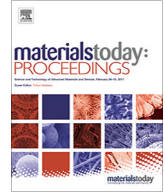




Contents lists available at ScienceDirect

Materials Today: Proceedings

journal homepage: www.elsevier.com/locate/matpr

Influence of basalt fiber on the behavior of beam - column joint under cyclic loading

G. Dineshkumar ^{a,*}, T. Palanisamy ^b

^a Department of Civil Engineering, Vaagdevi College of Engineering, Warangal 506005, Telangana, India

^b Department of Civil Engineering, National Institute of Technology Karnataka, Surathkal 575025, India

ARTICLE INFO

Article history:

Available online xxxx

Keywords:

Beam - Column Joints

Basalt fiber

Ductility

Stiffness

Energy absorption capacity

ABSTRACT

Beam-column joints are immensely complicated areas of reinforced concrete constructions. The strengthening of such components can have a significant impact on the earthquake resistant constructions because the rapid collapse of a building could occur if these beam-column joints fail. Recently, designing of reinforced concrete beam-column joints to resist earthquake load becomes more important using ductile design and high strength material. The fibers addition in a concrete directs to an improvement in cracking resistant, ductility, deformation and energy absorption capacity. However, there are currently many distinct types of fibres with various materials and geometric features are used in fiber reinforced concrete to improve the above said properties. The use of basalt fibre, an alternative material made from natural sources that comes from volcanic rock, is the main topic of this essay. The beam-column junction was used to assess the structural behaviour parameters for basalt fibre reinforced concrete, including load-deflection behaviour, ductility, stiffness value, energy absorption capacity, and energy index. From this work, it shows that the natural based basalt fiber shows excellent structural behavior when compared to control concrete. Basalt Fiber Reinforced Concrete (BFRC) has the potential for widespread application in the construction of concrete structures as well as in earthquake-prone regions.

Copyright © 2023 Elsevier Ltd. All rights reserved.

Selection and peer-review under responsibility of the scientific committee of the Advances in Construction Materials and Management.

1. Introduction

High energy absorbing materials that will reduce the risks are constantly required for constructions that are vulnerable to seismic loads [3,8]. Although fibres have a negligible impact on pre-cracking behaviour, their effectiveness is seen once the fragile concrete matrix has fractured [4,13]. Fibers that span cracks during the post-cracking stage significantly increase the composite's ductility and energy absorption capacity [6,23]. Many research initiatives are in the recent and earlier period have emphasis on utilizing steel fibres to improve the structural performance under seismic loads [5,12]. Even a slight improvement in the material's characteristics, given how much concrete is used now, will have a big technological and economical impact [1,15]. Fibers enhance the joint dimensional stability and integrity [19,24]. "The load carrying capacity of the beam column joint increased as the fibre content increased [2,22]. The dynamic damage is controlled by fiber reinforcement

under repeated impact [9,25]. This paper highlights the contribution of usage of natural based fiber will increase the structural behavior of member and also longevity of structures when compared to synthetic fibers used in concrete.

1.1. Basalt fiber

Basalts are igneous rocks with finer particles and a dark coloured. The lava flows quickly cool and harden, resulting in basalt rock [7,6]. There are certain intrusive basalts, which have cooled inside the Earth's interior, despite the fact that the majority of basalts are extrusive rocks that cooled at the Earth's crust [11,20,27]. Basalt rock is quickly drawn into a continuous fibre after melting at a high temperature (1450 °C). It is commonly known as Basalt roving or Continuous filament fiber [10,17]. If this continuous length is chopped into various lengths, it is said as Basalt Chopped strands Fiber (BCF) shown in Fig. 1. It might be brown, gold, or grey in colour. A type of inorganic fibre is basalt fibre [16,21]. It is very strong, has great fiber/resin adhesion, and is simple to manufacture using standard methods [14,18].

* Corresponding author.

E-mail address: gdkcivil@gmail.com (G. Dineshkumar).

<https://doi.org/10.1016/j.matpr.2023.04.232>

2214-7853/Copyright © 2023 Elsevier Ltd. All rights reserved.

Selection and peer-review under responsibility of the scientific committee of the Advances in Construction Materials and Management.



Fig. 1. Basalt fiber.

2. Materials and methods

2.1. Materials

2.1.1. Cement

In accordance with IS: 12269–1987, ‘Ordinary Portland Cement’ of grade 53 was utilised. The cement has a 3.15 specific gravity. The method outlined in Indian Standards IS: 4031–1988 was used to test the cement.

2.1.2. Fine Aggregate

Sand that retained on a 600 sieve after passing through a 4.75 mm screen was utilised as fine aggregate in tests conducted in accordance with IS: 2386 – 1963. Sand used has a fineness modulus 2.96 and a specific gravity 2.70. River sand complies with IS: 383–1970 grading zone III.

2.1.3. Coarse Aggregate

The coarse aggregates used were crushed blue granite with “average and cubic” shaped particles. According to IS: 2386–1963, the coarse aggregates were tested. In accordance with IS: 383–1970, coarse aggregate with a 20 mm size and specific gravity 2.70 was employed.

2.1.4. Water

The laboratory’s potable tap water, which complies with IS: 456–2000, was used to mix and cure the specimens.

2.1.5. Basalt fiber

The natural based Basalt chopped strands fiber was used. Basalt chopped strands fiber which was purchased from Kamenny Vek industries, Russia used for this work. Table 1 displays the specifications of basalt fibre as provided by the manufacturer.

2.1.6. Superplasticizer

In accordance with ‘IS 9103–1999, BS: 5075 part 3, and ASTM C-494’, superplasticizer based on sulphonated naphthalene polymers has been used.

Table 1
Basalt Fiber Specification.

Property	Values
Diameter	0.016 mm
Cut Length	12.mm
Aspect Ratio	794
Tensile Strength	4150 Mpa

2.2. Mix proportions

The mix were designed by using IS 10262–2009 method. Table 2 details the proportions of the mix used.

In this work, percentage of addition of Basalt fiber in concrete by weight was 0%, 0.05%, 0.1%, 0.15%, 0.20%, 0.25%, 0.30%, 0.35%, 0.40%, 0.45% and 0.50% and it is indicated as “B₀, B₁, B₂, B₃, B₄, B₅, B₆, B₇, B₈ B₉ & B₁₀” respectively.

2.3. Casting of specimen

2.3.1. Casting of cube specimens for compressive strength

In order to evaluate the compressive strengths of the control mix and basalt fibre reinforced concrete (BFRC), as well as to identify the proper percentage of basalt fibre addition to the concrete, a cube size 150 mm X 150 mm X 150 mm was prepared. For three sets of specimens with various fibre contents in concrete, moulds were cast. Three equal layers of freshly mixed concrete were poured into steel moulds, and each layer was gently crushed. They were cured in water for 28 days after being removed from the mould. The concreting of cubes was shown in Fig. 2.

2.3.2. Casting of beam – Column joint specimen for structural behaviour evaluation

For this investigation the exterior beam-column joint were preferred. One-fourth scale beam column joint was cast. The beam-column joint mould were fabricated by the plywood sheets in column size 110 mm × 200 mm × 785 mm and beam size 110 mm × 185 mm × 610 mm. Limit state method of design using IS 456:2000 was adopted for the design and detailed as per IS 13920:1993 codal provision. The detailing and casting of beam - column joint is shown in Figs. 3 & 4.

2.4. Testing Methodology:

2.4.1. Compressive strength evaluation

The key objective of determining the compressive strength of the concrete was to determine the optimal percentage of fibre addition. Fig. 5 depicts the results of cube specimens tested for various ages. Every specimen was examined in a saturated, dry environment. In each of the mixtures, three identical samples were evaluated.

2.4.2. Experimental test setup for beam - column joint specimen

The specimens of beam-column joints were evaluated in a 100 T loading frame. The experimental test arrangements was shown in Fig. 6.

In beam-column joint test setup, the axial load of 0.1f_{ck} applied on the top of column and cyclic load was applied at a distance of 100 mm from the beam end. The specimen placed in vertical position and load is applied on beam in downward and upward direction. Hydraulic jack were used for applying load at the end of the beam. A screw jack was used to apply the axial load on the column. For cyclic loading, observations were taken at load interval of 5 kN up to one load cycle of 10 kN in the each load cycle in both forward and reverse cycle loading simultaneously. The dial gauge was used to measure the deflection at opposite to the loading position. At each load cycle the load, deflection and crack pattern were recorded.

Table 2
Material requirement for 1 m³ of concrete (Kg/m³).

Grade	Cement	FA	CA	Water
M ₃₀	426	838	1105	136



Fig. 2. Concreting of Cubes.



Fig. 5. Test setup of Cube Compressive Strength.

at 7, 14, 28, and 56 days, as illustrated in Fig. 7. The maximum compressive strength was obtained in B5 mix with addition of 0.25% of fiber due to optimum dispersion of fiber content. The addition of fiber content above 0.30% in concrete mix the compressive strength falls down due to over dispersion of fiber in concrete. When the mechanical properties of basalt fibre reinforced concrete were evaluated, the B5 specimen with 0.25% basalt fibre showed the highest strength when compared to all other concrete combinations.

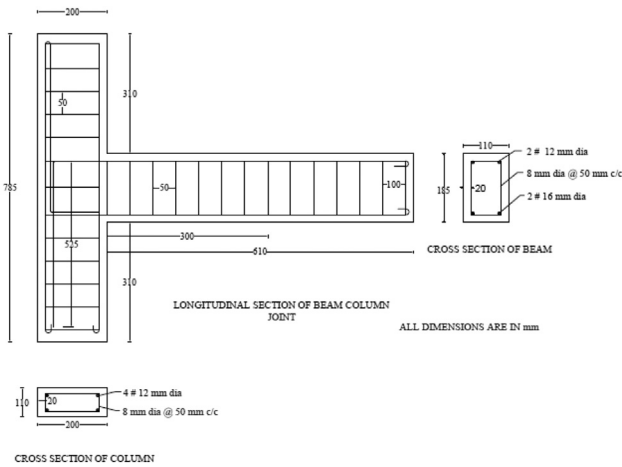


Fig. 3. Reinforcement Detailing of Beam - Column Joint specimen.



Fig. 4. Casting of Beam - Column Joint Specimen.

3. Results and discussion

3.1. Compressive strength of cube specimens

All plain concrete and basalt fibre reinforced concrete (BFRC) cubes were tested to determine compressive strength of concrete

3.2. Test results of beam – Column joint specimen

“For the study of structural behavior of beam - column joint, mixes such as B2, B4, B5, B6 and B10 were randomly selected with control specimen C0”.

3.2.1. Crack Development:

The first crack was observed in control specimen C0 at a load level of 15 kN. The first fracture was created at loads of 15 kN, 16 kN, 22 kN, 18 kN, and 15 kN for specimens B2, B4, B5, B6, and B10, with basalt fibre additions of 0.10%, 0.20%, 0.25%, 0.30%, and 0.50% by volume of concrete, respectively. Cracks were observed on some of the beam as the load level was raised. The hair line cracks were developed initially when the load level increasing there is a development of cracks till the ultimate load was obtained. Fig. 8 depicts the crack pattern of various beam column junction specimens.

3.2.2. Load deflection behavior

The load deflection behavior for the Beam Column joint specimen C0, B2,B4, B5, B6 and B10 are shown in Figs. 9 to 14. An increase in the fiber dosage level of basalt fiber increases the maximum load carrying capacity and deflection. The ultimate load carrying capacity of 32 kN, 35 kN, 40 kN, 35 kN and 30 kN are shown for the specimen B2, B4, B5, B6 and B10, respectively. For control specimen C0, the first crack was witnessed at the bottom of the beam at a load of 15 kN and ultimate load of 30 kN with a deflection of 8.26 mm and 7.54 mm in forward and reverse load cycle were noted. At load level of 15 kN, the crack was initially originated for the beam column joint specimen B2 and the specimen gradually tends to carry load, when the load level reaches 32 kN the ultimate load were reached and corresponding deflection recorded as 8.8 mm and 9.17 mm in forward and reverse load cycle. For the specimen B4, the first crack was witnessed on the beam at a load of 16 kN and ultimate load at 35 kN with a deflection of 8.36 mm and 9.21 mm in forward and reverse load cycle was noted. The first cracking load was observed as 22 kN and the ultimate load of 40 kN was recorded for B5 specimen and respective deflection is measured as 8.98 mm and 9.01 mm in forward



Fig. 6. Experimental Test Setup of Beam-Column Joint Specimen.

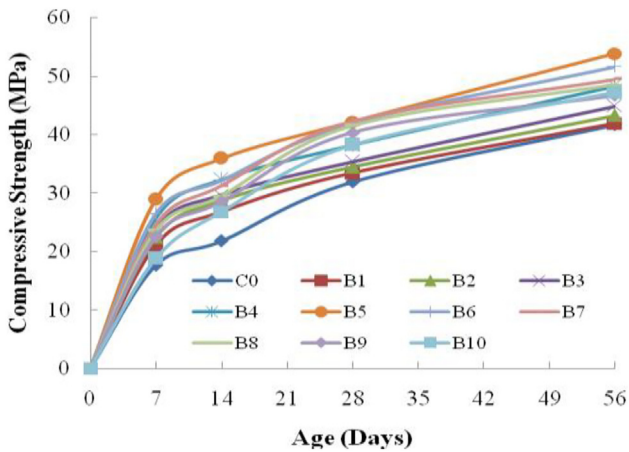


Fig. 7. Cube Compressive Strength of Control and Basalt Fiber Reinforced Concrete at the age of 7, 14, 28 and 56 Days.

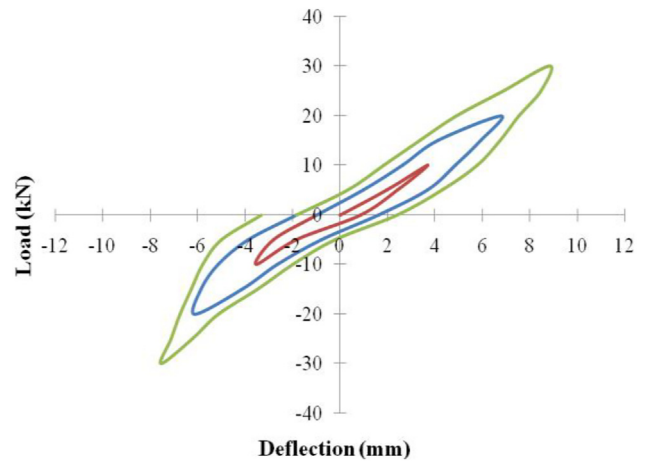


Fig. 9. Load - Deflection Curve for C0 Specimen.



Fig. 8. Crack Pattern of Control and Basalt Fiber Reinforced Concrete Beam-Column Joint Specimens.

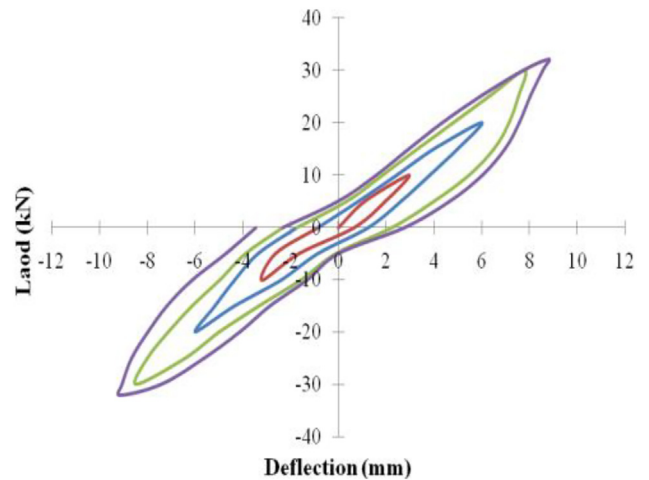


Fig. 10. Load - Deflection Curve for B2 Specimen.

and reverse load cycle. The specimen B6 withstands for the load of 35 kN its deflection is observed as 7.94 mm and 8.12 mm in forward and reverse load cycle, respectively. For the specimen B10, the first crack was witnessed at the bottom of the beam at a load of 15 kN and ultimate load at 30 kN with a deflection of 7.87 mm and 8.12 mm in forward and reverse load cycle.

3.2.3. Cumulative energy absorption capacity

“The energy absorption capacities were calculated as the area under the loops from the load deflection curve and the increasing energy absorption capacity was determined by the adding the

energy absorption capacity of the joint during each cycle considered and values are presented in the Figs. 15 and 16”. The cumulative energy absorption for forward cycle is about 116.73 kN mm and for the reverse cycle is 105.9 kN mm for control specimen C0. For the addition of fiber by 0.10% basalt fiber shows the cumulative energy absorption about 195.25 kN mm for forward cycle and for the reverse cycle it was about 186.28 kN mm. The specimen

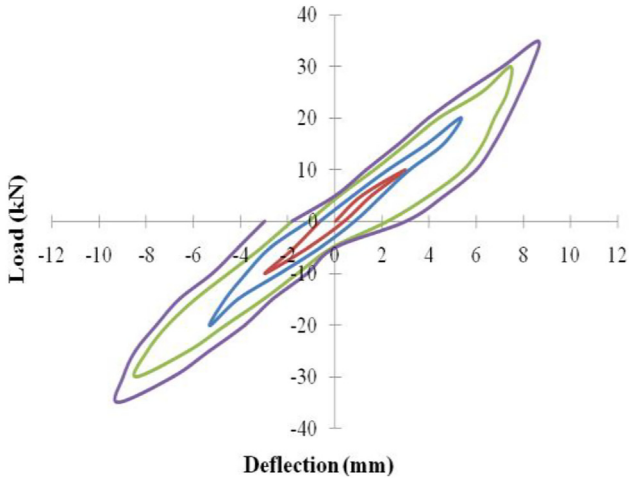


Fig. 11. Load - Deflection Curve for B4 Specimen.

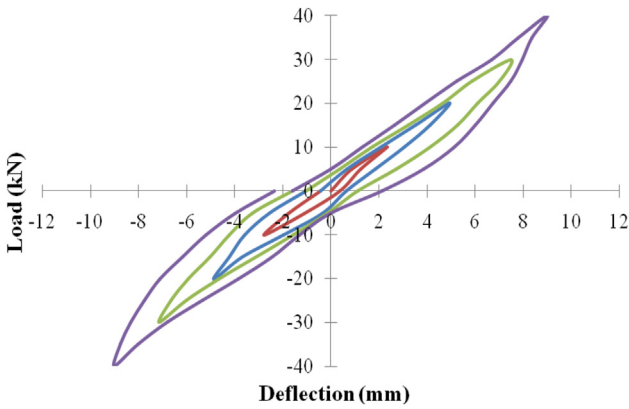


Fig. 12. Load - Deflection Curve for B5 Specimen.

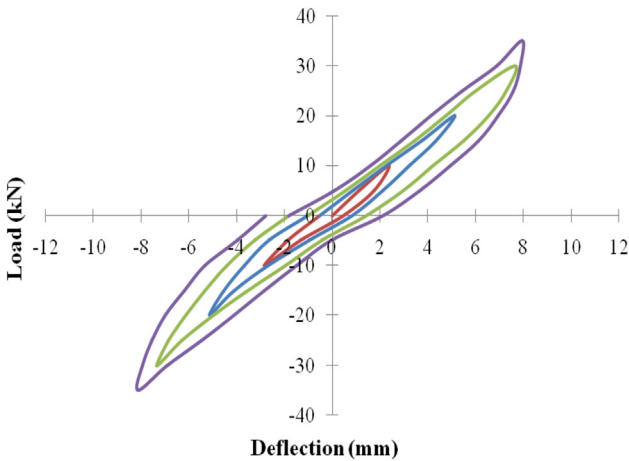


Fig. 13. Load - Deflection Curve for B6 Specimen.

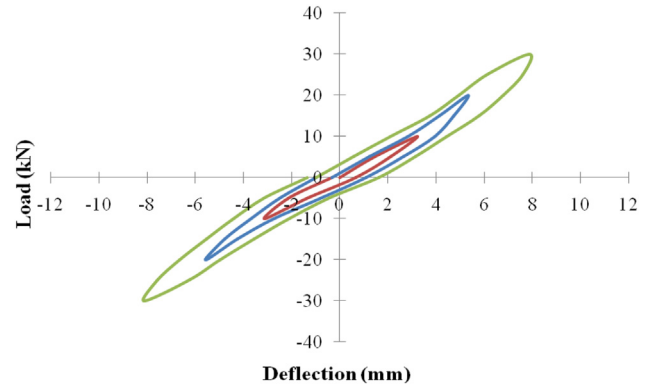


Fig. 14. Load - Deflection Curve for B10 Specimen.

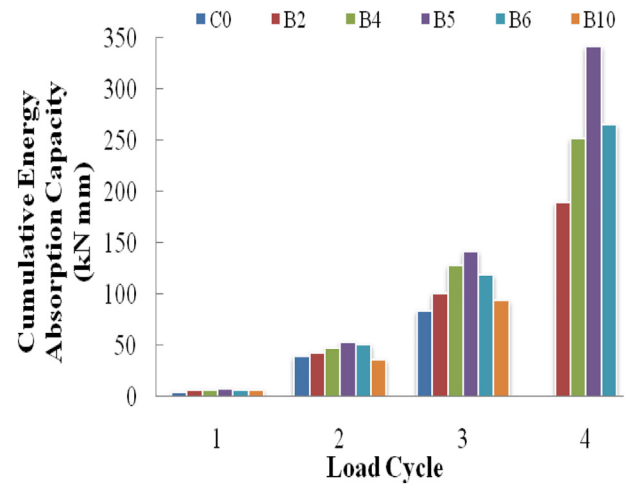


Fig. 15. Energy Absorption Capacity of Control and BFRC Beam - Column Joint (For Forward Load Cycle).

B4 with the fiber addition of 0.20% of basalt fiber shows the energy absorption about 228.21 kN mm in forward cycle and in the reverse cycle is 239.80 kN mm. The cumulative energy absorption capacity is observed as 248.35 kN mm for forward cycle and 301.43 kN mm for reverse cycle in B5 specimen with the basalt fiber addition of 0.40% by volume of concrete. The energy absorption capacity slightly decreases down for B6 and B10 specimen when

compared to the control specimen C0. The energy absorption capacity was obtained as 190.87 kN mm and 83.65 kN mm for forward cycle whereas for reverse cycle it was 202.74 kN mm and 73.15 kN mm. The specimen B5 with 0.25% of basalt fiber shows the maximum energy absorption capacity compared to all other mixtures

3.2.4. Ductility behaviour

“Ductility of a structure is its ability to undergo deformation beyond the initial yield deformation, while still sustaining load. In this investigation ductility factor is defined as the ratio of maximum deflection to the yield deflection”. Cumulative ductility behavior for BFRC beam-column joint is shown in Figs. 17 and 18. Cumulative ductility behavior for BFRC beam-column joint is shown in Figures 6.26 and 6.27. The ductility value for the control specimen is found as 4.47 in forward cycle and 4.15 in reverse cycle loading, respectively. For the fiber addition of 0.10% basalt fiber shows the ductility value of 6.3 and 4.3 was obtained on the B2 mix for forward and reverse cyclic loading, respectively, by the fiber addition of 0.20% of basalt fiber by volume concrete it obtains ductility value of 6.46 in forward cycle and 6.31 in reverse cycle. The addition of 0.25% basalt fiber B5 specimen increases the ductility value of 8.14 in forward cycle and 7.46 in reverse cycle. For B6 mix with 0.30% basalt fiber, the ductility value is marginally same as control mix. For B10 specimen with 0.50% basalt fiber addition decreases the ductility value when compared

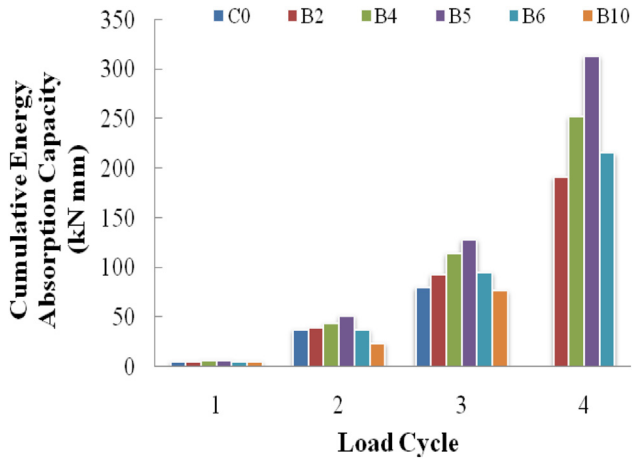


Fig. 16. Energy Absorption Capacity of Control and BFRC Beam - Column Joint (For Reverse Load Cycle).

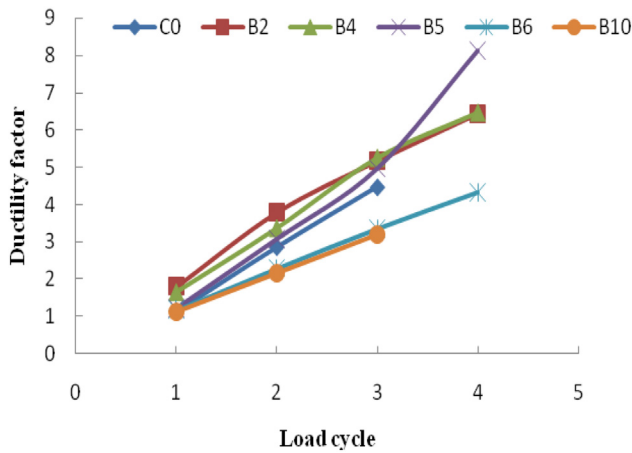


Fig. 17. Ductility Factor of Control and BFRC Beam - Column Joint.

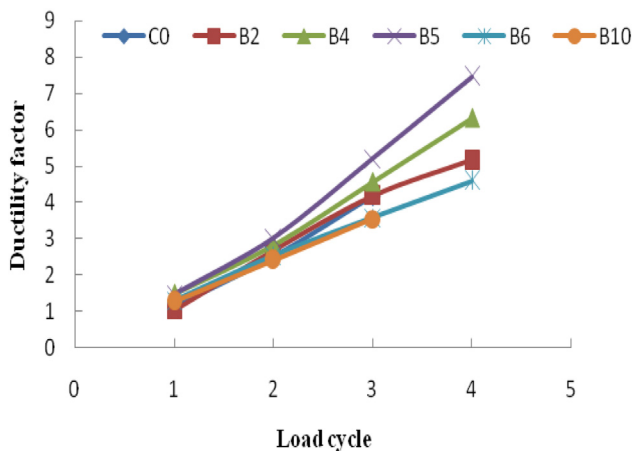


Fig. 18. Ductility Factor of Control and BFRC Beam - Column.

to control mix due to over dispersion of the fiber. The addition of 0.25% basalt fiber B5 specimen increases the ductility value.

3.2.5. Stiffness

“Stiffness is defined as the load required to causing unit deflection of the beam-column joint”. Figs. 19-20 show the stiffness for

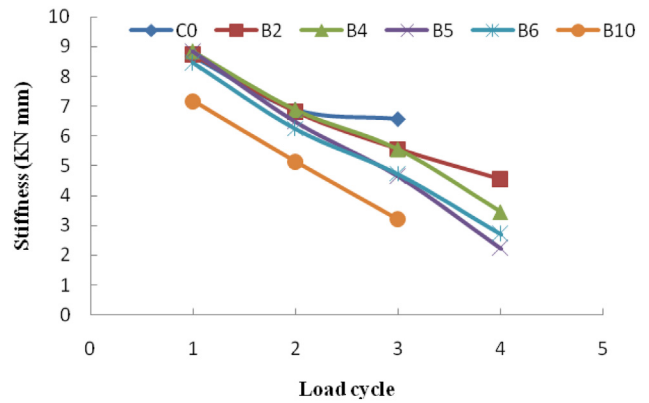


Fig. 19. Stiffness value of Control and BFRC Beam- Column Joint (For Forward Load Cycle).

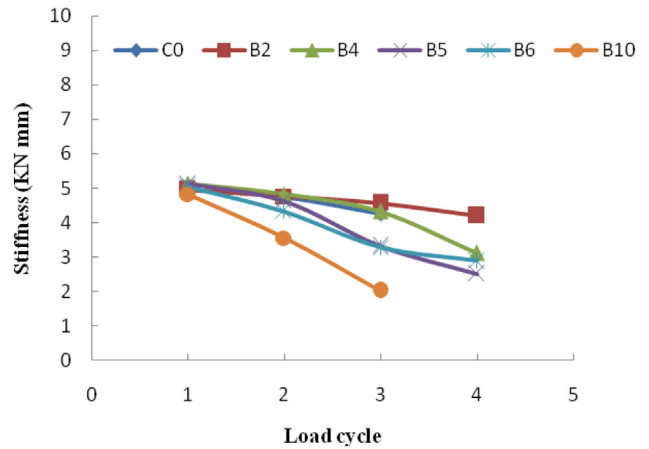


Fig. 20. Stiffness value of Control and BFRC Beam- Column Joint (For Reverse Load Cycle).

control specimen and the BFRC specimen. The stiffness value for the C0 mix at ultimate load is noted as 6.57 kN/mm for forward cycle and 4.26 kN/mm for reverse cycle. Whereas for the B2 mix the stiffness is found as 3.55 kN/mm for forward cycle and 2.11 kN/mm for reverse cycle in the addition of 0.10% Basalt Fiber by volume of concrete. By the addition of 0.20% of Basalt fiber gives the stiffness of 2.44 kN/mm and 1.77 kN/mm for forward and reverse cycle load, respectively, at an ultimate load level of 35 kN. There is stiffness degradation in the increase of load level to the specimen. For the ultimate load level of 40 kN the stiffness value showed as 1.23 kN/mm and 1.5 kN/mm for forward and reverse cycle at the B5 mix with the addition of 0.25% of basalt fiber by the volume of the concrete. Where B6 and B10 mix the stiffness value shows decrease on the ultimate load level. Stiffness degradation was noted when the load level increases. It is noted that, there is stiffness degradation in the increase of load level to the specimen.

4. Conclusions

By the experimental investigation, it was noted that B5 specimen in Basalt Fiber Reinforced Concrete shown the better performance characteristics compared to all other mixtures. The first crack load of B5 specimen with 0.25% of basalt fiber shows the 1.46 times more than of control specimen C0. The addition of

0.25% basalt fiber in concrete develops load carrying capacity about 1.33 times, compared control specimen C0. The cumulative energy absorption capacity for Basalt fiber reinforced concrete specimen B5 shows 2.22 times more than the control specimen in forward cycle and 2.80 times in reverse cycle at ultimate load level with 0.25% of fiber addition by volume of concrete. The ductility of B5 specimen with 0.25% basalt fiber shows the ductility value increases about 1.82 and 1.79 times in forward cycle and reverse cycle at ultimate load level when compared to control specimen C0. The stiffness value of Basalt Fiber Reinforced Concrete beam column joint shows the stiffness degradation when the load level increases. By the comparison of results, it is derived that the natural based basalt fiber has properties more than that of controlled concrete, which is due to better crack bridging mechanism and energy absorption capacity. Due to its overwhelming properties, the basalt fiber may be used in the earthquake prone areas to prevent the damage in the structures and increase the longevity of the structures. The addition of 0.25% basalt fiber by volume of concrete shows noticeable development in strength characteristics and structural behavior when compared to the control concrete.

CRedit authorship contribution statement

G. Dineshkumar: Methodology, Validation, Investigation, Writing – original draft. **T. Palanisamy:** Conceptualization, Resources, Supervision.

Data availability

Data will be made available on request.

Declaration of Competing Interest

The authors declare that they have no known competing financial interests or personal relationships that could have appeared to influence the work reported in this paper.

References

- [1] F.F. Wafa, Properties and applications of fiber reinforced concrete, JKAU: Eng. Sci. 2 (1990) 49–63.
- [2] N. Ganesan, P.V. Indira, R. Abraham, Steel fiber reinforced high performance concrete beam–column joints subjected to cyclic loading, ISET J. Earthquake Technol. 44 (3–4) (2007) 445–456.
- [3] N. Sudharsan, S. Praburanganathan, Y.B.S. Reddy, P. Pavan Kumar, Interaction of anthracite coal ash and Archis hypogaea shell ash on an innovative brick: an experimental and simulation study, Coal Preparation (2022), <https://doi.org/10.1080/19392699.2022.2089127>.
- [4] J. Gustavo, P. Montesinos, High- Performance fiber-reinforced cement composites: an alternative for seismic design of structures, ACI Struct. Journal 102 (5) (2005) 668–675.
- [5] M. Jamal Shannag, G. Abu-Farsakh, N. Dyya, Modeling the cyclic response of fiber Reinforced concrete joints, Eng. Struct. 29 (2007) 2960–2967.
- [6] J. Sim, C. Park, D.Y. Moon, Characteristics of basalt fiber as a strengthening material for concrete structures, Compos. Part B 36 (2005) 504–512.
- [7] S. Praburanganathan, N. Sudharsan, Y. Bharath Simha Reddy, C. Naga Dheeraj Kumar Reddy, L. Natrayan, P. Paramasivam, Force-Deformation study on glass fiber reinforced concrete slab incorporating waste paper, Adv. Civ. Eng. 2022 (2022), <https://doi.org/10.1155/2022/5343128>.
- [8] M. Palmieri, G. Plizzari, S. Pampanin, J. Mackechnie, Experimental investigation on the seismic behavior of SFRC columns under biaxial bending, Concrete Repair, Rehabilitation and Retrofitting II (2009) 1163–1171.
- [9] V. Ramakrishnan, N.S. Tolmare, V.B. Brik, Performance evaluation of 3-D basalt fiber reinforced concrete & basalt rod reinforced concrete, Final Report for Highway IDEA Project 45 (1998) 1–20.
- [10] N. Sudharsan, K. Sivalingam, Potential utilization of waste material for sustainable development in construction industry, Int. J. Recent Technol. Eng. 8 (3) (2019) 3435–3438.
- [11] L. Jianzhong, S. Wei, Dynamic mechanical behavior of ultra-high performance fiber reinforced concretes, J. Wuhan Univ. Technol.-Mater. Sci. Ed. (2008) 938–945.
- [12] V. Lopresto, C. Leone, I. De Iorio, Mechanical characterisation of basalt fiber reinforced plastic, Compos., Part B 42 (2011) 717–723.
- [13] M. Nehdi, A. Said, Performance of RC frames with hybrid reinforcement under reversed cyclic loading, Mater. Struct. 38 (2005) 627–637.
- [14] S.H. Chao, A.E. Naaman, G.J. Parra-Montesinos, Bond behavior of reinforcing bars in tensile strain-hardening fiber-reinforced cement composites, ACI Struct. J. 106–S84 (2009) 897–906.
- [15] S. Praburanganathan, S. Chithra, N. Divyah, N. Sudharsan, S.R. Yeddula Bharath, S. Vigneshwaran, Value-added waste substitution using slag and rubber aggregates in the sustainable and eco-friendly compressed brick production, Revista De La Construcción J. Construct. 21 (1) (2022) 5–20, <https://doi.org/10.7764/RDLC.21.1.5>.
- [16] P. Rajaram, A. Murugesan, G. Thirugnanam, Experimental study on behavior of interior RC beam column joints subjected to cyclic loading, Int. J. Appl. Eng. Res. 1 (1) (2010) 49–59.
- [17] N. Sudharsan, T. Palanisamy, S.C. Yaragal, Environmental sustainability of waste glass as a valuable construction material - A critical review, Ecol. Environ. Conservation 24 (2018) S331–S338.
- [18] M. Sivaraja, N. Velmani, M.S. Pillai, Study on durability of natural fiber concrete composites using mechanical strength and microstructural properties, Bull. Mater. Sci 33 (6) (2010) 719–729.
- [19] G. Sheldon, Forming Fibers from Basalt Rock, Platinum Metals Rev. 21 (1) (1977) 18–24.
- [20] A. Shende, A.M. Pande, Comparative study on Steel fiber reinforced Cum control concrete under flexural and deflection, Int. J. Appl. Eng. Res. 1 (4) (2011) 942–950.
- [21] T. Sen, H.N. Jagannatha Reddy, Application of sisal, bamboo, coir and jute natural composites in structural upgradation, Int. J. Innovation Manage. Technol. 2 (3) (2011) 186–191.
- [22] N. Sudharsan, B.C.J. Grant, Comparison of static response of laced reinforced concrete beams with conventional reinforced concrete beams by numerical investigations, Int. J. Civ. Eng. Technol. 9 (8) (2018) 700–704.
- [23] B. Vladimir, Brik, Advanced concept concrete Using Basalt Fiber/BF composite Rebar Reinforcement, Final Report for Highway-IDEA Project 86 (2003) 1–71.
- [24] N. Sudharsan, S. Saravananesh, Feasibility studies on waste glass powder, Int. J. Innovative Technol. Exploring Eng. 8 (8) (2019) 1644–1647.
- [25] T. Czigany, J. Vad, K. Poloskei, Basalt fiber as a reinforcement of polymer composites, Periodica Polytechnica Ser. Mech. Eng. 49 (1) (2005) 3–14.
- [27] T. Palanisamy, G. Dineshkumar, Performance evaluation and structural behaviour of Basalt Fiber Reinforced Concrete, Int. J. Earth Sci. Eng. 7 (2) (2014) 744–749.

Further reading

- [26] Y. Wang, S. Backer, C. Victor, Li, An experimental study of synthetic fibre reinforced cementitious composites, J. Mater. Sci. 22 (1987) 4281–4291.

See discussions, stats, and author profiles for this publication at: <https://www.researchgate.net/publication/375661753>

Customer Satisfaction towards Utilization of Services and Its Impact on Operational Performance of Bank of Baroda

Article · November 2023

CITATIONS

0

READS

568

1 author:



Venu Kesireddy

12 PUBLICATIONS 2 CITATIONS

SEE PROFILE

Customer Satisfaction towards Utilization of Services and Its Impact on Operational Performance of Bank of Baroda

1. Dr. Venu Kesireddy

Asst.Professor

Vaagdevi College of Engineering (Autonomous)

Bollikunta, Warangal.

Email id: kesireddyvenu@gmail.com

2. Dr. K. Prasad

Associate Professor, Head Department of MBA

Balaji Institute of Management Sciences,

Laknepally, Narsampet,

Warangal – District. (TS)

Mail ID: kushiniprasad7730@gmail.com

Abstract: The purpose of this study was to evaluate the quality of customer service provided by Bank of Baroda in Hyderabad. There is intense competition in consumer marketing companies and banks are not an exception. It is critical for service companies in general, and banks in particular, to focus on and effectively meet the needs of their customers. Customer satisfaction is a marketing term that refers to how well a company's products and services meet or exceed customer expectations. "The number of customers or percentage of total customers, whose reported experience with a firm, its products, or its services (ratings) exceeds specified satisfaction goals" is how customer satisfaction is defined. To measure the present Customer satisfaction level among the customers of the Bank of Baroda based on their region, the statistical tool chi square test was used. This study as well focuses on the three services of banks i.e., ATM services, mobile banking and internet banking to their customer satisfaction. This study is restricted to Hyderabad city only. The set of questionnaires were prepared and distributed to customers of the banks with Customer satisfaction levels with key determinants. The results of this analysis show that banks do indeed provide good services to their customers, and that they are satisfied with them. There are a few more service parameters that banks must follow in order to keep their customers.

Keywords: *Bank of Baroda, Customers, Services and Satisfaction levels*

1. Introduction

Banks are providing a client-based service in India and good customer service is the key to bank growth and stability. Banks need to work together to provide more efficient services that leverage technological capability and, at the same time, cost-effectiveness. The retention of customers is a critical factor for the banks. In the banking industry, customer service is a

key and broad concept. Banks are essentially service-oriented companies, with the majority of their activities involving service components. Although they sell banking and finance products, their products often have slight tangible product variation, which highlights the characteristics of the bank and thus facilitates the retention of customers. Banking sector reforms have provided significant improvement in the efficacy of services and the extensive utilization of technology in the banking sector. Customers can access a wide variety of utilities and therefore, it provides an excellent opportunity for the banks to provide efficient services and to retain customer's loyalty. An effort is made to cross-examine whether the customers from the three regions, i.e., Urban, Semi-urban and Rural display similar perceptions about availing of various utilities provided by Bank of Baroda.

2. Literature Review

Brahmbhatt, M. (2021), according to Parasuraman et al., bank customers' expectations are higher than their perceptions (1988). This disparity varies by banking sector. The dimensions of tangibility, assurance, empathy, reliability, responsiveness, and convenience are the explanatory variables for predicting customer satisfaction in Gujarat, according to factor analysis.

Kumar, T. S., &Vinothini, V. (2020), based on their findings, the banks are indeed providing good services to their customers, and the customers are satisfied. There are a few more service parameters that banks must follow in order to keep their customers.

Komulainen, H., &Saraniemi, S. (2019), by identifying customer experience and related value in a new mobile banking service, they demonstrate the importance of customer centricity in the mobile banking context. The study adds value to the process, the use situation, and the outcome, and it identifies temporality as influencing and connecting all of these factors. The study identifies a number of factors that help us understand what makes mobile banking services valuable to customers.

3. Objectives of the Study

1. To analyse the customers satisfaction levels towards utilization of services of Bank of Baroda
2. To give suitable suggestion to the customers and bank authorities.

4. Hypothesis of the Study

1. The three regions differ in using ATM services for cash withdrawals.
2. Customers from the three regions significantly differ in terms of usage of online banking services provided by Bank of Baroda.
3. The customers from the three regions are significantly different in terms of mobile banking services.

5. Research Methodology

Sample size:Total 300 customers are selected for the study from equal distribution in regions i.e., rural, semi-urban & urban.

Sample technique: Convenience sample technique was used to select the sample because of data collected from the customers according to their Convenience time.

Source of data: The study based on primary data. Through structure questionnaire data was collected from Bank of Baroda customers in Hyderabad region only.

Statistical tool: Chi square test was used to analyse the framed hypothesis to check whether the stated hypothesis are accepted or not.

6. Data Analysis

The satisfaction levels of Bank of Baroda customers towards their utilization of services i.e., ATM services, Mobile banking & Internet banking was analysed with the help of chi square test to check whether stated hypothesis are accept or not given below,

Table – 6.1 Satisfaction levels of the Customers towards utilities provided

Sl. No.	Region-wise classification of bank customers	Perception of the customers		Total
		Yes	No	
ATM services				
1	Urban	92	08	100
2	Semi-Urban	88	12	100
3	Rural	72	28	100
Chi-square Calculated value = 16.7 Tabular value = 5.99 Degrees of freedom=2 Results= Reject H ₀				
Online banking services				
1	Urban	68	32	100
2	Semi-Urban	54	46	100
3	Rural	24	76	100
Chi-square Calculated value = 40.2 Tabular value = 5.99 Degrees of freedom=2 Results= Reject H ₀				
Mobile banking/m-commerce				
1	Urban	64	36	100
2	Semi-urban	48	52	100
3	Rural	28	72	100
Chi-square Calculated value = 26.1 Tabular value = 5.99 Degrees of freedom=2 Results= Reject H ₀				

Source: Calculated from primary data

Table 6.1 shows the perception of bank customers towards utilities provided by Bank of Baroda. From the analysis of the results, it was observed that 92% of the urban customers, 88% of the Semi-urban and 72% of the rural customers have been using ATM services of Bank of Baroda for cash withdrawal. The comparison of results also shows that urban

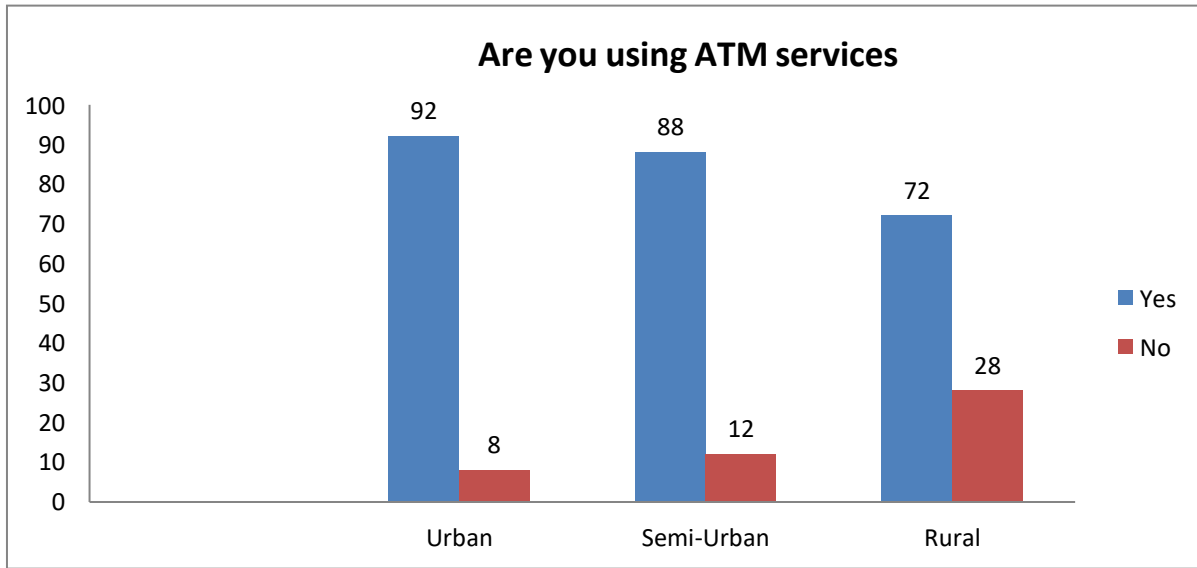
customers are far ahead of rural customers utilizing ATM services. The results of the Chi-square test reveal that the calculated value is above the value of the table, and therefore the null hypothesis is refused. It is concluded from the results that customers from the three regions differ in using ATM services for cash withdrawals.

Concerning Online banking services for online transfers, online purchases and online inquiry of deposits and withdrawal statuses, it is observed that 68% of the urban customers, 54% of the Semi-urban customers and 24% of the rural customers have opined that they are using the online banking services provided by Bank of Baroda. It shows that there is significantly less utilization of the online banking services of rural customers. Chi-calculated Square's value showing a considerably greater value of the table value indicates rejection of the null hypothesis. Therefore, it is proven that the customers from the three regions significantly differ in terms of usage of online banking services provided by Bank of Baroda. About mobile banking services, 64% of the urban customers, 48% of the Semi-urban customers and 28% of the rural customers have opined that they are using the services provided by Bank of Baroda.

The results prove that rural customers using mobile banking services are less in number. It might be due to the non-availability of a net facility in mobiles in rural areas and affordability to purchase Smartphone could have influenced them to not avail mobile banking services.

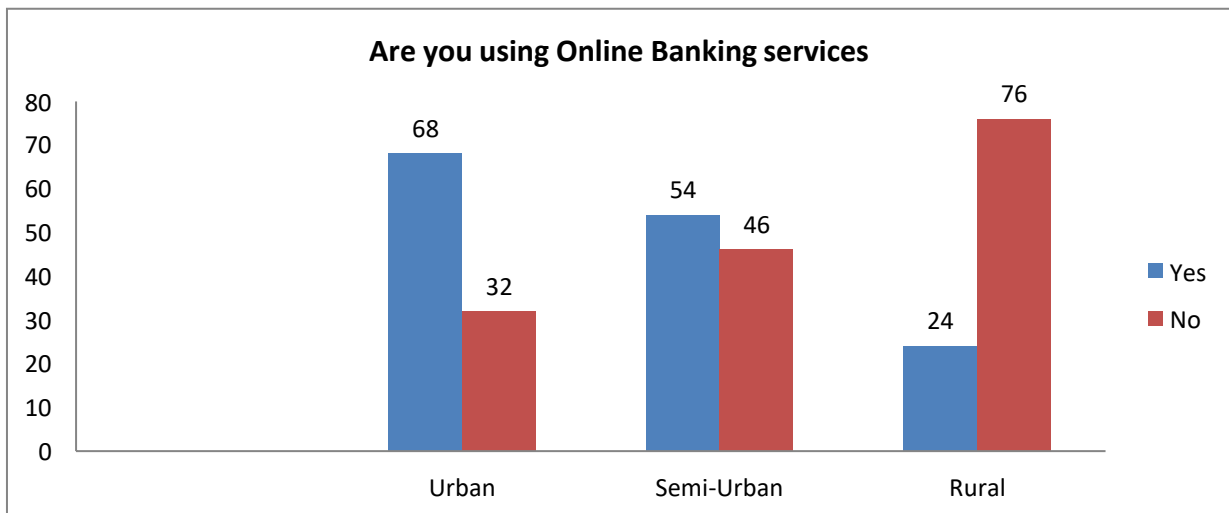
Further, the chi-square calculated values, i.e., 16.7, 40.2 26.1 respectively, are higher than the critical value, i.e., 5.99 at 2 degrees of freedom, hence it can be concluded that the customers from the three regions significantly differ when it comes to the use of ATM services, online banking & mobile banking services.

Graph -6.1 Satisfaction levels of the Customers towards ATM Services



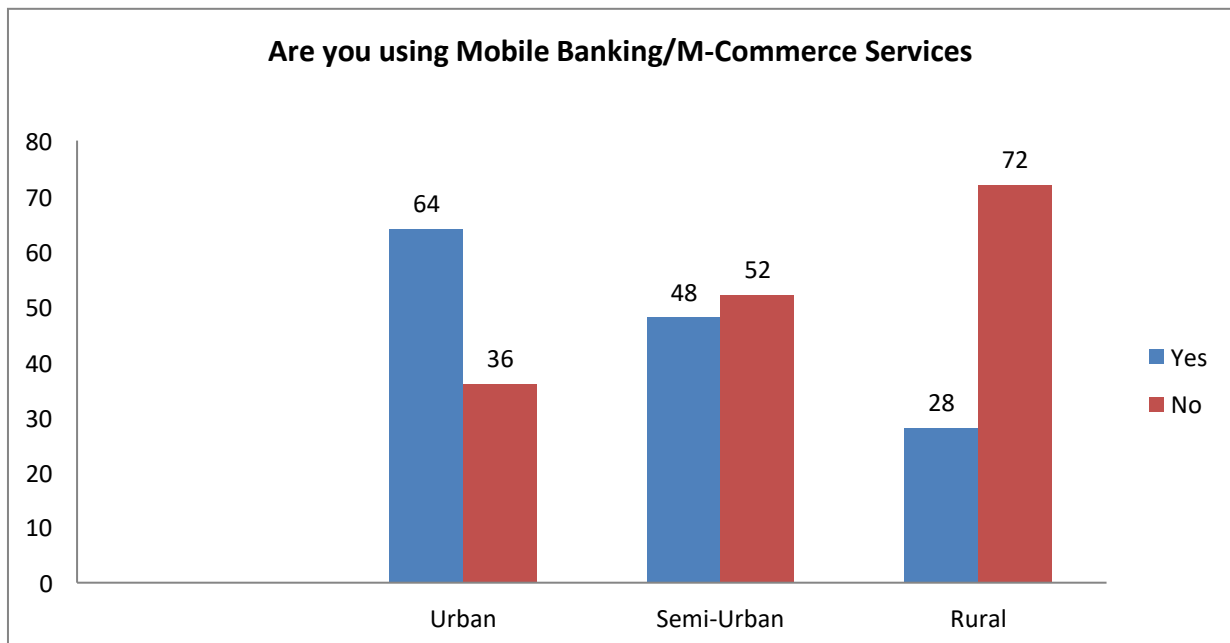
Source: Calculated from primary data

Graph -6.2 Satisfaction levels of the Customers towards Online Banking Services



Source: Calculated from primary data

Graph -6.3 Satisfaction levels of the Customers towards Mobile Banking/M-Commerce Services



Source: Calculated from primary data

Graph 6.1, 6.2 & 6.3 shows the perception of bank customers towards utilities provided by Bank of Baroda. From the analysis of the results, it was observed that 92% of the urban customers, 88% of the Semi-urban and 72% of the rural customers have been using ATM services of Bank of Baroda for cash withdrawal. The comparison of results also shows that urban customers are far ahead of rural customers utilizing ATM services. From the table 6.1, the results of the Chi-square test reveal that the calculated value is above the value of the table, and therefore the null hypothesis is refused. It is concluded from the results that customers from the three regions differ in using ATM services for cash withdrawals.

Concerning Online banking services for online transfers, online purchases and online inquiry of deposits and withdrawal statuses, it is observed that 68% of the urban customers, 54% of the Semi-urban customers and 24% of the rural customers have opined that they are using the online banking services provided by Bank of Baroda. From the table 6.1, it shows that there is significantly less utilization of the online banking services of rural customers. Chi-calculated Square's value showing a considerably greater value of the table value, indicates rejection of the null hypothesis. Therefore, it is proven that the customers from the three regions significantly differ in terms of usage of online banking services provided by Bank of Baroda. About mobile banking services, 64% of the urban customers, 48% of the Semi-urban

customers and 28% of the rural customers have opined that they are using the services provided by Bank of Baroda.

From the table 6.1, the results prove that rural customers using mobile banking services are less in number. It might be due to the non-availability of a net facility in mobiles in rural areas and affordability to purchase Smartphone could have influenced them to not avail mobile banking services.

7. Conclusion

Overall, it can be concluded that urban customers are far ahead of Semi-urban and rural customers in terms of usage of various facilities. There is clear evidence that the rural customers of Bank of Baroda have not been availing of the utilities provided by Bank of Baroda. All stated hypothesis are saying that the customers from different regions are having different satisfaction levels. The Bank of Baroda should concentrate on the region wise to establish ATM services, mobile banking services in the rural areas are still not up to mark. So while in the usage of internet banking most of the customers are don't know how to use internet banking. Bank has to improve their services in all three regions effectively for customers, which improves operational performance of Bank such as collecting more deposits and offering more loan and advances to customers.

8. Suggestions

1. The bank authorities should establish ATM services according to the population wise in the different regional areas.
2. The authorities should bring changes in the mobile banking app like user friendly and customised options for services etc.
3. In the Internet banking the banks makes certain security on the usage of services in the third parties sites.
4. Bank customer's satisfaction levels are changing day to day usage of services, so banks should change according to the satisfaction levels.
5. Banks are providing several services to their customer's like investment services, and personalized banking services. Customers should utilize services from the banks to fulfill their future goals.

References

1. Brahmabhatt, M. (2021). A study on measuring customers' expectation and perception in private and public sector banks. IJ Journal Of Management, extracted from <http://journal.ijharkhand.edu.in/A-study-on-measuring-customers.html>
2. Kumar, T. S., & Vinothini, V. (2020). A Study on Customer Satisfaction towards Banking Services of IndusInd Bank in Vadalur Town. *Humanities*, 8(1), 149-162.
3. Komulainen, H. and Saraniemi, S. (2019), "Customer centricity in mobile banking: a customer experience perspective", *International Journal of Bank Marketing*, Vol. 37 No. 5, pp. 1082-1102. <https://doi.org/10.1108/IJBM-11-2017-0245>
4. Bank of Baroda. (n.d.-b). *Bank of Baroda, India's International Bank*. Retrieved July 23, 2021, from <https://www.bankofbaroda.in/>
5. *What Is Banking?* (n.d.). The Balance. Retrieved July 23, 2021, from <https://www.thebalance.com/what-is-banking-3305812>
6. *Introduction: What is banking and why is it important?: MoneyCounts: A Penn State Financial Literacy Series.* (n.d.). https://psu.instructure.com/courses/1806581/Pages/Introduction-What-Is-Banking-and-Why-Is-It-Important?Module_item_id=26004136. Retrieved July 23, 2021, from https://psu.instructure.com/courses/1806581/pages/introduction-what-is-banking-and-why-is-it-important?module_item_id=26004136
7. User, S. (n.d.). *TechnoFunc - Introduction to Banking: What is a Bank?* <https://www.technofunc.com/index.php/domain-knowledge/banking-domain/item/what-is-a-bank>. Retrieved July 23, 2021, from <https://www.technofunc.com/index.php/domain-knowledge/banking-domain/item/what-is-a-bank>

See discussions, stats, and author profiles for this publication at: <https://www.researchgate.net/publication/375661753>

Customer Satisfaction towards Utilization of Services and Its Impact on Operational Performance of Bank of Baroda

Article · November 2023

CITATIONS

0

READS

568

1 author:



Venu Kesireddy

12 PUBLICATIONS 2 CITATIONS

SEE PROFILE

Customer Satisfaction towards Utilization of Services and Its Impact on Operational Performance of Bank of Baroda

1. Dr. Venu Kesireddy

Asst.Professor

Vaagdevi College of Engineering (Autonomous)

Bollikunta, Warangal.

Email id: kesireddyvenu@gmail.com

2. Dr. K. Prasad

Associate Professor, Head Department of MBA

Balaji Institute of Management Sciences,

Laknepally, Narsampet,

Warangal – District. (TS)

Mail ID: kushiniprasad7730@gmail.com

Abstract: The purpose of this study was to evaluate the quality of customer service provided by Bank of Baroda in Hyderabad. There is intense competition in consumer marketing companies and banks are not an exception. It is critical for service companies in general, and banks in particular, to focus on and effectively meet the needs of their customers. Customer satisfaction is a marketing term that refers to how well a company's products and services meet or exceed customer expectations. "The number of customers or percentage of total customers, whose reported experience with a firm, its products, or its services (ratings) exceeds specified satisfaction goals" is how customer satisfaction is defined. To measure the present Customer satisfaction level among the customers of the Bank of Baroda based on their region, the statistical tool chi square test was used. This study as well focuses on the three services of banks i.e., ATM services, mobile banking and internet banking to their customer satisfaction. This study is restricted to Hyderabad city only. The set of questionnaires were prepared and distributed to customers of the banks with Customer satisfaction levels with key determinants. The results of this analysis show that banks do indeed provide good services to their customers, and that they are satisfied with them. There are a few more service parameters that banks must follow in order to keep their customers.

Keywords: *Bank of Baroda, Customers, Services and Satisfaction levels*

1. Introduction

Banks are providing a client-based service in India and good customer service is the key to bank growth and stability. Banks need to work together to provide more efficient services that leverage technological capability and, at the same time, cost-effectiveness. The retention of customers is a critical factor for the banks. In the banking industry, customer service is a

key and broad concept. Banks are essentially service-oriented companies, with the majority of their activities involving service components. Although they sell banking and finance products, their products often have slight tangible product variation, which highlights the characteristics of the bank and thus facilitates the retention of customers. Banking sector reforms have provided significant improvement in the efficacy of services and the extensive utilization of technology in the banking sector. Customers can access a wide variety of utilities and therefore, it provides an excellent opportunity for the banks to provide efficient services and to retain customer's loyalty. An effort is made to cross-examine whether the customers from the three regions, i.e., Urban, Semi-urban and Rural display similar perceptions about availing of various utilities provided by Bank of Baroda.

2. Literature Review

Brahmbhatt, M. (2021), according to Parasuraman et al., bank customers' expectations are higher than their perceptions (1988). This disparity varies by banking sector. The dimensions of tangibility, assurance, empathy, reliability, responsiveness, and convenience are the explanatory variables for predicting customer satisfaction in Gujarat, according to factor analysis.

Kumar, T. S., &Vinothini, V. (2020), based on their findings, the banks are indeed providing good services to their customers, and the customers are satisfied. There are a few more service parameters that banks must follow in order to keep their customers.

Komulainen, H., &Saraniemi, S. (2019), by identifying customer experience and related value in a new mobile banking service, they demonstrate the importance of customer centricity in the mobile banking context. The study adds value to the process, the use situation, and the outcome, and it identifies temporality as influencing and connecting all of these factors. The study identifies a number of factors that help us understand what makes mobile banking services valuable to customers.

3. Objectives of the Study

1. To analyse the customers satisfaction levels towards utilization of services of Bank of Baroda
2. To give suitable suggestion to the customers and bank authorities.

4. Hypothesis of the Study

1. The three regions differ in using ATM services for cash withdrawals.
2. Customers from the three regions significantly differ in terms of usage of online banking services provided by Bank of Baroda.
3. The customers from the three regions are significantly different in terms of mobile banking services.

5. Research Methodology

Sample size:Total 300 customers are selected for the study from equal distribution in regions i.e., rural, semi-urban & urban.

Sample technique: Convenience sample technique was used to select the sample because of data collected from the customers according to their Convenience time.

Source of data: The study based on primary data. Through structure questionnaire data was collected from Bank of Baroda customers in Hyderabad region only.

Statistical tool: Chi square test was used to analyse the framed hypothesis to check whether the stated hypothesis are accepted or not.

6. Data Analysis

The satisfaction levels of Bank of Baroda customers towards their utilization of services i.e., ATM services, Mobile banking & Internet banking was analysed with the help of chi square test to check whether stated hypothesis are accept or not given below,

Table – 6.1 Satisfaction levels of the Customers towards utilities provided

Sl. No.	Region-wise classification of bank customers	Perception of the customers		Total
		Yes	No	
ATM services				
1	Urban	92	08	100
2	Semi-Urban	88	12	100
3	Rural	72	28	100
Chi-square Calculated value = 16.7 Tabular value = 5.99 Degrees of freedom=2 Results= Reject H ₀				
Online banking services				
1	Urban	68	32	100
2	Semi-Urban	54	46	100
3	Rural	24	76	100
Chi-square Calculated value = 40.2 Tabular value = 5.99 Degrees of freedom=2 Results= Reject H ₀				
Mobile banking/m-commerce				
1	Urban	64	36	100
2	Semi-urban	48	52	100
3	Rural	28	72	100
Chi-square Calculated value = 26.1 Tabular value = 5.99 Degrees of freedom=2 Results= Reject H ₀				

Source: Calculated from primary data

Table 6.1 shows the perception of bank customers towards utilities provided by Bank of Baroda. From the analysis of the results, it was observed that 92% of the urban customers, 88% of the Semi-urban and 72% of the rural customers have been using ATM services of Bank of Baroda for cash withdrawal. The comparison of results also shows that urban

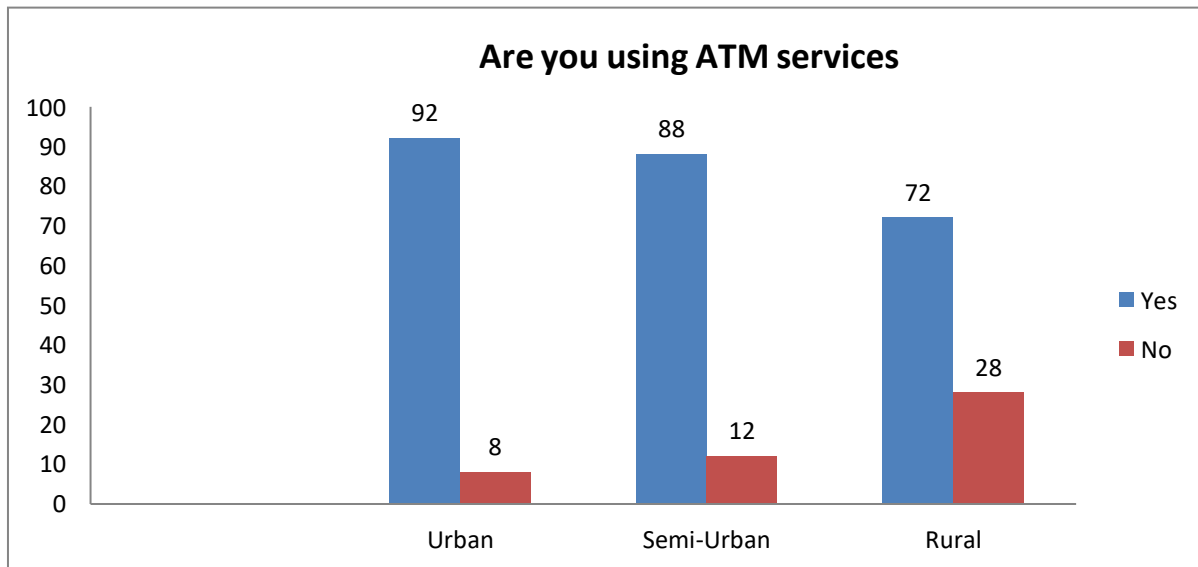
customers are far ahead of rural customers utilizing ATM services. The results of the Chi-square test reveal that the calculated value is above the value of the table, and therefore the null hypothesis is refused. It is concluded from the results that customers from the three regions differ in using ATM services for cash withdrawals.

Concerning Online banking services for online transfers, online purchases and online inquiry of deposits and withdrawal statuses, it is observed that 68% of the urban customers, 54% of the Semi-urban customers and 24% of the rural customers have opined that they are using the online banking services provided by Bank of Baroda. It shows that there is significantly less utilization of the online banking services of rural customers. Chi-calculated Square's value showing a considerably greater value of the table value indicates rejection of the null hypothesis. Therefore, it is proven that the customers from the three regions significantly differ in terms of usage of online banking services provided by Bank of Baroda. About mobile banking services, 64% of the urban customers, 48% of the Semi-urban customers and 28% of the rural customers have opined that they are using the services provided by Bank of Baroda.

The results prove that rural customers using mobile banking services are less in number. It might be due to the non-availability of a net facility in mobiles in rural areas and affordability to purchase Smartphone could have influenced them to not avail mobile banking services.

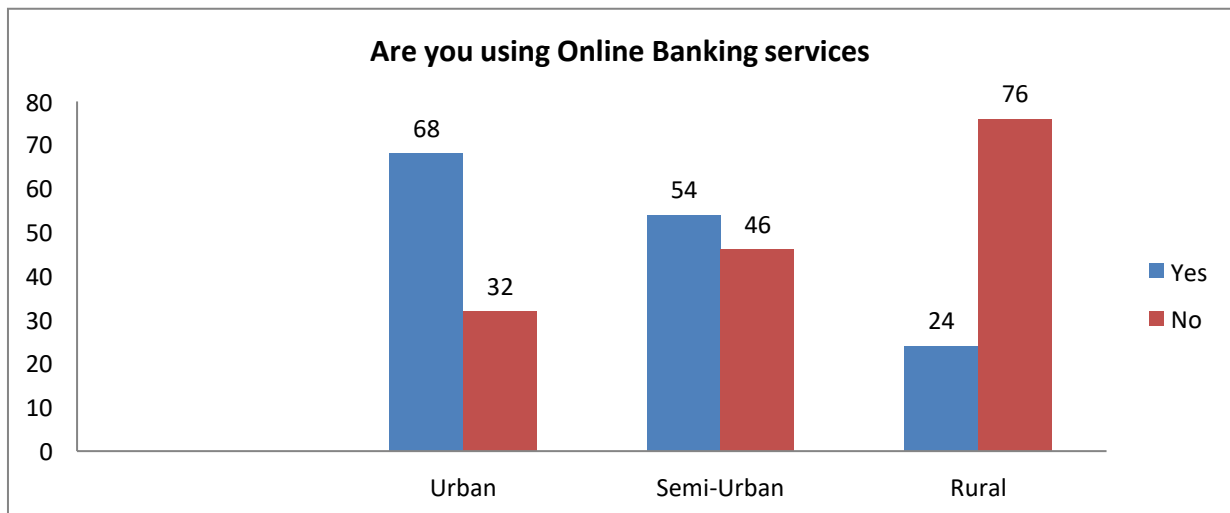
Further, the chi-square calculated values, i.e., 16.7, 40.2 26.1 respectively, are higher than the critical value, i.e., 5.99 at 2 degrees of freedom, hence it can be concluded that the customers from the three regions significantly differ when it comes to the use of ATM services, online banking & mobile banking services.

Graph -6.1 Satisfaction levels of the Customers towards ATM Services



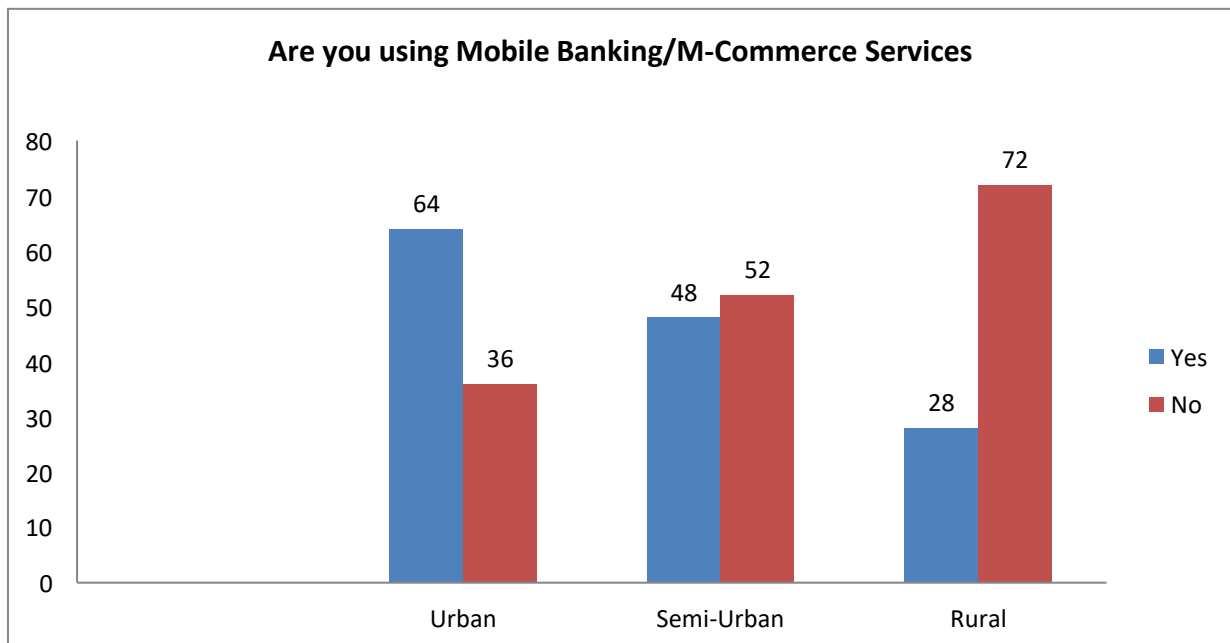
Source: Calculated from primary data

Graph -6.2 Satisfaction levels of the Customers towards Online Banking Services



Source: Calculated from primary data

Graph -6.3 Satisfaction levels of the Customers towards Mobile Banking/M-Commerce Services



Source: Calculated from primary data

Graph 6.1, 6.2 & 6.3 shows the perception of bank customers towards utilities provided by Bank of Baroda. From the analysis of the results, it was observed that 92% of the urban customers, 88% of the Semi-urban and 72% of the rural customers have been using ATM services of Bank of Baroda for cash withdrawal. The comparison of results also shows that urban customers are far ahead of rural customers utilizing ATM services. From the table 6.1, the results of the Chi-square test reveal that the calculated value is above the value of the table, and therefore the null hypothesis is refused. It is concluded from the results that customers from the three regions differ in using ATM services for cash withdrawals.

Concerning Online banking services for online transfers, online purchases and online inquiry of deposits and withdrawal statuses, it is observed that 68% of the urban customers, 54% of the Semi-urban customers and 24% of the rural customers have opined that they are using the online banking services provided by Bank of Baroda. From the table 6.1, it shows that there is significantly less utilization of the online banking services of rural customers. Chi-calculated Square's value showing a considerably greater value of the table value, indicates rejection of the null hypothesis. Therefore, it is proven that the customers from the three regions significantly differ in terms of usage of online banking services provided by Bank of Baroda. About mobile banking services, 64% of the urban customers, 48% of the Semi-urban

customers and 28% of the rural customers have opined that they are using the services provided by Bank of Baroda.

From the table 6.1, the results prove that rural customers using mobile banking services are less in number. It might be due to the non-availability of a net facility in mobiles in rural areas and affordability to purchase Smartphone could have influenced them to not avail mobile banking services.

7. Conclusion

Overall, it can be concluded that urban customers are far ahead of Semi-urban and rural customers in terms of usage of various facilities. There is clear evidence that the rural customers of Bank of Baroda have not been availing of the utilities provided by Bank of Baroda. All stated hypothesis are saying that the customers from different regions are having different satisfaction levels. The Bank of Baroda should concentrate on the region wise to establish ATM services, mobile banking services in the rural areas are still not up to mark. So while in the usage of internet banking most of the customers are don't know how to use internet banking. Bank has to improve their services in all three regions effectively for customers, which improves operational performance of Bank such as collecting more deposits and offering more loan and advances to customers.

8. Suggestions

1. The bank authorities should establish ATM services according to the population wise in the different regional areas.
2. The authorities should bring changes in the mobile banking app like user friendly and customised options for services etc.
3. In the Internet banking the banks makes certain security on the usage of services in the third parties sites.
4. Bank customer's satisfaction levels are changing day to day usage of services, so banks should change according to the satisfaction levels.
5. Banks are providing several services to their customer's like investment services, and personalized banking services. Customers should utilize services from the banks to fulfill their future goals.

References

1. Brahmabhatt, M. (2021). A study on measuring customers' expectation and perception in private and public sector banks. IJ Journal Of Management, extracted from <http://journal.ijharkhand.edu.in/A-study-on-measuring-customers.html>
2. Kumar, T. S., & Vinothini, V. (2020). A Study on Customer Satisfaction towards Banking Services of IndusInd Bank in Vadalur Town. *Humanities*, 8(1), 149-162.
3. Komulainen, H. and Saraniemi, S. (2019), "Customer centricity in mobile banking: a customer experience perspective", *International Journal of Bank Marketing*, Vol. 37 No. 5, pp. 1082-1102. <https://doi.org/10.1108/IJBM-11-2017-0245>
4. Bank of Baroda. (n.d.-b). *Bank of Baroda, India's International Bank*. Retrieved July 23, 2021, from <https://www.bankofbaroda.in/>
5. *What Is Banking?* (n.d.). The Balance. Retrieved July 23, 2021, from <https://www.thebalance.com/what-is-banking-3305812>
6. *Introduction: What is banking and why is it important?: MoneyCounts: A Penn State Financial Literacy Series.* (n.d.). https://psu.instructure.com/courses/1806581/Pages/Introduction-What-Is-Banking-and-Why-Is-It-Important?Module_item_id=26004136. Retrieved July 23, 2021, from https://psu.instructure.com/courses/1806581/pages/introduction-what-is-banking-and-why-is-it-important?module_item_id=26004136
7. User, S. (n.d.). *TechnoFunc - Introduction to Banking: What is a Bank?* <https://www.technofunc.com/index.php/domain-knowledge/banking-domain/item/what-is-a-bank>. Retrieved July 23, 2021, from <https://www.technofunc.com/index.php/domain-knowledge/banking-domain/item/what-is-a-bank>



Statistical Analysis on Post-Covid

¹ Dr. M. Srinivas, ² Martha Nuthana Priya

¹Professor, ²Student

¹Department of Mathematics,

¹Vaagdevi College of Engineering, Warangal, Telangana, India

Abstract: Most people's COVID-19 symptoms get better within a few weeks. Some patients experience long-term COVID-19 symptoms that can last for weeks or months. These symptoms vary widely. Some patients have few symptoms, while others have several. Symptoms can come and go, change over time, and range from mild to severe. This paper just focussed on the effect and analysis of the symptoms of the post-covid by the techniques of the Statistics.

IndexTerms – Statistics, Covid, Post-Covid, Symptoms, Pandemic.

I. INTRODUCTION

Most people who get COVID-19 recover within a few weeks. For some, symptoms can last weeks or months. Recovery can be prolonged, even if first COVID-19 illness was mild. This condition is called long-term COVID-19. Other terms that refer to the same condition include “long-haul COVID-19,” “post-COVID-19 syndrome,” and “long COVID.”

Symptoms of long-term COVID-19 can be different from initial COVID-19 illness. They can come and go and range from mild to severe.

Common long-term COVID-19 symptoms include:

- Fatigue
- Trouble breathing
- Cough
- Chest discomfort or pain
- Joint and muscle pain
- Headache
- Sleep problems
- Reduced sense of smell and taste
- Eating and digestive issues, such as diarrhea
- Fast or pounding heartbeat
- Fever that comes and goes
- Sweating

Complications can include:

- ❖ Heart muscle inflammation (myocarditis)
- ❖ Blood and vascular disorders (thrombosis and others)
- ❖ Lung function problems (breathing and other respiration issues)
- ❖ Kidney (renal) injury
- ❖ Severe depression and other mood disorders
- ❖ Sensory, memory, and cognitive and other neurological disorders
- ❖ Skin rashes or hair loss (that doesn't improve)

The COVID-19 pandemic has highlighted the importance of statistics in understanding and responding to public health crises. In the post-COVID era, statistics will continue to play a critical role in monitoring and managing the health of populations.

The percentage of people who have had COVID and currently report long COVID symptoms declined from 19% in June 2022 to 11% in January 2023. That decrease reflects a reduction in the share of people who have COVID and later report long COVID, which declined from 35% to 28% during the same period.

One of the key roles of statistics in the post-COVID era will be to track the spread of the virus and monitor the effectiveness of public health interventions. This will involve collecting and analyzing data on the number of cases, hospitalizations, and deaths, as well as information on vaccination rates and the prevalence of new variants of the virus.

The risk of long COVID-19 is significantly lower among vaccinated people compared to the unvaccinated, according to a new study. The research, which reviewed 41 studies involving more than 860,000 people, found that vaccination reduced the risk of long COVID by nearly half.



Effect of gamma irradiation, annealing on spectroscopic and thermal properties of some biopolymers – Gelatin

N. Srinivasa Rao ^a, D. Shireesh ^a, S. Kalahasti ^a, B. Sanjeeva Rao ^b  

Show more 

 Share  Cite

<https://doi.org/10.1016/j.matpr.2022.04.451> 




[Get rights and content](#) 

Abstract

Modification of chemical structure of gelatin is an important point of research due to its extensive applications in food and package industry. Various methods are prescribed in literature for this purpose. Among them the radiation method is very important due to its easiness and economy. The authors have used gamma irradiation for this purpose and studied the effect of gamma irradiation and annealing on spectroscopic and thermal properties of gelatins. For this purpose spectroscopic (Electron spin resonance (ESR) and Fourier transform infrared (FTIR)), thermal (differential scanning calorimetry) and scanning electron microscope are used. ESR spectra of irradiated gelatin have shown quartet structure at room temperature and the signal is annealed by heating the irradiated gelatin. FTIR spectra of gelatin are recorded under different conditions. After irradiation, change in intensity and shift in band position is observed, which are associated with the chemical changes brought out by radiation. Gamma irradiation brings changes in thermal and surface morphology of gelatin.



Investigations on nano composites of silver metalparticle embedded MAAMPS copolymer

D. Shireesh ^a , K. Rajendra Prasad ^b, S. Kalahasti ^a, B. Sanjeeva Rao ^c  

Show more 

 Share  Cite

<https://doi.org/10.1016/j.matpr.2022.04.525> 

[Get rights and content](#) 

Abstract

Effect of incorporation of silver metal nano particles (MNP) into the methacrylamide-2-acrylamido-2-methyl-propanesulphonic acid (MA-AMPS)[MA] copolymer matrix has been investigated by spectroscopic (UV-Vis, FTIR), thermal (DSC) and microscopic (SEM) techniques. The existence of reduced silver MNPs in the copolymer matrix is confirmed by the shift of UV absorption band, suggesting the complexation occurred between silver ion and reactive groups of copolymer. The results are further confirmed by monitoring the shift of FTIR absorption bands. DSC thermograms of the copolymer and nano composite indicate enhancement in thermal stability of copolymer due to the incorporation of silver nanoparticles. SEM micrograph reveals interaction between the silver particles and copolymer matrix.

Introduction

Insertion of metal nano particles into polymers drastically altered their optical [1], [2], electrical [3], [4], thermal [5], [6] and mechanical [7] properties. Such hybrid composite are suitable for various

Spectroscopic and Thermal Investigations on Methyl Methacrylate – co – Methacrylic Acid Copolymer

D. Shireesh¹, N. Srinivasa Rao¹, S. Kalahasti^{1*} and B. Sanjeeva Rao²

¹Department of Physics, Kakatiya University, Warangal, 506 009, Telangana State, India

²Department of Physics, AVV Degree and PG College, Warangal, 506 009, Telangana State, India

Gamma irradiation effects on methyl methacrylate (MMA) – methacrylic acid (MAA) copolymer were investigated by spectroscopic (ESR, FTIR) and thermal (DSC) methods. Electron spin resonance (ESR) spectra of the irradiated copolymer are analysed to be caused by different component spectra from the free radicals ($\sim \text{CH}_2 - \text{CH} - \text{CH}_2 \sim$ and $-\text{COOH}$ or $-\text{COOCH}_3$) as per computer simulation analysis. The ESR signals could be annealed near the transition temperature of the copolymer, and the free radicals formed irradiation might react to form stable structures at transition temperatures. Fourier transform infrared (FTIR) studies suggested that the 3380 cm^{-1} absorption band (due to COOH groups and or hydrogen bonding) and 1734 cm^{-1} absorption band (due to carbonyl groups) were mostly affected by irradiation. Differential scanning calorimeter (DSC) thermogram indicated that the copolymer is a two-phase system (PMMA and PMAA), and transition temperatures are influenced by gamma irradiation. The dosimetric application of copolymer is tested by the ESR technique, and it was found suitable for dosimetry.

Keywords: Bloch analysis; DSC; ESR; FTIR; Gamma irradiation; MAA; MMA

I. INTRODUCTION

Poly methyl methacrylate (PMMA), commercially known as Perspex, is one of the commercially known industrial polymers used in aerospace and high-altitude applications. PMMA has been used in biomedical (Amer *et al.*, 2014), photocatalytic (Camara *et al.*, 2014), solar cells (Yang *et al.*, 2008), organic memory devices as an organic insulator (Haik *et al.*, 2014) and sensors (Mishra *et al.*, 2014) applications. Similarly, PMAA-based coatings are also used in anti-cancer drugs (Yu *et al.*, 2004; Luo *et al.*, 2014) and insulin-releasing (Victor *et al.*, 2002) applications. Polymethacrylic acid is partially hydrophilic, and PMMA is hydrophobic; a mixture of these two has intermediate and interesting properties, which are needed to be investigated. In this context, the synthesis and characterisation of MMA-MAA copolymer and related compounds were reported by various authors (Girod *et al.*, 2013; Saboktakin *et al.*, 2011; Huang *et al.*, 2003; Sodeifian *et al.*, 2012). The copolymers and their derivatives

are reported to have interesting applications. They include coating film for tablets and granules (Paul *et al.*, 1976) in medical areas, microencapsulation (Georgiev *et al.*, 1994), anti-corrosion agents of metals coated on copolymer tablets (Gonsalves *et al.*, 2021), nano gels in biomedical applications (Lee *et al.*, 2001), intelligent material applications (Don *et al.*, 2008) and radiation dosimetry (Alashrah *et al.*, 2021).

With regard to studies on radiation-induced changes, PMMA is extensively investigated (Jebur *et al.*, 2020), and very few attempts are made on PMAA (Yin *et al.*, 2021).

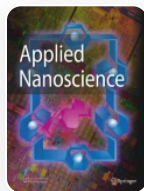
In this paper, we have explained the gamma irradiation effects of copolymer using spectroscopic (ESR and FTIR) and thermal (DSC) techniques. Thermal annealing characteristics and dosimetric aspects of the irradiated copolymer are investigated by ESR techniques. A computer simulation technique is used to analyse ESR spectra.



*Corresponding author's e-mail: skhasti@yahoo.co.in

[Home](#) [Applied Nanoscience](#) [Article](#)

Stilbene-containing carbazole-based fullerene derivatives as alternative electron acceptor for efficient organic solar cells

Original Article Published: 05 December 2022

Volume 13, pages 4101–4108, (2023) [Cite this article](#)[Applied Nanoscience](#)[Aims and scope](#)[Submit manuscript](#)

[Govindasamy Sathiyar](#) , [Gnyaneshwar Dasi](#), [Selva Kumar Ramasamy](#), [Prasenjit Kar](#), [Palanivel Sathishkumar](#), [Kuppusamy Thangaraju](#) & [Pachagounder Sakthivel](#) 

 257 Accesses  2 Citations [Explore all metrics](#) →



Abstract

We developed novel fluorine and nitro-containing stilbene-linked carbazole-based fullerene (C_{60}) derivatives for bulk heterojunction organic solar cells (BHJ-OSCs). The synthesized fullerene derivatives (FCz C_{61} BM and NCz C_{61} BM) have hexyl chains that possess good solubility in toluene and chlorobenzene organic solvents. The extended conjugation of FCz C_{61} BM and NCz C_{61} BM molecules showed broad absorption with strong absorption intensity. The FCz C_{61} BM and NCz C_{61} BM both have a low-lying lowest unoccupied molecular orbital (LUMO) level of -3.70 eV and -3.75 eV, respectively, due to extended conjugation with electron donor. These LUMO energy level was quite



Full Length Article

Solution processed highly transparent nitrogen-doped carbon quantum dots/ZnO hybrid thin films: A study on structural and enhanced UV emission

Lavanya Thyda ^a, Gnyaneshwar Dasi ^a, M.S. Abdul Azeez ^a, K. Naresh ^a, S. Suneetha ^a, P. Amaladass ^b, S. Vijayakumar ^c, Iftikhar Hussain ^d, R. Jayavel ^e, Kuppusamy Thangaraju ^a  

Show more 

 Share  Cite

<https://doi.org/10.1016/j.apsusc.2022.155664> 

[Get rights and content](#) 

Highlights

- Hydrothermal synthesized *N*-CQDs reveal narrow size distribution (2.5 to 3 nm).
- Spin-coated *N*-CQDs/ZnO hybrid films show higher transparency (above 81 %).
- *N*-CQDs get adsorbed onto the surface of ZnO nanoparticles (chemisorption).
- It facilitates non-radiative charge transfer between *N*-CQDs & ZnO ($\lambda_{\text{ex}}=325\text{nm}$).



ROLE OF STATISTICS IN ARTIFICIAL INTELLIGENCE

Srinivas Martha
Department of Mathematics
Vaagdevi College of Engineering
Warangal, Telangana, India

Martha Nuthana Priya
Department of ECE
University College of Engineering & Technology for Women
Kakatiya University, Warangal.

Abstract: Artificial intelligence (AI) is a rapidly developing field that involves the use of algorithms and machine learning to enable machines to perform human-like tasks. Statistics is a branch of mathematics that deals with collection, analysis, interpretation, presentation, and organization of data. Statistical methods are widely used in AI to improve performance and accuracy. The purpose of this paper is to examine the role of Statistics in AI. The paper aims to explore the theoretical foundations of AI and Statistics, the statistical methods used in AI, the applications of Statistics in AI, the benefits of integrating Statistics in AI, the challenges and limitations, and the future directions.

I. THEORETICAL FOUNDATIONS

AI is the simulation of human intelligence in machines that are programmed to think and act like humans. The goal of AI is to create intelligent machines that can perform tasks that typically require human intelligence, such as recognizing speech, image, and text, understanding natural language, playing games, and driving cars.

Statistics is the branch of mathematics that deals with data collection, analysis, interpretation, presentation, and organization. Statistical methods are used to analyze and interpret data to make inferences about populations from samples.

AI relies heavily on statistical methods to learn from data and make predictions. Statistical methods enable AI systems to detect patterns, identify relationships, and infer conclusions from data.

II. STATISTICAL METHODS IN ARTIFICIAL INTELLIGENCE

❖ Regression analysis

Regression analysis is a statistical method used in AI to identify the relationship between a dependent variable and

one or more independent variables. The method is used in AI to model and predict outcomes based on a set of input variables.

❖ Bayesian Statistics

Bayesian Statistics is a statistical method used in AI to estimate the probability of an event based on prior knowledge and new data. The method is used in AI to classify data, make predictions, and optimize decision-making.

❖ Machine learning algorithms

Machine learning algorithms are statistical methods used in AI to learn from data without being explicitly programmed. The algorithms are used in AI to identify patterns, classify data, and make predictions.

❖ Neural networks

Neural networks are a type of machine learning algorithm used in AI to mimic the structure and function of the human brain. Neural networks are used in AI for image and speech recognition, natural language processing, and robotics.

III. APPLICATIONS OF STATISTICS IN ARTIFICIAL INTELLIGENCE

❖ Natural language processing

Natural language processing (NLP) is a field of AI that deals with the interaction between computers and humans using natural language. Statistics is used in NLP to understand and interpret the meaning of natural language, classify text, and generate responses.

❖ Computer vision

Computer vision is a field of AI that deals with the interpretation of visual data from the world. Statistics is used in computer vision to classify images, recognize objects, and track movements.

SER Analysis of GFDM System over $\alpha - \mu$ Fading Channel for 5G Wireless Applications

Lingaiah Jada* and S.Shiyamala

School of Electrical and Communication Engineering, ECE, Vel Tech Rangarajan Dr.Sangunthala R&D Institute of Science and Technology, Avadi, Chennai-600 062, Tamilnadu, India

Received 13 June 2023; Accepted 27 December 2023

Abstract

A flexible radio waveform, generalised frequency division multiplexing (GFDM) allows for significant degrees of freedom in adjusting the number of time slots, subcarriers, and pulse shaping filters. The GFDM is one of the multi-carrier techniques that has been proposed to achieve 5G requirements. Initially, this study discusses about the derivation of novel analytical expression of symbol error rate under $\alpha - \mu$ fading channel using the GFDM system. The proposed derivation includes Rayleigh, Nakagami-m, and Nakagami-q fading channels as special cases for different α and μ values. Further, a simulation test-bed has been developed in MATLAB to access the simulation results and they are in good agreement with the derived theoretical results for various simulation parameters such as different roll-off factors, modulation orders and various fading parameters.

Keywords: GFDM, SER (symbol error rate), $\alpha - \mu$ fading channel, roll-off factor, SNR.

1. Introduction

In present days, 5G systems need to have very low latency, reliability, robust high throughput, and low value of out of band (OOB) emission. Several noteworthy waveforms have been designed in the literature for this situation. Because of its desirable qualities, including minimal OOB radiation to enable dynamic spectrum access and low latency, generalized frequency division multiplexing (GFDM) is one of the top options for future wireless applications. In GFDM, majority of the subcarriers are non-orthogonal to one another, which is the key difference between it and OFDM (orthogonal frequency division multiplexing) [1]. Cyclic prefixes (CP), which consume a lot of bandwidth, are not added to each subcarrier, which is another significant benefit of GFDM. We obtain the identical at the receiver in bits as those which are broadcast by the transmitter in GFDM because just to the combination of sub carriers, one CP is added [2]. According to [3-4], the GFDM system is less complex, achieves minimal OOB, and offers a viable 5G option. The authors of [5] addressed how the adaptable technology known as GFDM circumvents the problems with 4G technology. In a nutshell, GFDM sends data in the form of data blocks made up of K sub carriers and M sub-symbols. Each sub-carrier in GFDM has a low OOB radiation pulse with a circular shape.

As discussed earlier, GFDM is a non-orthogonal and we can make it orthogonal by employing different pulse shaping filters. Additionally, as GFDM is a less complicated method, it can be accomplished by combining it with orthogonal quadrature amplitude modulation (OQAM) [6-7]. To fulfil the demands of the most recent technologies, the GFDM system uses a variety of circular pulse shaping filters addressed in [8-10].

Numerous studies have been conducted on the performance of GFDM's bit error rate (BER) in various fading channels, considering a variety of pulse shaping candidates at receiver that include zero forcing (ZF) and matched filter (MF) in [11-16]. In order to eliminate self-interference, the ZF receiver is used in performance evaluation of GFDM for time-varying Rayleigh fading channels in terms of SER. However, noise enhance factor (NEF) [5] is used to boost up SER performance to overcome loss occur due to pulse shaping filter [17]. In [14-15], SER analytical expressions are provided under several fading environments. The SER expression over AWGN channel for GFDM system with a ZF receiver is shown in [5]. Nevertheless, multiple input multiple output (MIMO), which is one of the key enabler for 5G to achieve diversity is also suitable with GFDM [21-22]

One of the most important aspects of designing a communication system is modelling a wireless channel. The $\alpha - \mu$ distribution is generalized fading and it is used in non-line of sight (NLOS) channel environments. The Rayleigh, Nakagami-m, and Nakagami-q channels can be achieved for special values of $\alpha - \mu$ [3]-[23]. The GFDM system analysis under $\alpha - \mu$ fading is not much addressed in the literature. This motivates us to derive the analytical expressions of symbol error rate using GFDM system with ZF receiver under $\alpha - \mu$ fading channel. In particular, with the help of MATLAB software simulation results are validate with the analytical formulations.

The following major contributions are added to the literature with this article;

- The novel analytical SER expression for $\alpha - \mu$ fading channel is derived and Monte-Carlo simulated test bed has developed to valid theoretical results.

*E-mail address: vtd488@veltech.edu.in

ISSN: 1791-2377 © 2024 School of Science, DUTH. All rights reserved.

doi:10.25103/jestr.174.22

- The effect on SER is shown using the simulations for various fading parameters α and μ by fixing one parameter while varying the other.
- The GFDM system performance analysed for various roll-off factors.
- The effect of modulation order on the SER performance is studied.

The remaining four sections of the paper are structured as follows. The GFDM system model is discussed in section - 2. The innovative closed form of mathematical SER analysis under $\alpha - \mu$ fading is the subject of Section-3. Sections 4 and 5 present simulation analysis and results respectively.

2. System Model Description

2.1. Background of paper

Fig.1. depicts the GFDM transceiver. The vectorial data (\mathbf{b}) provided to the encoder that convert low bit rate input to a high bit rate data stream vectors (\mathbf{b}_c). The mapper block generates a $\mathbf{N} \times \mathbf{1}$ data vector as output (\mathbf{d}). This vectorial data is fed into an N -element GFDM modulator as input. The total vectorial data (\mathbf{d}) is divided into \mathbf{K} groups and \mathbf{M} data symbols;

$$\mathbf{d} = [(d_0)^T, (d_1)^T, \dots \dots (d_{K-1})^T]^T \quad (1)$$

with

$$d_k = [d_{k,0}, d_{k,1}, \dots \dots d_{k,M-1}]^T \quad (2)$$

The term $d_{k,m}$ in eq. (2) represents the data symbol which will be passed through k -th sub carrier at m -th time slot. Later, it is multiplied with pulse shaping filter $g_{k,m}(\mathbf{n})$. A GFDM block that uses \mathbf{K} subcarriers, each of which has \mathbf{M} data symbols, and generates $\mathbf{N} = \mathbf{K}\mathbf{M}$ samples. These sample values are filtered using a suitable transmit filter while using GFDM modulator is given as [11];

$$g_{k,m}[n] = g[(n - mk) \bmod N] e^{-\frac{j2\pi kn}{K}} \quad (3)$$

where $g_{k,m}(\mathbf{n})$ is both time and frequency shifted of $g(\mathbf{n})$. The GFDM signal $x(n)$ can be is expressed as follows given in [11];

$$x[n] = \sum_{k=0}^{K-1} \sum_{m=0}^{M-1} d_{k,m} g_{k,m}[n], \quad n = 0, 1 \dots \dots KM - 1 \quad (4)$$

The samples of pulse shaping filter is;

$$g_{k,m} = [g_{k,m}[0], g_{k,m}[1] \dots \dots g_{k,m}[MK - 1]]^T \quad (5)$$

The eq. (4) can be shown in matrix form as [12];

$$\mathbf{x} = \mathbf{A}\mathbf{d} \quad (6)$$

Where \mathbf{A} is GFDM matrix of size is $\mathbf{KM} \times \mathbf{KM}$ and it can be shown as [5];

$$\mathbf{A} = [g_{0,0} \dots g_{K-1,0} \quad g_{0,1} \dots g_{K-1,M-1}] \quad (7)$$

After GFDM block, cyclic prefix (CP) of length N_{cp} and cyclic suffix (CS) of length N_{cs} are added and then it transmitted through the channel.

2.2. Channel model

After removing CP, the received signal can propagate across the wireless channel using the following model:

$$r = \mathbf{H}\mathbf{x} + \mathbf{w} \quad (8)$$

Where $\mathbf{H} = \text{circ}\{\tilde{\mathbf{h}}\}$.

The GFDM signal is multiplied by the MRT coefficients and is represented mathematically as;

$$r = \sqrt{P_t} \sum_{i=0}^{N_t} h_i w_i x + w = \sqrt{P_t} h_F x + w \quad (9)$$

2.3. Reception of channel model

We have used ZF receiver as GFDM demodulator. The demodulated signal can be expressed as [5];

$$\hat{\mathbf{d}} = \mathbf{B}\mathbf{y} \quad (10)$$

Demodulation matrix is \mathbf{B} .

$B_{ZF} = A^{-1}$ is the receiver demodulation matrix for ZF receiver. The self-interference is eliminated by a ZF receiver, but noise effect is increased. When using a ZF receiver, NEF (ζ) mathematical expression is [5], indicates how much the SNR value is reduced;

$$\xi = \sum_{i=0}^{MK-1} |[B_{ZF}]_{k,i}|^2 \quad (11)$$

where ' ξ ' is equal for all $k = 0, 1, \dots, MK - 1$. We took $\alpha - \mu$ fading channel into consideration in this article. The analysis compress to some frequently used fading channels for some values of $\alpha - \mu$.

Table 1. Representation of various fading channels for different $\alpha - \mu$ values.

$\alpha - \mu$ values	Fading Environment
$\alpha=2$ and $\mu=1$	Rayleigh fading
$\alpha=2$ and $\mu > 1$	Nakagami- μ fading
$\mu=1$	Weibull fading

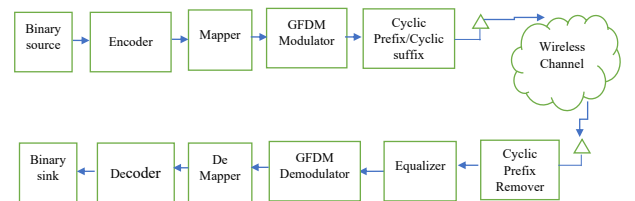


Fig. 1. GFDM Transceiver

$\alpha - \mu$ Distribution:

The $\alpha - \mu$ distribution can be used to model fading channels in the environment characterized by non-homogeneous obstacles that may be nonlinear in nature. The $\alpha - \mu$ fading also considers the received signal to be collection of clusters of multipath components.

The physical relation between resultants of received multipath clusters and fading amplitude for $\alpha - \mu$ distribution can be given as;

$$X^{\alpha,\mu} = \sum_{i=1}^n (I_i^2 + Q_i^2) \quad (12)$$

Where n is the number of clusters, I_i and Q_i are the resultant in-phase and quadrature phase components of i – th cluster in the received signal.

3. Symbol Error Rate Analysis

This section deals with the mathematical analysis of SER expression under $\alpha - \mu$ fading channel for GFDM system. Using a ZF receiver and the QAM modulation technique, the SER performance is assessed.

1). SER Calculation in AWGN Environment

The expression for SER utilising the GFDM scheme under the AWGN is [5];

$$P_{SER,AWGN}(\gamma) = 2 \left(\frac{p-1}{p} \right) \operatorname{erfc}(\sqrt{\gamma}) - \left(\frac{p-1}{p} \right)^2 \operatorname{erfc}^2(\sqrt{\gamma}) \quad (13)$$

Where

$$\gamma = \frac{3R_T}{2(2^m-1)} \frac{E_s}{\xi N_0} \quad \text{and} \quad R_T = \frac{KM}{KM+N_{CP}+N_{CS}} \quad (14)$$

In eq. (13) and eq. (14), $p = \sqrt{2m}$, m -represents number of bits, N_{CP} , N_{CS} are length of CP and CS respectively. K and M are number of subcarriers and data symbols. For various fading environments SER expression can be calculated using [5];

$$P_{SER} = \int_0^{\infty} P_{AWGN}(\gamma) P_{\gamma}(\gamma) d\gamma \quad (15)$$

In eq. (15), $P_{\gamma}(\gamma)$ represents the PDF of different fading channels.

2) $\alpha - \mu$ Fading Environment

$$A(\bar{\gamma}_{\alpha,\mu}) = 1 - \frac{1}{2\sqrt{\pi}} \frac{\alpha\mu^{\mu}\sqrt{k}(l)^{\alpha\mu/2}}{\Gamma(\mu)\gamma^{\frac{\alpha\mu}{2}}(2\pi)^{\frac{l+k-2}{2}}} G_{2l,k+l}^{k+l,l} \left[\frac{\mu^k l^l}{k^k \gamma^{\frac{\alpha\mu}{2}}} \left| \begin{matrix} \Delta\left(l, \frac{1-\alpha\mu}{2}\right), \Delta\left(l, 1-\frac{\alpha\mu}{2}\right) \\ \Delta(k, 0), \Delta\left(l, \frac{-\alpha\mu}{2}\right) \end{matrix} \right. \right] \quad (21)$$

$$B(\bar{\gamma}_{\alpha,\mu}) = 1 - \frac{2}{\pi} \frac{\mu^{\mu}}{\left(\frac{\alpha\mu}{\gamma}\right)^{\frac{\mu-1}{2}}} \sum_{j=0}^{\mu-1} \sum_{i=0}^{\infty} \frac{(-1)^i \left(\frac{\alpha\mu}{\gamma}\right)^{\frac{\alpha}{2}(\mu-j)} \sqrt{kl}^{\frac{i+j-1}{2}}}{j! i! \mu^{\mu-j} (2\pi)^{\frac{l+k-2}{2}}} G_{2l,k}^{k,2l} \left[\frac{l^i \mu^k}{\gamma^{\frac{\alpha k}{2}} k^k} \left| \begin{matrix} \Delta\left(l, \frac{1}{2}-i-cj\right), \Delta\left(l, -i-cj\right) \\ \Delta(k, 0), \Delta\left(l, -i-cj-\frac{1}{2}\right) \end{matrix} \right. \right] \quad (22)$$

The exact SER expression can be obtained by substituting eq. (21) and eq. (22) in eq. (17).

4. Results and Discussions

The findings of the simulation and their analysis are covered in this section. All simulations are run for 10^5 Monte-Carlo iterations with the following simulation parameters: length of CP and CS are $N_{cp}=8$, $N_{cs}=0$, $K=64$, $M=5$ and 16-QAM

The SER analysis is evaluated for various values of E_s/N_0 with single antenna ($N_t = 1$) and $\beta=0.1$ under $\alpha - \mu$ fading. The Fig.2 is simulated for different μ values and fixed α value ($\alpha=2$). The analytical values achieved from the derived

In order to calculate SER expression for $\alpha - \mu$ fading, we require PDF of $\alpha - \mu$ fading. It is given in [26] as;

$$P_{\gamma}(\gamma) = \frac{\alpha\mu^{\mu}\gamma^{\frac{\alpha\mu-1}{2}} e^{-\mu\left(\frac{\gamma}{\bar{\gamma}}\right)^{\frac{\alpha}{2}}}}{2\Gamma(\mu)\bar{\gamma}^{\frac{\alpha\mu}{2}}} \quad (16)$$

where $\bar{\gamma}$ is average channel SNR.

The SER expression for $\alpha - \mu$ fading can be calculated by substituting eq.(13) and eq.(16) in eq.(15) and it obtained as;

$$P_{\alpha-\mu}(e) = 2 \left(\frac{p-1}{p} \right) A(\bar{\gamma}_{\alpha-\mu}) - \left(\frac{p-1}{p} \right)^2 B(\bar{\gamma}_{\alpha-\mu}) \quad (17)$$

where $\bar{\gamma}_{\alpha-\mu}$ is equivalent SNR under $\alpha - \mu$ fading channel given by

$$\bar{\gamma}_{\alpha-\mu} = \frac{2R_T\sigma_{\alpha-\mu}^2 E_s}{(2^b-1)\xi N_0} \quad (18)$$

where b is number of bits per QAM symbol and $\phi = \sqrt{2^b}$.

$$R_T = \frac{NM}{NM+N_{cp}+N_{cs}} \quad (19)$$

The NEF value for ZF-receiver can be calculated as;

$$\xi = \sum_{n=0}^{NM-1} \left| (B_{ZF})_{i,n} \right|^2 \quad (20)$$

Eq. (17) consists of two unknown values such as $A(\bar{\gamma}_{\alpha-\mu})$ and $B(\bar{\gamma}_{\alpha-\mu})$ which can be computed as

theoretical expressions is in good agreement with the Monte-Carlo simulations. It is observed that SER performance reduces with the increases in μ value. At SNR=15dB, SER values are 0.163, 0.094, 0.0688 and 0.055 for $\mu=1, 2, 3$ and 4 respectively. It can be observed that for $\mu = 1$ the curve obtained in Fig. 2 matches to that of [5]. As discussed in the Section 3, $\alpha - \mu$ distribution covers Nakagami- m as special case for $\alpha=2$ and $\mu = m$. The results also confirm the same that Fig.2 is the plot for the SER performance of Nakagami- m distribution [28-30].

In Fig.3 also SER performance is investigated for different E_s/N_0 values under $\alpha - \mu$ fading. This simulation is evaluated using $N_t = 1$, $\beta=0.1$, and keeping one fading parameter is constant ($\mu=1$) and varying another fading

parameter ($\alpha=2,3,5,7$). This simulation is giving an exact SER response of Weibull fading with $\mu=1$ which is discussed in [30]. We can also deduce from the Fig.3 that SER values decrease with increase in α value.

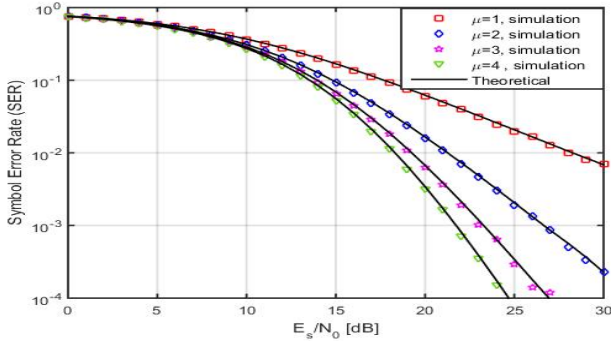


Fig. 2. SER vs E_s/N_0 performance for different μ and $\alpha=2$ values.

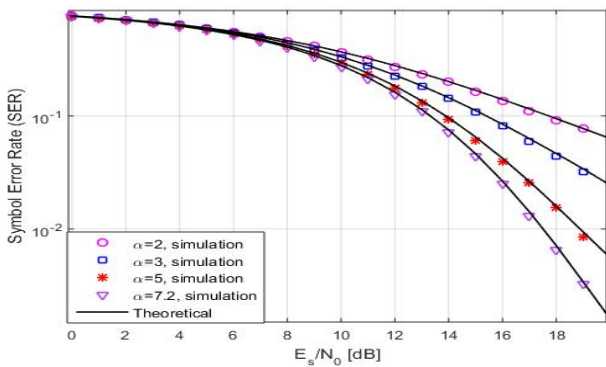


Fig. 3. SER vs E_s/N_0 analysis for various values of α and $\mu=1$.

At SNR=15dB, SER values are 0.1683, 0.117, 0.065 and 0.0462 for $\alpha= 2, 3, 5,$ and 7 respectively. The SER value decreases by almost 72.5%, as α value rises from $\alpha=2$ to $\alpha=7$, showing that fading becomes less severe as α increases. As discussed in the Section 3, $\alpha - \mu$ distribution covers Weibull as special case for α varies and $\mu = 1$.

The SER performance is analysed for various β values, different SNR values (10dB, 15dB, 18dB), $\mu = 3, \alpha = 2$, and employing the 16-QAM modulation technique in Fig.4. According to the simulation, the SER value decreases from 0.286 to 0.01781 at a value of $\beta=0.4$ as SNR value grows from 10dB to 18dB. This indicates that there is an almost 95% improvement in SER with the increase in SNR. The SER value decreases at lower values of β and it rises at higher levels of β . Finally, it can be said that it is always advisable to attain less SER at lower values of $\beta=0.1$ and greater SNR values (20dB). This occurs because of rise in β value, decrease the overlap between neighbouring subcarriers, which causes a rise in NEF value (ξ) and, ultimately, a decline in SER performance is observed. It is also observed that the SER value reduces due to rise in signal power as the SNR climbed from 10dB to 18dB.

The relationship between SER and E_s/N_0 is depicted in fig.5 for various roll-off factors (0.1, 0.6, and 0.9), $\mu = 4, \alpha = 2$, and employing 16-QAM modulation technique. The impact of the NEF parameter, which is important in GFDM, is also explained using Fig. 5. Because of the wider overlap of the subcarriers, which causes an increase in the NEF factor, so that we can observe noticeable change in the SER curve with the rise of roll-off factor's value. The SER values are 0.0034, 0.0074, and 0.0172 for $\beta=0.1, 0.6,$ and 0.9 at

SNR=20dB. The SER value lowers by 80.2% as the value of β falls from 0.9 to 0.1.

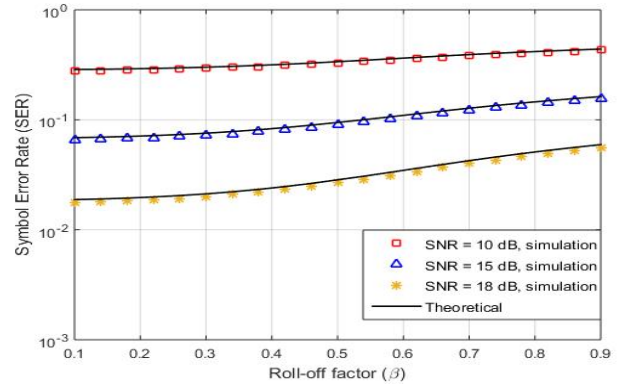


Fig. 4. SER vs roll-off factor for various SNR values.

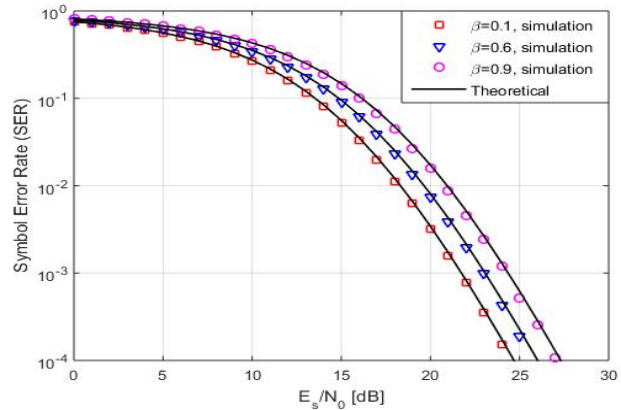


Fig. 5. SER vs E_s/N_0 analysis for various Roll-off factors.

The SER analysis for various SNRs is plotted in Fig. 6 for several modulation schemes (QPSK ($k=2$) and 16-QAM ($k=4$)), $N_t=1$, and $\alpha=2$ and $\mu=5$. We may conclude from this simulation that the SER value for the QPSK technique is lower than 16-QAM modulation method. For a specific scenario, the SER values for the 16-QAM and QPSK methods are 0.0251 and 0.0072, respectively at SNR=10dB.

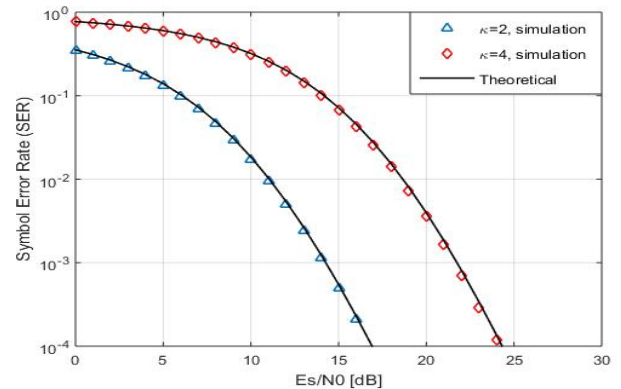


Fig. 6. SER vs E_s/N_0 analysis for various modulation schemes.

5. Conclusion

The performance of SER is examined in this study using GFDM system under $\alpha - \mu$ fading. The novel closed form of SER expression under $\alpha - \mu$ fading environment was initially derived in this paper. Later, using MATLAB simulations for a variety of simulation parameters such fading parameters, various roll-off factors, and various modulation orders, the performance of the SER is assessed. We have used the

published literature studies to validate our simulations as well. We have observed that the error rate is dropped as one fading parameter was fixed and another fading parameter was increased. Additionally, the overall performance of the SER using GFDM system is significantly influenced by the roll-off factor selection also. The studied system model under $\alpha - \mu$

fading is useful in designing the wireless communication system in a more generalized manner.

This is an Open Access article distributed under the terms of the Creative Commons Attribution License.



References

- [1] A. Farhang, N. Marchetti, and L. E. Doyle, "Low-Complexity Modem Design for GFDM," *IEEE Trans. Signal Process.*, vol. 64, no. 6, pp. 1507–1518, Mar. 2016, doi: 10.1109/TSP.2015.2502546.
- [2] Z. Sharifian, M. J. Omid, A. Farhang, and H. Saeedi-Sourck, "Polynomial-based compressing and iterative expanding for PAPR reduction in GFDM," in *2015 23rd Iranian Conf. Electr. Engin.*, Tehran, Iran: IEEE, May 2015, pp. 518–523. doi: 10.1109/IranianCEE.2015.7146271.
- [3] J. S. Ferreira *et al.*, "GFDM Frame Design for 5G Application Scenarios," *J. Commun. Inform. Sys.*, vol. 32, no. 1, pp. 54–61, 2017, doi: 10.14209/jcis.2017.6.
- [4] D. Zhang, M. Matthe, L. L. Mendes, and G. Fettweis, "A Study on the Link Level Performance of Advanced Multicarrier Waveforms Under MIMO Wireless Communication Channels," *IEEE Trans. Wireless Commun.*, vol. 16, no. 4, pp. 2350–2365, Apr. 2017, doi: 10.1109/TWC.2017.2664820.
- [5] N. Michailow *et al.*, "Generalized Frequency Division Multiplexing for 5th Generation Cellular Networks," *IEEE Trans. Commun.*, vol. 62, no. 9, pp. 3045–3061, Sep. 2014, doi: 10.1109/TCOMM.2014.2345566.
- [6] N. Michailow, L. Mendes, M. Matthe, I. Gaspar, A. Festag, and G. Fettweis, "Robust WHT-GFDM for the Next Generation of Wireless Networks," *IEEE Commun. Lett.*, vol. 19, no. 1, pp. 106–109, Jan. 2015, doi: 10.1109/LCOMM.2014.2374181.
- [7] I. Gaspar, L. Mendes, M. Matthe, N. Michailow, A. Festag, and G. Fettweis, "LTE-compatible 5G PHY based on generalized frequency division multiplexing," in *2014 11th Int. Symp. Wirel. Commun. Sys. (ISWCS)*, Barcelona, Spain: IEEE, Aug. 2014, pp. 209–213. doi: 10.1109/ISWCS.2014.6933348.
- [8] G. Fettweis, M. Krondorf, and S. Bittner, "GFDM - Generalized Frequency Division Multiplexing," in *VTC Spring 2009 - IEEE 69th Vehicul. Techn. Conf.*, Barcelona, Spain: IEEE, Apr. 2009, pp. 1–4. doi: 10.1109/VETECS.2009.5073571.
- [9] S. K. Antapurkar, A. Pandey, and K. K. Gupta, "GFDM performance in terms of BER, PAPR and OOB and comparison to OFDM system," presented at the *Adv. Sci. Technol.: Proceed. 2nd Int. Conf. Commun. Sys. (ICCS-2015)*, Rajasthan, India, 2016, p. 020039. doi: 10.1063/1.4942721.
- [10] A. Kumar and M. Magarini, "Improved Nyquist pulse shaping filters for generalized frequency division multiplexing," in *2016 8th IEEE Latin-American Conf. Commun. (LATINCOM)*, Medellin, Colombia: IEEE, Nov. 2016, pp. 1–7. doi: 10.1109/LATINCOM.2016.7811588.
- [11] N. Michailow and G. Fettweis, "Low peak-to-average power ratio for next generation cellular systems with generalized frequency division multiplexing," in *2013 Int. Symp. Intellig. Sign. Process. Commun. Sys.*, Naha-shi, Japan: IEEE, Nov. 2013, pp. 651–655. doi: 10.1109/ISPACS.2013.6704629.
- [12] S. K. Mishra and K. D. Kulat, "Approximation of peak-to-average power ratio of generalized frequency division multiplexing," *AEU - Int. J. Elec. Comm.*, vol. 99, pp. 247–257, Feb. 2019, doi: 10.1016/j.aeue.2018.12.001.
- [13] S. G. Neelam and P. R. Sahu, "Error performance of QAM GFDM waveform with CFO under AWGN and TWDP fading channel," in *2019 Nat. Conf. Commun. (NCC)*, Bangalore, India: IEEE, Feb. 2019, pp. 1–6. doi: 10.1109/NCC.2019.8732207.
- [14] M. Matthe, N. Michailow, I. Gaspar, and G. Fettweis, "Influence of pulse shaping on bit error rate performance and out of band radiation of Generalized Frequency Division Multiplexing," in *2014 IEEE Int. Conf. Commun. Worksh. (ICC)*, Australia: IEEE, Jun. 2014, pp. 43–48. doi: 10.1109/ICCW.2014.6881170.
- [15] V. Nivetha and V. Sudha, "BER Analysis of GFDM System Under Different Pulse Shaping Filters," in *2021 Sixth Int. Conf. Wirel. Commun., Sign. Proc. Networ. (WiSPNET)*, Chennai, India: IEEE, Mar. 2021, pp. 53–56. doi: 10.1109/WiSPNET51692.2021.9419396.
- [16] A. Nimr, M. Chafii, and G. Fettweis, *Practical GFDM-based Linear Receivers*. DE: VDE VERLAG GMBH, 2019. Accessed: Sep. 01, 2024. [Online]. Available: <https://doi.org/10.30420/454862039>
- [17] M. Carrick and J. H. Reed, "Improved GFDM equalization in severe frequency selective fading," in *2017 IEEE 38th Sarnoff Symp.*, Newark, NJ, USA: IEEE, Sep. 2017, pp. 1–6. doi: 10.1109/SARNOF.2017.8080391.
- [18] N. Michailow, S. Krone, M. Lentmaier, and G. Fettweis, "Bit Error Rate Performance of Generalized Frequency Division Multiplexing," in *2012 IEEE Vehicular Techn. Conf. (VTC Fall)*, Quebec City, QC, Canada: IEEE, Sep. 2012, pp. 1–5. doi: 10.1109/VTCFall.2012.6399305.
- [19] R. Datta, N. Michailow, M. Lentmaier, and G. Fettweis, "GFDM Interference Cancellation for Flexible Cognitive Radio PHY Design," in *2012 IEEE Vehicular Techn. Conf. (VTC Fall)*, Quebec City, QC: IEEE, Sep. 2012, pp. 1–5. doi: 10.1109/VTCFall.2012.6399031.
- [20] S. Tiwari, S. Sekhar Das, and K. K. Bandyopadhyay, "Precoded generalised frequency division multiplexing system to combat inter-carrier interference: performance analysis," *IET Commun.*, vol. 9, no. 15, pp. 1829–1841, Oct. 2015, doi: 10.1049/iet-com.2015.0081.
- [21] M. Matthe, L. L. Mendes and G. Fettweis, "Space-Time Coding for Generalized Frequency Division Multiplexing," *European Wireless 2014; 20th European Wireless Conf.*, Barcelona, Spain, May 2014, pp. 1-5.
- [22] M. Matthe, L. L. Mendes, N. Michailow, D. Zhang, and G. Fettweis, "Widely Linear Estimation for Space-Time-Coded GFDM in Low-Latency Applications," *IEEE Trans. Commun.*, vol. 63, no. 11, pp. 4501–4509, Nov. 2015, doi: 10.1109/TCOMM.2015.2468228.
- [23] J. Zhang, M. Matthaiou, Z. Tan, and H. Wang, "Performance Analysis of Digital Communication Systems Over Composite η - μ /gamma Fading Channels," *IEEE Trans. Veh. Technol.*, vol. 61, no. 7, pp. 3114–3124, Sep. 2012, doi: 10.1109/TVT.2012.2199344.
- [24] C. Ben Issaid, M.-S. Alouini, and R. Tempone, "On the Fast and Precise Evaluation of the Outage Probability of Diversity Receivers Over $\alpha - \mu$, $\kappa - \mu$, and η - μ fading Channels," *IEEE Trans. Wireless Commun.*, vol. 17, no. 2, pp. 1255–1268, Feb. 2018, doi: 10.1109/TWC.2017.2777465.
- [25] B. Sklar, *Digital communications: fundamentals and applications*, 3rd ed. Hoboken: Pearson Education, Inc, 2020.
- [26] M. D. Yacoub, "The $\alpha - \mu$ Distribution: A Physical Fading Model for the Stacy Distribution," *IEEE Trans. Veh. Technol.*, vol. 56, no. 1, pp. 27–34, Jan. 2007, doi: 10.1109/TVT.2006.883753.
- [27] I. S. Gradshteyn and D. Zwillinger, *Table of integrals, series, and products*, Eighth edition. Amsterdam; Boston: Elsevier, Academic Press is an imprint of Elsevier, 2015.
- [28] A. Yenilmez, T. Gucluoglu, and P. Remlein, "Performance of GFDM-maximal ratio transmission over Nakagami-m fading channels," in *2016 Int. Symp. Wirel. Commun. Sys. (ISWCS)*, Poznan, Poland: IEEE, Sep. 2016, pp. 523–527. doi: 10.1109/ISWCS.2016.7600960.
- [29] S. K. Bandari, V. V. Mani, and A. Drosopoulos, "Performance analysis of GFDM in various fading channels," *COMPEL: The Int. J. Comput. Mathem. Electric. Electr. Engineer.*, vol. 35, no. 1, pp. 225–244, Jan. 2016, doi: 10.1108/COMPEL-06-2015-0215.
- [30] L. Jada and S. Shiyamala, "Investigation on GFDM System for 5G Applications over Fading Channels," *J. Eng. Sci. Techn. Rev.*, vol. 15, no. 3, pp. 1–8, Feb. 2022, doi: 10.25103/jestr.153.01.

Channel Estimation Algorithm Based on Factor Graph for GFDM-UWA System

Lingaiah Jada* and S.Shiyamala

School of Electrical and Communication Engineering | ECE, Vel Tech Rangarajan Dr.Sagunthala R&D Institute of Science and Technology, Avadi, Chennai-600 062, Tamilnadu, India.

Received 12 August 2022; Accepted 10 June 2023

Abstract

According to the characteristics of the wireless channel, channel estimation algorithms based on the factor graph are proposed for Generalized Frequency Division Multiplexing over Underwater Acoustics (GFDM-UWA) system to improve the precision of channel estimation and bandwidth efficiency, which include two-dimension joint channel estimation and one-dimensional channel estimation algorithm. Time-varying frequency-selective fading channels can be modelled as 1st ordered autoregressive processes and approximating messages as Gaussian distribution, a novel channel estimation and symbol detection method for GFDM-UWA system is deduced by applying sum-product algorithm on the factor graph. Simulation results show that the algorithm can achieve good performance with low computational complexity.

Keywords: Generalized Frequency Division Multiplexing over Underwater Acoustics (GFDM-UWA); channel estimation; symbol detection; factor graph; Sum-product Algorithm (SPA).

1. Introduction

At present, there are limited channel estimation methods for Generalized Frequency Division Multiplexing over Underwater Acoustic channel (GFDM-UWA) technique, which is generally divided into pilot-based channel estimation and blind channel estimation. Blind estimation is difficult to implement in most application environments due to its complexity. The pilot-based channel estimation algorithms mainly include Least Square (LS) algorithm, Minimum Mean Square Error (MMSE) algorithm, and Decision Feedback (DF) algorithm. These algorithms are simple, but the performance is not enough ideal [1]. The Maximum Likelihood (ML) estimator can obtain theoretical optimal estimation performance, but computational complexity increases exponentially with increase of channel freedom, which limits its application in practice. Joint iterative channel estimation is an effective way to solve above Problem. It uses the pilot and detected data to iteratively estimate channel based on traditional auxiliary pilot channel estimation [2]. In [3], joint decoder and channel estimation module performs iterative channel estimation on OFDM system to improve channel estimation accuracy. On this basis, the blind multi-generation receiver of OFDM system based on factor graph has also received attention [4], but amount of computation is large and convergence speed is slow. In view of this, in this paper a new joint channel estimation algorithm is proposed. According to ML criterion, the optimal channel estimation problem is regarded and the observation information is solved using channel parameters and likelihood function of transmitted symbols. With the help of factor graph model [5], the initial channel parameter information is exchanged through time-frequency 2-D transfer function node, and optimal channel estimation result is obtained by using sum-product algorithm (SPA) rule. The algorithm reduces pilot

overhead while improving performance. However, due to two-dimensionality of pilot signal in GFDM-UWA system, there is a "ring" in the factor graph model of the algorithm. Therefore, in order to obtain better results, performance of the algorithm must be improved by multiple iterations, if factor graph model is constructed. If there is no loop, sum-product estimation algorithm can obtain accurate posterior estimation results, and the amount of calculation is also significantly reduced. In order to further reduce the computational complexity of the joint iterative algorithm, the characteristics of wireless channel is considered [6-7], in this paper 2-D joint channel estimation is decomposed in to cascaded two 1-D channel estimation algorithms.

2. System Model

The received frequency domain observation signal is expressed as:

$$Y[n, k] = X[n, k]H[n, k] + W[n, k] \quad (1)$$

Where $Y[n, k]$, $X[n, k]$ represent the received and transmitted signal on k^{th} subcarrier in the n^{th} GFDM-UWA symbol; $W[n, k]$ is a zero mean and σ^2 variance Gaussian white noise; $H[n, k]$ represents the k^{th} subcarrier channel frequency response (CFR) at n^{th} time.

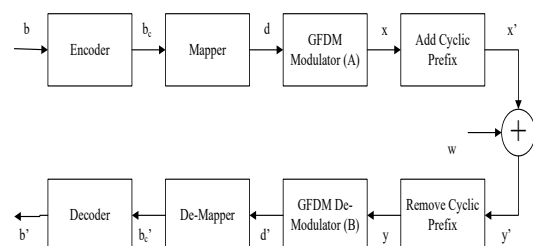


Fig. 1. Baseband Model for GFDM-UWA system.

*E-mail address: jadalangaiah69@gmail.com

ISSN: 1791-2377 © 2023 School of Science, IITU. All rights reserved.

doi:10.25103/jestr.163.08

Consider GFDM-UWA system (fig. 1) for a frequency selective channel, the correlation between two-point channel response with time interval Δn , frequency domain interval Δk can be expressed as:

$$r_H(\Delta n, \Delta k) = r_t(\Delta n)r_f(\Delta k) \quad (2)$$

Where r_t represents channel time domain correlation function, mainly depending on Doppler frequency shift caused by relative movement of transmitter and receiver; r_f represents frequency domain channel correlation function.

According to literature [9], transfer function $\Delta[\Delta n, \Delta k]$ is used to describe the information interchange between channel parameters, which reduces computational complexity of algorithm. In this paper, only first-order autoregressive (AR) model [10] is considered, i.e., $\Delta n + \Delta k = \pm 1$. According to characteristics of wireless channel parameters, the Gaussian distribution is approximated the transfer function i.e., $\Delta[\Delta n, \Delta k] \sim N(0, \sigma_\Delta^2[\Delta n, \Delta k])$. The variance for time domain transfer function Δt is:

$$\sigma_{\Delta t}^2 = 2 - 2J_0(2\pi f_d T_s) \quad (3)$$

Where τ_{max} is GFDM-UWA symbol interval; f_d is relative Doppler extension of transmitter and receiver; $J_0(\cdot)$ is 1st order Bessel function. The variance for frequency domain transfer function Δf is expressed as:

$$\sigma_{\Delta f}^2 = 2 - sinc(\tau_{max} F) \quad (4)$$

Where τ_{max} is maximum transmission delay; F is subcarrier spacing.

According to above GFDM-UWA system model, the optimal detection of the transmitted symbol using the ML algorithm can be expressed as:

$$\hat{X} = \underset{X}{arg \max} p(Y|X) \quad (5)$$

Where X represents sequence of transmitted symbols; Y represents sequence of received symbols.

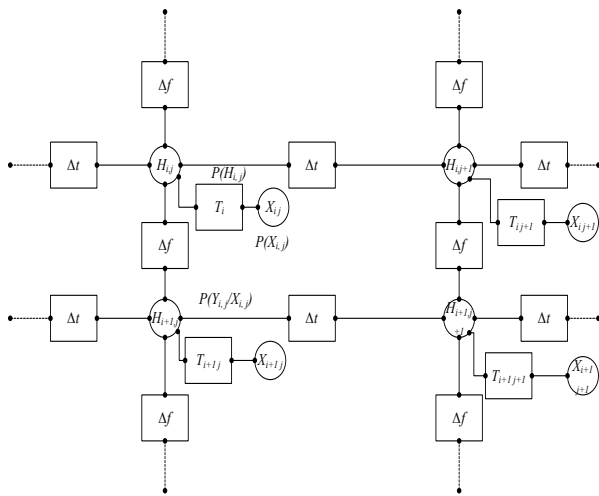


Fig. 2. Factor Graph based receiver model in GFDM-UWA system.

3. Joint Channel Estimation Based on Graph Factor

3.1. Two-Dimensional Joint Channel Estimation Algorithm Based on Factor Graph

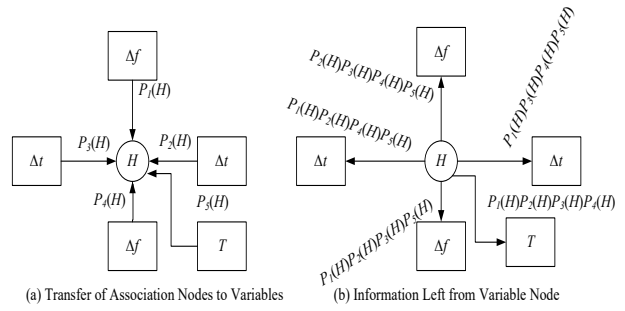


Fig. 3. Structure of Channel State Information Updater.

In fading environment, likelihood function in equation (5) is decomposed in to the correlation of symbol estimates at different time and frequency points:

$$p(Y|X) = \int_H p(Y|X, H)p(H)dH = \int_H \prod_{X \in X_p} p(Y|X, H) \prod_{X \in X_p} p(Y|H)p(H)dH \quad (6)$$

Where H is channel response matrix; X_p is training sequence of transmitted symbol.

According to characteristics of wireless channel, likelihood function is decomposed into product of local probability functions, and factor graph is used to represent relationship between each decomposed term and variable. A factor graph is a bidirectional graph consisting of function nodes, variable nodes, and graph edges. If function contains variable, edge of variable and function node need to be connected by the edge [4]. The factor graph model of the GFDM-UWA system receiver is shown in Figure 2. The squares in figure represent function nodes, the circles represent variable nodes, and straight lines represent edges of function nodes and variable nodes. $\Delta f, \Delta t$ represents frequency and time domain transfer function nodes between adjacent channel parameters $T_i \equiv p(Y_{i,j}|H_{i,j}, X_{i,j})$.

According to the above receiver model, a 2-D joint channel estimation algorithm is obtained by applying the sum product algorithm. From the factor graph model as shown in Fig. 2, each graph edge information is iteratively updated to each node until the algorithm converges. The factor graph based 2-D joint channel estimation algorithm in GFDM-UWA system is described as follows:

Step 1: Initialization. According to the received signal Y_0 and training sequence X_p , the initial channel estimation value H_0 is obtained by conventional LS algorithm. According to factor graph model as shown in Fig. 2, channel information at pilot position is exchanged by transfer function node by means of sum-product algorithm rule, and mean and variance of each node are iteratively updated in sequence. Assuming that the initial transmitted symbol have has equal priori probability, i.e., $p(X_{i,j}) = 0.5, i = 1, 2, \dots, K; j = 1, 2, \dots, N$, where K, N represents number of subcarriers and symbols in GFDM-UWA.

Step 2: Get the information of the variable node channel parameter based on symbol updated information and is given by:

$$p(H_{i,j}) = \sum_{X_{i,j} \in \{\pm 1\}} p(Y_{i,j}|H_{i,j}, X_{i,j})p(X_{i,j}) \quad (7)$$

Step 3: The channel parameters to gaussian channel model are updated, according to Fig. 3. Because it is assumed that $p(H)$ is subject to gaussian distributions, their products are still subject to Gaussian distributions

$$\prod_{j=1, j \neq m}^N p_n(H) \sim N(\mu_m, \sigma_m^2) \quad (8)$$

Where:

$$\mu_m = \frac{\sum_{n=1, n \neq m}^N \frac{\mu_n}{\sigma_n^2}}{\sum_{n=1, n \neq m}^N \frac{1}{\sigma_n^2}}, \sigma_m^2 = \frac{1}{\sum_{n=1, n \neq m}^N \frac{1}{\sigma_n^2}}$$

Step 4: The information passed from the observation function node to the symbol variable node based on the updated channel parameter information is gathered, and represented as:

$$p(Y_{i,j}|X_{i,j}) = \frac{1}{\pi(|X_{i,j}|^2 \sigma_{H_{i,j}}^2 + \sigma_n^2)} \times \exp\left(-\frac{|Y_{i,j} - \hat{H}_{i,j} X_{i,j}|^2}{|X_{i,j}|^2 \sigma_{H_{i,j}}^2 + \sigma_n^2}\right) \quad (9)$$

Repeat Step2~Step4 until the algorithm converges.

Step 5: The estimated value of the transmitted symbol from all the information related to the symbol is gathered: Step 5 is evaluated by all information related to the symbol to send the symbol.

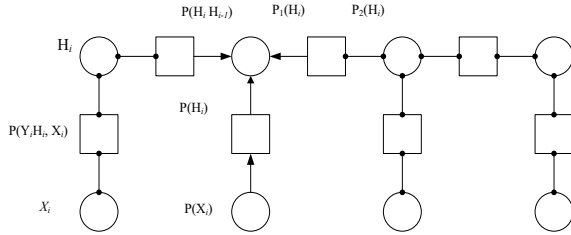


Fig. 4. 1-D Channel Estimation Factor Graph Model.

3.2. Two Cascaded 1-D Channel Estimation Algorithm

Since the factor graph of the above two-dimensional algorithm has a loop, multiple iteration operations are required, and the calculation amount is large, and the correlation of the wireless channel can be separated by the equation (2), so the two-dimensional joint channel estimation algorithm is passed through two cascade of one-dimensional channel estimation is implemented, that is, an appropriate factor graph model is established in the time domain and the frequency domain, respectively, when the channel parameter information is updated, only the transfer function in each direction is considered, and the other dimension is ignored. Correlation, the ring graph model no longer contains loops. Due to the incompleteness of channel parameter information transmission caused by algorithm approximation, the performance of the one-dimensional joint channel estimation algorithm is degraded compared to the performance of the two-dimensional joint channel estimation algorithm. The factor graph model of the one-dimensional channel estimation algorithm is shown in Figure 4. Consider the frequency domain channel estimation first in the time domain estimation.

Step 1: Time domain channel estimation

In this case, the factor graph model does not contain the symbol variable node and the observation node, so only the channel parameter information needs to be obtained. According to the channel parameter model, the channel parameter changes to a Markov process, and $p(H_i|H_{i-1})$ is the time domain transfer function and is represented by Δt in Fig.4. The output information of the channel can be calculated from (9), and then similar operations are performed in all subcarriers containing pilot symbols.

Step 2: Frequency domain channel estimation

The channel estimation value in the time domain is taken as known data, and then 1-D channel estimation is performed in the frequency domain, and the frequency domain transfer function Δf is used instead of $p(H_i|H_{i-1})$. Since each subchannel of the GFDM-UWA system is equivalent to a flat Rayleigh fading channel, the likelihood function $p(Y_{1:k}|X_{1:k})$ is decomposed into:

$$p(Y_{1:k}|X_{1:k}) = \int_{H_{1:k}} p(Y_{1:k}|X_{1:k}, H_{1:k}) p(H_{1:k}) dH_{1:k} = \int_{H_{1:k}} p(Y_i|X_i, H_i) p(H_0) p(H_i|H_{i-1}) dH_i \quad (10)$$

According to the factor graph model as shown in Fig. 4, the specific steps of 1-D joint channel estimation algorithm is expressed as follows:

1. Assume that the initial transmitted symbol a priori is equal probability, i.e., $(X_i) = 0.5, i = 1, 2, \dots, K$.
2. Obtain the channel parameter information, which is expressed as:

$$p(H_i) = \sum_{X_i \in \{\pm 1\}} p(Y_i|H_i, X_i) p(X_i) \quad (11)$$

3. Update the channel state information, because $p_1(H_i) \sim N(\mu_1, \sigma_1^2)$, $p_2(H_i) \sim N(\mu_2, \sigma_2^2)$, then $p_1(H_i) \cdot p_2(H_i) \sim N(\mu_H, \sigma_H^2)$.

$$\mu_H = \frac{\sigma_2^2 \mu_1 + \sigma_1^2 \mu_2}{(\sigma_2^2 + \sigma_1^2)}$$

$$\sigma_H^2 = \frac{\sigma_1^2 \sigma_2^2}{(\sigma_1^2 + \sigma_2^2)} \quad (12)$$

4. According to the updated channel state information, the information of the symbol variable node is:

$$p(Y_i|X_i) = \frac{1}{\pi(|X_i|^2 \sigma_{H_i}^2 + \sigma_n^2)} \cdot \exp\left(-\frac{|Y_i - \hat{H}_i X_i|^2}{|X_i|^2 \sigma_{H_i}^2 + \sigma_n^2}\right) \quad (13)$$

Repeat steps (2) to (4) until maximum iterations are met. According to (5), the symbol estimate using ML criterion is as follows:

$$\hat{X}_i = \arg \max_{X_i} p(Y_i|X_i) \quad (14)$$

4. Simulation Results

The simulation parameters of GFDM-UWA system is as follows: the number of subcarriers $K=64$, the number of GFDM-UWA symbols per frame is $N=13$, using BPSK modulation; under Rayleigh fading multipath channel, the number of multipath is 3; Normalized Doppler frequency

shift is $f_d T_s = 0.0114$ and the maximum delay $\tau_{max} = 3000ns$.

Fig. 5 shows performance comparison between the algorithm and accurate channel estimation (Bit Error Rate, BER).

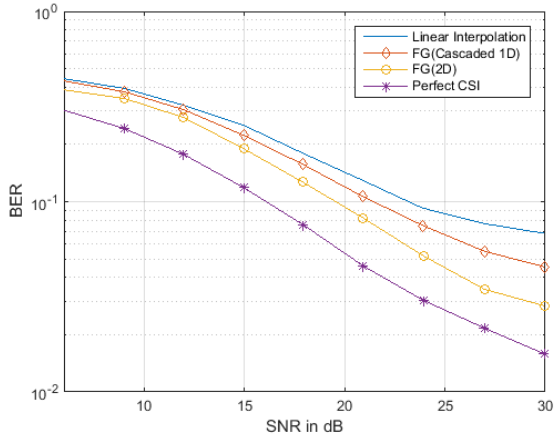


Fig. 5. BER Comparison of algorithm with the linear interpolation algorithm.

The linear interpolation algorithm represents the BER result of classical linear interpolation channel estimation algorithm, FG (cascaded 1D) and FG (2D) respectively represent two cascaded 1-D channel estimation and factor graph based 2-D channel estimation algorithm based on factor graph. The BER performance, perfect CSI, represents the BER performance of the ideal channel estimate. The simulation is based on the BER performance of the ideal channel estimation and the classical linear interpolation algorithm. It can be seen from the simulation results that the linear interpolation algorithm has the worst performance because the pilot interval cannot be tracked in time when the pilot interval is slightly larger, so the performance is not ideal. Compared with the linear interpolation algorithm, based on the factor graph, the joint channel estimation algorithm performs better, and the 1-D channel estimation algorithm takes the second place. The performance of the simplified 1-D channel estimation algorithm is lost because of the algorithm has an approximation in the channel estimation process, i.e., only the transfer function node in the 1-D direction is considered, resulting in loss of information when the channel parameter information is transmitted. On the other hand, since each function node is only connected to its associated variable node, the computational complexity of the simplified algorithm is significantly reduced. The two algorithms presented in this paper have a compromise between performance and complexity.

Fig.6 and Fig.7 show the BER performance comparison of 2-D and 1-D channel estimation algorithms for different pilot intervals in frequency domain.

In the simulation, the pilot intervals in frequency domain are $D_f = 6, D_f = 10$ and $D_f = 10$, respectively selected, and the time domain interval is 6. The simulation results show that pilot interval is also an important parameter affecting the performance of system. As pilot interval decreases, the channel estimation algorithm based on factor graph approximates the accurate channel state information (CSI). Therefore, pilot-assisted channel estimation must compromise spectral efficiency and estimation performance.

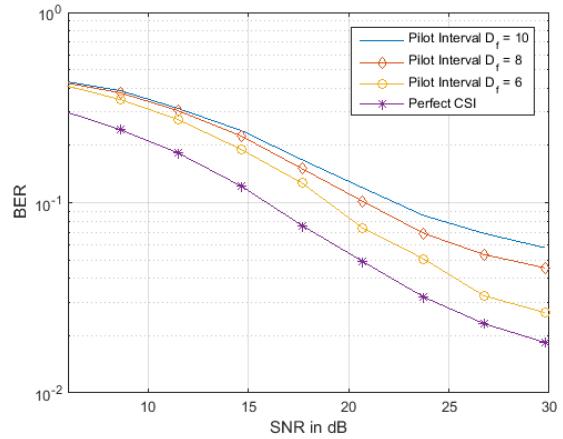


Fig. 6. BER comparisons of 2-D channel estimation algorithms at different pilot intervals.

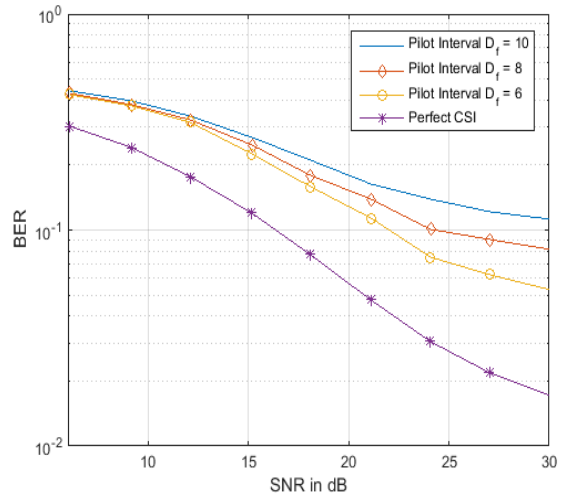


Fig. 7. Comparison of BER of cascaded 1-D channel estimation algorithm under different pilot intervals.

5. Conclusion

In this paper, channel estimation algorithm for GFDM-UWA system is proposed based on factor graphs. Firstly, the likelihood function that implements the optimal estimation of the transmitted symbols is decomposed to obtain a suitable factor graph model, and then the specific expression of the iterative estimation algorithm is derived according to the sum-product algorithm rules. The analysis and simulation results show that the proposed two-dimensional joint channel estimation algorithm can approximate the optimal estimation performance, and the simplified one-dimensional channel estimation algorithm can still achieve relatively good results under the condition of moderate computational complexity. Here the channel estimation is studied for SISO-GFDM-UWA system, and in future MIMO-GFDM-UWA channel estimation algorithms will be studied.

This is an Open Access article distributed under the terms of the Creative Commons Attribution License.







References

1. Proakis J G. "Digital Communication". New York, USA: McGraw Hill, 1995.
2. Tao Cui, C.Tellambura."Joint Channel Estimation and Data Detection for OFDM Systems via Sphere Decoding". In: *IEEE Global Telecommunications Conference*. Dallas, TX, USA, IEEE Press, 2004, pp. 3656-3660.
3. Panayirci, Erdal, Hakan Dogan, and H. Vincent Poor. "Low-complexity MAP-based successive data detection for coded OFDM systems over highly mobile wireless channels." *IEEE Transactions on vehicular Technology* 60(6), 2011, pp. 2849-2857.
4. Jiang Fan, Becker M R, Perez L C. "Time-varying Turbo Codes". *IEEE Communications Letters*,8(8), 2004, pp. 529-531.
5. Chen Rong, Zhang Haibin, Xu Youyun, et al. "Blind Receiver for OFDM Systems via Sequential Monte Carlo in Factor Graphs". *Journal of Zhejiang University -Science A*, 8(1), 2007, pp. 1-9.
6. Kchischang F R, Frey B J, Loeliger H A. "Factor Graphs and the Sum Product Algorithm". *IEEE Transactions on Information Theory*, 47(2), 2001, pp. 498-519.
7. Christian S, Jurgen L. "Estimation of Rapid Time-variant Channels for OFDM Using Wiener Filtering".In: *IEEE International Conference on Communications*. IEEE Press, Anchorage, AK, USEA, 2003, pp. 2930-2935.
8. Li Y, Cimini L J, Sollenberger N R. Robust "Channel Estimation for OFDM Systems with Rapid Dispersive Fading Channels". *IEEE Transactions on Communications*, 46(7), 1998, pp. 902-915.
9. Knievel C, Shi Z, Hoehner P A. "2D Graph-based Soft Channel Estimation for MIMO-OFDM". In: *Proc. of IEEE International Conference on Communications*. IEEE Press,Cape Town, South Africa, 2010, pp. 1-5.
10. Baddour K E, Beaulieu N C. "Autoregressive Modeling for Fading Channel Simulation". *IEEE Transactions on Wireless Communications*, 4(4), 2005, pp. 1650-1662.
11. Lingaiah.Jada and Shiyamala S., "Investigation on GFDM System for 5G Applications over Fading Channels", *Journal of Engineering Science and Technology Review*, 15(4), 2022, pp.1-8.
12. Farhang A., Marchetti N. and Doyle N., "Low Complexity Transceiver Design for GFDM," In: *IEEE Transactions on signal Processing*, 64(6), 2016, pp.1507-1518.
13. Michailow N., Mendes L., Matthe M., Gaspar I., Festag A. and Fettweis G., "Robust WHTGFDM for the Next Generation of Wireless Networks", *IEEE Communications. Lett.* 19, 2014, pp. 106-109.
14. Gaspar I., Mendes L., Matthe M., Michailow N., Festag A. and Fettweis G., "LTE- Compatible 5G PHY based on Generalized Frequency Division Multiplexing", In: *Proceedings of the 11th International Symposium on Wireless Communications Systems*, Spain: IEEE Press, 2014, pp. 209-213.
15. Fettweis G., M. Krondorf, and Bittner S., "GFDM – Generalized Frequency Division Multiplexing," In: *Vehicular Technology Conference*, Spain, 2009, pp. 1-4.
16. Antapurkar S., Pandey A and Gupta K., "GFDM Performance in terms of BER, PAPR and OOB and comparison to OFDM system", In: *2nd International Conference on Communication Systems*, Rajasthan, India, 2015, pp. 1-11.
17. Michailow N. and Fettweis G., "Low Peak-to-Average Power Ratio for Next Generation Cellular Systems with Generalized Frequency Division Multiplexing," In: *IEEE International Symp. on Int. Sig. Proc. and Comm. Sys.*,2013, pp. 651-655.
18. Michailow N., Matthe M., Gaspar I., Navarro Caldevilla A., Mendes L., Festag A., Fettweis G., "Generalized Frequency Division Multiplexing for 5th generation cellular Networks". *IEEE Transactions on Communications* 62(9), 2014, pp. 3045-3061.
19. Bandari S. K., Mani V., "Drosopoulos, Performance analysis of gfdm in various fading Channels", *COMPEL: The International Journal for Computation and Mathematics in Electrical and Electronic Engineering*, 35(1), 2016, pp. 225-244.
20. Bandari S. K., Drosopoulos A., Mani V. V., "Exact ser expressions of gfdm in nakagami-m and rician fading channels". In: *Proceedings of European Wireless, 21st Wireless Conference*, Budapest, Hungary, 2015, pp. 1-6.

Article

A Novel Integrated UWB Sensing and 8-Element MIMO Communication Cognitive Radio Antenna System

D Srikar¹, Anveshkumar Nella² , Ranjith Mamidi³, Ashok Babu⁴, Sudipta Das^{5,*} , Sunil Lavadiya⁶ ,
Abeer D. Algarni⁷ and Walid El-Shafai^{8,9} 

¹ Chaitanya Bharathi Institute of Technology, Hyderabad 500075, India

² School of EEE, VIT Bhopal University, Bhopal 466114, India

³ Vaagdevi College of Engineering, Warangal 506005, India

⁴ Institute of Aeronautical Engineering, Hyderabad 500043, India

⁵ Department of Electronics & Communication Engineering, IMPS College of Engineering and Technology, Malda 732103, India

⁶ Department of Information and Communication Technology, Marwadi University, Rajkot 360003, India

⁷ Department of Information Technology, College of Computer and Information Sciences, Princess Nourah bint Abdulrahman University, P.O. Box 84428, Riyadh 11671, Saudi Arabia

⁸ Security Engineering Lab, Computer Science Department, Prince Sultan University, Riyadh 11586, Saudi Arabia

⁹ Department of Electronics and Electrical Communications Engineering, Faculty of Electronic Engineering, Menoufia University, Menouf 32952, Egypt

* Correspondence: sudipta.das1985@gmail.com

Abstract: In this article, a cognitive radio (CR) integrated antenna system, which has 1 sensing and 24 communication antennas, is proposed for better spectrum utilization efficiency. In the 24 communication antennas, 3 different operating band antennas are realized with an 8-element MIMO configuration. The sensing antenna linked to port 1 is able to sense the spectrum that ranges from 2 to 12 GHz, whereas the communication 8-element MIMO antennas linked with ports 2 to 9, ports 10 to 17 and ports 18 to 25 perform operations in the 2.17–4.74 GHz, 4.57–8.62 GHz and 8.62–12 GHz bands, respectively. Mutual coupling is found to be less than -12 dB between the antenna elements. Peak gain and radiation efficiency of the sensing antenna are better than 2.25 dBi and 82%, respectively, whereas the peak gains and radiation efficiencies of all communication antennas are more than 2.5 dBi and 90%, respectively. Moreover, diversity characteristics of the MIMO antenna are assessed by parameters such as DG, ECC and CCL. It is found that ECC and CCL are less than 0.42 and 0.46 bits/s/Hz, respectively, and also DG is more than 9.1 dB.

Keywords: CCL; cognitive radio; DGG; ECC; MIMO; spectrum sensing; spectrum utilization efficiency



Citation: Srikar, D.; Nella, A.; Mamidi, R.; Babu, A.; Das, S.; Lavadiya, S.; Algarni, A.D.; El-Shafai, W. A Novel Integrated UWB Sensing and 8-Element MIMO Communication Cognitive Radio Antenna System. *Electronics* **2023**, *12*, 330. <https://doi.org/10.3390/electronics12020330>

Academic Editors: Naser Ojaroudi Parchin, Chan Hwang See and Raed A. Abd-Alhameed

Received: 22 November 2022

Revised: 12 December 2022

Accepted: 13 December 2022

Published: 8 January 2023



Copyright: © 2023 by the authors. Licensee MDPI, Basel, Switzerland. This article is an open access article distributed under the terms and conditions of the Creative Commons Attribution (CC BY) license (<https://creativecommons.org/licenses/by/4.0/>).

1. Introduction

In the licensed spectrum, channels are unutilized most of the time, thus leading to inefficient spectrum utilization. Hence, spectrum utilization efficiency deteriorates. The unutilized channels (i.e., licensed) can be used effectively for other applications to reduce the wastage of spectrum issue. CR technology mainly uses the concept of using the unutilized channels in the spectrum overlay approach. It is believed that the primary users in the spectrum overlay approach are the owners of the licensed spectrum and do not utilize their channels in the licensed spectrum completely. So, there exists a continuous monitoring in the radio environment to find the white spaces (i.e., spectrum holes). When a white space is detected at any moment, secondary users can use the channel that consists of the detected white space for other applications until the primary users want to use that channel. When primary users use that channel, secondary users should shift to any other unutilized licensed channels.

A new frequency-agile CR MIMO patch antenna was proposed in [1]. It comprises two patch antenna elements, which are hexagonal shaped. To achieve compactness and increase isolation, hexagonal-shaped defected ground structures are incorporated in the ground plane. The compactness is further attained by utilizing reactive loading. Varactor diodes are employed in the microstrip feed line to achieve frequency reconfigurability. Consequently, frequency tuning is achieved at 1.42–2.27 GHz. However, the proposed CR MIMO antenna cannot sense the spectrum as it does not have a sensing antenna. A frequency-reconfigurable CR MIMO antenna system for interweave scenario was presented in [2]. It comprises four reconfigurable antenna elements that are pentagonal slot-based. Varactor diodes are employed to alter the capacitance of the slot. As a result, a wide tuning range, which ranges from 3.2 GHz to 3.9 GHz, is achieved with a minimum of 100 MHz impedance bandwidth in each band. However, the proposed MIMO antenna does not have a sensing antenna. Additionally, the mutual coupling in the proposed CR MIMO antenna system is just less than -10 dB. A four-port CR MIMO antenna that works for overlay and underlay approaches for 5G applications in the 2.5–4.20 GHz range was proposed in [3]. This type of feature of the proposed antenna is obtained by controlling the operating modes of the multifunctional reconfigurable filter since the multifunctional reconfigurable filter, which works in three operational modes such as tunable bandpass filter, tunable band reject filter, and all pass filter, is integrated with UWB sensing antenna. Four filter antennas are integrated on FR-4 epoxy substrate to make a MIMO system. Additionally, they are well isolated with the help of reflectors. A two element MIMO antenna, which comprises sensing antenna operating at 2.2–7 GHz and two similar reconfigurable antennas, was proposed in [4]. By varying the capacitance of varactor diodes, reconfigurable antennas can be tuned to any frequency from 2.3 to 6.3 GHz. A four-port MIMO antenna in which two antennas are dedicated for sensing the spectrum 2.35–5.9 GHz and two other antennas are dedicated for communication was proposed. The reconfigurable narrowband antennas for communication can be tuned to any frequency from 2.6 to 3.6 GHz.

The undesired radio frequency interference can be avoided when sensing antenna and communication antennas are well isolated. Consequently, good performance is guaranteed for a CR device. When spectrum holes change rapidly in the radio environment and a single reconfigurable antenna is used for sensing the spectrum and performing the communication tasks, it becomes very hard for the antenna to switch from sensing mode to communication mode and vice versa. Moreover, in case of reconfigurable antennas, losses become high due to the presence of lumped elements, diodes, etc. Consequently, the performance of the antenna deteriorates to some extent. Additionally, it is noticed that the existing CR MIMO antennas in the literature [5–19] have a small tuning range since it is quite hard to tune the antenna to a desired frequency in a wide bandwidth. The drawbacks, which are associated with the available reconfigurable CR antennas in the literature, are power consumption, use of extra hardware, nonlinear effects of switches and biasing line effects. Moreover, the reconfigurable mechanisms may require the presence of motors and some additional biasing circuitry at times. Nevertheless, they have been extensively used by many researchers to make the antenna compact and tunable. Additionally, they are very difficult to implement in real time. In addition, the available reconfigurable CR antennas in the literature are able to perform only communication operations despite multiple spectrum holes being identified. Since it is well known that low profile planar antennas are advantageous and reconfigurable antennas have some unavoidable drawbacks [20,21], integrated sensing antennas and multiple communication antenna systems [22–26] are treated as the best alternative to reconfigurable antenna systems for CR applications. These antenna systems have a striking feature of performing multiple communication operations simultaneously due to the presence of multiple communication antennas. Since the spectrum is utilized in an efficient manner by performing multiple communication operations simultaneously, spectrum utilization efficiency increases significantly with these antenna systems. Whenever a white space (spectrum hole) identified by the sensing antenna matches with the operating frequency of the communication antenna, the respective communication antenna is given

access to the secondary users. Otherwise, it is terminated by a 50-ohm load. In integrated sensing antennas and multiple communication antenna systems, communication antennas are selected by an excitation switching reconfigurable mechanism.

In this article, a cognitive radio (CR) integrated antenna system, which has 1 sensing and 24 communication antennas, is proposed for better spectrum utilization efficiency. The sensing antenna linked to port 1 is able to sense the spectrum that ranges from 2 to 12 GHz, whereas the communication 8-element MIMO antennas linked with ports 2 to 9, ports 10 to 17 and ports 18 to 25 perform operations in the 2.17–4.74 GHz, 4.57–8.62 GHz and 8.62–12 GHz bands, respectively. Mutual coupling is less than -12 dB. The HFSS EM simulation tool is used for the proposed structure design. The fabricated prototype is verified and a good agreement is noted between the simulated and measured results. To the best of our knowledge, this is the only sensing and 8-element MIMO communication integrated antenna system that has the notable feature of performing a maximum of three communication operations concurrently in the CR environment. Moreover, this antenna system is the best alternative for all reconfigurable CR MIMO antenna systems. Additionally, it is less complex compared to all the other existing CR MIMO antennas in the literature.

The rest of the paper is organized as follows. The design of the proposed structure, UWB and narrow band antenna design steps, along with performance characteristics, are reported. Later, results and discussion on each and every performance parameter are provided. Thereafter, MIMO diversity characteristics are discussed. Finally, the conclusion of the work is given.

2. Twenty-Five Port CR Integrated Antenna System

The proposed CR integrated antenna system schematic is shown in Figure 1. The performance and 10 dB return loss bandwidth of each antenna are given in Table 1. The dimensions of the proposed CR integrated antenna system are given in Table 2. Sensing antenna is linked to port 1, whereas the communication 8-element MIMO antennas are linked with ports 2 to 9, ports 10 to 17 and ports 18 to 25. FR4 epoxy substrate of a thickness of 1.6 mm is used in the present design. Additionally, the design procedures for sensing and communication antennas are explained in this section.

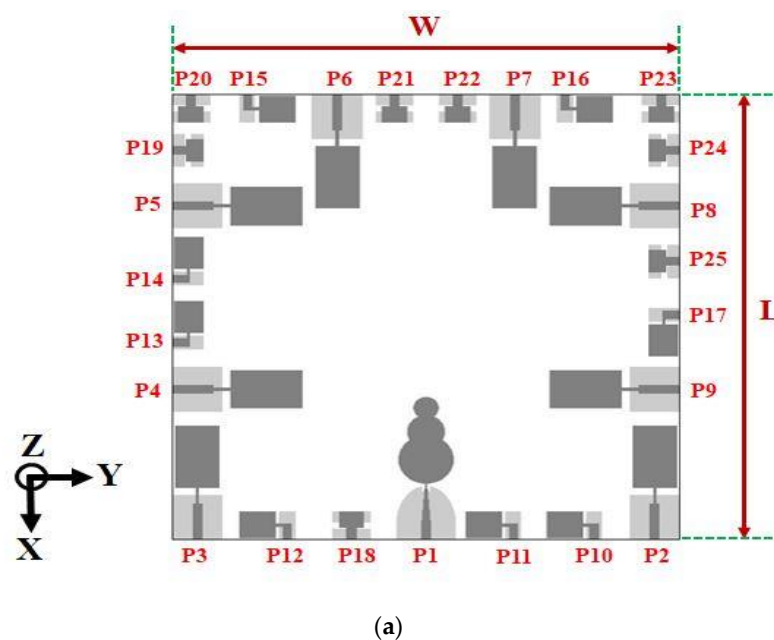


Figure 1. Cont.

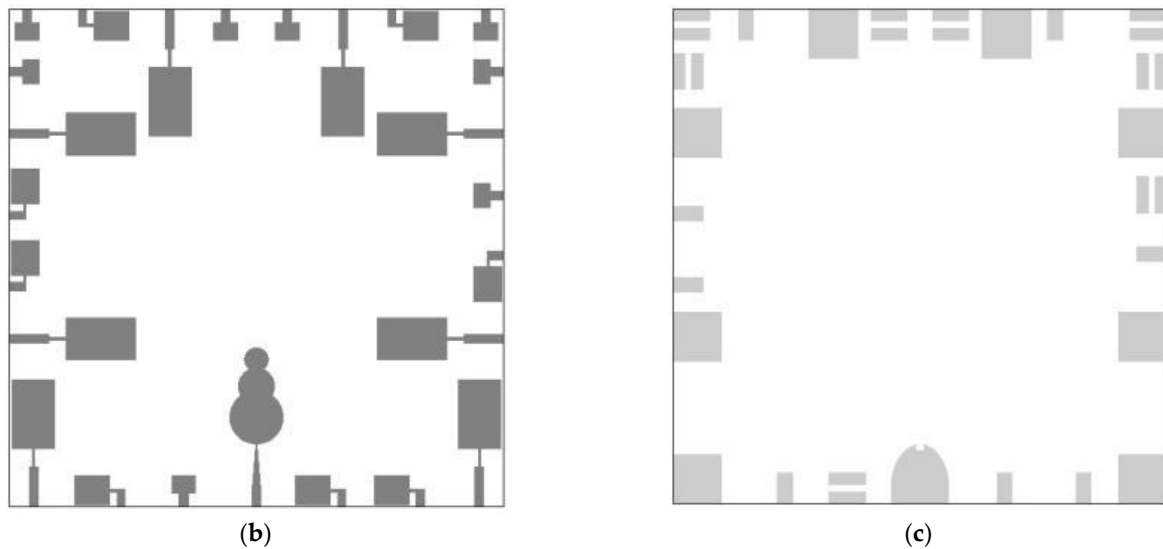


Figure 1. Geometry of the 25-port CR MIMO antenna. (a) Structure of the antenna. (b) Top view. (c) Back view.

Table 1. Specifications of the 25-port CR MIMO antenna.

Antenna	Usage	10 dB Return Loss Bandwidth
Ant (P1)	Sensing	2–12 GHz
Ant (P2) to Ant (P9)	Communication	2.17–4.74 GHz
Ant (P10) to Ant (P17)	Communication	4.57–8.62 GHz
Ant (P18) to Ant (P25)	Communication	8.62–12 GHz

Table 2. Dimensions of the 25-port CR MIMO antenna.

Parameter	Dimension (mm)	Parameter	Dimension (mm)
R1	8.78	l1	22.5
R2	5.28	w1	14
R3	4	lg1	16
p1	1.16	wg1	16
lg	5	ln1	5.5
wg	18.98	wn1	1
wf	3	p2	2.5
ln	1.57	lw1	13
wn	4.5	wf1	3
p4	0.2	l2	11.5
wf3	3.2	w2	9.5
W	160	L	160
lg2	5	w3	8
wg2	10	lm	4
wf2	3	wm	12
wn2	1.1	lg3	4
p3	0.95	wg3	12
l3	5.8	g1	1.16

3. Design Process of the Sensing Antenna Linked with Port 1

The structure of the sensing antenna that operates at 2–12 GHz is shown in Figure 2. As depicted in Figure 3, the design process is finished in five steps. A traditional circular shaped monopole antenna (i.e., Ant I in Figure 3) is designed in the first step, and its impedance bandwidth ranges from 2.6 GHz to 10.6 GHz, as illustrated in Figure 4. The electrical lengthening is performed in the second step by combining a circular patch of radius R2 with the circular radiator of radius R1, as depicted in Ant II in Figure 3. As

a result, the lower band edge (LBE) frequency of Ant II in Figure 1 is less than the LBE frequency of Ant I in Figure 4. However, the impedance matching of Ant II in Figure 4 at 3–5.75 GHz is poor. The electrical lengthening is further performed in the third step by combining a circular patch of radius R_3 with the radiator of Ant II. Consequently, the LBE frequency of Ant III in Figure 4 becomes 2.07 GHz, which is less than the LBE frequency of Ant II in Figure 4, but the reflection coefficient curve of Ant III in Figure 4 is below -10 dB at 2.55–4.3 GHz and 8.1–8.8 GHz. So, to attain impedance matching throughout a wideband, i.e., 2–12 GHz, the ground plane of Ant IV in Figure 3 is made semi-elliptical shaped and some portion of the 50-ohm feed line is tapered towards the radiator. Thus, better impedance matching is achieved compared to Ant III in Figure 4, but the reflection coefficient of Ant IV is a bit better than -10 dB at 2.82–3.57 GHz and 5.56–6.34 GHz, as shown in Figure 4. In the last stage, good impedance matching is achieved over a wideband (i.e., 2–12 GHz) by etching a rectangle-shaped notch in the ground plane of Ant V.

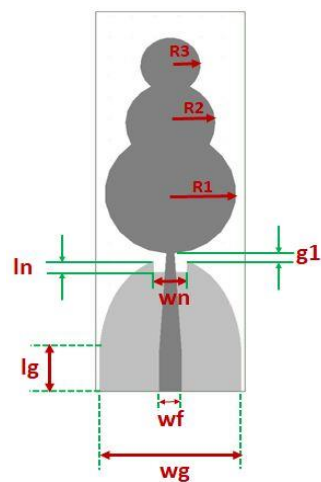


Figure 2. Schematic of the antenna linked with port 1.

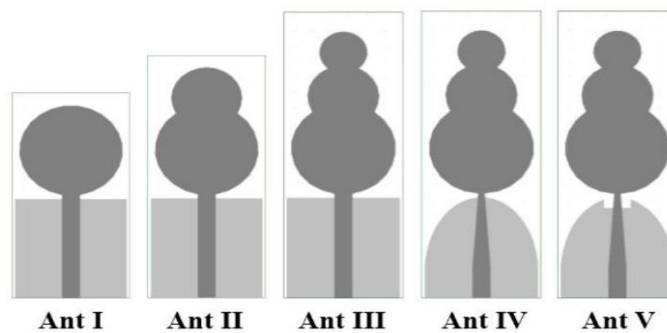


Figure 3. Evolution of antenna linked with port 1.

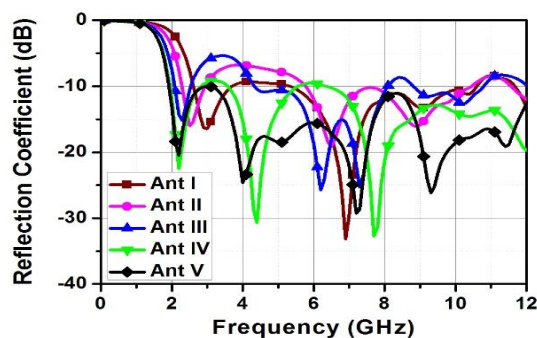


Figure 4. Evolution of the antenna linked with port 1.

As a result, the lower band edge (LBE) frequency of Ant II in Figure 1 is less than the LBE frequency of Ant I in Figure 4. However, the impedance matching of Ant II in Figure 4 at 3–5.75 GHz is poor. The electrical lengthening is further performed in the third step by combining a circular patch of radius R3 with the radiator of Ant II. Consequently, the LBE frequency of Ant III in Figure 4 becomes 2.07 GHz, which is less than the LBE frequency of Ant II in Figure 4, but the reflection coefficient curve of Ant III in Figure 4 is below -10 dB at 2.55–4.3 GHz and 8.1–8.8 GHz. So, to attain impedance matching throughout a wideband, i.e., 2–12 GHz, the ground plane of Ant IV in Figure 3 is made semi-elliptical shaped and some portion of the 50-ohm feed line is tapered towards the radiator. Thus, better impedance matching is achieved compared to Ant III in Figure 4, but the reflection coefficient of Ant IV is a bit better than -10 dB at 2.82–3.57 GHz and 5.56–6.34 GHz, as shown in Figure 4. In the last stage, good impedance matching is achieved over a wideband (i.e., 2–12 GHz) by etching a rectangle-shaped notch in the ground plane of Ant V.

4. Design Process of the Communication Antennas Linked with P2 to P9

The structure of the antenna linked with port 2 is depicted in Figure 5. The antenna linked with port 2 is targeted to operate at low frequencies and its design process ends in two stages. In the first stage, a normal monopole antenna with rectangle-shaped patch is designed, as illustrated in Figure 6. Furthermore, this antenna is realized with an 8-element MIMO configuration at ports P2 to P9. Dimensions of the rectangular radiator are selected in such a way that the LBE frequency of the antenna linked with port 2 is about 2.3 GHz. The mathematical formula for calculating the LBE of Ant I in Figure 6 is given below.

$$f_{LAntI(P2)} = \frac{7.2}{(l1 + r1 + p2) \times k} \text{ GHz} \tag{1}$$

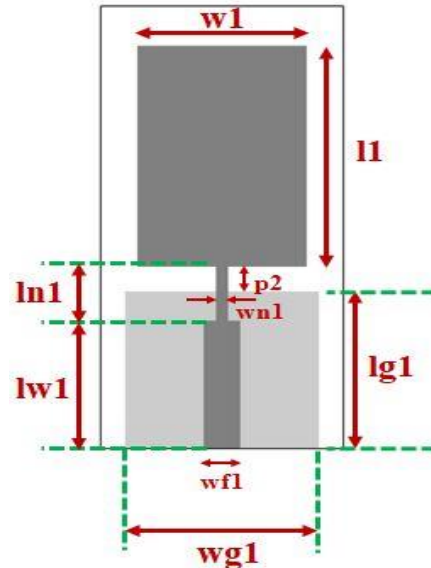


Figure 5. Schematic of the antennas linked with P2 to P9.

In Equation (1), $l1$ and $p2$ are the length of the rectangular patch and feed gap in centimeters, respectively. The term ' $r1$ ' in centimeters can be calculated from the width of rectangular patch since $r1 = \frac{w1}{2\pi}$. The term ' k ' is constant and is equal to 1.15.

After finding out the values of $l1$, $r1$, $p2$ and k , the LBE frequency of Ant I in Figure 1 is found as 2.3 GHz, whereas it is found as 2.34 GHz in simulation. It is evident from Figure 7 that Ant I operates at 2.34–2.9 GHz and 4.9–7.75 GHz. As the antenna linked with port 2 is aimed to operate at low frequencies, a 1 mm width narrow strip line is placed between rectangular patch and the 50-ohm feed line of 3 mm width in the second stage, as depicted in Ant II in Figure 6. A parametric study is performed by altering the length of the

1 mm strip line, as depicted in Figure 8. It is obvious from Figure 8 that lower band edge frequency does not change much when the 1 mm strip line’s length changes. Additionally, bandwidth slightly decreases when the 1 mm strip line’s length increases. Finally, the 1 mm strip line’s length is selected as 5.5 mm as good impedance matching and large -10 dB reflection coefficient bandwidth (i.e., 2.17–4.75 GHz) are achieved.

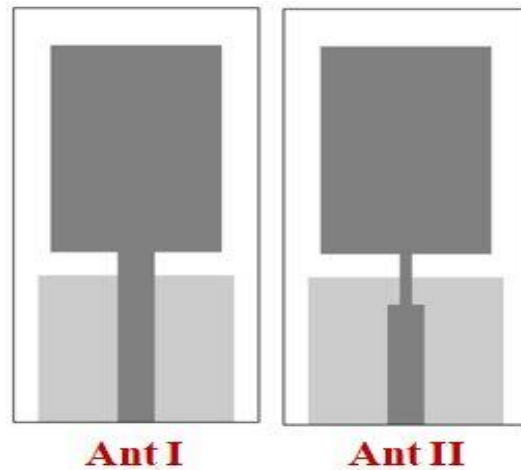


Figure 6. Evolution of the antennas linked with P2 to P9.

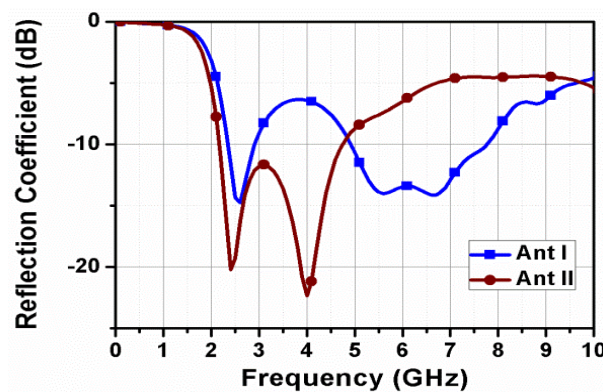


Figure 7. Reflection coefficients of the antennas in intermediate steps of the antenna linked with port 2.

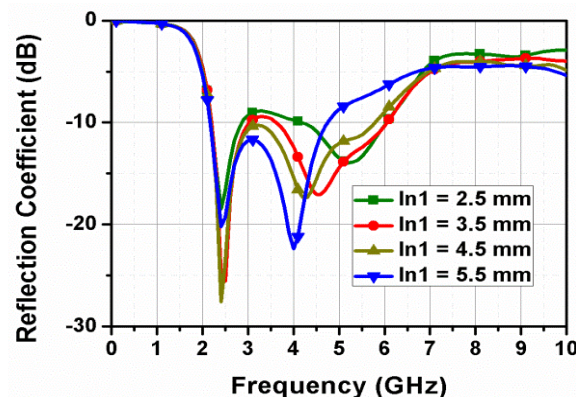


Figure 8. Reflection coefficients of the antenna linked with port 2 for different values of $ln1$.

5. Design Process of the Communication Antennas Linked with P10 to P17

The structure of the communication antennas linked with port 10 is depicted in Figure 9. A bent microstrip line feed is used to achieve good impedance matching in the appropriate band.

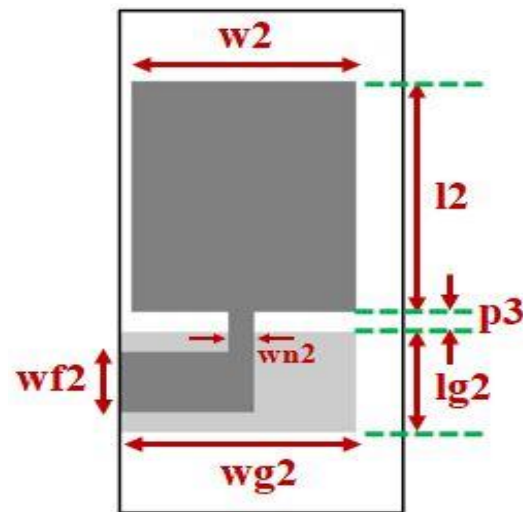


Figure 9. Schematic of the antennas linked with P10 to P17.

The design process of the communication antenna linked with port 10 ends in two stages. In the first stage, a rectangular radiator of length 11.5 mm and width 9.5 mm is fed by a bent microstrip line feed, as depicted in Ant I in Figure 10. Furthermore, this antenna is realized with an 8-element MIMO configuration at ports P10 to P17. The mathematical formula for calculating the LBE of Ant I in Figure 10 is given below.

$$f_{LAntI(P10)} = \frac{7.2}{(l2 + r2 + p3) \times k} \text{ GHz} \tag{2}$$

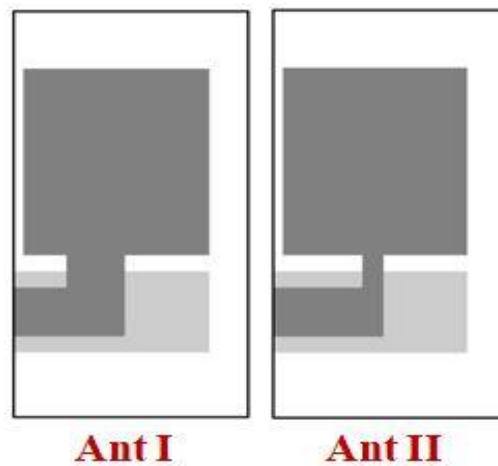


Figure 10. Evolution of the antennas linked with P10 to P17.

In Equation (2), $l2$ and $p3$ are the length of the rectangular patch and feed gap in centimeters, respectively. The term ' $r2$ ' in centimeters can be calculated from the width of the rectangular patch since $r2 = \frac{w2}{2\pi}$. The term ' k ' is constant and is equal to 1.15. After finding out the values of $l2$, $r2$, $p3$ and k , the LBE frequency of Ant I in Figure 10 is found as 5.15 GHz, whereas it is found as 4.95 GHz in simulation, as shown in Ant I in Figure 11. In the next stage, the reflection coefficient performance is analyzed by altering the width of the strip line of length l_n . As illustrated in Figure 12, the strip line of a width of 1.1 mm offers best impedance matching among different widths of strip line of length l_n and the return loss is better than 10 dB in 4.6–8.7 GHz.

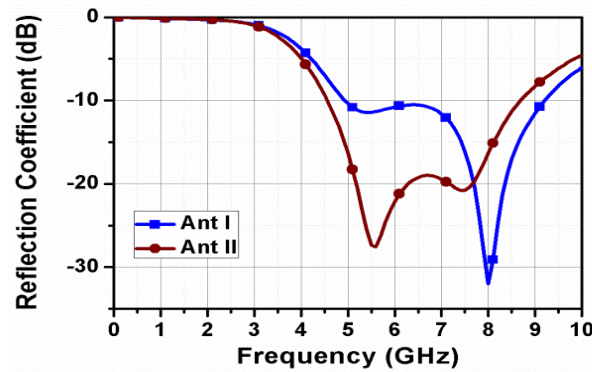


Figure 11. Reflection coefficients of the antennas in intermediate steps of the antenna linked with port 10.

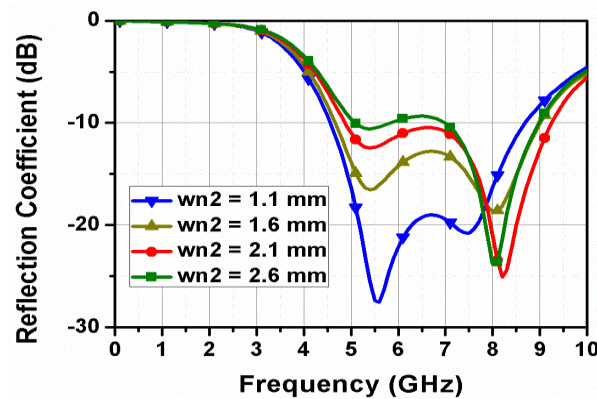


Figure 12. Reflection coefficients of the antenna linked with port 10 for different values of w_{n2} .

6. Design Process of the Communication Antennas Linked with P18 to P24

The structure of the communication antennas linked with P18 to P24 is depicted in Figure 13. Since the communication antennas linked with ports 2 and 10 are designed to operate at 2.17–4.74 GHz and 4.57–8.62 GHz, respectively, it is aimed to design a communication antenna that operates at frequencies which are greater than 8.62 GHz to cover the complete FCC UWB of 3.1–10.6 GHz. Furthermore, this antenna is realized with an 8-element MIMO configuration at ports P18 to P24. As depicted in Figure 14, the design process of the communication antenna linked with port 18 ends in two stages. In the first stage, a normal monopole antenna with a rectangle-shaped patch is designed, as illustrated in Figure 14. The length and width of the rectangular patch are selected in such a way that the LBE frequency is approximately 8.6 GHz.

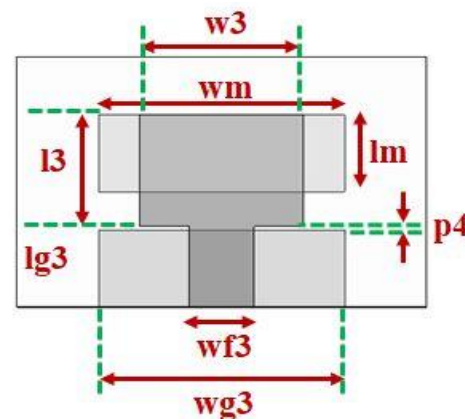


Figure 13. Schematic of the antennas linked with P18 to P24.

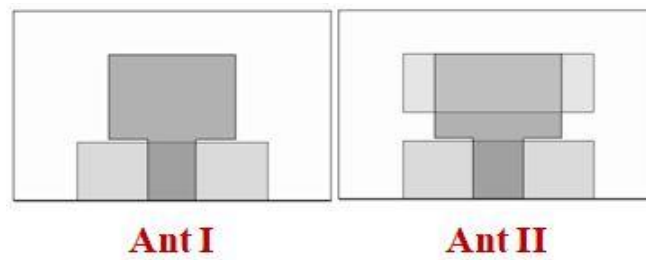


Figure 14. Evolution of the antennas linked with P18 to P24.

The mathematical formula for calculating the LBE frequency of Ant I in Figure 14 is given as:

$$f_{LAntI(P18)} = \frac{7.2}{(l3 + r3 + p4) \times k} \text{ GHz} \tag{3}$$

where l3 and p4 are length of the rectangular patch and feed gap in centimeters, respectively. The term 'r3' in centimeters is expressed in terms of width of the rectangular patch (i.e., $r3 = \frac{w3}{2\pi}$). The term 'k' is constant and is equal to 1.15. After substituting the values of l3, r3, p4 and k in Equation (3), the LBE frequency of Ant I in Figure 14 is found as 8.6 GHz, whereas it is found as 8.5 GHz in simulation, as shown in Ant I in Figure 15.

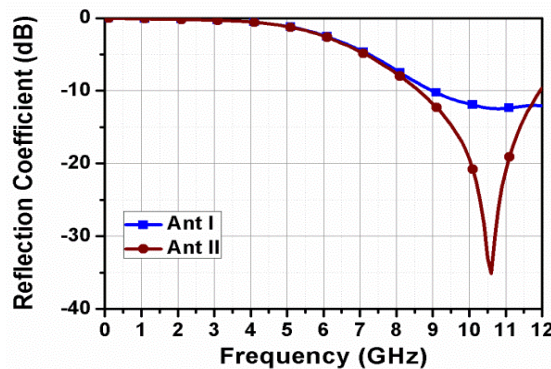


Figure 15. Reflection coefficients of the antennas in intermediate steps of the antenna linked with port 18.

It is seen from Figure 15 that the reflection coefficient curve of Ant I in Figure 1 is below -10 dB from 8.5 GHz and impedance matching is just decent. To make the lower band edge frequency 8.6 GHz and improve impedance matching, a rectangular-shaped patch is printed on the back portion of the substrate and the width of the 50-ohm feed line is chosen as 3.2 mm in the next stage. Figure 16 depicts a parametric study performed by altering the feed line's width. It is concluded from Figure 16 that the desired performance is achieved with a feed line of a width of 3.2 mm.

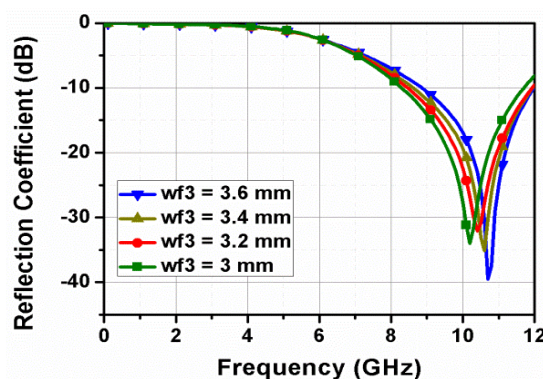


Figure 16. Reflection coefficient of the antenna linked with port 10 for different values of wf3.

7. Results and Discussions

After designing a sensing antenna and three communication antennas, the sensing antenna and eight copies of each communication antenna are placed as depicted in Figure 17.

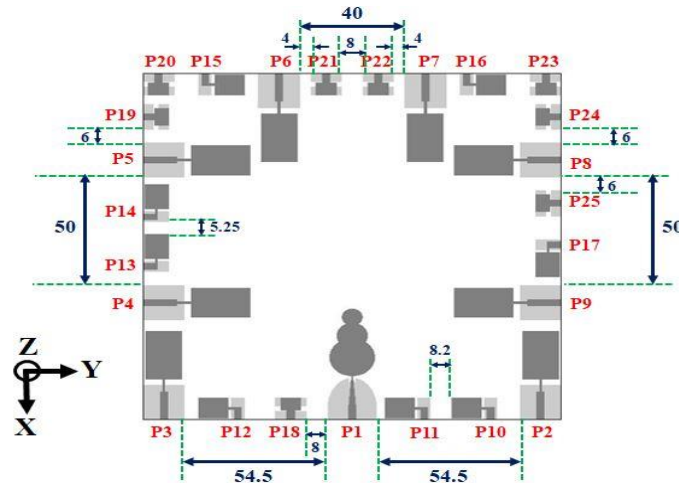


Figure 17. Inter-elemental spacing of the 25-port CR MIMO antenna.

The reflection coefficients of all antennas in the proposed 25-port CR MIMO antenna are depicted in Figures 18–20. An Agilent N5232A PNA-L network analyzer was used to check the correctness of the antenna. Good isolation between two antennas, without using any decoupling mechanism, can be attained in four possible cases. In the first case, low mutual coupling can be attained by placing two antennas in orthogonal fashion. In the second case, good isolation can be attained between two adjacent antennas that are similar to each other when the separation between those two antennas is greater than the one-fourth of the wavelength corresponding to their LBE frequency. In the third case, good isolation can be attained between two different antennas when the distance between them is greater than one-fourth of the wavelengths corresponding to their LBE frequencies. In the fourth case, if two similar antennas are even separated vertically at a distance that is slightly less than one-fourth of the wavelength corresponding to their LBE frequency, low mutual coupling can be attained between them. It can be seen from Figures 21–23 that an isolation of better than 12 dB is attained without using any decoupling mechanisms.

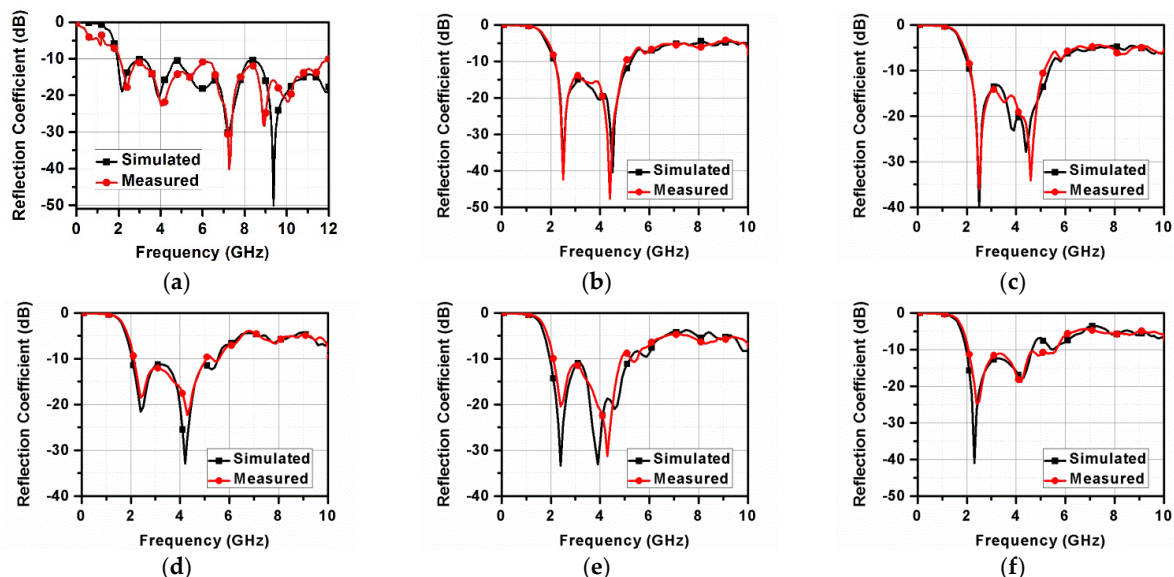


Figure 18. Cont.

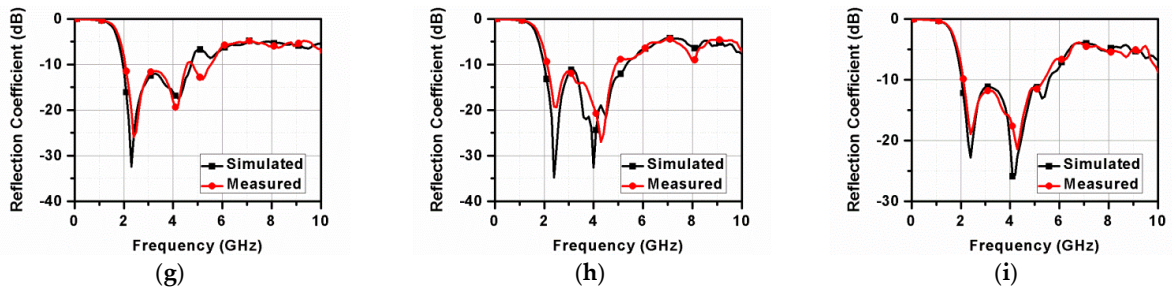


Figure 18. Plot of (a) S_{11} , (b) S_{22} , (c) S_{33} , (d) S_{44} , (e) S_{55} , (f) S_{66} , (g) S_{77} , (h) S_{88} , (i) S_{99} .

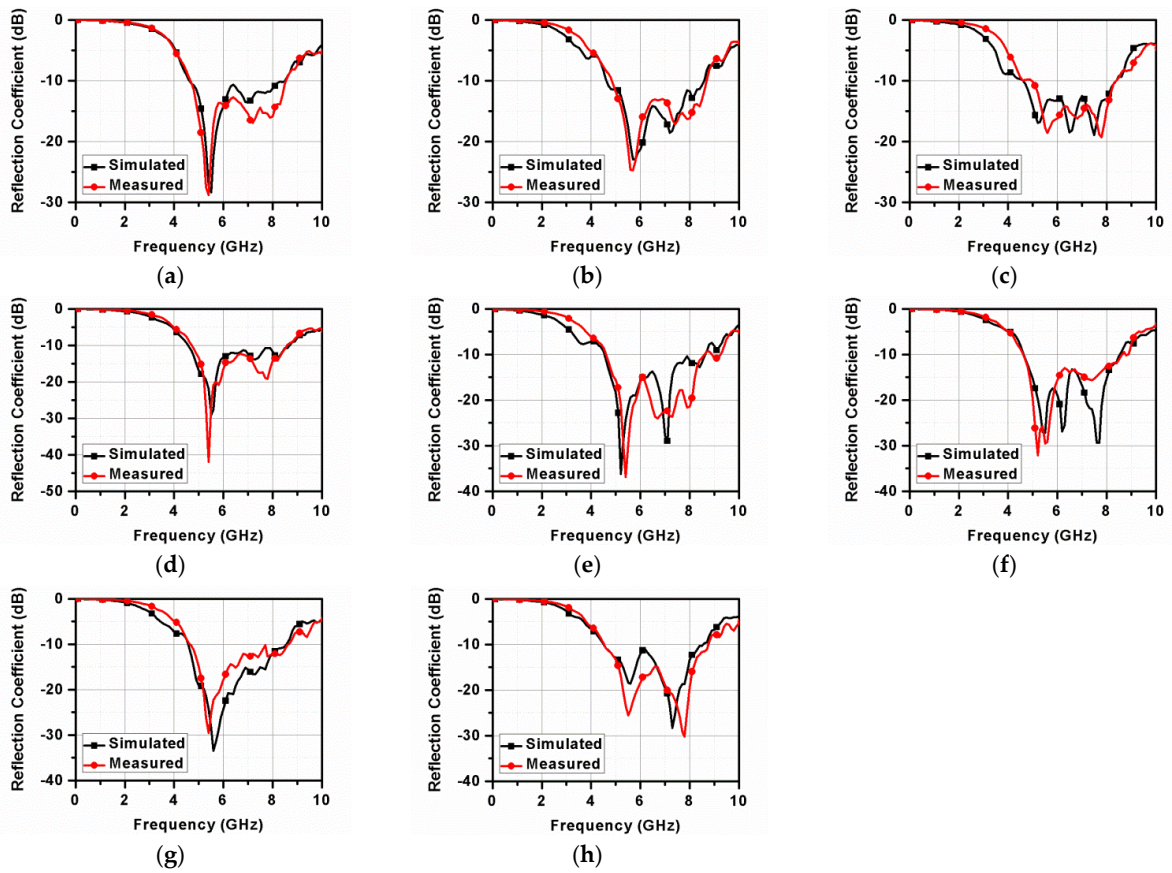


Figure 19. Plot of (a) $S_{10\ 10}$, (b) $S_{11\ 11}$, (c) $S_{12\ 12}$, (d) $S_{13\ 13}$, (e) $S_{14\ 14}$, (f) $S_{15\ 15}$, (g) $S_{16\ 16}$, (h) $S_{17\ 17}$.

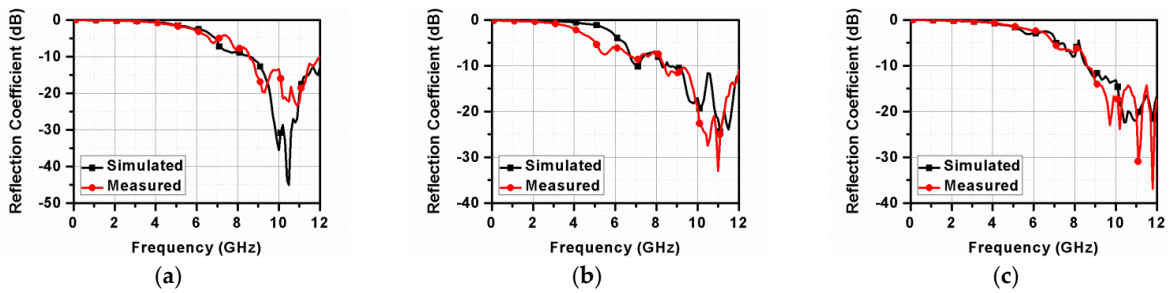


Figure 20. Cont.

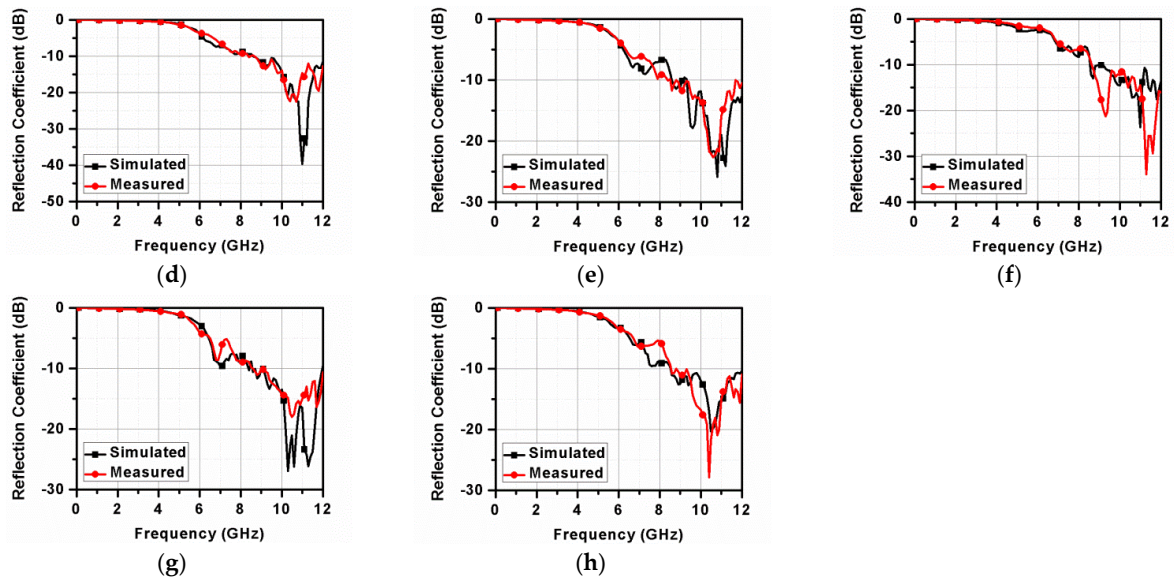


Figure 20. Plot of (a) $S_{18\ 18}$, (b) $S_{19\ 19}$, (c) $S_{20\ 20}$, (d) $S_{21\ 21}$, (e) $S_{22\ 22}$, (f) $S_{23\ 23}$, (g) $S_{24\ 24}$, (h) $S_{25\ 25}$.

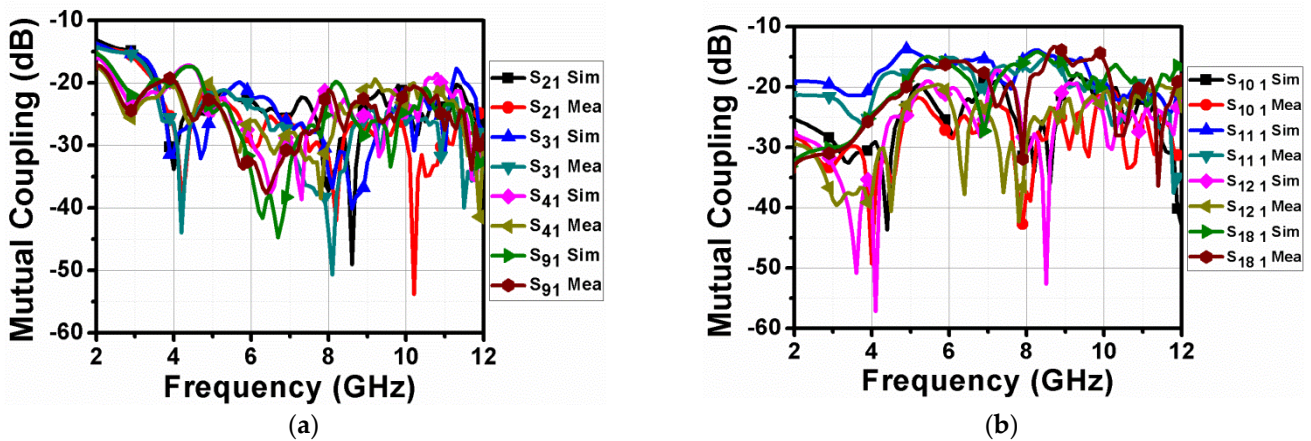


Figure 21. Mutual coupling between sensing and communication antennas (a) S_{21} , S_{31} , and S_{41} (b) $S_{10\ 1}$, $S_{11\ 1}$, $S_{12\ 1}$, and $S_{18\ 1}$.

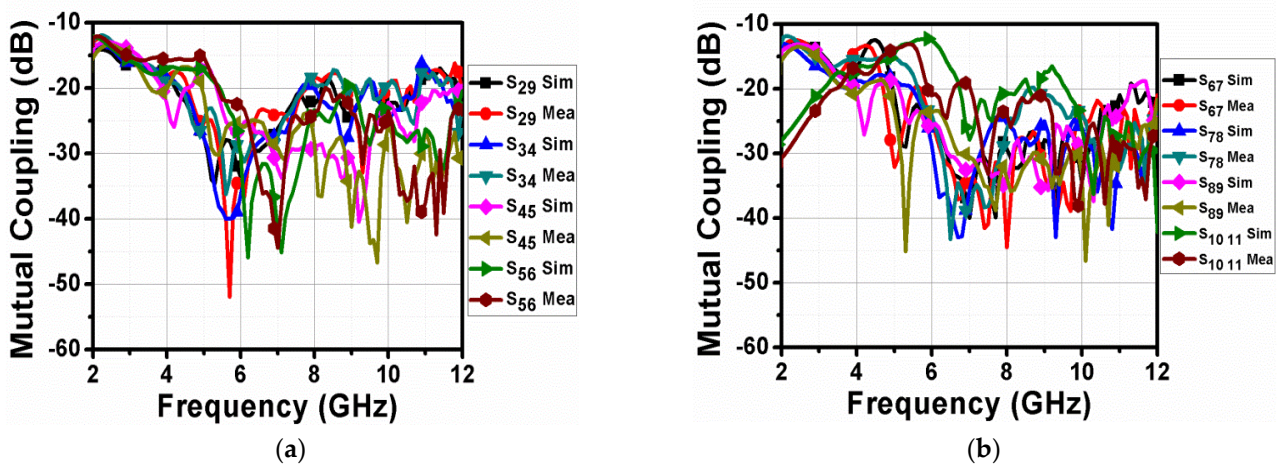


Figure 22. Cont.

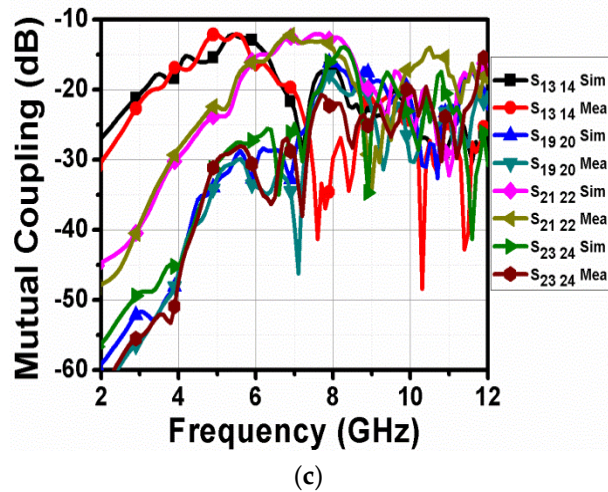


Figure 22. Mutual coupling between identical communication antennas (a) S_{29} , S_{34} , S_{45} , and S_{56} (b) S_{67} , S_{78} , S_{89} , and $S_{10\ 11}$ (c) $S_{13\ 14}$, $S_{19\ 20}$, $S_{21\ 22}$, and $S_{23\ 24}$.

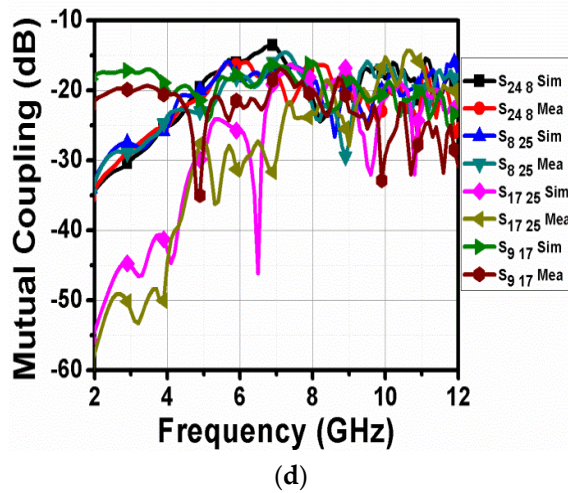
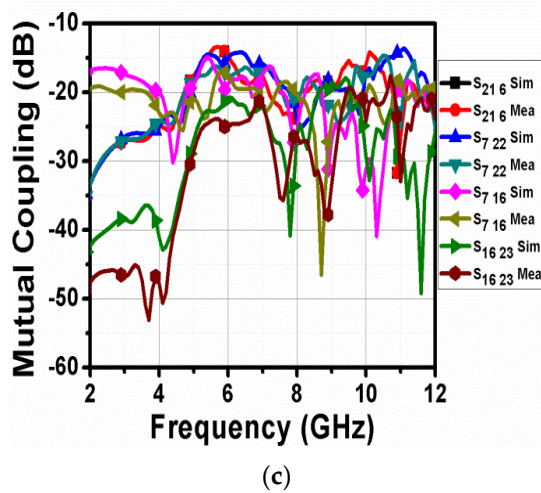
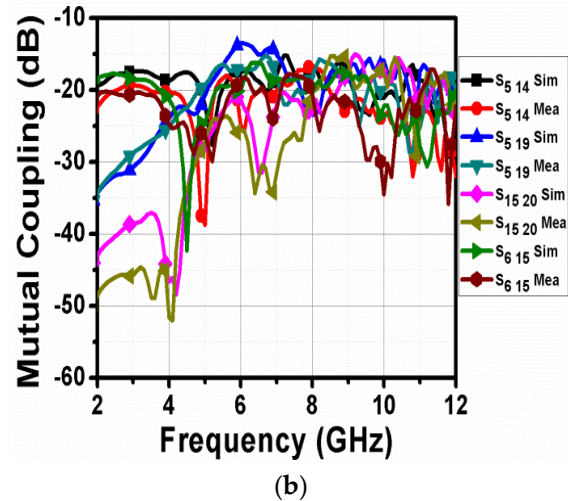
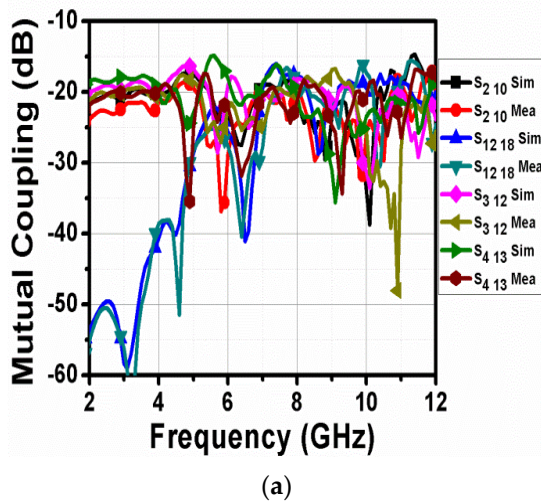


Figure 23. Mutual coupling between non-identical communication antennas. (a) $S_{2\ 10}$, $S_{12\ 18}$, $S_{3\ 12}$, and $S_{4\ 13}$ (b) $S_{5\ 14}$, $S_{5\ 19}$, $S_{15\ 20}$, and $S_{6\ 15}$ (c) $S_{21\ 6}$, $S_{7\ 22}$, $S_{7\ 16}$, and $S_{16\ 23}$ (d) $S_{24\ 8}$, $S_{8\ 25}$, $S_{17\ 25}$, and $S_{9\ 17}$.

In the proposed 25-port MIMO antenna system, if any two antennas are considered, they come under any one of the above four discussed cases. Hence, all the antennas in

the proposed 25-port CR MIMO antenna system are well isolated. The mutual coupling of other possible combinations is not shown in Figures 21–23 since two antennas in those combinations are separated by large distances. So, mutual coupling of better than -15 dB is guaranteed. Pyramidal horn antenna and the proposed CR MIMO antenna are used as transmitting and receiving antennas, respectively, in an anechoic chamber while measuring radiation patterns. A microwave analog signal generator is used to connect the transmitting antenna. In the far-field region, the designed antenna connected to a coaxial detector is kept in receiving mode and used as receiving antenna. The far-field patterns of the sensing antenna are depicted in Figure 24. The communication antennas linked with ports 2, 10 and 18 are illustrated in Figures 25–27, respectively. Dipole-natured patterns and nearly omnidirectional patterns are attained at low (2.5 and 5 GHz) and high frequencies (7.5 and 10 GHz), respectively, whereas dipole-natured patterns are attained in both the planes in case of communication antennas. The far-field patterns of the communication antennas accessed at ports 2, 10 and 18 are similar to that of a dipole antenna at 3 GHz, 6 GHz and 9 GHz, respectively, as depicted in Figures 25–27.

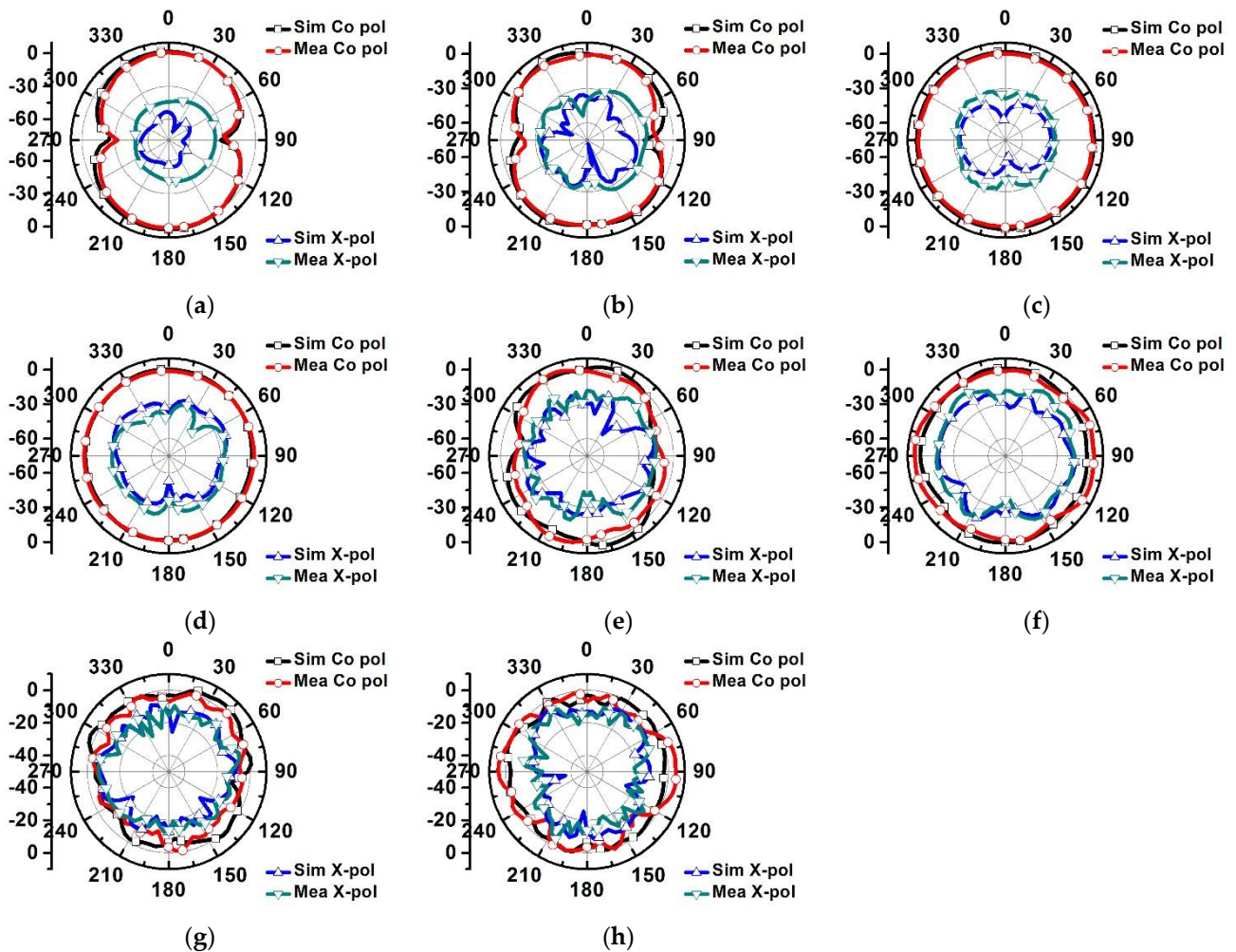


Figure 24. Far-field patterns of the sensing antenna in orthogonal planes at (a) 2.5 GHz (XZ), (b) 2.5 GHz (YZ), (c) 5 GHz (XZ), (d) 5 GHz (YZ), (e) 7.5 GHz (XZ), (f) 7.5 GHz (YZ), (g) 10 GHz (XZ), (h) 10 GHz (YZ).

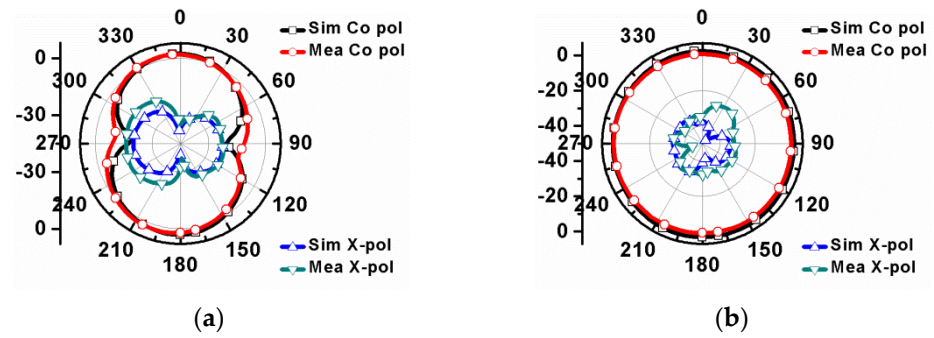


Figure 25. Far-field patterns of the communication antenna linked with port 2 at (a) 3 GHz (XZ) and (b) 3 GHz (YZ).

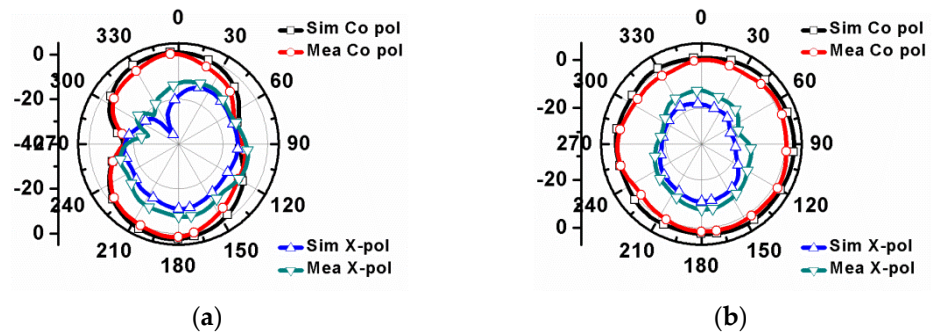


Figure 26. Patterns of the communication antenna linked with port 10 at 6 GHz in (a) XZ and (b) YZ.

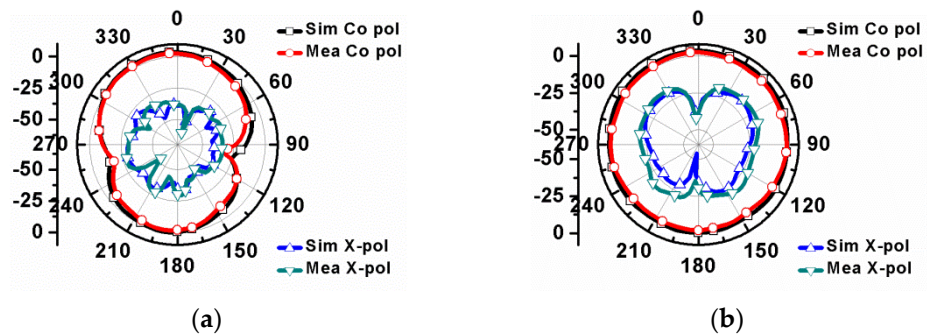


Figure 27. Far-field patterns of the communication antenna linked with port 18 at (a) 9 GHz (XZ) and (b) 9 GHz (YZ).

The slight shifts and little deviations in the resonances of the reflection coefficient curves may be because of the faults in fabrication of the prototype, material impurities, and imperfections in soldering and connector losses. However, the measured reflection coefficients of all the communication antennas in the 25-port MIMO antenna are below -10 dB in their impedance bandwidths, which indicates that the simulated reflection coefficient results of the 25-port CR MIMO antenna are in good agreement with the measured reflection coefficient results. The cross polarization levels of all the antennas in the proposed antenna are less than -20 dB, as shown in Figures 24–27. It indicates that the vertically polarized surface currents are more dominant than the horizontally polarized surface currents in all the antennas in the proposed 25-port CR MIMO antenna. Moreover, the obtained omnidirectional radiation patterns of all the antennas are well suitable for CR MIMO applications.

The radiation efficiency and peak gain of the sensing antenna are illustrated in Figures 28 and 29, respectively. It is seen that the simulated peak gain and radiation efficiency of the sensing antenna are better than 82% and 2.25 dBi, respectively. The radiation efficiencies and peak gains of the communication antennas are illustrated in

Figures 30 and 31, respectively. It is obvious from Figures 30 and 31 that the simulated peak gains and radiation efficiencies of the sensing antenna are better than 90% and 2.5 dBi, respectively. The measured peak gains are slightly less than the simulated peak gains because of substrate losses, magnetic field of the earth and errors in measurement. The fabricated prototype of the proposed 25-port CR MIMO antenna is provided in Figure 32.

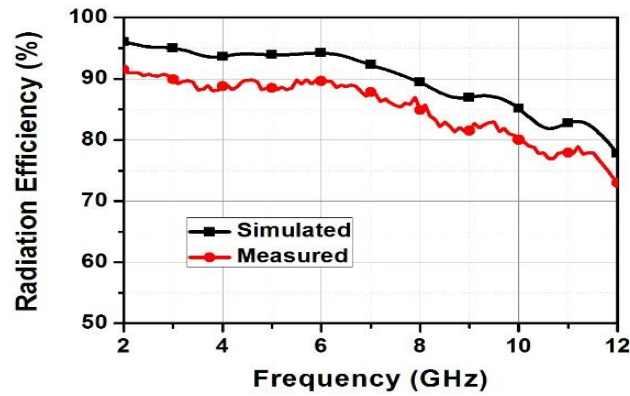


Figure 28. Radiation efficiency of the sensing antenna.

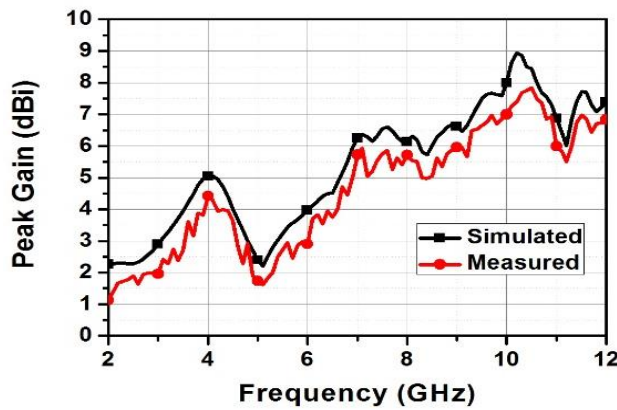


Figure 29. Peak gain of the sensing antenna.

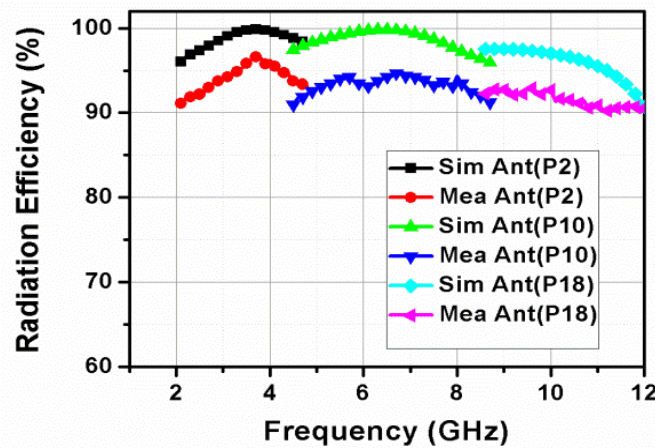


Figure 30. Radiation efficiencies of the communication antennas.

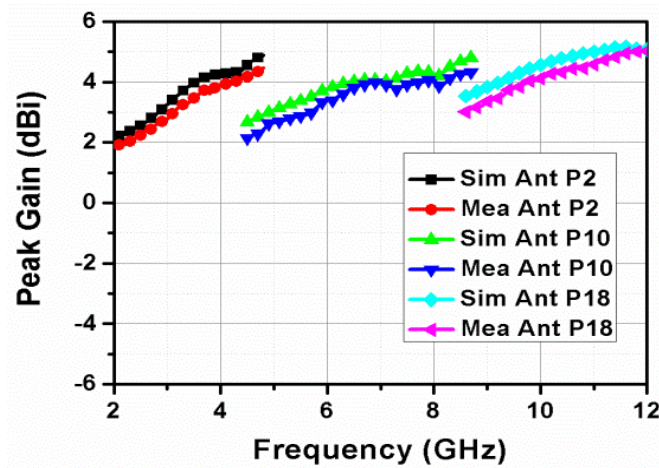


Figure 31. Peak gains of the communication antennas.

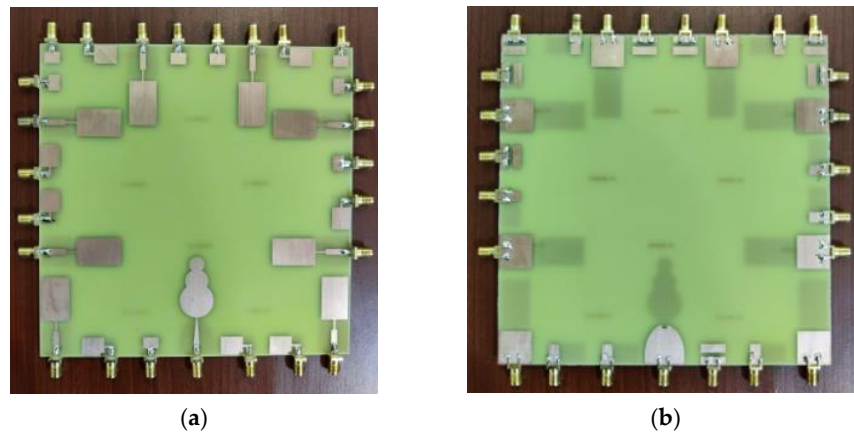


Figure 32. Fabricated prototype of the 25-port CR MIMO antenna. (a) Top view. (b) Bottom view.

It can be observed from Table 3 that no CR 8-element MIMO antennas appear in the existing literature. Additionally, the proposed 8-element MIMO antenna achieves polarization diversity and covers all communication bands from 2.17 to 12 GHz. Moreover, it does not have any switching elements such as PIN diodes, MEMS, varactor diodes, or other factors.

Table 3. Comparison of the 25-port CR MIMO antenna with other antennas in the literature.

Ref.	Size (mm ²)	Range of the Sensing Antenna (GHz)	Range Covered by Communication Antennas (GHz)	Min. Isolation (dB)	n-Element MIMO Antenna	Reconfiguration Mechanism
[1]	50 × 100	-	1.42–2.27	12	2	Varactor diodes
[2]	60 × 120	-	3.2–3.9	10	4	Varactor diodes
[3]	109 × 109	2–5.7	2.5–4.2	15	4	PIN and Varactor diodes
[4]	60 × 40	2.2–7	2.3–6.3	18	2	Varactor diodes
[5]	100 × 120	2.3–5.5	2.5–4.2	15	4	PIN and Varactor diodes
[6]	60 × 120	1–4.5	0.9–2.6	12.5	2	PIN and Varactor diodes
[7]	65 × 120	0.72–3.44	A few frequencies in 0.72–3.44	15.5	2	PIN and Varactor diodes
[8]	52.2 × 35	1.7–10.6	5.1–5.5, 6.6–7.2 and 9.7–10.2	15	2	-
[9]	110 × 110	-	1.73–2.28 and 2.45	10	2	Varactor diodes
[10]	110 × 70	2.45–5.3	2.5–3.6	12	4	Varactor diodes
[11]	152 × 126	2.4–6	5.8–6.3	20	4	PIN diodes
[12]	24 × 25	-	2.4, 3.5, 5.25	25	2	PIN diodes
This work	160 × 160	2–12	All frequencies in 2.17–12	12	8	-

8. Performance Analysis of the 25-port CR MIMO Antenna

The diversity characteristics of the proposed MIMO antenna can be assessed by the two parameters diversity gain (DG) and the envelope correlation coefficient (ECC) [27–30]. ECC can be calculated mathematically by using the S-parameters, as shown in Equation (4). An ideal MIMO antenna system has an ECC of 0. ECC of the proposed 8-element MIMO antenna is illustrated in Figure 1. DG can be determined mathematically once ECC is known using the equation given in Equation (1), and its ideal value for a good MIMO antenna system is 10 dB.

$$ECC(\rho) = \frac{|S_{ii}^* S_{ii} + S_{ji}^* S_{jj}|^2}{(1 - |S_{ii}|^2 - |S_{jj}|^2)(1 - |S_{ji}|^2 - |S_{ij}|^2)} \tag{4}$$

$$ECC(\rho) = \frac{\left| \iint_{4\pi} [F_i(\theta, f) * F_j(\theta, f)] d\Omega \right|^2}{\iint_{4\pi} |F_i(\theta, f)|^2 d\Omega \iint_{4\pi} |F_j(\theta, f)|^2 d\Omega} \tag{5}$$

where $i, j \in N, i < j, j \leq 4, F_i(\theta, \varnothing)$ is nothing but the far-field pattern of the antenna when port i and port j are excited, and $*$ denotes the Hermitian product. However, calculation of ECC using far-field patterns is very tedious. After ECC is calculated, DG in dB can be determined using Equation (6).

$$\text{Diversity Gain (dB)} = 10 \times \sqrt{1 - |0.99\rho|^2} \tag{6}$$

The quality of the proposed 25-port CR MIMO antenna system can be assessed by another crucial parameter called channel capacity loss (CCL). When the number of antennas increases, channel capacity increases under certain conditions without increasing transmitted power or bandwidth. However, channel capacity decreases when a correlation between the links exists. Additionally, as the correlation increases, CCL increases. CCL can be calculated from the equation [27–30] given below.

$$C_{\text{loss}} = -\log_2 \det(\Psi^R) \tag{7}$$

where Ψ^R represents correlation matrix of the receiving antenna. Its matrix representation is given below.

$$\Psi^R = \begin{pmatrix} \rho_{11} & \rho_{12} \\ \rho_{21} & \rho_{22} \end{pmatrix} \tag{8}$$

$$\rho_{ii} = 1 - |S_{ii}|^2 - |S_{ij}|^2 \text{ and } \rho_{ij} = -(|S_{ii}^* S_{ij} + S_{ji}^* S_{jj}|) \tag{9}$$

It is evident from Figure 33 that the ECC of the proposed 25-port CR MIMO antenna is less than 0.42 and DG of the proposed 25-port CR MIMO antenna is more than 9.1 dB. It can also be clearly seen that the CCL of the proposed 25-port CR MIMO antenna is less than 0.46 bits/s/Hz, as illustrated in Figure 34. Since the acceptable level of ECC and CCL of a good MIMO are 0.5 and 0.5 bits/s/Hz, the proposed 25-port CR MIMO antenna is well suitable for CR MIMO applications.

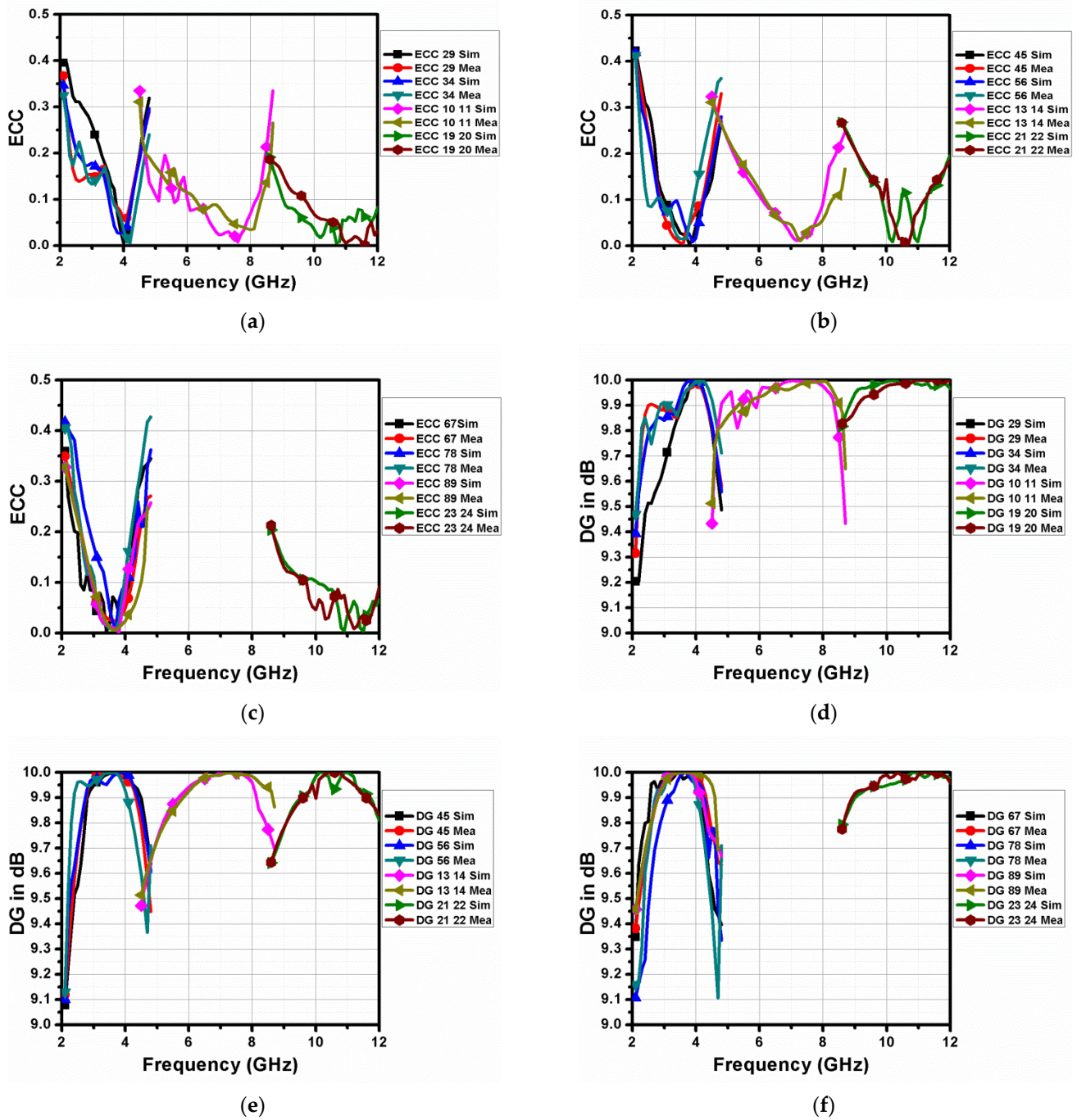


Figure 33. ECC and DG of the 25-port CR MIMO antenna. (a) ECC 29, ECC 34, ECC 10 11 and ECC 19 20 (b) ECC 45, ECC 56, ECC 13 14 and ECC 21 22 (c) ECC 67, ECC 78, ECC 89 and ECC 23 24 (d) DG 29, DG 34, DG 10 11 and DG 19 20 (e) DG 45, DG 56, DG 13 14 and DG 21 22 (f) DG 67, DG 78, DG 89 and DG 23 24.

The total active reflection coefficient (TARC) is one of the crucial parameters to evaluate the diversity performance of the antenna. It is nothing but the ratio of total incident power to the total power that is outgoing when a multiport antenna system is present. It can be calculated using the Equation (10) given in [27].

$$TARC = \frac{\sqrt{\sum_{k=1}^N |b_k|^2}}{\sqrt{\sum_{k=1}^N |a_k|^2}} \quad (10)$$

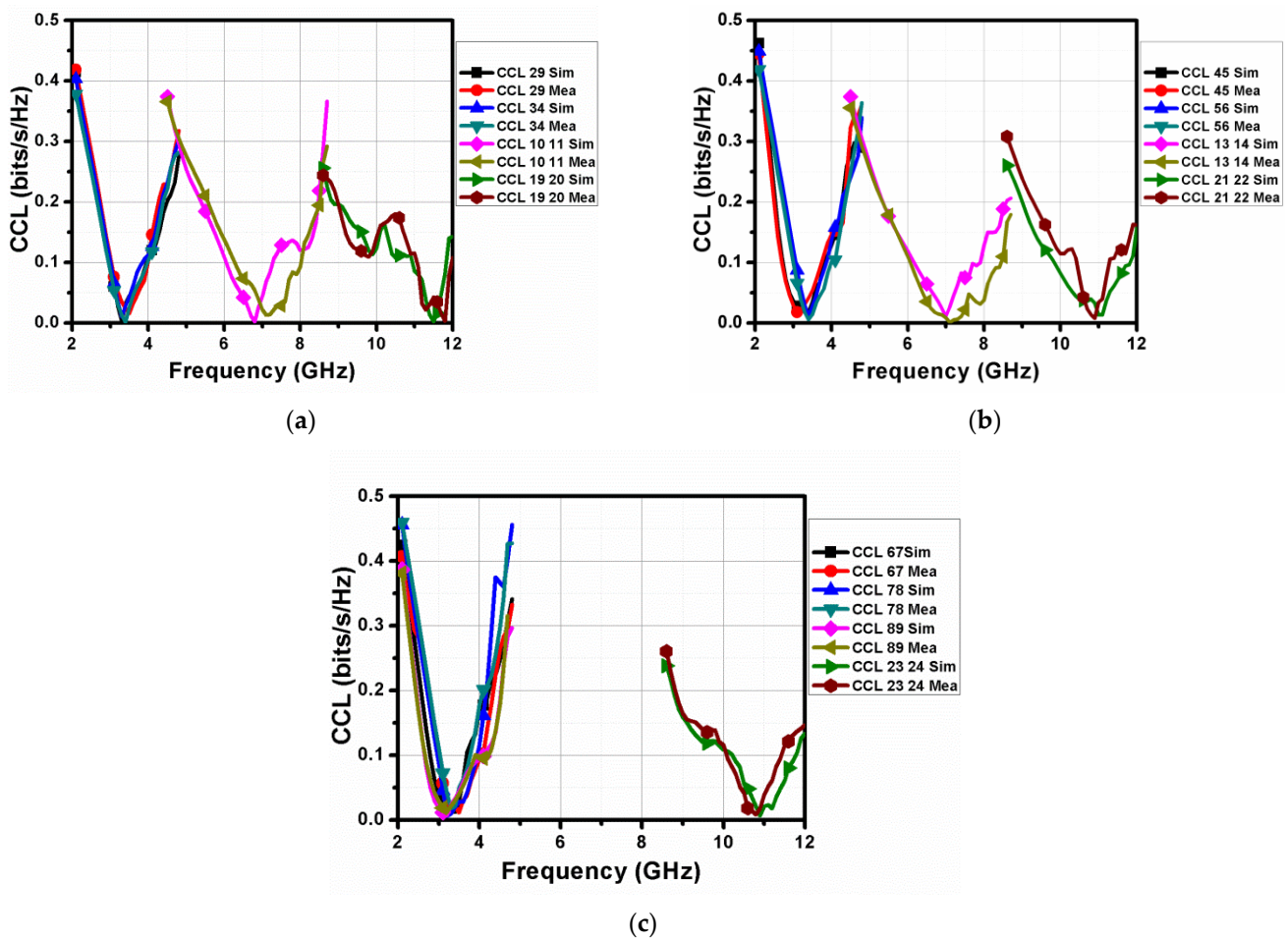
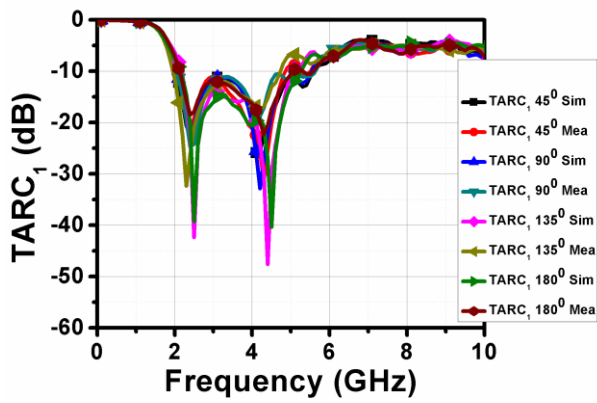


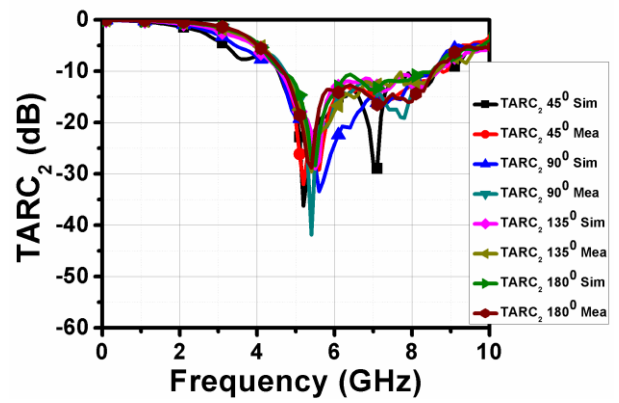
Figure 34. CCL of the 25-port CR MIMO antenna. (a) CCL 29, CCL 34, CCL 10 11 and CCL 19 20 (b) CCL 45, CC 56, CCL 13 14 and CCL 21 22 (c) CCL 67, CCL 78, CCL 89 and CCL 23 24.

where $|a|$ is the excitation parameter and $|b|$ is the scattering parameter in Equation (10). In order to check the effect of TARC on the 10 dB return loss bandwidth of the communication antennas, the proposed MIMO antenna is integrated with an ideal phase shifter in which scan angle is changed from 45° to 180° . It is obvious from Figure 35 that TARC for all 8-element communication antennas is less than -10 dB. So, it is confirmed that all the power that is delivered is accepted by the other antenna element without affecting the 10 dB return loss bandwidth of 8-element MIMO communication antennas.

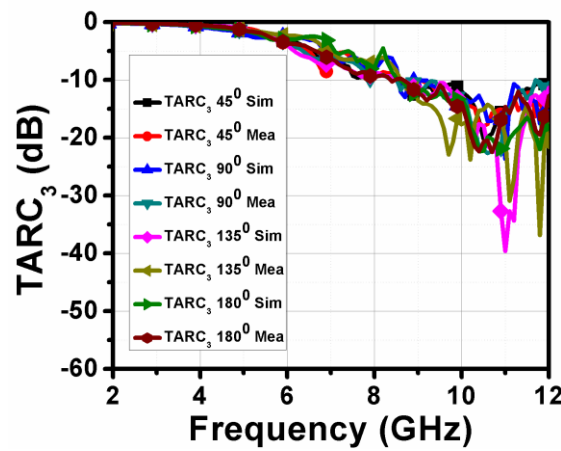
Mean effective gain (MEG) is another important parameter to assess the diversity performance of the antenna in wireless channels. It ascertains the antenna element’s ability to accept electromagnetic signals in the presence of rich fading channels. Practically, it ranges from -3 dB to -12 dB for a MIMO antenna with good diversity performance. It is evident from Figure 36 that the MEG for all MIMO communication antennas is less than -3 dB. So, it can be concluded that the 8-element MIMO communication antennas is a promising candidate for CR MIMO applications.



(a)

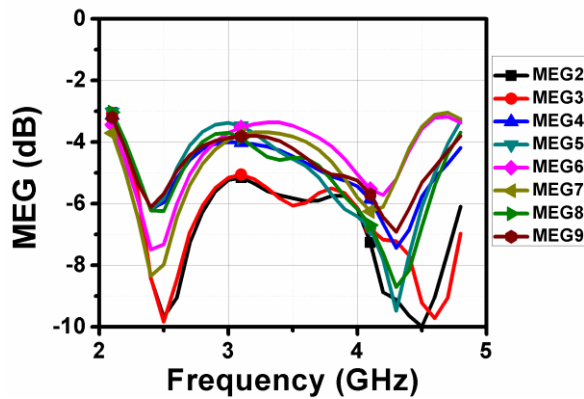


(b)

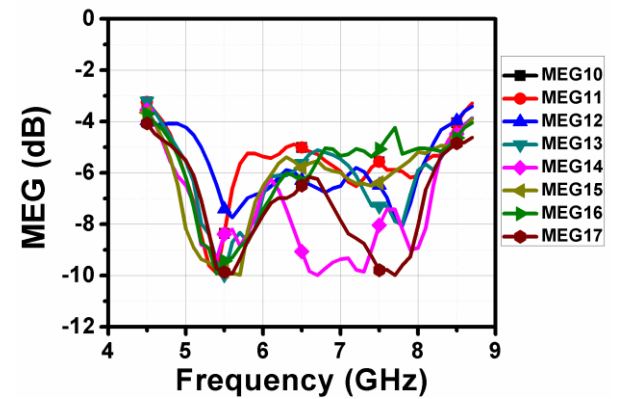


(c)

Figure 35. TARC of the 8-element communication antennas associated with (a) ports 2 to 9, (b) ports 10 to 17, and (c) ports 18 to 25.



(a)



(b)

Figure 36. Cont.

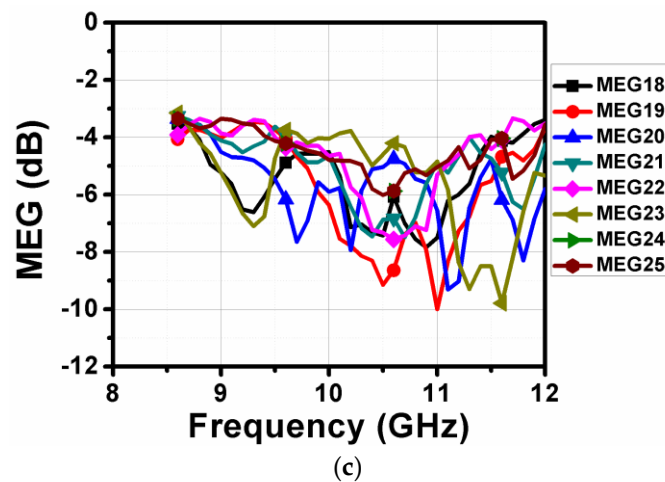


Figure 36. MEG of the 8-element communication antennas associated with (a) ports 2 to 9, (b) ports 10 to 17, and (c) ports 18 to 25.

9. Conclusions

In this article, a CR-integrated antenna system, which can perform maximum of three communication operations, has been presented to improve spectrum utilization efficiency. The sensing antenna linked to port 1 was able to sense the spectrum that ranges from 2 to 12 GHz, whereas the communication MIMO antennas linked with ports 2 to 9, ports 10 to 17 and ports 18 to 25 perform operations in the 2.17–4.74 GHz, 4.57–8.62 GHz and 8.62–12 GHz bands, respectively. Mutual coupling in the proposed CR MIMO antenna was less than -12 dB. Peak gain and radiation efficiency of the sensing antenna are found to be better than 2.25 dBi and 82%, respectively, whereas the peak gains and radiation efficiencies of all communication antennas were more than 2.5 dBi and 90%, respectively. It is inexpensive, easily implementable and has less complexity compared to the traditional reconfigurable CR MIMO antennas. Additionally, it can overcome all the drawbacks that are associated with reconfigurable CR MIMO antennas. Its performance has also been assessed by evaluating ECC, DG, CCL, TARC and MEG. The simulated and measured ECC, DG, CCL, TARC and MEG are within their acceptable limits. Hence, the proposed CR MIMO antenna is a promising candidate for CR MIMO applications.

Author Contributions: Conceptualization: D.S., A.N., R.M., A.B. and S.D.; methodology: D.S., A.N., S.D., S.L. and A.B.; software: D.S., A.B., A.D.A. and W.E.-S.; validation: A.D.A., W.E.-S. and S.L.; writing—original draft preparation: D.S., A.N. and S.D.; writing—review, and editing: S.L., W.E.-S. and R.M.; supervision: S.D., A.N., R.M. and A.B.; project administration: W.E.-S.; funding acquisition: A.D.A. All authors have read and agreed to the published version of the manuscript.

Funding: This work is supported by Princess Nourah bint Abdulrahman University Researchers Supporting Project number (PNURSP2023R51), Princess Nourah bint Abdulrahman University, Riyadh, Saudi Arabia.

Institutional Review Board Statement: Not applicable.

Informed Consent Statement: Not applicable.

Data Availability Statement: The data presented in this research are available on request from the corresponding author.

Acknowledgments: The authors would like to acknowledge the Princess Nourah bint Abdulrahman University Researchers Supporting Project number (PNURSP2023R51), Princess Nourah bint Abdulrahman University, Riyadh, Saudi Arabia.

Conflicts of Interest: The authors declare no conflict of interest.

References

1. Riaz, S.; Zhao, X.; Geng, S. A Frequency Reconfigurable MIMO Antenna with Agile Feedline for Cognitive Radio Applications. *Int. J. RF Microw. Comput. Aided Eng.* **2019**, *30*, e22100.
2. Hussain, R.; Raza, A.; Khan, M.U.; Shammim, A.; Sharawi, M.S. Miniaturized Frequency Reconfigurable Pentagonal MIMO Slot Antenna for Interweave CR Applications. *Int. J. RF Microw. Comput. Aided Eng.* **2019**, *29*, e21811. [\[CrossRef\]](#)
3. Alam, T.; Thummaluru, S.R.; Chaudhary, R.K. Integration of MIMO and Cognitive Radio for Sub-6 GHz 5G Applications. *IEEE Antennas Wirel. Propag. Lett.* **2019**, *18*, 2021–2025. [\[CrossRef\]](#)
4. Cheng, S.; Lin, K. A Reconfigurable Monopole MIMO Antenna with Wideband Sensing Capability for Cognitive Radio using Varactor Diodes. In Proceedings of the IEEE International Symposium on Antennas and Propagation & USNC/URSI National Radio Science Meeting, Vancouver, BC, Canada, 19–24 July 2015; pp. 2233–2234.
5. Thummaluru, S.R.; Ameen, M.; Chaudhary, R.K. Four-Port MIMO Cognitive Radio System for Midband 5G Applications. *IEEE Trans. Antennas Propag.* **2019**, *67*, 5634–5645. [\[CrossRef\]](#)
6. Zhao, X.; Riaz, S.; Geng, S. A Reconfigurable MIMO/UWB MIMO Antenna for Cognitive Radio Applications. *IEEE Access* **2019**, *7*, 46739–46747. [\[CrossRef\]](#)
7. Hussain, R.; Sharawi, M.S. A Cognitive Radio Reconfigurable MIMO and Sensing Antenna System. *IEEE Antennas Wirel. Propag. Lett.* **2015**, *14*, 257–260. [\[CrossRef\]](#)
8. Pahadsingh, S.; Sahu, S. Four Port MIMO Integrated Antenna System with DRA for Cognitive Radio Platforms. *AEU-Int. J. Electron. Commun.* **2018**, *92*, 98–110. [\[CrossRef\]](#)
9. Hussain, R.; Khan, M.U.; Sharawi, M.S. An Integrated Dual MIMO Antenna System with Dual-Function GND-Plane Frequency Agile Antenna. *IEEE Antennas Wirel. Propag. Lett.* **2018**, *17*, 142–145. [\[CrossRef\]](#)
10. Alam, T.; Thummaluru, S.R.; Chaudhary, R.K. Improved Multifunctional MIMO Cognitive Radio System for Integrated Interweave-Underlay Operations. *IEEE Trans. Microw. Theory Tech.* **2022**, *70*, 631–640. [\[CrossRef\]](#)
11. Jain, P.; Saptarshi, G. A Reconfigurable Four-Port MIMO Antenna for Sub-6 GHz Applications. In Proceedings of the IEEE Wireless Antenna and Microwave Symposium (WAMS), Rourkela, India, 5–8 June 2022; pp. 1–5.
12. Mansoul, A.; Mourad, N. Compact and Reconfigurable Multiband 2-Element MIMO Slot Antenna for Advanced Communication Systems. In Proceedings of the IEEE International Symposium on Antennas and Propagation and North American Radio Science Meeting, Montreal, QC, Canada, 5–10 July 2020; pp. 575–576.
13. Hussain, R.; Sharawi, M.S. 4-Element Planar MIMO Reconfigurable Antenna System for Cognitive Radio Applications. In Proceedings of the IEEE International Symposium on Antennas and Propagation & USNC/URSI National Radio Science Meeting, Vancouver, BC, Canada, 19–24 July 2015; pp. 717–718.
14. Hussain, R.; Sharawi, M.S.; Shamim, A. 4-Element Concentric Pentagonal Slot-Line-Based Ultra-Wide Tuning Frequency Reconfigurable MIMO Antenna System. *IEEE Trans. Antennas Propag.* **2018**, *66*, 4282–4287. [\[CrossRef\]](#)
15. Chacko, B.P.; Augustin, G.; Denidni, A. Electronically Reconfigurable Uniplanar Antenna with Polarization Diversity for Cognitive Radio Applications. *IEEE Antennas Wirel. Propag. Lett.* **2015**, *14*, 213–216. [\[CrossRef\]](#)
16. Hussain, R.; Sharawi, M.S.; Shamim, A. An Integrated Four-Element Slot-Based MIMO and a UWB Sensing Antenna System for CR Platforms. *IEEE Trans. Antennas Propag.* **2018**, *66*, 978–983. [\[CrossRef\]](#)
17. Tawk, Y.; Constantine, J.; Christodoulou, C.G. Reconfigurable Filtennas and MIMO in Cognitive Radio Applications. *IEEE Trans. Antennas Propag.* **2014**, *62*, 1074–1083. [\[CrossRef\]](#)
18. Islam, H.; Das, S.; Ali, T.; Bose, T.; Prakash, O.; Kumar, P. A Frequency Reconfigurable MIMO Antenna with Bandstop Filter Decoupling Network for Cognitive Communication. *Sensors* **2022**, *22*, 6937. [\[CrossRef\]](#)
19. Hussain, R.; Sharawi, M.S. An Integrated Slot-Based Frequency-Agile and UWB Multifunction MIMO Antenna System. *IEEE Antennas Wirel. Propag. Lett.* **2019**, *18*, 2150–2154. [\[CrossRef\]](#)
20. Nella, A.; Abhay, S.G. A survey on planar antenna designs for cognitive radio applications. *Wirel. Pers. Commun.* **2018**, *98*, 541–569. [\[CrossRef\]](#)
21. Nella, A.; Abhay, S.G.; Vigneswaran, D. Cognitive radio paradigm and recent trends of antenna systems in the UWB 3.1–10.6 GHz. *Wirel. Netw.* **2020**, *26*, 3257–3274.
22. Srikar, D.; Anuradha, S. Twelve Port MIMO Antenna with Polarisation Diversity for Cognitive Radio Applications. *Electron. Lett.* **2019**, *55*, 1165–1168. [\[CrossRef\]](#)
23. Srikar, D.; Anuradha, S. A Compact Six Port Antenna for Better Spectrum Utilization Efficiency in Cognitive Radio Applications. *Int. J. RF Microw. Comput. Aided Eng.* **2020**, *30*, e22383. [\[CrossRef\]](#)
24. Srikar, D.; Anuradha, S. A New Two-Element MIMO Antenna System for Cognitive Radio Applications. *Circuit World* **2022**, *48*, 111–125. [\[CrossRef\]](#)
25. Nella, A.; Gandhi, A.S. A Five-Port Integrated UWB and Narrowband Antennas System Design for CR Applications. *IEEE Trans. Antennas Propag.* **2018**, *66*, 1669–1676. [\[CrossRef\]](#)
26. Anvesh Kumar, N.; Gandhi, A.S. A Compact Novel Three-Port Integrated Wide and Narrow Band Antennas System for Cognitive Radio Applications. *Int. J. Antennas Propag.* **2016**, *2016*, 2829357.
27. Nandi, S.; Mohan, A. CRLH Unit Cell Loaded Triband Compact MIMO Antenna for WLAN/WiMAX Applications. *IEEE Antennas Wirel. Propag. Lett.* **2017**, *16*, 1816–1819.

28. Balaji, V.R.; Tathababu, A.; Arpan, D.; Anveshkumar, N.; Truong, K.N. An Inverted L-Strip Loaded Ground with Hollow Semi-Hexagonal Four-Element Polarization Diversity UWB-MIMO Antenna. *Trans. Emerg. Telecommun. Technol.* **2022**, *33*, e4381. [[CrossRef](#)]
29. Sharma, P.; Tiwari, R.N.; Singh, P.; Kumar, P.; Kanaujia, B.K. MIMO Antennas: Design Approaches, Techniques and Applications. *Sensors* **2022**, *22*, 7813. [[CrossRef](#)]
30. Addepalli, T.; Desai, A.; Elfergani, I.; Anveshkumar, N.; Kulkarni, J.; Zebiri, C.; Rodriguez, J.; Abd-Alhameed, R. 8-Port Semi-Circular Arc MIMO Antenna with an Inverted L-Strip Loaded Connected Ground for UWB Applications. *Electronics* **2021**, *10*, 1476. [[CrossRef](#)]

Disclaimer/Publisher's Note: The statements, opinions and data contained in all publications are solely those of the individual author(s) and contributor(s) and not of MDPI and/or the editor(s). MDPI and/or the editor(s) disclaim responsibility for any injury to people or property resulting from any ideas, methods, instructions or products referred to in the content.



An Hybrid Heuristic optimal relay selection strategy for energy efficient multi hop cooperative cellular communication

Uppula Kiran^{a,*}, Krishan Kumar^b

^a Department of Electronics & Communication Engineering, Lovely Professional University, Punjab 144001, India

^b Faculty in School of Electronics and Electrical Engineering, Lovely Professional University, Punjab 144001, India

ARTICLE INFO

Keywords:

Multi-hop cooperative cellular communication
Vehicular network
Energy efficient optimal relay selection
Best fitness-derived crow tunicate swarm optimization algorithm
Multi-objective function
Link reliability

ABSTRACT

One of the major constraints for mobile relay networks is energy-efficient communication owing to the restricted battery power of user terminals. Among them, the production method is cooperative cellular networks that focus on enhancing the data rate, network reliability, and network system capacity and also improving the spectrum resources in the Fifth Generation (5 G) networks. Thus, recent research works investigate the selection of mobile relays in vehicular networks and also the relay selection in cooperative communication. Here, the mobile relay is selected by the base station (operator) for every mobile user for reducing the cost with improved data rates and reducing the total transmission power. The selection of relay is performed by considering the benefits or utilities offered to three players such as mobile relay, mobile user, and operator. Conventional relay node selection approaches face challenges regarding reduced network lifetime, delay, increased energy consumption, and collusion attacks. For next-generation wireless networks, both energy efficiency and capacity are vital. To cope with these problems, a new multi-objective derived energy efficient accurate selection of relay in multi-hop cooperative cellular communication in the vehicular network through a hybrid heuristic strategy is implemented. The conventional approaches are utilized for probability-based multi-hop broadcasting for low latency. On the other hand, the major demerits of cellular communication are developing an effective multi-hop communication strategy that generates hidden node problems, and also it decreases the speed of the vehicles and the lack of infrastructure in network topology. Thus, this paper aims to propose a hybrid optimization model to choose the lowest count of multi-hops among the source and destination for the cooperative cellular vehicular communication network. The major issue well thought-out here is accurately choosing the count of hops or relays for appropriate communication, which is carried out through the multi-objective function regarding link reliability, energy consumption, outage probability, mobility factor, and transmission delay of the system. The adoption of the new hybrid algorithm with the aid of the Best Fitness-derived Crow Tunicate Swarm Optimization (BF-CTSO) algorithm is designed as the major contribution for optimally selecting the multi-hops between source and destination in a cooperative cellular communication network. Numerical results show that the proposed energy-efficient cooperative communication system outperforms traditional methods.

1. Introduction

Nowadays, the utilization of smart devices is emerging vastly, particularly in vehicular infrastructure, where they do not satisfy the demand for high data transmissions [1]. Even though there is a considerable increment in data transmission rates when compared with the first-generation mobile network, there is an urge in the requirement of services and data rates that is a big challenge and needed to be addressed in recent days. Thus, cooperative communication is a recent and essential paradigm that provides diversity, spectrum efficiency,

system capacity, network coverage, and a higher data rate in heterogeneous networks, and uses the broadcast nature of wireless networks [2]. Cooperation has occurred while the relay helps in the transmission from source to destination. For example, for increasing the capacity and network coverage, the fixed relays are installed in a deterministic manner in various positions such as buildings and towers [3] that offers services during busy hour. On the other hand, there are various circumstances in real-time applications, where there is a need of offering good quality service to a large number of users. The fixed relays do not give guaranteed service in non-uniform circumstances, so, the moving

* Corresponding author.

E-mail address: kiranuday411@gmail.com (U. Kiran).

relays are more economically appropriate than fixed relays and are utilized to share the traffic of congested cells [4]. Thus, moving relays are preferred concerning power consumption and deployment cost [5]. Though, various incentives and benefits must be offered for making them cooperate. The mobile relays may be static or randomly moving in any direction as the mobile users perform like mobile relays [6]. Additionally, there might be various numbers of mobile users, which can act as mobile relays for performing the transmission. On the other hand, in cooperative communication, the cautious selection of relays is more necessary to guarantee the effective transmission of packets [7]. Consequently, in cooperative communication, the most complicated problem is choosing a mobile relay when ensuring players benefits from their shared resources.

The fundamental concept of cooperative communications is that a virtual antenna array is acted as relay node for helping a source node for forwarding its information to its destination by utilizing the broadcasting nature of wireless channels [8]. The relationship between cooperative communication and security is to protect the MIMO system from active compromised nodes by securing the key management systems as a cryptographic approach. Moreover, the security protocol helps the MIMO system to process in high consumption. The secured CC transmission is utilized to minimize the computation time. The security protocol helps to improve secrecy and shows the efficiency of cooperative transmission [9]. In general, there are two cooperative communication modes “Decode-and-Forward (DF) and Amplify-and-Forward (AF)” which are presented with the variation in how the relay node processes the received signal [10]. The major problem in cooperative communications is choosing suitable relays for enhancing system efficiency. In recent days, a semi-distributed user relaying technique is suggested, where the decision is made by every relay node on their realistic relayed nodes individually. Cooperative beamforming-based transmission strategies are carried out to minimize the total energy consumption [11]. One of the promising technologies is cooperative relaying which aims to increase the effectiveness of a wireless system through several mechanisms like beamforming effects or increased spatial diversity [12]. These strategies can enhance the total throughput and the spectral efficiency of the complete system. Though, utilization of these methods usually results in higher power consumption [13].

Thus, relay approaches are necessary for cellular networks and improved the energy-efficiency since they show superiority to various methods for profitable and sustainable businesses, and commercial sense for operators [14]. The average energy efficiency of the relaying approaches may be restricted as the relays take more power and system resources. Hence, the major problem in the relaying system is to formulate whether a two-hop transmission is essential [15]. On the other hand, it is also necessary for selecting a relay between various candidates for maximizing the cooperation features for the entire system or the user [16]. The relay selection is broadly discussed in recent studies. The wireless communication system is rapidly developing however; some of the physical constraints have challenges. In general, the most complicated issues for the research are battery capacity, channel fading, and limited bandwidth which must address [17]. Cooperative communication is a more eminent technique for improving the wireless network quality of service capacity of data transmission and enhancing the battery lifetime. While considering the relay selection, the power losses must be eradicated, and performed the data transfer [18]. This paper plans to suggest a novel multi-hop cooperative cellular communication particularly for vehicular communication through a hybrid heuristic strategy.

The highlights of this research are illustrated here.

- To carry out new research work on multi-objective derived multi-hop cooperative cellular communication through a hybrid heuristic strategy for maximizing the performance in terms of energy-efficient relay selection. It helps to improve the energy efficiency of the multi-

hop cooperative cellular communication system without any path loss.

- To implement a heuristic strategy termed BF-CTSO with the integration of Crow Search Algorithm (CSA) and Tunicate Swarm Algorithm (TSA) techniques for selecting the number of relay nodes, especially for communication. The hybridized BF-CTSO is utilized to achieve the optimal solution and also it is used to achieve a better convergence rate.
- To derive the multi-objective function regarding various metrics such as link reliability, mobility factor, energy consumption, outage probability, and transmission delay for “optimal relay selection in multi-hop cooperative cellular communication” network. The generation of a multi-objective function is utilized for reducing energy consumption.
- To validate the efficacy of the designed multi-hop cooperative cellular communication model with diverse performance measures by estimating with conventional algorithms to demonstrate the superiority of this research work. The result analysis visualizes the achievements of the suggested method and also portrayed the issues of baseline approaches.

The remaining parts of this paper are ordered here. Segment II discusses the existing research works. Segment III demonstrates a design of a hybrid heuristic strategy for energy-efficient optimal relay selection. Segment IV formulates the multi-objective derived “energy efficient optimal relay selection” in multi-hop cooperative cellular communication. Segment V specifies the system model and cooperative mechanism in multi-hop cooperative cellular communication. Segment VI estimates the results. Segment VII shows the conclusion.

2. Literature works

This section analyzes the recent research approaches on cooperative communication networks with newly suggested algorithms along with the advantages and challenges of those studies. We have analyzed the given baseline approaches to show the improvements of this proposed method.

2.1. Related research studies

In 2020, Mohanakrishnan and Ramakrishnan [19] have considered the major aim of achieving effective transmission goals for any class of network. A routing protocol was integrated into cognitive radio technology to offer effective channel allocation. A tree-based structure was used for routing protocol for effective routing among and within networks. They have modified the tree routing protocols with the incorporation of an effective optimized strategy. A novel Genetic Whale Optimization Algorithm (GWOA) was implemented for transmission to select a root channel. The channels were disabled while the chosen root channel has become active. The Modified Cognitive Tree Routing Protocol (MCTRP) was implemented as a new objective in the recommended approach. This routing protocol has allocated the spectrum for satisfying the requirement of efficient channel usage, reduced the inherent delay, and maximized their transmission efficiency. They have performed effective channel utilization and minimized the overheads while estimating with the traditional protocols.

In 2022, Narayan et al. [20] designed a novel “Quantum Atom Search Optimization coupled with Blockchain aided Data Transmission (QASO-BDT) scheme” with security-derived data transmission for performing the relay node selection. This model has utilized three phases “registration, clustering, and transmission”. Firstly, a capillary gateway was used for registering each sensor node in the blockchain network during the node registration process. Then, the selection of cluster head was performed, and suggested an enhanced multi-view clustering scheme for clustering the nodes into several clusters in the clustering phase. Lastly, the QASO was used in the multi-hop transmission phase

for multi-hop transmission with the help of the optimal selection of relay nodes, and the security in the system was ensured by performing the blockchain-based transaction. The designed framework was experimented with in the MATLAB platform and achieved superior performance regarding metrics like reduced energy value and throughput and also guaranteed security in comparison with conventional methods.

In 2017, Wu et al. [21] examined a new “Energy Harvesting-Wireless Sensor Networks (EH-WSN)” for performing energy-efficient cooperation by jointly optimizing the relay selection and power allocation strategy. This suggests that EH-WSN has aimed for enhancing the energy efficiency of every node in a clustering scheme. Firstly, they have evaluated the impacts of cooperative communication, and further, they have considered the energy sustainability of each node. They have equated an online optimization issue for solving near-optimal solutions with lower computational complexity. The outstanding efficiency was noticed by the designed model through the performance evaluation regarding average working utility and transmitting power allocation. Moreover, this recommended joint optimization algorithm has outperformed different applications.

In 2016, Xu et al. [22] implemented an “Energy Awareness Optimal Relay Selection (EAORS) design” for determining the count of optimal relays by deriving a weighted objective function by taking energy consumption in both cooperative transmission and the spectrum sensing phases under the requirements of “secondary cooperative transmission Bit Error Rate (BER)” and global misdetection requirement. This method has concentrated on investigating the tradeoff between energy efficiency and detection accuracy and have constructed a weighted convex function as an objective function regarding relay numbers. They have solved the nonlinear convex problem for obtaining the best relay numbers. The EAORS scheme has shown the efficiency of the designed model regarding energy consumption analysis.

In 2015, Li et al. [23] derived the “double auction theory” to address the best relay formulation issue. They have focused on enhancing the efficiency of cell-edge users by optimizing energy efficiency. This optimization issue was solved by the existing standard algorithm. The simulation outcomes have verified that the efficiency of EE-MWM was examined regarding metrics like social welfare, capacity, and energy efficiency. This model has augmented the efficiency of cooperative cellular networks while estimating with traditional approaches.

In 2021, Hayati et al. [24] have taken “cooperative multicast D2D communication with NC”, where the relay was taken as femtocell base stations. This model has focused on maximizing energy efficiency for power allocation and relay selection. A new solution was provided by the designed model for performing network-coded cooperative D2D transmission and has considerably maximized the energy efficiency and spectral efficiency estimating with other approaches.

In 2010, Wei et al. [25] suggested a new cooperative cellular system with the recommendation of energy-efficient relaying strategies by choosing mobile relays with asymmetric traffic. This model has formulated the total energy consumption. Moreover, they have implemented a “Joint Uplink and Downlink Relay Selection (JUDRS)” scheme for minimizing the total energy consumption with an optimal selection of relays. In addition, they have examined the energy-efficient cooperation regions and discovered the optimal relay position with asymmetric traffic for systems. In addition, the simulation results have shown an important energy efficiency gain of the designed technique while estimating the best harmonic mean selection and previous best worst channel selection algorithms. They have exploited the “Diversity-Multiplexing Tradeoff (DMT)”. The recommended approach has achieved full spatial diversity in the amount of cooperating terminals in this network

In 2019, Sharfeen et al. [26] presented an auction-based strategy for selecting relays in cooperative communication. Thus, they have derived the utilities of three players. This model has introduced a centralized “Predicted Mobility Based Profitable Relay Selection Algorithm (PMPSRA)” by considering the random waypoint mobility model along

with the usage of auction theory for selecting a mobile relay. The experimental analysis has shown that the implemented PMPSRA strategy has chosen a mobile relay and provided elevated data rates and offered incentives to all the players.

In 2018, Sharfeen et al. [27] presented a bio-inspired unicast routing protocol for vehicular ad hoc networks. The selection of cellular attractor technique has been utilized to choose the next hops. The author has introduced a new routing protocol, which was utilized to alter the complicated dynamic platform with the help of routing reaction packets. The multiattribute decision-making scheme has been implemented to eliminate the count of unnecessary candidates for the selection of the next hop. Finally, the empirical findings have revealed its advanced performance.

In 2018, Sharfeen et al. [27] studied the issues of distributed information estimation. It has based on some of the existing network-aided applications, like optimization, cooperative localization, and distributed surveillance. The statistics have been introduced as a signal constraint, which has finite states related to a particular probability. The author has developed an adaptive distributed information fusion scheme to improve the local Bayesian rule-aided upgrading process.

2.2. Research gaps

Some of the recent research works are studied in cooperative communication networks.

- MCTRP [19] reduces the overhead of the network and guaranteed efficient channel utilization and has superior channel utilization capacity. It does not secure the designed model. In this present work, the relay selection process is utilized for secure transmission.
- QASO-BDT [20] has reduced the end-to-end delay and energy value and has maximized the lifetime of the nodes and achieved a higher throughput. This model does not discover the data paths for various relay nodes in dynamic MANET. The discovery of the data paths for various relay nodes in dynamic MANET will be considered an upcoming work.
- The joint optimization algorithm [21] has reached maximum precision and reached near optimal relay node selection and saving the efficiency of the model. This model does not solve the system outage probability. The outage probability analysis regarding nodes and field dimension variation is shown in the result analysis for this present work and exhibited higher performance.
- Compressed sensing [22] has offered a superior tradeoff between energy efficiency and accuracy and observes higher overhead. The experimental results confirmed that the efficiency of this present work is higher than the other approaches and thus, it reduces overhead.
- EE-MWM [23] gets superior efficiency of the cooperative cellular networks and ensures lower energy consumption among both relay users and source users. There is a need of enhancing the performance while matching one relay user with one CEU. The performance improvement while matching one relay user with one CEU will be taken as future work.
- Monte Carlo simulation [24] considerably improves the spectral efficiency and energy efficiency while estimating heterogeneous cellular networks and reduces the interference on femtocell networks regarding cooperative communication. Though, while considering the real scene, achieving accurate Channel State Information (CSI) is complicated. The investigation of the accurate CSI will be taken as future work.
- JUDRS [25] increases the considerable energy efficiency gain using the designed approach and minimizes the energy consumption of the network. It achieves a higher transmission error rate. The experiment shows that the error rate has lower than the other approaches.
- PMPSRA [26] offers a higher data rate and selects the optimal mobile relay. It does not focus on computing utilities for various operators

and does not focus on implementing multiple hexagons. The implementation of multiple hexagons has been considered an upcoming work.

3. A design of a hybrid heuristic strategy for accurate selection of relay with energy efficiency in multi-hop cooperative cellular communication

This section gives a detailed description of a new BF-CTSO algorithm along with a summary of the relay selection scheme in cooperative cellular communication.

3.1. Selection of relay scheme in multi-hop vehicular communication

In this designed multi-hop vehicular cooperative communication model, the selection of optimal relays is done by suggesting a novel BF-CTSO algorithm to maximize the efficiency of the communication and secrecy capabilities of cooperative strategy. The optimal relay selection scheme is also denoted as a designed Two-Round Relay Selection (2-RRS), in the initial step, a group of relays selection is done that can decode the source statistics. Accordingly, the selection of an accurate relay is forwarded to the recorded statistics to the target in the first round of selection. Generally, the relay selection is performed by taking two modules such as the “control module and transmission module”. The source node confirms that the buffer is empty or not in the control module. While it is noticed as empty, it is assigned as idle; otherwise, the handshake messages known as control frames are forwarded by the source node for performing the communication. After getting the handshake messages from the source node, the destination node exchanges the handshake messages with the utilization of advanced positioning algorithms [28] such as “Inertial Measurement Unit (IMU), Global Positioning System (GPS)”, assisted GPS, and differential GPS. Finally, it determines the re^* relays for engaging in cooperation via the “communication distance” between the source and destination.

In addition, the data frames are communicated in the transmission module by the source node in of Omni-directional broadcasting way while the destination performs the decoding of the data frame in a precise manner. At last, the transmission [29] of the data frame is done by the source node in the consequent Automatic Repeat Request (ARQ) round. On the other hand, the target node evaluates the ARQ round rq . While it is observed lesser than the maximum value of Q , it retransmits the messages or else it broadcasts a negative response via destination, and then, the value of rq is taken as 0. During the retransmission phase, the relays work in DF mode and the source node forwards the data frame and which is effectively decoded by $tp - \text{out-of-relays}re^*$. Consequently, the data frame is retransmitted via the starting node in the consequent ARQ round while $tp = 0$ otherwise the data frames are accordingly broadcasted to the target by $tp - \text{relays}$, where $re = 1, 2, 3, \dots, tp$. Further, $tp - \text{relays}$ continuously perform the retransmission process until Q reaches or receive an acknowledgement from the destination.

3.2. Hybrid BF-CTSO algorithm

A new algorithm called the BF-CTSO algorithm is implemented for selecting the optimal multi-hop relays in a cooperative cellular communication model to solve the multi-objective function. The optimal relay selection helps in minimizing the transmission delay and network energy consumption and increase the throughput with a better convergence rate.

This BF-CTSO algorithm is developed from the inspiration of both TSA and CSA techniques. TSA gives various benefits in recent research works like efficiency in handling the computational complexity and time complexity and getting optimal outcomes regarding robustness. However, TSA suffers from premature convergence and a lower convergence rate to address the limitations of TSA and reach a superior convergence speed, CSA is adopted in this paper due to its features like simpler

implementation, efficiency in finding feasible solutions, and get better convergence rate. Finally, the BF-CTSO algorithm solves the convergence issue and local optima issue and attains better development.

This BF-CTSO algorithm is implemented by recommending a new formation for the social forces between search agents \vec{F} of TSA technique with the help of initial speeds and subordinate speeds and also recent fitness function $F_s(j)$ whereas \vec{F} is updated in conventional TSA by only taking the initial speeds and subordinate speeds with the random number. The fitness-assisted parameter helps in efficiently updating the solutions. The formulation of the social forces between search agents \vec{F} is derived in Eq. (1), which replaces the conventional derivation in Eq. (3).

$$\vec{F} = \frac{[Z_{\max} - Z_{\min}]}{F_s(j)} \quad (1)$$

If $\vec{F} \leq F_{s_{\text{best}}}(j)$ is verified, then the search individuals are updated by TSA, otherwise, the upgrading is executed by CSA in the designed BF-CTSO algorithm.

TSA [30] is a “bio-inspired meta-heuristic optimization” technique, which is attracted to the behavior of the swarming nature of tunicates and jet populations during foraging and navigation procedures. Tunicates are one of the animals in the ocean and bright bio-luminescent nature that produces a pale green-blue light. Every tunicate is a few millimeters in size. TSA proves its efficiency in addressing engineering design problems and solving traditional optimization algorithms. Tunicate has the capability of discovering the source of food in the ocean. Though, they do not aware of the food location in the specific search area. For this purpose, the swarm intelligence and jet propulsion behaviors are modeled. A tunicate must satisfy three factors for modeling the jet propulsion constraint, which is eradicating the conflicts among search individuals, motion to the location of the optimal search agent, and persisting closer to the optimal search individual. The optimal best solutions are attained by updating the locations of other search individuals by taking the swarm behavior. The mathematical modeling of three conditions is formulated here.

- (i) “Avoiding the conflicts between search agents”: This behavior is modeled to determine the position of novel search individuals with the aid of a vector \vec{S} as formulated in Eq. (2).

$$\vec{S} = \frac{\vec{V}}{\vec{F}} \quad (2)$$

$$\vec{F} = [Z_{\min} + a_1 \cdot Z_{\max} - Z_{\min}] \quad (3)$$

$$\vec{V} = a_2 + a_3 - \vec{W} \quad (4)$$

$$\vec{W} = 2 \cdot a_1 \quad (5)$$

In the aforementioned conditions, the constants are framed as a_1, a_2 and a_3 in range of [0, 1], and the ocean’s water flow advection is defined as \vec{W} , the social forces among candidates are mentioned as \vec{F} , and the gravity force is specified as \vec{V} . The initial speeds and subordinate speeds are corresponding specified as Z_{\min} and Z_{\max} , that is assigned in the bounding limit of 1 and 4, respectively,

- (i) “Propagation with regards to the location of better candidates”: After eradicating the conflicts among the search individuals, the individuals are forwarded in search space to reach the location of optimal neighbors, which is done by finding the “distance among as the food source” and search individual that is specified as \vec{B} and formulated in Eq. (6).

$$\vec{B} = \left| \vec{Y} - c_m \cdot \vec{Z}_{tuni}(j) \right| \quad (6)$$

Here, the tunicate position is noted as $\vec{Z}_{tuni}(j)$ at j^{th} iteration, the variable \vec{Y} is defined as the location of the food source, and an arbitrary numerical lie in the limit of [0, 1] is denoted as c_m .

- (i) **“Convergence towards the best candidate”**: The food source or the best candidate is found by maintaining their position as equated in Eq. (7).

$$\vec{Z}_{tuni}(j) = \begin{cases} \vec{Y} + \vec{S} \cdot \vec{B} & \text{if } c_m \geq 0.5 \\ \vec{Y} - \vec{S} \cdot \vec{B} & \text{if } c_m < 0.5 \end{cases} \quad (7)$$

Here, the new position of tunicates owing to the food source position is denoted as $\vec{Z}_{tuni}(j')$.

- (i) **“Swarm behavior”**: The mathematical formulation of swarm behavior is formulated in Eq. (8).

$$\vec{Z}_{tuni}(j+1) = \frac{\vec{Z}_{tuni}(j) + \vec{Z}_{tuni}(j+1)}{a_1 + 2} \quad (8)$$

The final position will be attained in a random location within a cone or cylindrical shape that is described by the location of the tunicate.

If $\vec{F} > F_{S_{best}}(j)$ is verified, then the search individuals are updated by CSA in the designed BF-CTSO algorithm.

CSA [31] is inspired by the intelligent nature of crows, and it is a “population-based approach” performs by considering the concept of storing the crow’s excess food in safe places and they get it while it requires the food. This algorithm reveals competitive performance by achieving superior outcomes while evaluating conventional methods. Crows (corvids or crow family) represent the characteristics of an intelligent bird and it is also a greedy bird as they follow every other for getting optimal food sources. Moreover, crows observe other birds and notice where they preserve their food and then, they steal it without their knowledge. Then, they protect themselves from other birds. Some of the characteristics of CSA have to be studied to formulate the CSA. They live in flocks, have the capability of memorizing the location of their hiding places, crow follow other crows or birds to perform thievery, and finally, they protect themselves from catching as being pilfered through probability.

CSA is initialized by considering several crows in a dm – dimensional infrastructure, where the i^{th} crow’s position at j^{th} iteration in the search area is denoted as $Z^{i,j}$, where $i = 1, 2, 3, \dots, N$ and $j = 1, 2, 3, \dots, j_{max}$ the number of crows is indicated as N . Every crow consists of a memory, where they have memorized the location of their hiding place. The location of the hiding place of i^{th} the crow at j^{th} iteration is denoted as $H^{i,j}$, which is also known as the optimal or best solution attained so far.

It is assumed that crows try to explore their hiding location at j^{th} iteration. Consequently, the crow opts to go after the crow k for approaching and knowing the hiding location of the crow k . Thus, there will be two states that may occur.

State 1: Crow i opts to go after crow k for knowing the hiding location of crow k without their knowledge. For this case, the new location of the crow i is formulated in Eq. (9).

$$Z^{i,j+1} = Z^{i,j} + m_i \times l^{i,j} \times (H^{i,j} - Z^{i,j}) \quad (9)$$

Here, the flight length at j^{th} the iteration of i^{th} crow is denoted as $l^{i,j}$ and a random number with the range between [0, 1] is denoted as m_i .

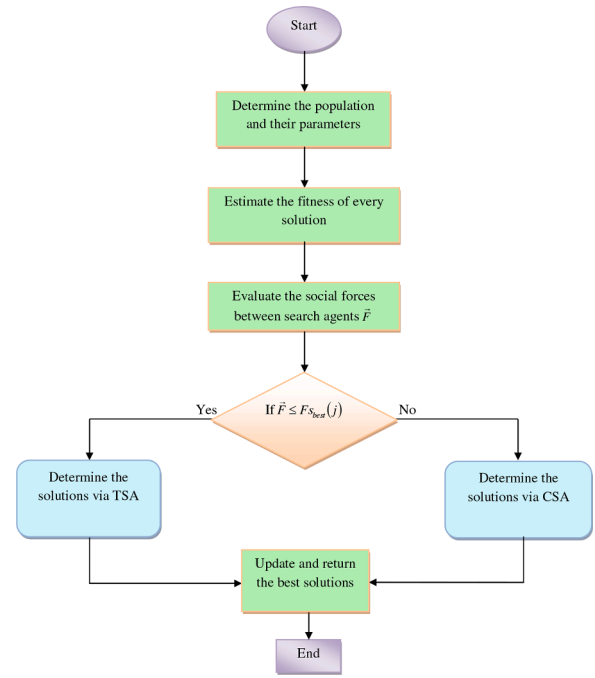


Fig. 1. Flow diagram of the offered BF-CTSO algorithm.

State 2: Here, the crow aware of the following strategy of crow i and decides to protect their hiding place from the crow j by fooling them by moving to a false location.

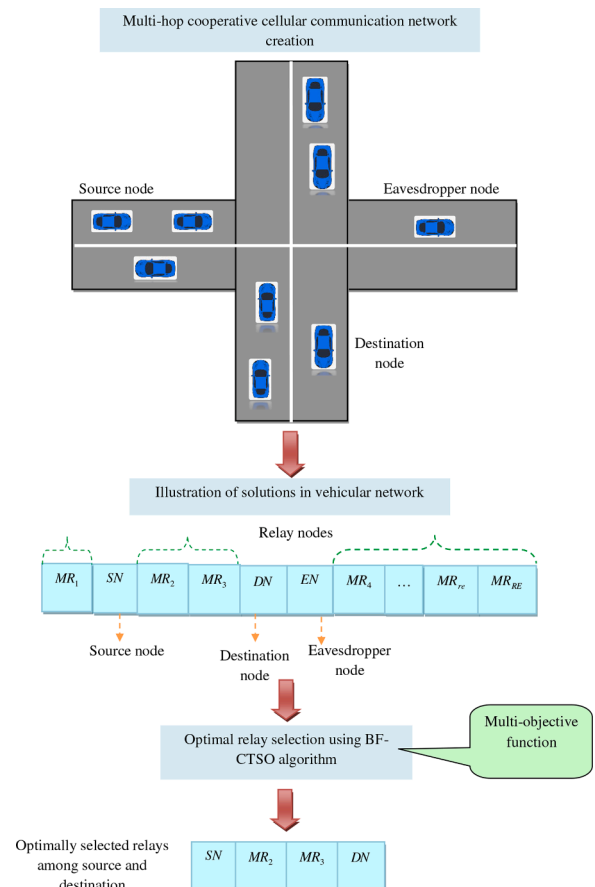


Fig. 2. Optimal relay nodes selection in the designed vehicular network using BF-CTSO algorithm.

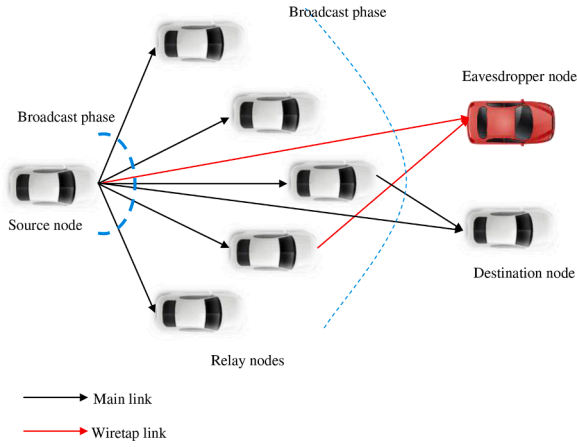


Fig. 3. A system model of a multi-hop cooperative vehicular communication network with a wiretap channel.

The determination of state 1 and state 2 is done by a random number and also the awareness probability, which is jointly derived in Eq. (10).

$$Z^{i,j+1} = \begin{cases} Z^{i,j} + m_i \times l^{i,j} \times (H^{i,j} - Z^{i,j}) & m_i \geq \rho^{i,j} \\ \text{Random location} & \text{else} \end{cases} \quad (10)$$

Here, the "awareness probability of crow" at j^{th} iteration is specified as ρ_j^i .

The proposed BF-CTSO algorithm works by initializing the population of search agents. Secondly, the maximum number of iterations and initial parameters are chosen. Thirdly, the fitness F of every search individual is computed. Then, the optimal candidate is found in the specified search area once determining the fitness value. The position of every search agent is updated by either CSA or TSA technique by updating the value \vec{F} . Alter the updated search individual that moves beyond the bounding range of a particular search space. Determine and update the search agent when there is a better solution. Finally, it verifies the termination condition and stops the execution of the algorithm, or else, the algorithm will be executed. The "pseudo code of the offered"

BF-CTSO algorithm is shown in Algorithm 1.

The flow diagram of the designed BF-CTSO algorithm is given in Fig. 1.

4. Multi-objective derived energy efficient optimal relay selection in multi-hop vehicular communication

This part discusses the multi-objective function derived for cooperative vehicular networks along with the description of various constraints.

4.1. Objective function on relay optimization

In this designed "energy efficient optimal selection of relay" strategy in the multi-hop vehicular network, a new algorithm named BF-CTSO is implemented to get the optimal relays between the source and destination nodes for enhancing communication with various constraints. This optimal relay selection is done by resolving the fitness function regarding various parameters like link reliability, mobility factor, and energy consumption, outage probability, transmission delay. Eq. (11) derives the objective of the designed vehicular network with a relay selection scheme.

$$F_s = \underset{\{MR,e\}}{\text{argmin}} \left(O_{out} + EC + MOF + T_j + \frac{1}{LR} \right) \quad (11)$$

In Eq. (11), the total number of relays used for the optimization is

Table 2
Simulation parameters utilized for Cooperative cellular network.

Parameters	Values
Total number of iterations	100
AL	2, 3
KL	5 frames/second
Communication range of antennas	1000 m
Number of population	10
sr	0.5 bits/slot/Hz
χ	105dB
Number of relay nodes	50
Number of nodes	[50, 100, 150]

Table 1
Advantages and issues of existing cooperative communication networks.

Author [citation]	Technique	Benefits	Issues
Mohanakrishnan and Ramakrishnan [19]	MCTRP	<ul style="list-style-type: none"> It reduces the overhead of the network and guarantees efficient channel utilization. It has superior channel utilization capacity. 	<ul style="list-style-type: none"> It does not secure the designed model.
Narayan et al. [20]	QASO-BDT	<ul style="list-style-type: none"> It has reduced the end-to-end delay and energy value. It has maximized the lifetime of the nodes and achieved a higher throughput. 	<ul style="list-style-type: none"> This model does not discover the data paths for various relay nodes in dynamic MANET.
Wu et al. [21]	Joint optimization algorithm	<ul style="list-style-type: none"> It has reached maximum precision and reached near optimal relay node selection. It saves the efficiency of the model. 	<ul style="list-style-type: none"> This model does not solve the system outage probability.
Xu et al. [22]	Compressed sensing	<ul style="list-style-type: none"> It has offered a superior tradeoff between energy efficiency and accuracy. 	<ul style="list-style-type: none"> It observes higher overhead.
Li et al. [23]	EE-MWM	<ul style="list-style-type: none"> It gets superior efficiency to the cooperative cellular networks. It ensures lower energy consumption among both relay users and source users. 	<ul style="list-style-type: none"> There is a need of enhancing the performance while matching one relay user with one CEU.
Hayati et al. [24]	Monte Carlo simulation	<ul style="list-style-type: none"> It considerably improves the spectral efficiency and energy efficiency while estimating heterogeneous cellular networks. It reduces the interference in the femtocell network regarding cooperative communication. 	<ul style="list-style-type: none"> Though, while considering the real scene, achieving accurate CSI is complicated.
Wei et al. [25]	JUDRS	<ul style="list-style-type: none"> It increases the considerable energy efficiency gained using the designed approach. It minimizes the energy consumption of the network. 	<ul style="list-style-type: none"> It achieves a higher transmission error rate.
Sharfeen et al. [26]	PMPRSA	<ul style="list-style-type: none"> It offers a higher data rate. It selects the optimal mobile relay. 	<ul style="list-style-type: none"> It does not focus on computing utilities for various operators and does not focus on implementing multiple hexagons.

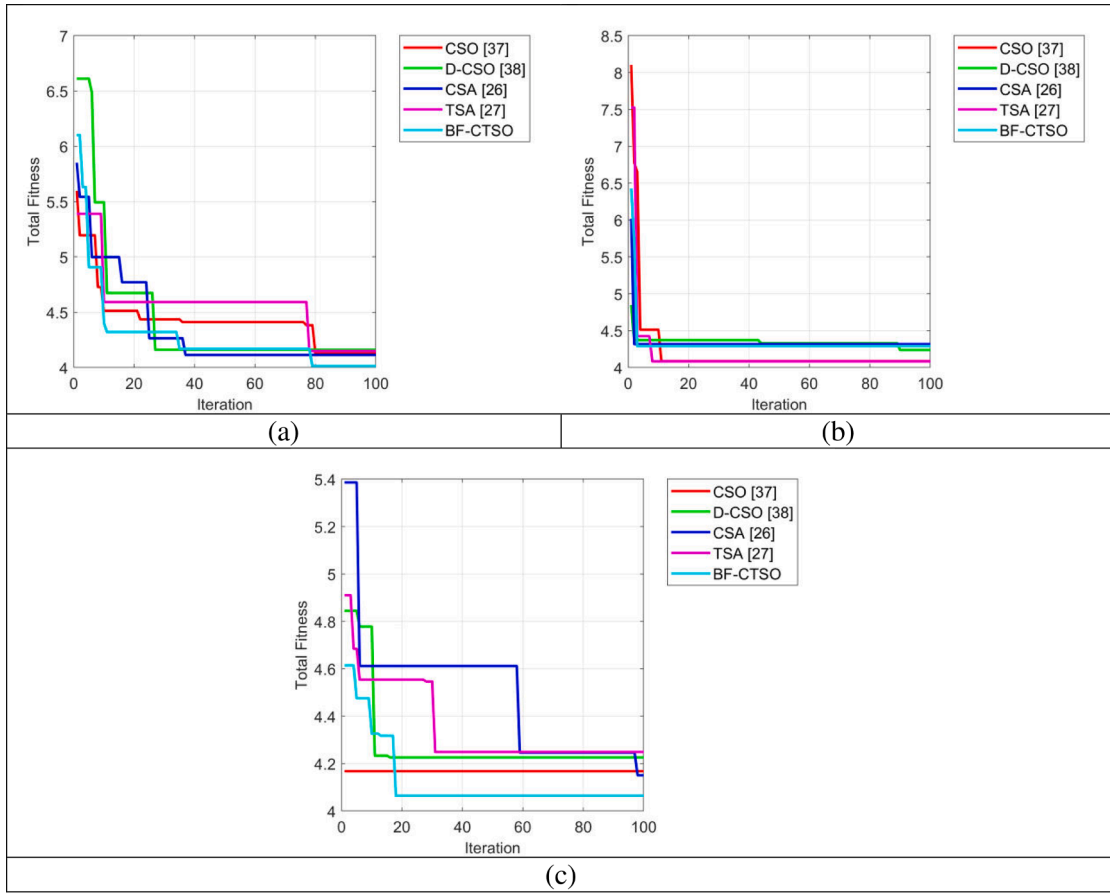


Fig. 4. Convergence analysis on designed “Energy Efficient selection of Optimal Relay in Multi-hop Cooperative Cellular Communication” with various algorithms for (a) scenario 1, (b) scenario 2, and scenario 3.

indicated as MR_{re} , and it is allocated among $[1, RE]$. Further, the constraints considered for deriving the multi-objective function are shown here, where outage probability is specified as O_{out} , the energy consumption is specified as EC , link reliability is given as LR , and the transmission delay T_j and mobility factor are shown as MOF . These parameters are derived in the upcoming sections.

The major goal of a cooperative vehicular network is to choose the multi-hops among the source and destination with the aid of the BF-CTSO algorithm, so, the unnecessary relay nodes or eavesdropper nodes are eradicated from the network. The optimal relay node selection in the designed vehicular network is illustrated in Fig. 2.

This diagrammatic illustration helps in understanding the relay selection strategy in the cooperative cellular communication model.

4.2. Constraints for multi-objective function

This proposed multi-hop relay selection in a vehicular communication network performs by selecting the number of relays by deriving the multi-objective function regarding constraints like link reliability, mobility factor, energy consumption, outage probability, and transmission delay, which are discussed here.

Link reliability [32]: “Link reliability” LR is described as “the possibility that a straight transmission link among two nodes will keep on constantly presented over a particular period”. The value LR is determined in Eq. (12).

$$LR = \int_{\hat{t}}^{\hat{t}+T_{fz}} ff(T_i)dti \quad \text{if } T_{fz} > 0 \quad (12)$$

Here, the continuous availability of a particular connection is known as T_{fz} , and the probability density function of the communications period (T_i) is denoted as $ff(T_i)$.

Average transmission delay [33]: It is described as the “average total transmission time per a data frame”. Here, one frame requires to be broadcasted $EP[T_{j_{DN}}(AL, re)]$ times on average before it is precisely reached by the destination under the relay number and arbitrary maximum transmission number AL , where the source broadcasts the first $EP[T_{j_{RE}}(AL, re)]$ times. Therefore, the formulation $T_j(AL, re)$ is derived in Eq. (13).

$$T_j(AL, re) = \frac{v \cdot EP[T_{j_{RE}}(AL, re)] + EP[T_{j_{DN}}(AL, re)] - EP[T_{j_{RE}}(AL, re)]}{KL} \quad (13)$$

$$EP[T_{j_{DN}}(AL, re)] = \sum_{is=1}^{AL} is \cdot \rho r(T_{j_{DN}} = is) \quad (14)$$

$$\rho r(T_{j_{DN}} = is) = \begin{cases} 1 - \rho r(SNDN_{out,1}) & is = 1 \\ \rho r(T_{j_{DN}} = \hat{is}) & 2 \leq is = \hat{is} \leq AL - 1 \\ \rho r(T_{j_{DN}} = AL) & is = AL \end{cases} \quad (15)$$

$$\rho r(T_{j_{DN}} = \hat{is}) = \rho r^{re}(SNRE_{out,AL-1}) \cdot \rho r(SNRE_{out,AL-1}) + \sum_{JH=1}^{AL-1} \sum_{re=1}^{RE} \rho r(T_{j_{MR}}^{re} = AL - JH) \cdot \rho r(SNDN_{out,AL-1}) \quad (16)$$

Once determining the $EP[T_{j_{DN}}(AL, re)]$, it is noticed that while re relays vanish for decoding the frames AL , they won't get it in AL^{th} the ARQ round. Consequently, $EP[T_{j_{RE}}(AL, re)]$ is determined in Eq. (17).

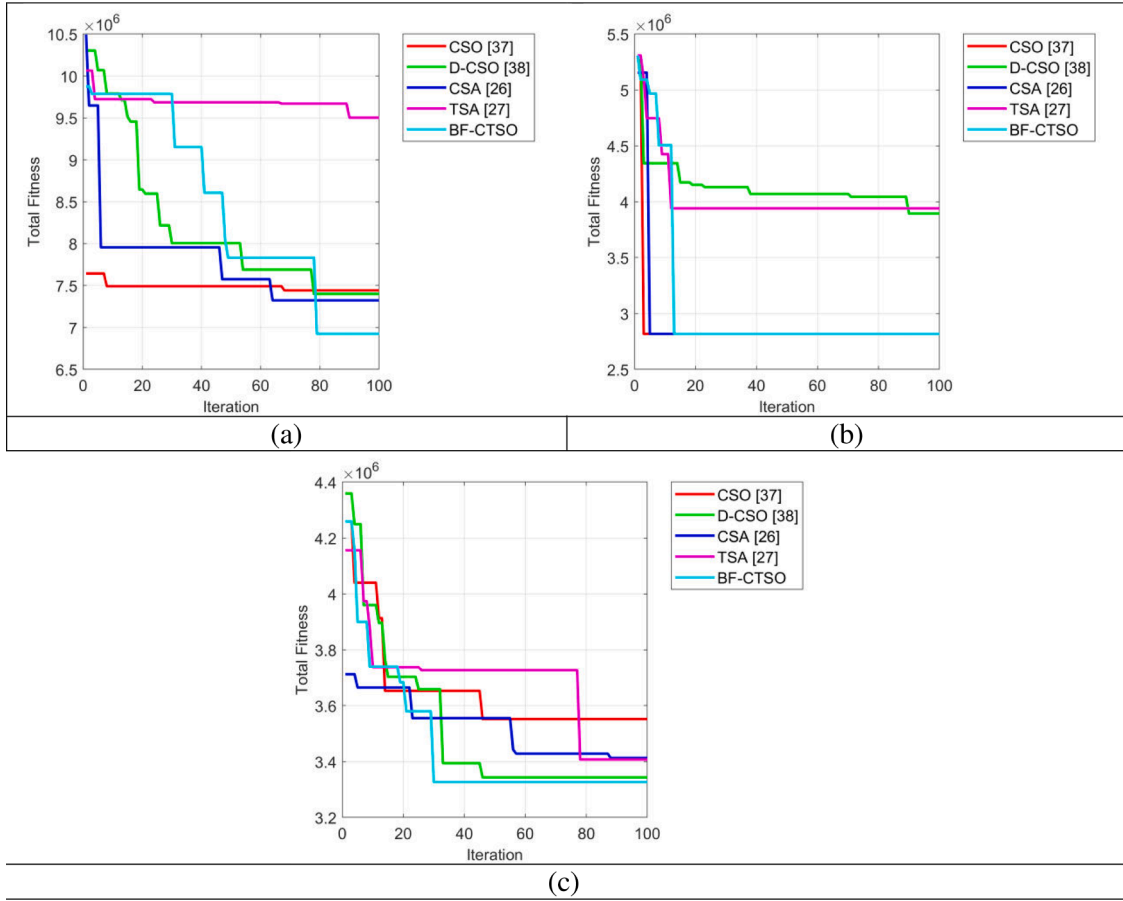


Fig. 5. The field dimension varied based on convergence analysis on designed “Energy Efficient selection of Optimal Relay in Multi-hop Cooperative Cellular Communication” with various algorithms for (a) scenario 1, (b) scenario 2, and scenario 3.

$$EP[Tj_{RE}(AL, re)] = \sum_{is=1}^{AL-1} \sum_{re=1}^{RE} is \cdot \rho r (Tj_{MR}^{re} = is) \quad (17)$$

Thus, the average transmission delay can be determined in the cooperative communication network.

“Energy consumption Model” [34]: The energy consumption EC for the designed multi-hop relay selection in a vehicular communication network is derived here.

In the entire communication path, the power consumption of a node during transmission includes both the circuit power consumption PW_{cp} and also the transmission signal power PW_{re} . Moreover, the data transmission rate s helps in determining the transmission signal power PW_{re} . Finally, for data transmission, the entire power utilized is derived in Eq. (18).

$$PW = PW_{re} + PW_{cp} \leq PW_{max} \quad (18)$$

In Eq. (18), the maximum obtainable battery power at the node is derived as PW_{max} . To estimate the energy efficiency in any network, the common measure is to estimate the energy consumption per information bit. While taking the cooperative networks, as the destination nodes, relay nodes, and source nodes has various power consumption issues, the sheer energy consumption measure is not applicable. Thus, there is a need of measuring the energy consumed by the source node and relay nodes, which is mathematically expressed in Eq. (19).

$$EC = \frac{(PW_{re} + PW_{SN})}{LT_{total}} \quad (19)$$

Hence, the energy consumption is measured for selecting the optimal relays.

Outage probability [33]: Eq. (20) formulates the outage probability of the data link with signaling rate s along with the transmitted signal bx with a Signal-to-Noise Ratio (SNR) \mathfrak{F} that is measured in the unit of bits/slot/Hz.

$$O_{out} = O\{Js(bx; by|ht)\langle sr \rangle\} = O\left\{\log_2\left(1 + \mathfrak{F}|ht|^2\right)\langle sr \rangle\right\} \quad (20)$$

Here, the attained signal is specified as by , the outage events at relays in the rq^{th} ARQ round are corresponding given as $SNMR_{out,rq}$, $SNMR_{DN_{out,rq}}$ and $SNDN_{out,rq}$ and the fading coefficient is noted as sh .

Moreover, the mathematical process of outage probability can be further simplified by taking the following assumptions $dq_{MR_1, DN} \neq dq_{MR_2, DN} \neq \dots \neq dq_{MR_{RE}, DN}$ and $dq_{SNMR_1} = dq_{SNMR_2} = \dots = dq_{SNMR_{RE}} = dq_{SNMR}$, where the expectation is specified as $EP[\cdot]$. On the other hand, it is noticed that $EP[|fs_{ijs,qs}|^2]$, in which the node pair is indicated as (is, js) , which is also expected as $EP[\omega_{ijs,qs}]$ that is proportional to $dq_{ijs}^{-\delta}$, the path loss factor is mentioned as δ .

Then, the communication of links from source to destination can be a failure, or else the outage happened for rq^{th} the ARQ round. This behavior is derived in Eq. (21).

$$O(SNDN_{out,q}) = \prod_{ut=1}^q O\left\{\log_2\left(1 + \eta|fs_{SNDN,ut}|^2\right)\langle sr \rangle\right\} = \prod_{ut=1}^q O\{\omega_{SNDN,ut} < \epsilon\} = \prod_{ut=1}^q HF_{\omega_{SNDN,ut}}(\epsilon) \quad (21)$$

Here, the “Cumulative Distribution Function (CDF)” of the arbitrary constraint RV is denoted by $HF_{RV}(bx)$, and $\epsilon = \frac{2^{sr}-1}{\eta}$, and the modules of power intensity gain matrixes are formulated as $EW_{SNMR} = [\omega_{SN,1}, \omega_{SN,2},$

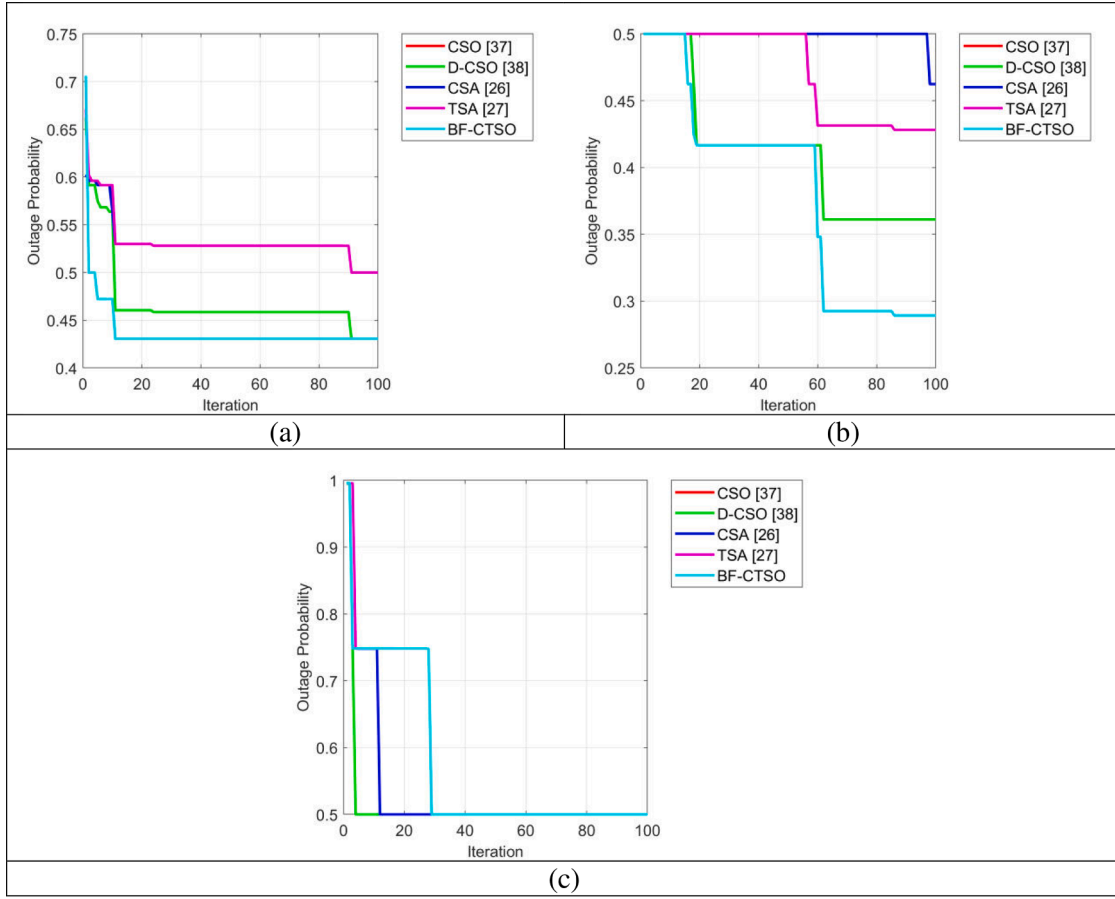


Fig. 6. Evaluation of outage probability for the designed “Energy Efficient selection of Optimal Relay in Multi-hop Cooperative Cellular Communication” with various algorithms for (a) scenario 1, (b) scenario 2, and scenario 3.

$$\dots, \omega_{SN,Q} \}_{1 \times Q}, EW_{SNDN} = [\omega_{SNDN,1}, \omega_{SNDN,2}, \dots, \omega_{SNDN,Q}]_{1 \times Q} \text{ and } \omega_{MRDN} = \begin{bmatrix} \omega_{MR_1DN,1} & \omega_{MR_1DN,2} & \dots & \omega_{MR_1DN,Q} \\ \omega_{MR_2DN,1} & \omega_{MR_2DN,2} & \dots & \omega_{MR_2DN,Q} \\ \vdots & \dots & \dots & \vdots \\ \omega_{MR_{RE}DN,1} & \omega_{MR_{RE}DN,2} & \dots & \omega_{MR_{RE}DN,Q} \end{bmatrix}_{RE \times Q}$$

The transmission of links from source to relay can be a failure or else the outage happened for rq^{th} the ARQ round. This behavior is derived in Eq. (22).

$$O(SNMR_{out,q}) = \prod_{ut=1}^q O\{\log_2(1 + \eta |f_{SNMR,ut}|^2) < sr\} = \prod_{ut=1}^q O\{\omega_{SNMR,ut} < \varepsilon\} = \prod_{ut=1}^q HF_{SNMN,ut}(\varepsilon) \quad (22)$$

Then, the transmission link among source and destination nodes along with there – relays has failed for rq^{th} ARQ rounds, which is derived in Eq. (23).

$$O(SNMRDN_{out,rq}) = \prod_{ut=1}^{T_{MR}^{re}} O\{\log_2(1 + \eta |f_{SNDN,ut}|^2) < sr\} \cdot \prod_{vp=T_{MR}^{re}+1}^q O\left\{\log_2\left(1 + \sum_{tj=1}^{re} \eta |f_{SMR_jDN,vp}|^2\right) < sr\right\} = \prod_{ut=1}^{T_{MR}^{re}} O\{\omega_{SNDN,ut} < \varepsilon\} \cdot \prod_{vp=T_{MR}^{re}+1}^q O\left\{\sum_{tj=1}^{re} \omega_{MR_jDN,vp} < \varepsilon\right\} \quad (23)$$

The “data frame at the first time” in the $(T_{MR}^{re})^{th}$ ARQ round is specified T_{MR}^{re} and it is decoded by there – out-of-neighbor nodes in the

network. Consequently, the probability T_{MR}^{re} is computed in Eq. (24).

$$O(T_{MR}^{re} = tj) = \binom{RE}{re} [O(SNMR_{out,tj-1}) - O(SNMR_{out,tj})]^{kr} \cdot O^{(RE-kr)}(SNMR_{out,tj}) \quad (24)$$

Until reaching the t^{th} ARQ round, this derivation illustrates that there – out-of-relays “will not decode the frame properly communicated from initial point”. A “Gamma arbitrary constraint with parameter” of $(ot_{ijs}, \frac{\Omega_{ijs}}{\omega_{ijs}})$ is indicated as $\omega_{ijs,q}$. Thus, Eq. (24) derives the CDF of the sum of re – “independents but not necessarily identical (i.n.i.d) Gamma random variables” with the constraints of $O\{\sum_{tj=1}^{re} \omega_{MR_jDN,vp} < lh\}$. Moreover, the “Possibility Distribution Function (PDF)” and CDF XH are computed here based on $XH = \sum_{tj=1}^{re} \alpha_{tj}$.

$$hf_{XH}(xh) = \prod_{tj=1}^{re} \left(\frac{ot_{tj}}{\Omega_{tj}}\right)^{ot_{tj}} FG_{\mathfrak{S},\mathfrak{S}}^{\mathfrak{S},0} \left[\exp(-xh) \right]_{\lambda_{\mathfrak{S}}^{(1)}, \lambda_{\mathfrak{S}}^{(2)}} \quad (25)$$

$$HF_{XH}(xh) = \prod_{tj=1}^{re} \left(\frac{ot_{tj}}{\Omega_{tj}}\right)^{ot_{tj}} FG_{\mathfrak{S}+1,\mathfrak{S}+1}^{\mathfrak{S}+1,0} \left[\exp(-xh) \right]_{\lambda_{\mathfrak{S}}^{(1)}, \lambda_{\mathfrak{S}}^{(2)}, 0} \quad (26)$$

Here, an integer is given $\mathfrak{S} = \sum_{tj=1}^{re} ot_{tj}$ and the Meiger-G function [35] is equated in Eq. (27).

$$\begin{aligned}
 FG_{pt,qt}^{kq,lq} \left[\begin{matrix} \lambda_{\mathfrak{S}}^{(1)} \\ \lambda_{\mathfrak{S}}^{(2)} \end{matrix} \right] &= FG_{pt,qt}^{kq,lq} \left[\begin{matrix} xh_1, xh_2, \dots, xh_{pt} \\ yh_1, yh_2, \dots, yh_{qt} \end{matrix} \right] \\
 &= \frac{1}{2\pi i s} \int_{CK} \frac{\prod_{js=1}^o \Gamma(yh_{j_s} - sg) \cdot \prod_{jt=1}^{RE} \Gamma(1 - xh_{j_t} + sg)}{\prod_{js=ot+1}^{qt} \Gamma(1 - yh_{j_s} + sg) \cdot \prod_{jt=RE+1}^{pt} \Gamma(xh_{j_t} - sg)} \zeta^{sg} ds g
 \end{aligned} \tag{27}$$

Term CK specifies the integral path by taking the relative size of the elements, and the Gamma function is equated as $\Gamma(\cdot)$, and $\lambda_{\mathfrak{S}}^{(1)}$ and $\lambda_{\mathfrak{S}}^{(2)}$ are respectively derived in Eq. (28) and Eq. (29).

$$\lambda_{\mathfrak{S}}^{(1)} = \left(\overbrace{\left(1 + \frac{ot_1}{\Omega_1} \right), \dots, \left(1 + \frac{ot_1}{\Omega_1} \right)}^{ot_1}, \dots, \overbrace{\left(1 + \frac{ot_{re}}{\Omega_{re}} \right), \dots, \left(1 + \frac{ot_{re}}{\Omega_{re}} \right)}^{ot_{re}} \right) \tag{28}$$

$$\lambda_{\mathfrak{S}}^{(2)} = \left(\overbrace{\left(\frac{ot_1}{\Omega_1} \right), \dots, \left(\frac{ot_1}{\Omega_1} \right)}^{o_1}, \dots, \overbrace{\left(\frac{ot_{re}}{\Omega_{re}} \right), \dots, \left(\frac{ot_{re}}{\Omega_{re}} \right)}^{o_p} \right) \tag{29}$$

In addition, the average power is mentioned $\Omega_{ij} \neq \Omega_q (t_j, q = 1, 2, 3, \dots, re, t_j \neq q)$ and then, Eq. (30) formulates the Rayleigh fading channel or the PDF of the sum of re Eq. (31).

$$h_{xh}^{Rayleigh} = \frac{1}{\prod_{ij=1}^{re} \Omega_{ij}} FG_{re,0}^{re,0} \left[\exp(-xh) \middle| \begin{matrix} 1 + \frac{1}{\Omega_1}, \dots, 1 + \frac{1}{\Omega_1} \\ \frac{1}{\Omega_1}, \dots, \frac{1}{\Omega_1} \end{matrix} \right] \tag{30}$$

$$h_{xh}^{Rayleigh} = \sum_{ij=1}^{re} \left(\prod_{sg \neq ij} \frac{1}{\frac{1}{\Omega_{sg}} - \frac{1}{\Omega_{ij}}} \right) \frac{1}{\Omega_{ij}} \exp\left(-\frac{xh}{\Omega_{ij}}\right) \tag{31}$$

Finally, the outage probability for all data links is determined. **Mobility Factor MOF** [36]: It is specified as the current stability of a potential relay and also determined as "a ratio among an exponential

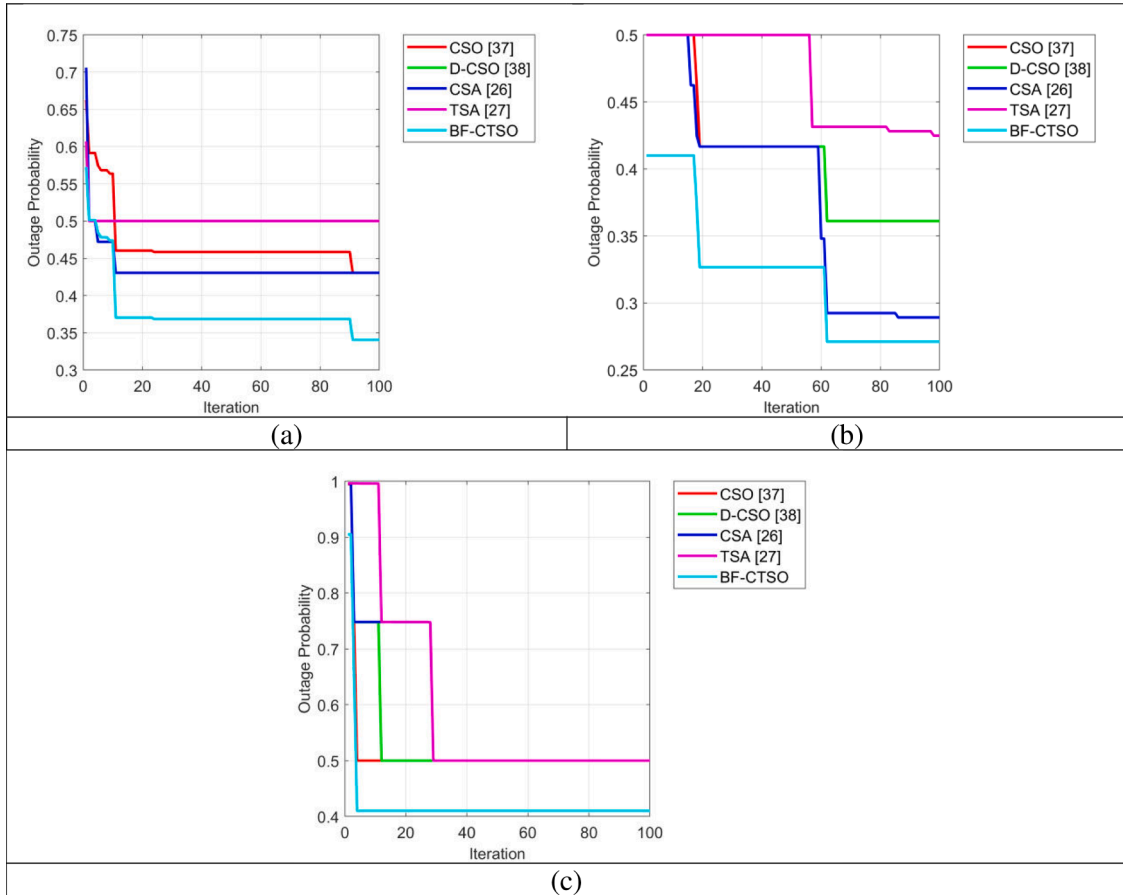


Fig. 7. The field dimension varied based on outage probability for the designed "Energy Efficient selection of Optimal Relay in Multi-hop Cooperative Cellular Communication" with various algorithms for (a) scenario 1, (b) scenario 2, and scenario 3.

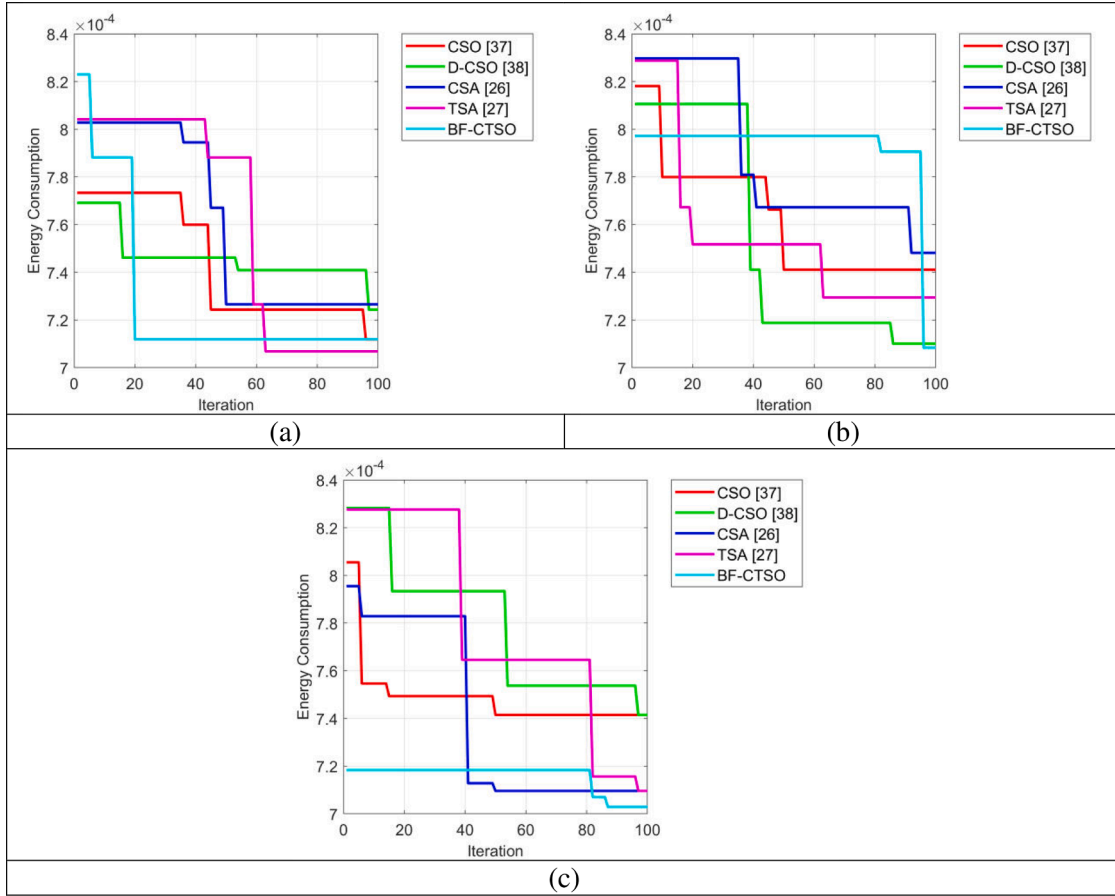


Fig. 8. Analysis of energy consumption for the designed “energy efficient optimal relay selection in multi-hop cooperative cellular communication” with various optimization algorithms for (a) scenario 1, (b) scenario 2, and scenario 3.

moving average of the pause time of the node AV_{pt} and the maximum detected pause time MD_{pt} that is derived from a time unit.

$$MOF = \frac{AV_{pt}}{MD_{pt}} \quad (32)$$

At last, this factor helps in selecting the relays as the most stable nodes.

5. System model and cooperative mechanism in multi-hop cooperative cellular communication

This section illustrates the cooperative strategy and system model of cooperative cellular communication for a multi-hop selection scheme.

5.1. Cooperative mechanism

The cooperative phase of the multi-hop cooperative vehicular communication network is explained here. The security of the cooperative phase is investigated by assuming the transmission of the signal bx done by the relay node with transmission power PW_{re} .

$$x_{MRDn,re} = \sqrt{PW_{re}} h_{sMRDn,re} bx + \beta'_{DN} \quad (33)$$

$$x_{MREN,re} = \sqrt{PW_{re}} h_{sMREN,re} bx + \beta'_{EN} \quad (34)$$

It has led to the reception of the corresponding signals at DN and EN . The AWGN at EN and DN with the similar power of β_0 are correspondingly indicated by β'_{DN} and β'_{EN} . It results in a higher privacy capability in the cooperative stage as shown in Eq. (35).

$$\mathfrak{R}_e^{CP,re} = \left[\log_2 \left(\frac{1 + \xi_1 |h_{sSNDN,re}|^2 + \xi_2 |h_{sMR,re,DN}|^2}{1 + \xi_1 |h_{sSNEV}|^2 + \xi_2 |h_{sMR,re,EN}|^2} \right) \right]^+ \quad (35)$$

$$\xi_2 = \frac{PW_{re}}{\beta_0} \quad (36)$$

However, the value ξ_2 is taken as zero, while the relay node cannot effectively make progress with the source message and it results in silence in this phase. At last, the complete instantaneous privacy capability from starting point to the target is shown in Eq. (37).

$$\mathfrak{R}_e^{re} = \frac{1}{2} \min \left\{ \left[\log_2 \left(\frac{1 + \chi_{SCS}^{re}}{1 + \chi_{SNEV}^{re}} \right) \right]^+, \left[\log_2 \left(\frac{1 + \chi_{SNDN}^{re} + \chi_{MRDn}^{re}}{1 + \chi_{SNEV}^{re} + \chi_{MREN}^{re}} \right) \right]^+ \right\} \quad (37)$$

Here, $\chi_{MREN}^{re} = \xi_2 |h_{sMREN,re}|^2$, $\chi_{MRDn}^{re} = \xi_2 |h_{sMRDn,re}|^2$, $\xi_{SNEV} = \xi_1 |h_{sSNEV}|^2$, and $\chi_{SCS}^{re} = \xi_1 |h_{sSCS}|^2$. During the broadcasting of every secret message in two-time slots, there is a need of using the coefficient $\frac{1}{2}$ in Eq. (37). Further, a “Generalized form of Optimal Relay Selection” (GORS) strategy is used for selecting the optimum relay in both cooperative and broadcast phases as formulated in Eq. (38).

$$\mathfrak{R}_e^{GORS} = \frac{1}{2} \max_{re \in \{1, \dots, RE\}} \{ \min \{ \mathfrak{R}_e^{BP,re}, \mathfrak{R}_e^{CP,re} \} \} \quad (38)$$

Through this formulation, it is clearly shown that the complete system security is affected owing to the leakage of secret data in either of cooperative or broadcast phase. Thus, the GORS approach maintains security by two diverse criteria, which are (i) the source-to-the-

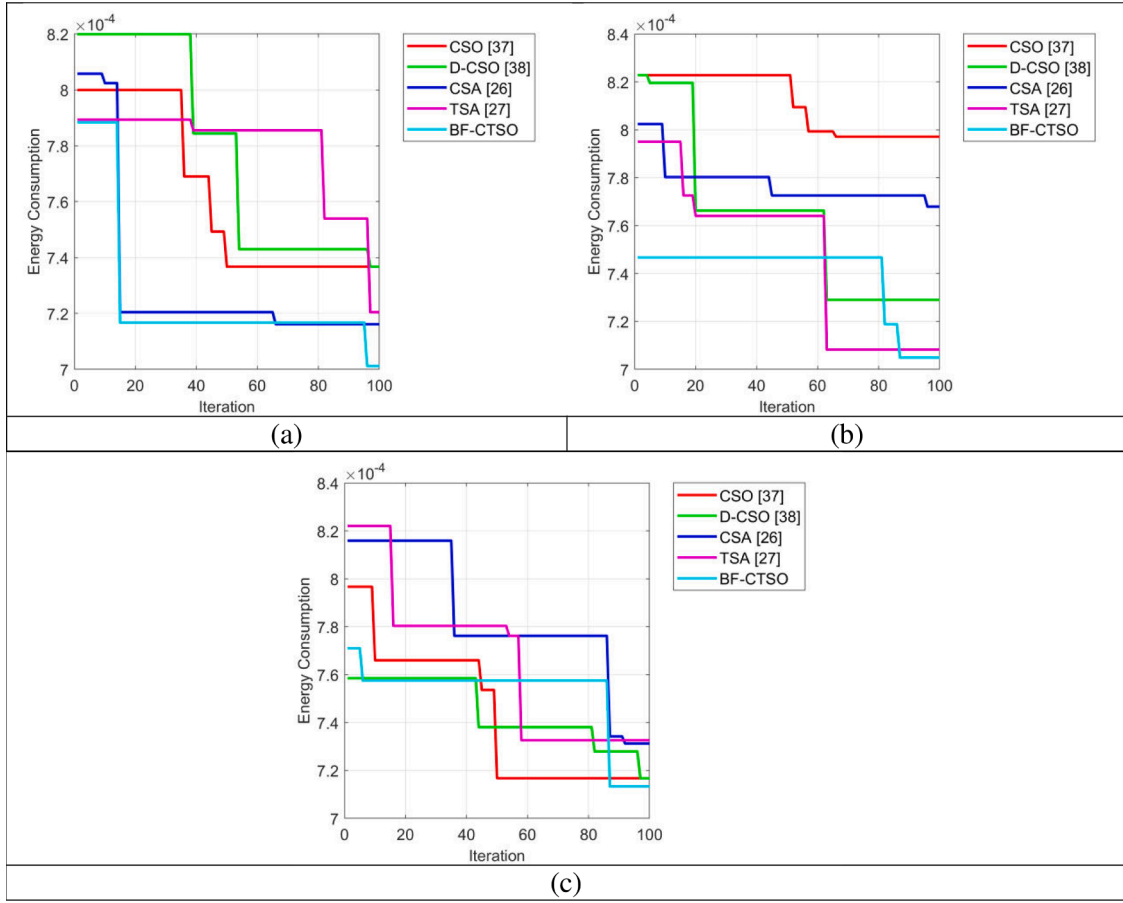


Fig. 9. The field dimension varied based on energy consumption for the designed “energy efficient selection of optimal relay in multi-hop cooperative cellular communication” with various algorithms for (a) scenario 1, (b) scenario 2, and scenario 3.

destination DN link, which is stronger than $SN - MR_{re}$, ($re = 1, \dots, RE$) links, and (ii) the source-to-destination DN link is weaker than the $SN - MR_{re}$, ($re = 1, \dots, RE$) links.

Thus, the secrecy capacity through GORS for the first constraint is derived in Eq. (39).

$$\mathfrak{R}_{\ell,1}^{GORS} = \frac{1}{2} \max_{re \in \{1, \dots, RE\}} \{ \min \{ \mathfrak{R}_{\ell}^{SNMR, re}, \mathfrak{R}_{\ell}^{CP, re} \} \} \quad (39)$$

Here, $\mathfrak{R}_{\ell}^{SNMR, re} = \left[\log_2 \left(\frac{1 + \chi_{SNMR}^{re}}{1 + \chi_{SNEN}} \right) \right]^+$ and $\chi_{SNMR}^{re} = \xi_1 |h_{SNMR, re}|^2$. Eq. (39) is similar to the maximum RE secrecy capacities [37]. The second case is derived in Eq. (40).

$$\mathfrak{R}_{\ell,2}^{GORS} = \frac{1}{2} \max_{re \in \{1, \dots, RE\}} \{ \min \{ \mathfrak{R}_{\ell}^{SNDN}, \mathfrak{R}_{\ell}^{CP, re} \} \} \quad (40)$$

In Eq. (40), $\mathfrak{R}_{\ell}^{SNDN} = \left[\log_2 \left(\frac{1 + \chi_{SNDN}}{1 + \chi_{SNEN}} \right) \right]^+$ that is similar to the “highest of RE privacy capabilities” and $\mathfrak{R}_{\ell}^{SNDN}$ demonstrates the “immediate privacy capability at the major target by direct communication”.

In the GORS strategy, the above-mentioned two criteria are applied; and factor 1/2 is used in Eq. (40) for minimizing the value of the transmission efficiency and also for enhancing the estimation of the wiretap link with the main channel. To select the optimal relay, the direct link is estimated by evaluating CSI in both receiving and transmitting nodes of each phase [38].

The overall CSI is accessible at receiver nodes [38], where the secret message can be forwarded to the source node at a specific rate δ_{ℓ} . Moreover, the decisions are carried out at the destination to get the source message with the ability of the direct link as formulated in Eq. (41).

$$\aleph : \mathfrak{R}_{\ell}^{SNDN} < \delta_{\ell} \quad (41)$$

It is performed by deriving the adaptive relaying, in which the secrecy capacity is maximized by a chosen best relay, or else the transmission of a new secret message is done through the source node, which is called AORS. The computational complexity can be minimized and spectral efficiency can be maximized with the help of the incremental relaying concept as given in Eq. (42) and further simplified in Eq. (43) [39].

$$\mathfrak{R}_{\ell}^{SNDN} < \left[\log_2 \left(\frac{1 + \xi_1 \max_{re \in \{1, \dots, RE\}} \{ |h_{SNMR, re}|^2 \}}{1 + \xi_1 |h_{SNEN}|^2} \right) \right]^+ \quad (42)$$

$$\eta : \chi_{SNDN} < \max_{re \in \{1, \dots, RE\}} \chi_{SNMR}^{re} \quad (43)$$

This AORS is implemented for increasing the secrecy capacity through performing the incremental collection of an optimal relay when estimating the \aleph .

5.2. System model

Cooperative communication has emerged in the recent day to enhance security by utilizing the characteristics of the physical layer. Here, among the source and major destination nodes, the relay nodes are used for improving the capacity of the main link compared with the wiretap ones. The secrecy efficiency can be amplified by maximizing the number of relays. On the other hand, relay selection is a most famous strategy with various relay cases for improving the effectiveness of the

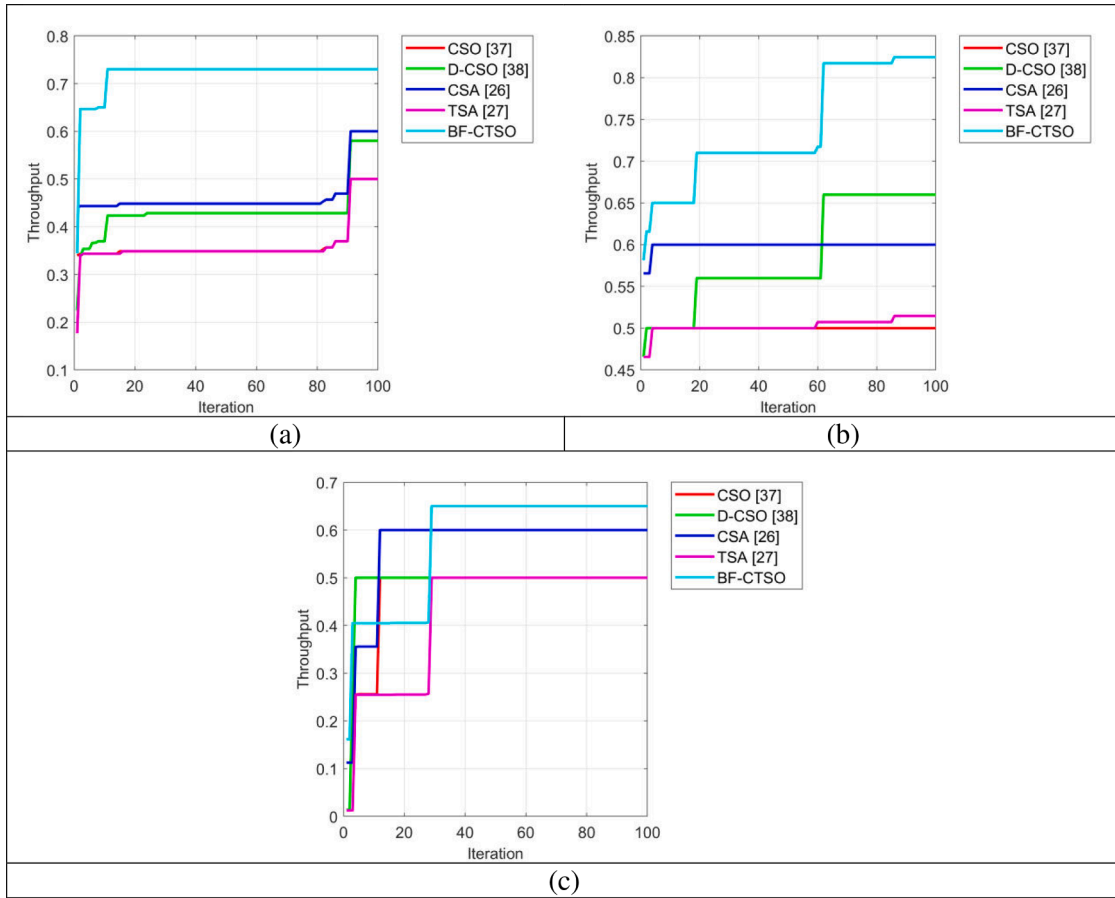


Fig. 10. Analysis of throughput for the designed “Energy Efficient Optimal Relay Selection in Multi-hop Cooperative Cellular Communication” with various optimization algorithms for (a) scenario 1, (b) scenario 2, and scenario 3.

cooperative systems [40] without or with security parameters. The relay selection schemes are utilized by taking the activity and passivity of the eavesdropper. Eavesdroppers nodes cause serious issues in the cooperative network by wiretapping from both relay and source nodes in the operational environments. Moreover, continuous monitoring of entire available channel links is required in various relay selection schemes, especially for a vehicular network that leads to an unwanted increase in system overhead. Thus, the performance of cooperative communication systems is mainly based on the selection strategy and the relaying protocol. Two eminent protocols are AF and DF. The efficient relay selection strategy for vehicular networks helps in various real-time applications including energy-saving improvements, road safety, and so on. Multi-hop cooperative vehicular communication network with various numbers of source and destination vehicles with active eavesdroppers is shown in Fig. 3.

Here, a time division multiplexing is used with different DF relay multi-hop “cooperative vehicular to vehicular communications system”. In a designed network, the nodes present in the vehicular network are the eavesdropper EN , destination DN, RE – relays $(MR_1, MR_2, \dots, MR_{RE})$, where $re = 1, 2, 3, \dots, RE$, and source node SN correlated with a single antenna. Moreover, all the available nodes are performed in a half-duplex way owing to the practical framework and so, they cannot broadcast and receive concurrently. However, they have direct paths from the “starting node” to the eavesdropper and major target nodes.

By taking the CSI of the wiretap and main channels, the precise estimation of channels in a communication network is possible. For this purpose, two conditions are formulated, in which via the error-free feedback link, CSI is offered at the transmitter nodes in the first scenario whereas the CSI is only accessible to the receiver nodes in the

second scenario [41]. Furthermore, the variance σ_{KcTr}^2 and zero mean are taken as the channel among every receiver node $Kc \in (MR_{RE}, EN, DN)$ for $re = 1, 2, \dots, RE$ that is h_{SKcTr} , and transmitter node $Tr \in (SN, MR_{RE})$. The source message Msg is encoded into a codeword $GS \in GS^{bg}$ by using capacity attaining codebook in the wiretap channel, where an alphabet of length bg is derived as GS^{bg} . The secret information is broadcasted by allocating the starting node which is known as the signal bx with communication power PW_{SN} .

The corresponding signals are achieved in this phase by the authorized nodes.

$$x_{DN} = \sqrt{PW_{SN}} h_{SNDN} bx + \beta_{DN} \tag{44}$$

$$x_{MR, re} = \sqrt{PW_{SN}} h_{SNMR, re} bx + \beta_{MR} \tag{45}$$

Here, the “Additive White Gaussian noise (AWGN)” at the diverse relays and considered destination are accordingly noted as β_{MR} and β_{DN} with the power of β_0 . Eq. (46) shows the received signal in the broadcast phase, where the eavesdropper node EN wiretaps from the source.

$$x_{EN} = \sqrt{PW_{SN}} h_{SNEN} bx + \beta_{EN} \tag{46}$$

Here, AWGN noise EN is specified as β_{EN} comprising density power β_0 . The best Gaussian codebook is used at the starting node with the Selection Combining Scheme (SCS). The secrecy capacities of the two broadcast phase and cooperative phases are separately derived, where a Single Input-Multiple Output (SIMO) channel is assumed as the secrecy capacity of the initial phase. The capacity of the SIMO channel from the source to the re^{th} relay and destination is derived in Eq. (47).

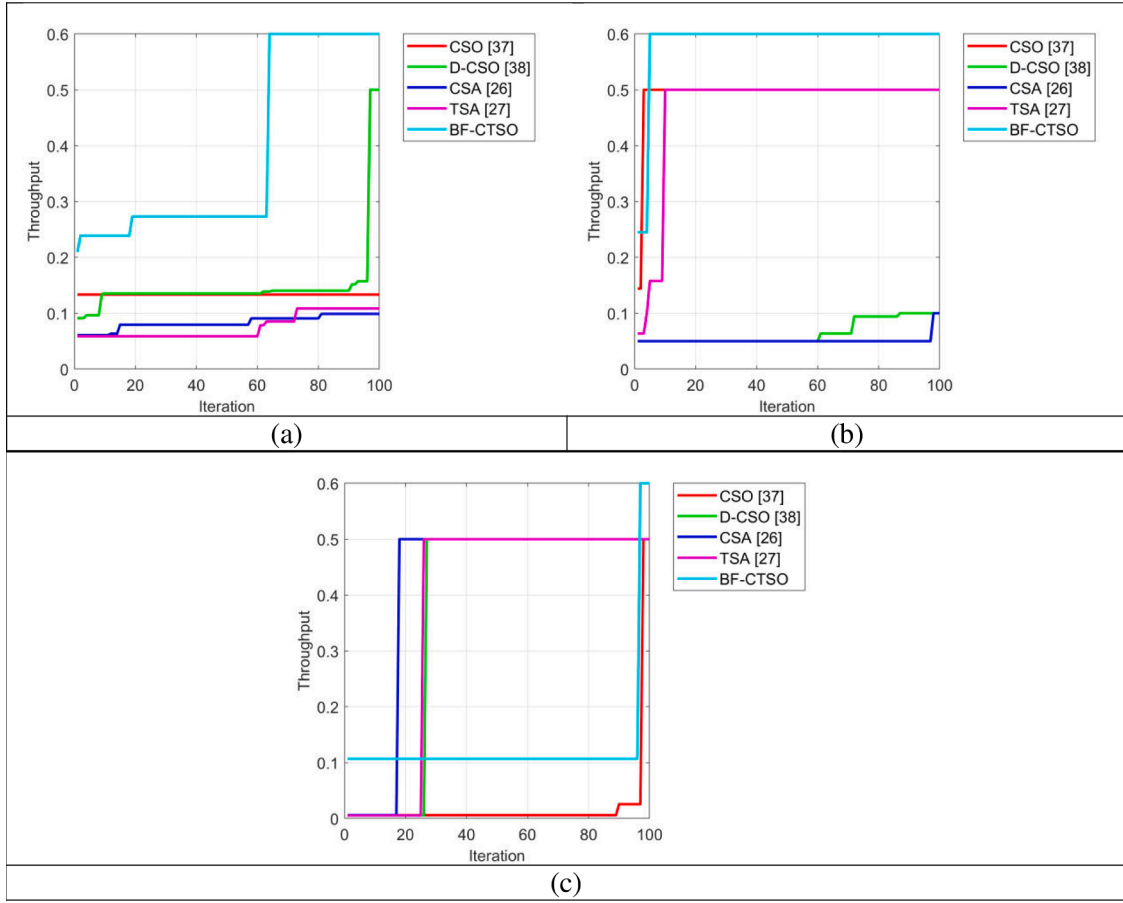


Fig. 11. The field dimension varies based on throughput for the designed “Energy Efficient selection of Optimal Relay in Multi-hop Cooperative Cellular Communication” with various algorithms for (a) scenario 1, (b) scenario 2, and scenario 3.

$$\Re_{SCS}^{re} = \log_2 \left(1 + \xi_1 |h_{SCS, re}|^2 \right) \quad (47)$$

$$h_{SCS, re} = \max \left\{ |h_{SNDN}|^2, |h_{SNMR, re}|^2 \right\} \quad (48)$$

$$\xi_1 = \frac{PW_{SN}}{\beta_0} \quad (49)$$

Consequently, the capacity of the wiretap channel is equated in Eq. (50).

$$\Re_{SNEV} = \log_2 \left(1 + \xi_1 |h_{SNEV}|^2 \right) \quad (50)$$

The secrecy capacity is derived from the variation among the capacities of wiretap and major links and so, the following capacity is utilized in the broadcast phase for performing secure communications at thereth relay.

$$\begin{aligned} \Re_e^{BP, re} &= [\Re_{SCS}^{re} - \Re_{SNEV}]^+ \\ &= \left[\log_2 \frac{1 + \xi_1 |h_{SCS, re}|^2}{1 + \xi_1 |h_{SNEV}|^2} \right]^+ \end{aligned} \quad (51)$$

In Eq. (51), the depiction $[bx]^+$ is specified as $\max(0, bx)$.

6. Results evaluation

This section discusses the experimental setup and the performance estimation on various constraints utilized for a cooperative vehicular communication network.

Table 1

6.1. Simulation setup

The recommended cooperative vehicle network was “developed in MATLAB 2020a”. The performance analysis was done by taking three diverse scenarios by differing the number of nodes as [50, 100, and 150] and experimental analysis was evaluated over the traditional algorithms such as Cat Swarm Optimization (CSO) [42], Dimension-based Cat Swarm Optimization (D-CSO) [43], CSA [31] and TSA [30], in terms of convergence analysis, transmission delay analysis, energy consumption, runtime, and outage probability analysis. The parameters taken for the experimentation are specified in Table 2. Here, the additional result shows that the variation of field dimension and also the variation of field dimension are considered as 50×50 m, 100×100 m, and 150×150 m for analyzing the performance of algorithms.

6.2. Evaluation of convergence

The efficiency of the suggested cooperative vehicular communication network is estimated over three scenarios with different heuristic approaches as depicted in Fig. 4. The field dimension varied based on convergence analysis of the designed cooperative vehicular communication network is shown in Fig. 5. The designed BF-CTSO algorithm shows the higher performance by reaching the lower fitness function as derived in abovementioned sections. For three cases, a cooperative vehicular communication network using the BF-CTSO algorithm for the selection of optimal relay improves the efficiency and attains competitive efficiency while estimating with existing heuristic algorithms.

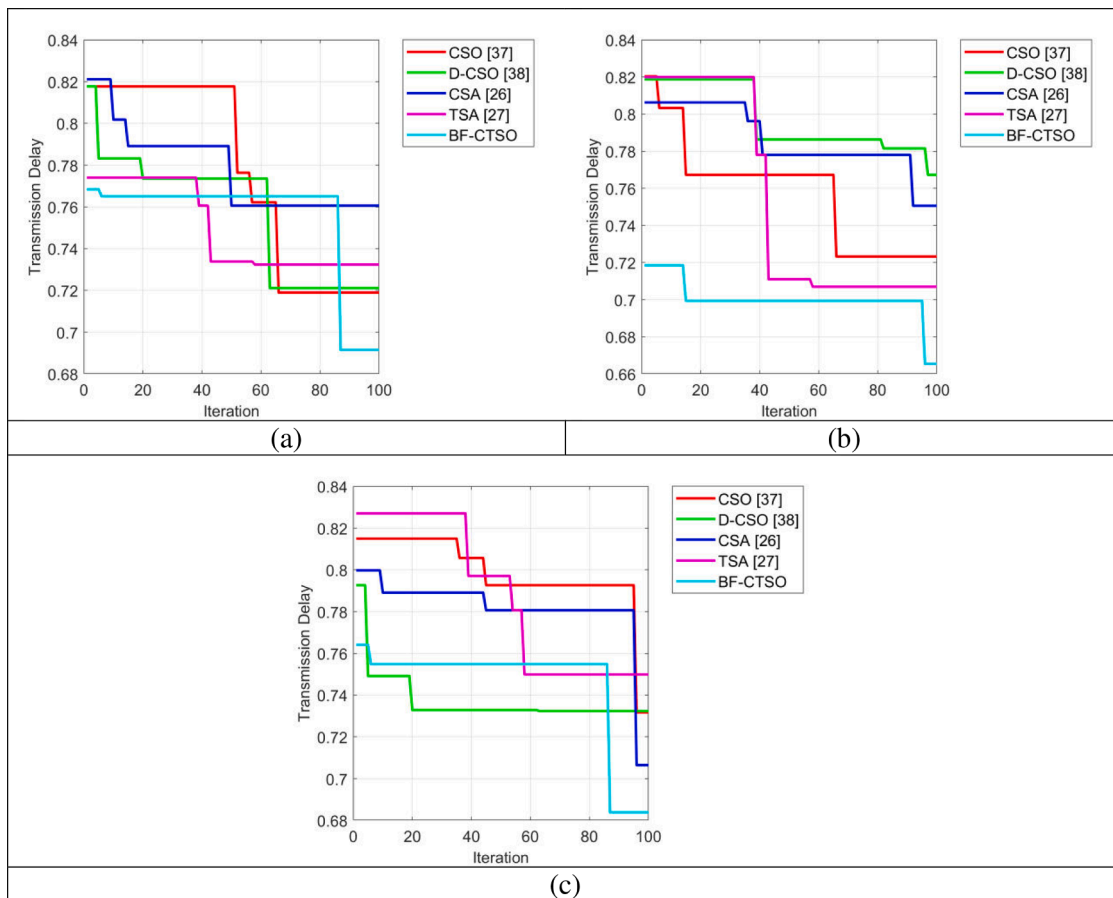


Fig. 12. Analysis of transmission delay for the designed “Energy Efficient selection of Optimal Relay in Multi-hop Cooperative Cellular Communication” with various algorithms for (a) scenario 1, (b) scenario 2, and scenario 3.

6.3. Analysis of outage probability

The performance estimation on the designed cooperative vehicular communication network in terms of outage probability is evaluated over three scenarios with various optimization methods as illustrated in Fig. 6. The field dimension varied based on outage probability analysis on the designed cooperative vehicular communication network is shown in Fig. 7. The recommended optimal relay selection using BF-CTSO algorithm shows the elevated performance by reaching the lower rate that demonstrates the superiority of the designed technique.

6.4. Estimation of energy consumption

The energy consumed by the suggested cooperative vehicular communication network is analyzed over three scenarios with different heuristic algorithms as shown in Fig. 8. The field dimension varied based on energy consumption analysis on the designed cooperative vehicular communication network is shown in Fig. 9. The designed optimal relay selection with BF-CTSO algorithm reaches lower energy consumption at the end of 100th iteration. Although the BF-CTSO reaches the higher energy consumption on initial iterations, at last, the lower energy consumption is taken by the nodes present in the designed cooperative network with the help of optimal relay selection using BF-CTSO.

6.5. Estimation of throughput

The overall performance of the recommended energy-efficient optimal relay selection in multi-hop cooperative cellular communication with various optimization algorithms over three scenarios is

estimated in Fig. 10. The field dimension varied based on throughput analysis on the designed cooperative vehicular communication network is shown in Fig. 11. The BF-CTSO technique gets higher efficiency regarding the higher range of throughput. As an example, while considering scenario 1, the designed BF-CTSO takes a higher throughput than others, which is 44%, 24%, 20, and 44% correspondingly elevated than CSO, D-CSO, CSA, and TSA techniques.

6.6. Estimation of transmission delay

The efficiency of the proposed energy-efficient optimal relay selection in multi-hop cooperative cellular communication is estimated in terms of transmission delay with various optimization algorithms over three scenarios as shown in Fig. 12. The field dimension varied based on transmission delay analysis on the designed cooperative vehicular communication network is shown in Fig. 13. The transmission delay of the designed cooperative network is reduced by BF-CTSO algorithm with the aid of optimal relay selection. For all three cases, the designed technique gets lower delay at the initial iterations itself while estimating with others. It finally ensures maximum performance with lower transmission delay and thus, this model is recommended for vehicular networks.

6.7. Analysis of runtime

The runtime analysis of the recommended optimal relay selection in a cooperative vehicular Network is portrayed in Table 3. The field dimension varied based on runtime analysis of the designed cooperative vehicular communication network as shown in Table 4. Moreover, the

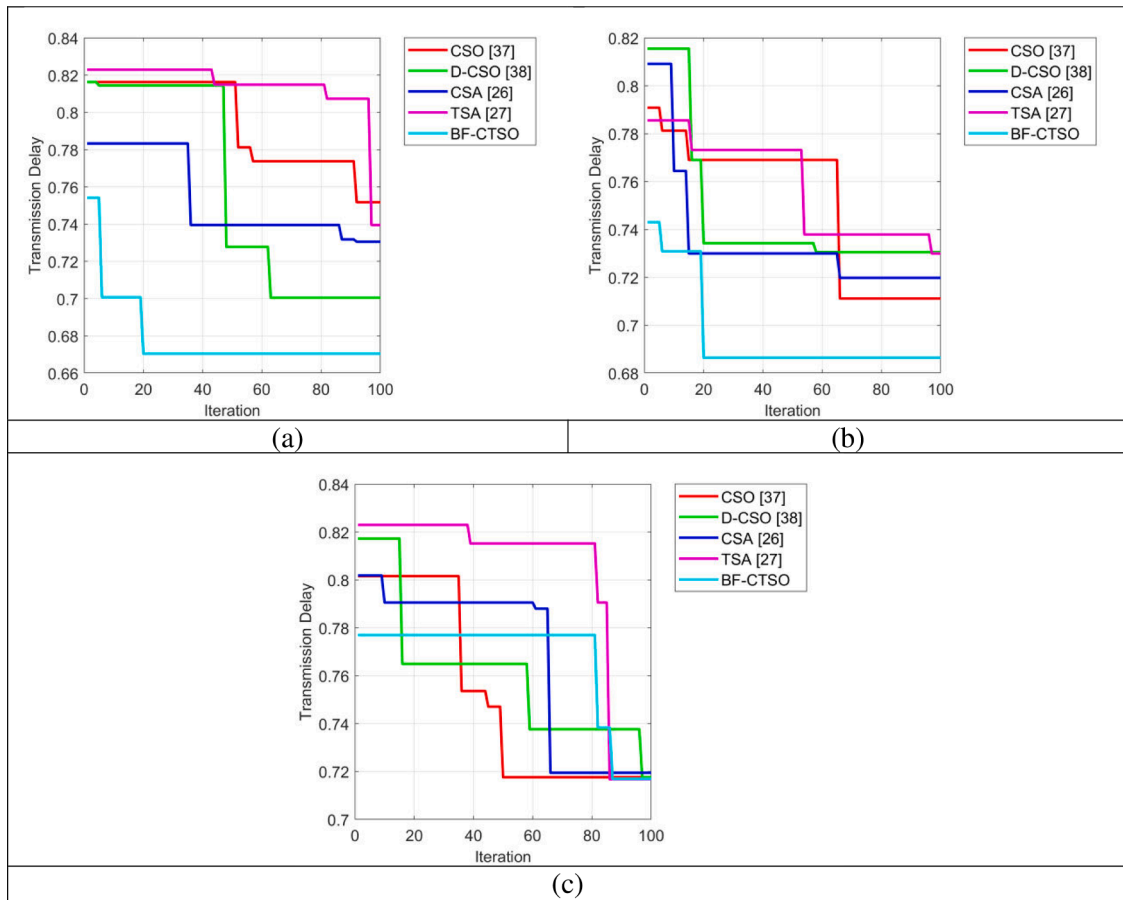


Fig. 13. The field dimension varied based on transmission delay for the designed “Energy Efficient selection of Optimal Relay in Multi-hop Cooperative Cellular Communication” with various algorithms for (a) scenario 1, (b) scenario 2, and scenario 3.

computation complexity of the designed BF-CTSO algorithm is shown in Table 5. In Table 5, the term Max_{iter} is denoted as the maximum number of iterations and the variable N_{pop} is represented as the number of populations. The term $chlen$ is indicated as chromosome length. While considering scenario 2, the designed BF-CTSO algorithm achieves 21.6%, 23%, 15%, and 2% accordingly enhanced than CSO, D-CSO, CSA, and TSA techniques.

6.8. Discussion

The heuristic algorithms are effective AI tools that can be helped to resolve real-time issues with low communication costs. For example, heuristic algorithms are utilized to adapt the high-mobility vehicular communication system to avoid road accidents by investigating the driving characteristic and environment by sensing data from the nearby environment. The adaption of a heuristic optimization algorithm to a high-mobility vehicular communication is extensively deployed in a cellular network which provides high immunity owing to its several

intrinsic advantages. Load balancing and offloading computation are the significant crucial elements that help to determine the maximum system utility in high-mobility vehicular communication systems. High-mobility vehicular communication using heuristic algorithms can provide improvements in these corresponding elements. Heuristic algorithms facilitate the sensitivity of vehicular environmental statistics’ real-time characteristics by communicating with the environment regarding the current state related to edge computing, cooperative caching, and offloading.

7. Conclusion

This research has focused on implementing an energy-efficient optimal relay selection model by deriving a new multi-objective function in a multi-hop cooperative vehicular communication network by implementing a hybrid heuristic strategy. A hybrid optimization model termed BF-CTSO algorithm was suggested to choose the optimal number of relays between the “source and destination” for the cooperative

Table 3 Analysis of run time of the designed optimal relay selection in cooperative vehicular Network over diverse heuristic algorithms for three scenarios.

Time	CSO [42]	D-CSO [43]	CSA [31]	TSA [30]	BF-CTSO
Scenario 1					
Time (sec)	0.88032	0.75789	0.58331	0.54135	0.5021
Scenario 2					
Time (sec)	0.53553	0.54636	0.49443	0.42809	0.41935
Scenario 3					
Time (sec)	0.24312	0.31229	0.21571	0.20897	0.080215

Table 4 The field dimension varied based on the run time of the designed optimal relay selection in a cooperative vehicular Network over diverse heuristic algorithms for three scenarios.

Time	CSO [42]	D-CSO [43]	CSA [31]	TSA [30]	BF-CTSO
Scenario 1					
Time (sec)	28.07	22.628	41.34	24.901	22.453
Scenario 2					
Time (sec)	27.136	26.869	29.802	25.576	24.38
Scenario 3					
Time (sec)	25.838	25.294	25.427	25.862	25.394

Table 5
Computational complexity of the designed BF-CTSO algorithm.

Proposed algorithm	Computational complexity
BF-CTSO algorithm	$O[(Max_{iter} * (N_{pop} + N_{pop} * chlen))]$

Algorithm 1

Proposed BF-CTSO algorithm.

Formulate a population of search individuals
 Validate the objective of every solution
 Set the social forces among search agents \vec{F}
 Initialization of the random parameters
 While ($j < j_{max}$)
 If $\vec{F} \leq F_{best}(j)$
 Update the solutions using TSA
 If $c_m \leq 0.5$
 Upgrade the search individuals with the help of the first constraint of Eq. (7)
 Else
 Upgrade the search individuals with the help of the second constraint of Eq. (7)
 End if
 Update swarm behavior using Eq. (8)
 Else
 Update the solutions using CSA
 If $r_{mi} \geq p^{ij}$
 Update the search individuals using the first constraint of Eq. (9)
 Else
 Update the search individuals using the second constraint of Eq. (9)
 End if
 Verify the feasibility of new positions
 Determine the fitness of new solutions
 Evaluate the new solutions
 $j = j + 1$
 End while
 Written the accurate solutions
 end

vehicular communication network. The multi-objective function regarding link reliability, energy consumption, outage probability, mobility factor, and transmission delay of the system was derived for offering the energy-efficient optimal relay selection. While considering scenario 3, the transmission delay of the recommended BF-CTSO algorithm has attained 9%, 9.3%, 4.2%, and 9% accordingly enhancing than CSO, D-CSO, CSA, and TSA techniques at the 100th iteration. However, there is a need of reducing energy consumption in the initial iterations themselves, which can be enhanced in the future. Since the current work focuses on the static vehicular system, it can be extended in the future by developing dynamic vehicular communication situations. The dynamic vehicular communication system will have the ability to consider dynamic characteristics like different vehicle mobility, transmit power interferences, time-varying channel quality, traffic flows, etc., which will overcome the problem of a static system.

Informed consent

Not Applicable.

Ethical approval

Not Applicable.

Funding

This research did not receive any specific funding.

CRediT authorship contribution statement

Uppula Kiran: Conceptualization, Methodology, Software, Data curation, Writing – original draft, Visualization, Investigation. **Krishan**

Kumar: Software, Validation, Writing – review & editing.

Declaration of Competing Interest

The authors declare no conflict of interest.

Data Availability

No data was used for the research described in the article.

Acknowledgements

I would like to express my very great appreciation to the co-authors of this manuscript for their valuable and constructive suggestions during the planning and development of this research work.

References

- [1] J. Li, L.J. Cimini, J. Ge, C. Zhang, H. Feng, Optimal and suboptimal joint relay and antenna selection for two-way amplify-and-forward relaying, *IEEE Trans. Wireless Commun.* 15 (2) (Feb. 2016) 980–993.
- [2] Y. Wu, L. p. Qian, L. Huang, X. Shen, Optimal relay selection and power control for energy-harvesting wireless relay networks, *IEEE Trans. Green Commun. Netw.* 2 (2) (June 2018) 471–481.
- [3] M. Najafi, V. Jamali, R. Schober, Optimal relay selection for the parallel hybrid RF/FSO relay channel: non-buffer-aided and buffer-aided designs, *IEEE Trans. Commun.* 65 (7) (July 2017) 2794–2810.
- [4] Q. Li, Q. Zhang, R. Feng, L. Luo, J. Qin, Optimal relay selection and beamforming in MIMO cognitive multi-relay networks, *IEEE Commun. Lett.* 17 (6) (June 2013) 1188–1191.
- [5] B.V. Nguyen, K. Kim, Secrecy outage probability of optimal relay selection for secure AnF cooperative networks, *IEEE Commun. Lett.* 19 (12) (Dec. 2015) 2086–2089.
- [6] M.M. Salim, D. Wang, Y. Liu, H. Abd El Atty Elsayed, M. Abd Elaziz, Optimal resource and power allocation with relay selection for RF/RE energy harvesting relay-aided D2D communication, *IEEE Access* 7 (2019) 89670–89686.
- [7] B. Klaiqi, X. Chu, J. Zhang, Energy-efficient and low signaling overhead cooperative relaying with proactive relay subset selection, *IEEE Trans. Commun.* 64 (3) (March 2016) 1001–1015.
- [8] P. Ubaidulla, S. Aissa, Optimal relay selection and power allocation for cognitive two-way relaying networks, *IEEE Wirel. Commun. Lett.* 1 (3) (June 2012) 225–228.
- [9] Abdullah Al Hayajneh, Md Zakirul Alam Bhuiyan, Ian McAndrew, A novel security protocol for wireless sensor networks with cooperative communication, *Computers* 1 (9) (2020) 4.
- [10] H. Gao, S. Zhang, Y. Su, M. Diao, M. Jo, Joint multiple relay selection and time slot allocation algorithm for the EH-abled cognitive multi-user relay networks, *IEEE Access* 7 (2019) 111993–112007.
- [11] J. Luo, S. Zhao, Z. Yang, G. Huang, D. Tang, Data-Driven-based relay selection and cooperative beamforming for non-regenerative multi-antenna relay networks, *IEEE Access* 9 (2021) 167154–167161.
- [12] P. Das, N.B. Mehta, Direct link-aware optimal relay selection and a low feedback variant for underlay CR, *IEEE Trans. Commun.* 63 (6) (June 2015) 2044–2055.
- [13] P. Lan, F. Sun, L. Chen, P. Xue, J. Hou, Power allocation and relay selection for cognitive relay networks with primary QoS constraint, *IEEE Wirel. Commun. Lett.* 2 (6) (December 2013) 583–586.
- [14] H. Feng, Y. Xiao, L.J. Cimini, Net throughput of centralized and decentralized cooperative networks with relay selection, *IEEE Wirel. Commun. Lett.* 3 (5) (Oct. 2014) 477–480.
- [15] C. Wang, J. Chen, Power allocation and relay selection for AF cooperative relay systems with imperfect channel estimation, *IEEE Trans. Veh. Technol.* 65 (9) (Sept. 2016) 7809–7813.
- [16] A. Dimas, D.S. Kalogerias, A.P. Petropulu, Cooperative beamforming with predictive relay selection for urban mmwave communications, *IEEE Access* 7 (2019) 157057–157071.
- [17] B. Choi, S.J. Bae, K. Cheon, A. Park, M.Y. Chung, Relay selection and resource allocation schemes for effective utilization of relay zones in relay-based cellular networks, *IEEE Commun. Lett.* 15 (4) (April 2011) 407–409.
- [18] A.H. Bastami, S. Habibi, Cognitive MIMO two-way relay network: joint optimal relay selection and spectrum allocation, *IEEE Trans. Veh. Technol.* 67 (7) (July 2018) 5937–5952.
- [19] Usha Mohanakrishnan, B. Ramakrishnan, MCTRP: an Energy efficient tree routing protocol for vehicular ad hoc network using genetic whale optimization algorithm, *Wirel. Personal Commun.* 110 (2020) 185–206.
- [20] Surya Narayan Mahapatra, Binod Kumar Singh, Vinay Kumar, A secure multi-hop relay node selection scheme based data transmission in wireless ad-hoc network via block chain, *Multimed. Tools Appl.* (2022).

- [21] Yin Wu, Wenbo Liu, Kaiyu Li, Power allocation and relay selection for energy efficient cooperation in wireless sensor networks with energy harvesting, *EURASIP J. Wirel. Commun. Netw.* 2017 (26) (2017).
- [22] X. Xu, J. Bao, H. Cao, Y. Yao, S. Hu, Energy-Efficiency-based optimal relay selection scheme with a ber constraint in cooperative cognitive radio networks, *IEEE Trans. Veh. Technol.* 65 (1) (Jan. 2016) 191–203.
- [23] Y. Li, C. Liao, Y. Wang, C. Wang, Energy-efficient optimal relay selection in cooperative cellular networks based on double auction, *IEEE Trans. Wireless Commun.* 14 (8) (Aug. 2015) 4093–4104.
- [24] Maryam Hayati, Hashem Kalbkhani, Mahrokh G. Shayesteh, Energy-efficient relay selection and power allocation for multi-source multicast network-coded D2D communications, *AEU - Int. J. Electron. Commun.* 128 (January 2021).
- [25] Y.A.N.G. Wei, L.I. Li-hua, S.U.N. Wan-lu, W.A.N.G. Ying, Energy-efficient relay selection and optimal relay location in cooperative cellular networks with asymmetric traffic, *J. China Univ. Posts Telecommun.* 17 (6) (December 2010) 80–88.
- [26] Benish Sharfeen Khan, Sobia Jangsher, Hassaan Khaliq Qureshi, Syed Hassan Ahmed, Predicted mobility based profitable relay selection in cooperative cellular network with mobile relays, *Phys. Commun.* 37 (December 2019).
- [27] Daxin Tian, Kunxian Zheng, Jianshan Zhou, Xuting Duan, Yunpeng Wang, Zhengguo Sheng, Qiang Ni, A microbial inspired routing protocol for VANETs, *IEEE Internet Things J.* 5 (4) (2018) 2293–2303.
- [28] Jagadeeshwar Tabjula, S. Kalyani, Prabhu Rajagopal, Balaji Srinivasan, Statistics-based baseline-free approach for rapid inspection of delamination in composite structures using ultrasonic guided waves, *Struct. Health Monitor.* (2021).
- [29] Deepjyoti Roy, Mala Dutta, A systematic review and research perspective on recommender systems, *J. Big Data* 9 (2022) 59.
- [30] Satnam Kaur, Lalit K. Awasthi, A.L. Sangal, Gaurav Dhiman, Tunicate Swarm Algorithm: a new bio-inspired based meta-heuristic paradigm for global optimization, *Eng. Appl. Artif. Intell.* 90 (April 2020).
- [31] Alireza Askarzadeh, A novel metaheuristic method for solving constrained engineering optimization problems: crow search algorithm, *Comput. Struct.* 169 (June 2016) 1–12.
- [32] Halbast Rasheed Ismael, Siddeeq Y. Ameen, Shakir Fattah Kak, Hajar Maseeh Yasin, Ibrahim Mahmood Ibrahim, Awder Mohammed Ahmed, Zryan Najat Rashid, Naaman Omar, Azar Abid Salih, Dindar Mikaeel Ahmed, Reliable communications for vehicular networks, *Asian J. Res. Comput. Sci.* 10 (2) (2021) 33–49.
- [33] S. Li, F. Wang, J. Gaber, Y. Zhou, An optimal relay number selection algorithm for balancing multiple performance in flying Ad Hoc networks, *IEEE Access* 8 (2020) 225884–225901.
- [34] Jianrong Bao, Jiawen Wu, Chao Liu, Bin Jiang, Xianghong Tang, Optimized power allocation and relay location selection in cooperative relay networks, *Advanced Wirel. Commun. Mobile Comput. Technol. Internet Things* (2017).
- [35] I.S. Gradshteyn, I.M. Ryzhik, Table of integrals, series and products, *Math. Comput.* 20 (96) (2007) 1157–1160.
- [36] Tauseef Jamal, Paulo Mendes, André Zúquete, Wireless cooperative relaying based on opportunistic relay selection, *Int. J. Adv. Netw. Serv.* (July 2012).
- [37] I. Krikidis, J.S. Thompson, S. McLaughlin, Relay selection for secure cooperative networks with jamming, *IEEE Trans. Wireless Commun.* 8 (10) (2008) 5003–5011.
- [38] Y. Zou, X. Wang, W. Shen, Optimal relay selection for physical-layer security in cooperative wireless networks, *IEEE J. Sel. Areas Commun.* 31 (10) (Oct. 2013) 2099–2111.
- [39] V.N.Q. Bao, N. Linh-Trung, M. Debbah, 'Relay selection schemes for dual-hop networks under security constraints with multiple eavesdroppers, *IEEE Trans. Wireless Commun.* 12 (12) (Dec. 2013) 6076–6085.
- [40] Daxin Tian, Jianshan Zhou, Zhengguo Sheng, An adaptive fusion strategy for distributed information estimation over cooperative multi-agent networks, *IEEE Trans. Inf. Theory* 63 (5) (2017) 3076–3091.
- [41] Sajad Poursajadi, Mohammad Hossein Madani, Adaptive optimal relay selection in cooperative vehicular communications under security constraints, *Vehic. Commun.* (October 2021) 31.
- [42] Abdelhamid Bouzidi, Mohammed Essaid Riffi, Mohammed Barkatou, Cat swarm optimization for solving the open shop scheduling problem, *J. Industr. Eng. Int.* 15 (2019) 367–378.
- [43] Uppula Kiran, Krishan Kumar", Throughput and outage probability-aware intelligent swarm-based multi-hop selection in vehicular network, *Commun. Cybern. Syst.* (2022).



wireless communications.

Mr. Kiran Uppula was born in India on February 10, 1987. He received B. Tech degree in Electronics and Communication Engineering from Vaagdevi College of Engineering-Warangal, Jawaharlal Nehru Technological University-Hyderabad, India in 2008, M. Tech (Wireless and Mobile Communication -ECE) from Vaagdevi College of Engineering-Warangal, Jawaharlal Nehru Technological University-Hyderabad, India in 2011 and Currently is a Ph.D (Electronics & Communication Engineering) Student in Lovely Professional University, Jalandhar-Delhi, Punjab-INDIA. He worked on wireless communication systems. He has published a good number of papers in referred conferences and journals. His present research interest includes



Dr. Krishan Kumar was born in India. He completed B.Tech and M.Tech in IT, Ph.D in ECE, Punjab, India. He has 25 years of experience teaching and industry. He is working as a professor at Lovely Professional University, Punjab, India. He worked in many government and non-government organizations in India and abroad, he has educated funded projects in India and abroad also. He is guiding M.Tech and Ph.D students. He has published more than 70 of papers in referred journals and conferences. And 4 books and more than 20 books chapters published. He is reviewer and editor few national and international journals.

DESIGN OF FINITE FIELD MULTIPLIERS WITH CRC-BASED ERROR DETECTION CONSTRUCTIONS IN CRYPTOGRAPHY APPLICATIONS

¹ YALAGANDHULA EESWARASAI, ² Mr. G. BABU

¹ PG Scholar, Dept. of ECE, Vaagdevi College of Engineering, Warangal, Telangana, India.

² Assistant professor, Dept. of ECE, Vaagdevi College of Engineering, Warangal, Telangana, India.

¹ eeswarasai@gmail.com, ² babugundlapally@gmail.com

Abstract— In this paper Finite-field multiplication has received prominent attention in the literature with applications in cryptography and error-detecting codes. For many cryptographic algorithms, this arithmetic operation is a complex, costly, and time-consuming task that may require millions of gates. In this work, we propose efficient hardware architectures based on cyclic redundancy check (CRC) as error-detection schemes for post quantum cryptography (PQC) with case studies for the Luov cryptographic algorithm. Luov was submitted for the National Institute of Standards and Technology (NIST) PQC standardization competition and was advanced to the second round. The CRC polynomials selected are in-line with the required error-detection capabilities and with the field sizes as well. We have developed verification codes through which software implementations of the proposed schemes are performed to verify the derivations of the formulations. Additionally, hardware implementations of the original multipliers with the proposed error-detection schemes are performed over a Xilinx field-programmable gate array (FPGA), verifying that the proposed schemes achieve high error coverage with acceptable overhead.

Keywords— Cyclic redundancy check (CRC), fault detection, field-programmable gate array (FPGA), finite-field multiplication.

I. INTRODUCTION

Many modern, sensitive applications and systems use finite-field operations in their schemes, among which finite-field multiplication has received prominent attention. Finite-field multipliers perform multiplication modulo, an irreducible polynomial used to define the finite field. For post quantum cryptography (PQC), the inputs can be very large, and the finite-field multipliers may require millions of logic gates. Therefore, it is a complex task to implement such architectures resilient to natural and malicious faults; consequently, research has focused on ways to

eliminate errors and obtain more reliability with acceptable overhead [1]–[6]. Moreover, there has been previous work on countering fault attacks and providing reliability for PQC. Sarker et al. [7] used error-detection schemes of number theoretic transform (NTT) to detect both permanent and transient faults. Mozaffari-Kermani et al. [8] performed fault detection for stateless hash-based PQC signatures. Additionally, error-detection hash trees for stateless hash-based signatures are proposed in [9] to make such schemes more reliable against natural faults and help protecting them against malicious faults. In [10], algorithm-oblivious constructions are proposed through recomputing with swapped cipher text and additional authenticated blocks, which can be applied to the Galois counter mode (GCM) architectures using different finite-field multipliers in $G F(2^{128})$. Several countermeasures based on error-detection checksum codes and spatial/temporal redundancies for the NTRU encryption algorithm have been presented in [11].

Our proposed error-detection architectures are adapted to the Luov cryptographic algorithm [12]; however, they can be applied to different PQC algorithms that use finite-field multipliers. The Luov algorithm was submitted for National Institute of Standards and Technology (NIST) standardization competition [13] and was advanced to the second round [14]. Cyclic redundancy check (CRC) error-detection schemes are applied in our proposed hardware constructions to make sure that they are overhead-aware with high error coverage. Our contributions in this brief are summarized as follows.

1) Error-detection schemes for the finite-field multipliers $G F(2^m)$ with $m > 1$ used in the Luov cryptographic algorithm are proposed. These error-detection architectures are based on CRC-5. Additionally, we explore and study both primitive and standardized generator

polynomials for CRC-5, comparing their complexity.

2) We derive new formulations for the error-detection schemes of Luov's algorithm, performing software implementations for the sake of verifications. We note that such derivation covers a wide range of applications and security levels. Nevertheless, the presented schemes are not confined to these case studies.

3) The proposed error-detection architectures are embedded into the original finite-field multipliers. We perform the implementations using Xilinx field-programmable gate array (FPGA) family Kintex Ultrascale+ for device xcku5p-ffvd900-1-i to confirm that the schemes are overhead-aware and that they provide high error coverage.

II. RELATED WORK

a) Reliable hardware architectures for the third-round sha-3 finalist grostl benchmarked on fpga platform:

The third round of competition for the SHA-3 candidates is ongoing to select the winning function in 2012. Although much attention has been devoted to the performance and security of these candidates, the approaches for increasing their reliability have not been presented to date. In this paper, for the first time, we propose a high-performance scheme for fault detection of the SHA-3 round-three candidate Grostl which is inspired by the Advanced Encryption Standard (AES). We propose a low-overhead fault detection scheme by presenting closed formulations for the predicted signatures of different transformations of this SHA-3 third-round finalist. These signatures are derived to achieve low overhead and include one or multi-bit parities and byte/word-wide predicted signatures. The proposed reliable hardware architectures for Grostl are implemented on Xilinx Virtex-6 FPGA family to benchmark their hardware and timing characteristics. The results of our evaluations show high error coverage and acceptable overhead for the proposed scheme.

b) Reliable hardware architectures for cryptographic block ciphers led and height:

Cryptographic architectures provide different security properties to sensitive usage models. However, unless reliability of architectures is

guaranteed, such security properties can be undermined through natural or malicious faults. In this paper, two underlying block ciphers which can be used in authenticated encryption algorithms are considered, i.e., light encryption device and high security and lightweight block ciphers. The former is of the Advanced Encryption Standard type and has been considered area-efficient, while the latter constitutes a Feistel network structure and is suitable for low-complexity and low-power embedded security applications. In this paper, we propose efficient error detection architectures including variants of recomputing with encoded operands and signature-based schemes to detect both transient and permanent faults. Authenticated encryption is applied in cryptography to provide confidentiality, integrity, and authenticity simultaneously to the message sent in a communication channel. In this paper, we show that the proposed schemes are applicable to the case study of simple lightweight CFB for providing authenticated encryption with associated data. The error simulations are performed using Xilinx Integrated Synthesis Environment tool and the results are benchmarked for the Xilinx FPGA family Virtex-7 to assess the reliability capability and efficiency of the proposed architectures.

III. CYCLIC REDUNDANCY CHECK

The cyclic redundancy check, or CRC, is a technique for detecting errors in digital data, but not for making corrections when errors are detected. It is used primarily in data transmission. In the CRC method, a certain number of check bits, often called a checksum, are appended to the message being transmitted. The receiver can determine whether or not the check bits agree with the data, to ascertain with a certain degree of probability whether or not an error occurred in transmission. If an error occurred, the receiver sends a "negative acknowledgement" (NAK) back to the sender, requesting that the message be retransmitted.

The technique is also sometimes applied to data storage devices, such as a disk drive. In this situation each block on the disk would have check bits, and the hardware might automatically initiate a reread of the block when an error is detected, or it might report the error to software.

The material that follows speaks in terms of a "sender" and a "receiver" of a "message," but it should be understood that it applies to storage writing and reading as well.

IV. PROPOSED SYSTEM

The proposed system are five popular PQC algorithm classes: code-based, hash-based, isogeny-based, lattice-based, and multivariate-quadratic equation-based cryptosystems [15]. Code-based cryptography differs from others in that its security relies on the hardness of decoding in a linear error-correcting code. Hash-based cryptography creates signature algorithms based on the security of a selected cryptographic hash function. The security of isogeny-based cryptography is based on the hard problem to find an isogeny between two given super singular elliptic curves. Lattice-based cryptography is capable of creating a public-key cryptosystem based on lattices. Lastly, the security of multivariate-quadratic-equation-based cryptography depends on the difficulty of solving a system of multivariate polynomials over a finite field. Such cryptographic schemes use large field sizes to provide the needed security levels.

Luov is a multivariate public key cryptosystem and an adaptation of the unbalanced oil and vinegar (UOV) signature scheme, but there is a restriction on the coefficients of the public key. Instead, the scheme uses two finite fields: one is the binary field of two elements, whereas the other is its extension of degree m . F_2 is the binary field and F_{2^m} is its extension of degree m . The central map $F: F_n 2^m \rightarrow F_o 2^m$ is a quadratic map, where o and v satisfy $n = o + v$, $\alpha_{i,j,k}$, $\beta_{i,k}$ and γ_k are chosen from the base field F_2 , and whose components f_1, \dots, f_o are in the form $f_k(x) = \sum_{i=1}^n \sum_{j=i}^n \alpha_{i,j,k} x_i x_j + \sum_{i=1}^n \beta_{i,k} x_i + \gamma_k$.

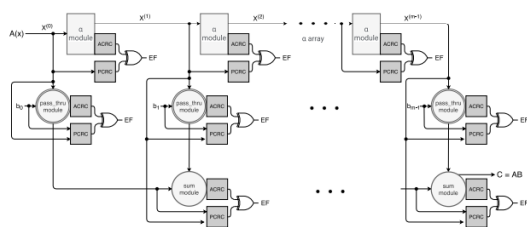


Figure-1: Finite-field multiplier with the proposed error-detection schemes based on CRC

These finite-field multiplications are very complex and require large-area footprint. Therefore, it is a complex task to implement such architectures resilient to natural and malicious faults. The aim of

this work is to provide countermeasures against natural faults and fault injections for the finite-field multipliers used in cryptosystems such as the Luov algorithm as a case study, noting that the proposed error-detection schemes can be adapted to other applications and cryptographic algorithms whose building blocks need finite-field multiplications. Readers who are interested in knowing more details about the Luov’s cryptographic algorithm are encouraged to refer to [12].

a) Proposed fault-detection architectures

The multiplication of any two elements A and B of $G F(2^m)$, following the approach in [16], can be presented as $A \cdot B \text{ mod } f(x) = \sum_{i=0}^{m-1} b_i \cdot (\sum_{j=0}^{m-1} a_j X^j) \text{ mod } f(x) = \sum_{i=0}^{m-1} b_i \cdot X(i)$, where the set of α_i ’s is the polynomial basis of element A , the set of b_i ’s is the B coefficients, $f(x)$ is the field polynomial, $X(i) = \alpha \cdot X(i-1) \text{ mod } f(x)$, and $X(0) = A$. To perform finite-field multiplication, three different modules are needed: sum, α , and pass-thru modules. The sum module adds two elements in $G F(2^m)$ using m two-input XOR gates, the α module multiplies an element of $G F(2^m)$ by α and then reduces the result modulo $f(x)$, and lastly, the pass-thru module multiplies a $G F(2^m)$ element by a $G F(2)$ element. One finite-field multiplication uses a total of $m - 1$ sum modules, $m - 1$ α modules, and m pass-thru modules to get the output. Fault injection can occur in any of these modules, and formulations for parity signatures in $G F(2^m)$ are derived in [16]. Parity signatures provide an error flag (EF) on each module. The major drawback of parity signatures is that their error coverage is approximately 50%, that is, if the number of faults is even, the approach would not be able to detect the faults. This highly predictable countermeasure can be circumvented by intelligent fault injection.

In this work, our aim is the derivation of error-detection schemes that provide a broader and higher error coverage than parity signatures and explore the application of such schemes to the

Luov algorithm. Thus, we derive and apply CRC signatures [17] to the finite-field multipliers used in Luov algorithm. This would be a step forward toward detecting natural and malicious intelligent faults, especially and as discussed in this brief, considering both primitive and standardized CRCs with different fault multiplicity coverage. CRC was first proposed in 1961 and it is based on the theory

of cyclic error-correcting codes. To implement CRC, a generator polynomial $g(x)$ is required. The message becomes as the dividend, the quotient is discarded, and the remainder produces the result. In CRC, a fixed number of check bits are appended to the data and these check bits are inspected when the output is received to detect any errors. The entire finite-field multiplier with our error-detection schemes is shown in Fig. 1, where actual CRC (ACRC) and predicted CRC (PCRC) stand for ACRC signatures and PCRC signatures, respectively. In Fig. 1, only one EF is shown for clarity; however, for CRC-5, which is the case study proposed in this brief, 5 EFs are computed on each module.

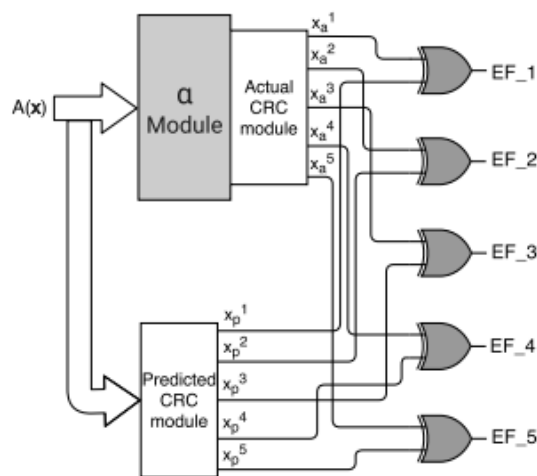


Figure-2: Proposed error-detection constructions for α module.

with its respective one to produce five EFs, which are represented as E F1–E F5. As an example, to obtain E F1, $x_1 p$ (or $a_{15} + a_{13} + a_{12} + a_{10} + a_9 + a_8 + a_6 + a_4$ for $g_0(x)$) is XORed with $x_1 a$ (or $\gamma_{14} + \gamma_{13} + \gamma_{11} + \gamma_{10} + \gamma_9 + \gamma_7 + \gamma_5 + \gamma_0$ for $g_0(x)$), which are calculated in (4) and (6), respectively. For our case study, the outputs are divided into five groups since we use CRC-5; however, if any other CRC-n is used, there will be n EFs and the actual and predicted outputs will be divided into n groups. In Table I, the CRC signatures for the different primitive polynomials are shown. We note that the choice of the utilized CRC can be tailored based on the reliability requirements and the overhead to be tolerated. In other words, for applications such as game consoles in which performance is critical (and power consumption is not because these are plugged in), one can increase the size of CRC. However, for deeply embedded systems such as

implantable and wearable medical devices, smaller CRC is preferred.

V. RESULTS

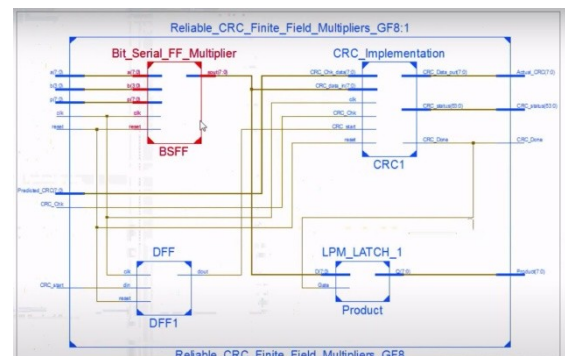


Figure-3: Proposed System

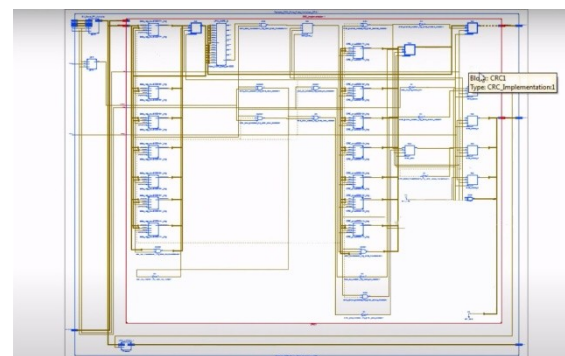


Figure-4: Schematic

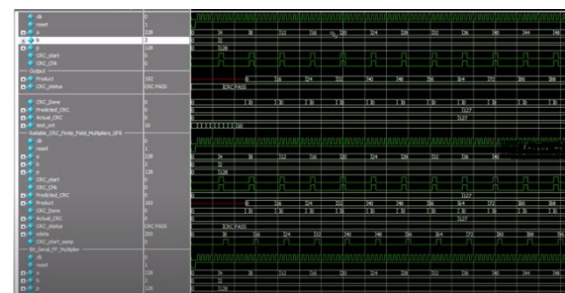


Figure-5: Output Wave forms

Table-1: Device Utilization Summary

Device Utilization Summary			
Resource	Used	Available	Used (%)
Number of 8-bit Registers	2191	307,360	0%
Number of 16-bit Registers	229	61,440	0%
Number of 32-bit Registers	6,001	307,360	1%
Number of 1-bit LUTs	6,001	307,360	1%
Number of 4-bit LUTs	1,200	76,800	1%
Number of 16-bit LUTs	31	1,920	1%
Number of 24-bit LUTs	31	1,920	1%
Number of 32-bit LUTs	31	1,920	1%
Number of 4-bit Multiplexers	6,001	6,001	100%
Number of 16-bit Multiplexers	1,200	1,200	100%
Number of 24-bit Multiplexers	31	31	100%
Number of 32-bit Multiplexers	31	31	100%
Number of 1-bit RAMs	298	1,024	29%
Number of 4-bit RAMs	31	31	100%
Number of 9-bit RAMs	31	31	100%
Number of 16-bit RAMs	2	63	3%
Number of 18-bit RAMs	31	31	100%
Number of 36-bit RAMs	2	2	100%

Table-2: Comparison of CRC – Based Error Constructions for Finite Field Multipliers

	Comparisons of Reliable CRC-Based Error Detection Constructions for Finite Field Multipliers	
	GF8 - CRC	GF32 CRC
Number of Slice Registers	96	214
Number of Slice LUTs	140	616
Number of Occupied Slices	43	229
I/Os	113	245
Delay (ns)	3.102	3.665
Power (W)	3.296	3.300

VI. CONCLUSION

In this work, we have derived error-detection schemes for the finite-field multipliers used in post quantum cryptographic algorithms such as Luov, noting that the proposed error-detection schemes can be adapted to other applications and cryptographic algorithms whose building blocks need finite-field multiplications. The error-detection architectures proposed in this work are based on CRC-5 signatures and we have performed software implementations for the sake of verification. Additionally, we have explored and studied both primitive and standardized generator polynomials for CRC-5, comparing the complexity for each of them. We have embedded the proposed error-detection schemes into the original finite-field multipliers of the Luov's algorithm, obtaining high error coverage with acceptable overhead.

REFERENCES

- [1] J. L. Danger et al., "On the performance and security of multiplication in $GF(2^N)$," *Cryptography*, vol. 2, no. 3, pp. 25–46, 2018.
- [2] M. Mozaffari-Kermani and A. Reyhani-Masoleh, "Reliable hardware architectures for the third-round SHA-3 finalist Grostl benchmarked on FPGA platform," in *Proc. DFT*, Oct. 2011, pp. 325–331.
- [3] M. Mozaffari-Kermani and A. Reyhani-Masoleh, "A low-cost S-box for the advanced encryption standard using normal basis," in *Proc. IEEE Int. Conf. Electro/Inf. Technol.*, Jun. 2009, pp. 52–55.
- [4] M. Yasin, B. Mazumdar, S. S. Ali, and O. Sinanoglu, "Security analysis of logic encryption against the most effective side-channel attack: DPA," in *Proc. IEEE Int. Symp. Defect Fault*

Tolerance VLSI Nanotechnol. Syst. (DFTS), Oct. 2015, pp. 97–102.

- [5] M. Mozaffari-Kermani, R. Azarderakhsh, A. Sarker, and A. Jalali, "Efficient and reliable error detection architectures of hash-counter-hash tweakable enciphering schemes," *ACM Trans. Embedded Comput. Syst.*, vol. 17, no. 2, pp. 54:1–54:19, May 2018.
- [6] M. Mozaffari-Kermani, R. Azarderakhsh, and A. Aghaie, "Reliable and error detection architectures of Pomaranch for false-alarm-sensitive cryptographic applications," *IEEE Trans. Very Large Scale Integr. (VLSI) Syst.*, vol. 23, no. 12, pp. 2804–2812, Dec. 2015.
- [7] A. Sarker, M. Mozaffari-Kermani, and R. Azarderakhsh, "Hardware constructions for error detection of number-theoretic transform utilized in secure cryptographic architectures," *IEEE Trans. Very Large Scale Integr. (VLSI) Syst.*, vol. 27, no. 3, pp. 738–741, Mar. 2019.
- [8] M. Mozaffari-Kermani, R. Azarderakhsh, and A. Aghaie, "Fault detection architectures for post-quantum cryptographic stateless hash-based secure signatures benchmarked on ASIC," *ACM Trans. Embedded Comput. Syst.*, vol. 16, no. 2, pp. 59:1–59:19, Dec. 2016.
- [9] M. Mozaffari-Kermani and R. Azarderakhsh, "Reliable hash trees for post-quantum stateless cryptographic hash-based signatures," in *Proc. IEEE Int. Symp. Defect Fault Tolerance VLSI Nanotechnol. Syst. (DFTS)*, Oct. 2015, pp. 103–108.
- [10] M. M. Kermani and R. Azarderakhsh, "Reliable architecture-oblivious error detection schemes for secure cryptographic GCM structures," *IEEE Trans. Rel.*, vol. 68, no. 4, pp. 1347–1355, Dec. 2019.
- [11] A. A. Kamal and A. M. Youssef, "Strengthening hardware implementations of NTRUEncrypt against fault analysis attacks," *J. Cryptograph. Eng.*, vol. 3, no. 4, pp. 227–240, Nov. 2013.
- [12] A. Kipnis, J. Patarin, and L. Goubin, "Unbalanced oil and vinegar signature schemes," in

Proc. Int. Conf. Theory Appl. Cryptograph. Techn. Berlin, Germany: Springer, 1999, pp. 206–222.

[13] D. Moody, “Post-quantum cryptography: NIST’s plan for the future,” Tech. Rep., Feb. 2016. [Online]. Available: <https://csrc.nist.gov/csrc/media/projects/post-quantum-cryptography/documents/pqcrypto-2016-presentation.pdf>

[14] D. Moody, “Post-quantum cryptography: Round 2 submissions,” Tech. Rep., Mar. 2019. [Online]. Available: <https://csrc.nist.gov/CSRC/media/Presentations/Round-2-of-the-NIST-PQC-Competition-Whatwas-NIST/images-media/pqcrypto-may2019-moody.pdf>

[15] D. J. Bernstein, “Post-quantum cryptography,” in *Encyclopedia of Cryptography and Security*, H. C. A. van Tilborg and S. Jajodia, Eds. Boston, MA, USA: Springer, 2011, pp. 949–950, doi: 10.1007/978-1-4419-5906-5_386.

[16] A. Reyhani-Masoleh and M. A. Hasan, “Error detection in polynomial basis multipliers over binary extension fields,” in *Proc. CHES*, 2002, pp. 515–528.

[17] EPC Radio-Frequency Identity Protocols Class-1 Generation-2 UHF RFID Protocol for Communications at 860 MHz 960 MHz, EPC Global, Brussels, Belgium, Version 1.0.23, 2008.

[18] T. V. Ramabadran and S. S. Gaitonde, “A tutorial on CRC computations,” *IEEE Micro*, vol. 8, no. 4, pp. 62–75, Aug. 1988.

[19] S. Subramanian, M. Mozaffari-Kermani, R. Azarderakhsh, and M. Nojoumian, “Reliable hardware architectures for cryptographic block ciphers LED and HIGHT,” *IEEE Trans. Comput.-Aided Design Integr. Circuits Syst.*, vol. 36, no. 10, pp. 1750–1758, Oct. 2017.

DESIGN OF DIGITAL CIRCUIT IMPLEMENTATION USING FULL SWING GDI TECHNIQUE AND CMOS TECHNOLOGY

¹BHUKYA TRIVENI, ²PANKAJ RANGAREE

¹PG Scholar, Dept.of ECE, Vaagdevi College of Engineering, Warangal, Telangana, India.

²Asst. Professor, Dept.of ECE, Vaagdevi College of Engineering, Warangal, Telangana, India.

¹triveni.bhukya410@gmail.com, ²phrangaree247@gmail.com

Abstract—This paper presents a design which provides full swing output for logic 1 and logic 0 for 1-bit full adder cell and reduces power consumption, delay, and area. In this design full adder consists of two XOR gate cells and one cell of 2x1 multiplexer (MUX). The performance of the proposed design compared with the different logic style for full adders through cadence virtuoso simulation based on TSMC 65nm technology models with a supply voltage of 1v and frequency 125MHz. The simulation results showed that the proposed full adder design dissipates low power, while improving delay and area among all the design taken for comparison.

Keywords— Full adder; Gate Diffusion Input (GDI); FS-GDI.

I. INTRODUCTION

In real time applications, ALU is an important component in all electronics, processors and embedded systems. In most of the circuits, power consumption as well as time depends on ALU configurations because all arithmetic and logical operations of circuits are performing in ALU. ALU is also one of the highest power density locations in the processor. The optimization of ALU can be done in three important VLSI parameters which include area, power dissipation and delay. The optimization of ALU for lower power dissipation and faster device performance is of mainly important. Power optimization is possible at every level of digital design flow; however, benefits are more at the architecture design level and transistor level.

In the design of low power digital logic circuits, CMOS is an important element which including microprocessors and ALU within it. Due to the leakage current problem, the static power consumption of CMOS device is almost negligible. However, the addition of the transient power consumption (PT) and capacitive load power consumption (PL) the dynamic power dissipation is

used significantly. Mostly this type of dynamic power is dissipated in translating charges in the parasitic capacitors in the CMOS gates.

In VLSI, There are different methods are used to control the power consumption at the architecture device level and module level which includes scaling, varying frequency of operation or supply voltage, changing the load capacitances, etc. Here, in this paper, we are concentrating about optimizing power requirements and delay at the module level. Power consumption, area and delay are the main important issues in VLSI industry, which triggered many research efforts are tried to minimize the power consumption, area and delay of VLSI circuits. There is only a limited amount of power available for electronic devices heavily used on a daily basis; these devices are low power high speed VLSI circuit works simultaneously. ALU has been a key element used in many applications such as microprocessor, image processing, digital signal processing etc., An essential component of arithmetic unit and almost all other arithmetic operations includes addition therefore any improvement in the adder cell is reflected as a major improvement in the ALU. Hence, the delay also becomes one of the important design parameters which need to be reduced as less as possible.

II. RELATED WORK

A. Morgenshtein, I. Shwartz, and A. Fish, “Gate Diffusion Input (GDI) logic in standard CMOS Nanoscale process,” 2010 IEEE 26th Convention of Electrical and Electronics Engineers in Israel, 2010.

In this paper CMOS compatible Gate Diffusion Input (GDI) design technique is proposed. The GDI method enables the implementation of a wide range of complex logic functions using only two transistors. This method is suitable for the design of low-power logic gates, with a much smaller area than Static CMOS and existing PTL techniques. As opposite to our originally proposed GDI logic, the

modified GDI logic is fully compatible for implementation in a standard CMOS process. Simulations of basic GDI gates under process and temperature corners in 40nm CMOS process are shown and compared to similar CMOS gates. We show that while having the same delay, GDI gates achieve leakage and active power reduction of up to 70% and 50%, respectively.

A. Morgenshtein, V. Yuzhaninov, A. Kovshilovsky, and A. Fish, "Fullswing gate diffusion input logic—Case-study of low-power CLA adder design," Integration, the VLSI Journal, vol. 47, no. 1, pp. 62–70, Jan. 2020.

In this paper, the design of a 4-Bit Arithmetic Logic Unit (ALU) using Modified Gate Diffusion Input technique is being done which is implemented using minimum transistor full adder and also adapts hardware reuse method which has advantages of minimum transistors requirement, more switching speed and low power consumption with respect to the conventional CMOS techniques. 4-Bit Arithmetic Logic Unit (ALU) is being implemented with MGDI technique in DSCH 3.5 and layout generated in Microwind tool. The Simulation is done using 65 nm technology at 1.2 v supply voltage The results show that the proposed design consume less power uses less number of transistors, while achieving full swing operation compared to previous work.

III. GATE DIFUSSION INPUT TECHNIQUE

In 2002 [3] A. Morgenstern, A. Fish and A. Wagner proposed Gate Diffusion Input Technique (GDI) for low power and small silicon area of VLSI digital design as an alternative to CMOS logic design. Presented in figure 1 (a) Primitive Proposed GDI cell

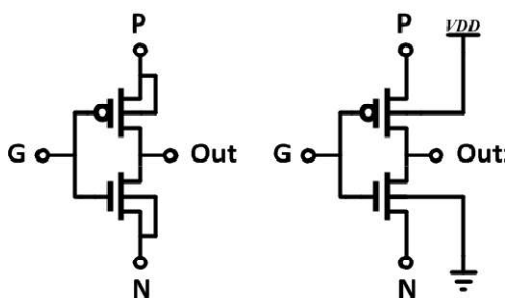


Figure: GDI cell; (a) Primitive Proposed GDI Cell, (b) MOD-GDI

Actually, this technique proposed for fabrication in silicon on insulator (SOI) and twin-well CMOS processes. Also, it provides an effective way for the design of fast, low power design using less number of transistors as compared to CMOS, PTL and TG techniques. This allows the design of many complex functions using only 2 transistors as listed in table I.

TABLE I. Different logic functions realization using GDI cell

N	P	G	OUT	Function
0	B	A	\overline{AB}	F1
B	1	A	$\overline{+B}$	F2
1	B	A	A+B	OR
B	0	A	\overline{AB}	AND
C	B	A	$\overline{AB+AC}$	MUX
0	1	A	$\overline{\quad}$	NOT

This logic style was suffering from some limitations such as reduced output voltage swing due to the threshold drops, this means that the output either high or low voltage is deviated from VDD or GND by threshold voltage drop (V_{th}), as that threshold drop causes performance degradation and increases short circuit power.

IV. METHODOLOGY

To solve existing problem we proposed a new approach to improve the output swing and overcome the threshold drop problem known as Full Swing (FS) GDI technique and utilizes only swing restoration transistor (SR) to ensure the full swing operation for F1 and F2 function. Either F1 or F2 gates or a combination of both can be used to realize any logical function. Although this technique uses more transistors than standard GDI but compared to CMOS logic style it uses a fewer number of transistors and achieves full swing output, low power, less delay and small area of the circuit.

i. Full Swing GDI based Full adder

In this paper the Full-Swing GDI technique is used to realize the circuits required to design the Full Adder as follows:

a) XOR Gate

XOR gate is the basic building block for the realization of various digital circuits such as multiplier, comparator, adder, decoder, and compressor[6]. The design XOR gate requires 4

transistors as shown in fig (a). The output can be expressed as:

$$A \text{ XOR } B = A \oplus B = \overline{A}B + A\overline{B}$$

At A=0, B=0 the NMOS transistor is switched off and PMOS transistor is switched on, where PMOS in the linear region.

At $V_{in} - V_{tp} < V_{out} < V_{DD}$, NMOS is cut off $V_{in} < V_{tn}$, then the output of XOR gate equal to (V_{tp}) threshold voltage of PMOS transistor.

At A=0, B=1 NMOS is cut off $V_{in} < V_{th}$, the PMOS in the linear region $V_{in} - V_{th} < V_{out} < V_{DD}$, then the output of XOR equal to VDD passes through PMOS.

At A=1, B=0 the PMOS transistor is switched off and NMOS transistor is switched on, where PMOS is cut off $V_{in} < V_{tp}$ and NMOS in the linear region $V_{in} - V_{tn} < V_{out} < V_{DD}$ then the output of the XOR gate is equal to $V_{DD} - V_{tn}$, (V_{tn}) threshold voltage of NMOS transistor.

At A=1, B=1 PMOS is cut off and NMOS in the linear region, then the output equal to ground passes through NMOS.

TABLE II. Truth Table Of XOR Gate.

A	B	A XOR B
0	0	V_{tp}
0	1	VDD
1	0	$V_{DD} - V_{tn}$
1	1	GND

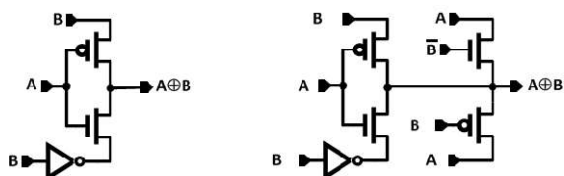


Figure: GDI cell; (a) 4T-XOR GATE, (b) 6T-XOR GATE

Implementation of MGDI

Design of primitive cells using MGDI

1) AND GATE USING MGDI The technique of manipulation of MGDI allowed by AND gate merely requires two transistors.

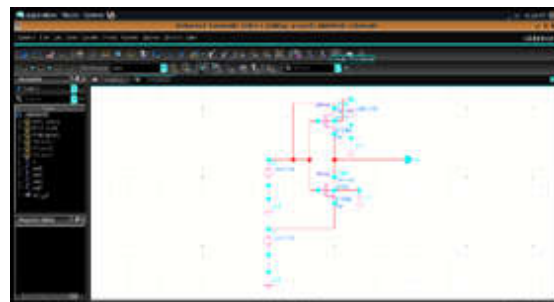


Figure: Demonstrates that gate schematic

View of AND gate using MGDI technique consumes fewer transistors than conventional logic technique in Figure.

a. OR GATE Using MGDI

The OR gate generated MGDI operation technique needs only 2 transistors which will be shown in figure.



Figure: Full Swing OR Gate

b. XOR GATE Using MGDI

For XOR gate implementation, three transistor numbers are provided using the MGDI shown in figure. Use this 3 XOR transistor the number of transistors can be reduced with full adder [7].

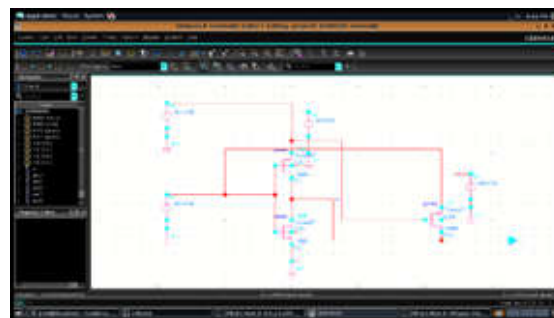


Figure: Full Swing XOR Gate

C. Design of Full Adder

A full adder is a combinational circuit that performs the arithmetic operation of 3 number of bits [8]. Addition considered an essential operation in arithmetic and logic unit digital signal processing and. The 1-bit full adder contains three input bits and two output bits, the first two bits of the inputs are A and B called operands and the third input bit Cin is a bit carried in from the previous less-significant stage, output bits called sum is the result of addition operation and carry out which will be the input carry to the next addition operation, and the expression.

$$SUM = A \oplus B \oplus C_{in} \tag{2}$$

$$COUT = A \overline{(A \oplus B)} + C_{in} (A \oplus B) \tag{3}$$

The proposed design consists of 16 transistors including two XOR gate cells to produce sum and one multiplexer cell to produce carry out, as shown in figure (4), the block diagram shown in figure (5), and the truth table of proposed full adder presented in table III

Table III. Truth Table Of Proposed Full Adder

A	B	Cin	SUM	Cout
0	0	0	0	0
0	0	1	1	0
0	1	0	1	0
0	1	1	0	1
1	0	0	1	0
1	0	1	0	1
1	1	0	0	1
1	1	1	1	1

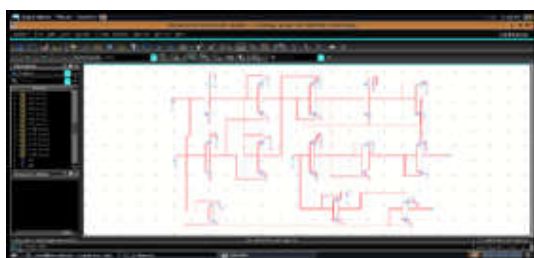


Figure: Proposed design for 1-Bit Full Adder

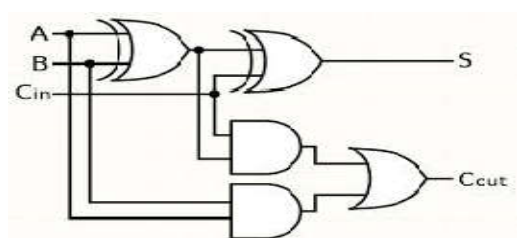


Figure: Block Diagram For Proposed Full Adder

4 BIT FULL ADDER Using MGDI

4-Bit Binary Adder to fast carry. The definition is general. Such full adders add up to two binary numbers of 4 bits. The sum outputs are given for every bit, and the resulting carry is obtained from the fourth bit. Both four bits of these adders feature a full internal look ahead.

1) FULL Subtractor Using MGDI

The complete subtractor is a hybrid circuit used to subtract three bits of input: the minuend Z, subtrahend X, borrow Y. The full subtractor generates two output bits: difference D, and borrow B. Y is set to borrow a corresponding Z digit. Therefore Y is subtracted from Z as well as the subtracting X.

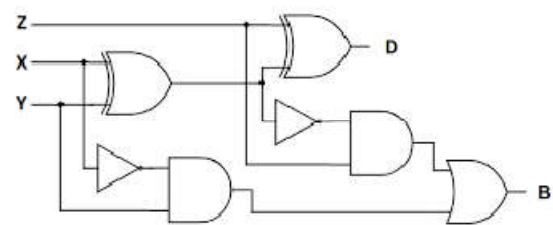


Figure: shows an absolute logic circuit for a subtractor

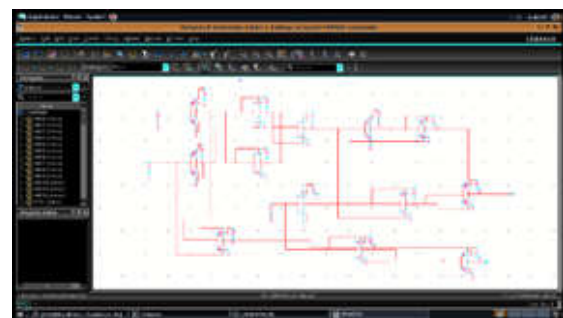


Figure: The logic circuit of full subtractor

With 26 transistors the full subtractor using MGDI has been developed. The schematic design of full subtractor will be displayed in figure. The circuit is operating at 1.8 V.

4 Bit Full Subtractor using MGDI

A binary adder-subtractor in digital circuits is one that is one that can add and deduce binary numbers in one circuit per se. The 4-bit full subtractor schematic architecture using MGDI is shown in fig. 12 [11], [12].

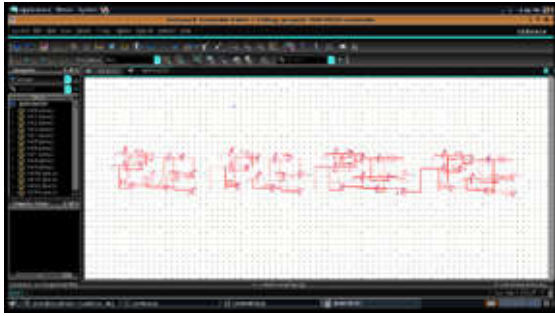


Figure: The logic circuit of 4-bit full subtractor

Design 4x4 multiplier using MGDI

The main block of a multiplier is full adder circuit as depicted using MGDI technique. Partial products are determined by multiplying the multiplier by each bit and then by summing the partial products. You will design an array multiplier to execute the multiplication that multiplies two 4-bit inputs and calculates an 8-bit output. Construction is made of the 4*4 array multiplier. The array multiplier is configured with a modified gate diffusion input technique to get the best low logic. In 180nm technology, the circuit has the 1.8V power supply. This configuration is being compared with the CMOS, and GDI will be done.

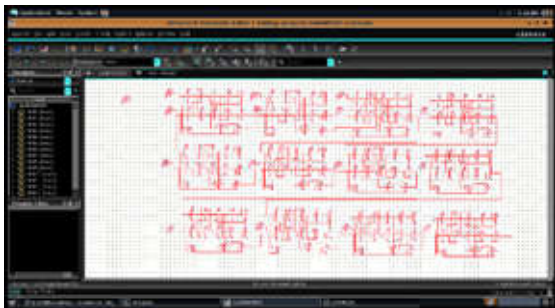


Figure: Displays the 4x4 multiplier schematic

V. RESULTS

i. Existing System

a) Device and node counts:

- MOSFETs - 14
- MOSFET geometries - 2
- Voltage sources - 4
- Subcircuits - 5
- Model Definitions - 6
- Computed Models - 2
- Independent nodes - 9
- Boundary nodes - 5
- Total nodes - 14

b) Power Results

VV1 from time 0 to 8e-008
 Average power consumed -> 3.258043e-007 watts

Max power 8.139258e-003 at time 4.001e-008
 Min power 0.000000e+000 at time 0
 VV2 from time 0 to 8e-008
 Average power consumed -> 3.678060e-006 watts
 Max power 9.211432e-003 at time 2.001e-008
 Min power 0.000000e+000 at time 0
 VV3 from time 0 to 8e-008
 Average power consumed -> 2.432820e-003 watts
 Max power 1.953101e-002 at time 4.001e-008
 Min power 1.492829e-009 at time 1.11e-009
 Measure information will be written to file
 "C:\Users\HOME\AppData\Local\Temp\Full_adder_gdi\Full_adder_gdi.measure"
 Measurement result summary
 delay = 201.9805p
Power values :
 Existing value:811.6 micro watt

ii. Proposed System

a) Device and node counts:

- MOSFETs - 28
- MOSFET geometries - 3
- Voltage sources - 4
- Subcircuits - 11
- Model Definitions - 6
- Computed Models - 2
- Independent nodes - 11
- Boundary nodes - 5
- Total nodes - 16

*** 1 WARNING MESSAGE GENERATED DURING SETUP

b) Power Results

VV1 from time 0 to 8e-008
 Average power consumed -> 2.670889e-005 watts
 Max power 1.462639e-003 at time 1.1e-008
 Min power 0.000000e+000 at time 0
 VV2 from time 0 to 8e-008
 Average power consumed -> 3.271979e-005 watts
 Max power 2.306265e-003 at time 2.08408e-008
 Min power 0.000000e+000 at time 0
 VV3 from time 0 to 8e-008
 Average power consumed -> 2.021329e-005 watts
 Max power 2.049975e-003 at time 4.1e-008
 Min power 0.000000e+000 at time 0
 Measure information will be written to file
 "C:\Users\HOME\AppData\Local\Temp\FULL_ADD\FULL_ADD.measure"
 Measurement result summary
 delay = 149.4834p
 Proposed value:26micro watt



Figure: Existing Full Adder



Figure: XOR Full Swing

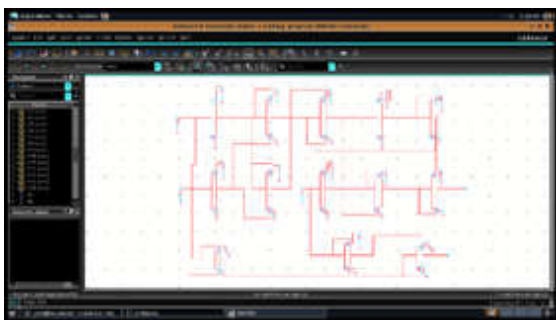


Figure: Proposed design for 1-Bit Full Adder



Figure: XOR Full Swing

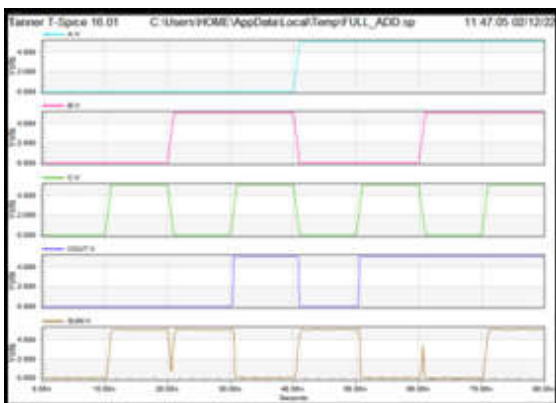


Figure: proposed Full adder circuit with SWING GDI TECHNIQUE



Figure: GDI XOR gate

This work presents a 1-bit Full Adder designed in 65nm TSMC process using the Full-Swing GDI technique and simulated using the Cadence Virtuoso simulator. Simulation results showed design in terms of power consumption and transistor count, while maintaining Full-Swing Operation. The proposed design consists of 16 transistors and operates under 1V supply voltage.

REFERENCES

[1] Wallace, C.S., "A suggestion for a fast multiplier", IEEE Transactions on Electronic Computers, EC-13, pp. 14-17, 1964.

[2] "Modelling of adders using CMOS and GDI logic for multiplier application". A VLSI based approach 2016 International Conference on Circuit , Power Computing Technologies (ICCPCT).

[3] Arkadiy Morgenshtein, Alexander Fish, and Israel A. Wagner, "Gate Diffusion Input (GDI): A power efficient method for digital combinatorial circuits", IEEE Transactions on VLSI Systems, Vol.10, No.5, October 2002.

[4] Naresh.N, Srinivasulu.M. "Design and implementation of various logic circuits using GDI technique". International Journal for

Research in Applied Science & Engineering Technology(IJRASET). Aug 2015; 3(8): 292-300p.

[5] Padmanabhan Balasubramanian and Johin John, "Low power digital design using Mod-GDI method", International Conference on Design and Test of Integrated Systems in Nanoscale Technology, IEEE, pp.190-193, September 2006.

[6] Krishnendu Dhar, "Design of a low power, high speed, energy efficient full adder using Mod-GDI and MVT scheme in 45nm technology", IEEE, International Conference on Control, Instrumentation, Communication and Computational Technologies (ICCICCT) pp.36-41, July 2014.

[7] Rashmi Kumari, Swapnil Rai, Subha Kaushik. "Design of basic gates using CMOS". International Journal of Research (IJR). May 2015; 2(5): 225-226p.

[8] Gangadhar Reddy "A novel power-aware and high performance full adder cell for ultra-low power design", IEEE International Conference on Circuit, Power and Computing Technologies, 2014, pp.1121-1126.

[9] R. Uma, "Bit fast adder design: Topology and layout with self-resetting logic for low power VLSI circuits", International Journal of Advanced Engineering Sciences and Technology, Vol No. 7, Issue No.2, 197-205, 2011.

[10] Uma.R, Dhavachelvan.P. "Mod-GDI technique: A new technique for enhancing performance in fulladder circuits", 2nd International Conference on Communication, Computing and Security. 2012.

[11] K.Dhar, A.Chatterjee (2014) "Design of an energy efficient, high speed, low power full subtractor using GDI technique", IEEE Conference on Technology Symposium.

IMPLEMENTATION OF RNS AND LNS BASED ADDITION AND SUBTRACTION UNITS FOR CRYPTOGRAPHY

¹YATA SOUJANYA, ²V.SABITHA

¹PG Scholar, Dept.of ECE, Vaagdevi College of Engineering, Warangal, Telangana, India.

² Associate Professor, Dept.of ECE, Vaagdevi College of Engineering, Warangal, Telangana, India.

¹soujanyayata99@gmail.com, ²sabitha_v@vaagdevi.edu.in

Abstract— The need for fast data processing and reducing the power dissipation of digital signal processing(DSP) algorithms and Cryptographic algorithms have provoked the development of efficient hardware implementations of residue number system (RNS) and logarithmic number system(LNS) arithmetic. This paper describes the implementation of adder and subtractor units by using RNS and LNS arithmetic. Addition and subtraction units are major and basic operations in public key cryptographic algorithms like Elliptic Curve Cryptography (ECC).

Keywords— Residue number system (RNS), logarithmic number system (LNS), adder, subtractor, power dissipation, digital signal processing (DSP), Cryptography.

I. INTRODUCTION

The biological sequence alignments for sequence of Deoxyribonucleic Acid (DNA) or protein present an insight into the natural mutations occurring in the strings. Also, similarities between two sequences might suggest evolution from the same genetic tree or mutations over time that occurred in one of the sequences in the given pair of sequences. A nucleotide consists of two parts viz: a phosphate group and a sugar group called deoxyribose; these two parts form the ribbon-like backbone of the DNA strand and are identical in all nucleotides. There are four different kinds of bases, which define the four different nucleotides viz: Adenine (A), Cytosine (C), Guanine (G) and, Thymine (T).

There are several algorithms for doing sequence alignment. The commonly used ones are Fast Alignment Search Tool –All (FASTA) and Basic Local Alignment Search Tool (BLAST). The Smith - Waterman Algorithm (SWA) is very sensitive algorithm but it has a very high computational cost. Due to this high computational cost, the real-life application of the SWA is much limited and the benefits that would have accrued from the field of

bioinformatics are yet to come to the fore. The high computational cost of the SWA has a direct link with the carry propagation Chains inherent to the Weighted Number Systems(WNS), e.g., binary number systems, decimal number systems. Because of this intrinsic performance limiter for arithmetic units and processors built based on WNS, several attempts have been made to overcome the speed.

II. RELATED WORK

In related work on bioinformatics with key reference to sequence alignment methods, Smith – Waterman Algorithm (SWA), and the computational cost of the SWA has a direct link with the carry propagation.

Now, Bioinformatics entails the creation and advancement of databases, algorithms, computational and statistical techniques, and theory to solve formal and practical problems arising from the management and analysis of biological data. Over the past few decades rapid developments in genomics and other molecular research technologies and developments in information technologies have combined to produce a tremendous amount of information related to molecular biology. It is the name given to these mathematical and computing approaches used to glean under Bioinformatics is the application of information technology and computer science to the field of molecular biology. The term bioinformatics was coined by Paulien Hogeweg in 1979[50] for the study of informatics processes in biotic systems. Its primary use since at least the late 1980s has been in genomics and genetics, particularly in those areas of genomics involving large-scale DNA sequencing.

Standing of biological processes, common activities in bioinformatics include mapping and analyzing DNA and protein sequences, aligning different DNA and protein sequences to compare

them and creating and viewing 3-D models of protein structures.

III. DESIGN

a) Digital System Implementation Process

In general, a digital system is a sequential circuit made up of interconnected flip - flops and gates. The system is partitioned into modular subsystems, each of which performs some functional tasks. Inter connecting the various subsystems through data and control signals results in a digital system.

In this digital system, we partition the system into two types of modules:

- i. Data path
- ii. Control unit.

Data Path: The Data path is responsible for all the operation performs on the data. It includes, Functional units such as adders, shifters, multipliers, Arithmetic and Logic Units(ALUs) and, comparators.

Control Unit: The control unit (controller) is responsible for controlling all the operations of the data path by providing appropriate control signals to the data path at the appropriate times.

b) The Module Design Flow

Design Entry: This is the first programming step. The circuit or system design must be entered into the design application software using text - based, graphic entry (schematic capture), or state diagram description.

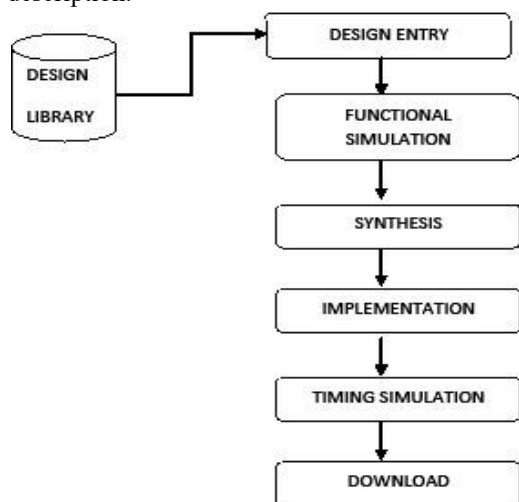


Figure-1: The Module Design Flow Diagram

c) Functional simulation

The entered and compiled design is simulated by soft- ware to confirm that the logic circuit functions as expected. The simulation will verify that correct outputs are produced for a specified set of inputs. A device - independent software tool for doing this is generally called a waveform editor. The steps involved are Synthesis, Implementation, Time simulation, Download.

d) Hardware Implementation of the RNS –SWA Architecture

In this section, we give a detail procedure of the hardware implementation of this step using RNS as tool, making use of its carry free, modularity and one step multiplication.

e) The RNS-SWA Forward Converter

The binary/decimal values are converted into residues numbers by the Binary to RNS Converter (BRC), which is termed the RNS forward conversion.

f) The Design Entry

The memory less RNS forward converter is entered into a Quartus II version 4.0 VHDL application software using the graphic entry or schematic capture tool embedded in the software.

g) The RNS Based Smith – Waterman Processor

The next step after the binary/decimal conversion to RNS phase is the RNS base SWA processor stage. This stage shows how the inherent properties of RNS are used to do carry free arithmetic’s on the SWA.

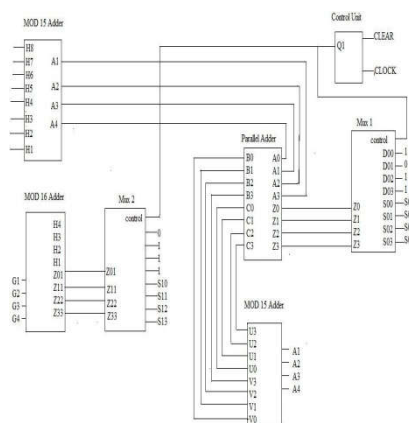


Figure - 2: The Schematic Diagram of RNS - SWA processor

h) Residue Number System Comparator

The RNS comparator architecture is made up of 256 words \times 8-bit ROM that contains the residue values and their decimal equivalents of all the decimal numbers within the dynamic range. The residue values, 8-bit numbers, are used as the address of the rivalries equivalent decimal numbers.

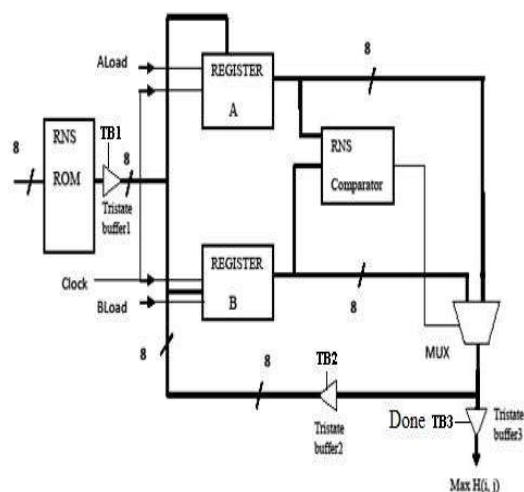


Figure - 3: The Schematic Diagram of RNS

IV. METHODOLOGY

a) Thermometer Encoding Representation of TC:

TABLE I
TC EXAMPLE

Regular Representation	TC
0	0000000
1	0000001
2	0000011
3	0000111
4	0001111
5	0011111
6	0111111
7	1111111

Thermometer Coding with TC [18], the value of each number is expressed as the number of ones in a string of bits. Since, in this coding, no weight is assigned to bit positions, it is not important where the ones are placed.

b) One-Hot Coding

The OHC is usually used to address lookup tables (LUTs) and at the output of some linear circuits.

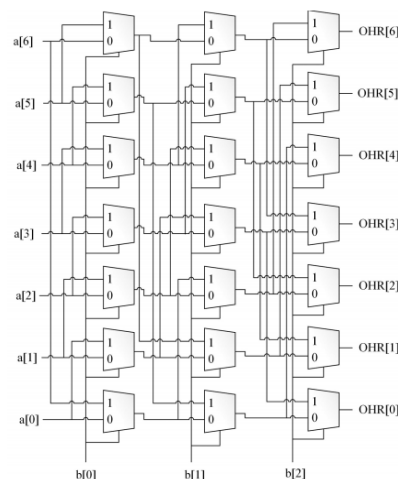


Figure - 4: OHR – Based module -7adder

c) The Logarithmic Number System

The representation of data as logarithms is long used as a means to simplify particular arithmetic operations and utilize improved numerical properties, even before the modern digital computer era. The logarithmic number system.

(LNS) is a formalization of the logarithmic representation of the data in a digital system and it can be conceived as a generalization of the floating-point representation. Swartzlander and Alexopoulos described the basics of the sign/logarithm arithmetic.

V. RESULTS

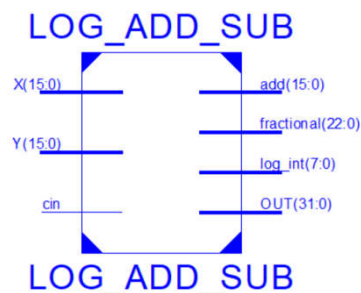


Figure - 5: Log Block Diagram

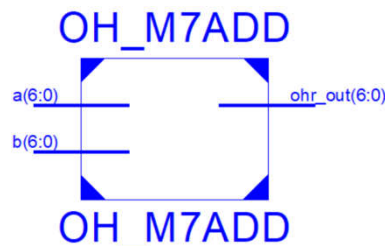


Figure - 6: OHR adder block diagram

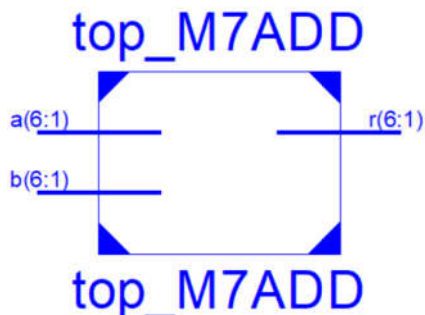


Figure - 7: thermometer block diagram



Figure - 8: log adder simulation



Figure - 9: OHR output

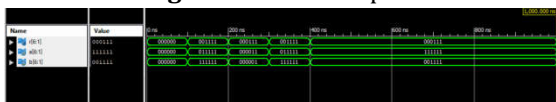


Figure - 10: thermometer results

```
Timing Summary:
-----
Speed Grade: -3

Minimum period: No path found
Minimum input arrival time before clock: 9.361ns
Maximum output required time after clock: 3.648ns
Maximum combinational path delay: 28.670ns
```

Figure - 11: Log adder Delay

```
Timing Summary:
-----
Speed Grade: -2

Minimum period: No path found
Minimum input arrival time before clock: No path found
Maximum output required time after clock: No path found
Maximum combinational path delay: 8.593ns
```

Figure - 12: OHR adder delay

```
Timing Summary:
-----
Speed Grade: -2

Minimum period: No path found
Minimum input arrival time before clock: No path found
Maximum output required time after clock: No path found
Maximum combinational path delay: 8.593ns
```

Figure - 13: thermometer Adder delay

VI. CONCLUSION

The possibility of accelerating the Smith-Waterman algorithm (SWA) using the arithmetic advantages of the Residue Number System (RNS). RNS is such an integer system exhibiting the

capabilities that support parallel computation, carry free addition, borrow-free subtraction, and single step multiplication without partial product. The theoretical analysis shows the advantages of implementing the SWA on an RNS platform. These advantages are exploited in this implementation to build an RNS-SWA architecture in order to reduce the computational time of the SWA. The RNS-SWA architecture consists of a Binary to RNS converter, two RNS processors, and RNS to Binary converter cum comparator.

REFERENCES

- [1] Zhining Lim, An RNS Enabled M Cryptography, 2010.
- [2] Dimitrios Soudris, Designing CM 2002.
- [3] Jean-claude Bajard, Nicolas Me “Efficient RNS for Cryptography Computation Applied Mathematics Paris (France), 2005.
- [4] Mohammad Esmaeildoust, Shirin Keivan Navi, “On the Design Multiplication, ” INTERNATIONAL SECURITY, VOL.16, NO.2, PP.11
- [5] Amos Omondi, Benjamin Premku theory and implementation ,vol.2.
- [6] R.A. Patel, M. Benaissa, N. Powe Power High-Speed Adder for Systems, 2004. SIPS 2004.
- [7] Melanie Dugdale, ”VLSI Implem Based on Binary Adders, ” CIRCUITS AND SYSTEMS-11: SIGNAL PROCESSING, VOL. 39,
- [8] Michael Haselman, “A Compar Logarithmic Number Systems on F Custom Computing Machines, 200 IEEE Symposium .
- [9] V. Paliouras and T.stouraitis, Lo Logarithmic Number System, 2001
- [10] K.Jhansson, O.Gustafsson, and L. of Elementary Functions for Loga COMPUTERS AND DIGITAL T PP.295-304. ES Micro processor for Public Key MOS circuits for low power, eloni and Thomas Plantard, y,”World Congress: Scientific s and Simulation, Jul 2005,
11. Hooshmand, M.; Zordan, D.; Testa, D.D.; Grisan, E.; Rossi, M. Boosting the battery life of

- wearables for health monitoring through the compression of biosignals. *IEEE Internet Things J.* 2017, 4, 1647–1662. [CrossRef]
12. Srinivasan, K.; Dauwels, J.; Reddy, M.R. Multichannel EEG compression: Wavelet-based image and volumetric coding approach. *IEEE J. Biomed. Health Inf.* 2013, 17, 113–120. [CrossRef] [PubMed]
13. Sriraam, N.; Eswaran, C. An adaptive error modeling scheme for the lossless compression of EEG signals. *IEEE Trans. Inf. Technol. Biomed.* 2008, 12, 587–594. [CrossRef] [PubMed]
14. Shaw, L.; Rahman, D.; Routray, A. Highly efficient compression algorithms for multichannel EEG. *IEEE Trans. Neural Syst. Rehabil. Eng.* 2018, 26, 957–968. [CrossRef] [PubMed]
15. Alvarez, G.D.; Favaro, F.; Lecumberry, F.; Martin, A.; Oliver, J.P.; Oreggioni, J.; Ramirez, I.; Seroussi, G.; Steinfeld, L. Wireless EEG system achieving high throughput and reduced energy consumption through lossless and near-lossless compression. *IEEE Trans. Biomed. Circuits Syst.* 2018, 12, 231–241. [CrossRef] [PubMed]
16. Zhou, P.Y.; Chan, K.C.C. Fuzzy feature extraction for multichannel EEG classification. *IEEE Trans. Cogn. Dev. Syst.* 2016, 10, 267–279. [CrossRef]
17. Chua, E.; Fang, W. Mixed bio-signal lossless data compressor for portable brain-heart monitoring systems. *IEEE Trans. Consum. Electron.* 2011, 57, 267–273. [CrossRef]
18. Chen, C.A.; Chen, S.L.; Huang, H.Y.; Luo, C.H. An efficient micro control unit with a reconfigurable filter design for wireless body sensor networks (WBSNs). *Sensors* 2012, 12, 16211–16227. [CrossRef] [PubMed]
19. Chen, S.L.; Wang, J.G. VLSI implementation of a low-power cost-efficient lossless ECG encoder design for wireless healthcare monitoring application. *Electron. Lett.* 2013, 49, 91–93. [CrossRef]
20. Chen, S.L.; Luo, G.A.; Lin, T.L. Efficient fuzzy-controlled and hybrid entropy coding strategy lossless ECG encoder VLSI design for wireless body sensor networks. *Electron. Lett.* 2013, 49, 1058–1060. [CrossRef]

DIAGONAL HAMMING BASED MULTI-BIT ERROR DETECTION AND CORRECTION TECHNIQUE FOR MEMORIES

¹ JALLELLA KAVITHA, ²Dr.V SUDHEER RAJA

¹PG Scholar, Dept.of ECE, Vaagdevi College of Engineering, Warangal, Telangana, India.

²Guide, Dept.of ECE, Vaagdevi College of Engineering, Warangal, Telangana, India.

¹kavithajallella54@gmail.com, ²sudheerraja.v@vaagdevi.edu.in

Abstract— In this paper, an advanced error correction 2-dimensional code based on divide-symbol is proposed to weaken radiation-induced MCUs in memory for space applications. For encoding data bits, diagonal bits, parity bits and check bits were analyzed by XOR operation. To recover the data, again XOR operation was performed between the encoded bits and the recalculated encoded bits. After analyzing, verification, selection and correction process takes place. Temporary errors which are classified under soft errors are created because of fluctuations in the voltage or external radiations. These errors are very common and obvious in memories. In this paper, multi-bit error detection and correction technique is proposed to identify errors 2 bits error for one row.

The proposed scheme is simulated and synthesized using Xilinx implemented in Verilog HDL.

Index Terms: Space Applications ,Diagonal Hamming, Multibit error correction, Random bit errors and correction techniques.

I. INTRODUCTION

Binary information is stored in a storage space called memory. This binary data is stored within metal-oxide semiconductor memory cells on a silicon integrated circuit memory chip. Memory cell is a combination of transistors and capacitors where capacitor charging is considered as 1 and discharging considered as 0 and this can store only one bit. Errors which are temporary or permanent are created in the memory cells and need to be eliminated. Single bit error correction is most commonly used technique which is capable of correcting up to one bit. Since technology is increasing rapidly, there are more probabilities of getting multiple errors [1]. Use of Diagonal Hamming method leads to efficient correction of errors in the memories. Memory was divided as SRAM, DRAM, ROM, PROM, EPROM, EEPROM and flash memory [2]. Main advantages of semiconductor memory is easy to use, less in

cost, and have high bits per square micrometers. Temporary errors are called transient errors which are caused because of fluctuations in potential level. Permanent errors are caused because of defects during manufacturing process or large amount of radiations [3].

For detection and correction of these soft errors, various methods have been proposed [4]. In this paper, memory bits which are affected by errors are recognized and rectified using Diagonal Hamming based multi-bit error detection and correction technique. The aim of this method is to detect effectively up to 8 bit errors and correcting them. In this project, Section-II gives overview of other coding techniques. The advantages and disadvantages of different coding techniques are discussed. Binary digits is stored in a space called memory. Errors occur in memory due to voltage fluctuations, manufacturing process or due to very high radiations. There are many coding techniques for error correction and detection. These techniques can correct from single to multiple bit errors. Coding methods like HVD, HVDD, HVPDH, DMC, MDMC, 3D parity check with Hamming are used to correct bits in memory. The 3 Dimensional parity check is used for checking and correcting the errors in message bits and hamming is used for correction of parity bits [3]. In HVPDH method, numbers of parity bits are reduced and hence reliability is increased [1]. HVD method [5] is used for correction of soft error bits and the power consumption is less in this method. In HVD method, the parity code uses four different directions in block of data.

Problem Statement Coding theory is interested in providing a reliability and trustiness in each communication system over a noisy channel. In the more communication systems, the error correction codes are used to find and correct the possible bit changing [2], for example, in wireless phones and etc. In any environment, Environmental interference, physical fault noise, electromagnetic radiation and other kinds of noises and disturbances

in the communication system affect communication direction to corrupted messages, an errors in the received codeword (message) or bit changing might be happened during a transmission of data [1] [2]. So, the data can be corrupted during a transmission and dispatching from the transmitter (sender) to the receiver, but during a data transmission, it might be affected by a noise, then the input data or generated codeword is not the same as received codeword or output data [1]. The error or bit changing which is happened in data bits can change the real value of the bit(s) from 0 to 1 or vice versa. In the following simple figure, a base structure of communication system is indicated. And this figure indicates that how the binary signal can be affected by a noise or other effects during a transmission on the noisy communication channel:

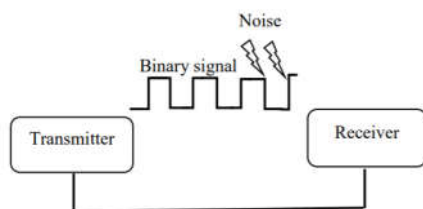


Figure: Data Transmission

To get the best idea of correction by using a redundancy in digital communication, first of all, it is necessary to model the main scheme contains two main parts called encoding and decoding like the following figure and in the next parts all of these parts will be explained in detail and implemented in verilog language.

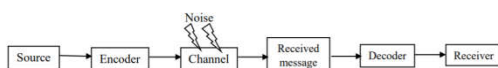


Figure: The main scheme of hamming code

According to this figure [2] [3], first of all, the code will be generated by a source, and then to do encoding part, the parity (redundancy) bits will be added by the encoder to the data bits which sent from a source. After that, the generated codeword which is a combination of data bits and parity bits will be transmitted to the receiver side, and during transmission, the error or bit changing might be happened in the communication channel over produced codeword. At the end, the corrupted error must be detected and corrected by decoder on the receiver side.

II. RELATED WORK

One of the proper subset of information theory is called coding theory, but the concept of these theories are completely different [2]. The main subject is began from a seminar paper which presented by Claude Shannon in the mid of 20th century. And in that paper, he demonstrated that good code exist, but his assertions were probabilistic. Then after Shannon’s theorem, Dr Hamming [1] [3] and Marcel Golay [5] presented their first error correction codes which called Hamming and Golay codes [2]. Source Encoder Channel Received message Decoder Receiver

In 1947, Dr Hamming introduced and invented the first method and generation of error correction code called hamming code [1] [6]. Hamming code is capable to correct one error in a block of the received message contains binary symbols [7]. After that, Dr Hamming has published a paper [1] in the Bell technical journal with a subject of error detection and error correction code. In 1960, other methods for error detection and error correction codes were introduced and invented by another inventor, for example, BCH code was invented by Bose, Chaudhuri and Hocquenghem who are a combination of the surname of the initial inventors' of BCH code [7].

Another error detection and error correction code which presented in 1960 was Reed Solomon (RS) code that invented by two inventors called Irving Reed and Gustave Solomon and this method was developed by more powerful computers and more efficient algorithm for decoding part [8]. 2.2. Types of Hamming Code There are three more significant types of hamming codes which called 1. Standard hamming code, 2. Extended hamming code [9], 3. Extended hamming product code, but in this research, the standard hamming code is used and implemented.

III. DESIGN METHODLOGY

Design of Diagonal Hamming method for memory Proposed design of Diagonal Hamming based multi-bit error detection and correction technique to the memory is shown in Figure. Using this approach of diagonal Hamming bits, the errors in the message can be recognized and can be rectified which are saved in the memory. In encoding technique message bits are given as input to the

Diagonal Hamming encoder and the Hamming bits are calculated. Message and Hamming bits (32+24 bits) are saved in the memory after the encoding technique.

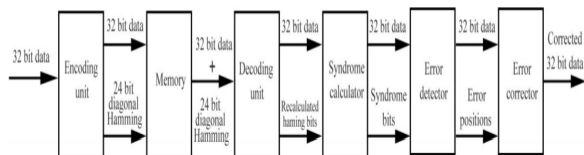


Figure: Proposed Architecture of Diagonal hamming method for memory

m3[7]	m3[6]	m3[5]	m3[4]	m3[3]	m3[2]	m3[1]	m3[0]
m2[7]	m2[6]	m2[5]	m2[4]	m2[3]	m2[2]	m2[1]	m2[0]
m1[7]	m1[6]	m1[5]	m1[4]	m1[3]	m1[2]	m1[1]	m1[0]
m0[7]	m0[6]	m0[5]	m0[4]	m0[3]	m0[2]	m0[1]	m0[0]

Figure: 32-bit message organization (C=8 and R=4)

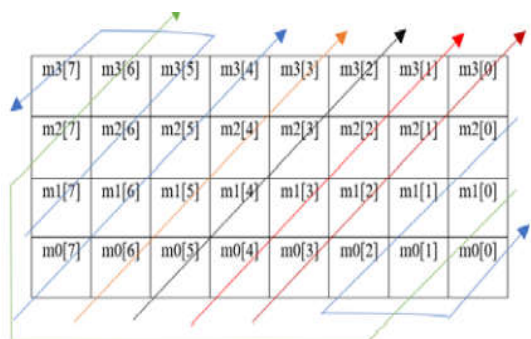


Figure: Grouping of the message bits to generate hamming bits

Errors which are occurring in the message bits, are saved in the memory and can be recognized and rectified in the decoding technique. B. Design of Diagonal Hamming Encoder For example, message of 32 bits is accounted in the proposed method. The message is represented in the form m x n matrix. The grouping of the message bits is depicted in Figure. The encoder generates the hamming bits and the hamming bits are obtained by grouping the message bits and the hamming bits are calculated with the help of hamming code. The message bits are patterned as shown in Figure. Eight diagonals

are considered in this Diagonal Hamming method and each diagonal consists of 4 message bits.

m3[7]	m3[5]	m2[6]	R1[3]	m1[7]	R1[2]	R1[1]
m3[6]	m2[7]	m0[1]	R2[3]	m1[0]	R2[2]	R2[1]
m0[0]	m0[2]	m1[1]	R3[3]	m2[0]	R3[2]	R3[1]
m3[4]	m2[5]	m1[6]	R4[3]	m0[7]	R4[2]	R4[1]
m3[3]	m2[4]	m1[5]	R5[3]	m0[6]	R5[2]	R5[1]
m3[2]	m2[3]	m1[4]	R6[3]	m0[5]	R6[2]	R6[1]
m3[1]	m2[2]	m1[3]	R7[3]	m0[4]	R7[2]	R7[1]
m3[0]	m2[1]	m1[2]	R8[3]	m0[3]	R8[2]	R8[1]

Figure: Positions of the hamming bits in accordance with the grouped message bits

Message bits are grouped as shown in the Fig. 3 in the specified directions. The first diagonal consists of m3[7], m3[5], m2[6], m1[7], the second diagonal has m3[6], m2[7], m0[1], m1[0], the third diagonal has m0[0], m0[2], m1[1], m2[0], the fourth diagonal has m3[4], m2[5], m1[6], m0[7], the fifth diagonal has m3[3], m2[4], m1[5], m0[6], the sixth diagonal has m3[2], m2[3], m1[4], m0[5], the seventh diagonal has m3[1], m2[2], m1[3], m0[4] and the eight diagonal has m3[0], m2[1], m1[2], m0[3]. Each one of the diagonals has four message bits. For the respective groups, the hamming bits are calculated as shown in Figure. The hamming bits are shown as R1, R2, R3, R4, R5, R6, R7, R8 arrays and these arrays consist of 3 bits. The hamming bits are calculated as given in equations (1)-(24) : For the first row:

$$R1[1] = m1[7] \oplus m2[6] \oplus m3[7]; (1) R1[2] = m1[7] \oplus m3[5] \oplus m3[7]; (2) R1[3] = m2[6] \oplus m3[5] \oplus m3[7]; (3) \text{ For the second row: } R2[1] = m1[0] \oplus m0[1] \oplus m3[6]; (4) R2[2] = m1[0] \oplus m2[7] \oplus m3[6]; (5) R2[3] = m0[1] \oplus m2[7] \oplus m3[6]; (6) \text{ For the third row: } R3[1] = m2[0] \oplus m1[1] \oplus m0[0]; (7) R3[2] = m2[0] \oplus m0[2] \oplus m0[0]; (8) R3[3] = m1[1] \oplus m0[2] \oplus m0[0]; (9) \text{ For the fourth row: } R4[1] = m0[7] \oplus m1[6] \oplus m3[4]; (10) R4[2] = m0[7] \oplus m2[5] \oplus m3[4]; (11) R4[3] = m1[6] \oplus m2[5] \oplus m3[4]; (12) \text{ For the fifth row: } R5[1] = m0[6] \oplus m1[5] \oplus m3[3]; (13) R5[2] = m0[6] \oplus m2[4] \oplus m3[3]; (14) R5[3] = m1[5] \oplus m2[4] \oplus m3[3]; (15) \text{ For the sixth row: } R6[1] = m0[5] \oplus m1[4] \oplus m3[2]; (16) R6[2] = m0[5] \oplus m2[3] \oplus m3[2]; (17) R6[3] = m1[4] \oplus$$

$m2[3] \oplus m3[2]$; (18) For the seventh row: $R7[1] = m0[4] \oplus m1[3] \oplus m3[1]$; (19) $R7[2] = m0[4] \oplus m2[2] \oplus m3[1]$; (20) $R7[3] = m1[3] \oplus m2[2] \oplus m3[1]$; (21) For the eight row: $R8[1] = m0[3] \oplus m1[2] \oplus m3[0]$; (22) $R8[2] = m0[3] \oplus m2[1] \oplus m3[0]$; (23) $R8[3] = m1[2] \oplus m2[1] \oplus m3[0]$; (24) In the encoder, the hamming bits are calculated for message. We get 24 hamming bits in total for 32-bit message. C. Proposed Diagonal Hamming Decoder The message bits which are encoded and kept in memory as a matrix as shown in Fig. 4, and are given as input to the decoder. The decoder now segregates message and hamming bits and it recalculates the hamming bits and evaluates syndrome bits. The syndrome bits are evaluated using the equations given in (25)-(48) : For first row $S1[1] = R1[1] \oplus m1[7] \oplus m2[6] \oplus m3[7]$; (25) $S1[2] = R1[2] \oplus m1[7] \oplus m3[5] \oplus m3[7]$; (26) $S1[3] = R1[3] \oplus m2[6] \oplus m3[5] \oplus m3[7]$; (27) For the second row: $S2[1] = R2[1] \oplus m1[0] \oplus m0[1] \oplus m3[6]$; (28) $S2[2] = R2[2] \oplus m1[0] \oplus m2[7] \oplus m3[6]$; (29) $S2[3] = R2[3] \oplus m0[1] \oplus m2[7] \oplus m3[6]$; (30) For the third row: $S3[1] = R3[1] \oplus m2[0] \oplus m1[1] \oplus m0[0]$; (31) $S3[2] = R3[2] \oplus m2[0] \oplus m0[2] \oplus m0[0]$; (32) $S3[3] = R3[3] \oplus m1[1] \oplus m0[2] \oplus m0[0]$; (33) For the fourth row: $S4[1] = R4[1] \oplus m0[7] \oplus m1[6] \oplus m3[4]$; (34) $S4[2] = R4[2] \oplus m0[7] \oplus m2[5] \oplus m3[4]$; (35) $S4[3] = R4[3] \oplus m1[6] \oplus m2[5] \oplus m3[4]$; (36) For the fifth row: $S5[1] = R5[1] \oplus m0[6] \oplus m1[5] \oplus m3[3]$; (37) $S5[2] = R5[2] \oplus m0[6] \oplus m2[4] \oplus m3[3]$; (38) $S5[3] = R5[3] \oplus m1[5] \oplus m2[4] \oplus m3[3]$; (39) For the sixth row: $S6[1] = R6[1] \oplus m0[5] \oplus m1[4] \oplus m3[2]$; (40) $S6[2] = R6[2] \oplus m0[5] \oplus m2[3] \oplus m3[2]$; (41) $S6[3] = R6[3] \oplus m1[4] \oplus m2[3] \oplus m3[2]$; (42) For the seventh row: $S7[1] = R7[1] \oplus m0[4] \oplus m1[3] \oplus m3[1]$; (43) $S7[2] = R7[2] \oplus m0[4] \oplus m2[2] \oplus m3[1]$; (44) $S7[3] = R7[3] \oplus m1[3] \oplus m2[2] \oplus m3[1]$; (45) For the eight row: $S8[1] = R8[1] \oplus m0[3] \oplus m1[2] \oplus m3[0]$; (46) $S8[2] = R8[2] \oplus m0[3] \oplus m2[1] \oplus m3[0]$; (47) $S8[3] = R8[3] \oplus m1[2] \oplus m2[1] \oplus m3[0]$; (48) If all the syndrome bits are equal to zero, then it represents that the message bits are not corrupted and if anyone of the syndrome bits in non-zero, then it represents the message bit(s) are corrupted. These corrupted bits need correction so, the message bits are sent to the error correction part. In the correcting of error part, the location of error is identified by doing the following calculations: Suppose if the error is in the third row of the

message organization, then the error position is calculated as: $(S3[3] * (22)) + (S3[2] * (21)) + (S3[0] * (20))$; (49) After the position is calculated, the error corrector negates the bit corresponding to that position to correct the data bit. This process is done till all the corrupted bits are corrected.

V. RESULTS

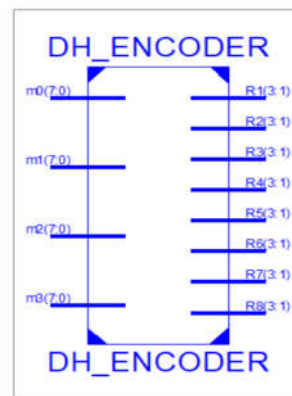


Figure: Encoder

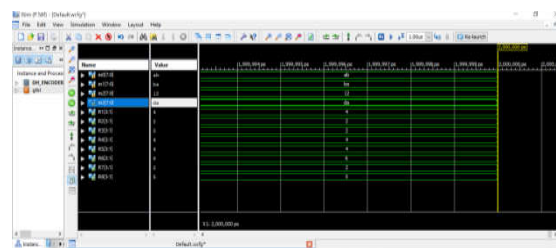


Figure: Encoder output

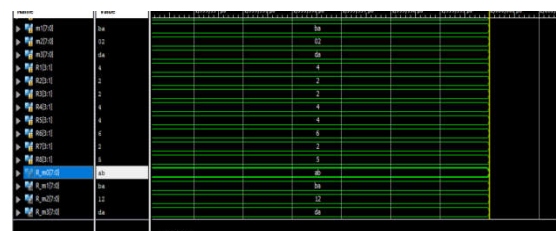


Figure: Decoder output

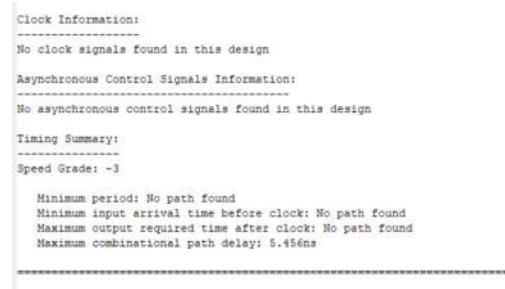


Figure: Delay

VI. CONCLUSION

Diagonal Hamming coding method is proposed in this paper and the main idea behind this work is to reduce maximum errors during transmission of bits in memory. Diagonal Hamming method identifies and corrects up to maximum of 8bit errors in a row for 32-bit input. Diagonal Hamming method ensures less area and delay by 91.76 percentage and 84.18 percentage respectively. Huge amount of error correction is possible using this Diagonal Hamming method.

REFERENCES

- [1] Paromita Raha , M. Vinodhini and N.S Murty, "Horizontal Vertical Parity and Diagonal Hamming Based Soft errors Detection and Correction of Memories," in Proc. Int Conf on Comp Com and Info, 2017.
- [2] S.ASAI, "Semiconductor memory trends," in Proc. of IEEE, Vol.74, 1986.
- [3] Shivani Tambatkar, Siddharth Narayana Menon, Sudarshan.V, M.Vinodhini and N.S.Murty, "Error Detection and Correction in Semiconductor Memories using 3D Parity Check Code with Hamming Code," in Proc. International Conf on Comm and Signal Processing, 2017.
- [4] Varinder Singh and Narinder Sharma, "A Review on Various Error Detection and Correction Methods Used in Communication," American International Journal of Research in Science, Technology, Engineering and Mathematics, pp. 252 - 257, 2015.
- [5] Mostafa Kishani, Hamid R. Zarandi, Hossein Pedram, Alireza Tadjary, Mohsen Raji and Behnam Ghavami, "HVD: Horizontal-Vertical-Diagonal error detecting and correcting code to protect against with soft errors," Design automation for embedded systems Journal, Vol. 15, no. 3, pp. 289- 310, May 2011.
- [6] S. Vijayalakshmi and V. Nagarajan (FEB 2019), "Design and Implementation of Low Power High-Efficient Transceiver for Body Channel Communications", Springer- Journal of Medical Systems
- [7] Md. Shamimur Rahman, Muhammad Sheikh Sadi, Sakib Ahammed and Jan Jurjens, "Soft Error Tolerance using Horizontal – Vertical Double – Bit Diagonal Parity Method," in Proc 2nd IEEE International Conference on Electrical Engineering and Information and Communication Technology (ICEEICT) , 21-23 May 2015.
- [8] Jing Guo, Liyi Xiao, Zhigang Mao and Qiang Zhao, "Enhanced Memory Reliability against Multiple Cell Upsets Using Decimal Matrix Code," IEEE Transactions on Very Large Scale Integration (VLSI) Systems, Vol. 22, Issue:1, pp. 127-135, Jan. 2014
- [9] Ahilan A. and Deepa P., "Modified Decimal Matrix Codes in FPGA Configuration Memory for Multiple Bit Upsets," in Proc.International Conference on Computer Communication and Informatics (ICCCI), pp. 1- 5, Jan. 2015
- [10] M.Vinodhini and N.S. Murty, "Reliable Low Power NoC Interconnect," Microprocessor and Microsystems-Embedded Hardware Design, Vol.57, March 2018.
- [11] U. Sai Himaja, M. Vinodhini, N.S. Murty, "Multi-Bit Low Redundancy Error control with Parity Sharing for NoC Interconnects," in Proc. International Conference on Communication and Electronics Systems, Oct. 2018.

Power Reduction of Domino Logic with clock gating using 16nm CMOS Technology

Bhukya Naveen Kumar¹, Dr. V. Sudheer Raja²

1(Department of ECE, Vaagdevi College of Engineering, Warangal
Email: naveennayakbhukya123@gmail.com)

2 (Department of ECE, Vaagdevi College of Engineering, Warangal
Email: sudheerraja.v@vaagdevi.edu.in)

Abstract:

In this paper, a new technique of power reduction in CMOS domino logic is proposed. The proposed technique uses clock gating as well as output hold circuitry. Clock is passed to the domino logic only during the active state of the circuit. During standby mode, clock is bypassed while the state of the circuit is retained. A 2:1 multiplexer is used for clock gating and for retaining the state of the circuit. Simulation results are being carried out in a 2-input NAND gate, 2-input nor gate and 1-bit conventional full adder cell in 16nm CMOS technology. The power of the proposed circuit is reduced to an average of 99.37 % with respect to standard domino logic. Propagation delay is slightly increased to an average of 4.53 %. Area of the proposed circuit increases to four transistors per domino module.

Keywords — Dynamic, Domino, static power, clock gating, CMOS.

I. INTRODUCTION

The modern technologies move towards smaller, faster, and cheaper computing systems. This has been facilitated by exponential increase in device density and operating frequency through VLSI technology scaling. This has led to an increase in power consumption that has reached limits of reliability and cost. In addition, continued scaling into the nanometer system has brought design robustness issues such as soft error, signal integrity, and process variability. In addition, the issues of power consumption and robustness are affected with time. This has created a predicament in computer system design that intimidated to be an uncertain block to future advancement [2].

The fast improvement of VLSI CMOS circuit technique is due to the wireless systems with low power budgets and increased use of small sized gadgets and very high speed processors. To attain this requirement, the supply voltages and size of transistors are scaled with technology. Due to larger number of devices per chip, the interconnection density increases [3]. The interconnection density

along with high clock frequency increases capacitive coupling of the circuit. Therefore, the noise pulses are generated leading to logic failure and delay of the circuit [6]. Again, when supply voltage is scaled, the threshold voltage of the device needs to be scaled to preserve the circuit performance, which leads to increase in the leakage current of the device. Due to low device count and high speed especially compared to complementary CMOS, dynamic-logic circuits are broadly used in a wide range of applications including dynamic memory, digital signal processors and microprocessors. Dynamic circuit contains a pull-down network which realizes our desired logic functions. According to the basic dynamic circuit operation, the dynamic node precharges at every clock cycle. As the clock signal frequency is high, the circuit generates a lot of noise which consumes extra power and slows the circuit.

II. LITERATURE SURVEY

A domino logic module consist of a pull down network (PDN), dynamically connected, followed by a static inverter [7] as shown in figure 1. The non-inverting output of domino is represented by

signal out while domino node is represented by X. The PDN is built exactly as that in complementary CMOS.

A. Standard Domino Logic Module

The domino module works in two phases - precharge and evaluation, where the signal clock controls the mode of operation as shown below:

$$clock = \begin{cases} 0, & \text{precharge phase} \\ 1, & \text{evaluation phase} \end{cases}$$

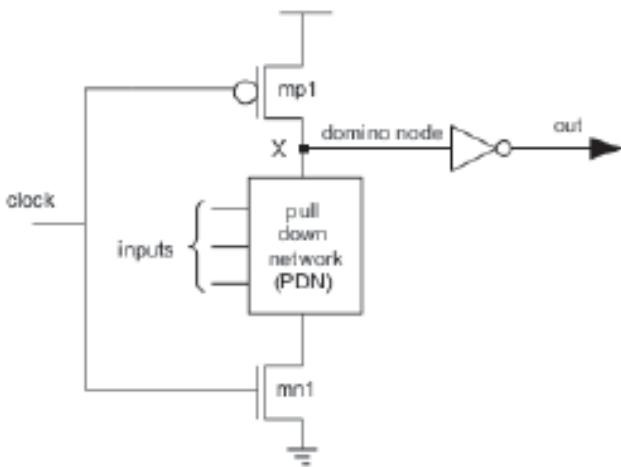


Figure: A Standard Domino Logic Module

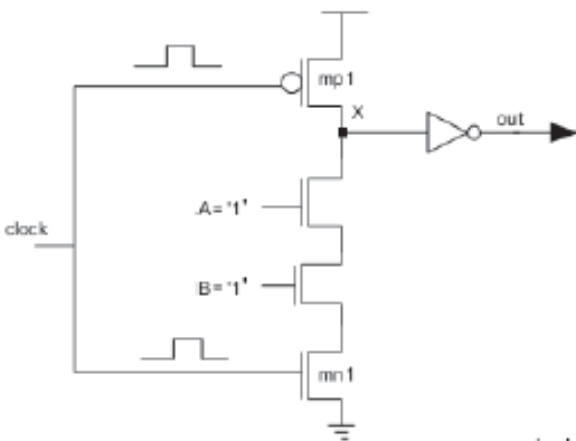


Figure: NAND gate using domino logic

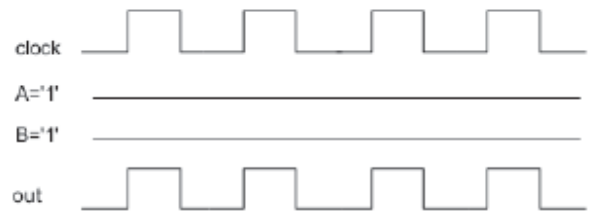


Figure: Waveforms for a 2-input NAND gate using domino logic during standby mode

During precharge phase, domino node X is charged to VDD by pmos transistor mp1. The nmos transistor mn1 is off during this phase. During evaluation phase, transistor mp1 is off while mn1 is in on state. If the input values are such that PDN conducts, node X discharges, otherwise it will hold the precharge value i.e. VDD. Figure 2 shows the domino logic module for a 2-input nand gate. Let the inputs of a 2-input nand gate domino logic are '11' i.e. A='1' and B='1' during standby mode. For this case, the out should be '1' but since the clock is present, out is a pulse as shown in figure 3. The presence of clock and the pulse shaped output dissipates a significant amount of power dissipation during standby mode. For the other combinations of standby inputs i.e. '00', '01' and '10', out is '0'. The presence of clock in domino logic leads to power dissipation in this case. Domino logic is faster than its static logic counterparts. Although, it is very sensitive to noise sources such as leakage current, crosstalk, charge sharing, power supply bump and ground bounce since its dynamic node cannot be recovered after the data is lost by those noise sources [4,5].

III. PROPOSED SYSTEM

We have presented a new scheme for the design of noise tolerant domino logic technique. This circuit contains a precharge transistor, an evaluation network, footer transistors and semi-dynamic inverter as depicted in figure. In the precharge period when the clock is low, the precharge pmos gets on and dynamic node is connected to v_{dd} and gets precharge to v_{dd}. When clock goes high, the evaluation phase starts and output gets evaluated with pull-down network that conditionally gets discharged if the pdn is on. During evaluation period when all the inputs are at logic 0, the

dynamic node stays at logic 1. However, in case of wide fan-in circuits, due to the sub threshold leakage pdn network leaks the charge stored in the capacitance at the dynamic node. When a noise voltage impulse occurs at gate input, voltage level of the dynamic node decreases resulting is change in output logic [8,9]. To stop that, the footer transistors (m_2 , m_3 and m_4) are connected. M_3 acts as stacking transistor [10,11]. At the evaluation period, when the dynamic node should be discharged, at that time m_2 makes a charge discharge path. In basic domino logic, the output pulses persist in the circuit, due to the precharge act.

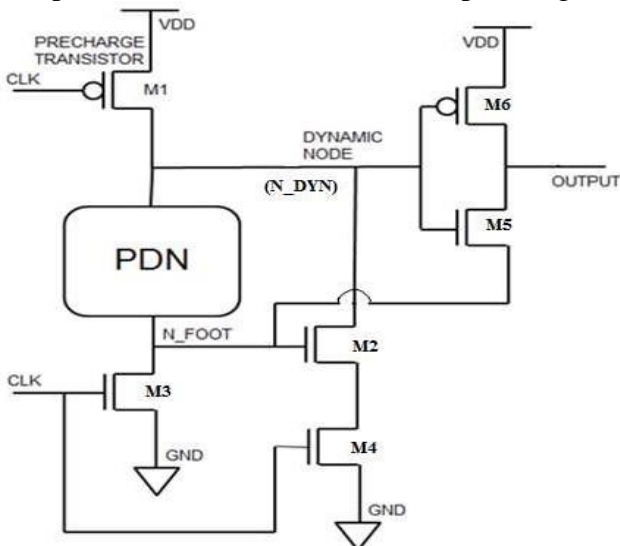


Figure: Proposed Circuit

The pulses of output node N_FOOT always propagated because of turning on the NMOS transistor present in the buffer by precharge pulse in the dynamic node. Therefore it can be easily said that we can avoid the precharge pulse propagating to the output of the buffer, if we can turn off the NMOS transistor of the buffer during precharge. Following this method, this unique circuit technique is proposed [13].

B. Circuit Analysis

The proposed novel domino circuit scheme is shown in Figure. Transistor M_3 is used as stacking transistor. Due to voltage drop across M_3 , gate-to-source voltage of the NMOS transistor in the PDN decreases. The proposed circuit has additional evaluation transistor M_4 with gate connected to the

CLK. When M_3 has voltage drop due to presence of noise-signals, M_2 starts leaking which causes a lot of power dissipation. This makes the circuit less noise robust. In proposed scheme, the transistor M_4 causes the stacking effect, which makes gate-to-source voltage V_{GS} of M_2 smaller (M_3 less conducting). Hence circuit becomes more noise robust and less leakage power consuming.

C. Noise Analysis

When PDN is OFF and the N_DYN is at high voltage, at that time the N_FOOT stays at low voltage. Due to the high voltage level of dynamic node, the gate of the NMOS (M_5) goes high and the low level of N_FOOT makes the source of the M_5 to 0. This makes M_5 ON and voltage of buffer output becomes same as the voltage of N_FOOT . It can be easily verified that if the NMOS transistor of buffer can be turned off permanently, by doing this, the pulses propagating to the output can be avoided. In the evaluation period, when the NMOS M_3 is ON, N_FOOT gets discharged to 0. When PDN is ON the N_DYN also gets discharged to ground. This makes the V_{GS} of buffer NMOS M_5 to 0 as $V_{GS} = V_G - V_S = 0$. This results in switching OFF the NMOS and the buffer output gets completely charged through PMOS M_6 .

In precharge the dynamic node will get charged to high, when PDN is ON the voltage of the N_FOOT is nearly same as N_DYN , as the NMOS M_3 is OFF. The V_{GS} of the buffer NMOS will be $V_G - V_S < V_{TH}$ which keeps the NMOS of the buffer at turned OFF stage. The PMOS of the buffer is also OFF due to the high level of N_DYN node. This makes the output of buffer LOW [14].

D. Power Analysis

The proposed structure uses semi-domino buffer structure. So the output node OUT has no pulses in precharge stage as shown in Figure. In the figure the first waveform shows the clock the second and third wave form shows the waveform of the input signals namely A and B.

IV. RESULTS

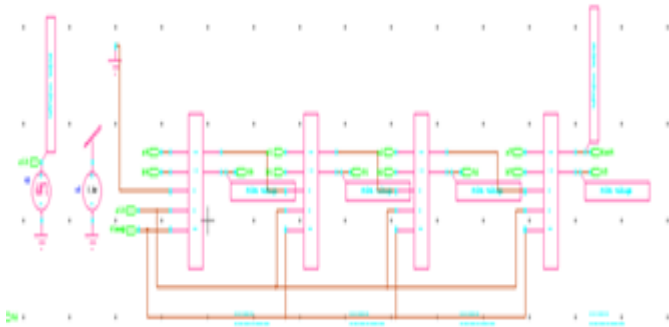


Figure: Proposed Circuit for 16nm 4bit Domino ADDER

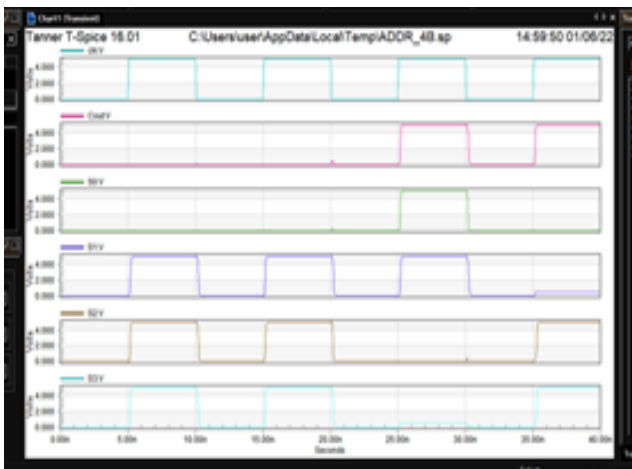


Figure: 2. Proposed Circuit 16nm Waveforms

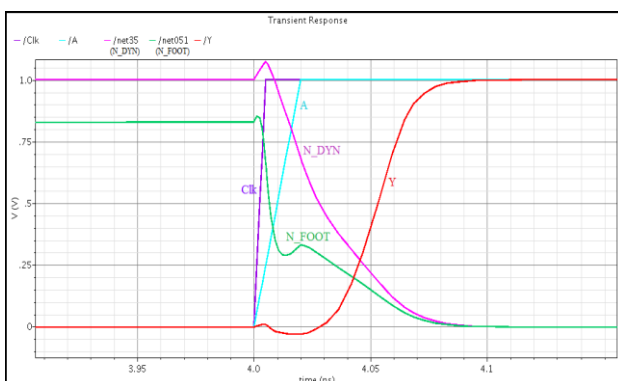


Figure: Simulated waveform of proposed scheme

V. CONCLUSION

In this dissertation, we have introduced and demonstrated a novel logic style. This logic consumes low power and is noise robust. This proposed logic is superior to domino and static CMOS logic in addition to some recent proposed logic styles in terms of energy and delay, and at the same time is more noise robust than any logic styles. In particular, we have shown 60 – 80 % power reduction vs. domino and 30 – 50 % speed improvement vs. static CMOS. In addition, we have presented that the logic also works efficiently with sequential circuits.

REFERENCES

1. J. M Rabaey, A. Chandrakasan, B, Nikolic, *Digital Integrated Circuits: A Design Perspective*, Upper saddle rive, NJ: 2e Prentice-Hall,2002.
2. S. M. Kang, Y. Leblebici, *CMOS Digital Integrated Circuits: Analysis & Design*, TATA McGraw- Hill Publication, 3e, 2003.
3. N. Weste, K. Eshraghian, *Principles of CMOS VLSI Design, A systems perspective*, Addison Wesley MA,1988.
4. J. P. Uyemura, *CMOS logic circuit design*, Kluwer Academic,2002.
5. K.S. Yeo, K. Roy, *Low- Voltage, Low-Power VLSI Subsystems*, McGraw Hill Professional, 2005.
6. K. Roy, S. Prasad, *Low-Power CMOS VLSI Circuit design*, Willey Interscience Publication, 2000.
7. A.P. Chandrakasan and R.W. Broderson, *Low Power Digital CMOS Design*, KluwerAcademic, 1995.

8. I.M.ElmarsyandA.Bellaouar, *LowPowerdigitalVLSIDesignCircuitsandSystems, Kluwer Academic, 1995.*
9. A.Devgan, "Efficientcouplenoiseestimationforon-chipinterconnects," in *ICCAD97*, pp.147- 151, 1997.
10. K. K. Kim, Y. -B. Kim, M. Choi, N. Park, "Leakage minimization technique for nanoscale CMOS VLSI based on macro-cell modelling," in *IEEE Design &Test of Computers*, Dec. 13, 2006.
11. M.Passlack, M.Uhle, H.Elschner, "Analysisofpropagationdelaysinhigh-speedcircuitsusing a distributed line model," *IEEE Transactions on Computer Aided DESIGN*, vol. 9, no. 8, Aug 1990.
12. I. -C. Wey, Y.-G. Chen, A.-Y. Wu, "Design and Analysis of Isolated Noise Tolerant (INT) Technique in Dynamic CMOS Circuits," *IEEE Transactions on Very Large Scale Integration (VLSI) Systems*, vol. 16, no. 12, pp. pp.1708-1712, Dec.2008.
13. P. Meher, K. K. Mahapatra, "Ultra low-power and noise tolerant CMOS dynamic circuit technique," in *IEEE Region 10 Conference TENCON 2011*, pp.1175-1179, Bali, 21-24 Nov. 2011.
14. F. Frustaci, P. Corsonello, S. Perri, G. Cocorullo, "High-performance noise-tolerant circuit techniquesforCMOSdynamiclogic," *IETCircuits, Devices&Systems*, vol.2,no.6,pp.

Design of Self- Recoverable SRAM Cell

Neelam Gurram

M. Tech, Scholar, Dept. of ECE

Vaagdevi College of Engineering, Warangal, Telangana State, India.

CH Anil Kumar

Assistant Professor, Dept. of ECE

Vaagdevi College of Engineering, Warangal, Telangana State, India

Abstract-In this paper, a profoundly dependable self-recoverable SRAM cell, to be specific SESRS cell, is proposed. More number of access semiconductors and an extraordinary input component among the inner hubs makes this SESRS cell novel SRAM cell with the accompanying benefits: 1. This planned SESRS cell can self-recuperate from both Twofold Hub Mistakes and Single Hub Blunders. 2.The power utilization is decreased by half around and the silicon region by 23% contrasted and the current SRAM cell. The reproduction results are utilized in the approval of the heartiness of the recently planned SESRS cell. Likewise, this proposed SRAM cell can diminish the read admittance time by 62% on a normal.

Keywords: SRAM, SESRS, Single Node Upsets(SNU), Double Node Upsets(DNU), Access Time, Power dissipation, Silicon Area

INTRODUCTION:

With the multiplication popular of low power gadgets like remote sensor organizations, implantable biomedical gadgets, and other battery-worked compact gadgets, power dispersal has turned into a key plan limitation. Static Irregular Access Memory (SRAM) is the significant supporter of the power dissemination, as they possess a huge piece of Frameworks on-Chip (SoCs), and their part will fill further in the future [1]. Besides, with the coming of super scaled innovations, spillage has turned into a serious danger. The power utilization will increment as spillage rises dramatically with a decrease in edge voltage (V_{th}) and door oxide thickness [2]. It is, in this way, important to limit the power related with SRAM to have a power-productive plan. Decreasing the stock voltage is a straight-forward method for accomplishing power proficiency on the grounds that the dynamic and spillage power diminish quadratically and dramatically individually with supply voltage [3]. Forceful innovation scaling is utilized for assembling current high level SRAM recollections, permitting high incorporation thickness and further developed execution. Notwithstanding, an unfriendly outcome is that how much basic charge put away on a hub of a SRAM cell diminishes due

to the steadily diminishing stockpile voltages and hub capacitances. Thus, high level SRAM cells are turning out to be increasingly more helpless to delicate blunders initiated by the striking of particles, like protons, neutrons, weighty particles, electrons, muons, and alpha particles [1-2]. Delicate blunders can invalidly change the qualities put away in SRAM recollections or even accident SRAM circuits in cutting edge innovations. In this way, it is vital to configuration solidified designs to accomplish high SRAM-unwavering quality as for delicate mistakes.

As of late, multi-chomped delicate blunder/upset (MCU) has compromised the security of SRAMs at super scaled innovation because of the decrease in successful distance between semiconductors [12]. The Piece interleaving (BI) compositional method is a productive method for managing this blunder. Notwithstanding, this method is appropriate to the cells that display completely half-select (HS) free activity. The straight-forward way to deal with accomplishing HS free activity is to utilize cross-point cell choice, where the compose way comprises of two access semiconductors constrained by various line and section based signals [9].

At the point when a patch strikes an OFF- state semiconductor in a SRAM cell, a thick track of electron- opening matches can be created. Hence, a flash twinkle, i.e., a solitary occasion flash(SET), might be created at the mecca that gathers the charge, and it veritably well may be honored at the result of the impacted explanation door. In the event that the SET twinkle engenders through the downstream combinational explanation entries, showing up at a capacity element, the beat might be caught, causing an invalid worth conservation in the capacity element(3). also again, the patch may directly strike an OFF- state semiconductor in a capacity element, causing a solitary mecca derangement(SNU). also, the joining consistence of SRAMs is continually expanding and mecca dividing is turning out to be a lot more modest. latterly, one striking- patch may at the same time influence two OFF- state semiconductors in a capacity element because of different mecca charge multifariousness systems(4), causing a twofold

mecca derangement(DNU). Without a mistrustfulness, SNU and DNU can beget invalid worth conservation in a SRAM cell. Consequently, to work on the vigor of SRAM cells to guard them against implicit information debasements, prosecution blunders, or indeed crashes, circuit itineraries need to palliate delicate miscalculations to work on the unvarying quality of SRAM cells for good introductory operations. The new event of FinFET advances can lessen the delicate mistake rate at the semiconductor or cell position(5). Be that as it may, this element of FinFET- grounded circuits is deficient to vindicate originators from giving significant and protean answers for delicate boob resistance, particularly for security introductory operations in cruel conditions.

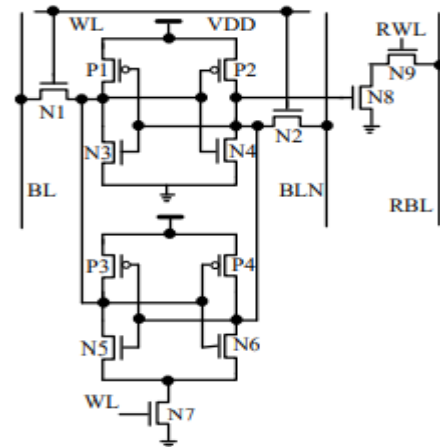
Many SRAM cell layouts [4], [11] have been presented using the Radiation Solidifying Plan (RHDD) method to reduce SNU or even DNU. RHBD can actually lessen the impact of radiation particles on SRAM cells. RHBD is also used for planning locks [16–17] and back-peddles [18–20]. There is a problem with the radiation-solidified SRAM cells as well:

- (1) Some SRAM cells are not capable of self-recovery after any SNU [6]. A portion of some SRAM cells' internal hubs can self-recover from SNU [7]. In the interim, certain SRAM cells, like RHD12T [7], can self-recover from DNU only for a portion of hub matches, whereas other SRAM cells can self-recover from DNU for all DNU.].
- (2) Some current solidified SRAM cells experience the ill effects of huge above, particularly as far as perused admittance time. Additionally, a portion of the cells actually experience the ill effects of high compose access times and from high power dissemination, for example, NASA13T [6] and DNUSRM [10].
- (3) Some current solidified SRAM cells utilize extra procedures to guarantee SRAM unwavering quality, for example, evaluating a few semiconductors [6], expanding dispersing between hubs [8], distinguishing delicate and heartless hubs [10], and so on. These arrangements increment the related region above and plan intricacy. Since the current SRAM cell in [12] still experiences the issue that it can't give total self-recoverability from blunders, despite the fact that it has a little above, In light of the RHBD approach, this paper presents a profoundly dependable SRAM cell with worked on self-recoverability from delicate mistakes. Likewise, with the diminished power utilization, silicon region and access time.

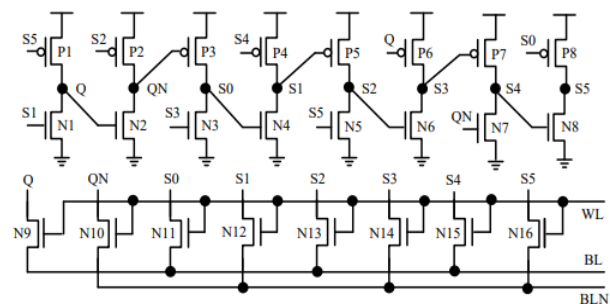
EXISTING SRAM CELLS

The current SRAM cells which can endure disturbs however experience the ill effects of the enormous

above, particularly as far as the entrance time and high-power scattering, are NASA13T and DNUSRM. These two SRAM cells are displayed in Fig. (1) and Fig. (2). The SRAM cell, which can endure both single-hub disturbs and twofold hub upsets and which has less power dissemination, is displayed in fig (3). In any case, this SRAM cell possesses more silicon region..



Fig(1): NASA13T

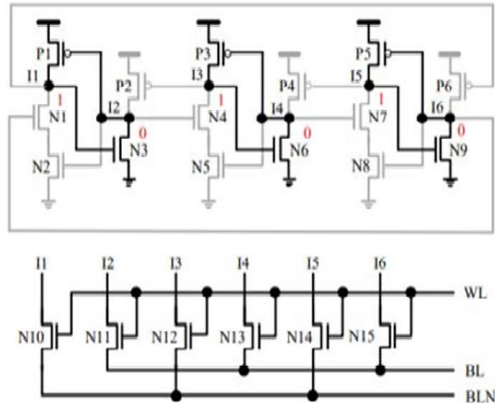


fig(2):DNUSRM

figFig. 1 shows the schematic of the NASA13T cell [6]. It is partitioned into three sections. The left-top part is utilized as an essential stockpiling module with a compose block. The left-base part goes about as an optional stockpiling module. The right part is an exceptional perused just block for understanding qualities. The read and compose blocks guarantee its comprehensibility and writeability. Contrasted and 6T, NASA13T gives an elevated degree of security against SNU to further develop delicate blunder resistance, yet it actually can't endure SNU brought about by high energy particles.

The design for the DNUSRM cell is shown in Fig. 2 [10]. The PMOS semiconductors P1 to P8 and the NMOS semiconductors N1 to N16 make up the 24 semiconductors that make up the DNUSRM cell. For maintaining value, semiconductors P1 to P8

and N1 to N8 are used. Access semiconductors that are restricted by word line WL are N9 to N16. Because of the remarkable growth of criticism circles, the DNUSRM cell can recover on its own from any potential SNUs and DNU. In any case, the DNUSRM cell experiences a huge above as far as power dissemination because of enormous current rivalry in its criticism circles and silicon region above because of the utilization of countless semiconductors.



Fig(3):SESRS 21T

In Fig. 3. The PMOS semiconductors P1 to P6 and the NMOS semiconductors N1 to N15 make up the 21 semiconductors that make up the SESRS cell. For maintaining value, semiconductors P1 to P6 and N1 to N9 are used. Access semiconductors that are restricted by word line WL are N10 to N15. Interior hubs I1 to I6 are connected to bit lines BL and BLN independently through access semiconductors N10 to N15. At the point when WL = 1, the entrance semiconductors are ON, permitting compose and peruse access tasks to be executed. At the point when WL = 0, the entrance semiconductors are OFF, and the cell holds the put away worth.

PROPOSED Framework

From Fig. 4, it should be possible to see the suggested self-recoverable SRAM cell's schematic. The PMOS semiconductors P1 to P8 and the NMOS semiconductors N1 to N8 make up the 16 semiconductors in this SESRS cell. 8 PMOS and 4 NMOS semiconductors, or semiconductors P1 to P8 and N1 to N4, make up the capacity of a portion of the cell. Semiconductors N5 through N8 are used for access operations, and word-line WL is connected to their entrance terminals. Interior hubs I1 to I4 in the proposed S8P4N cell are connected to bit lines BL and BLN by access semiconductors N5 to N8, respectively. The suggested S8P4N cell's architecture is seen in Figure 8 . At the point when WL = 1, the entrance semiconductors are ON, permitting compose and peruse access tasks to be executed. At the point when WL = 0, the entrance semiconductors are

OFF, and the cell holds the put away worth.

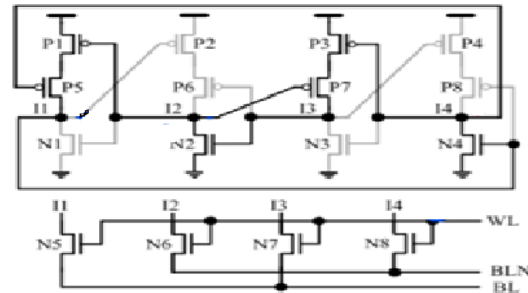


Fig (4): SESRS 16T

The characteristic charge and release of cell-hubs through access semiconductors can influence WATs and Rodents. We often consider that a cell with fewer semiconductors has a more constrained area and less power dispersion. To ensure its self-recoverability from all possible SNU and DNU, the suggested SESRS cell requires moderate region and power above. The suggested SESRS cell's high dependability and increased speed are primarily achieved at the sacrifice of critical area and power as compared to the existing solidified SRAM cells. Our suggested SESRS cell uses less space and energy.

Additionally, this can self-recover from all possible DNU and SNU, unlike the existing SRAM cell. Force scattering and the silicon area typically have PRCs of 23% and 50%, respectively.

SIMULATION RESULTS AND AREA CALCULATION

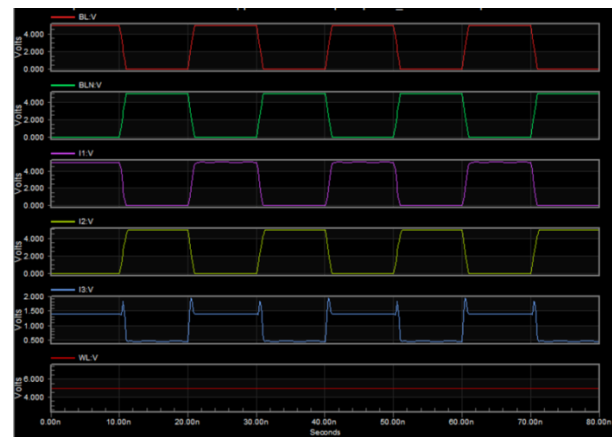


Fig (5): simulation waveforms

Area Calculations

Existing Method: Number of MOSFETS =16
 Area = No. of MOSFETS * Width * Length
 = 16 x 1.50 u x 0.25 u = 6 μmSq
 Proposed Method: Number of MOSFETS =21
 Area = No. of MOSFETS * Width * Length
 = 21 x 1.50 x0.25 = 7.875 μmSq
 Percentage of area decreased =1.875/7.875= 23%

CONCLUSION

The suggested 16T SESRS cell has less silicon region and power dispersion than the exceptional SRAM cell, which can self-recover from any possible DNU.

It may very well be effectively used in industries where high, constant quality and cost sufficiency are essential.

REFERENCES

- [1] M. Ebara, K. Yamada, K. Kojima, et al., "Process Dependence of Soft Errors Induced by α Particles, Heavy Ions, and High Energy Neutrons on Flip Flops in FDSOI," *IEEE Journal of the Electron Devices Society*, vol. 7, no. 1, pp. 817-824, 2019.
- [2] M. Gadlage, A. Roach, A. Duncan, et al., "Soft Errors Induced by High-Energy Electrons," *IEEE Transactions on Device and Materials Reliability*, vol. 17, no. 1, pp. 157-162, 2017.
- [3] S. Cai, W. Wang, F. Yu, et al., "Single Event Transient Propagation Probabilities Analysis for Nanometer CMOS Circuits," *Journal of Electronic Testing - Theory and Applications*, vol. 35, no. 2, pp. 163-172, 2019.
- [4] Y. Li, L. Li, Y. Ma, et al., "A 10-Transistor 65nm SRAM cell Tolerant to Single-Event Upsets," *Journal of Electronic Testing*, vol. 32, no. 2, pp. 137-145, 2016.
- [5] B. Narasimham, S. Gupta, D. Reed, et al., "Scaling Trends and Bias Dependence of the Soft Error Rate of 16 nm and 7 nm FinFET SRAMs," *International Reliability Physics Symposium*, pp. 1-4, 2018.
- [6] Y. Shiyanovskii, A. Rajendran, and C. Papachristou, "A Low Power Memory Cell Design for SEU Protection against Radiation Effects," *IEEE NASA/ESA Conference on Adaptive Hardware and Systems*, pp. 288-295, 2012.
- [7] C. Qi, L. Xiao, T. Wang, et al., "A Highly Reliable Memory Cell Design Combined with Layout-Level Approach to Tolerant Single-Event Upsets," *IEEE Transactions on Device and Materials Reliability*, vol. 16, no. 3, pp. 388-195, 2016.
- [8] C. Peng, J. Huang, C. Liu, et al., "Radiation-Hardened 14T SRAM Bitcell with Speed and Power Optimized for Space Application," *IEEE Transactions on Very Large Scale Integration (VLSI) Systems*, vol. 27, no. 2, pp. 407-415, 2019.
- [9] C. Hu, S. Yue, S. Lu, "Design of a Novel 12T Radiation Hardened Memory Cell Tolerant to Single Event Upsets (SEU)," *International Conference on Integrated Circuits and Microsystems*, pp. 182-185, 2017.
- [10] A. Yan, Z. Wu, J. Guo, et al., "Novel Double-Node-Upset-Tolerant Memory Cell Designs Through Radiation-Hardening-by-Design and Layout," *IEEE Transactions on Reliability*, vol. 68, no. 1, pp. 354-363, 2019.
- [11] J. Jiang, Y. Xu, W. Zhu, et al., "Quadruple Cross-Coupled Latch-Based 10T and 12T SRAM Bit-Cell Designs for Highly Reliable Terrestrial Applications," *IEEE Transactions on Circuits and Systems I: Regular Papers*, vol. 66, no. 3, pp. 967-977, 2019.
- [12] A. Yan, J. Zhou, Y. Hu, et al., "Novel Quadruple Cross-Coupled Memory Cell Designs with Protection against Single Event Upsets and Double-Node Upsets," *IEEE Access*, vol. 7, pp. 176188-176196, 2019.

DESIGN OF BIST (BUILT-IN-SELF-TEST) EMBEDDED MASTER-SLAVE COMMUNICATION USING SPI PROTOCOL

¹ R.SRAVANTHI, ² V.SABITHA

¹PG Scholar, Dept.of ECE, Vaagdevi College of Engineering, Warangal, Telangana, India.

² Associate professor, Dept.of ECE, Vaagdevi College of Engineering, Warangal, Telangana, India.

¹rangusravanthi456@gmail.com, ²sabitha_v@vaagdevi.edu.in

Abstract—The Serial-Peripheral Interface(SPI) Protocol also called as synchronous serial interface specification is used for communication between single master and single/multiple slaves. With the increase in number of slaves causing high complexity of circuit creates a demand in self testability feature for SPI module in order to test for fault free circuits. Built-InSelf-Test(BIST) is the answer for self-test in circuits as well as it helps in reduction of maintenance and testing cost. Design of BIST embedded SPI module with Single Master and Single Slave configuration has been introduced in this paper, here 8- bit data is transferred across the module ,where the circuit under test(CUT) is being self-tested with BIST feature for it's correctness. This SPI module is designed using Verilog Hardware Description Language(HDL) using EDA playground platform for applications like Application Specific Integrated Circuit(ASIC)or System on Chip(SOC).

Keywords— SPI, BIST,MISO, MOSI, TPG, ORA

I. INTRODUCTION

Motorola invented Serial Peripheral Interface(SPI) protocol in the mid 1980's to substitute parallel interfaces and provide high speed transfer of data between modules. SPI become most favoured serial communication protocol because of easy interfacing and high-speed transfer. SPI follows full duplex, master-slave communication while transferring and receiving data between them which synchronizes on the rising edge or falling edge of the clock. Data transmission can happen at the same time for both master and slave. There are basically two types of SPI interface, it can be either 3-wired or 4-wired.This research focuses on the popular 4-wired SPI interface.

SPI Protocol is followed even in embedded systems like so coprocessors and microcontrollers like Programmable Interface Controller(PIC),Advanced Virtual Risc (AVR). These chips may work as master or slave block which is operated by the in

built SPI controller in them. SPI is mostly used in those applications where high speed data transfer has to take place . SPI's exclusive features include master/slave operation, double buffered data register for transmission and reception, polarity and phase synchronization with serial clock, interrupt capability of CPU with fault deduction. SPI's functional registers are responsible for their recognition.

II. RELATED WORK

In the past few years, technology is increasing rapidly and the size of IC chips in VLSI industry is decreasing day by day and the incorporating new features in the small chip is a hectic work and beyond that the testing part is very crucial in any kind of circuit. A small test problem can cause a whole device failure and it can also cause whole version failure which can take billions of amounts. So, DFT (Design-For-Testability) became a preferable technique to decrease area over head and work efficiently.

Built In Self-Test is an approach for a system to test it self concept taken from Design for Testability model, This concept makes a simple and effective testing to reduce cost of ATE(Automatic Test Equipment) and reduce the reliability upon external testing process and also reduces the complexity. BIST is a unique feature in DFT test techniques where it self-test and consumes less overhead with most approximate results and contain only few blocks in the design which are Random pattern generator, Response analyzer etc.

III. DESIGN METHODOLOGY

In this research an SPI module having self-testing capability has been introduced. The basic components of BIST architecture has been introduced within SPI architecture block diagram where the designed CUT is able to self-test itself. The fig3 is the block diagram for BIST embedded

SPI protocol , where the test patterns are generated by the TPG block and they are send through Master block’s MOSI pin to the Slave.

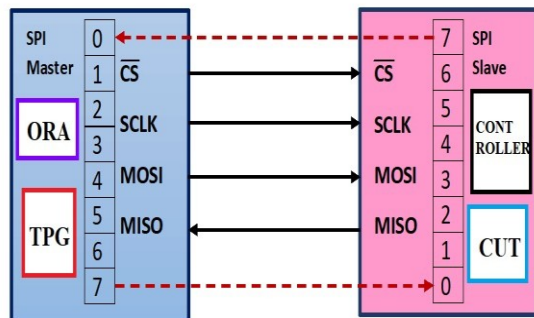


Figure: BIST embedded SPI Master-Slave block

Where slave reads the data sent from the master and segregates the received data and then finally passes to the CUT designed within the SPI slave block for performing the operation. After completion of the arithmetic operation. The results from the CUT are sent from the Slave block to the Master block through MISO pin .The received ALU results is then fed to the ORA block designed within the SPI Master for checking the correctness of the CUT.

a) Test Pattern Generator (TPG)

The TPG block proposed here uses LFSR(linear feedback shift register) technique to generate test patterns. Linear feedback shift register is also called as pseudo random pattern generator. An n bit LFSR has maximum sequence length of 2^n-1 .

For example if we take n=4 bit LFSR. The test patterns generation can be explained from the figure.

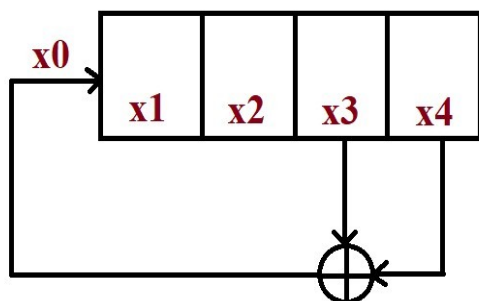


Figure: 4-bit Linear Feedback Shift Register(LFSR)

This 4 bit LFSR consists of a 4 bit shift register along with an exclusive OR gate in the feedback path. From the figure it is seen that 3rd and 4th bit

position of the data stream is exored and give as serial input to the first input. This exoring of 3rd and 4th bit are selected by a primitive polynomial(i.e. $F(x)=x^4+x^3+1$).Here, from the polynomial we take 4th bit and 3rd bit for exoring and it’s output is sent to x^0 (i.e. 1). Primitive polynomial is defined as a characteristic polynomial of an LFSR which determines maximum-length of the sequence generation. So for 4-bit LFSR, the number of pattern that can be generated is $15(2^4-1)$.

Table: Pseudo pattern generation for 4-bit LFSR

x1	x2	x3	x4	$x3 \oplus x4 = x0$	Clock cycle
1	1	1	1	0	1
0	1	1	1	0	2
0	0	1	1	0	3
0	0	0	1	1	4
1	0	0	0	0	5
0	1	0	0	0	6
0	0	1	0	1	7
1	0	0	1	1	8
1	1	0	0	0	9
0	1	1	0	1	10
1	0	1	1	0	11
0	1	0	1	1	12
1	0	1	0	1	13
1	1	0	1	1	14
1	1	1	0	1	15
1	1	1	1	0	16 (cycle repeats)

From the table it is clearly depicted that the LFSR goes through all possible code permutations except one(in this case it is 0000).This state is known as a locked state and such a state is eliminated due to it’s locking nature. In the proposed work an 8 bit LFSR has been designed which generates 255 pseudo random patterns(2^8-1).

b) ORA:

The ORA block presented in this research uses MISR (Multiple Input-Serial-Register) technique for compaction of the responses coming from the CUT . The compacted response is then compared to the golden signature which determines if there is any fault present or not. MISR operation can be explained from figure.

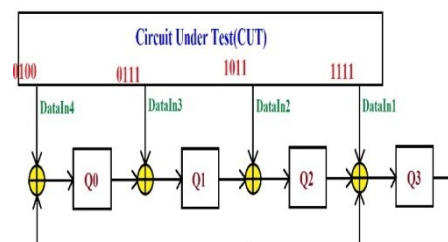


Figure: Proposed MISR model

Here we can see that four inputs enter into the MISR block from the CUT block for compaction of the responses received. The MISR block consists of 4 exor blocks before each D flip flop. Where the data inputs from the cut is exored one bit at a time. The right most bit from each data Input stream is exored first. Here also it is seen that output of Q3 goes as feedback to first and last exor which also follows the same primitive polynomial.

Table: Signature analysis for the given inputs

Clock cycle	Q0	Q1	Q2	Q3
0	0	0	0	0
1	0	1	1	1
2	1	1	0	1
3	0	0	1	0
4	0	0	1	0

From the table it is shown how the generated inputs in the CUT are compacted into single output signature.

IV. RESULTS

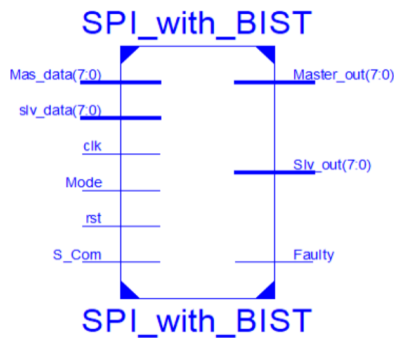


Figure: SPI with BIST block

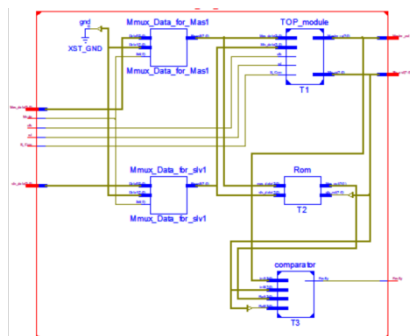


Figure: SPI with Internal Block

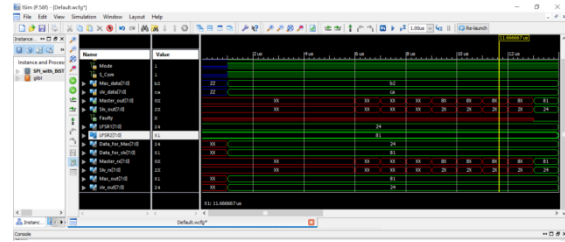


Figure: SPI with BIST

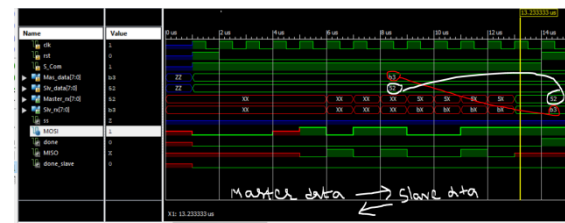
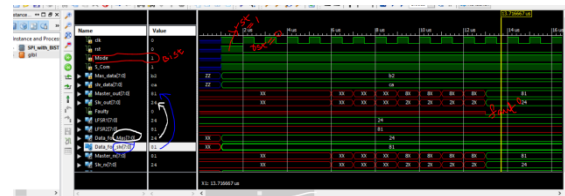


Figure: SPI with BIST highlighted

V. CONCLUSION

In this research, a BIST embedded SPI protocol with master-slave configuration has been designed successfully HDL and simulated using Xilinx in EDA Playground Platform. The self-testability feature has been well exercised in the proposed Model. Where, the designed CUT uses SPI protocol for data transfer and has the capability to test itself for checking the correctness of the Circuit under test.

REFERENCES

- [1] Choudhury, G.K.Singh, R.M.Mehra, "Design and Verification SerialPeripheralInterface (SPI) Protocol for LowPowerApplications", International Journal of Innovative Research in Science, Engineering and Technology, Vol. 3, Issue 10, October 2014
- [2] Vineeth B, Dr. B. Bala Tripura Sundari, "UVM Based TestbenchArchitecture for Coverage Driven Functional Verification of SPIProtocol", 2018 International Conference on Advances in Computing, Communications and Informatics (ICACCI)

- [3] PallaviPolsani, V. Priyanka B., Y. Padma Sai, “Design & Verification of Serial Peripheral Interface (SPI) Protocol”, International Journal of Recent Technology and Engineering (IJRTE) ISSN: 2277-3878, Volume-8 Issue-6, March 2020
- [4] Muhammad Hafeez, Azilah Saparon, “IP Core of Serial Peripheral Interface (SPI) with AMBA APB Interface”, IEEE 9th Symposium on Computer Applications & Industrial Electronics (ISCAIE), 2019
- [5] Shumit Saha, Md. Ashikur Rahman, Amit Thakur, “Design and Implementation of SPI Bus Protocol with Built-In-Self-Test Capability over FPGA” International Conference on Electrical Engineering and Information & Communication Technology (ICEEICT) 2014
- [6] Deepika, Jayanthi K Murthy “Interrupt Enabled Priority Based MasterSlave Communication using SPI Protocol”, International Journal of Innovative Technology and Exploring Engineering (IJITEE) , ISSN:2278-3075, Volume-9 Issue-9, July 2020
- [7] Xingchun Liu, Yandan Liu “Multi-functional Serial Communication Interface Design Based on FPGA”, 3rd IEEE International Conference on Computer and Communications, 2017
- [8] Bhagyashri, G. Allawagol, Vidyashree AC, Narendra Kumar, “Design of SPI IP to communicate with I2C bus of a microcontroller” International Journal of Industrial Electronics and Electrical Engineering, ISSN: 2347-6982, Special Issue, Sep.-2016
- [9] Xiaole Cui, Miaomiao Zhang, Qiujun Lin, Xiaoxin Cui, Anqi Pang, “Design and Test of the In-Array Build-In Self-Test Scheme for the Embedded RRAM Array”, IEEE ELECTRON DEVICE LETTERS, VOL. 38, NO. 5, MAY 2017
- [10] Abhas Singh, Gurram Mahanth Kumar, Abhijit Aasti, “Controller Architecture for Memory BIST Algorithms” IEEE International Students' Conference on Electrical, Electronics and Computer Science, MAY 2020/2021.

2064105701

LOW POWER DESIGN OF COUNTER USING DIGITAL SWITCHING CIRCUITS FOR COUNTING APPLICATIONS

¹Dr. M. Shashidhar, ²A. Shiva Skandhan

¹Associate professor, Dept.of ECE, Vaagdevi College of Engineering, Warangal, Telangana, India.

²PG Scholar, Dept.of ECE, Vaagdevi College of Engineering, Warangal, Telangana, India.

Abstract

A low-power VLSI circuit is intended to reduce power consumption, increase battery life, and reduce area. The performance of a circuit improves as the circuit's power consumption is reduced. The number of times a procedure or event has occurred in proportion to the clock signal is stored by a scaling circuit or counter. The main issue with scaling circuits is power consumption owing to the power supply. The low power was obtained by employing True Single Phase Clock Logic (TSPCL) and Self Controllable Voltage Level (SVL) technique to reduce power consumption in flipflops. The number of transistors and leakage power account for the majority of the power usage. By lowering the number of transistor counts, the proposed MGDI uses less power than TSPCL. TANNER EDA software is used to compare the simulation results of both MGDI and TSPCL techniques in terms of transistor count and power usage.

KEY POINTS:TSPCL SVL, TANNER EDA

I. INTRODUCTION:

In today's world, four elements - area, speed, delay, and power consumption - are critical in driving demand for compact handheld devices such as cell phones, laptops, palmtops, and electronic devices. Area, performance, affordability, and reliability were formerly the primary considerations of VLSI designers. In the past, reliability, cost, and performance were prioritised, and power conservation was a minor consideration. However, in recent years, power has been accorded equal weight to area and speed factors. Because of increased frequencies and chip sizes, power consumption has been a critical concern in recent years. Any VLSI circuit's performance is determined by its design architecture, which optimises power and ensures high reliability. Power optimization of circuits at many levels is required to design any circuit with low power consumption. Power dissipation reduction is a critical design issue in VLSI circuits.

The majority of system-level architectures are made up of sequential circuits, and the design of these circuits has a significant impact on the system's overall power consumption. The clock wastes a lot of electricity in many synchronous applications. The clock is the sole signal that switches continuously, therefore it typically has to drive a vast clock tree. The circuit itself is divided into several blocks. The power dissipation of the clock was lowered in asynchronous applications. Static and dynamic power

dissipation contribute the most power to any circuit. Sub threshold conduction, reverse biased p-n junction conduction, gate tunnelling current, drain source punchthrough, gate induce drain leakage, and other factors cause static power dissipation in the quiescent state of the circuit. When compared to dynamic power, however, static power makes a small contribution. The transition of signal and short circuit current causes dynamic power dissipation. The transient shorting of the power source and ground during signal transition causes short circuit power dissipation. The contribution of short circuit power to dynamic power is roughly 5-10%.

The proposal of an asynchronous counter employing the Modified Gate Diffusion Input (MGDI) design methodology is the paper's key contribution. Counters are circuits that count clock pulses in a sequential order. These are one of the most basic yet crucial building blocks in the construction of very large scale integration systems. It's been utilised in nearly all electronic systems for a long time, including microprocessors, memory, communication devices, scientific apparatus, and measuring systems. It keeps track of and occasionally displays the number of times a specific event or process has occurred, usually in relation to a clock signal. Other devices receive precise timing and control signals from them. It's been utilised in nearly all electronic systems for a long time, including microprocessors, memory, communication devices, scientific apparatus, and measuring systems. It keeps track of and occasionally displays the number of times a specific event or process has occurred, usually in relation to a clock signal. Other devices receive precise timing and control signals from them. In a synchronous counter, the clock pulse is applied to all flipflops at the same time, whereas in an asynchronous counter, the clock pulse is applied to the first flipflops first, and the output of the first flipflop is used as the clock for the remaining flipflops.

Section 2 discusses the various sources of power dissipation in the remainder of this work. The existing Flip-Flop and counter method is discussed in Section 3. The suggested counter method using the Modified Gate diffusion input technology is claimed in Section 4. Section 5 contains the results and analysis of the suggested work, whereas Section 6 contains the conclusion

MODIFIED PROBABILISTIC ESTIMATION EFFICIENT FIXED-WIDTH ADDER

¹Jarupula Koushik Kumar , ²M. Devadas

^{1,2}Dept. of Electronics and Communication Engineering

^{1,2}Vaagdevi College of Engineering, Warangal, Telangana, India

ABSTRACT

Customarily, fixed-width adder tree configuration is acquired from the full-width AT configuration by utilizing direct or post-truncation. In direct-truncation, one lower request piece of every snake result of full-width AT is post-shortened, and in the event of post-truncation, lower request pieces of definite stage adder yield are shortened, where $p = \text{dlog}_2 N_e$ and N is the information vector size. Both these techniques doesn't give a proficient plan. In this paper, a clever plan is introduced to get fixed-width AT configuration utilizing shortened input. A predisposition assessment recipe in view of probabilistic methodology is introduced to repay the truncation blunder. The proposed fixed-width AT plan for input-vector sizes 8 and 16 offers and region defer item putting something aside for word-length sizes (8,12,16), separately, and works out the result nearly with a similar precision as the post-shortened fixed-width AT which has the most noteworthy exactness among the current fixed-width AT. Further, we saw that Walsh-Hadamard change in view of the proposed fixed-width AT configuration reproduce higher-surface pictures with higher pinnacle sign to commotion proportion (PSNR) and moderate-surface pictures with practically a similar PSNR contrasted with those got utilizing the current AT plans. Plus, the proposed plan makes an extra benefit to improve different blocks show up at the upstream of the AT in a mind boggling plan

1. INTRODUCTION

- Low power, region proficient and superior execution registering frameworks are progressively utilized in compact and cell phones. For such applications, advanced signal handling calculations are executed in fixed-point VLSI frameworks. Adder tree ordinarily utilized in equal plans of inward item calculation and grid vector duplication. Multiplier configuration likewise includes a shift-adder tree for collection of fractional item bits. Word-length development is a typical issue experienced when duplication and expansion are acted in fixed-point number-crunching.
- The state of the piece framework of SAT is not the same as the AT. Therefore, word-length fills in an alternate request in SAT and AT. Additionally, there are not many different pieces likewise included the SAT to deal with negative incomplete results of multiplier. Explicit plans have been recommended for effective acknowledgment of fixed-width multipliers with less truncation blunder [1]. In any case, the plan utilized in fixed-width multiplier isn't fitting to foster a fixed-width AT plan because of various formed piece network. The full-width AT configuration produces $(w + p)$ bit yield for each N -point input-vector, where $p = \log_2 N$. For a similar size input-vector, the fixed-width AT configuration produces w -bit yield. Customarily, FX-AT configuration is gotten from the FL-AT configuration by utilizing direct or post-truncation. In direct-truncation, one lower request piece of every snake result of FL-AT is post-shortened, and in the event that post-truncation, $\{p\}$ lower request pieces of definite adder result of FL-AT are shortened. As of late, a few plans have been proposed for inexact calculation of expansion utilizing swell convey adder to save basic way postponement and region.

- The bio-propelled lower part OR snake is proposed in light of estimated rationale. Four distinct sorts of inexact snake plans are proposed. A surmised 2-cycle adder is proposed for inexact calculation of triple multiplicand without convey spread. These surmised plans can be utilized to carry out RCA with less deferral and region with some deficiency of exactness. The inexact RCA configuration can be utilized to acquire fixed-width AT utilizing post-truncation. Be that as it may, the inexact fixed-width AT doesn't offer a region postpone productive plan.
- Digit level streamlining of FL-AT for various steady duplication is proposed to exploit moving activity. A proficient FL-AT configuration is proposed utilizing the estimated snake of for loose acknowledgment of Gaussian channel for picture handling applications. We see that as the advanced AT of is intended for MCM based plan and none of the current plan talks about the issues connected with fixed-width execution of AT. It is seen that immediate truncation and post-truncation strategies doesn't give a proficient FX-AT plan. It is important to have an alternate methodology for creating proficient FX-AT plan which is presently missing in the writing. A productive FX-AT configuration unquestionably helps to work on the effectiveness of devoted VLSI frameworks executing complex DSP calculation.
- In this examination, we propose a plan to create a productive FX-AT plan with shortened input. Utilization of shortened input in FX-AT offers two crease benefits:
 - (1) region and defer saving inside the FX-AT because of decrease in adder width (by p-bits), and
 - (2) makes a degree to upgrade other registering blocks show up at the upstream of AT in a perplexing plan. In any case, the utilization of shortened input presents a lot of mistake in the FXAT yield which should be one-sided suitably.
- The principal commitment of the research are:
 - Utilization of shortened input in fixed-width AT plan.
 - Equation to assess the predisposition for mistake pay.

2. LITERATURE SURVEY

Uncertain adders for low-power Surmised Processing by Vaibhav Gupta, Debabrata Mohapatra, Sang Phill Park, Anand Raghunathan and KaushikRoy:

Low-power is a basic necessity for versatile interactive media gadgets utilizing different sign handling calculations and structures. In most media applications, the last result is deciphered by human detects, which are noticeably flawed.

Energy-effective sign handling by means of algorithmic commotion resilience, by R. Hegde; N.R. Shanbhag:

In this a structure for lowenergy computerized signal handling where the stock voltage is scaled past the basic voltage expected to match the basic way deferral to the throughput Design of low-power fast truncation-errortolerant snake and its application in computerized signal processing,by N. Zhu, W. L.

Goh, W. Zhang, K. S. Yeo, and Z. H. Kong: In current VLSI innovation, the event of a wide range of mistakes has become unavoidable. By taking on an arising idea in VLSI plan and test, blunder resistance (ET), a clever mistake open minded snake is proposed

Inaccurate plans for surmised low power expansion by cell substitution, by H. A. F. Almurib, T. N. Kumar, and F. Lombard:

It has three plans of an inaccurate snake cell for inexact processing. These cells require a significantly more modest number of semiconductors contrasted with a careful full adder cell as well as known vague plans Accuracyconfigurable snake for rough math plans by A. B. Kahng and S. Kang Guess can increment execution or diminish power utilization with a rearranged or erroneous circuit in application settings where severe necessities are loose.

A low-power, elite execution surmised multiplier with configurable halfway mistake recuperation by Cong Liu ;Jie Han; Fabrizio Lombard;

Rough circuits have been considered for blunder lenient applications that can endure a few loss of exactness with further developed execution and energy proficiency. Multipliers are key number juggling circuits in numerous such applications like computerized signal handling . In this an original estimated multiplier with a lower power. utilization and a more limited basic way than customary multipliers is proposed for elite execution DSP applications

3. PROPOSED SYSTEM

To gauge the predisposition of the shortened part more unequivocally the LSP of An is additionally parceled into two sections as major-part and minor-part. The main section of LSP comprises the major-part (MJP) and the leftover (p – 1) lower request segments comprise the minor-part (MNP). The predisposition for this situation is assessed involving the MJP and MNP of LSP as

$$\sigma = \sigma_{major} + \sigma_{minor}$$

where major and minor are the MJP and MNP of LSP's individually evaluated predispositions. The major is evaluated accurately using the MJP real sign value, whereas the minor is evaluated using a probabilistic approach. The quantified value of major is evaluated using the following:

$$E[MJP] = \left\lfloor \sum_{i=1}^N 2^{p-1} x_{i,p-1} \right\rfloor = 2^p \left\lfloor \sum_{i=1}^N \left(\frac{x_{i,p-1}}{2} \right) \right\rfloor$$

$$\sigma_{major} = \left\lfloor \sum_{i=1}^N \left(\frac{x_{i,p-1}}{2} \right) \right\rfloor$$

The quantized value of σ_{minor} is estimated as:

$$E[MNP] = \left(\frac{N}{4} \right) \cdot 2^p (1 - 2^{-p+1})$$

$$\sigma_{minor} = \text{round} \left[\left(\frac{N}{4} \right) (1 - 2^{-p+1}) \right] \approx \left(\frac{N}{4} \right)$$

For N = 8 and w = 8, Fig. 1(a) shows the information bit-network of the proposed superior truncated fixed-width adder tree (ITFX-AT). The convey bits c0, c1, c2, c3, c4, c5, and c6 are computed by the logic block related to major. These transmit data, and the least important part of MSP is given a fixed-predisposition pertaining to minor. According to (4b), the value of the minor for N = 8 is regarded as 2. Figure 1 depicts the proposed ITFX-design. AT's (b). The convey bits c0, c1, c2, c3, c4, c5, and c6 are calculated by the seven half-adders (A) connected in a tree topology. To add the fixed-bias(+4) to the MJP of LSP instead of the least-huge part of MSP,

four full-adders with fixed input-convey 1 are substituted for four of these seven half-adders. Additionally enhanced are full-adders with fixed input-convey '1' into a modified half-snake (A*) involving an XNOR and an entrance.

MSP										
7	6	5	4	3	2	1	0			
			x_{17}	x_{16}	x_{15}	x_{14}	x_{13}			
			x_{27}	x_{26}	x_{25}	x_{24}	x_{23}			
			x_{37}	x_{36}	x_{35}	x_{34}	x_{33}			
			x_{47}	x_{46}	x_{45}	x_{44}	x_{43}			
			x_{57}	x_{56}	x_{55}	x_{54}	x_{53}			
			x_{67}	x_{66}	x_{65}	x_{64}	x_{63}			
			x_{77}	x_{76}	x_{75}	x_{74}	x_{73}			
			x_{87}	x_{86}	x_{85}	x_{84}	x_{83}			
Fixed bias							1	0	0	
$y_4 = \{y_{47} \ y_{46} \ y_{45} \ y_{44} \ y_{43} \ y_{42} \ y_{41} \ y_{40} \ 0 \ 0 \ 0\}$										

(a)

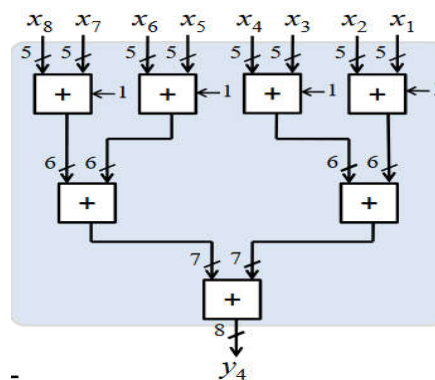


Fig. 1.(a) Input bit-matrix of proposed truncated fixed-width adder-tree (TFX-AT) with fixed-bias for error-compensation. (b) Structure of proposed TFX-AT design

MSP										MJP		MNP	
7	6	5	4	3	2	1	0						
			x_{17}	x_{16}	x_{15}	x_{14}	x_{13}	c_0	x_{12}	x_{11}	x_{10}		
			x_{27}	x_{26}	x_{25}	x_{24}	x_{23}	c_1	x_{22}	x_{21}	x_{20}		
			x_{37}	x_{36}	x_{35}	x_{34}	x_{33}	c_2	x_{32}	x_{31}	x_{30}		
			x_{47}	x_{46}	x_{45}	x_{44}	x_{43}	c_3	x_{42}	x_{41}	x_{40}		
			x_{57}	x_{56}	x_{55}	x_{54}	x_{53}	c_4	x_{52}	x_{51}	x_{50}		
			x_{67}	x_{66}	x_{65}	x_{64}	x_{63}	c_5	x_{62}	x_{61}	x_{60}		
			x_{77}	x_{76}	x_{75}	x_{74}	x_{73}	c_6	x_{72}	x_{71}	x_{70}		
			x_{87}	x_{86}	x_{85}	x_{84}	x_{83}		x_{82}	x_{81}	x_{80}		
σ_{minor}							1	0					
$y_5 = \{y_{57} \ y_{56} \ y_{55} \ y_{54} \ y_{53} \ y_{52} \ y_{51} \ y_{50} \ 0 \ 0 \ 0\}$													

Fig. 2 Input bit-matrix of proposed improved truncated fixed-width addertree (ITFX-AT) for $N = 8, w = 8$.

MJP and MNP represents the major part and minor part of LSP. $\{c_0, c_1, c_2, c_3, c_4, c_5, c_6\}$ represent the carry bits corresponding to the estimate of σ_{major}

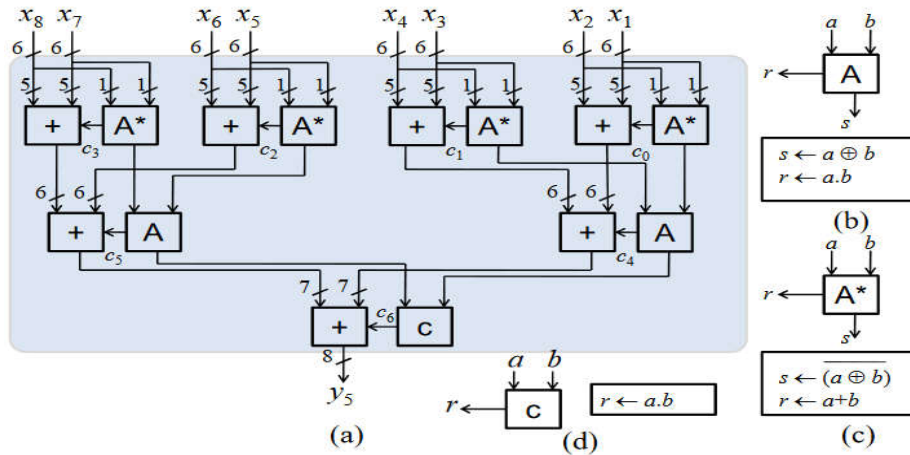


Fig.3 (a) Structure of proposed ITFX-AT. (b) Logic function of half-adder (A). (c) Logic function of modified adder (A*) (d) Logic function of carry cell

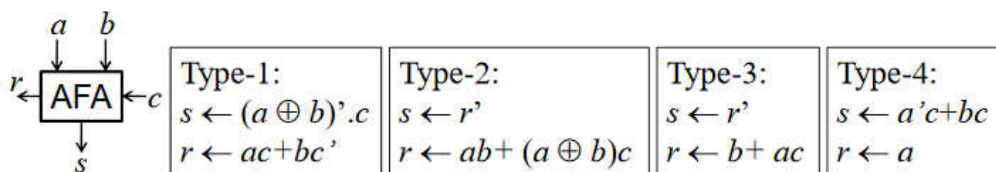
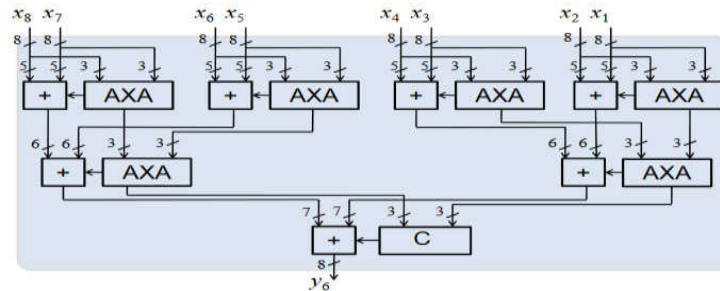


Fig. 4 (a) Structure of approximate fixed-width adder-tree using accurate RCA and 3-bit approximate RCA for $N = 8$ and $w = 8$. (b) Approximate Full Adder {Type-1, Type-2, Type-3, Type-4}

Inexact full-adders are considered to add the LSP of the info lattice to diminish the rationale intricacy and CPD of the FL-AT. The surmised adder is carried out utilizing the estimated full-snake Type1, Type-2, Type-3, and Type-4 of Post-shortened rough FX-AT is gotten from the inexact full-width adder tree to concentrate on the exhibition of the proposed FX-AT plans. Note that APX-FL-AT-Type-4 is indistinguishable from the APX-AT of the construction of APX-FX-AT-PT is displayed in Fig.4(a) utilizing exact RCA and 3-digit rough RCA for $N = 8$ and $w = 8$.

4. RESULTS

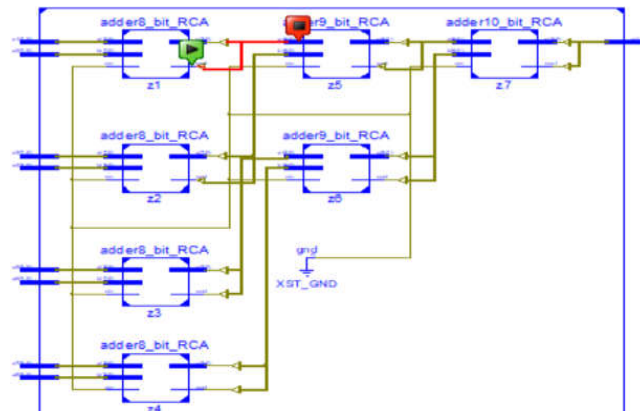


Fig 5: Internal Circuit

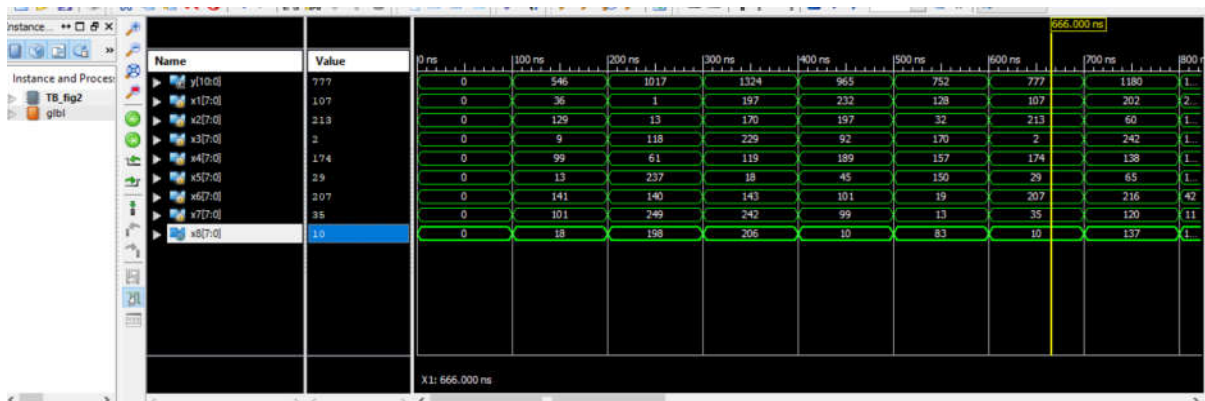


Fig 6: Output Wave Forms

```

Device utilization summary:
-----
Selected Device : 7a100tcsg324-3

Slice Logic Utilization:
Number of Slice LUTs:          88 out of 63400    0%
Number used as Logic:         88 out of 63400    0%

Slice Logic Distribution:
Number of LUT Flip Flop pairs used:  88
Number with an unused Flip Flop:    88 out of 88    100%
Number with an unused LUT:          0 out of 88    0%
Number of fully used LUT-FF pairs:  0 out of 88    0%
Number of unique control sets:      0

IO Utilization:
Number of IOs:                  75
Number of bonded IOBs:          75 out of 210    35%
    
```

Fig 7: LUTS

Data Path: x1<1> to y<9>

Cell:in->out	fanout	Gate Delay	Net Delay	Logical Name (Net Name)
IBUF:I->O	3	0.001	0.566	x1_l_IBUF (x1_l_IBUF)
LUT4:I0->O	2	0.097	0.698	z1/f2/Mxor_sum_xo<0>1 (k1<1>)
LUT6:I0->O	3	0.097	0.305	z5/f2/carry1 (z5/c<1>)
LUT3:I2->O	2	0.097	0.697	z5/f3/Mxor_sum_xo<0>1 (i1<2>)
LUT6:I0->O	3	0.097	0.389	z7/f3/carry1 (z7/c<2>)
LUT5:I3->O	3	0.097	0.389	z7/f5/carry1 (z7/c<4>)
LUT5:I3->O	3	0.097	0.389	z7/f7/carry1 (z7/c<6>)
LUT5:I3->O	2	0.097	0.688	z7/f9/carry1 (z7/c<8>)
LUT5:I0->O	1	0.097	0.279	z7/f10/Mxor_sum_xo<0>1 (y_9_OBUF)
OBUF:I->O		0.000		y_9_OBUF (y<9>)
Total		5.177ns	(0.777ns logic, 4.400ns route)	(15.0% logic, 85.0% route)

Fig 8: Delays

5. CONCLUSION AND FUTURE SCOPE

In this study, a novel idea is presented for obtaining a fixed-width AT architecture with shorter input. To correct the truncation error, an inclination assessment recipe based on a probabilistic technique is presented. Two distinct fixed-width AT layouts are chosen in consideration of the proposed plot. In comparison to the present fixed-width AT plans, each of the proposed proposals provide a considerable amount of investment cash for the region and CPD. The post-shortened fixed-width AT, which has the most notable accuracy among the present fixed-width AT, computes the output virtually with the same exactness as the proposed ITFX-AT for vector sizes 8 and 16, offering and ADP setting anything away for word-length sizes individually.

Additionally, we observed that the Walsh-Hadamard adjustment replicates larger images with a higher PSNR and moderate-surface images with virtually the same PSNR in comparison to those obtained using the present fixed-width adder designs. Additionally, a noteworthy feature of fixed-width AT plans is the use of reduced input tests, which provides an additional advantage for upgrading various blocks that appear upwards of the AT in a complex design.

REFERENCES

- [1] B. K. Mohanty and V. Tiwari, "Modified probabilistic estimation bias formulation for hardware efficient fixed-width Booth multiplier", *Circuits, Systems and Signal Processing*, Springer, vol.33, no.12, pp. 3981–3994, Dec., 2014
- [2] H. R. Mahdiani, A. Ahmadi, S. M. Fakhraie and C. Lucas, "Bioinspired imprecise computational blocks for efficient VLSI implementation of soft-computing applications", *IEEE Transactions on Circuits and Systems-I, Regular Papers*, vol. 57, no. 4, pp. 850–862, Apr.2010.
- [3] V. Gupta, D. Mahapatra, A. Raghunathan, and K. Roy, "Low-power digital signal processing using approximate adders", *IEEE Transactions on Computer Aided Design of Integrated Circuits and Systems*, vol. 32, no. 1, pp. 124–137, Jan.2013.
- [4] J. Liang, J. Han and F. Lombardi, "New metrics for the reliability of approximation and probabilistic adders", *IEEE Transactions on Computers*, vol. 62, no. 9, pp. 1760–1771, Sept.2013.
- [5] H. Jiang, J. Han, F. Qiao and F. Lambardi, "Approximate radix-8 Booth multipliers for low-power and high-performance operations", *IEEE Transactions on Computers*, vol. 65, no. 8, pp. 2638–2644, Aug.2016.
- [6] Y. Pan and P. K. Meher, "Bit-level optimization of adder-trees for multiple constant multiplications for efficient FIR filter implementation", *IEEE Transactions on Circuits and Systems-I, Regular Papers*, vol. 61, no. 2, pp. 455–462, Feb.2014.
- [7] R. O. Julio, L. B. Soares, E. A. C. Costa and S. Bampi, "Energy-efficient Gaussian filter for image processing using approximate adder", *In. Proc. International Conference on Electronics, Circuits and Systems, 2015*, pp.450-453, 2015.
- [8] D. Gizopoulos, M. Psarakis, A. Paschalis, and Y. Zorian, "Easily Testable Cellular Carry Lookahead Adders," *Journal of Electronic Testing: Theory and Applications* 19, 285-298, 2003.
- [9] S. Xing and W. W. H. Yu, "FPGA Adders: Performance Evaluation and Optimal Design," *IEEE Design & Test of Computers*, vol. 15, no. 1, pp. 24-29, Jan. 1998.
- [10] M. Bečvář and P. Štukjunger, "Fixed-Point Arithmetic in FPGA," *ActaPolytechnica*, vol. 45, no. 2, pp. 67-72, 2005.
- [11] P. M. Kogge and H. S. Stone, "A Parallel Algorithm for the Efficient Solution of a General Class of Recurrence Equations," *IEEE Trans. on Computers*, Vol. C-22, No 8, August 1973.
- [12][6]. P. Ndai, S. Lu, D. Somesekhar, and K. Roy, "Fine-Grained Redundancy in Adders," *Int. Symp. on Quality Electronic Design*, pp. 317-321, March 2007.
- [13][7]. T. Lynch and E. E. Swartzlander, "A Spanning Tree Carry Lookahead Adder," *IEEE Trans. on Computers*, vol. 41, no. 8, pp. 931-939, Aug. 1992. [8]. N. H. E. Weste and D. Harris, *CMOS VLSI Design*, 4th edition, Pearson–AddisonWesley, 2011.
- [14][9]. R. P. Brent and H. T. Kung, "A regular layout for parallel adders," *IEEE Trans. Comput.*, vol. C-31, pp. 260-264, 1982.
- [15][10]. D. Harris, "A Taxonomy of Parallel Prefix Networks," in *Proc. 37th Asilomar Conf. Signals Systems and Computers*, pp. 2213–7, 2003.

[16] <https://homepages.cae.wisc.edu/ece533/images/>

[17] <http://seamless-pixels.blogspot.in/2014/07/grass-2-turf-lawn-greenground-field.html>

[18] <https://www.decoist.com/2013-02-28/flower-beds/>

[19] <http://www.cosasexclusivas.com/2014/06/daily-overview-el-planetatierra-visto.html>

[20] <https://healthtipsfr.blogspot.com/2017/04/blog-post-40.html>

[21] <http://www.ugao.com/knowledge-center/how-to-design-a-flower-bed/>

A FULLY HOMOMORPHIC ENCRYPTION SCHEME WITH HIGH-PERFORMANCE POLYNOMIAL MULTIPLIERS

¹B. Soumya Sree, ²M. Devadas

^{1,2}Dept. of Electronics and Communication Engineering

^{1,2}Vaagdevi College of Engineering, Warangal, Telangana, India

ABSTRACT:

Completely Homomorphism Encryption is a method that permits calculations on scrambled information without the requirement for decoding, and it gives protection in different applications, for example, security safeguarding distributed computing. In this article, we present two equipment models streamlined for speeding up the encryption and decoding activities of the Fan-Vercauteren homomorphic encryption plot with elite execution polynomial multipliers.

We propose two streamlined equipment models for speeding up the encryption and decoding activities of the Fan-Vercauteren homomorphic encryption plot using elite execution polynomial multipliers in this article.

Our models will be used in a product code sign gas pedal system, in which the encryption and unscrambling chores will be offloaded to an FPGA device, while the remaining functions in the BFV plot will be done in programs running on a standard personal computer. Our gas pedal technology, in particular, has been modified to speed up the Straightforward Encoded Number juggling Library, which was produced by the Cryptography Exploration Gathering at Microsoft Exploration.

The equipment elements of the suggested system center around the XILINX VIRTEX7 FPGA gadget, which chats with its product portion by use of a fringe part interconnect express connection.

We will carry out our ideas independently for plaintext and figure text, concentrating on 1024-degree equations with 8-cycle and 32-digit coefficients. When compared to their unadulterated programming executions, the suggested structure achieves roughly 12 and 7 percent speedups, respectively, including I/O operations for the offloaded encrypting and decoding workloads.

Index Terms—Fan-Vercauteren (FV), FPGA, hardware, number theoretic transform, Simple Encrypted , arithmetic Library.

1. INTRODUCTION

Completely Homomorphic Encryption is the name given to any encryption scheme that allows number-crunching and consistent computations to be performed directly on the text. This characteristic deals with the secure management of sensitive data, which is a critical and as of now unfulfilled interest in distributed computing applications. Since its most memorable presentation, the possibility of homomorphism encryption has received wide consideration in the writing, and various homomorphism encryption plans have been presented. Although theoretically sound, homomorphism encryption plans are not exactly fit to be sent for practical applications due to execution limitations of PC structures.

Applications in view of current homomorphism encryption plans, which require productive executions of computationally costly numerical tasks, can be significant degrees more slow than customary programming applications that work on plain text information. For programming executions of homomorphism encryption , single center and multi center central processor exhibitions are basic. For single-center execution, recurrence of the processor straightforwardly influences execution, which can't be expanded considerably with contemporary innovation any further. Likewise, since central processor is expected to give great execution to a different arrangement of utilizations, equipment or potentially design enhancements for a computer chip focusing on just Homomorphism Encryption applications are not possible. Computer chip makers increment the exhibition of a processor with a multi center methodology. In any case, the quantity of centers that can be remembered for a multi center design is restricted because of costly single-center executions.

While Single Center Execution Of A Universally Useful Computer Processor Targets Consecutive Calculations, Multi Center Models Are More Reasonable For Equal Calculations. Most Homomorphism Encryption Plans Include A Blend Of Inherently Sequential And Exceptionally Parallelizable Calculations That Will At Last Perform Best On Heterogeneous Models Which Alludes To The Utilization Of Various Handling Centers To Expand Execution. In This Article, We Propose Such A Heterogeneous Gas Pedal Structure Highlighting A FPGA Center And A Computer Chip To Work On The Presentation Of Homomorphism Encryption Plans On A Framework Level.

Traditional crypto framework, for example, High level Encryption Standard doesn't have homomorphic property that permits number-crunching calculations to be performed Straight forwardly on figure text without decoding it. Then again, homomorphic encryption plans, for example, permit homomorphic tasks straightforwardly on the scrambled information and in this manner empower security protecting handling of data, particularly with regards to distributed computing where by security is a squeezing concern.

Also, HE conspires are evidently sluggish; thus, the case for speed increase is a lot more grounded than customary cryptosystems. With an always expanding interest for security in distributed computing applications, speed increase of homomorphic encryption plans is now a significant examination region.

The GPU execution is contrasted and the SEAL execution. The SEAL group as of late reported exceptionally productive Seal PIR, which is a confidential data recovery device that permits a client to download a component from an information base put away by a far off server without uncovering which component is downloaded . Our gas pedal system, while offloading exceptionally parallelizable encryption and unscrambling activities completely on the FPGA center, leaves the remainder of tasks of SEAL unblemished in programming.

By Conveying Our Edge Work, Any Cloud Design Using Seal For Homomorphism Encryption Applications Can Work On Its Exhibition By Using A Fpga Gadget Close To The Computer Processor,

Without Carrying Out The Whole Homomorphism Encryption Library In The FPGA. Our commitment in this article is recorded as follows.

1) We examine the iterative and the four-step Cooley Calculations for number hypothetical change activity and plan two novel, exceptionally parallelized equipment structures in light of these calculations.

We assess the consequences of our FPGA executions of the two equipment models concerning time and region and look at them against comparative works in the writing. We show that our equipment structures involving the original secluded multiplier calculation for any NTT-accommodating prime modulus, presented in our fundamental work give tantamount time execution to those involving exceptional primes in the writing.

We propose a gas pedal system, including a superior presentation FPGA gadget, associated with a host central processor. The structure interfaces the computer processor and the FPGA by means of a quick fringe part interconnect express association, accomplishing a 32-Gb/half-duplex I/O speed. The structure is utilized to speed up encryption and decoding tasks of SEAL. Each time an encode or decode capability is summoned via SEAL, the calculation is offloaded to the FPGA gadget through the PCIe association.

Our plan uses a development focusing on 128-digit security level. Counting the time spent on I/O, the latencies of the offloaded encryption and decoding tasks are worked on by $12\times$ and $7\times$, respectively, contrasted with their unadulterated programming executions on SEAL running on an Intel i97900X computer processor. As the structure gives a straightforward Despite the fact that the proposed unscrambling tasks of the BFV homomorphic encryption plot in our accommodation, it tends to be productively utilized to speed up different tasks in homomorphic applications.

To be sure, one of the main commitments of our work is to propose a superior presentation polynomial multiplier that can speed up the duplication of two exceptionally enormous degree polynomials, which is the computational container neck of all homomorphic tasks in the BFV plot or different plans.

Cryptography is the area of constructing cryptographic systems. Cryptology consists of two branches:

Cryptanalysis is the area of breaking cryptographic systems.

Cryptography is a field of computer science and mathematics that focuses on techniques for secure communication between two parties(Alice & Bob) while a third- party (Eve1 or Mallory2) is present (see Figure 1.1). This is based on methods like encryption, decryption, signing, generating of pseudo random numbers, etc.

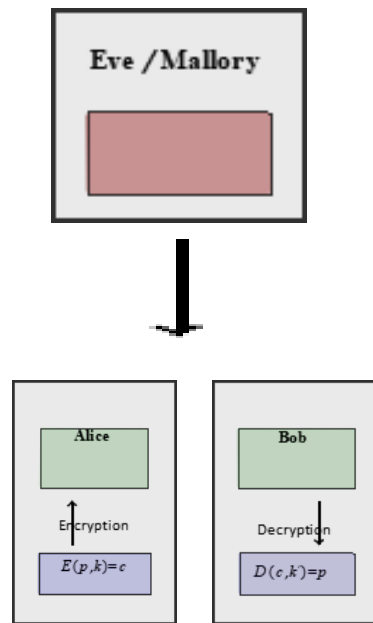


Figure1.1: A Basic Idea for Secure Communication

1. The four ground standards of cryptography are
2. Classification Characterizes as decides that cutoff points access or includes limitation certain data.
3. Information Honesty Deals with the consistency and exactness of information during its whole life-cycle.

Confirmation Affirms the reality of a property of a datum that is professed to be valid by some element.

4. Non-Disavowal Guarantees the powerlessness of a creator of an assertion resp. a snippet of data to deny it.
5. Presently a days there are in everyday two unique plans: From one perspective ,there are symmetric plans, where both, Alic eand Weave, need to have a similar key to scramble their correspondence.

For this, they need to at first safely trade the key. Then again, since Diffie and Hellman's key trade thought from 1976 (see likewise Alice and Sway both have a private and a public key.The public key can be imparted to anybody, so Weave can utilize it to encode a directive for Alice. In any case, just Alice, with the relating private key, can unscramble the scrambled message from Sway

There is the security of the structure itself, based on mathematics.

There is a normalization cycle for cryptosystems in light of hypothetical examination in math and intricacy hypothesis.

Then we have the execution of the designs in gadgets, for example SSL, TLS in your internet browser or GPG for marked resp. scrambled messages.

These executions shouldn't veer from the hypothetical norms.

MODES OF CIPHERS

For ciphers we have, in general, four different categories:

1. Symmetric and asymmetric ciphers (see Definition 2.20), and
2. Stream and block ciphers.

In the following we often assume binary representation of symbols, i.e. we are working with bits in $\mathbb{Z}/2\mathbb{Z}$. All of what we are doing can be easily generalized to other representations and other alphabets.

2. HOMOMORPHIC ENCRYPTION

2.1 BLOCK CIPHERS

It follows that the number of permutations of the form $\text{DES}_{k_2} \circ \text{DES}_{k_1}$ is much larger than the number of permutations of type DES_k .

Until now we always considered that our plaintexts have the same size as the key. Clearly, in general, one wants to encrypt longer documents or texts. For this problem there are several different modes one can apply block ciphers.

2.2 MODES OF BLOCK CIPHERS

Let us assume in this section that $\Sigma = \mathbb{Z}/2\mathbb{Z}$, block size is $n \geq 1$ and the key spaces \mathcal{K} are the same. We switch between representations of plain texts: For example let $n = 3$, then we can identify all natural numbers between 0 and 7. So we can represent 0 binary as 000 or $(0, 0, 0) \in (\mathbb{Z}/2\mathbb{Z})^3$, or 5 as 101 or $(1, 0, 1)$.

We further assume that there is some magic that randomly resp. pseudo and only and uniformly distributed chooses a key.

Assume we have a plain text p of arbitrary but finite length. We divide p into blocks of length n . If the length of p is not divisible by n then we add some random symbol at the end of p . In the end we receive a representation $p = (p_1, \dots, p_m)$ where all p_i are plaintext blocks of length n . Each plain text block p_i is encrypted to a corresponding cipher text block c_i using a given key k .

There are two main categories of ciphers in terms of key handling: If κ is feasible then \mathcal{K} and need to be kept secret and the cipher is called \mathcal{K} symmetric. Otherwise the cipher is called asymmetric.

We also call a cryptosystem symmetric resp. asymmetric if its corresponding cipher is symmetric resp. asymmetric. blocks of length n . If the length of p is not divisible by n then we add some random symbol at the end of p . In the end we receive a representation $p = (p_1, \dots, p_m)$ where all p_i are plaintext blocks of length n . Each plain text block p_i is encrypted to a corresponding cipher. An asymmetric cryptosystem is also called a public key cryptosystem as \mathcal{K} can be made public without weakening the secrecy of the "private" key set \mathcal{K} for keys.

This can be an arbitrary counter, usually one uses an increment counter: So for each block of the plain text or cipher text the counter is incremented by There are now various possible ways to combine then once with the counter.

Homomorphic Encryption is a leading edge new innovation which can empower private distributed storage and calculation arrangements, and numerous applications were portrayed in the writing over the most recent couple of years. However, before Homomorphic Encryption can be taken on in clinical, wellbeing, and monetary areas to safeguard information and patient and buyer security, it should be normalized, no doubt by different normalization bodies and government offices. A significant piece of normalization is expansive settlement on security levels for shifting boundary sets. Albeit broad examination and seat stamping has been finished in the exploration local area to lay out the establishments for this work, it is elusive all the data in a single spot, alongside substantial boundary suggestions for applications and sending.

This study is an attempt to capture (at least a portion of) the aggregate knowledge about the currently known state of security of these plans, to determine the plans, and to prescribe a wide range of limits to be used for

homomorphic encryption at various security levels. To produce these border proposals, we depict known attacks and their estimated running times. We also highlight additional features of these encryption plans that make them useful in a variety of applications and situations.

It is typical that future work outdate and expand this Homomorphic Encryption Standard will employ the accompanying numbering show:

We show a few viewpoints in the supplement that are not determined in this report and are expected to be covered by future records.

2.3 SECTION PROPERTIES:

Semantic Security or IND CPA Security: A homomorphic encryption scheme is thought to be secure if no adversary has a benefit in speculating (with a better than half chance) whether a given code message is an encryption of both of two similarly reasonable specific messages. This assumes that encryption will be randomized so that two distinct encryptions of a similar message do not appear to be identical.

Assume a client computes the key tuple by running the boundary and key-age calculations. A adversary is anticipated to have the limits, the assessment key EK, a public key PK(only in the public-key plan) and can receive encryptions of communications of its choice.

The enemy is then provided an encryption of one of two messages of its choice, registered by the aforesaid encryption computation, without recognizing which message the encryption.

The security of HE then ensures that the adversary cannot figure out which message the encryption compares to with critical benefit better than a half chance. This captures the fact that no information about the messages is revealed in the code message.

Minimization: The conservativeness property of a homomorphic encryption plot assures that homomorphic process on the code texts don't grow the length of the code texts. That is, any evaluator can play out an erratic upheld rundown of assessment capability calls and get a code text in the code text space (that doesn't rely upon the intricacy of the assessed capabilities).

Successful decoding: Profitable unscrambling attribute implies that the homomorphic encrypting plot typically ensures that the decoding runtime doesn't rely upon the capability which was assessed on the code texts

2.4 KEY ASSESSMENT

Assume a server has a corpus of code texts scrambled under a mystery key SK, and the client who claims SK is aware that SK may have been compromised.

It is appealing for an encryption strategy to have the associated key development property. Allow the client to generate another mystery key SK' to replace SK, another assessment key EK', and a change key TK so that: the server, given only TK and EK', can completely replace all code texts in the corpus with new code texts that (1) can be decoded using SK' and (2) fulfill semantic security in any event, for a foe who holds SK.

Any suitably homomorphic encryption scheme meets the following key development characteristic. Allow TK to serve as SK's encryption. To be more explicit, TK is a code text that, when unscrambled using secret key SK', provides SK. A server with TK and EK' can modify the wording of a code.

2.5 SIDE CHANNEL ASSAULTS

Side channel assaults take into account enemies who can obtain insufficient information about an encryption plot's mystery key, such as by running timing assaults during the decoding calculation. Versatility against such attacks, also known as leakage flexibility, is an important security requirement for an encryption strategy. That is, it ought to be difficult to abuse semantic security even in presence of side channel assaults. Normally, spillage strength can only withstand limited data spillage concerning the mystery key.

An appealing component of encryption plans in light of immovability of whole number cross section issues, and specifically realized HE conspires.

2.6 CHARACTER BASED ENCRYPTION

It is possible to deliver encoded messages to clients in a personality encrypted plot without knowing either a public key or a secret key, but only the personality of the beneficiary, where the personality can be a legitimate name or an email address.

This is possible as long as a trusted party distributes a few public borders PP and has an expert mystery key MSK . After authenticating herself, for example, by producing a government-issued ID, a client having character X will be given a secret key SK_x , which the client can use to decode any code message sent by the personality X .

To scramble message M to character X , all that is required is knowledge of the public bounds PP and X . Personality-based homomorphic encryption is an appealing version of public key homomorphic encryption. GSW modification maintains personality-based homomorphic.

3. BRAKERSKI / FAN-VERCAUTEREN (BFV)

We follow the same notations as the previous section.

$BFV.ParamGen(\lambda, PT, K, B) \rightarrow Params$.

We assume the parameters are instantiated following the commendations outlined in Section 5. Similarly to BGV, the parameters include:

Key-and error-distributions D_1, D_2 a ring R and its corresponding integer modulus integer modulus for the plaintext. In addition, the BFV parameters also include: Integer T , and $L = \log Tq$. T is the bit decomposition modulus. Integer $W = \lfloor q/p \rfloor$.

3.1 BFV.SecKeygen(Params) \rightarrow SK, EK

The secret key SK of the encryptions is a random element from the distribution defined as per Section 5. The evaluation key consists of LWE samples encoding the secret a specific fashion. In particular, for $i = 1, \dots, L$, sample a random a_i from R/qR and error e_i from D_2 , compute $EK = (EK_1, \dots, EK_L)$. $EK_i = -(a_i s + e_i) + T s^2$, a_i ,

3.2 BFV.PubKeygen(params) \rightarrow SK, PK, EK.

The secret key SK of the encryption scheme is a random element from the distribution. The public key is a random LWE sample with the secrets s . In particular, it is computed by sampling a random element a from R/qR and an error e from the distribution D_2 and setting $P = -(as + e)$, where all operations are performed over the ring R/qR . The evaluation key is computed as in BFV.SecKeygen.

3.3 BFV.PubEncrypt(PK, M) \rightarrow C

BFV.Pub. Encrypt first maps the message comes from the message space into an element in the ring R/p . To encrypt a message R/pR , parse the public key as a pair (pk_0, pk_1) . Encryption consists of two LWE samples using a secret where (pk_0, pk_1) is these are sample is auxiliary.

3.4 BFV.Decrypt(SK, C) \rightarrow M

The main in variant of the BFV scheme is that when we interpret the elements of a cipher text C as the coefficients of a polynomial then, $C(s) = WM + e$ for some "small" error e . The message M can be recovered by dividing the polynomial (by W , rounding each coefficient to the nearest integer, and reducing each coefficient modulo

3.5 PROPERTIES SUPPORTED.

The complete BFV scheme supports many features described in Section 6, including packed evaluations of circuits and can be extended into a threshold homomorphic encryption scheme. In terms of security, the BFV homomorphic evaluation algorithms can be augmented to provide evaluation privacy.

For details on the implementation of the full BFV scheme, were the reader to [B12], [FV12].

3.5.1 Comparison Between Bgv And Bfv

When implementing HE schemes, there are many choices which can be made to optimize performance for different architectures and different application scenarios. This makes a direct comparison of these schemes quite challenging.

3.5.2 The Gsw Scheme And Boot Strapping

Currently, the most practical homomorphic encryption schemes only allow to perform bounded depth computations. These schemes can be transformed into fully homomorphic ones (capable of arbitrary computations) using a “bootstrapping” technique introduced by Gentry [G09], which essentially consists of a homomorphic evaluation of the decryption algorithm given the encryption of the secret key.

Bootstrapping using the BGV or BFV schemes requires assuming that lattice problems are computationally hard to approximate within factors that grow super polynomials in the lattice dimension n . This is a stronger assumption than the in approximability with in polynomial factors required by standard (non-homomorphic) lattice-based public key encryption.

In [GSW13], Gentry, Sahai and Waters proposed a new homomorphic encryption scheme (still based on lattices) that offers a different set of trade-offs than BGV and BFV. An important feature of this scheme is that it can be used to bootstrap homomorphic encryption based on the assumption that lattice problems are hard to approximate within polynomial factors. Here we briefly describe the GSW encryption and show how both its security and applicability to boot strapping are closely related to LWE encryption, as used by the BGV and BFV schemes. property which we call threshold-HE is desirable. In threshold-HE the key-generation algorithms, encryption and decryption algorithms are replaced by a distributed-key-generation

The (DKG) algorithm, distributed-encryption (DE) and distributed-decryption (DD) algorithms. Both the distributed-key- generation algorithm and the distributed- decryption algorithm are executed via an interactive process among the participating users. The evaluation algorithms EvalAdd, Eval Mult, Eval Mult Const, Eval Add Const and Refresh remain unchanged. Bootstrapping is a very time-consuming operation and improving on its efficiency is still a 25very active research area. So, it may still not be ready for standardization, but it is the next natural step to be considered.

In [GSW13], Gentry, Sahai and Waters proposed a new homomorphic encryption scheme (still based on lattices) that offers a different set of trade-offs than BGV and BFV. An important feature of this scheme is that it can be used to bootstrap homomorphic encryption based on the assumption that lattice problems are hard to approximate within polynomial factors. Here we briefly describe the GSW encryption and show how both its security and applicability to bootstrapping are closely related to LWE encryption, as used by the BGV and BFV schemes. So, future standardization of bootstrapping (possibly based on the GSW scheme) could build on the current standardization effort. The cipher text encrypt the message as $(a+m, as+ e)$, but this is just a minor variant on LWE encryption, and equivalent to it from a security stand point.) Security rests on the standard LWE assumption, as used also by BGV and BFV, which says that the distribution $(A, A*S+E)$ is pseudorandom.

4. RESULT

Encryption and Decoding are the Significant Piece of Gotten correspondence, In homomorphic Encryption Plan Procedure on Chiper Text can be handily finished and without Need of any Unscrambling First.

The Engineering utilized gives improved Results in calculation speed, region, energy and power are of greater Need Result to be Exact i.e.,

By Utilizing ISE Plan SUITE Task Guide, Xilinx 14.7 adaptation in the recreation system the improved Results are Accomplished with Less Circuit Region With Low Power Utilization.

The encryption activity ought to be checked that the given information message is scrambled impeccably or not .on the off chance that any mistakes happen in the encryption activity, similar advances happen.

4.1 SIMULATION PROCEDURE

For clk: forcing a clock value: duty cycle: 50, period : 100. Rst: forcing a value: 1

Give any user input M=Msg= 34

Q = Modulus input= 8

T= poly modulus input= 4

Run simulation and again change rst: forcing a value: 1 Run simulation and again change rst: forcing a value: 0 And run simulation

For the above inputs the outputs for the encryption of the message is shown in the below images.

4.2 RESULTS OF ENCRYPTION OPERATION

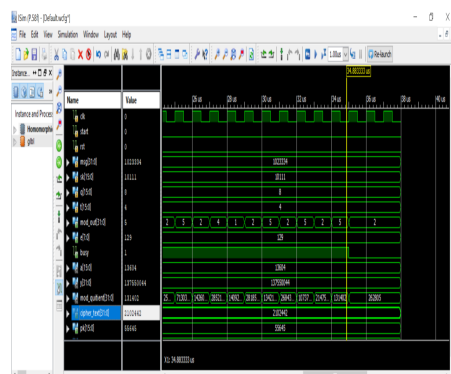
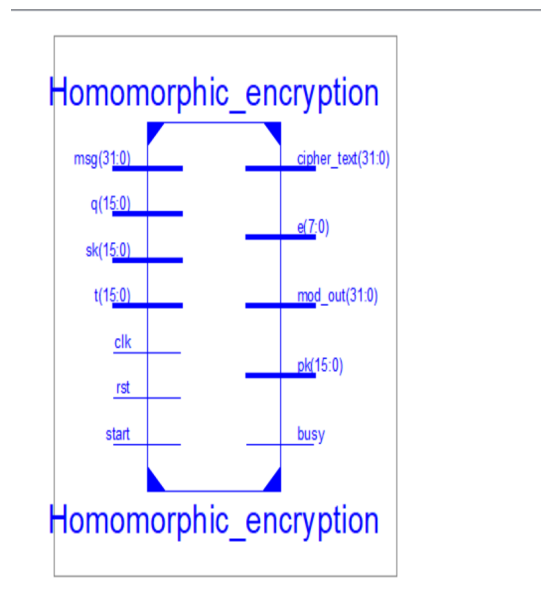


Figure 4.1: Results of Encryption Operation

After performing the encryption the received output message should be decrypted at the output end by performing decryption operation and the outputs of the decryption is shown below.

The outputs of the encryption will be verified and the decryption operation should be performed which is shown in below.

The outputs from the encryption operation should be verified that the given input message is encrypted perfectly or not .if any errors occur in the encryption operation then the same steps should be performed.

4.3 RESULTS OF DECRYPTION OPERATION

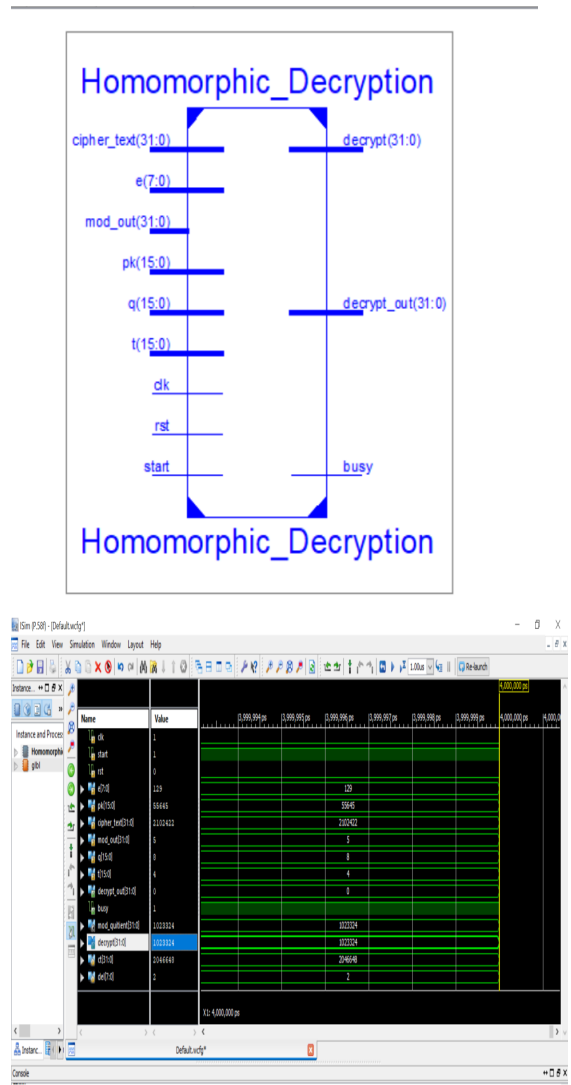


Figure 4.2: Results of Decryption Operation

The comparison table that shows the improved parameters for existing method to the proposed method is given below

```

Asynchronous Control Signals Information:
-----
No asynchronous control signals found in this design

Timing Summary:
-----
Speed Grade: -3

Minimum period: 1.943ns (Maximum Frequency: 514.646MHz)
Minimum input arrival time before clock: 27.715ns
Maximum output required time after clock: 2.150ns
Maximum combinational path delay: No path found

Timing Details:

```

Figure: Existing delay

Table 4.1: Comparison for Existing Method and the Proposed Method

Parameters	Existing Method	Proposed Method
Clock Frequency	200 MHz	514.64 MHz
LUT	800	526
Slice Registers	726	105
Delay (ns)	5.0	1.943

The comparison table that shows the improved parameters for existing method to the proposed method is given above. According to the above table, the suggested technique has a shorter latency than the present way, which improves the performance of the architectures employed.

5. CONCLUSION AND FUTURE SCOPE

Here this Project We Can Reduce the Power Consumption and Delay by Using Vedic Multiplier and Kogge stone Adder which is Fast in Performance. The greater values of frequency will results in the reduction in delay. So the performance of the system will be increased. And also the number of LUT's used in this project will also be reduced.

This work can be used Furtherly for 128 bits, 256 bits, can be Implemented by Further Different Multipliers and Fastest Adder to Increase the Performance of the Circuit. Ultimately, given minor adjustments, this accelerator's core logic modules may be utilized to construct ring arithmetic with bigger ring degrees and modulus sizes. We are now working on a new design based on our existing architecture that will lower energy usage using a parallel prefix adder (similar to the Kogge stone Adder), and the findings will be revealed in our future research.

REFERENCES

[1] Albrecht, M. R. (2017). On dual lattice attacks against small-secret LWE and parameter choices in HE lib and SEAL. In J. Coron & J. B. Nielsen (Eds.), EUROCRYPT 2017, part II (Vol.10211, pp. 103–129).Springer, Heidelberg.

- [2] Martin R. Albrecht, Robert Fitzpatrick, and Florian Gopfert: On the Efficacy of Solving by Reduction to Unique-SVP. In Hyang-Sook Lee and Dong-Guk Han, editors, ICISC 13, volume 8565 of LNCS, pages 293–310. Springer, November 2014.
- [3] Martin R. Albrecht, Rachel Player and Sam Scott. On the concrete hardness of Learning with Errors. *Journal of Mathematical Cryptology*. Volume 9, Issue 3.
- [4] Alkim, E., Ducas, L., Pöppelmann, T., & Schwabe, P. (2016). Post-quantum key exchange—A new hope. In T. Holz & S. Savage (Eds.), 25th USENIX security Alperin-Sheriff, J., Peikert, C.: Faster bootstrapping with polynomial error. In: Garay, J. A., Gennaro, R. (eds.) CRYPTO 2014. LNCS, vol. 8616, pp. 297–314.
- [5] László Babai : On Lovász' lattice reduction and the nearest lattice point problem, *Combinatorica*, 6(1):1-3, 1986.
- [6] Becker, A., Ducas, L., Gama, N., & Laarhoven, T. (2016). New directions in nearest neighbor searching with applications to lattice sieving. In R. Krauthgamer (Ed.),
- [7] W. Castryck, I. Iliashenko, F. Vercauteren, Provably weak instances of ring-LWE revisited. In: Eurocrypt 2016. vol. 9665, pp. 147–167. Springer (2016)
- [8] W. Castryck, I. Iliashenko, F. Vercauteren, On error distributions in ring-based LWE. *LMS Journal of Computation and Mathematics* 19(A), 130–145 (2016) 7.
- [9] Y. Chen, P.Q. Nguyen. BKZ 2.0: Better Lattice Security Estimates. In: Lee D.H., Wang X. (eds) *Advances in Cryptology – ASIACRYPT 2011*. ASIACRYPT .
- [10] Laarhoven, T. (2015). Search problems in cryptography: From fingerprinting to lattice sieving (PhD thesis). Eindhoven University of Technology.
- [11] Vadim Lyubashevsky, Chris Peikert, and Oded Regev : A tool kit for ring- LWE cryptography. *Annual International Conference on the Theory and Applications of Cryptographic Techniques*. Springer, Berlin, Heidelberg, 2013.

Research analysis on Spin Launch

Pothula Lolarkar Reddy^[1] Thokala Hruthik Reddy^[2] Sathwika veluguri^[3]

Department of Electronics and Communications^[1,2]

under supervision

Of

Ms.S. Vaishali M. Tech (Ph.D.)

Associate Professor

Department of Electronics and Communications

Vaagdevi College of Engineering

ABSTRACT:

Our world is advancing day by day, all the traditional gadgets are getting updated in our day-to-day life. If we see in the past years, we used the satellites that are very large in size, but now in the modern satellites all conventional constituents are replaced with the nano and micro components, which works more efficient and effective as compared with the conventional components. At present, we are launching numerous satellites in a single launch. This method of launching several satellites in a single launch is complicated and very cost-effective. From early stage to now, we are using the same conventional method of action and reaction method to launch a rocket and place the satellite into the orbit, this method needs chemical fuels which burns in and gives an opposite force that lifts a rocket into the sky. This customary method is suitable for satellites that have a large mass, for the nano satellites we doesn't require that much amount of fuel or force and cost that place them in orbit, so an alternative launching method is required to launch the nano satellites into the orbits. Here in the spin launch technique, it is one of the alternative techniques that differ from customary launching technique and cost effective

technique that works in placing a nano satellites which has less mass into the earth orbits.

1) INTRODUCTION

The spin launch technology is the new method of launching the rockets into the earth orbits. In the traditional method we use the chemical fuels that are burned in their chambers at the time of their combustion they exhibits the gases at high pressure, these gases lift up the rocket into the space, but this process is very costly and the gasses that are exhibited can cause damage to earth, even though these traditional satellites are used to lift high weight objects, but due to modernization of our world we are constructing the satellites with nano and micro objects that makes the satellite into the lighter weight, to launch these type of low weight satellites into the earth orbit we do not require adequate fuel and money, if we use traditional method then it costs more time and money, so to launch these type of satellites a new method is required with minimum cost and it must have ability to transport the satellite into the earth orbit, here our theory of spin launch can replace the traditional launch system and it has an ability to place a nano and micro satellite into the earth orbits. Unlike the

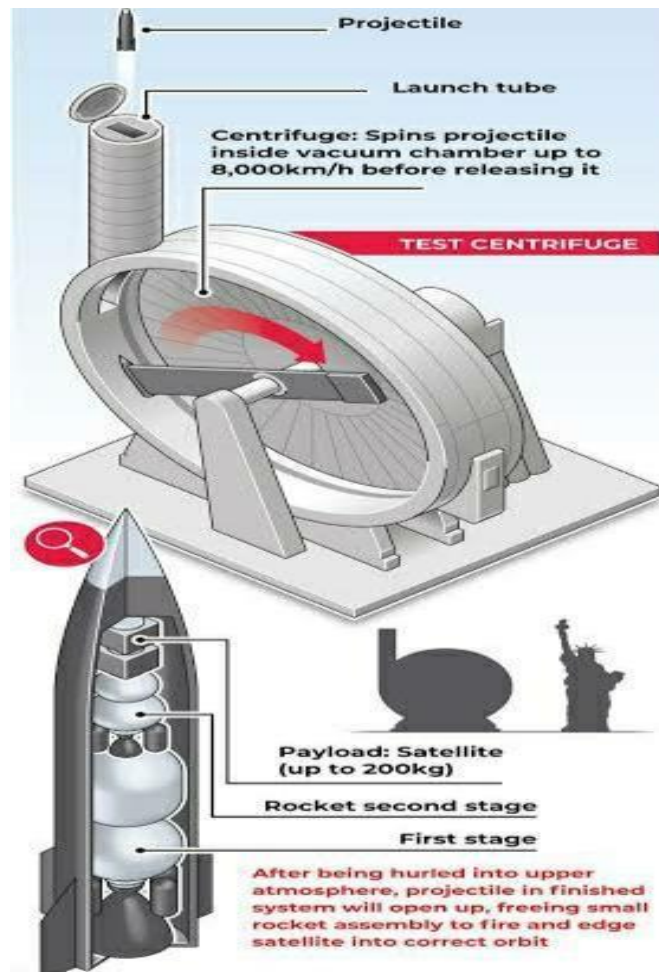
traditional launch the spin launch does not require much chemical fuel, this spin launch technique launches the rocket into space by the kinetic energy, this spin launch also requires some chemical fuel but it is not for the launch it is to correct and change the trajectory and path of the launched vehicle.

Here we use the vacuum chamber, because in vacuum chambers there is no air so the friction is less and there won't be any loss of the kinetic energy that is produced when the motor rotates.

CONSTRUCTION OF ROCKET THAT IS USED IN SPIN LAUNCH TECHNIQUE:

CONSTRUCTION OF THE SPIN LAUNCH

To construct the spin launch we mainly required a vacuum chamber, high rpm motors, that can be able to produce the required kinetic energy which is required to launch the rocket into the space, and a blade that one side is attached to the motor and the other to the rocket, and the blade should be able to eject the rocket after reaching the threshold kinetic energy, for the spin launch the construction is done in such a way that in a vacuum chamber the high rpm motor is fixed in the center and to the end of the motor the blade is connected, by this simple method the spin launch pad is prepared to launch the rockets into the earth's orbit.



As the spin launch technique is a special technique to launch the rocket into space, we need to design the special rockets that are suitable to

launch by using the spin launch technique, unlike the traditional rockets the spin launch rockets are very small in size and they carry less fuel when compared with the traditional rockets. The rocket should have a high resistance such that it can't get any damage while the launch pad is producing the kinetic energy by rotating. These rocket busters are the same but there is a chance of path deviation by these rockets. so the side busters of the rocket are given main importance in construction. The main busters of the rocket are opened, after the rocket reaches a

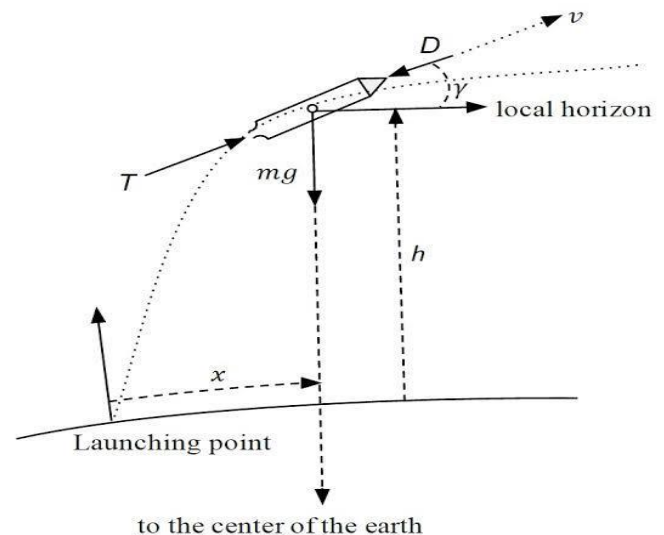
height by the kinetic energy produced. Mainly these rockets are designed to carry fewer payloads when compared with the traditional Cryogenic engine rockets.

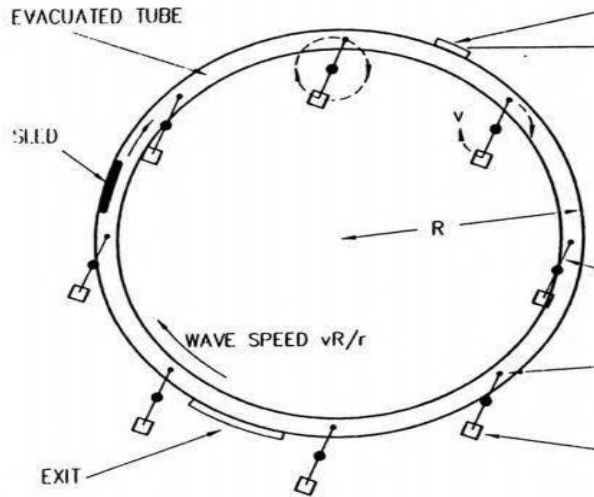


4) WORKING PRINCIPLE OF THE SPIN LAUNCH:

The spin launch mainly works on the principle of kinetic energy produced by the rotation of the rocket in the vacuum sealed chamber by the motors and then catapulted into space. For a simple demonstrate of spin launch, we can use a stone i.e., tied to the rope and then if we will the thread, the stone rotates and makes some energy at maximum speed, if we break the string then the stone escapes into the free sky and travels in a tangential path. And the stone falls on ground after its flight, here the force that required to escape the earth gravitational force is not produced by the stone so it falls on the ground, but if the stone can produce the enough energy that can suppress the earth gravitational force the stone can escape earth's gravitational field and it can enter into the space. Here according to our law, an object can be in rest or in uniform motion in a straight line until some external force acts on it, here in our case the gravitational force is an external force which pulls the stone into it. Hence the stone changes its path and falls on the ground. In spin launch technique the rocket is attached to the blade which is connected with the motor of high rpm, the rocket rotates with the motor at high speeds which is over hyper sonic speeds

approximately a speed of 450 revolutions per minute and then after achieving the required kinetic energy the rocket is catapulted into the sky. According to some test results the catapulted rocket can achieve the speed of 8000 KM/Hr, then the rocket can easily surpass the earth gravitational force, and the rocket after reaching a altitude of 61000 meters, the engine of the rocket is ignited and the rocket can roughly Achieve the speed of 28,200 Km/hr. If the rocket can achieve the speeds of 28,200 Km/hr then it is easy for the rocket to escape the earth's gravitational field. The side Propellers that are built for the rocket is used to correct the path of the rocket. If the spin launch is a successful technique to launch the rocket, then the use of the traditional rockets can be used less, the micro and nano satellites can be sent into space with low cost. However, the trials of the spin launch technique are done by many private and government space Agencies, if the trials are successful then a new launch technique is used to launch the rockets.





5) MERITS OF SPIN LAUNCH:

- 1) Spin launch requires low cost when compared with traditional launching techniques
- 2) Spin launch is more efficient and lower risk.
- 3) Requires less fuel when compared with traditional launching techniques.
- 4) Spin launch causes low pollution to the layers of the earth, because approximately at the height of 61000 meters the engine of the rocket is ignited.
- 5) We can launch multiple rockets from a single launch pad at a very quick time. So the buffer time is low for launching a second rocket from the same launch pad.
- 6) The spin launch method can also be able to launch the missiles for long ranges.

6) DEMERITS OF USING SPIN LAUNCH:

- 1) If the required kinetic energy is not produced by the launch pad then the rocket is unable to escape the earth's gravitational field.
- 2) Unlike the traditional rockets the spin launch rockets can carry only the low

amounts of payloads, approximately 100-250 kg's.

- 3) It is suitable only for launching the micro and nano satellites, not for the high weight satellites.
- 4) If the engine is not ignited in the mid-way of the launch, then the rocket may go uncontrollable and may fall in the human habitat areas on the earth.

7) CONCLUSION:

Hence, spin launch technique is an easier way to launch nano satellites and encourages the growth of living species by avoiding emission of harmful gases in the atmosphere. By this we'll increase the rate of exploring and emerging things in space and also for better communication and security, navigation and development. In simpler, we can say this technique is reliable, cost-effective, efficient and eco-friendly.

REFERENCES:

- STARTUP SPIN LAUNCH, Jonathan Yaney (CEO OF SPIN LAUNCH).
- GOOGLE WIKIPEDIA ARTICLE ON SPIN LAUNCH.

Throughput and Outage Probability-Aware Intelligent Swarm-Based Multi-Hop Selection in Vehicular Network

Uppula Kiran & Krishan Kumar

To cite this article: Uppula Kiran & Krishan Kumar (2022): Throughput and Outage Probability-Aware Intelligent Swarm-Based Multi-Hop Selection in Vehicular Network, Cybernetics and Systems, DOI: [10.1080/01969722.2022.2103232](https://doi.org/10.1080/01969722.2022.2103232)

To link to this article: <https://doi.org/10.1080/01969722.2022.2103232>



Published online: 04 Aug 2022.



Submit your article to this journal [↗](#)



View related articles [↗](#)



View Crossmark data [↗](#)



Throughput and Outage Probability-Aware Intelligent Swarm-Based Multi-Hop Selection in Vehicular Network

Uppula Kiran^a and Krishan Kumar^b

^aDepartment of Electronics & Communication Engineering, Lovely Professional University, Jalandhar, India; ^bFaculty in School of Electronics and Electrical Engineering, Lovely Professional University, Jalandhar, India

ABSTRACT

Cooperation is an emerging paradigm for improving spatial differentiation in Vehicular Ad-Hoc Networks (VANETs). Hence, many network solutions are motivated through cooperative communications for boosting VANET efficiency regarding specific network constraints like energy efficiency, network capacity, and outage probability. The main intention of this paper is to design and develop an optimization model for selecting the minimum number of multi-hops between the source and destination for the cooperative VANET networks. The first phase has a first-time slot, where a signal is transmitted by the source to the cooperative nodes (its relays) and their equivalent destination. The main problem considered here is to optimally select the number of hops or relays that are adaptable for communication, to solve the multi-objective functions concerning the target throughput and outage probability. The adoption of new Dimension-based Cat Swarm Optimization (D-CSO) is the main contribution here to optimally select the multi-hops among source and destination. Through the performance evaluation, it is observed that the designed model has achieved networks-wide fairness performance and a good convergence rate.

KEYWORDS

Cooperative communication; Dimension-based Cat Swarm Optimization; multi-hop selection; multi-objective function; outage probability; throughput; Vehicular Ad-Hoc Networks

1. Introduction

Cooperative communication has mainly emerged as a new paradigm for security improvement of the characteristics of the physical layer (Okeke et al. 2015; Nam, Jang, and Lee 2015). For offering a high ability to the major link compared to the wiretap one, the relay nodes are generally employed among source and destination nodes (Wang, Teh, and Li 2016). Consequently, to maximize the secrecy efficiency, it is noted that there is a need of enhancing the number of relays (Adam, Yanmaz, and Bettstetter 2014). Moreover, the selection of relay is a famous technique with several relay cases for maximizing the efficiency of cooperative systems without or with security parameters (Zhao et al. 2014). Several relay selection strategies

have been utilized in recent studies based on the activity or passivity of the eavesdropper. The relay selection is performed traditionally by utilizing the channel state information (CSI) of the major link while considering the passive eavesdropper (Feng, Xiao, and Cimini 2014). Moreover, depending on the accessibility of the CSI of the wiretap and main links, the selection of optimal relay is conducted when the known eavesdropper is considered (Xia and Aïssa 2015).

Generally speaking, wireless relay networks has been majorly focused on several physical layer security based on the cooperative phase scenario (Nguyen, Afolabi, and Kim 2013). On the other hand, the major problem requires additional emphasis with further examination of the broadcast phase in an operational platform when several direct links are available from the source node to the eavesdropper and destination nodes. Thus, proven and famous networks called cooperative communications have been taken as an efficient metric for enhancing the performance of wireless networks (Su et al. 2019). Generally, cooperative communication has been divided into two classes cooperative relaying and multi-hop communications. It has been utilized for cellular networks for increasing the “Quality of Service (QoS)” and/or coverage. The “Hybrid Ad hoc Network (HANET) or Multi-hop Cellular Network (MCN)” is often formed by integrating the cellular systems with multi-hop communications (Zheng et al. 2012; Kanithan et al. 2020). To realize MCN, the “Opportunity Driven Multiple Access (ODMA) protocol” (Zhang and Cimini, 2007) is introduced based on the “3rd Generation Partnership Project (3GPP) for Time-Division Duplexing (TDD) and Universal Mobile Telecommunications System (UMTS)”, which is suggested for offering the traffic hotspots and spot coverage, for increasing the capacity of the network and for maximizing the high data rate coverage (Abdulhadi, Jaseemuddin, and Anpalagan 2012).

In recent years, Vehicular Ad-Hoc Networks (VANETs) have inspired researchers due to their prospective exploration of several noteworthy telematic applications consisting of entertainment to safety-oriented applications, especially for intelligent transportation and traffic information systems (Seyfi et al. 2011; Agrawal et al. 2020). The connected vehicles also called a generalized VANET consist of wireless communication links between road-side access points and vehicles for supporting both vehicle-to-infrastructure (V2I) and vehicle-to-vehicle (V2V) communications (Hui et al. 2020; Singh et al. 2021). On the other hand, vehicular channels suffer from inherent space-time frequency differentiability due to the time-differing effects, multi-path propagation, and vehicular mobility. The emerging interest in the implementation of new communication architectures has to consider the complete exploitation of diversity. As cooperative communications have been extensively recognized as a powerful technique in several communities, it has to increase the

performance of wireless relay transmission systems from either cross-layer or physical-layer views (Achour, Alfayez, and Busson 2021). Hence, emerging cooperative communication technologies in VANETs propose a huge range of protocols and broader designs for solving the fast signal fading problem (Akin, Ilhan, and Özdemir 2015). Thus, there is a need of solving the throughput and outage probability in VANETs with the help of a heuristic-based algorithm for selecting the relays.

The major goal of the designed model is given here.

- To develop an optimization model for selecting the minimum number of multi-hops between the “source and destination” for the cooperative VANET networks to offer a good convergence rate and network-wide fairness performance.
- To develop a new D-CSO algorithm for selecting or optimizing the number of relays among the source and destination for effective communication or transmission of packets among them by solving the multi-objective function concerning throughput and outage probability.
- To study the performance of the suggested intelligent swarm-based multi-hop selection model in vehicular networks by convergence analysis, statistical analysis, and throughput and outage probability.

The residual parts of the suggested method are depicted below. [Section 2](#) describes the conventional works. [Section 3](#) describes the system model and cooperative mechanism in vehicular networks. [Section 4](#) narrates the optimal relay number selection model in vehicular networks. [Section 5](#) discusses the proposed relay selection strategy in vehicular networks based on outage probability and throughput. The result visualization is shown in [Section 6](#). In the end, this research work has concluded in [Section 7](#).

2. Literature Survey

VANETs are a class of Mobile Ad-Hoc Networks (MANET) and also it can be denoted as a group of smart vehicles interconnected together with wireless links. Here, VANETs have the vehicles move only on a predetermined road with the highest capability of data saver and computing power. The spreading of road safety messages is a difficult activity in VANETs. Few of the existing works based VANETs are depicted here.

2.1. Related Works

Saghezchi, Radwan, and Rodriguez (2017) have suggested a new “energy-aware cooperative relaying in future heterogeneous networks (HetNets)” to

reduce energy consumed by wireless devices. The problem was formulated as an assignment game and thus, this network has used game theory concepts. Initially, the selection of optimal relay was taken as a linear programming paradigm, where the appropriate relays have been selected as solutions from their possible sources. Ying and Nayak (2018) have considered an optimal relay selection issue by exploiting the social correlations from contributions and interaction between users for improving cooperative multi-hop D2D communications (Lim et al. 2021). This model has solved the above-mentioned problem through a new scheme. Here, the users were selected from the constructed social correlations, where relays were considered which have a stronger social relationship.

Tian et al. (2017) have implemented a relay selection technique with the help of the stochastic learning method, which has also evolved Nash equilibrium. They have also investigated the precise outage behavior of the cooperative communication networks by a multi-relay decode-and-forward scheme. Siddig, Ibrahim, and Ismail (2020) have suggested a new store-carry-forward strategy in a full-duplex way for exploiting the relay's capability for concurrent transmitting and receiving of information for delivering more data to the target vehicle in the uncovered area. The major aim of the designed model was to get optimal power allocation by determining the abilities of the links.

Li et al. (2020) have considered a new cooperative-node system model to propose a selection algorithm for getting the optimal relay number depending on a realistic networks model along with the distance measures among "Nakagami-m short-term static fading channel and relays", which was highly appropriate for unmanned aerial vehicles (UAVs). Poursajadi and Madani (2021) have examined the vehicular communication model with the help of adaptive optimal relay selection (AORS) for choosing the optimal relay with the constraints of security in terms of both cooperative and broadcast phases. Further, the incremental scheme was suggested for offering security.

Dan et al. (2010) have examined multi-user-based cooperative networks, the decode-and-forward relaying protocol was used for helping the intermediate relay nodes for forwarding the source forward information to the destination. In addition, they have implemented a new multi-relay nodes selection strategy with residual energy and instantaneous CSI for overcoming the imbalances in resource usage and for achieving the emergence of diversity gain. Dan et al. (2011) have suggested a power allocation strategy with distributed join relies on a node selection framework over multi-hop relaying cellular networks with the consideration of residual energy of relay nodes and wireless channel state (Yang et al. 2020). The residual energy state transitions and time-varying channels were characterized by using a first-order finite-state Markov chain.

Sadegh et al. have introduced a fuzzy logic-based routing (Agrawal et al. 2020; Yin 2020) method with authentication capacity in vehicular ad hoc networks. Here, vehicles were clustered using an effective strategy. Easy data packets have not followed the authentication strategy. Moreover, secure data packets have been utilized for an authentication strategy according to the Message Authentication Code (MAC) and symmetric key cryptography. Phull et al. have developed an approach for vehicular ad hoc networks. It utilized a game theory method to computerize vehicle combination and cluster head selection. The suggested method was utilized for eliminating the necessity for cluster improvement regularly. K-means algorithm was applied for the implementation of clusters on the social character of the cars. Numerous relay selection approaches have been reviewed in Table 1. These problems promote the research works to focus on implementing a new relay selection approach in Vehicular networks.

3. System Model and Cooperative Mechanism in Vehicular Networks

There are many advanced features there for VANETs to improve their commercial success. But, this system model includes many other advanced features to spread the messages from one vehicle to another. The system model for the suggested vehicular networks has shown here and also the cooperative mechanism for this system model that has briefly discussed below.

3.1. System Model

While considering the active eavesdropper in the system, a time division multiplexing is considered with several decode and forward (DF) relay cooperative vehicular to the vehicular communications system. Figure 1 shows a pair of vehicles with initial point and target point vehicular nodes along with some intermediate vehicular nodes.

In these networks, from the source node, the received messages are decoded and then forwarded to the destination. In these networks, entire nodes like destination D_s relay (M_1, M_2, \dots, M_R) , where $r = 1, 2, 3, \dots, R$ source S_r and eavesdropper E_v are communicated with a single antenna. Additionally, entire nodes are operated in a half-duplex manner regarding the real-time constraints, where they cannot receive and transmit simultaneously. An operational environment is considered here, where several direct paths are assumed from the source to eavesdropper and destination nodes. There is also an assumption that the accurate channel estimation is carried out based on the CSI of the wiretap and main channels. There are two scenarios assumed, where in the first case, CSI is available at the transmitter nodes through an error-free feedback



Table 1. Merits and demerits of relay selection approach in multi-hop communication networks.

Author [citation]	Techniques	Merits	Demerits
Saghezchi, Radwan, and Rodriguez (2017) Ying and Nayak (2018)	Game theory PSRS	<ul style="list-style-type: none"> It increases the lifetime of the battery. It saves energy. It reduces power consumption. 	<ul style="list-style-type: none"> It increases the energy-saving gain. It gets a lower success ratio of message deliveries.
Tian et al. (2017)	The decentralized self-organized relay selection algorithm	<ul style="list-style-type: none"> It enhances the network-wide fairness in terms of "transmission reliability, and high energy efficiency". It minimizes the computational complexity of the designed model. 	<ul style="list-style-type: none"> Though, the outage probability computation is complex. It has a high buffer time.
Siddiq, Ibrahim, and Ismail (2020)	Ergodic Maximization-Store-Carry-Forward (EM-SCF)	<ul style="list-style-type: none"> It enhances the system's performance. It gets lower average transmission delay and higher energy efficiency. 	<ul style="list-style-type: none"> This model is not suitable for smart internet of things (IoT)-based applications.
Li et al. (2020)	DTMC	<ul style="list-style-type: none"> It efficiently solves the generalized optimal relay selection and direct transmission. 	<ul style="list-style-type: none"> It is not suitable for real-time benefits.
Poursajadi and Madani (2021)	AORS	<ul style="list-style-type: none"> It has given complete secrecy and diversity order. 	
Dan et al. (2010)	Lagrangian dual-primal decomposition	<ul style="list-style-type: none"> It gets less implementation complexity. It guarantees energy efficiency. 	<ul style="list-style-type: none"> However, the performance of the model is slightly varied due to the poor channel conditions.
Dan et al. (2011)	Stochastic optimization	<ul style="list-style-type: none"> The computational complexity is low. 	<ul style="list-style-type: none"> The performance is affected due to the battery-limited relaying networks.

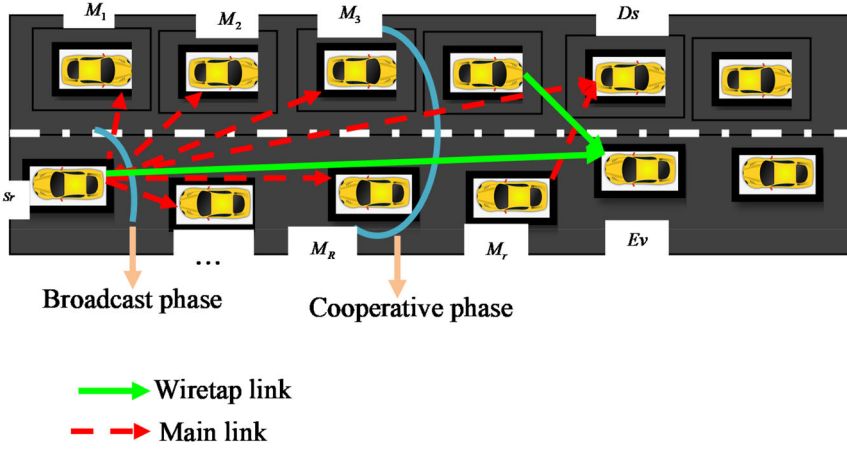


Figure 1. The cooperative mechanism in vehicular networks with several numbers of vehicular nodes.

link, while in the second case the CSI is only accessible to the receiver nodes (Dong et al. 2010). In addition, the channel among every receiver node $Bc \in (Sr, Ev, Ds)$ and transmitter node $Tn \in (Sr, Mr)$ for $r = 1, 2, \dots, R$ and h_{BcTn} is noticed as the Rayleigh distribution with quasi-static flat fading of variance σ_{BcTn}^2 and zero mean.

In the wiretap channel, the capacity attaining codebook is utilized that performs the encoding of the source message A into a codeword $A \in A^b$, where an input alphabet of length b is denoted as A^b . Here, a particular symbol is denoted as a unit power that is transmitted in a time slot. For broadcasting their secret information, the first slot of the time-division multiplexing protocol is assigned to the source node, which P_{Sr} represents a signal a with transmission power. The following signals are received by the authorized nodes in this phase.

$$z_{Ds} = \sqrt{P_{Sr}} h_{SrDs} a + b_{Ds} \quad (1)$$

$$z_{M,r} = \sqrt{P_{Sr}} h_{SrM,r} a + b_M \quad (2)$$

Here, the “Additive White Gaussian noise (AWGN)” at the different relays and major destinations are denoted as b_{Ds} and b_M , respectively with the same power of η_0 . Through the following received signal, the node Ev wiretaps from the source node in the broadcast phase.

$$z_{Ev} = \sqrt{P_{Sr}} h_{SrEv} a + b_{Ev} \quad (3)$$

In Eq. (3), AWGN noise Ev is termed as b_{Ev} including density power η_0 . In these networks, the broadcast phase and cooperation phase are executed separately which expresses the various secrecy capacities of the two phases. In the initial phase, the “Single Input-Multiple Output (SIMO) channel” is considered for presenting the secrecy capacity. Then, the capacity of the

SIMO channel is assumed by the optimal Gaussian codebook utilized from the source node to the r^{th} relay and destination node through the selection combining (SC) scheme (Yang et al. 2016) as given in Eq. (4).

$$\zeta_{\text{SC}}^r = \log_2(1 + \kappa_1 |h_{\text{SC},r}|^2) \quad (4)$$

$$h_{\text{SC},r} = \max\{|h_{\text{Sr}D_s}|^2, |h_{\text{SC},r}|^2\} \quad (5)$$

Here, $\kappa_1 = \frac{P_{\text{Sr}}}{\eta_0}$. Furthermore, the capability of the wiretap channel is formulated in Eq. (6).

$$\zeta_{\text{SE}} = \log_2(1 + \kappa_1 |h_{\text{SE}}|^2) \quad (6)$$

It has been verified that the variation among the capacities of the “main and wiretap links” is defined as the secrecy capacity (Li, Petropulu, and Weber 2011). Hence, the following derivation specifies the capacity of “secure communications” for the r^{th} relay in the broadcast phase.

$$\begin{aligned} \zeta_{\text{SS}}^{\text{BP},r} &= [\zeta_{\text{SC}}^r - \zeta_{\text{SE}}]^+ \\ &= \left[\log_2 \frac{1 + \kappa_1 |h_{\text{SC},r}|^2}{1 + \kappa_1 |h_{\text{SE}}|^2} \right]^+ \end{aligned} \quad (7)$$

In Eq. (7), the representation is given as follows $[a]^+ = \max(0, a)$.

3.2. Cooperative Mechanism

Consider the signal a of transmission power P_r is transmitted by relay node for examining “the security of the cooperative phase that has resulted in the reception of the corresponding signals” at E_v and D_s , respectively.

$$z_{\text{M}D_s,r} = \sqrt{P_r} h_{\text{M}D_s,r} a + b'_{D_s} \quad (8)$$

$$z_{\text{M}E_v,r} = \sqrt{P_r} h_{\text{M}E_v,r} a + b'_{E_v} \quad (9)$$

In the aforementioned equations, the AWGN at E_v and D_s with the same power of η_0 being represented as b'_{D_s} and b'_{E_v} , respectively, which leads to the secrecy capacity of the cooperative phase is formulated in Eq. (10), where $\kappa_2 = \frac{P_r}{\eta_0}$.

$$\zeta_{\text{SS}}^{\text{CP},r} = \left[\log_2 \left(\frac{1 + \kappa_1 |h_{\text{Sr}D_s,r}|^2 + \kappa_2 |h_{\text{M},D_s}|^2}{1 + \kappa_1 |h_{\text{SE}}|^2 + \kappa_2 |h_{\text{M},E_v}|^2} \right) \right]^+ \quad (10)$$

The cooperative phase becomes silence while the “relay node cannot recover the source message”, where $\kappa_2 = 0$. Lastly, the entire immediate secrecy capacity from source to destination is presented as the lower secrecy capabilities of both broadcast and cooperative phases as formulated here.

$$\zeta_{SS}^r = \frac{1}{2} \min \left\{ \begin{array}{l} \left[\log_2 \left(\frac{1+\gamma_{SC}^r}{1+\gamma_{SE}^r} \right) \right]^+, \\ \left[\log_2 \left(\frac{1+\gamma_{SrDs}^r+\gamma_{MDs}^r}{1+\gamma_{SE}^r+\gamma_{MEv}^r} \right) \right]^+ \end{array} \right\} \quad (11)$$

In Eq. (11), $\gamma_{MEv}^r = \kappa_2 |h_{MEv,r}|^2$, $\gamma_{MDs}^r = \kappa_2 |h_{MDs,r}|^2$, $\gamma_{SE} = \kappa_1 |h_{SE}|^2$, and $\gamma_{SC}^r = \kappa_1 |h_{SC,r}|^2$. To transmit every secret message, the coefficient $\frac{1}{2}$ is used in Eq. (11) as two-time slots are employed. In addition, the optimum relay is selected in both broadcast and cooperative phases by applying a generalized form of the ‘‘Optimal Relay Selection’’ (GORS) scheme, which is derived in Eq. (12).

$$\zeta_{SS}^{GORS} = \frac{1}{2} \max_{r \in \{1, \dots, R\}} \left\{ \min \left\{ \zeta_{SS}^{BP,r}, \zeta_{SS}^{CP,r} \right\} \right\} \quad (12)$$

However, the overall security can be destroyed when leaking secret information in many phases. There are two diverse constraints formulated for offering the security behavior of GORS, which are the source Sr to destination Ds link is weaker while compared with the $Sr-M_r, r = 1, \dots, R$ links and the source Sr to destination Ds link is stronger than $Sr-M_r, r = 1, \dots, R$ links. Thus, the secrecy capacity through GORS for the first constraint is derived in Eq. (13).

$$\zeta_{SS,1}^{GORS} = \frac{1}{2} \max_{r \in \{1, \dots, R\}} \left\{ \min \left\{ \zeta_{SS}^{SrM,r}, \zeta_{SS}^{CP,r} \right\} \right\} \quad (13)$$

In Eq. (13), $\zeta_{SS}^{SrM,r} = \left[\log_2 \left(\frac{1+\gamma_{SrM}^r}{1+\gamma_{SE}^r} \right) \right]^+$ and $\gamma_{SrM}^r = \kappa_1 |h_{SrM,r}|^2$. The ‘‘secrecy capacity of the GORS’’ strategy in the initial case is equivalent to the maximum R secrecy capacities (Krikidis, Thompson, and Laughlin 2009). The second case is derived in Eq. (14), which ζ_{SS}^{SrDs} indicates the ‘‘instantaneous secrecy capacity at the main destination through direct transmission’’.

$$\zeta_{SS,2}^{GORS} = \frac{1}{2} \max_{r \in \{1, \dots, R\}} \left\{ \min \left\{ \zeta_{SS}^{SrDs}, \zeta_{SS}^{CP,r} \right\} \right\} \quad (14)$$

In Eq. (14), $\zeta_{SS}^{SrDs} = \left[\log_2 \left(\frac{1+\gamma_{SrDs}^r}{1+\gamma_{SE}^r} \right) \right]^+$ that is equivalent to the maximum R -secrecy capacities.

These two conditions are utilized in the GORS strategy, the transmission efficiency can be decreased by relay via factor $1/2$, which also enhances the wiretap link compared with the main channel. The direct link is evaluated and the best relay is selected by accessing both CSI in the transmitter node or receiver nodes of every phase. The overall CSI is accessible at receiver nodes (Zou, Wang, and Shen 2013), where the secret message can be broadcasted at the source node at a particular rate \mathfrak{R}_{SS} . Additionally, the

decisions are made at the destination “about the capability of the direct link for recovering the source message” as given in Eq. (15).

$$\varepsilon : \zeta_{SS}^{SrDs} < \mathfrak{R}_{SS} \quad (15)$$

In this abovementioned equation, the adaptive relaying is derived while satisfying the Eq. (15), in which a selected best relay intends to maximize the secrecy capacity, or else a new secret message is transmitted by the source node. This strategy is named AORS. The incremental relaying is carried out for solving the complexity and for improving the spectral efficiency as given in Eq. (16).

$$\zeta_{SS}^{SrDs} < \left[\log_2 \left(\frac{1 + \kappa_1 \max_{r \in \{1, \dots, R\}} \{|h_{SrM, r}|^2\}}{1 + \kappa_1 |h_{SrEv}|^2} \right) \right]^+ \quad (16)$$

It is also simplified as shown in Eq. (17) (Bao, Trung, and Debbah 2013).

$$\psi : \gamma_{SrDs} < \max_{r \in \{1, \dots, R\}} \gamma_{SrM}^r \quad (17)$$

AORS is designed through the implementation of the incremental selection of an optimal relay for maximizing the secrecy capacity while satisfying the ψ .

4. Optimal Relay Number Selection Model in Vehicular Networks

The relay selection strategy in vehicular networks is explained below and also the development of D-CSO-based relay selection is depicted here.

4.1. Relay Selection Strategy

An optimal relay selection is carried out in the proposed vehicular networks through D-CSO to enhance the performance of the communication. In this section, the general relay selection strategy is discussed here. This scheme considers two modules like “control module and transmission module”. While considering the control module, the source verifies whether the buffer is empty or not. If it is empty, then it is kept idle, or else the control frames termed handshake messages are broadcasted by the source node for transmission. Once receiving the handshake messages by destination node from the source node, the handshake messages are exchanged by destination via advanced positioning techniques like inertial measurement unit (IMU), assisted GPS, GPS, and differential GPS, and then, it computes the r^* relays for participating in the cooperation by considering the “communication distance” among the source and destination.

On the other hand, in the transmission module, the data frames are transmitted by source in the way of omnidirectional broadcast while the data frame is decoded accurately by destination. Then, a new data frame is transmitted by the source in the consequent automatic repeat request (ARQ) round. In another case, the destination examines the ARQ round q , if it is lesser than the maximum value Q , then the retransmission phase is carried out in the system, or else a negative acknowledgment is forwarded back through the destination and further, q is assigned to 0. The relays perform in DF mode in the retransmission phase, where the data frame broadcasted by the source node is successfully decoded by p -out of relays r^* . Next, the retransmission of the data frame is done through the source node in the next ARQ round when $p = 0$ or else the data frames are transmitted directionally to the destination by p -relays, where $r = 1, 2, 3, \dots, p$. Likewise, until Q is reached or receives an acknowledgment from the destination, p -relays will not stop retransmission.

4.2. Proposed D-CSO-Based Relay Selection

The relay selection is carried out through the D-CSO algorithm due to its several features for maximizing the efficiency of vehicular networks.

Counts of Dimension to Change (CDC) in existing CSO (Bouzidi, Riffi, and Barkatou 2019) algorithm are defined by how many dimensions are altered with the interval of $[0, 1]$. CDC is developed according to the ratio between the latest fitness and worst fitness solutions. CSO has the ability for attaining accurate solutions with better balancing between the exploration and exploitation stages. It is utilized for resolving the premature convergence problem, owing to these advanced features CSO (Jose et al. 2014) is selected for this research work. Here, the D-CSO algorithm is initiated by calculating the CDC according to the latest and worst solutions.

CSO is one of the robust optimization algorithms (Jose et al. 2014; Jagadeeshwar et al. 2022) that get winning performance, where cat (solution) behaviors in resting and tracing modes decide the solution updating. The solution contains two modes such as seeking and tracing modes, here every solution denoted the cat with a fitness value and a flag, and its location. In this process, the location is a DS – dimension; here the flag is finalized whether the cat is in a seeking or a tracing mode. The fitness value represents the solution set and each dimension contains its velocity. At first, the count of cats is decided for each iteration, where the best cat is saved in the memory. The result is obtained by cats at the end of the iteration. The following steps help to find the accurate solution for the D-CSO algorithm (Illuri and Jose 2021; Jagadeeshwar et al. 2022). At first, the lower and upper bounds for the solution sets are described.

Then, the cats are classified based on the mixture ratio which is chosen in the bounding limit of $[0, 1]$. Then, the fitness value is evaluated for all the cats by taking the domain-specific fitness function. Then, the optimal cat is selected and stored in memory. Next, the cats are moved toward either tracing or seeking a model. Once forwarding the cats into either of the modes, the cats are randomly redistributed into seeking or tracing models through a mixture ratio. Finally, the termination condition is checked. When it is satisfied, then the program is terminated others the steps are repeated”.

“*Seeking Mode*”: It represents the resting nature of cats with the help of parameters like “Self-Position Considering (SPC), CDC, Seeking Range of the selected Dimension (SRD), and Seeking Memory Pool (SMP)”. SRD represents the mutative ratio for chosen dimensions, which is defined as the count of mutation and alterations for those dimensions, which are chosen by the CDC. Then, SMP shows the size of seeking memory for cats, which describes the “number of candidate positions in which one of them is going to be selected by the cat to go to”. Some of the steps of seeking mode in CSO are given here.

Initially, create several copies of SMP with the recent position of CT_j . Several CDC dimensions are mutated based on Eq. (18).

$$CDC = \frac{fit(k)}{worstfit(k)} \quad (18)$$

Moreover, arbitrarily, the SRD values are added or subtracted from “the current values to replace the old positions” as derived in Eq. (19).

$$Y_{kdsnew} = Y_{kdsold} * (1 + rn * SRD) \quad (19)$$

The arbitrary number is specified as rn that lies in the bounding limit of $[0, 1]$, the dimensions are represented as ds , the count of a cat is shown by k , Y_{kdsnew} derives the next location of cat and Y_{kdsold} derives the present location of cats.

The whole search agent locations are determined according to the fitness value. Choose one of the search agent’s solutions as the next location for the cat that is performed by probability, where the selection is performed by considering the higher fitness values as derived in Eq. (20).

$$\rho = \frac{|fit_i - fit_c|}{fit_{max} - fit_{min}} \quad (20)$$

When whole fitness values are similar, the complete selection probability is assigned for every candidate point to be 1. While taking the objective as the minimization, then the solution is taken as $fit_c = fit_{max}$ or else $fit_c = fit_{min}$, where $0 < i < k$.

“*Tracking Mode*”: It uses the tracing behavior of cats. At initial iterations, velocity values are randomly specified to the entire dimensions of the position of the cat. Though, there is a need of updating the velocity values for upcoming steps. Moving cats in the tracing mode are given here. Eq. (21) is used for updating the velocities for entire dimensions.

$$\vartheta_{j,ds} = \vartheta_{j,ds} + rs_1 cn_1(Y_{best,ds} - Y_{j,ds}) \quad (21)$$

If the velocity value is high, then it is similar to the highest velocity rate. Then, it updates the location CT_j through Eq. (22).

$$Y_{j,ds} = Y_{j,ds} + \vartheta_{j,ds} \quad (22)$$

Thus, the solution updating is carried out based on the seeking and tracing modes, where CDC is updated in the D-CSO algorithm based on fitness values. This modification results in getting optimal values and attaining a faster convergence rate for optimal relay selection in vehicular networks. The pseudo-code of the introduced D-CSO algorithm is shown in Algorithm 1.

Algorithm 1: Proposed D-CSO

```

Determine cat population and constraints
Formulate the fitness of whole solutions
Calculate CDC based on the recent fitness and worst fitness solutions
using Eq. (18)
Find the distance covered accurate and current search agents and average
distance
Evaluation of cats according to the fitness function
It  $CT_j$  is in the seeking mode
    Solution update by Eq. (19), according to seeking mode
else
    Solution update by Eq. (22), based on tracing mode
End if
Reallocate “the number of cats and assigned them into tracing mode
through mixture ratio and assign others to seek mode”
End for
End while
    Calculate fitness of all solution
    Upgrade best fitness value
end while
Return accurate solutions

```

The flow diagram of D-CSO is depicted in Figure 2.

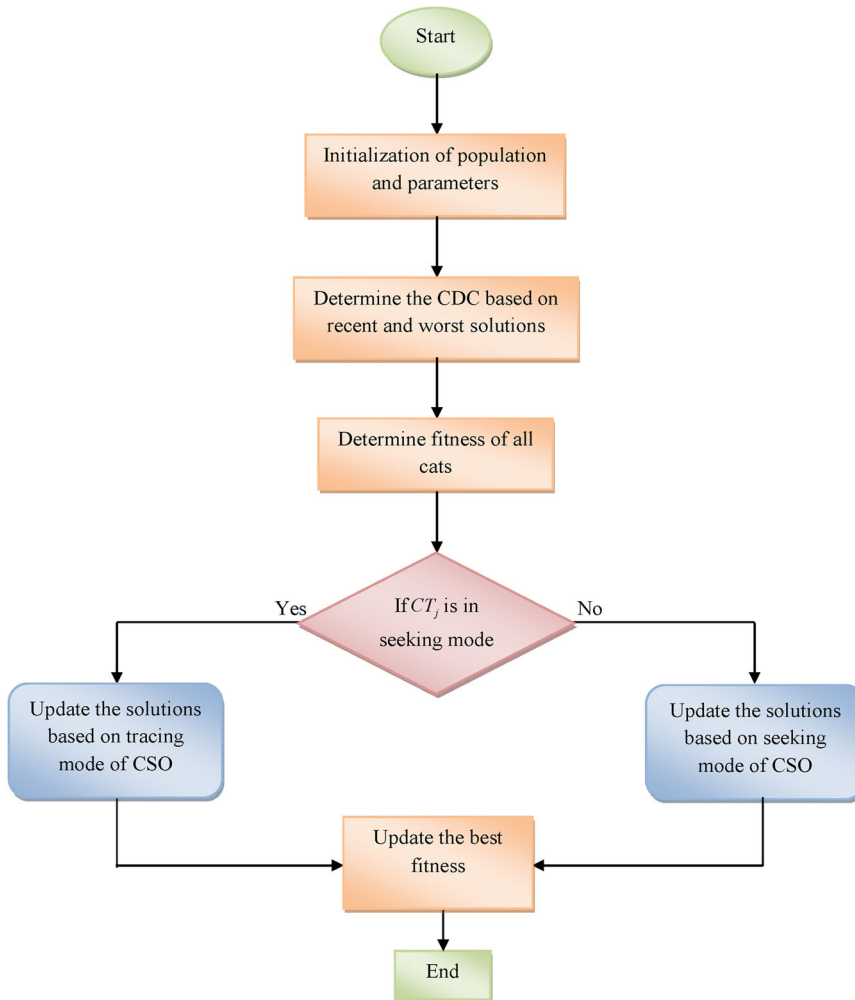


Figure 2. Flow diagram of the designed D-CSO algorithm.

5. Suggested Relay Selection Strategy in Vehicular Networks Based on Outage Probability and Throughput

Here, the suggested relay optimization process and the outage probability computation are formulated. Finally, the computation of throughput is explained in this section.

5.1. Proposed Relay Optimization

The relay optimization in the designed vehicular networks is carried out through the D-CSO algorithm by resolving the fitness functions like reduction of outage probability and maximization of throughput. The solution encoding of relay selection before and after optimization is given in Figure 3.

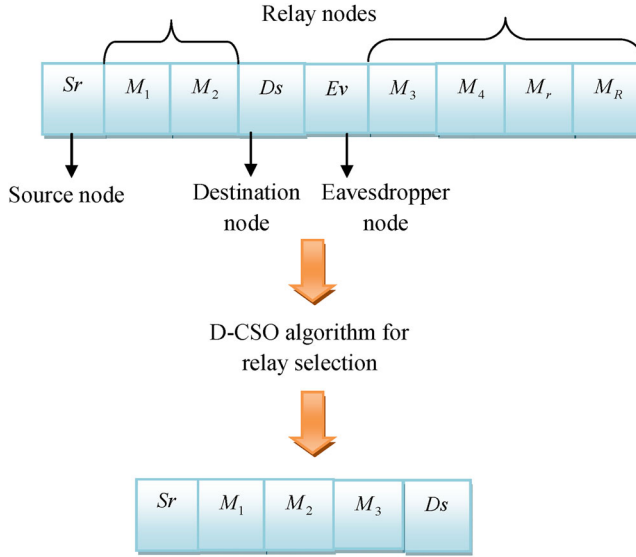


Figure 3. Optimal relay selection before and after encoding using the D-CSO algorithm.

The multi-hop selection is carried out by the D-CSO algorithm, where the unwanted relay nodes are removed from the networks through this D-CSO algorithm. The optimal relay nodes for solving the multi-objective function are chosen in Figure 3. Thus, the multi-hop selection is carried out through the D-CSO algorithm. The main scope of the introduced method is derived in Eq. (23).

$$fit = \underset{\{M_r\}}{\operatorname{argmin}} \left(OP_{out} + \frac{1}{Th} \right) \quad (23)$$

The mean count of relays is indicated as M_r the optimal relays selected with the help of the D-CSO algorithm for improving the efficiency of the vehicular networks to eliminate the entire computational complexity. The range M_r is assigned among $[1, R]$. In Eq. (23), outage probability is denoted as OP_{out} and throughput is termed as Th . These constraints are explained in upcoming sections.

5.2. Outage Probability Computation

Assume the “outage probability” of the data link with signaling rate $asrt$, the transmitted signal is considered as a with a “Signal-to-Noise Ratio (SNR)” of γ , is formulated in Eq. (24).

$$\begin{aligned} OP_{out} &= OP\{J(a; b|fh) < rt\} \\ &= OP\{\log_2(1 + \gamma|fh|^2) < rt\} \end{aligned} \quad (24)$$

In Eq. (24), the fading coefficient is noted as fh , the received signal is given as b , and the outage events that occur on link source to relay and source to destination with and without complete reception at relays in the q^{th} ARQ round are represented as $SrM_{out,q}$, $SrMDS_{out,q}$ and $SrDs_{out,q}$, respectively. Further, the following assumptions are considered for simplifying the process, which is $d_{M_1D_s} \neq d_{M_2D_s} \neq \dots \neq d_{M_R D_s}$ and $d_{SrM_1} = d_{SrM_2} = \dots = d_{SrM_R} = d_{SrM}$, where the expectation is given as $EX[\cdot]$. Moreover, it is observed that $EX\left[|fh_{ij,q}|^2\right]$, in which the node pair is given as (i,j) , which is also represented as $EX[\omega_{ij,q}]$ that is proportional to $d_{ij}^{-\beta}$, the path loss factor is termed as β , and the “probability of above outage events” is formulated with AWGN communication scenario in the “Nakagami-m short-term static fading channel”.

Equation (25) depicts the transmission of links source to relay has failed or outage happens for q^{th} ARQ round.

$$\begin{aligned} OP(SrM_{out,q}) &= \prod_{us=1}^q OP\{\log_2(1 + \gamma|fh_{SrM,us}|^2) < rt\} \\ &= \prod_{us=1}^q OP\{\omega_{SrM,us} < \varepsilon\} \\ &= \prod_{us=1}^q DF_{\omega_{SrM,us}}(\varepsilon) \end{aligned} \quad (25)$$

Here, Eq. (26) indicates the transmission of link source-destination that has been assisted by p - relays, which has failed for q^{th} ARQ rounds.

$$\begin{aligned} OP(SrMDS_{out,q}) &= \prod_{us=1}^{T_M^p} OP\{\log_2(1 + \gamma|fh_{SrDs,us}|^2) < rt\} \\ &\quad \times \prod_{vs=T_M^p+1}^q OP\left\{\log_2\left(1 + \sum_{t=1}^p \gamma|fh_{M_tD_s,vs}|^2\right) < rt\right\} \\ &= \prod_{us=1}^{T_M^p} OP\{\omega_{SrDs,us} < \varepsilon\} \cdot \prod_{vs=T_M^p+1}^q OP\left\{\sum_{t=1}^p \omega_{M_tD_s,vs} < \varepsilon\right\} \end{aligned} \quad (26)$$

Equation (27) depicts the transmission of links source to the destination have failed or outage happens for q^{th} ARQ round.

$$\begin{aligned}
OP(SrDs_{out,q}) &= \prod_{us=1}^q OP\{\log_2(1 + \gamma |fh_{SrDs,us}|^2) < rt\} \\
&= \prod_{us=1}^q OP\{\omega_{SrDs,us} < \varepsilon\} = \prod_{us=1}^q DF_{\omega_{SrDs,us}}(\varepsilon)
\end{aligned} \tag{27}$$

In the aforementioned equations, the ‘‘Cumulative Distribution Function (CDF)’’ of the arbitrary term A is shown as $DF_A(a)$, where $\varepsilon \sim \frac{2^{rt}-1}{\gamma}$, and the modules of power intensity gain matrixes $W_{SrM} = [\omega_{Sr,1}, \omega_{Sr,2}, \dots, \omega_{Sr,Q}]_{1 \times Q}$,

$$\begin{aligned}
W_{SrDs} &= [\omega_{SrDs,1}, \omega_{SrDs,2}, \dots, \omega_{SrDs,Q}]_{1 \times Q} \\
\text{and } \omega_{MDs} &= \begin{bmatrix} \omega_{M_1Ds,1} & \omega_{M_1Ds,2} & \cdots & \omega_{M_1Ds,Q} \\ \omega_{M_2Ds,1} & \omega_{M_2Ds,2} & \cdots & \omega_{M_2Ds,Q} \\ \vdots & \cdots & \cdots & \vdots \\ \omega_{M_RDs,1} & \omega_{M_RDs,2} & \cdots & \omega_{M_RDs,Q} \end{bmatrix}_{R \times Q} \quad \text{are indicated as}
\end{aligned}$$

$\omega_{SrM,us}$, $\omega_{SrDs,us}$, and $\omega_{M_iDs,vs}$, respectively.

The p –out-of-neighbor nodes in the vehicular networks that decode the ‘‘data frame for the first time’’ in the T_M^p ARQ round are represented by T_M^p . Further, the probability T_M^p is determined in Eq. (28).

$$OP(T_M^p = t) = \binom{R}{p} [OP(SrM_{out,t-1}) - OP(SrM_{out,t})]^k \cdot OP^{(R-k)}(SrM_{out,t}) \tag{28}$$

This derivation means that p –out of R relays ‘‘will not properly decode the frame transmitted from source’’ until the t^{th} ARQ round. A ‘‘Gamma random variable with parameter’’ $(o_{ij}, \frac{\Omega_{ij}}{o_{ij}})$ is denoted as $\omega_{ij,q}$. Thus, Eq. (26) is determined the CDF of the total of p ‘‘independents but not essentially same (i.n.i.d) Gamma arbitrary terms’’ with the solution of $OP\{\sum_{t=1}^p \omega_{M_tDs,vs} < h\}$. Representing $\xi_1, \xi_2, \dots, \xi_p$ as p (i.n.i.d) Gamma arbitrary terms with constraints of o_t , and Ω_t , where $t = 1, 2, \dots, p$. In addition, the ‘‘Probability Distribution Function (PDF)’’ and CDF of X is derived in the following equations by considering the $X = \sum_{t=1}^p \xi_t$.

$$df_X(x) = \prod_{t=1}^p \left(\frac{o_t}{\Omega_t}\right)^{o_t} GF_{\delta,\delta}^{\delta,0} \left[\exp(-x) \left| \begin{matrix} \lambda \\ \delta \\ \delta \end{matrix} \right. \begin{matrix} (1) \\ (2) \\ (2) \end{matrix} \right] \tag{29}$$

$$DF_X(x) = \prod_{t=1}^p \left(\frac{o_t}{\Omega_t}\right)^{o_t} GF_{\delta+1,\delta+1}^{\delta+1,0} \left[\exp(-x) \left| \begin{matrix} \lambda \\ \delta \\ \delta \end{matrix} \right. \begin{matrix} (1) \\ (2) \\ (2) \end{matrix} \right] \tag{30}$$

Here, the Meiger-G function (Gradshteyn and Ryzhik 2007) is derived in Eq. (31) and an integer is given as $\delta = \sum_{t=1}^p o_t$.

$$GF_{po, qo}^{ks, ls} \left[\mu \left| \begin{matrix} \lambda_{\delta}^{(1)} \\ \lambda_{\delta}^{(2)} \end{matrix} \right. \right] = GF_{po, qo}^{ks, ls} \left[\mu \left| \begin{matrix} x_1, x_2, \dots, x_{p_o} \\ y_{s_1}, y_{s_2}, \dots, y_{s_{q_o}} \end{matrix} \right. \right]$$

$$= \frac{1}{2\pi i} \int_{Ch} \frac{\prod_{j=1}^o \Gamma(y_{s_j} - su) \cdot \prod_{j=1}^R \Gamma(1 - x_j + su)}{\prod_{j=o+1}^{q_o} \Gamma(1 - y_{s_j} + su) \cdot \prod_{j=R+1}^{p_o} \Gamma(x_j - su)} \mu^{su} dsu \quad (31)$$

The integral path is denoted as Ch , which is dependent on the relative size of the constraints. In the aforementioned equations, the Gamma function is derived as $\Gamma(\cdot)$, terms $\lambda_{\delta}^{(1)}$ and $\lambda_{\delta}^{(2)}$ are expressed in Eqs. (32) and (33), respectively.

$$\lambda_{\delta}^{(1)} = \overbrace{\left(1 + \frac{o_1}{\Omega_1}\right), \dots, \left(1 + \frac{o_1}{\Omega_1}\right), \dots, \left(1 + \frac{o_p}{\Omega_p}\right), \dots, \left(1 + \frac{o_p}{\Omega_p}\right)}^{\delta} \quad (32)$$

$$\lambda_{\delta}^{(2)} = \overbrace{\left(\frac{o_1}{\Omega_1}\right), \dots, \left(\frac{o_1}{\Omega_1}\right), \dots, \left(\frac{o_p}{\Omega_p}\right), \dots, \left(\frac{o_p}{\Omega_p}\right)}^{\delta} \quad (33)$$

Moreover, the average power is given as $\Omega_t \neq \Omega_q (t, q = 1, 2, 3, \dots, p, t \neq q)$ and then, Eq. (34) specifies the Rayleigh fading channel or the PDF of the sum of p exponential random variables can be obtained.

$$df_X^{Rayleigh}(x) = \frac{1}{\prod_{t=1}^p \Omega_t} GF_{p,p}^{p,0} \left[\exp(-x) \left| \begin{matrix} 1 + \frac{1}{\Omega_1}, \dots, 1 + \frac{1}{\Omega_1} \\ \frac{1}{\Omega_1}, \dots, \frac{1}{\Omega_1} \end{matrix} \right. \right] \quad (34)$$

Equation (34) can be modified through the Meijer-G identity as given in Eq. (35).

$$df_X^{Rayleigh}(x) = \sum_{t=1}^p \left(\prod_{su \neq t} \frac{\frac{1}{\Omega_{su}}}{\frac{1}{\Omega_{su}} - \frac{1}{\Omega_t}} \right) \frac{1}{\Omega_t} \exp\left(-\frac{x}{\Omega_t}\right) \quad (35)$$

Thus, the outage probability for all data links is attained.

5.3. Throughput Computation

The network throughput is described as the mean count of data frames accurately transferred by the target point in one time period, in which the

mean “Discrete-Time Markov Chain (DTMC)” method in the initial point state can be related to the “steady-state probability” of state initial point. Thus, the steady probability of state initial point is given as π_{Sr} , and the steady-state distribution of the 3-D DTMC model is given as $\pi = (\pi_{Sr}, \pi_1, \dots, \pi_{DF})$. It is observed that throughput π_{Sr} is a binary function of Q and R . It can be formulated as $\begin{cases} \pi \cdot PO = \pi \\ \sum \pi = 1 \end{cases}$ and PO is a state transition probability vector of all one-step transition probability, which is derived as $\left[(Q+1) + R \sum_{i=1}^{Q-1} i \right] \times \left[(Q+1) + R \sum_{i=1}^{Q-1} i \right]$. Additionally, throughput $Th \leftarrow \pi_{Sr}$ is determined in Eq. (36).

$$Th = \pi_{Sr}(Q, R) = \frac{1 - FErr(Q, R)}{fh(Q, R)} \quad (36)$$

In Eq. (36), a binary function (Q, R) is denoted as $fh(Q, R)$ and the system frame fault rate is formulated as $FErr(Q, R)$, which are expressed below.

$$FErr(Q, R) = \begin{cases} OP_{SrM_{1,0,0}} \cdot OP_{M_{1,0,0}DF} \\ + \sum_{p=1}^R OP_{SrM_{1,p,0}} \cdot OP_{M_{1,p,0}DF}, & Q = 2 \\ Eq.(39), & Q \geq 3 \end{cases} \quad (37)$$

$$fh(Q, R) = \begin{cases} 1 + OP_{SrM_{1,0,0}} + \sum_{p=1}^R OP_{SrM_{1,p,0}}, & Q = 2 \\ Eq.(40), & Q \geq 3 \end{cases} \quad (38)$$

$$FErr(Q, R) = OP_{SrM_{1,0,0}} \cdot \prod_{i=1}^{Q-2} [OP_{M_{i,0,0}M_{i+1,0,0}}] \cdot OP_{M_{Q-1,0,0}DF} \\ + \sum_{p=1}^R OP_{SrM_{1,p,1}} \cdot \prod_{i=1}^{Q-2} [OP_{M_{i,p,i}M_{i+1,p,i+1}}] \cdot OP_{M_{Q-1,p,Q-1}DF} \\ + \sum_{p=1}^R \left(\begin{array}{c} \sum_{T_M^p=2}^{Q-1} \left(\begin{array}{c} OP_{SrM_{1,0,0}} \cdot \prod_{i=1}^{T_M^p-2} [OP_{M_{i,0,0}M_{i+1,0,0}}] \\ \cdot OP_{M_{T_M^p-1,0,0}M_{T_M^p-1,p,1}} \\ \cdot \prod_{i=T_M^p-2, j=Q-T_M^p-1}^{Q-1} [OP_{M_{i,p,j}M_{i+1,p,j+1}}] \\ \cdot \prod_{i=T_M^p, j=1}^{T_M^p-1} OP_{M_{Q-1,p,Q-T_M^p}DF} \end{array} \right) \end{array} \right) \quad Q \geq 3 \quad (39)$$

$$\begin{aligned}
& fh(Q-1, R) + OP_{Sr_1, 0, 0} \cdot \prod_{i=1}^{Q-2} [OP_{M_i, 0, 0} M_{i+1, 0, 0}] \\
& + \sum_{p=1}^R OP_{Sr_{M_1, p, 1}} \cdot [OP_{M_i, p, j} M_{i+1, p, i+1}] \\
fh(Q, R) = & \left(\begin{aligned}
& \sum_{T_M^p=2}^{Q-1} OP_{Sr_{M_1, 0, 0}} \cdot \prod_{i=1}^{T_M^p-2} [OP_{M_i, 0, 0} M_{i+1, 0, 0}] \cdot \\
& OP_{M_{(T_M^p-1), 0, 0} M_{T_M^p, p, 1}} \\
& \prod_{i=Q-2, j=Q-T_M^p-1}^{i=T_M^p, j=1} [OP_{M_i, p, j} M_{i+1, p, j+1}]
\end{aligned} \right) \quad Q \geq 3 \quad (40)
\end{aligned}$$

Thus, throughput can be obtained using Eq. (36) by substituting Eq. (37) with Eq. (40).

6. Results

This section explores the efficiency of the design in terms of various measures and it is discussed clearly.

6.1. Experimental Setup

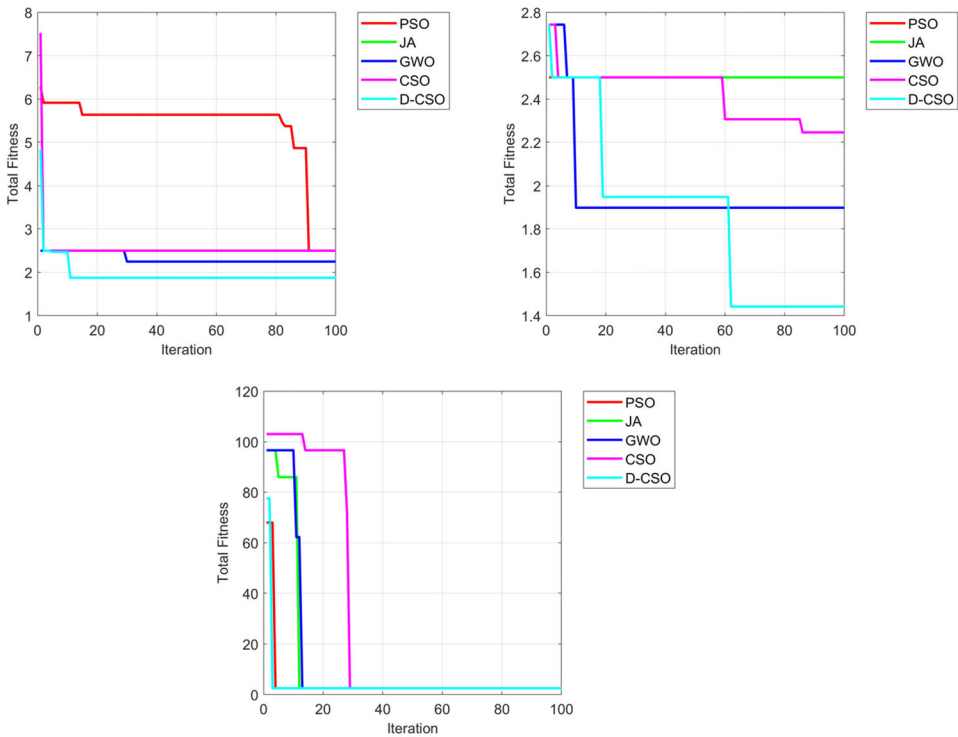
The proposed multi-hop selection in-vehicle networks were implemented in MATLAB 2020a, and the efficiency of the designed system was compared to the existing heuristic algorithms like particle swarm optimization (PSO) (Ai and Kachitvichyanukul 2009), Jaya Algorithm (JA) (Rao 2016), gray wolf optimizer (GWO) (Mirjalili, Mirjalili, and Lewis, 2014), and CSO (Bouzidi, Riffi, and Barkatou 2019) in terms of convergence analysis, throughput analysis, outage probability analysis, and statistical analysis. The simulation was managed by taking the three cases by differing the number of nodes as [50, 100, and 150]. The simulation parameters considered for the experimentation are given in Table 2.

6.2. Convergence Evaluation

The convergence evaluation of the designed multi-hop selection in-vehicle networks for the three test cases by differing the number of nodes is depicted in Figure 4. While considering case 1, at initial iterations, the highest fitness rate is observed by D-CSO as like other algorithms. At the 10th iteration, the lowest cost function with superior performance is noticed by D-CSO while

Table 2. Experimental constraints used for simulation in vehicular networks.

S.no	Symbols	Parameters	Values
1.	M	Number of nodes	[50, 100, 150]
2.	R	Number of relay nodes	50
3.	γ	Instantaneous SNR	105 dB
4.	rt	Outage probability of the data link with a signaling rate	0.5 bits/slot/Hz
5.	N_{pop}	Number of population	10
6.	–	Communication range of antennas	1000 m
7.	R	Relays	[1, 10]
8.	P	Binary function	5 frames/s
9.	Q	Binary function	2, 3
10.	Max_{iter}	Total number of iterations	100

**Figure 4.** Convergence evaluation of the designed Multi-hop Selection in Vehicular Networks with different heuristic algorithms in terms of (a) test case 1, (b) test case 2, and test case 3.

compared with other techniques. Similarly, for case 2, the highest fitness rate is observed at initial iterations, but the lowest fitness with a high-performance rate is attained by D-CSO at the 60th iteration only. Likewise, for case 3, the D-CSO gets the highest convergence rate at initial rates itself. From the analysis, for case 1, at the 100th iteration, the D-CSO correspondingly obtains 28%, 25%, 18%, and 28% superior to PSO, JA, GWO, and CSO. Therefore, elevated convergence behavior is observed by D-CSO for all the test cases.

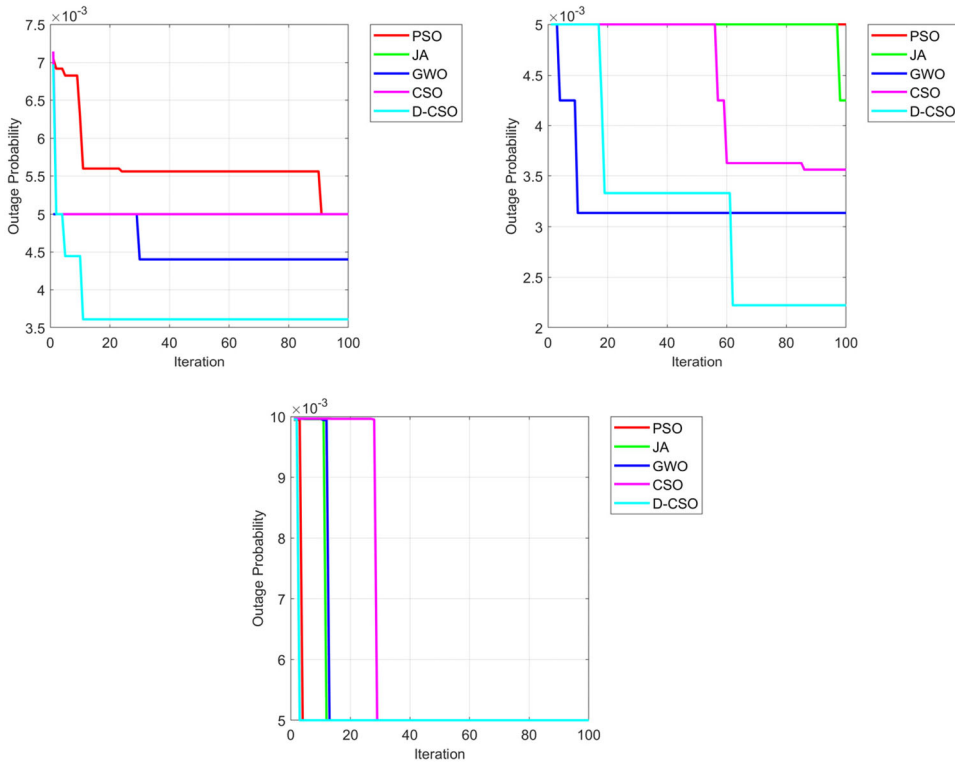


Figure 5. Analysis of outage probability of the designed Multi-hop Selection in Vehicular Networks with different heuristic algorithms in terms of (a) test case 1, (b) test case 2, and test case 3.

6.3. Analysis of Outage Probability

The proposed multi-hop selection in vehicular networks is validated regarding outage probability for three test cases as shown in Figure 5. The highest performance is observed by D-CSO by getting the lowest outage probability. Thus, for the first case, at the 10th iteration, the lowest rate with superior performance is attained by the D-CSO algorithm. While considering case 2, the D-CSO specifies the higher performance at the 60th iteration only. But, after that, consistent performance is observed by the proposed model than others. Likewise, for case 3, better performance is observed by D-CSO at initial iterations itself. However, all the other algorithms also show similar performance. Hence, in the future, it has to be improved for performance enhancement.

6.4. Analysis of Throughput

The efficiency of the suggested vehicular networks is verified regarding throughput for three test cases as given in Figure 6. The highest rate by D-CSO ensures the better efficiency of the developed multi-hop selection

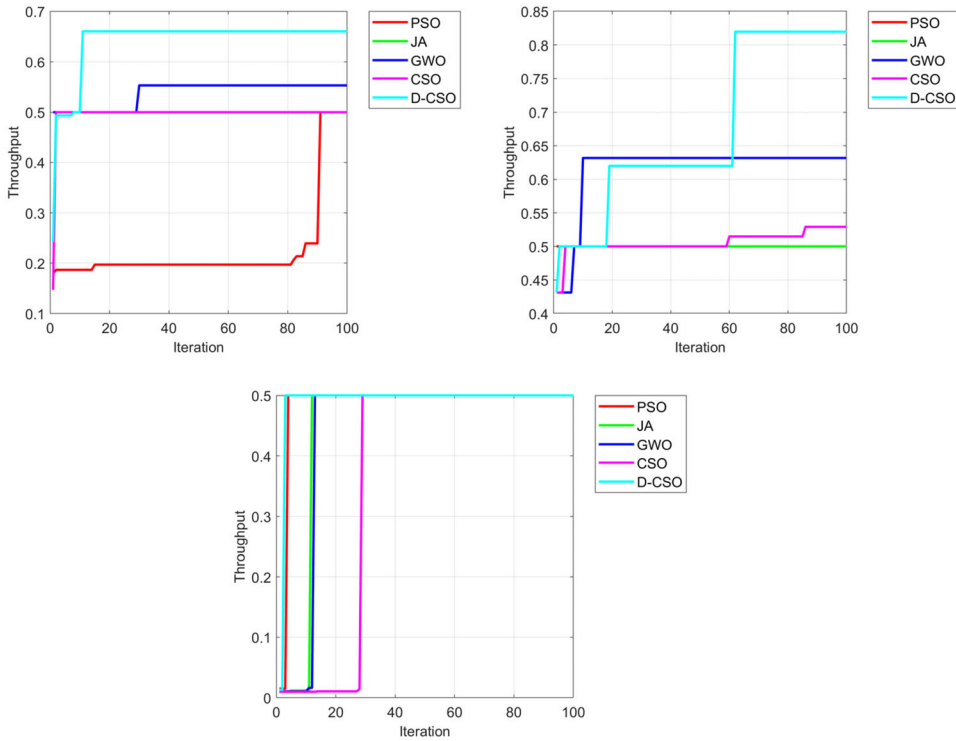


Figure 6. Analysis of throughput of the designed Multi-hop Selection in Vehicular Networks with different heuristic algorithms in terms of (a) test case 1, (b) test case 2, and test case 3.

Table 3. Statistical evaluation of the suggested Multi-hop Selection in Vehicular Networks over different heuristic algorithms for three test cases.

Algorithms	Best	Worst	Mean	Median	Standard deviation
Test case 1					
PSO (Ai and Kachitvichyanukul 2009)	2.50	6.28	0.97	5.63	5.31
JA (Rao 2016)	2.50	2.50	0.00	2.50	2.50
GWO (Mirjalili, Mirjalili, and Lewis 2014)	1.88	4.83	0.34	1.88	1.96
CSO (Bouzidi, Riffi, and Barkatou 2019)	2.50	7.51	0.50	2.50	2.55
D-CSO	2.25	2.50	0.11	2.25	2.32
Test case 2					
PSO (Ai and Kachitvichyanukul 2009)	2.50	2.50	0.00	2.50	2.50
JA (Rao 2016)	2.50	2.74	0.04	2.50	2.51
GWO (Mirjalili, Mirjalili, and Lewis, 2014)	1.44	2.74	0.39	1.95	1.85
CSO (Bouzidi, Riffi, and Barkatou 2019)	2.25	2.74	0.12	2.50	2.42
D-CSO	1.90	2.74	0.22	1.90	1.97
Test case 3					
PSO (Ai and Kachitvichyanukul 2009)	2.50	67.93	1.22	2.50	4.46
JA (Rao 2016)	2.50	96.62	7.52	2.50	12.11
GWO (Mirjalili, Mirjalili, and Lewis 2014)	2.50	77.50	0.55	2.50	3.99
CSO (Bouzidi, Riffi, and Barkatou 2019)	2.50	103.00	3.53	2.50	29.44
D-CSO	2.50	96.62	9.21	2.50	13.11

method in terms of throughput. Thus, for test case 1, the higher performance is noticed by the 10th iteration itself, while compared with other algorithms. In case 2, the D-CSO observes the highest performance at 60th iterations, and then, reliable and noteworthy performance is noticed by

evaluating existing algorithms. For test case 3, the highest performance is attained by the third iteration and then, similar performance is noticed by all the algorithms. For test case 3, at the 100th iteration, the D-CSO method correspondingly shows the highest throughput by 28%, 64%, 28%, and 50% progressed than PSO, JA, GWO, and CSO. Hence, the maximum performance is observed by D-CSO-based multi-hop selection in vehicular networks when compared with other algorithms.

6.5. Statistical Analysis

The statistical evaluation of the introduced multi-hop selection in vehicular networks is shown in Table 3. The mean is the average value of the best and worst values and the median is referred to as the center point of the best and worst values whereas the standard deviation is represented as the degree of deviation between each execution. The performance of the suggested D-CSO is correspondingly secured at 88.6%, 67.6%, and 78% more advanced than the PSO, GWO, and CSO for test case 1. Similarly, while taking test case 2, the performance of the suggested D-CSO is correspondingly secured at 81%, 43%, and 83.3% more advanced than the JA, GWO, and CSO. Likewise, for test case 3, the outperformance is noticed by D-CSO-based multi-hop selection in vehicular networks.

7. Conclusion

This work has designed and optimization method for the cooperative VANET networks to choose the minimum number of multi-hops among the initial pint and the target point using the D-CSO algorithm. This algorithm has optimally selected the number of hops or relays for effective communication, with the help of the multi-objective function concerning the system throughput and outage probability. Through the performance evaluation, D-CSO-based multi-hop selection with a cooperative mechanism was evaluated, where the performance of D-CSO was 36%, 42%, 25.2%, and 36% more advanced than PSO, JA, GWO, and CSO, respectively, for case 2 at 100th iteration. Thus, finally, superior performance was observed by D-CSO for all three test cases when compared with other heuristic algorithms. However, the equivalent performance was observed for both tests case 2 and test case 3 by D-CSO with other algorithms also.

References

- Abdulhadi, S., M. Jaseemuddin, and A. Anpalagan. 2012. A survey of distributed relay selection schemes in cooperative wireless ad hoc networks. *Wireless Personal Communications* 63 (4):917–35. doi:10.1007/s11277-010-0174-6.

- Achour, I., F. Alfayez, and A. Busson. 2021. A robust and efficient adaptive data dissemination protocol based on smart relay selection in vehicular networks. *Wireless Networks* 27 (7):4497–511. doi:10.1007/s11276-021-02726-8.
- Adam, H., E. Yanmaz, and C. Bettstetter. 2014. Medium access with adaptive relay selection in cooperative wireless networks. *IEEE Transactions on Mobile Computing* 13 (9): 2042–57. doi:10.1109/TMC.2013.97.
- Agrawal, S., N. Tyagi, A. Iqbal, and R. S. Rao. 2020. An intelligent greedy position-based multi-hop routing algorithm for next-hop node selection in VANETs. *Proceedings of the National Academy of Sciences, India Section A: Physical Sciences* 90 (1):39–47. doi:10.1007/s40010-018-0556-9.
- Ai, T. J., and V. Kachitvichyanukul. 2009. A particle swarm optimization for the vehicle routing problem with simultaneous pickup and delivery. *Computers & Operations Research* 36 (5):1693–702. doi:10.1016/j.cor.2008.04.003.
- Akin, A. I., H. Ilhan, and Ö. Özdemir. 2015. Relay selection for DF-based cooperative vehicular systems. *EURASIP Journal on Wireless Communications and Networking* 2015: 30. doi:10.1186/s13638-015-0251-3.
- Bao, V. N. Q., N. L. Trung, and M. Debbah. 2013. Relay selection schemes for dual-hop networks under security constraints with multiple eavesdroppers. *IEEE Transactions on Wireless Communications* 12 (12):6076–85. doi:10.1109/TWC.2013.110813.121671.
- Bouzidi, A., M. E. Riffi, and M. Barkatou. 2019. Cat swarm optimization for solving the open shop scheduling problem. *Journal of Industrial Engineering International* 15 (2): 367–78. doi:10.1007/s40092-018-0297-z.
- Dan, C., J. I. Hong, L. I. Xi, and L. I. Yi. 2010. QoS-guaranteed multi-relay selection and power allocation optimization in cooperative systems. *The Journal of China Universities of Posts and Telecommunications* 17 (6):25–31. doi:10.1016/S1005-8885(09)60521-5.
- Dan, C., J. I. Hong, L. I. Xi, and L. I. Yim. 2011. Energy-efficient joint relay node selection and power allocation over multihop relaying cellular networks toward LTE-advanced. *The Journal of China Universities of Posts and Telecommunications* 18 (3):1–7. doi:10.1016/S1005-8885(10)60055-6.
- Dong, L., Z. Han, A. P. Petropulu, and H. V. Poor. 2010. Improving wireless physical layer security via cooperating relays. *IEEE Transactions on Signal Processing* 58 (3):1875–88. doi:10.1109/TSP.2009.2038412.
- Feng, H., Y. Xiao, and L. J. Cimini. 2014. Net throughput of centralized and decentralized cooperative networks with relay selection. *IEEE Wireless Communications Letters* 3 (5): 477–80. doi:10.1109/LWC.2014.2331071.
- Gradshteyn, I. S., and I. M. Ryzhik. 2007. Table of integrals, series and products. *Mathematics of Computation* 20 (96):1157–60. <https://www.sciencedirect.com/book/9780123849335/table-of-integrals-series-and-products>
- Hui, Y., Z. Su, T. H. Luan, and C. Li. 2020. Reservation service: Trusted relay selection for edge computing services in vehicular networks. *IEEE Journal on Selected Areas in Communications* 38 (12):2734–46. doi:10.1109/JSAC.2020.3005468.
- Illuri, B., and D. Jose. 2021. Design and implementation of hybrid integration of cognitive learning and chaotic countermeasures for side channel attacks. *Journal of Ambient Intelligence and Humanized Computing* 12 (5):5427–41. doi:10.1007/s12652-020-02030-x.
- Jagadeeshwar, T., S. Kalyani, P. Rajagopal, and B. Srinivasan. 2022. Statistics-based baseline-free approach for rapid inspection of delamination in composite structures using ultrasonic guided waves. *Structural Health Monitoring* 147592172110733. doi:10.1177/14759217211073335.

- Jose, D., Kumar, P. Nirmal, Shirley, J. Abanah, and Ghayathrie, S. 2014. Implementation of genetic algorithm framework for fault-tolerant system on chip. *International Information Institute (Tokyo). Information; Koganei* 17(8):3921–45.
- Kanithan, S., N. A. Vignesh, E. Karthikeyan, and N. Kumareshan. 2020. An intelligent energy efficient cooperative MIMO-AF multi-hop and relay based communications for Unmanned Aerial Vehicular networks. *Computer Communications* 154:254–61. doi:10.1016/j.comcom.2020.01.029.
- Krikidis, I., J. S. Thompson, and S. M. Laughlin. 2009. Relay selection for secure cooperative networks with jamming. *IEEE Transactions on Wireless Communications* 8 (10): 5003–11. doi:10.1109/TWC.2009.090323.
- Li, J., A. P. Petropulu, and S. Weber. 2011. On cooperative relaying schemes for wireless physical layer security. *IEEE Transactions on Signal Processing* 59 (10):4985–97. doi:10.1109/TSP.2011.2159598.
- Li, S., F. Wang, J. Gaber, and Y. Zhou. 2020. An optimal relay number selection algorithm for balancing multiple performance in flying ad hoc networks. *IEEE Access* 8: 225884–901. doi:10.1109/ACCESS.2020.3044502.
- Lim, K. G., K. W. Teh, M. K. Tan, H. Lago, S. S. Yang, and K. T. Kin Teo. 2021. Enhanced multi-hop mechanism in vehicular communication system using swarm algorithm. 2021 IEEE International Conference on Artificial Intelligence in Engineering and Technology (IICAIET), 1–6. doi:10.1109/IICAIET51634.2021.9573842.
- Mirjalili, S., S. M. Mirjalili, and A. Lewis. 2014. Grey Wolf Optimizer. *Advances in Engineering Software* 69:46–61. doi:10.1016/j.advengsoft.2013.12.007.
- Nam, E., C. Jang, and J. H. Lee. 2015. Performance of reactive relay selection based on cumulative distribution function of SNRs for two-way relay networks. *IEEE Communications Letters* 19 (8):1378–81. doi:10.1109/LCOMM.2015.2441056.
- Nguyen, B. V., R. O. Afolabi, and K. Kim. 2013. Dependence of outage probability of cooperative systems with single relay selection on channel correlation. *IEEE Communications Letters* 17 (11):2060–3. doi:10.1109/LCOMM.2013.090313.131263.
- Okeke, G. O., W. A. Krzymien, Y. Jing, and J. Melzer. 2015. A novel low-complexity joint user-relay detection and association for multi-user multi-relay MIMO uplink. *IEEE Wireless Communications Letters* 4 (3):309–12. doi:10.1109/LWC.2015.2411657.
- Poursajadi, S, and M. H. Madani. 2021. Adaptive optimal relay selection in cooperative vehicular communications under security constraints. *Vehicular Communications* 31: 100360. doi:10.1016/j.vehcom.2021.100360.
- Rao, R. V. 2016. Jaya: A simple and new optimization algorithm for solving constrained and unconstrained optimization problems. *International Journal of Industrial Engineering Computations* 7 (1):19–34. doi:10.5267/j.ijiec.2015.8.004.
- Saghezchi, F. B., A. Radwan, and J. Rodriguez. 2017. Energy-aware relay selection in cooperative wireless networks: An assignment game approach. *Ad Hoc Networks* 56: 96–108. doi:10.1016/j.adhoc.2016.12.001.
- Seyfi, M., S. Muhaidat, J. Liang, and M. Uysal. 2011. Relay selection in dual-hop vehicular networks. *IEEE Signal Processing Letters* 18 (2):134–7. doi:10.1109/LSP.2010.2102017.
- Siddig, A. A., A. S. Ibrahim, and M. H. Ismail. 2020. An optimal power allocation and relay selection full-duplex store-carry-forward scheme for intermittently connected vehicular networks. *IEEE Access* 8:163903–16. doi:10.1109/ACCESS.2020.3020826.
- Singh, A. K., R. Pamula, P. K. Jain, and G. Srivastava. 2021. An efficient vehicular-relay selection scheme for vehicular communication. *Soft Computing* doi:10.1007/s00500-021-06106-4.

- Su, Y., X. Lu, Y. Zhao, L. Huang, and X. Du. 2019. Cooperative communications with relay selection based on deep reinforcement learning in wireless sensor networks. *IEEE Sensors Journal* 19 (20):9561–9. doi:[10.1109/JSEN.2019.2925719](https://doi.org/10.1109/JSEN.2019.2925719).
- Tian, D., J. Zhou, Z. Sheng, M. Chen, Q. Ni, and V. C. M. Leung. 2017. Self-organized relay selection for cooperative transmission in vehicular ad-hoc networks. *IEEE Transactions on Vehicular Technology* 66 (10):9534–49. doi:[10.1109/TVT.2017.2715328](https://doi.org/10.1109/TVT.2017.2715328).
- Wang, W., K. C. Teh, and K. H. Li. 2016. Generalized relay selection for improved security in cooperative DF relay networks. *IEEE Wireless Communications Letters* 5 (1):28–31. doi:[10.1109/LWC.2015.2488660](https://doi.org/10.1109/LWC.2015.2488660).
- Xia, M., and S. Aissa. 2015. Fundamental relations between reactive and proactive relay-selection strategies. *IEEE Communications Letters* 19 (7):1249–52. doi:[10.1109/LCOMM.2015.2418780](https://doi.org/10.1109/LCOMM.2015.2418780).
- Yang, M., D. Guo, Y. Huang, T. Q. Duong, and B. Zhang. 2016. Physical layer security with threshold-based multiuser scheduling in multi-antenna wireless networks. *IEEE Transactions on Communications* 64 (12):5189–202. doi:[10.1109/TCOMM.2016.2606396](https://doi.org/10.1109/TCOMM.2016.2606396).
- Yang, F., J. Han, X. Ding, Z. Wei, and X. Bi. June 2020. Spectral efficiency optimization and interference management for multi-Hop D2D communications in VANETs. *IEEE Transactions on Vehicular Technology* 69 (6):6422–36. doi:[10.1109/TVT.2020.2987526](https://doi.org/10.1109/TVT.2020.2987526).
- Yin, R. 2020. A multi-hop relay based routing algorithm for vehicular visible light communication networks. 2020 12th International Symposium on Communication Systems, Networks and Digital Signal Processing (CSNDSP), 1–6. doi:[10.1109/CSNDSP49049.2020.9249630](https://doi.org/10.1109/CSNDSP49049.2020.9249630).
- Ying, B., and A. Nayak. 2018. A power-efficient and social-aware relay selection method for multi-hop D2D communications. *IEEE Communications Letters* 22 (7):1450–3. doi:[10.1109/LCOMM.2018.2797877](https://doi.org/10.1109/LCOMM.2018.2797877).
- Zhang, L., and L. J. Cimini. 2007. Power-efficient relay selection in cooperative networks using decentralized distributed space-time block coding. *EURASIP Journal on Advances in Signal Processing* 2008 (1). doi:[10.1155/2008/362809](https://doi.org/10.1155/2008/362809).
- Zhao, D., H. Zhao, M. Jia, and W. Xiang. 2014. Smart relaying for selection combining based decode-and-forward cooperative networks. *IEEE Communications Letters* 18 (1): 74–7. doi:[10.1109/LCOMM.2013.112513.132216](https://doi.org/10.1109/LCOMM.2013.112513.132216).
- Zheng, Z., S. Fu, K. Lu, J. Wang, and B. Chen. 2012. On the relay selection for cooperative wireless networks with physical-layer network coding. *Wireless Networks* 18 (6):653–65. doi:[10.1007/s11276-012-0425-4](https://doi.org/10.1007/s11276-012-0425-4).
- Zou, Y., X. Wang, and W. Shen. 2013. Optimal relay selection for physical-layer security in cooperative wireless networks. *IEEE Journal on Selected Areas in Communications* 31 (10):2099–111. doi:[10.1109/JSAC.2013.131011](https://doi.org/10.1109/JSAC.2013.131011).



An intelligent dimension-based cat swarm optimization for efficient cooperative multi-hop relay selection in vehicular network

Uppula Kiran¹ · Krishan Kumar¹ · Ajay Roy¹ · Shamimul Qamar² · Abdul Azeem³

Received: 27 May 2022 / Accepted: 24 March 2023

© The Author(s), under exclusive licence to Springer-Verlag London Ltd., part of Springer Nature 2023

Abstract

A revolutionary concept for enhancing the geographical differentiations in vehicular ad hoc networks (VANET) is cooperation. Similar to multi-antenna systems such as Multiple-Input Multiple-Output (MIMO) systems, cooperative communication systems may enhance performance and geographical diversity. These systems are also easier to develop with dispersed hardware and traditionally constrained resources. In order to boost VANET efficiency with regard to certain network restrictions like energy efficiency (EE), network capacity (NC), and outage probability (OP), more network solutions are inspired by cooperative communication despite the fact that various successful research on VANET coupled with cooperative communications is mentioned, they have certain basic issues that they do not clearly address. This article primary goal is to develop and suggest an optimization technique for choosing the fewest possible multi-hops among source and destination for a cooperative VANET. The signal is transferred from the source to the cooperating nodes (their relays) and to their comparable destination during the first time slot of the first phase. In order to solve a multi-objective function including goal throughput and OP, how to choose the ideal amount of relays or hops to allow for flexible communication is the main problem being tackled here. The selection of the best source and destination multi-hop is significantly aided by the use of the novel Dimension-based Cat Swarm Optimization (D-CSO). The suggested model was shown to have a reasonable convergence rate and a fair performance over the whole network via the performance assessment.

Keywords Cooperative communication · Multi-hop selection · D-CSO · Throughput · OP

✉ Shamimul Qamar
sqamar@kku.edu.sa

Uppula Kiran
kiranuday411@gmail.com

Krishan Kumar
krishan.22397@lpu.co.in

Ajay Roy
ajayroy@live.com

Abdul Azeem
azeemnith@gmail.com

¹ Department of ECE, Lovely Professional University, Phagwara, Punjab 144411, India

² Computer Science and Engineering Department, College of Sciences and Arts, King Khalid University, Dhahran Al Janoub Campus, 64261 Abha, Kingdom of Saudi Arabia

³ Electrical Engineering Department, Jamia Millia Islamia University, New Delhi 110025, India

1 Introduction

Due to the capabilities of the physical layer, the development of cooperative communication is predominant as a fresh approach to enhancing security [1, 2]. Between sources and destinations, relay nodes are often utilized to provide the primary connection more capability than a wiretap connection [3]. As a consequence, it is shown that adding more relays is required to maximize the secrecy effectiveness [4]. Another well-known method for enhancing cooperative system performance, whether or not security restrictions are present, is relay selection [5]. Various relay selection approaches have been utilized depending on the eavesdropper's activity or passivity lately. By using the channel state information (CSI) and from the main channel taking into consideration the passive eavesdropper, the relay is chosen using the conventional technique [6]. In this situation, the best relay is chosen

while taking into account the known eavesdroppers, as well as the accessibility of the primary channel and the eavesdropping CSI [7].

According to a cooperative phase scenario, wireless transmission networks have generally focused largely on protecting numerous physical layers [8]. On the other hand, the broadcast phase of the operating platform, when the source, the eavesdropper, and the destination all have a lot of direct links, needs to be further investigated and given more attention as the main issue. Cooperative communication is a tried-and-true network, and it has been suggested that it could be used as a metric to measure how well wireless networks are performing [9]. Cooperative transmission and multi-hop communication are two general categories into which cooperative communication has been split and used to improve “Quality of Service (QoS)” and/or coverage for cellular networks. Cellular systems and multi-hop communications are frequently combined to create “Hybrid Ad hoc Network (HANET) or Multi-hop Cellular Network (MCN)” [10]. In order to implement MCN, the “Opportunity Driven Multiple Access (ODMA) protocol” [11] based on “3rd Generation Partnership Project (3GPP) for Time-Division Duplexing (TDD) and Universal Mobile Telecommunications System (UMTS)” is introduced. To increase network capacity, this protocol is indicated for providing traffic hot spots and spot coverage and to maximize coverage at high data rates [12].

Researchers have recently been motivated by VANETs to investigate a wide range of astounding telematics applications, especially for traffic intelligence and advanced transportation systems range from entertainment to ones that are safety-focused [13]. Wireless communication lines that enable vehicle-to-infrastructure (V2I) and vehicle-to-vehicle (V2V) communication make up connected automobiles, sometimes referred to as a generic VANET between automobiles and roadside access points [14, 15]. However, because of vehicle mobility, multi-path propagation, and time-varying impacts, due to inherent space-time frequency differentiability, vehicle channels are limited. The consideration of making full advantage of diversity is becoming increasingly important in the introduction of new communication designs. Wireless relay transmission systems’ performance must be enhanced by cooperative communication, whether seen from a cross-layer or physical-layer viewpoint because it has been widely acknowledged as a potent strategy in many cultures [16]. In order to solve the issue of rapid signal fading, developing in VANETs, cooperative communication technologies provide a broad range of protocols and more complex architectures [17]. Thus, a heuristic relay selection technique is required to handle throughput and OP in VANETs.

Here is where the proposed model’s major goal is presented.

- Enhancing the optimal method to choose fewest possible multi-hops among “source and destination” is necessary for a cooperative VANET to provide a high rate of convergence and equitable performance throughout the network.
- Use a new D-CSO method to solve a multi-objective throughput and OP function to choose or optimize the number of relays required for efficient packet transfer among a source and a destination.
- Intelligent swarm-based multi-hop relay selection strategy implementation to improve convergence analysis, OP, throughput and statistical analysis in VANETs.

The remainder of the suggested method is offered here. The literature review is described in Sect. 2. The system model and cooperative mechanism in the vehicular network are explained in Sect. 3. The model for selecting the best relay numbers in a vehicle network is described in Sect. 4. The suggested vehicular network relay selection approach based on throughput and OP is covered in Sect. 5. The findings and discussions are described in Sect. 6. This paper is concluded in Sect. 7.

2 Literature survey

2.1 Related works

For future heterogeneous networks (HetNets), Saghezchi et al. [18] have proposed “energy-aware cooperative relaying” to cut down on the energy used by wireless devices. Game theory principles have been incorporated in this network because the challenge was presented as an assignment game. The best relays were initially chosen using the linear programming paradigm, which involves choosing the best relays out of all of the candidates. In order to keep the participants from quitting the combination and to keep them satisfied, solutions were finally found for assuring distributing the reward among the participants in a fair manner. The obtained answer also proposed using a credit-based mechanism to reward the cooperative participants, which has kept the egotistical users out of joint federations. Intensive testing of this model was conducted.

By utilizing the social correlations from user contributions and interactions, Ying and Nayak [19] have taken into consideration an optimal relay selection (ORS) issue for improving cooperative multi-hop D2D communications. The aforementioned issue was resolved by this model using a novel strategy. Users were first chosen using social correlations that had been created, with greater social relationships being taken into consideration for relays.

Compared to evaluations using standard methods, the experimental findings demonstrate this model's lower average power usage. In order to achieve it, the best relays were chosen while taking advantage of the transmission power and ranges.

With the help of a stochastic learning method and a relay selection strategy, Tian et al. [20] realized this in 2017. Nash equilibrium has also emerged in this process. How precisely the cooperative communication network behaves during outages has also been investigated using a multi-relay decode-and-forward (DF) system. The lowest limit outage probability was also recommended to have minimal computation costs and two precise predictions. To establish the ideal power distribution in a cooperative network, they created an optimization model. The recommended method's analyses, along with the outage behaviours that lead to a Nash equilibrium state and their approximations, have been proven theoretically and quantitatively. The results demonstrated that the cooperative network performed pretty well in terms of fairness throughout the whole network, transmission reliability, and EE.

In 2020, Siddig et al. [21] proposed a full-duplex store-carry-forward method for making use of the relays' simultaneous transmission and reception of data to provide more information to target cars in inaccessible places. To achieve the best power distribution, the proposed model's primary objective was to ascertain the link's function. For decreasing the computational complexity with increased ECT, this model has proposed a new relay selection strategy. Comparing this model to other traditional half-duplex communication techniques, it was found to retain high target vehicle's ECT (effective communication time) while delivering additional data about the target vehicle.

In 2020, Li et al. [22] looked at a model of cooperative node systems and suggested a selection procedure on the basis of an accurate network model and the measurements of the distances between "Nakagami-m short-term static fading channel and relays," which was very suitable for unmanned aerial vehicles (UAVs). The probability of a system failure was estimated using the Meijer-G function, and a closed binary expression was developed while taking into consideration throughput, EE, and average transmission delay restrictions. In order to achieve a comprehensive system performance and balance the performances, a new trade-off factor known as EDT was created. This element has become more important in determining the appropriate number of relays. The findings validated the virtues of the provided strategy when taking into consideration the fixed relay number in addition to analysing the system performance and the impacts of network characteristics.

In 2021, Poursajadi and Hossein [23] analysed the vehicular communication model using adaptive ideal relay

selection (AORS) to choose the best relay while taking security precautions throughout both the cooperation and broadcast phases. The offering of the security was also considered using an incremental scheme. The outcomes assessed performance in terms of secrecy and outperformed previous schemes in terms of efficiency. Furthermore, an asymptotic analysis was performed, and it revealed that the suggested framework now possesses full secrecy diversity order. Finally, the results showed that the analysis was valid and that it had evaluated the system performance.

Within multi-hop relaying cellular networks, Chen et al. [25] introduced a distributed joint depend node selection method for power allocation in 2011. In order to do this, they considered the wireless interface condition and the residual energy of the relay nodes. Transitions while considering the time-varying channel and the residual energy state were described using a first-order finite-state Markov chain the indexability is a quality of the ideal policy, when paired using the formalism for stochastic optimization, has greatly decreased the computing complexity. The findings demonstrate that the created model greatly raised the projected system reward as compared to evaluations conducted using more conventional techniques.

2.2 Problem statement

Batteries last longer and use less energy according to game theory [18]. Gains in energy conservation are increased. The PSRS "(Power-efficient and Social-aware Relay Selection)" [19] technique lowers power use. Less messages are sent successfully. The overall network fairness is enhanced in relation to "transmission dependability, and high energy efficiency" via a [20]. It is hard to calculate the likelihood of an outage, though. EM-SCF [21] decreases the developed model's computational difficult. The buffer time is very long. The system performance is improved by DTMC [22], which also achieves shorter average transmission delays and increased energy efficiency. Smart Internet of Things (IoT)-based apps cannot use this approach. Direct transmission and generalized optimal relay selection, which provided complete secrecy diversity order, are successfully solved by AORS [23]. Real-time applications are uncomfortable using this technique. Lagrangian dual-primal decomposition [24] assures energy efficiency and has a lower implementation complexity. However, because of the unfavourable channel circumstances, the model's performance varies somewhat. The computational complexity is reduced using stochastic optimization [25]. The performance is impacted by the relaying networks' low battery life. These problems motivate academics to focus their efforts on developing an original relay selection method for vehicle networks.

3 Vehicular network system model and cooperative mechanisms

3.1 System model

A cooperative DF relay V2V communications system is examined using time division multiplexing (TDM) while taking the in the system, an active eavesdropper into account. The intermediate in Fig. 1 depicts the vehicles travelling the vehicle nodes at the sources and destinations.

The received messages in this network are decoded at the source node before being transmitted to the destination. A single antenna is used in this network to connect with whole nodes such as the eavesdropper Ev , source Sr , destination Ds , and R - relays (M_1, M_2, \dots, M_R), where $r = 1, 2, 3, \dots, R$. Furthermore, because of the real-time limits, the entire node is run in half-duplex mode so that it cannot broadcast and receive at the same time. In this case, a few straight paths among the source and the destination as well as eavesdropper nodes are considered in an operational setting. On the main channel's CSI and the eavesdropping channel is also supposed to be the foundation for correct channel estimate. Two possibilities are presumptive. When using an error-free feedback line, CSI is provided for free in the transmission region in the first scenario, but only on receiving nodes in the second [26]. Additionally, the Rayleigh distribution with zero mean and quasi-static flat fading of variance σ_{BcTn}^2 is seen for the channel among each receiver node $Bc \in (Sr, Ev, Ds)$ and transmitter node $Tn \in (Sr, M_r)$ for $r = 1, 2, \dots, R$ and h_{BcTn} .

The codebook that conducts the source message's A encoding and has the highest capacity into codeword $A \in A^b$ is used in the wiretap channel, and an input alphabet of length b is indicated as A^b . Here, a specific symbol is indicated by a having a certain level of strength and being transmitted within a particular window of time. The source

received the time slot that was initially available in the TDM protocol, P_{Sr} ; it refers to a signal with transmission strength and is used to broadcast their confidential information. The permitted nodes in this phase take in the following signals.

$$z_{Ds} = \sqrt{P_{Sr}}h_{SrDs}a + b_{Ds} \tag{1}$$

$$z_{M,r} = \sqrt{P_{Sr}}h_{SrM,r}a + b_M \tag{2}$$

where "Additive White Gaussian noise (AWGN)" is indicated as b_{Ds} and b_M , respectively, has the same strength as a primary destination. During the broadcast phase, the node receives the resultant signal and wiretaps the source node.

$$z_{Ev} = \sqrt{P_{Sr}}h_{SrEv}a + b_{Ev} \tag{3}$$

AWGN noise at Ev is referred to as b_{Ev} comprising with density power η_0 in Eq. (3). The broadcasting stage and the collaboration phase are carried out independently in this network, expressing the varied secret capabilities of the two phases. For showing the secret capacity, the "Single Input-Multiple Output (SIMO) channel" is taken into consideration first. Then, using the "Selection Combining" (SC) technique [27] as shown in Eq. (4), the best Gaussian codebook is used from the source site to the r th relay and destination node to assume the capacity of the SIMO channel.

$$\zeta_{SC}^r = \log_2 \left(1 + \kappa_1 |h_{SC,r}|^2 \right) \tag{4}$$

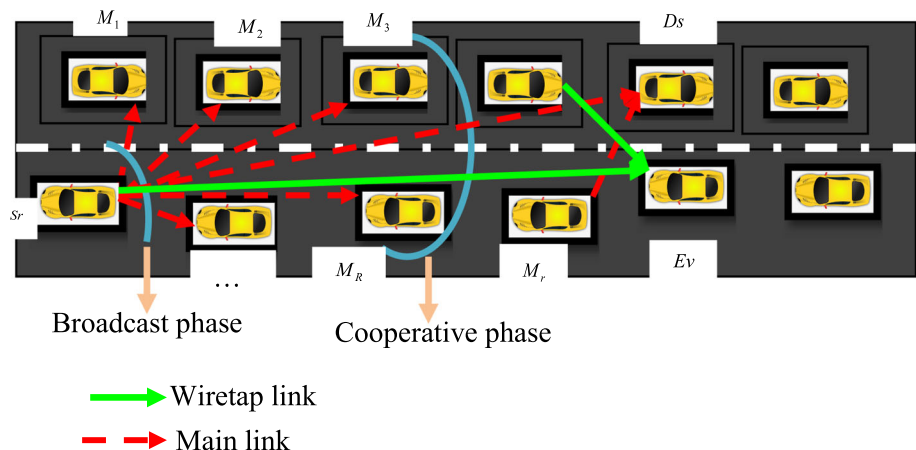
$$h_{SC,r} = \max \left\{ |h_{SrDs}|^2, |h_{SC,r}|^2 \right\} \tag{5}$$

where $\kappa_1 = \frac{P_{Sr}}{\eta_0}$. Additionally, Eq. (6) is used to determine the wiretap channel's capacity.

$$\zeta_{SE} = \log_2 \left(1 + \kappa_1 |h_{SE}|^2 \right) \tag{6}$$

Since then, confirmed that the "confidential capacity" is defined as the difference among the "main and wiretap

Fig. 1 Vehicle network cooperative mechanism with several vehicular nodes



connections” capabilities [28]. The capacity of “secure communications” for the r th relay in broadcast phase is therefore specified by the following derivation.

$$\begin{aligned} \zeta_{SS}^{BP,r} &= [\zeta_{SC}^r - \zeta_{SE}^r]^+ \\ &= \left[\log_2 \frac{1 + \kappa_1 |h_{SC,r}|^2}{1 + \kappa_1 |h_{SE}|^2} \right]^+ \end{aligned} \tag{7}$$

The representation is provided in Eq. (7) as follows $[a]^+ = \max(0, a)$.

3.2 Mechanism for cooperation

Assume the transmission power signal that is sent by the relay node to examine “obtaining the matching signals as a consequence of the cooperation phase’s security” at E_v and D_s , respectively.

$$z_{MDs,r} = \sqrt{P_r} h_{MDs,r} a + b'_{D_s} \tag{8}$$

$$z_{MEv,r} = \sqrt{P_r} h_{MEv,r} a + b'_{E_v} \tag{9}$$

In the aforementioned equations, the AWGN at E_v and D_s with the same power of η_0 are represented as b'_{D_s} and b'_{E_v} , respectively, it leads to the cooperation phase’s confidential capacity formulated in Eq. (10), where $\kappa_2 = \frac{P_r}{\eta_0}$.

$$\zeta_{SS}^{CP,r} = \left[\log_2 \left(\frac{1 + \kappa_1 |h_{SrDs,r}|^2 + \kappa_2 |h_{Mr,Ds}|^2}{1 + \kappa_1 |h_{SE}|^2 + \kappa_2 |h_{Mr,Ev}|^2} \right) \right]^+ \tag{10}$$

While the cooperative phase is silenced, the “The source message cannot be recovered by the relay node,” where $\kappa_2 = 0$. Finally, as articulated above, in both the broadcast and collaboration phases, the least-confidential capabilities are used to indicate the entire instantaneous secure transmission between the source and the destination.

$$\zeta_{SS}^r = \frac{1}{2} \min \left\{ \left[\log_2 \left(\frac{1 + \gamma_{SC}^r}{1 + \gamma_{SE}^r} \right) \right]^+, \left[\log_2 \left(\frac{1 + \gamma_{SrDs} + \gamma_{MDs}^r}{1 + \gamma_{SE} + \gamma_{MEv}^r} \right) \right]^+ \right\} \tag{11}$$

In Eq. (11), $\gamma_{MEv}^r = \kappa_2 |h_{MEv,r}|^2$, $\gamma_{MDs}^r = \kappa_2 |h_{MDs,r}|^2$, $\gamma_{SE} = \kappa_1 |h_{SE}|^2$, and $\gamma_{SC}^r = \kappa_1 |h_{SC,r}|^2$. The coefficient $\frac{1}{2}$ in Eq. (11) is utilized to send every secret message since two time slots are needed. Furthermore, in both the broadcast and cooperation stages, the finest relay is selected by using a “Generalized form of ORS (GORS)” scheme; it is derived in Eq. (12).

$$\zeta_{SS}^{GORS} = \frac{1}{2} \max_{r \in \{1, \dots, R\}} \left\{ \min \left\{ \zeta_{SS}^{BP,r}, \zeta_{SS}^{CP,r} \right\} \right\} \tag{12}$$

However, due to miscellaneous inducers and defaulters, the security can be reduced because the overall security can

be devastated with dripping at every phase or secret information leakage in multiple phases. Two different constraints are framed to address the security issues in GORS, when the source and destination links are weaker or stronger compared to $Sr - Mr, r = 1, \dots, R$ links.

$$\zeta_{SS,1}^{GORS} = \frac{1}{2} \max_{r \in \{1, \dots, R\}} \left\{ \min \left\{ \zeta_{SS}^{SrM,r}, \zeta_{SS}^{CP,r} \right\} \right\} \tag{13}$$

In Eq. (13), $\zeta_{SS}^{SrM,r} = \left[\log_2 \left(\frac{1 + \gamma_{SrM}^r}{1 + \gamma_{SE}} \right) \right]^+$ and $\gamma_{SrM}^r = \kappa_1 |h_{SrM,r}|^2$. The “confidential capacity of the GORS” in the first instance, strategy is equivalent to having plenty of R confidentiality [29]. Equation (14) is used to derive the second case, where ζ_{SS}^{SrDs} indicates the “immediate secrecy capability by direct transmission to the intended location.”

$$\zeta_{SS,2}^{GORS} = \frac{1}{2} \max_{r \in \{1, \dots, R\}} \left\{ \min \left\{ \zeta_{SS}^{SrDs}, \zeta_{SS}^{CP,r} \right\} \right\} \tag{14}$$

In Eq. (14), $\zeta_{SS}^{SrDs} = \left[\log_2 \left(\frac{1 + \gamma_{SrDs}}{1 + \gamma_{SE}} \right) \right]^+$ It is comparable to the highest of R – secrecy capacities.

These two circumstances are met by the GORS technique, which enhances the wiretap connection over the main channel by allowing for a relay through factor of 1/2 to degrade transmission efficiency. By obtaining access to CSI in each phase’s transmitter and receiver nodes, the direct connection is evaluated and the finest relay is opted. The source node’s secret message may be broadcast at a certain rate \mathfrak{R}_{SS} while still being able to obtain the total CSI at reception nodes [30]. Aside from that, choices are made where they will be implemented in Eq. (15).

$$\varepsilon : \zeta_{SS}^{SrDs} < \mathfrak{R}_{SS} \tag{15}$$

In order to meet Eq. (15), which states that a chosen optimal relay must maximize the capacity for secrecy or else the source node must broadcast a new secret message, the aforementioned equation for adaptive relaying is developed. AORS is the term given to this tactic. For the complexity described in Eq. (16) to be resolved and the spectral efficiency to be increased, incremental relaying is used.

$$\zeta_{SS}^{SrDs} < \left[\log_2 \left(\frac{1 + \kappa_1 \max_{r \in \{1, \dots, R\}} \left\{ |h_{SrM,r}|^2 \right\}}{1 + \kappa_1 |h_{SrEv}|^2} \right) \right]^+ \tag{16}$$

In Eq. (17) it is further simplified [31].

$$\psi : \gamma_{SrDs} < \max_{r \in \{1, \dots, R\}} \gamma_{SrM}^r \tag{17}$$

AORS is built by the application of incremental relay selection to maximize secrecy capacity while fulfilling the ψ .

4 Model for selecting the best relay numbers in a vehicle network

4.1 Strategy for relay selection

In order to become better communication performance, D-CSO is utilized to identify the appropriate relay in proposed VANETs in which a discusses about overall relay selection strategy is projected. Control module and transmission module are considered in this approach. Source determines whether or not the buffer is empty during control module consideration. If it is empty, it remains idle; otherwise, the source node broadcasts control frames for transmission known as handshake messages. The destination node responds with inertial measurement unit (IMU), GPS assistance, and differential GPS. Upon receiving the signals, transmitting data to the source node, the number of cooperative relays depends on the distance among the source and destination nodes.

In transmission module, source transmits the information frames via omnidirectional broadcast, while the destination precisely decodes the data frames. During the next Automatic Repeat Request (ARQ) round, source sends a new data frame. In alternative situation, after the destination assesses the ARQ round q ; the destination calls for retransmission or feedbacks negative acknowledgment, if the assessed value falls below the higher value. In retransmission stage DF relaying with p relays among r^* set is used to decode the source information. When the ARQ $p = 0$, the S_r retransmits the information frame. Similarly, p relays will not retransmit until destination is reached or until they receive a acknowledgment from the D .

4.2 D-CSO-based relay selection proposed

Due to its many advantages for increasing the effectiveness of the vehicular network, the relays are selected using the D-CSO method.

Counts of Dimension to Change (CDC) in the present CSO [32] method relates to how many dimensions will be modified within the range $[0, 1]$. Based on the ratio of the most current to the least effective fitness solutions, the suggested D-CSO algorithm applies CDC. The CSO was selected in this situation because to its high potential to arrive at suitable solutions via improved alignment between the testing and exploitation stages. However, premature assembly is an issue, which is why a novel idea was used in this case. In order to present the Dimension-based Cat Swarm Optimization technique, CDC was calculated using the best and worst solutions.

One of the most effective and reliable optimization strategies for superior performance is CSO, with the cat behaviour seeking and tracing modes selecting whether or not to change the solution. The majority of the time cats spend napping, making them sluggish creatures. The cats can still sense their environment, while they are resting. As a consequence, the cats will hunt. Cat distinguishes between two techniques: tracing and seeking modes; each outcome reveals each cat together with its flag, fitness score, and personal location. The DS - positions in the search region are dimensional, the flags indicate the searching or tracing modes of the cats, the fitness values denote sets, and the speeds of each dimension vary. We must first figure out how many cats there are in each iteration, with the best cat remembered. At the conclusion of the iteration, the ultimate result is obtained: cats. To determine the best course of action, the D-CSO is taking into account the following measures. In the beginning, the solution set's bottom and upper bounds are determined. X -Cats are randomly selected and distributed over the search area.

Once the selected combination's ratio to the bounding limit of $[0, 1]$ is known, the cats are then divided into several categories. The fitness value for each cat is then determined using the domain-specific fitness functions. The finest cats are then chosen and remembered after that. Cats are then encouraged to pursue tracing or model hunting. A random mixing ratio was used to reorganize the cats into searching or tracing models after forwarding them into one of the two modes. "Termination condition is verified," it says. The programme is terminated and the steps are replayed after it has been satisfied.

"Seeking mode": Using criteria like these, it simulates the way cats naturally relax. "Self-Position Considering (SPC), CDC, Seeking Range of the selected Dimension (SRD), and Seeking Memory Pool (SMP)." The user determines & optimizes all these settings using "trial-and error". A Boolean value called SPC is the total of all mutations and changes for a certain dimension, according to the CDC, indicating whether or not that dimension has experienced the most current cat mutation ratio. The cat's requesting memory size is then shown by SMP. This size indicates "there are several possible places, and the cat choose one of them to occupy." Here are several actions in the CSO seeking mode.

Create a number of clones of SMP with the most current position CT_j first. Based on Eq. (18) certain CDC dimensions are modified.

$$CDC = \frac{fit(k)}{worstfit(k)} \quad (18)$$

Additionally, add the SRD value at random, else deduct it from “to replace the previous places, use the current value” is derived in Eq. (19).

$$Y_{kds_{new}} = Y_{kds_{old}} * (1 + m * SRD) \tag{19}$$

where m represents arbitrary value ranging between [0, 1], k represents the number of cats, $Y_{kds_{old}}$ and $Y_{kds_{new}}$ indicate current location and next location of cats and d_s indicate dimension.

Then, all applicant roles’ fitness values are established. Select the best option for where the cat should go next. In other words, when selection is based on probability as determined by Eq. (20), it is done with greater fitness values.

$$\rho = \frac{|fit_i - fit_c|}{fit_{max} - fit_{min}} \tag{20}$$

When all fitness values are equal, every candidate point is given a full selection chance of one (1). The solution is considered as $fit_c = fit_{max}$ or otherwise $fit_c = fit_{min}$, where $0 < i < k$ the minimizing of the objective is taken as the goal.

“Tracking Mode”: Cats’ tracking habits are used. Every dimension of the cat placements’ starting velocity values are chosen at random. The velocity numbers for subsequent stages, however, should be updated. The following provides moving cats in tracing mode. Updates to the velocities across all dimensions are made using Eq. (21).

$$v_{j,ds} = v_{j,ds} + rs_1cn_1(Y_{best,ds} - Y_{j,ds}) \tag{21}$$

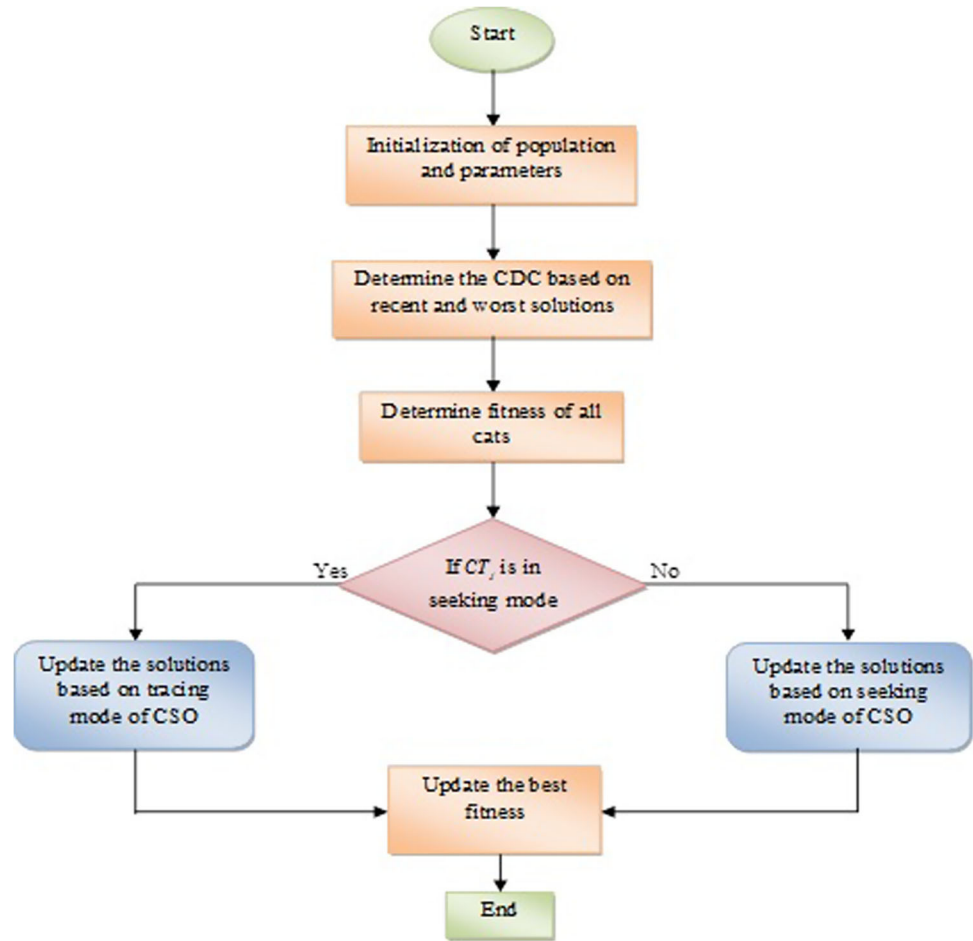
The maximum speed is equal to the velocity value when it reaches that value. Then, it uses Eq. (22) to update the position of CT_j .

$$Y_{j,ds} = Y_{j,ds} + v_{j,ds} \tag{22}$$

As a result, updating the solution is done using the searching and tracing modes, and the D-CSO algorithm updates the CDC depending on fitness values. With this adjustment, the ideal values and quicker convergence rate for the vehicular network’s optimal relay selection are obtained. Algorithm 1 contains the intended D-CSO algorithm’s pseudocode.

Algorithm 1: Proposed D-CSO
Determine cat population and constraints
Frame the fitness of whole solutions
Compute CDC based on the current fitness and vilest fitness solutions using Eq. (18)
Find the distance covered accurate and current search agents and average distance
Assessment of cats according to the fitness function
If CT_j is in the seeking mode
Solution update by Eq. (19), according to seeking mode
else
Solution update by Eq. (22), based on tracing mode
End if
Reallocate “the number of cats and allotted them into tracing mode through mixture ratio and assign others to seek mode”
End for
End while
Compute fitness of all solution
Elevate best fitness value
end while
Return accurate solutions

Fig. 2 Flowchart for the D-CSO algorithm that was created



In Fig. 2, the D-CSO flowchart is shown.

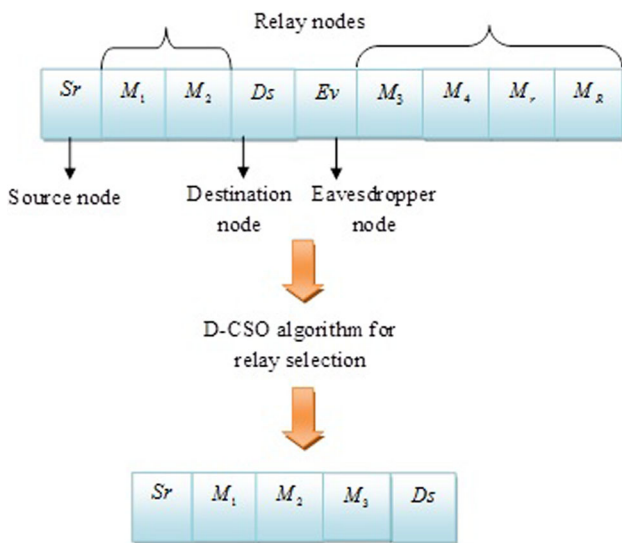


Fig. 3 Using the D-CSO technique, the best relays are chosen before and after encoding

5 Proposed vehicle network relay selection approach based on throughput and outage likelihood

5.1 Proposed relay optimization

The D-CSO method is used to solve multi-objective problems, such as minimizing outage probability and maximizing throughput, to optimize relays in the proposed vehicular network. Figure 3 shows the relay selection solution encoding both before and after optimization.

Proposed algorithm used to perform multi-hop selection, which eliminates unnecessary relay nodes from networks. This algorithm is used to select minimum number of relays and multi-hops to resolve multi-objective functions in the VANETS. The presented approach’s primary application is derived from Eq. (23).

$$fit = \arg \min_{\{M_r\}} \left(OP_{out} + \frac{1}{Th} \right) \tag{23}$$

The optimal relays under the cooperative aide are also termed as mean relays ($M_r \in [1, R]$) selected with the proposed algorithm to enhance the VANET efficiency by minimizing intricacy.

5.2 Calculation of outage probability

Assume the data link has a ‘‘outage probability’’ of and a signalling rate of rt , and the transmitted signal has a SNR of γ , as shown in Eq. (24).

$$OP_{out} = OP\{J(a; b|fh) < rt\} = OP\left\{\log_2\left(1 + \gamma|fh|^2\right) < rt\right\} \tag{24}$$

where fh represents fading coefficient and b as received signal. The OP of links between S, R and D in the q th ARQ is expressed as $SrM_{out,q}$, $SrMDs_{out,q}$ and $SrDs_{out,q}$, correspondingly.

$EX\left[|fh_{ij,q}|^2\right]$ represents the expectation function of fading coefficients between i and j nodes and $d_{ij}^{-\beta}$, where β represents the pathloss. The outage is computed considering Nakagami- m short-term static fading channel.

Equation (25) shows that an outage or failed transfer of connections from source to relay occurred for an q th ARQ cycle.

$$OP(SrM_{out,q}) = \prod_{us=1}^q OP\left\{\log_2\left(1 + \gamma|fh_{SrM,us}|^2\right) < rt\right\} = \prod_{us=1}^q OP\{\omega_{SrM,us} < \varepsilon\} = \prod_{us=1}^q DF_{\omega_{SrM,us}}(\varepsilon) \tag{25}$$

Here, Eq. (26) shows the transmission of the source–destination connection with relay p -assistance, which has failed for q th ARQ rounds.

$$OP(SrMDs_{out,q}) = \prod_{us=1}^{T_M^p} OP\left\{\log_2\left(1 + \gamma|fh_{SrDs,us}|^2\right) < rt\right\} \cdot \prod_{vs=T_M^p+1}^q OP\left\{\log_2\left(1 + \sum_{t=1}^p \gamma|fh_{M_tDs,vs}|^2\right) < rt\right\} = \prod_{us=1}^{T_M^p} OP\{\omega_{SrDs,us} < \varepsilon\} \cdot \prod_{vs=T_M^p+1}^q OP\left\{\sum_{t=1}^p \omega_{M_tDs,vs} < \varepsilon\right\} \tag{26}$$

The dissemination of connections from source to destination has failed or an outage has occurred q th ARQ round, as shown by Eq. (27).

$$OP(SrDs_{out,q}) = \prod_{us=1}^q OP\left\{\log_2\left(1 + \gamma|fh_{SrDs,us}|^2\right) < rt\right\} = \prod_{us=1}^q OP\{\omega_{SrDs,us} < \varepsilon\} = \prod_{us=1}^q DF_{\omega_{SrDs,us}}(\varepsilon) \tag{27}$$

$DF_A(a)$ represents the CDF of the term A, where $\varepsilon \triangleq \frac{2^{rt}-1}{\gamma}$.

The power density gain matrix can be simple represented as:

$$W_{SrM} = [\omega_{Sr,1}, \omega_{Sr,2}, \dots, \omega_{Sr,Q}]_{1 \times Q},$$

$$W_{SrDs} = [\omega_{SrDs,1}, \omega_{SrDs,2}, \dots, \omega_{SrDs,Q}]_{1 \times Q}$$

and

$$\omega_{MDs} = \begin{bmatrix} \omega_{M_1Ds,1} & \omega_{M_1Ds,2} & \dots & \omega_{M_1Ds,Q} \\ \omega_{M_2Ds,1} & \omega_{M_2Ds,2} & \dots & \omega_{M_2Ds,Q} \\ \vdots & \dots & \dots & \vdots \\ \omega_{M_RDs,1} & \omega_{M_RDs,2} & \dots & \omega_{M_RDs,Q} \end{bmatrix}_{R \times Q}$$

T_M^p defines the p relays in VANETS that can decode the information frame in the first ARQ round. And the probability of those p relays can be computed as:

$$OP(T_M^p = t) = \binom{R}{p} [OP(SrM_{out,t-1}) - OP(SrM_{out,t})]^k \cdot OP^{(R-k)}(SrM_{out,t}) \tag{28}$$

This expression represents the p relays out off R which cannot decode the information frame until t th ARD round.

$\omega_{ij,q}$ represents the Gamma random variable. $(o_{ij}, \frac{\Omega_{ij}}{o_{ij}})$ is denoted as. The overall p is evaluated with CDF which is not equal to the OP computed from the Gamma arbitrary terms (o_t, Ω_t) , where $t = 1, 2, \dots, p$ with $OP\{\sum_{t=1}^p \omega_{M_tDs,vs} < h\}$. The PDF and CDF of X ($X = \sum_{t=1}^p \xi_t$) are given as:

$$df_X(x) = \prod_{t=1}^p \left(\frac{o_t}{\Omega_t}\right)^{o_t} GF_{\delta,\delta}^{\delta,0} \left[\exp(-x) \Big|_{\lambda_3^{(2)}, \lambda_3^{(1)}}{\lambda_3^{(1)}}\right] \tag{29}$$

$$DF_X(x) = \prod_{t=1}^p \left(\frac{o_t}{\Omega_t}\right)^{o_t} GF_{\delta+1,\delta+1}^{\delta+1,0} \left[\exp(-x) \Big|_{\lambda_3^{(2)}, 0}{\lambda_3^{(2)}, 1}\right] \tag{30}$$

where Eq. (31) derives the Meijer-G function [33] and an integer is given as $\delta = \sum_{t=1}^p o_t$.

$$GF_{po,qo}^{ks,ls} \left[\mu_{\lambda_\delta^{(1)}} \right] = GF_{po,qo}^{ks,ls} \left[\mu_{|y_{s1}^{x1}, y_{s2}^{x2}, \dots, y_{s_{po}}^{x_{po}}|} \right]$$

$$= \frac{1}{2\pi i} \int_{Ch} \frac{\prod_{j=1}^o \Gamma(y_{sj} - su) \cdot \prod_{j=1}^R \Gamma(1 - x_j + su)}{\prod_{j=o+1}^{qo} \Gamma(1 - y_{sj} + su) \cdot \prod_{j=R+1}^{po} \Gamma(x_j - su)} \mu^{su} dsu \tag{31}$$

$\delta = \sum_{t=1}^p o_t$ represents an integer value. To consider the relative size an integral path is denoted by Ch , where is the relative size of the limitations, an integration is considered for Ch . The Gamma function is deduced from the aforementioned equations as $\Gamma(\cdot)$, where $\lambda_\delta^{(1)}$ and $\lambda_\delta^{(2)}$ are given as:

$$\lambda_\delta^{(1)} = \overbrace{\left(1 + \frac{o_1}{\Omega_1}\right), \dots, \left(1 + \frac{o_1}{\Omega_1}\right), \dots, \left(1 + \frac{o_p}{\Omega_p}\right), \dots, \left(1 + \frac{o_p}{\Omega_p}\right)}^\delta \tag{32}$$

$$\lambda_\delta^{(2)} = \overbrace{\left(\frac{o_1}{\Omega_1}\right), \dots, \left(\frac{o_1}{\Omega_1}\right), \dots, \left(\frac{o_p}{\Omega_p}\right), \dots, \left(\frac{o_p}{\Omega_p}\right)}^\delta \tag{33}$$

Furthermore, $\Omega_t \neq \Omega_q (t, q = 1, 2, 3, \dots, p, t \neq q)$ in Eq. (33) depicts the average power.

It is possible to get the PDF of the p-th random variable sum in the Rayleigh fading channel.

$$df_X^{Rayleigh}(x) = \frac{1}{\prod_{t=1}^p \Omega_t} GF_{p,p}^{p,0} \left[\exp(-x) \middle| \begin{matrix} 1 + \frac{1}{\Omega_1}, \dots, 1 + \frac{1}{\Omega_1} \\ \frac{1}{\Omega_1}, \dots, \frac{1}{\Omega_1} \end{matrix} \right] \tag{34}$$

The Meijer-G identity provided in Eq. (34) may be used to modify Eq. (35).

$$df_X^{Rayleigh}(x) = \sum_{t=1}^p \left(\prod_{su \neq t} \frac{1}{\Omega_{su}} \right) \frac{1}{\Omega_t} \exp\left(-\frac{x}{\Omega_t}\right) \tag{35}$$

So, all data connections have reached the OP.

5.3 Throughput computation

This statistic measures the typical number of frames that transmit successfully per unit of time, whereas the steady state probability is defined as the initial point with mean Discrete-Time Markov Chain (DTMC). The throughput is dependable on Q and R binary functions., where it can be articulated as $\begin{cases} \pi \cdot PO = \pi \\ \sum \pi = 1 \end{cases}$ and OP represents transition probability of one step and expressed as

$\left[(Q + 1) + R \sum_{i=1}^{Q-1} i \right] \times \left[(Q + 1) + R \sum_{i=1}^{Q-1} i \right]$. Throughput (Th) can be evaluated as

$$Th = \pi_{Sr}(Q, R) = \frac{1 - FErr(Q, R)}{fh(Q, R)} \tag{36}$$

$fh(Q, R)$ denotes a binary function of (Q, R) and $FErr(Q, R)$ represents frame fault rate and can be computed as:

$$FErr(Q, R) = \begin{cases} OP_{SrM_{1,0,0}} \cdot OP_{M_{1,0,0}DF} + \sum_{p=1}^R OP_{SrM_{1,p,0}} \cdot OP_{M_{1,p,0}DF}, & Q = 2 \\ \text{Eq. (39)}, & Q \geq 3 \end{cases} \tag{37}$$

$$fh(Q, R) = \begin{cases} 1 + OP_{SrM_{1,0,0}} + \sum_{p=1}^R OP_{SrM_{1,p,0}}, & Q = 2 \\ \text{Eq. (40)}, & Q \geq 3 \end{cases} \tag{38}$$

$$FErr(Q, R) = OP_{SrM_{1,0,0}} \cdot \prod_{i=1}^{Q-2} [OP_{M_{i,0,0}M_{i+1,0,0}}] \cdot OP_{M_{Q-1,0,0}DF}$$

$$+ \sum_{p=1}^R OP_{SrM_{1,p,1}} \cdot \prod_{i=1}^{Q-2} [OP_{M_{i,p,i}M_{i+1,p,i+1}}] \cdot OP_{M_{Q-1,p,Q-1}DF} \quad Q \geq 3$$

$$+ \sum_{p=1}^R \left(\begin{matrix} OP_{SrM_{1,0,0}} \cdot \prod_{i=1}^{T_M^p-2} [OP_{M_{i,0,0}M_{i+1,0,0}}] \\ \cdot OP_{M_{T_M^p-1,0,0}} \cdot M_{T_M^p-1,p,1} \\ \sum_{T_M^p=2}^{Q-1} \cdot \prod_{i=Q-2, j=Q-T_M^p-1}^{T_M^p-1} [OP_{M_{i,p,i}M_{i+1,p,i+1}}] \\ \cdot OP_{M_{Q-1,p,Q-T_M^p}DF} \end{matrix} \right) \tag{39}$$

$$fh(Q - 1, R) + OP_{Sr1,0,0} \cdot \prod_{i=1}^{Q-2} [OP_{M_{i,0,0}M_{i+1,0,0}}]$$

$$fh(Q, R) = + \sum_{p=1}^R OP_{SrM_{1,p,1}} \cdot [OP_{M_{i,p,i}M_{i+1,p,i+1}}] \quad Q \geq 3$$

$$+ \sum_{p=1}^R \left(\begin{matrix} \sum_{T_M^p=2}^{Q-1} OP_{SrM_{1,0,0}} \cdot \prod_{i=1}^{T_M^p-2} [OP_{M_{i,0,0}M_{i+1,0,0}}] \cdot \\ OP_{M_{(T_M^p-1),0,0}} \cdot M_{T_M^p,p,1} \\ \prod_{i=Q-2, j=Q-T_M^p-1}^{T_M^p-1} [OP_{M_{i,p,i}M_{i+1,p,i+1}}] \end{matrix} \right) \tag{40}$$

As a result, throughput may be calculated using Eq. (36) by adding Eqs. (37) to (40).

Table 1 Experimental parameters values employed in the vehicular network simulation

Parameters	Values
Numerous nodes	[50, 100, 150]
Numerous relay nodes	50
γ	105 dB
rt	0.50 bits/slot/Hz
Numerous population	10
Communication range of antennas	1000 m
R	[1, 10]
Frames, P	05 frames/s
Binary function Q	02, 03
Number of iterations overall	100

6 Results and discussion

6.1 Experimental arrangement

The suggested multi-hop selection procedure in VANETs is analysed using MATALB software tool, and it is compared with prevailing empirical algorithms such as Particle Swarm Optimization (PSO) [34], Jaya Algorithm (JA) [35], Grey Wolf Optimizer (GWO) [36, 37], and CSO [32]. The performance metrics like convergence, throughput, and OP was computed for three cases with different number of nodes (Table 1).

6.2 Analysis of convergence

Figure 4 illustrates the anticipated multi-hop selection in vehicle networks convergence analysis for the three test

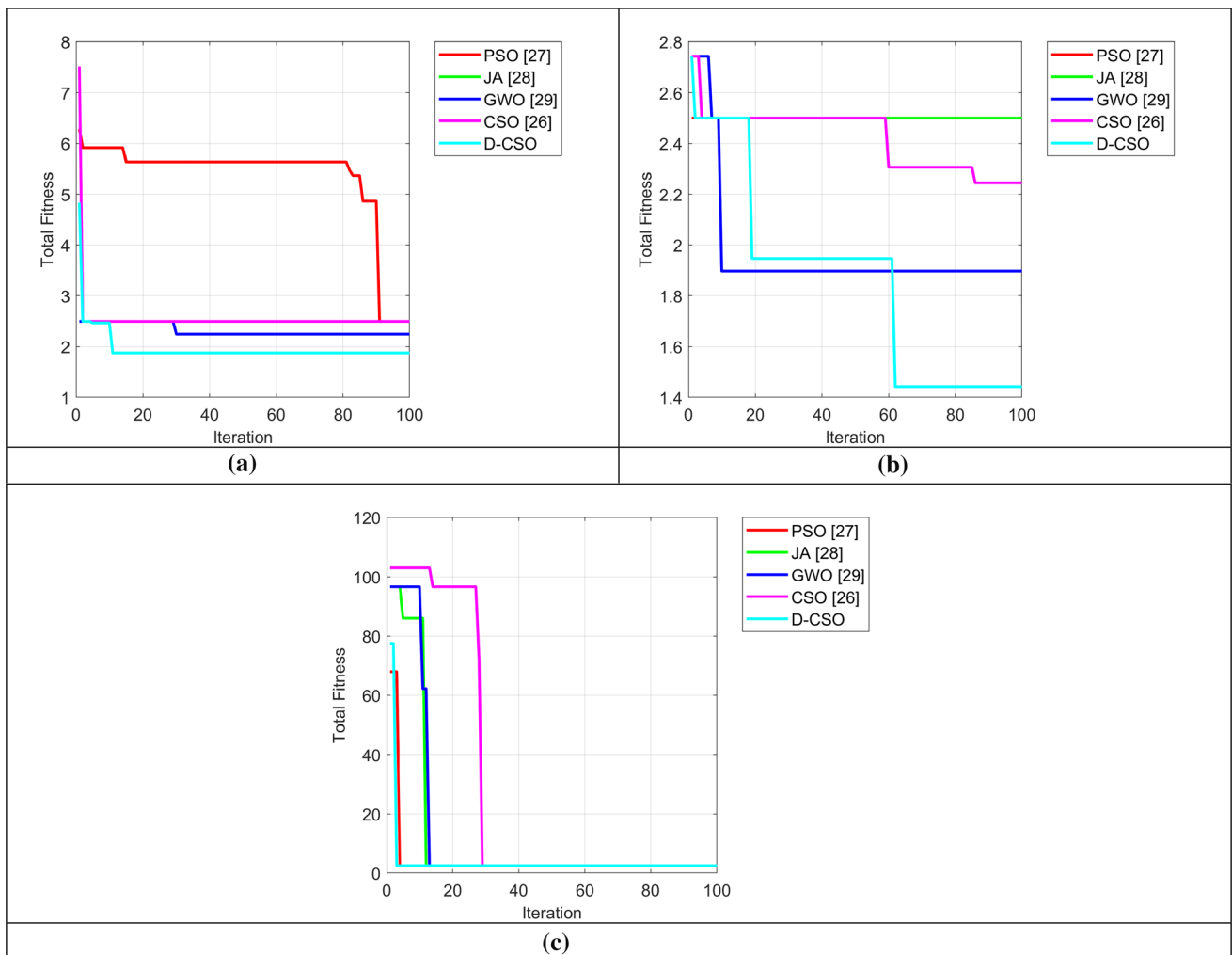


Fig. 4 Convergence evaluation of proposed algorithm with various empirical algorithms for **a** first case ($n = 50$), **b** second case ($n = 100$), and **c** third case ($n = 150$)

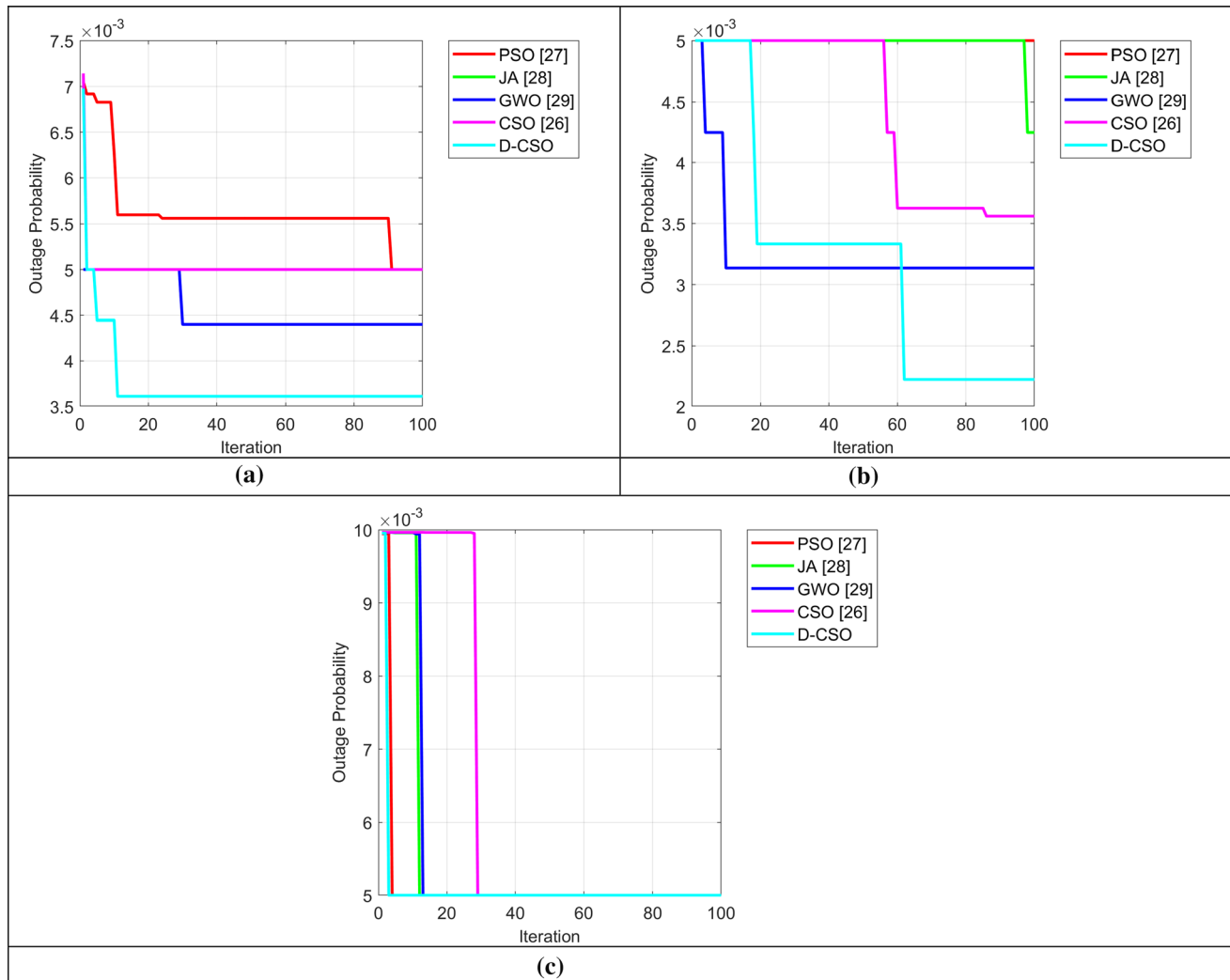


Fig. 5 OP analysis of proposed algorithm with various empirical algorithms for **a** first case ($n = 50$), **b** second case ($n = 100$), and **c** third case ($n = 150$)

scenarios by adjusting the node count. D-CSO, similar to other algorithms, observes the greatest fitness rate during first iterations while taking scenario 1 into consideration. The most affordable operation with the best performance is discovered by D-CSO in the tenth iteration when compared to other methods. Similar to instance 1, case 2 shows that the maximum fitness rate occurs during the first iterations, but D-CSO is the only one to perform well enough in the 60th iteration to get the lowest fitness. Similar to instance 2, in case 3 the D-CSO achieves the maximum convergence rate at beginning rates. According to the analysis, the D-CSO outperforms PSO, JA, GWO, and CSO by 28%, 25%, 18%, and 28%, respectively, at the 100th iteration for Case 1. D-CSO thus detects the superior convergence behaviour across all test cases.

6.3 Analysis of outage probability

Three test scenarios, shown in Fig. 5, are used to examine the recommended multi-hop option with regard to OP. D-CSO records the lowest OP and the maximum performance. So, for the first scenario, the D-CSO algorithm achieves the lowest rate with the best performance at the tenth iteration. When taking into account Case 2, the D-CSO merely defines the greater performance at the 60th iteration. But after that, the suggested model performs consistently better than the others. Similar to example 2, case 3 shows improved performance right from the start, according to D-CSO. However, the performance of all the other methods is comparable. Therefore, it has to be enhanced in the future for performance improvement.

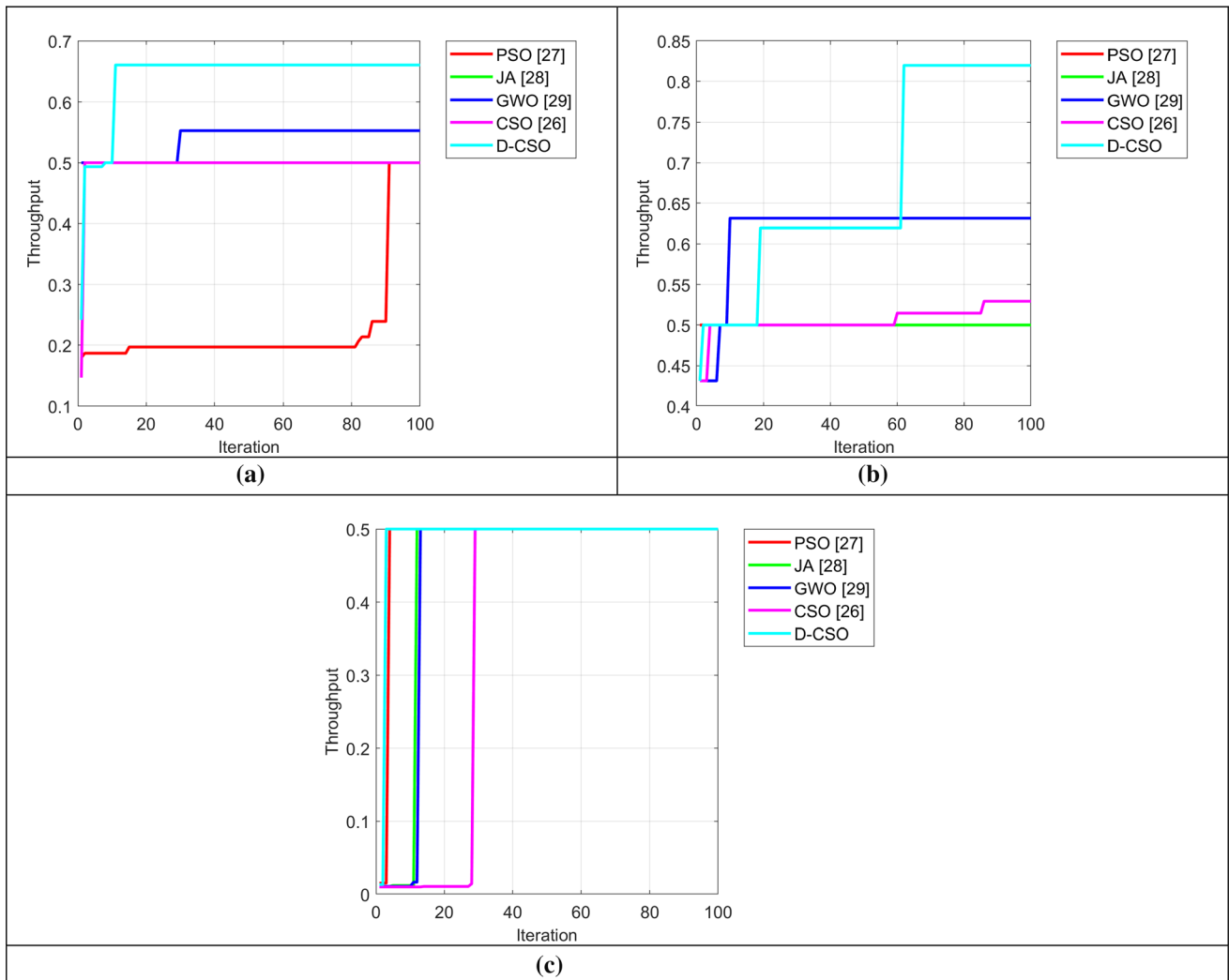


Fig. 6 Throughput analysis of proposed design with various empirical algorithms **a** first case ($n = 50$), **b** second case ($n = 100$), and **c** third case ($n = 150$)

6.4 Throughput analysis

In terms of throughput, the effectiveness of the recommended vehicular network is confirmed for the three test scenarios shown in Fig. 6. The multi-hop selection model is meant to perform better in terms of throughput at the greatest rate possible by D-CSO. In light of this, test case 1 shows improved performance even after 10 iterations when compared to other methods. In scenario 2, the D-CSO notices the maximum performance at the 60th iteration, and then, by assessing using current techniques, dependable and notable performance is discovered. For test case 3, the third iteration achieves the best performance, and all other iterations follow with performance that is comparable. At the 100th iteration of test case 3, D-CSO outperforms PSO, JA, GWO, and CSO by 28%, 64%, 28%, and

50%, respectively, in terms of throughput. In light of this, D-CSO-based multi-hop selection in the context of vehicular networks is shown to have the highest performance when compared to other algorithms.

6.5 Statistical analysis

The statistical assessment values of the proposed design in VANETs over other algorithms are depicted in Table 2. The values for the three cases are presented the degree of variation with standard deviation from finest to medium. From the statistical data of evaluation, it can be explored that the proposed D-CSO algorithm had outperformed in all the three cases with better performance.

Table 2 Statistical assessed values of proposed design with different empirical algorithms

Algorithms	Standard deviation	Best	Worst	Mean	Median
<i>First case</i>					
Ref. [34]	5.3	2.5	6.2	0.9	5.6
Ref. [35]	2.5	2.5	2.5	0.0	2.5
Ref. [36]	1.9	1.8	4.8	0.3	1.8
Ref. [32]	2.5	2.5	7.5	0.5	2.5
D-CSO [proposed]	2.3	2.2	2.5	0.1	2.2
<i>Second case</i>					
Ref. [34]	2.5	2.5	2.5	0.0	2.5
Ref. [35]	2.5	2.5	2.7	0.04	2.5
Ref. [36]	1.8	1.4	2.7	0.3	1.9
Ref. [32]	2.4	2.2	2.7	0.1	2.5
D-CSO [proposed]	1.9	1.9	2.7	0.2	1.9
<i>Third case</i>					
Ref. [34]	4.4	2.5	67.9	1.2	2.5
Ref. [35]	12.1	2.5	96.6	7.5	2.5
Ref. [36]	3.9	2.5	77.5	0.5	2.5
Ref. [32]	29.4	2.5	103	3.5	2.5
D-CSO [proposed]	13.1	2.5	96.6	9.2	2.5

7 Conclusion

In order to choose the fewest possible D-CSO technique for several hops among the source and destination, a cooperative VANET network optimization model has been developed in this research. Using a multi-objective function that takes system throughput and OP into account, this method has picked the no. of hops or relays for successful communication at the ideal value. Using a performance assessment, the effectiveness of a cooperative mechanism-based D-CSO multi-hop selection was evaluated. For case 2 at the 100th iteration, the performance of the D-CSO was 36%, 42%, 25.2%, and 36% better than that of the PSO, JA, GWO, and CSO, respectively. Finally, while comparing D-CSO to other heuristic algorithms, it was shown to have greater performance for all three test situations. However, D-CSO also noticed the same performance for test cases 2 and 3 using alternative techniques.

Acknowledgements The Deanship of Scientific Research of King Khalid University, Abha, Kingdom of Saudi Arabia, is acknowledged by the authors for sponsoring this study under Large Groups RGP.2/170/44.

Data availability The data that have been used are confidential.

Declarations

Conflict of interest The authors declare that they have no known competing financial interests or personal relationships that could have appeared to influence the work reported in this paper. There is no conflict of interest.

References

- Okeke GO, Krzymień WA, Jing Y, Melzer J (2015) A novel low-complexity joint user-relay selection and association for multi-user multi-relay MIMO uplink. *IEEE Wirel Commun Lett* 4(3):309–312
- Nam E, Jang C, Lee JH (2015) Performance of reactive relay selection based on cumulative distribution function of SNRs for two-way relay networks. *IEEE Commun Lett* 19(8):1378–1381
- Wang W, Teh KC, Li KH (2016) Generalized relay selection for improved security in cooperative DF relay networks. *IEEE Wirel Commun Lett* 5(1):28–31
- Adam H, Yanmaz E, Bettstetter C (2014) Medium access with adaptive relay selection in cooperative wireless networks. *IEEE Trans Mob Comput* 13(9):2042–2057
- Zhao D, Zhao H, Jia M, Xiang W (2014) Smart relaying for selection combining based decode-and-forward cooperative networks. *IEEE Commun Lett* 18(1):74–77
- Feng H, Xiao Y, Cimini LJ (2014) Net throughput of centralized and decentralized cooperative networks with relay selection. *IEEE Wirel Commun Lett* 3(5):477–480
- Xia M, Aïssa S (2015) Fundamental relations between reactive and proactive relay-selection strategies. *IEEE Commun Lett* 19(7):1249–1252
- Nguyen BV, Afolabi RO, Kim K (2013) Dependence of outage probability of cooperative systems with single relay selection on channel correlation. *IEEE Commun Lett* 17(11):2060–2063
- Su Y, Lu X, Zhao Y, Huang L, Du X (2019) Cooperative communications with relay selection based on deep reinforcement learning in wireless sensor networks. *IEEE Sens J* 19(20):9561–9569
- Zheng Z, Fu S, Lu K, Wang J, Chen B (2012) On the relay selection for cooperative wireless networks with physical-layer network coding. *Wirel Netw* 18:653–665
- Zhang L, Cimini LJ Jr (2007) Power-efficient relay selection in cooperative networks using decentralized distributed space-time block coding. *EURASIP J Adv Signal Process* 2008(362809):1–10

12. Abdulhadi S, Jaseemuddin M, Anpalagan A (2012) A survey of distributed relay selection schemes in cooperative wireless ad hoc networks. *Wirel Pers Commun* 63:917–935
13. Seyfi M, Muhaidat S, Liang J, Uysal M (2011) Relay selection in dual-hop vehicular networks. *IEEE Signal Process Lett* 18(2):134–137
14. Hui Y, Su Z, Luan TH, Li C (2020) Reservation service: trusted relay selection for edge computing services in vehicular networks. *IEEE J Sel Areas Commun* 38(12):2734–2746
15. Singh AK, Pamula R, Jain PK, Srivastava G (2021) An efficient vehicular-relay selection scheme for vehicular communication. *Soft Comput*. <https://doi.org/10.1007/s00500-021-06106-4>
16. Achour I, Alfayez F, Busson A (2021) A robust and efficient adaptive data dissemination protocol based on smart relay selection in vehicular networks. *Wirel Netw* 27:4497–4511
17. Akin AI, Ilhan H, Özdemir Ö (2015) Relay selection for DF-based cooperative vehicular systems. *EURASIP J Wirel Commun Netw* 2015(30):1–9
18. Saghezchi FB, Radwana A, Rodriguez J (2017) Energy-aware relay selection in cooperative wireless networks: an assignment game approach. *Ad Hoc Netw* 56:96–108
19. Ying B, Nayak A (2018) A power-efficient and social-aware relay selection method for multi-hop D2D communications. *IEEE Commun Lett* 22(7):1450–1453
20. Tian D, Zhou J, Sheng Z, Chen M, Ni Q, Leung VCM (2017) Self-organized relay selection for cooperative transmission in vehicular ad-hoc networks. *IEEE Trans Veh Technol* 66(10):9534–9549
21. Siddig AA, Ibrahim AS, Ismail MH (2020) An optimal power allocation and relay selection full-duplex store-carry-forward scheme for intermittently connected vehicular networks. *IEEE Access* 8:163903–163916
22. Li S, Wang F, Gaber J, Zhou Y (2020) An optimal relay number selection algorithm for balancing multiple performance in flying ad hoc networks. *IEEE Access* 8:225884–225901
23. Poursajadi S, Madani MH (2021) Adaptive optimal relay selection in cooperative vehicular communications under security constraints. *Veh Commun* 31:1003600
24. Dan CHEN, Hong JI, Xi LI, Yi LI (2010) QoS-guaranteed multi-relay selection and power allocation optimization in cooperative systems. *J China Univ Posts Telecommun* 17(6):25–31
25. Chen D, Ji H, Li X, Li Y (2011) Energy-efficient joint relay node selection and power allocation over multihop relaying cellular networks toward LTE-Advanced. *J China Univ Posts Telecommun* 18(3):1–7
26. Dong L, Han Z, Petropulu AP, Poor HV (2010) Improving wireless physical layer security via cooperating relays. *IEEE Trans Signal Process* 58(3):1875–1888
27. Yang M, Guo D, Huang Y, Duong TQ, Zhang B (2016) Physical layer security with threshold-based multiuser scheduling in multi-antenna wireless networks. *IEEE Trans Commun* 64(12):5189–5202
28. Li J, Petropulu AP, Weber S (2011) On cooperative relaying schemes for wireless physical layer security. *IEEE Trans Signal Process* 59(10):4985–4997
29. Krikidis I, Thompson JS, McLaughlin S (2008) Relay selection for secure cooperative networks with jamming. *IEEE Trans Wirel Commun* 8(10):5003–5011
30. Zou Y, Wang X, Shen W (2013) Optimal relay selection for physical-layer security in cooperative wireless networks. *IEEE J Sel Areas Commun* 31(10):2099–2111
31. Bao VNQ, Linh-Trung N, Debbah M (2013) Relay selection schemes for dual-hop networks under security constraints with multiple eavesdroppers. *IEEE Trans Wirel Commun* 12(12):6076–6085
32. Bouzidi A, Riffi ME, Barkatou M (2019) Cat swarm optimization for solving the open shop scheduling problem. *J Ind Eng Int* 15:367–378
33. Gradshteyn IS, Ryzhik IM (2007) Table of integrals, series and products. *Math Comput* 20(96):1157–1160
34. Ai TJ, Kachitvichyanukul V (2009) A particle swarm optimization for the vehicle routing problem with simultaneous pickup and delivery. *Comput Oper Res* 36(5):1693–1702
35. Venkata Rao R (2016) Jaya: A simple and new optimization algorithm for solving constrained and unconstrained optimization problems. *Int J Ind Eng Comput* 7(1):19–34
36. Mirjalili S, Mirjalili SM, Lewis A (2014) Grey wolf optimizer. *Adv Eng Softw* 69:46–61
37. Devulapalli PK, Pokkunuri PS, Maganti SB (2021) Energy efficient multi-hop cooperative transmission protocol for large scale mobile ad hoc networks. *Wirel Pers Commun (Springer)* 121(4):3309–3328

Publisher's Note Springer Nature remains neutral with regard to jurisdictional claims in published maps and institutional affiliations.

Springer Nature or its licensor (e.g. a society or other partner) holds exclusive rights to this article under a publishing agreement with the author(s) or other rightsholder(s); author self-archiving of the accepted manuscript version of this article is solely governed by the terms of such publishing agreement and applicable law.

VLSI IMPLEMENTATION OF ERROR DETECTION AND CORRECTION CODES FOR SPACE ENGINEERING

¹KANDULA BHARATH KUMAR, ²G VEDAVATHI

¹PG Scholar, Dept.of ECE, Vaagdevi College of Engineering, Warangal, Telangana, India.

²Associate professor, Dept.of ECE, Vaagdevi College of Engineering, Warangal, Telangana, India.

¹bharathbalu868@gmail.com, ²vedhavathi_g@vaagdevi.edu.in

Abstract— In this paper, On behalf of technology scaling, on-chip memories in a die undergoes bit errors because of single events or multiple cell upsets by the ecological factors such as cosmic radiation, alpha, neutron particles or due to maximum temperature in space, leads to data corruption. Error detection and correction techniques (ECC) recognize and rectify the corrupted data over communication channel. In this paper, an advanced error correction 2-dimensional code based on divide-symbol is proposed to weaken radiation-induced MCUs in memory for space applications. For encoding data bits, diagonal bits, parity bits and check bits were analyzed by XOR operation. To recover the data, again XOR operation was performed between the encoded bits and the recalculated encoded bits. After analyzing, verification, selection and correction process takes place. The proposed scheme is simulated and synthesized using Xilinx implemented in Verilog HDL.

Index Terms— Space Applications, Diagonal Hamming, Multibit error correction, Random bit errors and correction techniques.

I. INTRODUCTION

BINARY information is stored in a storage space called memory. This binary data is stored within metal-oxide semiconductor memory cells on a silicon integrated circuit memory chip. Memory cell is a combination of transistors and capacitors where capacitor charging is considered as 1 and discharging considered as 0 and this can store only one bit. Errors which are temporary or permanent are created in the memory cells and need to be eliminated. Single bit error correction is most commonly used technique which is capable of correcting upto one bit. Since technology is increasing rapidly, there are more probabilities of getting multiple errors [1]. Use of Diagonal Hamming method leads to efficient correction of errors in the memories. Memory was divided as SRAM, DRAM, ROM, PROM, EPROM,

EEPROM and flash memory [2]. Main advantages of semiconductor memory are easy to use, less in cost, and have high bits per square micrometers. Temporary errors are called transient errors which are caused because of fluctuations in potential level. Permanent errors are caused because of defects during manufacturing process or large amount of radiations [3].

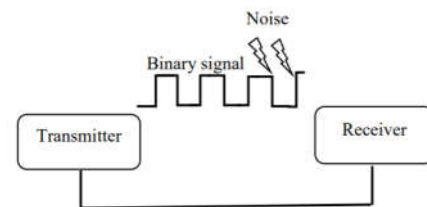


Figure: Data Transmission

II. RELATED WORK

1) Punctured Difference Set (PDS) code is a process to identify the multiple cell upsets in memories

2)The bits by the same logical word into different physical words which has been used in restrain multiple cell upsets in interleaving technique .

3) Built-in current sensors (BICS) are scheduled for reinforcement on correction single error detection and double error detection for granted fortification against multiple cell upsets.

4) 2-Dimensional matrix codes are prospective to conducive correct multiple cell upsets per word with a low decoding delay in which one word has been divided into multiple rows and column.

Drawbacks: 1) PDS codes require more area, power, and delay overheads since the encoding and decoding circuits are more complex in these complicated codes.

2) Interleaving technique may not be practically used in content-addressable memory (CAM),

because of the tight coupling of hardware structures from both cells and comparison circuit structures

3) BICS technique can only correct two errors in a word.

4) 2D MC is capable of correcting only two errors in all cases. In the recent technique names as FUEC–triple adjacent error correction (TAEC), is able to correct an error in a single bit, or an error in two adjacent bits (2-bit burst errors) or a 3-bit burst error, or it can detect a 4-bit burst error. This is possible by adding one more code bit. In this case, for a 16-bit data word, the FUEC– TAEC code needs eight code bits. The parity-check matrix H for this code is presented. As in the case of the FUEC–DAEC, Ci are the code bits and Xi are the primary data bits. Similarly, from H it is very easy to design the encoder/decoder circuitry. But this technique will be considered as less precision which could not correct the large number of data's.

III. HAMMING CODE

Hamming code are the linear block code which are invented by Richard.W. Hamming. They are an improvement over simple parity code method. The simple parity code cannot correct errors, and can only detect an odd number of errors. They are the type of binary codes. The idea of hamming distance is the central concept in coding the error Control. The hamming distance between the two words (of the same size) is the number of differences between the corresponding bits. The hamming distance can easily be found if we apply the Xor operation on the two words and count the number of 1s in the result. The hamming distance is a value always greater than zero. If we find the hamming distance between any two words it will be the result of the Xoring of the two bits. Like the hamming distance between d (000,011) is 2 because 000 xor 011 is 011 (two 1s) and the hamming distance between d (10101, 11110) is 3 because 10101 xor 11110 is 01011(three 1s). [3][7], if we calculate the number of redundancy bits for a 7 bit of information then it comes to be 4 redundancy bit. Redundancy bits are those extra bits which are required to detect and correct errors. The redundancy bits are added to the information bit at the transmitter and removed at the receiver. The receiver is able to detect the error and correct it because of the redundancy bits. Hamming codes are used as forward error correcting codes in the Bluetooth standard, and to

protect data stored in semiconductor memories. Hamming codes are generally used in computing, telecommunication, and other applications including data compression, and turbo codes. They are also used for low cost and low power applications.

IV. METHODOLOGY

The proposed system Design of Diagonal Hamming method for memory Proposed design of Diagonal Hamming based multi-bit error detection and correction technique to the memory is shown in Fig. Using this approach of diagonal Hamming bits, the errors in the message can be recognized and can be rectified which are saved in the memory. In encoding technique message bits are given as input to the Diagonal Hamming encoder and the Hamming bits are calculated. Message and Hamming bits are saved in the memory after the encoding technique.

a) Encoding Process

Here input is Data of 16 bits ,this 16bits are divided into 4 groups : a,b,c,d

Its Representation

Data				Dividing into Groups			
X[3]	X[2]	X[1]	X[0]	a[1]	a[2]	a[3]	a[4]
X[7]	X[6]	X[5]	X[4]	b[1]	b[2]	b[3]	b[4]
X[11]	X[10]	X[9]	X[8]	c[1]	c[2]	c[3]	c[4]
X[15]	X[14]	X[13]	X[12]	d[1]	d[2]	d[3]	d[4]

Diagonal Equation

$$D[1] = a[1]^b[2]^a[3]^b[4];$$

$$D[2] = b[1]^a[2]^b[3]^a[4];$$

$$D[3] = c[1]^d[2]^c[3]^d[4];$$

$$D[4] = d[1]^c[2]^d[3]^c[4];$$

Parity Equation

$$P[1] = a[1]^b[1]^c[1]^d[1];$$

$$P[2] = a[2]^b[2]^c[2]^d[2];$$

$$P[3] = a[3]^b[3]^c[3]^d[3];$$

$$P[4] = a[4]^b[4]^c[4]^d[4];$$

Check bits Equation

$$Ca = \{a[1]^a[3], a[2]^a[4]\};$$

$$Cb = \{b[1]^b[3], b[2]^b[4]\};$$

$$Cc = \{c[1]^c[3], c[2]^c[4]\};$$

$$Cd = \{d[1]^d[3], d[2]^d[4]\};$$

The output of encoding is 32bits i.e., original data with Diagonal bits, parity bits, Check bits arranged in matrix order

Output

O[19]	O[18]	O[17]	O[16]	O[3]	O[2]	O[1]	O[0]
O[23]	O[22]	O[21]	O[20]	O[7]	O[6]	O[5]	O[4]
O[27]	O[26]	O[25]	O[24]	O[11]	O[10]	O[9]	O[8]
O[31]	O[30]	O[29]	O[28]	O[15]	O[14]	O[13]	O[12]

Placing the bits

D[1]	P[1]	Ca[1]	ca[2]	X[3]	X[2]	X[1]	X[0]
D[2]	P[2]	Cb[1]	Cb[2]	X[7]	X[6]	X[5]	X[4]
D[3]	P[3]	Cc[1]	Cc[2]	X[11]	X[10]	X[9]	X[8]
D[4]	P[4]	Cd[1]	Cd[2]	X[15]	X[14]	X[13]	X[12]

b) Decoding Process

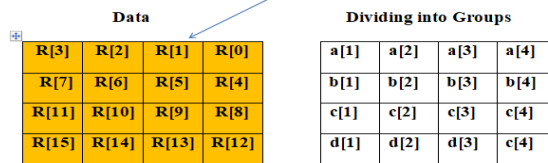
The encoded data ie., 32bits will be the input From that first 16bits will be having some error That's called Redundancy Bits.

Input for Decoding

X[19]	X[18]	X[17]	X[16]	X[3]	X[2]	X[1]	X[0]
X[23]	X[22]	X[21]	X[20]	X[7]	X[6]	X[5]	X[4]
X[27]	X[26]	X[25]	X[24]	X[11]	X[10]	X[9]	X[8]
X[31]	X[30]	X[29]	X[28]	X[15]	X[14]	X[13]	X[12]

And its pacing of bits Rbits are noting but It may have any Error D,P,C bit are the input What we got from Encoded output.

D[1]	P[1]	Ca[1]	ca[2]	R[3]	R[2]	R[1]	R[0]
D[2]	P[2]	Cb[1]	Cb[2]	R[7]	R[6]	R[5]	R[4]
D[3]	P[3]	Cc[1]	Cc[2]	R[11]	R[10]	R[9]	R[8]
D[4]	P[4]	Cd[1]	Cd[2]	R[15]	R[14]	R[13]	R[12]



Diagonal Equation

$$RD[1] = a[1]^b[2]^a[3]^b[4];$$

$$RD[2] = b[1]^a[2]^b[3]^a[4];$$

$$RD[3] = c[1]^d[2]^c[3]^d[4];$$

$$RD[4] = d[1]^c[2]^d[3]^c[4];$$

Parity Equation

$$RP[1] = a[1]^b[1]^c[1]^d[1];$$

$$RP[2] = a[2]^b[2]^c[2]^d[2];$$

$$RP[3] = a[3]^b[3]^c[3]^d[3];$$

$$RP[4] = a[4]^b[4]^c[4]^d[4];$$

Check bits Equation

$$RCa = \{a[1]^a[3], a[2]^a[4]\};$$

$$RCb = \{b[1]^b[3], b[2]^b[4]\};$$

$$RCc = \{c[1]^c[3], c[2]^c[4]\};$$

$$RCd = \{d[1]^d[3], d[2]^d[4]\};$$

Calculate Syndrome bits

$$Sd = D \text{ xor } RD$$

$$Sp = P \text{ xor } RP$$

$$Sc = C \text{ xor } RC$$

Select the Region From Equation Sd , Sp as given above

Region	Selection criteria
Region 1	$SD1+SD2+SP1+SP2 > SD3+SD4+SP3+SP4$
Region 2	$SD1+SD2+SP1+SP2 < SD3+SD4+SP3+SP4$
Region 3	$SD1+SD2+SP1+SP2 = SD3+SD4+SP3+SP4$

Correction Procedure: Correction will be done According with Region

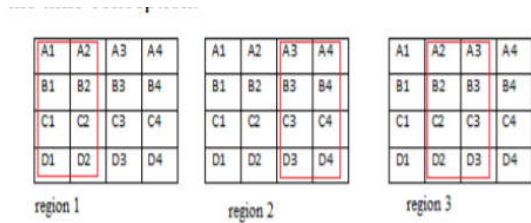


Figure: Regions of bits

Once Region is Selected

To get the final Output

The Particular Region is Xored with SC matrix .

V. RESULTS

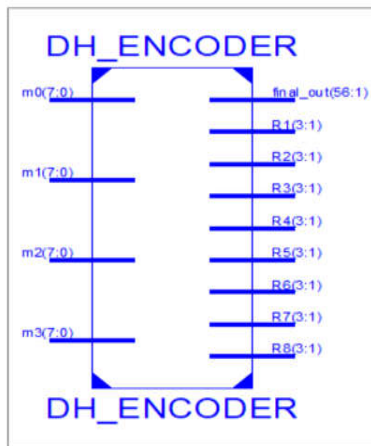
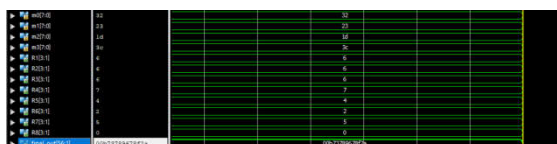


Figure: Block diagram for diagonal Hamming Encoder



The input given for this circuit is mo,m1,m2,m3 and output we get parity bit separate order and final_out .

R1,R2,R3,R4,R5,R6,R7,R8 is the parity bits

$$\begin{aligned} \text{Final_out} &= \text{Parity bits} + \text{msg_input} \\ &= 8 \times 3 \text{ (8 parities each having 3 bits) } + \\ &32 \text{ bit} \\ &= 56 \text{ bits} \end{aligned}$$

Error Corrector At Reciever side also called Decoder

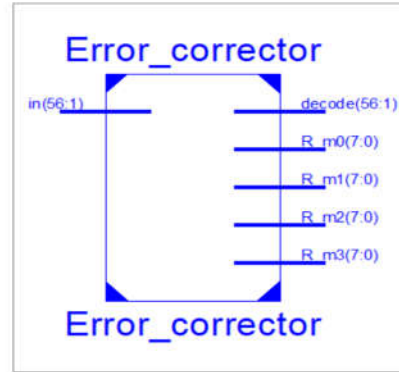


Figure: Block Diagram For Decoder

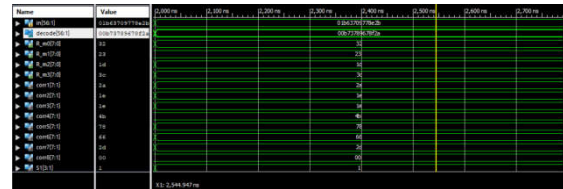


Figure: output Waveform for Error corrector

The output we got from encoding block is final_out 00b73789678f2a . Now, this is sent at the receiver side .But at the receiver side suppose the data getting with some Error Consider that as in = 01b63709778e2b input for Error corrector block or Decoding Block and Here at Output Error will be getting corrected and Getting Exact data whatever sent at Transmitter side .

$$\text{out} = 00b73789678f2a.$$

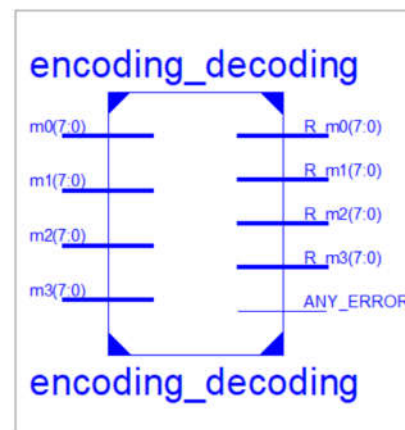


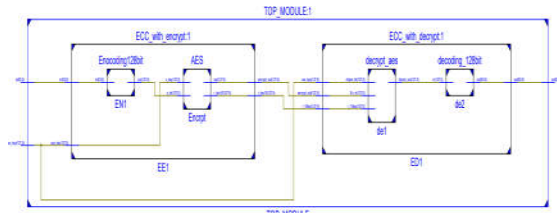
Figure: Encoding And Decoding Block

In this the 32bit input is grouped into 8bit msg_data ie., m0,m1,m2,m3;

Output is R_m0,R_m1,R_m2,R_m3 (Received_msg)

Output is also indicating Any_error Occured in Matching encoding and Decoding Data .

DIAGONAL HAMMING CODE 32 BIT with Cryptography .



With the help of advance encryption standard ,here error correction codes are designed .

In this Encoded Ouput will be the Input for AES Encryption By using Secured Key .

The Encrypted Output will forwarded to DecryptBlock with same Secured Key and the Decrypt Output will be given for Decoding Which is Decoding the input without any Error and The Required Data is Retrived At Reciever Side .

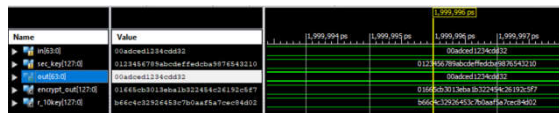


Figure: ECC with Cryptography output waveforms

REFERENCES

[1] Farahat, I.S., Tolba, A.S., Elhoseny, M. and Eladrosy, W., 2019. Data Security and Challenges in Smart Cities. In Security in Smart Cities: Models, Applications, and Challenges. Springer, Cham, pp. 117-142.

[2] Atzori, L., Iera, A. and Morabito, G., 2010. The internet of things: A survey. Computer networks, 54(15), pp.2787-2805.

[3] Zanella, A., Bui, N., Castellani, A., Vangelista, L. and Zorzi, M., 2014. Internet of things for smart cities. IEEE Internet of Things journal, 1(1), pp.22-32.

[4] Kuo, Y.W., Li, C.L., Jhang, J.H. and Lin, S., 2018. Design of a Wireless Sensor Network-Based IoT Platform for Wide Area and Heterogeneous Applications. IEEE Sensors Journal, 18(12), pp.5187- 5197.

[5] Sheng, Z., Yang, S., Yu, Y., Vasilakos, A., Mccann, J. and Leung, K., 2013. A survey on the ietf protocol suite for the internet of things: Standards, challenges, and opportunities. IEEE Wireless Communications, 20(6), pp.91-98.

[6] Gubbi, J., Buyya, R., Marusic, S. and Palaniswami, M., 2013. Internet of Things (IoT): A vision, architectural elements, and future directions. Future generation computer systems, 29(7), pp.1645- 1660.

[7] Hamming, R.W., 1950. Error detecting and error correcting codes. Bell System technical journal, 29(2), pp.147-160.

[8] Hsiao, M.Y., 1970. A class of optimal minimum odd-weight-column SEC-DED codes. IBM Journal of Research and Development, 14(4), pp.395-401.

[9] Reviriego, P., Liu, S.S., Snchez-Macin, A., Xiao, L. and Maestro, J.A., 2016. Unequal error protection codes derived from SEC-DED codes. Electronics Letters, 52(8), pp.619-620.

[10] Chowdhury, D.R., Gupta, I.S. and Chaudhuri, P.P., 1995. CA-based byte error-correcting code. IEEE Transactions on Computers, 44(3), pp.371-382.

[11] Chaudhuri, P.P., Chowdhury, D.R., Nandi, S. and Chattopadhyay, S., 1997. Additive cellular automata: theory and applications (Vol. 1). John Wiley and Sons. IEEE Computer Society Press, 1997.

[12] Bhaumik, J. and Chowdhury, D.R., 2010. New architectural design of CA-based codec. IEEE transactions on very large scale integration (VLSI) systems, 18(7), pp.1139-1144.

[13] Samanta, J., Bhaumik, J. and Barman, S., 2015. CA-Based Area Optimized Three Bytes Error Detecting Codes. J. Cellular Automata, 10(5-6), pp.409-423.

[14] Samanta, J., Bhaumik, J. and Barman, S., 2018. Compact CABased Single Byte Error

Correcting Codec. IEEE Transactions on Computers, (2), pp.291-298.

[15] Cha, S. and Yoon, H., 2012. Efficient implementation of single error correction and double error detection code with check bit pre-computation for memories. JSTS: Journal of Semiconductor Technology and Science, 12(4), pp.418-425.

[16] Kou, Y., Lin, S. and Fossorier, M.P., 2001. Low-density parity-check codes based on finite geometries: a rediscovery and new results. IEEE Transactions on Information Theory, 47(7), pp.2711-2736.

[17] Chen, X. and Men, A., 2008, November. Reduced complexity and improved performance decoding algorithm for nonbinary LDPC codes over GF (q). In Communication Technology, 2008. ICCT 2008. 11th IEEE International Conference on (pp. 406-409). IEEE.

[18] Richardson, T.J., Shokrollahi, M.A. and Urbanke, R.L., 2001. Design of capacity-approaching irregular low-density parity-check codes. IEEE transactions on information theory, 47(2), pp.619-637.

[19] Lin, C.L., Tu, S.W., Chen, C.L., Chang, H.C. and Lee, C.Y., 2016. An efficient decoder architecture for non-binary LDPC codes with extended min-sum algorithm. IEEE Transactions on Circuits and Systems II: Express Briefs, 63(9), pp.863-867.

[20] Wicker, S.B. and Bhargava, V.K. eds., 1999. Reed-Solomon codes and their applications. John Wiley and Sons.

[21] Gracia-Morn, J., Saiz-Adalid, L.J., Gil-Toms, D., Baraza, J.C. and Gil-Vicente, P.J., 2016. A very fast Single Error Correction-Double Error Detection Code for short data words.

[22] Saiz-Adalid, L.J., Gil, P., Ruiz, J.C., Gracia-Morn, J., Gil-Toms, D. and Baraza-Calvo, J.C., 2016, September. Ultrafast Error Correction Codes for Double Error Detection/Correction. In 2016 12th European Dependable Computing Conference (EDCC), IEEE, pp. 108-119.

[23] Liu, S., Reviriego, P., Xiao, L. and Maestro, J.A., 2017. A method to recover critical bits under

a double error in SEC-DED protected memories. Microelectronics Reliability, 73, pp.92-96.

[24] Alabady, S.A., Salleh, M.F.M. and Al-Turjman, F., 2018. LCPC Error Correction Code for IoT Applications. Sustainable Cities and Society.

[25] Alabady, S.A. and Al-Turjman, F., 2018. Low Complexity Parity Check Code for Futuristic Wireless Networks Applications. IEEE Access, 6, pp.18398-18407.

[26] Alabady, S.A., Salleh, M.F.M. and Al-Turjman, F., 2018. A novel approach of error detection and correction for efficient energy in wireless networks. Multimedia Tools and Applications, pp.1-29.

[27] Ming, Z., Yi, X.L. and Wei, L.H., 2011, October. New SEC-DEDDAEC codes for multiple bit upsets mitigation in memory. In VLSI and System-on-Chip (VLSI-SoC), 2011 IEEE/IFIP 19th International Conference, IEEE, pp. 254-259.

[28] Samanta, J. and Tripathi, S., 2018. Comments on "A novel approach of error detection and correction for efficient energy in wireless networks", Multimedia Tools and Application, vol. 78, no. 6, pp. 75797584, (DOI: 10.1007/s11042-018-6481-8).

Investigation On GFDM System For 5G Applications Over Fading Channels

Lingaiah Jada* and S.Shiyamala

School of Electrical and Communication Engineering | ECE, Vel Tech Rangarajan Dr.Sagunthala R&D Institute of Science and Technology, Avadi, Chennai-600 062, Tamilnadu, India

Received 22 February 2022; Accepted 20 July 2022

Abstract

The main goal of this paper is to investigate a generalized frequency division multiplexing (GFDM) system in Rician and Weibull fading settings utilizing the maximal ratio transmission (MRT) scheme. Now a day, most communication devices require low latency and low consumption of energy. In the literature, various multicarrier techniques are addressed and GFDM is one such technique that is new formulation research for future generations of mobile services. One of the major advantages of the GFDM technique is low out-of-band radiation. This paper initially explores the symbol error rate (SER) expression analysis in Rician and Weibull fading using the proposed GFDM-MRT system. Later on, performance is evaluated with MATLAB simulations for various simulation parameters such as the number of transmitting antennas, different roll-off factors, and various fading parameters. The performance is improved by 8dB to achieve the symbol error rate of 0.01 when we use the number of transmitting antennas ($N_t = 4$) compared to a single antenna ($N_t = 1$). Finally, it can be concluded that GFDM-MRT techniques are more reliable for high-speed communications.

Keywords: GFDM, Maximal Ratio Transmission, symbol error rate, Rician fading, Weibull Fading, 5G network.

1. Introduction

It is expected that the 5G cellular networks of fifth-generation will tackle several things at a time to meet user's satisfaction. To meet their expectations, 5G systems require very little latency for the tactile internet, a loose synchronization for the Internet of Things (IoT), reliability, efficient and robust high throughput to communicate via bit pipe communication, large coverage area, and a dynamic allocation of the spectrum with the low value of out of band emission. The main factor that distinguishes between GFDM and OFDM is that number of subcarriers are non-orthogonal to each other in GFDM [1]. One more major advantage with GFDM is that cyclic prefixes (CP) are not added to each subcarrier so a lot of bandwidth is saved. In GFDM, only one CP is added to the combination of subcarriers, hence, we receive the same bits at the receiver that are transmitted from the transmitter. For carrier aggregation, OFDM was having a high Out of Band (OOB) emission and it is low for GFDM [2]. GFDM system is less complex, achieves low OOB and it is promising 5G solution is stated in [3-4]. In [5], the authors discussed that GFDM is a flexible technology that overcomes the drawbacks presented in 4G technology. As a result, it suggests that GFDM is backward compatible with long-term evolution's accumulated knowledge.

The OOB emission of GFDM can be reduced if there is a smooth transition between the blocks of GFDM. The guard band is used in between the GFDM blocks by erasing the first sub-symbol and there will be the orientation of signal edges towards zero corresponding to that. This makes the transition between the blocks of GFDM smooth. This whole process is named guard-symbol GFDM (GS-GFDM) [6]. Generally, GFDM is a waveform that is non-orthogonal but

it can be made orthogonal by using various pulse shaping filters. It can also be done by making use of the combination of GFDM and orthogonal quadrature amplitude modulation (OQAM).

GFDM is a less complex approach, it can implement an LTE master clock for 5G Physical layers. Along with that the time-frequency structure of the nowadays cellular systems can also be implemented in [7]. Various circular pulse shaping filters are addressed in [8-10] which are used in the GFDM system to meet the requirements in the latest technologies. The GFDM signal is generated by multiplying and concatenating input symbols with an appropriate prototype filter [11].

ISI can be removed but noise value is enhanced using a zero forced (ZF) receiver. Further, the efficiency of the GFDM receiver can be increased with a minimum mean square estimation (MMSE) receiver [12]. ICI reduction approaches are suggested in [13]. A pre-coded GFDM system is discussed in [14]. To minimize ICI and the complexity of the receiver, the scheme was suggested in [14]. In [11], GFDM, OFDM, and single carrier frequency division (SC-FDM) analysis and their PAPRs performances were compared and it stated that GFDM achieves lower PAPR. The symbol error rate (SER) expression over the AWGN channel for the GFDM system with a ZF receiver is shown in [5].

The multiple-input and multiple-output (MIMO) based GFDM analysis is described in [15-16] which receiver complexity is more. This method uses a maximal ratio combining (MRC) scheme before demodulation. A large-scale MIMO transmission GFDM scheme is described in [17]. In [18], V-BLAST and spatial modulation schemes are used in the GFDM system and bit error rate (BER) performance is evaluated. The complexity of identification of MIMO-GFDM signals analysis is given in [19]. The detection complexity is further reduced in the MIMO-

*E-mail address: jadalingaiah69@gmail.com

ISSN: 1791-2377 © 2022 School of Science, ITHU. All rights reserved.

doi:10.25103/jestr.153.01

GFDM system using the Montecarlo algorithm in [20-21]. MIMO structure and MRT also reduces the complexity in [22-23]. Weibull fading is a basic statistical model that can be used in both indoor and outdoor settings, according to studies [31]. The importance of the Weibull fading channel in digital modulation systems is convincingly demonstrated in [32]. Some detailed analysis about the Weibull fading channel is provided in [33].

With the use of Maximal ratio transmission (MRT), receiver complexity in MIMO systems is reduced. There is not much work is addressed in the literature related to GFDM with MRT. The MRT-based GFDM system performance is evaluated over Nakagami- m fading channel in [24]. The above-stated references are useful to analyze the performance of GFDM with the MRT scheme in the Rician fading channel.

The remaining paper is structured in other four sections. The proposed GFDM based MRT scheme is described in section-2. Section-3 deals with the SER analysis in Rician and Weibull fading. Simulation analysis followed by conclusions is given in section-4 and section-5 respectively.

2. System Model Description

The proposed GFDM based MRT system model is shown in Fig. 1. The proposed system is having a transmitter and receiver. The transmitter consists of an encoder, mapper, and other various blocks. The vectorial data (\mathbf{b}) in the form of bits given as input to the encoder. The encoder converts the input from low bit-rate data stream into high bit-rate data stream and the output of the data vector is (\mathbf{b}_c). The output of the encoder is given as input to the mapper and it produces output as $N \times 1$ data vector (\mathbf{d}). This vectorial data is given as input to the GFDM modulator which consists of N elements. The vectorial data (\mathbf{d}) is decomposes into K groups M symbols as follows.

$$\mathbf{d} = [(d_0)^T, (d_1)^T, \dots, (d_{K-1})^T]^T \quad (1)$$

with

$$d_k = [d_{k,0}, d_{k,1}, \dots, d_{k,M-1}]^T \quad (2)$$

In eq. (2), $d_{k,m}$ is data symbol which is transmitted through k -th subcarrier at m -th time slot and $g_{k,m}(\mathbf{n})$ is filter coefficient. Let us assume that the GFDM block occupies K subcarriers, each subcarrier consists of M data symbols and it produces $N = KM$ samples. With GFDM modulator, samples are filtered with a corresponding transmit filter is given as [11]

$$g_{k,m}[n] = g[(n - mk) \bmod N] e^{-\frac{j2\pi kn}{K}} \quad (3)$$

The exponential term conducts frequency domain shift, and $g_{k,m}(\mathbf{n})$ is a time and frequency shifted version of $g(\mathbf{n})$. Finally, all the transmitted symbols are superimposed at one place that leads to GFDM signal which is given as $\mathbf{x}(\mathbf{n})$ in [11]

$$\mathbf{x}[n] = \sum_{k=0}^{K-1} \sum_{m=0}^{M-1} d_{k,m} g_{k,m}[n], \quad n = 0, 1, \dots, KM - 1 \quad (4)$$

The pulse-shaping filter samples can be shown as follows

$$g_{k,m} = [g_{k,m}[0], g_{k,m}[1] \dots g_{k,m}[MK - 1]]^T \quad (5)$$

and matrix representation of eq. (4) is [12]

$$\mathbf{x} = A\mathbf{d} \quad (6)$$

where A is a $KM \times KM$ dimension matrix which is also known as GFDM modulation matrix and is represented as [5]

$$A = [g_{0,0} \dots g_{K-1,0} g_{0,1} \dots g_{K-1,M-1}] \quad (7)$$

A cyclic prefix (CP) and cyclic suffix (CS) are added after GFDM block and then signal components are weighted with MRT coefficients as;

$$\mathbf{x}_i = w_i \mathbf{x} \quad (8)$$

where w_i is weighting factor (MRT coefficient) for i -th antenna and ($i = 1, 2, \dots, N_t$) [22];

$$w_i = \frac{h_i^*}{h_F} \quad (9)$$

$$h_F = \|\mathbf{h}\| = \sqrt{\sum_{i=1}^{N_t} |h_i|^2}$$

In eq. (9), h_i is channel coefficient. h_F Frobenius norm of channel vector $\mathbf{h} = [h_1, h_2, \dots, h_{N_t}]$.

Finally, the GFDM signal is multiplied with MRT coefficients is received at the receiver and its mathematical representation is

$$\mathbf{r} = \sqrt{P_t} \sum_{i=0}^{N_t} h_i w_i \mathbf{x} + \mathbf{w} = \sqrt{P_t} h_F \mathbf{x} + \mathbf{w} \quad (10)$$

Where \mathbf{w} is a noise vector $w \sim (0, \sigma_w^2)$. Later on, power is normalized by $P_t = 1/N_t$ at each antenna, so that channel coefficient in eq. (9) is equalized. Finally, an output signal from the equalizer is demodulated by matched filter (MF), ZF, and MMSE. The expression for the demodulated signal is [5]

$$\hat{\mathbf{d}} = B\mathbf{y} \quad (11)$$

where B is a demodulation matrix.

The demodulation matrix for the MF receiver is $B_{MF} = A^H$ which maximizes SNR and self-interference. Likely, for MMSE receiver B matrix is

$$B_{MMSE} = (R_n^2 + A^H H^H A H)^{-1} A^H H^H$$

which balances self-interference and noise enhancement and R_n^2 is the noise covariance matrix. Similarly, the B matrix for the ZF receiver is $B_{MF} = A^{-1}$. While the ZF receiver eliminates self-interference, it significantly improves noise efficiency.

The noise enhancement factor (NEF) ' ξ ' represents the amount of reduction in SNR value when uses ZF receiver and its mathematical expression is [5]

$$\xi = \sum_{i=0}^{MK-1} |[B_{ZF}]_{k,i}|^2 \quad (12)$$

where ' ξ ' is equal for all $k = 0, 1, \dots, MK - 1$.

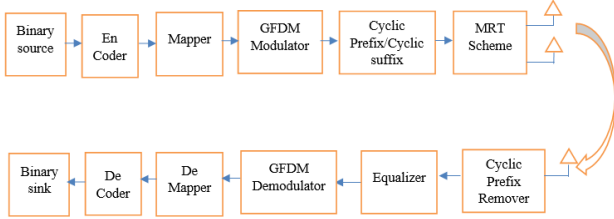


Fig. 1. Proposed GFDM Transceiver with MRT Scheme.

3. Symbol Error Rate Analysis

This section gives the analysis of GFDM based MRT scheme SER performance with ZF receiver in Rician and weibull fading environment. The usage of the ZF receiver in the proposed system reduces the self-interference but increases the noise value. The SER performance is evaluated using the QAM modulation scheme in the Rician and weibull channel. The channel impulse response of length N_{ch} can be represented as

$$h = [h_0, \dots, h_{N_{ch}-1}]^T \quad (13)$$

The received signal mathematical representation at the receiver is

$$r = Hx + w \quad (14)$$

In the above expression r and x are received and transmitted information respectively. Where $\mathbf{H} = \text{circ}\{\bar{h}\}$ and \bar{h} is a zero-padded version of h of the same length. For AWGN environment $\mathbf{H}=\mathbf{I}$, where \mathbf{I} is identity matrix. For the different fading environments in the wireless channel, \mathbf{H} value varies. In this paper, we are considering Rician and weibull fading in the wireless channel since it can be modeled as most of the cases because it consists of a line of sight (LOS) component.

3.1. Rician Channel Model

The Rician channel can be modeled if the signal amplitude in the wireless channel follows the Rician distribution. The envelopes of channel coefficients are $|h_i|$ for $i = 1, 2, \dots, N_t$ and PDF is given as [27].

$$f_{|h_i|}(|h_i|) = \left(\frac{1+K}{\bar{h}_i}\right) \exp\left[-\frac{(1+K)h_i + K\bar{h}_i}{\bar{h}_i}\right] I_0\left[\sqrt{\frac{4K(1+K)h_i}{\bar{h}_i}}\right]; \quad 0 \leq K < \infty \quad (15)$$

Where K is the Rician fading parameter

The instantaneous SNR value is

$$\gamma = \frac{P_t E_s}{\xi N_0} h_F^2 \quad (16)$$

In eq. (16), E_s and N_0 are average energy per symbol and noise power spectral density respectively. From eq. (9), the envelope of h_F can be computed as

$$h_F = \sqrt{X_1^2 + X_2^2 + \dots + X_{2mN_t}^2} \quad (17)$$

where $X_i \sim (0, \sigma_x^2)$ and $(i = 1, 2, \dots, 2mN_t)$ and $\bar{K} = KN_t$ [25], then the expression for PDF is

$$p_{h_F}(h_F) = \left(\frac{1+\bar{K}}{\bar{h}_F}\right) \exp\left[-\frac{(1+\bar{K})h_F + \bar{K}\bar{h}_F}{\bar{h}_F}\right] I_0\left[\sqrt{\frac{4\bar{K}(1+\bar{K})h_F}{\bar{h}_F}}\right]; \quad 0 \leq K < \infty \quad (18)$$

Then, the PDF in terms of SNRs is given in [26];

$$p_\gamma(\gamma) = \left(\frac{1+\bar{K}}{\bar{\gamma}}\right) \exp\left[-\frac{(1+\bar{K})\gamma + \bar{K}\bar{\gamma}}{\bar{\gamma}}\right] I_0\left[\sqrt{\frac{4\bar{K}(1+\bar{K})\gamma}{\bar{\gamma}}}\right]; \quad 0 \leq K < \infty \quad (19)$$

where $\bar{\gamma}$ is the average SNR value or $\bar{\gamma} = E[\gamma]$.

3.2. SER of GFDM-MRT

This section gives the exact expressions of SER of the GFDM-MRT system over the non-fading environment, Rician and weibull fading environment.

3.3 Non-fading (AWGN) Environment

The SNR is equally adjusted by NEF for GFDM at the receiver side. Hence, both OFDM SER and GFDM SER expressions for the AWGN environment are almost the same and they are differed in equivalent SNR [28]. The expression for SER under AWGN using GFDM system is [5];

$$P_{SER,AWGN}(\gamma) = 2\left(\frac{p-1}{p}\right) \text{erfc}(\sqrt{\gamma}) - \left(\frac{p-1}{p}\right)^2 \text{erfc}^2(\sqrt{\gamma}) \quad (20)$$

Where

$$\gamma = \frac{3RT}{2(2^\mu-1)} \frac{E_s}{\xi N_0} \text{ and } r = \frac{NM}{NM+N_{CP}+N_{CS}} \quad (21)$$

In eq. (20) and (21), $p = \sqrt{2\mu}$, μ represents the number of bits, N_{CP} , N_{CS} are the length of CP and CS respectively. N and M are number of subcarriers and sub-symbols.

The SER expression for different fading environments can be evaluated by averaging the error rates AWGN over PDF of other fading channels. It can be calculated using [5]

$$P_{SER} = \int_0^\infty P_{AWGN}(\gamma) P_\gamma(\gamma) d\gamma \quad (22)$$

In eq. (22), $P_\gamma(\gamma)$ represents the PDF of different fading channels.

3.4 Rician Fading Environment

To calculate SER expression in Rician fading, we require a PDF of Rician fading. The PDF expression is shown in eq. (19), it can be further modified by expressing it in infinite series form of a zeroth model of Bessel function [29];

$$I_0(x) = \sum_{q=0}^{\infty} \frac{\left(\frac{x^2}{4}\right)^q}{(q!)^2} \quad (23)$$

The modified PDF expression for the Rician fading environment is given in [25]

$$P_\gamma(\gamma) = \frac{1+K}{\bar{\gamma}_r} e^{-K} \sum_{q=0}^{\infty} \frac{1}{(q!)^2} \left(\frac{K(1+K)}{\bar{\gamma}_r}\right)^q \gamma^q \exp\left(-\frac{\gamma(1+K)}{\bar{\gamma}_r}\right) \quad 0 \leq K < \infty \quad (24)$$

Now, SER expression for Rician fading can be computed by substituting eq. (20) and eq. (24) in eq. (22), the bounded SER expression for GFDM system with single antenna is [25];

$$P_{SER,Ric}(\gamma) = \frac{2(p-1)}{p} I_3(\bar{\gamma}_r) - \left(\frac{p-1}{p}\right)^2 I_4(\bar{\gamma}_r) \quad (25)$$

Where $I_3(\bar{\gamma}_r)$ and $I_4(\bar{\gamma}_r)$ are expressed as given below;

$$I_3(\bar{\gamma}_r) = \frac{1+K}{\bar{\gamma}_r} e^{-K} \sum_{q=0}^{\infty} \frac{1}{(q!)^2} \left(\frac{K(1+K)}{\bar{\gamma}_r}\right)^q \frac{\Gamma(q+\frac{3}{2})}{\sqrt{\pi}(q+1)} {}_2F_1\left[q + 1, q + \frac{3}{2}; q + 2; + \left(\frac{1+K}{\bar{\gamma}_r}\right)\right] \quad (26)$$

$$I_4(\bar{\gamma}_r) = e^{-K} \sum_{q=0}^{\infty} \frac{K^q}{(q!)^2} \left(1 - \frac{4}{\pi} \sum_{j=0}^q \frac{\left(\frac{1+K}{\bar{\gamma}_r}\right)^j}{2j+1} {}_2F_1\left[j + \frac{1}{2}, j + 1; j + \frac{3}{2}; -\left(\frac{1+K}{\bar{\gamma}_r} + 1\right)\right]\right) \quad (27)$$

Similarly, for multiple antennas (N_t) case, SER expression for GFDM based MRT system is obtained by changing K to KN_t , the bounded SER expression for GFDM based MRT system with multiple antennas is

$$P_{SER,Ric}(\gamma) = \frac{2(p-1)}{p} I_3(\bar{\gamma}_r) - \left(\frac{p-1}{p}\right)^2 I_4(\bar{\gamma}_r) \quad (28)$$

$$I_3(\bar{\gamma}_r) = \frac{1+KN_t}{\bar{\gamma}_r} e^{-K} \sum_{q=0}^{\infty} \frac{1}{(q!)^2} \left(\frac{KN_t(1+KN_t)}{\bar{\gamma}_r}\right)^q \frac{\Gamma(q+\frac{3}{2})}{\sqrt{\pi}(q+1)} {}_2F_1\left[q + 1, q + \frac{3}{2}; q + 2; + \left(\frac{1+KN_t}{\bar{\gamma}_r}\right)\right] \quad (29)$$

$$I_4(\bar{\gamma}_r) = e^{-KN_t} \sum_{q=0}^{\infty} \frac{(KN_t)^q}{(q!)^2} \left(1 - \frac{4}{\pi} \sum_{j=0}^q \frac{\left(\frac{1+KN_t}{\bar{\gamma}_r}\right)^j}{2j+1} {}_2F_1\left[j + \frac{1}{2}, j + 1; j + \frac{3}{2}; -\left(\frac{1+KN_t}{\bar{\gamma}_r} + 1\right)\right]\right) \quad (30)$$

where

$$\bar{\gamma}_r = \frac{3R_T \sigma_r^2 E_s}{(2^\mu - 1) \xi N_0} \quad (31)$$

In the above eq. (31), $\bar{\gamma}_r$ is equivalent SNR in a Rician fading environment. Where ${}_2F_1[., .; .;]$ denotes the Gauss hypergeometric function [30]. It is assumed that σ_r^2 value is 0.5. If we substitute $K = 0$ for both single and multiple antennas cases, the expressions give the SER expressions for the Rayleigh fading environment. For $K = 0$, our simulation (Fig.2, black line) is exactly matching with the simulation (Fig.6, curve (i)) given in [25]. For $N_t = 1$, eq. (25) and eq. (28) are exactly match with each other.

4 Nakagami- m Fading Environment

The PDF expression for Nakagami- m fading environment is given in [24] as

$$p_\gamma(\gamma) = \left(\frac{m}{\bar{\gamma}}\right)^m \frac{\gamma^{m-1}}{\Gamma(m)} e^{-\frac{m\gamma}{\bar{\gamma}}} \quad (32)$$

To calculate SER expression in Nakagami- m fading, we require a PDF of Nakagami- m fading which is shown in eq. (32). Now, SER expression for Nakagami- m fading can be calculated by substituting equ. (20) and equ. (32) in equ. (22), the bounded SER expression for GFDM system with single antenna is given in [24];

$$P_{SER,Nak} = 2C_1 C_2^m \frac{\Gamma(m+\frac{1}{2})}{\sqrt{\pi}\Gamma(m+1)} {}_2F_1\left[m, m + \frac{1}{2}; m + 1; -C_2\right] - C_1^2 \left[1 - \frac{4}{\pi} \sum_{j=0}^{m-1} \frac{C_2^j}{2j+1} {}_2F_1\left[j + \frac{1}{2}, j + 1; j + \frac{3}{2}; -(C_2 + 1)\right]\right] \quad (33)$$

where C_1 and C_2 are expressed as follows;

$$C_1 = \frac{\sqrt{2^\mu - 1}}{\sqrt{2^\mu}}, \quad C_2 = \frac{m}{\bar{\gamma}_n} \quad (34)$$

Similarly, for multiple antennas (N_t) case, SER expression for GFDM based MRT system is obtained by changing m to mN_t , the bounded SER expression for GFDM based MRT system with multiple antennas is given in [24];

$$P_{SER,Nak} = 2C_1 C_2^{mN_t} C_4 {}_2F_1\left[mN_t, mN_t + \frac{1}{2}; mN_t + 1; -C_3\right] - C_1^2 \left[1 - \frac{4}{\pi} \sum_{j=0}^{mN_t-1} \frac{C_3^j}{2j+1} {}_2F_1\left[j + \frac{1}{2}, j + 1; j + \frac{3}{2}; -(C_3 + 1)\right]\right] \quad (35)$$

where C_3 and C_4 are expressed as follows

$$C_3 = \frac{mN_t}{\bar{\gamma}_n}, \quad C_4 = \frac{\Gamma(mN_t+\frac{1}{2})}{\sqrt{\pi}\Gamma(mN_t+1)} \quad (36)$$

$$\bar{\gamma}_n = \frac{3R_T P_t N_t \sigma_n^2 E_s}{(2^\mu - 1) \xi N_0} \quad (37)$$

In the above eq. (33), $\bar{\gamma}_n$ is equivalent to SNR in the Nakagami-fading environment. It is assumed that σ_n^2 value is 0.5. If we substitute $m = 1$ for both single and multiple antennas cases, the expressions give the SER expressions for the Rayleigh fading environment. For $m=1$, our simulation (Fig.2) is exactly matching with the simulation (Fig.2) given in [24]. For $N_t = 1$, eq. (33) and eq. (35) are exactly match with each other. For $m = 1$ and $K = 0$, eq. (25) and eq. (33) gives the same results and those two equations merge to Rayleigh's fading environment.

5 Weibull Fading Environment

The modified PDF expression for the Rician fading environment is given in [34];

$$P_\gamma(\gamma) = \left(\frac{v}{2(a\bar{\gamma})^{\frac{v}{2}}}\right) \gamma^{\frac{v}{2}-1} \exp\left(-\left(\frac{\gamma}{a\bar{\gamma}}\right)^{\frac{v}{2}}\right) \quad (38)$$

Now, SER expression for Weibull fading can be computed by substituting equ. (20) and equ. (38) in equ. (22), the bounded SER expression for GFDM system with single antenna is [33];

where $a = 1/\Gamma(1 + 2/v)$.

$$P_{Wbl}(e) = \frac{2(p-1)}{p} \frac{\frac{v}{2}}{(a\bar{\gamma})^{\frac{v}{2}}} I_3(\bar{\gamma}_{wb}) - \left(\frac{p-1}{p}\right)^2 \frac{\frac{v}{2}}{(a\bar{\gamma})^{\frac{v}{2}}} I_4(\bar{\gamma}_{wb}) \quad (39)$$

Where

$I_3(\bar{\gamma}_{wb})$ and $I_4(\bar{\gamma}_{wb})$ are expressed as given below;

$$I_3(\bar{\gamma}_{wb}) = \int_0^\infty \gamma^{\frac{v}{2}-1} e^{-\frac{\gamma}{(a\bar{\gamma}_{wb})^{\frac{v}{2}}}} \text{erfc}(\sqrt{\gamma}) d\gamma \quad (40)$$

$$I_4(\bar{\gamma}_{wb}) = \int_0^\infty \gamma^{\frac{v}{2}-1} e^{-\frac{\gamma}{(a\bar{\gamma}_{wb})^{\frac{v}{2}}}} \text{erfc}^2(\sqrt{\gamma}) d\gamma \quad (41)$$

Where

$$\bar{\gamma}_{wb} = \frac{3R_T \sigma_{wb}^2 E_s}{(2^\mu - 1) \xi N_0} \quad (42)$$

From [33], $I_3(\bar{\gamma}_{wb})$ and $I_4(\bar{\gamma}_{wb})$

$$I_3(\bar{\gamma}_{wb}) = \frac{2(a\bar{\gamma}_{wb})^{\frac{v}{2}}}{v} - \frac{\left(\frac{k}{2}\right)^{\frac{1}{2}} (\lambda)^{\frac{v}{2}}}{\sqrt{\pi}(2\pi)^{\frac{\lambda+k-2}{2}}} G_{2\lambda+k,\lambda}^{k+\lambda,\lambda} \left[\frac{\lambda^{\lambda-k}}{(a\bar{\gamma}_{wb})^{\frac{vk}{2}}} \middle| \begin{matrix} \Delta\left(\lambda, \frac{1-v}{2}\right), \Delta\left(\lambda, 1 - \frac{v}{2}\right) \\ \Delta(k, 0), \Delta\left(\lambda, -\frac{v}{2}\right) \end{matrix} \right] \quad (43)$$

$$I_4(\bar{\gamma}_{wb}) = \frac{2(a\bar{\gamma}_{wb})^{\frac{v}{2}}}{v} \left[1 - \frac{2 \sum_{i=0}^{\infty} \frac{(-1)^i}{i!} \left(\frac{k}{2}\right)^{\frac{1}{2}} (\lambda)^{\frac{i-1}{2}}}{\sqrt{\pi}(2\pi)^{\frac{\lambda+k-2}{2}}} G_{2\lambda+k,\lambda}^{k+\lambda,\lambda} \left[\frac{\lambda^{\lambda-k}}{(a\bar{\gamma}_{wb})^{\frac{vk}{2}}} \middle| \begin{matrix} \Delta\left(\lambda, \frac{1}{2} - i\right), \Delta(\lambda, -i) \\ \Delta(k, 0), \Delta\left(\lambda, -i - \frac{1}{2}\right) \end{matrix} \right] \right] \quad (44)$$

Similarly, for multiple antennas (N_t) case, SER expression for GFDM based MRT system is obtained by changing K to KN_t .

4. Simulation Analysis

This section discusses the simulation results and their analysis. All the simulations are performed with simulation values such as number of subcarriers $K=64$, length of CP $N_{CP}=8$ and length of $N_{CS}=0$.

4.1 Specifications used for simulation

Parameter	Variable	Value
Modulation Scheme	μ (Modulation Index)	QPSK , 16-QAM
Sub-carriers	K	64
Block-length	M	16
Filter type	-	RRC
Roll-off factor	α	0.1,0.6,0.9
Channel	$h(n)$	1, for AWGN
Cyclic prefix	CP	-
Fading Channels	-	Rician, Weibull
Fading Parameter	K	0,1,2,3 If $K=0$ Channel is Rayleigh fading $K= \infty$ Channel is AWGN
Transmitting Antennas	N_t	4

Fig. 2 represents the SER analysis of GFDM-MRT based system for various values of SNRs using multiple antennas at the transmitter ($N_t = 1,2,3,4$) and with a roll-off factor $\alpha = 0.1$. From the simulation, it is observed that simulation is evaluated for Rayleigh fading ($K = 0$) environment which is a special case of Rician fading with Rician fading parameter $K=0$. It is also observed that SER performance decreases as the number of antennas increases. In [24] SER performance was calculated for only $N_t=1$, the value of SER is $0.13 * 10^{-2}$ but in this paper we calculate SER performance for $N_t = 1, 2, 3, 4$ respectively. For a particular case at SNR = 15dB, SER values are $0.13 * 10^{-2}$, $0.09 * 10^{-3}$, $0.66 * 10^{-4}$ and $0.03 * 10^{-5}$ for $N_t = 1, 2, 3, 4$ respectively. At $N_t = 4$ SER performance is compared with $N_t=1$ in [24] minimized the SER to 99.97%. Finally, it can be concluded that the GFDM-MRT scheme with $N_t = 4$ gives 10dB, 4dB, and 2dB SNR gain for $N_t = 1, 2, 3$ transmit antennas at SER= 10^{-2} . Fig. 2 also compares the simulation results of [24] for different values of N_t , $K = 0$, and $\alpha = 0.1$.

Fig. 3 represents the SER analysis of GFDM-MRT based system for various values of SNRs using multiple antennas at the transmitter ($N_t = 2$), various Rician fading parameters $K = (0,1,2,3)$ and with a roll-off factor $\alpha = 0.1$. The curve for $K = 0$ is exactly matches with Rayleigh fading conditions and gives the same SER performance which matches with previous work [24]. But here, we can infer that as an increase in Rician fading parameter (K) from 0 to 3, the SER decreases.

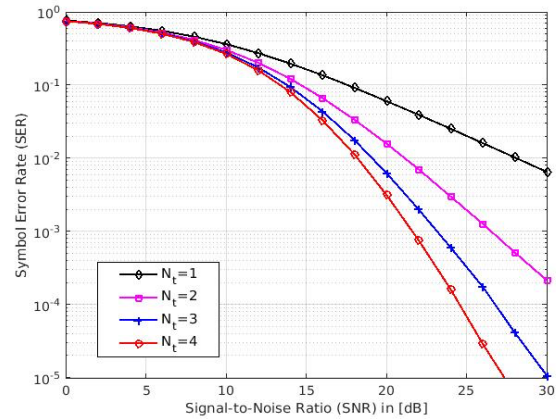


Fig. 2. SER vs SNR performance with the various number of transmitting antennas.

For a particular case at SNR=15dB, the error values for $K=0, 1, 2, 3$ are respectively 0.01596, 0.0103, 0.0060 and 0.003. At $K=4$ SER performance is compared with $K=0$ [24] i.e. approximately there is an 81.2% decrease in error from $K=0$ to $K=3$. Finally, it can be concluded that GFDM-MRT scheme with $N_t = 4$ gives 10dB, 4dB, and 2dB SNR gain for $N_t = 1, 2, 3$ transmit antennas at SER= 10^{-2} .

Fig. 4 is drawn between SER and SNR for different roll-off factors ($\alpha = 0.1, 0.6, 0.9$), $N_t = 2$, $K = 2$ and using a 16-QAM modulation scheme. Fig. 4 also explains the effect of the NEF parameter ζ which plays a key role in GFDM. As the value of the roll-off factor increases from 0.1 to 0.9, there is a significant change in the SER curve because as ζ increases there is a wider overlap of the subcarriers which increases the NEF factor. The SER values are 0.0216, 0.0116, 0.0060 at SNR=20dB for various values of $\alpha = 0.9, 0.6$ and 0.1 respectively. Here as α value decreases from 0.9

to 0.1, the SER value decreases by 72% but in literature[24] SER decreased by 50% as α value decreases from 0.9 to 0.1

Fig. 5 is drawn between SER and roll-off factor for different SNR values (10dB, 15dB, 20dB), $N_t = 3, K = 3$ and using 16-QAM modulation scheme. From the simulation it is observed that as SNR value increases from 10dB to 20dB, SER value decreases from 0.277 to 0.001 at $\alpha = 0.4$, it shows that there is an almost 95% improvement in SER with the increase in SNR. At a lower α value, the SER value is lower and it increases at higher α values. Finally, it can be concluded that to achieve less symbol error rate lower value at $\alpha=0.1$ and higher SNR=20dB values are always recommendable.

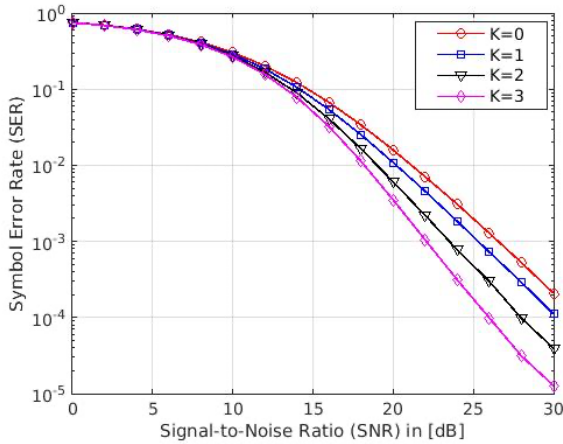


Fig. 3. SER vs SNR performance for various Rician fading parameters.

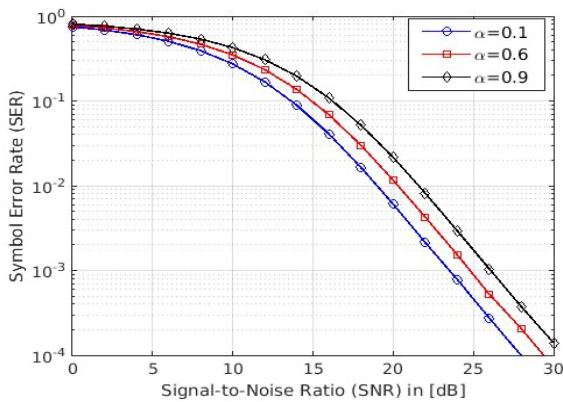


Fig.4. SER vs SNR performance for various Roll-off factors.

Fig. 6 is drawn between SER and SNRs for different modulation schemes (QPSK and 16-QAM), $K = 3, N_t = 3$ and $\alpha = 0.1$. From this simulation, we can state that the QPSK scheme achieves a lower value of SER compare to the 16-QAM modulation scheme. For a particular case, at SNR=10dB, SER values are 0.0251 and 0.0072 for 16-QAM and QPSK schemes.

Fig. 7 represents the SER performance of GFDM-MRT based system for various values of SNRs using multiple antennas at the transmitter ($N_t = 1,2,3,4$) and with a roll-off factor $\alpha = 0.1$ under the Weibull fading channel. In literature [33] only at $N_t = 1$ transmitter SER performance analysed. It is observed from Fig.7 that SER performance falls as N_t increases. For a particular case at SNR= 15dB, SER values are 0.04409, 0.03329, 0.02054 and 0.01554 for $N_t = 1, 2, 3, 4$ respectively. Finally, it can be concluded that the GFDM-MRT scheme with $N_t = 4$ gives 4dB, 3dB, and 2dB

SNR gain according to $N_t = 1, 2, 3$ transmit antennas respectively at SER= 10^{-2} .

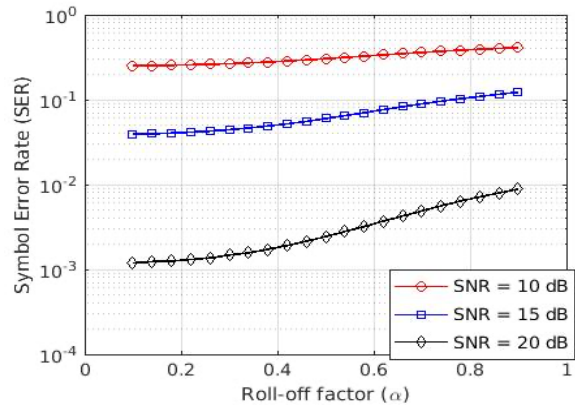


Fig. 5. SER vs roll-off factor for various SNR values.

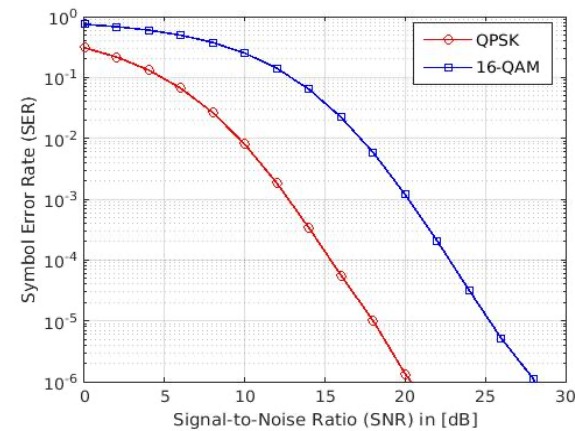


Fig.6. SER vs SNR performance for various modulation schemes.

Fig. 8 is drawn between SER and SNR for different roll-off factors ($\alpha = 0.1, 0.6, 0.9$), $N_t = 2$ and using a 16-QAM modulation scheme. Fig. 8 also explains the effect of the NEF parameter ζ which plays an important role in GFDM. The SER values are 0.04064, 0.02054, 0.01129 at SNR=16dB for various values of $\alpha = 0.9, 0.6$ and 0.1 respectively. As α value decreases from 0.9 to 0.1, the SER value decreases by 72.2%.

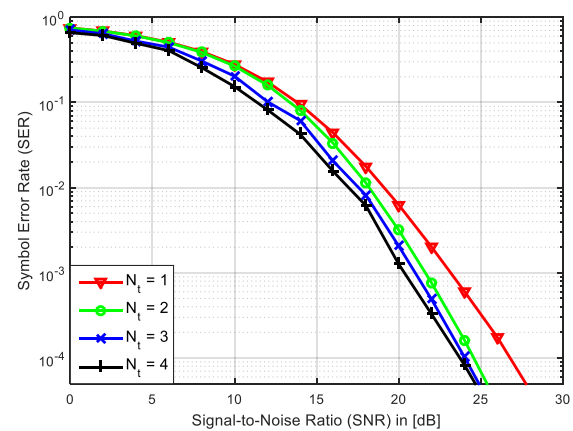


Fig.7. SER vs SNR performance with the various number of transmitting antennas.

Fig. 9 is drawn between SER and roll-off factor for different SNR values (10dB, 15dB, 20dB), $N_t = 3$ and using a 16-QAM modulation scheme. From the simulation, it is

observed that as SNR value increases from 10dB to 20dB, SER value decreases from 0.03525 to 0.05544 at $\alpha = 0.4$, which shows that there is an almost 57.2% improvement in SER with the increase in SNR. The SER value is less at lower values of α and it increases and is high at higher values of α .

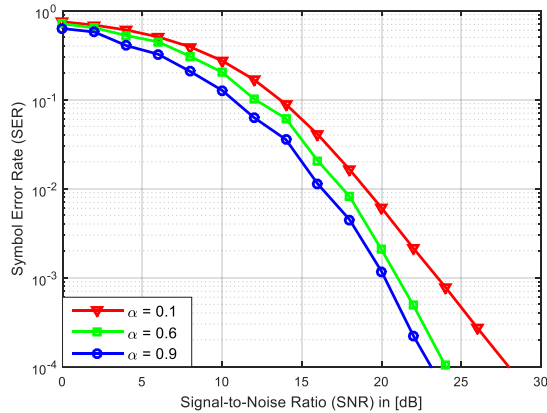


Fig.8. SER vs SNR performance for various Roll-off factors.

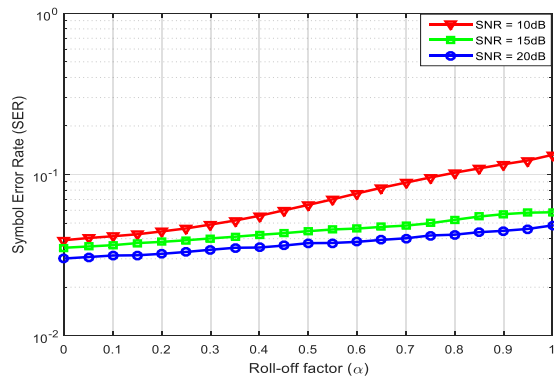


Fig.9. SER vs roll-off factor for various SNR values.

5. Conclusion

Under the Rician fading environment, the proposed GFDM-MRT scheme is suggested and its symbol error rate (SER) performance is investigated. Initially, the closed form of SER expression under Rician and Weibullfading environment for single and multiple antennas has provided. Later on, SER performance is evaluated with MATLAB simulations for various simulation parameters such as several transmitting antennas, different roll-off factors, and various fading parameters. We have also validated our simulations with the existing literature papers. The SNR performance is improved by approximately 6dB to achieve the symbol error rate of 0.01, when we use the number of transmitting antennas ($N_t = 4$) compared to a single antenna. ($N_t = 1$). Finally, it can be concluded that the GFDM-MRT technique is more reliable for high-speed communications.

This is an Open Access article distributed under the terms of the Creative Commons Attribution License.



References

1. A. Farhang, N. Marchetti, and L. Doyle, "Low Complexity Transceiver Design for GFDM", *IEEE Transactions on Signal Processing*, Vol. 64, Issue 6, pp.1507-1518, March-2016.
2. Z. Sharifian, M. Omid, A. Farhang and H. Source, "Polynomial-Based Compressing and Iterative Expanding for PAPR Reduction in GFDM", *23rd Iranian Conference on Electrical Engineering*, pp. 518-523, Iran, May-2015.
3. J. S. Ferreira, H. D. Rodrigues, A. A. Gonzalez, A. Nimr, M. Matthé, D. Zhang, L. L. Mendes, and G. Fettweis, "GFDM frame design for 5G application scenarios," *J. Commun. and Information Systems*, vol. 32, no. 1, pp. 54-61, 2017.
4. D. Zhang, M. Matthé, L. L. Mendes, and G. Fettweis, "A study on the link level performance of advanced multicarrier waveforms under MIMO wireless communication channels," *IEEE Trans. Wireless Commun.*, vol. 16, no. 4, pp. 2350 - 2365, Mar. 2017.
5. N. Michailow, M. Matthé, I. S. Gaspar, A. N. Caldevilla, L. L. Mendes, A. Festag, and G. Fettweis, "Generalized frequency division multiplexing for 5th generation cellular networks," *IEEE Trans. Commun.*, vol. 62, no. 9, pp. 3045-3061, Sep. 2014.
6. N. Michailow, L. Mendes, M. Matthe, I. Gaspar, A. Festag and G. Fettweis, "Robust WHTGFDM for the Next Generation of Wireless Networks", *IEEE Communications Letters*, Vol. 19, Issue 1, pp. 106-109, November-2014.
7. I. Gaspar, L. Mendes, M. Matthe, N. Michailow, A. Festag and G. Fettweis, "LTE- Compatible 5G PHY based on Generalized Frequency Division Multiplexing", in *Proceedings of the 11th International Symposium on Wireless Communications Systems*, pp. 209-213, Spain, August-2014.
8. G. Fettweis, M. Krondorf, and S. Bittner, "GFDM – Generalized Frequency Division Multiplexing," *Vehicular Technology Conference*, 2009.
9. S. Antapurkar, Pandey and K. Gupta, "GFDM Performance in terms of BER, PAPR and OOB and comparison to OFDM system", *2nd International Conference on communication systems*, India, October-2015.
10. A. Kumar, M. Magarini, "Improved Nyquist Pulse Shaping Filters for Generalized Frequency Division Multiplexing", *IEEE Latin American Conference on Communications*, pp. 1-7, November 2016.
11. N. Michailow and G. Fettweis, "Low Peak-to-Average Power Ratio for Next Generation Cellular Systems with Generalized Frequency Division Multiplexing," *IEEE International Symp. on Int. Sig. Proc. and Comm. Sys.*, Nov. 2013, pp. 651-655.
12. N. Michailow, S. Krone, M. Lentmaier and G. Fettweis, "Bit Error Rate Performance of Generalized Frequency Division Multiplexing," *Vehicular Technology Conference*, 2012
13. R. Datta, N. Michailow, M. Lentmaier, and G. Fettweis, "GFDM Interference Cancellation For Flexible Cognitive Radio PHY Design," *Vehicular Technology The conference*, 2012.
14. S. Tiwari, S. S. Das, K. K. Bandyopadhyay, "Precoded generalized frequency division multiplexing system to combat inter-carrier interference: performance analysis," *IET Comm.*, vol. 9, no. 15, pp. 1829-1841, May. 2015.
15. M. Matthe, L. L. Mendes and G. Fettweis, "Space-Time Coding for Generalized frequency Division Multiplexing," *European Wireless Conference*, 2014.
16. M. Matthe, L. L. Mendes, N. Michailow, D. Zhang, and G. Fettweis, "Widely Linear Estimation for Space-Time-Coded GFDM in Low Latency Applications," *IEEE Transactions on Communications*, vol. 63, no. 11, pp. 4501-4509, Nov. 2015.

17. N. E. Tunali, M. Wu, C. Dick, and C. Studer, "Linear Large-Scale MIMO Data Detection for 5G Multi-Carrier Waveform Candidates," *Conference on Signals, Systems and Computers*, 2015.
18. J. Datta, H.-P. Lin, and D.-B. Lin, A method to implement interference avoidance based MIMO-GFDM using spatial modulation," *Inter. Conf. on Advanced Tech. for Comm.*, 2015.
19. M. Matthe, I. S. Gaspar, D. Zhang, and G. Fettweis, "Near ML Detection" for MIMO-GFDM," *Vehicular Technology Conference*, 2015.
20. D. Zhang, M. Matthe, L. L. Mendes, and G. Fettweis, "A Markov Chain Monte Carlo Algorithm for Near-Optimum Detection of MIMO-GFDM Signals," *Inter. Symp. on Personal Indoor and Mobile Radio Communication*, 2015.
21. D. Zhang, M. Matthe, L. L. Mendes, I. S. Gaspar, N. Michailow, and G. Fettweis, Expectation Propagation for Near-Optimum Detection of MIMO-GFDM Signals," *IEEE Trans. on Wireless Comm.*, vol. 15, no. 2, pp. 1045-1062, Feb. 2016.
22. T. K. Y. Lo, "Maximum ratio transmission," *IEEE Trans. on Comm.*, vol. 47, no. 10, pp. 1458-1461, 1999.
23. E. Erdogan, T. Gucluoglu, "Performance Analysis of Maximal Ratio Transmission with Relay Selection in Two-way Relay Networks Over Nakagami-m Fading Channels," *Wireless Personal Communications Journal*, 2015.
24. A. Yenilmez, T. Gucluoglu, and P. Remlein, "Performance of GFDM-maximal ratio transmission over Nakagami-m fading channels," *2016 International Symposium on Wireless Communication Systems (ISWCS)*, Poznan, 2016, pp. 523-527.
25. S. K. Bandari, A. Drosopoulos, V.V. Mani, "Exact SER Expressions of GFDM in Nakagami-m and Rician fading channels," *European Wireless Conference*, 2015.
26. J. W. Browning, S. L. Cotton, D. Morales-Jimenez and F. J. Lopez-Martinez, "The Rician Complex Envelope Under Line of Sight Shadowing," in *IEEE Communications Letters*, vol. 23, no. 12, pp. 2182-2186, Dec. 2019.
27. M. Simon and M. Alouini, *Digital Communication over Fading Channels*, 2nd ed. Hoboken, NJ: Wiley Interscience, John Wiley & Sons, 2005.
28. B. Sklar, *Digital Communications: Fundamentals and Applications*, 2nd ed. New York, NY, USA: Prentice-Hall, 2001.
29. I. Abramowitz, M. amdStegun, *Handbook of Mathematical Functions*. Dover, 1970.
30. I. Gradshteyn and I. Ryzhik, *Table of Integrals, Series, and Products*, 5th ed. Academic Press, 1994.
31. Cheng, J., Tellambura, C. and Beaulieu, N. (2003), "Performance analysis of digital modulations on Weibull fading channels", 58th Vehicular Technology Conference, VTC 2003-Fall, 2003 IEEE, Vol. 1, pp. 236-240.
32. Sagias, N., Karagiannidis, G., Zogas, D., Mathiopoulos, P. and Tombras, G. (2004), "Performance analysis of dual selection diversity in correlated Weibull fading channels", IEEE Transactions on Communications, Vol. 52 No. 7, pp. 1063-1067.
33. Bandari, S.K., Mani, V.V. and Drosopoulos, A. (2016), "Performance analysis of GFDM in various fading channels", COMPEL - The international journal for computation and mathematics in electrical and electronic engineering, Vol. 35 No. 1, pp. 225-244.
34. Nalgonda, S., Bandari, S.K., Dhar Roy, S. and Kundu, S, "On the performance of weighted fusion-based spectrum sensing in fading channels", Journal of Computational Engineering, Vol.10, 2013.



Science, Technology and Development Journal

ISSN NO: 0950-0707, Impact Factor : 6.1

www.journalstd.com, Mail : editorstdjournal@gmail.com



CERTIFICATE OF PUBLICATION

This is to certify that the paper entitled

THE METHOD OF LOW POWER, HIGH PERFORMANCE AND AREA EFFICIENT ADDRESS DECODER DESIGN FOR SRAM

Authored by

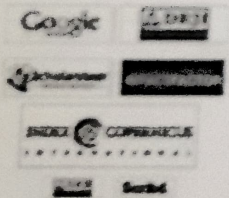
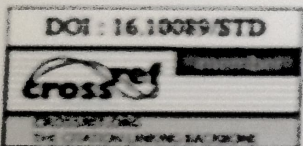
Mr. CH.ANIL KUMAR, Associate professor

From

Vaagdevi College of Engineering, Warangal, Telangana, India.

Has been published in

STD JOURNAL, Volume XI Issue VII JULY 2022



FRANCIS J. KEEFE, USA
EDITOR IN CHIEF
STD JOURNAL

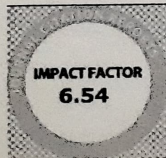
CERTIFICATE OF PUBLICATION

This is to certify that the paper entitled
**IMPLEMENTATION FOR ARRAY MULTIPLIER
AND DADDA MULTIPLIER**

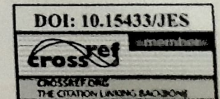
Authored by
CH.ANIL KUMAR

From
Vaagdevi College of Engineering, Warangal, Telangana, India.

Has been published in
JES JOURNAL, VOL 13, ISSUE 06, JUNE /2022



Dr. D. K. Umber
Editors-in-Chief
Dr. D.Karthikaran Umber
JES PUBLICATION





Preprint Submitted to Elsevier

A Comprehensive Analysis of Selection of Optimal Network Parameters For Cooperative Spectrum Sensing Network

M. Ranjeeth^{a,*}, B. Santosh Kumar^a, D. Srikar^b, M. Sashidhar^c and Srinivas Nallagonda^c^a Department of ECE, Vaagdevi College of Engineering, Warangal, Telangana, India, 506005.^b Department of ECE, Institute of Aeronautical Engineering, Dundigal, Hyderabad, Telangana, India, 500043^c Department of ECE, Marri Laxman Reddy Institute of Technology and Management, Dundigal, Hyderabad, Telangana, India, 500043

ARTICLE INFO

Article history:

Received xx Month 20xx

Revised xx Month 20xx

Accepted xx Month 20xx

Available online xx Month 20xx

Keywords:

Cognitive radio

Rayleigh fading

Improved energy detector

Optimal values

Total error rate

Average throughput

NUF

ABSTRACT

In this paper, we have addressed the cooperative spectrum sensing (CSS) network which has promising characteristics that can increase the detection performance. This study concentrates on the improved energy detector (IED) for identification of unknown signals in a Rayleigh fading. The CSS network is designed with several cognitive radio (CR) nodes, each node having M antennas and selection combining (SC) is used to determine which node has the highest detection probability value. Furthermore, the primary user (PU) activity is computed at the fusion center (FC) by utilizing fusion rules. Initially, the analytical expressions of missed detection and false alarm probabilities are skillfully extracted under Rayleigh fading. Further, mathematical assessment is provided to evaluate total error rate, network utility function (NUF) and average throughput. These parameters performance is discussed using various fusion rules at FC. Later, novel mathematical analysis of optimized CSS network parameters is provided for single and multiple antenna cases. Finally, simulation test-bed is implemented in MATLAB, analysis of optimized CSS network parameters, NUF and average throughput performances are assessed using simulations and it compared with analytical results. Finally, performance is enhanced with the proposed system compared to traditional systems.

1. Introduction

The radio spectrum (RS) is a significant asset for remote correspondence to perform different wireless applications. This RS is divided as number of chunks and each chunk is allocated for various applications. Most of the survey analysis are giving that much of these radio chunks are not utilized properly [1], hence there is a chance of occurrence of spectrum holes (vacant bands) in RS. To overcome this issue and for an effective usage of these spectrum holes, cognitive radio (CR) technology is employed [2]. The CR is an intelligent wireless technology which learn and adopt according to the environment [3]. The CR technology senses the available bandwidth, identify the large spectrum holes and uses this vacant bands for other applications with the help of cognitive users (CUs) without interrupting the function of primary user (PU). The approach called spectrum sensing (SS), sense the RS in order to identify the empty bands contained in it [1]. However, many factors may affect the SS execution, such as shadowing and

fading. These disadvantages can be avoided by incorporating several CUs in the network, reliably this is referred to cooperative spectrum sensing (CSS) technique [4]. The CSS network give reasonable detection probability in fading conditions [5]. According to the literature, the energy detection (ED) approach is widely used to identify the presence of PU [6]. There is a cap on identification of empty bands when ED method is employed in a CSS network under fading conditions [7]. Furthermore, the detection probability value is increased by employing an improved ED (IED) approach in each CR node with a number of antennas [8]. In [9], an experimental examination of an IED technique is discussed.

It is also essential to optimize the CSS network parameters accomplish the best efficiency and reduction in the cost as well as the network ambiguity. The CSS network optimization with the CFD scheme is addressed in [10]. Various parameters of CSS network are optimized and complete analysis is provided under Rayleigh fading in [11]. CSS network performance is measured using number of antennas with an IED over various fading channels is addressed in [12]-[14]. Similar and related study is done over various fading environments in [15]-[17]. The censoring concept based CSS in the presence of IED and multiple antenna analysis over fading channels is discussed in [18]. The ana-

* Corresponding author.

E-mail address(es): ranjeethm12@gmail.com (M. Ranjeeth).



Preprint Submitted to Elsevier

A Comprehensive Analysis of Selection of Optimal Network Parameters For Cooperative Spectrum Sensing Network

M. Ranjeeth^{a,*}, B. Santosh Kumar^a, D. Srikar^b, M. Sashidhar^c and Srinivas Nallagonda^c^a Department of ECE, Vaagdevi College of Engineering, Warangal, Telangana, India, 506005.^b Department of ECE, Institute of Aeronautical Engineering, Dundigal, Hyderabad, Telangana, India, 500043^c Department of ECE, Marri Laxman Reddy Institute of Technology and Management, Dundigal, Hyderabad, Telangana, India, 500043

ARTICLE INFO

Article history:

Received xx Month 20xx

Revised xx Month 20xx

Accepted xx Month 20xx

Available online xx Month 20xx

Keywords:

Cognitive radio

Rayleigh fading

Improved energy detector

Optimal values

Total error rate

Average throughput

NUF

ABSTRACT

In this paper, we have addressed the cooperative spectrum sensing (CSS) network which has promising characteristics that can increase the detection performance. This study concentrates on the improved energy detector (IED) for identification of unknown signals in a Rayleigh fading. The CSS network is designed with several cognitive radio (CR) nodes, each node having M antennas and selection combining (SC) is used to determine which node has the highest detection probability value. Furthermore, the primary user (PU) activity is computed at the fusion center (FC) by utilizing fusion rules. Initially, the analytical expressions of missed detection and false alarm probabilities are skillfully extracted under Rayleigh fading. Further, mathematical assessment is provided to evaluate total error rate, network utility function (NUF) and average throughput. These parameters performance is discussed using various fusion rules at FC. Later, novel mathematical analysis of optimized CSS network parameters is provided for single and multiple antenna cases. Finally, simulation test-bed is implemented in MATLAB, analysis of optimized CSS network parameters, NUF and average throughput performances are assessed using simulations and it compared with analytical results. Finally, performance is enhanced with the proposed system compared to traditional systems.

1. Introduction

The radio spectrum (RS) is a significant asset for remote correspondence to perform different wireless applications. This RS is divided as number of chunks and each chunk is allocated for various applications. Most of the survey analysis are giving that much of these radio chunks are not utilized properly [1], hence there is a chance of occurrence of spectrum holes (vacant bands) in RS. To overcome this issue and for an effective usage of these spectrum holes, cognitive radio (CR) technology is employed [2]. The CR is an intelligent wireless technology which learn and adopt according to the environment [3]. The CR technology senses the available bandwidth, identify the large spectrum holes and uses this vacant bands for other applications with the help of cognitive users (CUs) without interrupting the function of primary user (PU). The approach called spectrum sensing (SS), sense the RS in order to identify the empty bands contained in it [1]. However, many factors may affect the SS execution, such as shadowing and

fading. These disadvantages can be avoided by incorporating several CUs in the network, reliably this is referred to cooperative spectrum sensing (CSS) technique [4]. The CSS network give reasonable detection probability in fading conditions [5]. According to the literature, the energy detection (ED) approach is widely used to identify the presence of PU [6]. There is a cap on identification of empty bands when ED method is employed in a CSS network under fading conditions [7]. Furthermore, the detection probability value is increased by employing an improved ED (IED) approach in each CR node with a number of antennas [8]. In this paper, an experimental examination of an IED technique is discussed.

It is also essential to optimize the CSS network parameters accomplish the best efficiency and reduction in the cost as well as the network ambiguity. The CSS network optimization with the CFD scheme is addressed in [9]. Various parameters of CSS network are optimized and complete analysis is provided under Rayleigh fading in [10]. CSS network performance is measured using number of antennas with an IED over various fading channels is addressed in [11]. Similar and related study is discussed over various fading environments in [12]. The censoring concept based CSS in the presence of IED and multiple antenna analysis over fading channels is discussed in [13]. The ana-

* Corresponding author.

E-mail address(es): ranjeethm12@gmail.com (M. Ranjeeth).



Preprint Submitted to Elsevier

A Comprehensive Analysis of Selection of Optimal Network Parameters For Cooperative Spectrum Sensing Network

M. Ranjeeth^{a,*}, B. Santosh Kumar^a, D. Srikar^b, M. Sashidhar^c and Srinivas Nallagonda^c^a Department of ECE, Vaagdevi College of Engineering, Warangal, Telangana, India, 506005.^b Department of ECE, Institute of Aeronautical Engineering, Dundigal, Hyderabad, Telangana, India, 500043^c Department of ECE, Marri Laxman Reddy Institute of Technology and Management, Dundigal, Hyderabad, Telangana, India, 500043

ARTICLE INFO

Article history:

Received xx Month 20xx

Revised xx Month 20xx

Accepted xx Month 20xx

Available online xx Month 20xx

Keywords:

Cognitive radio

Rayleigh fading

Improved energy detector

Optimal values

Total error rate

Average throughput

NUF

ABSTRACT

In this paper, we have addressed the cooperative spectrum sensing (CSS) network which has promising characteristics that can increase the detection performance. This study concentrates on the improved energy detector (IED) for identification of unknown signals in a Rayleigh fading. The CSS network is designed with several cognitive radio (CR) nodes, each node having M antennas and selection combining (SC) is used to determine which node has the highest detection probability value. Furthermore, the primary user (PU) activity is computed at the fusion center (FC) by utilizing fusion rules. Initially, the analytical expressions of missed detection and false alarm probabilities are skillfully extracted under Rayleigh fading. Further, mathematical assessment is provided to evaluate total error rate, network utility function (NUF) and average throughput. These parameters performance is discussed using various fusion rules at FC. Later, novel mathematical analysis of optimized CSS network parameters is provided for single and multiple antenna cases. Finally, simulation test-bed is implemented in MATLAB, analysis of optimized CSS network parameters, NUF and average throughput performances are assessed using simulations and it compared with analytical results. Finally, performance is enhanced with the proposed system compared to traditional systems.

1. Introduction

The radio spectrum (RS) is a significant asset for remote correspondence to perform different wireless applications. This RS is divided as number of chunks and each chunk is allocated for various applications. Most of the survey analysis are giving that much of these radio chunks are not utilized properly [1], hence there is a chance of occurrence of spectrum holes (vacant bands) in RS. To overcome this issue and for an effective usage of these spectrum holes, cognitive radio (CR) technology is employed [2]. The CR is an intelligent wireless technology which learn and adopt according to the environment [3]. The CR technology senses the available bandwidth, identify the large spectrum holes and uses this vacant bands for other applications with the help of cognitive users (CUs) without interrupting the function of primary user (PU). The approach called spectrum sensing (SS), sense the RS in order to identify the empty bands contained in it [1]. However, many factors may affect the SS execution, such as shadowing and

fading. These disadvantages can be avoided by incorporating several CUs in the network, reliably this is referred to cooperative spectrum sensing (CSS) technique [4]. The CSS network give reasonable detection probability in fading conditions [5]. According to the literature, the energy detection (ED) approach is widely used to identify the presence of PU [6]. There is a cap on identification of empty bands when ED method is employed in a CSS network under fading conditions [7]. Furthermore, the detection probability value is increased by employing an improved ED (IED) approach in each CR node with a number of antennas [8]. In [9], an experimental examination of an IED technique is discussed.

It is also essential to optimize the CSS network parameters accomplish the best efficiency and reduction in the cost as well as the network ambiguity. The CSS network optimization with the CFD scheme is addressed in [10]. Various parameters of CSS network are optimized and complete analysis is provided under Rayleigh fading in [11]. CSS network performance is measured using number of antennas with an IED over various fading channels is addressed in [12]-[14]. Similar and related study is done over various fading environments in [15]-[17]. The censoring concept based CSS in the presence of IED and multiple antenna analysis over fading channels is discussed in [18]. The ana-

* Corresponding author.

E-mail address(es): ranjeethm12@gmail.com (M. Ranjeeth).

See discussions, stats, and author profiles for this publication at: <https://www.researchgate.net/publication/375524761>

Madhya Bharti (मध्या भर्ती)

Article · November 2023

CITATIONS
0

READS
130

1 author:



Venu Kesireddy

12 PUBLICATIONS 2 CITATIONS

SEE PROFILE

COMPOSITIONAL DUPONT ANALYSIS: A VISUAL TOOL FOR OVERALL FINANCIAL POSITION OF BANK OF BARODA

Dr. Venu Kesireddy, Asst. Professor, Department of MBA, Vaagdevi College of Engineering (Autonomous), Bollikunta, Warangal.

Y. Sravan Kumar, Asst. Professor, Department of MBA, Vaagdevi Engineering College, Bollikunta, Warangal.

Abstract

The main field of this work is to study the overall financial position of Bank of Baroda with the help of Du Pont analysis. To achieve the goal, this study has measured the ratios of ROE, ROA applying the DuPont analysis, which has been demonstrated with tables to show the change periodically. It is concluded from the study that, the parameters of ROE, ROI are showing comprehensive measures. The financial performance of BOB might be studied by several researchers all over India. The DuPont Analysis measures the wealth of the Owners, Investors with the ROE index, and the management's effectiveness with the ROA index, and one index affect the other. It is compared to the formation of a comparable size over a period of time.

Key Words: *Financial performance, Profitability, DUPONT, ROA, Bank of Baroda, ROI and ROE.*

I. INTRODUCTION

The DuPont analysis also known as the DuPont identity or DuPont Model is a framework for analyzing fundamental performance popularized by the DuPont Corporation. DuPont analysis is a useful technique used to decompose the different drivers of return on equity (ROE). The decomposition of ROE allows investors to focus on the key metrics of financial performance individually to identify strengths and weaknesses.

The analysis of the financial statements of a business includes besides the selection of the appropriate index and the comparison, without which the resulting conclusions do not have any meaning and most probably they do not lead to the correct explanation.

The comparison makes sense when it is done in relation to time and in relation to the similar businesses or the sector. This double comparison gives the capability of a more correct explanation of the indexes and consequently of the business condition (Papoulias, 2000).

Profitability of banks is measured mainly by two ratios. The Return on Equity (ROE) that increase the wealth of the shareholders and the Return on Assets (ROA) that show to the investors how cable is the bank management to yield earnings and how profitably use the whole assets of the bank.

Saunders (2000) provides a model of financial analysis for financial institutions that is based on the DuPont system of financial analysis return on equity model. The return on equity model disaggregates performance into the three components that determine return on equity: net profit margin, total asset turnover, and the equity multiplier. The profit margin allows the financial analyst to evaluate the income statement and the components of the income statement. Total asset turnover allows the financial analysis to evaluate the left-hand side of the balance sheet which is composed of the asset accounts. The equity multiplier allows the financial analyst to evaluate the right-hand side of the balance sheet which is composed of liabilities and owner's equity.

Return on equity analysis provides a system for planning (budgeting) in addition to analyzing the financial institution's performance. The net profit margin allows the analyst to develop a pro for income statement. An abbreviated income statement would be composed of net income equal to revenues minus expenses. The financial planner can determine the projected revenue level needed to meet the target net

II. RESEARCH METHODOLOGY

The research methodology means the way the research has been taken place to do the research work. It consists of objectives of study, scope of study and collection of data etc.

A). OBEJECTIVES OF THE STUDY

1. To study the financial performance of Bank of Baroda with the help of DUPONT analysis
2. To draw conclusions emerged from the study and offer appropriate suggestions.

B). SCOPE OF THE STUDY

The scope of the study is confined to financial performance of Bank of Baroda from 2007-08 to 2018-19. The study was focused financial performance with the help of Return on Equity, Return on Investment and DUPONT analysis.

C). COLLECTION OF DATA

The necessary data was collected from the secondary sources such as annual reports of Bank of Baroda, publications of Reserve Bank India, websites and other published sources.

III. DATA ANALYSIS AND INTERPRETATION

Du Pont analysis divides net operating profits into two multiple components: profit margin and asset turnover. This analysis is a common type of financial statement analysis. These two accounting ratios measure two different structures and therefore have two different characteristics. Previous research has shown that changes in asset sales are positively linked to changes in future income. The analysis of Du Pont takes into account three indicators to determine a company's profitability:

1. Return on Sales (ROS) or Net Profit Margin ratio
2. Return on Equity (ROE), and.
3. Return on Assets (ROA)

DuPont model basically segregates the ROE into three parts:

- ❖ Net Profit margin,
- ❖ Total Assets Turnover and
- ❖ Equity Multiplier.

NET PROFIT MARGIN

Net profit margin is a measure of the total profitability and also measures the profitability of the business on income. The margin of profit is the return of the assets of the company. The difference is between total income and total expenditure.

Net Profit Margin= Net Profit/ Total Income

Table -1: Net Profit Margin (NPM)

(2007-08 to 2018-19)

Year	Net profit (Rs. in crores)	Total Income (Rs. in crores)	Net Profit margin (In %)
2007-08	1435.52	13864.52	10.35
2008-09	2227.2	17849.24	12.48
2009-10	3058.33	19504.7	15.68
2010-11	4241.68	24695.11	17.18
2011-12	5006.96	33096.05	15.13
2012-13	4480.72	38827.27	11.54
2013-14	4541.08	43402.45	10.46
2014-15	3398.44	47365.56	7.17
2015-16	-5,396	49060.14	11.00
2016-17	1383.14	48957.99	2.83
2017-18	-2431.81	50305.69	-4.83

2018-19	433.52	56065.1	0.77
Sum	22378.78	442993.8	119.43
Average	1864.90	36916.15	9.95
STDEV	3120.04	14633.06	5.14
CAGR	-10	12	-0.20

Source: Compiled from the annual reports of Bank of Baroda

INTERPRETATION:

Table 1 shows the Net profit, Total Income and Net Profit Margin of BOB in 2007-08 to 2018-19. The Net Profit in 2007-08 is Rs. 1435.52 crores, at the end of the study period 2018-19 it is Rs. 433.52 crores and the average Net Profit is Rs.1864.90 crores. The Total Income in 2007-08 is Rs. 13864.52 crores, which has been increasing, reported highest Rs. 56065.1 crores in 2018-19. The Net Profit Margin in 2007-08 is 10.35 %, later on, fluctuated and reported highest 17.18 % in 2010-11. The average Net Profit Margin ratio during the study period is 9.95 %, with a standard deviation of 5.14%.

The Net Profit margin varies between 0.77 % and 17.18 % and average Net Profit Margin is 9.95 % with standard deviation of 5.14. At the end of the study period the Net Profit margin very lowest means there is significant problem regarding this year to report lowest Net Profit margin.

THE ASSET TURNOVER RATIO

The asset turnover ratio is the ratio of a company's assets to its sales or revenues. It's a metric for how efficiently a company generates revenue from its assets. As a result, a company's asset turnover ratio can be used to forecast its performance. The higher the ratio is the more profitable.

Formula:

Asset Turnover = (Total Income/ Total Assets)

**Table – 2: Asset Turnover Ratio
(2007-08 to 2018-19)**

Year	Total Income (Rs. In crores)	Total Assets (Rs. In crores)	Asset Ratio (In %)	Turnover
2008-09	13864.52	179599.5	7.72	
2008-09	17849.24	227406.7	7.85	
2009-10	19504.7	278316.7	7.01	
2010-11	24695.11	358397.2	6.89	
2011-12	33096.05	447321.5	7.40	
2012-13	38827.27	547135.4	7.10	
2013-14	43402.45	659504.5	6.58	
2014-15	47365.56	714988.6	6.62	
2015-16	49060.14	671376.5	7.31	
2016-17	48957.99	694875.4	7.05	
2017-18	50305.69	719999.8	6.99	
2018-19	56065.1	780987.4	7.18	
Sum	442993.8	6279909	85.69	
Average	36916.15	523325.8	7.14	
STDEV	14633.06	215530.6		
CAGR	12	14		

Source: Compiled from the annual reports of Bank of Baroda

INTERPRETATION:

Table 2 shows the Total income, Total Assets and Assets turnover ratio of BOB from 2007-08 to 2018-19. The Total Income in 2007-08 is Rs. 13864.52 crores, which has been increasing, reported highest Rs. 56065.1 crores in 2018-19 and the average income is Rs. 36916.15 crores; the Standard deviation is Rs. 14633.06 crores and the CAGR is 12%.

The table also shows the total assets of the Bank. The total assets in 2007-08 were Rs. 179599.5 crores, end of the study period 2018-19 is Rs, 780987.4 crores, and average assets Rs. 523325.8 crores. The standard deviation is Rs. 215530.6 crores and CAGR is 14 %.

The Assets turnover ratio is 2008-09 is highest at 7.85 %, later on fluctuated reported lowest 6.58 % in 2013-14 and at the end of the study period 2018-19 it is 7.18 %. The Average Asset turnover ratio during the study period is 7.14 %. So, we can conclude that the bank has regenerated the assets to generate income. It means on every Rs.100 worth of asset it is generating Rs.7.14 aggregate income every year. It should be better to generate at least Rs.10 on every Rs.100 worth of assets.

EQUITY MULTIPLIER

The third and final step of the DuPont model is the equity multiplier. Leverage ratio refers to the capital stock multiplier. It is a method of determining a company's financial leverage by evaluating its ability to use debt to fund its assets.

Formula: Equity Multiplier = Total Assets/ Stockholder's Equity

Table – 3: Equity Multiplier
(2007-08 to 2018-19)

Year	Total Assets (Rs. In crores)	Shareholder's Equity (Rs. In crores)	Equity Multiplier (Rs. In crores)
2007-08	179599.5	365.53	491.34
2008-09	227406.7	365.53	622.13
2009-10	278316.7	365.53	761.41
2010-11	358397.2	392.81	912.39
2011-12	447321.5	412.38	1084.73
2012-13	547135.4	422.52	1294.93
2013-14	659504.5	430.68	1531.31
2014-15	714988.6	443.56	1611.93
2015-16	671376.5	462.09	1452.91
2016-17	694875.4	462.09	1503.77
2017-18	719999.8	530.36	1357.57
2018-19	780987.4	530.36	1472.56
Sum	6279909	5183.44	14096.98
Average	523325.8	431.95	1174.75

STDEV	215530.6	57.65	
CAGR	14	0.34	

Source: Compiled from the annual reports of Bank of Baroda

INTERPRETATION:

Table 3 shows the Total Assets, Shareholder's equity and Equity multiplier ratio of BOB from 2007-08 to 2018-19. The total assets in 2007-08 were Rs. 179599.5 crores, end of the study period 2018-19 is Rs. 780987.4 crores, and average assets Rs. 523325.8 crores . The standard deviation is Rs. 215530.6 crores and CAGR is 14 %.The Shareholder's equity in 2007-08 is Rs. 365.53 crores, has reported the highest Rs. 530.36 crores at the end of the study period 2018-19. The average Shareholder's equity is Rs.431.95 crores. The standard deviation of the Shareholder's equity is Rs.57.65 crores and the CAGR is 0.34 % during the study period. The Equity multiplier ratio in 2007-08 is 491.34 %; later on, it fluctuated and reported the highest 1611.93 % in 2014-15 and at the end of the study period, 2018-19 was 1472.56 %. The average Equity multiplier ratio during the study period is 1174.75 %.

Being the equity multiplier ratio varies betweenRs. 491.34and Rs. 1611.93 and the average equity multiplier ratio during the study period is Rs.1174.75. Leverage ratio refers to the capital stock multiplier. It is a method of determining a company's financial leverage by evaluating its ability to use debt to fund its assets.

RESULT OF DUPONT ANALYSIS OF BOB

The following table 4 presents the summary of the results of ROE or Return on shareholders' equity or Return on Net worth of BOB for the period 2008-09 to 2018-19, which has been calculated from the secondary data collected and compiled from all the annual reports of all the financial parameters required for the formulae.

Table – 4: Summary of DUPONT Analysis of BOB, FY 2008-09 to 2018-19

Year	(A) NP Margin	(B) Asset turnover	(C) Equity Multiplier	ROE
	%	Times	(%)	$D=A/(B*C)$
2007-08	10.35	7.72	491.34	0.27
2008-09	12.48	7.85	622.13	0.26
2009-10	15.68	7.01	761.41	0.29
2010-11	17.18	6.89	912.39	0.27
2011-12	15.13	7.40	1084.73	0.19
2012-13	11.54	7.10	1294.93	0.13
2013-14	10.46	6.58	1531.31	0.10

2014-15	7.17	6.62	1611.93	0.07
2015-16	11.00	7.31	1452.91	0.10
2016-17	2.83	7.05	1503.77	0.03
2017-18	4.83	6.99	1357.57	0.05
2018-19	0.77	7.18	1472.56	0.01
Sum	119.43	85.69	14096.98	0.01
Average	9.95	7.14	1174.75	0.15
STDEV	8.28	0.44	4.04	
CAGR	-1.92	-0.01	0.09	

Source: Calculated and Compiled from the data collected from all the Annual reports of BOB

INTERPRETATION:

Table – 4: Shows Summary of DUPONT Analysis of BOB from 2007-08 to 2018-19. The NP Margin in 2007-08 was 10.35 %, increased to highest 17.18 % in 2010-2011, later gradually decreased to 0.77% in 2018-19. Asset turnover ratio in 2007-08 was 7.72 %, decreased to the lowest 6.58 % in 2013-2014, fluctuated and reported 7.18 % in 2018-19. Equity multiplier ratio in 2007-08 was 491.34 %, was highest 1611.93 % in 2014-15 and at the end of the study period 2018-19 it is 1472.56 %. ROE in 2007-08 was 6.15 % and reported highest 266.35 % in 2018-19.

The Return on Equity based on DUPONT analysis varies between 0.01 and 0.29 with an aggregate of 0.15. It means the Return on Equity is 15 on the investors amount on the real owners i.e., equity shareholders.

**Table – 5: Return on Assets & Return on Average Assets
(2007-08 to 2018-19)**

Year	Return On Assets(In %)	Return On Average Assets(In %)
2007-08	0.80	0.89
2008-09	0.98	1.10
2009-10	1.10	1.21
2010-11	1.18	1.33
2011-12	1.12	1.24
2012-13	0.82	0.90
2013-14	0.69	0.75
2014-15	0.48	0.49
2015-16	-0.80	-0.78

2016-17	0.20	0.2
2017-18	-0.34	-0.34
2018-19	0.06	0.06
Sum	6.29	7.05
Average	0.52	0.59
STDEV	0.63	0.67
CAGR	-0.21	-0.22

Source: Compiled from the annual reports of Bank of Baroda.

INTERPRETATION:

Table 5 presents the Return on Assets of the bank from 2007-08 to 2018-19 financial years. During the study period in 2007-08, the Return on Assets was 0.80 %. It is 0.06 % at the end of the study period 2018-19. The average Return on Assets is 0.52 % with a Compound Annual Growth Rate (CAGR) of -0.21 %. The Standard Deviation (STDEV) of Return on Assets during the study period is 0.63. The table also shows the Return on Average Assets of the bank from 2007-08 to 2018-19 financial years. During the study period in 2007-08, the Return on Average Assets was 0.89 %. It is 0.06 % at the end of the study period 2018-19. The average Return on Average Assets is 0.59 % with a Compound Annual Growth Rate (CAGR) of -0.22 %. The Standard Deviation (STDEV) of Return on Average Assets during the study period is 0.67%. The average Return on Assets is less than the benchmark of 1 %. So, the bank has to increase its income to improve return on assets.

The average Return on Average Assets is 0.59 %. The average Return on Assets is less than the benchmark of 1 %. So, the bank has to increase its income to improve return on assets.

IV. FINDINGS

1. The Net Profit margin varies between 0.77 % and 17.18 % and average Net Profit Margin is 9.95 % with standard deviation of 5.14. At the end of the study period the Net Profit margin very lowest means there is significant problem regarding this year to report lowest Net Profit margin.
2. The asset turnover ratio was representing here the relation between total assets and total income. The asset turnover ratio presenting as per every Rs.100 worth of asset it is generating Rs.7.14 aggregate income every year. It should be better to generate at least Rs.10 on every Rs.100 worth of assets.
3. Being the equity multiplier ratio varies between Rs. 491.34 and Rs. 1611.93 and the average equity multiplier ratio during the study period is Rs.1174.75. Leverage ratio refers to the capital stock multiplier. It is a method of determining a company's financial leverage by evaluating its ability to use debt to fund its assets.
4. The Return on Equity based on DUPONT analysis varies between 0.01 and 0.29 with an aggregate of 0.15. It means the Return on Equity is 15 on the investors amount on the real owners i.e., equity shareholders.
5. The average Return on Average Assets is 0.59 %. The average Return on Assets is less than the benchmark of 1 %. So, the bank has to increase its income to improve return on assets.

V. CONCLUSIONS

1. This paper presents a model for the financial analysis of a bank based on the Du Pont analysis of the world systemic banks and Du Pont system of financial analysis as presented in Saunders (2000). Equity returns are supplied to share holders from banks who utilize share holders' capital to offer loans to the banks clients.

2. To increase operating profits one bank must either increase sales (in a higher proportion than the cost of generating those sales) or reduce expenses. Since it is generally more difficult to increase sales than it is to reduce expenses, a small bank can try to lower expenses by offering innovating products and a big bank can do this by mergers and acquisitions.
3. Further, BOB can determine if they are using deposits loans and investments wisely. The ROE and ROA indexes are the most comprehensive measure of profitability of a bank. It considers the operating and investing decisions made as well as the financing and tax-related decisions.
4. The Du Pont mode is analysis that calculates the ROE ratio. The ROE ratio is decomposed in to net profit margin, total asset turnover and the equity multiplier. The DuPont model also show us how many times ROE ratio is bigger than the ROA ratio. In its simplest form, we can say that if a bank wants to improve the ROE ratio the only choices has is to increase operating profits, become more efficient in using existing assets to generate sales, recapitalize to make better use of debt and/or better control the cost of deposit and lending money.

References

1. Basel Committee on Banking Supervision (2011) “Global systemically important banks: Assessment methodology and the additional loss absorbency requirement “Consultative Document 7/2011.
2. Bodie, Z., Kane, A., and Alan, J.M., (2004) “Essentials of Investments” 5thedition, McGraw-Hill, Irwin,.
3. Boissay Frederic, Collard Fabrice and Smets Frank (2013) “Booms and Systemic Banking Crises.”: Working Paper Series No 1514/february 2011
4. Boran Milan (2010) “Market Dynamics & Systemic Risk” June 4, 2010 23rd Australasian Finance and Banking Conference 2010 Paper
5. Brandy, M., Walker, J., (2011) “What is an equity multiplier”, 2011
6. Collier W. H., McGowan, B. Mc., Muhammad, Jr. J., (2010) “Evaluating the impact of a rapidly changing economic environment on bank financial performance using the DuPont system of financial analysis”, Asia Pacific Journal of Finance and Banking Research Vol.4.No.4, 2010
7. CRMPG III (2008). “Containing Systemic Risk.”, The report of CRMPG III, August 6, 2008
8. Crosson, S., V., Belverd E., Needles, Jr., Belverd E., (2008) “Powers Marian Principles of accounting”. Houghton Mifflin, Boston 2008
9. Daula Tomas (2012). “Systemic Risk: Relevance, Risk Management Challenges and Open Questions”, June 2012
10. Ergung or Emre O. and Thomson James B. (2005) “Systemic Banking Crises” Federal Reserve Bank of Cleveland, issue 2/2005.

See discussions, stats, and author profiles for this publication at: <https://www.researchgate.net/publication/375524761>

Madhya Bharti (मध्य भारत)

Article · November 2023

CITATIONS
0

READS
130

1 author:



Venu Kesireddy

12 PUBLICATIONS 2 CITATIONS

SEE PROFILE

COMPOSITIONAL DUPONT ANALYSIS: A VISUAL TOOL FOR OVERALL FINANCIAL POSITION OF BANK OF BARODA

Dr. Venu Kesireddy, Asst. Professor, Department of MBA, Vaagdevi College of Engineering (Autonomous), Bollikunta, Warangal.

Y. Sravan Kumar, Asst. Professor, Department of MBA, Vaagdevi Engineering College, Bollikunta, Warangal.

Abstract

The main field of this work is to study the overall financial position of Bank of Baroda with the help of Du Pont analysis. To achieve the goal, this study has measured the ratios of ROE, ROA applying the DuPont analysis, which has been demonstrated with tables to show the change periodically. It is concluded from the study that, the parameters of ROE, ROI are showing comprehensive measures. The financial performance of BOB might be studied by several researchers all over India. The DuPont Analysis measures the wealth of the Owners, Investors with the ROE index, and the management's effectiveness with the ROA index, and one index affect the other. It is compared to the formation of a comparable size over a period of time.

Key Words: *Financial performance, Profitability, DUPONT, ROA, Bank of Baroda, ROI and ROE.*

I. INTRODUCTION

The DuPont analysis also known as the DuPont identity or DuPont Model is a framework for analyzing fundamental performance popularized by the DuPont Corporation. DuPont analysis is a useful technique used to decompose the different drivers of return on equity (ROE). The decomposition of ROE allows investors to focus on the key metrics of financial performance individually to identify strengths and weaknesses.

The analysis of the financial statements of a business includes besides the selection of the appropriate index and the comparison, without which the resulting conclusions do not have any meaning and most probably they do not lead to the correct explanation.

The comparison makes sense when it is done in relation to time and in relation to the similar businesses or the sector. This double comparison gives the capability of a more correct explanation of the indexes and consequently of the business condition (Papoulias, 2000).

Profitability of banks is measured mainly by two ratios. The Return on Equity (ROE) that increase the wealth of the shareholders and the Return on Assets (ROA) that show to the investors how able is the bank management to yield earnings and how profitably use the whole assets of the bank.

Saunders (2000) provides a model of financial analysis for financial institutions that is based on the DuPont system of financial analysis return on equity model. The return on equity model disaggregates performance into the three components that determine return on equity: net profit margin, total asset turnover, and the equity multiplier. The profit margin allows the financial analyst to evaluate the income statement and the components of the income statement. Total asset turnover allows the financial analysis to evaluate the left-hand side of the balance sheet which is composed of the asset accounts. The equity multiplier allows the financial analyst to evaluate the right-hand side of the balance sheet which is composed of liabilities and owner's equity.

Return on equity analysis provides a system for planning (budgeting) in addition to analyzing the financial institution's performance. The net profit margin allows the analyst to develop a pro forma income statement. An abbreviated income statement would be composed of net income equal to revenues minus expenses. The financial planner can determine the projected revenue level needed to meet the target net

II. RESEARCH METHODOLOGY

The research methodology means the way the research has been taken place to do the research work. It consists of objectives of study, scope of study and collection of data etc.

A). OBEJECTIVES OF THE STUDY

1. To study the financial performance of Bank of Baroda with the help of DUPONT analysis
2. To draw conclusions emerged from the study and offer appropriate suggestions.

B). SCOPE OF THE STUDY

The scope of the study is confined to financial performance of Bank of Baroda from 2007-08 to 2018-19. The study was focused financial performance with the help of Return on Equity, Return on Investment and DUPONT analysis.

C). COLLECTION OF DATA

The necessary data was collected from the secondary sources such as annual reports of Bank of Baroda, publications of Reserve Bank India, websites and other published sources.

III. DATA ANALYSIS AND INTERPRETATION

Du Pont analysis divides net operating profits into two multiple components: profit margin and asset turnover. This analysis is a common type of financial statement analysis. These two accounting ratios measure two different structures and therefore have two different characteristics. Previous research has shown that changes in asset sales are positively linked to changes in future income. The analysis of Du Pont takes into account three indicators to determine a company's profitability:

1. Return on Sales (ROS) or Net Profit Margin ratio
2. Return on Equity (ROE), and.
3. Return on Assets (ROA)

DuPont model basically segregates the ROE into three parts:

- ❖ Net Profit margin,
- ❖ Total Assets Turnover and
- ❖ Equity Multiplier.

NET PROFIT MARGIN

Net profit margin is a measure of the total profitability and also measures the profitability of the business on income. The margin of profit is the return of the assets of the company. The difference is between total income and total expenditure.

Net Profit Margin= Net Profit/ Total Income

Table -1: Net Profit Margin (NPM)

(2007-08 to 2018-19)

Year	Net profit (Rs. in crores)	Total Income (Rs. in crores)	Net Profit margin (In %)
2007-08	1435.52	13864.52	10.35
2008-09	2227.2	17849.24	12.48
2009-10	3058.33	19504.7	15.68
2010-11	4241.68	24695.11	17.18
2011-12	5006.96	33096.05	15.13
2012-13	4480.72	38827.27	11.54
2013-14	4541.08	43402.45	10.46
2014-15	3398.44	47365.56	7.17
2015-16	-5,396	49060.14	11.00
2016-17	1383.14	48957.99	2.83
2017-18	-2431.81	50305.69	-4.83

2018-19	433.52	56065.1	0.77
Sum	22378.78	442993.8	119.43
Average	1864.90	36916.15	9.95
STDEV	3120.04	14633.06	5.14
CAGR	-10	12	-0.20

Source: Compiled from the annual reports of Bank of Baroda

INTERPRETATION:

Table 1 shows the Net profit, Total Income and Net Profit Margin of BOB in 2007-08 to 2018-19. The Net Profit in 2007-08 is Rs. 1435.52 crores, at the end of the study period 2018-19 it is Rs. 433.52 crores and the average Net Profit is Rs.1864.90 crores. The Total Income in 2007-08 is Rs. 13864.52 crores, which has been increasing, reported highest Rs. 56065.1 crores in 2018-19. The Net Profit Margin in 2007-08 is 10.35 %, later on, fluctuated and reported highest 17.18 % in 2010-11. The average Net Profit Margin ratio during the study period is 9.95 %, with a standard deviation of 5.14%.

The Net Profit margin varies between 0.77 % and 17.18 % and average Net Profit Margin is 9.95 % with standard deviation of 5.14. At the end of the study period the Net Profit margin very lowest means there is significant problem regarding this year to report lowest Net Profit margin.

THE ASSET TURNOVER RATIO

The asset turnover ratio is the ratio of a company's assets to its sales or revenues. It's a metric for how efficiently a company generates revenue from its assets. As a result, a company's asset turnover ratio can be used to forecast its performance. The higher the ratio is the more profitable.

Formula:

Asset Turnover = (Total Income/ Total Assets)

**Table – 2: Asset Turnover Ratio
(2007-08 to 2018-19)**

Year	Total Income (Rs. In crores)	Total Assets (Rs. In crores)	Asset Ratio (In %)	Turnover
2008-09	13864.52	179599.5	7.72	
2008-09	17849.24	227406.7	7.85	
2009-10	19504.7	278316.7	7.01	
2010-11	24695.11	358397.2	6.89	
2011-12	33096.05	447321.5	7.40	
2012-13	38827.27	547135.4	7.10	
2013-14	43402.45	659504.5	6.58	
2014-15	47365.56	714988.6	6.62	
2015-16	49060.14	671376.5	7.31	
2016-17	48957.99	694875.4	7.05	
2017-18	50305.69	719999.8	6.99	
2018-19	56065.1	780987.4	7.18	
Sum	442993.8	6279909	85.69	
Average	36916.15	523325.8	7.14	
STDEV	14633.06	215530.6		
CAGR	12	14		

Source: Compiled from the annual reports of Bank of Baroda

INTERPRETATION:

Table 2 shows the Total income, Total Assets and Assets turnover ratio of BOB from 2007-08 to 2018-19. The Total Income in 2007-08 is Rs. 13864.52 crores, which has been increasing, reported highest Rs. 56065.1 crores in 2018-19 and the average income is Rs. 36916.15 crores; the Standard deviation is Rs. 14633.06 crores and the CAGR is 12%.

The table also shows the total assets of the Bank. The total assets in 2007-08 were Rs. 179599.5 crores, end of the study period 2018-19 is Rs, 780987.4 crores, and average assets Rs. 523325.8 crores. The standard deviation is Rs. 215530.6 crores and CAGR is 14 %.

The Assets turnover ratio is 2008-09 is highest at 7.85 %, later on fluctuated reported lowest 6.58 % in 2013-14 and at the end of the study period 2018-19 it is 7.18 %. The Average Asset turnover ratio during the study period is 7.14 %. So, we can conclude that the bank has regenerated the assets to generate income. It means on every Rs.100 worth of asset it is generating Rs.7.14 aggregate income every year. It should be better to generate at least Rs.10 on every Rs.100 worth of assets.

EQUITY MULTIPLIER

The third and final step of the DuPont model is the equity multiplier. Leverage ratio refers to the capital stock multiplier. It is a method of determining a company's financial leverage by evaluating its ability to use debt to fund its assets.

Formula: Equity Multiplier = Total Assets/ Stockholder's Equity

Table – 3: Equity Multiplier
(2007-08 to 2018-19)

Year	Total Assets (Rs. In crores)	Shareholder's Equity (Rs. In crores)	Equity Multiplier (Rs. In crores)
2007-08	179599.5	365.53	491.34
2008-09	227406.7	365.53	622.13
2009-10	278316.7	365.53	761.41
2010-11	358397.2	392.81	912.39
2011-12	447321.5	412.38	1084.73
2012-13	547135.4	422.52	1294.93
2013-14	659504.5	430.68	1531.31
2014-15	714988.6	443.56	1611.93
2015-16	671376.5	462.09	1452.91
2016-17	694875.4	462.09	1503.77
2017-18	719999.8	530.36	1357.57
2018-19	780987.4	530.36	1472.56
Sum	6279909	5183.44	14096.98
Average	523325.8	431.95	1174.75

STDEV	215530.6	57.65	
CAGR	14	0.34	

Source: Compiled from the annual reports of Bank of Baroda

INTERPRETATION:

Table 3 shows the Total Assets, Shareholder's equity and Equity multiplier ratio of BOB from 2007-08 to 2018-19. The total assets in 2007-08 were Rs. 179599.5 crores, end of the study period 2018-19 is Rs. 780987.4 crores, and average assets Rs. 523325.8 crores . The standard deviation is Rs. 215530.6 crores and CAGR is 14 %.The Shareholder's equity in 2007-08 is Rs. 365.53 crores, has reported the highest Rs. 530.36 crores at the end of the study period 2018-19. The average Shareholder's equity is Rs.431.95 crores. The standard deviation of the Shareholder's equity is Rs.57.65 crores and the CAGR is 0.34 % during the study period. The Equity multiplier ratio in 2007-08 is 491.34 %; later on, it fluctuated and reported the highest 1611.93 % in 2014-15 and at the end of the study period, 2018-19 was 1472.56 %. The average Equity multiplier ratio during the study period is 1174.75 %.

Being the equity multiplier ratio varies betweenRs. 491.34and Rs. 1611.93 and the average equity multiplier ratio during the study period is Rs.1174.75. Leverage ratio refers to the capital stock multiplier. It is a method of determining a company's financial leverage by evaluating its ability to use debt to fund its assets.

RESULT OF DUPONT ANALYSIS OF BOB

The following table 4 presents the summary of the results of ROE or Return on shareholders' equity or Return on Net worth of BOB for the period 2008-09 to 2018-19, which has been calculated from the secondary data collected and compiled from all the annual reports of all the financial parameters required for the formulae.

Table – 4: Summary of DUPONT Analysis of BOB, FY 2008-09 to 2018-19

Year	(A) NP Margin	(B) Asset turnover	(C) Equity Multiplier	ROE
	%	Times	(%)	$D=A/(B*C)$
2007-08	10.35	7.72	491.34	0.27
2008-09	12.48	7.85	622.13	0.26
2009-10	15.68	7.01	761.41	0.29
2010-11	17.18	6.89	912.39	0.27
2011-12	15.13	7.40	1084.73	0.19
2012-13	11.54	7.10	1294.93	0.13
2013-14	10.46	6.58	1531.31	0.10

2014-15	7.17	6.62	1611.93	0.07
2015-16	11.00	7.31	1452.91	0.10
2016-17	2.83	7.05	1503.77	0.03
2017-18	4.83	6.99	1357.57	0.05
2018-19	0.77	7.18	1472.56	0.01
Sum	119.43	85.69	14096.98	0.01
Average	9.95	7.14	1174.75	0.15
STDEV	8.28	0.44	4.04	
CAGR	-1.92	-0.01	0.09	

Source: Calculated and Compiled from the data collected from all the Annual reports of BOB

INTERPRETATION:

Table – 4: Shows Summary of DUPONT Analysis of BOB from 2007-08 to 2018-19. The NP Margin in 2007-08 was 10.35 %, increased to highest 17.18 % in 2010-2011, later gradually decreased to 0.77% in 2018-19. Asset turnover ratio in 2007-08 was 7.72 %, decreased to the lowest 6.58 % in 2013-2014, fluctuated and reported 7.18 % in 2018-19. Equity multiplier ratio in 2007-08 was 491.34 %, was highest 1611.93 % in 2014-15 and at the end of the study period 2018-19 it is 1472.56 %. ROE in 2007-08 was 6.15 % and reported highest 266.35 % in 2018-19.

The Return on Equity based on DUPONT analysis varies between 0.01 and 0.29 with an aggregate of 0.15. It means the Return on Equity is 15 on the investors amount on the real owners i.e., equity shareholders.

**Table – 5: Return on Assets & Return on Average Assets
(2007-08 to 2018-19)**

Year	Return On Assets(In %)	Return On Average Assets(In %)
2007-08	0.80	0.89
2008-09	0.98	1.10
2009-10	1.10	1.21
2010-11	1.18	1.33
2011-12	1.12	1.24
2012-13	0.82	0.90
2013-14	0.69	0.75
2014-15	0.48	0.49
2015-16	-0.80	-0.78

2016-17	0.20	0.2
2017-18	-0.34	-0.34
2018-19	0.06	0.06
Sum	6.29	7.05
Average	0.52	0.59
STDEV	0.63	0.67
CAGR	-0.21	-0.22

Source: Compiled from the annual reports of Bank of Baroda.

INTERPRETATION:

Table 5 presents the Return on Assets of the bank from 2007-08 to 2018-19 financial years. During the study period in 2007-08, the Return on Assets was 0.80 %. It is 0.06 % at the end of the study period 2018-19. The average Return on Assets is 0.52 % with a Compound Annual Growth Rate (CAGR) of -0.21 %. The Standard Deviation (STDEV) of Return on Assets during the study period is 0.63. The table also shows the Return on Average Assets of the bank from 2007-08 to 2018-19 financial years. During the study period in 2007-08, the Return on Average Assets was 0.89 %. It is 0.06 % at the end of the study period 2018-19. The average Return on Average Assets is 0.59 % with a Compound Annual Growth Rate (CAGR) of -0.22 %. The Standard Deviation (STDEV) of Return on Average Assets during the study period is 0.67%. The average Return on Assets is less than the benchmark of 1 %. So, the bank has to increase its income to improve return on assets.

The average Return on Average Assets is 0.59 %. The average Return on Assets is less than the benchmark of 1 %. So, the bank has to increase its income to improve return on assets.

IV. FINDINGS

1. The Net Profit margin varies between 0.77 % and 17.18 % and average Net Profit Margin is 9.95 % with standard deviation of 5.14. At the end of the study period the Net Profit margin very lowest means there is significant problem regarding this year to report lowest Net Profit margin.
2. The asset turnover ratio was representing here the relation between total assets and total income. The asset turnover ratio presenting as per every Rs.100 worth of asset it is generating Rs.7.14 aggregate income every year. It should be better to generate at least Rs.10 on every Rs.100 worth of assets.
3. Being the equity multiplier ratio varies between Rs. 491.34 and Rs. 1611.93 and the average equity multiplier ratio during the study period is Rs.1174.75. Leverage ratio refers to the capital stock multiplier. It is a method of determining a company's financial leverage by evaluating its ability to use debt to fund its assets.
4. The Return on Equity based on DUPONT analysis varies between 0.01 and 0.29 with an aggregate of 0.15. It means the Return on Equity is 15 on the investors amount on the real owners i.e., equity shareholders.
5. The average Return on Average Assets is 0.59 %. The average Return on Assets is less than the benchmark of 1 %. So, the bank has to increase its income to improve return on assets.

V. CONCLUSIONS

1. This paper presents a model for the financial analysis of a bank based on the Du Pont analysis of the world systemic banks and Du Pont system of financial analysis as presented in Saunders (2000). Equity returns are supplied to share holders from banks who utilize share holders' capital to offer loans to the banks clients.

2. To increase operating profits one bank must either increase sales (in a higher proportion than the cost of generating those sales) or reduce expenses. Since it is generally more difficult to increase sales than it is to reduce expenses, a small bank can try to lower expenses by offering innovating products and a big bank can do this by mergers and acquisitions.
3. Further, BOB can determine if they are using deposits loans and investments wisely. The ROE and ROA indexes are the most comprehensive measure of profitability of a bank. It considers the operating and investing decisions made as well as the financing and tax-related decisions.
4. The Du Pont mode is analysis that calculates the ROE ratio. The ROE ratio is decomposed in to net profit margin, total asset turnover and the equity multiplier. The DuPont model also show us how many times ROE ratio is bigger than the ROA ratio. In its simplest form, we can say that if a bank wants to improve the ROE ratio the only choices has is to increase operating profits, become more efficient in using existing assets to generate sales, recapitalize to make better use of debt and/or better control the cost of deposit and lending money.

References

1. Basel Committee on Banking Supervision (2011) “Global systemically important banks: Assessment methodology and the additional loss absorbency requirement “Consultative Document 7/2011.
2. Bodie, Z., Kane, A., and Alan, J.M., (2004) “Essentials of Investments” 5thedition, McGraw-Hill, Irwin,.
3. Boissay Frederic, Collard Fabrice and Smets Frank (2013) “Booms and Systemic Banking Crises.”: Working Paper Series No 1514/february 2011
4. Boran Milan (2010) “Market Dynamics & Systemic Risk” June 4, 2010 23rd Australasian Finance and Banking Conference 2010 Paper
5. Brandy, M., Walker, J., (2011) “What is an equity multiplier”, 2011
6. Collier W. H., McGowan, B. Mc., Muhammad, Jr. J., (2010) “Evaluating the impact of a rapidly changing economic environment on bank financial performance using the DuPont system of financial analysis”, Asia Pacific Journal of Finance and Banking Research Vol.4.No.4, 2010
7. CRMPG III (2008). “Containing Systemic Risk.”, The report of CRMPG III, August 6, 2008
8. Crosson, S., V., Belverd E., Needles, Jr., Belverd E., (2008) “Powers Marian Principles of accounting”. Houghton Mifflin, Boston 2008
9. Daula Tomas (2012). “Systemic Risk: Relevance, Risk Management Challenges and Open Questions”, June 2012
10. Ergung or Emre O. and Thomson James B. (2005) “Systemic Banking Crises” Federal Reserve Bank of Cleveland, issue 2/2005.

See discussions, stats, and author profiles for this publication at: <https://www.researchgate.net/publication/375524761>

Madhya Bharti (मध्या भर्ती)

Article · November 2023

CITATIONS
0

READS
130

1 author:



Venu Kesireddy

12 PUBLICATIONS 2 CITATIONS

SEE PROFILE

COMPOSITIONAL DUPONT ANALYSIS: A VISUAL TOOL FOR OVERALL FINANCIAL POSITION OF BANK OF BARODA

Dr. Venu Kesireddy, Asst. Professor, Department of MBA, Vaagdevi College of Engineering (Autonomous), Bollikunta, Warangal.

Y. Sravan Kumar, Asst. Professor, Department of MBA, Vaagdevi Engineering College, Bollikunta, Warangal.

Abstract

The main field of this work is to study the overall financial position of Bank of Baroda with the help of Du Pont analysis. To achieve the goal, this study has measured the ratios of ROE, ROA applying the DuPont analysis, which has been demonstrated with tables to show the change periodically. It is concluded from the study that, the parameters of ROE, ROI are showing comprehensive measures. The financial performance of BOB might be studied by several researchers all over India. The DuPont Analysis measures the wealth of the Owners, Investors with the ROE index, and the management's effectiveness with the ROA index, and one index affect the other. It is compared to the formation of a comparable size over a period of time.

Key Words: *Financial performance, Profitability, DUPONT, ROA, Bank of Baroda, ROI and ROE.*

I. INTRODUCTION

The DuPont analysis also known as the DuPont identity or DuPont Model is a framework for analyzing fundamental performance popularized by the DuPont Corporation. DuPont analysis is a useful technique used to decompose the different drivers of return on equity (ROE). The decomposition of ROE allows investors to focus on the key metrics of financial performance individually to identify strengths and weaknesses.

The analysis of the financial statements of a business includes besides the selection of the appropriate index and the comparison, without which the resulting conclusions do not have any meaning and most probably they do not lead to the correct explanation.

The comparison makes sense when it is done in relation to time and in relation to the similar businesses or the sector. This double comparison gives the capability of a more correct explanation of the indexes and consequently of the business condition (Papoulias, 2000).

Profitability of banks is measured mainly by two ratios. The Return on Equity (ROE) that increase the wealth of the shareholders and the Return on Assets (ROA) that show to the investors how cable is the bank management to yield earnings and how profitably use the whole assets of the bank.

Saunders (2000) provides a model of financial analysis for financial institutions that is based on the DuPont system of financial analysis return on equity model. The return on equity model disaggregates performance into the three components that determine return on equity: net profit margin, total asset turnover, and the equity multiplier. The profit margin allows the financial analyst to evaluate the income statement and the components of the income statement. Total asset turnover allows the financial analysis to evaluate the left-hand side of the balance sheet which is composed of the asset accounts. The equity multiplier allows the financial analyst to evaluate the right-hand side of the balance sheet which is composed of liabilities and owner's equity.

Return on equity analysis provides a system for planning (budgeting) in addition to analyzing the financial institution's performance. The net profit margin allows the analyst to develop a pro for income statement. An abbreviated income statement would be composed of net income equal to revenues minus expenses. The financial planner can determine the projected revenue level needed to meet the target net

II. RESEARCH METHODOLOGY

The research methodology means the way the research has been taken place to do the research work. It consists of objectives of study, scope of study and collection of data etc.

A). OBEJECTIVES OF THE STUDY

1. To study the financial performance of Bank of Baroda with the help of DUPONT analysis
2. To draw conclusions emerged from the study and offer appropriate suggestions.

B). SCOPE OF THE STUDY

The scope of the study is confined to financial performance of Bank of Baroda from 2007-08 to 2018-19. The study was focused financial performance with the help of Return on Equity, Return on Investment and DUPONT analysis.

C). COLLECTION OF DATA

The necessary data was collected from the secondary sources such as annual reports of Bank of Baroda, publications of Reserve Bank India, websites and other published sources.

III. DATA ANALYSIS AND INTERPRETATION

Du Pont analysis divides net operating profits into two multiple components: profit margin and asset turnover. This analysis is a common type of financial statement analysis. These two accounting ratios measure two different structures and therefore have two different characteristics. Previous research has shown that changes in asset sales are positively linked to changes in future income. The analysis of Du Pont takes into account three indicators to determine a company's profitability:

1. Return on Sales (ROS) or Net Profit Margin ratio
2. Return on Equity (ROE), and.
3. Return on Assets (ROA)

DuPont model basically segregates the ROE into three parts:

- ❖ Net Profit margin,
- ❖ Total Assets Turnover and
- ❖ Equity Multiplier.

NET PROFIT MARGIN

Net profit margin is a measure of the total profitability and also measures the profitability of the business on income. The margin of profit is the return of the assets of the company. The difference is between total income and total expenditure.

Net Profit Margin= Net Profit/ Total Income

Table -1: Net Profit Margin (NPM)

(2007-08 to 2018-19)

Year	Net profit (Rs. in crores)	Total Income (Rs. in crores)	Net Profit margin (In %)
2007-08	1435.52	13864.52	10.35
2008-09	2227.2	17849.24	12.48
2009-10	3058.33	19504.7	15.68
2010-11	4241.68	24695.11	17.18
2011-12	5006.96	33096.05	15.13
2012-13	4480.72	38827.27	11.54
2013-14	4541.08	43402.45	10.46
2014-15	3398.44	47365.56	7.17
2015-16	-5,396	49060.14	11.00
2016-17	1383.14	48957.99	2.83
2017-18	-2431.81	50305.69	-4.83

2018-19	433.52	56065.1	0.77
Sum	22378.78	442993.8	119.43
Average	1864.90	36916.15	9.95
STDEV	3120.04	14633.06	5.14
CAGR	-10	12	-0.20

Source: Compiled from the annual reports of Bank of Baroda

INTERPRETATION:

Table 1 shows the Net profit, Total Income and Net Profit Margin of BOB in 2007-08 to 2018-19. The Net Profit in 2007-08 is Rs. 1435.52 crores, at the end of the study period 2018-19 it is Rs. 433.52 crores and the average Net Profit is Rs.1864.90 crores. The Total Income in 2007-08 is Rs. 13864.52 crores, which has been increasing, reported highest Rs. 56065.1 crores in 2018-19. The Net Profit Margin in 2007-08 is 10.35 %, later on, fluctuated and reported highest 17.18 % in 2010-11. The average Net Profit Margin ratio during the study period is 9.95 %, with a standard deviation of 5.14%.

The Net Profit margin varies between 0.77 % and 17.18 % and average Net Profit Margin is 9.95 % with standard deviation of 5.14. At the end of the study period the Net Profit margin very lowest means there is significant problem regarding this year to report lowest Net Profit margin.

THE ASSET TURNOVER RATIO

The asset turnover ratio is the ratio of a company's assets to its sales or revenues. It's a metric for how efficiently a company generates revenue from its assets. As a result, a company's asset turnover ratio can be used to forecast its performance. The higher the ratio is the more profitable.

Formula:

Asset Turnover = (Total Income/ Total Assets)

**Table – 2: Asset Turnover Ratio
(2007-08 to 2018-19)**

Year	Total Income (Rs. In crores)	Total Assets (Rs. In crores)	Asset Ratio (In %)	Turnover
2008-09	13864.52	179599.5	7.72	
2008-09	17849.24	227406.7	7.85	
2009-10	19504.7	278316.7	7.01	
2010-11	24695.11	358397.2	6.89	
2011-12	33096.05	447321.5	7.40	
2012-13	38827.27	547135.4	7.10	
2013-14	43402.45	659504.5	6.58	
2014-15	47365.56	714988.6	6.62	
2015-16	49060.14	671376.5	7.31	
2016-17	48957.99	694875.4	7.05	
2017-18	50305.69	719999.8	6.99	
2018-19	56065.1	780987.4	7.18	
Sum	442993.8	6279909	85.69	
Average	36916.15	523325.8	7.14	
STDEV	14633.06	215530.6		
CAGR	12	14		

Source: Compiled from the annual reports of Bank of Baroda

INTERPRETATION:

Table 2 shows the Total income, Total Assets and Assets turnover ratio of BOB from 2007-08 to 2018-19. The Total Income in 2007-08 is Rs. 13864.52 crores, which has been increasing, reported highest Rs. 56065.1 crores in 2018-19 and the average income is Rs. 36916.15 crores; the Standard deviation is Rs. 14633.06 crores and the CAGR is 12%.

The table also shows the total assets of the Bank. The total assets in 2007-08 were Rs. 179599.5 crores, end of the study period 2018-19 is Rs, 780987.4 crores, and average assets Rs. 523325.8 crores. The standard deviation is Rs. 215530.6 crores and CAGR is 14 %.

The Assets turnover ratio is 2008-09 is highest at 7.85 %, later on fluctuated reported lowest 6.58 % in 2013-14 and at the end of the study period 2018-19 it is 7.18 %. The Average Asset turnover ratio during the study period is 7.14 %. So, we can conclude that the bank has regenerated the assets to generate income. It means on every Rs.100 worth of asset it is generating Rs.7.14 aggregate income every year. It should be better to generate at least Rs.10 on every Rs.100 worth of assets.

EQUITY MULTIPLIER

The third and final step of the DuPont model is the equity multiplier. Leverage ratio refers to the capital stock multiplier. It is a method of determining a company's financial leverage by evaluating its ability to use debt to fund its assets.

Formula: Equity Multiplier = Total Assets/ Stockholder's Equity

Table – 3: Equity Multiplier
(2007-08 to 2018-19)

Year	Total Assets (Rs. In crores)	Shareholder's Equity (Rs. In crores)	Equity Multiplier (Rs. In crores)
2007-08	179599.5	365.53	491.34
2008-09	227406.7	365.53	622.13
2009-10	278316.7	365.53	761.41
2010-11	358397.2	392.81	912.39
2011-12	447321.5	412.38	1084.73
2012-13	547135.4	422.52	1294.93
2013-14	659504.5	430.68	1531.31
2014-15	714988.6	443.56	1611.93
2015-16	671376.5	462.09	1452.91
2016-17	694875.4	462.09	1503.77
2017-18	719999.8	530.36	1357.57
2018-19	780987.4	530.36	1472.56
Sum	6279909	5183.44	14096.98
Average	523325.8	431.95	1174.75

STDEV	215530.6	57.65	
CAGR	14	0.34	

Source: Compiled from the annual reports of Bank of Baroda

INTERPRETATION:

Table 3 shows the Total Assets, Shareholder's equity and Equity multiplier ratio of BOB from 2007-08 to 2018-19. The total assets in 2007-08 were Rs. 179599.5 crores, end of the study period 2018-19 is Rs. 780987.4 crores, and average assets Rs. 523325.8 crores . The standard deviation is Rs. 215530.6 crores and CAGR is 14 %.The Shareholder's equity in 2007-08 is Rs. 365.53 crores, has reported the highest Rs. 530.36 crores at the end of the study period 2018-19. The average Shareholder's equity is Rs.431.95 crores. The standard deviation of the Shareholder's equity is Rs.57.65 crores and the CAGR is 0.34 % during the study period. The Equity multiplier ratio in 2007-08 is 491.34 %; later on, it fluctuated and reported the highest 1611.93 % in 2014-15 and at the end of the study period, 2018-19 was 1472.56 %. The average Equity multiplier ratio during the study period is 1174.75 %.

Being the equity multiplier ratio varies betweenRs. 491.34and Rs. 1611.93 and the average equity multiplier ratio during the study period is Rs.1174.75. Leverage ratio refers to the capital stock multiplier. It is a method of determining a company's financial leverage by evaluating its ability to use debt to fund its assets.

RESULT OF DUPONT ANALYSIS OF BOB

The following table 4 presents the summary of the results of ROE or Return on shareholders' equity or Return on Net worth of BOB for the period 2008-09 to 2018-19, which has been calculated from the secondary data collected and compiled from all the annual reports of all the financial parameters required for the formulae.

Table – 4: Summary of DUPONT Analysis of BOB, FY 2008-09 to 2018-19

Year	(A) NP Margin	(B) Asset turnover	(C) Equity Multiplier	ROE
	%	Times	(%)	$D=A/(B*C)$
2007-08	10.35	7.72	491.34	0.27
2008-09	12.48	7.85	622.13	0.26
2009-10	15.68	7.01	761.41	0.29
2010-11	17.18	6.89	912.39	0.27
2011-12	15.13	7.40	1084.73	0.19
2012-13	11.54	7.10	1294.93	0.13
2013-14	10.46	6.58	1531.31	0.10

2014-15	7.17	6.62	1611.93	0.07
2015-16	11.00	7.31	1452.91	0.10
2016-17	2.83	7.05	1503.77	0.03
2017-18	4.83	6.99	1357.57	0.05
2018-19	0.77	7.18	1472.56	0.01
Sum	119.43	85.69	14096.98	0.01
Average	9.95	7.14	1174.75	0.15
STDEV	8.28	0.44	4.04	
CAGR	-1.92	-0.01	0.09	

Source: Calculated and Compiled from the data collected from all the Annual reports of BOB

INTERPRETATION:

Table – 4: Shows Summary of DUPONT Analysis of BOB from 2007-08 to 2018-19. The NP Margin in 2007-08 was 10.35 %, increased to highest 17.18 % in 2010-2011, later gradually decreased to 0.77% in 2018-19. Asset turnover ratio in 2007-08 was 7.72 %, decreased to the lowest 6.58 % in 2013-2014, fluctuated and reported 7.18 % in 2018-19. Equity multiplier ratio in 2007-08 was 491.34 %, was highest 1611.93 % in 2014-15 and at the end of the study period 2018-19 it is 1472.56 %. ROE in 2007-08 was 6.15 % and reported highest 266.35 % in 2018-19.

The Return on Equity based on DUPONT analysis varies between 0.01 and 0.29 with an aggregate of 0.15. It means the Return on Equity is 15 on the investors amount on the real owners i.e., equity shareholders.

**Table – 5: Return on Assets & Return on Average Assets
(2007-08 to 2018-19)**

Year	Return On Assets(In %)	Return On Average Assets(In %)
2007-08	0.80	0.89
2008-09	0.98	1.10
2009-10	1.10	1.21
2010-11	1.18	1.33
2011-12	1.12	1.24
2012-13	0.82	0.90
2013-14	0.69	0.75
2014-15	0.48	0.49
2015-16	-0.80	-0.78

2016-17	0.20	0.2
2017-18	-0.34	-0.34
2018-19	0.06	0.06
Sum	6.29	7.05
Average	0.52	0.59
STDEV	0.63	0.67
CAGR	-0.21	-0.22

Source: Compiled from the annual reports of Bank of Baroda.

INTERPRETATION:

Table 5 presents the Return on Assets of the bank from 2007-08 to 2018-19 financial years. During the study period in 2007-08, the Return on Assets was 0.80 %. It is 0.06 % at the end of the study period 2018-19. The average Return on Assets is 0.52 % with a Compound Annual Growth Rate (CAGR) of -0.21 %. The Standard Deviation (STDEV) of Return on Assets during the study period is 0.63. The table also shows the Return on Average Assets of the bank from 2007-08 to 2018-19 financial years. During the study period in 2007-08, the Return on Average Assets was 0.89 %. It is 0.06 % at the end of the study period 2018-19. The average Return on Average Assets is 0.59 % with a Compound Annual Growth Rate (CAGR) of -0.22 %. The Standard Deviation (STDEV) of Return on Average Assets during the study period is 0.67%. The average Return on Assets is less than the benchmark of 1 %. So, the bank has to increase its income to improve return on assets.

The average Return on Average Assets is 0.59 %. The average Return on Assets is less than the benchmark of 1 %. So, the bank has to increase its income to improve return on assets.

IV. FINDINGS

1. The Net Profit margin varies between 0.77 % and 17.18 % and average Net Profit Margin is 9.95 % with standard deviation of 5.14. At the end of the study period the Net Profit margin very lowest means there is significant problem regarding this year to report lowest Net Profit margin.
2. The asset turnover ratio was representing here the relation between total assets and total income. The asset turnover ratio presenting as per every Rs.100 worth of asset it is generating Rs.7.14 aggregate income every year. It should be better to generate at least Rs.10 on every Rs.100 worth of assets.
3. Being the equity multiplier ratio varies between Rs. 491.34 and Rs. 1611.93 and the average equity multiplier ratio during the study period is Rs.1174.75. Leverage ratio refers to the capital stock multiplier. It is a method of determining a company's financial leverage by evaluating its ability to use debt to fund its assets.
4. The Return on Equity based on DUPONT analysis varies between 0.01 and 0.29 with an aggregate of 0.15. It means the Return on Equity is 15 on the investors amount on the real owners i.e., equity shareholders.
5. The average Return on Average Assets is 0.59 %. The average Return on Assets is less than the benchmark of 1 %. So, the bank has to increase its income to improve return on assets.

V. CONCLUSIONS

1. This paper presents a model for the financial analysis of a bank based on the Du Pont analysis of the world systemic banks and Du Pont system of financial analysis as presented in Saunders (2000). Equity returns are supplied to share holders from banks who utilize share holders' capital to offer loans to the banks clients.

2. To increase operating profits one bank must either increase sales (in a higher proportion than the cost of generating those sales) or reduce expenses. Since it is generally more difficult to increase sales than it is to reduce expenses, a small bank can try to lower expenses by offering innovating products and a big bank can do this by mergers and acquisitions.
3. Further, BOB can determine if they are using deposits loans and investments wisely. The ROE and ROA indexes are the most comprehensive measure of profitability of a bank. It considers the operating and investing decisions made as well as the financing and tax-related decisions.
4. The Du Pont mode is analysis that calculates the ROE ratio. The ROE ratio is decomposed in to net profit margin, total asset turnover and the equity multiplier. The DuPont model also show us how many times ROE ratio is bigger than the ROA ratio. In its simplest form, we can say that if a bank wants to improve the ROE ratio the only choices has is to increase operating profits, become more efficient in using existing assets to generate sales, recapitalize to make better use of debt and/or better control the cost of deposit and lending money.

References

1. Basel Committee on Banking Supervision (2011) “Global systemically important banks: Assessment methodology and the additional loss absorbency requirement “Consultative Document 7/2011.
2. Bodie, Z., Kane, A., and Alan, J.M., (2004) “Essentials of Investments” 5thedition, McGraw-Hill, Irwin,.
3. Boissay Frederic, Collard Fabrice and Smets Frank (2013) “Booms and Systemic Banking Crises.”: Working Paper Series No 1514/february 2011
4. Boran Milan (2010) “Market Dynamics & Systemic Risk” June 4, 2010 23rd Australasian Finance and Banking Conference 2010 Paper
5. Brandy, M., Walker, J., (2011) “What is an equity multiplier”, 2011
6. Collier W. H., McGowan, B. Mc., Muhammad, Jr. J., (2010) “Evaluating the impact of a rapidly changing economic environment on bank financial performance using the DuPont system of financial analysis”, Asia Pacific Journal of Finance and Banking Research Vol.4.No.4, 2010
7. CRMPG III (2008). “Containing Systemic Risk.”, The report of CRMPG III, August 6, 2008
8. Crosson, S., V., Belverd E., Needles, Jr., Belverd E., (2008) “Powers Marian Principles of accounting”. Houghton Mifflin, Boston 2008
9. Daula Tomas (2012). “Systemic Risk: Relevance, Risk Management Challenges and Open Questions”, June 2012
10. Ergung or Emre O. and Thomson James B. (2005) “Systemic Banking Crises” Federal Reserve Bank of Cleveland, issue 2/2005.

Social network Credibility analysis using various machine learning algorithms

Rapolu Vaishnavi¹, Deepika²

M.Tech Student, Department of CSE, Vaagdevi college of engineering, Hanamkonda, Bollikunta, warangal

506005(T.S) 1

Assi. Prof and Department of CSE, Vaagdevi college of engineering, Hanamkonda, Bollikunta, warangal

506005(T.S) 2

ABSTRACT

Internet-based communication and content-creation tools like social networking sites are widely used today. This data is often unreliable because it has not been checked for accuracy. There have been studies conducted on validating data, however they are typically restricted to very narrow cases. Hence, a more generic and adaptable design that is not tied to any particular social media network is required. We offer a framework to instantly and automatically analyze the trustworthiness of social media posts at the text, user, and social levels. Front-end, a light client proposed as a web plug-in for any browser; back-end, which implements the logic of the credibility model; and a module for third-party services make up the overall design of our framework. As a proof of concept, we create a framework for analyzing tweets for CREDibility and call it TCREo (Twitter CREDibility analysis framework). The key contributions of this work are the general framework design, an integrated credibility model that can be adapted to different social networks, and T-CREo, a proof of concept that proves the utility of the framework. As per outcomes of T-CREo is a highly scalable real-time service, demonstrating the framework's applicability and allowing evaluation of its performance for unstructured information sources. T-CREo implementation will be enhanced in the future to give a solid framework for the creation of third-party applications, and the credibility model will be expanded to take into account bots detection, semantic analysis, and multimedia analysis.

Keywords: twitter, svm, random forest, KNN, Decision tree, Logistic regression

1. INTRODUCTION

Nowadays, users mostly utilize social media platforms like Facebook, Twitter, and Instagram to share and read content related to a wide range of interests. This facilitates the free exchange of knowledge that has applications ranging from the dissemination of daily news and international events to the creation of cutting-edge technologies [1]-[3]. In the early 21st century, the proliferation of social media and other Internet platforms that enable people to connect, exchange, and generate content without explicit references to sources led to the creation of an enormous amount of data now known as Big Data. It might be challenging to use and interpret this data because it is often not documented or confirmed. Therefore, the idea of credibility, defined as the degree to which one has faith in (the veracity of) another person, thing, or process [4] has become crucial in many fields and points of view, including those of information technology, business, communications, journalism, information retrieval, and human-computer interaction, to name just a few. [5], [6].

Existing works, however, can only be used for credibility analysis in certain contexts (e.g., for a specific social platform, for a particular application). The extraction strategies used to acquire the information to feed the credibility models and the factors considered to determine credibility (e.g., qualities of the posts or of users who submitted them, the text of the posts, user social effect) vary among these publications (i.e., web scraping or API). That's why it's important to have a platform-agnostic, general-purpose architecture that can meet the specific needs of users and programmers.

To address these issues, we offer a system that can instantly and automatically evaluate the veracity of social network posts. Our earlier work [4] proposed a credibility model consisting of a publication-credibility analysis that can be adapted to different social networks; this model is instantiated in the framework. Text Credibility (determined via text analysis), User Credibility (determined via user account parameters such as creation date and verified account status), and Social Credibility make up the model's foundations. In this paper, we outline the framework's overall design and show how it may be put to use with unstructured information sources by using Twitter, one of the most popular social media platforms, as an example.

The following are some of the primary features of our proposed technique architecture that set it apart from prior works:

It automatically and in real-time performs credibility analysis; It consists of a front-end, which is suggested as a web plug-in to be incorporated on any browser, and a decoupled back-end which accesses the information needed for the credibility model via web scraping and social media API; Users/developers can configure the system to base the gathered information only with web scraping or integrating the use of the available API.

As proof of concept, we create TCREO (Twitter credibility analysis framework), the first version of the suggested system. T-CREO analyzes the trustworthiness of tweets in real time as a Google Chrome extension. According to the research reported in [7], around 500,000,000 tweets are posted daily on Twitter. As a result, research into the evaluation of trustworthiness in this setting has grown popular in recent years [8, 11]. Many studies [4, 8, 11, 12] and more comprehensive studies [13–18] have proposed frameworks for automatically and in real-time doing credibility analysis on Twitter. We provide a qualitative comparison of our solution to the state-of-the-art and demonstrate the performance evaluation of T-CREO across a range of situations and input parameters. According to the findings, T-CREO performs at a level that makes it suitable for use as a real-time, highly scalable service. In conclusion, the main contributions of this work are (i) the design of a framework to automatically perform credibility analysis on social networks in real time; (ii) the integration of a credibility model adaptable to different social networks into the structure; and (iii) T-CREO as a proof of concept that illustrates the applicability of the framework and allows a comparison study with current systems and an assessment of its performance.

2. LITERATURE SURVEY:

Current works take into account the extraction and analysis of various sorts of data to determine social media trustworthiness. Hence, other credibility concepts have been proposed [8, 9, 11, 19, 20]. Taking cues from these studies, we provide the following taxonomy of social network credibility terms:

- **Text Credibility (Post Credibility):** evaluates the text's veracity and reliability in general [8] or in relation to a specific issue [11]. Natural language processing and other text-analysis methods are used to arrive at this conclusion (NLP).
- **User Credibility:** determines the trustworthiness of a user account given its defining characteristics. For example, if the user's age is known, the age of the account might be used to determine the age of the user. A publication's social credibility can be determined using available information that represent the social influence of the user account and the post itself in relation to other users. This applies to publications on any topic. Followers, follows, and retweets are only some of the metrics used to determine this.
- **Subject Credibility** assesses how widely believed the text's subject matter or referenced event is. NLP and sentiment analysis methods are commonly used for this purpose, and they allow us to determine whether or not a piece of text is relevant to a given topic. All of these criteria of credibility add up to an overall assessment of the reliability of a piece of writing found in a social information source, but they aren't always taken into account together. In addition, most of the publications that have been published so far [4, 8, 11, 12, 20] simply reveal how the credibility model is implemented in a particular setting.

2 Our study centers on proposing and describing a general architecture to facilitate this procedure, and so Volume 4, 2016 of IEEE Access, Volume 9, Issue 19, February 2021. This is crucial for determining if the proposed method can be used in practical, time-sensitive situations. Existing research has also addressed the question of where the metrics used to determine credibility come from. While some of these

methods rely on the application programming interfaces (APIs) of social media platforms [19, 21], others rely on web scraping [23–26]. While online scraping offers far more flexibility than social network APIs, it also requires more effort and must be changed whenever the HTML structure changes. For credibility analysis [27] or to collect an endless volume of tweets [28], there have been few recent publications that compare both extraction approaches in Twitter. Research that proposes a structure, an architecture, or a method for assessing trustworthiness in online communities is more closely related to our own. Although our proposed architecture is adaptable to many social networks, we limit ourselves to Twitter here because that's where we'll be implementing it. We evaluate them in terms of the weighted believability levels, information extraction method, and usefulness in practical settings.

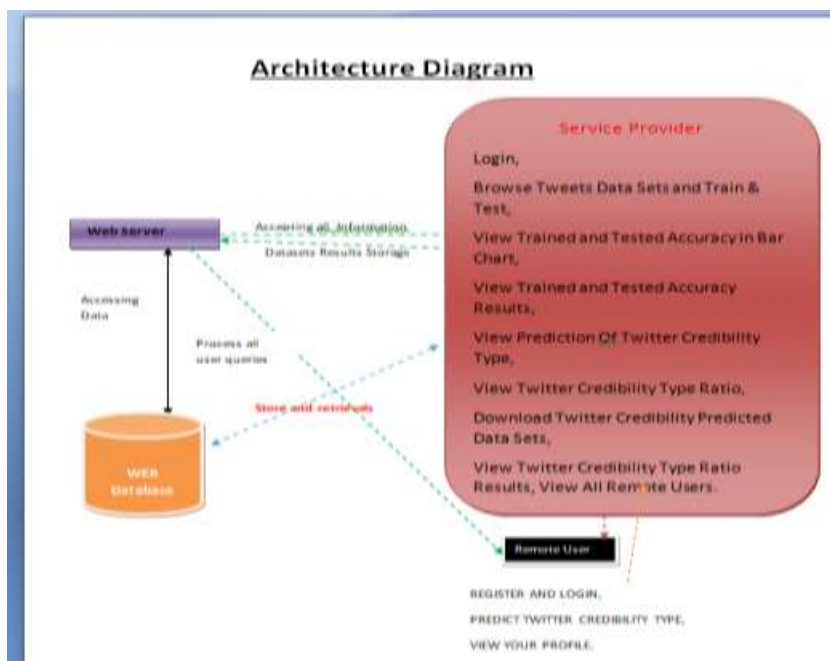
A. Twitter Analysis Tools for Reputability

While other works have presented architectures for real-time Twitter data analytics ([21], [22], [29–31]) or for pre-processing data for sentiment analysis ([32], for example), our focus here is on credibility analysis, which is outside the purview of these other works. Several research propose offline systems that can examine the veracity of tweets when requested by the user [33] or using previously collected data [34], [35]; these systems do not provide real-time veracity analysis. In [33], two methods are given for determining a topic's credibility: one uses the tweet's favorable and negative sentiments about the issue to determine its credibility, while the other uses the author's knowledge to determine its credibility. The system is made up of four parts plus a database of tweet opinions: The tweet sender/receiver is an interactive front-end module that takes user input and returns a result; the tweet credibility calculator module uses the tweet opinion classifier to determine both the topic and the opinion of a given tweet; and finally, it uses the tweet opinion database, which contains tweets collected by the tweet collector module and labeled with a topic-opinion label, to perform a majority decision on contradictory opinions in the same topic. Hoaxy [34] is a website that keeps tabs on the circulation of fake news across social media. The primary objective of this effort is to aid scholars, journalists, and the general public in keeping tabs on the spread of disinformation and the verification processes that surround it online. The system consists of a database (which also serves as a repository) and an analysis dashboard, as well as monitors (which include a URL tracker, scrapy spider, and an RSS parser). Web scraping, web syndication, and, where available, APIs from social networking platforms are used to compile data from the system's two primary sources, news websites and social media. The collected information is then evaluated to determine both the similarities and differences in the ways that users disseminate false information and the results of fact checks. These systems are not able to facilitate real-time analysis because they are off-line. In [35], the authors offer a method for identifying SOFNs through the analysis of the trustworthiness of tweets using graph Machine Learning. The Twitter API is used to collect data on user attributes (such as creation time, name, default profile, default profile image, favorites, statuses, and descriptions), the social graph of users (followers/following graph), and subject annotations. These features are used as inputs to binary Machine Learning classifier models for SOFN prediction. Other similar works have developed architectural frameworks for conducting real-time Twitter credibility assessments. [13]–[18]. In [13], we see an implementation of an

automated credibility assessment system for Twitter posts about news in Arabic. Together with the material itself, this method also evaluates the user account itself, taking into account things like its verified quality and Twittergrader.com score (i.e., text, user, and social credibility levels). Number of followers, impact of those followers, updates, news credibility, relationship between followers and following, and dedication are all factors that Twittergrader.com considers when calculating an account's overall authority and influence. The Twitter API underpins a four-part architecture that includes text pre-processing, feature extraction and computation, credibility calculation, and credibility assignment and rating. Described in [14] and [15], respectively, TweetCred and CredFinder are two useful solutions presented as Google Chrome plugins that determine a tweet's credibility in real time by analyzing its text, properties (such as publication time and source), and social influence. Twitter's application programming interface is used by both. The back-end of TweetCred [14] is in charge of calculating credibility scores by accessing the Twitter API to retrieve information about individual tweets and by using a Support Vector Machine (SVM) prediction model; the front-end is a local interface embedded in the Google Chrome browser, from which the tweets' IDs are scraped and sent to the back-end, and in which the credibility scores are displayed. Considerations such as the tweet's text (metadata and content) and social information about the person (e.g., followers, following) and the tweet's context are used to determine the tweet's trustworthiness (e.g., retweets, mentions). CredFinder [15] has a web-based backend and a frontend in the form of a Google Chrome extension. The former pulls tweets from Twitter searches and user timelines in real time, while the latter is built on four pillars: reputation, trustworthiness, user experience, and a rating algorithm for features. Tweets and their meta-data (the time of posting, the author name, the number of followers, the number of friends, the hash tags or mentions, etc.) are collected using the Twitter streaming API, VOLUME 4, 2016 3 IEEE Access, Volume:9, Issue Date:19.February.2021 et al. The algorithm that determines one's trustworthiness uses all of these factors as input. In [16], a different web interface structure is offered, this time as a web plug-in system. The goal is to assess the reliability of tweets about a certain topic in near-real time. The entailment, neutrality, or contradiction status of each tweet is determined just by analyzing the tweet's language. To help users determine the tweet's legitimacy, the system displays a selection of relevant news articles. Tweets are collected using the Twitter API, URLs mentioned in tweets are obtained using web scraping, and relevant articles and news headlines are located using the Bing news API. A credibility analysis paradigm for Twitter data is proposed in [17], along with catastrophe situation awareness. Using a database containing post text and external URLs, this approach can instantly determine the topic-level credibility (i.e., emergency situations) of a tweet by analyzing the content, connected URLs, number of retweets, and location data. A greater credibility score for an event therefore means that more people have tweeted about it, linked to it, and retweeted it. Information about tweets and their locations is gathered using the Twitter API and the Google Maps Geocoding API, respectively. The text is first assessed by the event identification module, which looks for terms that match with keywords that characterize a certain event (i.e., a disaster crisis issue), and then the credibility module determines how reliable the content is. In [18], we

learn about a technique developed more recently for instantaneous credibility evaluation. This system uses neural network models to analyze texts and user profiles in search of potentially fraudulent content and users. The number of pertinent words and the sentiment score are two measures of text credibility alongside the number of retweets, follows, and favorites (i.e. social impact) (i.e., the text content is analyzed). The trustworthiness of a Twitter user is determined by looking at their location, URL, whether or not the account has been verified, the account's geolocation, the account's creation date, and the user's most recent 20 tweets. These statistics are retrieved via the Twitter API. The system has a leaning module, a credibility module, and a module for monitoring tweets and users.

3. SYSTEM ARCHITECTURE



4. ALGORITHMS

4.1 Decision tree classifiers

Successful applications of decision tree classifiers can be found in a wide range of disciplines. The ability to extract descriptive decision-making knowledge from the provided data is their primary strength. From training data, a decision tree can be constructed. The following is the technique for generating such a set given a set (S) of objects, each of which belongs to a class (C1, C2, ..., Ck):

First, the decision tree for set S will have a single leaf labeled with the class C_i if all the items in S belong to that class.

Step 2. If not, then T is a test with results O_1, O_2, \dots, O_n . This test divides the set S into sets S_1, S_2, \dots, S_n , where each object in S_i has an outcome O_i for T . Since there is only one possible result for T , each object in S has an outcome O_i . T is the starting point for the decision tree, and for each possible outcome O_i , we construct a child decision tree by iteratively applying the same technique to the collection s .

4.2 Gradient boosting

The machine learning method of gradient boosting can be applied to a variety of problems, including classification and regression. A weak prediction model, such as a decision tree, is provided as part of an ensemble of such models. [1][2] Gradient-boosted trees is the resulting technique where a decision tree is the weak learner; it typically performs better than random forest. While similar to other boosting methods in that it involves a staged construction process, gradient-boosted trees generalizes these approaches by permitting the optimization of any differentiable loss function.

Classifies based on a similarity measure K-Nearest Neighbors (KNN) is a simple but powerful classification technique.

Does not "learn" until the test example is provided; is non-parametric; and employs lazy learning.

In order to categorize new data, we look for its K-nearest neighbors in the training data.

4.3 Logistic regression Classifiers

The goal of logistic regression analysis is to determine which factors best explain a categorical dependent variable. When the value of the dependent variable may only take on two possible forms, such as 0 and 1, Yes and No, etc., the statistical technique is referred to as logistic regression. When the dependant variable can take on at least three distinct values—for example, marital status—it is referred to as multinomial logistic regression. The dependent variable is measured differently than in multiple regression, although the process otherwise functions similarly.

Analyzing categorical response variables, logistic regression competes with discriminant analysis. Logistic regression, in the opinion of many statisticians, is more flexible and appropriate for modeling most situations than

discriminant analysis. This is because, unlike discriminant analysis, logistic regression does not require the independent variables to be regularly distributed.

Logistic regression, both binary and multinomial, can be calculated in this software using either numerical or categorical independent variables. The regression equation, likelihood, likelihood ratio, confidence interval, odds ratio, and standard deviation are all reported. A full residual analysis is carried out, complete with diagnostic residual reports and charts. It can search for the optimal regression model using the fewest number of independent variables, a process known as independent variable subset selection. You can use the ROC curves and confidence intervals on anticipated values to zero in on the optimal classification threshold. By automatically labeling rows that were not included in the analysis, it helps you verify your findings.

4.4 Naïve Bayes

The naive bayes approach is a type of supervised learning that operates under the assumption that the presence or lack of a feature in a class has no bearing on the presence or absence of any other feature.

Nonetheless, its apparent strength and effectiveness belie this. Its efficacy is on par with that of similar supervised learning methods. There are a number of explanations put out in the published works. In this guide, we focus on a justification that makes use of the representation bias. Like linear discriminant analysis, logistic regression, and linear support vector machines (SVMs), the naive bayes classifier is a type of linear classifier (support vector machine). The key distinction is in how the classifier's parameters are estimated (the learning bias).

Although the Naive Bayes classifier sees extensive use in academia, it has not caught on with practitioners who seek actionable insights. The researchers observed that, on the one hand, it is relatively simple to construct and apply, that its parameters are straightforward to estimate, that it can learn quickly even from very big databases, and that it provides reasonable accuracy when compared to alternative methods. But, the end users do not get a model that is simple to grasp and implement, and they do not see the value in using this method.

As a result, we show the results of the learning process in a fresh way. Both deployment and comprehension of the classifier are simplified. Part one of this course covers the naive bayes classifier's theoretical foundations. The method is then applied to a dataset using Tanagra. Results (model parameters) are compared to those found using various linear methods, including logistic regression, linear discriminant analysis, and linear support vector machine. The results are very consistent, as we have noted. This is largely responsible for the method's superior performance when compared to others. In the following section, we apply many programs to the same data set (Weka 3.6.0, R 2.9.2, Knime 2.1.1, Orange 2.0b and RapidMiner 4.6.0). Our primary goal is to comprehend the findings.

4.5 Random Forest

Decision trees are the backbone of many machine learning algorithms, and random forests, also known as random decision forests, are an ensemble learning method for classification, regression, and other tasks. The output of a random forest is the class chosen by the majority of trees, which is useful for classification tasks. When performing a regression job, the average or mean forecast from each tree is returned. Decision trees' tendency to overfit to their training set is mitigated by random decision forests. While they are superior to choice trees, random forests are less precise than gradient enhanced trees. However, its functionality may be impacted by data properties.

In 1995, Tin Kam Ho[1] developed the first algorithm for random decision forests by employing the random subspace method, which, in Ho's terminology, is a means of putting into practice Eugene Kleinberg's "stochastic discrimination" approach to classification.

In 2006, Leo Breiman and Adele Cutler trademarked "Random Forests," an expansion of the algorithm they had devised (as of 2019, owned by Minitab, Inc.).

To build a set of decision trees with limited variation, the extension combines Breiman's "bagging" approach with random feature selection, which was first suggested by Ho[1] and then independently by Amit and Geman[13].

Because of its ability to provide reliable predictions across a large variety of data types with minimal configuration, random forests are widely employed as "blackbox" models in enterprises.

4.6 SVM

A discriminant machine learning technique seeks to accurately predict labels for newly acquired instances by utilizing a training dataset that is both independent and identically distributed (iid). In contrast to the conditional probability distribution computations required by generative machine learning methods, a discriminant classification function simply accepts a data point x and assigns it to one of the classes involved in the classification task. Discriminant approaches require less computational resources and less training data, especially for a multidimensional feature space and when only posterior probabilities are needed, but they are less powerful than generative approaches, which are typically used when prediction involves outlier detection. Learning a classifier is geometrically comparable to solving an equation for a multidimensional surface that optimally divides the feature space into distinct classes.

SVM is a discriminant approach that, unlike genetic algorithms (GAs) and perceptrons, always returns the same optimal hyperplane value since it solves the convex optimization issue analytically. The solutions for perceptrons are quite sensitive to the parameters used to start and stop the process. While the perceptron and GA classifier

models are different every time training is begun, the SVM model parameters for a given training set are uniquely determined for a single kernel that translates the data from the input space to the feature space. As the goal of both GAs and perceptrons is to achieve the lowest possible training error, there will be multiple hyperplanes that satisfies this criterion.

4.7 Results:

classifier	Proposed work				Ref [31]			
	Accuracy	Precision	Recall	F1_score	Accuracy	Precision	Recall	F1_score
Random forest	83.4	83.1	95.6	88.6	78.4	79.6	91.6	85.2
KNN	71.3	75.3	84.5	82.3	66.2	72.5	78.9	75.5
SVM	73.5	71.2	93.4	81.3	67	68.7	91.9	78.6
Logistic regression	72.9	70.3	93	80	66.9	68.8	91.2	78.4
Naïve Bayes	72.8	71	96	82	66.7	67.7	94.8	79

Table1: algorithms comparison

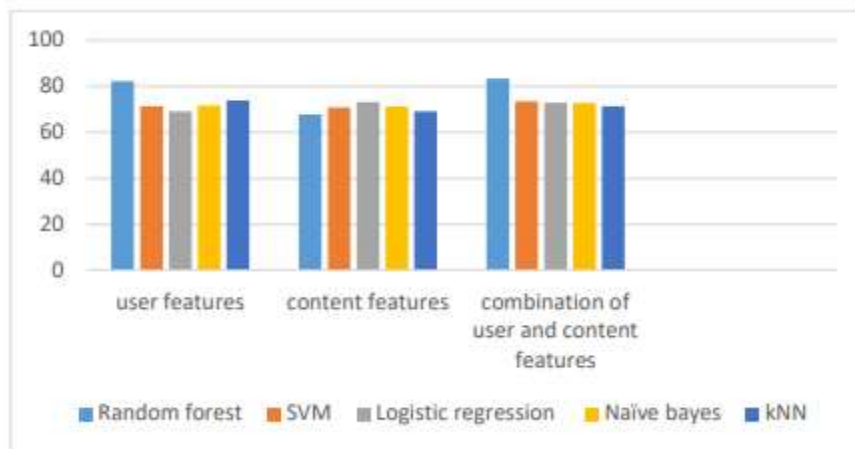


Figure 2: Comparison graph

5. CONCLUSIONS

In this work, we propose a general architecture of a framework for credibility analysis in social media based on a general credibility model. The framework is capable of calculating credibility on any social media in real-time, combining web-scraping and social media APIs to gather the parameters needed to instantiate

the credibility model. A proof of concept, for a specific use case of Twitter and to show the feasibility of the proposed architecture, named TCREO (Twitter credibility analysis framework), is developed and tested to evaluate its performance. Results show that our proposed framework can be implemented as a real time service and the scalability is ensured by increasing the level of concurrency. This experience allows outlining some suggestions to improve overall performance for high capacity servers. The modularity and simplicity of T-CREO, and the use of the credibility model, enable the creation of a real-time service; however, the connection time (latency) can be a determining factor, that might be considered in the deployment of the system.

Our future research is focused on the improvement of TCREO, starting with the suggestions from Section VI, such as the implementation of several instances or multi-threaded versions of the back-end to improve the performance, keep an external database of posts to overcome API limitations, and incorporate credibility analysis in other social platforms, to provide a robust architecture to the community for the development of third-party applications. We also plan to extend the credibility model by considering bots detection, semantic analysis of the text, and multimedia data analysis.

6. REFERENCES

- [1] D. Westerman, P. R. Spence, B. Van Der Heide, Social media as information source: Recency of updates and credibility of information, *J. of Computer-Mediated Comm.* 19 (2) (2014) 171–183. doi:10.1111/jcc4.12041.
- [2] Y. Kammerer, E. Kalbfell, P. Gerjets, Is this information source commercially biased? how contradictions between web pages stimulate the consideration of source information, *Discourse Processes* 53 (5-6) (2016) 430–456. doi:10.1080/0163853X.2016.1169968.
- [3] J. Slomian, O. Bruyère, J.-Y. Reginster, P. Emonts, The internet as a source of information used by women after childbirth to meet their need for information: A web-based survey, *Midwifery* 48 (2017) 46–52. doi:10.1016/j.midw.2017.03.005.
- [4] I. Dongo, Y. Cardinale, A. Aguilera, Credibility analysis for available information sources on the web: A review and a contribution, in: 2019 4th Internat. Conf. on System Reliability and Safety (ICSRS), IEEE, 2019, pp. 116–125. doi:10.1109/ICSRS48664.2019.8987623.
- [5] S. Y. Rieh, D. R. Danielson, Credibility: A multidisciplinary framework, *Annual Rev. Info. Sci & Technol.* 41 (1) (2007) 307–364. doi:10.1002/aris.144.v41:1.
- [6] T. J. Johnson, B. K. Kaye, Reasons to believe: Influence of credibility on motivations for using social networks, *Computers in human behavior* 50 (2015) 544–555. doi:10.1016/j.chb.2015.04.002.

- [7] Omnicore, Twitter by the Numbers: Stats, Demographics & Fun Facts, <https://www.omnicoreagency.com/twitter-statistics> (2020).
- [8] C. Castillo, M. Mendoza, B. Poblete, Information credibility on twitter, in: Proc. of Internat. Conf. on WWW, 2011, pp. 675–684. doi:10.1145/1963405.1963500.
- [9] B. Kang, T. Höllerer, J. O’Donovan, Believe it or not? analyzing information credibility in microblogs, in: Proc. of Internat. Conf. on Advances in Social Networks Analysis and Mining, 2015, pp. 611–616. doi:10.1145/2808797.2809379.
- [10] S. M. Shariff, X. Zhang, M. Sanderson, On the credibility perception of news on twitter: Readers, topics and features, *Computers in Human Behavior* 75 (2017) 785–796. doi:10.1016/j.chb.2017.06.026.
- [11] M. Alrubaian, M. Al-Qurishi, A. Alamri, M. Al-Rakhami, M. M. Hassan, G. Fortino, Credibility in online social networks: A survey, *IEEE Access* 7 (2019) 2828–2855. doi:10.1109/ACCESS.2018.2886314.
- [12] M. Viviani, G. Pasi, Credibility in social media: opinions, news, and health information—a survey, *Wiley Interdisciplinary Reviews: Data Mining and Knowledge Discovery* 7 (5) (2017) e1209. doi:10.1002/widm.1209.
- [13] H. S. Al-Khalifa, R. M. Al-Eidan, An experimental system for measuring the credibility of news content in twitter, *International Journal of Web Information Systems* 7 (2) (2011) 130–151. doi:10.1108/17440081111141772.
- [14] A. Gupta, P. Kumaraguru, C. Castillo, P. Meier, Tweetcred: Real-time credibility assessment of content on twitter, in: Proc. of Internat. Conf. on Social Informatics, 2014, pp. 228–243. doi:10.1007/978-3-319-13734-6_16.
- [15] M. AlRubaian, M. Al-Qurishi, M. Al-Rakhami, M. M. Hassan, A. Alamri, Credfinder: A real-time tweets credibility assessing system, in: Proc. Of Internat. Conf. on Advances in Social Networks Analysis and Mining, 2016, pp. 1406–1409. doi:10.5555/3192424.3192692.
- [16] T. Stephanie, Spot the lie: Detecting untruthful online opinion on twitter, Ph.D. thesis, Imperial College London, <https://www.doc.ic.ac.uk/oc511/reportStephanie.pdf> (2017).
- [17] J. Yang, M. Yu, H. Qin, M. Lu, C. Yang, A twitter data credibility framework—hurricane harvey as a use case, *ISPRS International Journal of Geo-Information* 8 (3) (2019) 111. doi:10.3390/ijgi8030111.
- [18] A. Iftene, D. Gîfu, A.-R. Miron, M.-S. Dudu, A real-time system for credibility on twitter, in: Proc. of The 12th Language Resources and Evaluation Conference, 2020, pp. 6166–6173. doi:10.3233/978-1-61499-900-3-453.

- [19] K. R. Saikaew, C. Noyunsan, Features for measuring credibility on facebook information, *International Scholarly and Scientific Research & Innovation* 9 (1) (2015) 174–177.
- [20] A. M. Idrees, F. K. Alsheref, A. I. ElSeddawy, A proposed model for detecting facebook news' credibility, *International Journal of Advanced Computer Science and Applications (IJACSA)* 10 (7) (2019) 311–316.
- [21] A. Black, C. Mascaro, M. Gallagher, S. P. Goggins, Twitter zombie:Architecture for capturing, socially transforming and analyzing the twittersphere,in: *Proc. of the 17th ACM Internat. Conf. on Supporting group work*, 2012, pp. 229–238. doi:10.1145/2389176.2389211.
- [22] M. Congosto, P. Basanta-Val, L. Sanchez-Fernandez, T-hoarder: A framework to process twitter data streams, *Journal of Network and Computer Applications* 83 (2017) 28–39. doi:10.1016/j.jnca.2017.01.029.
- [23] A. Hernandez-Suarez, G. Sanchez-Perez, K. Toscano-Medina, R. Toscano-Medina, V. Martinez-Hernandez, J. Olivares-Mercado, H. Pérez-Meana, V. Sanchez, Can twitter api be bypassed? a new methodology for collecting chronological information without restrictions, in: *SoMeT*, 2018, pp. 453–462. doi:10.3233/978-1-61499-900-3-453.
- [24] A. Hernandez-Suarez, G. Sanchez-Perez, K. Toscano-Medina, V. Martinez-Hernandez, V. Sanchez, H. Pérez-Meana, A web scraping methodology for bypassing twitter API restrictions, *CoRR* abs/1803.09875 (2018). arXiv:1803.09875.
- [25] D. Freelon, Computational Research in the Post-API Age, *Political Communication* 35 (4) (2018) 665–668. doi:10.1080/10584609.2018.1477506.

Forecasting Student Achievement: Exploring Data Mining Techniques in Education

^{*1,2}Dr. Nedendla Satyavathi and ²Dr. Eppakayala Balakrishna

^{*1,2}Associate Professor, Head, Department of CSE, Vaagdevi College of Engineering, Warangal, Telangana, India.

Abstract

The capability to forecast the performance trends of the students holds great significance in the field of education. Predictive analytics, using various data-driven methods, can help educators and institutions identify struggling students early on, tailor teaching methods to individual learning styles, and implement targeted interventions to improve overall academic outcomes. The suggested Data Mining (DM) methods for predicting the final grades of students using their past data are a valuable and realistic approach in the field of education. DM is a powerful method that involves the discovery of patterns and relationships within large datasets, and it can be particularly beneficial in predicting student performance and understanding the factors that influence academic outcomes. The use of three eminent DM methods (Naive Bayes, Random Forest, and Decision Tree) in experimental studies on two educational data-sets can yield precious approaching into student performance and academic outcomes. This result indicates that data mining methods can be valuable tools for educators and educational institutions to gain deeper insights into student outcomes and make informed decisions to improve teaching and learning practices.

Keywords: DM, student performance forecast, and classification

1. Introduction

The increasing availability of online systems in education and the abundance of student digital data have opened up new possibilities for leveraging data mining techniques [14, 16] to draw rules and forecasts about student's academic performance and outcomes. The accumulation of educational and informative data on a large scale often referred to as big data, enables researchers and educators to get deeper views into various aspects of student education and success.

The study's main focus is to estimate the scholars' successes at the end of the year by utilizing scholar data from two Portuguese schools. The eventual objective of this paper is to create a prediction model that can forecast the students' final grades [12], with the intention of assisting educators in identifying and supporting children who may be at risk of academic challenges or underperforming.

To achieve accurate predictions, the researchers applied several data preprocessing processes. Data preprocessing [13] is an essential step in DM and machine learning (ML), as it helps clean, transform, and prepares the data for analysis. The data preprocessing steps likely aimed to get better the quality of the data and ensure that the predictive model is reliable and effective.

Common data preprocessing techniques that might have been applied in the study include:

Data Cleaning: The researchers likely removed any noisy or irrelevant data points, corrected errors, and handled missing values to ensure the dataset is of high quality.

Feature Selection: Feature selection engages choosing the most relevant features (variables) from the dataset that have the most significant impact on the final grades. This helps

reduce computational complexity and improve model performance.

Feature Scaling: Feature scaling is employed to normalize the data so that features with different scales do not affect the model disproportionately.

Data Transformation: The researchers might have applied data transformations such as normalization, logarithmic transformations, or categorical encoding to make the data more suitable for the chosen predictive model.

Data Splitting: The dataset is typically divided into training and testing sets to train the predictive model on one portion of the data and evaluate its performance on unseen data.

Model Selection: Various predictive models, such as decision trees, random forests, naive Bayes, or others, may have been evaluated to recognize the most appropriate model for forecasting the students' final grades.

Model Evaluation: The predictive model's accuracy and performance were likely assessed by measurements, including recall, precision, accuracy or F1-score to find out its efficiency in predicting student outcomes.

The application of these data preprocessing techniques can significantly enhance the accuracy of the predictive model, ensuring that the educators receive reliable insights into student performance. By identifying students at risk of underperforming early on, educators can take proactive measures [17] and interventions to provide the necessary support, ultimately leading to improved educational outcomes. Additionally, the study's findings may contribute to the broader field of educational research and inform the development of tailored strategies to address the specific needs of students in secondary education.

2. Related Work

Forecasting students' educational performance [6, 7, 8] is a crucial area of focus in educational data mining, and technological advancements have played a significant role in enabling more accurate and effective predictions. The rise of e-Learning platforms and the integration of multimedia technologies have transformed the landscape of education, offering various benefits to both educators and students. Technological advancements, including e-Learning platforms and multimedia technologies, have revolutionized education, and provided valuable data for educational data mining. Predicting academic performance using DM techniques is an important research area that can significantly contribute to improving educational outcomes [17] and supporting both educators and students in achieving their goals.

The rise of online course teachings and the increasing prevalence of online communications and collaborative activities in schools have resulted in a significant increase in digital data within the education field. Costa's work [3] in 2017 highlighted the importance of data related to student failure rates, which raised crucial questions and concerns among educators regarding failure prediction.

The increase in the volume of data in training databases presents challenges when estimating students' performances. However, various techniques [5, 1] can be employed to effectively handle and analyze this large volume of data. Descriptive statistical analysis is able to give essential Knowledge about the data, but more sophisticated methods are required to make meaningful predictions and early identifications of student performance.

The exponential growth of automated data from universities presents a pressing essential to extract significant information from these vast volumes of data. Traditional methods of data analysis may not be sufficient to handle such large datasets, making data mining techniques invaluable for obtaining valuable insights and improving the quality of education developments.

DM procedures and algorithms have been widely useful in numerous and learning fields, offering valuable insights and predictive capabilities [2, 4]. Researchers have discovered the potential of DM methods in different domains of education. These studies have targeted different levels of education, ranging from high school students to higher education institutions.

3. Methods

The increase in digitalization has led to an explosion of data in virtually every field, including education. While having access to vast amounts of data is valuable, it becomes even more meaningful when we know how to extract meaningful insights and information from it [18]. DM, as a subset of ML, aims to do precisely that. In the context of education, DM plays a crucial role in leveraging the available data to make informed predictions and decisions about future educational outcomes [10, 11]. By applying numerous machine learning techniques to educational data, DM allows us to establish relationships between different variables, identify patterns, and make accurate predictions.

i). Naive Bayes Classifiers (NBC): NBC is a type of probabilistic algorithms commonly used for classification tasks in machine learning [16]. They are based on Bayes' theorem, a basic idea in probability theory and calculates the probability of an event happening based on the occurrence of related events. The key principle behind

Naive Bayes classifiers is the assumption of conditional independence among the features used for classification.

ii). Decision Tree Algorithm (DTA): DTA is a well-liked ML algorithm that uses a tree-like graph structure to make decisions based on features or attributes of the data. Each node in the tree denotes an attribute or feature, and each branch denotes a decision or result, based on that feature [15]. Decision trees are widely used in various applications due to their simplicity, interpretability, and ability to model complex decision-making processes. They are particularly useful when the goal is to understand and explain the reasoning behind predictions, making them a valuable tool in this study's context.

iii). Random Forest (RF): RF is an aggregation learning technique, meaning it forms multiple models (decision trees) and merges their predictions to make a final prediction. This ensemble approach often results in more robust and accurate predictions compared to using a single model. It is a common and powerful ensemble learning algorithm that creates a collection of decision trees through randomization and bagging [14]. By combining the predictions of multiple decision trees, Random Forest achieves higher accuracy and stability, making it a valuable tool for various classification tasks in machine learning.

The work-flow of a DM model for classification in the context of educational data analysis is shown in Figure 1. The process involves several steps, including feature selection, classification model building, model evaluation, and prediction for new student data. The iterative nature of the workflow, with feedback from the evaluation phase, allows for continuous improvement of the model's performance and adaptability to changing data patterns. This data mining model can be a powerful tool for educational institutions seeking to enhance student outcomes and optimize educational processes.

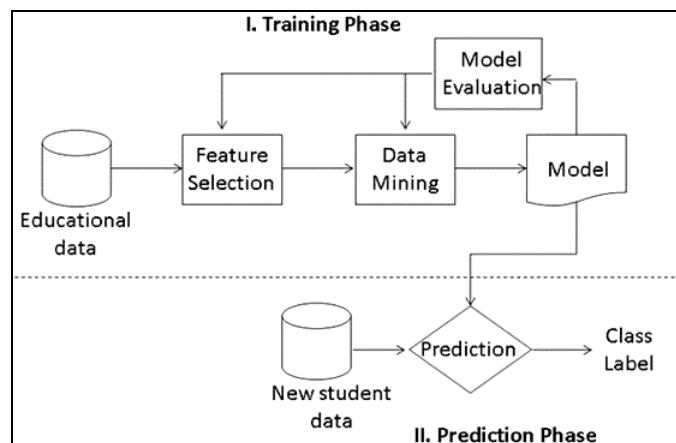


Fig 1: Structure of the DM model

4. Results and Experimental Analysis

To evaluate the performance of the classification models, we employed 10-fold cross-validation. Cross-validation is a re-sampling technique that helps assess how well the model will generalize to new, unseen data.

The Classification Accuracy (C.A) or correctness is a metric utilized to estimate the performance of a classification model. It measures or finds the percentage of properly classified instances out of the overall instances in the given data-set. The formula for Classification Accuracy (C.A) is:

$$C.A = \left[\frac{\text{No. of Correctly Classified Instances}}{\text{Total No. of Instances}} \right] \times 100$$

In this formula:

- "Number of Correctly Classified Instances" refers to the count of instances that were correctly predicted by the classification model. These are instances where the predicted class label matches the true class label.
- "Total Number of Instances" represents the total number of instances in the dataset, i.e., the sum of correctly classified instances and misclassified instances.
- The result is usually expressed as a percentage, indicating the proportion of correctly predicted instances over the entire dataset.

i). Data-Set Information

In this research, we utilized two publicly available datasets to forecast student performances. Both data-sets were gathered from two Portuguese minor education schools. The datasets comprise data concerning student grades and diverse demographic, social, and school-related characteristics.

By leveraging these datasets and conducting data mining and machine learning analyses, to gain insights into the factors influencing student performance and develop predictive models that can accurately predict academic outcomes for students in both Mathematics and Portuguese language lessons. Such insights can be valuable for educators and policymakers to tailor interventions and support strategies to improve student success and academic achievement in secondary education settings.

ii). Data Preprocessing Technique

The final grades of the students in the raw data-set, are represented as integer values in the range of 0 to 20, where 0 indicates the poorest grade and 20 represents the greatest score. However, for certain analysis and prediction tasks, it is often more convenient to work with categorical values rather than continuous numeric values. Therefore, they transformed the final grades into categorical values using two dissimilar grading schemes: five-level and binary grading.

Five-Level Grading System: In the five-level grading system, the continuous numeric values of the final grades (ranging from 0 to 20) were grouped into five distinct categories or levels. These levels may represent different performance levels, such as "Excellent," "Good," "Average," "Below Average," and "Poor." The specific grade ranges for each level were defined based on the grading policy.

Binary Grading System: In the binary grading system, the final grades were further simplified into two categories: "Pass" and "Fail." Students with final grades above a certain threshold (e.g., passing grade) were assigned to the "Pass" category, while those with grades below the threshold were categorized as "Fail."

Table 1: Five-level grading categories.

1	2	3	4	5
very good	Fine	Acceptable	Enough	Fail
16–20	14–15	12–13	10–11	0–9
A	B	C	D	F

iii). Experimental Results

Before classification and according to two dissimilar grading schemes, we have formed two versions of both the mathematics and Portuguese data-sets by categorizing the final grade attribute. This preprocessing step allows for a

comparison of the results obtained from these different versions, Offering valuable perspectives on how the grading system influences the effectiveness of the classification models.

The availability of two versions for each dataset (mathematics and Portuguese) with both binary and five-level grading systems presents an opportunity for a comparative analysis.

We compared the performance of mentioned algorithms for instance random forest, decision tree, and naive Bayes on both the grading versions of the Portuguese data-set.

The results of the experiment, as shown in Table 2, indicated the following:

Five-Level Grading Version: When using the five-level grading version of the Portuguese dataset (where the final grade was categorized into five performance levels), the best performance was achieved with the random forest algorithm. The accuracy rate for this version was reported as 75.35%.

Binary Grading Version: However, when the final grade of the Portuguese dataset was categorized into a binary form, representing "passing" or "failing," the accuracy rate significantly enhanced. For the binary grading version of the dataset, the random forest algorithm achieved an accuracy rate of 95.27%.

The comparison between the two grading versions revealed that the binary grading version led to a substantial improvement in the accuracy rate for the random forest algorithm. This suggests that the binary grading system may provide a more suitable and effective representation of the student performance for the prediction task.

The significant increase in accuracy with the binary grading version could be attributed to several factors such as Simplification of Classes, Class Imbalance, Generalization and Decision Boundary.

Table 2 shows the classification accuracy rates for the Portuguese lesson dataset using three classification algorithms. The accuracy values are provided for both the five-level grading version and the binary label dataset version.

Table 2: Accuracy rates of classification for the data-set containing Portuguese lesson data.

Name of the Algorithm	Five-Level Grading Accuracy	Binary Grading Accuracy
DTA	67.80%	91.37%
RF	75.35%	95.27%
NBC	68.26%	88.44%

Among the five-level grading version of the Portuguese lesson dataset, the Decision Tree algorithm (J48) yielded the highest accuracy rate of 75.35%. In the binary grading version of the Portuguese lesson data-set, the Random Forest ensemble method achieved the best accuracy rate of 95.27%.

Table 3: Accuracy rates of classification for the data-set containing mathematics lesson data.

Name of the Algorithm	Five-Level Grading Accuracy	Binary Grading Accuracy
DTA	73.42%	89.11%
RF	71.14%	91.39%
NB	70.38%	86.33%

In the five-level grading version of the Mathematics lesson dataset, the best accuracy rate of 73.42% was achieved using the Decision Tree algorithm (J48). In the binary grading

version of the Mathematics lesson dataset, the Random Forest ensemble method showed the best performance, with an accuracy rate of 91.39%.

Overall, the results indicate that the Random Forest algorithm performed remarkably well in both the Portuguese and Mathematics lesson datasets, especially in the binary grading versions, where it achieved the highest accuracy rates among the three algorithms. The Decision Tree Algorithm also demonstrated competitive performance, particularly in the five-level grading versions of both datasets.

These findings can help guide the selection of appropriate algorithms and grading systems for predicting student performances effectively in educational settings.

5. Conclusions and Recommendations for future work

This research suggests the DM methods to forecast the final grades of students using their past data. The main goal is to build predictive models that can accurately map student features to their final grades. To achieve this, we compared the performance of three famous classification techniques such as naive Bayes, random forest, and decision tree. The research findings could help educators and educational institutions get precious approaches into predicting student performance and identifying at-risk students. This research could contribute to the advancement of educational DM and provide important guidance for educators in utilizing predictive models to enhance the teaching and learning process.

In future research and applications of data mining for predicting student performance, there are several avenues for exploration and improvement, including feature selection methods, classification algorithms and deep learning. By exploring these directions and incorporating advanced techniques, future research in educational data mining can continue to advance our understanding of student performance and contribute to more effective and personalized educational interventions.

References

1. Fan Y, Liu Y, Chen H, Ma J. Data mining-based design and implementation of college physical education performance management and analysis system. *International Journal of Emerging Technologies in Learning*. 2019; 14(06):87-97
2. Guruler H, Istanbulu A. Modeling student performance in higher education using data mining. *Studies in Computational Intelligence*. 2014; 524:105-124
3. Costa EB, Fonseca B, Santana MA, de Araújo FF, Rego J. Evaluating the effectiveness of educational data mining techniques for early prediction of students' academic failure in introductory programming courses. *Computers in Human Behavior*. 2017; 73:247-256
4. Shahiri AM, Husain W. A review on predicting student's performance using data mining techniques. *Procedia Computer Science*. 2021;72:414-422
5. Fernandes E, Holanda M, Victorino M, Borges V, Carvalho R, Van Erven G. Educational data mining: Predictive analysis of academic performance of public school students in the capital of Brazil. *Journal of Business Research*. 2019; 94:335-343
6. Marbouti F, Diefes-Dux HA, Madhavan K. Models for early prediction of at-risk students in a course using standards-based grading. *Computers in Education*. 2016; 103:1-15
7. Miguéis VL, Freitas A, Garcia PJ, Silva A. Early segmentation of students according to their academic performance: A predictive modelling approach. *Decision Support Systems*. 2018; 115:36-51
8. Asif R, Merceron A, Ali SA, Haider NG. Analyzing undergraduate students' performance using educational data mining. *Computers in Education*. 2020; 113:177-194
9. E. Balakrishna, Dr. B. Rama, Dr. A. Nagaraju "Mining of Negative Association Rules using Improved Frequent Pattern Tree" published in IEEE Explorer proceedings of ICCCT-2014, Hyd Publisher: IEEE, INSPEC Accession Number: 15022153, DOI:10.1109/ICCCT.2.2014.7066748.
10. Buenano-Fernandez D, Villegas-CH W, Lujan-Mora S. The use of tools of data mining to decision making in engineering education-A systematic mapping study. *Computer Applications in Engineering Education*. 2019; 27(3):744-758
11. Zhu S. Research on data mining of education technical ability training for physical education students based on Apriori algorithm. *Cluster Computing*. 2019; 22(6):14811-14818
12. Lu M. Predicting college students English performance using education data mining. *Journal of Computational and Theoretical Nanoscience*. 2017; 14(1):225-229
13. Marquez-Vera C, Cano A, Romero C, Noaman AYM, Mousa FH, Ventura S. Early dropout prediction using data mining: A case study with high school students. *Expert Systems*. 2016; 33(1):107-124
14. Amjad Abu S, Al-Emran M, Shaalan K. Factors affecting students' performance in higher education: A systematic review of predictive data mining techniques. *Technology, Knowledge and Learning*. 2022; 24(4):567-598
15. Fujita H. Neural-fuzzy with representative sets for prediction of student performance. *Applied Intelligence*. 2021; 49(1):172-187
16. Satyavathi N, Dr. Rama B, Dr. Nagaraju A. "Present State-of-the-Art of Dynamic Association Rule Mining Algorithms", titled published in International Journal of Innovative Technology and Exploring Engineering (IJITEE), in Regular Issue, ISSN: 2278-3075(Online), 2019, 9(1).
17. Cortez P, Silva A. Using data mining to predict secondary school student performance. In: Brito A, Teixeira J, editors. *Proceedings of 5th Annual Future Business Technology Conference. EUROSIS-ETI*; 2018, 5-12
18. Rodrigues MW, Isotani S, Zárata LE. Educational Data Mining: A review of evaluation process in the e-learning. *Telematics and Informatics*. 2018; 35(6):1701-1717.

EXTRACTION OF FUEL FROM WASTE PLASTIC BY PYROLYSIS PROCESS WITH ZEOLITE CATALYST

Kedala Pranay¹ Dr. Sanjeev Kumar Sanjjan² Dr. Srinivasulu Pulluru³

¹M.Tech (Thermal Engineering)Department of mechanical engineering vaagdevi college of engineering (UGC autonomous) approved by AICTE & permanent affiliation to jntuh, hyderabad.p.o, bollikunta, Warangal urban- 506005.

² Assistant professor Department of mechanical engineering vaagdevi college of engineering (UGC autonomous) approved by AICTE & permanent affiliation to jntuh, Hyderabad. p.o, bollikunta, Warangal urban- 506005.

³Professor and Head of the Department of mechanical engineering vaagdevi college of engineering (UGC autonomous) approved by AICTE & permanent affiliation to jntuh, hyderabad. p.o, bollikunta, Warangal urban- 506005.

Abstract

The present rate of economic growth is unsustainable without saving of fossil energy like crude oil, natural gas, or coal. There are many alternatives to fossil energy such as biomass, hydropower, and wind energy. Also, suitable waste management strategy is another important aspect. Development and modernization have brought about a huge increase in the production of all kinds of commodities, which indirectly generate waste. Plastics have been one of the materials because of their wide range of applications due to versatility and relatively low cost.

Some 299 million tons of plastics were produced in 2013, representing a 4 percent increase over 2012. Recovery and recycling, however, remain insufficient, and millions of tons of plastics end up in landfills and oceans each year. Approximately 10 to 20 million tons of plastic end up in the oceans each year. A recent study conservatively estimated that 5.25 trillion plastic particles weighing a total of 268,940 tons are currently floating in the world's oceans. And since plastic being a non-biodegradable material it remains into the soil, thereby polluting the environment.

Our Project deals with the extraction of OIL/DIESEL from the waste plastics termed as PLASTIC PYROLYZED OIL which can be marketed at much cheaper rates compared to that present in the market. As we know that both Plastics and Petroleum derived fuels are Hydrocarbons that contain the elements of Carbon & Hydrogen. Pyrolysis process becomes an option of waste-to-energy technology to deliver bio-fuel to replace fossil fuel. The advantage of the pyrolysis process is its ability to handle unsorted and dirty plastic. The pre treatment of the material is easy. Plastic is needed to be sorted and dried. Pyrolysis is also non toxic or non environmental harmful emission unlike incineration.

1. INTRODUCTION

Plastic plays a vital role in enhancing the standard lives of human being for more than 50 years. It is a key of innovation of many products in various sectors such as construction, healthcare, electronic, automotive,

packaging and others. The demand of commodity plastics has been increased due to the rapid growth of the world population. The global production of plastic has reached about 299 million tons in 2013 and has increased by 4% over 2012. The continuous rising of plastic demand led to the growing in waste accumulation every year. It was reported that 33 million tons of plastic waste are generated in the US based on 2013 statistic. As in Europe, 25 million tons of plastic ended up in waste stream during the year of 2012. Based on the statistic established in Europe, about 38% of the plastic waste still went to the landfill, 26% were recycled while 36% were utilized for energy recovery. The continuous disposal of plastic in the landfill would definitely cause serious environmental problem.

Although plastic recycling able to reduce some amount of plastic waste, the more reliable and sustainable method has been established. Since high demand of plastics have been received each year, the reduction of fossil fuel such as coal, gas and especially petroleum that made up plastic itself has gained great interest of many researchers to discover and develop potential energy resources due to the rising in energy demand. Some of the new energy resources that have been explored include solar energy, wind power, geothermal and hydropower technology. Recently, the energy conversion from waste has been an intelligent way to fully utilize the waste to meet the increased energy demand. The conversion of plastics to valuable energy is possible as they are derived from petrochemical source, essentially having high calorific value. Hence, pyrolysis is one of the routes to waste minimization that has been gaining interest recently.

pyrolysis:-

- Pyrolysis is a process of chemically decomposing organic materials at elevated temperatures in the absence of oxygen. The process typically occurs at temperatures above 430°C (800°F) and under pressure. It simultaneously involves the change of physical phase and chemical composition and is an irreversible process.

- Pyrolysis process becomes an option of waste to energy technology to deliver nibio-fuel to replace fossil fuel. The advantages of this process is its ability to handle unsort and dirty plastic. Plastic is needed to be sorted and dried.
- The whole process is done in a reactor or a vessel fabricated with the help of a catalyst for its sole purpose.



Fig 1: Pyrolysis

Pyrolysis of plastic waste: -

- The pyrolysis of plastic starts with collection of plastic waste from surroundings and feeding them in to the vessel.
- Continued by closing the vessel cap air tight followed by switching on the heating coils which is used to heat the vessel.
- After constant heating the vessel at about 430°C the heat and pressure developed inside vessel melts the plastic forming vapour.
- The vapour from the vessel is to be collected or discharged directly into the water to condense it to oil form.
- The condensed oil is to be collected and by purification process, the oil can be used along with diesel as a blend fuel for diesel engines.

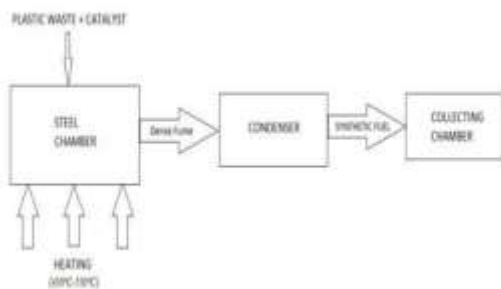


Fig 2: Pyrolysis of plastic waste

2. LITERATURE REVIEW

Chanashetty and Patil [1] have investigated fuel from waste plastic; they used condenser and reactor for pyrolysis process. They found this method is suitable for large plastic waste problems and helping fuel storage by means of products as diesel, kerosene, and lubricant oil. In this investigation, they used the waste plastic as rigid film, sheet plastic, and expanded foam materials.

Karad and Havalammanavar [2] investigated waste plastic to fuel, petrol, diesel, and kerosene by pyrolysis method on the temperature range 350–500 °C and waste plastic bags, food wrap, vegetable oil bottles, automotive parts garments bags, some carpets refrigerated containers, and they concluded that it saves 1000000 species of oceanic life and green future. Due to eco-friendly, it is involved in Swachh

Arunkumar and Nataraj [3] explored change of waste plastic into fuel oil within the sight of bentonite as an impetus and utilized materials condenser, reactor strategy is pyrolysis. It gives us outputs that are petrol, diesel, and fuel oil and inputs are PET bottles, shopping bags, plastic packages. They concluded that it provides perfect and green future and fuel efficiency, control of nitrogen, halogen, sulfur which is hazardous for human beings.

Mathur et al. [4] investigated extraction of pyrolysis fuel from Plastic Waste: A Review 849 oil from waste plastic where pyrolysis process is using, and the waste plastic inlet is all the types of plastic and outputs are waste oil and diesel fuel. It concludes that the process is carried out grade 5 types of plastic materials, 1.65 l of oil is obtained by using 1.5 kg of plastic.

Verma et al. [5] examined engine fuel creation from waste plastic pyrolysis and execution advancement in a CI Motor with diesel mix. Inputs are every one of the sorts of waste plastic and yield plastic pyrolysis oil by utilizing

pyrolysis technique. The materials are used: condenser, oil collector, furnace reactor, load controller, gas analyzer, fuel meter, dynamometer, and computer. The conclusion is plastic oil saves 40% blended with diesel without loss of power reduction in exhaust emission.

Bezergini et al. [6] investigated alternate diesel from waste plastic by use of

pyrolysis plant. The products are diesel fuel, heavy oils, naphtha, kerosene and inlets are bags, bottles, and liquid containers. They got the conclusion from investigation nearly 70–85% less production cost, and this method is promising alternate diesel fuel.

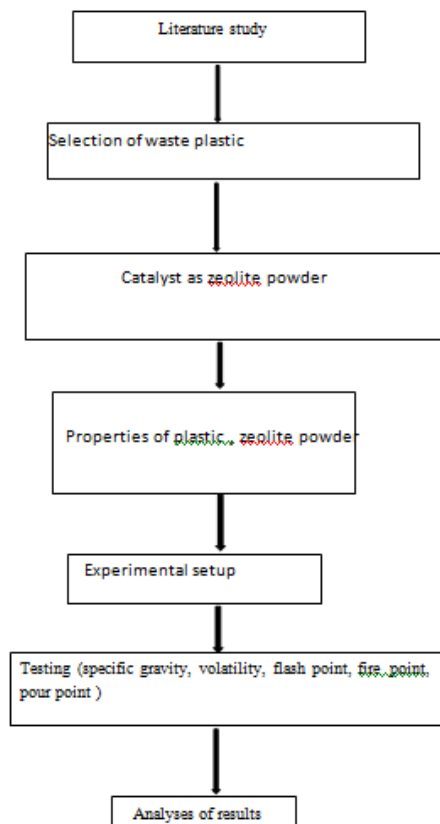
Mustafa Kamal and Zainuri [7] researched green result of fluid fuel from plastic waste by pyrolysis at 900 °C, where yields are fluid fuel and bays are

delicate destroyed plastic, drain bottles, cleanser parcels, water funnels receptacles They concluded that in 900 °C of pyrolysis providing more calorific value of the fuel compare to 425 °C, boric acid and cyclopentanone is reduced at 900 °C.

2.1 PROBLEMS STATEMENT

Based on the above discussions it is noted that there are few reports available on the Extraction Of Fuel From Waste Plastic By Pyrolysis Process. This motivating me to conduct detailed study about the effect of waste plastic to produce a fuel by using the zeolite powder. The relevance of the present study is to improve the performance of blended biodiesel mixture in automobiles. The present work deals with the addition of prepared waste plastic and polymer to extract the fuel by adding the zeolite powder as catalyst. The performance and combustion characteristics such as flash point, fire point, viscosity of the prepared fuel.

3. METHODOLOGY



Objectives: -

The main objectives of this project are:

- To establish the basis for the development and implementation of waste plastics recycling with the application of environmentally sound technologies to promote resource conservation and greenhouse gases.
- To raise awareness in developing countries like INDIA on plastic waste and its possible reuse for conversion into diesel or fuel, this could be generated and marketed at cheaper rates compared to that of the available diesel or oil in the market.
- To reduce the dependency on gulf countries for fossil fuels, thereby contributing to the Economic growth of the country.

Characteristics of pyrolytic oil: -

Before looking at the process options for the conversion of plastic into oil products, it is worth considering the characteristics of these two materials, to identify where similarities exist, and the basic methods of conversion. The principal similarities are that they are made mostly of carbon and hydrogen, and that they are made of molecules that are formed in chains of carbon atoms.

Plastic is a generic term for a wide range of polymers produced using highly refined fractions of crude oil, or chemicals derived from crude oil, known as monomers. Polymers are formed by the reaction of these monomers, which results in chain lengths of tens or hundreds of thousands of carbon atoms. Some polymers also contain oxygen polyethylene terephthalate, whereas others contain chlorine polyvinyl chloride. It is worth noting that only a small proportion of the crude oil processed in the world is used to produce the monomers e.g. ethane, propene, used in the manufacture of polymers e.g. polyethene, polypropylene. The similarity between oil products and plastics are explained.

Process parameters condition: -

Parameters play major role in optimizing the product yield and composition in any processes.

In plastic pyrolysis, the key process parameters may influence the production of final end products such as liquid oil, gaseous and char. Those important parameters may be summarized as temperature, type of reactors, pressure, residence time, catalysts, type of fluidizing gas and its rate. The desired product can be achieved by controlling the parameters at different settings. In-depth discussions of the operating parameters are reviewed in the following subsections.

4. EXPERIMENTAL SETUP

Basic instruments used are

- Pyrolysis chamber

- Temperature controller
- Condenser
- Temperature sensor
- Heating coil
- Insulator
- Storage tank
- Valve
- Gas exit line



Fig : Experimental set up

REACTOR

Type of reactor used: -

The batch or semi-batch reactors are the best reactors to be used in thermal pyrolysis to obtain high liquid yield since the parameters can be easily controlled. However, these reactors were not suggested for catalytic pyrolysis in consideration of the potential coke formation on the catalyst outer surface that would disturb the overall product yield. In addition, batch operation was not suitable for large scale production since it required high operating cost for feedstock recharging and thus, it was more appropriate for laboratory experiment.



Fig 4: Reactor

Information about Catalyst

The aim of this study was to determine the quality and applications of liquid oil produced by thermal and catalytic pyrolysis of polystyrene (PS) plastic waste by using a small pilot scale pyrolysis reactor. Thermal pyrolysis produced maximum liquid oil (80.8%) with gases (13%) and char (6.2%), while catalytic pyrolysis using synthetic and natural zeolite decreased the liquid oil yield (52%) with an increase in gases (17.7%) and char (30.1%) production. The lower yield but improved quality of liquid oil through catalytic pyrolysis are due to catalytic features of zeolites such as microporous structure and high BET surface area. The liquid oils,

Both from thermal and catalytic pyrolysis consist of around 99% aromatic hydrocarbons, as further confirmed by GC-MS results. FT-IR analysis further showed chemical bonding and functional groups of mostly aromatic hydrocarbons, which is consistent with GC-MS results. The produced liquid oils can be suitable for energy generation and heating purposes after the removal of acid, solid residues and contaminants. Further upgrading of liquid oil and blending with diesel is required for its potential use as a transport fuel.

Zeolite: -

The lower yield but improved quality of liquid oil through catalyst pyrolysis are due to catalytic features of zeolites such as Microporous structure and high BET surface area. The liquid oils, both from thermal and catalytic pyrolysis consist of around 99% aromatic hydro carbons, as further confirmed by GC-MS results.



Fig : Zeolite Powder



Fig: Catalyst used Zeolite
Equipment:

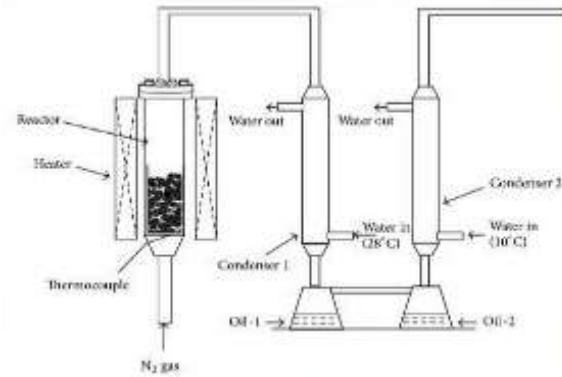


Fig 4.3: Schematic Diagram



Assembly of Pyrolysis Setup: -

Assembly of the setup follows the fabrication and testing of the components required for the process. The stand is placed where the setup is to be installed so as to conduct the experiment. The experiment is performed outdoors for safety. The frame is carefully placed on the stand. The next step involves carefully installing the furnace and the insulation bricks. Then carefully place the furnace in the centre. The wires of the electric furnace are sealed in insulating material. Bricks are placed in the rest of the space surrounding the furnace. This ensures minimum heat loss from the furnace in all directions except the top. The frame lid is then used to cover the furnace inside the frame. The lid prevents heat loss. The penultimate step is inserting the heating chamber through the lid into the furnace. The final step of the assembly is placing the helical coil heat exchanger assembly on the stand. Final setup For performance of the experiment, the material selected is first added to the heating chamber. The next step is placing the heat sealing gasket between the flanges and fastening the flanges using nut bolting. The fasteners are tightened so that the gasket properly seals the flanges. No air leakage is tolerated as this may result into combustion of the polymers being used. The empty water tank is filled with water before starting the test. The water is filled so that the major part of the coil is immersed under water. This helps to increase the effectiveness in heat exchange. After final inspection the electric supply to the furnace is switched on and the experiment begins. A stopwatch is used so as to keep a track of observations with respect to time. After switching on the apparatus, approximately 15 minutes later it is observed that furnace starts heating considerably. This can be said as the hot fumes are seen rising up from the little gaps in the frame and the heating chamber. Approximately 40 minutes after the start it is observed that milky fumes are obtained from the outlet. Also the heat sealing gasket is seen to

emit some fumes as it heats up. However these observations last for a few minutes until the entire setup attains high temperature 400°C . Using 1.5 kg of plastic in the experimentation 85 minutes after the start of the experiment it is observed that drops of oil start falling from the outlet. A funnel and a flask for oil collection are placed below the outlet.



Fig : Final set of the experiment

Fabrication and Analysis of Extracted Oil: -

Once the raw fuel is obtained it is further subjected to distillation process so as to obtain the fuel i.e., diesel in its pure form by removing the impurities present in it which can be then tested into diesel engines for its efficiency.



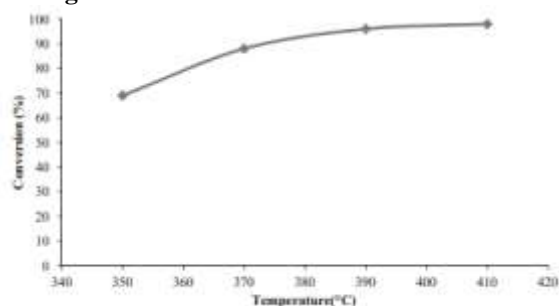
Fig : Burning of fuel (fire)



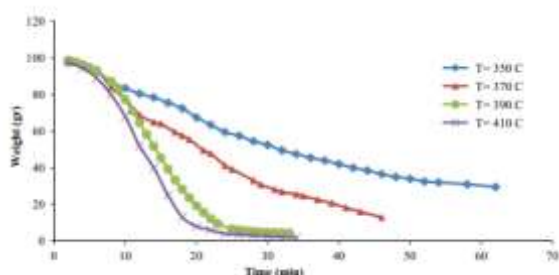
Fig : Test of Fuel Characteristic
After Producing Fuel: -

- The oil produced is to be tested for
- Dynamic viscosity by Redwood viscometer
- Flash point by pensky martins closed cup apparatus
- Fire point by pensky martins closed cup apparatus
- Calorific value by Bomb Calorimeter.

Testing of Zeolite: -



Graph : Effect of temperature on catalytic degradation of polystyrene

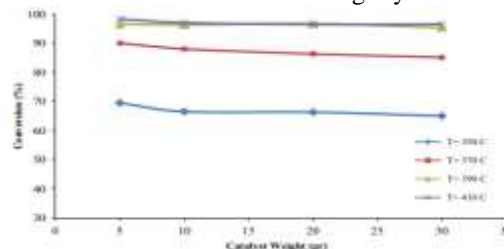


Graph: Polystyrene Weight loss in Different temperatures

Effect of temperature on product yield: -

The gases, liquids, and residues on the catalyst from the degradation experiment. The amounts of gaseous products were calculated by subtracting the sum of weights for liquids and residues, from the total weight of Polystyrene sample and fresh catalyst that was initially loaded to the reactor. Carbonaceous compounds adhering to the reactor body were dissolved in n-hexane and were measured as degradation residues. In all cases, the liquid oils were main products. From Table 6, it can be figured out that the amount of liquid products increase with temperature increase, while the residues decrease within the same condition. In low temperatures, the amount of catalyst residues was high (31 and 18 wt% in 350 and 370 C,). However, these amounts are very small at higher temperatures. This indicates that the

competitive cross-linking reactions take place first, especially in low temperatures; therefore, cracking of the resulting cross-linked polymer becomes more difficult. Even though the amount of liquid products is small in low temperatures, aromatics are the main liquid products. With the increase of temperature, the amount of aromatics increases slightly.



Graph: Influence of catalyst on polystyrene

Temperature (°C)	Contents of products (wt%)		
	Gases	Liquids	Residues
350	3.5	65	31.5
370	2.4	78.8	18.8
390	1.4	95.7	2.9
410	1	97.3	1.7

Table : Product Yield from the catalytic pyrolysis of polystyrene

RESULTS

Throughout experiment we find the all-values flash point, fire point, four-point, kinematic viscosity, specific gravity, volatility, gross heating value

SI NO	SUBJECT	Zeolite as catalyst liquid & fuel
1	Flash point	40
2	Fire point	50
3	Pour point	-12
4	Kinematic viscosity	1.167
5	Specific gravity	0.7673
6	Gross heating value	41.86

2Advantages: -

- Recycle energy of waste plastics into usable fuel
- Crude oil & gas is used for generation of electricity
- Environment pollution is controlled

Limitations: -

1. High Carbon monoxide emissions compared to that of currently available diesel in the market.
2. High emissions at lesser loads compared to that of higher load working engines.
3. For efficient use of diesel grade fuel of waste plastic, blending it with normal diesel is necessary.

Application of Project & Future Work: -

- The obtained fuel could be utilized in diesel generators, vehicles such as tractors and also passenger vehicles such as cars.
- The fuel has to be refined at the industrial establishments, based on the results of which small scale industry can be established.
- As there is a high demand of crude oil and due to its sky reaching prices, we could take up this project to setup large or small scale industries and produce the fuel locally at much cheaper rates directly benefiting the National economy and also a step towards swachh Bharat by recycling the waste plastic.
- The application of this project could help in reducing the dependency on the gulf countries and promote a step towards innovation

CONCLUSION

It is very difficult to find out alternative of plastic. Even plastic's demand is increasing every day as well as their waste. This project analysis has observed the use of waste plastics, a factory planning and its feasibility in Metropolitan City. It is easily assumed that, when the use of waste plastic will increase then the solid waste management will search more ways to find out to collect them. The implementation of this project can develop so many opportunities in the city. It can be a solution to control waste plastic, develop a new technique or idea, and detect the source of diesel for the country. India is such a country where this kind of project could be very promising and effective in the future.

The use of plastic pyrolysis oil in diesel engine in the aspect of technical and economical is compared and found that oil is able to replace the diesel oil. Though the plastic pyrolysis oil offers lower engine performance, the plastic waste amount is enormous and it needed to be process to reduce the environmental problems. Moreover, the engine can be modify follow the combustion condition of plastic pyrolysis oil. The waste plastic used in the process must be PE or PP or LDPE in order to protect the contamination of chlorine in the oil.

- Thus thermal pyrolysis of mixed plastics leads to the production of fuel oil which is valuable resource energy
- It also reduce the problem of disposal of waste plastics pollution.

References

1. Elliott, D.C., Sealock, L.J. and Burner, R.S. (1988) Product analysis from direct liquefaction of several high-moisture biomass feedstocks, *Pyrolysis Oils from Biomass — Producing, Analyzing, and Upgrading*, (eds. Soltes, E.J., Milne, T.A.), ACS, Washington, pp. 179–188.
2. Fagernäs, L. (1995) Chemical and physical characterization of biomass-based pyrolysis oils — Literature review. VTT Research Notes, Vol. 1706.
3. McKinley J. (1989), Biomass Liquefaction Centralized Analysis, prepared for Science Branch, Science Procurement Department of Supply and Services, Hull, Quebec, DSS file No. 23216–4–6192, Final report, Project No 4–03–837.
4. *Pyrolysis Liquids Upgrading and Utilisation*, (eds. A.V. Bridgwater, and G. Grassi), Elsevier Applied Science, p 177–218, 1991
5. *Bio-oil Production and Utilisation-Proceedings of the 2nd EU-Canada workshop on Thermal Biomass Processing*, (eds. A.V. Bridgwater, and E.N. Hogan), CPL Press, Newbury, 1996.
6. *Proceedings Biomass Pyrolysis Oil Properties and Combustion Meeting*, (ed. Milne, T.A.), US DoE, 1994, available from NTIS.
7. Diebold, J.P. et al. (1996) Specifications of fast pyrolysis liquids for use as a fuel, paper to be presented to this conference.
8. Rick, F. and Vix, U. (1991) Product Standards for Pyrolysis Liquids for use as fuel in industrial firing plants, *Pyrolysis Liquids Upgrading and Utilisation* (eds. Bridgwater, A.V. and Grassi, G.), Elsevier Applied Science, pp. 177–218.
9. Garrett, D.E. and Mallan, G.M., *Pyrolysis Process for Solid Wastes*, US Patent no 4153514, approved 8 May 1979.
10. Oasmaa, A., Leppämki, E., Koponen, P., Levander, J., Tapola, E. (1996) Physical characterization of biomass-based pyrolysis oils. Application of standardised fuel oil analyses for pyrolysis oils, to be published in VTT Research Notes.

360-DEGREE ROTATING CONVEYOR BELT WITH TILT UP & DOWN MECHANISM

Banoth Suresh¹ Chinnala Venkatesh² Paripalli Navaraj³ Macharla Sai Krishna⁴
Pangunuri Akshay Kumar⁵ P.Raju⁶

^{1,2,3,4, and 5} B.Tech Department of Mechanical Engineering, vaagdevi college of engineering (UGC autonomous) approved by AICTE & permanent affiliation to jntuh, hyderabad. p.o, bollikunta, Warangal urban- 506005

⁶ Assistant professor department of Mechanical Engineering, vaagdevi college of engineering (UGC autonomous) approved by AICTE & permanent affiliation to jntuh, hyderabad. p.o, bollikunta, Warangal urban- 506005.

Abstract:

Bulk material transportation requirements have continued to stress the belt conveyor industry to carry higher tonnages, larger distances and more diverse routes. In order to keep up these criteria significant technology advances have been incorporated in the field of the belt conveyor design, analysis and numerical simulation. The application of traditional components in nontraditional applications requiring horizontal curves and intermediate drives have changed and expanded belt conveyor possibilities. Examples of complex conveying applications along with the numerical tools required to insure reliability and availability will be reviewed. This work indicates the new developments in belt conveyor technology. The present work deals with the new trend in the field of belt conveyor system. A 360 degree rotating belt conveyor system has been designed for prototype operation and the details of the design, fabrication, modeling and economics of the rotating belt conveyor system is presented in this work.

INTRODUCTION

A conveyor system is a part of mechanical handling equipment that moves materials from one location to another. Conveyors are especially useful in applications involving the transportation of heavy or bulky materials. Conveyor systems allow quick and efficient transportation for a wide variety of materials, which make them very popular in the material handling and packaging Material handling is an important sector of industry, which is consuming a considerable proportion of the total power supply. Belt conveyors are being employed to form the most important parts of material

handling systems because of their high efficiency of transportation. It is significant to reduce the energy consumption or energy cost of material handling sector. This task mainly depends on the improvement of the energy efficiency of belt conveyors. Now in industries only fixed type belt conveyors are available. But a prototype model of a 3600 rotating belt conveyor belt with updown mechanism is designed.

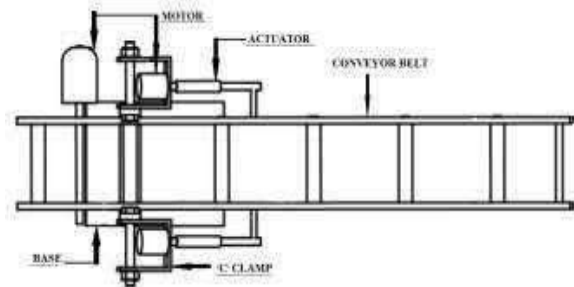
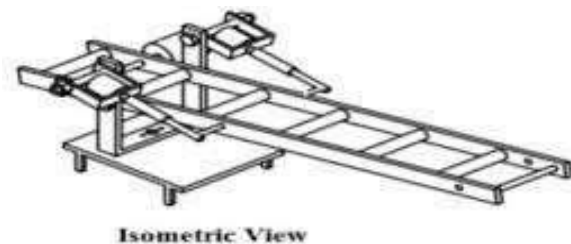


Fig 1.1 : Line diagram of conveyor



Throughout the world bulk materials handling operations perform a key function in a great number

and variety of industries. While the nature of the handling tasks and scale of operations vary from one floor to another and, on the international scene, from one country to another according to the industrial and economic base, the relative costs of storing and transporting bulk materials are, in the majority of cases, quite significant. It is important, therefore, that handling systems be designed and operated with a view to achieving maximum efficiency and reliability. Bulk material transportation requirements have continued to press the belt conveyor industry to carry higher tonnages some distances and more diverse routes. In order to keep up, significant technology advances have been required in the field of system design, analysis and numerical simulation.

The application of traditional components in non-traditional applications requiring horizontal curves and intermediate drives have changed and expanded belt conveyor possibilities. Example of complex conveying applications along with numerical tools require insuring reliability and availability will be reviewed. The system design tools and methods used to put components together into unique conveyance system designed to solve ever expanding bulk material handling needs. In industry for material handling many fixed conveyor belt is required. So, the installation and maintenance charge of fixed conveyor belt is increased for solution of this problem. New creation is 360 degree rotating flexible conveyor belt.

1.1OBJECTIVE: Now in industries only fixed type belt conveyor is available. But we will make the conveyor belt such that it can be rotate 360° and up-down mechanism with proto type model.

1.2PROBLEM STATEMENT: Now a days generally in industry Fix type belt conveyor system is available. But we will Make the conveyor belt such that it can be rotate 360 degree & Up-Down Mechanism with prototype model. The system is designed and develop the system for safely store or insert the material in appropriate compartment.

2. LITERATURE REVIEW

Conveyors are durable and reliable components used in automated distribution and warehousing, as well as manufacturing and production

facilities. In combination with computer-controlled pallet handling equipment this allows for more efficient retail, wholesale, and manufacturing distribution. It is considered a labor saving system that allows large volumes to move rapidly through a process, allowing companies to ship or receive higher volumes with smaller storage space and with less labor expense.

Rubber conveyor belts are commonly used to convey items with irregular bottom surfaces, small items that would fall in between rollers (e.g. a sushi conveyor bar), or bags of Product that would sag between rollers. Belt conveyors are generally fairly similar in construction consisting of a metal frame with rollers at either end of a flat metal bed. The belt is looped around each of the rollers and when one of the rollers is powered (by an electrical motor) the belting slides across the solid metal frame bed, moving the product. In heavy use applications the beds which the belting is pulled over are replaced with rollers. The rollers allow weight to be conveyed as they reduce the amount of friction generated from the heavier loading on the belting.

Belt conveyors can now be manufactured with curved sections which use tapered rollers and curved belting to convey products around a corner. These conveyor systems are commonly used in postal sorting offices and airport baggage handling systems. A sandwich belt conveyor uses two conveyor belts, face-to-face, to firmly contain the item being carried, making steep incline and even vertical-lift runs achievable.

Belt conveyors are the most commonly used powered conveyors because they are the most versatile and the least expensive.[citation needed] Product is conveyed directly on the belt so both regular and irregular shaped objects, large or small, light and heavy, can be transported successfully. These conveyors should use only the highest quality premium belting products, which reduces belt stretch and results in less maintenance for tension adjustments. Belt conveyors can be used to transport product in a straight line or through

changes in elevation or direction. In certain applications they can also be used for static accumulation or cartons.

Material Handling involves the movement of materials from one place to another for the purpose of processing or storing. According to American Material Handling society, 'Material Handling is an art and science of involving the movement, packing and storing of subsystems in any form. Thus material handling function includes all types of movements vertical, horizontal or combination of both and of all types of material fluid, semi fluid and discrete items and of movements required for packing and storing. The material handling function is considered as one of the most important activities of the production function as out of total time spent by the materials inside the plant area, about 20% of the time is utilized for actual processing on them while remaining 80 % of the time is spent in moving from one place to another, waiting for processing or finding place in sub-stores. Moreover about 20 % of the total production cost is traceable as material handling cost

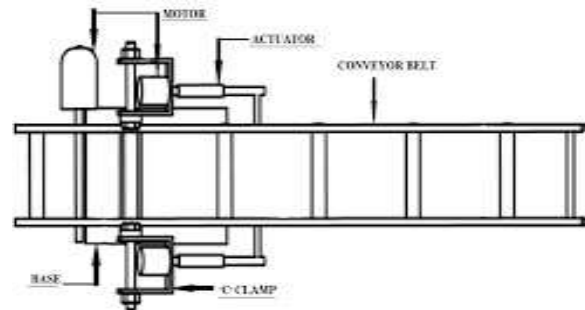
PROJECT BACKGROUND:-

- One motor is connected with the shaft of the belt which will rotate the conveyor belt.
- Two motors and two actuator will be use for making the up-down mechanism.
- Two motor are connected with those actuator and when the motor will rotate the actuator will move in the up-down position.
- One another motor is provided in the bottom of the base and the shaft will be connect to the clamp which is connected with that motor shaft with the help of brass coupling.
- So with the help of this we can rotate the conveyor belt at 360°.
- So with the help of this 360° rotated conveyor belt the material handling can be done easily at desired place

3.WORKING

One motor is connected with the shaft of the belt which will rotate the conveyor belt. Two motors and two actuators will be used for making the up-down mechanism. Two motor are connected with those actuators and when the motor will rotate the actuator will move in the up-down

position. One another motor is provided in the bottom of the base and the shaft will be connecting to the clamp which is connected with that motor shaft with the help of brass coupling. So, with the help of this we can rotate the conveyor belt at 360°.So with the help of this 360°rotated conveyor belt the material handling can be done easily at desired place.



DESIGN CONSIDERATIONS:

According to the design of an effective and efficient material handling system which will increase productivity and minimize cost, the guidelines normally followed are: 1)Designing the system for continuous flow of material (idle time should be zero)

2)Going in for standard equipment which ensures low investment and flexibility

3)Incorporating gravity flow in material flow System

4)Ensuring that the ratio of the dead weight to the payload of material handling equipment is minimum

WORKING OF CONVEYOR THROUGH IOT MOBILE CONTROL:

Robo can be control from any where with IOT , we can give the commands through mobile android app this command send to the cloud , after that data in the cloud updated to the hardware microcontroller unit.

When ever the controller receive the data from the cloud it executes the robotic operations like forward backward,lefr right and stop.

Design Calculations:-

Weight carrying Capacity: Capacity is the product of speed and belt cross sectional area.

Generally, belt capacity B.C (kg/sec) is given as:

$$BC = 3.6A V \rho$$

Where,

A= belt sectional area (m²) ρ = material density (kg/m³) V= belt speed (m/s)
Area of Belt

$$A = \text{Length} \times \text{Width} A \\ = 815 \times 100 \\ A = 81500 \text{ mm}^2$$

$$A = 0.081500 \text{ m}^2. \quad 1.2 \\ \text{Belt Speed:}$$

$$V = 0.01745 \text{ m/sec.}$$

1.3 Density of Material:

P = Density of material Material used for Belt is flexible Plastic. Density of plastic is 0.15 x 10³ kg/m³. (Considered)

$$C = 3.6 \times A \times V \times \rho$$

$$B.C = 3.6 \times 0.081500 \text{ m}^2 \times 0.01745 \text{ m/sec} \times 0.15 \times 10^3$$

$$B.C = 0.767 \text{ Kg/sec.}$$

3.2 Diameter of Roller (Drive Pulley): The roller support belt and facilitates easy as well as free rotation of the belt conveyor in all direction. The correct choice of roller diameter must take into consideration the belt width. The relationship between the maximum belt speed, roller diameter and the relative revolution per minute is give as

Where,

N = RPM of Belt

V = Speed of Belt D = Dia. Of Roller

$$D = 33.32 \text{ mm} \quad D = 34 \text{ mm.}$$

Power at Drive Pulley:-

Where,

T = Torque of Drive motor

$$T = 2 \text{ kg.m}$$

$$T = 19.61 \text{ N.m}$$

$$P_p = 20 \text{ Watt.} \quad P_p = 0.02 \text{ Kw}$$

Belt Tension at Steady State:-

$$T_{ss} = 1.37 \times F \times L \times g (2 \times M_i + (2 \times M_b + M_m) \times \cos\theta) + H \times g \times M_m \text{ Where,}$$

T_{ss} = Belt tension at steady state (N).

F = Coefficient of friction (0.02).

L = Conveyor length (m). (Conveyor belt is approximately half of the total belt length). = 832mm = 0.832m.

g = Acceleration due to gravity (9.81 m/sec²).

M_i = Load due to the idlers (Considering no load).

M_b = Load due to belt (0.18304 kg).

M_m = Load due to conveyed materials (Considering no load). θ = Inclination angle of the conveyor.

H = Vertical height of the conveyor.

EXPERIMENTAL PHOTOS



Fig : base connected with motor



Fig : Actuator



R.P.M Motor In The Bottom Of Base



Fig : ROLLER



IOT PROGRAM CONTROL CHIP

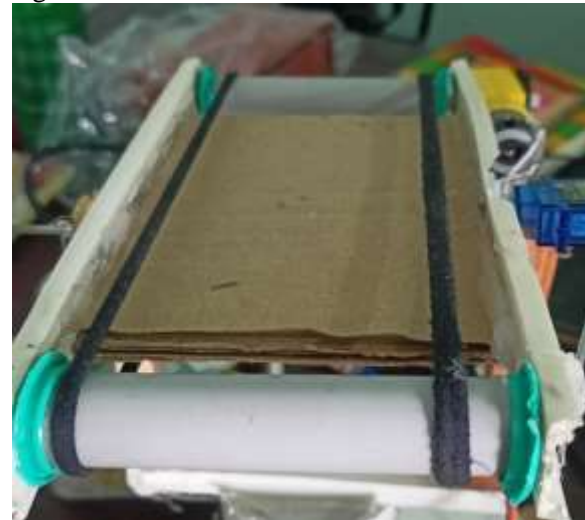


Fig : CONVEYOR BELT



Fig : FINAL PRODUCT

CONCLUSION

Considering the practical working conditions of the respective warehouse, we have reached a conclusion that it needs a directional conveyor system to regulate the workload at the place. It will help reducing the workload, human labour, mishandling, damage and injuries while loading and unloading of goods from the carrier vehicles to the desired stacking place and increase the efficiency of workplace. The design has comparatively more portability and utility for versatile tasks. Overall, the above deigned system would help out to solve the problem faced at the workplace to the maximum extent. So in all matter it is the better than fixed conveyor belt.

- Low manufacturing cost of the equipment.
- Easy to handle.
- Less weight.
- Compact in size.

- Cost of checking the error is less.

- All kinds of material can be handled.

- Even a lay man can work in it.

REFERENCES

1. "Recent Research Developments In Beltconveyor Technology"
2. Sunderesh S. Heragu And Banuekren "Materials Handling System Design"
3. Aniket.A. Jagtap Et Al [3] "Design Of Material Handling Equipment: Belt Conveyor System For Crushed Biomass Wood Using V Merge Conveying System" Ijmerr Vol. 4, No. 2, April 2015 Issn 2278 – 0149
4. Michael G. Kay [4] "Material Handling Equipment"
5. "ABB-Process Industries Variable-Speed Drives for Belt Conveyor Systems", pp. 1-7, (2000).
6. Anath K N and Rakesh V (2013), "Design and Selecting Proper Conveyor Belt", Int. Journal of Advanced Technology, Vol. 4, No. 2, pp. 43-49.
7. Besser Service Bulletin (2006), "Conveyor Belt Basic Rules and Procedure for Tracking", pp. 1-7.
8. . "Conveyor Equipment Manufacturers Association (CEMA)", Belt Conveyors for Bulk\ Materials, 6th Edition, pp. 200-205
9. Fenner Dunlop (2009), "Conveyor Handbook", Conveyor Belting Australia, pp. 1-70.
10. "Phoenix Conveyor Belt Systems", Design Fundamentals Hamburg, pp. 1-16 (2004).

DESIGN AND THERMAL ANALYSIS OF STEAM BOILER USED IN POWER PLANTS

Shahidul Islam¹

Dr.Sanjeev Kumar Sajjan²

Dr.P.Srinivasulu³

¹M.Tech department of Mechanical Engineering, vaagdevi college of engineering (UGC autonomous) approved by AICTE & permanent affiliation to jntuh, hyderabad. p.o, bollikunta, Warangal urban- 506005

²Assistant professor department of Mechanical Engineering, vaagdevi college of engineering (UGC autonomous) approved by AICTE & permanent affiliation to jntuh, hyderabad. p.o, bollikunta, Warangal urban- 506005.s

³Professor and Head of the department of Mechanical Engineering, vaagdevi college of engineering (UGC Autonomous) approved by AICTE & permanent affiliation to jntuh, hyderabad. p.o, bollikunta, Warangal urban- 506005.

Abstract: Steam boiler is a closed vessel in which water or other fluid is heated under pressure and the steam released out by the boiler is used for various heating applications. In this thesis the steam flow in steam boiler is modeled using CATIA parametric design software. The thesis will focus on thermal and CFD analysis with different inlet velocities (10, 25, 35 & 45m/s). In this paper, the CFD analysis is to determine the heat transfer coefficient, heat transfer rate, mass flow rate, pressure drop. Thermal analysis to determine the temperature distribution, heat flux for models steam boiler with different materials such as EN 31 steel, stainless steel 316L and copper.

3D modeled in parametric software CATIA and analysis done in ANSYS.

Keywords: CFD analysis, CATIA, ANSYS and velocities .

1. INTRODUCTION

A boiler is a closed vessel in which fluid (generally water) is heated. The liquid doesn't really bubble. (In North America, the expression "heater" is regularly utilized if the design isn't to heat up the liquid. The warmed or disintegrated liquid leaves the evaporator for use in different procedures or warming applications, including water warming, focal warming, heater based force age, cooking, and sanitation.

Water-tube heater: In this sort, tubes loaded up with water are orchestrated inside a heater in various potential arrangements. Regularly the water tubes interface huge drums, the lower ones containing water and the upper ones steam and water; in different cases, for example, a mono-tube heater, water is coursed by a siphon through a progression of curls. This sort for the most part gives high steam creation rates, however less capacity limit than the abovementioned. Water tube boilers can be intended

to misuse any warmth source and are commonly favored in high-pressure applications since the high-pressure water/steam is contained inside little breadth pipes which can withstand the weight with a more slender divider. These boilers are generally built set up, generally square fit as a fiddle, and can be various stories tall.

Steam Boiler

At the point when water is heated up the outcome is soaked steam, additionally alluded to as "wet steam." Saturated steam, while generally comprising of water fume, conveys some unelaborated water as beads. Soaked steam is helpful for some reasons, for example, cooking, warming and sanitation, yet isn't alluring when steam is relied upon to pass on vitality to apparatus, for example, a boat's impetus framework or the "movement" of a steam train. This is on the grounds that unavoidable temperature as well as weight misfortune that happens as steam ventures out from the heater to the hardware will cause some buildup, bringing about fluid water being conveyed into the apparatus. The water entrained in the steam may harm turbine edges or on account of a responding steam motor, may cause genuine mechanical harm because of hydrostatic lock.

2. LITERATURE SURVEY

Structural and thermal analysis of a boiler using finite element Analysis[1] Steam boiler is a closed vessel in which water or other liquid is warmed under tension and the steam discharged out by the kettle is utilized for different warming applications. The primary contemplations in the structure of a kettle for a specific application are Thermal plan and investigation, Design for produce, physical size and cost. In the current work a fire tube kettle is dissected for static and Thermal stacking. The geometric model of kettle is made in CATIA V5 programming according to the drawing. This model is imported to HYPERMESH through IGES arrangement and FEA

model with combined work is created utilizing shell components. To this FEA model different stacking conditions like plan pressure, warm loads and working conditions are applied. One of the supporting legs is captured in all the headings and the other one is captured uniquely in X, Z-bearings and all turns. All these are made by utilizing HYPERMESH and it is sent out to ANSYS for answer for acquire the redirections, stresses. Those qualities are associated with material reasonable qualities according to the ASME Section VIII Division 2. Analysis of New Boiler Technologies [2] The thermodynamics of fare cogeneration direct that higher HP steam conditions bring about greater power created, something which has driven the business to accomplish ever higher weights and temperatures without thinking about the financial aspects. Practically speaking, as conditions are expanded, the extra capital expense surpasses the extra power. The higher HP conditions have likewise determined a second pattern : to receive single drum boilers as opposed to proceeding to utilize bi-drum plans. While this is the correct methodology at high conditions, care should be taken in choosing the subtleties of the design. A Study Analysis and Performance of High Pressure Boilers with its Accessories [3] Power establishes the fundamental and basic contribution for quick financial improvement. Right now vitality place a crucial job both in modern improvement, which thusly prompts the thriving age offices created in AP to satisfy developing need for power. By utilizing adornments in the evaporator. The effectiveness of the plant increments. For instance the extras like Economizer expands the feed water temperature while super radiator builds the temperature of the steam created in the heater. The air pre radiator expands the delta air temperature, which goes into the heater. The fundamental goal of present undertaking work is to break down the proficiency of economizer, super heater& air pre warmer by changing the different parameters in evaporator section. Design and examination of the model of kettle for steam pressure control [4] to get high vitality productive force plant activity it is important to effectively control the steam pressure. Thus an exertion has been made right now control such a basic parameter for example steam pressure by building up a model of kettle pack utilizing PLC based PID controller which utilizes IMC strategy for tuning the parameters of the PID. Introduced work additionally incorporates the demonstrating of the procedure and reenactment has been finished with the fitting exchange work utilizing feed forward input control methodology. Further down to earth reactions and hypothetical reaction has been thought about. Likewise open circle approval

has been done to approve the model model. Shuhas R Bamrotwar,[6],2014 Boiler tube disappointment is the prime explanation of constrained blackouts at coal terminated warm force plants. With consistently expanding interest for power, it is exceptionally important for the force plants to create power without constrained blackouts. This paper delineates cause and impact examination of kettle tube disappointments. The information relating to heater tube disappointments for one of Thermal Power Plant in Maharashtra State of most recent ten years was alluded. Out of all out 144 disappointments, 43 disappointments were seen in economizer zone. Economizer is the fundamental piece of the heater in the heater second pass. It is the mechanism for transportation of the feed water to kettle drum. It assists with expanding the heater proficiency.

Problem description

The objective of this project is to make a 3D model of the steam boiler and study the CFD and thermal behavior of the steam boiler by performing the finite element analysis. 3D modeling software (CATIA) was used for designing and analysis software (ANSYS) was used for CFD and thermal analysis.

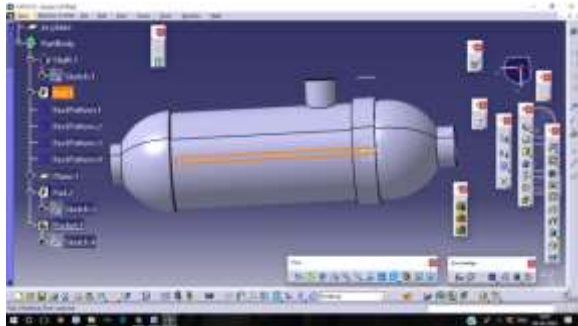
- The methodology followed in the project is as follows:
- Create a 3D model of the steam Boiler assembly using parametric software pro-engineer.
- Convert the surface model into Para solid file and import the model into ANSYS to do analysis.
- Perform thermal analysis on the steam Boiler assembly for thermal loads.
- Perform CFD analysis on the existing model of the surface steam boiler for Velocity inlet to find out the mass flow rate, heat transfer rate, pressure drop.

MODELING AND ANALYSIS

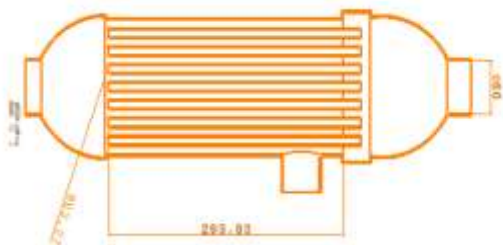
Computer-aided design (CAD) is the use of computer systems (or workstations) to help in the creation, alteration, investigation, or upgrade of a structure. PC supported structure writing computer programs is used to grow the productivity of the organizer, improve the idea of arrangement, improve correspondences through documentation, and to make a database for amassing. PC helped configuration yield is normally as electronic records for print, machining, or other gathering assignments. The term CADD (for Computer Aided Design and Drafting) is moreover used. CATIA is a condensing for Computer Aided Three-dimensional Interactive Application. It is one of the fundamental 3D programming used by relationship in different

organizations stretching out from flight, vehicle to purchaser things. CATIA is a multi organize 3D programming suite made by Systems, including CAD, CAM similarly as CAE. Dassault is a French structure mammoth dynamic in the field of flying, 3D structure, 3D progressed bogus ups, and thing lifecycle the officials (PLM) programming.

3D Model of steam boiler



2D model of steam boiler



Surface model of boiler



FEM/FEA helps in evaluating complicated structures in a system during the planning stage. The strength and design of the model can be improved with the help of computers and FEA which justifies the cost of the analysis. FEA has prominently increased the design of the structures that were built many years ago.

CFD

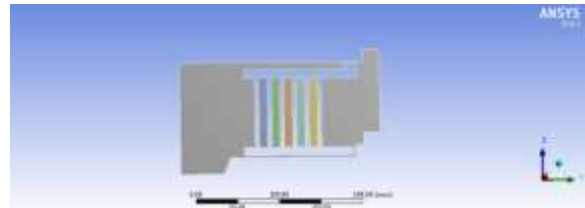
Computational fluid dynamics, usually abbreviated as CFD, is a branch of fluid mechanics that uses numerical methods and algorithms to solve and analyze problems that involve fluid flows.

CFD ANALYSIS OF STEAM BOILER

Geometry

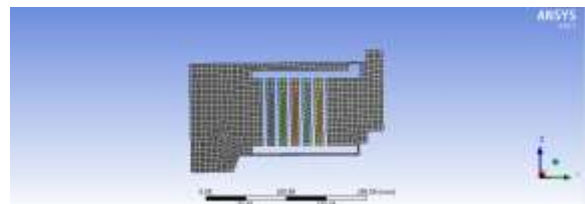
Steam boiler is built in the ANSYS workbench design module. It is a counter-flow Steam boiler. First, the fluid flow (fluent) module from the workbench is selected. The design modeler opens as a new window as the geometry is double clicked.

Imported model



Meshing

The model is designed with the help of CATIA and then import on ANSYS for Meshing and analysis. The analysis by CFD is used in order to calculating pressure profile and temperature distribution. For meshing, the fluid ring is divided into two connected volumes. Then all thickness edges are meshed with 360 intervals. A tetrahedral structure mesh is used. So the total number of nodes and elements is 6576 and 3344.



Steam boiler model after Meshing

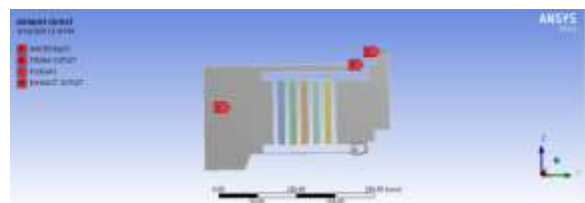
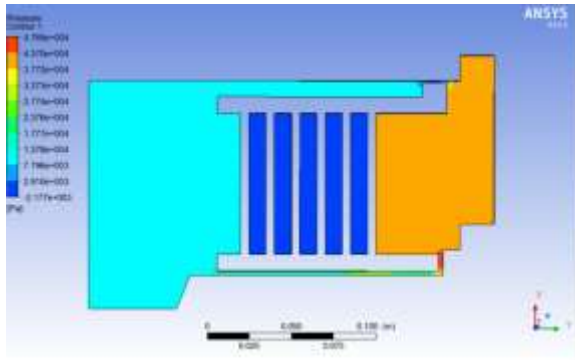


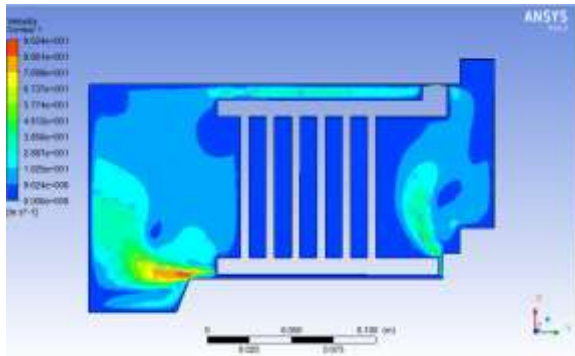
Fig: inlet and outlet conditions

Inlet velocity-45 m/s

Static Pressure



Velocity Magnitude



Mass flow rate

Mass Flow Rate	(kg/s)
interior-fluegas	23.602331
interior-split.2_	0
steam_outlet	-0.47910237
wall-fluegas	0
wall-split.2_	0
water_inlet	0.67500001
Net	0.19589764

Heat transfer rate

Total Heat Transfer Rate	(w)
steam_outlet	-143318.86
wall-fluegas	0
wall-split.2_	-0.0010746096
water_inlet	224623.13
Net	81304.265

THERMAL ANALYSIS OF STEAM BOILER

Used Materials steel, copper, brass & stainless steel

Copper material for tube

EN 31 Steel, brass & stainless steel 316L for boiler casing

Copper material properties

Thermal conductivity = 385w/m-k
 Specific heat = 0.385j/g⁰C
 Density = 0.00000776kg/mm³

Steel material properties

Thermal conductivity = 93.0w/m-k
 Specific heat = 0.669j/g⁰C
 Density = 0.0000075kg/mm³

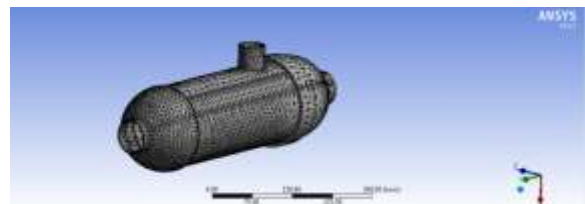
Stainless Steel material properties

Thermal conductivity = 34.3w/m-k
 Specific heat = 0.620j/g⁰C
 Density = 0.00000901kg/mm³

Imported Model



Meshed model

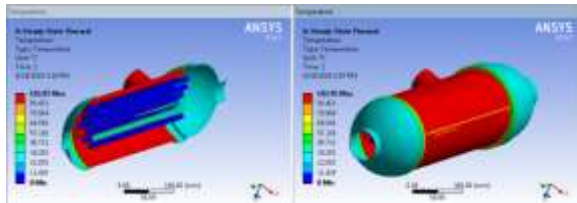


Finite element analysis or FEA representing a real project as a “mesh” a series of small, regularly shaped tetrahedron connected elements, as shown in the above fig. And then setting up and solving huge arrays of simultaneous equations. The finer the mesh, the more accurate the results but more computing power is required.

Boundary Conditions

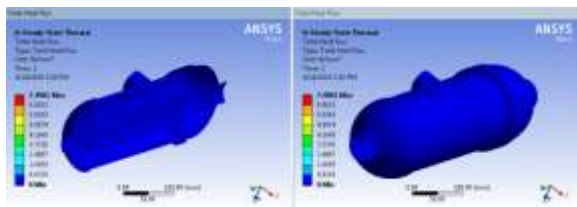


MATERIAL- STEEL FOR BOILER CASING, COPPER FOR TUBES
Temperature



According to the contour plot, the temperature distribution maximum temperature at tubes because the steam passing inside of the tube. So we are applying the temperature inside of the tube and applying the convection except inside the tubes. Then the maximum temperature at tubes and minimum temperature at steam boiler casing.

Heat flux



According to the contour plot, the maximum heat flux at inside the tubes because the steam passing inside of the tube. So we are applying the temperature inside of the tube and applying the convection except inside the tubes. Then the maximum heat flux at inside the tubes and minimum heat flux at steam boiler casing and outside of the tubes.

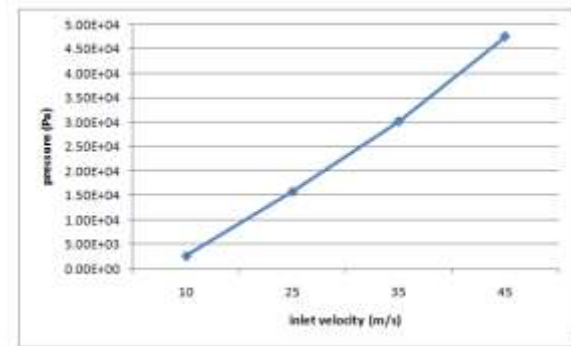
According to the above contour plot, the maximum heat flux is 7.496 w/mm² and minimum heat flux is 0.8329 w/mm².

RESULT TABLES

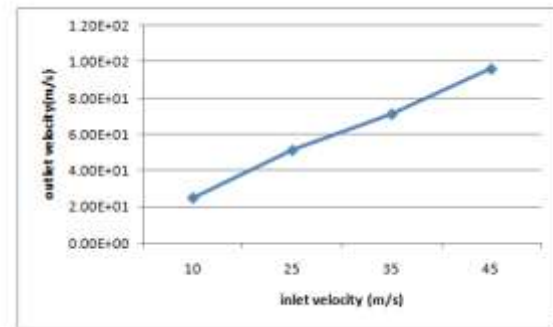
Velocity (m/s)	Pressure (Pa)	Velocity (m/s)	Mass flow rate (kg/s)	Heat transfer Rate(W)
10	2.60e+03	2.51e+01	0.04368	21681.532
25	1.58e+04	5.14e+01	0.11344	52773.632
35	3.02e+04	7.13e+01	0.15603	9596.454
45	4.76e+04	9.62e+01	0.19589	81304.165

Thermal Analysis Result Table

Materials	Temperature (°C)	Heat flux
Mild steel	102.85	7.4961
Stainless steel 316L	103.04	19.821
Copper	103.17	49.672

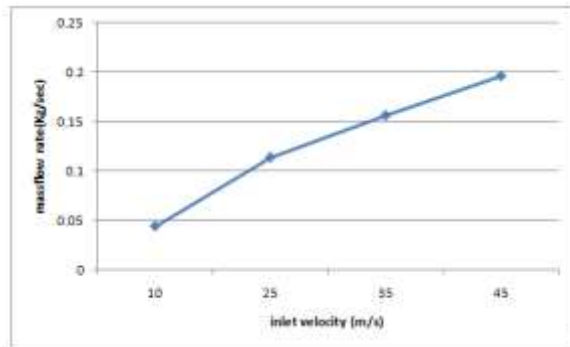


A plot between maximum pressure and velocities by FEA approach is shown in above fig. From the plot the variation of maximum static pressure is observed. Maximum static pressure increases with increases in velocities.

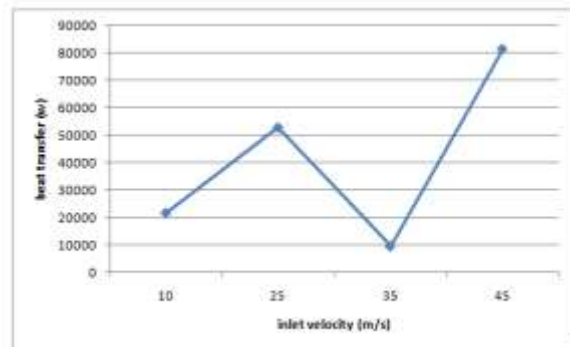


A plot between maximum velocity and velocities by FEA approach is shown in above fig. From the plot the variation of maximum static velocity is observed. Maximum velocity increases with increases in velocities.

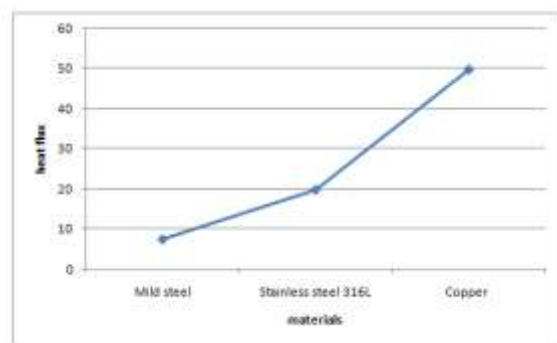
Mass Flow Rate Plot



A plot between maximum mass flow rate and velocities by FEA approach is shown in above fig. From the plot the variation of maximum mass flow rate is observed. Maximum mass flow rate increases with increases in velocities.



A plot between maximum heat transfer rate and velocities by FEA approach is shown in above fig. From the plot the variation of maximum heat transfer rate is observed. Maximum heat transfer rate increases with increases in velocities.



A plot between maximum heat flux and velocities by FEA approach is shown in above fig. From the plot the variation of maximum heat flux is observed. Maximum heat flux increases with increases in

velocities. Heat flux value is decreases steel than stainless steel & copper.

CONCLUSION

In this thesis, the steam boiler is modeled using CATIA design software. The thesis will focus on thermal and CFD analysis with different velocities (10, 25, 35 & 45m/s). Thermal analysis done for the steam boiler by steel, stainless steel & copper.

By observing the CFD analysis the pressure drop, velocity, heat transfer coefficient, mass flow rate & heat transfer rate increases by increasing the inlet velocities.

By observing the thermal analysis, the taken heat transfer coefficient values are from CFD analysis. Heat flux value is more for copper material than steel & stainless steel.

So we can conclude the brass material is better for steam boiler.

REFERENCES

1. Finite Element Analysis of Steam Boiler Used In Power Plants 1M. Suri Babu, 2 Dr.B.Subbaratnam 1M.Tech understudy, 2Professor, Dept of Mechanical Engineering, Kits, Markapur, A.P, India.
2. Structural and warm examination of a kettle utilizing limited component Analysis D.Kondayya Department of Mechanical Engineering, Author Correspondence: Department of Mechanical Engineering, Sreenidhi Institute of Science and Technology, Ghatkesar, Hyderabad – 501301.
3. Analysis of New Boiler Technologies Dr Mike Inkson
4. A Study Analysis and Performance of High Pressure Boilers With its Accessories J. Suresh babu¹, R.Latha², B.Praveen³, V.Anil kumar⁴, R Rama kumar⁵, s.peerulla⁶ 1 Assistant Professor in MED, K.S.R.M College of designing, AP, India 2 3 4 5 6 Student, mechanical office, K.S.R.M College of building, AP, India
5. Design and investigation of the model of heater for steam pressure control 1 Akanksha Bhoursae, 2 Jalpa Shah, 3 Nishith Bhatt Institute of Technology, Nirma

University, SG parkway, Ahmedabad-382481,India

3Essar steels limited,Hazira,Surat-394270,India

6.Lou Roussinos, P. E., "Kettle Design and Efficiency" [online], Available:

[http://www.forestprod.org/drying06williamson .pd f,](http://www.forestprod.org/drying06williamson.pdf)

Accessed: September 1, 2010.

7.Murdock, K. L., "3ds max 9 Bible, Wiley Publishing Inc. Indianapolis, Indiana, 2007.

8.Nagpal, G. R., 1998, Power Plant Engineering, Khanna, Delhi.

9.Steam Pressure Reduction: Opportunities and Issues by U.S Department of vitality,

EVALUATION OF PERFORMANCE AND EMISSION CHARACTERISTICS OF ALGAE OIL BIODIESEL OIL BLEND WITH ALUMINIUM OXIDE AS NANO ADDITIVE

Shaik Yakubpasha¹ Dr. Srinivasulu Pulluru²

¹M.Tech (Thermal Engineering)Department of mechanical engineering vaagdevi college of engineering (UGC autonomous) approved by AICTE & permanent affiliation to jntuh, hyderabad.p.o, bollikunta, Warangal urban-506005.

²Professor and Head of the Department of mechanical engineering vaagdevi college of engineering (UGC autonomous) approved by AICTE & permanent affiliation to jntuh, hyderabad. p.o, bollikunta, Warangal urban-506005.

Abstract

The biodiesel can be extricated from various sources and mix with motor energizes to counter factors like fuel shortage, contamination, cost and expanding of customers. The utilization of Nano added substance in algal oil Diesel-Biodiesel mix is one of the method to diminish the outflows and expanding execution of IC Motor. In the current task chlorella green growth oil is utilized as elective fuel with aluminum oxide (Al₂O₃) as nano added substance to accomplish better execution and lower outflows. In this work green growth oil is utilized as an elective fuel which is mixed with diesel in various extents with and without aluminum oxide as nano added substance. Green growth fuel is mixed with diesel on volume premise, specifically B20, B25 and B30 are made to run in CI diesel motor. The properties of the fuel were seen as indicated by American Culture for Testing and Materials Principles. Exploratory testing was carried out in a solitary cylinder four stroke water cooled diesel motor. Among the different mixes tried B20 shows improved results when contrasted and diesel in brake warm efficiency (BTE), brake explicit fuel utilization (BSFC) and lower (HC and CO₂) discharges. Be that as it may, the other outflow like Nitrogen oxide (NO_x) and Carbon monoxide (CO) were shown possibly higher. Aluminium oxide (Al₂O₃) as nano added substance is mixed with green growth biodiesel (B20) in various extents of added substance, for example, 0.08gram, 0.1gram and 0.12gram (80ppm, 100ppm and 120ppm) were taken. By utilizing the aluminum oxide (Al₂O₃) as nano added substance with green growth biodiesel (B20) shows nearer assessment with diesel brings about higher warm proficiency and lower NO_x, HC, CO₂ outflows. Nonetheless, different emanations carbon monoxide (CO) was possibly higher. At long last the exhibition and emanations, for example, NO_x, CO₂, HC and CO are looked at and introduced.

Keywords: Al₂O₃, biodiesel, chlorella algae, BSFC and NO_x.

1. INTRODUCTION

Alternative fuels for diesel engines have become progressively significant because of a few financial viewpoints and expanded ecological worries. A worldwide temperature alteration worries because of the creation of ozone depleting substances have considered one of main consideration the advancement of the utilization of biofuels. Carbon dioxide (CO₂) from fuel burning is a significant supporter of nursery gases and caused a change in the environment framework. However the utilization of biodiesel as an elective fuel for oil diesel fuel works in pressure start (CI) diesel motors is exceptionally successful for the decrease of CO₂ emanation since it is delegated green and sustainable power got from inexhaustible biomass assets like vegetable oils and creature fats.

In activity of a four stroke CI motor just air is enlisted into the chamber during pull while the fuel is infused into the chamber not long before the burning happens. In the event that the fuel is infused into a pre-burning chamber prior to being brought into the chamber then it is fathom as roundabout CI motor. Then again when the fuel is infused straightforwardly into the chamber, it is supposed direct CI motor. The admission air is packed and in the process the temperature additionally climbs to around 800K. The pressure proportion of CI motor is typically higher than for SI motor.

Biodiesel is a spotless consuming fuel delivered from oil, vegetable oils, or creature fats. Biodiesel is delivered by transesterification of oils with short-chain alcohols or by the etherification of unsaturated fats. The transesterification response comprises of changing fatty oils into unsaturated fat alkyl esters, within the sight of a liquor, like methanol or ethanol, and an impetus, like a soluble base or corrosive, with glycerol as a side-effect. Since biodiesel is made altogether from vegetable oil or creature fats, it is sustainable and biodegradable. Most of biodiesel today is created by soluble base catalyzed transesterification with methanol, which brings about a moderately short response time.

ALGAE FUEL

Algae fuel or algal biofuel is one more type of petroleum derivative that utilizes microalgae as its wellspring of regular stores. A portion of the interesting qualities of algal energizes are as per the following: they can be developed with irrelevant effect on new water assets, they can be integrated utilizing sea and wastewater, and they are biodegradable and moderately innocuous to the climate whenever spilled. Green growth cost more per unit mass because of the great capital and creation costs. The US Branch of Energy's Sea-going Species Program, 1978-1996, was immersed in biodiesel from microalgae. The last report suggested that biodiesel could be the main attainable technique to create sufficient fuel to impact current world diesel utilization. Algal fuel is exceptionally good and plausible connected with other biofuels, as they don't need to create underlying mixtures and they can switch higher parts of biomass over completely to oil contrasted with other developed crops. Concentrates in plain view that a types of green growth can create up to 60% of their dry load as oil. Since the cells fill in fluid suspension, where they have more powerful admittance to water, CO₂ and supplements are fit for delivering a lot of biomass and usable oil in either high rate algal lakes or photograph bioreactors.

2. LITERATURE REVIEW

A lot of exploration going on the plan and improvement of the motors. Today a gigantic improvement was conveyed for accomplish a decent exhibition and lessen discharges. These is accomplish by utilizing different fuel mixes, fuel infusion timing, bio diesel utilizing with and without utilization of additive, the added substance utilized in this work is Al₂O₃ in view of having great ignition attributes. In these fields a ton of exploration was happening with various mixes blended in with diesel.

Cheng Chen et al. [1] They led probe Impact of sequential and equal designs on the two-stage stream ways of behaving for double ignition chambers with a pushed body and presumed that the different multi-faceted stream and energy transformation ways of behaving of the burning gas and fuel grains in two ordinary designs of double chambers with a moved body. Joining the two-liquid model (TFM) and the lumped boundary technique (LPM), a coupled methodology is proposed to portray the gas-strong stream with response in the double chamber framework, which considers gas creation, interphase drag, intergranular stress, and intensity move between two stages.

Varun, et al [2] They researched on Adjustment in ignition chamber calculation of CI motors for appropriateness of biodiesel and reasoned that

biodiesel doesn't give a similar exhibition as diesel. This follows the way that a few changes are to be integrated into the motor. Burning chamber (CC) math is perhaps of the main element that influence the presentation of the motor. Varieties in these calculations, just barely have shown a colossal change in the presentation and outflow boundaries. In this article, different ignition chamber calculations have been thought of and results acquired from exploratory and mathematical examination was talked about.

G. Najafi et al. [3] They carried out on the impact of burning administration on diesel motor emanations powered with biodiesel-diesel mixes and reasoned that the consequences of compelling systems incorporate; ignition the executives, fuel added substances and after-treatment innovation which are accounted for in different exploration studies are examined. The general outcomes demonstrated the way that utilizing one system can not diminish every one of the discharges of diesel motors. Be that as it may, utilizing a few systems all the while can decrease all the diesel motor outflows. The outcome from an overview showed that the best proposed answer for decrease of diesel motor poisons is utilizing biofuels, which comprise of a blend of diesel, biodiesel and ethanol.

L.X. Sang et al. [4] They researched probe Alteration of Ternary Carbonates with Added substances lastly came about that to work on the warm actual properties of ternary carbonates, potassium, lithium, and sodium carbonates were changed by adding added substances CaO, CaCO₃, Ca(OH)₂ and KOH. Their softening point, starting crystallization point, and deterioration temperature were broke down by utilizing the Simultaneous Warm Analyzer. Albeit the added substances have less impact on the underlying crystallization temperatures and the disintegration temperatures of ternary carbonates, they contrastingly affect the liquefying point of ternary carbonates.

Md. Hasan ali et al. [5] They directed probe Biodiesel from Neem Oil as an Elective Fuel for Diesel Motor and expressed that powers". Vegetable oil can't be straightforwardly utilized in the diesel motor for its high consistency, high thickness, high glimmer point and lower calorific worth. So it should be changed over into biodiesel to make it steady with fuel properties of diesel. Biodiesel creation is an important interaction which needs a proceeded with study and improvement process. The current review was expected to consider angles connected with the creation of biodiesel from Neem oil and exploring its fuel properties. The seeds of Neem contain 30-40% oil. This report manages biodiesel acquired from

Neem oil which are mono alkyl esters created utilizing 'Transesterification' process.

Shruthi H et al. [6] They directed an investigation on Creation of Biofuel from Unrefined Neem Oil and its Presentation and inferred that This paper manages Biodiesel creation from neem oil, which is monoester delivered utilizing transesterification process. It has high lubricity, clean consuming fuel and can be a fuel part for use in existing unmodified diesel motor. The fuel properties of biodiesel including streak point and fire point were inspected.

Ahmed et al. [7] They researched the impact of Al₂O₃ NPs on jojoba biodiesel-diesel mixes. The outcome showed that there was impressive change in fuel properties. The writers detailed that the fuel test JB20DA produced the most extreme measure of BSFC (~760 g/kW-hr) at 50 mg Al₂O₃ added substance focus in contrast with different mixes (15). One of the new examinations directed in 2018, showed the decrease in brake explicit fuel utilization around 12% with the option of Al₂O₃ nanoparticles and emanations, for example, NO_x and CO₂ are diminished.

Mohankumar et al. [8] Did a test examination on execution, ignition and emanation qualities of DI diesel motor involving green growth as a biodiesel. In these work green growth is utilized as an elective fuel with various mix blend with diesel and the outcomes got are summed up. Green growth fuel is mixed with diesel on a volume premise, specifically A10, A20, A30, A40 and A100 and made to run in diesel motors.

S. Karthikeyan et al. [9] They conveyed an investigation by utilizing *Caulerpa racemosa* green growth biofuel mixed with Bi₂O₃ as nano added substance. Execution and discharge investigation have been led with the help of a Kirloskar make four-stroke, single-chamber diesel engine utilizing *C. racemosa* green growth oil biodiesel with Bi₂O₃ nano additives and its diesel mixes. The BSFC for B20 + 100 ppm at maximum load is 0.294 kg/kWh which is extremely near that of diesel. BTE of the multitude of tried fills shows a comparative pattern and B20+ 100 ppm rules (15%) contrast with the B20 mix. CO (3% vol) and HC (200 ppm) emanation for Bi₂O₃ and its mixes are seen as lower than that for B20.

2.1 OBJECTIVE

Numerous specialists have performed probes CI motor with various vegetable oils, Virgin feedstock, Creature fats, Multi-feedstock and Sewage sludge. Biodiesel fuel can possibly be utilized as an elective fuel that can decrease discharges of carbon dioxide (CO₂), carbon monoxide (CO), nitrogen

oxide (NO_x) and hydrocarbons (HC) outflows and can be further developed execution of gas powered motor. In this study green growth oil is utilized as biodiesel is elective fluid non-renewable energy source. Green growth are photosynthetic living beings connected with plants that fill in water and produce energy from carbon dioxide and daylight. Single-celled microalgae can be utilized to deliver enormous measure of fat, which can be changed over into biodiesel. In numerous experiments biodiesel had taken at various extents of mix, in that ideal mix extents are B20, B25 and B30 are thought about for this study. But biodiesel fuel emits higher NO_x discharges.

Numerous specialists are found nano added substances is one of the most mind-blowing choice for bringing down the discharges and working on the presentation of a motor. There are many kinds of nano added substances like ethanol and methanol. In this study aluminum oxide is utilized as nano added substance, Nanoparticles when utilized as fuel added substances in IC motors further develop the ignition qualities, give better atomization, better fire supportability, diminishes BSFC and furthermore lessen NO_x. In many experiments added substances were taken at various extents, in that ideal extents are 80 ppm, 100 ppm and 120 ppm are thought about for this review.

The goal of this trial study is to assess the impact of Aluminum oxide as Nano added substance in algal oil mixed with diesel in single chamber diesel engine. To assess the exhibition and outflows qualities with optimum mix proportion's.

2.2 METHODOLOGY

This concentrations to the bit by bit strategies and procedures involved towards the finish of the undertaking alongside accomplishing the goals of the exploration. In view of writing review, readings and synopses made in the past section, the accompanying trial test will be done comprises of four significant works:

(I) Readiness of biodiesel fills (BDF) from Algae based as well as their combinations with diesel fuel.

(ii) Playing out the motor activities by utilizing the different kinds and mixing extents of biodiesels as fills as well as standard diesel fuel (DSL).

(iv) Estimating the fumes gas emanations set free from the burning of biofuels in pressure start (CI) diesel motor like CO, CO₂, HC and NO_x.

The general examination strategy or exploratory stream is improved on in a stream diagram in the ensuing point.

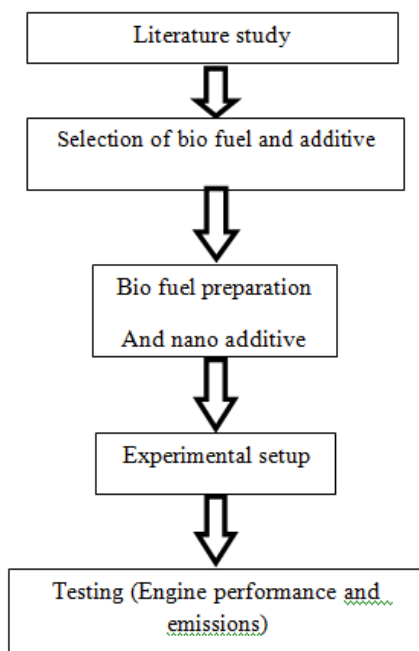


Fig : Flow chart of work

3.MATERIALS PREPARATION

In the initial step of study, 20%, 25% and 30 % of Chlorellamicroalgae biofuel is considered as fuel and aluminum oxide (Al_2O_3) is considered as the nano-added substance to assess the motor presentation. In second step motor changes with advanced motor boundaries. At long last, in third step exploratory consequences of (discharge qualities) the both altered fuel and motor are contrasted and the current pattern motor.

In the ongoing review, 80 ppm (0.08 gm) ,100 ppm (0.1 gm) and 120 ppm (0.12) of Al_2O_3 nanoparticles particles are added to oneliter of 20% journal filth biodiesel and nano particles are scattered well with biodiesel mix utilizing ultrasonicator and mechanical stirrer.

To control the sedimentation of nano particles CTAB(Cetyl Trim ethyl Ammonium Bromide) surfactant is utilized to give the negative charge to the particles to accordingly sedimentation of molecule is stayed away from. To keep away from the sedimentation of the nanoparticles, the fuel mixes are shaken well prior to directing the experimentation. The schematic view of the nano added substance fuel mix arrangement and use is shown in Figure 3.1. The schematic perspective on the nano particles and fuel mix responses is displayed in the Figure 3.2.

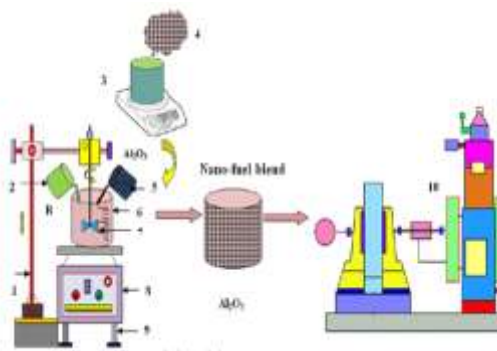


Figure 3.1. Ultrasonicator and Mechanical stirrer for preparation of nano fuel blends.

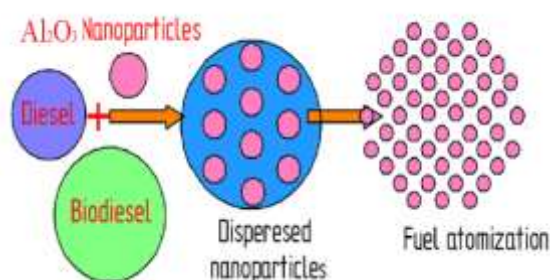


Figure 3.2. Atomization of nanoparticles dispersed test fuel.

3.1Chlorellagreen microalgae bio fuel Identification and Preparation for Oil extraction Collected

Green growth test was analyzed under Shroud E200 Compound Magnifying lens. The photo in figure was taken by broadening it multiple times and multiple times. The examples were spread under the sun in the top of the inn for 2 days (48 hours) to vanish how much water. The dried examples were ground with the assistance of pestle and processor and the fine powder was gone through various micron strainers, to get different cross section size algal biomass, figure 2. The ground green growth were dried for 30 min at $80^{\circ}C$ in a hatchery for delivering extra water. Then, at that point, the green growth powder was put away in various containers for extraction explore in a fixed holder.



Figure:3.4 Collection of algae from the open pond

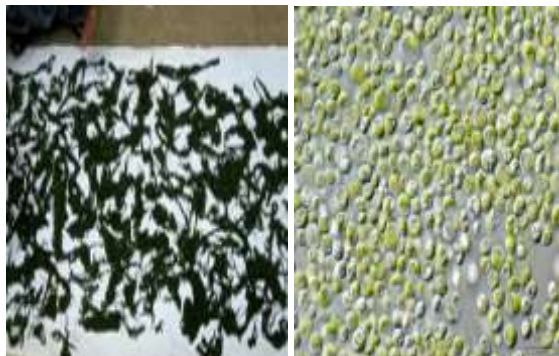


Figure.3.5 Chlorella green microalgae bio fuel identification and drying associated with the algal biomass.

Oil extraction from Algae

The green growth tests gathered were dried (100 percent) and powdered. Hexane was blended in with the dried ground green growth to remove oil in isolating channel of 250 ml. Then, at that point, the combination was saved for 24 h for settling and for detachment of the two layers in the channel. The natural stage containing the green growth oil was exhausted in the pre-weighted 50 ml measuring utencil. The Algal oil was isolated from Green growth biomass by filtration and weighted it by utilizing electronic weight balance.



Fig :3.6 samples

3.2 Nanoparticle Size Analysis using XRD

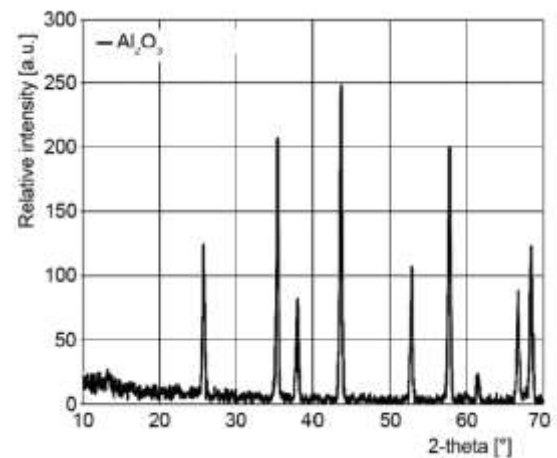


Fig3.7. XRD patterns for Al₂O₃ nanoparticle

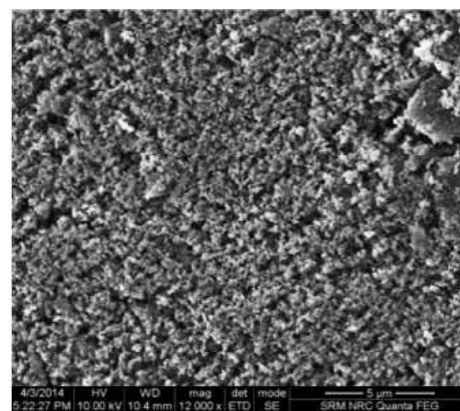


Fig3.8: The SEM image

Details of Al₂O₃ nanoparticle

Specific Surface area	40 m ² /g
Number of CAS	1344-28-1
Molecular Weight	101.96
Color	White
Linear Formula	Al ₂ O ₃
Size of particle	<50nm
MDL number	MFCD00003424

The physical and chemical properties measured based on ASTM standard for diesel and algae biodiesel blend B20 and its Al₂O₃ blend fuels.

Properties	Method	Diesel	Algae oil	B20	B20 +0.08g Al ₂ O ₃	B20+ 0.1g Al ₂ O ₃	B20+ 0.12g Al ₂ O ₃
Density (kg/m ³)	ASTM D1298	830	882	810	842	848	855
Kinematic viscosity at 40°C (mm ² /s)	ASTM D88	3.58	5.53	4.73	5.62	5.67	5.69
Calorific value (kJ/kg)	ASTM D240	43,000	33,860	38,960	39,890	40,126	41,264
Cetane number	ASTM D613	48	62	54	51	53	57
Flash point (°C)	ASTM D92	52	129	98	81	83	87
Fire point (°C)	ASTM D92	78	61	71	90	98	11

Table 3.2 physical and chemical properties of diesel and algae oil and its blend

3.3 Problems with emissions

Carbon Monoxide (CO)

Carbon monoxide is a noxious gas. It has no smell, however can kill without acknowledging what's going on. The principal solution for carbon monoxide emanations of petroleum motors has been the presentation of exhaust systems.

- Increment fuel utilization.
- Effectively harmed and quit working.
- Effectively precisely harmed

Nitrogen Oxides (NO_x)

Nitrogen is significant component of the air that we relax. At the point when it is presented to top strain and temperatures with oxygen all around to deliver nitrous oxides. Nitrous oxides later structure a mist with lessen level ozone. As the diesel motor works, the motor will have a high air content nitrous oxides are bound to be shaped. EGR decline the ignition temperature beneath the place where the nitrogen actually consume.

Hydro carbons (HC)

The difference in HC emanation stages as for proportionality proportion for a SI motor was

examined before. Obviously this is areas of strength for an in wind energy proportion. Fuel added substance blend doesn't have adequate oxygen to take all carbon impressions, last exhaust items HC, CO. This is particularly obvious when the air combination blend is deliberately begun when it is more extravagant. This is additionally least during the heap less quick speed increase.

Carbon dioxide (CO₂)

carbon dioxide (CO₂) makes up most of ozone harming substance outflows from area, however more modest measure of methane (CH₄) and nitrous oxide (N₂O) are likewise transmitted. These gases are delivered during the ignition of petroleum products, for example, coal oil, flammable gas, to create power.

Particulate matter (PM)

Particulate matter is the general term used to portray strong particles and fluid drops tracked down in the air. The piece and size of these airborne particles and beads differ in two sizes. The two sizes ranges known as PM10 and PM2.5, are broadly observed, both at significant outflows sources and in encompassing air.

4. EXPERIMENTAL SETUP

Tests have been performed on a Kirlosker Water cooled single-chamber diesel engine with 4-stroke, the Table 1 shows details of which are given. Figure shows the schematics for the trial set-up. To control the motor, a consistent speed of 1500 rpm was utilized. Tests were carried on diesel motor by Al₂O₃ nano particulate substitute, Algaeoil. With load in 3.5 kw, from 0 burden to 12 load. The engine was coupled to the electrical dynamometer to give the brake load. For the diesel fuel and sesame oil, two different gas tanks were utilized. For the volumetric fuel stream rate estimation, a 50 cm³ burette and a stop watch were utilized. Utilizing the AVL-444 5 gas analyzer, outflows, for example, CO, HC and NO_x were examined and smoke was estimated by the Bosch smoke siphon and the smoke meter is appended to the motor's ventilation system.



Fig :4.1 Kirlosker engine experimental setup

Table 4.1: Specifications of test engine

Power (Kw)	3.3 kw
Bore (mm)	87.50
Stroke (mm)	110.00
Compression ratio	18:0
Speed	1500
Injection pressure (Bar)	200
Injection timing	230 BDC

4.1 Combustion Parameters:

Specific Gas Const (kJ/kg K): 1.00

Air Density (kg/m³): 1.17

Adiabatic Index: 1.41

Polytropic Index : 1.06

Number Of Cycles: 10

Cylinder Pressure Reference : 5

TDC Reference: 0

4.2 Performance Parameters:

Orifice Diameter (mm): 20.00

Orifice Co-eff. Of Discharge: 0.60

Dynamometer Arm Length (mm): 185

Fuel Pipe dia (mm): 12.40

Ambient Temp. (0C): 29

Pulses Per revolution: 360

Fuel Type: Diesel

Fuel Density (Kg/m³): 830

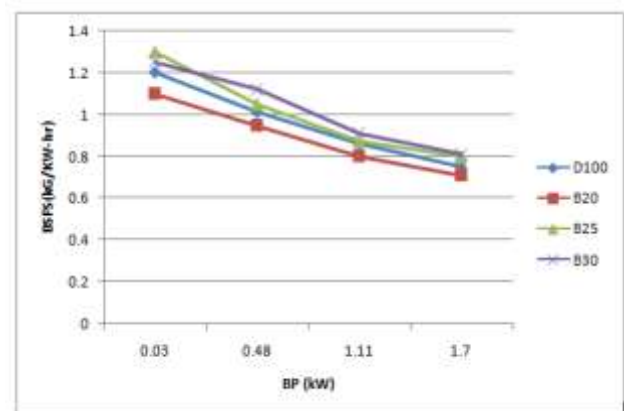
Calorific Value Of Fuel (kJ/kg): 43,000

4.3 EXPERIMENTAL PROCEDURE

Explore has been led with diesel and green growth biodiesel. The tests are carried out in Motor. In first stage the exploratory examination is finished to get gauge boundaries by utilizing standard diesel. In second phase of examination the green growth biodiesel mixes are utilized i.e. B20, B25, and B30 as a fuel in the motor. In third phase of examination the green growth Bio-diesel with Al₂O₃ additive 80, 100 and 120 ppm is utilized as fuel in the Engine. The cooling of the motor is achieved by flowing water through the jackets of the chamber head and the motor block. In the experimental examinations, different instruments are utilized for the estimation of various parameters. The major vaporous discharges estimated in the ongoing review are HC, CO, CO₂ and NO_x. Possibly, the justification for the event of these emanations are general and relies up upon the type of fuel being utilized, motor working and configuration condition, motor stacking condition.

5. RESULTS AND DISCUSSIONS

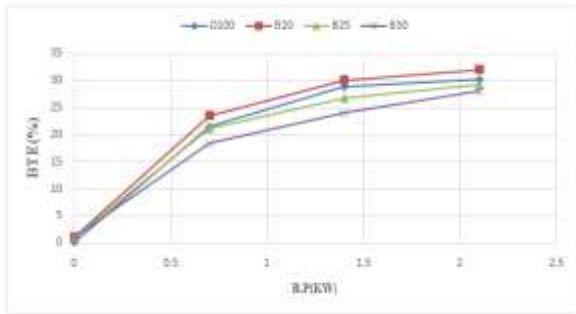
PERFORMANCE ANALYSIS OF BIO-DIESEL BLENDS



Graph 5.1 BP Vs BSFC

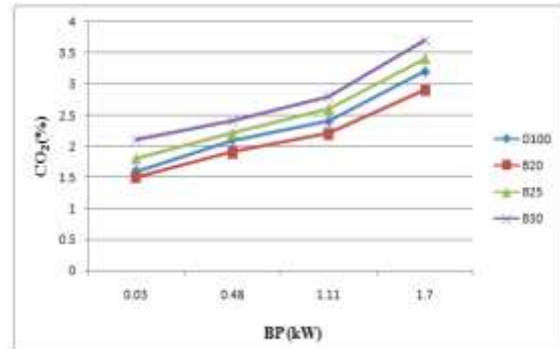
The above chart is plotted between Brake power and Brake explicit fuel utilization (BSFC). The diagram analyzes the BSFC of different energizes (D100, B20, B25, B30) utilized in the diesel motor. Brake explicit fuel consumption (BSFC) measures how much info energy foster one-kilowatt power. The BSFC is a significant foster boundary of a motor since it deals with both mass stream rate and warming worth of the fuel. The above chart shows that while expanding in the brake power naturally it diminishes the brake explicit fuel utilization. It diminishes with expanding load for all test loads. As speed increment B.P increments. The above diagram shows that biodiesel

mix B20 is lower than the diesel (D100) fuel under stacking condition.



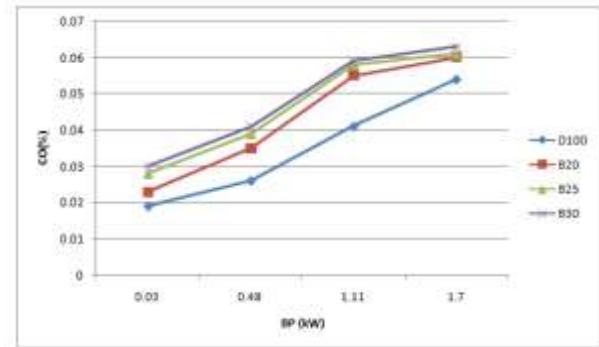
Graph 5.2 BP Vs BTE

higher temperature and oxygen present in its construction. Since the biodiesel atom contains oxygen in its construction, how much oxidizer expected by the motor gets decreased.



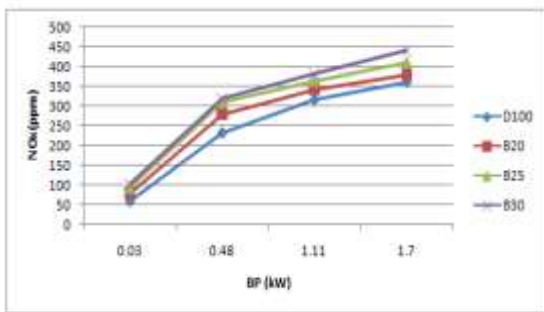
Graph 5.4 B.P vs CO₂

The above chart is plotted between Brake power and Brake warm productivity (BTE). The chart looks at the BTE of different powers (D100, B20, B25, B30) utilized in the diesel motor. It shows that while expanding the brake power consequently the BTE is likewise increments. BTE builds because of expansion in oxygen content in test fills and in motor burdens. It expansions in load in the event of all the mixed fuel tried. This can be ascribed to decrease in heat misfortune and expansion in influence with expansion in load. The above diagram shows that biodiesel mix B20 is lower than the diesel (D100) fuel under stacking condition.



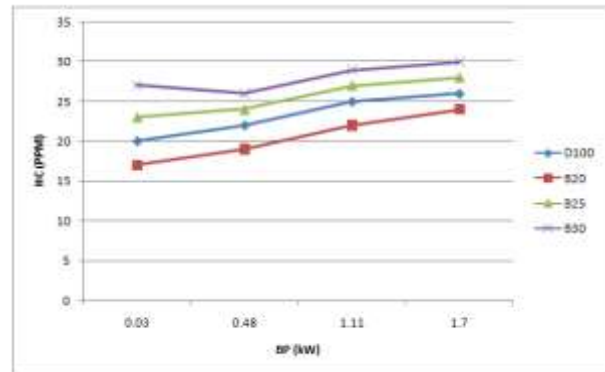
Graph 5.5 B.P Vs CO

EMISSION CHARACTERISTICS OF BIO-DIESEL BLENDS:



Graph 5.3 B.P Vs NO_x

The above diagram is plotted between Brake power and NO_x. The chart thinks about the NO_x outflows of different fills (D100, B20, B25, B30) utilized in the diesel motor. It shows that rising in brake power naturally expansion in NO_x emissions. NO_x levels are higher for biodiesel contrasted with diesel activity. NO_x discharges expansions in biodiesel activity because of the receptive idea of biodiesel particle at

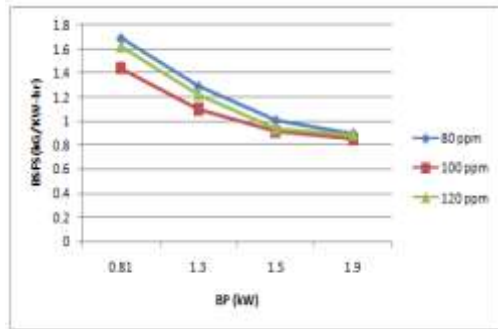


Graph 5.6 B.P Vs HC

The above chart is plotted between the brake power and HC emanations. The diagram thinks about the HC outflows of different fills (D100, B20, B25, B30) utilized in the diesel engine. Hydrocarbon discharges are delivered because of some of hydrocarbon present in the powers doesn't take part in burning. Hydrocarbon outflows are delivered because of some

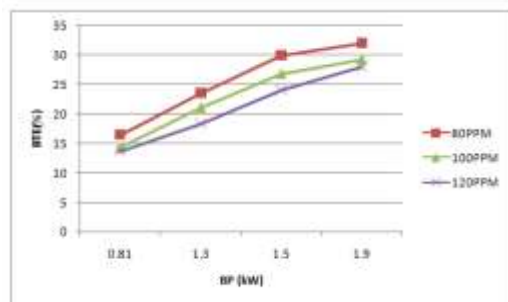
of hydrocarbon present in the energizes doesn't take part in burning. The decrease in HC is expected to biodiesel has higher consistency it has longer start postpone it further leadsto delayed dispersion burning term prompts complete burning of fuel. Another center explanation is that green growth fuel contains oxygen content in its fuel structure normally this further enhances oxidation prompts total consuming of fuel Hydrocarbon emanations are viewed as low for biodiesel fuel blendB20 contrasted with diesel (D100) fuel under all stacking condition.

Performance And Emission Characteristics With Aluminium Oxide As Nano Additive



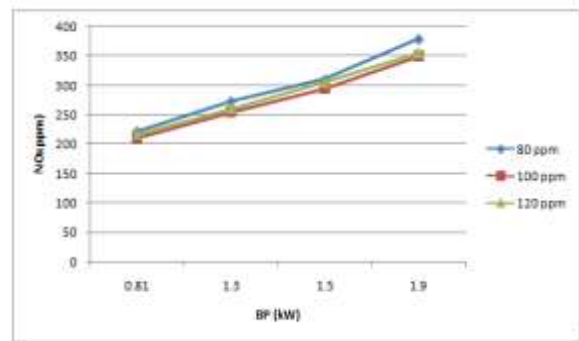
Graph 5.7 B.P Vs BSFC

The above chart is plotted between Brake power and Brake explicit fuel utilization (BSFC).The diagram thinks about theBSFC of different energizes (B20+80ppm, B20+100ppm, B20+120ppm) utilized in the diesel motor. Brake explicit fuel utilization (BSFC) is a proportion of the eco-friendliness of any main player that consumes fuel and creates rotational, or shaft power. With the expansion in load, brake explicit fuel utilization diminishes. At higher burden conditions the brake warm proficiency is expanded and brake explicit fuel utilization diminished. It was observed that BSFC is least for green growth biodiesel B20 with 100ppm of aluminum oxide (Al₂O₃) contrasted and other nano added substance rates (B20+80ppm, B20+120ppm) under stacking condition.



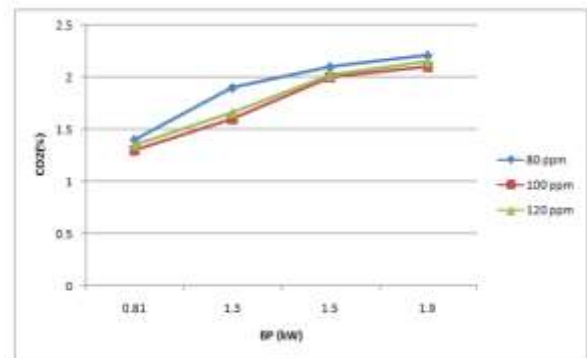
Graph 5.8 B.P Vs BTE

EMISSION ANALYSIS WITH ADDITIVE:



Graph 5.9B.P Vs NOx

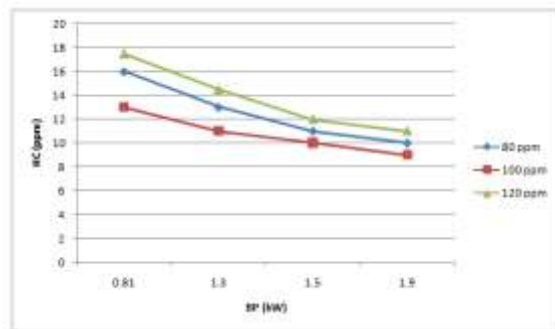
The above chart is plotted between Brake power and Nitrogen oxide (NO_x).The graph thinks about the NO_x of different fills (B20+80ppm, B20+100ppm, B20+120ppm) utilized in the diesel motor. NO_x levels are higher for biodiesel contrasted with diesel activity. NO_x discharges expansions in biodiesel activity because of the receptive idea of biodiesel particle at higher temperature and oxygen present in its construction. Since the biodiesel particle contains oxygen in its construction, how much oxidizer expected by the motor gets decreased. By adding aluminum oxide (Al₂O₃), there is decrease in NOX discharge. This is because calcium carbonate contains 48% of oxygen goes about as an oxygen cushion and donates surface grid oxygen. It was seen that green growth bio diesel B20 with 100ppm added substance has less NOX discharges than different added substances at higher burdens.



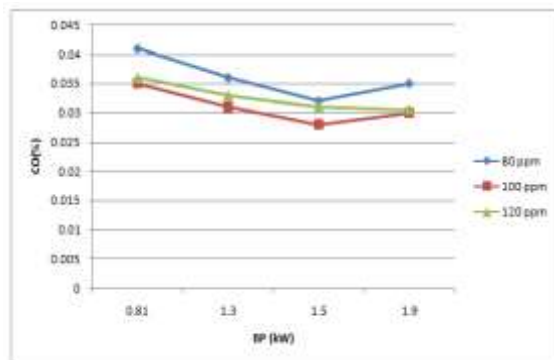
Graph 5.10 B.P Vs CO2

The above graph is plotted between Brake power and Carbon dioxide (CO₂). The graph compares theCO₂of various fuels (B20+80ppm, B20+100ppm, B20+120ppm) used in the diesel engine. The CO₂ emission increases with increases in load, as expected. As the engine load increases, CO₂

emissions increased due to the higher fuel consumption associated with load increase. Lower CO₂ emissions were noticed in biodiesel blend B20 with 100ppm nano additive compared to other additives blends(B20+80ppm,B20+ 120ppm).



Graph 5.11 B.P(KW) Vs HC (ppm)



Graph 5.12 BP (KW) VS CO(%)

6. CONCLUSIONS

In this present investigation biodiesel extracted from chlorella algae is tested in single cylinder diesel engine. In Initial part of this study, Physical and chemical characteristics of diesel and algae blends and along with aluminium oxide as nano additive were analyzed. Then experimental studies are carried out by running the engine at various load conditions and the corresponding performance and emission characteristics were studied. The various conclusions made from the present study are as follows.

Performance and emission characteristics of Bio-diesel blends:

It is observed that applied load increases brake specific fuel consumption (BSFC) decreases for both algae blends and diesel. Regarding BSFC among the blends of algae biodiesel B20 shows better results. However, at maximum load conditions algae blends B20 shows 0.71 kg/kW-hr and diesel 0.75 kg/kW-hr,

it clearly shows biodiesel blend B20 has marginally 0.04kg/kW-hr less BSFC when compared with diesel. It is observed that applied load increases brake thermal efficiency (BTE) increases for both algae blends and diesel. Regarding BTE among the blends of algae biodiesel B20 shows better results. However, at maximum load conditions algae blends B20 shows 32% and diesel 30.23%, it clearly shows that biodiesel blend B20 has marginally 1.77% more when compared with diesel.

It is observed that applied load increases nitrogen oxide (NO_x) emission increases for both algae blends and diesel. Regarding NO_x emission among the blends of algae biodiesel B20 shows better results. However, at maximum load conditions algae blends B20 shows 380ppm and diesel 360ppm, it clearly shows that biodiesel blend B20 has 20ppm more when compared with diesel.

It is observed that applied load increases carbon dioxide (CO₂) emission increases for both algae blends and diesel. Regarding CO₂ emission among the blends of algae biodiesel B20 shows better results. However, at maximum load conditions algae blends B20 shows 2.9% and diesel 3.2%, it clearly shows that biodiesel blend B20 has 0.3% less when compared with diesel.

It is observed that applied load increases carbon monoxide (CO) emissions increases for both algae blends and diesel. Regarding CO emission among the blends of algae biodiesel B20 shows better results. However, at maximum load conditions algae blends B20 shows 0.06% and diesel 0.054%, it clearly shows that biodiesel blend B20 has 0.006% more when compared with diesel.

It is observed that applied load increases hydro carbons (HC) increases for both algae blends and diesel. Regarding HC emission among the blends of algae biodiesel B20 shows better results. However, at maximum load conditions algae blends B20 shows 24ppm and diesel 26ppm, it clearly shows biodiesel blend B20 has 2ppm less when compared with diesel.

From the above studies, it concludes that algae biodiesel blend B20 shows better results when compared with diesel and other blends. However, regarding biodiesel blend B20 has more emissions(CO and NO_x) values when compared to diesel. So for reducing emissions we are using aluminium oxide as nano additive with algae biodiesel blend B20.

Performance and Emission characteristics algae biodiesel blend B20 with Additive of 80,100 and 120ppm Al₂O₃

It is observed that applied load increases brake specific fuel consumption (BSFC) decreases for algae biodiesel blend B20 with additives (80ppm, 100ppm,

120ppm).. However, at maximum load conditions algae biodiesel blend B20+ 80ppm shows 0.8932 kg/kW-hr, B20+100ppm shows 0.8543kg/kW-hr, B20+120ppm shows 0.8865kg/kW-hr. Regarding BSFC among the additives of aluminium oxide (80ppm, 100ppm, 120ppm) with algae biodiesel B20, which concludes 100ppm nano additive shows better results when compared with other additives.

It is observed that applied load increases brake thermal efficiency (BTE) increases for algae biodiesel blend B20 with additives (80ppm, 100ppm, 120ppm). However, at maximum load conditions algae biodiesel blend B20+ 80ppm shows 29.15%, B20+100ppm shows 30.55%, B20+120ppm shows 28.91%. Regarding BTE among the additives of aluminium oxide (80ppm, 100ppm, 120ppm) with algae biodiesel B20, which concludes 100ppm nano additive shows better results when compared with other additives.

It is observed that applied load increases nitrogen oxide (NO_x) emission increases for algae biodiesel blend B20 with additives (80ppm, 100ppm, 120ppm). However, at maximum load conditions algae biodiesel blend B20+ 80ppm shows 379ppm, B20+100ppm shows 350ppm, B20+120ppm shows 355ppm. Regarding NO_x emission among the additives of aluminium oxide (80ppm, 100ppm, 120ppm) with algae biodiesel B20, which concludes 100ppm nano additive shows better results when compared with other additives.

It is observed that applied load increases carbon dioxide (CO₂) emission increases for algae biodiesel blend B20 with additives (80ppm, 100ppm, 120ppm). However, at maximum load conditions algae biodiesel blend B20+ 80ppm shows 2.21%, B20+100ppm shows 2.1%, B20+120ppm shows 2.15%. Regarding CO₂ emission among the additives of aluminium oxide (80ppm, 100ppm, 120ppm) with algae biodiesel B20, which concludes 100ppm nano additive shows better results when compared with other additives.

It is observed that applied load increases carbon monoxide (CO) emission first decreases and slightly increases for algae biodiesel blend B20 with additives (80ppm, 100ppm, 120ppm). However, at maximum load conditions algae biodiesel blend B20+ 80ppm shows 0.035%, B20+100ppm shows 0.030%, B20+120ppm shows 0.03%. Regarding CO₂ emission among the additives of aluminium oxide (80ppm, 100ppm, 120ppm) with algae biodiesel B20, which concludes 100ppm nano additive shows better results when compared with other additives.

It is observed that applied load increases hydrocarbons (HC) emission decreases for algae biodiesel blend B20 with additives (80ppm, 100ppm, 120ppm). However, at maximum load conditions algae

biodiesel blend B20+ 80ppm shows 10ppm, B20+100ppm show 9ppm, B20+120ppm shows 11ppm. Regarding HC emission among the additives of aluminium oxide (80ppm, 100ppm, 120ppm) with algae biodiesel B20, which concludes 100ppm nano additive shows better results when compared with other additives.

From the above studies, which concludes that algae biodiesel blend B20 with 100ppm aluminium oxide nano additive is effective when compared with other additives.

References

- [1] Gaurav Dwivedi, Siddharth Jain, M.P. Sharma, 'Diesel engine performance and emission analysis using biodiesel from various oil sources – Review', *J. Mater. Environ. Sci.* 2013, 4, pp 434-447.
- [2] Barnwal B K and Sharma M P., 'Prospects of Biodiesel Production from Vegetable oil in India.' *Renewable and Sustainable Energy Reviews*, 2005, 9, pp363-378.
- [3] Avinash Kumar Agarwal, "Biofuels (alcohols and biodiesel) applications as fuels for internal combustion engines", *Progress in Energy and Combustion Science*, 2007, pp: 233–271.
- [4] Murugesan A, Umarani C, Subramanian R, "Bio-diesel as an alternate fuel for diesel engines- A review", *Journal of Renewable and sustainable energy reviews*, 2009, pp: 653-662.
- [5] I.M. Rizwanul Fattah, H.H.Masjuki, A.M.Liaquat, RahizarRamli, M.A. Kalam, V.N.Riazuddin, 'Impact of various biodiesel fuels obtained from edible and non-edible oils on engine exhaust gas and noise emissions', *Journal of Renewable and Sustainable Energy Reviews* 18, 2013, pp 552–567
- [6] Md. NurunNabi, Md. MustafizurRahman, Md. ShamimAkhter, 'Biodiesel from cotton seed oil and its effect on engine performance and exhaust emissions, *Applied Thermal Engineering*, 2009, 29, pp2265–2270
- [7] T. VenkateshwaraRao, G. prabhakarrao, K. Hema Chandra reddy. 'Experimental investigation of pongamia, Jatropha, Neem methyl esters as biodiesel in CI engine. *JJMIE*. 2008, 2, pp117-122.
- [8] A.E. Atabani, A.S.Silitonga, H.C.Ong, T.M.I.Mahlia, H.H.Masjuki, IrfanAnjumBadruddin, H.Fayaz, 'Non-edible vegetable oils: A critical evaluation of oil extraction, fatty acid compositions, biodiesel production, characteristics, engine performance and emissions production, *Renewable and Sustainable Energy Reviews*' , 2013, 18, pp 211–245
- [9] Yie Hua Tan, Mohammad Omar Abdullah, Cirilo Nolasco-Hipolito, Nur Syuhada Ahmad Zauzi, Georgie Wong Abdulla "Engine performance and

emissions characteristics of a diesel engine fueled with diesel-biodiesel-bioethanol emulsions”

[10] Rao et al, G. L. K. . Relationships among the physical properties of biodiesel and engine fuel system design requirement. *International Journal of Energy And Environment*,2010, Vol. 1, Issue. 5, pp. 919- 926.

[11] Ganesh, G. Gowrishankar, ‘Effect of Nano-fuel additive on emission reduction in a Biodiesel fuelled CI engine’,2011, IEEE, DOI: 10.1109/ICECENG.2011.6058240

[12] Kumar B Rajesh, Saravanan S, Rana D, Anish V and Nagendran A 2016 Effect of a sustainable biofuel – n-octanol – on the combustion, performance and emissions of a DI diesel engine under naturally aspirated and exhaust gas recirculation (EGR) modes *Energy Conversion and Management* 118 (2016) 275–86.

[13] J. Sadhik Basha, R. B. Anand, “ The influence of nano additive blended biodiesel fuels on the working characteristics of a diesel engine” *Braz. Soc. Mech. Sci. Eng.*,2013, 35:257–264

[14] Sadhik Basha J, Anand RB ‘Performance and emission characteristics of a DI compression ignition engine using carbon nanotubes blended diesel’. *Int J Adv Ther Sci Eng*,2010, 1:67–76

[15] DeLuca LT, Galfetti L, Severini F ‘Combustion of composite solid propellants with nanosized aluminium’. *Combust Explos Shock Waves*,2010, 41:680–692

EXPERIMENTAL AND CFD ANALYSIS OF A LITHIUM-ION BATTERY COOLING SYSTEM FOR ELECTRIC VEHICLES USING A PHASE-CHANGE MATERIAL AND HEAT PIPES

Gangula Chiranjeevi Reddy¹

Mr. Raju perala²

Dr. Srinivasulu Pulluru³

¹M.Tech (Thermal Engineering)Department of mechanical engineering vaagdevi college of engineering (UGC autonomous) approved by AICTE & permanent affiliation to jntuh, hyderabad.p.o, bollikunta, Warangal urban- 506005.

² Assistant professor Department of mechanical engineering vaagdevi college of engineering (UGC autonomous) approved by AICTE & permanent affiliation to jntuh, Hyderabad. p.o, bollikunta, Warangal urban- 506005.

³Professor and Head of the Department of mechanical engineering vaagdevi college of engineering (UGC autonomous) approved by AICTE & permanent affiliation to jntuh, Hyderabad. p.o, bollikunta, Warangal urban- 506005.

Abstract

Lithium-ion power battery has become one of the main power sources for electric vehicles and hybrid electric vehicles because of superior performance compared with other power sources. In order to ensure the safety and improve the performance, the maximum operating temperature and local temperature difference of batteries must be maintained in an appropriate range. The effect of temperature on the capacity fade and aging are simply investigated. The electrode structure, including electrode thickness, particle size and porosity, are analyzed. It is found that all of them have significant influences on the heat generation of battery.

In this paper, the modeling in CREO parametric software and analysis done in ANSYS. The model designed with different type of heat pipe shapes and analyzes the heat pipe with different mass flow inlets (30, 40, 50, 60& 70L/min). In this thesis CFD analysis to determine the pressure, velocity, heat transfer coefficient, mass flow rate and heat transfer rate for the different designs of heat pipe and different mass flow inlets. In this thesis the thermal analysis to determine the temperature distribution and heat flux for two types of phase change materials (RT50 & Li Fe PO4).

Furthermore we are conducting the experimental study with different type of heat pipe shapes and analyzes the heat pipe with different mass flow inlets (30, 40,50,60& 70L/min).**Key words:** CFD, Mass flow rate, CREO, Lithium- ion battery, PCM.

1.Introduction

Lithium-ion battery (LIB) has received considerable attention for traction uses due to the higher energy density (70-170 Wh/kg), power capabilities, lowest standard reduction voltage ($E_0 = -3.04V$) and low atomic mass compared to previous battery technologies. Figure shows the relationship between various types of secondary batteries in a Ragone plot. The required amount of energy stored in PHEVs and EVs is much higher than for HEVs in order to be able to travel long distances in all electric range. In the 2000s, the LIB are considered as one of the most promising solutions for environment-friendly transportation such as HEVs, PHEVs and EVs. Basically, LIB includes different components (cathode, anode, separator and electrolyte) and work according to the so-called "extraction/insertion" process. The LIB cells are configured in various shapes such as coin, cylindrical, pouch and prismatic.

Phase Change Materials PCM Manufacturers Building & Electronic Air Condition

T-series 18Cto29C: Phase Change Materials, PCM Latest TM 29T Brand with Melting Point 29°C and Latent Heat of fusion 175 K Joule/Kg or 260 K Joule/liter. Its best suited for Air-Condition Back-up to BT Shelter or Telecom Shelter. Temperatures from 18°C to 29°C are used in Air Conditioning. Other M.P. grades are summarized in the link. S-series 32Cto48C: Phase Change Material PCM Latest TM 36S Brand with Melting Point 36°C and Latent Heat of fusion 260 K Joule/Kg or 357 K Joule/liter. It is best suited for Air-Cooled Telecom Shelters. Other M.P. grades are summarized in the link. Hot Pads and Solar Heating systems use our PCM Latest TM 58, melting at 58°C. Electronic or Telecom Enclosure: PCM are widely used in Electronic or Telecom Enclosures (BT Shelters) is Latest TM 29T for Air-condition AC Air Conditioning with PCM and you may also visit our page AC Backup by PCM or Phase Change Latest TM 36S for Free Cooling. We also offer Polymer-based PCM-Filled Profiles Panels and Aluminum PCM-Filled Profiles or any other Container like Balls or Bottles or Heat Sinks and so on. We also supply Telecom Shelters and provide engineering services for Back-up Cooling in Existing and New Shelters. If your interest is only in PCM for Telecom Shelter then go to our Page Telecom Shelters PCM.

2.Literature Review

Kusekar S.K et, al (2015) has conducted an experiment in Design and development of electrical car to illustrate an implementation of electric vehicle technology on a small scale. Here we observed how to design an electric car with less cost and have studied about various components that is required to design an electric car. It shows that electrical battery operated vehicle is more suitable than other vehicle because the cost of the electricity is low and also maintenance cost is less. Also we got an idea about how to calculate the torque required moving the vehicle. In this study we understand the basic principles of chassis designing, steering system, caster, camber, drift, acceleration, top speed and performance tuning of the vehicle.

K.Vignesh et, al (2015) performed an experiment in the Design and fabrication of Free Energy Bicycle which would produce a cheaper and effective result than the existing system. In this, they have fitted a dynamo in the bicycle which is in contact with the rear wheel. The motor is also connected

with a rear wheel via main shaft to transmit power to the wheel and other end of dynamo is connected with the two terminals of the battery for the recharging purpose. Awash Tekle et, al (2014) performed an experiment on the topic Renewable Energy Use for Continuous electric vehicles Battery charging capacity in mobile. This paper presents and studies on renewable energy use, by integrating solar and wind energy for continuous electric vehicle battery charging capacity in mobility. Here, the power for electric vehicle is generated from solar cells and wind turbine and it is fed to the battery for charging the inverter.

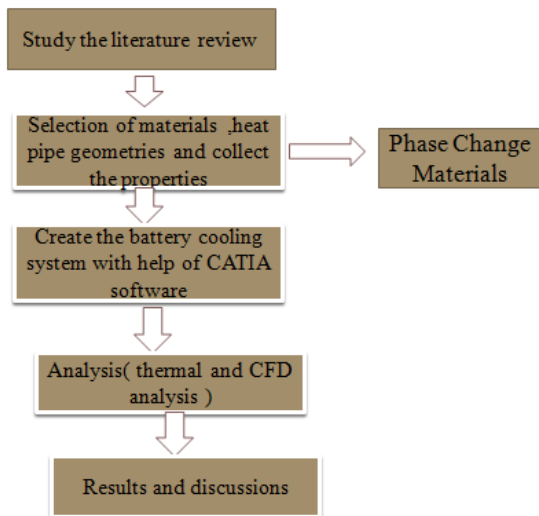
S.M.Ferdous et, al (2011) conducted an experiment on Electric vehicle which is based on the concept of charging the batteries of an electric vehicle when it is in motion. In general the energy storage capacity of the battery used in electric vehicle is very low compare to the conventional fuels used in modern automobiles. Hence they have found out a method to recharge the battery using renewable resource.

A A Pesaran et al. introduced the thermal performance of electric car battery modules and packs. With the purpose of precisely design the thermal management system for electric cars, so thermal analysis should be conducted. Therefore, to get the estimate of the thermal performance, the heat transfer principles and finite element analysis software have been used.

Objectives

- To increase the heat transfer coefficient and mass flow rate at various heat pipe geometries.
- To increase the heat flux at various heat pipe geometries with phase change materials.

Methodology



3. Modeling and Analysis

Computer-aided design (CAD) is the use of computer structures (or workstations) to useful resource within the introduction, modification, evaluation, or optimization of a layout.

In mechanical layout it is referred to as mechanical layout automation (MDA) or laptop-aided drafting (CAD), which incorporates the procedure of making a technical drawing with

the use of laptop software program. CAD software program for mechanical layout uses either vector-primarily based photographs to depict the items of conventional drafting, or may also produce raster pix showing the general look of designed objects. However, it involves extra than just shapes.

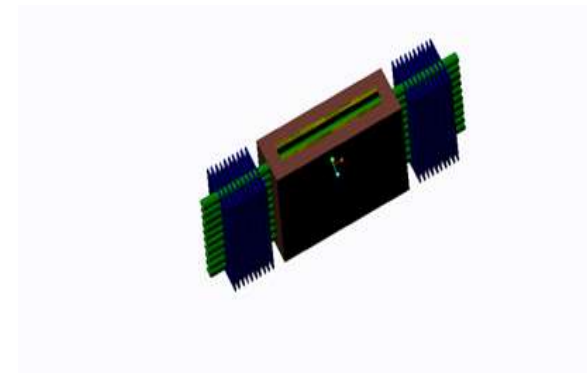
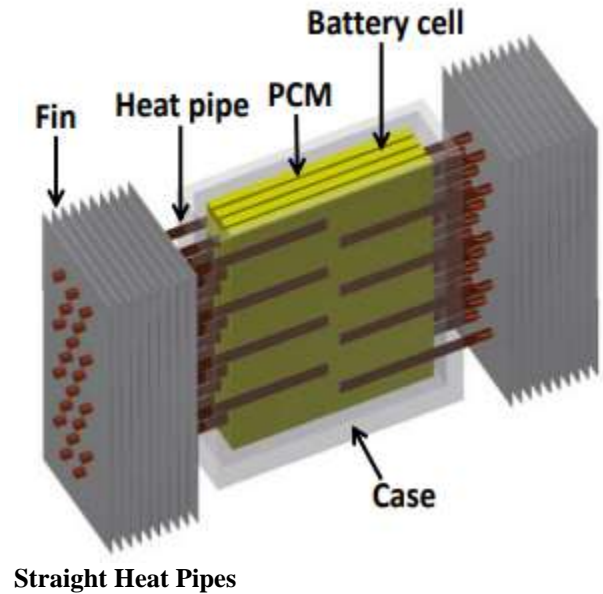


Figure1: Straight Heat Pipes

Bend Type Heat Pipes

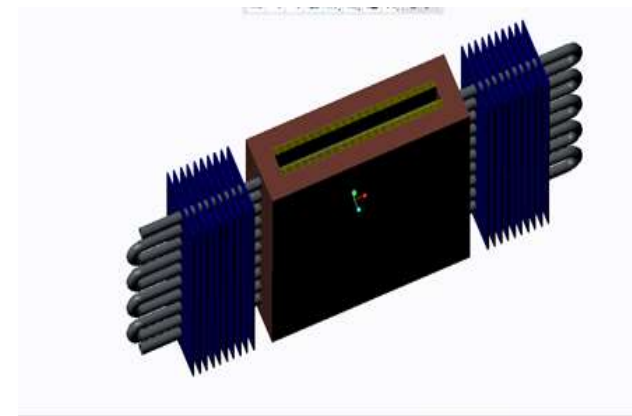


Figure 3: Bend type Heat Pipes

Introduction To FEA

Finite element evaluation is a way of solving, commonly about, sure issues in engineering and science. It is used in particular for troubles for which no precise solution, expressible in some mathematical shape, is to be had. As such, it is a numerical rather than an analytical approach. Methods of this type are wished because analytical techniques can not address the actual, complex problems which are met with in engineering. For instance, engineering strength of materials or the mathematical theory of elasticity may be used to calculate analytically the stresses and strains in a dishonest beam, however neither may be very successful in locating out what is occurring in part of a car suspension system for the duration of cornering.

Introduction to CFD

Computational fluid dynamics, usually abbreviated as CFD, is a branch of Fluid mechanics that uses numerical techniques and algorithms to solve and analyze troubles that contain fluid flows. Computers are used to carry out the calculations required to simulate the interaction of fluids and gases with surfaces defined through boundary conditions. With excessive-speed supercomputers, better answers may be achieved. Ongoing research yields software that improves the accuracy and pace of complex simulation eventualities along with transonic or turbulent flows. Initial experimental validation of such software is carried out the usage of a wind tunnel with the very last validation coming in complete-scale trying out, e.g. Flight tests.

CFD Methodology

In all of those processes the same fundamental system is followed:

- During preprocessing
- The geometry (bodily bounds) of the problem is described.
- The extent occupied by the fluid is split into discrete cells (the mesh). The mesh can be uniform or non-uniform.
- The bodily modeling is described – as an example, the equations of movement + enthalpy + radiation + species conservation.

Material Properties

For cooling fans

Density = 2719kg/m³

Specific heat = 871j/kg-k

Thermal conductivity =202.4w/m-k

For heat pipes

Density = 2920kg/m³

Specific heat = 126.8j/kg-k

Thermal conductivity = 11940w/m-k

For battery outer case

Density = 2688kg/m³

Volume XIV, Issue XI, November/2022

Specific heat = 905j/kg-k

Thermal conductivity = 1 w/m-k

Phase change materials

RT50

Density = 753kg/m³

Specific heat = 2000 j/kg-k

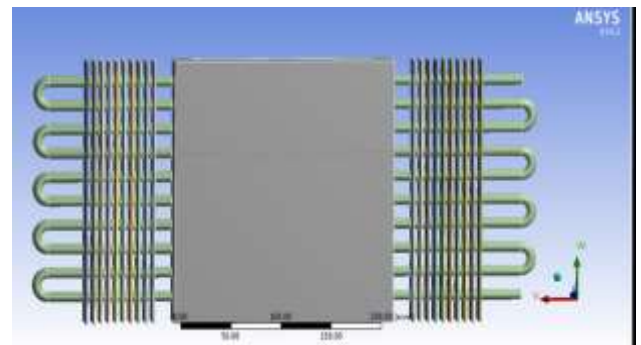
Thermal conductivity = 0.2w/m-k

Li Fe PO4

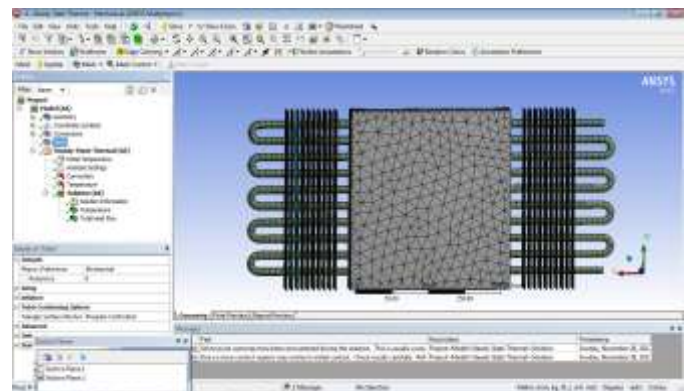
Thermal conductivity = 0.35w/m-k

CFD and Thermal Analysis of Lithium-Ion Battery Cooling System

Imported model



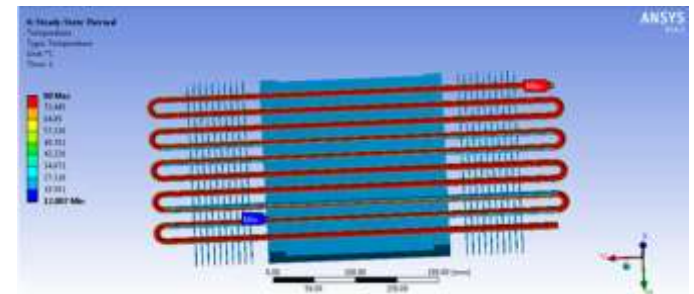
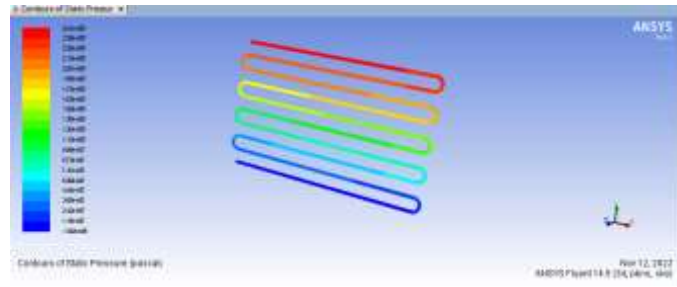
Meshed model



Pressure

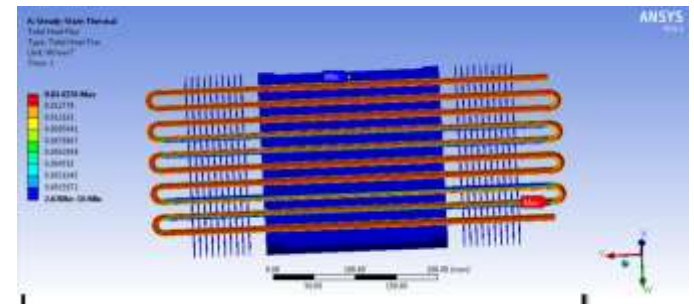
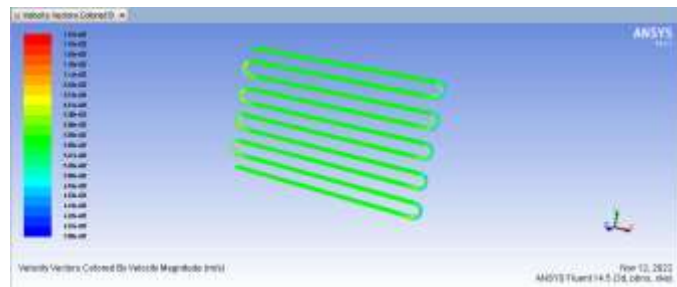
Material- RT50 (Phase Change Material)

Temperature



Velocity

Heat flux

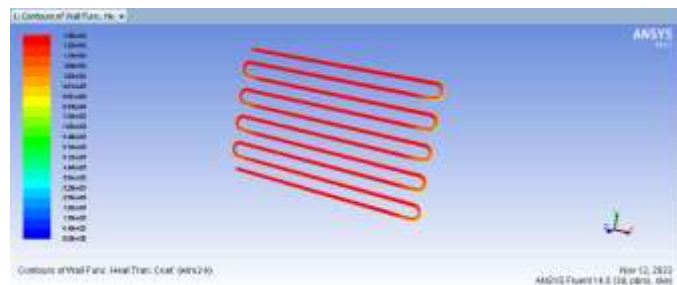


Heat Transfer Coefficient

Analysis Results and discussions

CFD analysis results tables

Case 1: straight type



Mass Flow Rate & Heat Transfer Rate

At mass flow rate (L/min)	Pressure (Pa)	Velocity (m/s)	Heat transfer coefficient (w/m2-k)	Mass flow rate (kg/sec)	Heat transfer rate
30	5.33e+06	2.15e+03	4.8e+03	0.000380	2.228
40	9.93e+06	3.00e+03	6.16e+03	0.000748	4.423
50	1.36e+07	3.56e+06	7.08e+03	0.001036	6.12
60	1.91e+07	4.29e+03	8.28e+03	0.00151	8.92
70	2.51e+07	5.02e+03	9.51e+03	0.00084	4.9250

Mass Flow Rate	(kg/s)
inlet	0.19999996
interior-partbody	746.15308
outlet	-0.19846933
wall-partbody	0
Net	0.0015306324

Case 2: Bend type

Total Heat Transfer Rate	(w)
inlet	1177.5229
outlet	-1168.5139
wall-partbody	0
Net	9.0090332

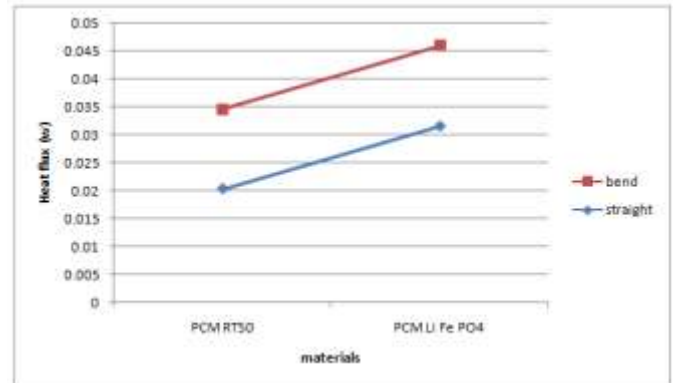
At mass flow rate (L/min)	Pressure (Pa)	Velocity (m/s)	Heat transfer coefficient (w/m2-k)	Mass flow rate (kg/sec)	Heat transfer rate (w)
30	3.97e+07	3.93e+03	7.24e+03	0.000281	1.666
40	2.31e+08	7.97e+03	1.28e+04	0.001530	9.009

50	2.48e+08	1.12e+04	1.80e+04	00.00150	9.00329
60	7.87e+08	1.60e+04	2.29e+04	0.000625	3.2189
70	1.34e+09	2.00e+04	2.76e+04	0.0002172	2.3659

According to the plot, the maximum mass flow rate at 70 lit/min with bend type heat pipes.

Thermal analysis results tables

Models	Material	Temperature(°C)		Heat flux(w/mm ²)
Design1 (straight heat pipes)	PCM RT50	19.213	80	0.020264
	PCM Li Fe PO4	17.838	80	0.031486
Design 2(bend type heat pipes)	PCM RT50	12.913	80	0.014391
	PCM Li Fe PO4	12.007	80	0.014376

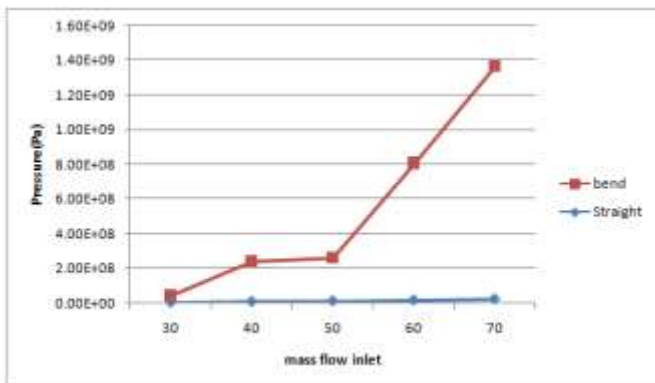


EXPERIMENTAL SETUP

In this study, the cooling system used paraffin PCM with embedded heat pipes. We intend to measure both the normal heat emission of the LiB in the charging and discharging states, and the abnormal heat emission of the LiB during thermal runaway. Each battery in our device was in contact with a number of narrow heat pipes, and the surrounding space of the LiB was filled by the PCM. The cooling system had two heat transfer routes through the heat pipes from the surface of the LiB to the outside of the device, namely (1) LiB–HP–outside and (2) LiB–PCM–HP–outside, as shown in Fig. 1. It seemed as if there was a relatively large amount of thermal resistance between the LiB surfaces and the heat pipes that came into contact with them, but the thermal resistance must have been quite small between the LiB surfaces and the PCM, and between the PCM and the HP surfaces because the PCM was poured in the liquid phase into the space around the LiB and HPs before solidifying, which produced an almost ideal contact interface between the materials. Cooling fins on the condensation area of the heat pipes released the thermal energy into the atmosphere.

Graphs

Pressure



According to the plot, the maximum pressure at 70 lit/min with bend type heat pipes.

Mass flow rate

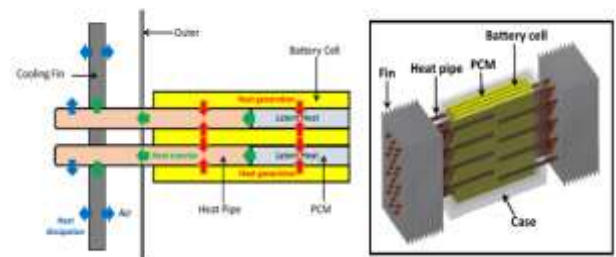
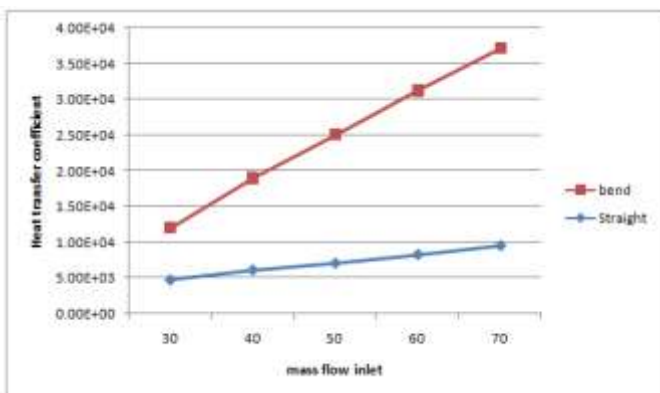


Fig. Conceptual diagram of the hybrid cooling system using HPs and a paraffin PCM. (a) The path of heat transfer in the system, and (b) an overview of the general construction of the system.

Four A4 sized mimic battery were made, as shown in Fig. 2, in which a polyimide heater ($194 \times 144 \times 0.2 \text{ mm}^3$) was placed between two aluminum plates ($200 \times 175 \times 4 \text{ mm}^3$) and was covered with a laminated film composed of synthetic resin and aluminum foil. A vinyl chloride ($\text{CH}_2=\text{CHCl}$) container (inner height = 220 mm, inner width = 200 mm, inner depth = 49 mm) contained four mimic batteries, as shown in Fig. 3. The thickness of the container body was 10–35 mm, and its thermal conductivity was $0.17 \text{ W m}^{-1} \text{ K}^{-1}$. A cooling unit composed of 20 heat pipes and 10 cooling fins was put in the condensation area, as shown in Fig. 4. The HPs had an inner radius of 9 mm, length of 220 mm, width of 10 mm, and a thickness of 3 mm, which resulted in the flat shape at the evaporator area. The working fluid was pure water.

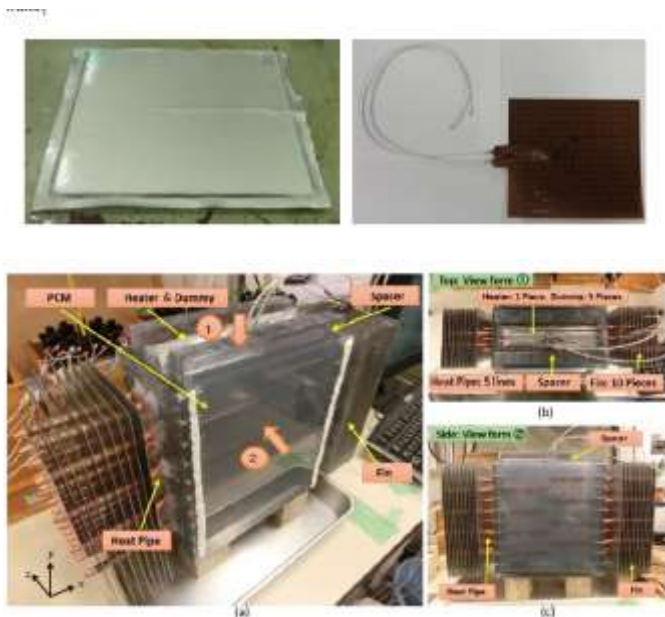


Fig. The experimental setup using the PCM, HPs, and cooling fins (a) as viewed from above and slightly to the side, (b) as viewed from directly above, and (c) as viewed from the front. This test module considered a potential size miniaturization that may be needed for future EV applications, and the length of the condensation part of the unit was 80 mm, while the ratio between the evaporation and condensation areas was 4:3. In this prototype setup, little consideration was given to the capillary limit and the subsequent maximum amount of heat that could be transported during the design of the length of the heat pipes. The cooling fins were designed so that there would be 7.5 mm of space between each element. Overall, the maximum heat release of this system was at $70 \text{ }^\circ\text{C}$ – $80 \text{ }^\circ\text{C}$, which was when abnormal heat emissions would occur.

RT50 was applied to the PCM in the test module; the physical properties of RT50 are shown in Table 1. RT50 is a paraffin wax PCM with a fusion temperature range of $46 \text{ }^\circ\text{C}$ – $50 \text{ }^\circ\text{C}$. Previous studies have recommended the fusion range of the PCM used in an LiB be mostly $40 \text{ }^\circ\text{C}$ – $44 \text{ }^\circ\text{C}$ because the

optimum temperature range for operating LiBs is approximately $15 \text{ }^\circ\text{C}$ – $40 \text{ }^\circ\text{C}$. However, the aim of the present study is to explore countermeasures for the abnormal heat emission of LiBs that eventually leads to thermal runaway; as such, we decided to use an organic PCM with a somewhat higher melting temperature. In the test module, 842 cm^3 of RT50 was filled as the PCM, and the total amount of latent heat was $1.24 \times 10^5 \text{ J}$.

Experiments

After 120 s from the start time of the experiment, the temperature of “No device” setup exceeded $80 \text{ }^\circ\text{C}$, becoming dangerous temperature leading to thermal runaway. After 240 s from the start time, the temperature of “PCM” and “HP” setups were exceeded $80 \text{ }^\circ\text{C}$. Afterwards, the experiment of “No device” setup was finished because the temperature gradient became suddenly large after 300 s. After 720 s, all experimental setup was exceeded $80 \text{ }^\circ\text{C}$. The experiment of “PCM” was finished because the temperature gradient became suddenly large after 1500 s. The temperature difference between “HP” and “HP + PCM” setups became 39.3°C , 32.5°C and $28.4 \text{ }^\circ\text{C}$ at 1500 s, 2700 s and 3600 s, respectively. The time to reach 80°C , which is dangerous temperature leading to thermal runaway, are 104 s, 187s, 216 s and 708 s in “No device”, “PCM”, “HP” and “HP + PCM” setups, respectively. The condition of “HP + PCM” setup extended the time to reach 80°C , by about 7-times more than “No device” setup.

Initially, from the result of the “No device” setup, as has been predicted, as the test module did not have any cooling measures, it could not control the temperature increase under the assumed abnormal heating condition.

As for the “PCM” setup, basically, it could not control the temperature increase under the assumed abnormal heating condition. However, from 600–900 s, it stopped increasing and stayed within a range of $\pm 3 \text{ }^\circ\text{C}$. This result shows that the temperature rise in the mimic battery was restricted by the latent heat capacity of the PCM. The reason why the temperature remained at a temperature somewhat higher than that of the melting point of the PCM is thought because although the temperature around the melting interface of the PCM was near the material’s melting point, there was a large temperature gradient inside the melted PCM because of its small thermal conductivity ($0.2 \text{ W m}^{-1} \text{ K}^{-1}$). To balance the heat from the mimic battery and the melting rate of the PCM, the temperature of the melted PCM, and the mimic battery adjacent to it, increased to approximately $120 \text{ }^\circ\text{C}$. Figure 8 (a) also shows that after most of the PCM had melted, the temperature rose again. This result led us to believe that the melting point of the PCM, and its quantity in the setup, greatly influences the temperature that is maintained and the total amount of heat absorbed.

In the “HP” setup, it could not control the temperature increase under the assumed abnormal heating condition either. However, the temperature became almost steady at this point, as it changed only within $\pm 10 \text{ }^\circ\text{C}$ between 1,800–3,600 s (at which point the experiment ended). At the end of the measuring time, the inner temperature was $147.2 \text{ }^\circ\text{C}$. Under this condition, heat generated inside the system was transported to the ambient air through the heat pipes and heat sink; when both of the amounts of heat were equal to one another, the temperature became stationary. The heat transfer rate of the fins can be determined by Eq. (2), and the heat

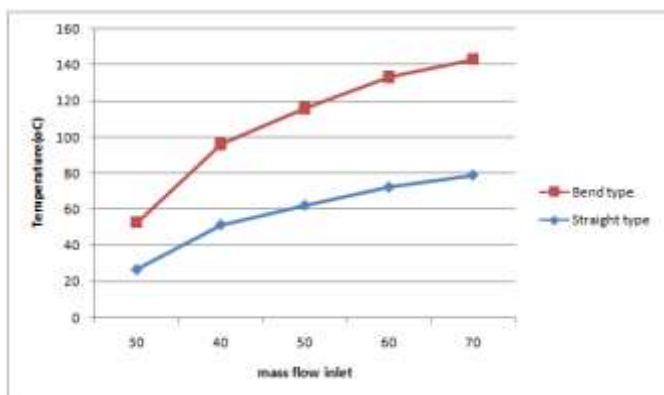
removal from the fins was determined by the temperature difference, ΔT , between the fins and the ambient air. As the fins were tightly connected with the heat pipes and because the temperature difference between the two ends of the heat pipe itself was small, the fin temperature was strongly related to the temperature inside the system. In this experiment, depending on the thermal efficiency of the particular fins used and the resultant fin–surface temperature, the temperature of the mimic battery became approximately 140 °C to balance out the inner heat generated and the heat lost to the air. Therefore, if the efficiency of the fins is improved, the temperature at which the mimic battery is maintained could be lowered.

In the “HP + PCM” setup, the inner temperature of the mimic battery exceeded 80 °C after 708 s, and it reached 100.8 °C after 1,800 s. The inner temperature at the end of the measuring time (*i.e.*, 3,600 s) was 118.8 °C. The experiment indicated that by using this experimental setup, the inner temperature of the mimic battery was 28.4 °C lower at the end of the measuring time than in the “HP” setup. However, under this condition, the temperature still kept increasing after 3,600 s, and it seemed to take longer to reach a steady state. The final steady temperature will be determined by the thermal performance of the heat sink. The PCM is thought to have reduced the increase in the heating rate of the mimic battery in this setup. The reason why a very long time was needed to reach the steady state is because the thermal conductivity of the PCM used is extremely small (0.2 W m⁻¹ K⁻¹). We think that if the thermal conductivity of the PCM was increased, the system would have a more evenly distributed temperature inside the PCM, which would reduce the rate at which the temperature increases.

Table: experimental results of temperatures

Mass flow inlet (L/min)	Temperature (oC)	
	Straight type	Bend type
30	26.82	25.8
40	51.61	44.3
50	62.35	53.4
60	72.35	60.7
70	79.06	63.9

Graph: mass flow inlet and cases Vs temperatures



Conclusion

Lithium-ion power battery has become one of the main power sources for electric vehicles and hybrid electric vehicles because of superior performance compared with other power sources. In order to ensure the safety and improve the performance, the maximum operating temperature and local temperature difference of batteries must be maintained in an appropriate range. The effect of temperature on the capacity fade and aging are simply investigated. The electrode structure, including electrode thickness, particle size and porosity, are analyzed. It is found that all of them have significant influences on the heat generation of battery.

In thesis the modeling in CREO parametric software and analysis done in ANSYS. The model designed with different type of heat pipe shapes and analyzes the heat pipe with different mass flow inlets (30& 50L/min).

By observing the CFD analysis mass flow rate, heat transfer rate, heat transfer coefficient values are increases by increasing the mass flow inlets and heat transfer rate more at design2 (bend type heat pipes).

By observing the thermal analysis the heat Flux value is more for lithium ion phosphate phase change material than RT50 phase change material at design2 (U-bend heat pipes)

So it can be concluded the design2 (U-bend type heat pipes) is better model for Lithium-ion power battery cooling system.

References

1. Wagner, R. Valve regulated lead-acid batteries for telecommunications and UPS applications. In Valve-Regulated Lead-Acid Batteries; Rand, D.J., Ed.; Elsevier B.V.: Oxford, UK, 2004; pp. 435–465.
2. Percy, K. Ausnet Testing New Battery System to Curb Power Outages in Summer. Available online: <http://www.abc.net.au/news/2015-01-07/ausnet-trialling-new-system-to-curb-power-outages-on-hot-days/6004454> (accessed on 30 May 2015). Energies 2015, 8 10172
3. Pesaran, A.A. Battery thermal models for hybrid vehicle simulations. J. Power Sci. 2002, 110, 377–382.
4. Rothgang, S.; Rogge, M.; Becker, J.; Sauer, D.U. Battery design for successful electrification in public transport. Energies 2015, 8, 6715–6737.
5. Shabani, B.; Andrews, J. Standalone solar-hydrogen systems powering fire contingency networks. Int. J. Hydrogen Energy 2015, 40, 5509–5517.
6. Pesaran, A.; Vlahinos, A.; Stuart, T. Cooling and Preheating of Batteries in Hybrid Electric Vehicles; National Renewable Energy Laboratory (NREL): Colorado, CO, USA, 2003.
7. Ji, Y.; Wang, Y. Heating strategies for Li-ion batteries operated from subzero temperatures. Electrochim. Acta 2013, 107, 664–674.
8. Szenté-Varga, D.; Horvath, G.; Rencz, M. Thermal characterization and modelling of lithium-based batteries at low ambient temperature. In Proceedings of the 14th International Workshop on Thermal Investigation of ICs and Systems, 2008 (THERMINIC 2008), Rome, Italy, 24–26 September 2008.

EXPERIMENTAL INVESTIGATION AND CFD MODELLING OF A THERMOSYPHON

Tejavath Narendar¹Dr. K.Parvesh Kumar²Dr. Srinivasulu Pulluru³

¹M.Tech (Thermal Engineering)Department of mechanical engineering vaagdevi college of engineering (UGC autonomous) approved by AICTE & permanent affiliation to jntuh, hyderabad.p.o, bollikunta, Warangal urban-506005.

²Professor Department of mechanical engineering vaagdevi college of engineering (UGC autonomous) approved by AICTE & permanent affiliation to jntuh, Hyderabad. p.o, bollikunta, Warangal urban- 506005.

³Professor and Head of the Department of mechanical engineering vaagdevi college of engineering (UGC autonomous) approved by AICTE & permanent affiliation to jntuh, hyderabad. p.o, bollikunta, Warangal urban-506005.

Abstract

A bibliographical review on design & modelling & heat transfer in gravity assisted Closed Loop Two Phase Thermosyphons (CLTPT) with channels having a hydraulic diameter of the order of some millimeters and input power below 1 kW is proposed. The available experimental works quoted in the open literature are critically analyzed in order to highlight the main results obtained paying special attention to between void factor and heat transfer, velocity, pressure.

In this project analysis of two phase thermosyphon has been considered in the present study, under steady state conditions using thermodynamic and heat transfer correlation to find heat transfer & overall heat transfer coefficient in evaporator, condenser, riser, downcomer. By help of correlation used to find pressure balance within the system. CFD and Experimental analysis was carried out to predict how phase change takes place within the loop.

1. INTRODUCTION

Thermosyphon is a method of passive heat exchange, based on natural convection, which circulates a fluid without the necessity of a mechanical pump. Thermosiphoning is used for circulation of liquids and volatile gases in heating and cooling applications such as heat pumps, water heaters, boilers and furnaces. Thermosiphoning also occurs across air temperature gradients such as those utilized in a wood fire chimney or solar chimney.

This circulation can either be open-loop, as when the substance in a holding tank is passed in one direction via a heated transfer tube mounted at the bottom of the tank to a distribution point—even one mounted above the originating tank—or it can be a vertical closed-loop circuit with return to the original container. Its purpose is to simplify the transfer of

liquid or gas while avoiding the cost and complexity of a conventional pump.

A two-phase thermosyphon is highly effective passive heat transfer system. Generally, it consists of an evacuated tube that filled with working fluid at a rated filled ratio to transport heat throughout the system. A thermosyphon is divided into three parts; an evaporator section, adiabatic section (transport) and condenser section. It may have multiple heat sources or sinks with or without adiabatic sections depending on specific application and design. It works by absorbing latent heat of vaporization from a heat source. It is a fact that thermosyphons are very effective, low cost and reliable heat transfer device for many thermal and heat recovery applications. The TPT technology has found increase interest of the researches in a wide range of applications from small-scale to large-scale systems. TPTs are use in chemical and petroleum industries, electronic cooling, telecommunication devices, energy storage systems, thermoelectric power generators, seasonal cooling, and load reduction of buildings.

As heat generation from various systems increased and there is limit on heat transfer rate in air cooling system the interest for using liquid cooling for high heat flux applications has risen. Thermosyphon cooling is an alternative liquid cooling technique in which heat is transferred as heat of vaporization from evaporator to condenser with a relatively small temperature difference. The thermosyphon has been proved as a promising heat transfer device with very high thermal conductance. High-capacity passive cooling system studied in this project is a thermo loop device that utilizes the thermo loop heat transfer concept. This device is an assemblage of Evaporator, Condenser, Cooling liquid, Non-return valve and Reservoir charged with a liquid for removing heat from any source upon which the evaporator is attached. Thermal management of electronic systems is one of the major focal points of the design system and is primarily concerned in keeping the

temperature of the various components within a maximum allowable limit.

1.1 WORKING OF THERMOSYPHON

In the evaporator, where the circulating fluid is heated, the liquid boils and in the condenser, where the heat is rejected to environment, the vapour completely comes back to liquid phase. The system relies on gravity for the liquid return to the evaporator. In these applications the loop thermosyphons usually operate at low pressure and temperatures comprise into the range 20–120 °C. The operating principle of those devices with respect to the well-known single tube thermosyphon, deals with the separation of the pathways of the replenishment liquid from that of the vapour escaping from the evaporation zone.

In such a way a meaningful increase of heat transport with respect to the conventional two phases closed thermosyphons is obtained and the classical operative limitations like flooding or entrainment limitations are overcome. These effects are more remarkable as the size of the devices decreases. Several key parameters influences the performances of the close loop two phase thermosyphon systems like:

- Heat input.
- Internal tube diameter.
- Distance between evaporator and condenser.
- Thermo-physical properties of the working fluid.
- Operating pressure.
- Sub-cooling of the fluid.
- Volumetric filling ratio (fill charge ratio).
- Pressure drops and thermal resistances at different part of the thermosyphon.

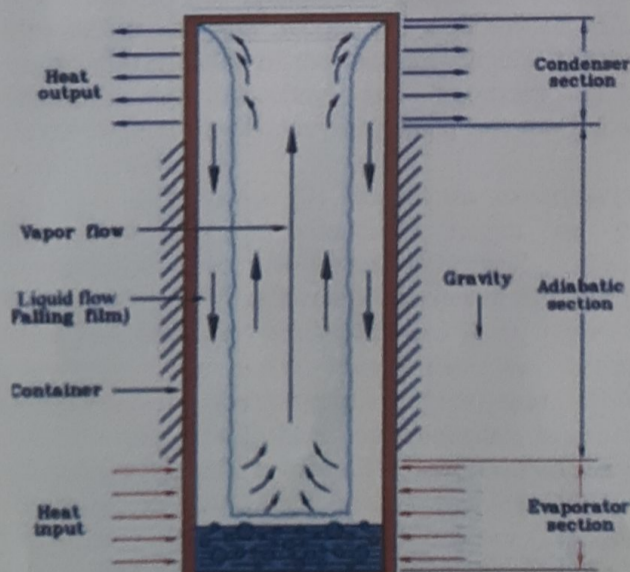


Fig. . Basic Working Principle of a Thermosyphon

2.LITERATURE REVIEW

Many investigations been carried out in order to analyze the thermal performance of a thermosyphon and many have looked into different factors that influence its performance. These are as follows.

Faghri [1] utilization of the two-phase thermosyphons (TPTs) is expanding for some warmth exchange applications. The performance of thermosyphon systems. The impact of the influencing parameters on the execution of for example geometry, filling ratio, working liquid and the inclination angle by different researchers. The various working limits happening in a thermosyphon that includes dry out, and flooding affects likewise examined. Based on many factors reviewed it shows that the filling ratio exerts small influence in heat transfer and influence is more noticeable for inclination angles. Circulation of working fluid that aided by effects of gravity disable thermosyphon to perform in horizontal position. In addition, it is expected dry out effect could easily occur in the case of high-power input, low fill ratio and high inclination angle. This paper could utilize as the beginning point for the researches keen on and their renewable energy applications.

Amatachaya et al [2] compared the heat transfer characteristics of a flat two-phase closed thermosyphon (FTPCT) and a conventional two-phase closed thermosyphon (CTPCT). In the investigation thermosyphons with inner diameter of 32 mm and length of 980 mm were compared by varying the heat input, filling ratio and aspect ratio. From the results it was reported that the heat transfer coefficient of the CTPCT and FTPCT increased with decrease in filling ratios. Based on their finding it shows that thermosyphon structure has significant effect on overall heat transfer coefficient.

Kyung Mo et al [3] compared the thermal performance between annular and concentric thermosyphons with individual length of 215 mm and inner and outer diameter of 22 mm and 25.4 mm at different fill ratios. Both the thermosyphons performance were studied based on changes of the entrainment limit at different fill ratio. Based on their findings concentric thermosyphons has enhanced the entrainment limit far better than an annular thermosyphon as the fill ratio increases. This is because reduction of the cross-sectional area for vapor flow results in increase of the shear at the vapor-liquid interface causes such enhancement.

Hasna Louahlia et al [4] studied the evaporation and condensation heat transfer coefficients for looped thermosyphon. The investigation carried out by varying the heat load throughout the experiment. Result shows that condenser and evaporator thermal

OBJECTIVES

- a) Geometry of loop is defined by using correlation.
- b) The physical parameter is defined like heat transfer, pressure, velocity by help of correlation.
- c) The systems having small heat generation rate may be used to carry heat at relatively small temperature difference in system.
- d) Reduce moving mechanical devices and Noise generation as conventional system has moving components which affects environment.
- e) To overcome continuous power consumption in conventional system and reduce power consumption.
- f) To verify heat dissipation rate and effectiveness of thermosyphon cooling system to compare result with conventional cooling system.

3.MATERIALS AND METHODS

Water is a colorless, odorless and tasteless liquid, stable and nontoxic. Its solid and vapor forms are ice and steam, although the term "water" is sometimes used for all three phases. With a narrow liquid range, it is one of the few chemicals known to exist commonly in all three phases.

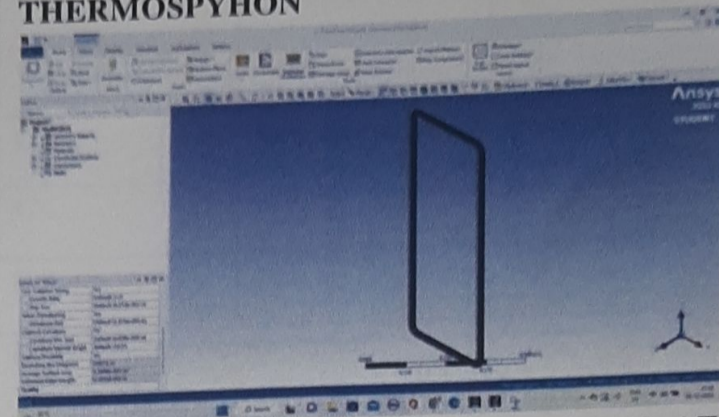
Physical Properties

Water is a relatively "light" molecule with a molar mass (molecular weight) of 18.01, giving the vapor a density of 0.623 relative to air. The high dielectric constant (Table 2) of water is largely responsible for its good solvent properties. It is, however, a weak electrolyte when pure, but with dissolved ions increases its conductivity by several orders of magnitude. The molecule's small size (O-H bond length is 96 pm) gives high permeability through membranes. In many ways water is an anomalous fluid largely explained by strong hydrogen bonding resulting in the formation of loose clusters of molecules. It has a high latent heat (see Steam Tables) and high melting point, and expands on freezing. Above the critical point (Table 1) water is "supercritical" and the distinction between liquid and vapor disappears.

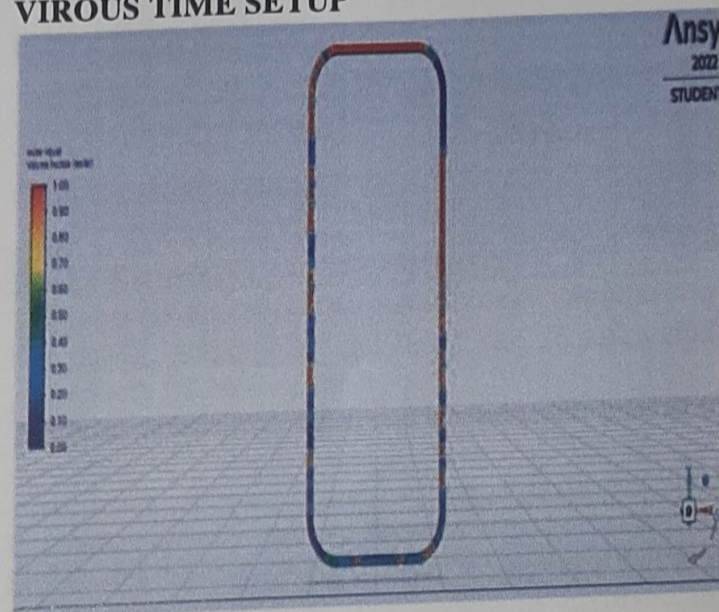
CFD analysis for liquid flow, gas flow, or heat transfer can help you deliver innovative designs and greater product efficiency. Typical problems solved include:

- Pressure drop for a valve to calculate its efficiency
- Airflow inside a home or office environment to calculate thermal comfort factors

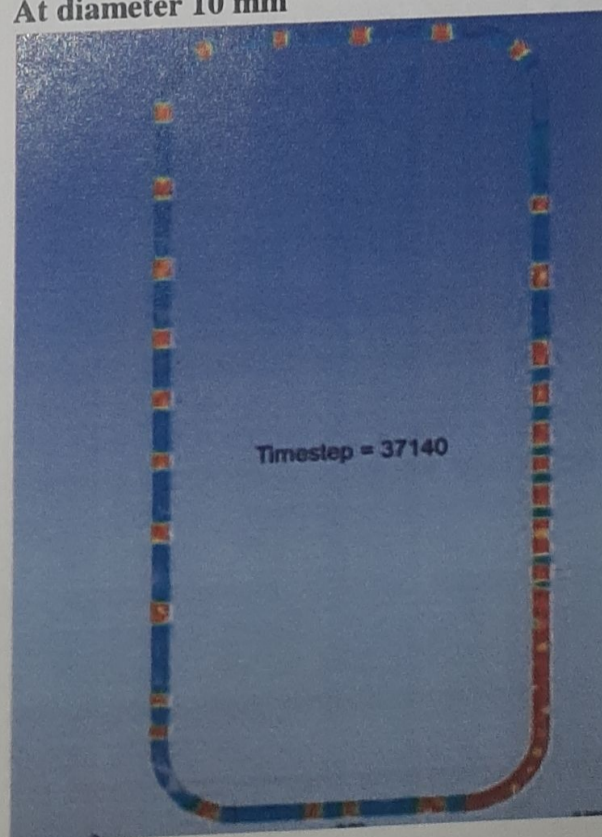
MODELING AND CFD ANALYSIS OF THERMOSYPHON



WATER LIQUID VOLUME FRACTION AT VIROUS TIME SETUP



At diameter 10 mm



4. Theoretical calculations

Fluid properties

Fluid	Temperature (oC)	Density (kg/m ³)	Surface tension (n/m)	Viscosity(ns /m ²)
Water (Liquid)	100	1000	0.720	0.000282
Water (vapor)	100	0.6	0.0588	0.00013

Nomenclature

ρ_L = density of liquid ($\frac{kg}{m^3}$)

ρ_V = density of Vapour ($\frac{kg}{m^3}$)

$\Delta \rho = \rho_L - \rho_V$

ϵ = filling ratio

μ = viscosity

σ = surface tension

M = mass flow rate

Capillary length (l) = $\frac{\sigma}{g(\rho_L - \rho_V)}$

Filling ratio or void factor (ϵ) = $\frac{1 - \frac{H}{L}}{\frac{\Delta \rho}{\rho_L}}$

Lockhart martinelli parameter = $\Psi^2 = \frac{(\frac{dp}{dx})_{sl}}{(\frac{dp}{dx})_{sg}}$

Lockhart martinelli correlation = $(\frac{dp}{dx})_{tp} =$

$\phi^2_2 (\frac{dp}{dx})_{sl} = \phi^2_2 (\frac{dp}{dx})_{sg}$

Kandilkar (flow boiling heat transfer for evaporator)

$h_{tp} = C_1 C_0 (25 Fr Lo)^{C_5} h_{Liquid} + C_3 B_0^C C_4 h_{liquid} F_f L$

	Convective	Nuclear
--	------------	---------

	region	boiling region
C1	1.1360	0.6683
C2	-0.9	-0.2
C3	667.2	1058
C4	0.7	0.7
C5	0.3	0.3

DittusBoelter (down corner)

$h_2 \phi = 0.023 (Re_m)^{0.8} (Pr_{Liq})^{0.4}$

$(\frac{KLiq}{d})$

Shah correlation (condenser)

$h_2 \phi = h_{liquid} [(1-x)^{0.8} + (\frac{3.8x^{0.76}(1-x)^{0.04}}{(Pr_{Liq})^{0.38}})]$

Chan Correlation (riser)

$h_2 \phi = h_{macro} + h_{micro}$

5. EXPERIMENTAL METHODOLOGY

This chapter describes the methodology employed in this study, explaining in detail the experimental procedures for each of the tests.

Three experimental tests were conducted, the first consisting of a single thermosyphon test. The second experiment involved a heat exchanger equipped with 6 thermosyphons and it furthers the experimental knowledge by extracting a value of average thermal conductivity (k) for the thermosyphons involved in the study using the thermal network analysis. Six thermosyphons were used for two main reasons; they represent a module that has been used for Econotherm (the funding body) for sizing purposes and it is also one of the smallest representations of a staggered arrangement for further study.

A third experiment took place involving the same heat exchanger as the second experiment but doubling the heat transfer area on the evaporator side through addition of a "second pass" on the evaporator-side.

The main objective of the last two experiments was to create a relation between the inlet conditions and the internal thermal conductivity of the thermosyphons. The thermosyphons were modelled as superconductors with a thermal conductivity determined analytically, in a hope to simplify the task of predicting the thermal performance of a heat exchanger equipped with thermosyphons.

Design of test rig

The thermosyphons used were made of carbon steel, measured 1,760 mm in length and had a diameter of

28 mm. Both of them were equipped with water as a working fluid filled to 100% of the evaporator section (100% filling ratio). The evaporator section of each thermosyphon measured 1 m and was surrounded by two heating ropes of 500 W, for a maximum of 1 kW of heat energy per thermosyphon. The condenser section measured 200 mm and consisted of a coiled tube surrounding the thermosyphon. Water was used as the shell-side fluid. The experimental apparatus and its schematic representation is presented in Figure .



Figure: Experimental apparatus of single thermosyphon experiment with thermocouple locations

Heat Exchanger equipped with six thermosyphons

The second experimental rig consisted of a heat exchanger equipped with six thermosyphons in a cross-flow arrangement. The design of the rig was based on a scaled-down version of a real working example of a heat exchanger used by Econotherm and can be considered to be a modular design, allowing for future adaptation of different flow configurations. A simple cross flow was investigated in the second experiment.

Design of test rig

The test rig was equipped with six thermosyphons vertically arranged in two staggered rows. The unit was divided into two sections: a hot air circuit and a cold water circuit.

The thermosyphon tube was made of carbon steel, measuring 2 m in length and had a diameter of 28 mm with a surrounding wall with an average

thickness of 2.5 mm. The working fluid was distilled water and the filling ratio was 100% (100% of the evaporator section), roughly translated into 0.7 m in height from the bottom of the thermosyphon. All tubes were chemically treated before insertion of water to avoid corrosion.



Figure: – Experimental apparatus of the heat exchanger in cross flow

From left to right: the heat exchanger before installation; the heat exchanger after being thermally insulated; representative schematic of the thermosyphon heat exchanger and the size of its respective sections.

Experimental Results and Discussions

This chapter outlines the main outcomes of the experimental study. The results from the single thermosyphon experiments are presented first followed by the experiments conducted with the heat exchanger equipped with six thermosyphons in single pass and double pass.

Assumptions

The assumptions made during all the tests are the following:

- Constant mass flow rate across the heat exchanger in both flow sides
- Constant specific heat capacity across the fluid side(s) of the heat exchanger
- Neglectable axial heat transfer from conduction across the thermosyphon wall
- No heat transfer across the walls of heat exchanger
- No heat transfer at the adiabatic section of the thermosyphon
- Steady-state flow

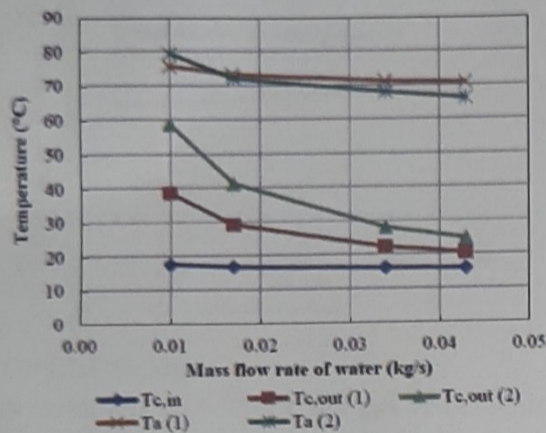
g) Same thermal conductivity for all the thermosyphons

Temperature Comparison

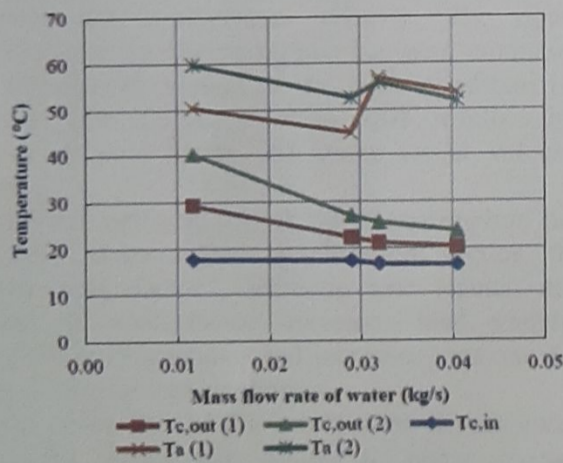
The temperature profile of the two thermosyphons was plotted against the mass flow rate of water on the condenser side. Since the outlet of Thermosyphon #1 is the inlet of Thermosyphon #2, they may be displayed on the same graph (Figure 1, Figure 2 and Figure 3):

Tc,in and Tc,out represent the inlet and outlet temperatures of the condenser and Ta the temperature in the adiabatic section and simultaneously the saturation temperature of the working fluid. The numbers (1) and (2) refer to the Thermosyphons #1 and #2. As may be observed in the following figures, the inlet temperature of the water (Tc,in) was kept constant and by increasing the mass flow rate of water, the outlet temperature decreased as may be observed from the decreasing gap between Tc,in and Tc,out.

Temperature distribution within the condenser section for 985 W



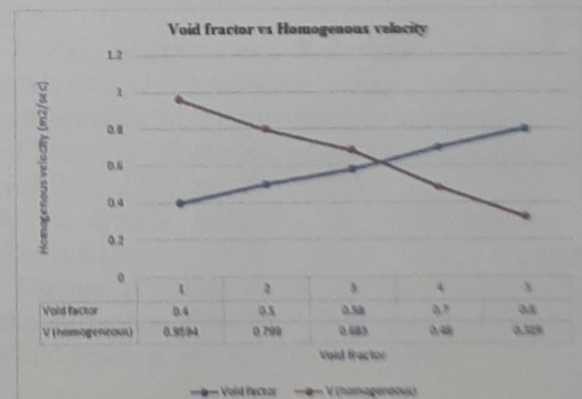
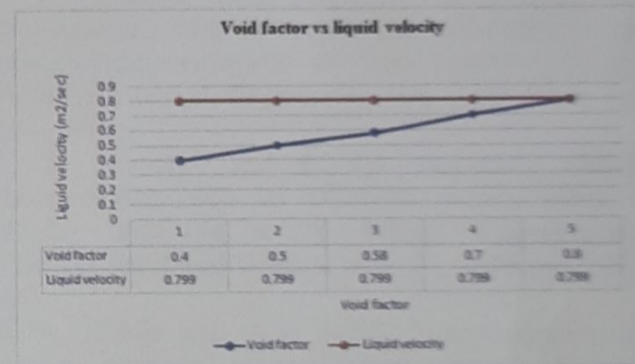
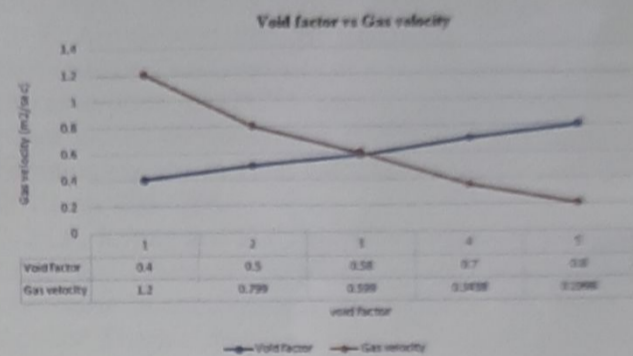
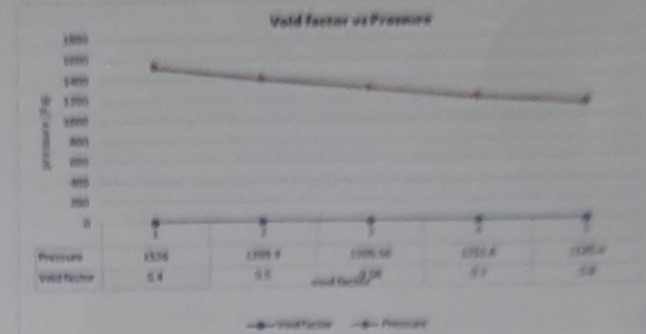
Figure— Temperature distribution within the condenser section for 685 W

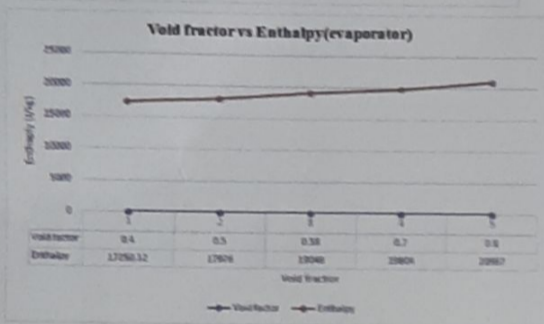
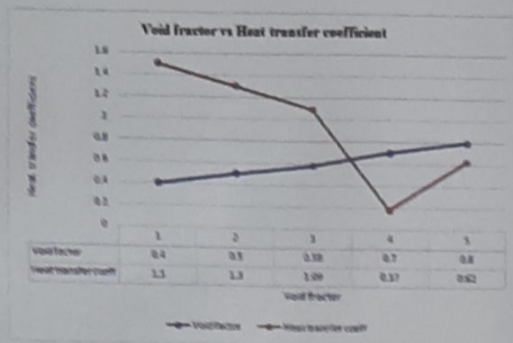
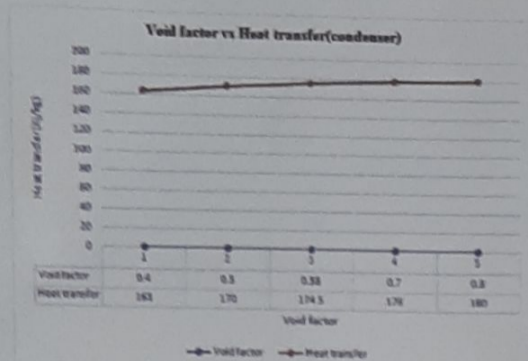


In the adiabatic region, the saturation temperature of the working fluid is observed to decrease with decreasing outlet temperatures, as expected, since the

saturation temperature tends to be located in between the temperatures at the evaporator and the condenser. The temperature of the evaporator is not available as the thermocouple was found to be in contact with the heater thus giving a reading that was not as accurate as desired.

RESULTS & DISCUSSION





CONCLUSION

The homogenous velocity and gas velocity along the thermosyphon has been compared with the analytic results at the same condition for different void factor, showing that results, that increase of void factor decreases the homogenous velocity. The liquid velocity along the thermosyphon has been compared with the analytic results at the same condition for different void factor, showing that results, that increase of void factor will make liquid velocity constant.

The thermal performance of the thermosyphon has also been characterized at different section for different void factor, showing that results, that increase of void factor decreases heat transfer coefficient in downcomer and increases heat transfer rate in condenser and evaporator.

The main objective of this work is the development of a CFD model that allows to phase change simulations of the evaporation and condensation phenomena in a thermosyphon & to verify how bubble growth takes place.

Through this paper, void fraction between 0.55 to 0.7 is recommend to single loop thermosyphon & diameter of loop should be in the range of 5mm to 47.5mm for water as working fluid.

FUTURE SCOPE OF WORK

A new concentrated solar desalination system based on a two-phase working fluid with volumetric solar absorption. This system improves overall solar to thermal efficiency and reduce parasitic power by taking advantage of the passive flow circulation of a loop thermosyphon. To predict system performance, a two-phase loop thermosyphon model around well-validated. The model continues to be developed and will be validated against a larger-scale prototype system.

REFERENCES

1. A. Faghri, "Heat Pipes: Review, opportunity and challenges," *Frontiers in Heat Pipes*, 2014, pp. 1-48.
2. P. Amatachaya and W. Srimuang, "Comparative heat transfer characteristics of a flat two-phase closed thermosyphon (FTPCT) and a conventional two-phase closed thermosyphon (CTPCT)," *International communications in Heat and Mass Transfer*, vol. 37, 2010, pp. 293- 298.
3. M.K. Kyung and C.B. In, "Comparison of flooding limit and thermal performance of annular and concentric thermosyphons at different fill ratios," *Applied Thermal Engineering* vol. 99, 2016, pp. 179-188.
4. L.G. Hasna, L.M. Stephane and C. Ali, "An experimental study of evaporation and condensation heat transfer coefficients for looped thermosyphon," *Applied Thermal Engineering* vol. 110, 2016, pp. 931- 940.
5. S. Thanapol and P., "A two-phase closed thermosyphon with an adiabatic section using a flexible hose and R-134a filling," *Experimental Thermal and Fluid Science*, vol. 77, 2016, pp. 317-326.
6. A. Khalid and A.M Joudi, "Improvements of gravity assisted wickless heat pipes," *Energy Conversion & Management* vol. 41, 2000, pp. 2041-2061.
7. P.G. Anjankar and R.B. Yarasu, "Experimental analysis of condenser length effect on the performance of thermosyphon," *International Journal of Emerging Technology and Advanced Engineering*, vol. 2(3), 2012, pp. 2250-2459.
8. A. Brusly Solomon, K. Arun Mathew, B.C. Ramachandran, V.K. Pillai, and Karthikeyan, "Thermal performance of anodized two phase closed thermosyphon (TPCT)," *Experimental Thermal and Fluid Science*, vol. 48, 2013, pp. 49-57.

EXPERIMENTAL STUDY OF HEAT TRANSFER IN DOUBLE TUBE HAIR-PIN HEAT EXCHANGER

Veldi Akhila¹ Dr.Sanjeev Kumar Sajjan² Dr.Srinivasulu Pulluru³

¹M.Tech (Thermal Engineering)Department of mechanical engineering vaagdevi college of engineering (UGC autonomous) approved by AICTE & permanent affiliation to jntuh, hyderabad.p.o, bollikunta, Warangal urban-506005.

²Associate Professor Department of mechanical engineering vaagdevi college of engineering (UGC autonomous) approved by AICTE & permanent affiliation to jntuh, Hyderabad. p.o, bollikunta, Warangal urban- 506005.

³Professor and Head of the Department of mechanical engineering vaagdevi college of engineering (UGC autonomous) approved by AICTE & permanent affiliation to jntuh, hyderabad. p.o, bollikunta, Warangal urban-506005.

Abstract:

Heat can be transferred between one or more fluids using a heat exchanger. The fluids may be in direct touch or separated from one another by a solid wall to prevent mixing. Single-tube (Double Pipe) and multiple-tube (Multitude) hairpin exchangers are also available, as well as bare tubes, finned tubes, U-tubes, straight tubes (with the possibility to pass a rod through them), fixed tube sheets, and removable bundles.

In this research, the properties of the combination of the nano fluid and the base fluid, water, are calculated. Magnesium oxide and silver nanoparticle volume fractions of 10%, 20%, and 25% are the nanofluids, which are moving at various speeds of 0.5, 1, 1.5, and 2 m/s. The properties of nanofluids are determined using theoretical calculations, and these qualities are then employed as analyses' inputs. Using CREO parametric software, a 3D model of the hair pin heat exchanger with and without twisted tape is created. The hair pin heat exchanger is subjected to CFD analysis at various nanofluid volume fractions. The pressure drop, Reynolds number, heat transfer coefficient, and Nusselt number are all determined using CFD analysis.

Keywords: Finite element analysis, Hair pin heat exchanger, CFD analysis, thermal analysis.

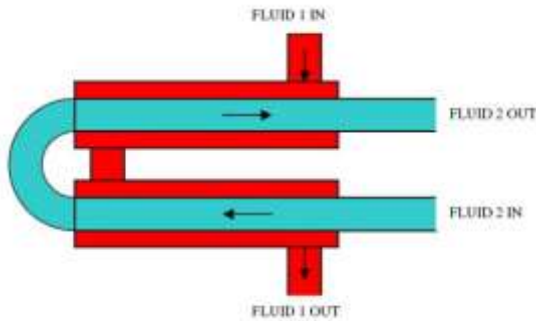
1. INTRODUCTION

Heat exchangers are one of the in general used gadget inside the procedure industries. Heat Exchangers are used to switch warmness between two system streams. One can understand their usage that any technique which involve cooling, heating, condensation, boiling or evaporation would require a heat exchanger for these purpose. Process fluids, typically are heated or cooled earlier than the system or undergo a section exchange. Different heat exchangers are named in step with their application. For instance, heat exchangers getting used to

condense are known as condensers, in addition warmth exchanger for boiling purposes are called boilers. Performance and efficiency of warmth exchangers are measured thru the quantity of warmth switch the usage of least location of warmth transfer and strain drop. A higher presentation of its efficiency is performed by calculating over all heat switch coefficient. Pressure drop and region required for a positive quantity of heat transfer, affords an insight about the capital value and energy necessities (Running value) of a warmness exchanger. Usually, there is lots of literature and theories to layout a warmth exchanger according to the requirements.

HEAT EXCHANGER DESIGN, INC. Gives a entire line of Hairpin Exchangers. These exchangers offer authentic counter-contemporary float and are especially appropriate for hot temperature crossing, high strain, excessive temperature, and low to moderate surface vicinity requirements. Our Hairpin Exchangers are available in single tube (Double Pipe) or multiple tubes inside a hairpin shell (Multitube), bare tubes, finned tubes, U-tubes, straight tubes (with rod-via capability), constant tube sheets and detachable package deal. The floor region levels from (1) square foot to six,000 square toes (Finned tubes). Pressure abilities are full vacuum to over 14,000 PSI (restrained by size, fabric, and layout circumstance). Hairpin Exchangers are designed and fabricated per ASME code, and TEMA standards.

Pressure drop and area required for a certain quantity of heat transfer, provides an perception about the capital cost and power necessities (Running price) of a warmth exchanger. Usually, there is a lot of literature and theories to layout a heat exchanger in keeping with the necessities.



Advantages:

- Tube bundle is removable; therefore mechanical cleansing is feasible at the shell aspect.
- The U form package is free for growth and contraction in the Hairpin shell casting off the need for enlargement joint.
- Are able to sporting the maximum strain allowable by using ASME Code per given wall thickness. (Up to 14600 psi and not using a corrosion allowance). Higher pressure rankings are feasible the use of substances with higher stress values
- For approaches that require frequent mechanical cleaning, naked tube gives ease of cleaning and accessibility.
- Bare Multi-Tube and Double-Pipe Exchangers provide the least strain drop amongst most exchangers.

2.LITERATURE REVIEW

W.H. Azmi [1] The heat switch coefficient and friction element of TiO₂ and SiO₂ water based totally nanofluids flowing in a round tube underneath turbulent drift are investigated experimentally below consistent heat flux boundary situation. TiO₂ and SiO₂ nanofluids with an average particle size of fifty nm and 22 nm respectively are used in the operating fluid for extent concentrations up to three.0%. Experiments are carried out at a bulk temperature of 30 °C in the turbulent Reynolds wide variety variety of 5000 to 25,000. The improvements in viscosity and thermal conductivity of TiO₂ are extra than SiO₂ nanofluid. However, a most enhancement of 26% in warmness transfer coefficients is obtained with TiO₂ nanofluid at 1.0% attention, while SiO₂ nanofluid gave 33% enhancement at three.Zero% awareness. The heat switch coefficients are decrease in any respect other concentrations. The particle concentration at which the nanofluids supply maximum warmness switch has been decided and validated with assets enhancement ratio. It is located that the pressure drop is at once proportional to the density of the nanoparticle.

P.K. Sharma et.Al. [2] Presented a new method to are expecting the convective heat transfer coefficient in a

tube with twisted tape inserts of different types of pitch to diameter ratios. Modification is proposed to Van Driest eddy diffusivity expression to the case of swirl float generated by using twisted tape inserts. Heat switch performance can be expanded by growing the thermal conductivity of the running fluid. Water, ethylene glycol and engine oil which are usually used as warmness switch fluids have tremendously low thermal conductivities whilst compared to that of the solids. High thermal conductivity of solids can be used to boom the thermal conductivity of a fluid by way of including small strong debris to that fluid.

K.V.Reddy et.Al. [2] Double pipe warmth exchangers are easy in creation and efficient in operation. Enhancement in warmness transfer in warmth exchangers can be executed by way of the usage of exceptional strategies. Et.Al [3, 4, 5, 6] Passive method is one of the first-rate strategies in this insertion of twisted tape inserts growth the warmth switch coefficient, boom turbulence and thus growth the price of warmth transfer insides the tubes of the heat exchanger. Cut twisted taped similarly increase the turbulence which complements the turbulent warmness switch.

Pak and Cho [7] achieved experiments on convective warmth switch of nanofluids underneath turbulent drift conditions using Al₂O₃ and TiO₂ dispersed in water.

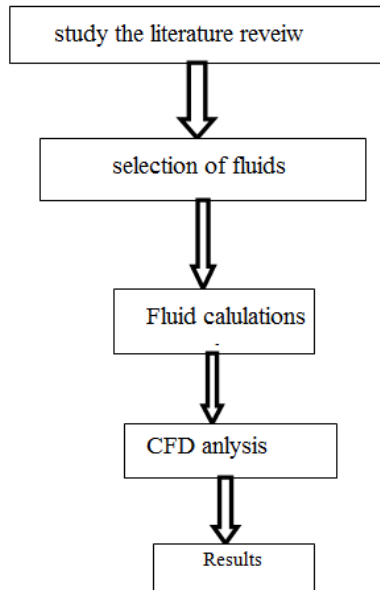
P.V.Durga Prasad et.Al. [8] achieved experimental research to enhance the warmth transfer via the usage of Silver nanofluids at low volume concentrations and trapezoidal cut twisted tapes . The results confirmed that there is a huge enhancement in warmth transfer with nano fluids whilst as compared with that of the bottom fluid and the trapezoidal cut twisted tapes greater the turbulence which in turn extended the rate of warmth transfer.

Objectives of the project

The following are the main objectives of the present work:

- The objective of this project is to make the double pipe heat exchanger and study the heat transfer of the heat exchanger by performing the experimentally .
- To increase the heat transfer coefficient ,friction factor and heat transfer rate at different volume fraction nano fluid
- To identify suitable fluid for the based on results obtained from finite element analysis.

3.METHODOLOGY



4. MODELING AND ANALYSIS

Computer-aided design (CAD) is using pc systems (or workstations) to aid inside the introduction, change, evaluation, or enhancement of a structure. Computer aided design programming is utilized to enlarge the performance of the planner, improve the nature of configuration, improve correspondences via documentation, and to make a database for assembling. Computer aided layout yield is regularly as electronic records for print, machining, or different assembling duties. The term CADD (for Computer Aided Design and Drafting) is moreover utilized. CATIA is an abbreviation for Computer Aided Three-dimensional Interactive Application. It is one of the main 3-D programming used by associations in numerous agencies extending from aviation, vehicle to purchaser gadgets. CATIA is a multi level 3-D programming suite created by means of Systems, such as CAD, CAM just as CAE. Dassault is a French building monstrous dynamic inside the field of flying, three-D structure, three-D advanced false ups, and item lifecycle the executives (PLM) programming.

Dimensions of designed double tube Hair-pin heat exchanger:

Outer pipe specification Inner tube specification

Copper tube of U bends
 I.D. of shell= 19.05 mm
 I.D. of tube = 8.4 mm
 Copper tube of U bends

I.D. of shell= 19.05 mm
 I.D. of tube = 8.4 mm
 O.D. of shell = 22 mm O.D. of tube = 9.5 mm
 Center to center distance is taken
 Wall thickness= 0.55 mm
 1.5 - 1.8 times of outer dia. of shell.
 Thermal conductivity of wall= 385 w/m2K
 Length of each G.I. pipe = 22.86cm
 Effective length of copper tube through which heat transfer could take place= 45cm
 Total length of the copper tube = straight part (51cm) + U-shaped bend part (9cm) =60cm

3D model of hair pin heat exchanger



FEM/FEA helps in evaluating complex systems in a device in the course of the starting stage. The strength and design of the version can be progressed with the assist of computers and FEA which justifies the value of the analysis. FEA has prominently accelerated the design of the systems that have been constructed a few years in the past.

CFD

Computational fluid dynamics, normally abbreviated as CFD, is a branch of fluid mechanics that uses numerical methods and algorithms to solve and analyze troubles that contain fluid flows.

Calculations To Determine Properties Of Nano Fluid By Changing Volume Fractions Nano Fluid Calculations:

Nomenclature

ρ_{nf} = Density of nano fluid (kg/m³)

ρ_s = Density of solid material (kg/m³)

ρ_w = Density of fluid material (water) (kg/m³)

ϕ = Volume fraction

C_{pw} = Specific heat of fluid material (water) (j/kg-k)

C_{ps} = Specific heat of solid material (j/kg-k)

μ_w = Viscosity of fluid (water) (kg/m-s)

μ_{nf} = Viscosity of Nano fluid

K_w = Thermal conductivity of fluid material (water)
(W/m-k)

K_s = Thermal conductivity of solid material
(W/m-k)

Density of Nano Fluid

$$\rho_{nf} = \phi \times \rho_s + [(1-\phi) \times \rho_w]$$

Specific Heat Of nano Fluid

$$C_{p\ nf} = \frac{\phi \times \rho_s \times C_{ps} + (1-\phi)(\rho_w \times C_{pw})}{\phi \times \rho_s + (1-\phi) \times \rho_w}$$

Viscosity Of Nano Fluid

$$\mu_{nf} = \mu_w (1+2.5\phi)$$

Thermal Conductivity of Nano Fluid

$$K_{nf} = \frac{K_s + 2K_w + 2(K_s - K_w)(1 + \beta)^3 \times \phi}{K_s + 2K_w - 2(K_s - K_w)(1 + \beta)^3 \times \phi} \times k_w$$

5. RESULTS AND DISCUSSION

CFD Analysis of Hair Pin Heat Exchanger

Silver Nano Fluid

Volume Fraction - 0.25

Imported model



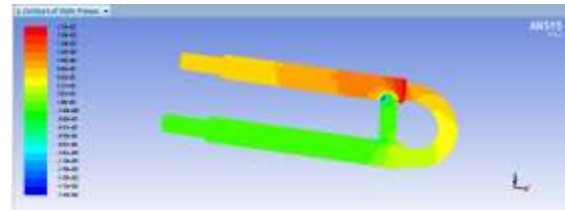
Fig: 1 imported model from 3D modeling software



Fig: 2 meshed model

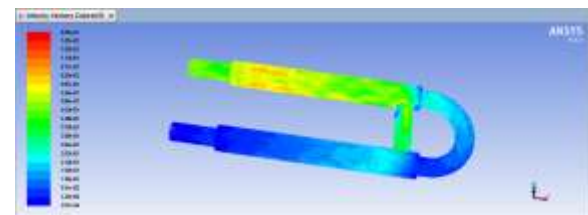
The model is designed with the help of CATIA and then import on ANSYS for Meshing and analysis. The analysis by CFD is used in order to calculating pressure profile and temperature distribution. For meshing, the fluid ring is divided into two connected volumes. Then all thickness edges are meshed with 360 intervals. A tetrahedral structure mesh is used. So the total number of nodes and elements is 6576 and 3344.

STATIC PRESSURE

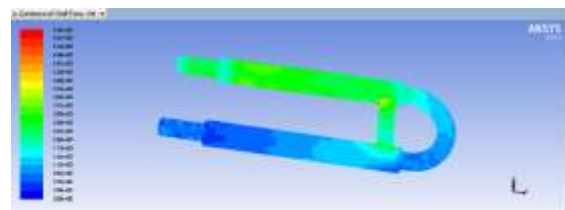


According to above the plot the maximum pressure at inlet of the tube and minimum pressure at outlet of the tube

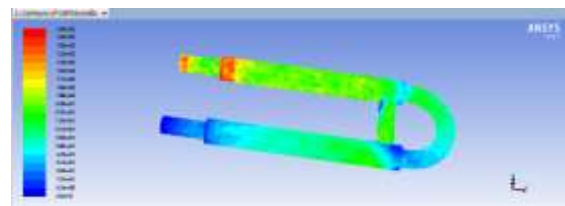
Velocity



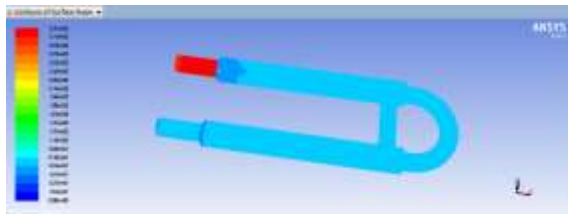
Heat Transfer Co-Efficient



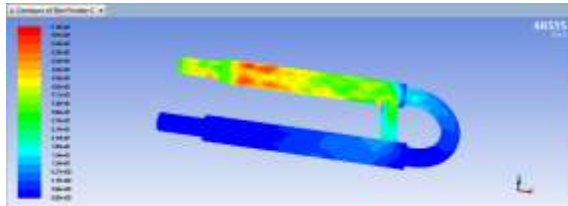
Re



Nu



Friction factor



6.RESULT TABLES

CFD RESULT TABLES

Fluid	Inlet velocity (m/s)	Pressure (pa)	Velocity (m/s)	Re	Friction Factor	Nu	Heat transfer coefficient (w/m ² -k)
Water	0.5	1.78e+02	0.83	1.66e+02	3.02	3.27e+02	5.76e-03
	1	5.35e+02	1.62	2.74e+02	12.74	3.46e+02	1.05e-04
	1.5	1.05e+03	2.40	4.66e+02	1.73e+01	3.52e+02	1.44e-04
	2	1.81e+03	3.22	7.64e+02	2.90e+01	3.55e+02	1.81e-04

Fluid	Inlet velocity (m/s)	Pressure (pa)	Velocity (m/s)	Re	Friction Factor	Nu	Heat transfer coefficient (w/m ² -k)
MgO (10%)	0.5	3.50e+02	0.831	1.49e+02	6.93	7.31e+01	1.24e-04
	1	1.003e+03	1.612	1.84e+02	2.09e+01	7.48e+01	2.18e-04
	1.5	2.16e+03	2.380	2.72e+02	3.92e+01	7.64e+01	2.96e-04
	2	3.38e+03	3.16	3.88e+02	6.18e+01	7.69e+01	3.75e-04
MgO (20%)	0.5	3.61e+02	0.8312	1.52e+02	7.33	6.74e+01	1.44e-04
	1	1.34e+03	1.61	1.92e+02	2.17e+01	6.86e+01	2.45e-04
	1.5	2.31e+03	2.37	2.93e+02	4.11e+01	7.02e+01	3.43e-04
	2	4.36e+03	3.21	4.64e+02	6.67e+01	7.07e+01	4.31e-04
MgO (25%)	0.5	3.68e+02	0.8291	1.55e+02	7.62	6.53e+01	1.59e-04
	1	3.68e+02	1.61	2.03e+02	26e+01	6.63e+01	2.80e-04
	1.5	1.25e+03	2.19	3.25e+02	4.30e+01	6.76e+01	3.81e-04
	2	4.36e+03	3.19	4.90e+02	6.93e+01	6.79e+01	4.78e-04

Fluid	Inlet velocity (m/s)	Pressure (pa)	Velocity (m/s)	Re	Friction Factor	Nu	Heat transfer coefficient (w/m ² -k)
Silver nano fluid (10%)	0.5	7.84e+02	0.831	2.42e+02	1.26e+01	6.86e+01	1.84e-04
	1	2.71e+03	1.63	6.14e+02	3.94e+01	7.01e+01	2.96e-04
	1.5	3.54e+03	2.41	1.33e+03	7.91e+01	7.06e+01	3.87e-04
	2	9.4e+03	3.21	2.7e+03	3.27e+02	7.10e+01	4.68e-04
Silver nano fluid (20%)	0.5	7.95e+02	0.834	3.48e+02	1.38e+01	6.6e+01	2.01e-04
	1	2.73e+03	1.632	6.28e+02	4.93e+01	6.77e+01	3.22e-04
	1.5	5.55e+03	2.412	1.45e+03	8.13e+01	6.89e+01	4.05e-04
	2	9.43e+03	3.25	2.82e+03	1.41e+02	7.01e+01	4.95e-04
Silver nano fluid (25%)	0.5	8.01e+02	0.837	2.38e+02	1.33e+01	6.27e+01	2.19e-04
	1	2.83e+02	1.619	6.47e+02	4.09e+01	6.41e+01	3.52e-04
	1.5	5.65e+02	2.431	1.59e+03	8.13e+01	6.56e+01	4.55e-04
	2	9.49e+02	3.251	2.96e+03	1.311e+02	6.66e+01	5.12e-04

7. EXPERIMENTAL SETUP

The schematic of experimental setup has been proven in figure 7.1. The setup includes centrifugal pumps, a check section (concentric double-tube hairpin warmth exchanger), hot water reservoir, bloodless fluid reservoir and manometer. The effective duration of the check phase is forty five cm via which warmth was being transferred. The perimeter of U-kind return bend is 9 cm. There become a counter flow of fluids inside the horizontal check segment where, the cold circulation became flowing in the tube at the same time as warm water inside the annulus. The internal tube is made of copper material with inner and the outer diameter is 8.43 and nine.50 mm respectively; while, the outer tube is made up of Galvanized Iron with internal and the outer diameter is nineteen.05 and 22 mm respectively. Installed miniature double tube Hair-pin warmth exchanger and the experimental setup hooked up inside the laboratory are proven in figure 7. 2 and determine 7.3 respectively.

The test segment has been thermally insulated by using the use of cotton rope and asbestos mud to lessen the heat loss in radial outward path. The differential pressure transmitter has been installed for the dimension of strain drop therefore the frictional loss throughout the ends of the internal tube. Mercury thermometers had been anchored on each cease of the test phase to measure the temperatures at inlet and outlet of both the streams. From hot water reservoir and cold fluid reservoir the new and bloodless move have been constantly furnished to the take a look at phase. The temperature of both the new water and cold fluid reservoir changed into maintained through inbuilt PID controller which ensures constant temperature inside the reservoirs at their preferred set factor. A common glass U – tube manometer full of mercury become also used for pressure dimension. Silver is pretty miscible in water. So, water – Silver nano particles mixtures have been organized via blending regarded quantity of Silver in water as in step with requirement. The mixture was routinely stirred for 15 mins and additionally stored inside the

shaker to ensure proper mixing of both the fluids. Hot water changed into constantly provided at regular temperature (50°C) and constant flow rate (3 lit/min.) within the annulus of the check segment Whereas, Cold water at 30°C turned into supplied at exclusive flow rate various from 1-5 litre/minute. At constant flow rate, pressure, temperature and flow rate with the flow rate of the streams were measured. Frictional losses have been analyzed with various flow rate of the fluid movement. Firstly Cold flow was taken as pure distilled water after which water – Silver (10%, 20%, and 25% Silver with the aid of volume) have been used. A coiled copper tube with dimension 9.5 mm of outer diameter became submerged in a cold water reservoir, i.e. A chiller with temperature controller set at favored temperature. The cold flow popping out from the inner tube of the heat exchanger turned into surpassed through the coiled copper tube to lose the power and consequently come to the inlet temperature of the fluid stream.

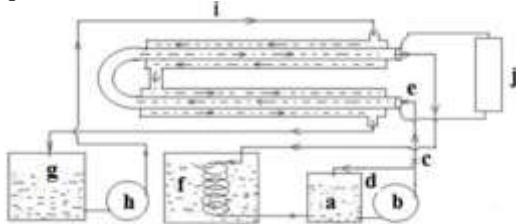


Figure .Schematic diagram of the experiment d. Bypass, e. Cold stream, f. Coolant, g. Hot water



Figure.: Installed miniature double tube Hairpin heat exchanger in laboratory.

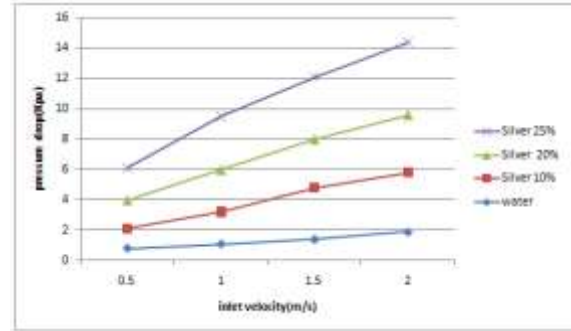


Figure.: Installed experimental setup in the laboratory. a. Cold fluid reservoir, b. Pump, c. Rotameter, d. Cooling system w PID controller, e. Double tube Hair-pin heat exchanger, f. Mercury thermometer, g. Mercury manometer, h. Hot water reservoir with PID temperature controller

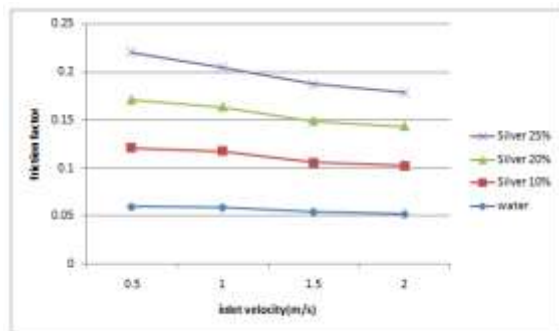
8.RESULTS AND DISCUSSIONS

The experiments have been conducted for unpaired segment with the flow of water and water – Silver nano particles composites inside the inner tube of miniature double tube Hair-pin heat exchanger for varying flow rate 1 – 5 litre/minute. The internal diameter of the inner tube is 8.40 mm. The received speed changed into numerous within the degrees from 0.5 to 2 m/s. A fully developed condition became assumed for theoretical calculations. Experimentally measured friction factors became compared towards the values acquired theoretically by using correlations are given in equations for laminar and turbulent flow respectively. The experimentally discovered pressure drop in differential manometer throughout the test section became additionally compared with the theoretically calculated pressure drop.

Fluid	Inlet velocity (m/s)	Friction factor	Pressure drop(kpa)
Water	0.5	0.06	0.81
	1	0.0593	1.1
	1.5	0.0545	1.4
	2	0.0521	1.9
Water +Silver nano fluid 10%	0.5	0.061	1.3
	1	0.0583	2.1
	1.5	0.0513	3.4
	2	0.0501	3.9
Water + Silver nano fluid 20%	0.5	0.05	1.9
	1	0.046	2.8
	1.5	0.0432	3.2
	2	0.041	3.8
Water + Silver nano fluid 25%	0.5	0.049	2.1
	1	0.041	3.5
	1.5	0.038	4.1
	2	0.035	4.8



Graphs



Above graph represents the variation of experimental and theoretical friction factor values against Reynolds number for both distilled water and water – silver nano particles mixtures (0%, 10%, 20% and 25% silver by volume). The experimental results of friction factor in miniature double tube Hair-pin heat exchanger was compared with Darcy’s friction factor and friction factor obtained from Blasius equation in laminar and turbulent flow respectively. It is observed that friction factor decreases with increase in velocity as well as with concentration of the Silver nano fluid. It is also observed that friction factor decreases more rapidly with Reynolds number in laminar compared to turbulent flow. In this study, a mixture of silver and water was taken as heat transfer fluid which has more density and viscosity and less thermal conductivity than pure distilled water. But here for friction factor study; viscosity and flow rate played the major role.

From above figure, it is clear that pressure drop rapidly increases with the increase in concentration of silver in the mixture for the same Reynolds number. For varying flow rate 1-5 litre/minute, the fluid was in turbulent flow only for distilled water and 10% ethylene silver nano particles mixture but it was in laminar flow for lower flow rate whereas, turbulent flow for higher flow rate for both the concentrations 20% and 25% of silver in water. For higher pressure drop, higher will be the requirement of pumping cost and thus, lowered the mechanical stability of the system. So, pressure drop and velocity profile analysis is more important in designing of the flow system.

9.CONCLUSION

- In this Thesis, nano fluid is mixed with base fluid water are calculated for their combination properties. The nano fluids are magnesium Oxide and silver nano particles volume fractions 10%, 20% and 25% at different velocities (0.5,1,1.5and 2 m/s).
- Theoretical calculations are done determine the properties for nano fluids and those properties are used as inputs for analysis.
- 3D model of the hair pin heat exchanger with and without twisted tape model is done in CREO parametric software. CFD analysis is done on the hair pin heat exchanger at different nano fluid volume fractions.
- CFD analysis is to determine the pressure drop, Reynolds number, heat transfer coefficient and Nusselt number.
- By observing the CFD analysis results the increasing the velocities increases the friction factor and heat transfer coefficient values.
- By observing the CFD analysis results the friction factor and heat transfer coefficient values more at silver nano particles (0.25%).
- So, it can be concluded the silver nano particles (0.25%) is the better fluid for hair pin heat exchanger.

REFERENCES

- [1] P.K.Sarma , T. Subramanyam , P.S. Kishorea, V. Dharma Rao, Sadik Kakac ,2002, A new approach to are expecting convective warmness transfer in a tube with twisted tape inserts for turbulent waft, Journal of Thermal Sciences, pp 955-960.
- [2] K.Vijaya Kumar Reddy , Naga Sarada Somanchi, Rangisetty Sri Rama Devi , Ravi Gugulothu and B. Sudheer Prem Kumar ,2015, Heat Transfer Enhancement in a Double pipe Heat Exchanger Using Nano Fluids, Proceedings of the 17th ISME Conference ISME17 October three-four, 2015, IIT Delhi, New Delhi,PP:1-7
- [3] Indrakant Singh, D.R.Nilesh Diwakar , 2013, Heat switch enhancement using extraordinary geometry of twist tape turbulators: a evaluation, International Journal of Applied Research in Mechanical Engineering (IJARME) ISSN: 2231 – 5950, Vol-three, Iss-2,
- [4] S.Tabatabaeikia, H.A.Mohammed, N.Nik-Ghazali, and B.Shahizare, 2014, Heat Transfer Enhancement by means of Using Different Types of Inserts, Advances in Mechanical Engineering, Article ID 250354, pp:1-13.
- [5] Mukesh P Mangtani and K M Watt, April 2015, Effect of Twisted-tape inserts on warmness switch in a tube—a evaluation, , ISSN 2278 – 0149 ,Vol. Four, No. 2.
- [6] A Dewan, P Mahanta, K Sumithra Raju and P Suresh Kumar,Review of passive warmth switch augmentation techniques, Proc. Instn Mech. Engrs Vol. 218 Part A: J. Power and Energy.
- [7] Pak, B.C., Cho Y.I. 1998, Hydrodynamic and warmth transfer examine of dispersed fluids with submicron steel oxide debris, Experimental Heat Transfer 11, pp 151-170.
- [8] P.V. Durga Prasad, A.V.S.S.K.S. Gupta and K. Deepak, 2014, Investigation of Trapezoidal-Cut Twisted Tape Insert in a Double Pipe U-Tube Heat Exchanger the usage of Al₂O₃/Water based totally Nanofluid, 2d International Conference on Nanomaterials and Technologies (CNT 2014), Procedia Materials Science10(2015) 50 – 63, Pp: 50-sixty three
- [9] B. Raei1, F. Shahraki1, M. Jamialahmadi, S.M. Peyghambarzadeh, 2017, Experimental research on the warmth transfer performance and stress drop traits of γ -Al₂O₃/water nanofluid in a double tube counter glide warmness exchanger , Trans. Phenom. Nano Micro Scales, 4(1), Pp: sixty four-77
- [10] V. Murali Krishna,2016, Experimental research of warmth switch enhancement with the aid of the use of al₂o₃water nanofluid in a concentric tube warmth exchanger , International Journal of Mechanical Engineering and Technology (IJMET)

Volume 7, Issue 6, November– December 2016,
Pp.449–458.

FEA INVESTIGATION OF THE DISCHARGE VALVE DYNAMICS IN A RECIPROCATING COMPRESSOR FOR TRANS-CRITICAL CO₂ REFRIGERATION CYCLE

Nunavath Saikumar ¹

Dr.Sanjeev Kumar Sajjan ²

Dr.P.Srinivasulu ³

¹M.Tech department of Mechanical Engineering, vaagdevi college of engineering (UGC autonomous) approved by AICTE & permanent affiliation to jntuh, hyderabad. p.o, bollikunta, Warangal urban- 506005

² Assistant professor department of Mechanical Engineering, vaagdevi college of engineering (UGC autonomous) approved by AICTE & permanent affiliation to jntuh, hyderabad. p.o, bollikunta, Warangal urban- 506005.

³ Professor and Head of the department of Mechanical Engineering, vaagdevi college of engineering (UGC autonomous) approved by AICTE & permanent affiliation to jntuh, hyderabad. p.o, bollikunta, Warangal urban- 506005.

Abstract

CO₂ is gaining in popularity as an ecologically friendly refrigerant. CO₂ compressors have been created by many universities and businesses for various uses. Japan has produced some tiny CO₂ compressors for use in residential heat pump water heaters and automotive air conditioners. Analytical experiments are conducted in this study to assess the compressor's thermodynamic performance. The movement of the discharge valve in the reciprocating CO₂ compressor is measured while modifying the design parameter compressor speed 50m/s, 75m/s, 80m/s, and 100m/s in order to explore the key parameters that impact valve dynamics. In CREO, a 3D model of the valve is created, and in ANSYS, a CFD and thermal study of the discharge valve is performed. Thermal analysis is done by varying the materials Stainless Steel, En9 Steel and Cast Iron.

Keywords: CO₂,CFD,CREO and EN 9steel

1.INTRODUCTION

As a harmless to the ecosystem refrigerant, CO₂ has acquired and more consideration. Various organizations and organizations have created CO₂ blowers for various applications. Some little CO₂ blowers have been created in Japan for the utilization in homegrown intensity siphon water warmer and auto climate control system. These blowers are for the most part parchment and moving cylinder types, with power around 1-2kW and COP around 4. Huge and medium CO₂ blowers have been delivered by Dorin and Bock for the utilization in business applications.

Contrasted and conventional fluorocarbon-based refrigerants, CO₂ has lower basic temperature (31.6) yet higher basic tension (7.37MPa). Due to the transcritical activity of the cycle, CO₂ blower is working under a lot higher tension, 5-10 times higher than the standard blower. This high tension causes huge powers, which significantly challenges the plan of key parts like wrench, associating pole, course and pull/release valves.CO₂ has a high volumetric limit (22.6MJ/m³ at 0°C), which is 1.58, 5.12 and 8.25 times as much as NH₃, R22 and R12 separately. In this manner, the cleared volume of CO₂ blower is more modest than the standard blower. Along these lines, it very well may be feasible to plan the blower reduced and savvy blower. Nonetheless, it turns out to be more challenging to orchestrate the valves with adequate stream region in a generally little space.

RECIPROCATING COMPRESSOR

A responding blower or cylinder blower is a positive-dislodging blower that utilizes cylinders driven by a driving rod to convey gases at high tension.

The admission gas enters the attractions complex, then, at that point, streams into the pressure chamber where it gets compacted by a cylinder driven in a responding movement by means of a driving rod, and is then released. Applications incorporate petroleum treatment facilities, gas pipelines, substance plants, flammable gas handling plants and refrigerationplants. One specialty application is the blowing of plastic jugs made of polyethylene terephthalate (PET).

In the ionic fluid cylinder blower many seals and course were taken out in the plan as the ionic fluid

doesn't blend in with the gas. Administration life is quite a bit longer than a standard stomach blower with decreased support during use, energy costs are diminished by as much as 20%. The intensity exchangers that are utilized in an ordinary cylinder blower are taken out as the intensity is eliminated in the actual chamber where it is created. Practically 100 percent of the energy going into the cycle is being utilized with little energy squandered as reject heat.

CO₂ As Refrigerant: The Tran critical Cycle

In three past articles, we have introduced an outline of CO₂ (R-744) as a refrigerant, its applications in modern refrigeration, and a contextual analysis of a CO₂ overflow framework in an European general store. The frameworks introduced were all subcritical - that is, the refrigeration cycles were altogether beneath the basic place of CO₂. Presently, after a concise survey of CO₂ qualities, contrasting subcritical and transcritical cycles, we will introduce a working transcritical framework with an airtight CO₂ blower and talk about plan contemplations.

CO₂ is a part of our environment that is fundamental for life. It has no ozone exhaustion potential and immaterial an Earth-wide temperature boost potential, so CO₂ has no administrative responsibility, as do HFCs. There is compelling reason need to represent the sum utilized, and it needn't bother with to be recovered. (Attributes of CO₂, contrasted and those of R-134a and R-404A, are displayed in Table 1.)

Refrigerant And Properties	R-134a	R-404A	CO ₂
Natural substance	No	No	Yes
Ozone depletion potential (ODP)	0	0	0
Global warming potential (GWP)	1300	3260	1
Critical point	590 psia 214°F	541 psia 161°	1,067 psia 88.0°
Triple point	0.058 psia -153.4°	0.406 psia -148°	75.1 psia -69.9°
Flammable or explosive	No	No	No
Toxic	No	No	No

Table 1. Properties of CO₂ (R-744) compared with those of R-134a and R-404A.

2.LITERATURE REVIEW

CO₂ in transcritical refrigeration

The frameworks for both straightforward R134a (subcritical) and CO₂ (transcritical) frameworks are displayed on the consolidated strain enthalpy charts in Figure 2 - the term 'transcritical' essentially implying that the cycle passes across the basic point. Utilizations of transcritical refrigeration have required off over the most recent 20 years, especially with little refrigeration frameworks - at first for auto and little marine applications - that are by and large recognized to have created from work embraced by Gustav Lorentzen in the last part of the 1980s. Helpfully, the low basic temperature sits in the scopes of temperature that are every now and again found in HVAC and R applications.

In transcritical refrigeration cycles, CO₂ works at a lot higher tensions than customary HFC and alkali frameworks. Present day fabricating strategies have empowered the development of minimal expense parts equipped for working at the high tensions expected for CO₂ refrigeration. This incorporates little homegrown units, heat siphons, grocery store applications, and, less significantly, modern applications. More modest CO₂ systems will generally utilize unitary transcritical frameworks, while bigger, business and modern frameworks are bound to utilize CO₂ as a low temperature refrigerant in overflow frameworks, along with different refrigerants, for example, alkali being utilized as the high temperature refrigerant. There have been improvements in little parchment blowers and responding blowers explicitly for transcritical CO₂ frameworks. CO₂ has a higher volumetric refrigeration limit than conventional refrigerants (so requiring less dislodging) however at a lot higher tension differentials. The diminished volume streams of the refrigerant gives open doors to more modest parts.

CO₂ can likewise be utilized as an immediate refrigerant, where fluid CO₂ is basically siphoned under the gun to an evaporator providing the cooling load, with the disintegrated CO₂ then, at that point, went through a low temperature heat exchanger (still at high strain) and consolidated, prepared to be recycled to the heap.

Subcritical and transcritical cycles

Taking a gander at Figure1, the R134a cycle has the vanishing system getting going base left, where the low temperature refrigerant is a blend of fume and fluid. As the refrigerant increases heat from the encompassing cooling burden (or intensity hotspot for heat siphon), its enthalpy ascends with the refrigerant at consistent strain, until it turns into a superheated gas at the admission of the blower. The blower expands the tension, additionally adding intensity to the refrigerant, and consuming ability to drive the engine. The hot, high-pressure, superheated gas enters the condenser, where intensity is dismissed (or, in an intensity siphon, passed to the intensity move medium) and the gas returns to a fluid. The warm, high-pressure fluid (frequently subcooled) goes through a strain decreasing gadget (an extension gadget) at steady enthalpy. The entire cycle is beneath the basic point, so is known as a 'subcritical' process. The development gadget is planned basically to guarantee that superheated gas enters the blower by detecting the state of the low-pressure refrigerant leaving the evaporator to control the stream.



Attractions cooling is taken on to keep the engine moving along as expected and proficiently. A blend valve is intended to procure adequate stream region in the restricted space. Sandvik 7C27Mo2 is utilized as the valve material, which has great erosion opposition, high durability, and brilliant weakness strength properties. Hydrodynamic diary orientation are chosen because of the enormous cylinder force.

3. MODELING AND ANALYSIS

(CAD), otherwise called PC helped plan and drafting (CADD), is the utilization of PC innovation for the course of endlessly plan documentation. PC Aided Drafting depicts the most common way of drafting with a PC. CADD programming, or conditions, give the client input-instruments to smooth out plan processes; drafting, documentation, and assembling processes. CADD yield is many times as electronic documents for print or machining activities. The advancement of CADD-based programming is in direct relationship with the cycles it tries to streamline; industry-based programming (development, producing, and so forth) normally utilizes vector-based (straight) conditions though realistic based programming uses raster-based (pixelated) conditions.

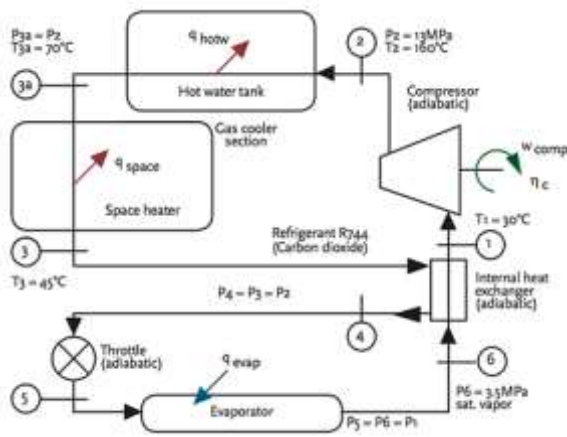


Fig :1 CO2 transcritical heat pump operation schematic

Design of the structure



Fig: 3d Model Of Discharge Valve

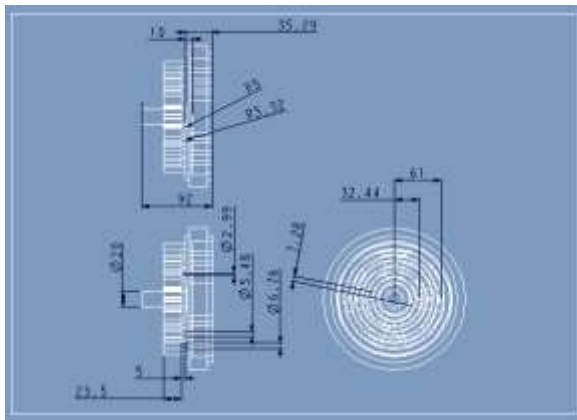


Fig: 2D Drawing Of Discharge Valve

Thermal

ANSYS is fit for both consistent state and transient investigation of any strong with warm limit conditions. Consistent state warm investigations work out the impacts of consistent warm loads on a framework or part. Clients frequently play out a consistent state examination prior to doing a transient

warm investigation, to assist with laying out starting circumstances. A consistent state investigation likewise can be the last advance of a transient warm examination; performed after all transient impacts have decreased. ANSYS can be utilized to decide temperatures, warm slopes, heat stream rates, and intensity transitions in an article that are brought about by warm loads that don't shift over the long run. Such loads incorporate the accompanying

Computational liquid elements, normally curtailed as CFD, is a part of liquid mechanics that utilizes mathematical strategies and calculations to take care of and investigate issues that include liquid streams. PCs are utilized to play out the computations expected to reenact the connection of fluids and gases with surfaces characterized by limit conditions. With rapid supercomputers, improved arrangements can be accomplished.

4.THERMAL ANALYSIS OFRECIPROCATING COMPRESSOR DISCHARGE VALVE

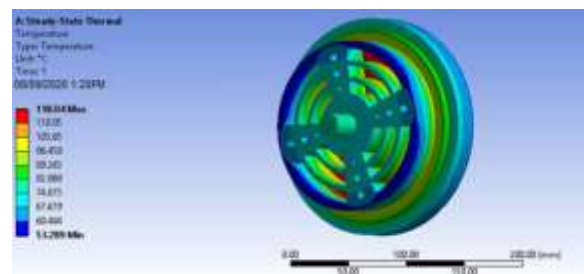
MATERIAL –EN 9 STEEL

Thermal conductivity of aluminum = 59.1W/mK

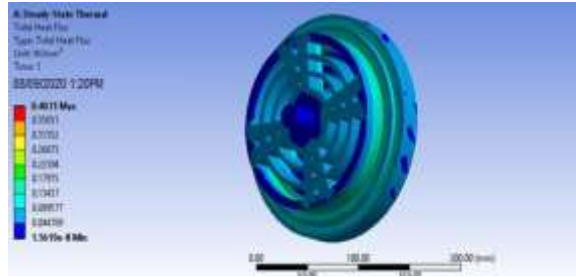
Specific heat =421 J/Kg K

Density = 0.00000771Kg/mm3

Temperature



Heat flux



CFD ANALYSIS OF RECIPROCATING COMPRESSOR DISCHARGE VALVE

CO₂ propeties

Thermal conductivity-0.0146w/m-k

Specific heat-0.895kj/kg-k

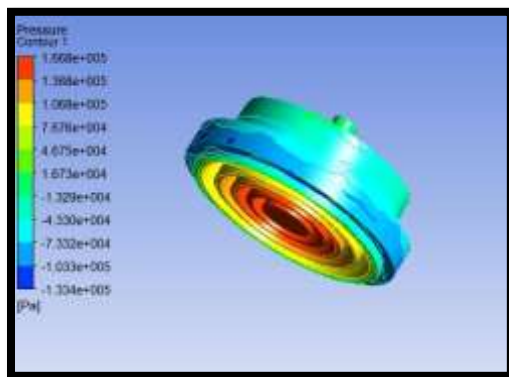
Viscosity-1.85*10⁻⁵pa.s

Density -1.997kg/m³

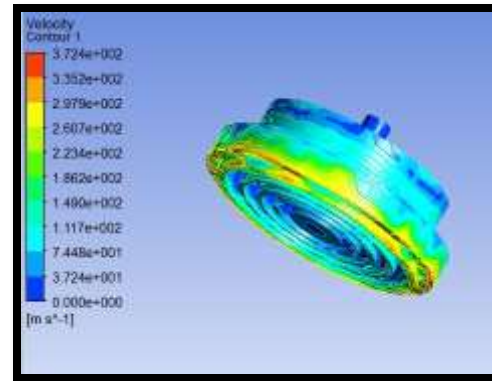
Boundary conditions

<i>Inlet temperatures(T)</i>	394k			
<i>Inlet pressure(P)</i>	101325 pa			
<i>Inlet velocity(V)</i>	50	75	80	100

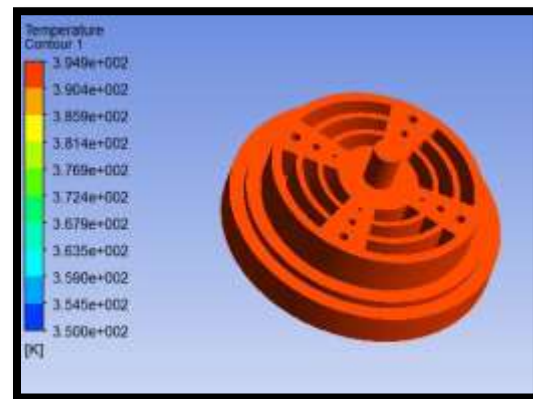
Pressure



Velocity



Temperature



Heat transfer co-efficient

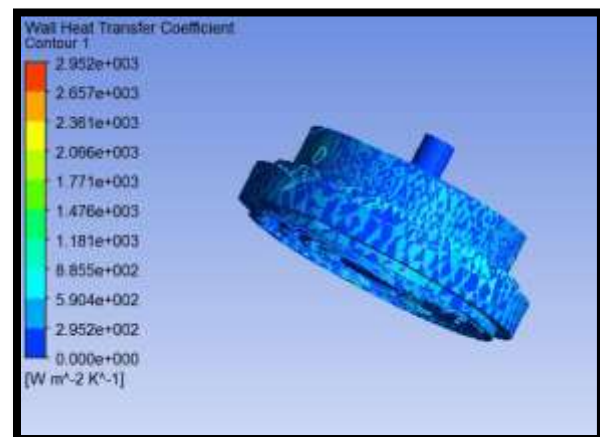


Table:1 CFD Results

Speed (m/s)	Pressure (Pa)	Velocity (m/s)	Temperature (°C)	Heat transfer coefficient (W/m ² -k)	Mass flow rate (Kg/s)	Heat transfer rate (W)
50	4.157e+004	1.881e+002	3.943e+002	6.971e+002	0.017766	1517.524
75	7.404e+004	2.482e+002	3.944e+002	1.028e+003	0.025038	2138.6226
80	1.160e+005	3.100e+002	3.960e+002	1.935e+003	0.034672	3064.5336
100	1.668e+005	3.724e+002	3.949e+002	2.952e+003	0.04242	3561.9091

speed 50m/s, 75m/s, 80m/s and 100m/s. 3D model of the valve is done in CREO and CFD analysis and thermal analysis is done on the discharge valve in ANSYS. Thermal analysis is done by varying the materials Stainless Steel, EN9 Steel and Cast Iron.

By comparing the CFD analysis results, the heat transfer rate, heat transfer coefficient, pressure, velocity and mass flow rate are increasing by increasing the compressor speed. By observing the thermal analysis results, EN9 Steel has more heat flux (i.e) heat transfer rate is more.

Table :2 Thermal Analysis Result Table

Materials	Temperature(°C)		Heat flux(W/m ² -K)
	Max.	Min.	
Stainless steel	118.09	39.865	0.16399
Cast iron	118.05	50.886	0.37049
EN13 steel	118.04	53.289	0.4031

So it can be concluded that increasing the compressor speed and using EN9 steel is better for better performance.

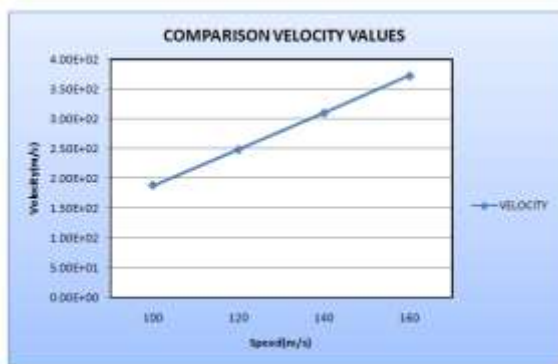
References

[1] Junghyoun Kim, et al. Valve Dynamic Analysis of a Hermetic Reciprocating Compressor International Compressor Engineering Conference. Purdue, 2006

[2] Jeffrey J. NIETER. Encounters with Application of a COR 2R Reciprocating Piston Compressor for a Heat Pump Water Heater, International Compressor Engineering Conference. Purdue, 2006

[3] Hsinheng. Li, T. E. Rajewski. "Trial investigation of oil contender for the COR 2R refrigeration framework." The procedures of the fourth IIR - Gustav Lorenten Conference on Natural Working Fluids at Purdue, P409 - 416, Li Hsinheng, Rajewski T E. Exploratory investigation of ointment contender for the COR 2R refrigeration framework//The procedures of the fourth IIR-Gustav Lorentzen Conference on Natural Working Fluids. Purdue, 2000: 409-416.

[4] Jurgen Sub, Horst Kruse. "Effectiveness of the showed interaction of COR 2R compressor." Int J . Refrig. Vol. 21 , No. 3. pp194-201 , 1998.



CONCLUSION

In this project, analytical investigations are made to determine the thermodynamic performance of the compressor by varying design parameter compressor

[5] Officinal Mario Dorin SPA. Semi-airtight COR 2R Compressors for business applications. In: IEA Heat siphon focus/IIR Workshop on COR 2R innovation in refrigeration, heat siphon and cooling frameworks, Trondheim Norway. 1997. 5

[6] Neksa.P, et al. Improvement of two phase semihermetic COR 2R blowers. In: fourth IIR Gustav Lorentzen gathering on regular working liquids, Purdue University, USA. 2000 :355 362.

[7] Experimental Investigation of the Dynamics of SelfActing Valve in a Reciprocating Compressor for Transcritical CO₂ Refrigeration Yuan Ma Xi'an Jiaotong University Yanan Gan Xi'an Jiaotong University Xueyuan Peng Xi'an Jiaotong University Ziwen Xing Xi'an Jiaotong University.

[8] Decade Developments of Rotary Compressor Pravin K. Katare, Vilayat M. Kriplani.

[9] Analytical and Experimental Investigation of RotaryVane Two-Phase Expanders in Vapor Compression Refrigeration Systems by Ahmad Mahmoud. 23TMahmoud, Ahmad

HEAT TRANSFER ENHANCEMENT USING TRAPEZOIDAL TWISTED TAPE & NANO FLUID IN A PLAIN TUBE HEAT EXCHANGER

Namala Srikanth¹, M.Tech I (Thermal Engineering) Mr.P.Raju² Assistant Professor², Dr.P.Srinivasulu,³ Professor³ (Head of the Department) Vaagdevi College Of Engineering (UGC Autonomous), P.O, Bollikunta, Warangal Urban-506005.

ABSTRACT

In the current scenario, water availability is the major element restraining the nations around the globe to meet the increasing food and energy needs. Water plays a crucial role in energy and food production around the globe. Due to the limited availability of fresh water, it is becoming a difficult task for the nations to use the available water resources for the production of food and energy. The emerging competition for water resources between the food and energy production sectors is recognized in the “food-energy-water nexus”. Desalination of sea/brackish water has the potential to reduce the water scarcity. Integration of desalination systems with power generation systems will be a major benefit in energy-water nexus. In this study, rankine cycle is integrated with a multiple-effect desalination system. During power generation using rankine cycle, huge amountsof energy is being liberated to ambient through condensers. In this study, the developed system utilizes the condensation energy to drive a multiple-effect desalination system instead of dumping to the environment.

*Thermodynamic model of the system is being developed to verify the feasibility and parametric studies are being conducted to determine the optimum System configuration and operating point.***Key words:** CFD, Heat transfer

Augmentation, twisted tape, and reduced width twisted tape, Thermal performance

INTRODUCTION

Effective utilization, conservation and recovery of heat are critical engineering problems faced by the process industry. The economic design and operation of process plants are often governed by the effective usage of heat. A majority of heat exchangers used in thermal power plants, chemical processing plants, air conditioning equipment, and refrigerators, petrochemical, biomedical and food processing plants serve to heat and cool different types of fluids. Both the mass and overall dimensions of heat exchangers employed are continuously increasing with the unit power and the volume of production. This involves huge investments annually for both operation and capital costs. Hence it is an urgent problem to reduce the overall dimension characteristics of heat exchangers. The need to optimize and conserve these expenditures has promoted the development of efficient heat exchangers. Different techniques are employed to enhance the heat transfer rates, which are generally referred to as heat transfer enhancement, augmentation or intensification technique.

1.1. Heat Transfer Enhancement

Heat transfer enhancement is one of the key issues of saving energies and compact designs for mechanical and chemical devices and plants. In the recent years, considerable emphasis has been placed on the development of various augmented heat transfer surfaces and devices. Energy and materials saving considerations, space considerations as well as economic incentives have led to the increased efforts aimed at producing more efficient heat exchange equipment through the augmentation of heat transfer. The heat exchanger industry has been striving for enhanced heat transfer coefficient and reduced pumping power in order to improve the thermo hydraulic

efficiency of heat exchangers. A good heat exchanger design should have an efficient thermodynamic performance, i.e. minimum generation of entropy or minimum destruction of energy in a system incorporating a heat exchanger. It is almost impossible to stop energy loss completely, but it can be minimized through an efficient design. The major challenge in designing a heat exchanger is to make the equipment compact and to achieve a high heat transfer rate using minimum pumping power. Heat transfer enhancements can improve the heat exchanger effectiveness of internal and external flows. They increase fluid mixing by increasing flow vorticity, unsteadiness, or turbulence or by limiting the growth of fluid boundary layers close to the heat transfer surfaces. In some specific applications, such as heat exchangers dealing with fluids of low thermal conductivity like gases or oils, it is necessary to increase the heat transfer rates. This is further compounded by the fact that viscous fluids are usually characterized by laminar flow conditions with low Reynolds numbers, whose heat transfer coefficient is relatively low and thus becomes the dominant thermal resistance in a heat exchanger. The adverse impact of low heat transfer coefficients of such flows on the size and cost of heat exchangers adds to excessive energy, material, and monetary expenditures. As the heat exchanger becomes older, the resistance to heat transfer increases owing to fouling or scaling. Augmented surfaces can create one or more combinations of the following conditions that are indicative of the improvement of performance of heat exchangers: Decrease in heat transfer surface area, size, and hence the weight of a heat exchanger for a given heat duty and pressure drop or pumping power

- Increase in heat transfer rate for a given size, flow rate, and pressure drop.
- Reduction in pumping power for a given size and heat duty
- Reduction in fouling of heat exchangers

1.2. Heat transfer augmentation techniques

Heat transfer augmentation techniques are generally classified into three categories namely: Active techniques, Passive techniques and Compound techniques.

1.3. Swirl flow devices

This is coming under category of passive heat transfer enhancement technique. These include a number of geometric arrangements or tube inserts for forced flow that create rotating and/or secondary flow i.e. inlet vortex generators, twisted-tape inserts and axial-core inserts with a screw-type winding etc.

1.5.1. Twisted tape inserts

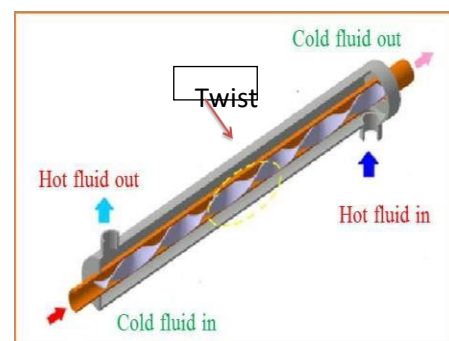


Fig.1.1. View of the twisted tape inside a plain tube

Terms used in twisted tape insert

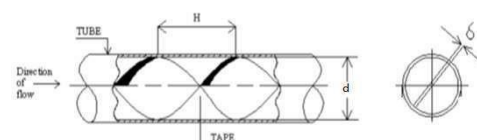
Pitch (H): Axial distance for 180° rotation of the tape **Twist**

Ratio (y): The twist ratio is defined as the ratio of pitch to inside diameter of the tube.

LITERATURE REVIEW

With the desired objectives as explained in the preceding chapter, literature survey is carried out to ascertain the progress in the field of heat transfer enhancement with twisted tape inserts. The literature in enhanced heat transfer is growing faster. At least fifteen percent of the heat transfer literature is directed towards the techniques of heat transfer augmentation now.

A lot of research has been done in heat transfer equipment by using twisted tape inserts, both experimentally and numerically.



2.1. Twisted tape in laminar flow

A summary of important investigations of twisted tape in a laminar flow is represented in Table

2.1. Twisted tape increases the heat transfer coefficient with an increase in the pressure drop. Different configurations of twisted tapes, like full-length twisted tape, short length twisted tape, full length twisted tape with varying pitch, reduced width twisted tape and regularly spaced twisted tape have been studied widely by many researchers.

Manglik and Bergles^[7] developed the correlation between friction factor and Nusselt number for laminar flows including the swirl parameter, which defined the interaction between viscous, convective inertia and centrifugal forces. These correlations pertain to the constant wall temperature case for fully developed flow, based on both previous data and their own experimental data.

2.2 Twisted tape in turbulent flow

The important investigations of twisted tape in turbulent flow are summarized in Table 2.2. In turbulent flow, the dominant thermal resistance is limited to a thin viscous sublayer. A tube inserted with a twisted tape performs better than a plain tube, and a twisted tape with a tight twist ratio provides an improved heat transfer rate at a cost of increase in pressure drop for low Prandtl number fluids. This is because the thickness of the thermal boundary layer is small for a low Prandtl number fluid and a tighter twist ratio disturbs the entire thermal boundary layer, thereby increasing the heat transfer with increase in the pressure drop. Manglik and Bergles^[23] developed correlations for both turbulent flow and laminar flow. For an isothermal friction factor, the correlation describes most available data for laminar, transitional and turbulent flows within 10 per cent. However, a family of curves is needed to develop correlation for the Nusselt number on account of the non-unique nature of laminar turbulent transition. Their correlations are as follows

Methodology

Computational Fluid Dynamics (CFD) is the use of computer-based simulation to analyse systems involving fluid flow, heat transfer and associated phenomena such as chemical reaction. A numerical model is first constructed using a set of mathematical equations that describe the flow. These equations are then solved using a computer programme in order to obtain the flow variables throughout the flow domain. Since the arrival of the digital computer, CFD has received extensive attention and has been widely used to study various aspects of fluid dynamics. The development and application of CFD have undergone considerable growth, and as a result it has become a powerful tool in the design and analysis of engineering and other processes.^[35]

3.1 CFD analysis procedure

CFD analysis requires the following information:

- A grid of points at which to store the variables calculated by CFD
- Boundary conditions required for defining the conditions at the boundaries of the flow domain and which enable the boundary values of all variables to be calculated
- Fluid properties such as viscosity, thermal conductivity and density etc.
- Flow models which define the various aspects of the flow, such as turbulence, mass and heat transfer.
- Initial conditions used to provide an initial guess of the solution variables in a steady state simulation.
- Solver control parameters required to control the behavior of the numerical solution process.

NUMERICAL INVESTIGATIONS

This chapter deals with the numerical analysis of water flowing through a horizontal circular tube at constant wall temperature, for estimation of the heat transfer and friction factor characteristics. The results obtained from numerical investigations are validated by comparing with the available

correlations

4.1. Physical model

Considered the problem of water flowing through a circular tube with length (L) and inside diameter of 2200 mm and 22 mm respectively.

4.2. FLUENT Simulation

4.2.1. Geometry Creation and Mesh generation

A circular pipe of diameter 22 mm and length 2200 mm was used as the geometry. A 3-D geometry is created by using ANSYS workbench and schematic view is shown in the Fig. 4.2. Structured meshing method is used for meshing the geometry. It is meshed into 55,806 nodes and 1, 95,569 elements as shown in Fig. 4.3.

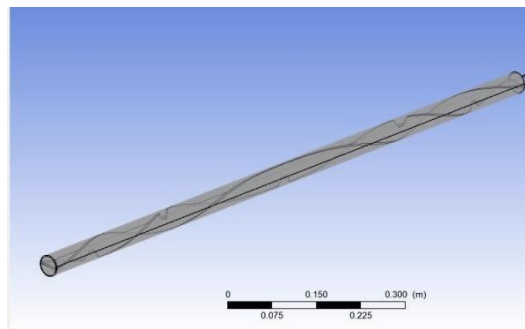


Fig 4.2 tube geometric created by ANSYS workbench

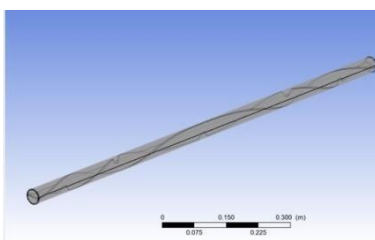
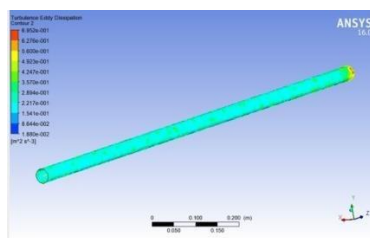


Fig 4.3 Meshing of plain tube geometry



Fing No 4.12 kinetic energy Nano

4.2.2. Defining the Material Properties

This section of the input contains the options for the materials

S.No.	properties	value
1	Density, ρ	998.2 kg/m ³
2	Specific heat capacity, C_p	4182 J/kg K
3	Thermal conductivity	0.6 W/m K
4	Viscosity, μ	1.003 x 10 ⁻³ kg/m s

tube chosen. Water is passing in the horizontal tube under constant wall temperature condition in the present work. Under materials Tab in FLUENT, fluid considered is water -liquid. Solid (tube wall) material considered for analysis is copper. The selection of material is done. Material selected is water-liquid. The properties of water- liquid is taken as follows

4.2.4 Boundary Conditions

Water at a temperature of 25⁰C was used as the working fluid. The numerical studies were carried out with uniform velocity profile at the inlet of the horizontal pipeline. The direction of the flow was defined normal to the boundary. Inlet velocity and temperature were of water while passing through the plain tube. Because of the frictional resistance offered to fluid flow, water pressure drops across flow field. Pressure drop varied from 6.042 Pa to 330.05 Pa for the range of Reynolds numbers considered for numerical analysis.

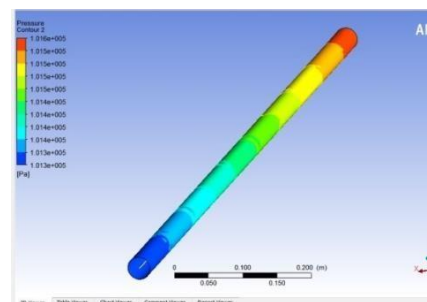


Fig 4.4 pressure nano contour

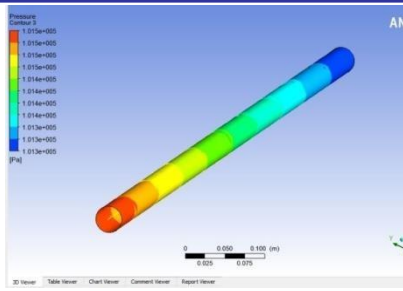


Fig 4.5 Pressure water

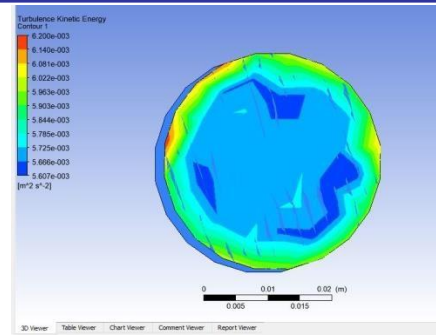


Fig no 4.5 kinetic energy Nano fluid

4.2.3. Laminar Region

Nusselt number for the base fluid (water) in the laminar region was compared with equations (4.3) and (4.4). It can be seen from Fig.4.6. Friction factor for the base fluid (water) in the laminar region was compared with equation (4.7). It can be seen from Fig.4.7.

4.2.4. Turbulent Region.

Nusselt number for the base fluid (water) in the turbulent region was compared with equation (4.5). It can be seen from Fig.4.8.

Friction factor for the base fluid (water) in the turbulent region was compared with equation (4.8). It can be seen from Fig.4.9.

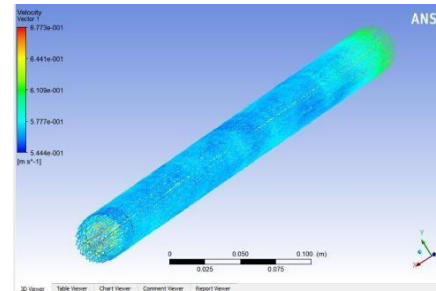


Fig no 4.7 Velocity Nano

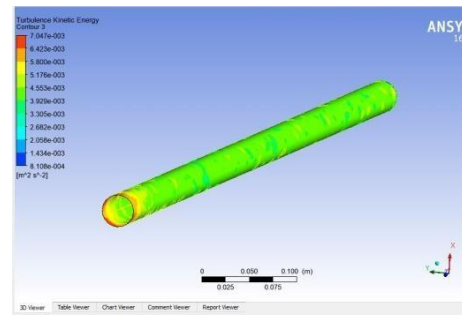


Fig no 4.8 tur ke water

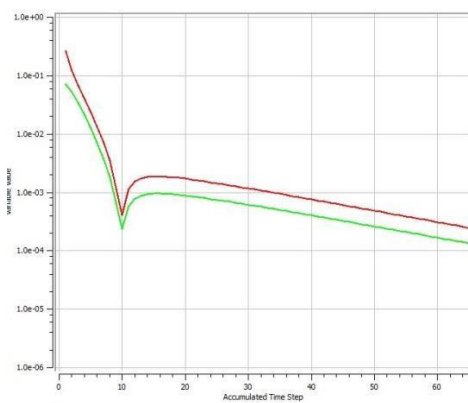


Fig.4.6. kinetic energy Nano

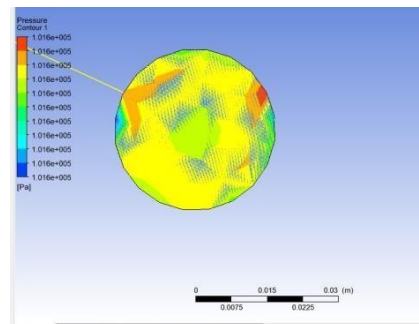
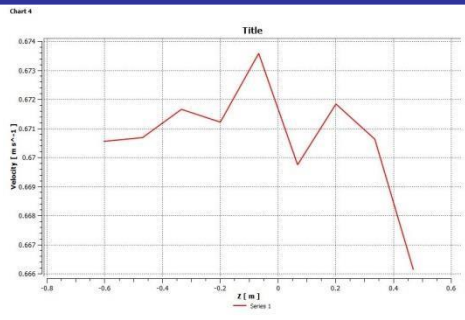
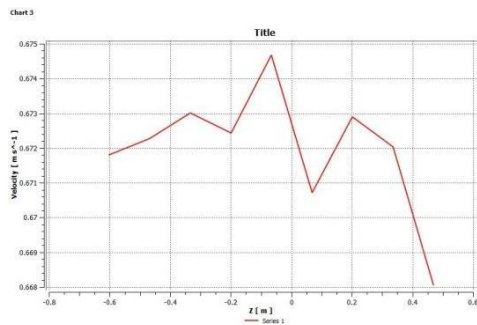


Fig No 4.10 pressure Nano



Fin no 4.11 vel water



Fin No 4.12 Velocity Nano

CONCLUSION

The numerical analysis of heat and fluid-flows through a constant wall temperature circular plain tube and finned tube fitted with twisted tape is carried out, with the aim to investigate the effect of tape twist ratio ($\gamma=H/d$) and tape width on heat transfer (Nu), friction factor (f) and thermal performance (η) behaviors in the laminar and turbulent flow regime.

The main findings can be drawn as follows.

4. Turbulent modeling was done with standard $k-\epsilon$ turbulence model, the Renormalized Group (RNG) $k-\epsilon$ turbulence model, the standard $k-\omega$ turbulence model, and the Shear Stress Transport(SST) $k-\omega$ turbulence model. The CFD results of Nusselt number and friction factor are compared with those obtained from Manglik and Bergles equations. It is clearly seen that the predicted Nusselt numbers obtained from the SST $k-\omega$ turbulence models is in better agreement compared to those from other models. The SST $k-\omega$ turbulence model is valid within $\pm 20.2\%$ error limit with measurements for Nusselt number and $\pm 26.4\%$ for friction factor. Therefore this model used for

further studies. Plain tube with full width twisted tape inserts, (FWTT) of twist ratio, ($\gamma=2, 3, 4, 5$) results show that Nusselt number and friction factor values were found to decrease with increasing in twist ratio. Twisted tape inserts for twist ratio ($\gamma=2$) can enhance heat transfer rates up to 3.5 times at Reynolds number 2000 and increase in friction factors nearly 9 times in comparison with those of the plain tube. Thermal performance factor (η) was found to increase with increase in Reynolds number in the laminar region and decrease in the turbulent region. The maximum value of the thermal performance factor was found to be 1.6 for Twisted tape ($\gamma=3$) in plain tube at a Reynolds number of 2000

5. Finned tube with reduced width twisted tape, (RWTT) simulation results are shown that the twisted tape inserts of twist ratio ($\gamma=2$) can enhance heat transfer rates up to 3.76 times at Reynolds number 2000 with tape width of 16 mm and the corresponding increase in friction factors nearly 14 times in comparison with those of the plain tube. Thermal performance factor (η) was found to initially increase with increase in Reynolds number then decrease in the laminar region and increase with increase Reynolds number in the turbulent region. The maximum value of the thermal performance factor was found to be 1.31 for Twisted tape ($\gamma=5$) and tape width of 12 mm in a Reynolds number of 10000

REFERENCES

1. Bergles.A.E. (2001), the implications and challenges of enhanced heat transfer for the chemical process industries! Trans IChemE Vol.79 pp.437-444
2. Syam sundar, L. sharma, K.V. (2011), Laminar convective heat transfer and friction factor of Al_2O_3 nanofluid in circular tube fitted with twisted tape inserts, International Journal of Automotive and Mechanical Engineering, Volume 3, pp. 265-278
3. Adrian, B. Allan, D. K. (2003), Heat transfer enhancement. In Heat Transfer Handbook, Chapter 14, pp.1033, -1101, Wiley-interscience.

4. Bergles, A.E. Blumenkrantz, A.R. Taborek, J. (1974), Performance evaluation criteria for enhanced heat transfer surfaces. Proc. of 5th Int. Heat Conf., Tokyo, Vol. 2, pp. 239-243
5. Lokanath, M. S. (1997), Performance evaluation of full length and half-length twisted tape inserts on laminar flow heat transfer in tubes. In Proceedings of 3rd ISHMT–ASME Heat and Mass Transfer Conference, India, pp. 319–324
6. Ray, S. Date, A.W. (2001), Laminar flow and heat transfer through square duct with twisted tape insert, International journal of Heat and Fluid Flow, Vol. 22, pp. 460-472
7. Manglik, R. K. and Bergles, A. E. (1993), Heat transfer and pressure drop correlations for twisted-tape inserts in isothermal tubes: Part I: laminar flows. Trans. ASME, J. Heat Transfer, Vol.115, pp.881–889.
8. Saha, S. K. and Dutta, A. (2001), Thermo-hydraulic study of laminar swirl flow through a circular tube fitted with twisted tapes. Trans. ASME, J. Heat Transfer, Vol.123, pp. 417–421.
9. Tariq, A. Kant, K. and Panigrahi, P. K. (2000), Heat transfer enhancement using an internally threaded tube. In Proceedings of 4th ISHMT–ASME Heat and Mass Transfer Conference, India, pp. 277–281.
10. Saha, S. K. and Bhunia, K. (2000), Heat transfer and pressure drop characteristics of varying pitch twisted-tape-generated laminar smooth swirl flow. In Proceedings of 4th ISHMT– ASME Heat and Mass Transfer Conference, India, pp. 423–428.
25. Ray, S. and Date, A. W.(2003), Friction and heat transfer characteristics of flow through square duct with twisted tape insert, Int. J. Heat and Mass Transfer, Vol. 46, pp.889–902.

PERFORMANCE AN IMPROVEMENT OF AN AUTOMOBILE RADIATOR USING DIFFERENT NANO FLUIDS

Guguloth Anitha¹ P Raju² Dr. Srinivasulu Pulluru³

¹M.Tech (Thermal Engineering)Department of mechanical engineering vaagdevi college of engineering (UGC autonomous) approved by AICTE & permanent affiliation to jntuh, hyderabad.p.o, bollikunta, Warangal urban-506005.

²Assistant professor Department of mechanical engineering vaagdevi college of engineering (UGC autonomous) approved by AICTE & permanent affiliation to jntuh, Hyderabad. p.o, bollikunta, Warangal urban- 506005.

³Professor and Head of the Department of mechanical engineering vaagdevi college of engineering (UGC autonomous) approved by AICTE & permanent affiliation to jntuh, hyderabad. p.o, bollikunta, Warangal urban-506005.

Abstract

In cooling system of automobile engine the water is evaporate at high temperature, so we need to add water and also water is low capacity of absorb heat. Cooling system plays important roles to control the temperature of car's engine. One of the important elements in the car cooling system is cooling fluid. The usage of wrong cooling fluid can give negatives impact to the car's engine and shorten engine life. An efficient cooling system can prevent engine from overheating and assists the vehicle running at its optimal performance. In this Paper, different nano fluids mixed with base fluid water are analyzed for their performance in the radiator. The nano fluids are magnesium Oxide and silver nano particle at different volume fractions such as 0.25%. Theoretical calculations are done determine the properties for nano fluids and those properties are used as inputs for analysis.

3D model of the radiator is done in CREO. CFD analysis is done on the radiator for all nano fluids and volume fraction.

Key words: CREO, NANO FLUID,CFD AND COOLING SYSTEM

1.1 INTRODUCTION TO AUTOMOBILE RADIATOR

Radiators are heat exchangers used to transfer thermal energy from one medium to another for the purpose of cooling and heating. The majority of radiators are constructed to function in automobiles, buildings, and electronics. The radiator is always a source of heat to its environment, although this may be for either the purpose of heating this environment, or for cooling the fluid or coolant supplied to it, as for engine cooling. Despite the name, radiators generally transfer the bulk of their heat via convection, not by thermal radiation, though the term

"convector" is used more narrowly; see radiation and convection, below.



1.2 RADIATION AND CONVECTION

One might expect the term "radiator" to apply to devices that transfer heat primarily by thermal radiation (see: infrared heating), while a device which relied primarily on natural or forced convection would be called a "convector". In practice, the term "radiator" refers to any of a number of devices in which a liquid circulates through exposed pipes (often with fins or other means of increasing surface area), notwithstanding that such devices tend to transfer heat mainly by convection and might logically be called convectors. The term "convector" refers to a class of devices in which the source of heat is not directly exposed.

1.3 WORKING OF AUTOMOBILE RADIATORS

Almost all automobiles in the market today have a type of heat exchanger called a radiator. The radiator

is part of the cooling system of the engine as shown in Figure below. As you can see in the figure, the radiator is just one of the many components of the complex cooling system.

2. LITERATURE SURVEY

Yiding Cao and KhokiatKengskool [1], had gave application of the heat pipe in an automotive engine was introduced. In this application, heat pipes were incorporated into the radiator of the automotive engine for more efficient heat transfer. The cooling load of the radiator can be increased for heavy-duty engines, while the power consumption of the cooling fan can be reduced for higher energy efficiency. Heat pipes including two-phase closed thermo siphon were two-phase heat transfer devices with an effective thermal conductance hundreds of times higher than that of copper. For the terrestrial applications, gravity was often used to assist the return of the liquid condensate and no wick structure was needed inside the heat pipe.

M. Naraki and S.M. Peyghambarzadeh [2], In this research, the overall heat transfer coefficient of CuO/water Nano fluids is investigated experimentally under laminar flow regime ($100 < Re < 1000$) in a car radiator. The Nano fluids in all the experiments have been stabilized with variation of pH and use of suitable surfactant. The results show that the overall heat transfer coefficient with Nano fluid is more than the base fluid. The overall heat transfer coefficient increases with the enhancement in the Nano fluid concentration from 0 to 0.4 vol. %.

Rahul Tarodiya, J. Sarkar, J. V. Tirkey [3], the used of "Nano fluids" have been developed and these fluids offer higher heat transfer properties compared to that of conventional automotive engine coolants. Energetic analyses as well as theoretical performance analyses of the flat fin tube automotive radiator using Nano fluids as coolants have been done to study its performance improvement. Effects of various operating parameters using Cu, SiC, and Al₂O₃ and TiO₂ Nano fluids with 80% water-20% ethylene glycol as a base fluid are presented in this article. Use of Nano fluid as coolant in radiator improves the effectiveness, cooling capacity with the reduction in pumping power. SiC-80% H₂O-20% EG (base fluid) yields best performance in radiator having plate fin geometry followed by Al₂O₃-base fluid, TiO₂-base fluid and Cu-base fluid. The maximum cooling improvement for SiC is 18.36%, whereas that for Al₂O₃ is 17.39%, for TiO₂ is 17.05% and for Cu is 13.41% as coolants. Present study reveals that the Nano fluids may effectively use as coolant in automotive radiators to improve the performance.

Vincent Enontiemonria, Ohiozua, OhiremeNathaniel [5], The cooling properties of a locally formulated coolant (sample C) vis-a-vis, its boiling

characteristics and specific heat capacity were investigated alongside with a common coolant-water (as sample A) and a commercial coolant (sample B). The results of the investigation showed that sample C gave the best performance compared to the other two samples A and B: the boiling points of sample C was 110°C, sample A 100°C, and sample B 101°C. This means that the possibility of a boil-out of sample C from the radiator is little compared to samples A and B. Also, for the same quantity of coolant more heat would be required to raise sample C to its boiling point than for samples A and B. In other word, better cooling would be achieved using sample.

Problem identification

In Current era, it becomes an need to Design an Automobile with higher efficiency , more life and environment friendly. For that purpose it is necessary to run the engine at favourable condition; so Radiator acts as an catalyst in the functioning of Engine.

For effective utilization of Radiator Following changes can be made:

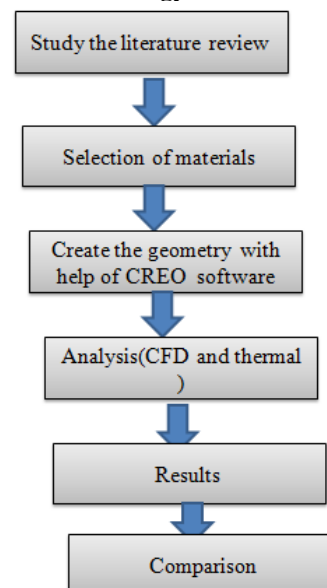
- Used of nano fluid
- Helical tubes

Objective and novelty

The main objective of this project to increase the cooling efficiency with different nano fluids when we compared to water. Furthermore we are changing the geometry i.e straight tube in replace of helical tube Present now a days in radiator fluid used as water now we are replacing the nano fluids due increase cooling efficiency.

Radiator tube is a straight tube we replace the helical tube.

2.3 Methodology



3. MODELING AND ANALYSIS RADIATOR SPECIFICATIONS

Maruti Alto:

- Size: 300*335*23 mm
- Make: SUZUKI
- Model no. DL-A039
- Material: Copper

Maruti 800

- Downward flow type
- Cu tubes, Cu plates
- 37 plates, dia of tubes-10mm
- Capacity= 3lit.

Cooling fan

- Rpm: 1200-2400 rpm
- 220/240 V
- Single phase AC

Water Pump

- Submersible pump
- 165-220V/50 Hz
- Power -19W
- Output -1100 L/H

Energy wire

- 1 phase, 2 wire
- AC 240V , 50Hz
- I (max)- 30A

Heating elements

- Power = 2000W, 1500W

Reservoir

- Material: Stainless steel
- Capacity: 25-30L

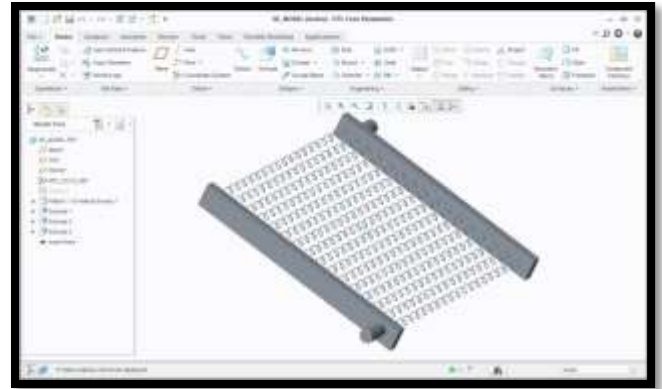


Fig: 3d Model of Radiator

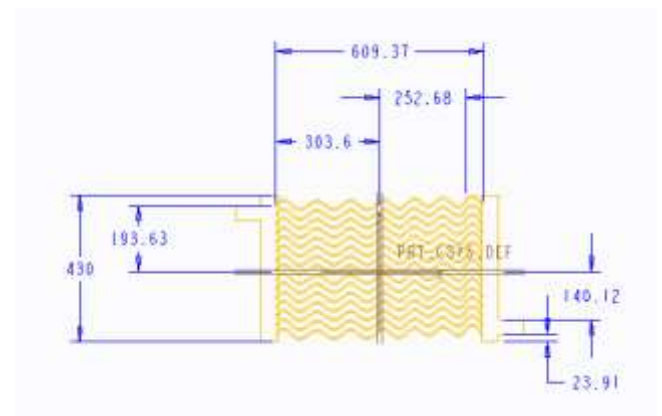


Fig: 2D model

CFD (Computational Fluid Dynamics)

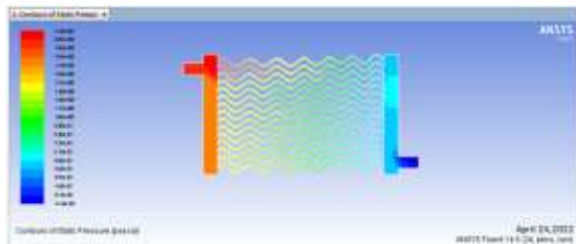
The ANSYS/FLOTRAN CFD (Computational Fluid Dynamics) offers comprehensive tools for analyzing two-dimensional and three-dimensional fluid flow fields. ANSYS is capable of modeling a vast range of analysis types such as: airfoils for pressure analysis of airplane wings (lift and drag), flow in supersonic nozzles, and complex, three-dimensional flow patterns in a pipe bend. In addition, ANSYS/FLOTRAN could be used to perform tasks including.

Nano Fluid Properties

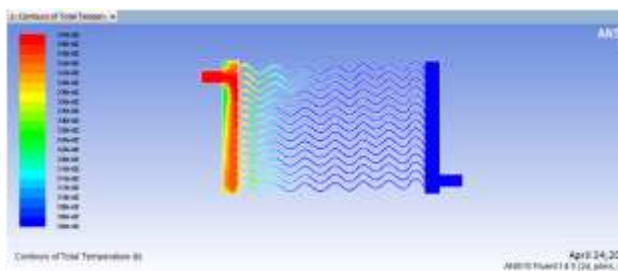
FLUID	Volume fraction	Thermal conductivity (w/m-k)	Specific heat (J/kg-k)	Density (kg/m ³)	Viscosity (kg/m-s)
MAGNESIUM OXIDE	0.25	1.4586	2465.67	1643.47	0.001629
SILVER		1.4917	1575.17	3373.65	0.001629

4. CFD Analysis of Radiator

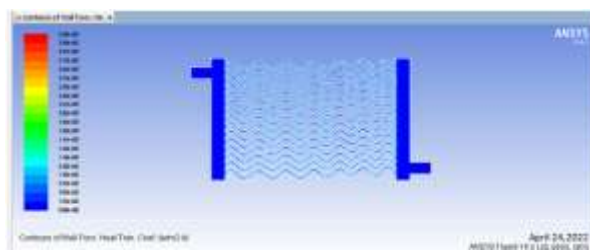
Static Pressure



Static Temperature



Heat Transfer Co-Efficient



Total Heat Transfer Rate (w)	
inlet	129598.88
outlet	-11532.23
wall_trm_srf	-118045.85
Net	20.792969

Mass Flow Rate (kg/s)	
inlet	1.5
interior_trm_srf	7.3168697
outlet	-1.4991596
wall_trm_srf	0
Net	0.00084042549

5.RESULTS AND DISCUSSIONS

CASE 1-STRAIGHT TUBE

Fluid	Pressure (Pa)	Heat transfer coefficient (W/m ² k)	Mass flow rate (Kg/sec)	Heat transfer rate (w)
Air	1.61e+03	4.84e+00	0.00046002	6.1064413
Water	3.00e+02	1.20e+02	0.0000059604	4.23437
Magnesium oxide	1.96e+02	2.60e+02	0.0000108409	1.140675
Silver nano fluid	1.05e+01	3.60e+02	0.0001062	0.71875

CASE 2 -HELICAL TUBE

Fluid	Pressure (Pa)	Heat transfer coefficient (W/m ² k)	Mass flow rate (Kg/sec)	Heat transfer rate (w)
Air	3.61e+03	4.96e+01	0.00111	49.08
Water	6.24e+02	1.23e+03	0.000837	151.32
Magnesium oxide	4.47e+02	2.96e+03	0.000892	56.37
Silver nano fluid	2.18e+01	3.68e+03	0.0008404	20.297

6.CONCLUSION

In this thesis, different NANO fluids mixed with base fluid water are analyzed for their performance in the radiator. In this project the different types of fluids are applied in radiator. The fluids are water, air and aluminum oxide NANO fluid.

3D model of the radiator is done in CREO parametric software. CFD analysis is done on the radiator for all fluids and thermal analysis is done in ANSYS.

By observing the CFD analysis the heat transfer coefficient values are increases by increasing the mass flow inlet. The heat transfer coefficient more at silver nano fluid when we compared other fluids.

When we compare the different geometries of radiator the helical type tube is the better model because the heat transfer rate value is more for helical type tube radiator is better model.

REFERENCES

- [1] Yiding Cao and KhokiatKengskool, "An Automotive Radiator Employing Wickless Heat Pipes" Florida International University, Miami, Conference Paper, 1992.
- [2] Hwa-Ming Nieh, Tun-Ping Teng, Chao-Chieh Yu "Enhanced heat dissipation of a radiator using oxide nano-coolant". International Journal of Thermal Sciences 77 (2014) 252-261.
- [3] M.Naraki and S.M. Peyghambarzadeh, "Parametric study of overall heat transfer coefficient of CuO/water Nano fluids in a car radiator". International Journal of Thermal Sciences 66 (2013) 82-90.
- [4] RahulTarodiya, J. Sarkar, J. V. Tirkey, "Performance of flat fin tube automotive radiator using Nano fluids as coolants". National Conference on Emerging Trends in Mechanical Engineering (ETME – 2012).
- [5] Efeovbokhan, Vincent Enontiemonria, Ohiozua, Ohireme Nathaniel, "Comparison of the cooling effects of a locally formulated car radiator coolant with water and a commercial coolant". The International Journal of Engineering And Science (IJES) ||Volume|| 2 ||Issue|| 01 ||Pages|| 254-262 ||2013|| ISSN: 2319 – 1813 ISBN: 2319 – 1805.
- [6] S.M. Peyghambarzadeh , S.H. Hashemabadi , S.M. Hoseini , M. SeifiJamnani "Experimental study of heat transfer enhancement using water/ethylene glycol based Nano fluids as a new coolant for car radiators". International Communications in Heat and Mass Transfer 38 (2011) 1283–1290.
- [7] S.M. Peyghambarzadeh, S.H. Hashemabadi, M. Naraki, Y. Vermahmoudi," Experimental study of overall heat transfer coefficient in the application of dilute Nano fluids in the car radiator".Applied Thermal Engineering 52 (2013) 8-16.
- [8] D. Madhesh, R. Parameshwaran, S. Kalaiselvam" Experimental investigation on convective heat

transfer and rheological characteristics of Cu–TiO₂ hybrid nanofluids".Experimental Thermal and Fluid Science 52 (2014) 104–115.

EFFECT OF PISTON BOWL GEOMETRY ON PERFORMANCE AND EMISSION WITH TOBACCO BIODIESEL BLEND

Jarupula Revanth Kumar¹ Mr.Y. Umashankar² Dr. Srinivasulu Pulluru³

¹M.Tech (Thermal Engineering)Department of mechanical engineering vaagdevi college of engineering (UGC autonomous) approved by AICTE & permanent affiliation to jntuh, hyderabad.p.o, bollikunta, Warangal urban-506005.

²Assistant professor Department of mechanical engineering vaagdevi college of engineering (UGC autonomous) approved by AICTE & permanent affiliation to jntuh, Hyderabad. p.o, bollikunta, Warangal urban- 506005.

³Professor and Head of the Department of mechanical engineering vaagdevi college of engineering (UGC autonomous) approved by AICTE & permanent affiliation to jntuh, hyderabad. p.o, bollikunta, Warangal urban-506005.

Abstract

Non-edible oils are considered as one of the most productive alternatives for internal combustion engine fuels because of very little to no food insecurity and good combustion properties. Tobacco plant grows well between 20° and 30°C which are well suitable conditions for Andhra Pradesh state climate, also it is a very remunerative crop therefore it is very difficult to substitute, FCV (Flue-Cured Virginia) is cultivated in Andhra Pradesh locally and its leaves are fully utilized in production of cigarette and other tobacco products, its seeds can be used to produce biodiesel. Test fuel is made out of Tobacco seed oil (B20, B30, B50) and distilled water (additive) micro emulsion using SPAN 80 (0.2%) TWEEN 80 (0.1%) as non-ionic surfactant and emulsifier at various blends of 5, 10 and 15ml in 1-liter B20 fuel. This project has two stages in which Experiments are conducted to reach the full conclusion.

Stage-1: To study the performance parameters of a toroidal shaped combustion chamber and a hemispherical combustion chamber and conclude which performs better.

Stage-2: To study the effect of varied piston bowl geometry on the performance and emission characteristics of tobacco seed oil micro emulsion (TSOME) biodiesel on four stroke single cylinder diesel engines at constant speed of 1500 rpm for different loads. It is noticed that, at 20% blend of Tobacco seed oil and 10ml distilled water micro emulsion biodiesel, the stability and emission parameters were improved compared to pure diesel fuel operation. Hence the same optimal blend is adapted for conducting experiments by changing piston bowl geometry as well as the additive composition in the fuel mixture. The experiments are conducted duly ensuring the same compression ratio which was used with standard hemispherical geometry.

1. INTRODUCTION

Diesel engines have found wide applications in many industrial, agricultural and transport sectors due to their better fuel to power conversion efficiency and fuel economy. Apart from being a fuel of wide applications, it is also a major contributor to the atmospheric emissions leading to shrinking snow and ice, rise in sea level, severe droughts and floods. Reportedly, 57% of greenhouse gases are from fossil fuel combustion owing to transport and industrial sectors. Emissions from fossil fuel combustion not only harm the nature but also deteriorate human health by forming nitrogen oxides and particulate matter. The emissions from diesel engines include carbon monoxide (CO), carbon dioxide (CO₂), unburned hydrocarbons (HC), nitrogen oxides (NOX), particulate matters (PM) and traces of Sulphur oxides (SOX).

Bio-diesel

Bio diesel is form of fuel which is derived from animals, plants or other organic matter which contains long-chain fatty acid esters. It is made by a process called as transesterification, in which the principal oil lipids react with alcohol and produce methyl, ethyl or propyl ester.

Unlike other fuels which require small changes in the engine specifications, biodiesel is a drop-in fuel, means it is simply compatible with existing diesel engines without any modifications or alterations in the engine specifications.

Market places are mostly distributed with pure biodiesel and its blends, A system known as “B” factor is used to recognize the amount of biodiesel fuel used in any fuel mixture.

- 1.B100- Stands for 100% pure biodiesel.
- 2.B50- Stands for 50% pure biodiesel and 50% pure Petro diesel.
- 3.B20- Stands for 20% pure biodiesel and 50% pure Petro diesel.
- 4.B2- Stands for 2% pure biodiesel and 98% pure Petro diesel.

Selection of Tobacco Variety

FCV Tobacco seeds are used in this analysis as a source to obtain biodiesel. This variety is produced only in three states in India, and Andhra Pradesh is one among them. It grows best in climatic conditions ranging from 200C to 300C and Mild rains. FCV stands for (Flue Cured Virginia) which is generally used in production of cigars, cigarettes and beedi. Its leaves are fully utilized in consumer grade products but the seeds are left only for propagation. Each plant produces thousands of seeds in its lifetime, also it's a crop which propagates into a full-grown plant very quickly (within 6 months of plantation). The seeds are very small and large in quantity, to the general eye the seeds look like roughly grated powder and are dark brown in colour.



Fig-1 Tobacco plant, its leaves and cigar making



Fig 2 FCV Tobacco Seeds

Emulsion Fuels

Emulsions are obtained from a dispersion of two non-miscible fluids. The dispersion produces a continuous and finely dispersed droplets phase. A surfactant added to the mixture reduces the oil and water surface tension, activates their surfaces, and maximizes their superficial contact areas to make emulsions. The surfactant molecule has both lipophilic group and hydrophilic group. The hydrophilic group is polarized and oil repelling, whereas the nature of a lipophilic group is the opposite. Therefore, the amount of hydrophilic group and lipophilic group in a surfactant can be estimated by testing its soluble ability in chemical compounds. The surfactant increases the electric charge in the disperse phase droplets and increases the droplet repulsion force to prohibit droplets from merging. The water oil emulsion is prepared using either a mechanical, chemical, or electric homogenizing machine to stir water and oil mixture. Most of the properties of the emulsion systems (stability, viscosity, etc.) depend on the droplets size and size

distribution. The mean droplet diameter depends on the intensity and on the amount of introduced energy for the particular preparation technique.

A commonly used classification of emulsions is based on the polarity of the phases. In almost all the applications, water is one of the fluids, while the other is characterized by a lower dielectric constant indicated as oil. Therefore, emulsions are generally indicated as dispersions of water droplets in oil (water-in-oil emulsions, W/O) or oil droplets in water (oil-in-water emulsions, O/W).

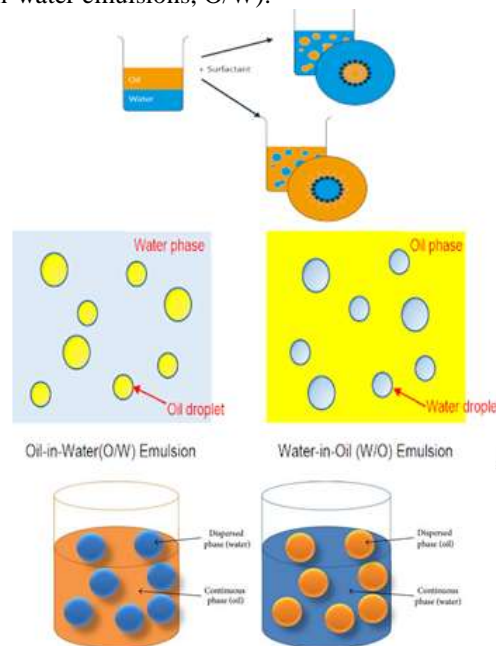


Fig 3 Emulsions

Surfactants

Surfactants are compounds that lower the surface tension (or interfacial tension) between two liquids, between a gas and a liquid, or between a liquid and a solid.

Surfactants may act as detergents, wetting agents, emulsifiers, foaming agents, or dispersants. The word "surfactant" is a blend of surface-active agent coined in 1950.

Table: Fuel Properties

Test Fuel	Viscosity at 40°C (Centi-Poise)	Density at 25°C	Cetane Number	Calorific Value (kJ/kg)
Diesel	4.0	0.84	55	42000
Tobacco Seed Oil (crude) (CTSO)	24.0	0.91	45	38438
Tobacco Seed Oil (Biodiesel) (TSOBD)	12.0	0.87	0.52	38000

Reasons why tobacco oil is chosen as a safe alternative.

1. The yield percentage of tobacco seed oil is 33-40%. Depending upon the crop quality.

2. More than one hundred and thirty-four hectares of land is used for tobacco cultivation, which in result leaves so many tons of seeds which can be properly utilised in tobacco oil production.

3. Only 315 Tonnes of tobacco oil is produced every year without the need for commercial biodiesel, if biodiesel is produced then all the wastage seeds can be properly utilized.

4. Cetane number of tobacco seed oil biodiesel is 47 which is just below Karanja oil biodiesel which is 48. So, the compression ratio can be the same which is generally used for the diesel engine, Therefore, there is no requirement of any modifications to the engine.

5. Density of the tobacco seed oil biodiesel is 0.87 which is just 0.3 times more than diesel which is 0.84, this means the biodiesel can be stored in a normal sealed tank just like diesel without any need for special modifications in the storage tank.

6. The viscosity of the biodiesel is 12 centi-poise which is relatively high compared to diesel, therefore the distilled water additive should be helping in gradually reducing the viscosity to a point that there comes no need for any additional modification in the engine.

2. LITERATURE SURVEY

Habibullah et al. [1] have investigated the effect of blends from palm and coconut oil methyl ester on diesel engine. The test results showed the biodiesel blends produced low brake torque and high brake specific fuel consumption. Reduced emission of HC, CO and smoke emissions were observed with an increase in NO_x emission. However, the combined blend of palm and coconut oil biodiesel showed superior performance and emission when compared to performance of individual biodiesel blends and emission characteristics.

Ozturk et al. [2] have done investigation of the performance and emission study of a compression ignition engine using biodiesel derived from cananol-hazelnut soap stock. Decrease in the ignition delay and maximum heat release rates with the 44 addition of biodiesel blends was seen. Using B5 biodiesel blend, HC, CO and smoke emissions decreased with an increase in NO_x emission. However, there was deterioration in the combustion process due to higher biodiesel blend as a result of higher density, viscosity and surface tension. An increase in HC, CO and smoke emission was seen with decrease in NO_x emission.

Ramadhas et al. [3] have carried out tests with methyl esters of rubber seed oil as fuel in a diesel engine. The results showed an improvement in thermal efficiency due to the use of biodiesel of lower concentration. B10 biodiesel blend provided a better thermal efficiency with lower emission gases. The exhaust gas temperature and NO_x emission increased

with an increase in biodiesel blend. Agnew et al. [26] have used Croton megalocarpus (musine) methyl ester as fuel in a three-cylinder Perkins D3.142 engine. The tests indicated a lower brake thermal efficiency for croton biodiesel blend than standard diesel fuel. The specific fuel consumption increased by 2.65%, 3.8%, 4.7% and 4.7% for B5, B20, B50 and B100 respectively than with diesel fuel. CO, CO₂ and HC emissions were higher for the croton biodiesel with lower smoke emission.

Kalam et al. [4] have conducted experiments in a four-cylinder diesel engine fueled with B5, B10 and B20 blends of palm and Jatropha biodiesel and compared to standard diesel fuel in the speed range of 1000 rpm to 4000 rpm. The brake power was decreased by 2.3% to 10.7% on an average with the use of B10 and B20 blends of palm and jatropha biodiesel. BSFC was increased by 26.4% on an average for biodiesel blends. CO and HC emissions were reduced by 30.7% and 25.8% on an average for B20 biodiesel blends when compared to diesel fuel. NO_x emission decreased by 3.3% on average for palm 3 biodiesel blends of B10 and B20, whereas NO_x emission increased by 3.0% on an average for jatropha biodiesel blends of B10 and B20 when compared to diesel fuel.

However, there seems to be very less research in the field of tobacco oil and its applications, for this project we have selected a local variety of tobacco crop cultivated in Andhra Pradesh State, it is widely used in production of cigars, cigarettes and beedi, FCV (Flue Cured Virginia) tobacco is a type of tobacco plant which produces high quality tobacco yield. V.B. Veljkovic[5] used Nicotiana Tabacum L seed to produce biodiesel, FAME (Fatty acids preferably Methyl Esters) from the crude TSO having the high FFA content was investigated The tobacco biodiesel obtained had the fuel properties within the limits prescribed by the latest American (ASTM D 6751-02) and European (DIN EN 14214) standards, except for a somewhat higher acid value than that prescribed by the latter standard Thus, tobacco seeds, as agricultural wastes and with quite high oil content, might be a cheap and valuable renewable raw material for biodiesel production .

Problem Recognition

Based on the above discussions it is noted that there is less research and few reports available on the investigation of local Andhra Pradesh FCV tobacco variety oil biodiesel and its emulsions. This is motivating me to conduct detailed study about the characteristics of tobacco seed oil biodiesel micro emulsion as fuel. The relevance of the present study is to improve the performance of 20% blended tobacco oil biodiesel micro emulsion mixture in

automobiles maintaining the current emission standards (BS VI).

The present work also deals with the study of combustion chamber performance of the experimental engine rig, characteristics such as BTE, BSFC, Specific Fuel, Mechanical Efficiency of a diesel engine were evaluated at different loads along with the emission characteristics like CO, HC, and NO_x. The effects on piston bowl geometry will also be analysed.

Objective

This present investigation, shows the combustion and emission characteristics of FCV Tobacco seed biodiesel micro-emulsion (5ml, 10ml, 15ml blends) and its effects on varying piston bowl geometry and combustion chamber performance in direct injection diesel engine, the piston bowl geometry was modified to have tangential grooves and from the baseline cylindrical shape. Blends containing 0% of diesel required preheating up to 80°C. Performance and emission characteristics of 90% (B10) and 80% (B20) are better than the other blends followed by 70% blend. The maximum efficiency of 90% and 80% blend is well comparable with diesel. However unburned HC emissions are increased up to 4.1kW load by 10%, 18.5%, 37.14% and 45% for 90%, 80%, 70% and 0% blends but HC is reduced by 16%, 18% and 24% for the blends B10, B20 and B30 respectively compared with diesel at full load condition. CO emission, CO₂ emissions reduced 1.9%, 7.7%, 9.7% and 12.1% for the blends B10, B20 and B30 respectively when compared with diesel. Decrease in the brake thermal efficiency of tobacco biodiesel blends B10, B20, B30 and B100 are 24.13%, 26.50%, 29.06% and 31.29% respectively when compared with the diesel. Brake specific fuel consumption higher than diesel and BSFC for the blends B10, B20, B30 and B100 is respectively 1.3 times, 1.39 times, 2.21times, and 2.86 times the consumption of diesel. Performance of tobacco biodiesel is validated as results are in well comparison with the results of pongamia biodiesel.

3. METHODOLOGY

Materials Required

In this project the materials obtained were from the trusted retail seller and were verified for the product

quality in terms of fuel. Since the entire study is based on two stages, the fuel with analytical grade quality is procured and after that the piston assembly is purchased for varying combustion chamber geometry.

Since toroidal shape geometry is unusual in the market and is not commercially produced, we had to machine the piston to our requirements. Initially the piston when purchased had hemispherical geometry, to reduce the depth of hemispherical chamber additional material was added using arc welding and later smoothen using lathe machining. Milling process was used to cut slots tangentially on the piston bowl to bring it into toroidal shape and finally the entire piston was polished to obtain surface quality in order to achieve maximum performance.



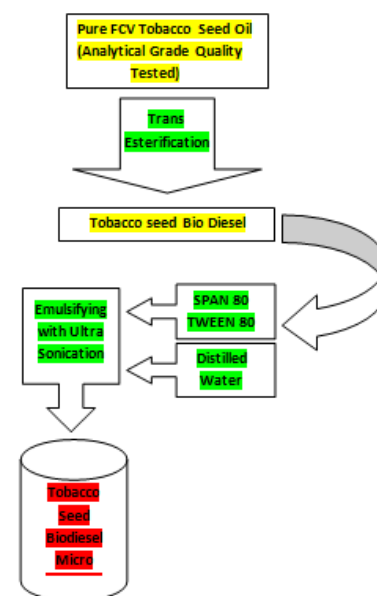
Fig Tobacco Seed Oil



Fig Hemispherical Piston

Distilled water, Emulsifier, and Surfactant was obtained from a trusted industrial chemicals supplier, all these were stored at normal room temperature as none of these materials required any special storage conditions. Further it was noted that the engine didn't require any further modifications and was able to fully function with the test fuels without any modifications. The method of load imposed on the engine was by means of electrical motor.

Overview Flow Chart



Trans-Esterification

It is a general term used to indicate the direct conversion of triacylglycerol's lipids by alcohols to alkyl esters without first isolating the free fatty acids (FFA). More specifically in alcoholics, the triacylglycerol's in a fat or oil are reacted with excess alcohol in the presence of a catalyst.

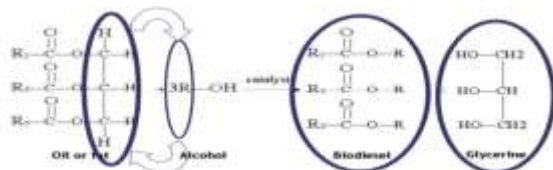


Fig 3.3 Chemical Reaction of Biodiesel

The catalyst may be acidic (example: sulphuric acid, hydrogen chloride, boron trifluoride, etc.) or alkaline (e.g., metal alkoxide, alkaline hydroxide, etc.), with the alkaline catalysts giving faster reactions. The well-known mechanisms of acid and alkaline alcoholysis are depicted. All the steps in the trans esterification process are reversible but the equilibrium can be shifted with excess alcohol so that trans esterification proceeds practically to completion. In acid catalysed trans esterification, fatty acids can be formed by the reaction of carbocation II with the water in the reaction mixture. Thus, the preferred conditions for acid catalysed esterification of triacylglycerol's are, therefore, a large excess of an appropriate alcohol and the absence of water.

Surfactants

We are using combination of non-ionic surfactants SPAN 80 (surfactant) TWEEN 80 (emulsifier). The surfactant (SPAN 80) maintains the even nature of surface tension between oil and water emulsion, so that it is not too viscous or too runny unevenly. The emulsifier (TWEEN 80) works as a binding agent between the oil and water micro droplets, it has both a hydrophilic end and a lipophilic end in its molecules which attracts an oil and water droplet together resulting in an emulsion. The combination of this chemical was procured from a local homeopathy drug store, as they use this chemical in preparation of medicine emulsions, 0.1% of this chemical combination will be used in 1 liter of emulsified fuel preparation.



Fig TWEEN-80

Fig SPAN-80

3D Solid Modeling in Catia

CATIA is the use of computer systems to aid in the 3D model creation, modification, analysis, or optimization of a design. CATIA software is used to increase the productivity of the designer, improve the quality of design, improve communications through documentation, and to create a database for manufacturing. A 3D solid modeling of the piston bowl geometry was designed with perfect symmetry and used further in CFD analysis.

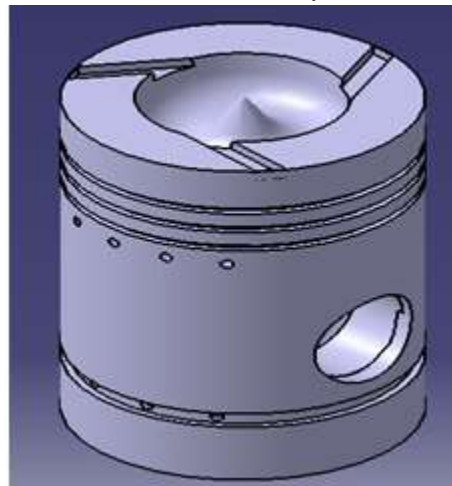


Fig :Tangential Groove Piston ANSYS Modeling & Analysis

Modification of Standard Piston

In this piston we are going to modify the piston into three tangential grooves has been made on top surface of the piston and also to design toroidal shape on piston bowl and slight increasing in piston bowl diameter on standard piston. The tangential grooves make homogeneous mixing of air and fuel during combustion by enhancing the swirl within combustion chamber and increased bowl diameter

decrease the compression ratio and its effect on emission reduction are observed.



Fig :Standard Piston

The above piston will be further machined to house the tangential grooves and will be bored to form a reverse toroidal geometry so that when it is introduced to the jet of fuel spray, it forms toroidal motion inside the combustion chamber.



Fig :Tangential Grooved Piston

The tangential groove depth is kept constant at 3 mm. Groove width is 6.5 mm.

4. Experimental Set Up

The experiment was conducted on Kirloskar TV-1, single cylinder, four-stroke, water cooled DI diesel engine with a displacement of 661cc. The rated power of the engine is 5.2 kW at 1500 rpm with constant speed. The schematic view of the experimental setup is shown in Fig below. The

engine had a hemispherical bowl piston, 3 holes injector. The inline mechanical fuel pump was operated at a standard injection pressure of 220 kg/cm² and the recommended TDC. The governor was used to control the speed of the engine. Cooling of the engine was injection timing of 23 accomplished by supplying water through the jackets in the engine block and cylinder head. A hole was made on the top of the cylinder head surface area to place the piezoelectric pressure transducer for measuring the heat release rate and cylinder pressure. The engine was stabilized for a particular operating point, fuel flow rate and exhaust gas temperatures are recorded. The engine was allowed to run for 15 to 20 minutes to attain the steady state condition to reach cooling water temperature of 70 centigrade



Fig :Test Rig Engine Setup

This experimental test was conducted in single cylinder, direct injection, water cooled, compression ignition engine. The engine is fully instrumented for measurements of necessary operating parameters.

TABLE- The specifications of D.I. Diesel engine

Make	Kirloskar
Type	4 stroke, single cylinder diesel engine.
Number of Cylinders	One
Bore	80 mm
Stroke	110 mm
Compression Ratio	16.5:1
Capacity	5 H.P
Speed	1500 rpm(constant)
Injection timing	23 ⁰ BTDC
Type of loading	Electrical resistance
Dynamometer	swinging field dynamometer

Exhaust Gas Analyzer

Exhaust gas analyser also gives you the ability to measure the effectiveness of repairs by comparing before and after exhaust readings. The combustion chemistry equation:

Fuel (hydrogen, carbon, sulphur) + Air (nitrogen, oxygen) = Carbon dioxide + water vapour + oxygen + carbon monoxide + hydrocarbon + oxides of nitrogen + sulphur oxides.

Good combustion is simply put this way:

$$\text{HC} + \text{O}_2 + \text{N}_2 = \text{H}_2\text{O} + \text{CO}_2 + \text{N}_2$$

Bad combustion is simply put this way

$$\text{HC} + \text{NO}_x + \text{Still air} + \text{Sunlight} = \text{Smog.}$$

- HC = Hydrocarbons, concentration of the exhaust in parts per million (ppm). = Unburned Petroleum diesel, represents the amount of unburned fuel due to incomplete combustion exiting through the exhaust. This is a necessary evil. We don't want it so try to keep it as low as possible. An approximate relationship between the percentage of wasted fuel through incomplete combustion and the ppm of HC is about 1/200 (1.0% partially burned fuel produces 200 ppm HC, 10%=2000 ppm HC, 0.1%=20 ppm HC)

- CO = Carbon Oxide, concentration of the exhaust in percent of the total sample. = Partially burned petroleum diesel, this is the petroleum diesel that has combusted, but not completely. This gas is formed in the cylinders when there is incomplete combustion and an excess of fuel. Therefore, excessive CO contents are always a sign of an overly rich mixture preparation. (The CO should have become CO₂ but did not have the time or enough O₂ to become real CO₂ so it is exhausted as CO instead.) CO is highly poisonous odourless gas

- CO₂ = Carbon Dioxide, concentration of the exhaust in percent of the total sample. Completely Burned Petroleum diesel, represents how well the air/fuel mixture is burned in the engine (efficiency). This gas gives a direct indication of combustion efficiency. It is generally 1-2% higher at 2500 RPM than at idle. This is due to improved gas flow resulting in better combustion efficiency. Maximum is around 16%. At night the trees convert CO₂ in to Oxygen. Preserve them.

- NO_x = Oxides of Nitrogen (This is only seen by a 5-gas analyser) Only seen with dynamometer or engine under load. NO_x emissions rise and fall in a reverse pattern to HC emissions. As the mixture becomes

leaner more of the HC's are burnt, but at high temperatures and pressures (under load) in the combustion chamber there will be excess O₂ molecules which combine with the nitrogen to create NO_x. NO_x increases in proportion to the ignition timing advance, irrespective of variations in A/F ratio.



Fig : Gas analyser

OBSERVATIONS

Procedure

The experiment was performed firstly with standard piston with diesel. And then Toroidal piston bowl with tangential grooves is fitted in to the engine then experiment repeated with diesel and blend of nonionic surfactants (5, 10 and 15ml). The steps used are described as below:

1. Firstly, the diesel was filled in a fuel tank.
2. After setting the water supply, the cooling water and calorimeter flow was set up at 250 LPH and 150 LPH respectively.
3. All the electrical connections were checked properly and then the electric supply was started.
4. Then the valve provided at the Burette was opened to supply the diesel to the engine.
5. Then engine was started and run for few minutes at no load conditions.
6. All readings are speed, load, manometer readings, time taken for 10cc Of fuel consumption, temperatures, voltage and current are noted.
7. The engine is loaded with 25 at first condition.
8. The same steps were repeated for different loads.
9. All the readings were saved and then same procedure was done for TCC tangential grooves with diesel and blend of nonionic surfactants.
10. After noting all the readings engine was brought to no load conditions and after that engine fuel supply was stopped after some time.

Experimental Procedure for Exhaust Gas Analysis

1. Sensors were inserted into the provided outlet for exhaust gases for the required load condition.
2. The analyzer was attached to the exhaust outlet and the exhaust gases were passed to the analyzer with the help of sensors.

3. After this the displayed readings on the digital screen of analyzer were noted.
4. Mean value of these readings were calculated.
5. Then the sensors were removed.
6. The above steps are repeated for different fuels and different load condition.

4.1.2 Performance Parameters

Engine performance is an indication of the degree of success of the engine performs its assigned task, i.e., the conversion of the chemical energy contained in the fuel into the useful mechanical work. The performance of an engine is evaluated on the basis of the following:

1. Brake Power
2. Break thermal efficiency
3. Specific Fuel Consumption
4. Mechanical Efficiency
5. Volumetric Efficiency
6. Exhaust Smoke and Other Emission

Initial Experimental DATA & VALUES.

The Engine test rig was initially tested in order to evaluate whether the engine meets the expected requirements of the study or not, six sensors were implemented in order to check all the prerequisites, the values obtained during the initial runs is represented in three sets which are represented in the table given below and further generated into a graph to show the stability of the engine.

Table :Initial Engine Parameters

S. No	Speed	LOAD	Manometer readings		Time taken for 10cc	Temperatures						Volt age	AMP S
			H1	H2		T1	T2	T3	T4	T5	T6		
Set - 1													
1	1560	25	19	28	33.3	68	76	77	360	43	43	239	165
2	1536	30	20	20	31.5	67	73	76	400	43	43	241	168
3	1356	75	21	29.3	35.8	66	43	41	300	43	43	243	300
4	1240	100	22	28	33.25	68	41	40	338	43	43	244	476
Set - 2													
5	1360	25	21	29	30	40	40	40	150	41	43	240	0
6	1480	30	20	30	34.3	37	45	40	211	41	43	248	160
7	1400	75	19	31	32.3	39	53	39	257	40	44	260	230
8	1300	100	17	31.5	30.2	38	57	38	302	42	45	280	310
Set - 3													
9	1480	25	21.5	29.5	48	40	40	40	160	56	40	230	0
10	1400	30	20.5	31.5	33	36	44	39	220	58	41	260	170
11	1300	75	18.5	32.5	31	38	50	40	270	58	42	270	288
12	1260	100	17.1	33.3	29	37	55	39	320	58	42	280	468

From the above three sets we can compare the values and it can be noted that the exhaust temperature is consistent and other parameters of the engine's output are in line with the basic requirements necessary to carry out the experimental studies. Therefore, we can iterate a graph on these values and see how the consistency of the engine can be represented.

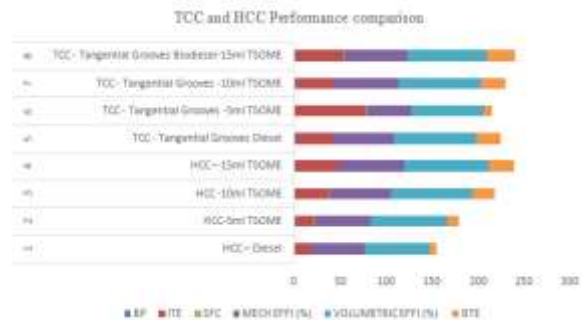
Comparison of Hemispherical Combustion Chamber and Tangential Combustion Chamber.

In our next experiment we will be comparing Hemispherical Combustion Chamber (HCC) with Tangential Combustion Chamber (TCC) in order to check which combustion chamber performs better. The results will determine how much swirl is being generated in a particular profile which will further be the basis for analysing the emissions, because better swirl results into further reduced emissions.

Table :Performance Parameters

S.NO	Piston	BP	IME	SFC	MECH EFFI (%)	VOLUMETRIC EFFI (%)	BTE
1	HCC - Diesel	1.084	16.35	0.55	58.94	71.2	7.2
2	HCC-5ml TSOME	1.674	20.88	0.38	61.60	83.4	12.73
3	HCC -10ml TSOME	2.196	32.1	0.40	66.82	88.9	24.05
4	HCC - 15ml TSOME	2.315	46.14	0.41	71.80	91.1	27.4
5	TCC - Tangential Grooves Diesel	2.200	39.85	0.44	66.71	85.6	26.58
6	TCC - Tangential Grooves -5ml TSOME	1.057	77.39	0.62	49.00	79.3	8.62
7	TCC - Tangential Grooves -10ml TSOME	2.196	41.66	0.46	69.62	90.2	26.54
8	TCC - Tangential Grooves Biodiesel-15ml TSOME	2.415	51.56	0.45	68.68	87.5	29.87

From the above results we can see already that the parameters like BP, SFC, BTE are better in TCC compared to HCC, therefore TCC can be further used in our next experiment which is emission analysis. The values here in the above table can be represented in a comparative graph.

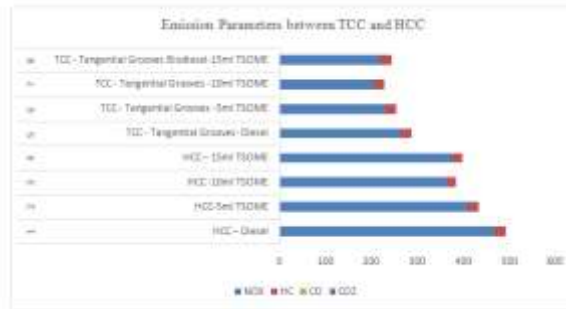


Graph :TCC and HCC Performance comparison

From the above graphical representation, we can see that TCC satisfies our requirements and to further cement our claims we will be doing an emission analysis and compare the values between TCC and HCC.

Table : Emission Parameters

S.NO	Piston	NOx	HC	CO	CO2
1	HCC - Diesel	468	22	0.02	2.9
2	HCC-5ml TSOME	411	20	0.019	2.4
3	HCC -10ml TSOME	363	19	0.018	2.2
4	HCC - 15ml TSOME	375	21	0.021	2.5
5	TCC - Tangential Grooves- Diesel	263	23	0.03	2
6	TCC - Tangential Grooves -5ml TSOME	251	22	0.025	2.4
7	TCC - Tangential Grooves -10ml TSOME	205	21	0.023	2.1
8	TCC - Tangential Grooves Biodiesel-15ml TSOME	220	23	0.024	2.3



Graph- Emission Parameters between TCC and HCC Hence, it is evident from the values and graph that TCC (Toroidal combustion chamber) gives better performance compared to HCC (Hemispherical combustion chamber).Therefore we can now proceed towards the core of our study experiments which will be covered in the next chapter.

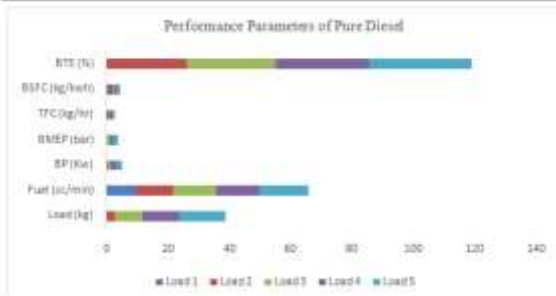
5.RESULTS AND DISSCUSION

Performance Parameters

Engine performance is an indication of the degree of success of how the engine performs its assigned task, i.e., the conversion of the chemical energy contained in the fuel into the useful mechanical work. As it is already evident that toroidal shape gives better performance compared to hemispherical combustion chamber (HCC), we will be performing all our analysis on toroidal combustion chamber (TCC). The performance of an engine is evaluated on the basis of the following:

Table : Experimental values for pure Diesel

S.No	Load (kg)	Fuel (cc/min)	BP (Kw)	BMEP (bar)	TFC (kg/hr)	BSFC (kg/kwh)	BTE (%)
1	0	10	0.03	0.04	0.4	1.2	0.05
2	3	12	0.48	0.06	0.5	1.01	26.43
3	9	14	1.11	1.09	0.6	0.82	28.87
4	12	14	1.7	1.31	0.6	0.75	30.23
5	15	16	1.9	1.40	0.8	0.82	33.46



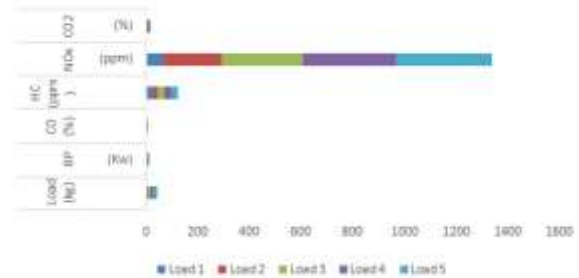
Graph :Performance Parameters of Pure Diesel

In the above results table and graph, we can see the performance values obtained for pure diesel as fuel and these performance factors will be further used to compare with the Tobacco seed oil biodiesel blends, we will be using three different blends of the biodiesel which are B20, B30, B50 and compare which blend is the most optimal for making a micro emulsion which gives us better stability, reliable and consistent performance.

Table :Emissions values for pure Diesel

S.No	Load (kg)	BP (Kw)	CO (%)	HC (ppm)	NO _x (ppm)	CO ₂ (%)
1	0	0.03	0.019	20	60	1.6
2	3	0.48	0.026	22	230	2.1
3	9	1.11	0.041	25	315	2.4
4	12	1.7	0.054	26	360	3.2
5	15	1.9	0.062	28	372	3.8

Emission parameters for Pure Diesel

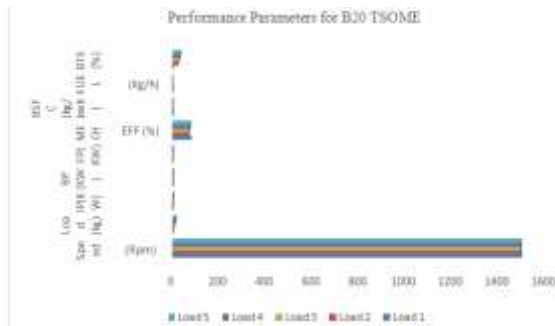


Graph :Emission parameters for Pure Diesel

Here, are the emission values of pure diesel which are theoretically and experimentally obtained, since there is not much of a difference between the theoretical values and experimentally obtained values, we will be considering the experimentally obtained values and then these values will be used as a medium of comparison between B20, B30 and B50. Now we will be running the engine on a standard B20 tobacco seed oil biodiesel blend to obtain the performance parameters as well as emission values to compare them with others.

Speed (Rpm)	Load (kg)	IP(KW)	BP (KW)	FP(KW)	MECH EFF (%)	BSFC (kg/kwh)	FUEL (Kg/h)	BTE (%)
1500	0	1.11	0.81	0.3	77.72	1.1	0.891	1.02
1500	3	2.1	1.3	0.8	69.23	0.95	0.62	23.5
1500	9	2.2	1.5	0.7	71.87	0.8	0.53	29.88
1500	12	2.7	2	0.7	75.21	0.71	0.44	32
1500	15	2.9	2.2	0.9	76.89	0.83	0.48	35

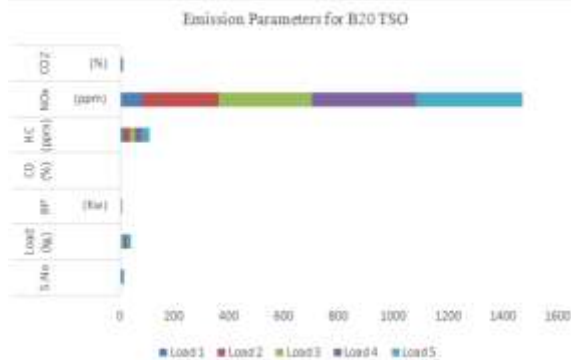
Table: Experimental values for Tobacco oil with B20 Blend



Graph :Performance Parameters for B20 TSOME
Here we can clearly see that there is a gradual difference in the performance parameters namely the BP, BSFC, BTE are at least 0.2, 0.4, 0.1 values different compared to diesel and by this we can now have a look at the emission values to see if there is any reduction in the pollution.

S.No	Load (kg)	BP (Kw)	CO (%)	HC (ppm)	NO _x (ppm)	CO ₂ (%)
1	0	0.81	0.023	17	80	1.5
2	3	1.3	0.035	19	280	1.9
3	9	1.5	0.055	22	342	2.2
4	12	2	0.060	24	380	2.9
5	15	2.2	0.072	26	388	3.2

Table :Emissions Values ForTobacco Oil With B20 Blend



Graph:Emissions Parameters forTobacco Oil with B20 Blend.
Here we can see that CO values are 0.004 ppm more compared to diesel but there is a significant reduction in the HC values which are at least 3ppm less compared to diesel, although the NOx values are 20ppm more, the CO2 values are 0.1% less and by this we can now further compare these values with the B30 and B50 blends.

Performance And Emission Characteristics Of Bio –Diesel With Spaan- Tween (Surfactant And Emulsifier) And Distilled Water.

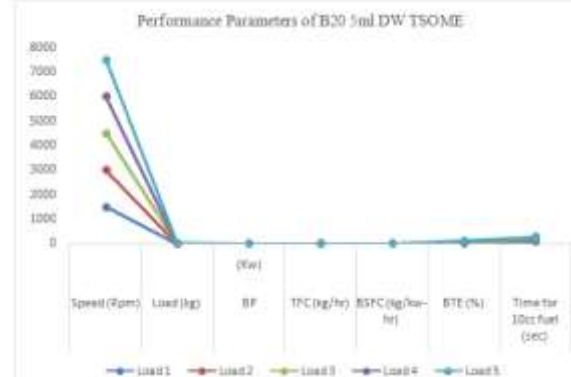
We will now undergo a performance analysis on B20 tobacco seed oil with 5ml, 10ml, 15ml additive blends to see which blend is the most optimal and high stability as well as it has better performance to sustainability factor.

Since we have already determined that a Tangential combustion chamber (TCC) gives a better swirl to the fuel vapour compared to a Hemispherical combustion chamber (HCC), we will be then using TCC as primary means of analysis for all the B20 TSOME blends.

We will be starting the analysis with a 5ml distilled water blend, and further on we will be undergoing the emission analysis to compare the values with other two blends.

Table: Experimental values of B20 Blend with 5ml of Additives (Distilled water)

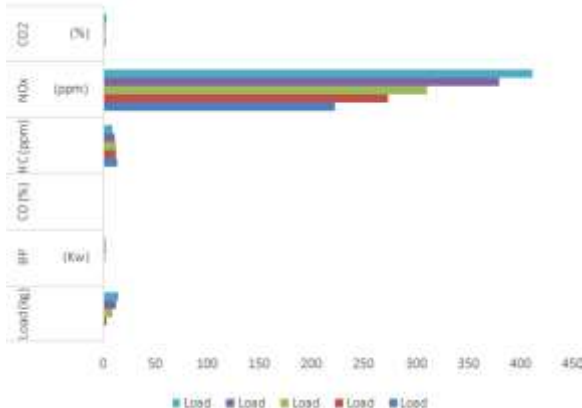
Speed (Rpm)	Load (kg)	BP (Kw)	TFC (kg/hr)	BSFC (kg/kwhr)	BTE (%)	Time for 10cc fuel (sec)
1500	0	0.82	0.7856	1.4367	16.45	93.56
1500	3	1.4	1.2346	1.0987	23.42	71.23
1500	9	1.72	1.4568	0.9145	28.87	64.51
1500	12	2.0	1.7853	0.8932	29.15	59.08
1500	15	2.67	2.2612	0.6231	30.21	53.23



Graph :Performance Parameters of B20 blend with 5ml DW TSOME

Table :Emissions values of B20 Blend with 5ml of Additive (Distilled water)

S.No	Load (kg)	BP (Kw)	CO (%)	HC (ppm)	NO _x (ppm)	CO ₂ (%)
1	0	0.82	0.041	14	222	1.4
2	3	1.4	0.036	13	273	1.9
3	9	1.72	0.032	12	310	2.1
4	12	2.0	0.035	11	379	2.21
5	15	2.42	0.038	9	410	3.16



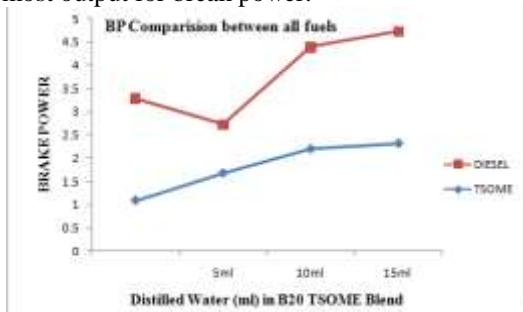
Graph: Emission Parameters of B20 5ml DW TSOME
 Here we can already see that we have obtained pretty promising HC and CO₂ values, although there is not much of a change in the CO and NO_x values. So, we will be further carrying out a performance study of 10ml TSOME blend.

Now we will be doing a performance and emission analysis of B20 TSOME 10ml distilled water additive blend to check whether we get better values compared to 5ml B20 TSOME blend

Performance Analysis Graphs Of B20 Tsome Blends

Brake Power:

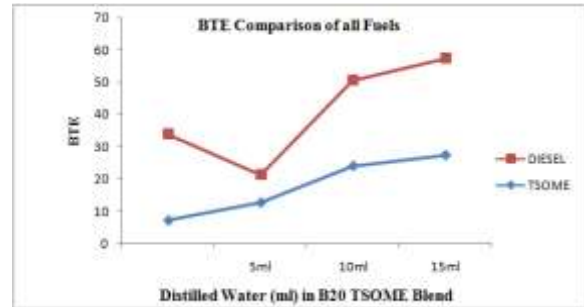
Break power of an CI Engine is the power available at the crank shaft. The break power of an CI Engine is usually measured by means of a break mechanism. Here we can see that 15ml TSOME blend has the most output for break power.



Graph :Comparison of Break Power between all fuels

BREAK THERMAL EFFICIENCY:

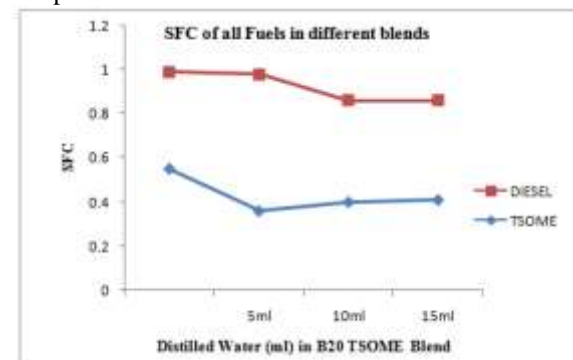
It is defined as a break power of a heat engine as a function of the thermal input from the fuel. It is used to evaluate how well a energy converts the heat from a fuel to mechanical energy. Here we can see that 15ml TSOME blend has the most BTE value.



Graph :BTE Comparison of all Fuels

SPECIFIC FUEL CONSUMPTION

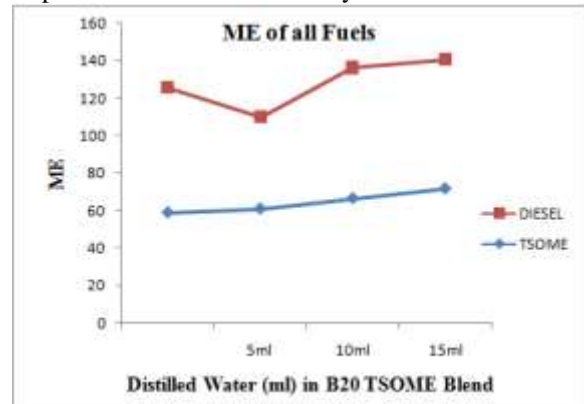
Here we can see that specific fuel consumption is of 5ml B20 TSOME blend is the most optimal compared to all the fuels.



Graph :SFC Comparison of all Fuels

MECHANICAL EFFICIENCY:

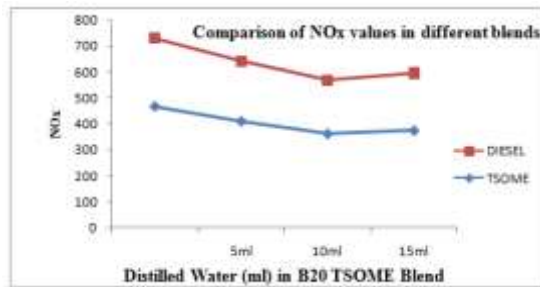
It measures the effectiveness of a machine in transforming the energy and power that is input to the device into an output force and movement. Here we can see that 15ml B20 TSOME blend has the best output for mechanical efficiency.



Graph ME of all Fuels

Oxides of Nitrogen (NOx)

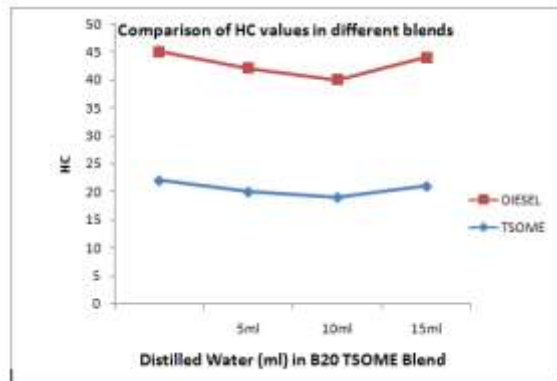
Here we can see that 10ml B20 TSOME has the best output for reduced NOx emissions compared to other blends.



Graph :Comparison of NOx values of all Fuels

Hydrocarbons (HC)

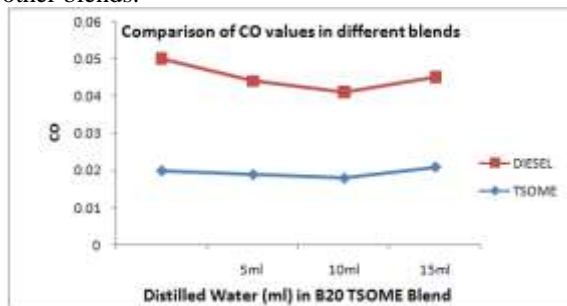
Here we can see that HC emissions are less in 10ml B20 TSOME compared to other blends although diesel has the highest value for HC emissions.



Graph :Comparison of HC values of all Fuels

CARBON OXIDE (CO)

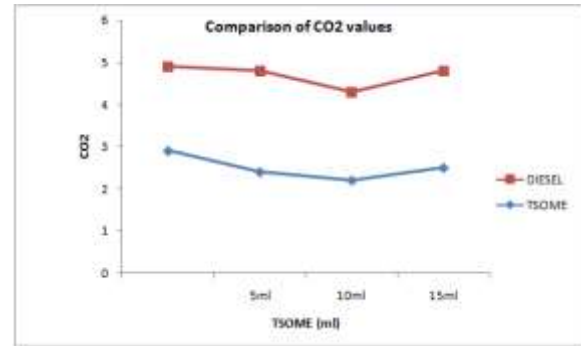
Here we can see that 10ml B20 TSOME has the best output for reduced CO emissions when compared to other blends.



Graph :Comparison of CO values of all Fuels

CARBON DIOXIDE (CO2)

Here we can see that 10ml B20 TSOME the best output for reduced CO2 emissions when compared to all the other blends.



Graph :Comparison of CO2 values of all Fuels

Since low exhaust gases values as well as the performance to stability factor are the primary prerequisites of our study. We can hence conclude that all the three characteristics are best obtained in 10ml B20 TSOME.

Therefore, we can finally say that 10ml B20 TSOME blend is the most stable and sustainable fuel compared to other blends, hence we have got the most optimal fuel in this study to work with the tangential combustion chamber to obtain best performance and reduced emissions for tobacco seed oil biodiesel.

6.CONCLUSION

Final Statement

In this investigation biodiesel fuel extracted from FCV Tobacco seed oil is emulsified with distilled water and tested in the single-cylinder diesel engine. In the initial analysis of this study, Physical and chemical characteristics of diesel and tobacco seed oil as well as Tobacco seed oil microemulsion (TSOME) were analysed. Then experimental studies are carried out by running the engine on varied piston geometry (Toroidal shape) and well as varying load conditions, the corresponding performance and emission characteristics were studied. The conclusions made from the present study are as follows.

STABILITY, PERFORMANCE AND EMISSION CHARACTERISTICS OF TOBACCO SEED BIODIESEL AND ITS BLENDS:

- It is observed that after cold mechanical pressed yield obtained from tobacco seeds was 34 percent and after transesterification the maximum yield of biodiesel obtained in the due process from tobacco seed oil was 85 percent.
- Initially the colour of biodiesel had tint of green colour but later on after coming back to the room temperature it was observed to be dark yellow or in colour similar to Karanja oil. Although the nature of tobacco biodiesel was found to be non-hazardous, unlike pure diesel.
- After addition of surfactants (SPAAN-TWEEN), the stability of the fuel for various blends of distilled

water varied greatly and 10ml B20 blend was observed to execute highest stability.

- It is observed that all the performance parameters like BP, SFC, Mechanical Efficiency, Brake Thermal Efficiency have a drastic difference in performances of Hemispherical combustion chamber and Toroidal combustion chamber. Since the performance of TCC is better, it was used in the engine to analyse the performance of TSOME blends as well as pure diesel.

- It is observed that lowest volumetric efficiency was seen in the pure biodiesel B100 fuel whereas the highest volumetric efficiency was seen in pure diesel.

- Mechanical Efficiency has a steady rising peak as we go from pure tobacco biodiesel to B20(15ml) TSOME. However, the highest mechanical efficiency was observed in case of pure diesel only.

- NOx emissions are observed to be the lowest when the load is maximum in case of B20(10ml) and the highest peak was observed in case of pure diesel when the load is lowest.

- It is observed that applied load increases carbon dioxide (CO₂) emission increases for both TSOME blends and diesel. Regarding CO₂ emission among the blends of TSOME, biodiesel B20 (10ml) shows better results. However, at maximum load conditions, TSOME blends B20 (10 ml) shows 2.1% and diesel 4.2%, which clearly shows that biodiesel blend B20 (10ml) has 0.3% less when compared with diesel.

- It is observed that applied load increases carbon monoxide (CO) emissions increase for both TSOME blends and diesel. Regarding CO emission among the blends of TSOME biodiesel B20 shows better results. However, at maximum load conditions TSOME blend B20(10ml) shows 0.019% and diesel 0.042%.

- It is observed that applied load increases hydrocarbons (HC) increase for both TSOME blends and diesel. However, at maximum load conditions TSOME blends B20(10ml) shows 18ppm and diesel 40ppm, it clearly shows biodiesel blend B20(10ml) has 22ppm less when compared with diesel.

- A comparative study of all the fuel blends which were used in the experiment have been observed in the form of line graphs, which clearly shows us the performance of various TSOME blends and various performance parameters which can be selectively considered to obtain the required fuel characteristics. However, the most stable specimen is finalized as the best fuel because a microemulsion needs to be stable for longer periods of time to be able to sustain in the commercial market. In the studies we have observed that TSOME B20 (10ml) has a shelf life of 58 - 60 days. After the shelf life the fuel simply separates itself into a colloidal solution.

From the above studies, it concludes that TSOME biodiesel blend B20 (10ml) shows better results when compared with diesel and other blends.

Hence, the above studies, conclude that Tobacco seed oil biodiesel blend (B20) with Surfactants SPAAN TWEEN and distilled water 15ml forms a microemulsion which is more stable and effective in performance when compared with other blends.

REFERENCES

- [1] F.L. Dryer, Proc. Combust. Inst. 16 (1977) 279–295. [https://doi.org/10.1016/S0082-0784\(77\)80332-9](https://doi.org/10.1016/S0082-0784(77)80332-9)
- [2] Recep Altın, Selim Çetinkaya, Hüseyin Serdar Yücesu, the potential of using vegetable oil fuels as fuel for diesel engines, Energy Conversion and Management, Volume 42, Issue 5, 2001, [https://doi.org/10.1016/S0196-8904\(00\)00080-7](https://doi.org/10.1016/S0196-8904(00)00080-7).
- [3] T. Kadota, H. Yamasaki, Prog. Energy Combust. Sci. 28 (2002) 385–404.
- [4] Dennis Y.C. Leung, Xuan Wu, M.K.H. Leung, A review on biodiesel production using catalyzed transesterification, Applied Energy, Volume 87, Issue 4, 2010, <https://doi.org/10.1016/j.apenergy.2009.10.006>.
- [5] B.S. Gottfried, C.J. Lee, K.J. Bell, Int. J. Heat Mass Transfer 9 (1966) 1167–1188.
- [6] İmdat Taymaz, An experimental study of energy balance in low heat rejection diesel engine, Energy, Volume 31, Issues 2–3, 2006, <https://doi.org/10.1016/j.energy.2005.02.004>.
- [7] R.W. Temple-Pediani, Proc. Inst. Mech. Engrs. 184, Pt. 1, 38 (1969–1970) 677–696.
- [8] C.O. Pedersen, Int. J. Heat Mass Transfer 13 (1970) 369–381
- [9] Usta N. Use of tobacco oil methyl ester in turbocharged indirect injection diesel engine. Biomass Bioenergy 2005; 28:77–86.
- [10] Can Haşimoğlu, Murat Ciniviz, İbrahim Özsert, Yakup İcingür, Adnan Parlak, M. Sahir Salman, Performance characteristics of a low heat rejection diesel engine operating with biodiesel, Renewable Energy, Volume 33, Issue 7, 2008, <https://doi.org/10.1016/j.renene.2007.08.002>.
- [11] Canakci M, Van Gerpen J. Biodiesel production from oils and fats with high free fatty acids. Trans ASAE 2001; 44:1429–36.
- [12] Wilfried Wunderlich and Morihito Hayashi, “Thermal cyclic fatigue analysis of three aluminium piston alloys”, International Journal of Material and Mechanical Engineering, June 2012.

[13] Piotr Szurgott and Tadeusz Niezgodą, “Thermo mechanical FE analysis of the engine piston made of composite material with low hysteresis” Journal of KONES Powertrain and Transport, Vol. 18, No. 1, 2011.

[14] V. B. Bhandari, “Design of Machine Elements”, 3rd Edition, McGraw Hill.

[15] F. S. Silva, “Fatigue on engine pistons – A Compendium of case studies”, Department of Mechanical Engineering, University of Minho, Portugal, Engineering Failure Analysis 13 (2006) 480–492.

Study of Non-Conventional Air Conditioning System Feasibility for an Office Space

Noushad Ahmed Shaik¹, Raju.P², Srinivasulu.P³,

^{1,2,3}*Mechanical Department, JNTUH*

¹M.Tech (Thermal Engineering)Department of mechanical engineering vaagdevi college of engineering (UGC autonomous) approved by AICTE & permanent affiliation to jntuh, hyderabad.p.o, bollikunta, Warangal urban- 506005.

² Assistant Professor Department of mechanical engineering vaagdevi college of engineering (UGC autonomous) approved by AICTE & permanent affiliation to jntuh, hyderabad. p.o, bollikunta,Warangal urban- 506005.

³Professor and Head of the Department of mechanical engineering vaagdevi college of engineering (UGC autonomous) approved by AICTE & permanent affiliation to jntuh, Hyderabad. p.o, bollikunta, Warangal urban- 506005.

Abstract— The purpose of this study about the feasibility of non-conventional air conditioning systems is mainly implied to discover new and more effective air condition systems in terms of expenses as well as reduced adverse effects on the environment. The resources which are available by nature can be implemented in air conditioning applications and energy conservation or savings can be achieved. During the study, an energy-efficient hybrid geothermal system is designed for an office space, where a major part of the air conditioning need is fulfilled by the geothermal heat exchange principle, and an auxiliary conventional air conditioning system is used to fulfil the additional temperature requirements for that particular space. A geothermal heat exchange system is based on heat transfer through a ground looping system which comprises an array of loops sheathed under the ground up to a significant depth. At a certain depth underneath, the soil temperature remains constant and significantly low throughout, irrespective of the ambient temperature. Thus, this temperature source is used for heat exchange in an air conditioning process, thereby reducing the major energy requirement. Major advantages of using this system for an air conditioning application over conventional systems are greater energy efficiency, minimal operating expenses, higher reliability, reduced environmental hazards to a great extent, etc.

Keywords—Geothermal, Heat transfer, Air conditioning, Non-conventional energy, Closed Loop

I. INTRODUCTION

The non-conventional air conditioning i.e., geothermal air conditioning system works on the principle of heat transfer through the earth's surface for either heating or cooling applications as desired. Heat transfer takes place between the temperature source beneath and the air which is a primary medium of an air conditioning system [3]. The use of Ground source heat pumps (GSHPs) for air conditioning is observed as one of the best renewable energy technologies which are both cost-effective and energy-efficient[4].It is observed that the temperature underneath at a certain depth of soil remains constant and is considerably low compared to that of the ambient condition [6].The difference between the ambient and underground soil temperature sources varies between 10 and 25 degrees [5]. Thus, accordingly, the rate of heat transfer takes place. During the summer season, the underground source acts as a heat sink and in the winter season, the underground heat source acts as a heating medium. And other controlling parameters such as humidity, indoor air quality, air changes per hour, and zone control can be achieved by means of the usual equipment of an air conditioning application. This study helps in understanding the feasibility of the design which is carried out based on the International Ground Source Heat Pump Association (IGSHPA) and also the thumb rules of the American Society Of Heating, Refrigeration And Air Conditioning Engineers (ASHRAE) with respect to geothermal systems [1, 2]. The energy demand is increasing very rapidly with the growth of the population and to fulfill this requirement, conventional energy sources are being used which are resulting in many adverse effects like global warming and air pollution [7]. The use of renewable energy like geothermal energy is a promising solution to meet a significant part of demand.

II. LITERATURE REVIEW

Abdul Ghani Olabi et al. [8] studied various geothermal energy Technologies and compared their hybrid versions. This work studies the various applications of geothermal-based hybrid technologies and investigates the effectiveness of renewable energy sources. It was described that the combination of renewable energy sources and geothermal energy results in efficient hybridization. In this study, more emphasis was given to the adoption of flexible control methods which can help in controlling each energy source effectively so that overall energy production can be optimized.

Masih Alavy et al. [9] discussed about hybrid geothermal air conditioning system for cooling and heating of an conditioned space by using a common loop distribution system. The crucial parameter involved in these hybrid systems is to design an optimized regeneration cycle to meet the load demand and heating requirements. Geothermal energy plants will not produce any

harmful emissions when compared with conventional fossil fuel-based systems for the same load requirement. Geothermal energy extraction is not much efficient due to its low-grade nature and in general, it is used in combination with hybrid systems to meet the demand which is not possible by using geothermal energy sources alone [10,11].

NimaBonyadind et al. [12] studied the different hybrid system combinations and their main selection criteria which are to reduce the operating cost throughout the year and also to prevent the environment from emissions. Martina Ciani et al. [13] compared the geothermal-solar power plant which was coupled with thermal energy storage to develop an efficient hybrid design. Montaser Mahmoud et al. [14] investigated the use of phase change materials (PCM) integration with Geothermal energy as one of the most stable renewable energy applications which can be used to avoid thermal fluctuations during peak loads. In this article, the PCM-based hybrid system is used to enhance the rate of heat transfer and also to stabilize thermal imbalances.

Ceyhun Yilmaz [15] studied the adsorption cooling system powered by the geothermal system for cooling buildings. In this study, the thermodynamic performance and economic analysis of the system are studied to analyze the annual cost and coefficient of performance (COP). The outcome of this study can help design sustainable buildings and reduce the cost of energy with greater efficiency per unit.

S.A. El- Agouz et al. [16] investigated the performance of a geothermal system integrated with a desiccant air conditioning system under the influence of various climatic conditions. The thermal analysis of this system is performed under different stimulated weather conditions which resulted in obtaining optimum comfortable temperature in different climatic conditions. The different climatic zones are studied to analyze the consumption of ground and solar energy in this hybrid system.

WahibaBendaikha et al. [17] performed the feasibility of a geothermal heat pump coupled with a hybrid fuel cell for application in air conditioning. The experimental analysis is done for heating and cooling requirements in the Northern part of Algeria. It was concluded that the use of Hybrid Energy Systems (HES) when integrated with proton exchange fuel cells is effective in air conditioning by using absorption sub-systems that can reduce the overall cost as the electricity consumption of the compressor is eliminated.

Baccoli, R et al. [18] studied the energy and exergy analysis conditioning system by using the geothermal heat pump. This investigation uses vertically placed heat exchangers attached to the ground to analyze the thermal conductivity, boundary conditions, and diffusivity of the system so that maximum efficiency can be obtained comparatively. The theoretical and mathematical calculations were performed to develop the feasible Ground Source Heat Pump (GSHP).

2.1 PROBLEM DESCRIPTION:

The geothermal energy resources are combined with the other sources of energy to form a hybrid system but the initial capital requirement of these systems is very high also there are many factors to be considered before installing these systems such as ambient temperature, ground soil properties, cost of drilling, machinery, and material requirements. The most crucial aspect to employ these hybrid systems is to select an efficient control method by considering the nature of the individual energy source.

Apart from various environmental conditions, it is also important to perform a feasibility study so that the running cost can be minimized and the high initial capital requirement can be justified in the long run.

III. GEOTHERMAL SYSTEM

The Geothermal Air conditioning system uses the heat of Earth's crust which is usually maintained at constant temperature respect of the ambient environmental conditions. As we go deep into the earth from ground level, for every 70 feet the temperature rises to 1°F. There are three main types of geothermal Technologies which uses earth's energy. They are:

- Direct use geothermal
- Ground source heat pumps
- Deep and enhanced geothermal systems

These systems are coupled to form a continuous loop through which cooling medium is circulated. The air conditioned space where the conditioned air is circulated through geothermal system or hybrid auxiliary systems. The auxiliary systems are used where the geothermal system alone cannot fulfil the load demand. A series of pipes are installed in the form of loops which act as a heat exchanger through which continuous circulation of cooling medium takes place from a conditioned space to the ground. The cooling medium like water is continuously circulated through these loops which transfers heat from the ground to conditioned space or vice versa. This underground pipe loop is made up of plastics or metals which are coupled with an air handling unit or an auxiliary system to fulfil the load requirements.

A. Closed Loop Geothermal Air Conditioning System

The geothermal air conditioning system of the closed loop type employs continuous loops connected in series or parallel arrays which are used to circulate the solution continuously throughout the closed system where heat transfer occurs. The same solution is circulated constantly in the closed loop. The underground loop system is widely used in areas where water scarcity is present while on the other hand, this system can also be coupled by means of nearby water body like ponds

or lakes where efficient heat transfer takes place. There are two types of closed-loop systems depending on their configuration one is Horizontal and the other is Vertical. In places where ground area availability is less, a vertical closed loop system is used which uses vertically drilled deep boreholes and in every hole different loop configurations can be set up like simple coaxial, complex coaxial, single U pipe, Double U pipe, etc.

While designing this loop system it is very important to maintain proper distance between the two adjacent vertical boreholes to avoid ineffective heat transfer between the loops and as per standards, it is around 15 to 20 feet.

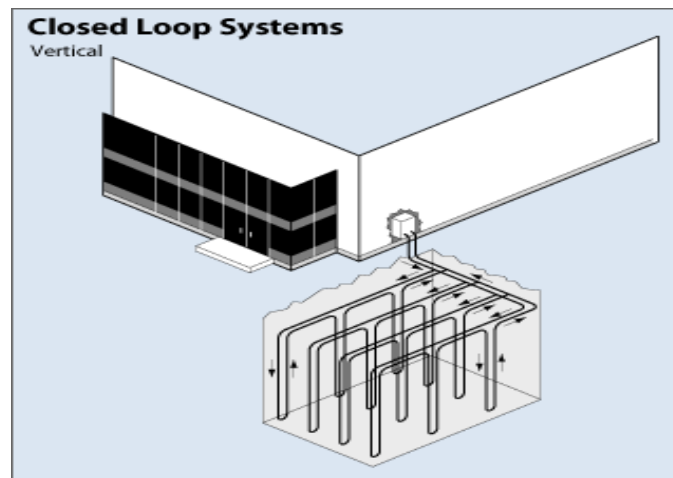


Fig. 1 Closed Loop Vertical System

IV. BUILDING DETAILS

The space to be conditioned in this study is considered to be an office space. The location of such space is Bangalore, India. The north and eastern facing of that office space is a complete glass section. And the other two sides of the space are referred to as conditioned partitions. Typical office space on the first floor of a building is taken into consideration and the system being executed shall be located at ground level. The office space elements a total area of about 4349 square feet and a large number of workstations are incorporated into that space along with void spaces such as passages and corridors. The indoor air handling system used for air conditioning is installed in a dedicated room remote to the office space and the adjoining spaces are considered to be conditioned spaces. Hence, particular office space is taken into consideration for studying the feasibility of the geothermal system in executing the purpose of supplying the conditioned air to that space. A capacity of about 119 persons can be accommodated into the space with relevance of sedentary style work since it is an office space, while the system is being designed as per standards of ASHRAE [1,2]. The occupancy is finalized based on the number of existing workstations within that particular space. Henceforth, the heat load calculation is done based on this occupancy rate, and also other important aspects of heat intake into the space which is majorly from the glass exposures have been considered while designing the system

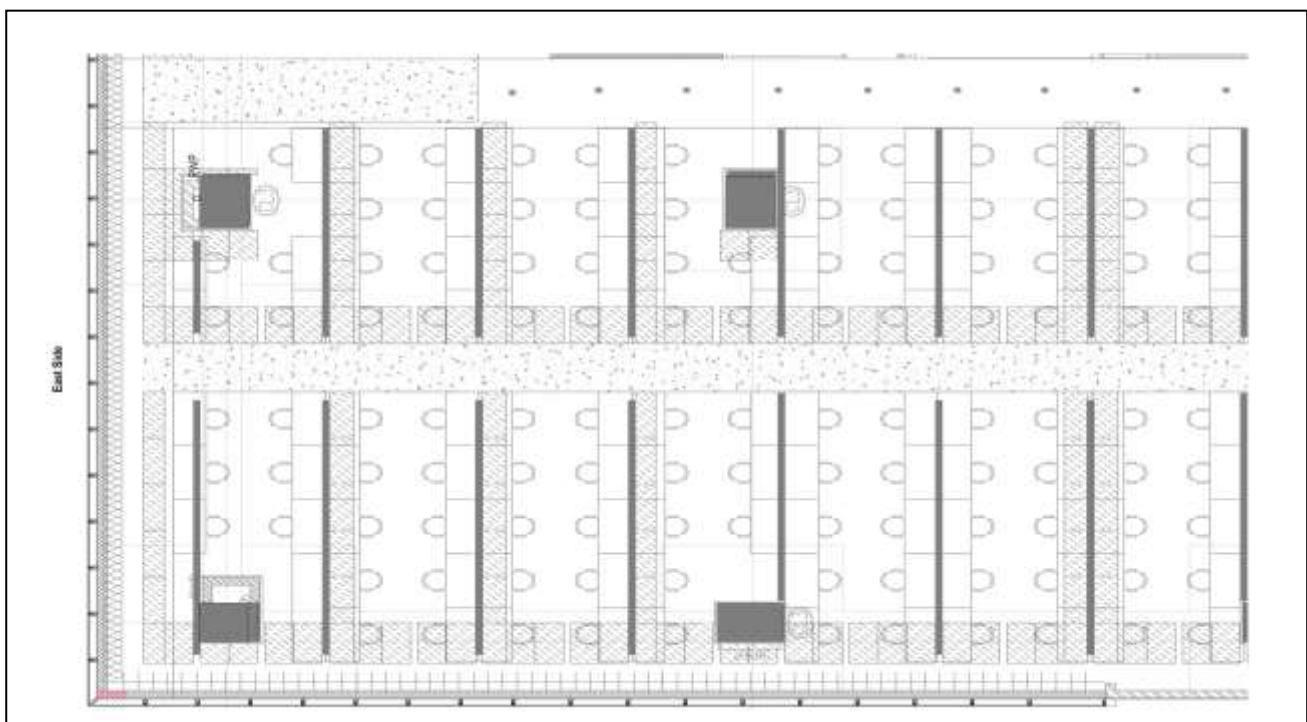


Fig. 2 Building Plan

V. CALCULATIONS

A. Heat Load Estimation for an office space

The total heat load of office space in consideration is evaluated by using a software called hourly analysis program (HAP). The calculated cumulative heat load is 16.3 T.R resulting from the above-said software. And the flow rate of air required to maintain the specified temperature within the zone is estimated to be 9463 CFM i.e, cubic feet per minute.

B. Pipe Sizing

The pipe size designed to allow the circulation of low-temperature water throughout the system is evaluated by using Mc Quay pipe sizer software. While designing the size of piping an important parameter required to calculate the pipe size is the water consumption rate desirable within the system and the same is estimated based on the standard recommendation for geothermal conditioning system. A general value of consumption rate varies between 2 and 3 GPM but the rate considered in this study is taken as 2.4 GPM per T.R which is an effective consideration while designing the pipe size.

- Rate of Water consumption – 2.4 GPM per TR for a loop which is considered a closed cycle heat exchange.
- Total estimated GPM for office space = 16.3 × 2.4 = 39.12GPM
- Desirable Pipe size resulted from evaluation = Ø 2”

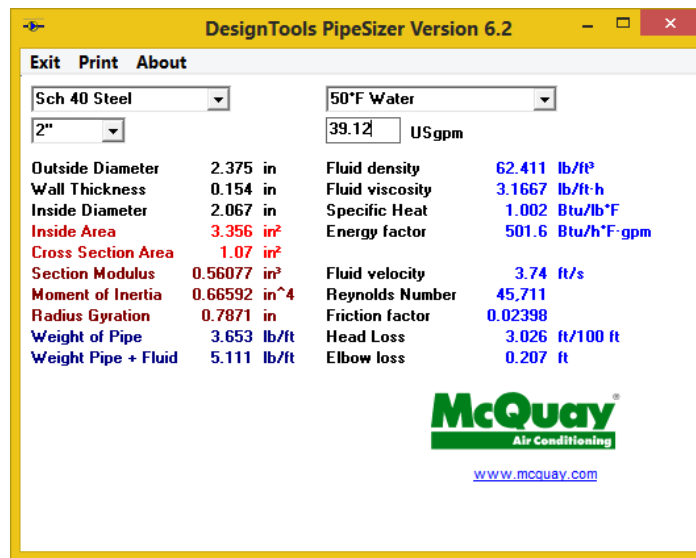


Fig. 3 Pipe Sizer

C. Loop Length Evaluation

An important parameter in the geothermal system of air conditioning is the length of closed-loop piping that is to be sheathed underneath the earth’s surface and the loop length for the respective heat load of the considered space can be calculated by an expression determined by the International Ground Source Heat Pump Association (IGSHPA) stated as follows.

Expression for loop length,

$$L = \frac{572 \times \left(\frac{COP-1}{COP}\right) (R_p + R_s F_C)}{(T_2 - T_1)} \times C_C$$

Where,

- R_p – Pipe resistance
- R_s – Soil resistance
- C_C – Cooling capacity
- T_1 – Minimum ground temperature
- T_2 – Maximum attainable fluid temperature
- F_C – Cooling factor = 0.6
- COP – 2 to 4 for cooling application

$$L = \frac{572 \times \left(\frac{3-1}{3}\right) ((4.94 \times 10^{-5}) + (0.939 \times 0.6))}{(27 - 22)} \times 16.3 \times 3.156$$

The optimum temperature of the source underground for the selected region is 22°C.

And the maximum temperature of fluid achieved during heat transfer through loops is about 27°C based on the thermal conductivity of the loops.

C.O.P for cooling application is considered between a range of 2 to 4 i.e., '3'.

$$\therefore L = 2186.76 \text{ feet}$$

Thus single – U bend loop system is desirable and the depth of the loop significant for heat transfer is considered 100 feet, as recommended according to the thumb regulation subsequently,

∴ Total number of U – loops to be installed underneath,

$$= \frac{2186.76}{2 \times 100} = 10.93$$

$$\therefore N \cong 12$$

Therefore, an array of 4 × 3 vertical parallel loop systems is to be installed as per the design.

The intermediate distance between each loop is considered to be 15'

The piping in the closed loop system is made up of galvanized iron (G.I) which is preferable due to advantages like lower initial cost compared to other metals such as copper and enhanced thermal conductivity. Also, it has longer service life with consistent performance.

D. Hybrid System Selection

The requirement of a hybrid system occurs while the cooling load demand is not fulfilled by using only a geothermal system. As a result, the integration of a geothermal air conditioning system with other conventional or auxiliary systems is incorporated which helps in meeting the part load requirement of a conditioned space. During water circulation through the ground loops, the peak temperature that can be attained per site is limited to 27° C, but during the peak ambient temperature condition the preferred temperature inside the conditioned space is to be maintained at 16°. Therefore by using only a geothermal system 60% of the required cooling can be attained in a conditioned space.

- $16 \div 27 = 0.592$ i.e. 0.6 or 60 %

Therefore, the rest 40 % of the cooling demand is fulfilled by means of an air-cooled chiller system which is coupled with the geothermal system. This auxiliary system is used here as the net heat load is less than 100 T.R which makes it highly suitable in this kind of application.

E. Cost Comparison

TABLE I
COST COMPARISON WITH CONVENTIONAL SYSTEM FOR SAME APPLICATION

S.No	Type of Cost	Air Cooled Chiller System	Geothermal System
1	Capital Cost	₹420000/-	₹956740/-
2	Running costs per month	₹142524/-	₹65066/-

The cost analysis is done here to compare the conventional air conditioning systems with this unconventional system from the actual market analysis point of view.

VI. CONCLUSIONS

The major difference in terms of financial analysis of these two systems is that the cost of a Hybrid geothermal air conditioning system is 75% more than compared the regular conventional air conditioning systems. But the major differentiating factor here is the operating costs which result in 45% of savings per month that can be achieved if a geothermal system is used in place of conventional systems. This is due to the high efficiency of the geothermal system, particularly in the winter season where the auxiliary system is not required as the required comfort temperature can be obtained in the conditioned space just by using geothermal heat transfer from the ground loops.

By using these Hybrid geothermal energy system there is not much difference in electricity consumption but if groundwater is used as a circulating medium the space requirement and water consumption are reduced and no heat is released into the atmosphere thereby helping in prevent global warming. It is observed that there has been significant growth in solar-assisted air conditioning systems as it's one of the promising solutions towards sustainable future.

REFERENCES

- [1] ASHRAE. 2001. ASHRAE Handbook - 2001 Fundamentals. Atlanta, GA: American Society of Heating, Refrigerating and Air-Conditioning Engineers, Inc.
- [2] ASHRAE Handbook (2007) - 'Heating, Ventilating, and Air-Conditioning – Applications'.
- [3] M. Carlini and S. Castellucci, "Efficient energy supply from ground coupled heat transfer source," in *Proceedings of the International Conference on Computational Science and Applications (ICCSA '10)*, vol. 6017 of *Lecture Notes in Computer Science*, part 2, pp. 177–190, Springer, Fukuoka, Japan, 2010.
- [4] J. W. Lund, D. H. Freeston, and T. L. Boyd, "Direct application of geothermal energy: 2005 worldwide review," *Geothermics*, vol. 34, no. 6, pp. 691–727, 2005.
- [5] Energy Saver, U.S. Department of Energy's (DOE) report [Online]. Available, <https://www.energy.gov/energysaver/geothermal-heat-pumps#:~:text=Depending%20on%20latitude%2C%20ground%20temperatures,the%20air%20in%20the%20summer>.
- [6] P. Bayer, D. Saner, S. Balay, L. Rybach, and P. Blum, "Greenhouse gas emission savings of ground source heat pump systems in Europe: a review," *Renewable and Sustainable Energy Reviews*, vol. 16, no. 2, pp. 1256–1267, 2012.
- [7] B. Mullan, J. Haqq-Misra, Population growth, energy use, and the implications for the search for extraterrestrial intelligence, *Futures* 106 (2019) 4e17. ISSN 0016-3287, <https://doi.org/10.1016/j.futures.2018.06.009>
- [8] Olabi, Abdul-Ghani & Mahmoud, Montaser& Soudan, Bassel& Wilberforce Awotwe, Tabbi& Ramadan, Mohamad. (2019). Geothermal based hybrid energy systems, toward eco-friendly energy approaches. *Renewable Energy*. 147. 10.1016/j.renene.2019.09.140.
- [9] Masih Alavy, Seth B. Dworkin, Wey H. Leong, A design methodology and analysis of combining multiple buildings onto a single district hybrid ground source heat pump system, *Renew. Energy* 66 (2014) 515e522, <https://doi.org/10.1016/j.renene.2013.12.030>.
- [10] Benjamin Henault, Philippe Pasquier, Micha elKummert, Financial optimize- € tion and design of hybrid ground-coupled heat pump systems, *Appl. Therm. Eng.* 93 (2015) 72e82, <https://doi.org/10.1016/j.applthermaleng.2015.09.088>.
- [11] Hackel Scott, Amanda Pertzborn, Effective design and operation of hybrid ground-source heat pumps: three case studies, *Energy Build.* 43 (2011) 3497e3504, <https://doi.org/10.1016/j.enbuild.2011.09.014>.
- [12] NimaBonyadi, Evan Johnson, Derek Baker, Technoeconomic and exergy analysis of a solar geothermal hybrid electric power plant using a novel combined cycle, *Energy Convers. Manag.* 156 (2018) 542e554. ISSN 0196- 8904, <https://doi.org/10.1016/j.enconman.2017>.
- [13] Martina CianiBassetti, Daniele Consoli, Giovanni Manente, Andrea Lazzaretto, Design and off-design models of a hybrid geothermal-solar power plant enhanced by a thermal storage, *Renew. Energy* (2017), 0960-1481, <https://doi.org/10.1016/j.renene.2017.05.078>.
- [14] Mahmoud, Montaser& Ramadan, Mohamad &Naheer, Sumsun& Pullen, Keith &Abdelkareem, Mohammad &Baroutaji, Ahmad &Olabi, Abdul-Ghani. (2021). Investigation on the Use of Phase Change Materials in Geothermal Energy Applications. 10.1016/B978-0-12-815732-9.00059-0.
- [15] Yilmaz, Ceyhun. (2017). Thermodynamic and economic investigation of geothermal powered absorption cooling system for buildings. *Geothermics*. 70. 239-248. 10.1016/j.geothermics.2017.06.009.
- [16] El-Agouz, S.A. &Kabeel, Abd Elnaby. (2014). Performance of desiccant air conditioning system with geothermal energy under different climatic conditions. *Energy Conversion and Management*. 88. 464–475. 10.1016/j.enconman.2014.08.027.
- [17] Paper, Research & Larbi, Salah & Bouziane, Mahmah. (2011). Feasibility study of hybrid fuel cell and geothermal heat pump used for air conditioning in Algeria. *International Journal of Hydrogen Energy*. 36. 4253-4261. 10.1016/j.ijhydene.2010.09.058.
- [18] R. Baccoli, C. Mastino, G. Rodriguez, Energy and Exergy analysis of a geothermal heat pump air conditioning system, *Applied Thermal Engineering* (2015), doi: 10.1016/j.applthermaleng.2015.03.046.

THERMAL BARRIER COATING (TBC) ONTO THE PISTON CROWN AND VALVES FOR IMPROVING ENGINE PERFORMANCE AND EMISSION CHARACTERISTICS BY USING DIESEL AND MAHUA METHYL ESTER (MME) AS A FUEL

Kothuri Dhiraj¹ Mr. Y. Umashankar² Dr. Srinivasulu Pulluru³

¹M.Tech (Thermal Engineering) Department of mechanical engineering vaagdevi college of engineering (UGC autonomous) approved by AICTE & permanent affiliation to jntuh, hyderabad.p.o, bollikunta, Warangal urban-506005.

² Assistant professor Department of mechanical engineering vaagdevi college of engineering (UGC autonomous) approved by AICTE & permanent affiliation to jntuh, Hyderabad. p.o, bollikunta, Warangal urban-506005.

³ Professor and Head of the Department of mechanical engineering vaagdevi college of engineering (UGC autonomous) approved by AICTE & permanent affiliation to jntuh, hyderabad. p.o, bollikunta, Warangal urban-506005.

ABSTRACT:

The present research work aims to apply Thermal Barrier Coating (TBC) onto the piston crown and valves for improving engine performance and emission characteristics by using diesel and Mahua Methyl Ester (MME) as a fuel. For this utility, a Direct Injection (DI) conventional diesel engine was renewed to an LHR engine by applying 0.5 mm thickness of $3Al_2O_3-2SiO_2$ (as TBC) onto the piston crown and valves, the MME is used in the LHR (Low Heat Rejection) engine. The fuel injector pressure was maintained at 200 bar for investigation. The result shows that the application of TBC, increases the brake thermal efficiency to 13.65% at 25% load with diesel as compared to conventional DI diesel engine. The significant improvement of specific fuel consumption and the brake thermal efficiency of LHR engine with MME fuel were observed at full load. Using MME and diesel fuels with TBC achieves lower exhaust gas temperature. It was also observed that the smoke density of MME with and without TBC was significantly reduced. It was also found that the carbon monoxide emission was very moderately reduced under all loads by the use of MME fuel with TBC. Furthermore at all loads, MME with TBC were found to significantly reduce hydrocarbon emission.

KEYWORDS: Mahua methy ester biodiesel, Diesel fuel, Thermal barrier coating, Low heat rejection engine.

1. INTRODUCTION

Biodiesel is a one the preeminent renewable fuel, non-toxic and biodegradable. Biodiesel is a oxygenated with ester-based fuel that is obtained from first-generation oils, second-generation oils, and third-generation oils. Biodiesel is formed by a simple chemical reaction between edible or non-edible oils

with an acid-base catalyst and alcohols. The biodiesel has around 9% to 12% in-built O_2 content by weight basis, it has good lubricity properties, free sulphur content, and mixable with petro-diesel fuel with various blends of propagation. Thus the biodiesel has more impact than the petro-diesel fuels Sudheer [1]. In India, the production of non-edible oils is poor so due to this some of the developmental works have been carried out by the government of India for producing biodiesel from non-edible oils such as Mahua, Jatropha, Karanja, Linseed, Cotton, Mustard, Neem, etc. In India, most of the states are tribal regions where the Mahua seeds are found profusely Padhi et al. [2]. The Mahua tree has the ability to give seeds from the 7th year of plantation. Mahua seed oil is a common ingredient of Indian hydrogenated fat. The Mahua raw oil is extracted from the seed kernels and its oil seems to be like semi-solid fat at room temperature, pale yellow due to the high presence of viscous in oil. Mahua raw oil the free acids contain around 30 to 40%. During the production of biodiesel, various products can be produced by the manufacturer from the glycerin Agarwal et al. [3] and Padhi et al. [4]. Generally, the raw Mahua oil contains high percentage of Free Fatty Acids (FFA) and the conversion of FFA to biodiesel is very much essential by means of transesterification or esterification process Vijay et al. [5] and Azam et al. [6]. It is also observed that the properties and chemical composition of Mahua oil is almost similar to the other in-edible oil such as Cotton, Neem, Karanja, etc. but the Mahua has a high content of viscosity and FFA. There is some renowned process such as transesterification, esterification, dilution, micro-emulsion and pyrolysis process are utilized to reduce the viscosity in order to produce the biodiesel. However, the transesterification is one of the best processes for obtaining maximum yield with some of

the effective properties as compared to diesel properties Chauhan et al. [7] and Sirurmath et al. [8]. For the present work experimental investigations, the biodiesel MME and diesel has been used and also determined the properties of MME and diesel. During the combustion of IC engines, it is noticed that heat loss is one of the major problems and plays a vital role in all the aspects of engine operation such as engine efficiency, fuel consumption, and emissions. Due to the loss of heat energy the performance of the engine and efficiency will reduce. This will happens when the combustion gases takes places the thermal energy will be rejected to the atmosphere and passes through the other modes of heat transfer. Where the gas temperature and pressure will lost due to that engine output is getting lost. Consequently, loss of heat transfer energy in engine decreases the overall engine performance. Many experimental studies have been conducted in an attempt to gain a better understanding of the mechanisms which affect heat transfer within the combustion chamber. Each of these fundamental studies has contributed to the understanding of heat transfer in the IC engine, with the ultimate goal of improved engine performance and efficiency. Thus many have demonstrated that the most basic factors affecting heat transfer include: engine load, speed, compression ratio, ignition timing, fuel pressure variation and equivalence ratio. By applying TBC onto the piston crown and valve, the direct injection (DI) conventional diesel engine is transformed to an LHR engine to reduce heat loss Karaoglanli et al. [9]. Enhancing the LHR engine by effective TBC it promises the lower fuel consumption, higher thermal efficiency, lowering the emissions and elimination of the cooling system Buyukkaya et al. [10]. A number of ceramic coatings such as Mullite, Al_2O_3 , TiO_2 , $CaO/MgO-ZrO_2$, Ytria-stabilized Zirconia (YSZ) have been used in several engine application Cao et al. [11], Mohamed et al. [12] and Lima et al. [13]. Thermal barrier coating like Al_2O_3 , $Ca/Mg-PSZ$, Mullite, and TiO_2 be capable of be good quality substitute to YSZ due to their appropriate properties for engine application.

2. LOW HEAT REJECTION ENGINE

Since many years ago the ceramics have been used before the LHR Engines. The ceramic materials have a lower heat conduction coefficient and in weight compared to the other materials that are used in conventional engines. Nowadays, it is observed that ceramic materials have great growth in achieving the better performance of diesel engines Gatowski et al. [14] and Kamo et al. [15].

2.1 Selection of TBC material for IC engines

To fulfill the requirement of good TBC we need to find out appropriate TBC with good bond coating materials that can resist in rigorous conditions in the diesel engine combustion chamber. The essential requirements of a good quality TBC are mentioned below.

- Chemical inertness.
- Good adherence capability with a metallic substrate.
- High melting point.
- Low thermal conductivity.
- No Phase change in the room temperature range
- Same thermal expansion coefficient with the metallic substrate Kam et al. [15] and Abedin et al. [16].

Even though numerous ceramic materials have been used as TBC in diesel engines, but Mullite physical properties is being showed good such as thermal conductivity, high corrosion resistance, High hardness, good thermal shock resistance below 1273 K, etc. There are some physical properties of Mullite as TBC as shown in the below table. 1. From this below table, we can expect this coating material is quite suitable for an IC engine application.

Table 1: Properties of Mullite

Name	Properties				
	Melting Point	Poisson's Ratio	Thermal Conductivity (λ)	Young's Modulus (E)	Thermal Expansion Coefficient (α)
Mullite ($3Al_2O_3 \cdot 2SiO_2$)	2123 K	0.25	3.3 W/mk (1400k)	127 GPa (293 K)	5.3×10^{-6} (293-1273 K)

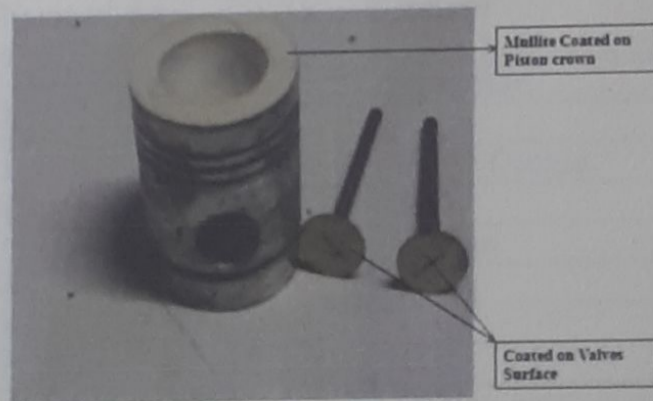


Figure 1: Mullite coated to Piston crown and valves surface

The purpose of this research work is to concern LHR engine to upgrade the engine performance with diesel and biodiesel fuels at a constant fuel injection pressure. For this purpose, single cylinder diesel engine is converted to LHR engine by applying the Mullite of 0.5mm thickness onto the valves and piston crown as shown in figure 1. Here the experiment is conducted with standard diesel and biodiesel with and without TBC to analyse the performance and emission characteristics.

3. TRANSESTERIFICATION PROCESS

In this transesterification process, initially the Mahua oil is preheated at 65°C to 70°C temperature for 30 minutes to get rid of the moisture content. After the preheating process, 1000ml of Mahua oil is taken with 14grams of potassium hydroxide and 300ml of methanol. The potassium hydroxide and methanol is added in a 1000ml of Mahua oil, then it is heated at 55°C and simultaneously the solution has to be stirred for 60 minutes. During the process the chemicals reacts with the Mahua oil and produces the MME. After finishing the process, the mixture is allowed to settle down in a separating flask for 24 hours. Once the reaction process is completed, then it is observed that the glycerine gets settled down and the methyl ester should be separated in a separate container. After the separation the MME should be washed with distilled warm water. The distilled water is heated at 45 °C then the heated distilled water is mixed with MME and after mixing solution, it must be shaken gently to remove residual catalyst or soap content. Then later distilled water is removed. Now the MME is heated at 100°C for 30 minutes to remove the trace of water left over in it. Finally the Mahua Biodiesel is obtained with maximum yield as shown in the below figure 2.

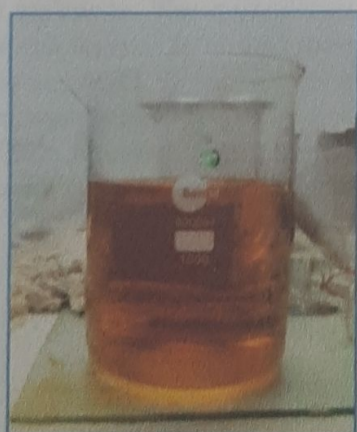


Figure 2: Final Product of Pure Mahua Biodiesel

4. FUEL PROPERTIES

Various physical properties of diesel and MME fuels were mentioned in below table 2. Some of the physical properties were tested in laboratory of Malla Reddy Engineering College (A), Secunderabad, Telangana, India. The properties of the MME fuel are within the standard of ASTM D 6751 and EN 14214.

Table 2: Properties of the Fuels

Properties	Diesel	MME
Density(15°C), kg/m ³	835	872
Specific gravity	0.850	0.916
Kinematic viscosity at 40°C, mm ² /s	2.4	4.0
Calorific Value (KJ/kg)	42930	39400
Flash Point °C	70	127
Fire Point °C	76	136
Cloud point °C	-10 to -15	6
Pour point °C	-35 to -15	1
Colour	Light brown	Dark yellow
Cetane number	51	46
Aniline point °C	69	63
Iodine value	NM	60
Diesel index	150	145

Note: NM = Not measured

5. EXPERIMENTAL SETUP

5.1 Engine test

A 3.5 kW single bore diesel engine with a fixed speed 1500rpm water cooled is used for the investigation to progress the performance and to diminish the harmful emissions. The Schematic of the experimental set up is shown in figure 3. A hydraulic dynamometer is used for loading the engine.

Table 3: Engine Specifications

Name of the specifications	Values
Name of Engine	Kirloskar
Stroke	4
Type of cooling	Water Cooled
B.H.P.	5
Stroke length	110mm
Bore	80mm
No. of Cylinder	1
Compression Ratio	16.5:1
Speed	1500rpm

Fuel Injection Pressure	200 Bar
Rated output	3.68kw (5.0 hp)
Connecting Rod Length	230.0mm
Exhaust Valve Open	340°
Exhaust Valve Closes	554°
Inlet Valve Open	527°
Inlet Valve Close	750°
Injection Advance	27° BTDC
Loading Type	Hydraulic

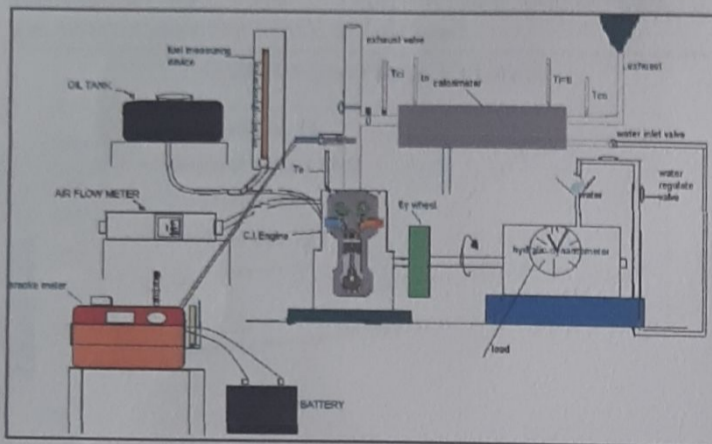


Figure 3: Schematic Plan of Experimental Setup

6. RESULTS AND DISCUSSIONS

The LHR engine was investigated for the various load conditions for different diesel and biodiesel fuels with TBC and without TBC. The results was analyzed and presented in the following sections.

6.1 Performance and Emission Parameters

6.1.1 Brake specific fuel consumption

The variation of brake specific fuel consumption (BSFC) with load at 200 bar pressure which shows with and without TBC for different fuels is presented in figure 4. Here fuel consumption of diesel is less when compare to MME oil. The BSFC without TBC of diesel at full load is 0.40 kg/kw-hr and for biodiesel is 0.44 kg/kw-hr. The comparison of with TBC of diesel at full load is 0.37 kg/kw-hr and for biodiesel is kg/kw-hr. At 25 % load diesel with TBC fuel consumption was found less. The use of with and without TBC increases the biodiesel fuel consumption because of lower calorific value.

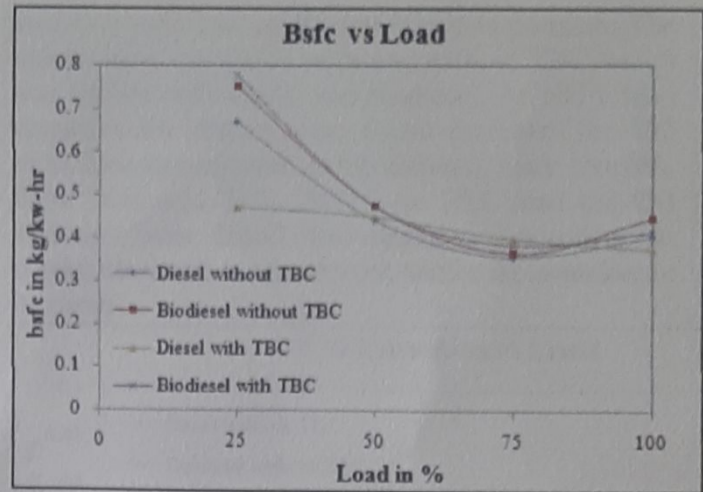


Figure 4: BSFC vs Load

6.1.2 Brake thermal efficiency

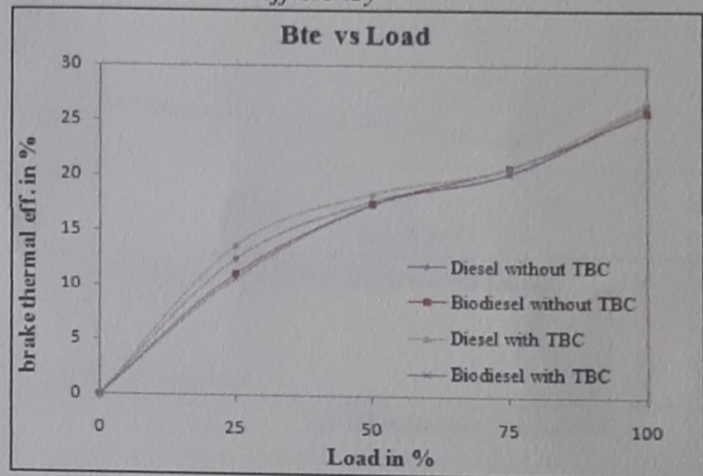


Figure 5: BTE vs Load

The above figure 5. shows the variation of brake thermal efficiency (BTE) with load at 200 bar pressure. The experiment was conducted with and without TBC for different fuel is presented. At 25% load condition diesel with TBC was found to be improved. At full load condition, there was no much remarkable improvement that was not found because of higher viscosity leads poor atomization, fuel vaporization and combustion. Hence there was no much improvement in thermal efficiency.

6.1.3 Exhaust gas temperature

The below figure 6. shows the variation of exhaust gas temperature with a load at 200 bar injection pressure. The results showed that, in all cases, the exhaust gas temperature increased with the increase in load. The diesel and biodiesel which was fuelled without TBC, the MME oil is the highest value of exhaust gas temperature of 265°C, whereas the corresponding value with diesel was found to be 255°C and for MME oil with TBC is the highest value of exhaust gas temperature of 427°C, whereas

the corresponding value with diesel was found to be 337°C only. The exhaust temperature having a higher percentage of MME oil was found to be higher at the entire load in comparison to diesel oil with TBC. The MME and Diesel without TBC were found to lower Exhaust gas temperature compared to others with TBC. This may be due to the higher combustion temperature of TBC, which gains more heat during the combustion process, and the presence of more oxygen in biodiesel, resulting in a higher peak combustion temperature. Thus increase the exhaust gas temperature for MME at full load.

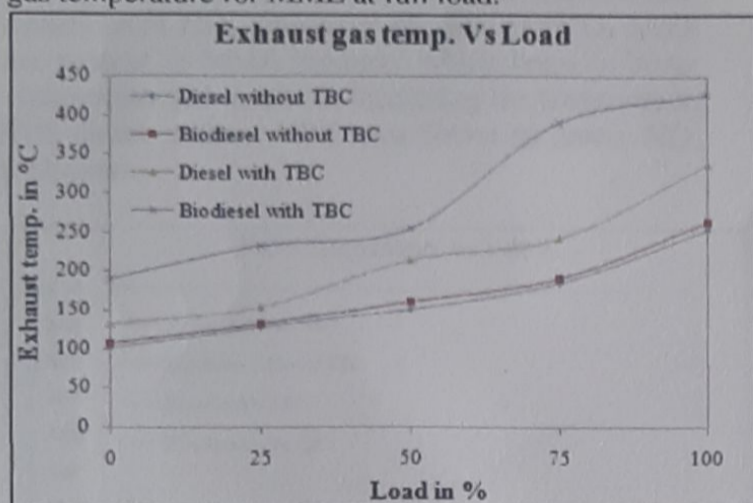


Figure 6: Exhaust Gas Temperature vs Load

6.1.4 Smoke density

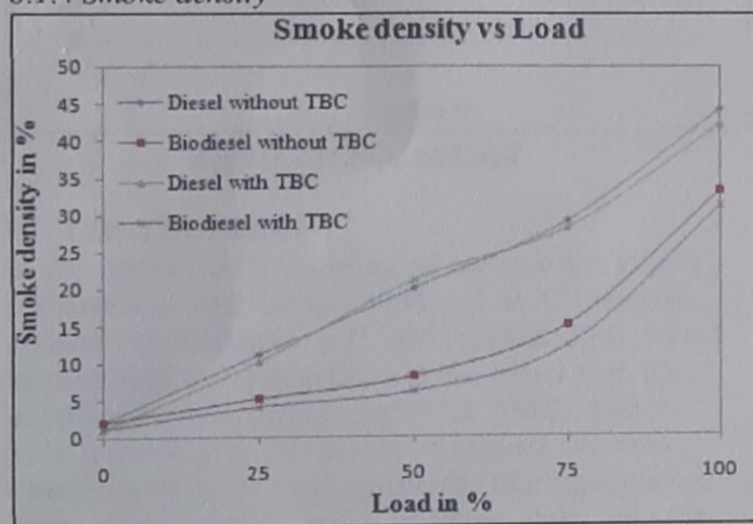


Figure 7: Smoke Density vs Load

The variation of smoke density with load is shown in figure 7. The smoke density of MME with and without TBC was found significantly reduced compared to Diesel with TBC and without TBC. This is because biodiesel has a better vaporization effect at higher combustion temperatures, and there is more oxygen in biodiesel.

6.1.5 CO Emissions

Figure 8. shows the variation of carbon monoxide

emission with load at 200 bar injection pressure. The results were compared with and without TBC which was fuelled with diesel and biodiesel. At 100% load condition the results were found increased the CO emissions as compared to the different loads like 0%, 25%, 50% and 75%. At 1% to 75% load the CO emission was found less because improving in combustion and more oxygen molecule contains in biodiesel.

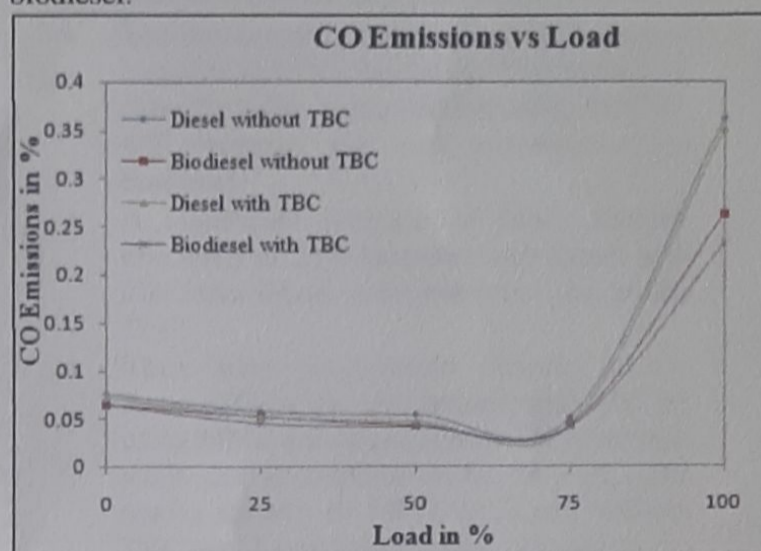


Figure 8: CO Emissions vs Load

6.1.6 HC Emissions

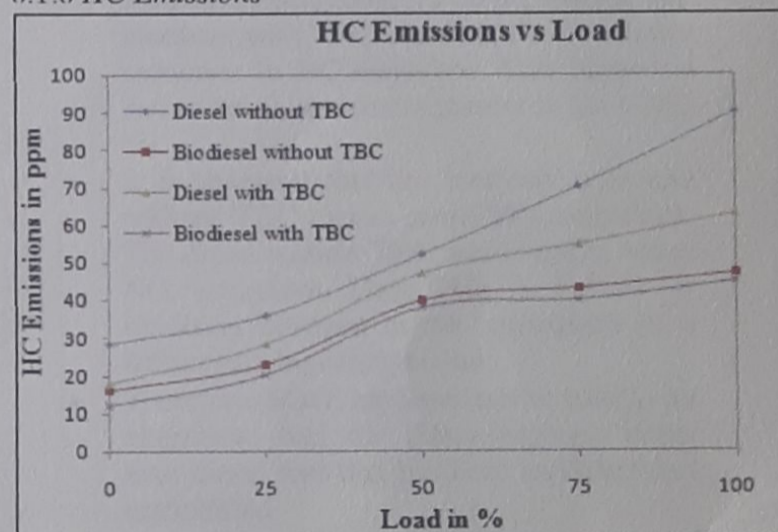


Figure 9: HC Emissions vs Load

The comparisons of hydrocarbon emissions of diesel and biodiesel at 200 bar injection pressure with and without TBC are shown in figure 9. The biodiesel is was found very less HC emissions as compared to the diesel. At maximum load without TBC, the HC emissions is 90(PPM) for diesel and for MME 47(PPM). At 100% load without TBC the biodiesel is very less CO emissions as compared to the diesel. At maximum load, there was a remarkable reduction of HC emissions is 63 (PPM) for diesel and for

biodiesel 45 (PPM) with TBC. This may be due to an increase in combustion temperature as results of a decrease in heat losses and more O_2 present in biodiesel.

6.1.7 NO_x Emissions

The variation of Nitrogen oxide (NO_x) with load at 200 bar pressure which shows with and without TBC for diesel and MME fuels is presented in figure 10. NO_x is formed by oxidizing nitrogen in the atmosphere at a sufficiently high temperature. It was well noted that the biodiesel with and without TBC causes more NO_x emissions because more O_2 levels are present in MME biodiesel which helps in better combustion and results in increasing the temperature. The diesel without TBC was found to lower NO_x emissions.

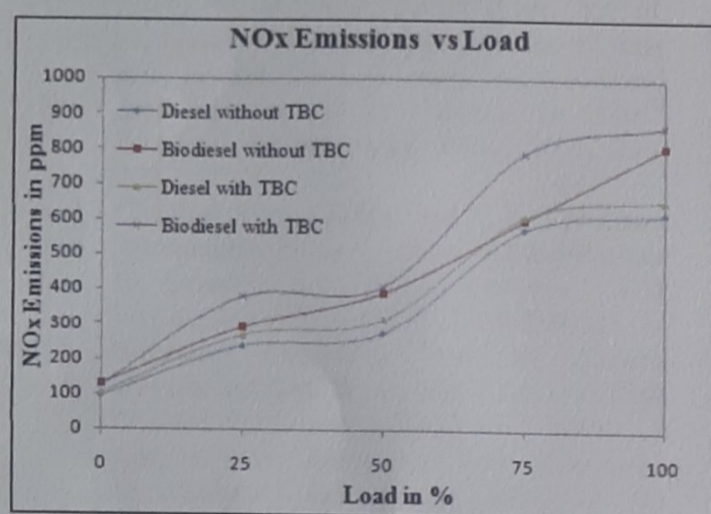


Figure 10: NO_x vs Load

7. CONCLUSIONS

In the current work, in order to improve the engine performance with Mahua biodiesel in C.I engines, different technologies with and without TBC have been studied and compared with the diesel fuel. Here experiments were conducted with MME fuel and TBC technologies and has been studied extensively through performance and emissions. The experiments were demonstrated with constant fuel injector pressure 200 bar and at a constant speed 1500 rpm. After investigating and analyzing the LHR engine, the important conclusions are revealed below.

- The Mahua methyl ester properties of Density, Fire point, Flash point and Kinematic viscosity were observed to be within the limits of ASTM D 6751 and EN 14214 specifications. The properties values are observed to be very close and higher than the diesel. The calorific value (CV) was observed to be lower than the diesel. Due to

this, there will a cause of increasing of Ignition Delay during the combustion process in LHR Engine.

- DI diesel engine was transformed to an LHR engine with the modification of 0.5 mm thickness of $3Al_2O_3-2SiO_2$ as TBC onto the piston crown and valves. Later, the performance and emission characteristics were investigated and analyzed.
- The fuel consumption of diesel is less when compare to MME biodiesel. Due to the low calorific value, using and not using the TBC will increase the fuel consumption of biodiesel.
- A significant increase of brake thermal efficiency at 25% load condition diesel with TBC was found to be improved due to the TBC.
- There were good results obtained at the lower exhaust gas temperature with TBC by using MME and Diesel, due to the more heat attain during combustion by the TBC. The smoke density of MME with and without TBC was found significantly reduced due to the more O_2 present in the biodiesel.
- The CO emissions were observed that at all loads; the biodiesel with TBC was very moderately decreased. At all the loads MME biodiesel with TBC was found a remarkable reduction in HC emissions. This happened due to the O_2 molecules present in the MME oil.
- It is observed that the biodiesel with and without TBC causes more NO_x emissions. The diesel without TBC was found to lower NO_x emissions. Here, NO_x is formed by oxidizing nitrogen in the atmosphere at a sufficiently high temperature.
- Therefore, MME biodiesel can be used as an alternative fuel for diesel engines, rather than diesel fuel that has been modified and unmodified.

REFERENCES

- Sudheer Nandi. "Performance of CI Engine by Using Biodiesel-Mahua Oil." *American Journal of Engineering Research*, 2(10), 2013, 22-47.
- Padhi, S. K., and R. K. Singh. "Optimization of esterification and transesterification of Mahua (*Madhuca Indica*) oil for production of biodiesel." *Journal of Chemical and Pharmaceutical Research*, 2(5), 2010, 599-

- 608.
- III. Agarwal, Avinash Kumar, and L. M. Das. "Biodiesel development and characterization for use as a fuel in compression ignition engines." *J. Eng. Gas Turbines Power*, 123(2), 2001, 440-447.
- IV. Padhi, Saroj K., and R. K. Singh. "Non-edible oils as the potential source for the production of biodiesel in India: a review." *Journal of chemical and pharmaceutical Research*, 3(2), 2011, 39-49.
- V. Vijay Kumar, M., A. Veeresh Babu, and P. Ravi Kumar. "Producing biodiesel from crude Mahua oil by two steps of transesterification process." *Australian Journal of Mechanical Engineering*, 17(1), 2019, 2-7.
- VI. Azam, M. Mohibbe, Amtul Waris, and N. M. Nahar. "Prospects and potential of fatty acid methyl esters of some non-traditional seed oils for use as biodiesel in India." *Biomass and bioenergy*, 29(4), 2005, 293-302.
- VII. Chauhan, Prema Singh, and V. K. Chhibber. "Non-edible oil as a source of bio-lubricant for industrial applications: a review." *Int J Eng Sci Innov Technol*, 2, 2013, 299-305.
- VIII. Sirurmah, Shivkumar, Pavan M. Vikram, and Govind Das. "Transesterification of Fish Oil And Performance Study on 4-Stroke CI Engine With Blends of Fish Biodiesel." *International Journal of Research in Engineering and Technology*, 3(3), 2014, 608-612.
- IX. Karaoglanli, Abdullah C., Hasan Dikici, and Yilmaz Kucuk. "Effects of heat treatment on adhesion strength of thermal barrier coating systems." *Engineering Failure Analysis*, 32, 2013, 16-22.
- X. Buyukkaya, Ekrem, and Muhammet Cerit. "Experimental study of NOx emissions and injection timing of a low heat rejection diesel engine." *International journal of thermal sciences*, 47(8), 2008, 1096-1106.
- XI. Cao, X. Q., Robert Vassen, and Detler Stöver. "Ceramic materials for thermal barrier coatings." *Journal of the European Ceramic Society*, 24(1), 2004, 1-10.
- XII. MohamedMusthafa, M., S. P. Sivapirakasam, and M. Udayakumar. "Comparative studies on fly ash coated low heat rejection diesel engine on performance and emission characteristics fueled by rice bran and pongamia methyl ester and their blend with diesel." *Energy*, 36(5), 2011, 2343-2351.
- XIII. Lima, C. R. C., and J. M. Guilemany. "Adhesion improvements of thermal barrier coatings with HVOF thermally sprayed bond coats." *Surface and Coatings Technology*, 201(8), 2007, 4694-4701.
- XIV. Gatowski, Jan A. "Evaluation of a selectively-cooled single-cylinder 0.5-L diesel engine." *SAE transactions*, 1990, 1580-1591.
- XV. Kamo, Roy, Dennis N. Assanis, and Walter Bryzik. "Thin thermal barrier coatings for engines." *SAE Transactions*, 1989, 131-136.
- XVI. Abedin, M. J., Masjuki, H. H., Kalam, M. A., Sanjid, A., & Ashraful, A. M. "Combustion, performance, and emission characteristics of low heat rejection engine operating on various biodiesels and vegetable oils." *Energy conversion and management*, 85, 2014, 173-189.

ESTABLISHMENT OF SCR TEST FACILITY AND EVALUATION OF 8MM PITCH HONEYCOMB TYPE CATALYST IN A 20 LITER CAPACITY SCR TEST FACILITY

Vanaparthi Mahesh¹

Mr. Raju perala²

Dr. Srinivasulu Pulluru³

¹M.Tech (Thermal Engineering)Department of mechanical engineering vaagdevi college of engineering (UGC autonomous) approved by AICTE & permanent affiliation to jntuh, hyderabad.p.o, bollikunta, Warangal urban-506005.

² Assistant professor Department of mechanical engineering vaagdevi college of engineering (UGC autonomous) approved by AICTE & permanent affiliation to jntuh, Hyderabad. p.o, bollikunta, Warangal urban- 506005.

³Professor and Head of the Department of mechanical engineering vaagdevi college of engineering (UGC autonomous) approved by AICTE & permanent affiliation to jntuh, hyderabad. p.o, bollikunta, Warangal urban-506005.

ABSTRACT

Selective Catalytic Reduction (SCR) is an advanced active emissions control technologies that offers an economic and effective means of reducing Oxides of Nitrogen (NO_x) emissions from flue gas by injecting a reductant agent through a special catalyst into the exhaust stream of flue gas. SCR is typically capable of removing 80 to 90 percent of NO_x emissions from fossil fuel power plants, and is widely considered the most effective technology demonstrated up to date for this purpose. SCR technology is designed to permit nitrogen oxide (NO_x) reduction reactions to take place in an oxidizing atmosphere. It is called "selective" because it reduces levels of NO_x using ammonia as a reducing agent with in a catalyst system. The chemical reaction is known as "reduction" where the flue gas is the reducing agent that reacts with NO_x to convert the pollutants into nitrogen, water and tiny amounts of CO₂.

The objective of this paper was to establish the 20 litres capacity Selective Catalytic Reduction (SCR) test facility in Advanced Pressurized Fluidized Bed Gasification (APFBG) test facility and also evaluate the performance of 11.8mm pitch Honeycomb type catalyst for NO_x reduction by operating APFBG test facility in combustion mode with high ash Indian coal. The Honeycomb type catalyst was tested with high dust conditions by varying the flue gas temperature from 300 Deg. C to 350 deg. C. The results showed that the SCR test facility with honeycomb type catalyst has been established successfully and also achieved very satisfactory performance with high dust conditions. The honeycomb catalysts was removing minimum of 67% and Maximum 80% NO_x from flue gas with 30-52 grams/Nm³ dust concentration. Ammonia slip was measured in the range of 4 to 6 ppm and the ratio of 2 ammonia (NH₃) to oxides of nitrogen (NO_x) was maintained as 1.0 for all experiments.

1.INTRODUCTION

Fossil fuels play a crucial role in the energy mix, and will continue to play a major role in decades to come. Coal is the most common source for heat and power production, and the role of coal will continue to be very important in the near future. According to EIA statistics for 2016, coal remains the second largest energy source worldwide until 2030 and from 2030 through 2040, it is the third-largest energy source. World coal consumption increases from 2012 to 2040 at an average rate of 0.6%/year [1]. The coal combustion generates solid and gaseous combustion products and is inevitably associated with environmental pollutants among which Oxides of Nitrogen (NO_x) are major ones. The nitrogen monoxide (NO), nitrogen dioxide (NO₂) and nitrous oxide (N₂O) molecule belongs to the family of nitrogen oxides (NO_x) compounds. NO_x is used to refer to the total amount of nitrogen oxides. About 95 % of oxides of nitrogen from industrial activities come from combustion processes. NO_x can cause severe health problems and have strong environmental impacts. The main effects are: Formation of ground-level ozone, formation of acid aerosols, formation of acid rain, deterioration of water quality, formation of toxic chemicals and global warming.

Selective Catalytic Reduction (SCR):

SCR is a process, where ammonia (NH₃) is injected into flue gas stream, allowing the ammonia (NH₃) to selectively react with nitrogen oxides NO_x (NO & NO₂) and decompose them into water (H₂O) and Nitrogen (N₂) in presence of catalyst. An ammonia is injected into exhaust gases containing NO_x. The gases mix thoroughly in a turbulent zone, and then pass through the catalyst where the NO_x is reduced. The technique is known as "selective" because the reducing agent will preferentially react with NO_x instead of O₂ at the proper temperature. The term "reduction" is used

because the nitrogen is chemically reduced from an oxidized form to molecular nitrogen.

2. LITERATURE REVIEW

So far numerous investigations have been done in the selective catalytic reduction of NO by NH₃ as a reducing agent over vanadium and titanium based catalysts to improve the reduction performances. Also, in an effort to improve the NO_x conversion efficiency, several investigations have been performed using parameters such as space velocity, the temperature of the SCR catalyst and the volume of oxidation catalyst at different raw NO_x concentrations.

Hubner et al. (1996) carried out an experimental investigation on NH₃-SCR of NO with a filter medium made from ceramic fibers on laboratory and bench scales, using model flue gases and a real flue gas from fuel oil combustion; filter candles were used and impregnated with various SCR catalysts (vanadium-oxide and others).

Zurcher et al. (2008) experimentally investigated NH₃-SCR of NO over two catalyst configurations namely ceramic candle and ceramic sponges, impregnated with V₂O₅/TiO₂/WO₃-based catalysts, in a fixed-bed reactor and individually. Results showed that the highest conversion values at 300 °C for both configurations in a fixed-bed reactor were generally lower in multifunctional reactors.

(Nam, 2007). Lietti et al. (1997) performed numerical investigations to determine the DeNO_x behavior over a V₂O₅ SCR catalyst by changing various parameters such as NH₃ concentration, the temperature of the SCR catalyst, and NH₃/NO ratio.

Furthermore, Nova et al. (2006; 2009) conducted a kinetic modelling of SCR reactions over a Vanadia based catalysts for heavy duty diesel applications. Even so, there are few investigations concerning NH₃-SCR of NO over Vanadia-based catalysts in a catalytic filter and honeycomb reactor. These multifunctional reactors for the simultaneous filtration and selective catalytic reduction (SCR) of NO_x in high temperature gas cleaning are of industrial interest since they allow substitution of two or more process units with a single reactor, where all the operations of interest are executed simultaneously. They have been suggested to save energy, space and cost and are capable of carrying out, besides the chemical reactions, other functions, such as separation or heat exchange.

Schaub et al. (2003) studied NH₃-SCR of nitric oxide (NO) over V₂O₅/TiO₂ in a catalytic filter using numerical kinetic modelling. They found that NO conversion of 60-80% is possible on the time scales of gas flow through the catalytic filter medium for temperatures around 250-350 °C. They also

developed their model to indirectly reach some sort of validation for a SCR honeycomb reactor.

Roduit et al. (1998) developed a 3D modelling for selective catalytic reduction of NO_x by NH₃ over Vanadia honey- Selective Catalytic Reduction (SCR) of NO by Ammonia Over V₂O₅/TiO₂ Catalyst in a Catalytic Filter Medium and Honeycomb Reactor 877 Brazilian Journal of Chemical Engineering Vol. 32, No. 04, pp. 875 - 893, October - December, 2015 comb catalysts.

Winkler et al. (2003) developed a one-dimensional numerical model for chemical reactions to describe the DeNO_x behaviour of a current commercial SCR catalyst by considering both standard and fast SCR reactions with the oxidation of NH₃.

They also carried out a parametric study by changing the concentrations of various components such as NO, NH₃ etc. to find the effects on SCR performance using FTIR spectrometry and computational investigation. The heterogeneous chemical reactions taking place on the catalytic surface are also taken into account based on the Langmuir-Hinshelwood (LH) mechanism, while the NH₃ storage phenomena are adopted through the DubininRadushkevich adsorption isotherm (Tsinoglou and Koltsakis, 2007). To evaluate the DeNO_x performance, Gieshoff et al. (2000) carried out studies and changed parameters such as the NH₃/NO_x and the NO₂/NO_x ratios over a V₂O₅ catalyst.

3. Properties of Feedstock

3.1 Sub Bituminous Coal

Raw sub bituminous coal of grade E and of –10 mm size from Singareni calories was obtained for this experimentation. The various analysis of coal has been pursued using in-house available techniques and shown in table 4, 5, 6, 7 & 8. The raw coal was crushed and sieved to 0.5 mm to – 4 mm sizes and used for generation of flue gas for testing of inhouse developed catalyst.

3.1.1 Physical properties of Sub-bituminous coal:

S.No	Physical properties of Sub-bituminous coal	
01	The mean diameter of the particle (mm)	1.75
02	Bulk Density of coal (kg/m ³)	810.04

03	Particle Density of coal (kg/m ³)	1665.1
----	-----------------------------------------------	--------

Table : Physical properties of Sub-bituminous coal

3.1.2 Proximate analysis of Sub-bituminous coal (Wt %):

S.No	Proximate analysis of Sub-bituminous coal	
01	Moisture (%)	2.55
02	Ash (%)	29.25
03	Volatile Matter (%)	28.93
04	Fixed Carbon (%)	39.27

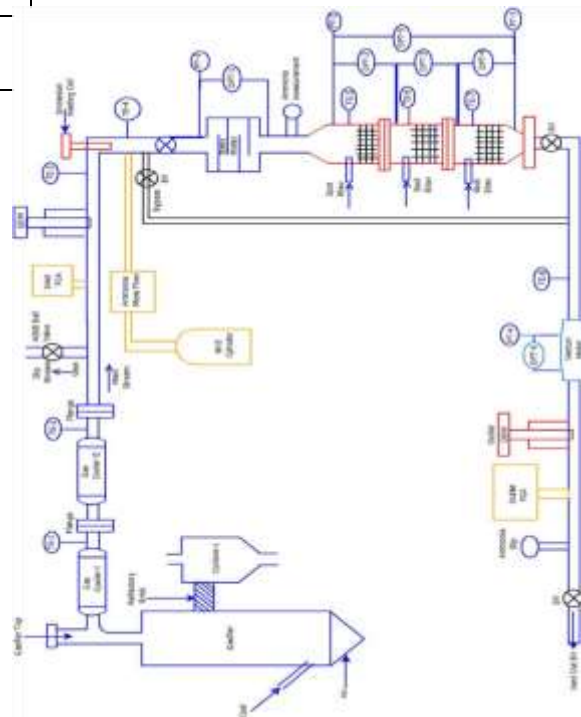
Table : Proximate analysis of Sub-bituminous coal

05	Ammonia Injection system
06	Static Mixture
07	SCR Reactor Housing
08	SCR Catalyst
09	Venturi Flow Meter

Table : The experimental setup systems/sub-systems

Process & Instrumentation Diagram (P&ID) of 20 Liters SCR test Facility

Figure : Process & Instrumentation Diagram (P&ID) of 20 Liters SCR test Facility.



4. EXPERIMENTAL SYSTEM DESCRIPTION

The experiments were conducted in 20 litres capacity Selective Catalytic Reduction (SCR) test facility with 8mm pitch honeycomb type SCR catalysts. The 8mm pitch honeycomb type catalyst supplied by BHEL Corp. R&D, CTI Group Bangalore and is installed in 20 litres capacity Selective Catalytic Reduction (SCR) test facility to evaluate the performance. The existing 200mm dia pilot plant was operated in a combustion mode and generated flue gas for testing of 20 litres capacity honeycomb type catalysts for NOx reduction. The Process and Instrumentation Diagram (P&ID) and Pictorial View of SCR test facility for De-NOx process is shown in Figure 1(a) & 1(b) respectively. The performance of honeycomb type catalyst was tested with dust concentration of 30-52 grams/Nm³ in flue gas. The experimental setup comprises of the following systems/sub-systems and are explained subsequently,

S.No	Sub System
01	Ø200mm Pilot Plant Test Facility
02	Flue Gas Cooler-I & II
03	On-line Dust Monitoring system
04	NOx Measurement System



Figure: Pictorial View of 20 litres capacity SCR test facility

Ø200mm Pilot Plant Test Facility:

The Process Flow Diagram (PFD) and pictorial view of Ø200mm Pilot Plant Test Facility are shown in Figure 2. The pilot scale plant is operated in combustion mode to generate the flue gas (NO_x, SO₂, CO₂, CO & O₂) for testing of 8mm honeycomb type catalyst.

The Ø200mm Pilot Plant Test Facility consists of three main sections: The feeding and extraction system, the reactor system and the gas cleaning system. The feeding system consists of one rotary feeder for coal and rotary extractor for extract the ash content from the reactor. The gas cleaning system path was completely blocked with high alumina brick to avoid the dust going in to cyclones. Since the present testing was recommended with high ash content (30-52 grams/Nm³), the flue gas is not allowed to enter in to gas clean-up system.

Apart from the main systems, the following sub systems also available in a pilot plant: air compressor and electric heater. The reactor consists of three zones; the plenum, reactor and free board section. Refractory bricks and insulation castables are laid inside the fluidized bed reactor to minimize the heat losses. The coal was introduced with help of rotary feeder inside the fluidized bed reactor with help of transport air. Thermocouples are installed radially and axially to measure the reactor temperature and pressure difference across the reactor is measured

using Differential Pressure Transmitters (DPTs). Immediately after the flue gas generation, gas was sent in to SCR reactor without cleaning of dust particles.

NO_x Measurement System:

A flue gas analyser is used to measure the oxides of nitrogen from flue gas at inlet and outlet of SCR reactor. A flue gas analyser is a portable electronic device, which measures and displays the products of combustion from both domestic and commercial fossil fuelled appliances. Additionally, they can measure the ambient air quality in rooms or buildings. Flue gas analysers are used for measure the following composition from flue gas i.e. O₂, CO, CO₂, SO_x and NO_x and these components are measured using NDIR (Non- Dispersive Infrared) Technology. The flue gas analyser along with measured composition is shown in figure 3.

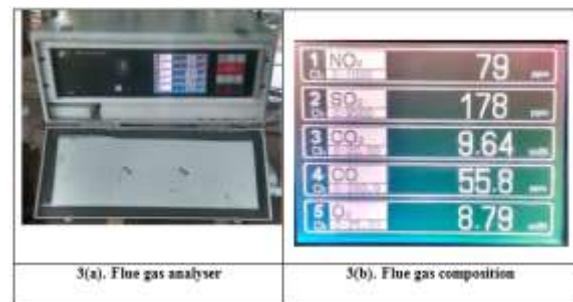
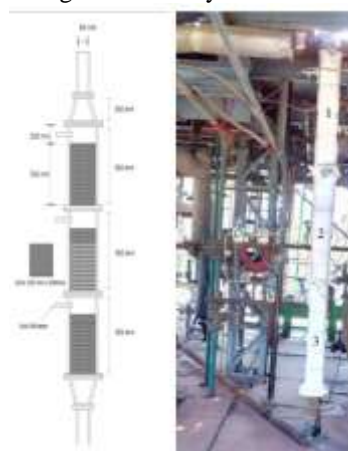


Figure: Flue gas analyser and measured composition

SCR Reactor Housing:

The honeycomb catalyst is enclosed in a fabricated stainless steel housing called SCR reactor. The size of the SCR reactor is 100 mm x 100 mm x 900 mm of 3 modules. The drawing of SCR reactor module casing for honeycomb is shown in figure .



SCR Catalyst:

Catalyst is the heart of DeNO_x process. There are two types of catalysts are available; Honeycomb type catalyst. The Honeycomb type catalysts with 8mm

pitch has been used for reduction of oxides of nitrogen (NO_x) from flue gas. Anhydrous gaseous ammonia reacts with NO_x in flue gas to form nitrogen (N₂) and water vapour (H₂O) in presence of honeycomb type SCR catalyst. The primary base material of catalyst is titanium dioxide (TiO₂), with smaller amounts of other metal oxides including tungsten oxide (WO₂) for thermal support and vanadium pentoxide (V₂O₅), which is the primary active material.

The size of honeycomb catalyst is offered with 94mm X 94mm X 750mm of 3 Modules with 8mm pitch and 1mm wall thickness. The total volume of honeycomb catalyst is 0.0198 m³ (or) 19.8 litres (0.094*0.094*0.75 *3). The pictorial view of 8mm pitch honeycomb type SCR catalysts have been shown in figure 06. To provide a large gas contact area with a minimum pressure loss, the honeycomb catalyst is provided as 64 elements containing a large number of parallel channels (corrugated or extruded honeycomb catalysts).



Figure 6(a). Pictorial View of 8mm honeycomb SCR type catalyst



Figure 6(b). Pictorial View of 8mm plate type SCR catalyst

5. EXPERIMENTAL PROCEDURE

The existing Ø200mm Pilot Plant Test Facility was operated in a combustion mode and generated flue gas for testing of 8mm pitch honeycomb type SCR catalysts. The Process and Instrumentation Diagram (P&ID) and Pictorial view of SCR test facility for De-NO_x process is shown in Figure 1 (a) & 1 (b) respectively. The performance of honeycomb type SCR catalysts were tested with high dust (30-52 grams/Nm³) concentration in flue gas.

For testing of honeycomb type catalyst with dust, flue gas generated from the gasifier and sent directly to dust measurement system where the dust concentration was measured with help of on-line dust monitoring system. The gasifier and its pipe lines are shown in figure 7(a) & 7(b) respectively. Once the dust measured using on-line dust measurement system, the flue gas was sent to immersion heating coil to heat the flue gas to a required SCR inlet

temperature (300 to 350 Deg.C) and is shown in figure 8(a). Then the inlet NO_x concentration was measured using flue gas analyser and is shown in figure 3.

Subsequently the required quantity of Anhydrous Ammonia was admitted with help of ammonia mass flow controller in to flue gas pipe line through ammonia injection nozzle. The pictorial view of ammonia mass flow controller and ammonia flow nozzle is shown in figure 4 (a) & 4 (b). The quantity of anhydrous ammonia is calculated based on the flue gas flow rate and NO_x concentration in the flue gas. Once the anhydrous ammonia injected in to flue gas, the mixture of Ammonia (NH₃) and Oxides of Nitrogen (NO_x) gas was sent to static mixture for better mixing of ammonia and oxides of nitrogen in the flue gas. The pictorial view of static mixture system is shown in figure 9 (a). Then the mixture sent in to SCR reactor to reduce the oxides of nitrogen (NO_x) in presence of honeycomb type SCR catalysts for NO_x reduction at required SCR inlet temperatures. The line diagram and pictorial view of 20 litre capacity SCR reactor module is shown in Figure 5. The temperature, pressure and differential pressures are measured across the SCR reactor using E-type thermocouples, pressure transmitters and differential transmitters respectively. Once the reaction completed in SCR reactor, the flue gas passes through gas Venturi flow meter to measure the flue gas flow rate for calculating the space velocity. The outlet NO_x concentration and ammonia slip also measured before vent off to the atmosphere using flue gas analyser and ammonia gas analyser respectively. The NO_x conversion rate was calculated based on the inlet and outlet NO_x concentration of the SCR reactor.



Fig 8 (a). Combustor & 8 (b). Flue Gas Pipe Lines



Fig 9 (a). Heater & Static Mixture



Fig 9 (b). Ammonia Injection Nozzle

6.EXPERIMENTAL RESULTS

The existing Ø200mm Pilot Plant Test Facility was operated in a combustion mode and generated flue gas for testing of 8mm honeycomb type catalyst for generating the performance curves. The size of the each honeycomb is 94mm X 94mm X 750 mm long to get about 20 liter catalyst volume. The Process and Instrumentation Diagram (P&ID) of 20 litres SCR test Facility for De-NOx system is shown in Figure 1.

Coal was procured from Singareni calories, to generate the flue gas for testing of in-house developed catalyst. The physical properties, proximate and ultimate analysis of coal was shown in table 04, 05 & 06 respectively. Feed particle size has been maintained more or less same for all the experiments and which was + 0.5 to -4.0 mm.

The performance of honeycomb type catalyst was evaluated by varying the dust concentration from 38-50 grams/nm³ in flue gas. For testing of honeycomb catalyst the flue gas flow rate varied at 31.80, 41.75 & 51.70 Nm³/hr and space velocity 2102 /hr respectively. Also the SCR inlet temperature varied in the range of 300 to 350 Deg.C and the molar ratio of ammonia (NH₃) to oxides of nitrogen (NO_x) varied in the range of 0.9 to 1.0 for all experiments.

The Ø200mm Pilot Plant Test Facility generates the flue gas by operating in combustion mode. The flue gas composition consists of carbon di-oxide (CO₂), water (H₂O), oxygen (O₂), nitrogen (N₂), nitrous oxide (NO), nitrogen di-oxide (NO₂), sulphur di-oxide (SO₂), and Argon (Ar). The generated flue gas composition in volume percentage wise is shown in table 15.

SCR Honeycomb Type Catalyst Performance Curves:

Inlet NOx concentration Vs De-NOx efficiency

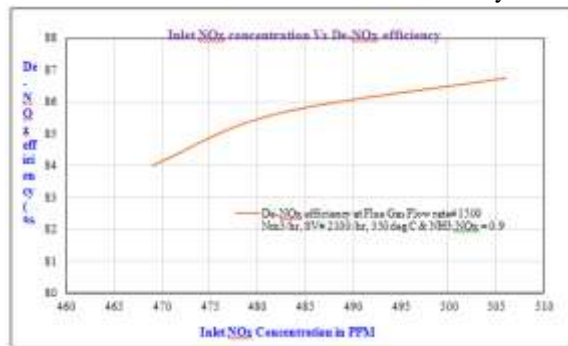


Figure 10 Inlet NOx concentration Vs De-NOx efficiency

Figure 10. Shows the De-NOx efficiency as a function of inlet NOx concentration. This experiment was conducted in a 20 litre capacity SCR test facility by maintaining the flue gas flow rate of 41.75 Nm³/hr and space velocity 2100 /hr. Also varied the molar ratio of ammonia (NH₃) to oxides of nitrogen

(NO_x) was in the range of 0.9 to 1.0 but reported only 0.9 (NH₃: NO_x=0.9) due to avoid more ammonia slip.

The results show that the increase in inlet NO_x concentration in flue gas leads to increase in De-NO_x efficiency which could be attributed due to reaction kinetics [2]. When the inlet NO_x concentration is increases from 469-506 ppm, the De-NO_x efficiency also increased from 84 to 86.75%. The concentration of the reactants also affects the reaction rate of the NO_x reduction process. However, NO_x concentrations higher than approximately 150 parts per million (ppm) generally do not result in increased performance [3]. Low NO_x inlet levels result in decreased NO_x removal efficiencies because the reaction rates are slower, particularly in the last layer of catalyst [2].

Temperature vs. De-NOx efficiency:

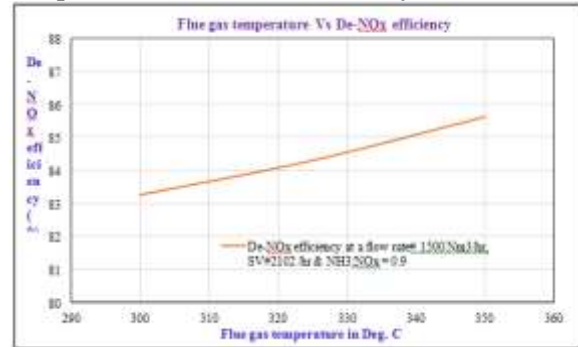


Figure. Shows the De-NOx efficiency as a function of SCR inlet temperature. this experiment was conducted in a 20 litre capacity SCR test facility by maintaining the flue gas flow rate of 41.75 Nm³/hr and space velocity 2102 /hr. Also varied the SCR inlet temperature in the range of 300 to 350 Deg.C and the molar ratio of ammonia (NH₃) to oxides of nitrogen (NO_x) in the range of 0.9 to 1.0 but reported only 0.9 (NH₃: NO_x=0.9) due to avoid more ammonia slip.

The results show that the De-NOx efficiency increases as the temperature of the SCR inlet gas is increased which could be attributed due to more NO conversion at relatively high operating temperatures. When the SCR inlet temperature increases from 300 to 350 Deg.C,

the De-NOx efficiency also increased from 83.26 to 85.62% at a space velocity of 2102 /hr. The higher SCR inlet temperature favours the reaction kinetics between NO_x and NH₃. When the SCR inlet temperature increases the reaction rate also increases, which in turn increases the De-NOx efficiency.

Flue gas flow rate Vs De-NOx efficiency:

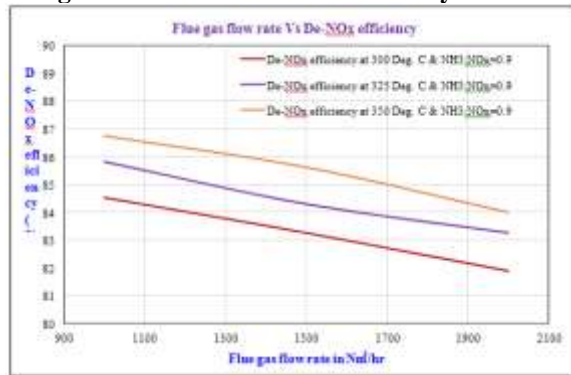


Figure 12. Shows the De-NOx efficiency as a function of flue gas flow rate. This experiment was conducted in a 20 litre capacity SCR test facility by varying the flow rate of 31.80, 41.75 & 51.70 Nm³/hr. Also the SCR inlet temperature varied in the range of 300 to 350 Deg.C and the molar ratio of ammonia (NH₃) to oxides of nitrogen (NO_x) varied in the range of 0.9 to 1.0 but reported only 0.9 (NH₃: NO_x=0.9) due to avoid more ammonia slip.

The results show that the De-NOx efficiency increases with decrease in flue gas flow rate which could be attributed due to less residence time. The residence time is the major parameter which greatly affects the DeNOx efficiency in SCR catalyst. When the flue gas flow rate increases, the residence time decreases which means the flue gas spent very less time in SCR reactor which leads to reduction in reaction rate between NO_x and NH₃. When the flue gas flow rate increases from 31.80, 41.75 & 51.70 Nm³/hr, the De-NOx efficiency decreased from 86.75 to 81.89% at different temperatures (300 -350 Deg.C).

NOx/NH3 molar ratio Vs Outlet NOx concentration

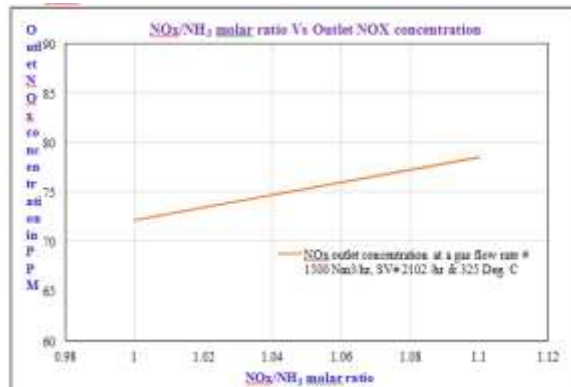


Figure 14 NO_x/NH₃ molar ratio Vs Outlet NOx concentration

Figure 13. Shows the outlet NOx concentration as a function of NO_x/NH₃ molar ratio. This experiment was conducted in a 20 litre capacity SCR test facility by maintained the flue gas flow rate of 41.75 Nm³/hr

and space velocity i.e. 1500 Nm³/hr and 2102 /hr. Also the SCR inlet temperature has been maintained 325 deg. C and the molar ratio of oxides of nitrogen (NO_x) to ammonia (NH₃) is varied in the range of 1.0 to 1.1.

The results show that the outlet NOx decreases with decrease in NO_x/NH₃ molar ratio which could be attributed due to less ammonia concentration in NO_x/NH₃ molar ratio. When the availability ammonia in the SCR catalyst increases, the reaction rate also increases which leads to reduction in out let NOx. When the ratio of oxides of nitrogen to ammonia decreases from 1.1 to 1, the out let NOx concentration reduced from 72.15 to 78.50 ppm.

Ammonia slip Vs Flue gas flow rate

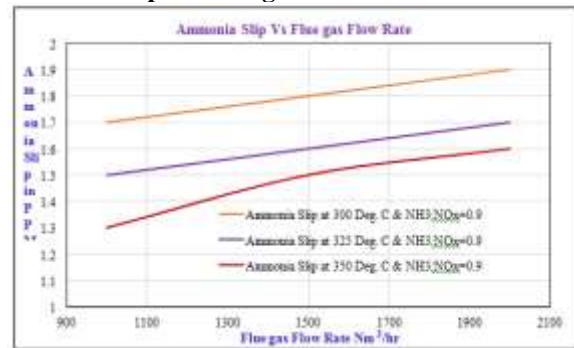


Figure 17. Shows the ammonia slip as a function of flue gas flow rate. This experiment was conducted in a 20 litre capacity SCR test facility by varying the flue gas flow rate of 31.80, 41.75 & 51.70 Nm³/hr. Also varied the SCR inlet temperature in the range of 300-350 deg. C and the molar ratio of ammonia (NH₃) to oxides of nitrogen (NO_x) in the range of 0.9 to 1.0 but reported only 0.9 (NH₃: NO_x=0.9) due to avoid more ammonia slip.

The results show that the Ammonia slip increases as the flue gas flow rate increases which could be attributed due lower residence time. When the flue gas flow rate increases from 31.80, 41.75 & 51.70 Nm³/hr, the ammonia slip increases from 1.3 to 1.9ppm at the molar ratio of ammonia (NH₃) to oxides of nitrogen (NO_x) in the range of 0.9. When the flue gas flow increases, the residence time decreases when the residence time decreases the reactivity also decreases. When the reactivity decreases the ammonia slip increases. Ammonia slip also increases as the catalyst activity decreases. The allowable ammonia slip approximately less than 2 ppm .

7. CONCLUSIONS

Experiments were carried out to generate the performance curves with in-house developed 8mm Pitch Honeycomb type catalyst in a 20 litre volume capacity SCR test facility. The flue gas was generated from Ø200mm Pilot Plant Test Facility by operating in combustion mode. The NO_x removal efficiency and ammonia slip was investigated with dust concentration of 38-50 grams/Nm³ in flue gas by varying the space velocities (2500-1500 per hr.) and flue gas temperatures (300–350⁰C) using anhydrous ammonia as reducing agent.

- In-house developed 8mm pitch honeycomb type SCR catalysts were tested in a 20-liter capacity SCR test facility with dust concentration in the range of 38-50 grams/nm³ by varying the space velocities (2500-1500 per hr.) and flue gas temperatures in the range of 300–350⁰C using anhydrous ammonia as reducing agent.
- NO_x reduction efficiency achieved with honeycomb was 81.89 – 86.75% at 2500-1500 per hr. space velocities and the ratio of ammonia (NH₃) to oxides of nitrogen (NO_x) was maintained at 0.9.
- NO_x reduction efficiency achieved with honeycomb was 82.72– 88.23% at 2500-1500 per hr. space velocities and the ratio of ammonia (NH₃) to oxides of nitrogen (NO_x) was maintained at 1.0.
- Ammonia slip measured was in the range of 1.4 to 3.8 ppm for honeycomb catalyst at 0.9 & 1.0 for ammonia to oxides of nitrogen.
- The total Differential Pressure (DP) across Honeycomb SCR catalyst was 25-38 mmWc over a 2250mm length.

Finally, it can be concluded that, the 8mm pitch honeycomb type SCR catalysts are very much suitable for reduction of Oxides of Nitrogen (NO_x) in the range of 80-90% in flue gas with dust concentration of 30-52 grams/Nm³ which are meeting the NTPC requirements. Hence, based on the performance achieved in 20 litre SCR test facility, the honeycomb type SCR catalysts were selected and finalized for establishment of 1500 Nm³/hr slip stream De-NO_x system in Left Hand (LHS) side and Right Hand (RHS) Side at Unit-2 of NTPC Simhadri power plant as per MOU.

REFERENCES

1. International Energy Outlook 2016, report no. DOE/EIA-0484(2016) I May 2016.
2. The Cadmus Group, Inc., Bechtel Power Corporation, and Science Applications International Corporation. Selective Catalytic Reduction for NO_x Control on Coal-fired Boilers, Draft Report. Prepared for the U.S. Environmental Protection Agency. May 1998.
3. Selective Catalytic Reduction Draft public comment. Prepared by John L. Sorrels, Air Economics Group Health and Environmental Impacts Division Office of Air Quality Planning and Standards U.S. Environmental Protection Agency. June 2015.
4. Institute of Clean Air Companies (ICAC). White Paper. Selective Catalytic Reduction (SCR) Control of NO_x Emissions from Fossil Fuel-Fired Electric Power Plants. May 2009.

Credit card fraud detection using Machine Learning Model

Dashamukhi Sudhathi¹, Sravankumar Bethi²

M.Tech Student, Department of CSE, Vaagdevi college of engineering, Hanamkonda , Bollikunta,warangal
506005(T.S)¹

Assist. Prof, Department of CSE, Vaagdevi college of engineering, Hanamkonda , Bollikunta,warangal
506005(T.S)²

Abstract

With the growth of e-commerce has come an upsurge in credit card theft. Due to the industry's stratospheric expansion, banks are finding it more challenging to detect credit card fraud. The detection of unauthorised purchases is one of the most critical responsibilities that machine learning performs in combatting credit card fraud. Banks use a variety of machine learning algorithms to forecast these kinds of transactions, drawing on previous data and introducing unique features to increase prediction accuracy. The success of credit card fraud detection is highly dependent on data set sampling technique, variable selection, and detection mechanism. This study investigates the effectiveness of logistic regression, decision trees, and random forest in detecting credit card fraud. A dataset of 2,84,808 credit card transactions from a European bank collected using kaggle. It defines fraudulent transactions as "positive class" and valid purchases as "negative class," but the data set is considerably skewed, with just about 0.172% being fraudulent and the rest being legitimate. Because to the author's frame interpolation efforts, the dataset now contains 60% fraudulent and 40% valid transactions. The dataset is subjected to each of the three approaches, and the output code is written in the programming R. Several metrics, including as sensitivity, specificity, accuracy, and error rate, are utilised to analyse the efficacy of the approaches in relation to the aforementioned criteria. The accuracy of the logistic regression, decision tree, and random forest classifiers was 90.0, 94.3, and 95.5%, respectively. When evaluated to logistic regression and decision trees, the Random forest outperforms both.

1. Introduction

Credit card fraud includes theft and fraud performed at the time of payment with a credit card, with the goal to make a purchase without paying or to withdraw cash from an account without authorisation. Identity theft is commonly associated with credit card fraud. Identity theft increased by 21% in 2008, according to data provided by the Federal Trade Commission in the United States, after being relatively stable throughout the middle of the millennium.

The overall number of ID theft cases fell, as did the proportion of complaints involving credit card fraud. Annual transactions totaled roughly 13 billion in 2000, with approximately 10 million (or one in every 1300) being fraudulent. Furthermore, 5% of all monthly active accounts were fake (5 out of every 10,000). Even though only one-twelfth of all transactions are currently monitored by fraud detection systems, the resulting losses amount to billions of dollars. Credit card fraud is one of the most serious threats that modern businesses face. To effectively resist the illusion, it is necessary to first understand its mechanisms. Credit card thieves use a variety of techniques. The unauthorised use of another person's credit card for financial gain while both the card's rightful owner and the card issuer are unaware of the transaction is a common definition of credit card fraud. Card fraud typically begins with the loss or theft of the card itself or of the card account number or other sensitive data associated with the account that must be made available to a merchant during a legal transaction. The data is recorded on a magnetic stripe on the back of the card in a machine-readable format, and the card number, which is frequently the Primary Account Number (PAN), is displayed on the front. Cardholder's name, Card number, Expiration Date, Verification/CVV code, and Card Type are required fields. Credit card fraud can also be committed in a variety of other ways. Con artists are very skilled and can act quickly. This article will assist in identifying Application Fraud, which occurs when a person knowingly provides inaccurate information when applying for a credit card using the standard approach. Lost or stolen credit cards account for a large share of credit card theft. Aside from the traditional techniques of credit card fraud, more sophisticated fraudsters use skimming and tampering to steal money from unsuspecting victims. The magnetic strip on the back of the card or the information stored on the smart chip on the card can be copied from one card to another, providing the recipient access to the required information.

2. Literature review

The book by Rimpal R. Popat and Jayesh Chaudhary discusses They conducted a survey regarding the detection of credit card fraud, focusing on its three primary subfields: bank fraud, business fraud, and insurance fraud. They have prioritised the two primary methods of processing credit card transactions: I remotely (card not present) and ii in person. They have focused on techniques such as Regression, classification, Logistic regression, Support vector machine, Neural network, Artificial Immune system, K-nearest Neighbor, Naive Bayes, Genetic Algorithm, Data mining, Decision Tree, etc. They give a conceptual framework for six data mining approaches (classification, clustering, prediction, outlier detection,

Regression, and visualisation). The Artificial Immune System (AIS), Bayesian Belief Network (BBN), Neural Network (NN), Logistic Regression (LR), Support Vector Machine (SVM), Tree, Self-Organizing Map (SOM), and Hybrid Methods were among the various statistical and computational techniques covered (HM). All of the above-mentioned machine learning techniques, they reasoned, can deliver a high detection rate of accuracy, and businesses are eager to discover fresh ways to boost their earnings and cut expenses. Machine learning could be a viable alternative if you're seeking for a solution.

Authors MohamadZamini

Aiming to use autoencoder-based clustering for unsupervised fraud detection. They have employed the autoencoder, which is an autoassociator neural network, to reduce the dimensionality, extract the relevant features, and boost the network's learning performance. They trained their autoencoder-based clustering with the following parameters using a European dataset of 284,807 transactions, of which 0.17 percent were fraudulent. Three Hundred Iterations Cluster count = 2 When starting to cluster, k-means++ is the initialization to use. Acceptable level of divergence = 0.001 The model's learning rate is 0.01%. Epoch count = 200 The activation function is denoted by the symbols elu and Relu. Their context-free model design yielded a training loss of 0.024, a validation loss of 0.027, and a mean non-fraud data error of 75% less than the mean of reconstructive error, which was 25%. Regarding the model's predictions, the True positives equal 56,257, the False negatives equal 607, the False positives equal 18, the True negatives equal 80, and the best preferred equals $(56,257 + 80 = 56,337)$. A total of 56,337 out of a possible 284,807 forecasts were accurate.

ShiyangXuan was presented, and a comparison was done between two random forests. Forests constructed using a combination of random trees (CART) and randomization (random). While both systems classify transactions as normal or abnormal, their basis classifications and performance are different, therefore they employ separate random forest strategies to train the behaviour aspects of each. Using data from a Chinese e-commerce firm, they tested both systems. where the percentage of fraudulent transactions in the subgroups ranges from one to ten. As a result, the CART-based random forest achieves a 96.7% accuracy, whereas the random-tree-based random forest achieves just 91.96 percent. Many issues, such as uneven data, have arisen because of the use of the B2C dataset. As a result, the algorithm can be enhanced.

These machine learning algorithms for detecting credit card fraud were proposed by author DejanVarmedja, who also conducted the research necessary to get these conclusions. Logistic Regression, Naive Bayes, Random Forest, and Multilayer Perceptron are some of the many machine learning techniques available. To achieve the best results, we employ an artificial neural network (ANN) called a multilayer perceptron, which consists of four hidden layers, a relu activation function (to prevent the usage of negative values), and an optimizer called Adam. Therefore, the Logistic regression accuracy score is 97.46%, with 56962 samples and 98 fraud transactions making up the data set. Accuracy scores of 99.23% and 99.96% are achieved by Naive Bayes and Random Forest, respectively, on the same dataset. The final ANN accuracy was 99.93%, and it was found that random forest provides the greatest outcome when it comes to detecting credit card fraud.

Authors Changjun Jiang proposed a new four-stage approach to fraud detection. The first stage involves using historical transaction data to divide transactions into clusters of similar behaviour. The authors then developed a sliding window strategy to aggregate transactions. This algorithm is used to characterise a cardholder's behavioural pattern. Behavior patterns and responsibilities are finally sorted out and classified. Therefore, when compared to other methods, their approach, which combines Logistic Regression with raw data (RawLR), Random Forest with aggregation data (AggRF), and a feedback mechanism with aggregation data (AggRF +FB), achieves 80% accuracy.

Methodology

Keeping up with the Modeling and pattern of illicit transactions is getting harder as technology evolves. This labor-intensive method of detecting credit card fraud can now be automated, thanks to advancements in machine learning, artificial intelligence, and other related areas of information technology. In this research, the provided methods are applied to the problem of credit card fraud detection. Machine learning techniques like Logistic Regression, Decision Trees, Random Forest, Naive Bayes, SVM, and the K-Nearest classifier are compared to find the most effective one for detecting fraudulent credit card purchases.

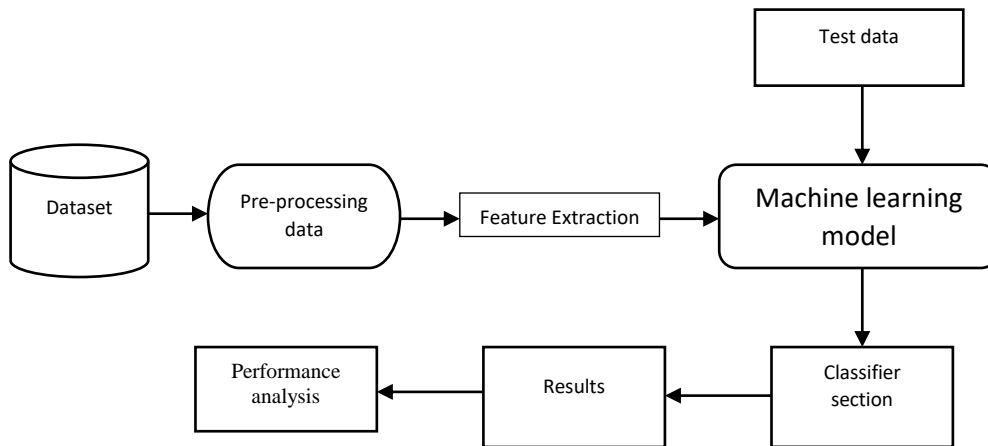


Fig. 1 proposed architecture

Simply said, it's predicated on a Machine Learning model that could boost the efficiency of specialised computer vision programmes. The proposed method is grounded in particular configurations of the Machine Learning model, as shown in Figure 1.

Algorithm

Algorithm: Credit Card fraud Detection Using Machine Learning Techniques.(CCFD-ML)

Inputs: Credit card dataset as S, prediction models M

Output: Fraud detection Results as R

1. **Start**
2. **Input dataset(S)**
3. **Pre-processing (S)**
4. **Extract features from training set()**
5. **For each model m in M**
6. **Train the model m**
7. **End For**
8. **For each model m in M**
9. **Use model for testing**
10. **Evaluate**

11. **Display results**
12. **End For**
13. **End**
14. **Return R**

Fig.2 Proposed algorithm.(CCFD-ML)

(HDP-MLT) utilises an input dataset to generate a set of prediction models in a pipeline format. At a ratio of 80:20, it separates the dataset into training and testing data. After then, a number of ML models are cycled through in an iterative process to spot signs of transaction fraud. Various indicators are used to compare the effectiveness of the various models. Accuracy, precision, recall, and F1-score are all calculated using the model-specific confusion matrices. The method returns both the results of the fraud detection and performance statistics.

3.3 Performance Evaluation Metrics

In many ML-based situations, the confusion matrix serves as the foundation for creating metrics used to evaluate performance. Many works, including [2], [3], [7], and [10], investigate the usefulness of the confusion matrix. There are two examples where the predictions are accurate (TP and TN) and two examples where the forecasts are off (FP and FN).

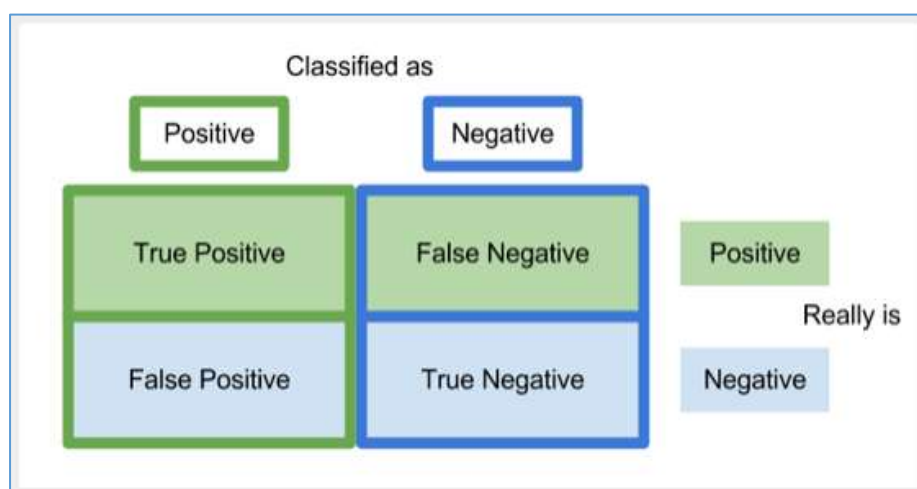


Figure 3: Confusion matrix model

Figure 3 shows how the performance metrics are derived by applying the confusion matrix to a variety of scenarios. The metrics for success are given in Equations (4)–(6). (7).

$$\text{Precision} = \frac{TP}{TP+FP} \quad (4)$$

$$\text{Recall} = \frac{TP}{TP+FN} \quad (5)$$

$$\text{F1-measure} = 2 * \frac{(\text{precision} * \text{recall})}{(\text{precision} + \text{recall})} \quad (6)$$

$$\text{Accuracy} = \frac{TP+TN}{TP+TN+FP+FN} \quad (7)$$

The values of these indicators range from 0 to 1, with 0 being the worst potential performance and 1 the best. When talking about values, higher means better.

4. Dataset description

This dataset represents hypothetical charges made to credit cards between January 1, 2019, and December 31, 2020, and may include both genuine and fraudulent charges. It protects the credit card accounts of one thousand people who shop at a select group of 800 stores. Using Brandon Harris's Sparkov Data Generation | Github tool, we generated this. The time span of this simulation was from January 1, 2019, to December 31, 2020. Together, the files were transformed into a universal standard.

Card numbers and other sensitive information were hashed because of a confidentiality agreement between the bank and the paper's authors. As a result of the discrepancy between the number of honest dealings and the number of scams, the overall data set had an extremely asymmetrical distribution.

5. RESULTS AND DISCUSSION

Using AI for detecting fraudulent activity is a hot issue right now. An algorithm designed to detect credit card fraud looks for specific types of suspicious activity by comparing them to known fraud patterns. There are three distinct categories of machine learning, although the supervised and hybrid methods are best suited to detecting fraudulent activity. Here, we take a look at some of the latest developments in credit card fraud detection algorithms and compare them to some of the established methods of classification.

	Model	Train score	Test Score/Accuracy	Precision	Recall	F1-score	specificity
2	Decision Tree	94.78	94.92	94.013	94.139	94.076	95.500
3	Random Forest	90.22	89.68	96.216	79.041	86.787	97.667
5	K Nearest Neighbour	87.91	81.91	84.850	70.382	76.942	90.567
0	Logistic Regression	86.84	86.60	94.178	73.268	82.418	96.600
4	Naive Bayes	81.55	81.53	97.411	58.481	73.085	98.833
1	Support Vector Machines	47.79	45.49	43.992	99.334	60.979	5.067

Fig 4. Comparison table for performance of models

As shown in Figure 3, ML are utilised for the identification of credit card fraud. The accuracy of various models is compared to that of other employed models. There is significant performance improvement when recommended method is applied. Each method exhibited an increased F1-score compared to the models utilised in conventional methods.

5.1 Confusion matrix of proposed algorithms

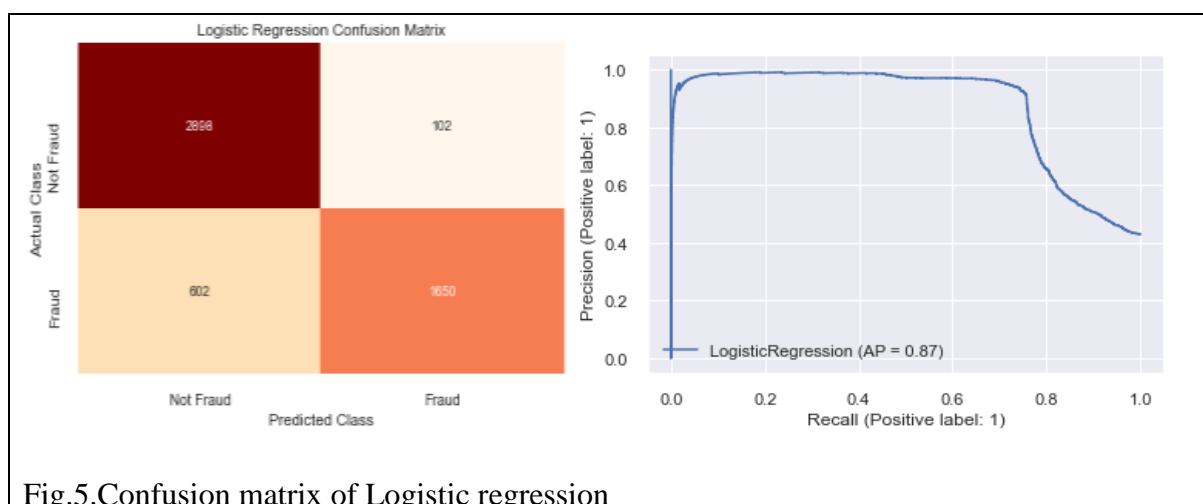


Fig.5. Confusion matrix of Logistic regression

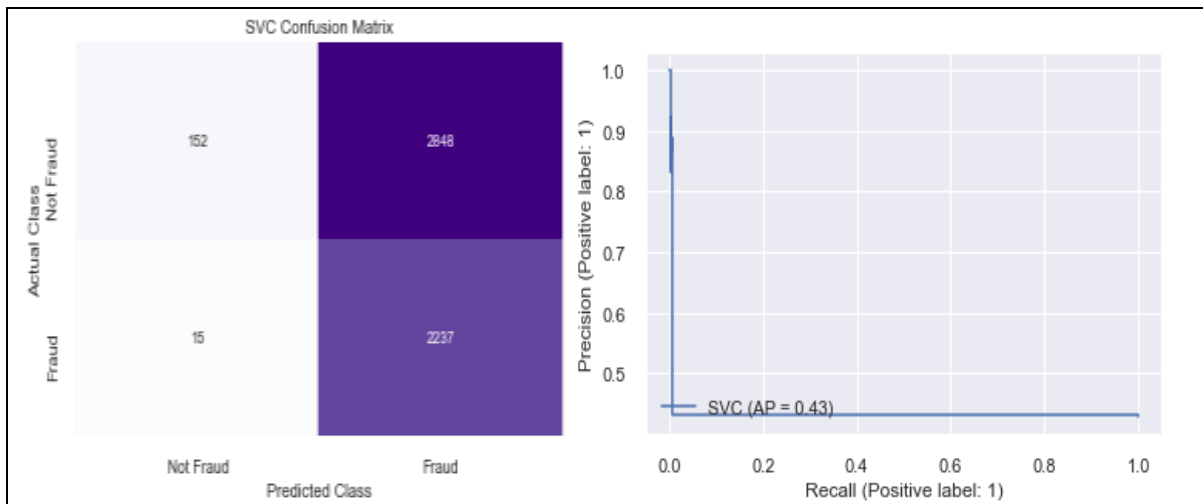


Fig.6.Confusion matrix of SVC

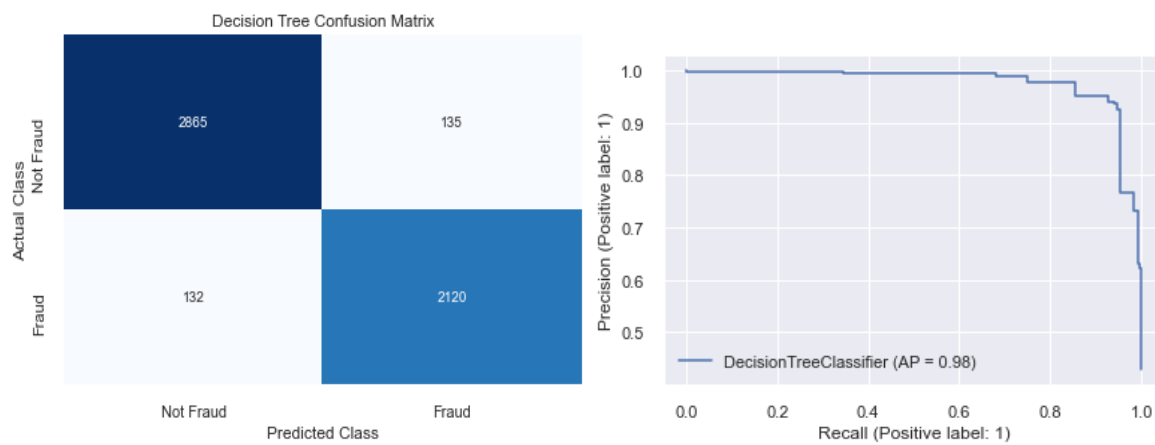


Fig.7.Confusion matrix of Decision Tree

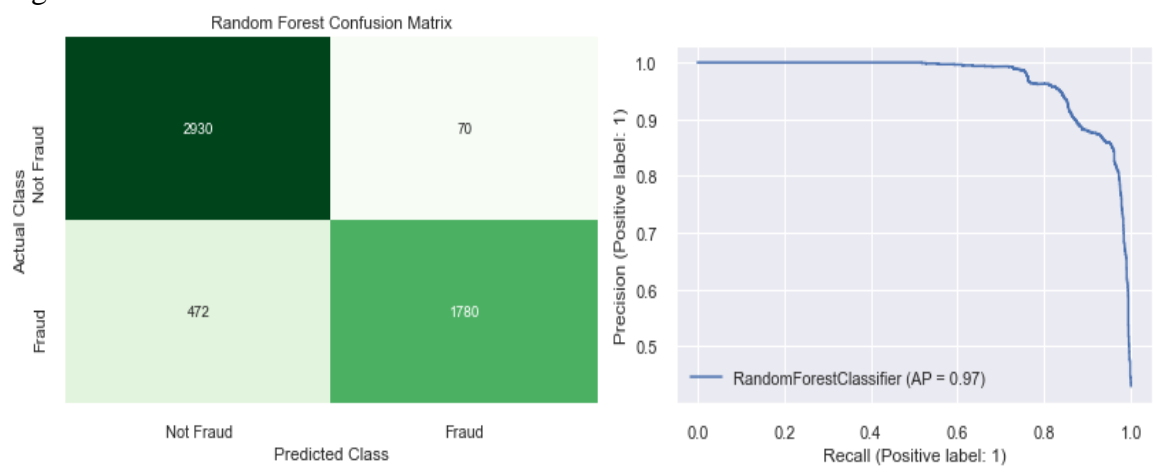


Fig.8.Confusion matrix of Random Forest

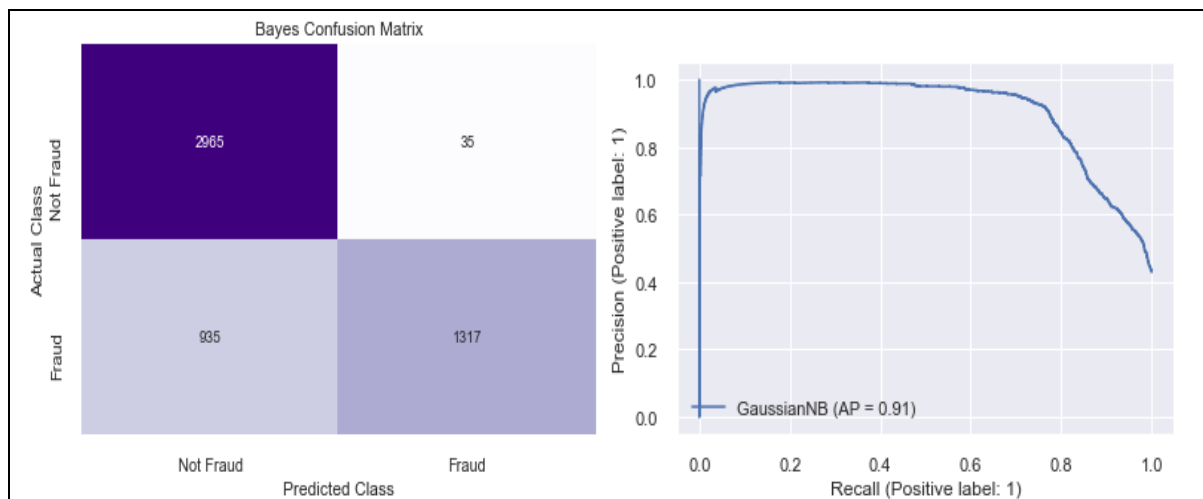


Fig.9. Confusion matrix of Naïve Bayes

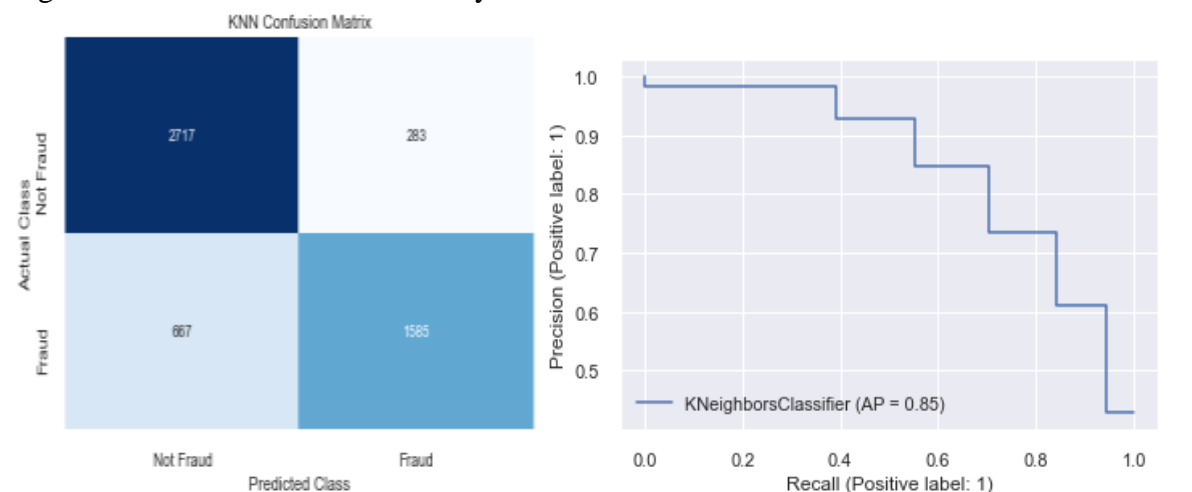


Fig.10. Confusion matrix of KNN

A confusion matrix, which is depicted in the graphics above, is a table used to characterise the performance of a classification method. A confusion matrix is a graphical representation and summary of the performance of a classification algorithm. The confusion matrix consists of four fundamental properties (numbers) utilised to define the classifier's measuring metrics. These four digits represent:

TP (True Positive): TP indicates the number of transactions who have been correctly identified as having malignant lymph nodes, indicating that they have the illness.

TN (True Negative): TN indicates the number of accurately identified healthy patients.

FP (False Positive): FP is the number of incorrectly transactions who are truly healthy. FP is referred to as a Type I error.

4. FN (False Negative): FN shows the number of patients misclassified as healthy although actually they are suffering from the disease. FN is also known as a Type II mistake.

Performance measures of an algorithm are accuracy, precision, recall, and F1 score, which are determined on the basis of the above-stated TP, TN, FP, and FN.

6. Conclusion

As a result of applying our refined Decision tree algorithm to the problem of credit card fraud detection, we have obtained an accuracy value of 94.79. The proposed module can be applied to a bigger dataset and produces more reliable results than those obtained using the existing modules. With more training data, the Random forest algorithm improves performance, but it still lags behind in testing and actual use. Additionally, more pre-processing methods being used would be useful.

7. References

- [1]ShiyangXuan, GuanJun Liu, Zhenchuan Li, LutaoZheng, Shuo Wang, ChangJun Jiang, Random Forest for Credit Card Fraud Detection,2018 (IEEE).
- [2]. DejanVarmedja, MirjanaKaranovic, SrdjanSladojevic, Marko Arsenovic, and AndrasAnderla,Credit Card Fraud Detection - Machine Learning methods, Publish in:18th International Symposium INFOTEH-JAHORINA, 20-22 March 2019 (IEEE).
- [3]. ShantanuRajora, Dong-Lin Li, ChandanJha, NehaBharill, Om Prakash Patel, Sudhanshu Joshi, Deepak Puthal, MukeshPrasad,A Comparative Study of Machine Learning Techniques for Credit Card Fraud Detection Based on Time Variance,2018 (IEEE).
- [4]. Rimpal R. Popat and JayeshChaudhary,A Survey on Credit Card Fraud Detection using Machine Learning, 2018 (IEEE), pp. 1120 - 1125
- [5]. ChangJun Jiang, Jiahui Song, GuanJun Liu, Member, IEEE, LutaoZheng, and WenjingLuan,Credit Card Fraud Detection: A Novel Approach Using Aggregation Strategy and Feedback Mechanism,2018 (IEEE), pp. 2327-4662.
- [6]. Shail Machine, Emad A. Mohamad, BehrouzFar,Supervised Machine Learning Algorithms for Credit Card Fraudulent Transaction Detection: A Comparative Study, 2018(IEEE) computer society, pp.122-125.
- [7]. SamanehSorournejad, Zahra Zojaji, Reza EbrahimiAtani, Amir Hassan Monadjemi,A Survey of Credit Card Fraud Detection Techniques: Data and Technique Oriented Perspective.

- [8]. Kuldeep Randhawa, Chu Kiong Loo, ManjeevanSeera, Chee Peng Lim, Ashoke K. Nandi, Credit Card Fraud Detection Using AdaBoost and Majority Voting, Published in: IEEE Access on 15 February 2018, vol. no.6, pp. 14277 – 14283.
- [9]. N. Sivakumar, Dr.R. Balasubramanian, Fraud Detection in Credit Card Transactions: Classification, Risks and Prevention Techniques, Published in (IJCSIT) International Journal of Computer Science and Information Technologies, vol no. 6 (2), 2015, pp. 1379-1386.
- [10]. SaiKiran, Jyoti Guru, Rishabh Kumar, Naveen Kumar, Deepak Katariya, MaheshwarSharma, Credit card fraud detection using Naïve Bayes model based and KNN classifier, Published in: International Journal of Advance Research, Ideas and Innovations in Technology, Issue no. 3, vol.no. 4, 2018, pp.44-47.
- [11]. Rishi Banerjee, Gabriela Boursal, Steven Chen, MehalKashyap, Sonia Purohit, Jacob Battipagali, Comparative Analysis of Machine Learning Algorithms through Credit Card Fraud Detection, 2018.
- [12]. KaithekuzhicalLeenaKurien and Dr.AjeetChikkamannur, Detection and prediction of credit card fraud transactions using machine learning, Published in: International Journal of engineering science & research technology (IJESRT), 2019, pp. 199-208.
- [13]. Md.Akster Hossain and Mohammed NazimUddin, A Differentiate Analysis for Credit Card Fraud Detection, Published in: Int. Conf. on Innovations in Science, Engineering and Technology (ICISSET), 27- 28 October 2018 (IEEE), pp. 328-333.
- [14]. Suresh K Shirgave, Chetan J. Awati, Rashmi More, Sonam S. Patil, A Review on Credit Card Fraud Detection Using Machine Learning, Published in International journal of Science and Technology Research, vol.no.8, Issue no. 10, October 2019, pp. 1217-1220.
- [15]. S P Mani raj, Aditya Saini, Swarna Deep Sarkar ShadabAhmed, Credit Card Fraud Detection using Machine Learning and Data Science, Published in: International Journal of Engineering Research & Technology (IJERT), vol.no.8, Issue no. 09, September 2019, pp.110-115.

User interests mining and Meta route discovery-based personal product recommendations

Gandrakoti Anil Kumar¹, Mr.Salim Amirali Jiwani²

M.Tech Student, Department of CSE, Vaagdevi College of Engineering, Bollikunta, Warangal 506005(T.S)¹

AssistantProfessor, Department of CSE(AI & ML), Vaagdevi College of Engineering, Bollikunta, Warangal 506005(T.S)²

ABSTRACT

Any modern e-commerce or social media platform would be incomplete without a robust recommendation system. One example of a legacy recommendation system is the product recommendation system, which has two main flaws: unnecessary advice repetition and unpredictability with respect to new products (cold start). These restrictions arise because traditional recommendation systems rely solely on the user's past purchasing patterns to provide product suggestions. Incorporating the user's social qualities, such as personality traits and topical interests, could reduce the need for a fresh start and eliminate redundant recommendations. Thus, in this work, we develop Meta-Interest, a product recommendation system that takes the user's unique characteristics into account and is based on interest mining and meta-path finding. Even if the user's history doesn't include these items or similar ones, Meta-Interest can nonetheless forecast the user's interests and the items linked with these interests. This is achieved by examining the user's shopping habits in order to suggest products they are more likely to enjoy. The implemented system is "personality aware" in two ways: (1) it uses the user's personality attributes to make predictions about the kind of content that would pique his interest, and (2) it uses the user's personality characteristics to determine which products will be most appealing to him. It was compared to modern recommendation techniques like deep-learning-based recommendation systems and session-based recommendation systems. The implemented strategy improves the recommendation system's precision and recall, especially in cold-start conditions, as demonstrated by the experiments.

Keywords: recommendation system, Meta-interest recommendations process.HIN

1. INTRODUCTION

One-fourth of the world's population, or 2.14 billion people, will be digital shoppers by the end of the decade because of the proliferation of smartphones and internet connectivity. With so many customers and so many products on the market, an online shop's success is determined by how well it is able to pair each customer with the best item for them; this is where product recommendation algorithms come in. Generally speaking, there are two broad categories of product recommendation systems:

(1) Collaborative filtering (CF): CF systems suggest new products to a user based on that user's past (rating, viewing, or purchasing) behaviour.

CBF systems suggest new products by gauging their similarity with previously rated, viewed, or purchased products.



Figure1: Collaborative Filtering and Content-based Filtering

Instead, many people today use platforms like Facebook, Twitter, and Instagram to voice their opinions on a variety of issues (or, in some cases, to convey their desire to buy a certain product). That's why it's so useful to mine social media posts for insights into user motivations and preferences [1]. However, the development of personality computing [2] has opened up fresh avenues for enhancing the effectiveness of user modelling in general and recommendation systems in particular through the incorporation of the user's personality qualities. This project involves the development of a product suggestion system that can anticipate a user's demands and the connected things, even if his past purchases did not include these or similar items. The user's topics of interest are

analysed to determine which products to suggest. The implemented system takes the user's personality into account in two ways: (1) to make predictions about the user's likely interests, and (2) to link the user's personality facets with the corresponding products. In Figure 2, we can see that the suggested system makes use of a combination of a hybrid filtering method and interest mining that takes the user's individuality into account.

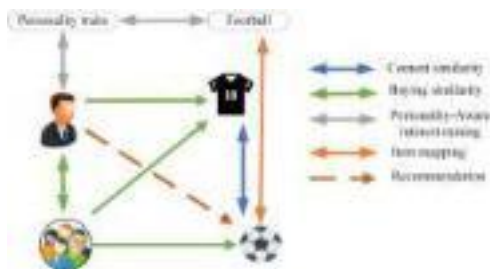


Figure 2: Interest Mining-based Product Recommendations

The system is described as a heterogeneous information network (HIN) due to the presence of different types of nodes (people, items, and themes) and the links between them. In our scenario, product suggestion can be recast as link prediction in the hierarchical information network [3]. The difficulty depicted in Figure 2 is determining whether or not a connection exists between the user and the product based on the user's

past ratings and topics of interest as represented by an HIN (the ball). How to strike a good balance between the volume of data needed to create an accurate forecast and the algorithmic complexity of the methods used to get it is one of the key problems of link prediction in HIN. HIN's link prediction algorithm needs to be highly efficient because, in practice, networks can contain millions of nodes. However, in particularly sparse networks, processing solely local information could result in inaccurate predictions. Thus, in our method, we aim to fuse information from these meta-paths, which originate at user nodes and terminate at the predicted node (product nodes), in order to make the prediction.

The following is a brief overview of the work's contributions:

- 1) Establish a mechanism for suggesting products to users based on their interests.
- 2) The implemented system makes use of the user's Big Five personality features to improve interest mining and carry out personality-aware product filtering.
3. The system uses graph-based meta route discovery to anticipate the relationship between consumers and

products, allowing for the prediction of both implicit and explicit preferences.

2. Literature survey:

Due to the variability in review patterns, the existing online product recommendation system has significant shortcomings. The information comes from customers' comments left on online stores' pages. It's possible that this information contains fabricated testimonials, which introduces uncertainty. As a result, the current system's output is confusing when applied to the current data. Instead, the new algorithm delivers more meaningful results by using only authentic reviews and factoring in the credibility of the user. The suggested system automatically gathers user feedback from around the web and analyses it using opinion mining and sentiment analysis. In addition to the review's star rating, the buyer's profile and purchase history, and whether or not the review was written before or after the purchase, are also considered. The website from which the customer should purchase the product will be suggested based on these characteristics and the user's credibility.

Author(s): Zhibo Wang, Mengyuan Wan, Xiaohui Cui, Lin Liu, Zixin Liu, Wei Xu, Linlin He

Against the backdrop of the internet's exponential growth, e-commerce has become an integral part of people's daily lives. However, the advent of such large datasets has also brought about issues, such as information overload, which can be mitigated through the strategic application of a recommendation system. However, as e-commerce grows in popularity, the number of product catalogues and users increases, resulting in decreased performance from the conventional recommendation system. In this article, we develop a custom recommendation algorithm for improving the effectiveness of the new recommendation system by mining data from customer evaluations. The product's features were distilled, and the polarity of the users' opinions was studied. In order to determine an appropriate recommendation, this article creates a system that takes into account both the user's preference model and the characteristics of the product under consideration. Based on experimental data, a personalised recommendation system greatly outperforms a conventional recommendation system in terms of both accuracy and recall.

Author(s):PriyadarsiniPatnaik An integral aspect of artificial intelligence (AI) is the recommendation system it employs to ensure users can get to their data whenever and wherever they need it. The use of online product recommender systems to make recommendations to customers based on their individual tastes is widespread. When presented with massive amounts of data, typical recommendation algorithms used by recommendation engines fail to live up to users' expectations, resulting in poor suggestion efficiency in an AI setting. A custom-tailored suggestion engine was developed as a solution. These PRS are a vital part of the Indian e-commerce landscape for all of the major firms in the industry. Since individualised recommendations are growing in popularity, this research looks at how they relate to information processing theory and how they affect user happiness. Through regression analysis, we also looked at the connections between the variables and discovered that the level of pleasure of the end user is positively correlated with the degree to which the product was specifically recommended to them.

Analysis of the Literature on Product

Recommendation Systems
Author(s):KetkiKinkar These days, it might be challenging to zero in on exactly what we're looking for amidst the plethora of results that pop up when we conduct a search. The recommendation system is helpful in overcoming these obstacles. A recommender system is a filtering framework that uses a variety of algorithms to sift through data and provide users with suggestions for what they're most likely to find useful. Effective customization mechanisms and recommendation systems are frequently up-to-date and make suggestions based on current consumer preferences. These methods have proven to be extremely useful in the fields of e-commerce, education, media, publishing (including books and films), and research (including scientific papers). In this paper, we take a look at a wide range of recommendation techniques, discussing their advantages and disadvantages along with a variety of performance metrics. We have looked at a number of articles and analysed their methodology, the main points of the algorithm they used, and the places where they could be strengthened.

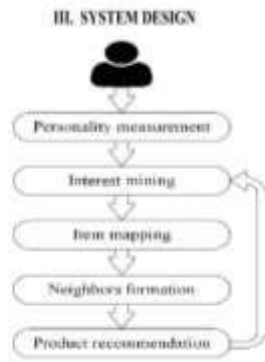


Fig 3: Meta-interest recommendations process.

In this section, the conceptual underpinnings of the proposed system will be outlined. The goal of MetaInterest is to provide users with the best possible recommendations based on their topical interests as determined by their social network profiles. The overarching structure of the meta-interest system is depicted in Fig. 1. There are five stages to making a suggestion. First, the user takes a personality test, or the system performs an automated analysis of their social media profiles to determine the user's personality attributes. Because personality qualities have been shown to be generally stable throughout time, the process of measuring personality is the only constant in the system. The next step is to determine the user's interests in a particular field, either explicitly or implicitly. The process of explicit interest mining involves the

examination of For implicit interest mining, a complex examination of the user's social network and other hidden aspects that may affect the user's topical interests is required. Step 3 entails categorising objects based on their meta-interest. The connections made are many-to-many, meaning that one subject can be linked to numerous objects. The same goes for the possibility that a given object has more than one category it belongs to. In the fourth stage, we identify the group of users who are most comparable to the subject user. Meta-Interest takes three different types of similarity into account here: personality, viewing, buying, and rating, and shared interests. In Step 5, item recommendations are fine-tuned by revising the collection of neighbours and the user's topical interest profile and topics-items matching.

Obtaining Personal Interests: Our method has the potential to improve the accuracy of system recommendations and mitigate the cold-start effects because it takes the user's interests and personality information into account. Users' topical interests can be inferred from data posted on social networks. Automatic topic extraction methods like latent Dirichlet allocation (LDA) and frequency-inverse category

frequency analysis (FICA) can accomplish this task (TFICF). But these methods are designed for longer pieces of writing, and they don't work well on the user's short, sparse, and loud contributions like tweets. Therefore, we have enriched each user-generated post with semantic annotators to improve topic detection accuracy by reducing noise and ambiguity in the post. Items are mapped to their respective subjects after the public space for those topics has been populated with ODP ontology categories. It is possible to recommend an item to a user based on their topical interests because each item is tagged with one or more topics. Newly added items that have not yet been viewed by any user are directly associated with the corresponding topic category in the ODP ontology, while items that have survived the cold start phase are associated with the interests of those that are related to the personality traits shared by users who purchased this item. After constructing the users-topics-items heterogeneous graph $G = (GU, GT, GP)$ that includes the user, topic, and item subgraphs and their connections, meta-paths can be discovered. As things stand, the goal is to predict the N-most recommended items that a user will find interesting based on his or

her topical interests and past purchasing or viewing behavior.

Methodology: As a link prediction in HIN [3], product suggestion is a potential outcome of the proposed system. For instance, in this system, the objective is to anticipate whether or not a link exists between the user and the product based on the user's past ratings and thematic interests as reflected in an HIN (the ball). One of the main problems with link prediction in HIN is how to find a good balance between the amount of data needed to make a prediction and the algorithmic complexity of the ways to get that data.

The mechanism used to accomplish link prediction in HIN must be exceedingly efficient because, in practise, networks are typically formed of hundreds of thousands or even millions of nodes.

But in networks with few nodes, making predictions based on local knowledge alone may not be accurate.

Thus, in our method, we employ meta-paths that originate at user nodes and terminate at the predicted node (product nodes in our case), and we attempt to fuse the

information from these meta-paths to make the forecast.

4. PERFORMANCE METRICS

Any product recommendation system is evaluated by measuring the accuracy and coverage of its recommended items. To test the efficiency of Meta-Interest and compare it to the afore-mentioned baselines, we determine the recommended items by each baseline and displayed it in the user’s feed along with other irrelevant items, and measure the accuracy rate of the relevant items. Formally, Let $F = R \cup I$ be the set that represents all items in user u ’s feeds, where $R = \{p1, p2, \dots, pr\}$ is the set relevant items, and $I = \{p1, p2, \dots, pi\}$ is the set of irrelevant items. After showing F in user u ’s feeds, we denote $V = \{p1, p2, \dots, pv\}$ as the set of viewed items. In this context we are interested in the following values: (1) true positives: the group of relevant items that have been viewed by the user $TP = \{x / x \in R \cap V\}$, (2) false positives: the group of irrelevant items that have been viewed by the user $FP = \{x / x \in I \cap V\}$ and (3) false negatives: the group of relevant items that have not been viewed by the user $FN = \{x / x \in R, x \notin V\}$. We have used the following metrics: Precision: the portion of relevant

viewed items in the total viewed items, and it is computing using

(5) P precision =

$$\text{Precision} = \frac{\text{True Positive}}{\text{True Positive} + \text{False Positive}} = \frac{\text{True Positive}}{\text{Total Predicted Positive}}$$

(5) Recall: the portion of relevant viewed items in the total relevant items, and it is computing using

$$\text{Recall} = \frac{\text{True Positive}}{\text{True Positive} + \text{False Negative}}$$

(6) F-Measure: also called the balanced F-Score, it is the harmonic average of the precision and recall, and it is computing using

		true class		
		EFR	LFR	total
predicted class	EFR	True Positives (TP)	False Positives (FP)	predicted EFR
	LFR	False Negatives (FN)	True Negatives (TN)	predicted LFR
		true EFR	true LFR	

$$PR = \frac{TP}{TP+FP}$$

$$RE = \frac{TP}{TP+FN}$$

$$CA = \frac{TP+TN}{TP+TN+FP+FN}$$

$$F_1 = \frac{2TP}{2TP+FP+FN}$$

5. RESULTS:

Model Type	Accuracy
Naive Bayes	87.42836676217765
SVM	88.2163323782235
Logistic Regression	89.18338108882521

Figure 2: accuracy



Figure 3: Recommendation

6. CONCLUSION

This work provides a personality-aware product recommendation system that anticipates a user's requirements and suitable items by using interest mining and meta route discovery. A product suggestion algorithm is created based on the user's declared interests in a certain topic. The suggested system is sensitive to the user's individual personality in two ways. The first is that it predicts the kind of material that will most likely interest the user based on his personality traits. Second, it associates the user's personal characteristics with the products chosen. Experiments reveal that the proposed approach outperforms state-of-the-art systems in accuracy and recall during the cold start phase for new items and users.

7. REFERENCES

- [1] G. Piao and J. G. Breslin, "Inferring user interests in microblogging social networks: a survey," *User Modeling and User-Adapted Interaction*, vol. 28, no. 3, pp. 277–329, aug 2018. [Online]. Available: <http://link.springer.com/10.1007/s11257-018-9207-8>
- [2] A. Vinciarelli and G. Mohammadi, "A Survey of Personality Computing," *IEEE Transactions on Affective Computing*, vol. 5, no. 3, pp. 273–291, jul 2014. [Online]. Available: <http://ieeexplore.ieee.org/document/6834774/>
- [3] V. Mart'nez, F. Berzal, and J.-C. Cubero, "A Survey of Link Prediction in Complex Networks," *ACM Computing Surveys*, vol. 49, no. 4, pp. 1–33, feb 2017.
- [4] H.-C. Yang and Z.-R. Huang, "Mining personality traits from social messages for game recommender systems," *Knowledge-Based Systems*, vol. 165, pp. 157–168, feb 2019. [Online]. Available: <https://linkinghub.elsevier.com/retrieve/pii/S095070511830577X>

- [5] W. Wu, L. Chen, and Y. Zhao, "Personalizing recommendation diversity based on user personality," *User Modeling and User-Adapted Interaction*, vol. 28, no. 3, pp. 237–276, 2018.
- [6] H. Ning, S. Dhelim, and N. Aung, "PersoNet: Friend Recommendation System Based on Big-Five Personality Traits and Hybrid Filtering," *IEEE Transactions on Computational Social Systems*, pp. 1–9, 2019. [Online]. Available: <https://ieeexplore.ieee.org/document/8675299/>
- [7] B. Ferwerda, M. Tkalcic, and M. Schedl, "Personality Traits and Music Genres: What Do People Prefer to Listen To?" in *Proceedings of the 25th Conference on User Modeling, Adaptation and Personalization*. ACM, 2017, pp. 285–288.
- [8] B. Ferwerda, E. Yang, M. Schedl, and M. Tkalcic, "Personality and taxonomy preferences, and the influence of category choice on the user experience for music streaming services," *Multimedia Tools and Applications*, pp. 1–34, 2019. [9] Z. YusefiHafshejani, M. Kaedi, and A. Fatemi, "Improving sparsity and new user problems in collaborative filtering by clustering the personality factors," *Electronic Commerce Research*, vol. 18, no. 4, pp. 813–836, dec 2018. [Online]. Available: <http://link.springer.com/10.1007/s10660-018-9287-x>
- [10] S. Dhelim, N. Huansheng, S. Cui, M. Jianhua, R. Huang, and K. I.-K. Wang, "Cyberentity and its consistency in the cyber-physical-social-thinking hyperspace," *Computers & Electrical Engineering*, vol. 81, p. 106506, jan 2020. [Online]. Available: <https://linkinghub.elsevier.com/retrieve/pii/S0045790618334839>
- [11] A. Khelloufi, H. Ning, S. Dhelim, T. Qiu, J. Ma, R. Huang, and L. Atzori, "A Social Relationships Based Service Recommendation System For IIoT Devices," *IEEE Internet of Things Journal*, pp. 1–1, 2020. [Online]. Available: <https://ieeexplore.ieee.org/document/9167284/>
- [12] F. Zarrinkalam, M. Kahani, and E. Bagheri, "Mining user interests over active topics on social networks," *Information Processing & Management*, vol. 54, no. 2, pp. 339–357, 2018.

- [13] A. K. Trikha, F. Zarrinkalam, and E. Bagheri, "Topic-Association Mining for User Interest Detection," in European Conference on Information Retrieval. Springer, 2018, pp. 665–671.
- [14] J. Wang, W. X. Zhao, Y. He, and X. Li, "Infer user interests via link structure regularization," *ACM Transactions on Intelligent Systems and Technology (TIST)*, vol. 5, no. 2, p. 23, 2014.
- [15] S. Dhelim, H. Ning, M. A. Bouras, and J. Ma, "Cyber-Enabled Human-Centric Smart Home Architecture," in 2018 IEEE SmartWorld). IEEE, oct 2018, pp. 1880–1886. [Online]. Available: <https://ieeexplore.ieee.org/document/8560294/>
- [16] S. Faralli, G. Stilo, and P. Velardi, "Automatic acquisition of a taxonomy of microblogs users' interests," *Web Semantics: Science, Services and Agents on the World Wide Web*, vol. 45, pp. 23–40, 2017.
- [17] S. Dhelim, N. Aung, and H. Ning, "Mining user interest based on personality-aware hybrid filtering in social networks," *Knowledge-Based Systems*, p. 106227, jul 2020. [Online]. Available: <https://linkinghub.elsevier.com/retrieve/pii/S0950705120304354>
- [18] J. Kang and H. Lee, "Modeling user interest in social media using news media and wikipedia," *Information Systems*, vol. 65, pp. 52–64, 2017.
- [19] Qi Liu, Enhong Chen, HuiXiong, C. H. Q. Ding, and Jian Chen, "Enhancing Collaborative Filtering by User Interest Expansion via Personalized Ranking," *IEEE Transactions on Systems, Man, and Cybernetics, Part B (Cybernetics)*, vol. 42, no. 1, pp. 218–233, feb 2012. [Online]. Available: <http://ieeexplore.ieee.org/document/6006538/>
- [20] Y. Dong, N. V. Chawla, and A. Swami, "metapath2vec: Scalable Representation Learning for Heterogeneous Networks," in *Proceedings of the 23rd ACM SIGKDD International Conference on Knowledge Discovery and Data Mining*. New York, NY, USA: ACM, aug 2017, pp. 135–144. [Online]. Available: <https://dl.acm.org/doi/10.1145/3097983.3098036>
- [21] C. Shi, B. Hu, W. X. Zhao, and P. S. Yu, "Heterogeneous Information

Network Embedding for Recommendation,”
IEEE Transactions on
Knowledge and Data Engineering, vol. 31,
no. 2, pp. 357–370, feb 2019.

[Online]. Available:
<https://ieeexplore.ieee.org/document/8355676/>

[22] M. Zhang and Y. Chen, “Link
prediction based on graph neural networks,”
in Advances in Neural Information
Processing Systems, 2018, pp. 5165–5175.

[23] W. Song, Z. Xiao, Y. Wang, L. Charlin,
M. Zhang, and

J. Tang, “Session-Based Social
Recommendation via Dynamic
Graph Attention Networks,” in Proceedings
of the Twelfth ACM
International Conference on Web Search
and Data Mining. New
York, NY, USA: ACM, jan 2019, pp. 555–
563. [Online]. Available:
<https://dl.acm.org/doi/10.1145/3289600.3290989>

[24] P. I. Armstrong and S. F. Anthony,
“Personality facets and
RIASEC interests: An integrated model,”
Journal of Vocational
Behavior, vol. 75, no. 3, pp. 346–359, dec
2009.[Online]. Available:

<https://linkinghub.elsevier.com/retrieve/pii/S0001879109000657>

[25] U. Wolfradt and J. E. Pretz, “Individual
differences in creativity: Personality,
story writing, and hobbies,” European
Journal of Personality, 2001

Seamless Integration of Edge Computing and Cloud Resources for Enhanced Data Analysis

Dr. E. Balakrishna

Associate Professor

Department of CSE

Vaagdevi College of Engineering

Dr.N.Satyavathi

Associate Professor

Head, Department of CSE

Vaagdevi College of Engineering

Abstract-The primary objective of the seamless integration of edge computing and cloud resources for enhanced data analysis is to create a powerful and efficient data processing ecosystem that leverages the strengths of both edge devices and cloud infrastructure. This integration aims to provide real-time and resource-intensive data analysis capabilities, enabling organizations to make more informed decisions, respond quickly to events, and extract valuable insights from their data. It is an enhanced data analysis to create a holistic ecosystem that combines real-time responsiveness with robust analysis, enabling organizations to harness the full potential of their data for effective decision-making and innovation. In this paper we addressed what are the factors that influence and how we can improve the data privacy and security in the seamless integration of edge computing and cloud resources for enhanced data analysis

Key words: edge computing, security and cloud resources

1. Introduction:

The seamless integration of edge computing and cloud resources represents a transformative approach in the realm of data analysis, offering a dynamic synergy between localized real-time processing and expansive cloud-based analytics. This innovative integration aims to harness the strengths of both edge computing, which enables rapid processing at the edge of the network, and cloud resources, which provide extensive computational power and storage capabilities. By seamlessly combining these two computing paradigms [1,2], organizations can achieve enhanced data analysis, informed decision-making,

and operational efficiency across a spectrum of applications and industries.

In this integration, edge devices situated closer to data sources perform initial processing and filtering, minimizing data transmission to the cloud. This approach not only reduces latency and supports real-time responsiveness but also addresses privacy concerns by processing sensitive data closer to its source. Simultaneously, cloud resources offer the computational might require for in-depth historical analysis, machine learning, and advanced data modelling. This duality of edge and cloud forms the foundation for a comprehensive data analysis

ecosystem, capable of addressing the diverse needs of modern applications.

However, this integration is not without its challenges. Balancing tasks between edge and cloud, orchestrating dynamic workload distribution, ensuring data privacy and security, and maintaining consistency pose intricate technical and strategic considerations. Addressing these challenges demands a holistic approach that spans technology, security measures, orchestration mechanisms, and compliance adherence.

This integration holds immense potential across a myriad of domains. From optimizing industrial processes and enhancing IoT applications to enabling intelligent decision-making[3] in healthcare and retail, the seamless integration of edge computing and cloud resources promises to redefine how data is analysed, insights are derived, and strategies are formulated. As this paradigm continues to evolve, organizations are poised to unlock new dimensions of efficiency, agility, and innovation through the convergence of edge computing and cloud resources for the purpose of enhanced data analysis.

Integration Benefits for Data Analysis:

Latency Reduction: Integrating edge computing and cloud resources reduces latency by performing real-time analysis at the edge. Critical decisions can be made promptly without waiting for data to travel to a distant cloud server and back. Cloud resources can then be utilized for more in-depth analysis.

Real-Time Responsiveness: Edge computing allows for immediate data processing and response, making it suitable for applications that require instant reactions.

By integrating with cloud resources, historical data and complex analyses can be performed to inform long-term strategies.

Scalability and Flexibility: Cloud resources provide scalability for computationally intensive tasks. During peak demands, cloud resources can be allocated to handle the load, while edge devices handle routine processing. This dynamic allocation ensures efficient resource utilization.

Bandwidth Efficiency: Integrating edge and cloud computing optimizes bandwidth usage. Only relevant insights or summarized data need to be transmitted to the cloud, reducing the amount of data transferred and lowering associated costs.

Data Privacy and Security: Edge computing enhances data privacy and security by processing sensitive information locally. Only aggregated or anonymized data is sent to the cloud, minimizing the risk of exposing critical data during transmission.

Distributed Analysis: The integration enables a distributed approach to data analysis. Edge devices can preprocess and filter data, while cloud resources handle more extensive analysis. This division of labour maximizes resource utilization and speeds up overall processing.

Resource Allocation: Edge devices perform tasks that require minimal latency, leaving cloud resources available for computationally demanding tasks. This efficient resource allocation enhances the overall system's performance.

Hybrid Architectures: Integrating edge and cloud computing allows for hybrid architectures that

leverage the benefits of both paradigms. This flexibility accommodates diverse use cases, workloads, and network connectivity scenarios.

Redundancy and Reliability: The integration provides redundancy and reliability. If an edge device fails, the cloud can seamlessly take over the workload, ensuring uninterrupted data analysis and decision-making.

The seamless integration of edge and cloud resources has led to improved data analysis and decision-making in various real-world scenarios. Here are some examples:

Smart Manufacturing: In manufacturing plants, sensors installed on machinery collect real-time data about equipment performance. Edge computing processes this data locally to detect anomalies and potential failures. Critical alerts are sent to cloud platforms for more in-depth analysis. This integration allows manufacturers to predict maintenance needs, reduce downtime, and optimize production schedules.

Healthcare Monitoring: Wearable health devices, such as fitness trackers and medical sensors, collect data about individuals' health metrics [4]. Edge devices on these wearables process immediate health data, while cloud resources analyse historical trends. This integration helps doctors make informed decisions about patient care and identify potential health risks.

Autonomous Vehicles: Self-driving cars use edge computing to process sensor data in real-time for immediate navigation decisions. Cloud resources are employed for high-level route planning, map updates,

and long-term traffic pattern analysis. The integration ensures real-time safety and comprehensive navigation optimization.

Smart Grids: In the energy sector, edge devices within power distribution networks monitor and analyse energy consumption patterns. Immediate feedback is provided for load balancing and grid stability. Cloud resources are used for long-term energy consumption trends and optimizing energy distribution across regions.

Agricultural Precision: IoT sensors in agriculture collect data on soil conditions, weather, and crop health. Edge devices process this data locally to make real-time decisions about irrigation and fertilizer application. Cloud resources analyze long-term data to enhance planting strategies and predict crop yields.

Retail Analytics: In retail environments, edge devices track foot traffic and customer behaviours in real time. Cloud resources analyse this data to identify trends [6] in customer preferences and optimize store layouts. This integration helps retailers enhance customer experiences and tailor marketing strategies.

Environmental Monitoring: Sensors deployed in environmental monitoring stations gather data on air quality, pollution levels, and weather conditions. Edge devices process immediate data to provide real-time alerts and updates. Cloud resources analyse long-term data to study environmental trends and support policy decisions.

Supply Chain Management: Edge devices in warehouses monitor inventory levels and track shipments. Immediate data processing ensures

accurate stock management and quick order fulfilment. Cloud resources analyse historical data to optimize supply chain operations and anticipate demand patterns.

Smart Cities: Urban environments use edge devices for real-time traffic monitoring and pollution detection. Cloud resources analyse this data to make informed decisions about traffic management and urban planning. The integration improves city services and enhances residents' quality of life.

Disaster Response: During natural disasters, edge devices in disaster-stricken areas provide real-time information on conditions and casualties. Cloud resources process this data to coordinate emergency responses and allocate resources efficiently, thereby minimizing human loss and damage.

The balance between processing data at the edge and sending it to the cloud has a significant impact on data latency and real-time decision-making[6]. Here's how this balance influences these factors:

Processing Data at the Edge:

Low Latency: Edge computing involves processing data locally, closer to the data source. This significantly reduces the time taken for data to travel to a distant cloud server and back, leading to lower latency.

Real-Time Decision-Making: Edge processing allows for immediate data analysis and decision-making. Time-sensitive actions can be taken in real time based on locally processed data, enabling quick responses to events.

Efficiency: Edge processing is efficient for tasks that require immediate attention and do not necessitate the extensive computational resources of cloud servers.

Bandwidth Conservation: By processing data at the edge, the amount of data that needs to be transmitted to the cloud is reduced, conserving bandwidth and minimizing data transmission costs.

Sending Data to the Cloud:

Higher Latency: Transmitting data to the cloud introduces latency due to the time it takes for data to travel over the network to the remote data centre and back to the edge. This latency can be variable depending on network conditions.

Complex Analysis: Cloud resources offer more computational power and memory, allowing for more complex data analysis, machine learning, and advanced analytics that may not be feasible at the edge.

Historical Insights: Cloud analysis can provide insights based on historical data trends, which may require larger datasets and computational capabilities not available at the edge.

Resource-Intensive Tasks: Tasks that demand significant computational resources or involve analysing vast amounts of data can be offloaded to the cloud, where scalability is readily available.

Balancing Latency and Decision-Making:

Use Case Dependence: The balance between edge and cloud processing depends on the specific use case. Applications requiring immediate actions benefit from edge processing to minimize latency, while those needing in-depth analysis leverage cloud capabilities.

Hybrid Approach: A hybrid approach can be employed, where time-sensitive data is processed at the edge for quick actions, while non-time-sensitive data is sent to the cloud for comprehensive analysis.

Edge Orchestration: Intelligent edge orchestration mechanisms can dynamically determine whether data should be processed locally or sent to the cloud, considering factors such as data type, urgency, and available resources.

The integration of edge computing and cloud resources has a profound impact on the development and deployment of Internet of Things (IoT) applications and devices. It addresses key challenges and enhances the capabilities of IoT solutions. Here's how this integration influences IoT development and deployment:

Reduced Latency and Real-Time Responsiveness:

IoT devices often require real-time responsiveness, especially in applications like industrial automation, healthcare monitoring, and autonomous vehicles. Edge computing enables immediate data processing at the device level, minimizing latency and enabling real-time decision-making.

Cloud resources can be used for more comprehensive analysis and long-term trends, enhancing the quality of insights derived from IoT data.

Improved Scalability:

Edge computing and cloud resources offer a scalable approach to IoT deployment. Edge devices can handle localized data processing, while cloud platforms provide scalability for processing data from a large number of devices.

Bandwidth Optimization:

Transmitting large volumes of raw data from IoT devices to the cloud can strain network bandwidth and increase costs. Edge computing reduces the amount of data transmitted by processing and filtering data locally before sending relevant insights to the cloud.

Enhanced Privacy and Security:

Edge computing enhances data privacy and security by processing sensitive information locally, reducing the exposure of critical data during transmission. Only aggregated or summarized data is sent to the cloud, reducing risks associated with data breaches.

Flexibility in Application Design:

IoT applications can leverage the integration's flexibility. Real-time processing at the edge can cater to time-critical tasks, while cloud resources can handle historical analysis, predictive modelling, and resource-intensive computations.

Optimal Resource Utilization:

IoT devices often have limited computational resources. Edge computing offloads processing tasks from central servers, optimizing the usage of device resources while leveraging cloud resources for more complex computations.

Resilience and Redundancy:

The integration provides redundancy in case of device failure. If an edge device malfunctions, cloud resources can take over processing, ensuring continuous data analysis and decision-making.

Edge Orchestration:

Edge orchestration platforms dynamically allocate tasks between edge devices and cloud resources based

on factors such as data type, processing requirements, and network conditions. This enhances efficiency and response times.

Location-Dependent Services:

Certain IoT applications require services that are location-dependent, such as navigation in autonomous vehicles. Edge computing enables local processing of location data, reducing dependency on cloud resources for real-time navigation.

Cost Efficiency:

IoT applications often have budget constraints. The integration can lead to cost savings by minimizing the need for transmitting data to the cloud and optimizing resource allocation based on workload.

2. Literature Survey:

A comprehensive literature survey on the topic of "Seamless Integration of Edge Computing and Cloud Resources for Enhanced Data Analysis" involves exploring various research [7, 8, 9 and 10] that discuss the challenges, techniques, benefits, and applications of integrating edge computing and cloud resources for improved data analysis.

The literature survey often delve into the technical aspects, algorithms, architectures, and case studies of integrating edge and cloud resources. It summarizes the findings and trends in the integration of edge computing and cloud resources for data analysis.

Security and Privacy Studies:

As security and privacy are crucial aspects of integration, literature discussing the techniques,

challenges, and solutions for ensuring data security and privacy in this context is highly valuable.

Orchestration and Load Balancing Techniques [11]:

Explore literature that discusses dynamic orchestration and load balancing mechanisms to allocate tasks effectively between edge devices and cloud resources.

IoT and Industrial Applications:

Look for studies focusing on the integration's applications in the Internet of Things (IoT) and industrial sectors. These studies often showcase how the integration enhances data analysis and decision-making in specific domains.

Cloud Resource Management:

Literature on cloud resource management explores how to optimize the utilization of cloud resources while balancing workloads and ensuring efficient data analysis.

Latency Reduction Techniques:

Studies on latency reduction techniques discuss methods to minimize data transmission delays and achieve real-time or near-real-time analytics [13].

Data Aggregation and Compression:

Explore research on techniques that aggregate and compress data at the edge before transmission to the cloud, optimizing network bandwidth and reducing data transmission costs.

Energy Efficiency and Resource Constraints:

Look for literature that addresses how to manage energy-efficient processing on resource-constrained edge devices while maintaining security and privacy.

Federated Learning and Edge AI:

Research on federated learning and edge AI discusses how these techniques can be applied in the integration to enable collaborative machine learning models without sharing raw data.

The seamless integration of edge computing and cloud resources plays a crucial role in addressing issues of network congestion and bandwidth limitations [12]. Here's how this integration contributes to alleviating these challenges:

Local Data Processing:

Edge computing enables data processing to occur at or near the source of data generation. This reduces the need to transmit large volumes of raw data over the network to centralized cloud servers.

By processing data locally at the edge, only relevant insights or summarized information are sent to the cloud, reducing the amount of data that needs to traverse the network.

Minimized Data Transmission:

Transmitting data over networks, especially in scenarios with limited bandwidth, can lead to network congestion and increased latency. Edge computing reduces the need for frequent data transmission, easing network traffic.

Bandwidth Conservation:

Edge devices process and filter data, sending only necessary information to the cloud. This approach conserves bandwidth by avoiding the unnecessary transfer of large datasets to the cloud for analysis.

Real-Time Insights at the Edge:

Immediate data processing at the edge enables quick decisions and actions without relying on cloud resources. This reduces the dependency on continuous data transmission to the cloud for real-time responsiveness.

Dynamic Data Prioritization:

The integration allows for dynamic data prioritization. Critical or time-sensitive data can be processed at the edge to ensure immediate responses, while less urgent data can be sent to the cloud for more comprehensive analysis.

Edge Caching:

Edge devices can store frequently accessed or critical data locally using caching mechanisms. This reduces the need to retrieve data from the cloud repetitively, thus alleviating network congestion.

Distributed Load:

Offloading computational tasks to edge devices distributes the processing load across the network. This avoids overburdening a single centralized cloud server and reduces the risk of network congestion.

Improved Scalability:

As the number of IoT devices and data sources increases, the integration ensures that edge devices process local data, reducing the strain on the network and cloud infrastructure.

Redundancy and Failover:

The integration provides redundancy by allowing for failover mechanisms. If an edge device or network segment becomes congested, the system can route data

to alternative edge devices or the cloud to maintain uninterrupted data flow.

Data Aggregation at the Edge:

Edge devices can aggregate data from multiple sources before sending aggregated insights to the cloud. This aggregation reduces the frequency and volume of data transmission, easing network congestion.

Several factors influence the seamless integration of edge computing and cloud resources for enhanced data analysis. These factors impact the technical, operational, and strategic aspects of the integration.

Here are some key factors to consider:

Use Case and Application Requirements:

The specific use case and application requirements determine the balance between edge and cloud processing. Consider whether real-time responsiveness, historical analysis, or a combination of both is needed.

Latency Tolerance:

Applications with low-latency requirements, such as autonomous vehicles or industrial automation, need to prioritize edge processing to minimize delays in decision-making.

Data Volume and Velocity:

The volume and velocity of incoming data influence whether processing should occur at the edge or in the cloud. High data volumes might necessitate initial filtering at the edge before sending data to the cloud.

Network Connectivity and Bandwidth:

The quality of network connectivity, available bandwidth, and potential network congestion impact

the feasibility of transmitting data to the cloud. Edge processing can alleviate these constraints.

Data Privacy and Security:

The sensitivity of data and privacy concerns influence whether data should be processed locally at the edge to minimize data exposure during transmission.

Computational Resources of Edge Devices:

The computational capabilities of edge devices determine the complexity of analysis they can handle.

Tasks requiring significant processing power might be more suitable for cloud resources.

Scalability Requirements:

Consider the scalability requirements of your application. Will the number of devices increase? Can cloud resources handle the workload during peak demands?

Real-Time Decision-Making:

Applications that require immediate responses, such as real-time sensor data analysis, benefit from edge processing to ensure rapid decision-making.

Historical Analysis and Advanced Analytics:

Cloud resources are advantageous for tasks that involve historical data analysis, machine learning, and other advanced analytics that require substantial computational resources.

Resource Constraints and Cost Efficiency:

Edge devices might have resource constraints in terms of processing power, memory, and energy. Choose the processing location based on optimizing resource utilization and cost efficiency.

Edge Orchestration:

The implementation of dynamic edge orchestration mechanisms influences how tasks are allocated between edge devices and cloud resources based on real-time conditions.

User Experience and Data Presentation:

Consider how insights and analysis results will be presented to end-users. Ensure a seamless user experience regardless of whether data originated from edge or cloud processing.

Redundancy and Failover:

Plan for redundancy and failover mechanisms in case of edge device failures. Determine how seamlessly the system can transition processing tasks to other devices or the cloud.

Regulatory and Compliance Considerations:

Regulatory requirements and compliance standards might influence data storage, processing, and transmission decisions.

Industry and Vertical Specifics:

Different industries and verticals have unique requirements. Consider factors like healthcare regulations, industrial automation standards, and retail trends.

By carefully considering these factors, you can tailor your approach to seamlessly integrate edge computing and cloud resources for enhanced data analysis, ensuring that the integration aligns with your application's goals and requirements.

Data privacy and security are critical considerations in the seamless integration of edge computing and cloud resources for enhanced data analysis. Here's how data privacy and security are addressed in this integration:

Edge Data Privacy:

Sensitive data can be processed and analysed locally on edge devices, reducing the need to transmit raw data to the cloud. This limits exposure of sensitive information during transmission.

Data Encryption:

Implement end-to-end encryption to protect data during transmission between edge devices and the cloud. This ensures that data remains secure even if intercepted.

Access Control:

Implement access controls at both the edge and cloud levels to restrict data access to authorized personnel. Only authorized users should be able to interact with and analysed the data.

Data Anonymization:

Anonymize data before transmitting it to the cloud. This ensures that individual users' identities cannot be easily linked to the data.

Secure Protocols:

Use secure communication protocols such as HTTPS and MQTT with proper authentication and authorization mechanisms to ensure data integrity and prevent unauthorized access.

Secure Edge Devices:

Secure edge devices with proper authentication, regular updates, and security patches to prevent unauthorized access and potential vulnerabilities.

Data Minimization:

Minimize the data transmitted to the cloud by processing data at the edge and sending only relevant

insights. This reduces the risk associated with transmitting large volumes of data.

Cloud Security Measures:

Utilize cloud provider security features such as encryption at rest, access controls, and intrusion detection to safeguard data stored in the cloud.

Compliance with Regulations:

Ensure that data processing and transmission comply with relevant data protection regulations, such as GDPR or HIPAA, depending on the industry and region.

Monitoring and Auditing:

Implement monitoring and auditing mechanisms to track data access and usage. This helps detect unauthorized activities and provides an audit trail for compliance purposes.

User Consent and Transparency:

Ensure that users are informed about data processing and obtain their consent, especially if sensitive data is involved. Transparency builds trust and ensures compliance.

Data Lifecycle Management:

Develop a clear data lifecycle management strategy, including data retention and deletion policies, to minimize the risk of unauthorized access to outdated data.

Security Testing and Audits:

Regularly conduct security testing and audits of both edge devices and cloud resources to identify vulnerabilities and address potential security gaps.

Employee Training:

Train employees and personnel handling data on best practices for data privacy and security. Human error is a common cause of data breaches.

Incident Response Plan:

Have a well-defined incident response plan in place to quickly address and mitigate any potential data breaches or security incidents.

By implementing these measures, organizations can ensure that data remains private and secure throughout the seamless integration of edge computing and cloud resources for enhanced data analysis. It's essential to adopt a comprehensive approach that addresses data privacy and security at every stage of the data's journey, from edge to cloud.

3.Results and Analysis:

The following are the overview of the types of outcomes that have emerged from previous and ongoing research in this field up to that point:

Latency Reduction and Real-Time Responsiveness:

Research has demonstrated that processing data at the edge reduces latency and enables real-time decision-making, leading to improved responsiveness in applications such as industrial automation and IoT.

Network Bandwidth Optimization:

Studies have shown that by processing data locally at the edge and sending summarized insights to the cloud, network bandwidth can be conserved, reducing the risk of congestion and transmission costs.

Privacy Enhancement and Data Security:

Research has emphasized the importance of processing sensitive data locally to enhance privacy

and minimize data exposure during transmission. This aligns with data protection regulations.

Hybrid Analytics for Better Insights:

Previous research has highlighted the value of combining real-time edge analytics with cloud-based historical analysis to provide a more comprehensive view of data and yield deeper insights.

Resource Utilization Optimization:

Studies have explored how balancing processing between edge and cloud resources optimizes the utilization of computational resources and improves overall system efficiency.

Edge-Cloud Orchestration Techniques:

Research has proposed and evaluated orchestration mechanisms that dynamically allocate tasks between edge devices and cloud resources based on factors like data type, latency requirements, and workload.

Scalability and Workload Management:

Research has addressed strategies for handling scalability challenges, ensuring that the integration can scale to accommodate increased data volumes and device connections.

Edge Device Selection and Optimization:

Previous studies have analysed the selection of appropriate edge devices, considering factors such as processing power, energy efficiency, and compatibility with cloud platforms.

Fault Tolerance and Redundancy:

Research has investigated failover mechanisms and redundancy strategies to maintain uninterrupted data analysis and decision-making in case of edge device failures.

Industry-Specific Applications: - Studies have focused on specific industries, such as healthcare, manufacturing, and smart cities, showcasing how the integration benefits various sectors through enhanced data analysis.

Performance Benchmarking and Evaluation: - Previous research has evaluated the performance of different integration approaches, comparing factors like latency, resource usage, and overall system efficiency.

Energy Efficiency Considerations: - Some research has explored how the integration can improve energy efficiency by offloading tasks from power-hungry cloud servers to energy-efficient edge devices.

Challenges and Open Research Questions: - Previous studies have identified challenges in terms of load balancing, data consistency, security, and seamless handoff between edge and cloud resources, which require further investigation.

Keep in mind that the field of edge computing and cloud integration is rapidly evolving, and new research findings are continuously being published. Improving data privacy and security in the seamless integration of edge computing and cloud resources for enhanced data analysis involves a combination of technical techniques, best practices, and tools. Here are some advanced techniques to enhance data privacy and security:

Multi-Layer Encryption:

Implement end-to-end encryption using strong cryptographic algorithms for data in transit between edge devices and cloud resources. Use encryption

libraries and protocols like TLS/SSL to ensure data remains confidential.

Homomorphic Encryption:

Explore homomorphic encryption, which allows computations to be performed on encrypted data without decrypting it. This technique ensures that sensitive data remains encrypted even during analysis.

Differential Privacy:

Integrate differential privacy techniques to add noise or randomness to aggregated data before transmission, preserving individual privacy while allowing accurate analysis.

Secure Enclaves:

Utilize hardware-based security features, such as Intel SGX or ARM Trust Zone, to create secure enclaves on edge devices. These enclaves isolate sensitive computations from the rest of the system.

Zero-Trust Architecture:

Adopt a zero-trust architecture that assumes no device or user can be trusted by default. Implement strong authentication, access controls, and continuous monitoring across both edge and cloud components.

Federated Learning:

Implement federated learning techniques, where model training occurs on edge devices while only aggregated model updates are sent to the cloud. This minimizes the need to transmit raw data.

Attribute-Based Encryption:

Use attribute-based encryption to define access controls based on attributes (e.g., roles, user characteristics). This allows fine-grained control over who can access specific data.

Block chain Technology:

Consider using block chain for secure and tamper-resistant data storage and auditing. Block chain can provide an immutable ledger for data transactions and access history.

Threat Detection and Intrusion Prevention:

Deploy intrusion detection systems (IDS) and intrusion prevention systems (IPS) on edge devices and in the cloud to monitor for unauthorized access and potential threats.

Secure Key Management: - Implement secure key management practices to protect encryption keys used for data protection. Use Hardware Security Modules (HSMs) for enhanced key security.

Data Masking and Tokenization: - Implement data masking or tokenization techniques to replace sensitive data with pseudonyms or tokens. This way, even if data is compromised, it remains unusable.

Privacy-Preserving Analytics: - Utilize techniques such as secure multi-party computation (SMPC) or secure function evaluation (SFE) to perform analytics on encrypted data without revealing the data itself.

Regular Security Audits: - Conduct regular security audits and vulnerability assessments to identify and address potential security weaknesses in both edge and cloud components.

Privacy Impact Assessments: - Conduct privacy impact assessments to evaluate potential risks to privacy and identify mitigation strategies. This helps ensure that privacy is considered throughout the integration process.

Continuous Monitoring and Response: - Implement continuous monitoring of edge devices and cloud resources to detect anomalies and respond to security incidents in real-time.

By incorporating these advanced techniques into the integration of edge computing and cloud resources, organizations can significantly enhance data privacy and security. It's important to approach data privacy and security as an ongoing process, continuously adapting to emerging threats and evolving technologies.

Research on the seamless integration of edge computing and cloud resources for enhanced data analysis has yielded valuable insights and findings. While I don't have access to the most current research beyond my

While integrating edge computing and cloud resources for enhanced data analysis offers numerous benefits, there are also several drawbacks and challenges related to data privacy and security that need to be considered and addressed. Some of these drawbacks include:

Increased Attack Surface:

The integration introduces additional points of entry for potential cyberattacks, as both edge devices and cloud resources need to be secured. This broader attack surface requires comprehensive security measures.

Data Transmission Risks:

Transmitting data between edge devices and the cloud can expose it to interception and potential breaches if

encryption and secure transmission protocols are not properly implemented.

Cloud Vulnerabilities:

Cloud environments are not immune to security vulnerabilities. Misconfigurations, unauthorized access, and data breaches can occur if cloud security is not managed effectively.

Complexity of Orchestration:

Orchestrating tasks between edge and cloud resources dynamically adds complexity. Incorrect orchestration decisions can lead to data exposure or inefficient resource usage.

Data Consistency Challenges:

Maintaining data consistency across edge and cloud components can be challenging. Ensuring that aggregated data sent to the cloud is accurate and up-to-date requires careful management.

Resource Constraints:

Edge devices often have limited computational resources, which might constrain the implementation of robust security measures. Balancing security and resource efficiency is a challenge.

Key Management Complexity:

Managing encryption keys for secure communication between edge and cloud resources can become complex, requiring careful key distribution and rotation strategies.

Compliance Variability:

Ensuring compliance with data protection regulations across edge and cloud environments can be complex

due to differences in data processing and storage practices.

Edge Device Vulnerabilities:

Some edge devices might lack proper security features, making them susceptible to attacks. Securing a diverse range of devices can be challenging.

Limited Processing for Security: - Edge devices might prioritize data processing over security measures due to resource constraints, potentially leading to vulnerabilities if not properly managed.

Insider Threats: - Insiders with access to edge devices or cloud resources can pose security risks. Proper access controls and monitoring are needed to mitigate this threat.

Lack of Standards: - The lack of standardized security practices for edge-cloud integration can lead to inconsistent security implementations and potential vulnerabilities.

Data Aggregation Risks: - Aggregating data at the edge before sending it to the cloud can lead to exposure of potentially sensitive insights if not carefully managed and anonymized.

Overhead of Privacy Techniques: - Implementing advanced privacy-preserving techniques like homomorphic-encryption or differential privacy can introduce processing overhead that affects overall system performance.

Human Factors: - Human error, such as misconfigurations or inadequate user training, can compromise security and privacy, underscoring the importance of proper training and education.

To address these drawbacks, it's crucial to implement a comprehensive security strategy that encompasses both edge and cloud components, considering the unique challenges and requirements of each. Regular security assessments, audits, and staying updated with security best practices are essential to mitigating these challenges and ensuring a secure integration of edge computing and cloud resources for enhanced data analysis.

4. Conclusion and future scope:

In conclusion, the seamless integration of edge computing and cloud resources presents a paradigm-shifting approach that bridges the gap between localized real-time processing and expansive cloud-based analytics. This integration holds the promise of revolutionizing data analysis by leveraging the strengths of both edge and cloud computing to drive enhanced decision-making, operational efficiency, and innovation across various industries and applications.

Through this integration, organizations can tap into the power of edge devices positioned closer to data sources, enabling rapid initial processing and reducing latency for time-sensitive applications. This localized processing not only supports real-time responsiveness but also addresses concerns around data privacy and security by minimizing data transmission to the cloud. Simultaneously, cloud resources provide the computational muscle needed for in-depth analysis, complex modelling, and long-term trend identification.

The future scope of seamless integration of edge computing and cloud resources is dynamic and evolving. As these technologies continue to merge and mature, they will drive innovation, reshape industries, and empower organizations to harness data in unprecedented ways. To make the most of this potential, collaboration between researchers, industry practitioners, and policymakers will be vital in shaping the direction of this integration.

References



1. Muralidhara, P. (2017). IoT applications in cloud computing for smart devices. *INTERNATIONAL JOURNAL OF COMPUTER SCIENCE AND TECHNOLOGY*, 1(1), 1-41.
2. Serrano, N., Gallardo, G., & Hernantes, J. (2015). Infrastructure as a service and cloud technologies. *IEEE Software*, 32(2), 30-36.
3. Muralidhara, P. (2019). Load balancing in cloud computing: A literature review of different cloud computing platforms. Page | 8
4. Elmurzaevich, M. A. (2022, February). Use of cloud technologies in education. In *Conference Zone* (pp. 191-192).
5. G'ayratovich, E. N. (2022). The Theory of the Use of Cloud Technologies in the Implementation of Hierarchical Preparation of Engineers. *Eurasian Research Bulletin*, 7, 18-21.
6. Ekanayake, J., Gunarathne, T., & Qiu, J. (2010). Cloud technologies for bioinformatics applications. *IEEE Transactions on parallel and distributed systems*, 22(6), 998-1011.
7. Aziz, M. A., Abawajy, J., & Chowdhury, M. (2013, December). The challenges of cloud technology adoption in e-government. In *2013 International Conference on Advanced Computer Science Applications and Technologies* (pp. 470-474). IEEE.
8. Sharmili, N., Yonbawi, S., Alahmari, S., Lydia, E. L., Ishak, M. K., Alkahtani, H. K., ... & Mostafa, S. M. (2023). Earthworm Optimization with Improved SqueezeNet Enabled Facial Expression Recognition Model. *Computer Systems Science & Engineering*, 46(2).
9. Rutskiy, V., Aljarbouh, A., Thommandru, A., Elkin, S., Amrani, Y. E., Semina, E., ... & Tsarev, R. (2022). Prospects for the Use of Artificial Intelligence to Combat Fraud in Bank Payments. In *Proceedings of the Computational Methods in Systems and Software* (pp. 959-971). Cham: Springer International Publishing.
10. Aljarbouh, A., Tsarev, R., Robles, A. S., Elkin, S., Gogoleva, I., Nikolaeva, I., & Varyan, I. (2022). Application of the K-medians Clustering Algorithm for Test Analysis in Elearning. In *Proceedings of the Computational Methods in Systems and Software* (pp. 249- 256). Cham: Springer International Publishing.
11. Albarakati, A. J., Boujoudar, Y., Azeroual, M., Eliysaouy, L., Kotb, H., Aljarbouh, A., ... &

Pupkov, A. (2022). Microgrid energy management and monitoring systems: A comprehensive review. *Frontiers in Energy Research*, 10, 1097858.

12. Albarakati, J. A., Azeroual, M., Boujoudar, Y., EL Iysaouy, L., Aljarbouh, A., Tassaddiq, A., & EL Markhi, H. (2022). Multi-Agent-Based Fault Location and Cyber-Attack Detection in Distribution System. *Energies*, 16(1), 224. Page | 9
13. Haq, I., Mazhar, T., Nasir, Q., Razzaq, S., Mohsan, S. A. H., Alsharif, M. H., ... & Mostafa, S. M. (2022). Machine Vision Approach for Diagnosing Tuberculosis (TB) Based on Computerized Tomography (CT) Scan Images. *Symmetry*, 14(10), 1997



Asymmetric resistive switching by anion out-diffusion mechanism in transparent Al/ZnO/ITO heterostructure for memristor applications

Suman Gora ^a, Lavanya Thyda ^a, Gnyaneshwar Dasi ^a, Reddivari Muniramaiah ^a, Atul Thakre ^b, Jitendra Gangwar ^c, D. Paul Joseph ^a, M. Kovendhan ^d, P. Abdul Azeem ^a, D. Dinakar ^a, Kuppusamy Thangaraju ^a, Hitesh Borkar ^a  

Show more 

 Share  Cite

<https://doi.org/10.1016/j.surfin.2022.101950> 

[Get rights and content](#) 

Abstract

In this report, the monovalent cations of sodium and potassium are doped into the ZnO matrix to explore for resistive switching. The structural analysis confirms that Na⁺ and K⁺ cations are incorporated into the interstitial sites of ZnO lattice. The Na⁺ and K⁺ doped ZnO thin films (NZO and KZO) have exhibited improved transparency slightly higher than 80 % for the wavelength range 400–1000 nm. Hall and impedance measurements confirms that resistance of the thin films increased after incorporation of Na⁺ and K⁺ cations into the ZnO lattice. The fabricated NZO and KZO thin films-based memory devices exhibited bipolar resistive switching phenomenon with excellent ON/OFF ratio of 10⁴, endurance of ~ 100 cycles, and charge retention of 10⁴ s in both the resistive states. These results imply that NZO and KZO films to have enormous potential to serve as an efficient resistive switching device.



EXPLORATIONS IN ARTIFICIAL INTELLIGENCE AND MACHINE LEARNING

Zareena Begum¹ and Kerla Raju²

¹Assistant Professor, Department of Computer science and Engineering(DS),
Vaagdevi college of Engineering, Bollikunta (JNTUH).

²Assistant Professor, Department of Computer Science,
Vaagdevi Degree and PG college, Hanamkonda (KU).

Abstract:

Man-made reasoning(AI) seems the characterizing age within recent memory. Google has just re-marked its Google Research division to Google AI as the venture seeks after patterns within the area of manufactured insight. John McCarthy characterizes AI, again in 1956 like this " AI involves machines that can do liabilities which can be capability of mortal insight". This Free Book offers you a short introduction to Artificial Intelligence, Machine Learning, and Deep Learning. In any case, what are the guideline varieties among Artificial Intelligence, Machine

DOI Number: 10.14704/nq.2022.20.10.NQ55008

NeuroQuantology 2022; 20(10): 64-74

Learning, and Deep Learning?

To set it just, Machine proficiency is a way of arriving at AI. Arthur Samuel's depiction of Machine proficiency(ML) is from 1959 " Machine proficiency Field of investigate that offers PC frameworks the usefulness to analyze with out being unequivocally modified". Commonplace inconveniences answered with the guide of utilizing Machine education are

- Retrogression.
- Section.
- Division.
- Network investigation.

What has changed decisively considering the ones spearheading days is the vertical pushed of Big Information and of computing power, making it plausible to analyze enormous segments of realities at scale! Simulated intelligence wants Big Data and Machine Learning to check. Machine education is a way of? preparing? an arrangement of decides all together that it could look at. Gigantic segments of realities are utilized to instruct

calculations and allowing calculations to " look at" and enhance. Profound education is a subset of Machine proficiency and changed into invigorated with the guide of utilizing the shape and normal for the brain. As a representation, Artificial Neural Networks(ANNs), are calculations that demonstrate the home grown state of the cerebrum, videlicet the interconnecting of various neurons. This Free Book offers a gentle prelude to Machine proficiency, records brilliant ML strategies equivalent as decision tree education, Hidden Markov Models, supporting education, Bayesian organizations, as well as overlaying a couple of elements of Profound Literacy and the way this relates to AI. It need to help you gain an expertise of some of the advances within the area of AI and Machine proficiency while providing you with an idea of the specific hacks you will need to get initiated on the off chance that you need to compositions as a Machine Learning brains.

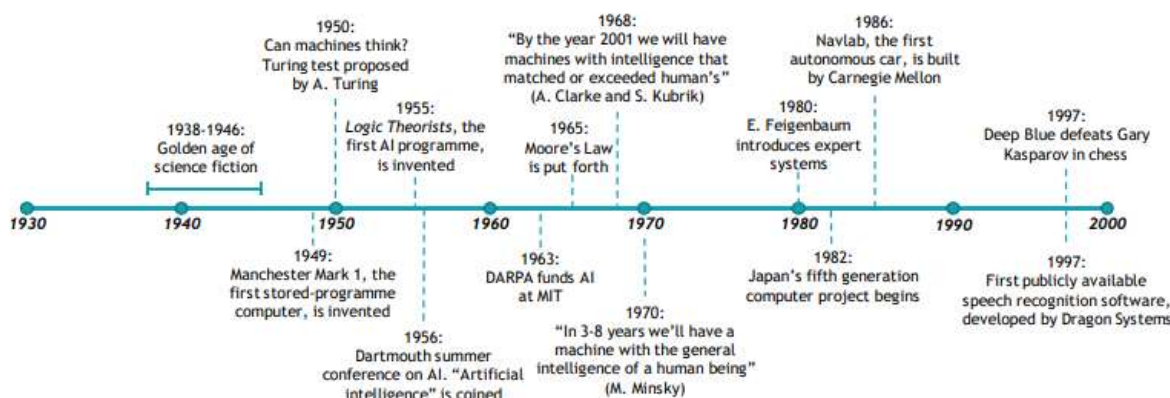
1. INTRODUCTION:

In 1950, British mathematician Alan Turing posted a paper on working out servicealso, knowledge(Turing, 1950(1)) representing the question of whether machines can assume. Hehigh level a simple heuristic to check his proposition might need to a PC have a conversation

furthermore, arrangement inquiries in a way that could fool a dubious human into allowing thePC transformed into truly a human? 1 The performing " Turing test " keeps on being utilized second. That equivalenttime, Claude Shannon proposed the presentation of a framework that would be guided to play chess(Shannon, 1950(2)). The framework can be gifted with the guide of utilizing the utilization of savage strain or with the guide of utilizing evaluating alittle arrangement of an adversary's essential moves(UW, 2006(3)).Various remember the Dartmouth Summer Research Project withinside the late spring time of 1956 as thecountry of manufactured insight(AI). At this manufacturing plant, the statute of AI transformed into conceptualizedwith the

guide of utilizing John McCarthy, Alan Newell, Arthur Samuel, Herbert Simon and Marvin Minsky.While AI investigation has logically worked on over the when multiple times, the promises of early Aladvertisers ended up being excessively favorable. This caused a " AI margin time " of diminished sponsorshipfurthermore, leisure activity in AI investigation all through the 1970s. New sponsorship andleisure activity in AI appeared with propels in estimation power that came to be had withinside the Nineties(UW, 2006(3)). Figure1.1 presents a course of events of AI's initial improvement. The AI margin time finished withinside the Nineties as computational powerand measurements storage facility had been progressingto the variable that confounded commitments had been getting possible. In 1995, AI moved forwardwith Richard Wallace's improvement of the Artificial verbal Internet Computer truth thatmight need to keep up with initial trades. Likewise withinside the Nineties, IBM progressed a PC named DeepBlue that utilized a savage strain procedure to play towards global chess champion Gary Kasparov.

Figure 1.1. Timeline of early AI developments (1950s to 2000)



Source: Adapted from Anyoha (28 August 2017[4]), "The history of artificial intelligence", <http://sitn.hms.harvard.edu/flash/2017/history-artificial-intelligence/>.

Dark Blue might appearance ahead of time six way or moreover and will at any point

ascertain 330 million positionspredictable with second(Somers, 2013(5)). In 1996, Deep

Graphical Exploratory Data Analysis (GEDA): A Case Study on Employee Attrition

Dr. Ayesha Banu, Dr. Sharmila Reddy, M. Rama

Associate Professor & Head, CSE(Data Science).Vaagdevi College of Engineering

headcsd@vaagdevi.edu.in

Associate Professor & Head, CSE(Data Science).Vaagdevi Engineering College

sharmilakreddy@vecw.edu.in

Assistant Professor,CSE,Vaagdevi College of Engineering

rama_m@vaagdevi.edu.in

To Cite this Article

Dr. Ayesha Banu, Dr. Sharmila Reddy, M. Rama, **Graphical Exploratory Data Analysis (GEDA): A Case Study on Employee Attrition**”,*Journal of Science and Technology*, Vol. 07, Issue 09,-November 2022, pp01-11

Article Info

Received: 28-09-2022

Revised: 17-09-2022

Accepted: 25-10-2022

Published: 5-11-2022

Abstract

Exploratory Data Analysis (EDA) popularly performs some preliminary investigations on the dataset to understand its content and structure. EDA is a mandatory step in the complete process of data analysis, since its mandatory to analyze the data in order to produce good results and in turn help in decision making. There are several Graphical EDA techniques which not only analyze the data but also present the results in graphical form. This paper uses the Python programming language for both data analysis and visualization of results. The rich set of python libraries including pandas, numpy, matplotlib, seaborn etc greatly supports the process of GEDA. This paper works on the “Employee Performance and Attrition” dataset to analyze and extract potential information and present results in graphical form.

Keywords: Graphical Exploratory Data Analysis, Python, Data Visualization,matplotlib, seaborn.

1. INTRODUCTION

In today’s world of technology data is growing very fast in both volumes and variety and it has become highly impossible to understand and analyze the data manually. Data analysis is collection of different processes to inspect, clean, transform, and model the data with an objective of discovering potentially useful information, drawing several conclusions, and finally supporting decision-making.Exploratory Data Analysis (EDA)evaluates or comprehends data and is a significant component of any process in data science or machine learning.It helps in exploring the data; understanding the structure and relationships between variables andbuilds a consistent and valuable output.

Python is a very popular programming language today due its flexibility andwide collection of inbuilt libraries, which are very essential to performdata analytics and complex computations.Pythonsupports multiple libraries for data analytics like NumPy for mathematical and statistical calculations and PandasthePython Data Analysis Library.Data visualization plays a vital role in representingthe data and also complex data relationships graphically such that it is easy to understand. Python has many libraries that support for displaying data in the form of charts, graphs , plots and animations. Two such popular libraries used in this work are Matplotlib and Seaborn.

This paper works on the “Employee Performance and Attrition” dataset to perform Exploratory Data Analysispresent results in graphical form using python. The paper is organized in to four sections. Section 2 briefs the review of literatureand section 3 explains the differenttechniques for EDA both non graphical and graphical. In section 4, the graphical exploratory data analysis is studied on the Employee Attrition dataset using python.

2. LITERATURE SURVEY

Aindrila et al. [1] made a study on the tools for data visualization with respect to their efficacy in the EDA process. They also examined the scalability of the exploration tools for analyzing large datasets. Matthew Ntow Gyamfi et al. [2] investigated the commercial banks practices regarding credit risk and loan default to find the causes of nonperforming loans. X. Francis Jency et al. [5] have performed EDA on bank data to understand the nature of clients who apply for loans in banks. Based on the results they applied machine learning algorithms for loan prediction and classified the clients as good customer and bad customer.

K. Ulaga Priya et al. [4] have done EDA on bank dataset using random forest algorithm to predict customers loan privilege in R programming for analysis. Kiranbala & Deepika [5] have performed EDA both numerical and graphical on the World Happiness report 2021 to understand the various aspects of data analysis. Kabita Sahoo et al. [6] have done EDA using python to understand the different libraries of python for data analysis and graphical representation of results.

3. TECHNIQUES FOR EDA

In the complete process of data analysis, after collecting the data and pre processing it, EDA is the very important step for data manipulation, plotting and visualization. Most of the EDA techniques are graphical and few are quantitative which help in analyzing the data sets with respect to their statistical characteristics. The techniques available for Exploratory Data Analysis (EDA) are broadly classified into Non-Graphical EDA and Graphical EDA where in both the techniques are classified into two types namely univariate and multivariate [7]. Some of the EDA techniques depend on the type of data on which they are applied and some depend on the purpose of the analysis. Table 1 shows the preferable EDA technique that can be adopted for a given type of data and purpose of analysis.

3.1. Non-Graphical Exploratory Data Analysis: NGEDA

These techniques help in providing an idea about the description and distribution of the variable(s). There are two methods under this category namely univariate and multivariate.

3.1.1 Univariate NGEDA: This is a principal form of data analysis that involves only one variable to identify underlying data distribution and the characteristics of population distribution. This analysis also covers outlier detection. For any quantitative variable Univariate EDA helps making initial assessments on the variable distribution using the data sample.

See discussions, stats, and author profiles for this publication at: <https://www.researchgate.net/publication/371379251>

An Efficient Deep Learning Algorithm for MRI Segmentation Using Kernel based CNN with M-SVM An Efficient Deep Learning Algorithm for MRI Segmentation Using Kernel based CNN with M-...

Article in *NeuroQuantology* · December 2022

DOI: 10.48047/NQ.2022.20.20.NQ109035

CITATIONS

0

READS

82

1 author:



Ayesha Banu Mohd

Vaagdevi College of Engineering

30 PUBLICATIONS 51 CITATIONS

SEE PROFILE



An Efficient Deep Learning Algorithm for MRI Segmentation Using Kernel based CNN with M-SVM

Dr. Ayesha Banu¹, Associate Professor & Head, Dept. of CSE(DS), Vaagdevi College of Engineering, Warangal, India.
Santhosh Ramchander. N², Associate Professor, Dept. of CSE, Sreyas Institute of Engineering and Technology, Hyderabad, India.
and Ramya Laxmi. K³, Assistant Professor, Dept. of CSE, Sreyas Institute of Engineering and Technology, Hyderabad, India.

Abstract.

Image segmentation has contributed majorly on long-standing medical image processing. It used earlier considered as a minor study field in computer vision. But today the rapid evolution of deep learning and image processing in medical field using CNN model has become a major focus of study. This paper examines deep learning-based image segmentation. Initially the ideas and features of deep learning-based medical image processing are introduced. The prospective development route is widened by analyzing the three basic approaches of medical image segmentation including their precincts. A list of troublesome tissues or organs and their conventional segmentation procedures are also discussed. However, research on deep learning-based picture segmentation is still in its infancy. Medical photographs are scarce, and the data set contains only a few of these images. The generated photos are not clinically correct. These challenges are addressed by deep learning-based brain tumour segmentation. Using a database of brain tumours, this study used a kernel-based CNN with M-SVM to increase quality and minimise error rates. It is obvious that the proposed work is superior to previous work.

Keywords: M-SVM, CNN, LoG, CLAHE, Feature Extraction, SGLDM

DOI Number: 10.48047/NQ.2022.20.20.NQ109035

NeuroQuantology 2022; 20(20): 309-317

1. Introduction

Image segmentation is considered as the complicated operation in image processing. This is a hotspot in pattern recognition. This is a hindrance to 3D modelling and other cutting-edge technology. Segmentation divides a huge image into manageable parts. To be readily visible, a picture's target must be separated from its background. Background subtraction methods are currently being improved. [1] By combining new ideas and technology, we've discovered a general segmentation method that works on every image. With the advancement of hospital care, new medical enterprises are becoming increasingly popular. Clinicians most typically use CT, MRI, PET, X-ray, and ultrasound imaging, followed by CT and MRI (UI). Images of microscopy, peritoneum, and other usual RGB images are given.

To make a clinical diagnosis, doctors use CT and other MRI scans [2]. So computer vision researchers focused on medical image processing. The rapid progression in the area of artificial intelligence and deep learning (DL) applied on picture segmentation has shown good performance in image categorization [3]. Deep learning outperforms traditional AI and computer imaging approaches in separation precision and reliability. Using artificial intelligence to divide medical data can assist doctors assess the extent of malignant tumours, quantify therapy effects, and reduce doctor workload. To adequately describe the various strategies, we used Google and ArXiv to obtain the most recent research on computer-aided diagnosis and learning.

Medical image processing conferences, like other premier events, are important information sources (Information Processing in Medical Imaging). We looked for papers that incorporated deep learning techniques. We promise to verify all findings. To assess the merits and downsides of current developments in medical image segmentation, this study looks at machine learning rather than past evaluations [4–6]. This research reviews the current state of the art in deep learning medical image segmentation and outlines potential stumbling blocks. This paper

See discussions, stats, and author profiles for this publication at: <https://www.researchgate.net/publication/371379314>

CHRONIC DISEASE DIAGNOSIS USING MACHINE LEARNING ALGORITHM

Article in *Multimedia Systems* · May 2023

CITATIONS

0

READS

135

2 authors:



Ayesha Banu Mohd
Vaagdevi College of Engineering

30 PUBLICATIONS 51 CITATIONS

SEE PROFILE



Zareena Begum
Madras School of Economics

10 PUBLICATIONS 37 CITATIONS

SEE PROFILE



CHRONIC DISEASE DIAGNOSIS USING MACHINE LEARNING ALGORITHM

¹ Dr. Ayesha Banu, ² Zareena Begum

¹Associate Professor, ²Assistant Professor

¹ Department of Computer Science and Engineering (Data Science)

¹Vaagdevi college of Engineering, Bollikunta, Warangal, Telangana, India.

Abstract : Chronic kidney disease (CKD), which is also a key risk factor for other diseases, kills and disables people all over the world. Because there are no evident signs in the early stages of CKD, it might go unnoticed. Medicine that decreases the progression of renal disease can be used to prevent it from progressing in patients who are diagnosed early. Clinicians can achieve their objectives more quickly by using machine learning models. This study suggests a CKD diagnosis approach based on machine learning. In the UCI machine learning repository, missing values in the CKD data set were discovered. The most similar measures from a large number of full samples were used to fill in the missing data in each partial sample using KNN imputation. Patients may forget to take measures in the real world for a variety of reasons, resulting in missing data. Six machine learning approaches were employed to construct models when the missing data set was completed: logistic regression, k-nearest neighbor, naive Bayes classifier, and feed forward neural network. With a diagnosis accuracy of 99.75 percent, Random Forest is the most accurate of these machine learning models. After ten simulations based on the errors generated by the constructed models utilizing the integrated model, an average accuracy of 99.83 percent can be achieved. As a result, we came to the conclusion that this method may be used to diagnose more complex clinical disorders.

Keywords: Machine Learning, Logistic Regression, KNN, Neural Network, Random Forest.

I. INTRODUCTION

Chronic kidney disease (CKD) affects roughly 10% of the world's population, making it a significant public health issue. [3] Chronic kidney disease (CKD) affects 10.8% of Chinese individuals, compared to 10–15% in the US. Unemployment in Mexico has risen to 14.7 percent, according to a new survey. Renal function declines over time, and the kidneys eventually cease to function. When kidney disease is in its early stages, there are no visible indicators of it. It's likely that the illness won't be diagnosed until the kidney has lost around 25% of its function. Chronic kidney disease has a severe impact on the human body, with high rates of morbidity and mortality. It can lead to cardiovascular disease. Once CKD has started, it is impossible to stop it. Patients who are recognized earlier in the disease's progression can receive treatment to halt or stop it, which is why early identification and diagnosis are so critical. A computer programme that combines data and deductive reasoning to learn the features of a particular pattern is an example of machine learning. This technology may be a viable tool for diagnosing CKD in patients due to its capacity to reliably and economically diagnose illnesses. Electronic health records have evolved into a new type of medical equipment with a wide range of uses as a result of their rapid expansion. Machine learning has previously been used in the medical field to identify human body status, analyze disease factors, and diagnose a variety of diseases.

Heart disease, diabetes, retinopathy, acute renal injury, cancer, and other disorders are just a few examples which can be diagnosed using machine learning algorithms. Regression tree, neural network, probability and decision surface approaches were used in these models. Hodneland et al used image registration to discover kidney morphological alterations in order to diagnose CKD. Vasquez-Morales et al. used large CKD datasets to construct classifiers that had a 95% accuracy rate on their test data.

Chemo metrics can be used to investigate the relationships between various items and factors using a multivariate method. The application of chemo metric-based multivariate classifiers in the diagnosis of chronic kidney disease (CKD) may be beneficial. Fuzzy logic and fuzzy mathematics diagnostic methods can be used on patients data with chronic kidney disease to better understand and diagnose their illness.

L.A. Zadeh released his seminal work on fuzzy set theory in 1965. "Fuzzy set theory," an infinite-valued logic, allows for less-than-perfect reasoning. Crisp ingredients may or may not be included in the kit. Components in fuzzy sets are only marginally significant. The

See discussions, stats, and author profiles for this publication at: <https://www.researchgate.net/publication/371702144>

Data mining functionalities on Web and Semantic Web A Survey

Article · June 2023

CITATIONS

0

READS

121

2 authors:



Ayesha Banu Mohd
Vaagdevi College of Engineering

30 PUBLICATIONS 51 CITATIONS

SEE PROFILE



Ayesha Ameen
Deccan College of Engineering and Technology

24 PUBLICATIONS 194 CITATIONS

SEE PROFILE

Data mining functionalities on Web and Semantic Web

A Survey

*Dr. Ayesha Banu

* Associate Professor & Head, Dept. CSE(DS), Vaagdevi College of Engineering, Warangal, ayeshabanuvce@gmail.com, 9949204894

Dr. Ayesha Ameen

Professor, Dept. of IT, Deccan College of Engineering & Technology, Hyderabad, ameenayesha@gmail.com

1. Introduction

Data Mining has attracted a great deal of attention in the information industry and in the society in recent years due to the availability of huge amounts of data and the immediate requirement for transforming such data into useful information and knowledge. The information and knowledge gained can be used for applications ranging like Business analysis, fraud detection and customer retention, production control, science exploration and many more. The amount of data stored in databases continues to grow at faster rates and this large amount of stored data contains valuable hidden knowledge, which could be used to improve the decision-making process of an Enterprise or business and many other popular areas of science and Information technology.

The number of human data analysts grows at a much smaller rate than the amount of stored data. Thus, there is a necessity for (semi-)automatic methods for extracting knowledge from data. This need has led to the emergence of a field called **Data Mining** and knowledge discovery. This is an interdisciplinary field, using methods of several research areas like Machine Learning, Statistics, Information Science, Database Technology and many more to extract high level knowledge from real-world data sets. Data mining is the core step of a broader process, called knowledge discovery in databases, or knowledge discovery, for short [1]. The World Wide Web serves as a huge, widely distributed, global information service centre for news, advertisements, consumer information, financial management, education, government, e-commerce and many other information services. The Web also contains a rich and dynamic collection of hyperlink information and web page access and usage information providing rich sources for data mining. **Web Mining** refers to the use of data mining techniques to automatically retrieve, extract and evaluate information for knowledge discovery from Web documents and services.

The great success of the current WWW leads to a new challenge: a huge amount of data is interpretable by humans only; machine support is limited. The **Semantic Web** is a vision of Tim Berners-Lee which suggests enriching the Web by machine-processable information which supports the user in his tasks. The **Semantic Web** is nothing but today's Web enriched by a formal semantics in form of ontologies that captures the meaning of pages and links in a machine-understandable form. The main idea of the Semantic Web is to enrich the current Web by machine-processable information in order to allow for semantic-based tools supporting the human user.

Semantic Web Mining is a combination of two areas: **Semantic Web** and **Web Mining**. The nature of most data on the Web is so unstructured that they can only be understood by humans and the Semantic Web addresses this challenge by trying to make the data (also) machine understandable. The amount of data on the web is so huge that they can only be processed efficiently by machines and Web Mining addresses this by (semi-)automatically extracting the useful knowledge hidden in these data, and making it available as an aggregation of manageable proportions.[4]

See discussions, stats, and author profiles for this publication at: <https://www.researchgate.net/publication/371379166>

GRAPH SIGNAL PROCESSING ANALYSIS BASED ON GRAPH DATA SCIENCE: INTERPRETABILITY, REPLICABILITY

Article · June 2023

DOI: 10.5281/zenodo.7766284

CITATIONS

0

READS

296

3 authors:



Zareena Begum

Madras School of Economics

10 PUBLICATIONS 37 CITATIONS

SEE PROFILE



Rama M A

Maharani Lakshmi Ammanni College for Women

18 PUBLICATIONS 149 CITATIONS

SEE PROFILE



Ayesha Banu Mohd

Vaagdevi College of Engineering

30 PUBLICATIONS 51 CITATIONS

SEE PROFILE

GRAPH SIGNAL PROCESSING ANALYSIS BASED ON GRAPH DATA SCIENCE: INTERPRETABILITY, REPLICABILITY

Zareena Begum

Assistant Professor, Dept. of Computer science and engineering (DataScience)
Vaagdevi College of Engineering

M.Rama

Assistant Professor, Dept. of Computer science and engineering
Vaagdevi College of Engineering

Dr. Ayesha Banu

Associate Professor, Dept. of Computer science and engineering (DataScience)
Vaagdevi College of Engineering

ABSTRACT

There are numerous modern data science challenges that make use of graphs (networks) as a representation of data, including those dealing with social, biological, and communication networks. There has been a rise in the use of signal processing and ML techniques for graph-based data analysis in the past decade. The prevalence of graphs and graph-based learning challenges across a wide range of applications has increased the interest in exploring explainability in graph data science. Since identifying communities is the first order of business when mining graphs for insights, we'll utilise that as a lens through which to investigate the challenge of explaining graph data science. Communities are formed when people with shared interests get together, and they are dense subnetworks of the larger network. Though many approaches to community discovery work well with artificial networks that have a clear modular structure, the quality and impact of these algorithms' results when applied to real-world networks with a more nuanced modular structure are less certain. In this paper, motivated by recent advances in explainable AI and ML, we offer methods and metrics from network science to quantify three separate elements of explainability in the context of community detection: interpretability, replicability, and reproducibility.

1. INTRODUCTION

Model explainability, interpretability, and reproducibility

Data is fed into the model, and then the model "does its thing" and spits out a prediction. The lack of clarity is problematic in many ways, and is often encapsulated by the vaguely related concepts of explainability, interpretability, and reproducibility.

- Explainability: Providing the human-friendly explanation of how a Machine Learning (ML) model works
- Interpretability: Indicates the ability to:
 - o Learn how model inputs, features, and outputs are connected.
 - o Anticipate outputs based on inputs.

PERFORMANCE ANALYSIS OF EXTERNALLY STRENGTHENED BEAM-COLUMN JOINT USING BASALT FIBRE FABRIC UNDER CYCLIC LOADING

G. GOKILA*, G. DINESHKUMAR

**K.S.R. College of Engineering, Tiruchengode, Namakkal, India*

E-mail: gokilagksr2007@yahoo.com

Abstract. The joint between beam and column (BCJ) in concrete structures is considered a crucial part of the load-bearing structure. Failure in this joint leads to structural collapse or major structural distress due to exceptional loading and seismic waves. Strengthening of this joint in structures is a mandatory part of infrastructure development all over the earth. The sustainable alternative solution is the utilisation of natural-based basalt fibre fabric. This work presents the impact of the BCJ wrapped by 300 and 450 GSM (g/m^2) basalt fabrics. A total of three concrete BCJ specimens are experimented using cyclic loading conditions to analyse the structural behaviour. The experimental results are compared with the analytical data.

Keywords: basalt fabric, confinement, crack resistance, absorption capacity, cyclic loading, strengthening.

AIMS AND BACKGROUND

Nowadays strengthening and retrofitting RC structures is mandatory due to the seismic activity. Existing Beam-column joint (BCJ) in RC structures are not designed to earthquake design philosophy and strong column weak beam criteria of design. More techniques are implemented in the field of structural design for strengthening the joint members¹. Usage of steel and concrete jacketing in RC beam-column joint enhances ultimate strength and rigidity. Many research projects² utilise the steel in the plain plate and corrugated sheets. Retrofitting by externally bonded steel plates influences reduced site disruption and minimum changes in cross-section. However³, this technique is affected by corrosion of the plate, difficulty in plate handling due to heavyweight, and unenviable shear failure. That includes repair using epoxy, stitching, steel jacketing, and Fibre-reinforced polymer (FRP) materials. In recent years many research results reveal that joints retrofitted with fibre fabric produce promising results⁴. Strengthening of BCJ using various fibre fabrics was compared⁵ and this was highlighted⁶. Among these works, researchers suggested different ways of utilising fibre fabric sheets to improve the shear capacity of the joint region. It was investigated⁷ the impact of wrapping on shear

* For correspondence.

strength and discussed the curing procedure. The CFRP-pull out tests using CFRP laminates on concrete were discussed⁸⁻¹⁰. Fibre orientation in CFRP wrapping is more efficient in improving combined tension and bending, 45° inclination to the main member produces higher deformation capacity.

EXPERIMENTAL

Ordinary Portland Cement (OPC) conforming to IS 12269: 2013 and all materials used in this work were chosen based on Indian standard (IS) code of practice. The fine aggregate used in this work falls under Zone II classification, according to IS 383-1970, with a fineness modulus of 2.32. Crushed coarse aggregate with nominal sizes of 20 mm and with specific gravity of 2.64 was used. The properties of materials utilised in this research are presented in Tables 1–6.

Table 1. Physical properties of OPC (Ordinary Portland cement)

S. No	Parameter	Value
1	Fineness of cement particles (retained on 90 µm sieve)	3%
2	Consistency	31%
3	Specific gravity	3.26
4	Initial setting time	36 min
5	Final setting time	276 min
6	Compressive strength	
	7 days	28.2 MPa
	28 days	53.5

Table 2. Fine aggregate properties

S. No	Parameter	Value obtained
1	Fineness modulus	2.32
2	Specific gravity	2.57
3	Water absorption (%)	0.80
4	Bulk density (kg/l)	1.28
5	Zone of grading	II

Table 3. Coarse aggregate properties

S. No	Parameter	Value obtained
1	Type	Crushed
2	Nominal size	20.00
3	Fineness modulus	6.78
4	Specific gravity	2.64
5	Water absorption (%)	1.87

Table 4. Steel bar properties

S. No	Steel bar diameter (mm)	Yield strength (MPa)	Ultimate strength (MPa)	Elongation
1	16	547.00	668.00	21.2
2	12	542.00	651.13	24.5
3	6	431.85	621.80	7.02

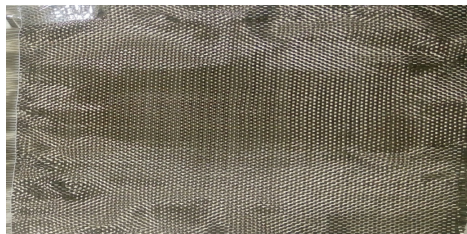
Table 5. Mix proportions of M₃₀ grade concrete

Grade	Cement (kg/m ²)	Fine aggregate (kg/m ²)	Coarse aggregate (kg/m ²)	Water (l/m ³)
M ₃₀	437.78	660.97	1111.88	197
Mix ratio	1	1.5	2.5	0.45

Table 6. Properties of epoxy resin

S. No	Parameter	Value obtained
1	Type	Hanson's epoxy resin
2	Resin hardener ratio	1:2
3	Density of resin	1.10 g/cm ²
4	Tensile strength	50 MPa
5	Tensile strain	2.1%
6	Elastic modulus	3.2 GPa

Basalt fabric properties. Igneous rock is the main source for the production of basalt products. This igneous rock (molten state) was extruded into the nozzle to form the basalt continuous filament. By using the weaving techniques the filaments are weaved as fabric. Depending on the weaving pattern, it was sub grouped as unidirectional, bi- directional and multi directional fabric. This work utilises the basalt bidirectional fabric shown in Fig. 1. The fabric is purchased from Arrow Technical Textiles Pvt.Ltd, Mumbai.

**Fig. 1.** Basalt bi-directional fabric

The fabric was tested using uniaxial fabric tensile testing machine available in the department of textile technology laboratory at K. S. Rangasamy College of technology based on the ASTM D3039. Six numbers of basalt fabric specimens

were chosen for fabric testing and the dimensions are shown in Fig. 2. Among six, three specimens had 300 (g/m²) and another three – 450 (g/m²). These specimens were provided with 2 mm thickness glass fabric laminates tabs at the end. It was done to fix the fabric sample at the testing machine.

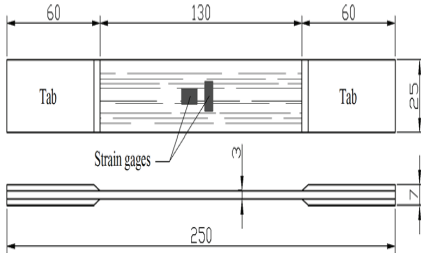


Fig. 2. Dimension of basalt fabric for tensile test



Fig. 3. Failure patterns of basalt fabric sample

Table 7. Basalt fabric properties

S. No	Parameter	Value obtained	
		300 (g/m ²)	450 (g/m ²)
1	Density	2.45 g/cm ²	2.67 g/cm ²
2	Thickness	1.2 mm	
3	Tensile strength	2143 Mpa	2410 MPa
4	Tensile strain	3.112%	3.15%
5	Modulus of elasticity	81 GPa	89 GPa

The failure pattern of samples is shown in Fig. 3. From the test results the basalt fabric properties are presented in table 7. In this work, three external BCJ were prepared using M₃₀ grade concrete and steel of Fe415. This mix ratio was 1:1.6:2.7 with water cement ratio of 0.45. These BCJ were tested using 100T capacity loading frame in structural engineering laboratory at K.S.R. College of Engineering (Figs 6 and 7).

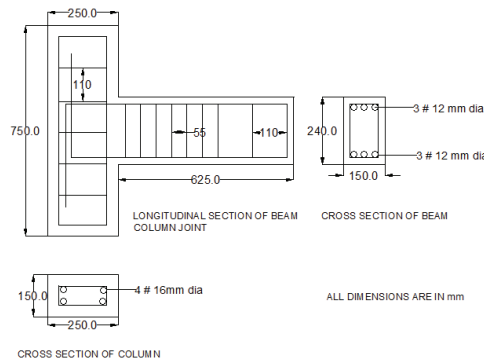


Fig. 4. Reinforcement details of beam column joint

The three specimens consist of four numbers of 16 mm diameter rods in column main reinforcement, and three numbers of 12 mm diameter rods in tension zone of the beam, and three numbers of 12 mm diameter rods in the compression zone. These reinforcement details are shown in Fig. 4. Grinder roller was used to spread the epoxy over the BCJ surface. Then the fabric was placed over the epoxy with the help of roller as shown in Fig. 5.



Fig. 5. Basalt fabric wrapped beam column joint

The detailing of exterior beam-column joint was done based on IS 13920: 2016 codal provision. One-fourth scale of reinforced concrete exterior beam-column joint specimens was cast for this work. In all six joints the column main reinforcement consisted of 4 numbers of 16 mm diameter whereas in the beam portion, the reinforcement consisted of 3 numbers of 12 mm diameter bars in tension and compression zone.

Table 8. Beam column joint nomenclature

S. No	Specimen identification	Description
1	CS1	Control specimen
2	BF1	Strengthening of beam column joint using 300 (g/m ²) basalt fabric wrapping
3	BF2	Strengthening of beam column joint using 450 (g/m ²) basalt fabric wrapping



Fig. 6. Reverse loading arrangement of beam column joint



Fig. 7. Forward loading arrangement of beam column joint

RESULTS AND DISCUSSION

The first crack was witnessed at the load level of 15 kN for control specimen CS and the crack was initiated at load of 24 and 28 kN for specimen BF 1, BF 2, respectively. Specimen wrapped with 450 (g/m²) basalt fabric produce delayed crack initiation than 300 (g/m²) basalt fabric. The hair line cracks were developed in first load cycle for control specimen. But for BF1 and BF2 the hair line cracks are developed at the end of second load cycle. Then cracks were developed into wider one in the third and fourth load cycle.

Load deflection behaviour. Deflection is the degree to which a structural element is displaced under a load. It may refer to an angle or a distance. For a given load, the deflection observed within the elastic limit is known as load deflection rate. The load deflection behaviour of CS, BF 1, BF 2 are represented by hysteresis loop shown in Figs 8, 9 and 10, respectively.

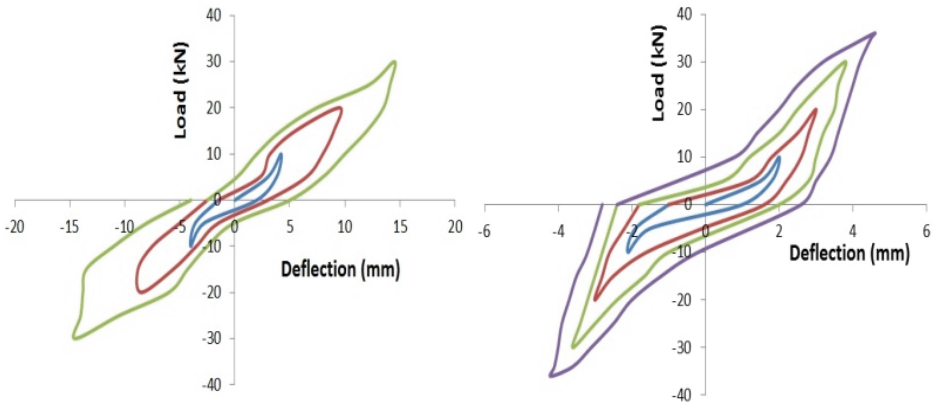


Fig. 8. Load deflection (hysteresis) curve for CS specimen

Fig. 9. Load deflection (hysteresis) curve for BF1

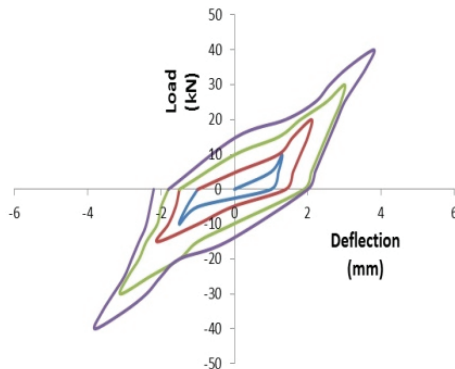


Fig. 10. Load deflection (hysteresis) curve for BF2

Ductility of beam column joint. Ductility of a structure is its ability to undergo deformation beyond the initial yield deformation, while still sustaining load. In this investigation ductility factor is defined as the ratio of maximum deflection to the yield deflection. The ductility behaviour for forward cycle is about 3.67 and for the reverse cycle is 3.56 for control specimen CS. Strengthening of beam-column joint wrapped with basalt fabric BF1 shows the ductility factor of 6.5 for forward cycle and for the reverse cycle it is 6.45 and for specimen BF 2 has the value of 6.98 for forward cycle and 6.88 for reverse cycle. These values are graphically represented in Figs 11 and 12.

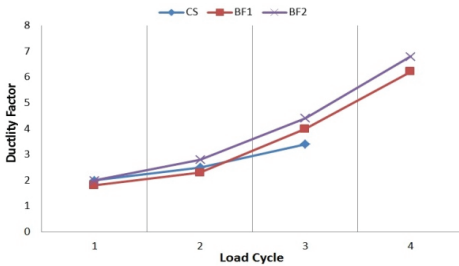


Fig. 11. Ductility factor for forward loading

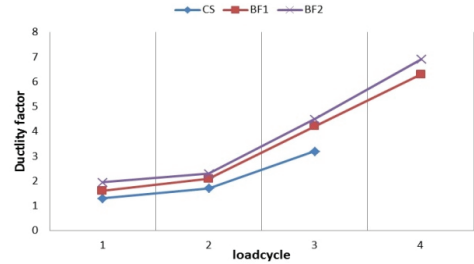


Fig. 12. Ductility factor for reverse loading

Stiffness. Resistance to deformation while applying a load is simply called stiffness. Stiffness is defined as the load required to causing unit deflection of the beam-column joint. A tangent was drawn for each cycle of the hysteric curves at a load of $P = 0.75 P_u$, where P_u – was the maximum load of that cycle. Determine the slope of the tangent drawn to each cycle, which gives the stiffness of that cycle. The stiffness for the control specimen (CS) and FRP wrapped specimen are presented in Figs 13 and 14.

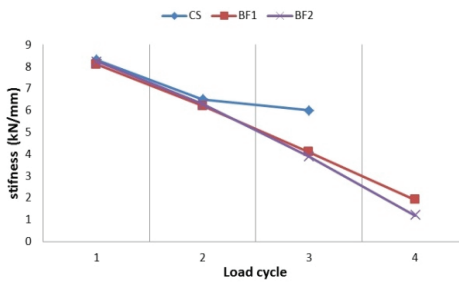


Fig. 13. Stiffness for forward loading

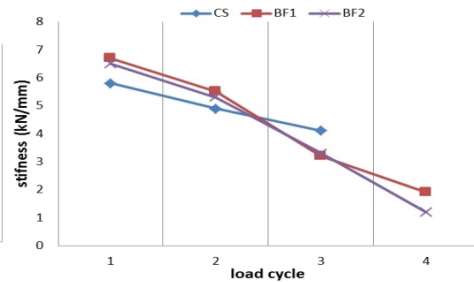


Fig. 14. Stiffness for reverse loading

Strengthening of beam-column joint using basalt fabric BF1 shows a stiffness value of 1.5 kN/mm for forward cycle and 1.67 kN/mm for reverse cycle. Similarly specimen BF2 has the value of 1 kN/mm for forward cycle and 1.2 kN/mm for reverse cycle.

Cumulative energy absorption capacity. The energy absorption capacities during each load cycle were calculated as the area under the hysteresis loops from the load deflection curve and the cumulative energy absorption capacity of the beam-column joint was determined by the adding the energy absorption capacity of the joint during each cycle considered and values are presented in Figs 15 and 16.

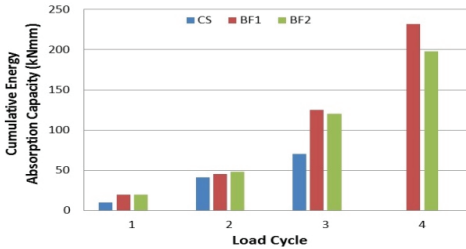


Fig. 15. Cumulative energy absorption capacity for forward loading

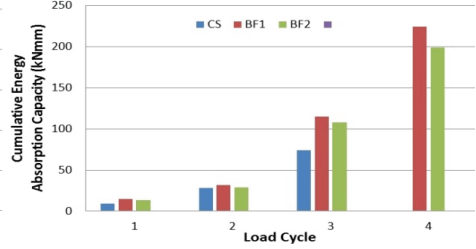


Fig. 16. Cumulative energy absorption capacity for reverse loading

The numerical analysis in this work includes the construction of non-linear finite element model to simulate the seismic behaviour of beam-column joints reinforced with FRP. The available finite element software package, ANSYS program was used for this purpose. The finite element analysis considered both geometrical and material non-linearity.

Meshing. Square configuration of mesh is generated, to obtain the accurate result from Solid65 element. The volume sweep command of ANSYS is used to mesh the support. This properly sets the width and length of elements in the concrete support and makes it consistent with the elements and nodes in the concrete portions of the model. Figures 17 and 18 show the analytical modelling and meshing of beam column joint specimen, respectively.

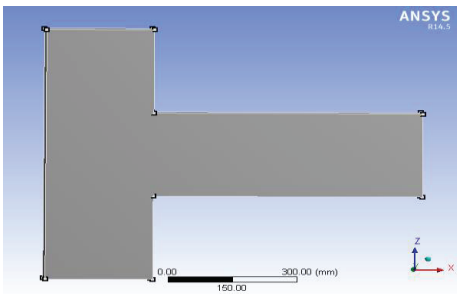


Fig. 17. Analytical modelling of beam column joint

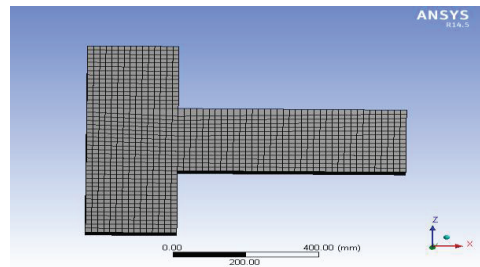


Fig. 18. Meshing beam – beam column joint

FRP wrapping. The structural geometry of exterior beam column joint has been modelled for the mentioned dimension and analysed using ANSYS. The exterior beam column joint has been analysed with and without wrapping on plastic hinge. The loads are applied on the column, the axial load applied on the centre of the column. Figures 19 and 20 show the modelling and meshing of beam-column joint with wrapping, respectively.

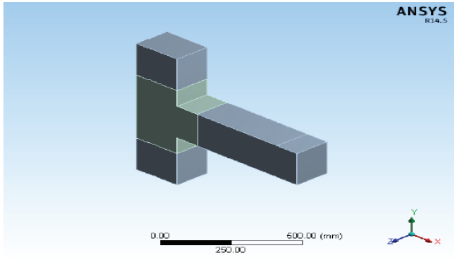


Fig. 19. Modelling of beam-column joint with wrapping

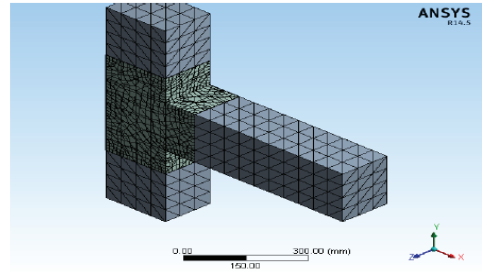


Fig. 20. Meshing of beam-column joint with wrapping

Deflection diagram from ANSYS analysis is shown in Figs 21–23.

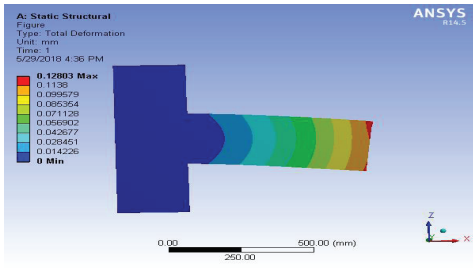


Fig. 21. Deflection diagram for CS specimen

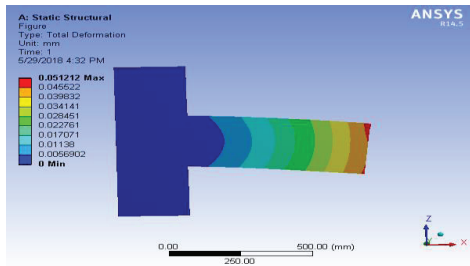
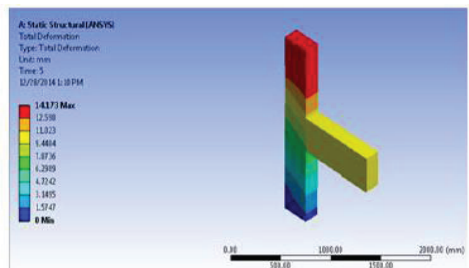
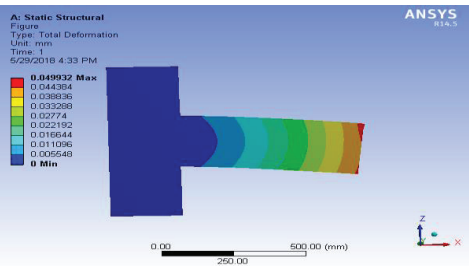


Fig. 22. Deflection diagram for BF1 specimen



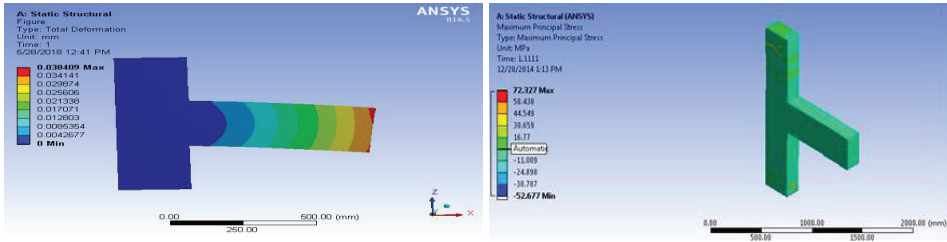


Fig. 23. Deflection diagram for BF2 specimen

The comparison of experimental test results with analytical test results are shown in Table 9.

Table 9. Comparison of ultimate load with experimental and analytical modelling

S. No	Beam – column joint identification	Ultimate load (kN)		Difference (%)
		experimental	analytical	
1	CS	30	33	9.09
2	BF1	36	38	5.26
3	BF2	40	42	4.76

The ultimate load of the control specimen CS has a 9.09% difference when compared to the experimental result. For specimen BF 1, BF 2 the difference between these results is about 5.26 and 4.76%, respectively. The comparison in deflection of experimental test results with analytical test results is shown in Table 10.

Table 10. Comparison of deflection with experimental and analytical modelling

S. No	Beam – column joint identification	Deflection (mm)		Difference (%)
		experimental	analytical	
1	CS	14.5	13.562	6.46
2	BF1	4.6	4.004	13.00
3	BF2	3.9	3.554	8.87

Difference of 6.46 % is obtained for CS specimen. For BF 1, BF 2, specimen the difference was obtained as 13 and 8.87%, respectively.

CONCLUSIONS

Beam column joint strengthened with 450 (g/m^2) basalt fabric wrapped specimen (BF2) produces better performances than 300 (g/m^2) basalt fabric wrapped specimen (BF1). Compared with control specimen, the basalt wrapped beam column joint produces better structural performance. Basalt wrapping at joints reduces the shear cracks and flexural cracks at early stage of loading. Control specimen fail before the completion of three cycles of load. Basalt wrapped specimen BF1 cre-

ates 20% higher load carrying capacity than control specimen and BF2 produces 33.33% higher load than CS specimen. The maximum difference in predicting the failure load is 9.09% while the maximum difference in deflection is 13%. From this work, it is derived that the natural based basalt fabric has better properties which is due to better crack bridging mechanism and energy absorption capacity. Due to its overwhelming properties, the basalt fabric may be used in the earthquake prone areas to prevent the damage in the structures and increase the longevity of the structures.

REFERENCES

1. N. ILIES, V. FARCAS, C. GHERMAN, V. CHIOREAN, D. POPA: Soils Efficient Improvement Solutions with Waste Materials and Binders. *J Environ Prot Ecol*, **16** (4), 1397 (2015).
2. S. SAKTHIVEL, S. JAGADEESAN: Flexural Performance of Recycled Coarse Beams Made with Recycled Coarse Aggregate Incorporating Alccofine. *J Environ Prot Ecol*, **23** (1), 119 (2022).
3. XING ZHAO, XIN WANG, ZHISHEN WU, JIN WU: Experimental Study on Effect of Resin Matrix in Basalt Fibre Reinforced Polymer Composites under Static and Fatigue Loading. *Constr Build Mater*, **242**, (2020).
4. N. PANG: Study on the Relevance of Environmental Awareness and Local Identity Based on Visual Imagery. *J Environ Prot Ecol*, **22** (6), 2338 (2021).
5. M. A. ALAM, A. HASSAN, Z. C. MUDA: Development of Kenaf Fibre Reinforced Polymer Laminate for Shear Strengthening of Reinforced Concrete Beam. *Mater Struct*, **49** (3), 795 (2016).
6. S. GURUSIDESWAR, R. VELMURUGAN, N. K. GUPTA: High Strain Rate Sensitivity of Epoxy/Clay Nano Composites Using Non-contact Strain Measurement. *Polymer*, **86**, 197 (2016).
7. S. RAVICHANDRAN V. K. STALIN: Data Behavior of Multiple Footings on Geocomposite Reinforced Gravel-Sand Bed Formation. *J Environ Prot Ecol*, **23** (1), 280 (2022).
8. M. S. KUMAR, K. ARUNACHALAM: Strength and Toughness Response of High Strength Concrete Beams Reinforced with Polypropylene and Steel Fibres. *J Balk Tribol Assoc*, **25** (3), 793 (2019).
9. LARISA GARCIA-RAMONDA, LUCA PELA, PERE ROCA, GUIDO CAMATA: In-plane Shear Behaviour by Diagonal Compression Testing of Brick Masonry Walls Strengthened with Basalt and Steel Textile Reinforced Mortars. *Constr Build Mater*, **240**, (2020).
10. K. ASLANI, O. KOHNEPOOSHI: Structural Behavior of FRP Strengthened Reinforced Concrete Shear Walls with Openings Using Finite Element Method. *Adv Struct Eng*, **21** (7), 1072 (2018).

*Received 7 October 2021
Revised 28 November 2021*

Article

Experimental Prognostication of Ultra-High-Performance Lightweight Hybrid Fiber-Reinforced Concrete by Using Sintered Fly Ash Aggregate, Palm Oil Shell Aggregate, and Supplementary Cementitious Materials

Diptikar Behera ^{1,*}, Kuang-Yen Liu ^{1,*}  and Dineshkumar Gopalakrishnan ² ¹ Department of Civil Engineering, National Cheng Kung University, Tainan 701, Taiwan² Department of Civil Engineering, Vaagdevi College of Engineering, Warangal 506005, India; gdkcivil@gmail.com

* Correspondence: diptiharibol@gmail.com (D.B.); kyliu@gs.ncku.edu.tw (K.-Y.L.)

Abstract: To create cost-effective structures, the modern construction industry has sought to reduce the dead load of buildings. Lightweight concrete is a quick way to reduce dead load. The current study is primarily concerned with identifying modern substitutes for coarse aggregate likely to aid in waste management and offer potential alternatives to the most exploited natural resources. According to ACI C 39-M, this study developed a novel lightweight hybrid fiber-reinforced concrete (LWHFRC) with a density of less than 1825 kg/m³ and compressive strength of 50 to 75 MPa. Ordinary Portland cement (53 Grade) was mixed with fly ash, silica fume, and GGBS. Sintered fly ash aggregate (SFA) and palm oil shell aggregate (POS) were used as coarse aggregates. Hooked steel fibers and polyvinyl alcohol fibers were combined in a hybrid form to improve crack propagation properties at the initial and subsequent stages. The water-to-binder ratio was kept constant at 0.30 to 0.35 with a 1% superplasticizer. Four volume fractions of hybrid fibers (both steel and PVA with $V_f = 0\%$, 1%, 1.5%, and 2%) were added. In addition, XRD, SEM, EDS, and EDS mapping tests were performed to finalize the material's chemical composition and crystalline structure. Furthermore, beams and cylinders were tested to determine the modulus of rupture, which was determined to be between 9.5 and 14 MPa by ACI code C 1609-M, and indirect tensile strength, achieved as 10 to 14 MPa by ACI code C 496-M. The researcher altered the modulus of elasticity (E_c) formula for lightweight concrete and discovered a relationship between f_c' and f_{cb} , f_c' and f_{spt} , and f_{cb} and f_{spt} . Finally, ANOVA and regression tests were run to check the significance of the experiment. The cost analysis revealed that the cost of LWHFRC increased by approximately 16.46%, while the strength increased by 55.98% compared to regular concrete.

Keywords: reinforced lightweight concrete; hybrid fiber; silica materials; XRD; SEM; EDS; ANOVA; regression



Citation: Behera, D.; Liu, K.-Y.; Gopalakrishnan, D. Experimental Prognostication of Ultra-High-Performance Lightweight Hybrid Fiber-Reinforced Concrete by Using Sintered Fly Ash Aggregate, Palm Oil Shell Aggregate, and Supplementary Cementitious Materials. *Materials* **2022**, *15*, 5051. <https://doi.org/10.3390/ma15145051>

Academic Editor: Francesco Fabbrocino

Received: 6 June 2022

Accepted: 18 July 2022

Published: 20 July 2022

Publisher's Note: MDPI stays neutral with regard to jurisdictional claims in published maps and institutional affiliations.



Copyright: © 2022 by the authors. Licensee MDPI, Basel, Switzerland. This article is an open access article distributed under the terms and conditions of the Creative Commons Attribution (CC BY) license (<https://creativecommons.org/licenses/by/4.0/>).

1. Introduction

Advancements in expertise enhance not only human comforts but also impairment the environment. In the world, most industries are accompanied by many materials such as fly ash [1–4], silica fume, and GGBS. As a natural vegetable aggregate, palm oil shell is a vegetable product from palm trees with low density that satisfies lightweight coarse aggregate criteria. As an artificial aggregate, sintered fly ash aggregate with low density and good strength is also an artificial aggregate for the palletization process in industries [5,6]. Palletization is a worldwide process used to manufacture artificial aggregates named sintered fly ash aggregate [7]. Fly ash is a by-product of coal-based thermal power plants. If not properly disposed of, fly ash can cause water and soil contamination, consequently interrupting the ecological cycles. China, the USA, and India consume around 70% of

the total coal worldwide [8]. According to a CEA [9] report, about 166 million tons of fly ash in India are generated from 132 thermal plants annually. About 56% of fly ash is utilized effectively through various methods, and the remaining fly ash is still a concern to society. Most attention is devoted to commercial applications such as the replacement of cement. This process simultaneously consumes the generated industrial wastes and reduces the requirement for cement clinker. High-quality fly ash with a low carbon content is used as a mineral additive to manufacture cement and concrete. Low-quality fly ash with higher and variable carbon content is generally used in landfills. Production of artificial aggregates from fly ash [10] is a great leap toward fly ash disposal in large quantities. Generally, the aggregate phase occupies 60–80% of the concrete matrix by volume. The depletion of natural aggregate resources is another significant concern for sustainable development worldwide [11].

Steel fiber and polyvinyl alcoholic fiber (PVA) were also used independently and combined to produce high-performance fiber-reinforced lightweight concrete by a few researchers. The researcher's primary goal is to use an environmentally harmful material as a light component to create high-performance, lightweight concrete. However, few researchers have already developed ultra-high-performance fiber-reinforced lightweight concrete, which is most suitable for structural members such as beams, columns, floors, and precast members. However, this was very expensive in the concrete industry because most researchers did not use coarse aggregate in their ultra-high-performance concrete (UHPC). In addition, many researchers developed only lightweight concrete. We plan to create new inventive concrete that will be high-performance and lightweight with truncated cost. There are numerous benefits of lightweight structural concrete over normal-weight concrete in the construction industry, particularly in high-rise buildings. The original method of fabricating lightweight structural concrete uses lightweight aggregates instead of ordinary aggregates in concrete. Due to the insufficient resources for natural and artificial lightweight aggregates, the substitute sources for lightweight aggregates should be revealed from industrial wastes. Oil palm shell (OPS) and oil palm-boiler clinker (OPBC) are two solid wastes from the palm oil industry [12,13] and are obtainable in abundance in tropical regimes. In this paper, the effects of using fly ash (FA), silica fume (SF), ground granulated blast slag (GGBS), [14] and numerous combinations of them such as sintered fly ash aggregate (regular round shape) and palm oil shell aggregate (irregular triangular shape) [15] with two different fibers such as steel fiber and PVA fiber were evaluated. Another goal of the researcher was to investigate multiaggregate (SFA and POS) without natural coarse aggregate (NCA) because circular SFA [16] and triangular POS have different workability and water absorption criteria for maintaining the perfect bonding of lightweight concrete [17] in construction industries. The effect of fibers on mortars and concrete has recently been demonstrated to increase the ductility chattels of cementitious composites.

Superior tensile strength, flexibility, toughness, and crack resistance were proven as the main properties enhanced by fiber reinforcement. Hybrid fiber-reinforced composites were renowned for further improving the properties at the early and future stages of crack and propagation. The key is to combine various beneficial properties of fiber into a single matrix, resulting in superiority in both aspects. Steel fiber and PVA fiber [18,19] were combined with two lightweight aggregates, palm oil shell, sintered fly ash aggregate, and three mineral admixtures, fly ash, silica fume, and GGBS in this study. The first series is industrialized with the optimum mineral admixture in different percentages, while the second series is settled with the lightweight concrete [20] with optimum mineral admixture. Finally, the third series explores the optimum lightweight concrete [21,22] with different percentages of two fibers [23]. The most crucial aspect of this research was maintaining the W/B ratio of 0.30 and 1% of high-range water-reducing admixture (HRWRA) throughout all three series. The compressive strength, flexural strength, split tensile strength, water absorption test, workability test, XRD test, SEM test, EDS test, and EDS mapping were carried out in the first stage of the research. The second stage of the study is to perform the bond shear test (slant shear and pull out) of lightweight concrete with regular concrete

for the retrofitting field of the construction industries. In addition, the researcher plans to perform different durability tests for the new LWHFRC. After completing the material level of the research, the researcher will test other beam loadings to satisfy the new mix design concrete for high-performance, lightweight concrete. This paper investigates the provision of two different fibers, steel, and PVA fiber, in hybrid form with multi-lightweight aggregate by adding all three mineral admixtures to develop high-strength and high-performance concrete. Analysis shows that performance enhancement was obtained by using fibers in the hybrid form. Hooked steel fibers with an aspect ratio of 40 and 80 and PVA fibers [24] with an aspect ratio of 800 were used in this research. The size of the normal coarse aggregate (NCA), sintered fly ash aggregate (SFA) of size 12.5 to 18 mm, and palm oil shell aggregate (POS) of 10 to 12.5 mm were used. This study achieved better lightweight concrete strength and high-performance hybrid fiber-reinforced concrete. The cost of lightweight concrete [25] was also reduced in this research. According to the cost analysis, the cost of LWHFRC increased by approximately 16.46%, while the strength increased by 55.98% compared to regular concrete in the same mix design without mineral admixture.

The mix design is based upon ACI-213 R-03 and ACI-211.2. In this research, 20 to 50% SFA and 10 to 30% POS gave better results. The higher volume of GGBS has a tremendous role in the high strength of concrete. Finally, ANOVA and regression analyses were performed to identify the lightweight hybrid fiber-reinforced [26–29] concrete (LWHFRC). The researcher modified the modulus of elasticity (E_c) with a compressive strength (f_c') formula for lightweight concrete and created a relationship equation between compressive strength and flexural strength (f_c' and f_{cb}), compressive strength and split tensile strength (f_c' and f_{spt}), flexural strength [30], and split tensile strength [31] (f_{cb} and f_{spt}) (ACI-318-05). The forthcoming paper will discuss hybrid fiber-reinforced lightweight concrete's bond strength and durability. In the next research phase, beam structural behavior parameters such as load-carrying capacity, ductility factor, stiffness, energy absorption capacity, and energy index will be evaluated.

The development of lightweight concrete without sacrificing performance or strength is a novel aspect of this study. This novel material alters design considerations and reduces the self-weight of the structure. This study will cover the numerous practical applications in civil engineering practices. Because of their overwhelming strength and performance, these innovative concrete composites may be used in earthquake-prone areas. Because sintered fly ash aggregate (SFA) and palm oil shell aggregate (POS) have regular and irregular shapes in structure, researchers had the brilliant idea of combining both totals with a high volume of cementitious materials without natural aggregate to achieve lightweight, high-performance concrete at a lower cost for bridge structures and high-rise building applications.

2. Materials and Methods

Twenty-four mix designs with varying volumes of steel and PVA fibers were prepared to investigate the effect of steel and PVA fibers on the properties of lightweight aggregate concrete. The volume fraction of steel fibers and PVA fibers in concrete ranged from 0% to 2%. Figure 1 depicts the raw materials with sizes. Figure 2 summarizes the fiber contents of all 18 assorted designs. All other parameters, such as cement content ($c = 600 \text{ kg/m}^3$), water/cement ratio ($w/c = 0.3$ to 0.35), superplasticizer dosage ($SP = 1\%$), and weight ratio of coarse lightweight aggregate to natural river sand ($LWA/S = 1.5$), remained constant across all mixtures. The water absorption of aggregates was determined within the mixing time, and the batch proportions were adjusted accordingly.

2.1. Material Properties

The properties of the materials are listed in Table 1 below. In this mix, two mineral admixtures with 10% silica fume and 35% GGBS by partial replacement of cement, two coarse aggregates such as SFA and POS without NCA, and two fibers such as steel fibers and PVA fibers of 0 to 2% fraction by volume to make hybrid fiber-reinforced con-

crete, 0.30 to 0.35 W/B ratio, with high volume cementitious materials around 600 kg/m³ are used.



Figure 1. Raw materials.

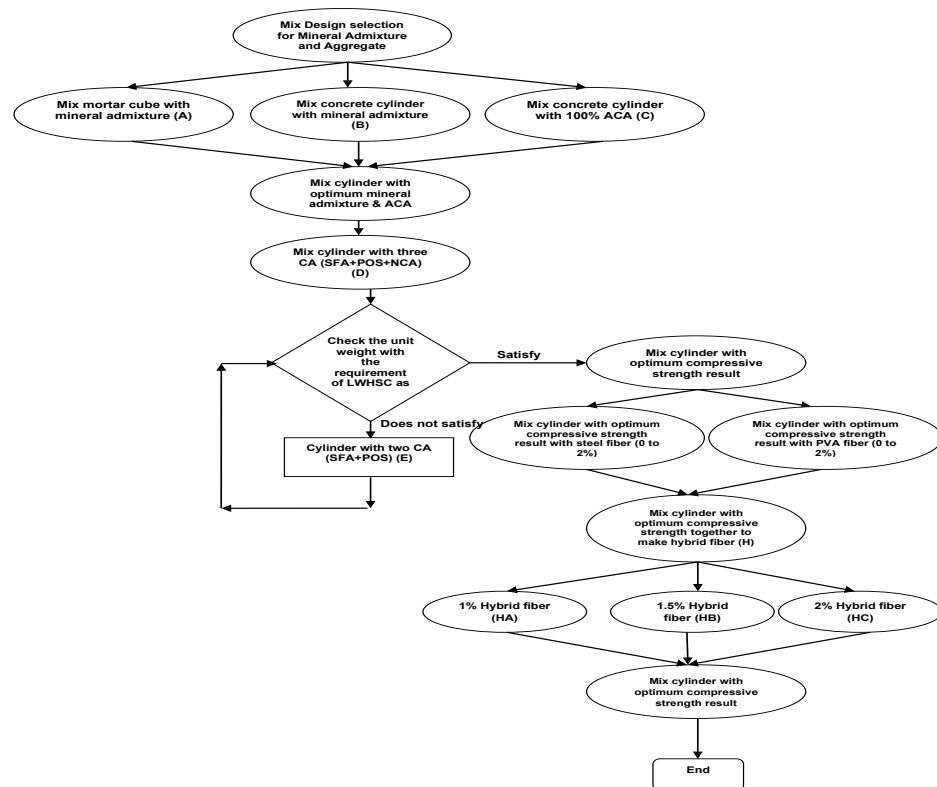


Figure 2. Flow chart of primary mix design.

Table 1. Mechanical properties of materials.

Materials	Mechanical Properties
Cement	53 grades, OPC
Silica fume	Self-compaction, but SP required
Fly ash	Class F, unit weight 1380 kg/m ³
GGBS	1000–1100 kg/m ³ (loose), 1200–1300 kg/m ³ (vibrated)
CA (NCA)	12 to 18 mm, an angular shape
CA (SFA)	12.5 to 18 mm, density 678 to 879 kg/m ³ , water absorption <10% for 24 h, round shape
CA (POS)	10 to 12.5 mm, density 610 to 860 kg/m ³ , water absorption < 15%, triangular shape
FA	Dune sand is 0.6 mm, and coarse sand is 4.75 mm
Water	Normal (pure)
SP	Sulfated naphthalene
Fiber—Steel	MS13/0.32 and MS16/0.2 of tensile strength 2800 MPa with an aspect ratio of 40 and 80
Fiber—PVA	6 mm and 12 mm with aspect ratio 800 and tensile strength 1500 MPa

2.2. Mix Proportion

The 24-mix design (E1 to E6, HA1 to Ha6, HB1 to HB6, and HC1 to HC6) used in this experiment is as follows. The quantity of the materials used in this experiment was calculated from that mixed design. The number of specimens in this experiment is 576 pieces divided into four series. All mixing and preparation of samples were performed at room temperature. The first series consists of a cylinder specimen (100 mm × 200 mm) for compressive strength. The second series consists of the flexural specimen (150 mm × 150 mm × 530 mm) for flexural strength, and the third series consists of a cylinder specimen (150 mm × 300 mm) for the split tensile strength of concrete. The fourth series consists of a cylinder specimen (100 mm × 200 mm) for the water absorption test. The volume fraction (V_f) of both the steel fiber and PVA fiber was also categorized in a hybrid form of 1% (HA series), 1.5% (HB Series), and 2% (HC Series). The amount of each material used in this experiment is shown in Tables 2 and 3. All the materials shown in Tables 2 and 3 are magnified with a 1.3 amplification factor for casting. According to the flow chart given in Figure 2, we decided on the mix design by ACI code 213 R-03 and ACI-211.2. The flow chart in Figure 2 depicts the complete summary of our research work mix design stage. The results of hybrid fiber-reinforced lightweight concrete (HA, HB, and HC Series) were only highlighted in this paper. In another article, the researcher attached the other results of individual fiber-reinforced lightweight concrete.

The fine and coarse aggregates were mixed in a concrete mixer for about 2 min before cement was added to the concrete mixtures. The ingredients were re-mixed until a uniform color was achieved. The steel fiber and PVA fiber were then gradually added to the mixture. The water had been split in half. The first half was added to the ingredients in the mixer and mixed for 2–3 min before adding the remaining water and superplasticizer. After that, the ingredients were mixed for another 2–3 min. The concrete was then poured into the molds and consolidated on a vibrator. The specimens were cured under laboratory conditions by covering them with a plastic sheet for 24 h, followed by wet curing. Figure 2 depicts a summary of casting details. Tables 2 and 3 also include a mix design summary for hybrid fiber-reinforced concrete and lightweight concrete.

2.3. Evaluation

The effect of partial/complete substitution of coarse artificial aggregate with POS on mechanical properties such as unit weight, compressive strength, flexural strength, split tensile strength, modulus of elasticity, water absorption test, and workability test was evaluated (slump cone).

Table 2. Mix design of hybrid fiber-reinforced concrete (kg/m³).

Mix	Cement	Silica Fume	Fly Ash	GGBS	CA (NCA)	CA (SFA)	CA (POS)	FA	Water	SP	Steel Fiber	PVA Fiber	Total
HA1	330.00	60.00	0.00	210.00	0.00	345.43	82.82	613.47	176.64	6.00	0.00	0.00	1824.35
HA2	330.00	60.00	0.00	210.00	0.00	345.43	82.82	613.47	176.64	6.00	9.12	9.12	1824.35
HA3	330.00	60.00	0.00	210.00	0.00	345.43	82.82	613.47	176.64	6.00	13.68	4.56	1824.35
HA4	330.00	60.00	0.00	210.00	0.00	345.43	82.82	613.47	176.64	6.00	4.56	13.68	1824.35
HA5	330.00	60.00	0.00	210.00	0.00	345.43	82.82	613.47	176.64	6.00	18.24	0.00	1824.35
HA6	330.00	60.00	0.00	210.00	0.00	345.43	82.82	613.47	176.64	6.00	0.00	18.24	1824.35
HB1	330.00	60.00	0.00	210.00	0.00	345.43	82.82	613.47	176.64	6.00	0.00	0.00	1824.35
HB2	330.00	60.00	0.00	210.00	0.00	345.43	82.82	613.47	176.64	6.00	9.12	18.24	1824.35
HB3	330.00	60.00	0.00	210.00	0.00	345.43	82.82	613.47	176.64	6.00	18.24	9.12	1824.35
HB4	330.00	60.00	0.00	210.00	0.00	345.43	82.82	613.47	176.64	6.00	22.80	4.56	1824.35
HB5	330.00	60.00	0.00	210.00	0.00	345.43	82.82	613.47	176.64	6.00	27.37	0.00	1824.35
HB6	330.00	60.00	0.00	210.00	0.00	345.43	82.82	613.47	176.64	6.00	0.00	27.37	1824.35
HC1	330.00	60.00	0.00	210.00	0.00	345.43	82.82	613.47	176.64	6.00	0.00	0.00	1824.35
HC2	330.00	60.00	0.00	210.00	0.00	345.43	82.82	613.47	176.64	6.00	9.12	27.37	1824.35
HC3	330.00	60.00	0.00	210.00	0.00	345.43	82.82	613.47	176.64	6.00	18.24	18.24	1824.35
HC4	330.00	60.00	0.00	210.00	0.00	345.43	82.82	613.47	176.64	6.00	27.37	9.12	1824.35
HC5	330.00	60.00	0.00	210.00	0.00	345.43	82.82	613.47	176.64	6.00	36.49	0.00	1824.35
HC6	330.00	60.00	0.00	210.00	0.00	345.43	82.82	613.47	176.64	6.00	0.00	36.49	1824.35

Table 3. Mix design of normal and lightweight concrete (kg/m³).

Mix	Cement	Silica Fume	Fly Ash	GGBS	CA (NCA)	CA (SFA)	CA (POS)	FA	Water	SP	Steel Fiber	PVA Fiber	Total
C1	600.00	0.00	0.00	0.00	1053.16	0.00	0.00	651.96	176.64	6.00	0.00	0.00	2487.76
C2	600.00	0.00	0.00	0.00	0.00	458.88	0.00	651.96	176.64	6.00	0.00	0.00	1893.48
C3	600.00	0.00	0.00	0.00	0.00	0.00	389.53	577.08	248.64	6.00	0.00	0.00	1821.25
E1	330.00	60.00	0.00	210.00	0.00	431.79	0.00	613.47	176.64	6.00	0.00	0.00	1827.89
E2	330.00	60.00	0.00	210.00	0.00	388.61	41.41	613.47	176.64	6.00	0.00	0.00	1826.12
E3	330.00	60.00	0.00	210.00	0.00	345.43	82.82	613.47	176.64	6.00	0.00	0.00	1824.35
E4	330.00	60.00	0.00	210.00	0.00	302.25	124.23	613.47	176.64	6.00	0.00	0.00	1822.58
E5	330.00	60.00	0.00	210.00	0.00	259.07	165.64	613.47	176.64	6.00	0.00	0.00	1820.81
E6	330.00	60.00	0.00	210.00	0.00	215.89	207.04	613.47	176.64	6.00	0.00	0.00	1819.04

2.3.1. Unit Weight

After 28 days of curing, three cylindrical concrete specimens measuring 100 mm in diameter and 200 mm in height were prepared from each concrete mixture to determine the unit weight. The specimens were air-dried for 48 h before being measured to ensure uniform moisture content. The weight-to-volume ratio was expressed as the unit weight of concrete. For each mixture, triplicate measurements were taken, and the average values were reported. Tables 2 and 3 provide information on unit weight.

2.3.2. Workability Test

Workability tests such as slump, compaction factor, and vee bee consistometer were performed on various lightweight concrete and lightweight hybrid fiber-reinforced concrete mixtures. Table 4 displays the results. A sulfated naphthalene-based superplasticizer was used in additional trials to improve the workability and cohesiveness of fresh concrete [32]. A superplasticizer content of 1% by mass of binder was used.

2.3.3. Slump Test

The slump test was carried out following ACI-C143/C143M 12. A 300 mm high frustum of a cone with a leveled surface was placed in the mold. The concrete was filled in three layers, with each layer tamped 25 times with a 16 mm steel rod with a rounded

nose. The top was not level, and the mold was firmly pressed against the slab base. The mold was gently lifted, and the decrease in concrete height was measured and recorded in Table 4 [32].

Table 4. Workability test results.

E Series (Without Fiber)—LWC				
Mix	Slump (mm)	Compaction Factor	Vee Bee Time in Seconds	Water Absorption %
E1/CS	270	0.89	8	2.5
E2	255	0.87	11	3.4
E3	240	0.8	13	3.7
E4	233	0.78	15	4.6
E5	210	0.77	18	5.3
E6	190	0.75	20	5.5
HA Series (With 1% Hybrid fiber)				
Mix	Slump (mm)	Compaction Factor	Vee Bee Time in Seconds	Water Absorption %
HA1/CS	240	0.8	13	3.7
HA2	201	0.83	14	4.5
HA3	192	0.71	15	4.9
HA4	180	0.79	17	7.6
HA5	173	0.76	20	8.2
HA6	165	0.71	22	9.5
HB Series (With 1.5% Hybrid fiber)				
Mix	Slump (mm)	Compaction Factor	Vee Bee Time in Seconds	Water Absorption %
HB1/CS	240	0.8	13	3.7
HB2	210	0.74	14	4.6
HB3	194	0.71	16	5.2
HB4	180	0.68	18	5.7
HB5	162	0.69	20	11.8
HB6	154	0.64	23	12.4
HC Series (With 2% Hybrid fiber)				
Mix	Slump (mm)	Compaction Factor	Vee Bee Time in Seconds	Water Absorption %
HC1/CS	240	0.8	13	3.7
HC2	206	0.87	11	2
HC3	192	0.8	13	3.5
HC4	180	0.78	15	4
HC5	168	0.65	21	6.2
HC6	140	0.67	23	13.7

2.3.4. Compaction Factor Test

The compacting factor test was performed following ACI-C143/C143M-12 using a compacting factor test apparatus. The top hopper was filled gently with concrete, while the bottom hopper was kept closed. The top hopper was opened, and the concrete fell from the upper to the lower hopper and then from the lower hopper to the mold. Table 4 summarizes the test values. The density of partially compacted concrete was divided by the density of fully compacted concrete to determine the degree of compaction.

2.3.5. Vee Bee Time Test

The vee bee time apparatus measured the workability of concrete as per ACI-C143/C143M-12. The time required for the complete remolding of concrete was measured. The vee bee times are tabulated in Table 4 [32].

2.3.6. Water Absorption Test

At 28 days of curing, the cylinder samples were tested for water absorption capacity. First, the dry masses of concrete specimens were saturated in the water basin for 28 days in the methodology. Following that, the saturated concrete samples were reweighed, and the soaked mass of the samples was subtracted from the dry mass to determine the mass of water absorption and thus the percentage of water absorption relative to dry mass. The rates of water absorption by the sample cylinder specimen are shown in Table 4 [32].

2.3.7. Cylinder Compressive Strength Test

The cylinder compressive strength test was performed on the 100 mm diameter and 200 mm high cylinder specimens at the ages of 7 and 28 days, respectively, using a 100-ton capacity compression testing machine following ACI-C39/C39M-20 [32].

2.3.8. Split Tensile Strength Test

The split tensile strength test is an indirect tensile strength test for cylindrical specimens. Splitting tensile strength tests were performed at 28 days for concrete cylinder specifications of 150 mm in diameter and 300 mm in length, using an ASTM-C496 [33]. Figure 6 depicts the test specimen. The load was applied gradually until the specimen split and readings were noted.

The splitting tensile strength was estimated after 28 days by using the following relationship:

$$f_{\text{spt}} = 2P / \pi ld$$

where

f_{spt} = splitting tensile strength of the specimen (MPa);

P = maximum load applied to specimen (N).

l = length of the specimen (mm).

d = cross-sectional diameter of the specimen (mm).

2.3.9. Flexural Strength Test

A flexural strength test was performed on the 150 mm × 150 mm × 530 mm beam specimen at 28 days using a 50-ton capacity universal testing machine by subjecting the specimen to four-point bending to determine the flexural strength as per ASTM C 1609 M. The flexural strength was calculated using the result analysis and test configuration formula.

3. Results and Discussion

3.1. Unit Weight

As a substitute for SFA, the unit weight of concrete specimens prepared with varying amounts of POS is used. In Tables 2 and 3, these values ranged from 1819 to 2487 kg/m³. The unit weight of concrete from the C1 to C3 series was used to replace NCA, SFA, and POS completely. However, the unit weights of C2 and C3 fell within the ACI 213 R-03 lightweight concrete criteria. The E1 to E6 series were also within the light concrete unit weight range of 1819–1828 kg/m³.

3.2. Workability and Water Absorption Test

Fresh concrete is usable when it can be easily transported, placed, compacted, and finished without segregation. Slump tests were performed on concrete with lightweight aggregate from E1 to E6 as lightweight concrete (LWC) and HA to HC series as lightweight hybrid fiber-reinforced concrete (LWHFRC) to determine comparable workability. Before the fresh concrete specimens were cast in the molds, four batches of all concrete types were tested for workability. Table 4 displays the test results for the average slump of control lightweight concrete and all LWHFRC concretes. The average slump flow diameter (E3—without fiber) was 51 cm, with a slump height of 24.2 cm, as shown in Figures 3a and 3b, respectively.



Figure 3. Slump cone test (height = 24.2 cm and slump flow diameter = 51 cm).

At 28 days of curing, the cylinder samples were tested for water absorption capacity. First, the dry masses of concrete specimens were saturated in a water basin for 28 days. Following that, the saturated concrete samples were reweighed. Finally, the soaked mass of the samples was subtracted from the dry mass to determine the mass of water absorption and, thus, the percentage of water absorption relative to dry mass. Table 4 shows the rates of water absorption by a cylinder specimen sample. Because of the hydrophilic nature of fiber and the larger interfacial area between the fiber and the matrix, water absorption increased gradually as fiber content increased.

3.3. Compressive Strength

(a) E Series (LWC)

Table 5 shows the cylinder compressive strength of LWC (lightweight concrete) and LWHFRC (lightweight hybrid fiber-reinforced concrete) at 7 and 28 days. At 28 days, the compressive strengths (E1-E6) of LWC were increased by 80.44%, 61.53%, 55.99%, 11.83%, 18.78%, and 4.93%, respectively, when compared to control concrete (C1). At 28 days, the compressive strength of 100% SFA (E1) was 64.145 MPa, nearly as high as the other results in this series. The scores for 90% SFA + 10% POS (E2) and 80% SFA + 20% POS (E3) were 57.425 and 55.453, respectively. So, for this next stage, the researcher used the E3 series to keep the unit weight below the lightweight criteria (below 1850 kg/m^3) set by ACI-213 R-03 and developed a strong bond between irregular triangular coarse aggregate (POS) and regular circular coarse aggregate (SFA) at a 1:4 ratio (POS: SFA). Figure 4 shows the cylinder compressive strength test with LVDT. Figure 5a graph shows the compressive strength of concrete without fiber.

(b) HA Series (1% Hybrid Fiber)

At the age of 28 days, the compressive strengths (HA1-HA6) of LWHFRC (1% hybrid fiber) were increased by 55.99%, 57.96%, 64.44%, 57.48%, 69.97%, and 47.50%, respectively, when compared to control concrete (C1). At 28 days, the compressive strength of 1% steel fiber (HA5) was 60.425 MPa, nearly as high as the other results. Figure 5b graph shows the compressive strength of concrete with 1% hybrid fiber.

(c) HB Series (1.5 % Hybrid)

At the age of 28 days, the compressive strengths (HB1-HB6) of LWHFRC (1.5% hybrid fiber) were increased by 55.99%, 56.24%, 67.59%, 78.58%, 86.34%, and 23.42%, respectively, when compared to control concrete (C1). At 28 days, the compressive strength of 1.5% steel fiber (HB5) was 66.245 MPa, nearly as high as the other results in this series. Figure 5c graph shows the compressive strength of concrete with 1.5% hybrid fiber.

(d) HC Series (2% Hybrid)

At the age of 28 days, the compressive strengths (HC1-HC6) of LWHFRC (2% hybrid fiber) were increased by 55.99%, 56.24%, 58.81%, 75.63%, 95.29%, and 5.85% (-ve), respec-

tively, when compared to control concrete (C1). At 28 days, the compressive strength of 2% steel fiber (HC5) was 69.425 MPa, nearly as high as other results in this series. Figure 5d graph shows the compressive strength of concrete with 2% hybrid fiber.

Table 5. A mix of unit weight ≤ 1825 kg/m³ fc' (MPa) without fiber.

Mix	7 Days		28 Days		% Increase Strength	
	fc'	σ	fc'	σ	7 Days	28 Days
E1	43.37	5.25	64.15	3.26	72.66	80.44
E2	38.43	5.41	57.43	5.43	52.97	61.53
E3	37.85	3.09	55.45	4.82	50.69	55.99
E4	28.52	5.24	39.75	3.5	13.53	11.83
E5	25.93	4.07	42.23	2.77	3.24	18.78
E6	22.89	3.03	37.30	2.05	−8.88	4.93
Mix of 1% Hybrid Fiber fc' (MPa)						
Mix	7 Days		28 Days		% Increase Strength	
	fc'	σ	fc'	σ	7 Days	28 Days
HA1	37.85	1.77	55.45	3.73	50.69	55.99
HA2	35.43	2.95	56.16	7.60	41.02	57.96
HA3	42.58	9.59	58.46	7.56	69.50	64.44
HA4	39.75	4.75	55.98	1.80	58.26	57.48
HA5	42.49	3.93	60.43	4.96	69.14	69.97
HA6	37.15	2.53	52.44	2.41	47.87	47.50
Mix of 1.5% Hybrid Fiber fc' (MPa)						
Mix	7 Days		28 Days		% Increase Strength	
	fc'	σ	fc'	σ	7 Days	28 Days
HB1	37.85	2.14	55.45	2.90	50.69	55.99
HB2	37.43	3.78	55.55	3.81	48.98	56.24
HB3	40.85	5.11	59.58	4.20	62.63	67.59
HB4	43.28	4.53	63.49	2.20	72.29	78.58
HB5	43.58	2.35	66.25	1.57	73.47	86.34
HB6	27.42	3.85	43.88	7.60	9.17	23.42
Mix of 2% Hybrid Fiber fc' (MPa)						
Mix	7 Days		28 Days		% Increase Strength	
	fc'	σ	fc'	σ	7 Days	28 Days
HC1	37.85	2.25	55.45	2.84	50.69	55.99
HC2	37.43	3.17	55.55	2.69	49.00	56.24
HC3	38.62	2.28	56.46	4.38	53.76	58.81
HC4	41.87	3.93	62.44	4.92	66.68	75.63
HC5	48.66	8.27	69.43	3.86	93.70	95.29
HC6	22.43	2.13	33.47	2.17	−10.72	−5.85
C1—Control Specimen $fc' = 25.12$ MPa (7 Days) and 35.55 MPa (28 Days)						



Figure 4. Cylinder compressive strength test with LVDT.

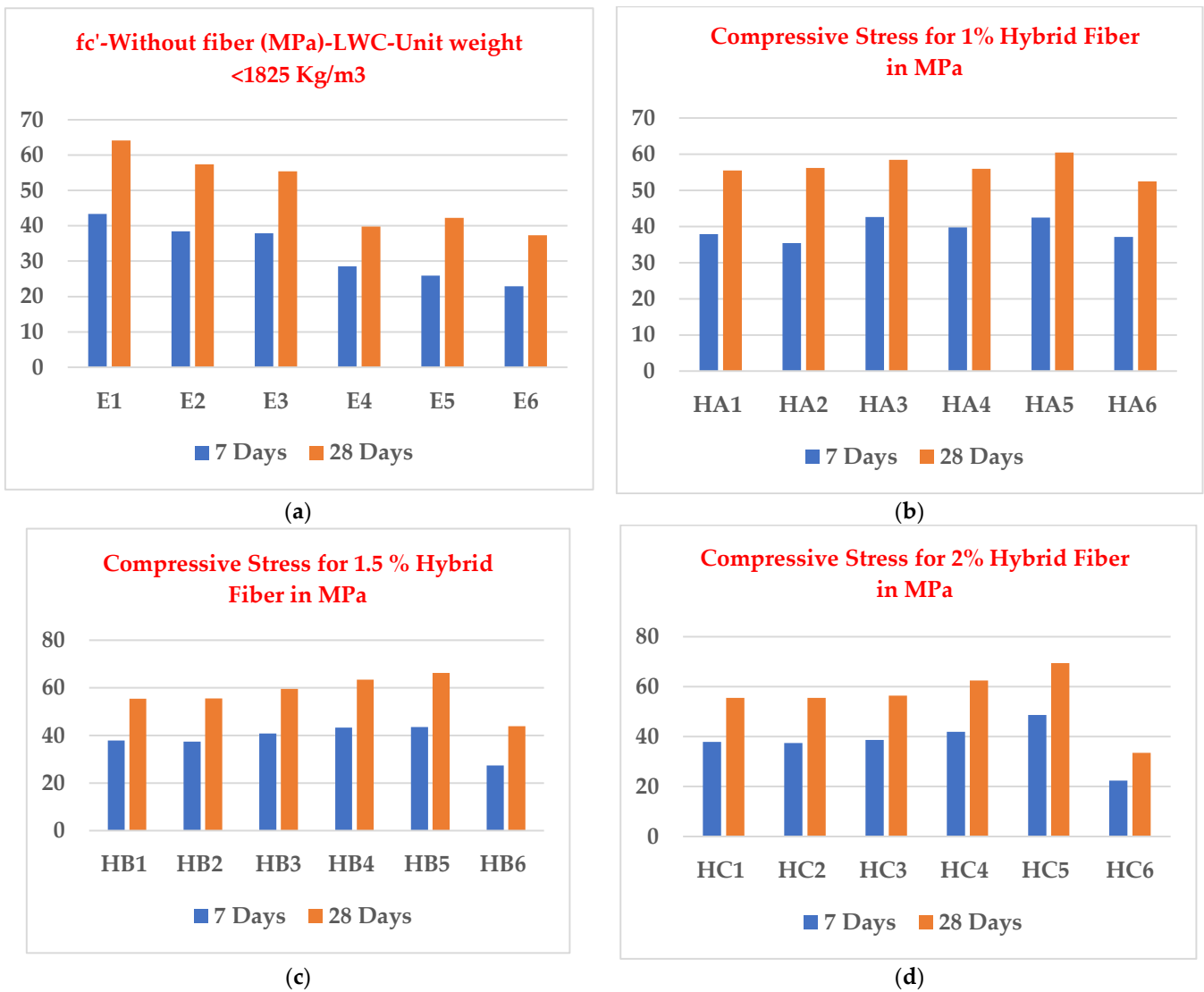


Figure 5. Compressive strength of concrete with different fiber contents.

3.4. Split Tensile Strength Test

At 7 and 28 days, the split tensile strength of the concrete specimens was determined.

Table 6 summarizes the average test results of the split tensile strength in their specified curing periods of 7 and 28 days. Figure 6 shows the split tensile test of the cylinder specimen.

Table 6. Experimental results for f_c' , f_{cb} , f_{spt} , and E_c .

Mix Stage	7 Days				28 Days			
	f_c' (MPa)	f_{cb} (MPa)	f_{spt} (MPa)	E_c (GPa)	f_c' (MPa)	f_{cb} (MPa)	f_{spt} (MPa)	E_c (GPa)
HA1	37.85	7.81	7.59	21.96	55.45	11.09	10.82	24.96
HA2	35.43	8.12	7.95	22.15	56.15	11.65	11.28	25.12
HA3	42.58	8.15	8.16	22.54	58.45	11.76	11.54	25.63
HA4	39.75	7.84	7.68	22.01	55.98	11.23	10.85	25.08
HA5	42.49	9.23	8.71	23.12	60.42	12.91	12.35	26.06
HA6	37.15	8.11	7.10	21.32	52.43	11.56	10.21	24.27
HB1	37.85	7.81	7.59	22.93	55.45	11.09	10.82	24.96
HB2	37.43	8.05	7.65	21.97	55.54	11.57	10.93	24.98
HB3	40.85	8.42	8.49	22.77	59.57	12.43	12.13	25.87
HB4	43.28	8.72	8.64	23.53	63.48	12.69	12.34	26.71
HB5	43.58	9.64	9.62	23.95	66.24	13.48	13.35	27.28
HB6	27.42	6.72	7.04	19.47	43.87	9.56	10.05	22.20
HC1	37.85	7.81	7.59	21.93	55.45	11.09	10.82	24.96
HC2	37.43	7.82	7.87	22.10	56.12	11.23	11.21	25.11
HC3	38.62	8.25	7.96	22.13	56.45	11.85	11.34	25.19
HC4	41.87	8.63	8.67	23.27	62.43	12.49	12.34	26.49
HC5	48.66	9.71	9.84	24.50	69.42	13.96	13.85	27.93
HC6	22.43	6.75	7.22	21.20	51.54	9.53	10.45	24.07



Figure 6. Split tensile test of the cylinder.

3.5. Flexural Strength Test

The concrete specimens' flexural strength was measured after 7 and 28 days. Table 6 summarizes the average flexural strength test results in their specified curing periods of 7 and 28 days. Figure 7 shows the flexural test of the beam specimen.

Finally, we concluded that adding a certain percentage of fiber in concrete increased the specimen's compressive, tensile, and flexural strength since the randomly oriented fibers arrest a microcracking mechanism and limit crack propagation, thus improving stability and elasticity.



Figure 7. Flexural test of beam specimen (four-point loading).

3.6. Relationship between Compressive Strength (f_c') Test and Modulus of Elasticity Test

According to ACI 318-19, the modulus of elasticity was calculated by the following formulas:

$$E_c = 0.043 \times W_c^{1.5} \times \sqrt{f_c'} \text{ (in MPa)} \dots\dots\dots \text{Lightweight Concrete}$$

$$E_c = 4700 \times \sqrt{f_c'} \text{ (in MPa)} \dots\dots\dots \text{Normal Concrete}$$

Figure 8 depicts that the cylinder compressive strength and modulus of elasticity of LWHFRC are closely related. The relationship was discovered to be as follows:

$$E_c = 3.3525 f_c'^{0.5}$$

$$R^2 = 1$$

We concluded from Figure 8 that our current study’s LWHFRC regression value is close to 1, and the present study graph is close to LWC ACI 318-05. The LWC graph is higher than the normal concrete graph of E_c and f_c' .

3.7. Relationship between Flexural Strength (f_{cb}) and Split Tensile Strength (f_{spt}) Test

Figure 9 shows that the cylinder split tensile strength and beam flexural strength of LWHFRC are related. The relationship was discovered to be as follows:

$$f_{cb} = 0.9782 f_{spt}^{1.0175}$$

$$R^2 = 0.8426$$

We also concluded from Figure 9 that our current study’s LWHFRC regression value is close to 0.8426, and the present study graph was similar to a normal concrete ACI 318-14 graph. However, the other normal concrete relationship graphs were higher than the current study graph [33–35].

3.8. Relationship between Split Tensile Strength (f_{spt}) Test and Compressive Strength (f_c') Test

Figure 10 shows that the cylinder split tensile strength and compressive strength of LWHFRC are closely related. The relationship was found to be as follows:

$$f_{spt} = 0.4309 f_c'^{0.8103} \tag{1}$$

$$R^2 = 0.8875 \tag{2}$$

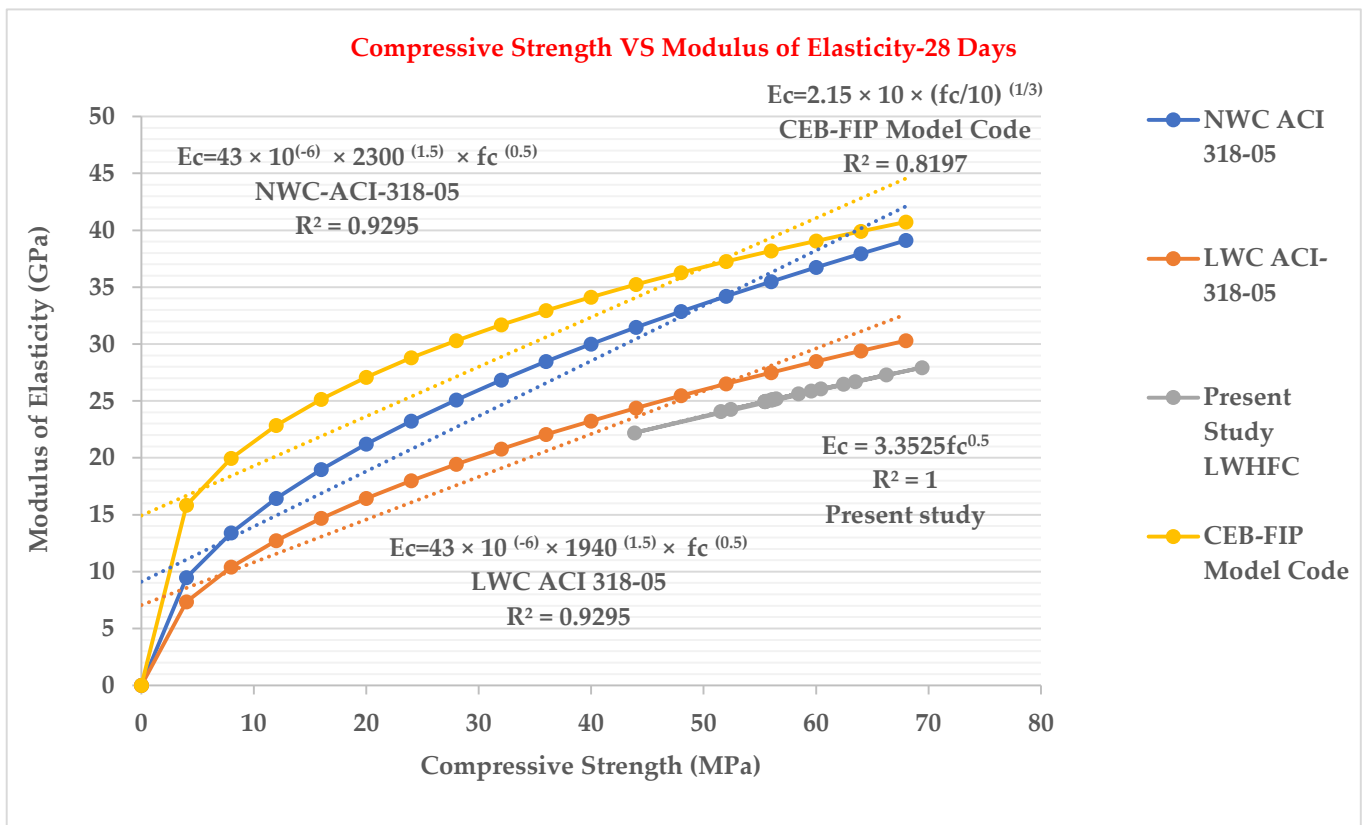


Figure 8. Relation between compressive strength and modulus of elasticity.

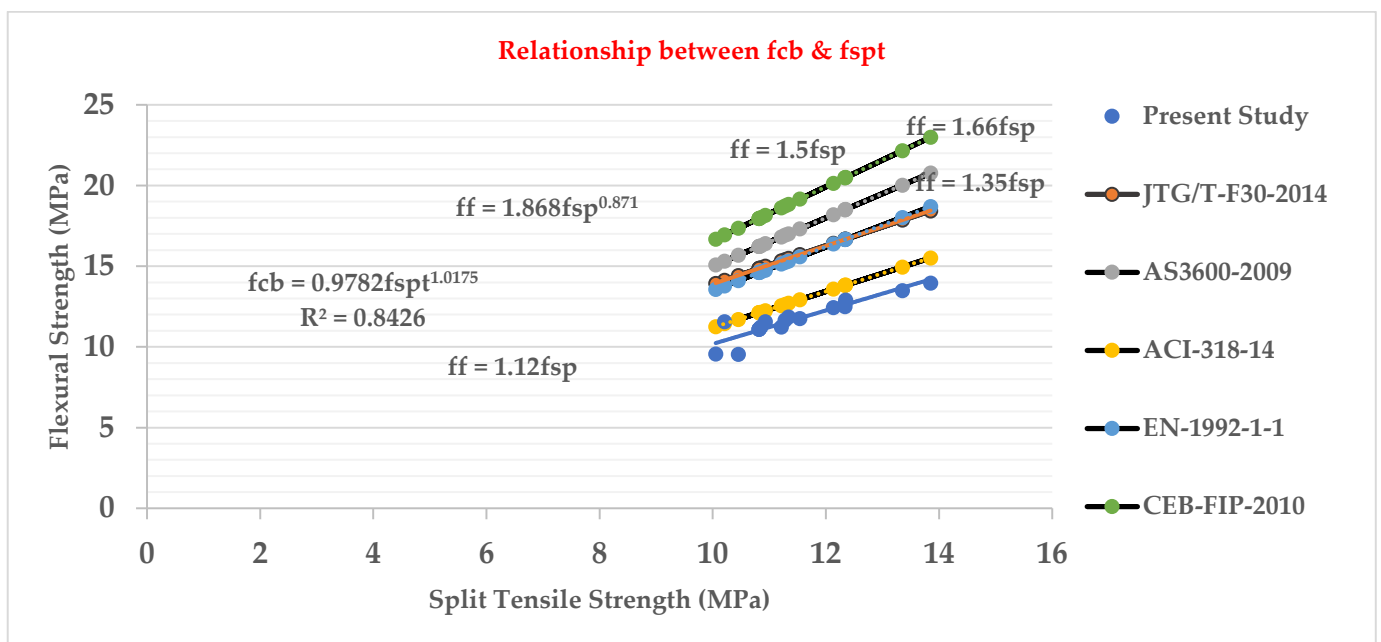


Figure 9. Relation between flexural strength and split tensile strength.

From Figure 10, we also concluded that our present study’s LWHFRC regression value is nearly 0.8875, and the present study graph was too much higher than other graphs for normal concrete [33–35].

3.9. Relationship between Flexural Strength (f_{cb}) Test and Compressive Strength (f_c') Test

Figure 11 shows that the beam flexural strength and compressive strength of the cylinder of LWHFRC are closely related. The relationship was found to be as follows:

$$f_{cb} = 0.2984 f_c'^{0.9062}$$

$$R^2 = 0.868$$

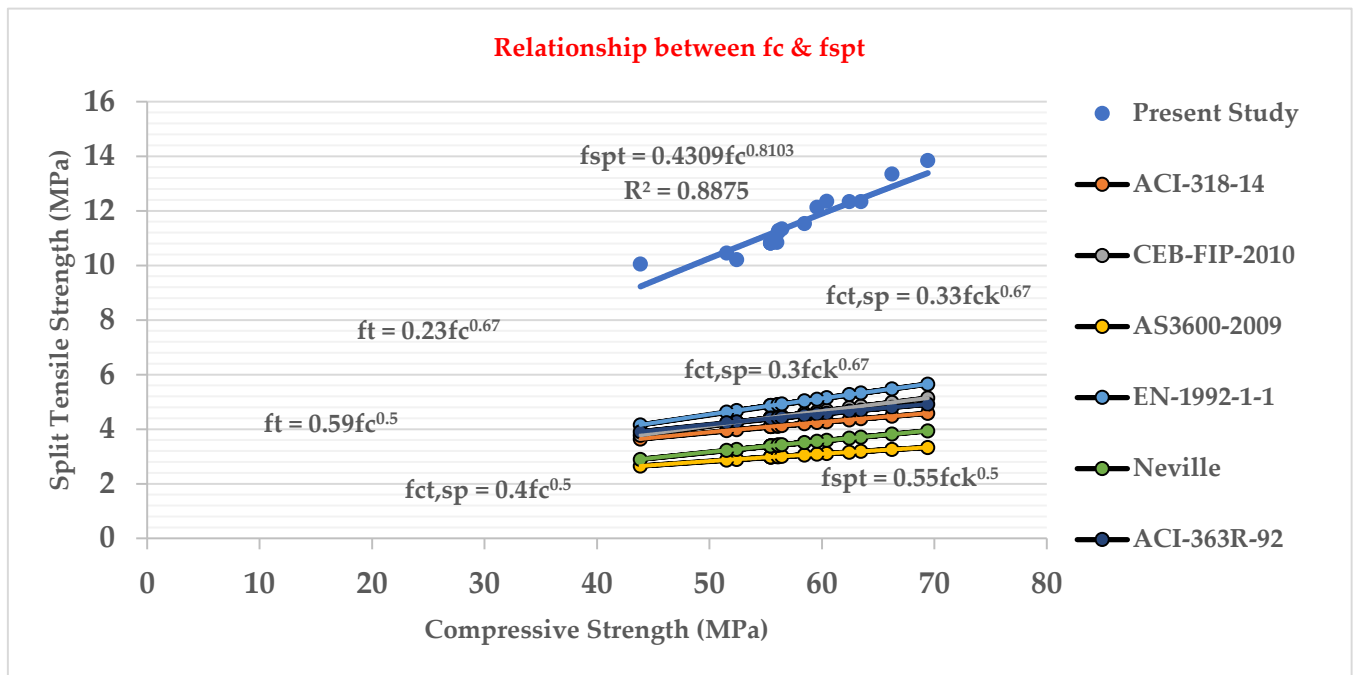


Figure 10. Relation between split tensile strength and compressive strength.

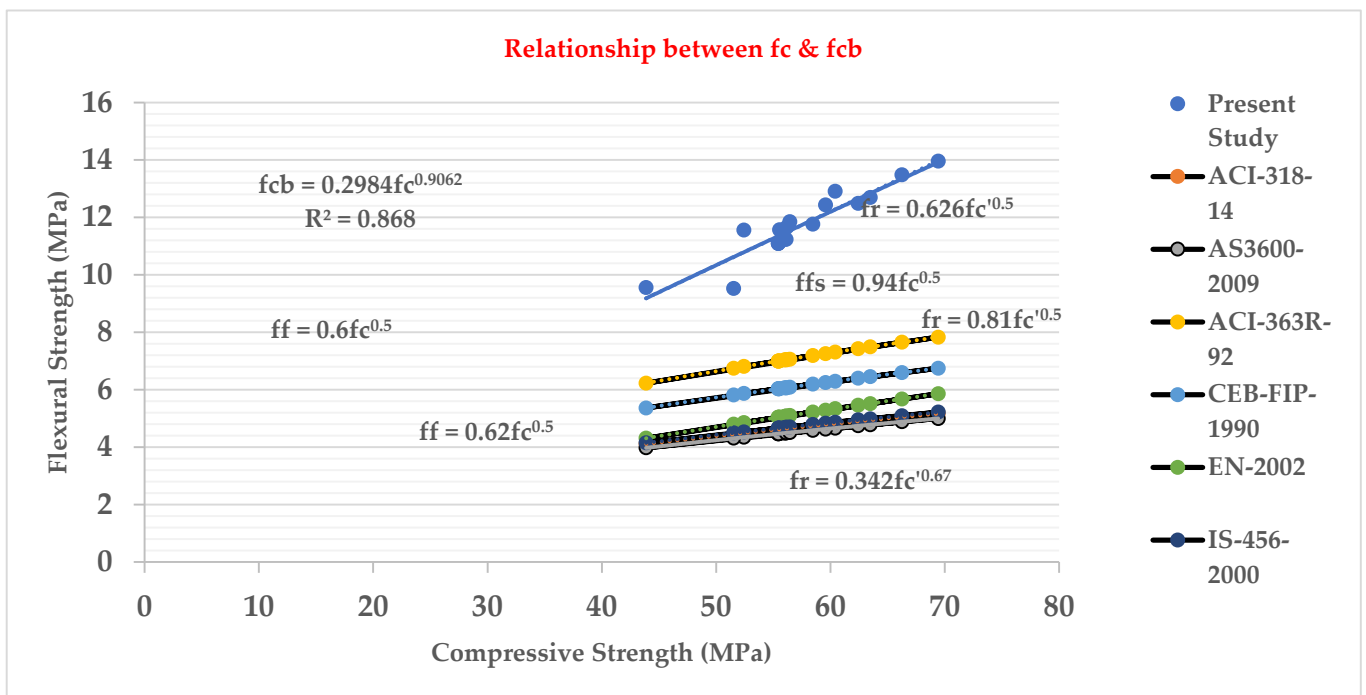


Figure 11. Relation between flexural strength and compressive strength.

From Figure 11, we also concluded that our present study's LWHFRC regression value is nearly 0.868, and the present study graph was too much higher than other graphs for normal concrete [33–35].

3.10. Cost Analysis Report

From Tables 7–9, we concluded that if the concrete cost was increased by 16.46%, strength increased by around 55.98%; however, unit weight decreased by about 26.67%.

Table 7. C-1-100%—normal concrete in NTD.

Material	Unit Volume (m ³)	Quantity (kg/m ³)	Price/Ton	Total Cost (NTD)
Cement	0.19	600.00	5500.00	3300.00
Sand (FA)	0.25	651.96	450.00	293.38
NCA	0.38	1053.17	450.00	473.92
SFA	0.00	0.00	0.00	0.00
POS	0.00	0.00	0.00	0.00
Silica Fume	0.00	0.00	0.00	0.00
GGBS	0.00	0.00	0.00	0.00
Fly Ash	0.00	0.00	0.00	0.00
SP	0.01	6.00	0.00	0.00
Water	0.18	176.64	100.00	17.66
Total Quantity		2487.76		4084.97

Table 8. E-3 lightweight high strength concrete (80% SFA + 20% POS) in NTD.

Material	Unit Volume (m ³)	Quantity (kg/m ³)	Price/Ton	Total Cost (NTD)
Cement	0.10	330.00	5500.00	1815.00
Sand (FA)	0.23	613.47	450.00	276.06
NCA	0.00	0.00	450.00	0.00
SFA	0.28	345.43	350.00	120.90
POS	0.07	82.82	5600.00	463.79
Silica Fume	0.02	60.00	30000.00	1800.00
GGBS	0.09	210.00	1200.00	252.00
Fly Ash	0.00	0.00	800.00	0.00
SP	0.01	6.00	2000.00	12.00
Water	0.18	176.64	100.00	17.66
Total Quantity		1824.36		4757.42

NCA—normal coarse aggregate, NTD—New Taiwan Dollar

Table 9. Cost comparison results in NTD (New Taiwan dollar).

Mix	Unit Weight (kg/m ³)	Cost (NTD)	Fc' (MPa)	Increment Cost	Increment Strength	Decrease Unit Weight
C1 (NC)	2487.76	4084.97	35.55			
E3 (LWC)	1824.36	4757.42	55.45	16.46%	55.98%	26.67%

3.11. Scanning Electron Microscopy (SEM), EDS Analysis, EDS Mapping, XRD

(a) XRD Report

The SFA peak was higher than fly ash and silica fume peaks [36,37]. Figure 12 shows the XRD report.

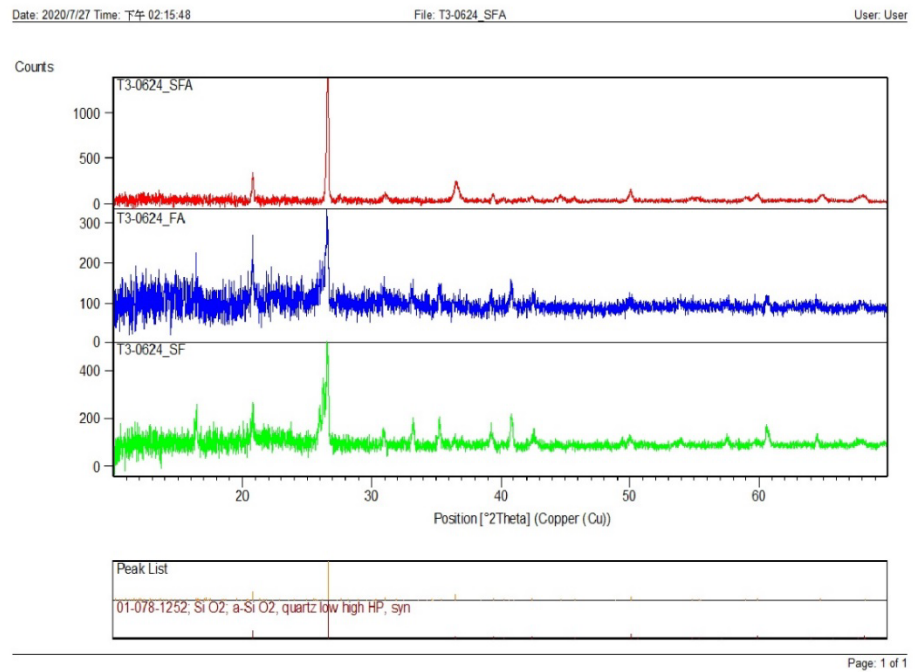


Figure 12. XRD report.

(b) EDS Analysis

According to the EDS analysis report from Table 10, carbon was 55.39%, oxygen was 33.64%, and silicon was 4.82% [36,37]. Figure 13 shows the EDS analysis report.

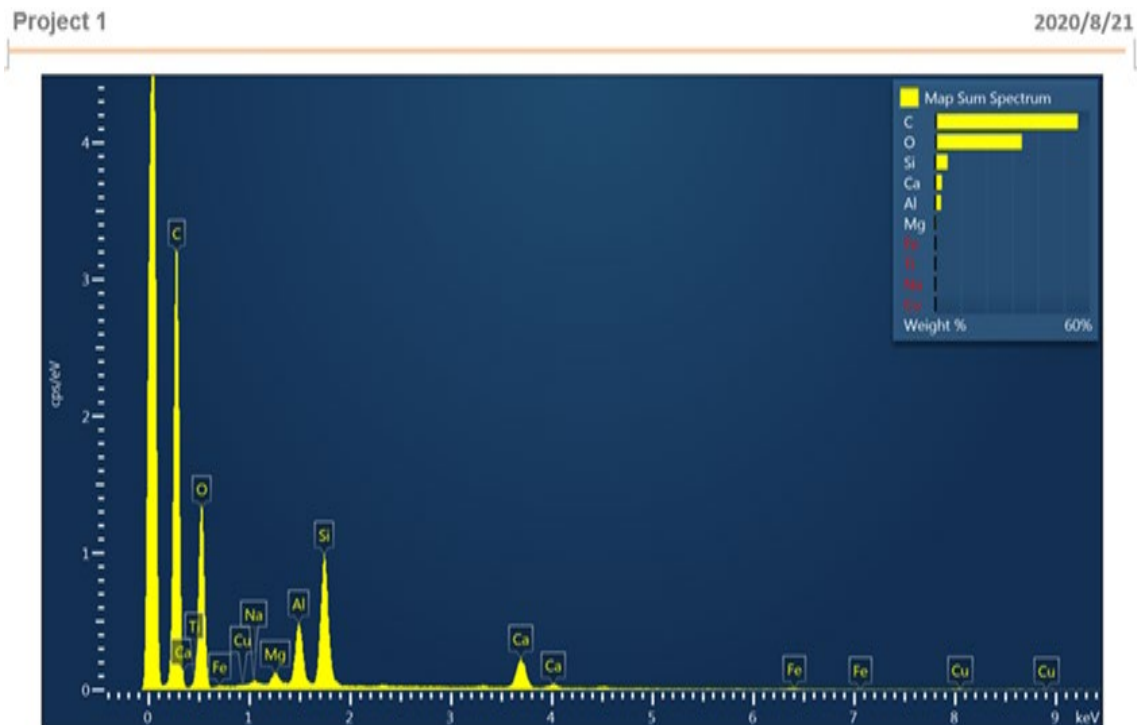


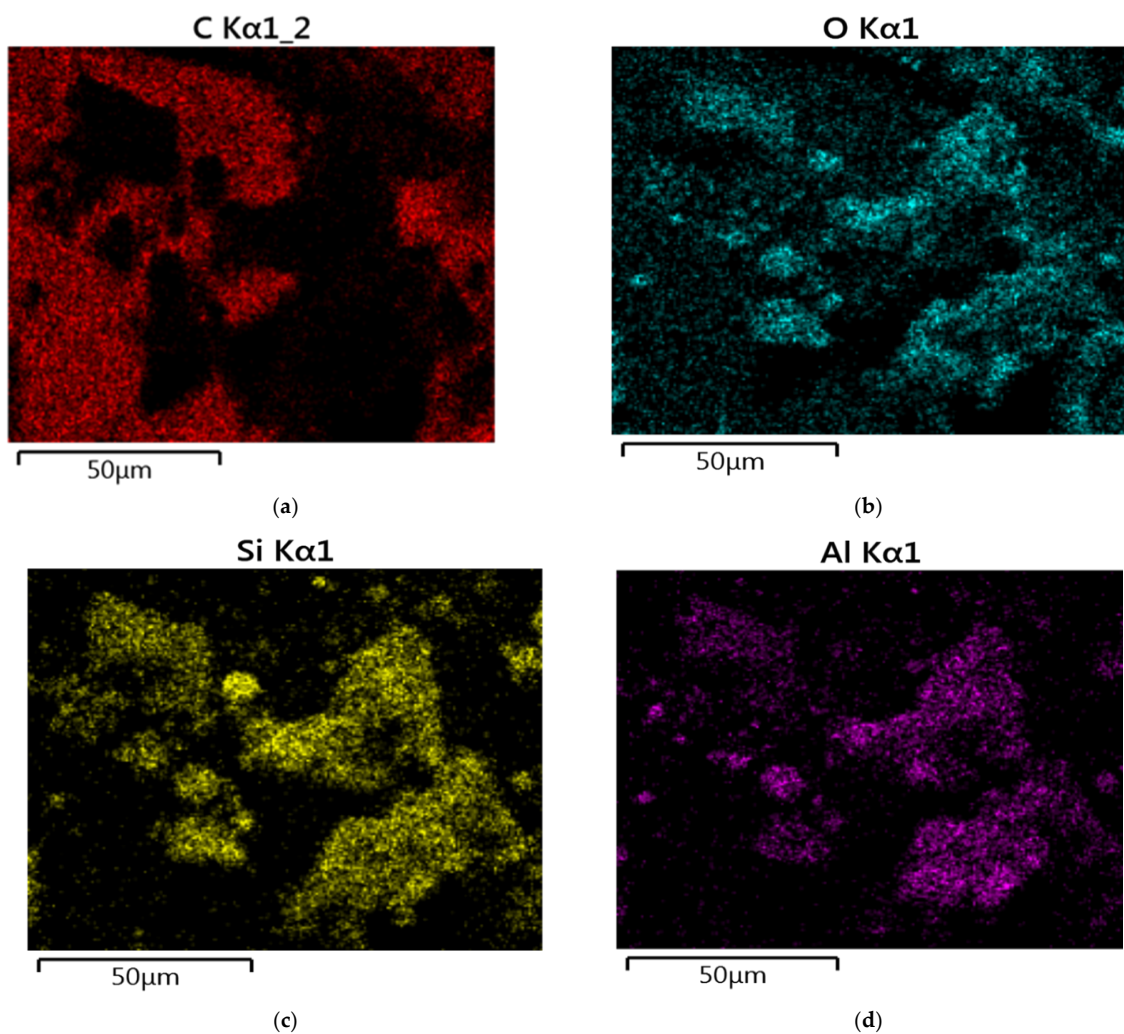
Figure 13. EDS analysis.

Table 10. EDS Analysis Report.

Elements	Weight %
C	55.39
O	33.64
Na	0.18
Mg	0.43
AL	2.27
Si	4.82
Ca	2.6
Ti	0.26
Fe	0.33
Cu	0.08
Total	100

(c) SEM Report

The SEM image in Figure 14a below showed that the carbon image is much brighter than the other image since the carbon content is greater than that of other chemicals. Similarly, in Figure 14b–f, the percentages of oxygen, silicon, aluminum calcium, and boron are simultaneously lesser; therefore, the image of oxygen, silicon, aluminum, calcium, and boron are less bright than that of carbon [36,37].

**Figure 14.** Cont.

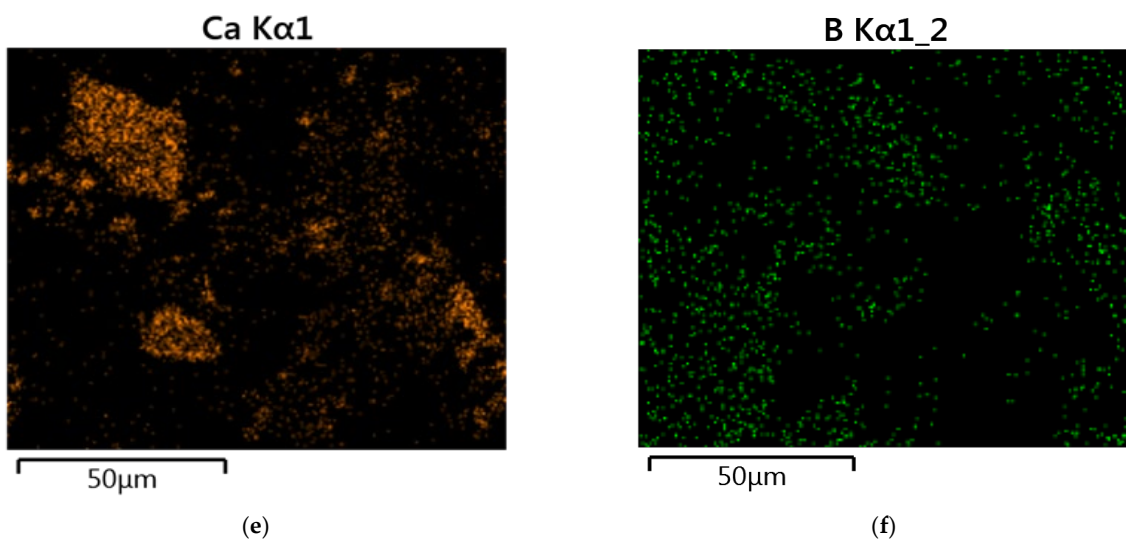


Figure 14. SEM image.

(d) SEM Report—EDS mapping

Morphological characteristics were found by using the JEOL-IT-100 instrument. It gives the direct result of the significant depth of field [36,37]. Figures 15 and 16 show the SEM image and EDS mapping on a 10 μm scale and 100 μm scale, respectively.

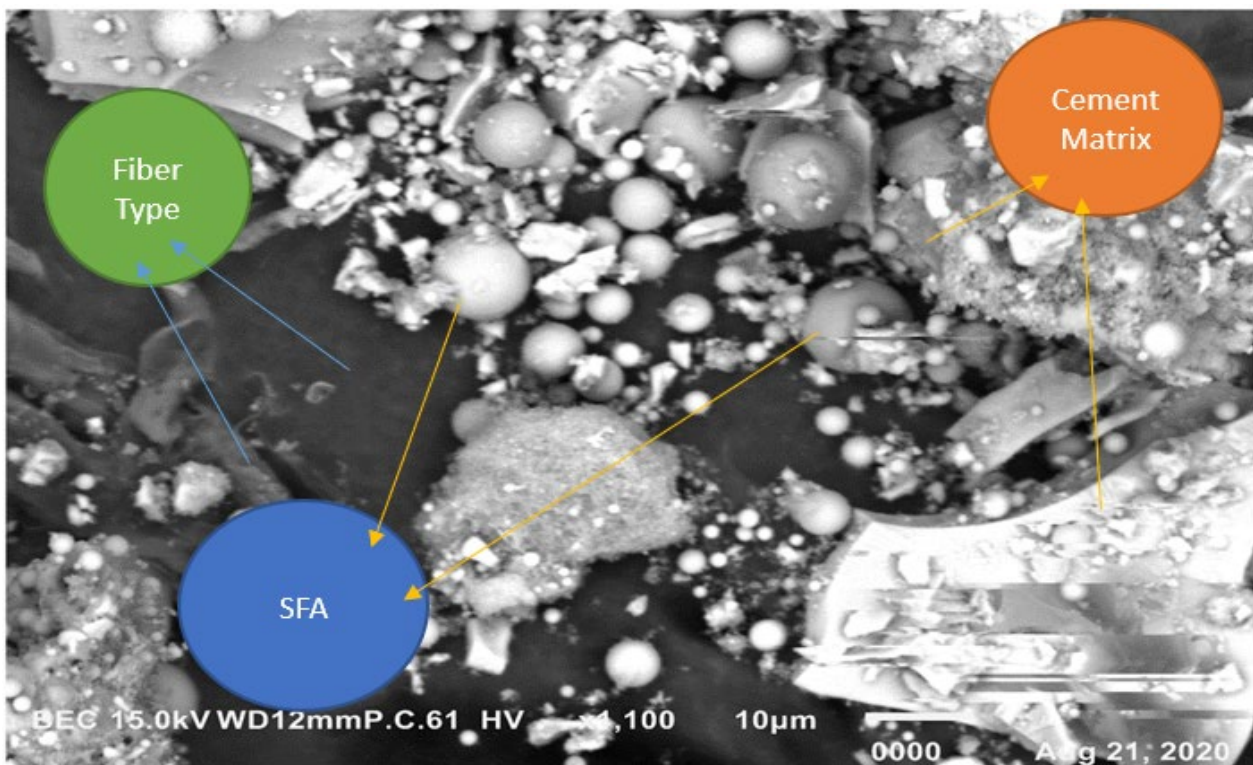


Figure 15. SEM image—EDS mapping on a 10 μm scale.

3.12. ANOVA and Regression Analysis for Bulk Density, Water Absorption, Slump, and Compressive Strength of Lightweight Concrete and Lightweight Hybrid Fiber-Reinforced Concrete

The ANOVA and regression analysis confirmed whether our findings were significant or not. The summary of ANOVA and regression analysis are shown in Table 11. The ANOVA and regression results are shown in Tables 12 and 13, respectively. According to

the ANOVA analysis, results are significant if F statistics are greater than F critical values. ANOVA results are significant if the *p*-value is less than 0.05. The bulk density ANOVA analysis [38–40] for lightweight concrete was insignificant, but there was significance within SFA, POS, and LWC. Water absorption was significant between light concrete stages but not between lightweight hybrid fiber-reinforced concrete sets. Slumps were not substantial between lightweight concrete stages but were significant within the lightweight hybrid fiber-reinforced concrete stages. The difference in compressive strength for lightweight concrete was insignificant. Furthermore, there was no significance within light hybrid fiber-reinforced concrete stages.

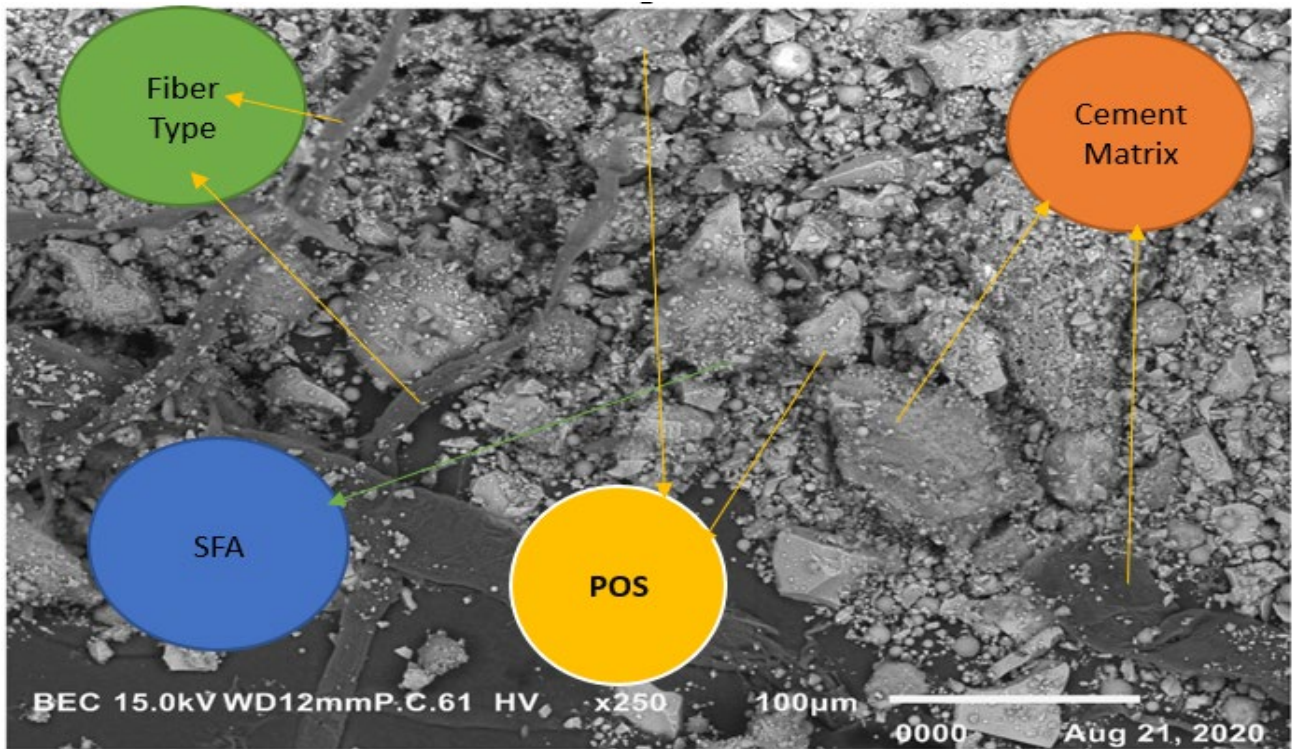


Figure 16. SEM image—EDS mapping on a 100 μm scale.

Table 11. Summary of ANOVA analysis—LWHFRC.

	Bulk Density	Water Absorption	Slump	Compressive Strength
Row (Between Group)	Insignificant	Significant	Significant	Insignificant
Column (Within Group)	Significant	Insignificant	Insignificant	Insignificant
Summary Of Regression Analysis—LWHFRC				
	Bulk Density	Water Absorption	Slump	Compressive Strength
Column (Within Group)	Significant	Significant	Significant	Insignificant
Column (Within Group)	Significant	Significant	Significant	Insignificant
Column (Within Group)	Significant	Significant	Significant	Insignificant

Table 12. ANOVA for bulk density—E series (POS, SFA, LWC).

Source of Variation	SS	DF	MS	F	p-Value	F Crit
Rows (Between Group)	73.06899	5	14.6138	0.002334	0.999999	3.32585
Columns (Within Group)	10,511,267	2	5,255,633	839.347	7.28×10^{-12}	4.10281
Error	62,615.74	10	6261.574			
Total	10,573,956	17				

ANOVA for Water Absorption—LWHFRC						
Source of Variation	SS	DF	MS	F	p-value	F crit
Rows (Between Group)	161.3783	5	32.27567	11.13594	0.000783	3.325835
Columns (Within Group)	8.843333	2	4.421667	1.525589	0.26409	4.102821
Error	28.98333	10	2.898333			
Total	199.205	17				

ANOVA for Slump						
Source of Variation	SS	DF	MS	F	p-value	F crit
Rows	14,160.5	5	2832.1	77.45032	1.15×10^{-7}	3.325835
Columns	52.33333	2	26.16667	0.715588	0.512325	4.102821
Error	365.6667	10	36.56667			
Total	14,578.5	17				

ANOVA for fc' —Lightweight Hybrid Fiber-Reinforced Concrete						
Source of Variation	SS	DF	MS	F	p-value	F crit
Rows (Between Group)	826.0872	5	165.2174	6.623388	0.005707	3.325835
Columns (Within Group)	10.83689	2	5.418447	0.21722	0.808452	4.102821
Error	249.4455	10	24.94455			
Total	1086.37	17				

Table 13. Regression for bulk density.

Factors	R Square	Adjusted R Square	DF	F	Significance F
POS	1	1	1	5.94355×10^{32}	1.69848×10^{-65}
SFA	1	1	1	3.11206×10^{31}	6.19518×10^{-63}
LWC	1	1	1	1.9908×10^{27}	1.51389×10^{-54}

Regression for Water Absorption					
HA	0.953685964	0.942107455	1	82.36690647	0.000817123
HB	0.836947333	0.796184166	1	20.53195076	0.010567519
HC	0.635757264	0.544696581	1	6.981687786	0.057442761

Regression for Slump					
HA	0.875740011	0.844675014	1	28.19057099	0.006048326
HB	0.969230769	0.969230769	1	126	0.000358735
HC	0.963329455	0.954161818	1	105.0793708	0.000510568

Regression for Compressive Strength					
HA	0.008658483	−0.239176896	1	0.034936428	0.860826386
HB	0.022056558	−0.222429303	1	0.090216087	0.778866104
HC	0.076118739	−0.154851577	1	0.3295607	0.596656068

Regression analysis revealed significant regression for bulk density, water absorption, and slump. Nonetheless, within the lightweight hybrid fiber-reinforced concrete group, only the deterioration for compressive strength was not significant (HA, HB, and HC). We concluded that regression analysis was substantial for bulk density, water absorption, and the slump in lightweight hybrid fiber-reinforced concrete. Both ANOVA and regression analysis revealed that the compressive strength of the lightweight hybrid fiber-reinforced

concrete was not significant (LWHFRC). As a result, the experimental results matched the ANOVA and regression results.

4. Conclusions and Future Perspectives

The unit weight of concrete was around 1825 kg/m³ for all three stages of hybrid fiber-reinforced lightweight concrete, which met the ACI 318-19 light concrete criteria. The water binder ratio remained constant throughout all three stages at 0.30 to 0.35. (HA, HB, and HC). The average slump flow diameter is around 51 cm. The average slump height is 24.2 cm for lightweight concrete without fiber (E3). The slump value decreases gradually while the fiber percentage increases.

1. The compressive strengths (E1–E6) of LWC at 28 days were increased by 80.44%, 61.53%, 55.99%, 11.83%, 18.78%, and 4.93%, respectively, when compared to control concrete (C1).
2. Similarly, at 28 days, the compressive strengths (HA1–HA6) of LWHFRC were increased by 55.99%, 57.96%, 64.44%, 57.48%, 69.97%, and 47.50%, respectively (1% hybrid fiber). At 28 days, the compressive strengths (HB1–HB6) of LWHFRC (1.5% hybrid fiber) increased by 55.99%, 56.24%, 67.59%, 78.58%, 86.34%, and 23.42%, respectively. At the age of 28 days, the compressive strengths (HC1–HC6) of LWHFRC were increased by 55.99%, 56.24%, 58.81%, 75.63%, 95.29%, and 5.85% (-ve), respectively (2% hybrid fiber).
3. The strength of lightweight concrete without fiber increased by 55.98%, while the cost of lightweight concrete increased by approximately 16.46%, and unit weight decreased by about 26.67% compared to normal concrete without mineral admixture.
4. The significant effect of replacing 50% of the GGBS with cement played an essential role in increasing compressive strength.
5. SFA outperforms POS and NCA in compressive strength. However, the workability of SFA is lower than that of the other two aggregates. The researchers also discovered that the 90% SFA and 10% POS mixture and the 80% SFA and 20% POS mixture had higher strength and unit weight, meeting lightweight structural criteria.
6. The series of 2% steel fiber and 0.5% PVA fiber had higher compressive strength than the other percentages. The compressive strength of the 2% hybrid fiber (1.5% steel + 0.5% PVA) was higher.
7. In the flexural strength test of the beam, PVA fiber deflected more than steel fiber. As a result, the modulus of rupture of a steel fiber beam was higher.
8. The relationship between the beam flexural strength, and the cylinder split tensile strength of LWHFRC was $f_{cb} = 0.9782 f_{spt}^{1.0175}$, $R^2 = 0.8426$.
9. A relationship was formed between the cylinder split tensile strength and compressive strength of LWHFRC: $f_{spt} = 0.4309 f_c^{0.8103}$, $R^2 = 0.8875$.
10. The LWHFRC beam flexural and compressive strengths formed a relationship $f_{cb} = 0.2984 f_c^{0.9062}$, $R^2 = 0.868$.
11. The cylinder modulus of elasticity and LWHFRC compressive strength formed a relationship $E = 3.3525 f_c^{0.5}$, $R^2 = 1$.
12. The ACI-318-19- E_c lightweight concrete equation matched the current lightweight hybrid fiber-reinforced concrete study.
13. Mineral admixtures improve the structure of the aggregate's contact zone, resulting in a better bond between aggregates and cement paste, as demonstrated by the SEM micrograph and XRD report.
14. ANOVA and regression analysis produced the most significant results with 5 to 10% error.

Author Contributions: D.B.: data curation, formal analysis, investigation, methodology, visualization, writing—original draft. K.-Y.L.: investigation, review, editing, conceptualization, funding acquisition, project administration, supervision, validation, writing—review, and editing. D.G.: investigation, review, and editing. All authors have read and agreed to the published version of the manuscript.

Funding: The first author’s financial support provided by the Satu JRS project (No. NCKU-42-2021) and the Department of Civil Engineering, National Cheng Kung University, is gratefully acknowledged.

Institutional Review Board Statement: Not applicable.

Informed Consent Statement: Not applicable.

Data Availability Statement: Not applicable.

Acknowledgments: The authors acknowledge the support of the Department of Civil and Structural Engineering, National Cheng Kung University, Tainan, Taiwan.

Conflicts of Interest: The authors declare that no known competing financial interests or personal relationships could have appeared to influence the work reported in this paper.





References

1. Narattha, C.; Chaipanich, A. Phase characterizations, physical properties, and strength of environment-friendly cold-bonded fly ash lightweight aggregates. *J. Clean. Prod.* **2018**, *171*, 1094–1100. [\[CrossRef\]](#)
2. Sathyam, D.; Srikanth, K.; Desai, B.V. Brief Study on Concrete Modified with Artificial Cold Bonded Pelletized Light Weight Fly Ash Aggregates. *IOSR J. Eng.* **2017**, *7*, 35–41.
3. Majhi, R.K.; Padhy, A.; Nayak, A.N. Performance of lightweight structural concrete produced by utilizing the high volume of fly ash chemosphere and sintered fly ash aggregate with silica fume. *Clean. Eng. Technol.* **2021**, *3*, 100121. [\[CrossRef\]](#)
4. Reddy, B.D.; Jyothy, S.A.; Kumar, N.K.; Kumar, K.H. An Experimental Investigation on Concrete by Partial Replacement of Cement by Fly Ash and Fine Aggregate by Quarry Dust. *IOP Conf. Ser. Mater. Sci. Eng.* **2020**, *1006*, 012033. [\[CrossRef\]](#)
5. Hasani, H.; Soleymani, A.; Hashem Jahangir, H.; Azizi, M.B. Investigating the effect of sintered fly ash aggregate on mechanical properties of concrete: A review. In Proceedings of the 13th National Congress on Civil Engineering, Isfahan, Iran, 10–11 May 2022.
6. Nadesan, M.S.; Dinakar, P. Mix design and properties of fly ash waste lightweight aggregates in structural lightweight concrete. *Case Stud. Constr. Mater.* **2017**, *7*, 336–347. [\[CrossRef\]](#)
7. Nadesan, M.S.; Dinakar, P. Structural concrete using sintered fly ash lightweight aggregate: A review. *Constr. Build. Mater.* **2017**, *154*, 928–944. [\[CrossRef\]](#)
8. Yao, Z.T.; Ji, X.S.; Sarker, P.K.; Tang, J.H.; Ge, L.Q.; Xia, M.S.; Xi, Y.Q. A comprehensive review on the application of coal fly ash. *Earth Sci. Rev.* **2015**, *141*, 105–121. [\[CrossRef\]](#)
9. Central Electricity Authority. *Report on Flyash Generation at Coal/Lignite Based Thermal Power Stations, and Its Utilization in the Country for the Year 2015–2016*; Central Electricity Authority: New Delhi, India, 2016.
10. Ramamurthy, K.; Hari Krishnan, K.I. Influence of binders on properties of sintered fly ash aggregate. *Cem. Concr. Compos.* **2006**, *28*, 33–38. [\[CrossRef\]](#)
11. Prakash, R.; Raman, S.N.; Subramanian, C.; Divyah, N. Eco-friendly fiber-reinforced concrete. In *Handbook of Sustainable Concrete and Industrial Waste Management*; Woodhead Publishing: Sawston, UK, 2022. [\[CrossRef\]](#)
12. Sobuz, H.R.; Hasan, N.M.S.; Tamanna, N.; Islam, S. Structural Lightweight Concrete Production by Using Oil Palm Shell. *J. Mater.* **2014**, *2014*, 870247. [\[CrossRef\]](#)
13. Aslam, M.; Shafiq, P.; Jumaat, M.Z. High Strength Light Weight Aggregate Concrete using Blended Coarse Lightweight Aggregate Origin from Palm Oil Industry. *Sains Malays.* **2017**, *46*, 667–675. [\[CrossRef\]](#)
14. Kamaldeep, M.G.; Chamberlin, S. Experimental Study on Performance of Concrete by using Combination of Fly ash and Ggbs as Blended Material. *Int. J. Recent Technol. Eng. IJRTE* **2019**, *7*, 490–495.
15. Bashar, I.I.; Alengaram, U.J.; Jumaat, M.Z.; Islam, A.; Santhi, H.; Sharmin, A. Engineering properties and fracture behavior of high-volume palm oil fuel ash-based fiber reinforced geopolymer concrete. *Constr. Build. Mater.* **2016**, *111*, 286–297. [\[CrossRef\]](#)
16. Gomathi, P.; Sivakumar, A. An accelerated curing effect on the mechanical performance of cold bonded and sintered fly ash aggregate concrete. *Constr. Build. Mater.* **2015**, *77*, 276–287. [\[CrossRef\]](#)
17. Kockal, N.U.; Ozturan, T. Effects of lightweight fly ash aggregate properties on the behavior of lightweight concrete. *J. Hazard. Mater.* **2010**, *179*, 954–965. [\[CrossRef\]](#)
18. Abbass, W.; Khan, M.I. Mechanical properties of Hybrid steel/PVA fiber reinforced high strength concrete. *MATEC Web Conf.* **2018**, *199*, 11005. [\[CrossRef\]](#)
19. Feng, J.; Sun, W.; Zhai, H.; Wang, L.; Dong, H.; Wu, Q. Experimental Study on Hybrid Effect Evaluation of Fiber Reinforced Concrete Subjected to Drop Weight Impacts. *Materials* **2018**, *11*, 2563. [\[CrossRef\]](#)
20. Bijen, J. Manufacturing processes of artificial lightweight aggregates from fly ash. *Int. J. Cem. Compos. Lightweight Concr.* **1986**, *8*, 191–199. [\[CrossRef\]](#)

21. Oti, O.P.; Nwaigwe, K.N.; Okereke, N.A. Assessment of palm kernel shell as a composite aggregate in concrete. *CIGR J.* **2017**, *19*, 34–41. Available online: <http://www.cigrjournal.org> (accessed on 18 August 2017).
22. Basha, S.I.; Ali, M.R.; Al-Dulaijan, S.U.; Maslehuddin, M. Mechanical and thermal properties of lightweight recycled plastic aggregate concrete. *J. Build. Eng.* **2020**, *32*, 101710. [[CrossRef](#)]
23. Sudhikumar, G.S.; Prakash, K.B.; Rao, M.S. Effect of Aspect Ratio of Fibers on the Strength Characteristics of Slurry Infiltrated Fibrous Ferrocement. *J. Civ. Struct. Eng.* **2014**, *3*, 29–37.
24. Nagarkar, R.; Patel, J. Polyvinyl Alcohol: A Comprehensive Study. *Acta Sci. Pharm. Sci.* **2019**, *3*, 34–44.
25. Verma, C.L.; Handa, S.K.; Jain, S.K.; Yadav, R. Techno-commercial perspective study for sintered fly ash lightweight aggregates in India. *Constr. Build. Mater.* **1998**, *12*, 341–346. [[CrossRef](#)]
26. Zhang, R.; Jin, L.; Tian, Y.; Dou, G.; Du, X. Static and dynamic mechanical properties of eco-friendly polyvinyl alcohol fiber-reinforced ultra-high-strength concrete. *Struct. Concr.* **2019**, *20*, 1051–1063. [[CrossRef](#)]
27. Noushini, A.; Samali, B.; Vessalas, K. Effect of polyvinyl alcohol (PVA) fiber on dynamic and material properties of fiber reinforced concrete. *Constr. Build. Mater.* **2013**, *49*, 374–383. [[CrossRef](#)]
28. Hassanpour, M.; Shafiq, P.; Bin Mahmud, H. Lightweight aggregate concrete fiber reinforcement—A review. *Constr. Build. Mater.* **2012**, *37*, 452–461. [[CrossRef](#)]
29. Libre, N.A.; Shekarchizadeh, M.; Mahoutian, M.; Soroushian, P. Mechanical properties of hybrid fiber reinforced lightweight aggregate concrete made with natural pumice. *Constr. Build. Mater.* **2011**, *25*, 2458–2464. [[CrossRef](#)]
30. Georgiou, A.; Pantazopoulou, S. Determination of the direct tensile stress-strain curve from simple three-point bending tests. *ResearchGate* **2014**, *2014*, 1–11. [[CrossRef](#)]
31. Hamad, A.J.; Sldozian, R.J.A. Flexural and Flexural Toughness of Fiber Reinforced Concrete—American Standard Specifications Review. *GRD J. Glob. Res. Dev. J. Eng.* **2019**, *4*, 5–13.
32. Deepak, T.J.; Jalam, A.A.; Loh, E.; Siow, Y.T.; Nair, S.; Panjehpour, M. Prognostication of Concrete Characteristics with Coconut Shell as Coarse Aggregate Partial Percentile Replacement. *IJSRSET Themed Sect. Eng. Technol.* **2015**, *1*, 45–50. Available online: <http://ijsrset.com/archive.php?v=4&i=6&pyear=2015> (accessed on 15 September 2015).
33. Franklin, S.O.; Kangootui, F.I. Tensile/Compressive/Flexural Strength Relationships for Concrete using Kgale Aggregates with Botchem as Binder. *Int. J. Sci. Eng. Res.* **2020**, *11*, 5.
34. Xie, F.; Zhang, C.; Cai, D.; Ruan, J. Comparative Study on the Mechanical Strength of SAP Internally Cured Concrete. *Front. Mater.* **2020**, *7*, 588130. [[CrossRef](#)]
35. Juki, M.I.; Awang, M.; Annas, M.M.K.; Boon, K.H.; Othman, N.; Kadir, A.B.A.; Roslan, M.A.; Khalid, F.S. Relationship Between Compressive, Splitting Tensile and Flexural Strength of Concrete Containing Granulated Waste Polyethylene Terephthalate (PET) Bottles as Fine Aggregate. Available online: <https://doi.org/10.4028/www.scientific.net/AMR.795.356> (accessed on 15 September 2013).
36. Moretti, L.; Natali, S.; Tiberi, A.; D'Andrea, A. Proposal for a Methodology Based on XRD and SEM-EDS to Monitor Effects of Lime-Treatment on Clayey Soils. *Appl. Sci.* **2020**, *10*, 2569. [[CrossRef](#)]
37. Kanniyappan, S.P.; Kumar, S.; Muthukumar, T. Analyzing the Microstructural Properties of Nanomaterial in OPC by SEM, TEM, XRD and Corrosion Rate by TAFEL Techniques. *Int. Res. J. Eng. Technol. IRJET* **2017**, *4*, 1497–1503.
38. Geetha, S.; Ramamurthy, K. Properties of sintered low calcium bottom ash aggregate with clay binders. *Constr. Build. Mater.* **2011**, *25*, 2002–2013. [[CrossRef](#)]
39. Yusuf, S.; Islam, N.; Akram, W.; Ali, H.; Siddique, A. Prediction of the best tensile and flexural strength of natural fiber reinforced epoxy resin-based composite using taguchi method. In Proceedings of the International Conference on Industrial & Mechanical Engineering and Operations Management, Dhaka, Bangladesh, 26–27 December 2020.
40. Artoglu, N.; Girgin, Z.C.; Artoglu, E. Evaluation of Ratio between Splitting Tensile Strength and Compressive Strength for Concretes up to 120 MPa and its Application in Strength Criterion. *ACI Mater. J.* **2006**, *103*, 18–24.

Research Article

Synthesis and Enhanced Photocatalytic Activity of Zinc Oxide-Based Nanoparticles and Its Antibacterial Activity

R. Ragunathan ¹, **Sampathkumar Velusamy** ², **Jothi Lakshmi Nallasamy**,²
Manoj Shanmugamoorthy ², **Jesteena Johney**,¹ **Senthilkumar Veerasamy**,³
Dineshkumar Gopalakrishnan,⁴ **Muralimohan Nithyanandham**,⁵ **Dhivya Balamoorthy** ⁶
and **Prabu Velusamy**⁷

¹Centre for Bioscience and Nano Science Research, 641021, Coimbatore, India

²Department of Civil Engineering, Kongu Engineering College, Perundurai, Erode 638060, India

³Department of Civil Engineering, M.Kumarasamy College of Engineering, Karur 639113, India

⁴Department of Civil Engineering, Vaagdevi College of Engineering, Warangal 506005, India

⁵Department of Civil Engineering, K.S.R. College of Engineering, Tiruchencode 637215, India

⁶Department of Hydraulic and Water Resource Engineering, Wollega University, Ethiopia

⁷Department of Construction Technology and Management, Wollega University, Ethiopia

Correspondence should be addressed to R. Ragunathan; cbnrcindia@gmail.com
and Dhivya Balamoorthy; dhivyabalamoorthy@wollegauniversity.edu.et

Received 18 May 2022; Revised 30 May 2022; Accepted 3 June 2022; Published 15 June 2022

Academic Editor: Samson Jerold Samuel Chelladurai

Copyright © 2022 R. Ragunathan et al. This is an open access article distributed under the Creative Commons Attribution License, which permits unrestricted use, distribution, and reproduction in any medium, provided the original work is properly cited.

Nanotechnology is an emerging technology for the treatment of waste water. Nanoparticles have its own advantages as the higher surface area to volume ratio compared to the bulk material. In this study, zinc oxide-based nanoparticles were synthesized. Synthesized nanoparticles are characterized by UV-visible spectroscopy, Fourier transform infrared spectroscopy, scanning electron microscopy, and energy dispersive X-ray spectroscopy (EDX). The antibacterial study was carried out using the synthesized nanoparticle. The photocatalytic degradation for methyl blue, methyl red, and Orange G is also done in this study using the synthesized nanoparticles. The shape and size of the nanoparticles obtained are rounding spherical with 80 to 110 nm. The optimum result obtained from the dye degradation study is 94% for methyl blue.

1. Introduction

Nanometric zinc oxide can have many different forms. It can be found in structures that are one dimensional (1D), two dimensional (2D), and three dimensional (3D). Needles, helixes, nanorods, ribbons, belts, wires, and combs are among the most common one-dimensional structures. Nanopellets, nanosheet/nanoplate, and other two-dimensional structures of zinc oxide can be found [1]. Nanotechnology is the manufacture and application of materials on the tiniest scale possible [2].

Nanoscale particles have lately emerged as possible antibacterial agents due to its higher surface area to volume

ratio, which is attracting researchers, due to the development of microbial resistance to metal ions, antibiotics, and the generation of resistant strains.

The recent expansion in the field of porous and nanometric materials generated through nontraditional techniques has sparked interest in finding new uses for ZnO nanoparticles [3]. Zinc oxide is also a fascinating semiconductor material because of its use in solar cells, gas sensors, ceramics, catalysts, cosmetics, and varistors [4].

Zinc oxide nanoparticles are widely known for their antibacterial properties. Using the disc diffusion approach, Wahab et al. employed this feature to suppress *Bacillus subtilis* and *Escherichia coli* growth. The potential antibacterial

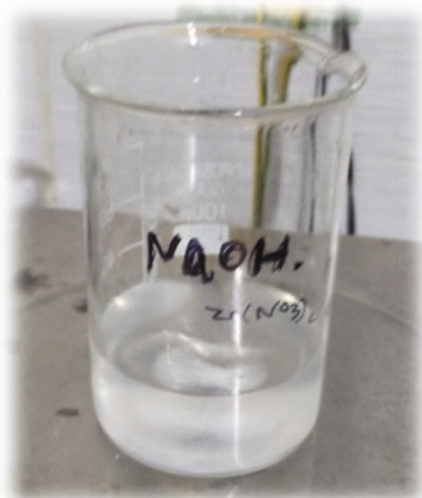


FIGURE 1: Before nanoparticle synthesis.

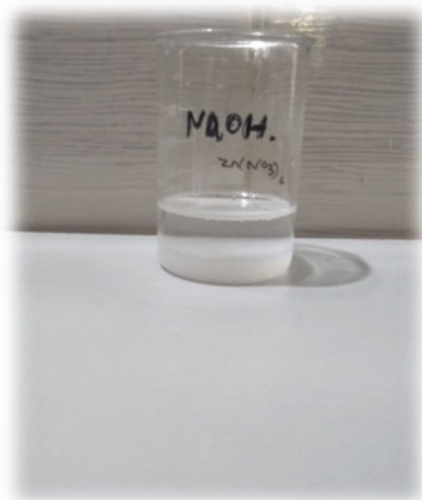


FIGURE 2: After nanoparticle synthesis.

activity of zinc oxide nanoparticles was then assessed [5, 6].

The old known techniques such as metal organic chemical vapor deposition (MOCVD), spray pyrolysis, laser ablation, sputter deposition, ion beam-assisted deposition, template-assisted growth, and chemical vapor deposition have also been used for the zinc oxide nanostructure synthesis.

Further, literature reports [7] have demonstrated the synthesis of zinc oxide nanoparticles with sizes ranging from 50 to 200 nm using the solution-combustion method with zinc acetate dihydrate and ethylene glycol, as well as the synthesis of zinc oxide nanoparticles using the solvothermal method at 180°C for 24 hours with zinc acetate dihydrate and urea. When compared to inorganic antibacterial agents, antibacterial researches on organic materials are frequently unstable, especially at high temperatures and/or pressures [8].

It has been claimed that eco-friendly plant extracts can be used to synthesis nanoparticles. Because ZnO is nontoxic, it can be employed as a photocatalytic degradation material for contaminants in the environment [9].

Zinc oxide has additional properties that make it an efficient antibacterial agent. That Zn²⁺, in addition to being a nontoxic metal, is a necessary nutrient found in practically every cell, is required for a variety of physiological processes, and must be eaten in the diet to maintain good health [10]. This study focuses on the chemical synthesis of ZnO nanoparticles, as well as their characterization and antibacterial activity against the human bacterial pathogen *Staphylococcus aureus* [11].

Germination tests on maize and rice were used to assess the phytotoxicity of seven metal oxide NPs: titanium oxide (nTiO₂), silicon di oxide (nSiO₂), cerium dioxide (nCeO₂), magnetite (nFe₃O₄), aluminium oxide (nAl₂O₃), zinc oxide (ZnO), and copper oxide (nCuO). As toxicity markers, root length and shoot length were chosen since they are susceptible to an unfavourable environment [12]. This study contributed to the application of metal oxide NPs in agriculture and the assessment of environmental safety.

2. Materials and Methods

2.1. Chemicals, Glasswares, and Cultures Required. The chemicals, glasswares, and cultures required are the following: zinc nitrate, zinc sulphate, sodium hydroxide, potassium hydroxide, Petri plate, *Staphylococcus aureus*, *Escherichia coli*, methyl blue, methyl red, Orange G (all the chemicals used were AR grade).

2.2. Preparation of Zinc Oxide Nanoparticles

2.2.1. Zinc Nitrate (HiMedia, Mumbai). Zinc oxide nanoparticle was prepared from 0.1 M of zinc nitrate (1.487 g weighed and 50 ml distilled water dissolved) separated into two portions each of 25 ml. Then, 0.2 M of 0.04 g weighed and 5 ml water and sodium hydroxide (NaOH) and 0.2244 g weighed and 5 ml of potassium hydroxide (KOH) were prepared.

First, a portion of 25 ml of zinc nitrate and 5 ml of prepared sodium hydroxide (NaOH) (NaOH was added to enhance the formation of the alkoxide phase during the zinc oxide nanoparticle synthesis) are added drop by drop and stirred constantly with magnetic stirrer (100 rpm) for 2-3 hrs and incubated at room (37°C) temperature without light contact for overnight. After the incubation period, zinc oxide nanoparticles are formed [13, 14].

A second portion of 25 ml of zinc nitrate and 5 ml of prepared potassium hydroxide (KOH) are added drop by drop and constant stirred with magnetic stirrer for 2-3 hrs and incubated at room temperature without light contact for 24 hours. After the incubation, white color zinc oxide nanoparticles are formed.

2.2.2. Zinc Sulphate. Zinc oxide nanoparticle was prepared from 0.1 M of zinc sulphate (1.4377 g weighed and 50 ml distilled water dissolved) separated into two portions each of 25 ml. Then, 0.2 M of 0.04 g weighed and 5 ml water and

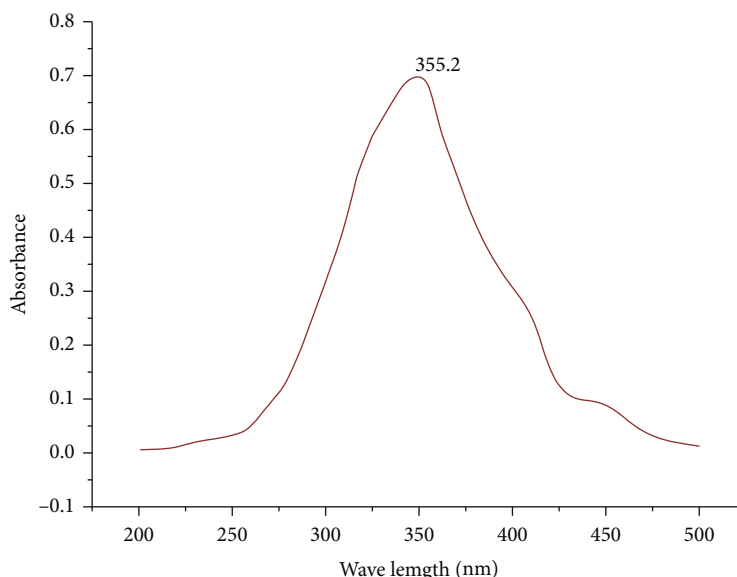


FIGURE 3: UV-visible.

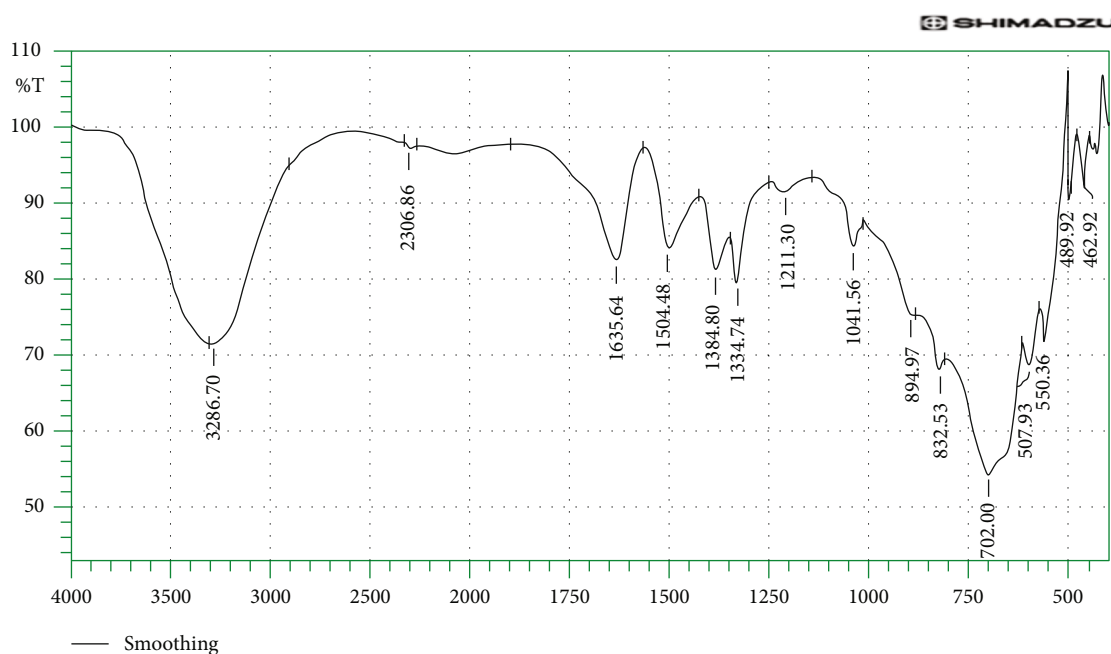


FIGURE 4: FTIR-zinc oxide nanoparticle.

sodium hydroxide (NaOH) and 0.2244 g weighed and 5 ml of potassium hydroxide (KOH) were prepared [15].

To compare the best catalytic agent, first, a portion of 25 ml of zinc sulphate and 5 ml of sodium hydroxide (NaOH) are added drop by drop and constant stirred with magnetic stirrer for 2-3 hrs and incubated at room temperature without light contact for overnight. After the incubation, the white color formed the presence of zinc oxide nanoparticle.

A second portion of 25 ml of zinc sulphate and 5 ml of potassium hydroxide (KOH) are added drop by drop and constant stirred with magnetic stirrer for 2-3 hrs and incubated at room temperature without light contact for over-

night. After the incubation, the white color formed the presence of zinc oxide nanoparticle [16].

2.3. Characterization of Nanoparticle. UV-visible spectroscopy, FTIR, and SEM were used to analyse the produced ZnO nanoparticles (among the two). To acquire the structural figure of the created nanoparticles and to determine their size, the liquid solution is utilized for UV-visible spectroscopy, and the powder form of zinc oxide nanoparticles was used for FTIR, SEM, and EDX images.

2.3.1. UV-Visible Spectroscopy. The absorption plasmon peak of ZnO nanoparticles was observed at 300 to 400 nm

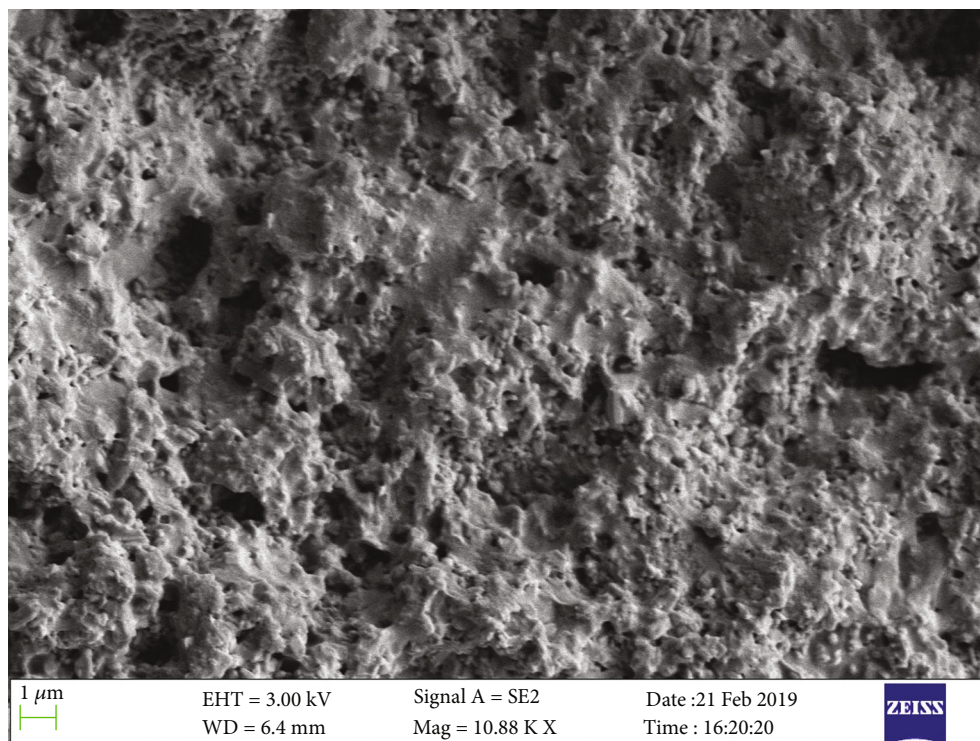


FIGURE 5: SEM-zinc nanoparticles.

using Labotronic LT 291 UV–VIS and microprocessor spectrophotometer with 5 nm interval.

2.3.2. FTIR (Fourier Transform Infrared Spectroscopy). Pellets of samples were made into 1 mm pellets using a hydraulic press and scanned more than a wave number range of 4000 cm^{-1} to 400 cm^{-1} using Shimadzu FTIR spectrometer.

2.3.3. SEM (Scanning Electron Microscopy). Characteristic X-rays are produced when one electron is removed from the sample's inner shell, prompting a higher-energy electron to occupy the shell and release energy in the form of X-rays. These distinctive X-rays are then utilized to determine the material's composition as well as to determine the presence of components and contaminants in the sample. Magnification in a scanning electron microscopy technique can be adjusted across 6 orders of magnitude range, from around 10 to 500,000 times.

2.3.4. EDX (Energy-Dispersive X-Ray). Energy-dispersive X-ray spectroscopy (EDS or EDX) also known as energy dispersive X-ray analysis is a chemical characterization and elemental analysis technique.

2.3.5. Antimicrobial Activity. The antimicrobial activity of produced zinc oxide nanoparticles was tested using the Agar well diffusion assay method in Mueller Hinton agar, which was produced by diluting 28 gm in 1000 ml distilled water and sterilized under autoclave. After sterilization, media was poured to Petri dish and allowed for solidification. Pure culture of *Staphylococcus aureus* and *Escherichia coli* (Sneha Clinical Laboratory, Coimbatore) bacteria was swabbed in two different Petri dishes. Make four wells using a well

maker. Then, the wells are filled with ZnO NP (1), ZnO NP (2), ZnO NP (3), and ZnO NP (4), and antibiotic disc was used as a positive control, and the Mueller Hinton agar plates are kept for incubation at 37°C for 24 h [17].

2.3.6. Photocatalytic Study. Photocatalysis is well-established for the efficient and long-term elimination of organic and inorganic contaminants from water, and this technology is especially valuable for industrial water treatment. The percentage of dye decolorization was calculated by the following formula [18]:

$$\% \text{ of dye decolourisation} = \frac{C - T}{C} \times 100, \quad (1)$$

where C is the control and T is the absorbance value.

2.4. Methyl Blue. Methyl blue was prepared by adding 40 ml methyl blue and 20 ml of distilled water that are mixed well. Separate each 30 ml dyes in two beakers. First beaker is taken as a control, and in the second beaker, zinc oxide nanoparticles were added and then place the beakers in the sunlight (or) UV light. Color change is notified in every 1 hour, and OD value is notified.

2.5. Methyl Red. Methyl red was prepared on 40 ml methyl red and 20 ml of distilled water that are mixed well. Then, separate each 30 ml dyes in two beakers. The first beaker was control, and the second beaker was zinc oxide nanoparticles and then placed it under sunlight (or) UV light. After one hour, color changes were observed, and OD values were observed.

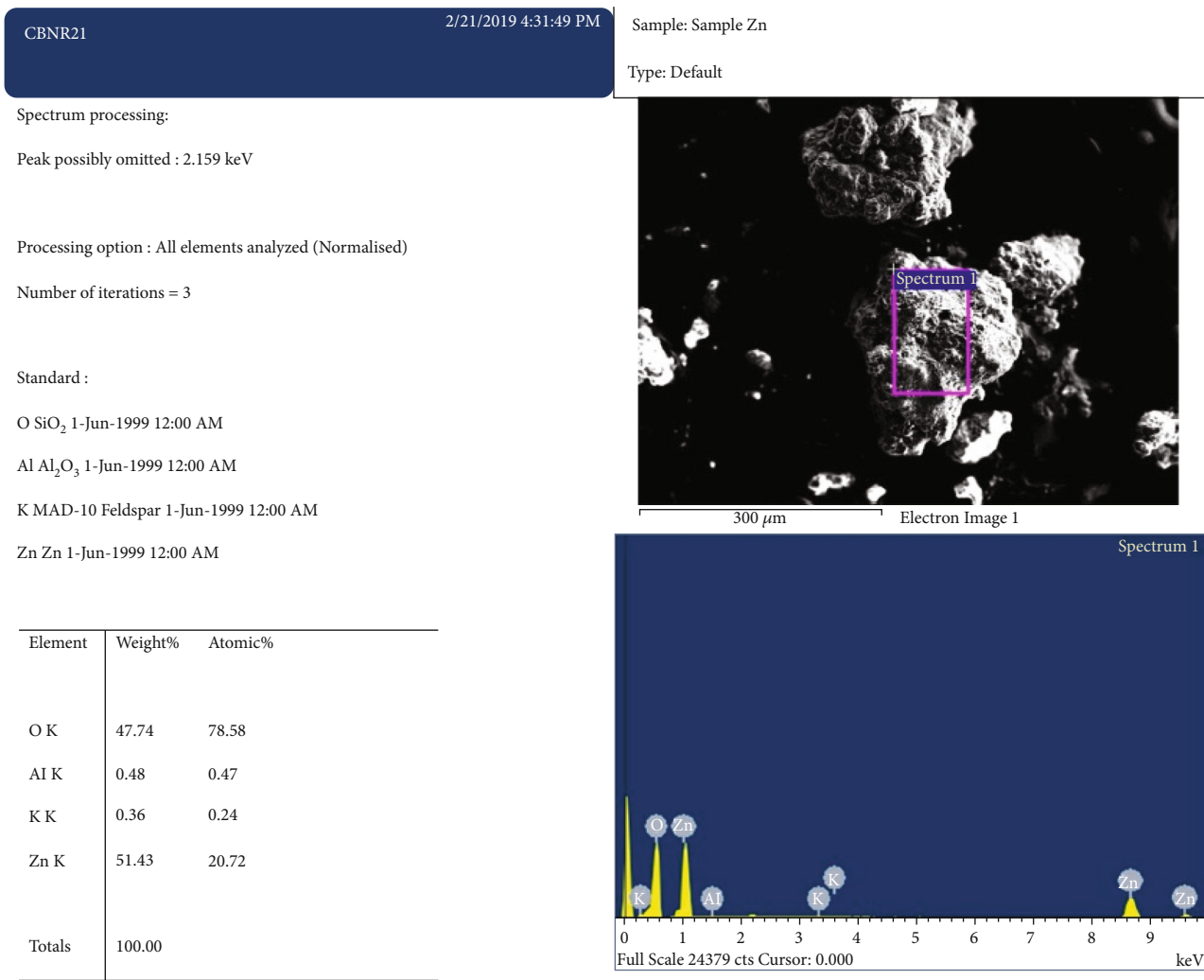


FIGURE 6: EDX-zinc nanoparticle.

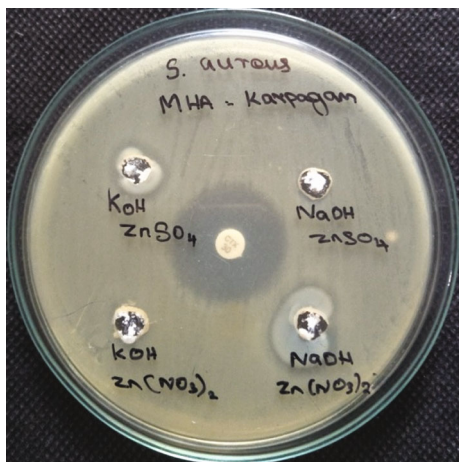


FIGURE 7: Staphylococcus aureus.

2.6. Orange G. 0.025 mg of Orange G and 120 ml distilled water were taken and mixed well, and it was divided into three portions. First portion as 60 ml of Orange G was taken

as control. Second portion as 20 ml of Orange G was taken and added with 5 mg of zinc oxide nanoparticles. Third portion as 40 ml of Orange G was taken and added with 5 mg of zinc oxide nanoparticles and then put under sunlight (or) UV light. After one hour, color changes were observed, and OD values were taken.

2.7. Seed Germination. For germination, the green gram seeds were rinsed with sterile water several times for surface sterilization. Four cups were taken the seed germination, and plant growth was processed in the respective cups. In all the four cups, soil was added in half of the size which was essential for seed germination. The soil was added with tap water, control Orange G, treated Orange G, and the nanoparticle, respectively, in each cup. Then, the 10 seeds were soaked in all the cups. Incubate the cups under the sunlight for germination. The seed germination and the plant growth were observed within 2-3 days of incubation. After that, the plant grown in each cup was picked up from the soil, and then, the leaf counting and the length of the stem and root were measured [19].

TABLE 1: Staphylococcus aureus zone measurement.

S. no	Components	Zone of inhibition
1	Cefotaxime plate (CTX 30)	8 mm
2	ZnO NP (1): Zn(NO ₃) ₂ NaOH	6 mm
3	ZnO NP (2): Zn(NO ₃) ₂ KOH	Nil
4	ZnO NP (3): ZnSO ₄ NaOH	Nil
5	ZnO NP (4): ZnSO ₄ KOH	3 mm



FIGURE 8: Escherichia coli.

TABLE 2: Escherichia coli zone measurement.

S. no	Components	Zone of inhibition
1	Cefotaxime plate (CTX 30)	7 mm
2	ZnO NP(1): Zn(NO ₃) ₂ NaOH	6 mm
3	ZnO NP(2): Zn(NO ₃) ₂ KOH	3 mm
4	ZnO NP(3): ZnSO ₄ NaOH	4 mm
5	ZnO NP(3): ZnSO ₄ KOH	5 mm

TABLE 3: Photocatalytic study of methyl blue.

S. no	Methyl blue	24 hours	48 hours
1	Control	100%	100%
2	1 hour	27%	94%
3	2 hour	31%	92%

TABLE 4: Photocatalytic study of methyl red.

S. no	Methyl red	24 hours	48 hours
1	Control	100%	100%
2	Absorbance	33%	66%

2.8. *Extraction of Chlorophyll Content.* After the plant growth, 1 gm of leaf was taken from each plant; then, the leaves were grinded along with acetone in mortar and pestle. The leaf extract of each plant was prepared of about 2-3 ml. Then, the OD value of each leaf extract was taken under UV-

TABLE 5: Photocatalytic study of Orange G.

S. no	Orange G	24 hours	48 hours
1	Control	100%	100%
2	20 ml	69%	90%
3	40 ml	99%	82%

Vis spectrophotometer at both 663 and the 646 nm at an interval of 24 hrs and 48 hrs after the plant growth. Based on the OD value, the chlorophyll content of each plant was measured and calculated by using the following formula/equation [20]:

$$\text{Chlorophyll} = 12.25A_{663.2} - 279A_{646.8} \quad (2)$$

3. Result and Discussion

Zinc nanoparticle was prepared from 0.1 M of 1.487 g zinc nitrate and dissolved in 50 ml distilled water. Then, 0.2 M of 0.04 g sodium hydroxide (NaOH) was prepared.

3.1. *Visual Observation.* As shown in Figures 1 and 2, zinc nitrate and 5 ml of sodium hydroxide (NaOH) are added drop by drop and stirred constantly with magnetic stirrer for 2-3 hrs and incubated at room temperature without light contact for overnight. After the incubation, the presence of zinc oxide nanoparticles is observed by the formation of white color.

3.2. *UV-Visible.* From Figure 3, UV-visible spectra, ZnO nanoparticles were obtained between 300 and 550 nm. The ZnO nanoparticles in the solution are confirmed by the surface plasma resonance band at 355.2 nm, as shown. The amount of absorption within the wave length of 200–500 nm was observed by UV-Vis spectroscopy for analytical investigation of the prepared sample of ZnO nanoparticles (Figure 3). Surface plasmon resonance in ZnO nanoparticles produces an absorption band at about 355.2 nm [21].

3.3. *FTIR (Fourier Transform Infrared Spectroscopy).* To determine the quality and composition of the metal nanoparticles, infrared examinations were conducted. Interatomic vibrations cause absorption bands in metal oxides in the fingerprint area, which is below 1000 cm⁻¹. Peaks at 3286.70 cm⁻¹ and 1041.56 cm⁻¹ represent O-H stretching and deformation due to water adsorption on the metal surface (Figure 4). The peaks at 1634.00 cm⁻¹ correspond to stretching and deformation vibrations in ZnO, respectively [22, 23].

3.4. *SEM (Scanning Electron Microscopy).* A scanning electron microscope (SEM) is a microscopy technique that creates a high beam of electrons to view a material. Zinc oxide nanoparticle was synthesized from the chemical reduction method on powdered sample placed under the sunlight and dried, and the morphology was observed under the scanning electron microscopy [24].

SEM (ZEISS) shows that lateral dimension of particles (including the reducing agent, which may be agglomerated



FIGURE 9: Before nanoparticle, seed was added.



FIGURE 10: After nanoparticle, plant grows.

of the nanoparticles) is of the order of 310 nm synthesized zinc oxide nanoparticles that are spherical, crystal, and cuboids in nature; external morphology of synthesized nanoparticles in the range of 3 μm can be seen (Figure 5).

3.5. EDX (Energy-Dispersive X-Ray Analysis). The EDX profile shows the chemical analysis of synthesized ZnO nanoparticle. EDX pattern shows major emission energy at 1 kg which is the binding energy for zinc with the weight of 51.43% and the atomic range of 20.72%, whereas the 0.5 Kev which is the binding energy for oxygen with the weight of 47.74% and atomic range of 78.58% which confirms that ZnO has been correctly identified (Figure 6).

3.6. Antimicrobial Activity

3.6.1. *Staphylococcus aureus*. The organism used is *Staphylococcus aureus* bacteria (Figure 7), and the antibiotic used is cefotaxime disc (CTX 30), ZnO NP (1), ZnO NP (2), ZnO NP (3), and ZnO NP (4) zone formed in the Mueller Hinton agar (38.0 g in 1000 ml distilled water, HiMedia) Petri plates and measured, as shown in Table 1.

3.6.2. *Escherichia coli*. Antibacterial activity is defined as anything that kills bacteria or inhibits their growth or reproduction. The four compounds produced from Mueller Hinton agar (38.0 g in 1000 ml distilled water, HiMedia) were utilized as the medium in antibacterial investigations of ZnO using the well diffusion method. The organism used is *Escherichia coli* bacteria (Figure 8), and the antibiotic is

cefotaxime plate (CTX 30), ZnO NP (1), ZnO NP (2), ZnO NP (3), and ZnO NP (4) zone formed (Table 2) in the Petri plates and measured [25].

3.7. Photocatalytic Study

3.7.1. Methyl Blue. In this study, chemically synthesized zinc oxide nanoparticle was added to the methyl blue dye, and the control was maintained. The control and the nanoparticle added dye were placed under the sunlight for the activity of zinc oxide nanoparticle against the dyes and maintained as such for 48 hrs. After 24 hrs, the absorbance was measured under the UV-Vis spectroscopy at a time interval of 1 hour. After 48 hrs, the absorbance value was taken at an interval of about 2 hrs for the discoloration of dye by the zinc oxide nanoparticles synthesized, and the result was observed by the taken absorbance value (Table 3).

3.7.2. Methyl Red. In this study, chemically synthesized zinc oxide nanoparticle was added to the methyl red dye, and the control was maintained. The control and the nanoparticle added dyes were placed under the sunlight for the activity of zinc oxide nanoparticle against the dye and maintained as such for 48 hrs. After 24 hrs, the absorbance was measured under the UV-Vis spectroscopy at a time interval of 1 hour. After 48 hrs, the absorbance value was taken at an interval of about 2 hrs for the discoloration of dye by the zinc oxide nanoparticle, and the result was observed by the taken absorbance value (Table 4).

3.8. Orange G. In this study, chemically synthesized zinc oxide nanoparticle was added to the Orange G dye, and the control was maintained. The control and the nanoparticle added dye were placed under the sunlight for the activity of zinc oxide nanoparticle against the dye and maintained as such for 48 hrs. After 24 hrs, the absorbance was measured under the UV-Vis spectroscopy at a time interval of 1 hour. After 48 hrs, the absorbance value was taken at an interval of about 2 hrs for the discoloration of dye by the zinc oxide nanoparticle, and the result was observed by the taken absorbance value (Table 5).

3.9. Seed Germination

3.9.1. Before Seeding. The toxicity study was conducted using seed germination assay and found that the treated water seeds grown well on par with the control seed and correlated that the treated water does not contain any toxic elements. In these cups, 10 seeds are soaked for seed germination process with respective samples and allowed for growth under sunlight of about 2 weeks (Figures 9 and 10).

3.9.2. After 1 Week. After 1 week of incubation, seed germination was observed in all the cups. In each cup, the number of plant seed germination occurred was observed as follows:

- (i) Control (tap water): 8-plant seed germination present
- (ii) Treated Orange G: 6-plant seed germination present

(iii) Control Orange G: 6-plant seed germination present

(iv) Control nanoparticle: 7-plant seed germination present

3.10. Examination of Chlorophyll Content. Based on the OD value, the chlorophyll content of each plant was measured and calculated by using the formula/equation:

$$\text{Chlorophyll} = 12.25A_{663.2} - 279A_{646.8} \quad (3)$$

The control nanoparticle contained plant has a good seed germination and good root, shoot, and growth compared to the treated Orange G and the control Orange G. It has high chlorophyll content compared with control tap water plant. It showed that the nanoparticle can be easily eliminated soil toxic compounds and helped for plant seed germination and growth development process [26]. Recently, [27] studied the photocatalytic studies of methylene blue using zinc oxide nanoparticles and found the degradation of 85%.

4. Conclusion

In the present study, zinc oxide nanoparticle was synthesized using chemical reduction method. The nanoparticle was characterized using UV-visible spectroscopy, and the plasma peak was found to be 355.2 nm, confirmed the zinc oxide nanoparticle synthesis. The FTIR was also carried out to characterize the zinc oxide nanoparticle. The morphology of the nanoparticle was studied using SEM. The round spherical with 80 to 110 nm size of the nanoparticle was obtained. Further, the EDX was carried out, and the zinc 51.43% confirmed zinc oxide nanoparticles.

The antibacterial study was carried out against *E.coli* and *Staphylococcus aureus*, and the zone of inhibition was measured. The zone of inhibition was maximum in *E. coli*. The photocatalytic study was carried out against methyl blue, methyl red, and Orange G under sunlight. The maximum percentage of dye decolorization after two days in methyl blue is 94%, in methyl red is 66%, and in Orange G is 90%.

The seed germination assay was also studied using zinc oxide nanoparticles of treated water, tap water, control dye, and treated dye. Among the control dye, the treated one showed the maximum chlorophyll content.

Data Availability

The data used to support the findings of this study are included within the article.

Conflicts of Interest





The authors declare that there are no conflicts of interest regarding the publication of this paper.

References

- [1] D. Xrd, A. C. Mohan, and B. Renjanadevi, "Preparation of zinc oxide nanoparticles and its characterization using scanning electron microscopy (SEM) and X-ray diffraction(XRD)," *Procedia Technology*, vol. 24, pp. 761–766, 2016.
- [2] H. Amekura, N. Umeda, Y. Sakuma et al., "Zn and ZnO nanoparticles fabricated by ion implantation combined with thermal oxidation, and the defect-free luminescence," *Applied Physics Letters*, vol. 88, no. 15, p. 153119, 2006.
- [3] A. Gupta, H. S. Bhatti, D. Kumar, N. K. Verma, and D. R. Tandon, "Nano and bulk crystals of ZnO : synthesis and characterisation," *Digest Journal of Nanomaterials and Biostructures*, vol. 1, no. 1, pp. 1–9, 2006.
- [4] X. Wang, Y. Ding, C. J. Summers, and Z. L. Wang, "Large-Scale synthesis of six-nanometer-wide ZnO nanobelts," *Journal of Physical Chemistry B*, vol. 108, no. 26, pp. 8773–8777, 2004.
- [5] R. Wahab, S. G. Ansari, Y. S. Kim, M. A. Dar, and H. S. Shin, "Synthesis and characterization of hydrozincite and its conversion into zinc oxide nanoparticles," *Journal of Alloys and Compounds*, vol. 461, no. 1-2, pp. 66–71, 2008.
- [6] J. Sawai, "Quantitative evaluation of antibacterial activities of metallic oxide powders (ZnO, MgO and CaO) by conductimetric assay," *Journal of Microbiological Methods*, vol. 54, no. 2, pp. 177–182, 2003.
- [7] G. Priyanka, P. Brian, B. W. David, H. Wenjie, J. P. William, and A. J. Anne, "Antimicrobial activities of commercial nanoparticles against an environmental soil microbe, *Pseudomonas putida* KT2440," *Pseudomonas putida Journal of Biological Engineering*, vol. 3, no. 1, pp. 1–13, 2009.
- [8] D. Gnanasangeetha and D. SaralaThambavani, "One pot synthesis of zinc oxide nanoparticles via chemical and green method," *International Science Congress Association–Research Journal of Material Sciences*, vol. 2320, no. 7, p. 6055, 2013.
- [9] C. T. Walsh, H. H. Sandstead, A. D. S. Prasad, P. M. Newberne, and P. J. Fraker, "Zinc: health effects and research priorities for the 1990s," *Environmental Health Perspectives*, vol. 102, no. 2, pp. 5–46, 1994.
- [10] G. Narasimha, A. Sridevi, B. Devi Prasad, and B. Praveen Kumar, "Chemical synthesis of zinc oxide (ZnO) nanoparticles and their antibacterial activity against a clinical isolate *Staphylococcus aureus*," *International Journal of Nano Dimension*, vol. 5, no. 4, pp. 337–340, 2014.
- [11] M. H. Huang, S. Mao, H. Feick et al., "Room-temperature ultraviolet Nanowire Nanolasers," *Science*, vol. 292, no. 5523, pp. 1897–1899, 2001.
- [12] L. Vayssieres, K. Keis, A. Hagfeldt, and S.-E. Lindquist, "Three-dimensional array of highly oriented crystalline ZnO microtubes," *Chemistry of Materials*, vol. 13, no. 12, pp. 4395–4398, 2001.
- [13] P. K. Stoimenov, R. L. Klinger, G. L. Marchin, and K. J. Klambunde, "Metal oxide nanoparticles as bactericidal agents," *Langmuir*, vol. 18, no. 17, pp. 6679–6686, 2002.
- [14] C.-H. Hsieh, "Spherical zinc oxide nano particles from zinc acetate in the precipitation method," *Journal of the Chinese Chemical Society*, vol. 54, no. 1, pp. 31–34, 2007.
- [15] J. Sawai, E. Kawada, F. Kanou et al., "Detection of active oxygen generated from ceramic powders having antibacterial activity," *Journal of Chemical Engineering of Japan*, vol. 29, no. 4, pp. 627–633, 1996.
- [16] S. S. Kumar, P. Venkateswarlu, V. R. Rao, and G. N. Rao, "Synthesis, characterization and optical properties of zinc oxide nanoparticles," *International Nano Letters*, vol. 3, no. 1, pp. 1–6, 2013.
- [17] L. F. A. Anand Raj and E. Jayalakshmy, "Biosynthesis and characterization of zinc oxide nanoparticles using root extract of *Zingiber officinale*," *Oriental Journal of Chemistry*, vol. 31, no. 1, pp. 51–56, 2015.
- [18] Z. Yang, J. Chen, R. Dou, X. Gao, C. Mao, and L. Wang, "Assessment of the phytotoxicity of metal oxide nanoparticles on two crop plants, maize (*Zea mays* L.) and rice (*Oryza sativa* L.)," *International Journal of Environmental Research and Public Health*, vol. 12, no. 12, pp. 15100–15109, 2015.
- [19] R. P. Singh, V. K. Shukla, R. S. Yadav, P. K. Sharma, P. K. Singh, and A. C. Pandey, "Biological approach of zinc oxide nanoparticles formation and its characterization," *Advanced Medicinal Letters*, vol. 2, no. 4, pp. 313–317, 2011.
- [20] O. A. Fouad, A. A. Ismail, Z. I. Zaki, and R. M. Mohamed, "Zinc oxide thin films prepared by thermal evaporation deposition and its photocatalytic activity," *Applied Catalysis B: Environmental*, vol. 62, no. 1-2, pp. 144–149, 2006.
- [21] M. Nirmala, M. G. Nair, K. Rekha, A. Anukaliani, S. Samdarshi, and R. G. Nair, "Photocatalytic activity of ZnO nanopowders synthesized by DC thermal plasma," *African Journal of Basic & Applied Sciences*, vol. 2, no. 5-6, pp. 161–166, 2010.
- [22] M. G. Nair, M. Nirmala, K. Rekha, and A. Anukaliani, "Structural, optical, photo catalytic and antibacterial activity of ZnO and Co doped ZnO nanoparticles," *Materials Letters*, vol. 65, no. 12, pp. 1797–1800, 2011.
- [23] S. Kandasamy, S. Velusamy, P. Thirumoorthy et al., "Adsorption of chromium ions from aqueous solutions by synthesized nanoparticles," *Journal of Nanomaterials*, vol. 2022, Article ID 6214438, 8 pages, 2022.
- [24] A. C. Janaki, E. Sailatha, and S. Gunasekaran, "Synthesis, characteristics and antimicrobial activity of ZnO nanoparticles," *Spectrochimica Acta Part A: Molecular and Biomolecular Spectroscopy*, vol. 144, pp. 17–22, 2015.
- [25] N. Sumanta, C. I. Haque, J. Nishika, and R. Suprakash, "Spectrophotometric analysis of chlorophylls and carotenoids from commonly grown fern species by using various extracting solvents," *Research Journal of Chemical Sciences*, vol. 2231, p. 606X, 2014.
- [26] H. Kumar and R. Rani, "Structural and optical characterization of ZnO nanoparticles synthesized by microemulsion route," *International Letters of Chemistry, Physics and Astronomy*, vol. 14, pp. 26–36, 2013.
- [27] J. López-López, A. Tejada-Ochoa, A. López-Beltrán, J. Herrera-Ramírez, and P. Méndez-Herrera, "Sunlight photocatalytic performance of ZnO nanoparticles synthesized by green chemistry using different botanical extracts and zinc acetate as a precursor," *Molecules*, vol. 27, no. 1, pp. 6–17, 2022.

Review Article

Maintenance Methodologies Embraced for Railroad Systems: A Review

Priyanka Prabhakaran ¹, **Anandakumar Subbaiyan**,¹ **Dineshkumar Gopalakrishnan** ²,
Harsha Vardhana Balaji.M.,³ **S. Ramkumar** ⁴, **Suresh Veluswamy**,⁵
Dinesh Kumar Murugesan,⁵ **Satheeshkumar Seerangagounder**,⁶
Sivakumar Arunachalam,¹ **Prabhu Velusamy** ⁷, and **Priyanka Bhaskaran**⁸

¹Department of Civil Engineering, Kongu Engineering College, Perundurai, Erode 638060, India

²Department of Civil Engineering, Vaagdevi College of Engineering, Warangal 506005, Telangana, India

³Department of Civil Engineering, Sona College of Technology, Salem 636005, India

⁴Department of Civil Engineering, M. Kumarasamy College of Engineering, Karur 639113, India

⁵Department of Civil Engineering, Hindusthan College of Engineering, Coimbatore 641032, India

⁶Department of Agriculture Engineering, Kongunadu College of Engineering and Technology, Trichy 621215, India

⁷Department of Construction Technology and Management, Wollega University, Wollega, Ethiopia

⁸Department of Mechatronics Engineering, Kongu Engineering College, Perundurai, Erode 638060, India

Correspondence should be addressed to Priyanka Prabhakaran; priyacivil80@gmail.com and Prabhu Velusamy; prabhuvelusamy@wollegauniversity.edu.et

Received 5 July 2022; Revised 20 July 2022; Accepted 27 August 2022; Published 14 September 2022

Academic Editor: K. Raja

Copyright © 2022 Priyanka Prabhakaran et al. This is an open access article distributed under the Creative Commons Attribution License, which permits unrestricted use, distribution, and reproduction in any medium, provided the original work is properly cited.

Congestion on land, hike in fuel costs, and critical need to cut down environmental emissions have generated the urge to shift from conventional rail transit systems to metro rail and high-speed rail for a mass mode of transportation. The conventional railway network especially in India stages an effective space in the means of mass transit systems. Subsequently, periodic inspection of the state of railway tracks is vital for ensuring rail safety, as tracks are critical components of train transportation networks. Tracks are designed to withstand zero critical incidents, and with the advent of new high-speed train services, there is a greater need to focus on track performance. Track maintenance methods are customized to suit local conditions for enhancing safety and reducing disruptions while guaranteeing the resilience and sustainability of any rail system. In recent years, various aspects of the TMSs (track maintenance systems) have been introduced within the railway industry for both ballasted and ballastless track systems. This study reviewed various approaches to track maintenance measures using traditional methods, statistical methods, and geometry-based methods based on track deterioration. Among all the reviewed methods, track maintenance based on the geometry is said to cater to the needs of the maintainers. The outcomes of this study are expected to support and assist in track maintenance decisions in the railway industry.

1. Introduction

Railways have always played an important role in the transportation of commodities and passengers. Massive consignments get transported through railways mainly due to their cost efficiency and reduced environmental emissions. Currently, most of the goods and commuters are

shifted by this mode of transport increasing their loads and indirectly the tracks on which they run. Railway tracks on which trains run encompass switches, ballasts, sleepers, and rails, where ballasts are used globally in railway tracks [1]. Though slabs are also substituted in a few parts, ballasted tracks are conventionally used due to their reduced costs and ability to handle dynamic loads. Over years these ballasted

track systems have been replaced by ballastless tracks. In a ballasted railway track, the ballast consists of crushed granular material. This ballast layer has sleepers embedded inside of it, which are used as a support mechanism for the superstructure. The ballast is placed on top of the sub-ballast. The ballast has many key functions such as supporting the weight of the track, absorbing and distributing loads (static and dynamic) of trains running on the tracks, and providing good water or fluid drainage capabilities [2]. The ballast also increases track stability in the lateral and longitudinal directions and, therefore, they must be maintained regularly. Throughout history, loads and speeds have been steadily increasing in rail transportation, and throughout this evolution, railway tracks have experienced changes. One such advancement is a full rebuild of track structures, which renders them ballastless. Traditional ballasts are replaced by firm supporting slabs consisting of concrete, steel, or asphalt, which transfers the load and provides stability. As numerous comparable components characterize them, there are several varieties of ballastless track systems available based on different manufacturers. As a stiffer alternative to ballasted track systems, additional precautions must be taken to maintain flexibility. A common feature embedded in most of the ballastless track systems is that they have highly elastic rail fastening systems. For further elasticity, other elastic components can be installed, such as pads, bearings, or springs [3]. The major advantages of using ballastless tracks are described as follows: large reduction in maintenance cost (20–30% of maintenance cost of ballasted ones), fewer traffic interruptions, contributing to higher availability, less restrictive use of electromagnetic wheel brakes, reduced structural height and weight, and preventing the release of ballast dust in the environment.

Figure 1 represents an overview of the ballastless track systems in practice within the Indian Metro Rail System. There are two approaches to express track conditions, namely track geometries and track structures. Track geometry flaws and irregularities are primarily used to represent track conditions and plan track repair. Track geometries deteriorate with age and use and can have detrimental impacts on track performances. When track parametric values fall below the satisfactory level, it causes derailment, with serious outcomes which may include increased railway operating costs, economic losses, damage to railway assets, the environment, and loss of human lives. Correction of inadequate track geometries results in expensive track maintenance. Their maintenance activities should be scheduled to restore track parametric values to an appropriate state. The state of rail transportation and track structures includes numerous components. Their service life and performances are primarily determined by maintenance techniques used throughout their life cycles.

Efficient rail infrastructure maintenance necessitates the correct allocation of resources to various operations, posing a number of practical and operational problems [4]. Maintaining railways can be categorized as follows:

- (1) PM (preventive maintenance) involves carrying out activities (inspection, identification, and repair)

based on periodic schedules where each equipment's operating condition is checked and reconditioned.

- (2) CM (corrective maintenance): all measures are taken if there is an unexpected or abrupt maintenance event in terms of repair of an item/equipment due to perceived faults by the users.
- (3) PRM (predictive maintenance) is required wherever contemporary measurement and signal processing technologies are required to correctly anticipate and diagnose item/equipment condition during operation.

PMs are time-based activities for assessing track deteriorations and have been studied [5–7]. Though maintenance activities need to be preplanned and executed within a short time frame after on-site inspections, [85], it is difficult to plan them. Moreover, these operations disrupt sequences of regular PMs which keep railway track elements in tune and fine conditions. PM actions can assist to return the component to a better state, and they are frequently less expensive than component replacement [7–9]. To take advantage of the cost-benefit of PMs, a PM intervention can be performed a number of times repeatedly on a particular component prior to its renewal [10, 11]. As a result, track maintenance via a predictive process has traditionally been addressed as a series of independent phases, with each track component controlled separately. Various layers of management assess each stage for each key component of the rail system. Several studies have systematically classified various models and optimization models. The shortcomings in the field of track maintenance management have been highlighted, and future potential study fields have been recommended. The specifics of various track maintenance systems were investigated in terms of conventional approaches, statistical methods, geometry-based methods, machine learning methods, and bioinspired optimization methods in this review work. The track maintenance model's best operational performance in terms of maintenance policy, maintenance cost, and reliability metrics is being evaluated and debated.

2. Overview of the Pioneering Analysis Undertaken in Track Maintenance Systems

2.1. Traditional Methods for Track Maintenance. Railway tracks are subjected to preventive as well as CMs. Among these, the PM's activities are scheduled prior to providing a systematic way of monitoring the track performance. Various other numerical experiments were performed on track scheduling models by implementing superior computational methods, and these systems were applied to a railroad network to improvise the maintenance schedule decisions where rail temperatures were focused. A study's design included a heavy rail haul network of 60 kg/m using rail stress sensors, strain gauges, and thermocouples. The temperature of the rails varies regularly according to the temperature of the surrounding air. SFT might fluctuate by 2–3 times over the day, according to field experiments. Based on

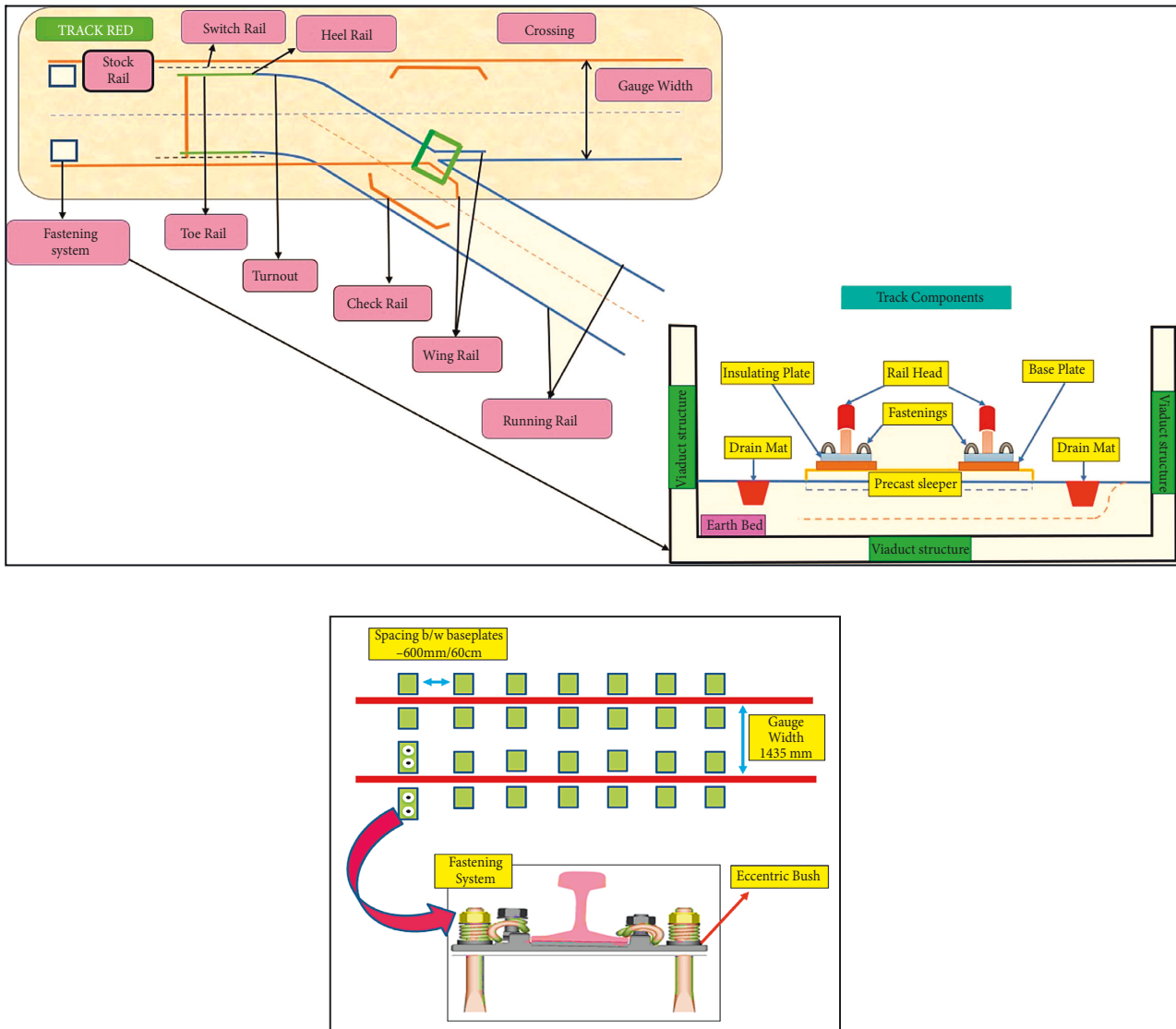


FIGURE 1: Overview of a ballastless track system.

these findings, an improvement in assessing track conditions using rail creep measurements was reported. TSMs (track stability management) are tools that identify requirements for PRMs. These tools stress the importance of rail stability and stress while defining rail modification priorities. Their assessments consider MS (margin of safety) or differences between TBs (track strengths) and TR-TN (rail stress) on the track. TR is the highest rail temperature while TBs are temperatures in which buckling might occur. TSMs use three elements, namely safety, track conditions, and prioritization of stress to obtain parameter values and act accordingly. RSMs (rail stress monitors) and strain gauges were installed on two (4 and 6 meters) 60 kg/m rails and tested with vertical loads of 5000 kgs where a hydraulic actuator was used. The test results were calibrated using finite element analysis. Computational results on strain gauges and thermocouples showed reduced SFTs at higher rail temperatures and contrary to RSM values which had increased SFTs at higher rail temperatures. Track

maintenance decision support systems have also made use of computational approaches such as big data. Big data methods have been presented to help with railway track maintenance choices. A large quantity of data on railway track condition monitoring is being gathered from various sources in numerous countries. These data are not being properly utilized due to a lack of appropriate methodologies for extracting key events and critical historical information. As a result, important information is concealed by massive amounts of data from various sensors. For railway track condition monitoring, general approaches that may support effective track maintenance decisions are provided. In Dutch tracks, As a benchmark, axle box acceleration (ABA) measurements are utilized, and generic reduction formulations are addressed to manage failures [12].

Moreover, the risk matrix application focused on identifying track zones that were bottlenecks and limited the operating strength and standard of tracks. A critical analysis method was presented to generate a hierarchical

TABLE 1: Inferences of traditional track maintenance methods.

<i>Author Reference</i>	<i>Evaluation Scheme</i>	<i>Concentrated segment</i>	<i>Parameters involved</i>	<i>Tools employed</i>	<i>Research gap</i>
[20]	Real time	Track maintenance schedule	Time window/travel cost/penalty cost	Time-space network model	Running time/renewal cost of rail
[12]	Case study	Track maintenance	Axle box acceleration measurements	Big data techniques	Maintenance frequency
[13]	Case study	Track maintenance analysis and rail infrastructure	Railway track operational factors	Risk matrix modelling	Weak overhead cable
[14]	Case study	Track deterioration	Track geometry measurements	RMMS	Life cycle costing
[16]	Case study	Electrically insulated rail joint	Inspection time variations/periodic replacement interval	Fault tree analysis	Inaccurate prediction/frequency of usage
[17]	Case study	Track maintenance schedule	Time periods/set up cost/key performance indicators	Capacitated arc routing problem	Maintenance crew scheduling
[18]	Case study	Track fault detection	Temperature/current/voltage	Remote condition monitoring	Database management/decision-making
[19]	Real time	Track maintenance schedule	Train timetable	Mathematical modelling	Speed restrictions
[21]	Real time	Track buckling	Rail temperature	Finite element analysis	Weather parameters
[22]	Case study	Rail maintenance	Squats/ballast defects	MILP solver	Multiple track defects (corrugation/ballast degradation)

improvement list in order to solve the issue of train mission interruption and lower operational capacity. The study's findings categorized the track line section into distinct risk zone categories based on their capacity and punctuality loss [13]. The process illustrates the analysis of track geometry simulation while optimizing the schedule with regard to tracking possession time as the research intends to decrease track possession cost. The analysis and modelling method for track maintenance planning and optimization will aid in the decrease of track possession time. Rather than maintenance schedule models, the bulk of studies on the tracks has focused on its deterioration process with regard to age and climate behavior. M&R (maintenance and renewal) was also targeted in a study that created a generic deterioration model by simulating track behavior. The model's life cycle costing and numerical optimization techniques minimized costs by balancing maintenance or renewals and could also produce qualitative inspections including disruptions to traffic. The scheme assisted in achieving the global objectives of RMMSs (railway maintenance management systems) [14]. The proposed M&R approach connected inventories, work history, and resource allocations to automatically predict deteriorations. Two critical components of the proposed PMs were namely localizing defects in infrastructures and accounting for parameters that were uncertain in their prediction of future deteriorations [15]. Impacts of an EI (electrically insulated) railway junctions regarded as a vital asset for railroad track identification as well as a major source of train interruptions were also examined. The maintenance aspects were added to FMTs (fault

maintenance trees) to determine the complexity and correctness of the parameters involved. The study's findings indicated that it was feasible to enhance joint reliability, for example, by doing more inspections, but the increased maintenance costs exceeded lower costs due to failures [16]. Consumed time due to maintenance can be constant or may change. Hence, the minimum time required to maintain segments was targeted where maintenance schedules were modified based on three distinct variations.

The scheme CARPF (capacitated arc routing problem with fixed cost) has resolved these issues by considering the parameters as a node routing issue [17]. Most track maintenance programs are designed to save money or time, but very few are designed to decrease the downtime of the equipment used to accomplish them. This optimization approach aided in the early discovery of problems thus reducing equipment downtimes and increasing production [18]. The majority of conventional track maintenance approaches have focused on studying track behavior owing to deterioration and wear prediction models. Reference [19] presented a mathematical programming approach for modifying train schedules on a single track based on maintenance activities. The unpredictability of maintenance activities may cause delays in the original maintenance plan, which may also conflict with predetermined train schedules. By adding buffer time into the redesigned schedule, this study tackles the unpredictability of maintenance tasks. In the modified timetable, the operational restrictions via speed limit due to maintenance activities were also addressed. The model produces a revised timetable that contains a

maintenance plan and train operation schedules for railway planners. Table 1 summarizes the conclusions drawn from traditional track maintenance methods:

The findings from conventional practices have revealed the usage of Weiner process, undirected graphical method, and fixed location-based monitoring method by the researchers for track maintenance practices. Many other methods like mixed integer linear programming (MILP) model, reliability-centered maintenance signalling system, and global sensitivity analysis based on distribution technique were utilized for forecasting and assessing track performance and resilience [15, 23]. With the introduction of metro rail transit systems, most of these methods are no longer extensively used. The majority of the studies mentioned above were well suited for the conventional railway system; thus, there is a need to use sophisticated prediction methods and forecasting models for track preventative maintenance.

2.2. Statistical Methods for Track Maintenance. Most of the statistics-based maintenance techniques are catered to create models or optimizations. Track geometry was predicted by [24] based on Petri nets. Their study projected conditions of the track with their estimated lifetime costs. The study altered inspection, maintenance, and ballast renewal parameters to achieve efficient predictions. Maintaining high-speed rail corridors using shared/dedicated operation patterns was examined, where descriptive parameter tables analyzed a corridor's response to changes in track maintenance strategies [25]. A modelling technique assessed existing data on track geometry and ballast condition, collected at regular intervals. Using the provided degradation distributions, a track section model was created that integrated maintenance and renewal processes and allowed the prediction of the ballast section's state over time frames. The model employs a Petri net formulation with a Monte Carlo solution routine to examine the efficacy of various maintenance techniques [26]. Most of the track maintenance schedules corresponded to train timetables. Several studies have modified the railway schedule based on the repair schedule. Physical inspections and visual examinations were the base for assessing track geometry issues. The scheme pointed out discrepancies in inspection data of tracks using a specialized instrument (track geometry vehicle). The model eliminated all positional errors from inspection data irrespective of noises in parameter measurement values. The model took 1.5004 s to correct 1 km track segment's positional errors. Further, the model also adapted itself to a variety of other applications: track geometries of trolleys, highway inspection data from LiDAR (Light Detection and Ranging) vehicles, and railroad catenary wire geometry inspection [27]. Despite periodic maintenance and considerable noise, the results line up exactly. Grindings are used in this study to eliminate fractures based on their depth. The rate of expansion of cracks on the head rail remains constant and the crack grows by 1% for every 1% increase in ridership [Mega gross tons]. It is expected that a single machine pass can repair a crack with a depth of h mm and a

cost of $ascg$. The increase in track growth was represented by a typical track section with the final limit as T_i . If the length of the track segment I exceed the limit T_i , the track is replaced at a cost $cr \gg cg$. An increase in rate correlates with a decrease in the duration of cost function intervals. The last PMs are to be replaced at a higher co at the limit T_i . Similar research was proposed for solving issues in interactions between high-speed night trains and maintenance schedules by utilizing MILPCPLEX solver. The study rearranged maintenance schedules to accommodate high-speed night trains running early morning or late evenings resulting in enhanced maintenance plans and timetables [28]. The midnight train timetable typically overlaps with the daytime train repair schedule. The service line is closed during maintenance of any railway section; therefore, to avoid conflicts, the maintenance period for specific segments is shortened to less than 4 hours or postponed accordingly. Night trains utilize the spare time available between consecutive railway segment repairs (G). In order to avoid the conflicts between the train schedule amidst the maintenance schedule, certain trains were even cut off from service line. Thus, the work presented a modular approach for railway maintenance schedule optimizations.

A predictive technique for railway track maintenance scheduling was implemented taking into consideration risk assessment strategies based on ISO 55000 standards as well as real-time track conditions. A unique feature of this method is the inclusion of the idea of risk management in railway maintenance scheduling, suggesting that maintenance activity priorities are based on asset criticalities, such as track degradation conditions and repair prices, as well as users' unmet demand caused by asset failures [29]. To deal with nonlinearity concerns, predicted track degradation models are used. Tracks are classified into four conditions: good where there is negligible degradation, waiting maintenance where the tracks are close to failure but the degradation process has commenced, acceptable track degradation where failure is expected to take place within ds time, and unacceptable degradation level where the tracks are expected to be renewed or replaced. As a result, a MILP approach integrating cost, hazards, and appropriate weights is developed to forecast correct maintenance priority within a time horizon. The asset management approach used on a railway track segment was investigated using a Markov model. The number of model parameters employed forecasts the condition of a track segment over time for a specific asset management approach in order to illustrate the effects of maintenance interventions on the track's lifetime. The Markov model offers a simple yet effective mechanism for evaluating the effects of an asset management strategy on a railway track section [30]. Tracks are classified according to their standard deviation (SD), namely ∂ : good, ∂_{crit} : critical, ∂_{spd} : speed restriction, and ∂_{cls} : line closure. Once a track section reaches ∂_{crit} , the section requires maintenance. As the track deteriorates more, the SD value obtained will strike ∂_{spd} , implying that speed limitations will be applied to that portion. In case of further deterioration, the track segment reaches ∂_{cls} which indicates there is an immediate need for closure of that segment. Theoretical prediction of track

irregularities was proposed by [31]. The study's grey model was compared with linear and exponential models. The study computed longitudinal standard deviations with the use of regression while their grey model was based on inspection data. In their assessment of prediction accuracies, the study found that modifying their model using the Fourier series resulted in the best performances with minimal errors. The work was an asset to the planning and scheduling of PMs. In addition, track inspectors were used to undertake an enhanced method of track geometry monitoring as data related to tracking geometry behavior was manually captured. After the advent of modern rail track inspection vehicles, this had altered as the vehicles run along train tracks and collected data about the state of infrastructures. Based on this information, a degradation model for train tracks was built in order to anticipate track deterioration and estimate future maintenance operations. To forecast tram track degradation, an ANFIS (adaptive network-based fuzzy inference system) was proposed where ANFIS estimated gauges. The system was found capable of accurate predictions even in jumbled data [32].

PMs were scheduled by [33] using optimization on a combination of PMs and renewals and arriving at the best between them. Resource optimization solutions such as grouping and balancing are used to reduce maintenance costs while maintaining the same level of service. Mixed integer linear programming is used to lower the costs of maintenance and renewal projects, as well as the associated labor and downtime charges, across the planning horizon. According to experimental data, the integrated optimization strategy minimizes the cost of preliminary work by effectively arranging it. The combined strategy resulted in a 14% reduction in maintenance and renewal expenses. Another research on preventative maintenance schedule was recommended to keep railway infrastructures in excellent working order while also taking into consideration limited resources available. The challenge of scheduling preventative railway maintenance operations was defined using MIP (mixed integer programming) and VNSs (variable neighborhood searches) to address large instances of the problem [34]. Many studies have focused on preventative maintenance scheduling techniques, while only a few of them focused on CM scheduling. Following their discovery as part of an inspection procedure, a methodology was presented in the study for optimizing CMs in rail networks. A study modelled integer programming for minimizing passenger delays due to low operational speeds on degraded rail segments while giving importance to intensively operating segments, train loads, staffing, budgets, and other constraints [35]. Figure 2 shows the degradation of rails, which was monitored on a real-time basis. These figures represent the lack of greasing along the sliding chair of check rails, rusting of check rail locks, worn-out base plates/rail plates that control the friction between the eccentric bushes and the anchor bolts, and the lack of greasing in the nosing areas. These defects indicate high chances of track slips that might create pits on the tracks thereby causing damage to the rolling stock.

The idea of RAMS (reliability, availability, maintainability, and safety) has been embraced by most metro rail

depots, and a similar approach was recommended to assist choices on train track design and maintenance methods. RAMS management is often used in the railway industry, but the proposed LCCA supported decisions on design alternatives and maintenance methods through an economic analysis that considered costs and performances. As a result, a decision support system was created based on life cycle costing (LCC) analysis for balancing immediate and long-term costs with performance and targeting RAMS. The suggested model incorporated not just agency (e.g., construction, inspection, maintenance, and renewal) and user expenses (e.g., delay-related) but also environmental costs into a full life cycle cost analysis (e.g., related to CO₂ emissions). The RAMS of a slab track was typically greater than that of a ballasted track, according to the findings [36]. A comparable analysis of life cycle costs was recently offered as a reasonably inexpensive alternative maintenance strategy for existing lines. This research seeks to evaluate the technology's potential benefits while also developing a new maintenance approach for existing ballasted rail beds. A protocol for the use of the BSB technology, as well as its related maintenance plan, has been established. The acquired results are also submitted to a sensitivity analysis. The use of BSS is projected to result in a considerable increase in the time between minor and major maintenance tasks [37]. Using the binary integer programming (IP) paradigm, a study has proposed a maintenance schedule optimization model for various components of a railway track. In general, grouping and maintaining several track components under one ownership saves the cost incurred as the track tends to be occupied. A sensitivity analysis is used to emphasize the effects of available possession time on the number of necessary possessions as well as the total cost involved [38].

In the same way as the prior integer programming model [39], a MIP model for routing vehicles with restrictions was proposed targeting Class-I railroads. Very few or limited studies have explored MDMs (Markov decision models), but one study used MDMs to obtain predicted values as impacted by present scenarios. The proposed MDMs used the train wheel's distinct conditions including their diameter, renewal distance based on time, and damages based on conditions. The study's estimated Markov transition matrices considered PMs and proposed an optimal strategy for ideal actions based on wheel conditions/states [40]. Another study was also based on MDMs and used conditions of the rails to define an optimal strategy that reduced overall costs. Rail conditions were assessed by the MDM using height, weight, MGTs (million gross tons), and damage incidences of the rails. The proposed optimum policy was a set of three PMs for railway managers to decide on the best PMs based on the state of the rail [41]. MPCs (model predictive controls) were proposed for multilevel decisions on optimum railway network's PMs. The study differentiated sections using independent stochastic degradations. They used a controller to compute and arrive at long-term section-wise PMs, thus helping reduce deteriorations and maintenance costs while ensuring degradations did not cross a defined threshold. The study's Dantzig-Wolfe decompositions optimized both continuous and discrete variables for best

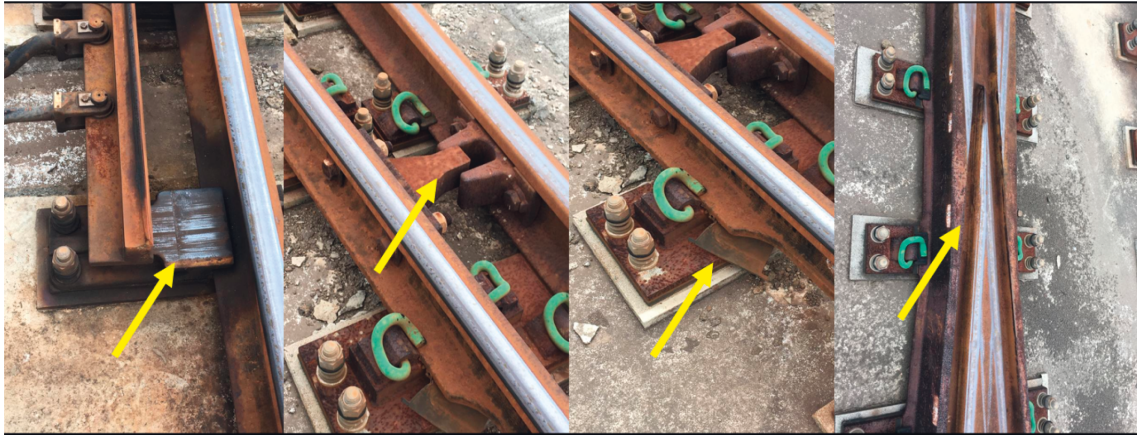


FIGURE 2: Common visible track defects [source: Chennai Metro Rail Depot].

decisions. Short-term schedules for maintenance using a high-level controller were proposed where maintenance staff routing was optimized. The study handled the issue assuming it as a routing issue and was found to be resilient, nonconservative, and scalable in simulations. Maintenances were scheduled based on average deteriorations and did not extend upto 6 months as a buffer time was allotted between average degradations and maintenance threshold values. The maintenance plan for certain sections had raised above maintenance thresholds and had to be grounded to zero after 6 months. In case of maximum deteriorations, time steps near maintenance threshold values and this occurs only during rail breakages. Table 2 lists the inferences obtained from the statistical maintenance methods. Most of the statistical methods employed for the maintenance of tracks have left a leap in the area of renewal cost.

2.3. Maintenance Methods Based on Track Geometry.

Bayesian models are probabilistic models that are thought to describe the connection between conditionally independent and dependent variables. Only a few investigations have been using this technique to evaluate rail track geometry deterioration over time in order to improve rail track geometry degradation uncertainty. Inspection historical data were used to assess uncertainties and were updated after every inspection. After each update of inspection history, uncertainties were assessed and degradations were measured by computing subsequent probabilities [42]. Similarly, the same approach was used to forecast and track degradations for guiding maintenance/renewals. This study used conditional auto regressions on track geometry data for interactions between successive track sections and lines [43]. The study simulated multiple correlations in consecutive track section components including degradation rates using HBMs (hierarchical Bayesian model). Their HBM assessed quality by comparing sensitivities of their generated candidate model's past distributions. Reference [44] used HBMs to evaluate railway track deteriorations. In addition, the study illustrates track maintenance histories with renewals in terms of percentage in the period 2001 to 2009, where the ratio of renewals shows a rise from 0.34 (2001) to 0.65

(2009). The authors also recommended MDMs for quantitative maintenance and thus prevent deterioration in Portugal's railway tracks. PMs/CMs/renewals costs, infrastructural delays for accommodating maximum allowable speeds, and unexpected infrastructure delays for temporary speed limitations were all accounted for alerting according to international standards. Threshold warning for key quality indicators of railway tracks that assists in determining the optimal choice of indicators were studied using sensitivity analysis, and in addition, penalties were levied on delay in trains [45]. The VirMaLab formalism was extended to provide an assistance tool for rail maintenance in an automated metro environment for standard steel-wheeled trains.

The theory of dynamic Bayesian networks provides an intriguing framework for addressing this problem since it allows for the use of probability distributions to characterize degradation processes as well as stochastic representations of maintenance agents. It not only simulated the rail degradation and the whole maintenance process but also the maintenance action decisions. The software's indicators assist in determining the most appropriate maintenance parameters. Because a metro rail track segment is made up of n number of elementary rail sections, developing a maintenance model for the entire stretch is considered unrealistic. As a result, the model only represents the elementary rail sections, which are extrapolated to larger sections based on reliability indicators. The VirMaLab model can estimate track degradation from hour to hour, including the effects of broken rail during peak hours. According to the VirMaLab Bayesian network, each condition of the rail is classified as OK (the rail with null defect), X1 (rail with internal cracks that are larger than 2 mm), X2 (rail with both internal and surface cracks less than 30 mm large), or BR (broken rail). The model's initial block is made up of rail deterioration, followed by the second block, which is made up of diagnosis devices. Ultrasound vehicles (USV), walking survey teams (WT), metro drivers (Drv), and track circuits are the devices that trigger periodic rail changes based on traffic, peak hours, and operational stops (TC). TC is thought to be the first to discover 80% of the broken rail problems. In the case of a warm season, rail dilation aids in maintaining electric

TABLE 2: Inferences of statistical track maintenance methods.

<i>Author Reference</i>	<i>Evaluation Scheme</i>	<i>Concentrated segment</i>	<i>Parameters involved</i>	<i>Tools employed</i>	<i>Research gap</i>
[5]	Case study	Track maintenance	Frequency of tamping operation	Mixed integer programming model (MILP)	Cost structure/schedule generation
[6]	Case study	Track maintenance	Rail grinding schedule/ rail crack detection	Integer programming model (ILP)/polyhedral analysis	Maintenance decision-making process/frequency of inspections
[24]	Case study	Track geometry	Inspection/ intervention/renewal	Petri net formulation	Track length/tamping machine
[25]	Real time	Track maintenance	Segments/routine works/possession cost	TMS strategy/Sensitivity analysis	Calibration of the PMSP model
[29]	Case study	Track maintenance schedule	Maintenance activities/ risk assessment	Modular model architecture/ ILP	Online recovery tool to determine stochastic delays
[32]	Case study	Track degradation	Rail load, rail type, rail profile	Adaptive network-based fuzzy inference system (ANFIS) model	Gauge value prediction
[33]	Case study	Track maintenance	Time period/track component replacement	Integer programming model (ILP)/Heuristic algorithms	Unexpected interventions/ corrective maintenance decisions
[36]	Case study	Track maintenance	User cost/ environmental cost	RAMS/LCCA	Database management
[37]	Case study	Track maintenance	Ballast type/lab test/ traffic	Life cycle approach	Life cycle cost analysis (LCCA) and life cycle assessment (LCA)
[38]	Case study	Track maintenance	Rail, ballast, sleepers, and switches	Binary integer programming (IP) model	Limitation of possession time
[39]	Real time	Track maintenance clustering	Project duration/job cluster type	Mixed integer mathematical programming model (MIMP)	Randomness of algorithm
[40]	Case study	Track interactive rolling sets	Wheel diameter/ mileage	Markov decision process/ MDP toolbox-MATLAB	Markov transition matrix (MTM)/inspection modes/ precision
[41]	Case study	Track maintenance	Rail grinding/renewal	Markov decision process	Rail curvature

contact with the BR, reducing the capacity of the TC to identify a fault by 50% [46]. Stochastic models are financial models that predict the likelihood of obtaining various outcomes under various limitations using randomly chosen variables. These models are used to characterize the process of geometrical track deterioration over time. For each vehicle speed category, a statistical analysis is carried out. The novel aspect of this study is that the Dagum distribution, which is commonly used to depict income distributions, is used to represent the geometrical track degradation process at the longitudinal level [47]. As part of condition-based preventative maintenance, a stochastic mathematical model is being created to optimize and anticipate tamping operations on ballasted rails. The model is described as a mixed 0–1 nonlinear program with real technical restrictions such as longitudinal standard deviation deterioration rate, track layout, track recovery dependency on its quality at the time of the repair operation, and preventative maintenance limits. This model looks at a 51.2 km long section of railway during a 10-year period. The deterioration model was found to be stochastic in nature, and it displayed the longitudinal standard deviation decreasing with time. The rate of degradation of the longitudinal standard deviation was

modelled using Monte Carlo techniques, with three parameters taken into consideration. Dagum's probabilistic distribution blended well with real-world data. The results of two simulations, namely stochastic simulation in space and stochastic simulation in space and time, were compared to one another. [48] The suggested condition-based maintenance model could provide optimum schedules in a reasonable amount of time. Only a few other researchers have focused on establishing an analytical framework that aids in decision-making. Reference [49] provided an analytical methodology for determining the best geo-defect repair options by minimizing anticipated costs including derailments/repairs. The study's major contributions were in integrating three models: track deteriorations of Class II geo-defects; survival of tracks from derailment risks, and optimization of track repairs under uncertain conditions. The proposed models showed a 20% reduction in overall composite costs and the percentage rose when longer track sections were considered.

Another study that followed this proposal using the same approach except that their model was an optimization was based on cost-based formulations and risk-based formulation (RBFs). These schemes addressed optimal rectification

planning challenges of railways. To improve track rectification decisions, existing railroads are presented with decision queries such as how yellow tags slip into red tags, how unrectified yellow tags slip into the risk of derailment, and what should be the correct time horizon within which an activity is prevented from falling into the red tag area [50]. Because track geometry is regarded as a hotspot in any railway industry, few research have focused on the degradation of track geometry by utilizing the Weibull technique and regression approaches. Reference [51] presented a Weibull method for analyzing time distributions for track geometry to deteriorate to defined states after repair. The quality of the track is determined by the rail alignment, particularly the vertical alignment. Higher wavelengths that have little bearing on ride quality are filtered out. The train engineers use a wavelength filter of around 35m to screen the track condition. The standard deviation for a 220-m yard segment is then determined. In addition to the tamping action, the quality of the track geometry is assessed. The findings of this study demonstrate that traffic speed and the history of any line's maintenance have an impact on geometrical degradation. Furthermore, the notion that tamping affects railway ballast is supported.

Meanwhile, [52] used a logistic regression technique to add unplanned maintenance requirements for rail track geometry deterioration. Unplanned maintenance for tracks based on European Standard EN 13848 was proposed in a study. The study considered bridges and switches data from inspection records and analyzed them statistically. Standard deviations from longitudinal values and errors in horizontal alignments were used as main indicators for unplanned maintenances. The study also proposed trade-offs between planned/unplanned maintenances and catering to EN 13848 limitations. Most optimization approaches focused on track conditions and costs of renewing them. PMs were forecast using biobjective optimizations where renewals were linked to track geometry. From the standpoint of infrastructure management, the challenge was treated as an objective integer optimization problem. The overall expenditures of planned repair and renewal activities, as well as the total number of delays in runtime induced by speed limits, were both minimized. The optimal Pareto frontier was determined using a simulated annealing approach in a tiny example for a basic network [53]. In a railroad track degradation study, [54] developed a short-range track condition forecast technique. Its purpose is to inform railway maintenance managers about the track condition ahead of time so that track maintenance activities may be scheduled. Track geometrical exceptions are derived from track conditions assessed using track geometry vehicles, and the projected values revealed that they did not offer a trustworthy condition. Track geometry data from Jiulong-Beijing train track geometry cars were used for error and comparability tests. The improved model is strong enough to generate trustworthy predictions, according to the analysis results. Reference [55] suggested a new approach for forecasting track geometry defects that is comparable to existing track records and combined prediction with inspection and maintenance planning. Broken rail faults are frequently

preceded by visual and ultrasonic cracks. The recommended strategy's underestimation of flaws is controlled by a novel application of a risk-averse and hybrid prediction approach.

MDM forecasts identified suitable inspection and maintenance strategies. Moreover, Whittle indices using an updated transition kernel (multi-bandit formulations) offered optimum dynamic policies to handle limitations. The study forecastings were highly accurate and suitable to forming long-term scheduling rules which could be changed based on changing conditions. Reference [56] reduced ballast costs for maintenance/unit traffic by their optimization of track geometry inspections. The study considered inspection and maintenance timings along with incurred costs for inspections, tampering, and risk of accidents based on track conditions. The study's probabilities were based on northern Sweden's track geometry data where passenger and freight trains were considered. Constructions, operations, designs, and maintenance account to track geometry degradations. Reference [57] assessed PM limits for Iran's railway lines to reduce overall maintenance costs. The study's cost model included PMs, CMs, inspections, and penalties when CMs limits were exceeded. The study used standard deviation values of longitudinal levels for quality of railway geometry assessments. The study minimized model's uncertainties in maintenances. The most comparable track sections were classified using the K-means clustering method. Thereafter, a linear function was used to indicate the degradation of rail sections for each cluster. To anticipate track geometry behavior and calculate the appropriate maintenance limit that minimizes overall maintenance expenditures, the Monte Carlo approach was utilized. According to his results, putting in place an adequate limitation can save overall yearly maintenance expenditures by 27 to 57%.

Among the previously described track geometry models, [58] proposed a method for allocating an effective track geometry maintenance limit that results in the lowest overall yearly maintenance cost. The cost model integrated inspections, PMs, CMs, and emergency CMs using standard deviation and outlier values of singular faults on longitudinal scales to derive quality indicators for PMs and CMs. The study used Monte Carlo approach to model track behavior after maintenance operations, limiting it to certain scenarios thus minimizing overall maintenance costs. Sensitivity analysis on inspections and maintenance response times was used to suggest effective restrictions in railway operations. However, the study proposed a lower bound optimal value for operations. Track geometry is evaluated at discrete time intervals (s) to determine its condition, as previously indicated. Each inspection interval measures the standard deviation of the longitudinal level (DLL), and if it exceeds the action limit AL (DLL AL), the track will be examined for PM tamping during the first maintenance window (T_{tamp}). This means that PMs will not be performed on the track until the predetermined PMs period has passed, even if the DLL between two maintenance cycles is greater than the AL. Track geometry is evaluated at discrete time intervals (s) to determine its condition, as previously indicated. This study concentrates on the efficient determination of maintenances,

and catering to isolated faults has been outlined for future scope. Examining reaction times of regular CMs, track degradations can be categorized into normal tracks in CMs or CMs in an emergency. The categorization can be applied only when the time taken to react exceeds inspection intervals. In this study, the degradation of track geometry was modelled using a linear model and the degradation parameters. The degradation parameters in the suggested degradation model are (???? and bs) considered as random variables. The difference between the projected value and the measured value is said to be degradation, where t is the time in days and t_n is the time at the most recent tamping operation. Various parameters encompass degradations resulting in a change of behavior in track sections. The AD (Anderson–Darling) test found suitable distribution where the likelihood of degradations assisted in estimating distribution parameters. It can be inferred that linear model residues get distributed normally in tests. Minitab software computed mean and variances of degradation model's errors [58].

The increasing trend observed in the track length is represented in Figure 3 which indicates the critical need to monitor track geometry. Datasets related to track geometry cannot be easily obtained since they are not kept in a repository. Despite the fact that data gathering is uncommon, a few real-time studies have been developed and carried out using data-driven models, and a few of them are discussed here. Based on track quality evaluations over time, [97] developed a data-driven tamping forecast. A study database comprising asset information completed maintenance activities and measured data over a 4,400-km stretch of the Austrian rail network during a 16-year period has been made public. For planning and anticipating tamping operations, the modified standard deviation of vertical track geometry has been found as an excellent track quality indicator. Further analysis reveals that a linear regression function is most suited for characterizing track quality between two tamping activities and for forecasting track quality in the future with the highest accuracy. The linear regression function was used to create an algorithm that allows for the analysis of track quality behavior over time for large time series and the whole network. Based on measurement data gathered from the field study, a comparable data-driven analytical approach for prediction of isolated track geometry problems was created. A new defect-based model was suggested to determine the deterioration pattern of isolated longitudinal level faults of railway tracks. In the deterioration route, the suggested model considered the occurrence of shock events.

The efficiency of tamping intervention in correcting longitudinal-level faults was also investigated. The results demonstrate that the linear model is considered to be a good fit for exhibiting the longitudinal-level defect of the track degradation pattern. In addition, a section-based model based on binary logistic regression has been created to forecast the likelihood of isolated faults occurring in segments of railroad systems. As explanatory variables, the model included standard deviation and

kurtosis of longitudinal levels. The kurtosis of the longitudinal level is a statistically significant predictor of individual track section levelling problems. The validation findings show that the proposed binary logistic regression model can detect the presence of isolated defects in a track segment with high accuracy [59]. Table 3 groups the inferences from the geometry-based maintenance techniques.

3. Identification of Real-Time Constraints in the Indian Metro Rail System

PMs are carried out by the maintainers in every Indian metro, and the values obtained at every section of the rail are recorded manually in registers which will further be verified by the section engineers.

The section engineers are responsible for deciding if any maintenance is to be performed by their team at the particular section after obtaining a work permit from the operation and control center of the railway. Therefore, there is a time-lapse analyzed here and this, in turn, may sometimes result in an emergency maintenance requirement. To offer a realistic prediction for track maintenance restrictions and real-time constraints, the most modern PMs for railway tracks rely heavily on inspection and degradation evaluation. To solve these constraints, recently several algorithms have been introduced which are discussed in the above section. The majority of the studies have concentrated on optimal routes for the maintenance crew, rerouting of vehicles as per maintenance schedule, clustering track maintenance jobs, cost for undertaking the early and late maintenance tasks, corrective maintenance programming model, considering actual infrastructure condition, minimizing the maintenance cost while maintaining the tracks at acceptance fit levels, minimizing the track possession time, and track degradation models. To the best of our knowledge, the major constraints encountered along the maintenance of tracks [Figure 4] are climatic conditions, lack of automated schedule, equipment availability, labour availability, track restoration time, block time, availability of parallel department, unskilled outsourced labor, implementation of additional stretch, budget constraints (hidden), maintenance tender, rail availability, train rerouting, trip frequency, material availability, budget approval time, and material processing time. The on-site constraints observed during the preparatory works of this study are as follows: outsourced technicians and maintainers-technical barrier, lack of preplanned maintenance activity, lack of systemized track maintenance schedule incorporating the constraints, climatic hindrances to complete the allotted activity, and lack of integrated (rolling stock, signaling) track maintenance scheduling

4. Workplan for Future

Track maintenance system of Indian metros is possibly done during night time as the run time of metro train

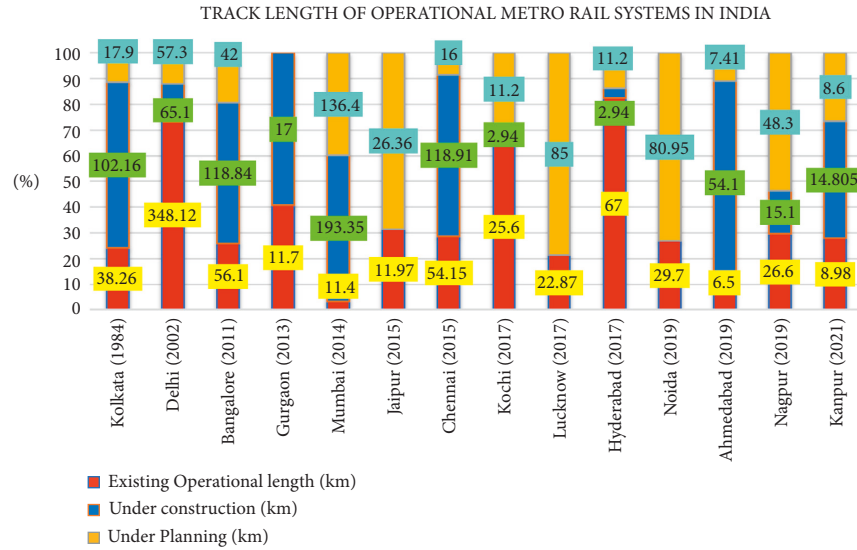


FIGURE 3: Increasing trend of metro rail track length [Source: https://en.wikipedia.org/wiki/Urban_rail_transit_in_India].

TABLE 3: Inferences of geometrical track maintenance methods.

Author Reference	Evaluation Scheme	Concentrated segment	Parameters involved	Tools Employed	Research Gap
[7]	Case study	Track maintenance	Track alignment defects	Decision support systems	Probability prediction of alert limits
[8]	Case study	Track maintenance	Total cost/renewal actions/speed restrictions	Mathematical modelling	Degradation parameters/different network configuration
[9]	Case study	Track maintenance	Track alignment parameters	HBM/Monte Carlo Simulation	Model sensitivity/correlation of formulation
[10]	Case study	Track maintenance	Track alignment parameters	Markov decision process	Permissible speed restriction
[15]	Case study	Track maintenance	Track alignment parameters	Weibull approach	Improvement of TPI
[47]	Case study	Rail maintenance	Rail parameters	VirMaLab/Bayesian models	Integration of meta-heuristics
[51]	Case study	Rail maintenance	Location/time of defect occurrence/defect type	Markov decision process/Whittle indices	Crew assignment for maintenance operations
[57]	Case study	Track maintenance	Rail type length/allowable speed/ballast type/fastener type/passenger capacity	Monte Carlo simulation/K-means clustering algorithm	Reduction of maintenance cost
[58]	Case study	Track maintenance	Maintenance window/frequency of inspection	Monte Carlo simulation/sensitivity analysis	Increase frequency and response time for maintenance
[59]	Case study	Track maintenance	Track geometry inspection values	Heuristics/analytical framework	Time optimization
[60]	Case study	Track quality	Track indices/longitudinal level	Linear regression analysis	Best fit integrated model
[47]	Case study	Track maintenance	Longitudinal level, alignment, gauge, twist, and cross-level.	Dagum distribution	Fitness of the model for varying track components
[48]	Case study	Track maintenance	Track alignment levels/standard deviation	Mathematical modelling/MILP/Monte Carlo process	Maintenance cost

begins every day on an average at 6 : 00 AM and ends by 9 : 30 PM and therefore the time slot available for preventive track maintenance is only during night time after

all train sets are back to stabling sheds. The work time available for any track maintenance activity is hardly 4 hours. The maintainers walk along the planned sections

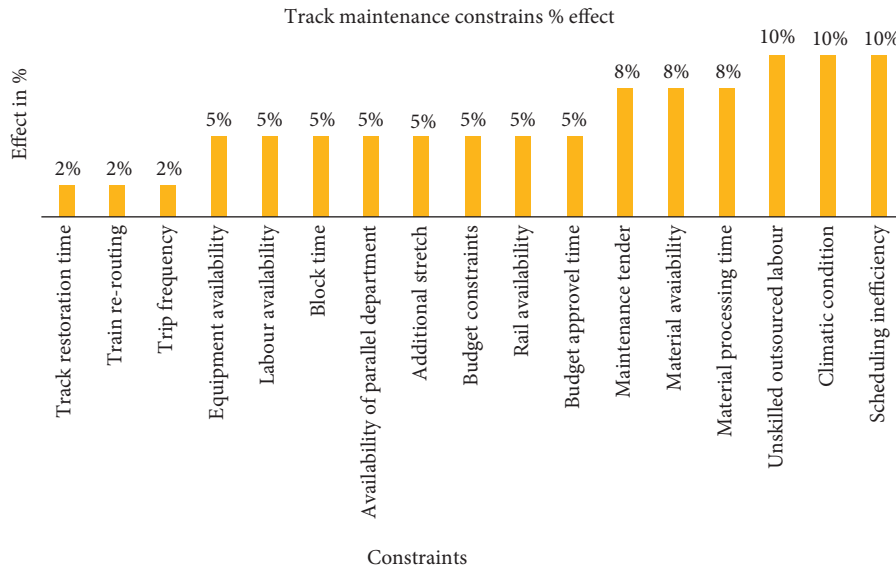


FIGURE 4: Constraint measurement in percentage wise.

of tracks and inspect visually during the nighttime which is very difficult at times to predict the exact track geometry measure. Most of the metro rail system has a parallel line known as a walkway along which the keyman can walk to inspect the lines in case of any reported issues observed during daytime. With the increase in track length, this is considered to be a critical task. In order to reduce the construction space and cost, walkways have not been included in any further projects. Therefore, in order to avoid a time-lapse in taking speedy action at the segment which requires immediate attention, a maintenance management model is believed to serve the purpose. Usually, the track geometry values are entered manually and recorded in separate registers. The section engineers in turn further check for the value accuracy and decide upon any need to directly inspect the particular section that has deviated from the tolerance/permissible value limits. There occurs a time-lapse for carrying out the maintenance activity, in case there is a need for immediate attention. Hence, it is necessary to have a planned scheduling system for allotting the maintenance activity along the track sections in between the service run during day time. As the Indian metros are on the verge of expanding their operational routes with a greater number of depots for stabling, it is highly necessary to plan the track maintenance activities systematically. Therefore, from all the previously referred reviews and methods, it is understood that most of the studies have been carried out on a real-time basis and the developed models are deployed into the respective systems to acquire better results. Through this work, the authors of the study have planned to develop a track maintenance alerting system for the Indian metros by developing a track cloud which will have a predefined set

of datasets from historical records. This database acts as a base layer to identify the difference in parameter threshold values if they fall beyond the limits. The developed system will serve as a decision assistant to the maintainer who can determine whether the track requires immediate attention or not which will then be reported systematically to the policymakers.

5. Conclusion

Railway infrastructure is one of a country's most valuable assets in terms of passenger and freight transit. The track is an essential aspect of the railway system among these components. As a result, maintenance planning for a busy railway track is difficult due to increased strain on increasing operation time, which limits the infrastructure-accessible time for repair. As a result, track maintenance has traditionally been regarded as a series of processes, with each track component being administered independently. Each phase for each major element of the rail system is evaluated at various levels of management. This review work studied the details of various track maintenance systems in terms of conventional methods, statistical methods, and geometry-based methods. The best operating performance of the track maintenance model with respect to the maintenance policy, maintenance cost, and reliability measures are reviewed. From every developed model, it can be inferred that railway track maintenance via ballastless has given more results than the ballasted track model. This review completely provides the methods adopted for tracking maintenance practices along with their constraints. Further, the review has also proposed a

maintenance model for Indian metro rail for future endeavors. From every reviewed analysis, it is notable that time plays a major important role in all systems. Therefore, in order to avoid a time-lapse in taking speedy action at the track segment which requires immediate attention, a new system that integrates the database cloud is planned to be introduced in future work for the betterment of the Indian Metro Rail System.

Data Availability

There are no separate data associated with this article.

Conflicts of Interest

The authors declare that there are no conflicts of interest in this study

Acknowledgments

The authors would like to extend their gratitude to the maintainers of Kochi Metro Rail Limited (Depot) and Chennai Metro Rail Limited (Depot) team for providing their valuable support and guidance.

References





- [1] D. Prescott and J. Andrews, "Modelling Maintenance in Railway Infrastructure Management," in *Proceedings of the Annual Reliability and Maintainability Symposium*, pp. 1–6, Orlando FL USA, January 2013.
- [2] C. Zhang, Y. Gao, L. Yang, Z. Gao, and J. Qi, "Joint optimization of train scheduling and maintenance planning in a railway network: a heuristic algorithm using Lagrangian relaxation," *Transportation Research Part B: Methodological*, vol. 134, pp. 64–92, 2020.
- [3] S. A. Kollo, A. Puskas, and G. Kollo, "Ballasted track versus ballastless track," *Key Engineering Materials*, vol. 660, pp. 219–224, 2015.
- [4] T. Liden, "Railway infrastructure maintenance - a survey of planning problems and conducted research," *Transportation Research Procedia*, vol. 10, pp. 574–583, 2015.
- [5] E. Gustavsson, "Scheduling tamping operations on railway tracks using mixed-integer linear programming," *EURO Journal on Transportation and Logistics*, vol. 4, no. 1, pp. 97–112, 2015.
- [6] E. Gustavsson, M. Patriksson, A. B. Stromberg, A. Wojciechowski, and M. Onnheim, "Preventive maintenance scheduling of multi-component systems with interval costs," *Computers & Industrial Engineering*, vol. 76, pp. 390–400, 2014.
- [7] M. Wen, R. Li, and K. B. Salling, "Optimization of preventive condition-based tamping for railway tracks," *European Journal of Operational Research*, vol. 252, no. 2, pp. 455–465, 2016.
- [8] C. Stenstrom, P. Norrbin, A. Parida, and U. Kumar, "Preventive and corrective maintenance–cost comparison and cost-benefit analysis," *Structure and Infrastructure Engineering*, vol. 12, no. 5, pp. 603–617, 2016.
- [9] Z. Zhu, Y. Xiang, M. Li, W. Zhu, and K. Schneider, "Preventive maintenance subject to equipment unavailability," *IEEE Transactions on Reliability*, vol. 68, no. 3, pp. 1009–1020, 2019.
- [10] T. P. Carvalho, F. A. Soares, R. Vita, R. D. P. Francisco, J. P. Basto, and S. G. S. Alcalá, "A systematic literature review of machine learning methods applied to predictive maintenance," *Computers & Industrial Engineering*, vol. 137, Article ID 106024, 2019.
- [11] Q. Wang, S. Bu, and Z. He, "Achieving predictive and proactive maintenance for high-speed railway power equipment with LSTM-RNN," *IEEE Transactions on Industrial Informatics*, vol. 16, no. 10, pp. 6509–6517, 2020.
- [12] N. Balac, T. Sipes, N. Wolter, K. Nunes, B. Sinkovits, and H. Karimabadi, "Large scale predictive analytics for real-time energy management," in *Proceedings of the IEEE international conference on big data*, pp. 657–664, Silicon Valley, CA, USA, October 2013.
- [13] S. M. Famurewa, M. Asplund, M. Rantatalo, A. Parida, and U. Kumar, "Maintenance analysis for continuous improvement of railway infrastructure performance," *Structure and Infrastructure Engineering*, vol. 11, no. 7, pp. 957–969, 2015.
- [14] S. Jovanovic, H. Guler, and B. Coko, "Track degradation analysis in the scope of railway infrastructure maintenance management systems," *Gradevinar*, vol. 67, no. 3, pp. 247–258, 2015.
- [15] R. Schenkendorf, J. C. Groos, and L. Johannes, *IFAC-PapersOnLine*, vol. 48, no. 21, pp. 964–969, 2015.
- [16] E. Ruijters, D. Guck, M. Van Noort, and M. Stoelinga, "Reliability-centered maintenance of the electrically insulated railway joint via fault tree analysis: a practical experience report," in *Proceedings of the 46th Annual IEEE/IFIP International Conference on Dependable Systems and Networks*, pp. 662–669, Toulouse, France, June 2016.
- [17] Z. Su and B. D. Schutter, "Optimal scheduling of track maintenance activities for railway networks," *IFAC-PapersOnLine*, vol. 51, no. 9, pp. 386–391, 2018.
- [18] S. B. Singh, R. Suresha, and K. H. Sachidananda, "Reliability centered maintenance used in metro railways," *Journal Européen des Systèmes Automatisés*, vol. 53, no. 1, pp. 11–19, 2020.
- [19] M. Bababeik, S. Zerguini, M. Farjad-Amin, N. Khademi, and M. Bagheri, "Developing a train timetable according to track maintenance plans: a stochastic optimization of buffer time schedules," *Transportation Research Procedia*, vol. 37, pp. 27–34, 2019.
- [20] F. Peng and Y. Ouyang, "Track maintenance production team scheduling in railroad networks," *Transportation Research Part B: Methodological*, vol. 46, no. 10, pp. 1474–1488, 2012.
- [21] S. S. Ahmad, N. K. Mandal, G. Chattopadhyay, and J. Powell, "Development of a unified railway track stability management tool to enhance track safety," *Proceedings of the Institution of Mechanical Engineers - Part F: Journal of Rail and Rapid Transit*, vol. 227, no. 5, pp. 493–516, 2013.
- [22] Z. Su, A. Jamshidi, A. Nunez, S. Baldi, and B. De Schutter, "Integrated condition-based track maintenance planning and crew scheduling of railway networks," *Transportation Research Part C: Emerging Technologies*, vol. 105, pp. 359–384, 2019.
- [23] S. Sharma, Y. Cui, Q. He, R. Mohammadi, and Z. Li, "Data driven optimization of railway maintenance for track geometry," *Transportation Research Part C: Emerging Technologies*, vol. 90, pp. 34–58, 2018.
- [24] J. Andrews, D. Prescott, and F. De Rozières, "A stochastic model for railway track asset management," *Reliability Engineering & System Safety*, vol. 130, pp. 76–84, 2014.
- [25] P. Lautala and H. Pouryousef, "Sensitivity analysis of track maintenance strategies for the high-speed rail (HSR)

- services,” *ASME/IEEE Joint Rail Conference*, vol. 54594, pp. 141–150, 2011.
- [26] J. Andrews, “A modelling approach to railway track asset management,” *Proceedings of the Institution of Mechanical Engineers - Part F: Journal of Rail and Rapid Transit*, vol. 227, no. 1, pp. 56–73, 2013.
- [27] P. Xu, R. Liu, Q. Sun, and L. Jiang, “Dynamic-time-warping-based measurement data alignment model for condition-based railroad track maintenance,” *IEEE Transactions on Intelligent Transportation Systems*, vol. 16, no. 2, pp. 799–812, 2015.
- [28] D. Wang, S. Zhan, Q. Peng, and W. Zhou, “Integrated overnight train scheduling and maintenance planning for high-speed railway lines,” *Transportation Research Record*, vol. 2675, no. 3, pp. 222–237, 2021.
- [29] A. Consilvio, A. Di Febbraro, and N. Sacco, “A Modular Model to Schedule Predictive Railway Maintenance Operations,” in *Proceedings of the 2015 International Conference on Models and Technologies for Intelligent Transportation Systems*, pp. 426–433, Budapest, Hungary, June 2015.
- [30] D. Prescott and J. Andrews, “Investigating railway track asset management using a Markov analysis,” *Proceedings of the Institution of Mechanical Engineers - Part F: Journal of Rail and Rapid Transit*, vol. 229, no. 4, pp. 402–416, 2015.
- [31] T. Xin, S. M. Famurewa, L. Gao, U. Kumar, and Q. Zhang, “Grey-system-theory-based model for the prediction of track geometry quality,” *Proceedings of the Institution of Mechanical Engineers - Part F: Journal of Rail and Rapid Transit*, vol. 230, no. 7, pp. 1735–1744, 2016.
- [32] M. Karimpour, L. Hitihamillage, N. Elkhoury, S. Moridpour, and R. Hesami, “Nonlinear Estimation Model for Rail Track Deterioration,” *International Conference on Transportation Economics and Transportation Systems*, vol. 11, no. 9, 2017.
- [33] F. Pargar, O. Kauppila, and J. Kujala, “Integrated scheduling of preventive maintenance and renewal projects for multi-unit systems with grouping and balancing,” *Computers & Industrial Engineering*, vol. 110, pp. 43–58, 2017.
- [34] R. Macedo, R. Benmansour, A. Artiba, N. Mladenovic, and D. Urosevic, “Scheduling preventive railway maintenance activities with resource constraints,” *Electronic Notes in Discrete Mathematics*, vol. 58, pp. 215–222, 2017.
- [35] K. Argyropoulou, C. Iliopoulou, and K. Kepaptsoglou, “Model for corrective maintenance scheduling of rail transit networks: application to Athens metro,” *Journal of Infrastructure Systems*, vol. 25, no. 1, Article ID 04018035, 2019.
- [36] F. G. Pratico and M. Giunta, “An Integrative Approach RAMS-LCC to Support Decision on De-sign and Maintenance of Rail Track,” in *Proceedings of the International Conference on Environmental Engineering. ICEE; Vilnius, Lithuania, April 2017*.
- [37] F. Sajedi and H. A. Razak, “Comparison of different methods for activation of ordinary Portland cement-slag mortars,” *Construction and Building Materials*, vol. 25, no. 1, pp. 30–38, 2011.
- [38] C. Dao, R. Basten, and A. Hartmann, “Maintenance scheduling for railway tracks under limited possession time,” *Journal of Transportation Engineering Part A: Systems*, vol. 144, no. 8, Article ID 04018039, 2018.
- [39] F. Peng and Y. Ouyang, “Optimal clustering of railroad track maintenance jobs,” *Computer-Aided Civil and Infrastructure Engineering*, vol. 29, no. 4, pp. 235–247, 2014.
- [40] J. A. Braga and A. R. Andrade, “Optimizing maintenance decisions in railway wheelsets: a Markov decision process approach,” *Proceedings of the Institution of Mechanical Engineers - Part O: Journal of Risk and Reliability*, vol. 233, no. 2, pp. 285–300, 2019.
- [41] L. C. B. Sancho, J. A. P. Braga, and A. R. Andrade, “Optimizing maintenance decision in rails: a Markov decision process approach,” *ASCE-ASME Journal of Risk and Uncertainty in Engineering Systems, Part A: Civil Engineering*, vol. 7, no. 1, Article ID 04020051, 2021.
- [42] A. Lopez-Pita, P. F. Teixeira, C. Casas, A. Bachiller, and P. A. Ferreira, “Maintenance costs of high-speed lines in Europe state of the art,” *Transportation Research Record*, vol. 2043, no. 1, pp. 13–19, 2008.
- [43] A. R. Andrade and P. F. Teixeira, “Hierarchical Bayesian modelling of rail track geometry degradation,” *Proceedings of the Institution of Mechanical Engineers - Part F: Journal of Rail and Rapid Transit*, vol. 227, no. 4, pp. 364–375, 2013.
- [44] A. R. Andrade and P. F. Teixeira, “Statistical modelling of railway track geometry degradation using hierarchical Bayesian models,” *Reliability Engineering & System Safety*, vol. 142, pp. 169–183, 2015.
- [45] A. R. Andrade and P. F. Teixeira, “Exploring different alert limit strategies in the maintenance of railway track geometry,” *Journal of Transportation Engineering*, vol. 142, no. 9, Article ID 04016037, 2016.
- [46] O. Francois, L. Bouillaut, and S. Dubois, “A Multi-Nets Approach for Modeling and Evaluating Rail Maintenance Strategies,” in *Proceedings of the 9th World Congress on Railway Research*, pp. 22–26, France, May 2011.
- [47] C. Vale and S. M. Lurdes, “Stochastic model for the geometrical rail track degradation process in the Portuguese railway Northern Line,” *Reliability Engineering & System Safety*, vol. 116, pp. 91–98, 2013.
- [48] C. Vale and I. M. Ribeiro, “Railway condition-based maintenance model with stochastic deterioration,” *Journal of Civil Engineering and Management*, vol. 20, no. 5, pp. 686–692, 2014.
- [49] Q. He, H. Li, D. Bhattacharjya, D. P. Parikh, and A. Hampapur, “Railway track geometry defect modeling: deterioration, derailment risk and optimal repair,” in *Proceedings of the Transportation Research Board Annual Meeting. The Academy of Transportation Research Board, Washington DC US, January 2013*.
- [50] Q. He, H. Li, D. Bhattacharjya, D. P. Parikh, and A. Hampapur, “Track geometry defect rectification based on track deterioration modelling and derailment risk assessment,” *Journal of the Operational Research Society*, vol. 66, no. 3, pp. 392–404, 2015.
- [51] M. Audley and J. D. Andrews, “The effects of tamping on railway track geometry degradation,” *Proceedings of the Institution of Mechanical Engineers - Part F: Journal of Rail and Rapid Transit*, vol. 227, no. 4, pp. 376–391, 2013.
- [52] A. R. Andrade and P. F. Teixeira, “Unplanned-maintenance needs related to rail track geometry,” *Proceedings of the Institution of Civil Engineers-Transport*, vol. 167, no. 6, pp. 400–410, 2014.
- [53] A. R. Andrade and P. F. Teixeira, “Biobjective optimization model for maintenance and renewal decisions related to rail track geometry,” *Transportation Research Record*, vol. 2261, no. 1, pp. 163–170, 2011.
- [54] P. Xu, C. Jia, Y. Li, Q. Sun, and R. Liu, “Developing an Enhanced Short-Range railroad Track Condition Prediction Model for Optimal Maintenance Scheduling,” *Mathematical Problems in Engineering*, vol. 2015, Article ID 796171, 12 pages, 2015.

- [55] P. C. Lopes Gerum, A. Altay, and M. Baykal-Gürsoy, "Data-driven predictive maintenance scheduling policies for railways," *Transportation Research Part C: Emerging Technologies*, vol. 107, pp. 137–154, 2019.
- [56] I. A. khouy, P. O. Larsson-Kraik, A. Nissen, U. Juntti, and H. Schunnesson, "Optimisation of track geometry inspection interval," *Proceedings of the Institution of Mechanical Engineers - Part F: Journal of Rail and Rapid Transit*, vol. 228, no. 5, pp. 546–556, 2014.
- [57] A. Kasraei, J. A. Zakeri, and A. Bakhtiary, "Optimal track geometry maintenance limits using machine learning: a case study," *Proceedings of the Institution of Mechanical Engineers - Part F: Journal of Rail and Rapid Transit*, vol. 235, no. 7, pp. 876–886, 2021.
- [58] H. Khajehei, A. Ahmadi, I. Soleimanmeigouni, and A. Nissen, "Allocation of effective maintenance limit for railway track geometry," *Structure and Infrastructure Engineering*, vol. 15, no. 12, pp. 1597–1612, 2019.
- [59] I. Soleimanmeigouni, A. Ahmadi, and U. Kumar, "Track geometry degradation and maintenance modelling: a review," *Proceedings of the Institution of Mechanical Engineers - Part F: Journal of Rail and Rapid Transit*, vol. 232, no. 1, pp. 73–102, 2018.
- [60] J. Neuhold, I. Vidovic, and S. Marschnig, "Preparing track geometry data for automated maintenance planning," *Journal of Transportation Engineering, Part A: Systems*, vol. 146, no. 5, pp. 1–11, 2020.

Research Article

Treatment of Tanning Effluent Using Seaweeds and Reduction of Environmental Contamination

V. Sampathkumar ¹, S. Southamirajan,² Elango Subramani,³ Senthilkumar Veerasamy,⁴ D. Ambika,¹ Dineshkumar Gopalakrishnan ⁵, G. E. Arunkumar,⁶ K. Raja,¹ S. Arulmozhi ⁷, and Dhivya Balamoorthy ⁸

¹Department of Civil Engineering, Kongu Engineering College, Perundurai, Erode 638060, India

²Department of Civil Engineering, Kongunadu College of Engineering and Technology, Tholurpatti 621215, India

³Department of Civil Engineering, K.S.R. College of Engineering, Namakkal, Tiruchengode 637 215, India

⁴Department of Civil Engineering, M.Kumarasamy College of Engineering, Karur 639113, India

⁵Department of Civil Engineering, Vaagdevi College of Engineering, Warangal 506005, Telangana, India

⁶Department of Civil Engineering, Shree Venkateshwara HI-Tech Engineering College, Gobi 638452, India

⁷Department of Civil Engineering, Erode Sengunthar Engineering College, Perundurai, Erode 638057, Tamil Nadu, India

⁸Department of Hydraulic and Water Resource Engineering, Wollega University, Nekemte, Ethiopia

Correspondence should be addressed to V. Sampathkumar; anbusampathcivil@gmail.com and Dhivya Balamoorthy; dhivyabalamoorthy@wollegauniversity.edu.et

Received 14 July 2022; Revised 31 July 2022; Accepted 8 August 2022; Published 6 September 2022

Academic Editor: Shankar Karuppannan

Copyright © 2022 V. Sampathkumar et al. This is an open access article distributed under the Creative Commons Attribution License, which permits unrestricted use, distribution, and reproduction in any medium, provided the original work is properly cited.

One of the main sources of dangerous chemicals that are dumped untreated into land and water bodies and have a negative influence on the ecosystem are industrial effluents. Seaweeds are currently used for treating industrial effluent effectively. The technology is at a maturing stage. This paper reviews the characterization and cultivation of seaweeds for wastewater treatment. In this present study, different extracts of four seaweeds such as *Gracilaria edulis*, *Sargassum wightii*, *Turbinaria ornata*, and *Kappaphycus alvarezii*, from the Mandapam coastal regions were analyzed. The seaweeds are used to treat the leather industry effluents collected from EKM leather processing company, Erode, Tamil Nadu, India. Among all, extracts of *Gracilaria edulis* survived at different concentrations of TDS: 15,000, 25000, and 35000 mg/l. Out of these different ranges, TDS of about 25000 mg/l seaweed named *Gracilaria edulis* reduced more amounts of chemicals present in the effluent like TDS (93.90%), phosphates (72.71%), nitrate (75.08%), nitrite (76.92%), and turbidity (99.01%) content. Additionally, we produce the quality and strength of agar gel from the cultivation of *Gracilaria edulis* by the Nikansui method. Finally, we got the extraction procedure to obtain a higher yield of about 10.26% and a maximum gel strength of 92.06 g·cm⁻² while maintaining the melting point at 78°C.

1. Introduction

Waste is produced by every area of our society, including consumers, manufacturing, farming, mines, energy, transport, and construction. Pollutants in waste include chemicals, process byproducts, and waste materials [1]. When these contaminants are released in excess of what the ecosystem can absorb, pollution may occur. Industrial wastes are produced by a variety of industrial processes, and each production method has a unique impact on the quantity and

severity of the pollution discharged [2]. The biggest contaminant of all industrial wastes is tannery effluent. The leather industry plays a significant role in the Indian economy, supplying 2 billion US dollars in exports and 2% of global trade. Nearly, 2.5 million people are currently in the leather sector, and the bulk of the leather industries is classified as small- and medium-sized businesses [3]. The country's enormous animal population is a significant factor in the development and expansion of the leather industry. Nearly, 10% of the world's supply of raw hides and skins, the

essential raw resources for leather industry, are available in India. In India, the states of Tamil Nadu, Andhra Pradesh, Karnataka, Punjab, West Bengal, and Uttar Pradesh are home to the majority of tanning salons.

The quantity of chemicals used in tanning processes is almost in the same range as that in all the regions in India. Depending on the availability of water, the wash water volume usage varies, and wash water contains chemicals in various concentrations in the sectional and composite wastewater [4, 5]. The concentration of the pollutants present in the wastewater also depends on the clean technology adopted in the tanneries like dusting of salt, recovery and reuse of chromium, and the quality of the chemicals used. In Tamil Nadu, it is mandatory for tannery processing, raw to semifinish (chrome tanning process), to have a chrome recovery system [6, 7]. Due to scarcity of water, the quantity of water used for washing is less in Tamil Nadu when compared with that of other parts of the country. Due to this, the concentrations of chemical oxygen demand (COD) and biochemical oxygen demand (BOD) are comparatively high in wastewater [8, 9]. However, in the case of tanneries in Uttar Pradesh, Punjab, and West Bengal, the volume of water used for washing is high and this results in dilution of the pollutants [10, 11]. In Andhra Pradesh and Tamil Nadu, soak and pickle liquor are segregated and conveyed to solar evaporation pans. However, in other parts of the country, no segregation of the soak and pickle is done and they are combined with the remaining sectional streams [12–14].

Seaweed is the common name for countless species of marine plants and algae that grow in the ocean as well as in rivers, lakes, and other bodies of water [15]. Seaweeds are used for a variety of things, including integrated aquaculture, fertilizers, animal feed, and nourishment for humans and animals. Presently, soak effluent is treated by solar evaporation pan. In this process, a coagulant is added to reduce the odor and turbidity of soak effluent and to increase the evaporation rate of effluent [16]. To provide a solution, this study focuses on the treatment of soak effluent by phytoremediation technique. This technique not only treats the effluent but also uses it to produce useful byproducts like agar gel by the Nikansui method. In the soak effluent having basic parameters like TDS, turbidity was found to be in a high range [17, 18]. For treating this effluent, the conventional methods are suitable but not an economical one. To overcome this, an ecofriendly method called phytoremediation technique (It is a method of “bio remediation” where different kinds of plants are used to transfer, remove, and stabilize toxins from the soil and ground water.) is adopted instead of the phytoaccumulation (The contaminants, along with other nutrients and water, are absorbed by plant roots during this process) process.

2. Materials and Methods

2.1. Collection of Seaweeds. The seaweeds (Figure 1 and Figure 2) were collected from the Mandapam coastal regions (latitude 9° 16' 32.56" N and longitude 79° 07' 25.03" E), India's southeast coast. A sample of seaweed was manually

collected, and any extraneous materials, sand particles, and epiphytes were quickly rinsed away with seawater [19]. It was immediately brought to the laboratory and extensively cleansed, utilizing normal water to remove the salt from the sample's surface while being maintained in an icebox filled with slush ice [20].

2.2. Collection of the Soak Effluent. The effluent was collected from E. K. M. Leather Processing Company at Erode (Figure 3). Many industries were using normal water in the soak process, but this industry was using reverse osmosis (RO) reject wastewater, which has more organic and inorganic constituents and other trace compounds. Therefore, the soaking effluent contains more organic and inorganic constituents [21]. These effluents were analyzed the raw and diluted effluent for physical and chemical characteristics such as pH, turbidity, BOD, COD, and phosphate by using APHA (33) methods. Physical and chemical characteristics of raw soak effluent are pH is 7.0–8.5, turbidity is > 1000 NTU, TDS is 30000–40000 mg/L, BOD is 1560 mg/L, COD is 3000 mg/L, TSS is 9800 mg/L, phosphate is 18 mg/L, NO₃ is 9.80 mg/L, and NO₂ is 0.08 mg/L, and biochemical parameters are total protein is 1800 µg/l, lipid is 12 mg/l, and carbohydrate is nil.

2.3. Aqua Culturing Technique. Marine or freshwater species may be raised by aquaculture, sometimes known as “fish farming,” in the marine or on shore. The farming technique employed heavily influences how environmentally friendly farmed seafood is [22].

2.3.1. Floating Raft Method. Floating rafts for hydroponically produced plants. The rafts can be used to improve water quality by filtering, consuming, or decomposing contaminants (such as nutrients, silt, and metals) from the wastewater [23]. They float on a wet pond top.

FRM might be a viable and reasonably affordable engineered the best management practice (BMP) for lowering wastewater pollution (Figure 4).

2.3.2. Determination of Growth of Seaweeds from the Soak Effluent. I have chosen 4 types of seaweeds like *Gracilaria edulis*, *Turbiaria ornata*, *Kappaphycus alvarezii*, and *Sargassum wightii* that were cultivated by the low tide method. In this method, for 1 liter of the soak effluent, 10 g of seaweeds was used for each species. Furthermore, aeration is provided [24]. After a period of 20 days, only the species called *Gracilaria edulis* alone has shown growth. It is found by measuring the final weight of that species [25].

Growth Rate = (Initial weight – Final weight)/(Final weight).

2.3.3. Determination of Optimum TDS for the Growth of *Gracilaria edulis*. An optimum dosage for the growth of *Gracilaria edulis* was identified by diluting the soak effluent with water to make different concentrations like 15,000,



FIGURE 1: Brown algae.



FIGURE 2: Red algae.



FIGURE 3: Collection of the soak effluent from E.K.M. Leather Processing Company.

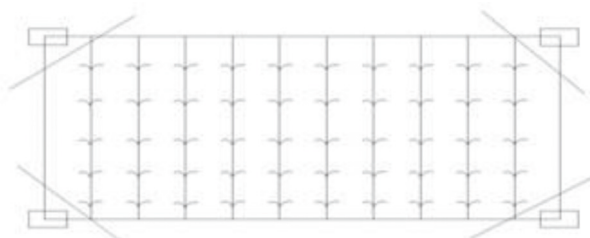


FIGURE 4: Floating raft method.

25,000, and 35,000 mg/l. Finally, that seaweed survived at a TDS range of 25,000 mg/l. Then, the plant was cultivated using the diluted soak effluent to determine the optimum TDS for the growth of the plant [26].

2.3.4. *Aqua Culture Study for Gracilaria edulis*. This study was conducted on three different samples (Figure 5).

- (1) Tannery soaking effluent of 15,000 TDS
- (2) Tannery soaking effluent of 25,000 TDS
- (3) Tannery soaking effluent of 35,000 TDS

2.4. Treatment of Wastewater Using *Gracilaria edulis*

2.4.1. *Determination of the Soak Effluent after Treatment at 5 Days Retention Time*. An optimum dosage for the growth of *Gracilaria edulis* was identified by diluting the soak effluent with water to make different concentrations of 15,000, 25,000, and 35,000 mg/l of TDS. Finally, it was determined that this plant can survive at 25,000 mg/l TDS [27]. Then, the plant was cultivated using the diluted soak effluent to determine the treated soak effluent. The initial weight of the seaweeds is tested for its soak effluent parameters for 5 days' retention time. We take the final weight of seaweeds after 15 days. These 25,000 mg/lit of TDS of the soak effluent has high removal efficiency of physical-chemical parameters by using *Gracilaria edulis*.

2.4.2. *Analysis of the Soak Effluent at 5 Days Retention Time*. The tannery effluent was collected through the soaking process and tested for its physical-chemical parameters by the AHPA method. Then, the cultivation of seaweed is weighted after 15 days by a weighing machine (Figure 6).

2.5. *Removal of BOD and COD from Treated Wastewater*. It was found that the treated soak effluent had high COD and BOD content. It will be removed by adding a large amount (2pinch) of coagulant dose like alum and polyelectrolyte [28].

2.6. *Production of Agar Gel from Gracilaria edulis*. The best combinations of alkali/acid and thermal processing were found to improve the yield and quality of agar from the red seaweed *Gracilaria edulis* [29].

2.6.1. *Soaking*. To study the effect of the soaking period, 20 g of dried *Gracilaria edulis* were soaked in 400 ml of potable water. Time units such as 4 h, 8 h, and 12 h were selected [30].

2.6.2. *Acid Pretreatment*. To determine the effect of acid soaking, the seaweeds were soaked in a dilute solution of HCL/NaOH at a concentration of 0.5 N for 1 hr. Presoaked samples in potable water for 11 h were transferred to a concentration of NaOH/HCL (0.5 N–3.0 N) for 1 h in a water bath at 82°C. To this mixture, 10 ml of CaCl₂·2H₂O was added to reduce the loss of agar while processing [31].

2.6.3. *Agar Extraction*. The treated plant was washed with running tap water to remove traces of NaOH/HCL. The dry sample of about 20 g was boiled in a 1 liter beaker after adding 400 ml of distilled water and maintaining pH in the range of 6.0–6.5 in an autoclave for 2 h. The hot extract was recovered after filtration through a muslin cloth. The residue was re-extracted with 100 ml of hot (80–85°C) distilled water. The filtrated samples were maintained at room temperature at –20°C for 12 h. The frozen gel was allowed for thawing. Alternatively, change the freezer and thaw the filtrated samples two times. The thawed gels were kept in the sun to dry for 3 days. Agar samples after complete drying were weighted accurately to calculate the percentage yield of agar [32].

2.6.4. *Agar Gel Strength Measurement*. The agar gel strength is measured by the FMC gel tester or by the Nickansui Method [33]

We calculate the gel strength formula according to the following equation:

$$G = X \left(\frac{W}{200} \right), \quad (1)$$

where $G = X$ gel strength in grams. W = millimetre of water necessary to break the gel. X = weight of gel in grams.

3. Results and Discussion

3.1. *Analysis of Sea Water*. The nutrient status of seawater for the selection of seaweed should be surveyed for basic physicochemical parameters like TDS, pH, NO₂, DO, NO₃, and phosphate by APHA (33) methods. From Table 1, it can be observed the TDS has a maximum value of 37,000 mg/l and the minimum value was NO₂ as 0.06 mg/Lit.

3.2. *Analysis of the Lime Effluent*. The lime effluent should be analyzed by the AHPA method. The lime effluent comes from the tannery process. It is also one of the tannery effluents [34]. It was analyzed for the physicochemical parameters like BOD, COD, TDS, pH, nitrate, nitrite, phosphate, and hardness of the lime effluent. From Table 2, it can be seen that NO₂, NO₃, and phosphate values fall to less than 0.01 mg/lit. Selection of seaweeds survived at 7.2–8.5 of pH, 30,000–37,000 of TDS, 0.3–1.74 mg/lit of nitrate, 0.17–0.98 mg/lit of nitrite, and 0.65–4.23 mg/lit of phosphate. However, the lime effluent has the minimum amount of nutrients. Therefore, the seaweeds are not able to survive in lime effluent. However, the lime effluent should not be taken for treating purposes because the effluent has nutrients of less than 0.001 mg/lit.

3.3. *Analysis of Soak Effluent*. The first nutrient content of soak effluent was found. The selection of seaweed should be based on physicochemical parameters like TDS, pH, NO₂, DO, NO₃, and phosphate by APHA (33) methods. The soak effluent is from the tannery process [35].

Two water samples, like fresh water and RO rejected water, are used for the soaking process. Here, we have chosen

FIGURE 5: Growth of *Gracilaria edulis* constructed in Aquaculture.

Diluted Soak Effluent at 15,000 TDS Diluted Soak Effluent at 25,000 TDS Raw Soak Effluent at 35,000 TDS

FIGURE 6: Initial soak Effluent for treating wastewater by seaweeds.

TABLE 1: Characteristics of sea water.

S.NO	Parameters	Range
1	TDS	37,000 mg/lit
2	DO	1.2 mg/lit
3	pH	7.2–8.5*
4	Temperature	25°C–35°C
5	NO ₂	0.06 mg/lit
6	NO ₃	20.0 mg/lit
7	Phosphate	4.80 mg/lit

*value on the pH scale.

the fresh water only, because the fresh has 33,000 mg/lit of TDS. The RO rejects wastewaters having 40,000–50,000 mg/lit (Table 3).

3.4. Aqua Culturing Study for *Gracilaria edulis*

3.4.1. Method for the Growth of Seaweeds from the Soak Effluent. *Gracilaria edulis* was cultivated by the low tide method. In this method, for 1 liter of soak effluent, 10 g of

TABLE 2: Characteristic of lime effluent.

S.NO	Parameters	Range
1	TDS	22,000 mg/lit
2	BOD	3000 mg/lit
3	COD	11,000 mg/lit
4	pH	12–14*
5	Hardness	2250 mg/lit
6	NO ₂	<0.01 mg/lit
7	NO ₃	<0.01 mg/lit
8	Phosphate	<0.01 mg/lit

*value on the pH scale.

TABLE 3: Characteristics of the soak effluent.

S.NO	Parameters	Range
1	TDS	33800 mg/lit
2	pH	7.5*
3	COD	2960 mg/lit
3	Total protein	1800 µg/lit
5	NO ₂	0.06 mg/lit
6	NO ₃	20.00 mg/lit
7	Phosphate	4.80 mg/lit
8	Temperature	28°C

*value on the pH scale.



(1) Treated Soak Effluent (2) Diluted Soak Effluent (3) Raw Soak Effluent

FIGURE 7: Treated soak effluents at 5 days retention time.

TABLE 4: Physical and chemical characteristics of feed and treated effluent—5 days retention time.

S.NO	Parameters	Feed effluent	After treatment	Removed from waste water	Removal percentage
1	pH	8.30*	8.22*	0.08*	—
2	TDS	12150 mg/lit	11410 mg/lit	740 mg/lit	93.90%
3	BOD	845 mg/lit	720 mg/lit	125 mg/lit	85.06%
4	COD	3400 mg/lit	2920 mg/lit	480 mg/lit	85.35%
5	NO ₂	0.013 mg/lit	0.010 mg/lit	0.003 mg/lit	76.92%
6	NO ₃	2.878 mg/lit	2.161 mg/lit	0.717 mg/lit	75.08%
7	Phosphate	52.38 mg/lit	38.09 mg/lit	14.29 mg/lit	72.71%
8	Turbidity	0.5 NTU	0.3 NTU	0.2 NTU	90.73%

*value on the pH scale.

TABLE 5: Characteristic of BOD and COD.

S.NO	Parameters	Initial BOD	Final BOD
1	BOD	845 mg/lit	338 mg/lit
2	COD	3400 mg/lit	1360 mg/lit

TABLE 6: Quality of agar gel from *Gracilaria edulis*.

S.NO	Treatment	Agar yield (%)	Gel strength (g.cm ⁻²)	Melting point (°C)
1	Control	12.132	52.36	66
2	2 hrs	11.440	68.80	73
3	4 hrs	10.812	69.06	81
4	8 hrs	10.275	82.26	82
5	11 hrs	10.361	95.05	78

seaweed was used for each species. Further aeration is provided. After a period of 20 days, only the species called *Gracilaria edulis* showed growth. It is found by measuring the final weight of that species [5].

Number of plant: 1.

Initial weight of plant: 20 g.

Final weight of plant: 26 g.

3.4.2. Analysis of Soak Effluent Characteristics after Phytoremediation. During the growth, different parameters of effluent were analyzed like pH, TDS, turbidity, BOD (biological oxygen demand), COD (chemical oxygen demand), and TSS (total suspended solids).

In this study, the best removal efficiency and retention time of 5 days were taken for *Gracilaria edulis*, such as 5 days [36, 37]. Effluent characteristics was analyzed for phytoremediated water after the retention time of 5 days (Figure 7). Plant feed is the soak effluent for growth. During growth plant parameters and characteristics of effluent from aquaculture was monitored and analyzed (Table 4).

3.5. Removal of BOD and COD in the Treated Soak Effluent. The effluent should have high COD and BOD content, if it is not treated. It will be removed by adding a large amount (2 pinch) of coagulant dose like alum and polyelectrolyte (Table 5).

3.6. Quality of Agar Gel from *Gracilaria edulis*. The FMC Gel tester measures the agar gel. This method is done by following procedures such as the soaking process, alkali/acid Pre-treatment process, and agar extraction process (Table 6). Finally, we find out the agar gel strength [38, 39].

From the above table, the maximum agar gel strength (95.05 g cm⁻²) was achieved 11 hours treatment at 78°C and the minimum agar gel strength (52.36 g.cm⁻²) was achieved at 66°C.

4. Conclusion

Results from this study show that soak effluent has a higher concentration of TDS and odor. Seaweeds like *Gracilaria edulis* were found to be effective compared to the other three species for treating soak effluent. The maximum removal efficiency of (physicochemical characteristics) soak effluent is given with retention time. The turbidity of treated soak effluent is reduced to 90.73% in 5 days of retention time. The phosphate of treated soak effluent is reduced to 72.71% in 5 days of retention time. The nitrate of treated soak effluent is reduced to 76.92% in 5 days of retention time. The nitrite of treated soak effluent is reduced to 75.08% in 5 days of retention time. The TDS of treated soak effluent is reduced to 93.90% in 5 days' retention time. The pH of the soak effluent is reduced to 99.03% in 5 days' retention time. Then, the extraction procedure to obtain a higher yield is 10.361% and the maximum gel strength is 95.05 g.cm⁻² while maintaining the melting point at 78°C.

Data Availability

All data are included in the manuscript.

Conflicts of Interest

The authors declare that they have no conflicts of interest.

References

- [1] V. Kannan, M. Vijayanthi, and M. Chinnasamy, "Bioremediation of chromium in tannery effluent by filamentous Cyanobacteria *anabaena flos-aquae* west," *International Journal of Environmental Sciences*, vol. 2, no. 4, 2012.
- [2] P. Vijayabaskar and V. Shiyamala, "Antibacterial activities of Brown marine algae (*Sargassum wightii* and *Turbinaria ornata*) from the Gulf Of Mannar biosphere reserve," *Advances in Biological Research*, vol. 5, pp. 99–102, 2011.
- [3] K. P. Kumar, K. Murugan, K. Kovendan, A. N. Kumar, J. S. Hwang, and D. R. Barnard, "Combined effect of seaweed (*Sargassum wightii*) and *Bacillus thuringiensis* var. *israelensis* on the coastal mosquito, *Anopheles sondaicus* Tamil Nadu, India," *Science Asia*, vol. 38, pp. 141–146, 2012.
- [4] S. Abirami, S. Srisudhaand, and P. Gunasekaran, "Comparative study of chromium biosorption using brown, red and green macro algae," *International Journal of Biological and Pharmaceutical Research*, vol. 4, pp. 115–129, 2013.
- [5] P. Raag Harshvardhan, A. Subbaiyan, U. Vasavi et al., "Enhanced biodegradation of battery-contaminated soil using *Bacillus* sp.(mz959824) and its phytotoxicity study," *Advances in Materials Science and Engineering*, vol. 2022, Article ID 5697465, 7 pages, 2022.
- [6] L. Wang, M. Min, Y. Li et al., "Cultivation of green algae *Chlorella* sp. in different wastewaters from municipal wastewater treatment plant," *Applied Biochemistry and Biotechnology*, vol. 162, no. 4, pp. 1174–1186, 2010.
- [7] M. Thomas, P. Drzewicz, A. Więckol-Ryk, and B. Panneerselvam, "Effectiveness of potassium ferrate (VI) as a green agent in the treatment and disinfection of carwash wastewater," *Environmental Science and Pollution Research*, vol. 29, no. 6, pp. 8514–8524, 2022.
- [8] V. K. Gupta, A. K. Shrivastava, and N. Jain, "Biosorption of chromium (vi) from aqueous solutions by green algae *Spirogyra* species," *Water Research*, vol. 35, no. 17, pp. 4079–4085, 2001.
- [9] M. Thomas, P. Drzewicz, A. Więckol-Ryk, and B. Panneerselvam, "Influence of elevated temperature and pressure on treatment of landfill leachate by potassium ferrate (VI)," *Water, air and Soil Pollution*, vol. 232, no. 11, pp. 1–15, 2021.
- [10] B. Sivaprakash, N. Rajamohan, and A. Mohamed Sadhik, "Batch and column sorption of heavy metal from aqueous solution using a marine alga *Sargassum tenerrimum*," *International Journal of ChemTech Research*, vol. 2, pp. 155–162, 2010.
- [11] S. Kandasamy, S. Velusamy, P. Thirumoorthy et al., "Adsorption of chromium ions from aqueous solutions by synthesized nanoparticles," *Journal of Nanomaterials*, vol. 2022, Article ID 6214438, 8 pages, 2022.
- [12] S. Sharmila and L. Jeyanthi Rebecca, "A comparative study on the degradation of leather industry effluent by marine algae," *International Journal of Pharmaceutical Science Review and Research*, vol. 25, pp. 46–50, 2014.
- [13] P. Balamurugan, K. Shunmugapriya, and S. Arunkumar, "Design of systems for recycling of wastewater for sustainable development," *International Journal of Civil Engineering and Technology*, vol. 2, no. 9, pp. 955–962, 2018.
- [14] M. Naveenkumar, K. Senthilkumar, V. Sampathkumar, S. Anandakumar, and B. Thazeem, "Bio-energy generation and treatment of tannery effluent using microbial fuel cell," *Chemosphere*, vol. 287, Article ID 132090, 2022.
- [15] A. A. Belay, "Impacts of chromium from tannery effluent and evaluation of alternative treatment options," *Journal of Environmental Protection*, vol. 01, no. 01, pp. 53–58, 2010.
- [16] R. Seenivasan, M. Rekha, H. Indu, and S. Geetha, "Antibacterial activity and phytochemical analysis of selected seaweeds from Mandapam coast India," *Journal of Applied Pharmaceutical Science*, vol. 2, no. 10, pp. 159–169, 2012.
- [17] K. M. Gopalakrishnan, V. Sampathkumar, G. Nithya Prakash, and G. Boobalakrishnan, "Bioelectrochemical treatment of sugarcane wastewater using microbial fuel cells and methane production," *Indian Journal of Environmental Protection*, vol. 35, no. 7, pp. 548–568, 2015.
- [18] B. Panneerselvam and S. Priya K, "Phytoremediation potential of water hyacinth in heavy metal removal in chromium and lead contaminated water," *International Journal of Environmental Analytical Chemistry*, pp. 1–16, 2021.
- [19] B. Suyasa and W. Dwijani, "Biosystem treatment approach for seaweed processing wastewater," *Journal of Environment and Waste Management*, vol. 2, no. 2, pp. 059–062, 2015.
- [20] S. Gatew and W. Mersha, "Tannery waste water treatment using *Moringa stenopetala* seed powder extract wyno academic," *Journal of Physical Science*, vol. 1, no. 1, pp. 1–8, 2013.
- [21] K. Manivannan, G. Thirumaran, G. Karthikai Devi, A. Hemalatha, and P. Anantharaman, "Biochemical composition of seaweeds from Mandapam coastal regions along southeast Coast of India American-Eurasian," *Journal of Botany*, vol. 1, no. 2, pp. 32–37, 2008.
- [22] R. Jayasankar and S. Varghese, "Cultivation of marine red alga *Gracilaria edulis* (Gigartinales, Rhodophyta) from spores," *Indian Journal of Marine Sciences*, vol. 35, no. 1, pp. 75–77, 2002.
- [23] C. D. G. Harley, K. M. Anderson, K. W. Demes et al., "Effects of climate change on global seaweed communities," *Journal of Phycology*, vol. 48, no. 5, pp. 1064–1078, 2012.
- [24] L. P. Machado, S. T. Matsumoto, C. M. Jamal et al., "Chemical analysis and toxicity of seaweed extracts with inhibitory activity against tropical fruit anthracnose fungi," *Journal of the Science of Food and Agriculture*, vol. 94, no. 9, pp. 1739–1744, 2014.
- [25] M. Beutler, K. H. Wiltshire, B. Meyer et al., *APHA (2005), Standard Methods for the Examination of Water and Wastewater*, Vol. 1, American Public Health Association, Washington, DC, USA, 2005.
- [26] B. Johnson and G. Gopakumar, *Farming of the Seaweed *Kappaphycus Alvarezii* in Tamil Nadu Coast-Status and Constraints*, Central Marine Fisheries Research Institute, Kochi, Kerala, 2011.
- [27] N. Kaliaperumal and S. Kalimuthu, *Seaweed Potential and its Exploitation in India*, Central Marine Fisheries Research Institute, Kochi, Kerala, 2010.
- [28] S. Sathesh and S. G. Wesley, "Diversity and distribution of seaweeds in the Kudankulam coastal waters, south-eastern coast of India," *Biodiversity Journal*, vol. 3, no. 1, pp. 79–84, 2012.
- [29] G. M. Castro, F. Pérez-Gil, E. Rosales, and R. E. Manzano, "The seaweed (*Sargassum sinicola* Setchel and Gardner) as an

- alternative for animal feeding,” *Cuban Journal Science*, vol. 26, pp. 177–184, 1992.
- [30] I. Laing, *Cultivation of Marine Unicellular Algae*, Conwy: Ministry of Agriculture, Fisheries and Food, London, UK, 1991.
- [31] M. M. Nielsen, A. Bruhn, M. B. Rasmussen, B. Olesen, M. M. Larsen, and H. B. Møller, “Cultivation of *Ulva lactuca* with manure for simultaneous bioremediation and biomass production,” *Journal of Applied Phycology*, vol. 24, no. 3, pp. 449–458, 2012.
- [32] A. J. Sellers, K. Saltonstall, and T. Davidson, “The introduced alga *Kappaphycus alvarezii* (Doty ex P.C. Silva, 1996) in abandoned cultivation sites in Bocas del Toro, Panama,” *BioInvasions Records*, vol. 4, pp. 1–7, 2015.
- [33] J. Munoz, Y. Freile-Peigrín, and D. Robledo, “Mariculture of *Kappaphycus alvarezii* (Rhodophyta, Solieriaceae) color strains in tropical waters of Yucatán, México,” *Aquaculture*, vol. 239, no. 1–4, pp. 161–177, 2004.
- [34] A. H. Buschmann and M. C. Hernández-González, “Seaweed cultivation, product development and integrated aquaculture studies in Chile,” *World Aquaculture*, vol. 36, no. 3, 2005.
- [35] A. Saravanan, P. S. Kumar, and M. Yashwanthraj, “Sequestration of toxic Cr (VI) ions from industrial wastewater using waste biomass: a review,” *Desalination and Water Treatment*, vol. 68, pp. 245–266, 2017.
- [36] M. Arputha Bibiana, K. Nithya, M. Manikandan, P. Selvamani, and S. Latha, “Antimicrobial evaluation of the organic extracts of *Sargassum wightii* (Brown algae) and *Kappaphycus alvarezii* (red algae) collected from the coast of Meemesal Tamilnadu,” *International Journal of Pharmaceutical, Chemical and Biological Sciences*, vol. 2, no. 4, pp. 439–446, 2012.
- [37] V. Kumar, “Application of marine macroalgae in agriculture,” *Seaweed Research Utiln.* vol. 37, no. 1, pp. 1–4, 2015.
- [38] N. Shanmugam, P. Rajkamal, S. Cholan et al., “Biosynthesis of silver nanoparticles from the marine seaweed *Sargassum wightii* and their antibacterial activity against some human pathogens,” *Applied Nanoscience*, vol. 4, no. 7, pp. 4881–4888, 2014.
- [39] W. A. Kasim, E. A. M. Hamada, G. Nehal, and S. K. Eskander, “Influence of seaweed extracts on the growth, some metabolic activities and yield of wheat grown under drought stress,” *International Journal of Agronomy and Agricultural Research (IJAAR)*, vol. 7, pp. 173–189, 2015.

NON-DESTRUCTIVE ANALYSIS OF THE VARIOUS CHARACTERISTICS OF A SUSTAINABLE CONCRETE WITH INDUSTRIAL WASTE

**Dr. K Thirupathi Rao¹ Dr. G Dineshkumar² Riyaz Syed³ Dr. Sumanth Kumar Bandaru⁴
Asaboyina Sravanthi⁵**

¹Professor, ^{2,4}Associate Professor, ^{3,5}Assistant Professor

^{1,2,3,5} Department of Civil Engineering, Vaagdevi College of Engineering, Warangal, Telangana, India-506005

⁴ Department of Civil Engineering, Kakatiya Institute of Technology and Science, Warangal, Telangana, India-506015

Abstract Sustainability in structural materials is now becoming more and more popular all around the world. The easiest ways to make construction more ecologically friendly are to reuse natural resources, construction and demolition trash, and solid waste. Industrial waste concrete is said to be more socially and economically practical and less durable, stronger, and more ecologically friendly than traditional concrete. The development of non-destructive testing (NDT) over time has not been thoroughly studied by academics. In order to provide non-destructive procedures that would allow us to evaluate the compressive strength of concrete without causing damage, an experimental investigation was conducted. Concrete prisms (150 mm 150 mm 150 mm) containing varying amounts of industrial waste (coal bottom ash (CBA) and waste glass sludge (WGS)) were cast. With the aid of the data, we were able to establish correlations between the concrete's compressive strength and both the Schmidt hammer rebound value and the ultrasonic pulse velocities. Microstructural research demonstrated the suitability of these industrial wastes as partial cement replacements by demonstrating that adding 10% of CBA and WGS enhanced the porosity of concrete examples. Traces of calcium alumino-silicate hydrate (C-A-S-H), portlandite, and C-S-H were visible under scanning electron microscopy (SEM), indicating the binding properties of CBA and WGS. The polynomial work expectation supported the idea of the response surface method (RSM) for cement and industrial waste substitution optimisation. When the ANOVA fluctuation was analysed using a p value and a significance level of 0.05, the model was statistically significant. According to the study's findings, concrete's strength may be greatly increased by using 15% CBA and 10% WGS as cementitious additives and cement replacements, respectively.

Keywords: concrete; industrial waste; mechanical properties; non-destructive testing; ANOVA; SEM; CBA; WGS

¹ Introduction

One of the most popular and widely used building materials is concrete. Because of its durability and long-term viability in retaining structures like walls and channels, buildings are created around it. Cement is one of several ingredients used to make concrete. To give concrete its variety of properties, additional admixtures are added to the mix in addition to these basic ingredients. Because there is more demand for concrete, there is more need for cement. As a by-product of making cement, the following gases are released: CO₂, nitrogen, and sulphur dioxide. The bulk of greenhouse gases that warm the globe, CO₂, makes up 76% of the total [1]. In order to minimise

the amount of cement used in concrete, various industrial byproducts are employed as fractional replacements. Environmental pollution is rising as a result of multi-waste landfilling [2]. This issue may be resolved by the possible use of a variety of waste materials in the building sector [3-5], leading to more efficient waste management [6-8]. Due to a rise in cement consumption, carbon dioxide gas (CO₂) is emitted into the environment. In order to lessen the CO₂ emissions from cement factories, various industrial wastes or by-products are being utilised in concrete as a partial replacement for cement. Two of the most typical waste materials in the world are waste glass sludge and coal bottom ash. Utilising these waste materials in landfills has detrimental impacts on the environment, including elevated soil alkalinity, contaminated ground or surface water, and harm to plants and other living things. The use of these waste materials as a cement alternative will benefit the environment by lowering CO₂ emissions as well as the risks associated with landfilling [9,10]. With the application of industrial wastes like marble powder and carbon black, mechanical qualities, including durability features like water permeability and chloride migration, greatly increase [10–12]. Rubberized concrete, an industrial waste, was researched by Tayeh et al. [13] in order to enhance the serviceability and durability features [14–17].

In this project, waste materials were effectively mixed into concrete, producing substantial societal and financial advantages. Coal bottom ash (CBA), sometimes referred to as bottom ash, is a byproduct of coal-fired thermal power plants. The aggregate coal fiery debris produced by these facilities contains 10–20 percent CBA on a regular basis. When CBA is dumped in a landfill, its hazardous components can spread and contaminate groundwater or surface water, endangering plants and other living things. CBA has a lot of potential to be used in the building industry as a cement replacement material (CRM), according to researchers who started using it as a partial substitute for cement. Sulphate, magnesium, calcium, and other minerals are also present in CBA in addition to silica, iron, and alumina. To examine the impact and application of various nano-sized fillers and binders in concrete, researchers have utilised them as fillers and binders [20–22].

The chemical makeup of CBA makes it a superior cement alternative. Researchers have successfully partially substituted CBA for cement in the past with encouraging results. A by-product of the glass cutting and finishing procedure used in industry is waste glass sludge (WGS). The bulk of WGS is now disposed of in landfills, which is leading to a number of environmental issues. The physical properties of the material are influenced by the particle size, surface area, and total concentration of Al₂O₃ and SiO₂ in the admixture. Al₂O₃, SiO₂, and large-surface-area particles are abundant in WGS. In order to enhance the mechanical qualities of concrete, it may be rational to substitute WGS for cement. Concrete is put through a range of tests, some of which are destructive, some of which are semi-destructive, and some of which are not.

A concrete construction's quality and long-term performance are the main goals of non-destructive testing (NDT). Since non-destructive testing (NDT) does not affect the structure's look, quality, or performance, many nations have adopted it. Ultrasonic pulse velocity (UPV) is a non-destructive test that is frequently used to assess structural problems. This method's foundation is the propagation of pulses at a particular frequency through concrete. The amount of time the pulse needs to pass through a certain substance is noted. Once the gap and duration are shown, it is feasible to calculate the typical pulse speed, which can vary depending on a number of factors, including the material's properties and the volume of water in the sample. Concrete homogeneous and non-uniform zone identification is frequently accomplished using an

ultrasonic wave propagation variance research.

Concrete faults can also be found using this technique. The properties of concrete can be continually monitored throughout its usable life thanks to the UPV technique. The rebound hammer test is one of the non-destructive testing techniques. The hammer mass strikes the concrete when the tester's plunger retracts up against a spring, which is mechanically released when it is fully tensioned. Members and tangible characteristics (such mixture type, binder content, and binder type) all have an impact.

There are various studies on the connection between the quantity of rebounders and the compressive strength of concrete. Contrarily, industrial trash and concrete exhibit unity since there is no obvious connection between the two. The use of non-destructive testing (NDT) methods for concrete structures has a number of benefits, according to the investigation's findings, including the fact that NDT procedures take less time than destructive testing methods and no structural components are damaged during them. There is very little research on how destructive testing and NDT interact with concrete that contains waste materials. The current study focuses on NDT techniques, as well as how these correlations relate to the characteristics of concrete when combined with industrial waste. To investigate the relationships between compressive strength, rebound number, and ultrasonic pulse velocity, various ratios of industrial waste were utilised. This work offers a novel approach to the issue of NDT-based concrete quality estimation. Additionally, the response surface method (RSM) for optimisation is utilised to forecast the qualities of the concrete. The findings of optimisation are consistent and match those of experiments. Additionally, predictions on the use of CBA and WGS are made using the investigated approach to show its utility.

Research Significance

In contrast to other studies, ours advances the field by employing the RSM approach to examine various outcomes. To use less cement, certain industrial wastes that are harmful to the environment, such CBA and WGS, are integrated. Both destructive and non-destructive methods are used to analyse test findings. To further investigate the C-S-H, portlandite, and other cementitious characteristics of CBA and WGS, a microstructural examination was conducted.

2. Materials and Methods

The tests for determining the physical characteristics of the aggregates and binders to be used, the workability of the fresh mixes (changing% replacement values), compressive tests, and non-destructive testing on the hardened mixes (rebound hammer and UPV) are necessary in order to perform a series of laboratory tests on a specimen. In preliminary testing, specific gravity and density are also taken into account. The casting and testing of prism samples, as well as the manufacture of the concrete mix and preparatory material testing, all adhered to the most recent ASTM standards.

2.1. Materials and Mix Proportioning

In this experiment, regular Portland cement was utilised. While a coarse aggregate with a fineness modulus of 4.3 was included, fine aggregates with a fineness modulus of 2.7 were utilised. To keep the concrete workable, a superplasticizer with a polycarboxylate basis was used. Until consistency in the concrete matrix was achieved, concrete components were blended in a

rotating pan-type mixer for around 10 minutes at an average speed of 32 rpm. Fresh concrete was placed in three fairly equal strata inside a steel prism that measured 150 mm in width, 150 mm in length, and 150 mm in height. The concrete was then tightly compacted using a vibrating table. According to the advice offered in ACI 211.1, mixing and casting were carried out. The qualities of the coarse and fine aggregates were taken into account during the calculation for the concrete mix design, and at first a mix percentage of 1: 1.22: 2.7 was chosen.

The amount predicted from the mix design was far below this restriction since the aggregate was ordered in a significant quantity with the factor of safety applied. We wanted to get the material from the same batch so that the qualities were constant, therefore we first ordered a bigger quantity of it. To perform the slump test (ASTM C 143), a trial mix was created. The experimental mix produced a droop more than 150 mm even though the desired slump was between 75 and 100mm. CBA fume, WGS, cement, water, fine and coarse aggregates, and superplasticizer were combined to create concrete. Ordinary Portland cement of grade 43 was used for the testing of cement.

2.2. Mixing and Casting Procedure

The amount of WGS in the modified high-volume CBA concrete was calculated using the design of experiments (DOE) approach and the Design Expert software. The percentage of CBA varied from 0% to 20%, whereas that of WGS varied from 0% to 20%, according to the RSM research. Table 3 displays the overall mixture with varying CBA and WGS content levels. Three minutes of dry mixing, three minutes of wet mixing, three minutes of adding SP, and at least four minutes of final mixing were performed. The features of fresh concrete were then examined. The freshly mixed concrete was then poured into a conventional mould that had dimensions of 100 millimetres in diameter, 200 millimetres in height, and 500 millimetres in width. In order to measure compressive strength, a hardened prism was utilised. The hardened prisms were validated after an average of 28 and 90 days, with three samples analysed in each case, for each combination, with the loading rate set at 3.0 KN/s. As specified by ASTM C293M-10, the splitting tensile strength of the specimens was measured after 28 and 90 days of curing.

2.3. Testing Program

The slump test was used to evaluate the workability of concrete, whereas just one test on new concrete specimens was used to evaluate the mechanical parameters (compressive strength, split tensile strength, ultrasonic pulse velocity, and rebound number). According to ASTM C192/C 192 M-06, these tests were conducted. The samples were cast in addition to regular concrete, CBA, and WGS concrete, and the prisms utilised were 150 mm 150 mm 150 mm in size.

2.4. Response Surface Method

A quantitative way for developing mathematical models that display one or more replies within a set of input variables is the response surface method (RSM). When determining the effect and importance of each input element and the answer, the RSM gives a polynomial connection between them. This example may be used to forecast and improve a mixed design's reaction. The initial stage in creating a statistical model is gathering experimental data, which is then followed by choosing the best model to fit the data. At this stage, the demonstration centres on whether the evaluation is sufficient. A quantifiable computer programme called Design Expert v11 comprises

test plans, mathematical formulae, factual analysis, and response optimisation. To plan the interaction between input components and their influence on the response, the analysis of variance (ANOVA) tool is employed. The responses examined in this study (y_4) are the compressive strengths (y_1) of the specimens as measured by the slump test. The controlling variables in these reactions are WGS/B (x_1) and CBA/B (x_2), which stand for the relative amounts of fly ash and silica fume. They each account for the total vent gas composition of the cement.

3. Results and Discussion

Lab tests on the strength and modulus of elasticity indices of concrete were performed using both destructive and non-destructive techniques. It must be demonstrated that NDT and the common compressive and modulus of elasticity tests on the same concrete specimens are connected. A thorough explanation of the concrete mix was provided in the preceding section.

3.1. Compressive Strength

Figure 1 shows concrete with various ages and percentages of waste glass sludge and coal bottom ash. Concrete's compressive strength was first measured at 28 and 90 days after control specimens were cast. At 28 days and 90 days, the compressive strength was 39.2 MPa and 39.4 MPa, respectively. The control specimen was found to have a lower compressive strength than concrete specimens with 5% to 10% coal bottom ash and waste glass sludge. The strength of 10% CBA concrete was the greatest of any other form of concrete. The solid particle aggregation was lessened, increasing the material's compressive strength. One of the potential causes of the better compressive outcomes is the Concrete is a heterogenous material, and the micro- and nano-sized particles of WGS and CBA improved its porosity structure. This caused the porosity of hardened concrete to diminish and the flow ability of new concrete to improve, both of which had a big influence on the strength and longevity of concrete. The results of this experiment are consistent with those of other investigations, which discovered that adding coal bottom ash to concrete in amounts up to 10% increased its compressive strength. As shown in the 2D contour plot, the red zone in the plots denotes a portion of concrete that is stronger than the green zone, and vice versa. The green region has the lowest compressive strength value, whereas the yellow and red zones have the highest compressive strength values. 38 MPa at 10% WGS was the optimal compressive strength for concrete mixed with WGS. Because of the skewed look of the contours, the factors (% of WGS) do not have a strong interface. The compressive strength rapidly reduces as the WGS concentration rises, as seen by the 3D response surface plot.

How the compressive strength of all concrete mixes varies when they are blended in different ways. According to the 2D contour plot the red zone denotes a section of concrete with a higher strength, while the green zone denotes a region with a lower strength. The greatest compressive strength value is in the red zone, followed by the yellow region, and the minimum compressive strength value is in the green zone. The optimal compressive strength for concrete and CBA was 42.0 MPa at 10% CBA, respectively. The presence of the skewed outlines indicates a poor interface between the components (percentage of CBA). The 3D response surface plot in Figure 3b shows a sharp decline in compressive strength as the WGS concentration rises.

3.2. Ultrasonic Pulse Velocity

We also measured the ultrasonic pulse velocity of concrete treated with various concentrations of CBA and WGS using ultrasonic pulse velocity equipment. In the UPV findings at 28 and 90 days following the casting of all types of concrete, CBA and WGS may have a negligible impact. The addition of coal bottom ash caused a little rise in UPV at 90 days, whereas the addition of 15 percent CBA and WGS caused a reduction at all ages. One of the main contributors to the development of UPV is the porosity of concrete. Due to the decrease in porosity brought on by an increase in density, UPV rises as the concrete hardens [10]. The smaller particle sizes of CBA and WGS when added to concrete decrease porosity, increasing the UPV of the finished product. The UPV drops with a 15% substitution of these components, as illustrated, since the inclusion of CBA and WGS lowers the cement concentration, resulting in less CSH gel and less dense concrete. The graphs show relationships between the compressive strength and the percentage of industrial waste in the concrete. The statistics show a similar pattern in the strength improvements. The compressive strength of concrete rises with time, as seen by the linear trends in ultrasonic pulse velocity.

3.3. Compressive Strength and Rebound Hammer

The outcomes of the rebound number. At 28 and 90 days, concrete containing 5-10% CBA and WGS had greater rebound values than control concrete. Despite this, when the CBA and WGS content was raised by above 10%, the rebound number was discovered to be a little lower than that of the reference concrete. This phenomenon can explain the cementitious impact of additional fillers since the surface hardness of concrete grows with age and the amount of industrial waste in concrete rises. According to the CBA and WGS percentages, this type of concrete has a relatively modest amount of cement, which reduces the surface hardness by 15-20%.

The statistics show a similar pattern in the strength improvements. The graph shows that the rebound number grows together with the compressive strength of concrete as it ages.

The rebound number findings at 28 and 90 days. Control concrete rebounded less than concrete adding 5-10% CBA and WGS. The rebound value was lower than that of the reference concrete when the CBA and WGS content was above 10%. The explanation for this phenomena is that the surface hardness of concrete rises with age and as the amount of industrial waste grows. The surface hardness of this kind of concrete was reduced by 15–25%, according to results from CBA and WGS. The figures below show the rebound and compressive strength of concrete with various quantities of industrial waste. The research shows that there is a regular pattern in the strength improvements. The graph shows that as concrete ages, both its compressive strength and rebound number increase. Following correlations were also proposed by the multiple regression analysis for concrete strengths between 20 MPa and 46 MPa.

3.4. Anova Analysis

On concrete strength, the effects of three independent factors, including a combination of 10% CR (B), 15% SF, and 10% FA, were examined (A). The model's compressive strength for CBA and WGS at 42.1 MPa and 38.0 MPa, respectively, had a F value of 13.05. A high F value indicates the model's applicability and usefulness. The figures demonstrate the importance of each model. Noise has a 0.01 percent chance of affecting the model's F value. Models with p values under 0.05 are regarded as necessary. To show that the model is reliable, its coefficient of

determination, also known as R-squared (R_2), should be close to 0.88. The difference between the corrected R_2 and the anticipated R_2 is less than 0.2. This shows that there is some consistency between the modified R_2 and the anticipated R_2 . For optimal (Adeq) accuracy, the signal-to-noise ratio measurement is also a prerequisite. All models are capable of navigating the design area. Plotting the residual normal plot as a straight line might be used as a method to evaluate the model. As a result, the projected value will yield more accurate results than anticipated if all points are nearly parallel to the normal line. the model's accuracy and your ability to choose the right extraction.

3.5. Optimization and Experimental Validation

Response surface methodology (RSM) was used to predict how the interaction of two factors—silica fume and rubber particles—affected the mechanical strength. The final model, was produced after 13 other mixture designs were created based on the first RSM mixture design and successfully fed into the RSM to test their efficacy. This was done after all of the data from the initial mixture had been successfully obtained. The comparison results show a minor discrepancy between the experiment and RSM findings, however this is still acceptable. The desired value is 0.592, which means that 42.1 MPa and 38.0 MPa compressive strengths may be attained with 10% CBA and 10% WGS, respectively.

4. Microstructure Analysis by SEM

4.1. Waste Glass Sludge (WGS)

It is possible to discern crushed and angular particles by looking at the WGS SEM. In WGS samples, more C-S-H of the gel-type may be detected. Less holes and voids can be seen in WGS 10% than in calcium silicate hydrate (C-S-H), which also suggests that it has a higher compressive strength than other samples because to its favourable pozzolanic properties, as was confirmed previously. The C-S-H phase makes the tiny glass flecks easy to observe. A honeycomb structure is produced by the combined phase. The amorphous small particles that react with the portlandite to speed up the C-S-H production are thought to be the primary cause of the WGS's pozzolanic activity. Additionally, the CBA and WGS particles support

4.2. Coal Bottom Ash (CBA)

The SEM images clearly show traces of needle-like ettringite content. Although it is not as comprehensive as WGS, the C-S-H may also be seen. Due to its outstanding pozzolanic quality and strong compressive strength, CBA 10% exhibits fewer pores and voids. CBA also contains calcium alumino-silicate hydrate (C-A-S-H), as was previously demonstrated. C-S-H exhibits the portlandite phase, which is also supported by earlier study. The CH that is readily accessible aids in the production of additional C-S-H in the concrete, enhancing its strength and density.

4.3. Calculation of Porosity by Analysing Particles Using Image J Software

The Image J programme may be used to do a porosity investigation [16]. The SEM picture is enhanced in the picture J programme for this study, and the image channels are then split for

greater visibility and a suitable threshold level is used to discover the particles that need to be examined. The report of our analysis of the particles will then show the precise location of the pores. The threshold level used to see the particles for analysis. Table 8 displays the particles' specifics. CBA and WGS had the lowest porosity at a 10% cement replacement rate. These two samples likewise exhibited the greatest compressive strength as a result. Their pozzolanic behaviour, which eventually fills the gaps and fissures, may have been the cause of this.

5. Conclusions and Recommendations

5.1. Conclusions

In the first of the two stages of this experiment, prisms' concrete strength was evaluated using destructive and non-destructive techniques. Testing on hammer and ultrasonic pulse velocities validated the associations.

The experimental and analytical debates led to the following results. After 28 days, 10% CBA and WGS addition led to the greatest improvement in compressive strength, and this may be regarded as the ideal amount of coal bottom ash for normal-strength concrete. The samples were evaluated using Design Expert software at all ages, and a similar pattern to that of compressive strength was seen. Additionally, RSM was verified to estimate compressive strength at various ages; nevertheless, around 15% higher experimental values were noted. In this work, relationships between compressive strength and ultrasonic pulse velocity, rebound number and compressive strength, and dynamic modulus of elasticity and static modulus of elasticity were proposed for all percentages (5%, 10%, 15%, and 20%) of CBA and WGS. The combination of pundit and rebound hammer as non-destructive test methods for the evaluation of both young-age and ageing concrete produced more favourable results than either technique alone.

Additionally, general relationships for concrete with CBA and WGS incorporation were put out for strengths between 20 MPa and 46 MPa. Due to the increased number of variables employed to create these associations, it was discovered that the coefficients of determination for these relationships were less than 90% (0.85, 0.82). We used a two-way ANOVA with a p value less than 0.05 as the significance threshold to assess the statistical significance of the prediction models. To compare the compressive strength of CBA and WGS concrete, an equation was put out. The RSM model and the equations used to determine the compressive strength of CBA and WGS concrete were precise. The experimental findings were corroborated by the prediction model results, which also showed a little variation. The use of coal bottom ash and waste glass sludge as partial substitutes for cement in concrete is strongly advised based on the findings of this and previous research because they not only offer improved mechanical properties but also provide suitable solutions to achieve sustainable and environmentally friendly processes.

References

1. Anderson, T.R.; Hawkins, E.; Jones, P.D. CO₂, the greenhouse effect and global warming: From the pioneering work of Arrhenius and Callendar to today's Earth System Models. *Endeavour* **2016**, *40*, 178–187.
2. Yildizel, S.A.; Tayeh, B.A.; Calis, G. Experimental and modelling study of mixture design optimization of glass fiber-reinforced concrete with combined utilization of Taguchi and Extreme Vertices Design Techniques. *J. Mater. Res. Technol.* **2020**, *9*, 2093–2106.

3. Karalar, M.; Özkılıç, Y.O.; Deifalla, A.F.; Aksoylu, C.; Arslan, M.H.; Ahmad, M.; Sabri, M.M.S. Improvement in Bending Performance of Reinforced Concrete Beams Produced with Waste Lathe Scraps. *Sustainability* **2022**, *14*, 12660.
4. Qaidi, S.; Najm, H.M.; Abed, S.M.; Özkılıç, Y.O.; Al Dughaihi, H.; Alosta, M.; Sabri, M.M.S.; Alkhatib, F.; Milad, A. Concrete Containing Waste Glass as an Environmentally Friendly Aggregate: A Review on Fresh and Mechanical Characteristics. *Materials* **2022**, *15*, 6222. Çelik, A.I.; Özkılıç, Y.O.; Zeybek, Ö.; Özdöner, N.; Tayeh, B.A. Performance Assessment of Fiber-Reinforced Concrete Produced with Waste Lathe Fibers. *Sustainability* **2022**, *14*, 11817.
5. Amin, M.; Zeyad, A.M.; Tayeh, B.A.; Agwa, I.S. Engineering properties of self-cured normal and high strength concrete produced using polyethylene glycol and porous ceramic waste as coarse aggregate. *Constr. Build. Mater.* **2021**, *299*, 124243.
6. Breyse, D.; Balayssac, J. Non-Destructive In Situ Strength Assessment of Concrete. 2008.
7. Hamidian, M.; Shariati, A.; Khanouki, M.M.A.; Sinaei, H.; Toghroli, A.; Nouri, K. Application of Schmidt rebound hammer and ultrasonic pulse velocity techniques for structural health monitoring. *Sci. Res. Essays* **2012**, *7*, 1997–2001.
8. Hussain, Z.; Pu, Z.; Hussain, A.; Ahmed, S.; Shah, A.U.; Ali, A.; Ali, A. Effect of fiber dosage on water permeability using a newly designed apparatus and crack monitoring of steel fiber-reinforced concrete under direct tensile loading. *Struct. Health Monit.* **2021**, *21*, 2083–2096.
9. Ahmed, S.; Hussain, A.; Hussain, Z.; Pu, Z.; Ostrowski, K.A.; Walczak, R. Effect of Carbon Black and Hybrid Steel-Polypropylene Fiber on the Mechanical and Self-Sensing Characteristics of Concrete Considering Different Coarse Aggregates' Sizes. *Materials* **2021**, *14*, 7455.
10. Ali, A.; Hussain, Z.; Akbar, M.; Elahi, A.; Bhatti, S.; Imran, M.; Zhang, P.; Ndam, N.L. Influence of Marble Powder and Polypropylene Fibers on the Strength and Durability Properties of Self-Compacting Concrete (SCC). *Adv. Mater. Sci. Eng.* **2022**, *2022*, 9553382.
11. Ismail, M.H.; Megat Johari, M.A.; Ariffin, K.S.; Jaya, R.P.; Wan Ibrahim, M.H.; Yugashini, Y. Performance of High Strength Concrete Containing Palm Oil Fuel Ash and Metakaolin as Cement Replacement Material. *Adv. Civ. Eng.* **2022**, *2022*, 6454789.
12. Antonio, B.; Giancarlo, C.; David, P.; Giuseppe, R. Calibration and reliability of the Rebound (Schmidt) Hammer Test. *J. Civ. Eng. Archit.* **2013**, *1*, 66–78.
13. Alaloul, W.S.; Musarat, M.A.; Tayeh, B.A.; Sivalingam, S.; Rosli, M.F.B.; Haruna, S.; Khan, M.I. Mechanical and deformation properties of rubberized engineered cementitious composite (ECC). *Case Stud. Constr. Mater.* **2020**, *13*, e00385.
14. Rezaifar, O.; Hasanzadeh, M.; Gholhaki, M. Concrete made with hybrid blends of crumb rubber and metakaolin: Optimization using Response Surface Method. *Constr. Build. Mater.* **2016**, *123*, 59–68.
15. Abed, M.; Nemes, R.; Tayeh, B.A. Properties of self-compacting high-strength concrete containing multiple use of recycled aggregate. *J. King Saud Univ.-Eng. Sci.* **2020**, *32*, 108–114.
16. Cai, C.; Wu, Q.; Song, P.; Zhou, H.; Akbar, M.; Ma, S. Study on diffusion of oxygen in coral concrete under different preloads. *Constr. Build. Mater.* **2021**, *319*, 126147.

17. Argiz, C.; Moragues, A.; Menéndez, E. Use of ground coal bottom ash as cement constituent in concretes exposed to chloride environments. *J. Clean. Prod.* **2018**, *170*, 25–33.
18. Chingalata, C.; Budescu, M.; Lupas,teanu, R.; Lupas,teanu, V.; Scutaru, M.C. Assessment of the concrete compressive strength using non-destructive method. *Bulentinul Inst. Politeh. Din Iasi*, **2017**, *63*, 43–56.
19. Zaghoul, M.M.Y.; Mohamed, Y.S.; El-Gamal, H. Fatigue and tensile behaviors of fiber-reinforced thermosetting composites embedded with nanoparticles. *J. Compos. Mater.* **2019**, *53*, 709–718.
20. Zaghoul, M.M.Y.; Zaghoul, M.M.Y. Influence of flame retardant magnesium hydroxide on the mechanical properties of high density polyethylene composites. *J. Reinf. Plast. Compos.* **2017**, *36*, 1802–1816.
21. Zaghoul, M.Y.M.; Zaghoul, M.M.Y.; Zaghoul, M.M.Y. Developments in polyester composite materials—An in-depth review on natural fibres and nano fillers. *Compos. Struct.* **2021**, *278*, 114698.

EVALUATION OF GROUNDWATER QUALITY FOR SUSTAINABLE DRINKING AND IRRIGATION

**Dr. K Thirupathi Rao¹, Dr. Syed Omar Ballari², Dr.N Muralimohan³, Dr. G
Dineshkumar⁴, Dr. M Anil⁵, Syed Riyaz⁶**

¹Professor, Department of Civil Engineering, Vaagdevi College of Engineering, Warangal, Telangana-506005.

²Associate Professor & Head, Department of Civil Engineering, Guru Nanak Institutions Technical Campus, Khanapur (V), Ibrahimpatnam, Hyderabad, Telangana-501506.

³ Associate Professor, Department of Civil Engineering, K.S.R College of Engineering, Tiruchengode, Namakkal, Tamilnadu-637215.

⁴Associate Professor, Department of Civil Engineering, Vaagdevi College of Engineering, Warangal, Telangana-506005.

⁵Associate Professor, Department of Civil Engineering, Kamala Institute of Technology and Science, Singapur, Karimnagar-505468.

⁶Assistant Professor, Department of Civil Engineering, Vaagdevi College of Engineering, Warangal, Telangana-506005.

Abstract: The preservation of freshwater resources in arid and semi-arid regions, which is crucial for sustainable development, depends heavily on the identification and management of the groundwater quality. Local authorities and water resource managers might divide the use of resources between agricultural and drinking purposes depending on the quality of the groundwater in different places. In the Tabriz aquifer, which is situated in the province of East Azerbaijan, northwest Iran, this study seeks to pinpoint regions where water pumping is appropriate for harvesting and use for drinking. A groundwater compatibility study was carried out using data from 39 wells collected between 2003 and 2014, including electrical conductivity (EC), total dissolved solids (TDS), chloride (Cl), calcium (Ca), magnesium (Mg), sodium (Na), potassium (K), sulphate (SO₄), total hardness (TH), bicarbonate (HCO₃), pH, carbonate (CO₃), and sodium adsorption ratio (SAR). Due to their significant significance in determining the quality of water resources for irrigation and drinking, the Water Quality Index (WQI) and Irrigation Water Quality (IWQ) indexes are used in conjunction with one another. Water was zoned as excellent, good, or bad according to the WQI index for drinking water. The research comes to the conclusion that the majority of drinking water gathered for urban and rural regions is "excellent water" or "good water".

Keywords: sustainable water harvesting; water quality index (WQI); irrigation water quality (IWQ); groundwater quality; hydro informatics; hydrologic cycle; earth system models; hydrology; climate change; water resource management; sustainable development

1. Introduction

There is a severe lack of freshwater resources. The amount of water on earth that is appropriate for human consumption is less than 1%. Freshwater resources must be managed and safeguarded as a result [1]. One of the key initiatives of local and national governments has been to regulate and limit freshwater consumption for agricultural purposes in order to safeguard this priceless resource for sustainable development. However, agriculture continues to be a significant part of the global economy [2]. The largest consumer of clean water is agriculture, which is also a significant factor in the degradation of surface and groundwater assets and quality [2]. In locations that are arid and nearly bone dry, groundwater assets are especially important for financial growth [3]. The natural, physical, and chemical conditions of the water are considered to represent its quality, together with any alterations that may have been brought on by anthropogenic activity [4–

7]. The process of handling water from the moment it is first collected until it is kept in a well, which is frequently governed by many physicochemical characteristics, has an impact on the quality of the groundwater [8].

Groundwater resources have been severely depleted and corrupted as a result of population increase and excessive groundwater use [9]. Furthermore, it is obvious that the quality of agricultural water affects the quality of the soil and, consequently, the yields that are produced. Due to population increase, interest in farming regions and the goods produced by these farms has risen fast in the most recent century. Additionally, experts have noted that a number of factors, including an increase in the number of metropolitan areas, industrialised spaces, poorly managed fields, and ecological pollution, have added additional pressure to the production of agricultural goods [10,11]. Therefore, a key component, if not the primary purpose, of many agricultural improvement and administration designs has been the viably utilisation of both the farmed land and the irrigation water. Therefore, it is crucial to assess the quality of groundwater. A typical assessment of groundwater quality is simple, but it necessitates a step-by-step procedure taking each element into account [12]. As a result, it is inadequate for giving a detailed picture of the quality of the water. In order to get water quality information in a configuration that is both efficiently expressible and defensible, water quality indexes have been developed [13,14]. The character of a water system source is typically determined by its (a) salinity level, (b) danger of penetration or porousness, (c) quality of certain toxic ions, (d) harmfulness of trace elements, and (e) numerous other impacts. It should be highlighted that various risks or adverse consequences might manifest concurrently, making it more challenging to conduct water evaluations [15]. Simsek and Gunduz [15] proposed an irrigation water quality (IWQ) list based on the five risk areas mentioned above for harvests to characterise the quality of water systems.

The IWQ index is an approach that linearly blends the elements of the water system quality that adversely impact soil quality and crop yield [16]. Due to its simplicity of use, especially for non-technical individuals, many analysts have employed this index to meet irrigation water system goals in light of various hydrochemical characteristics [17–20]. The selection and presentation of an accumulation function led to the creation of the main water quality index (WQI) [21]. The WQI index has been used in several research works, including those of Effendi and Wardiatno [22], Chen et al. [23], Bodrud-Doza et al. [24], and Fijani, for qualitative zoning of the aquifers for drinking purposes as well as for finding the best sites for drinking water wells. A Geographical Information System (GIS) is an effective tool for storing, managing, reviewing, and mapping spatial information for choices in several locations at once, which aids in addressing pertinent basic concerns. Many research, like Narany et al. [18] and Manap et al., have successfully used GIS to show how water quality metrics are distributed. Because groundwater in the research region is primarily utilised for agricultural as well as for drinking water in rural and urban areas, GIS is essential to maintaining the sustainability of the investigated aquifer's quality. Therefore, the following goals were established in order to better understand the processes and the state of groundwater quality in the research area:

1. Identifying areas of aquifer feeding
2. Determining the WQI in the aquifer
3. Investigating the alterations in WQI for drinking water through the statistical period
4. Checking the water quality status in tapping drinking wells and determining suitable locations for extracting drinking water
5. determining the IWQ in the aquifer
6. Investigating the variations in WQI for agricultural water during the statistical period
7. Checking water quality status in the agricultural wells and determining appropriate and inappropriate locations for extracting agricultural water.

2. Materials and Methods

2.1. Water Quality

The irrigation water's quality is determined by the kind and quantity of dissolved substances present. In general, the quality of irrigation water is assessed using salinity, specific ion toxicity, trace element toxicity, and other impacts on delicate crops.

In general, crops may experience physiological drought when exposed to high electrical conductivity. Typically, waters classified as appropriate irrigation waters have EC values lower than 700 S/cm. The sodium adsorption ratio (SAR) and salinity are the two frequently occurring variables that influence penetration.

Irrigation water's SAR value is calculated as follows:

$$SAR = \frac{[Na^+]}{\sqrt{\frac{[Ca^{++}] + [Mg^{++}]}{2}}} \quad (1)$$

where $[Na^+]$, $[Ca^{++}]$, and $[Mg^{++}]$ represent, respectively, the concentrations of sodium, calcium, and magnesium ions in water. To assess the potential danger of penetration in the soil, a grouping of the EC-SAR paradigm was used [15]. According to reports, when soil is inundated by fluids with a high sodium content, a high sodium surface is produced that weakens the soil's structural integrity. The soil contracts, and as a result, its pores are damaged and it is dispersed into smaller components. The amount of clay in the soil is another crucial factor. Because the soil mud particles disperse when the SAR value is high, this has an adverse effect on the soil structure [15].

When the concentration of some ions in water or soil is too high, plants become poisonous, including salt, chloride, and boron. Ion concentrations in plants are considered hazardous when they are predicted to damage the plant or reduce yield. The level of toxicity varies depending on the type of plant and how well ions are absorbed. Crops that are long-lasting and resilient are more vulnerable to this form of toxicity than plants that are harvested within a year. If chloride ions build up in plants, they can reduce yields since they might come through the water system [2]. Low quantities of chloride are extremely beneficial to crops. However, toxicity begins to emerge when the concentration levels above 140 mg/L. The burning of leaves or the drying of leaf tissue are indications of injury. In contrast to other particles' obvious harmful nature, toxic sodium concentrations are subtly bothersome. The scorching of leaves or dead tissues around the exterior edges of leaves are typical toxicity manifestations on the plants. Contrarily, the negative consequences of poisonous chloride concentration typically begin with the emergence of atypical leaf tips.

It is a truth that plants and other living things require trace elements in small proportions, but larger concentrations of these elements are harmful to both plants and humans. Chromium, selenium, and arsenic pose a significant threat to groundwater resources [20]. The use of nitrogen fertilisers, farming practises, and other human activities all contribute to an increase in groundwater nitrate [2]. pH values are related to the alkalinity of water.

2.2. Irrigation Groundwater Quality Index (IWQ Index)

Simsek and Gunduz as well as Ayers and Westcot were taken into consideration while choosing the hydrochemical criteria used to assess the irrigation water quality [15]. Based on how crucial they are to the quality of irrigation water, pH and EC have been given minimum and maximum weights of 1 and 5, respectively. Furthermore, according to the magnitude of their impacts on irrigation water quality, various weights between 1 and 5 were taken into consideration for additional dangers that have a variety of effects on sensitive crops. Additionally, the rating scale was changed for every parameter [15,20] from 1 indicating a low appropriateness for irrigation to 3 indicating a good suitability for irrigation. Equations (2) and (3) were used to produce the proposed IWQ index, which evaluates the combined influence of quality characteristics.

$$W_i = \frac{w}{N} \sum_{i=1}^N R_i \quad (2)$$

$$IWQIndex = \sum W_i \quad (3)$$

where W is the contribution of each of the five hazards—salinity, infiltration, particular ion toxicity, trace element toxicity, and other effects—mentioned above. N is the total number of parameters, w is the weight of each hazard, and R is the rating value.

In order to assess the quality of the aquifer utilised for agricultural water supplies in the research zone, four risk groups centred on salinity, infiltration, and permeability, specifically ion toxicity and other consequences to sensitive plants, were implemented.

Following the determination of the index value, the three distinct classes listed in Table 1 were appropriately examined. Table 1 shows that the IWQ was classified as low if it was lower than 19, medium if it was between 19 and 32, and high if it was more than 32. Each parameter's measurement coefficients were left unchanged while several rating factors (i.e., 1, 2, and 3) were used to get the attributes, resulting in three distinct index values (i.e., 39, 26 and 13). The upper and lower limits for each given categorization were determined by taking the average of these values [15].

Table 1. The evaluation limits of the IWQ index.

IWQ Index	Suitability of Water for Irrigation
<19	Low
19–32	Medium
>32	High

2.3. Water Quality Index (WQI Index)

Horton was the first to use indices to indicate groundwater quality. The Water Quality Index (WQI) is one of the many instruments available for displaying data on the nature of water [34]. A grading system known as WQI is used to show how different parameters affect the general quality of water [35]. It serves as a crucial marker for the assessment and management of groundwater in that capacity. WQI is evaluated in light of how suitable the groundwater is for human use.

For the purposes of determining WQI, three steps are taken. Due to its importance for drinking water, the weight (W_i) of each water quality parameter is assessed in the first phase. Equation (4) uses the following equation to get the relative weight (W_i): w_i

$$W_i = \frac{w}{\sum_{i=1}^n w} \quad (4)$$

In the formula above, n is the number of parameters. In the second step, a rating of quality (q_i) is ascertained for every parameter, and the ratio of its individual standard value is measured based on the rules from the WHO:

$$q_i = \frac{C_i \times 100}{S_i} \quad (5)$$

In the formula above, C_i is the concentration of chemical parameters for water samples which is expressed in mg/L, and S_i is the WHO's standard of drinking water for every substance parameter in mg/L. In the third step, the WQI is measured as:

$$WQI = \sum_{i=1}^n W_i q_i \quad (6)$$

As shown in Table 2, WQI results are typically analysed and then categorised into five categories of drinking water: excellent, good, bad, extremely poor, and improper. The weighted arithmetic method of determining WQI included twelve parameters. Each characteristic is given a weight according on how important it is for drinking, with 5 representing total dissolved solids (TDS) and EC, 4 representing SO_4 and TH, 3 representing pH, Cl, and Na, and 2 representing K, Mg, Ca, CO_3 , and HCO_3 .

Table 2. Water quality classification based on WQI value.

Classification of Drinking Water Quality		
WQI Range	Class	Type of Water
below 50	I	Excellent water
50–100	II	Good water
100–200	III	Poor water

200–300	IV	Very poor water
above 300	V	Water unsuitable for drinking

2.4. Study Area

The research region is the 791 km² Tabriz plain aquifer in Iran's East Azerbaijan province (Figure 1). Apples, pears, apricots, peaches, cherries, green beans, leeks, spinach, and squash are all grown on the majority of the land in the region. The same aquifer also supplies around 40% (50 million cubic metres) of Tabriz city's (population: 1.7 million) potable water. The average annual precipitation of Tabriz is close to 290 mm, which is extremely less when compared to the 800 mm global average. The research area may be classified as a semiarid region because of the average temperature of 12.5 C and the De Martonne aridity index. The aquifers' water resources come from rainfall and flow through streams, while the nearby mountains' groundwater seeps out. The water system also recycles industrial and municipal waste waters. In the research region, there are typically three different types of harvesting: harvests for supplying urban water, rural water, and agricultural water. In the research region, there are 81, 50, and 3884 water harvesting wells for agricultural, rural, and urban purposes, respectively. The drinking water wells in Tabriz are buried at the point where the aquifer's groundwater enters to provide the highest possible quality of drinking water. The average water depth in the region is 21 metres, however it may range from 1.5 to 186 metres.

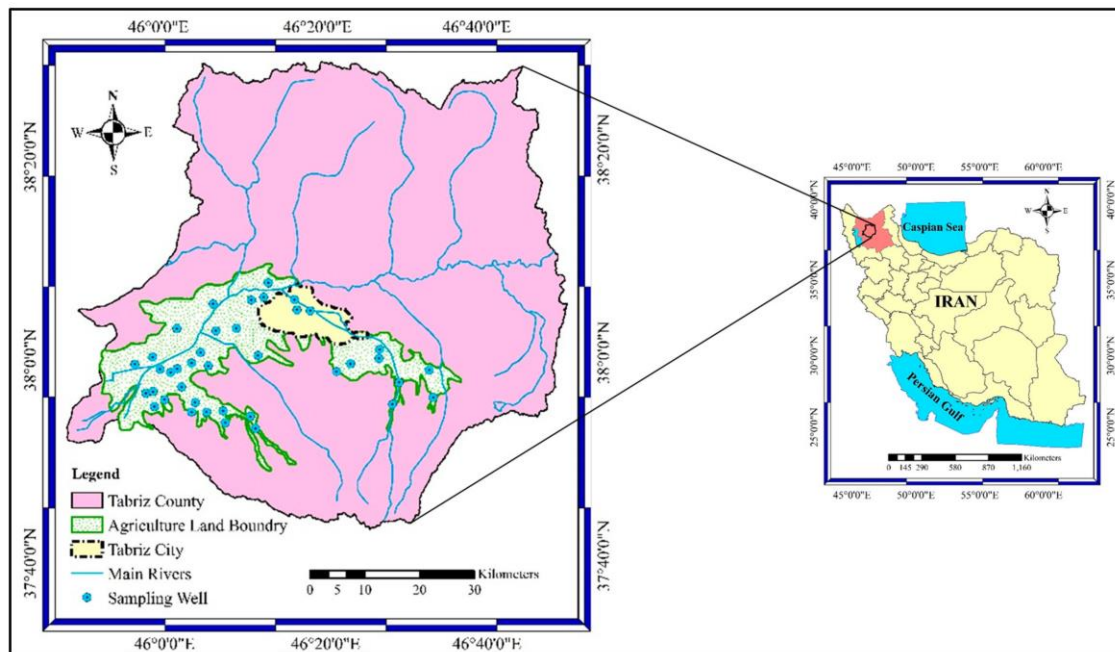


Figure 1. The geographical position of the study area with sites of sampled wells.

2.5. Data Collection

39 wells from the years 2003 to 2014 were sampled twice, in May and September, for electrical conductivity (EC), total dissolved solids (TDS), chloride (Cl), calcium (Ca), magnesium (Mg), sodium (Na), potassium (K), sulphate (SO₄), total hardness (TH), bicarbonate (HCO₃), pH, carbonate (CO₃), and sodium adsorption ratio (SAR) data (Figure 1). Only two measurements of the water quality in the study region were made, one in May when the groundwater level was at its peak and the other in September when it was at its lowest. Additionally, the usefulness of the aforementioned criteria for irrigation and drinking purposes was taken into consideration. 936 samples in total were used for the analysis. Table 3 shows brief statistical characteristics of each well throughout the time period under consideration.

Table 3. The statistical properties of the qualitative parameters in Tabriz plain aquifer during the period between 2003 to 2014.

Parameters	Unit	Min	Max	Average	Standard Deviation
------------	------	-----	-----	---------	--------------------

SO ₄	(mg/L)	0.08	22.13	4.76	4.52
Cl	(mg/L)	0.20	102.50	15.05	20.47
HCO ₃	(mg/L)	0.58	10.97	4.05	2.07
Co ₃	(mg/L)	0.00	1.03	0.12	0.19
pH	-	6.35	9.45	7.91	0.58
EC	(μ mho/cm)	186.55	11,560.00	2393.27	2406.94
K	(mg/L)	0.00	0.78	0.23	0.16
Na	(mg/L)	0.44	48.25	10.85	12.58
Mg	(mg/L)	0.25	22.60	4.97	4.76
Ca	(mg/L)	0.80	50.00	7.93	9.34
TH	(mg/L)	31.35	3625.00	620.24	682.19
TDS	(mg/L)	111.93	7514.00	1550.23	1563.50
SAR	-	0.40	24.83	3.91	3.89

3. Results and Discussion

Between 2003 and 2014, the WQI index was calculated 24 times, twice in May and once in September. The WQI index ranged from 12.14 as the least value to 300.53 as the greatest value. To evaluate the general WQI index processes in each of the investigated wells, the regression equation between the WQI index and time (t) was obtained (Table 4).

Table 4. The linear regression equation between the WQI index and time from 2003 to 2014.

Well Number	Regression Equation	Correlation Coefficient	Well Number	Regression Equation	Correlation Coefficient
1	$WQI = 1.6939t + 15.355$	0.55	21	$WQI = -0.2128t + 28.505$	0.40
2	$WQI = 0.2421t + 18.094$	0.94	22	$WQI = -0.3667t + 24.643$	0.55
3	$WQI = -0.2941t + 49.447$	0.63	23	$WQI = 1.0321t + 44.451$	0.84
4	$WQI = -0.0729t + 19.488$	0.61	24	$WQI = 0.1134t + 17.292$	0.36
5	$WQI = 0.3631t + 15.272$	0.71	25	$WQI = -0.9066t + 171.89$	0.49
6	$WQI = 3.0499t + 7.8392$	0.82	26	$WQI = -1.3891t + 149.53$	0.63
7	$WQI = 3.288t + 171.85$	0.83	27	$WQI = -1.5646t + 97.094$	0.71
8	$WQI = 3.1769t + 21.563$	0.69	28	$WQI = -5.2218t + 210.01$	0.73
9	$WQI = -0.7188t + 77.803$	0.57	29	$WQI = 0.0781t + 45.126$	0.08
10	$WQI = 3.4849t + 109.04$	0.98	30	$WQI = -0.3709t + 64.842$	0.50
11	$WQI = -0.0508t + 19.439$	0.26	31	$WQI = 1.149t + 19.474$	0.93
12	$WQI = -0.038t + 22.085$	0.52	32	$WQI = -0.3804t + 53.272$	0.44
13	$WQI = 1.9223t + 131$	0.74	33	$WQI = -0.1622t + 17.845$	0.71
14	$WQI = -1.3849t + 63.949$	0.83	34	$WQI = 0.0509t + 16.505$	0.18
15	$WQI = 1.2416t + 118.07$	0.62	35	$WQI = -0.9229t + 79.56$	0.66
16	$WQI = 0.1337t + 23.677$	0.47	36	$WQI = -3.5949t + 128.41$	0.90

17	$WQI = 7.9565t + 208.11$	0.78	37	$WQI = -0.1744t + 17.907$	0.37
18	$WQI = 1.1912t + 51.941$	0.89	38	$WQI = -0.0247t + 13.77$	0.10
19	$WQI = 1.7036t + 66.614$	0.88	39	$WQI = 2.015t + 98.716$	0.96
20	$WQI = 0.1387t + 28.494$	0.46			

Table 4 shows that the WQI index value has reduced in 19 wells while showing a rising tendency in the remaining wells. Drinking groundwater quality has increased as shown by the WQI index procedure, but has worsened as shown by an increasing trend. Out of the 936 samples collected from 39 wells between 2003 and 2014, 497 samples were labelled as having "excellent water," 217 samples as having "good water," 188 samples as having "poor water," 31 samples as having "very poor water," and three samples were labelled as having "unsuitable water for drinking." After calculating the size of Thiessen polygons for each of the 39 analysed wells based on the region impacted by each well, the average value of the WQI index was established. The average WQI index for the study region for the statistical period is shown in Figure 2a. This data shows that the WQI index for the region is trending upward. Drinking-quality groundwater has gotten worse over time. The average WQI index of the aquifer remains in the "good water" class across the research period, despite the deterioration in the quality of drinking groundwater. As a result, the aquifer, which provides water to both urban and rural areas, cannot be proved to pose a major and widespread danger of unsuitable water quality.

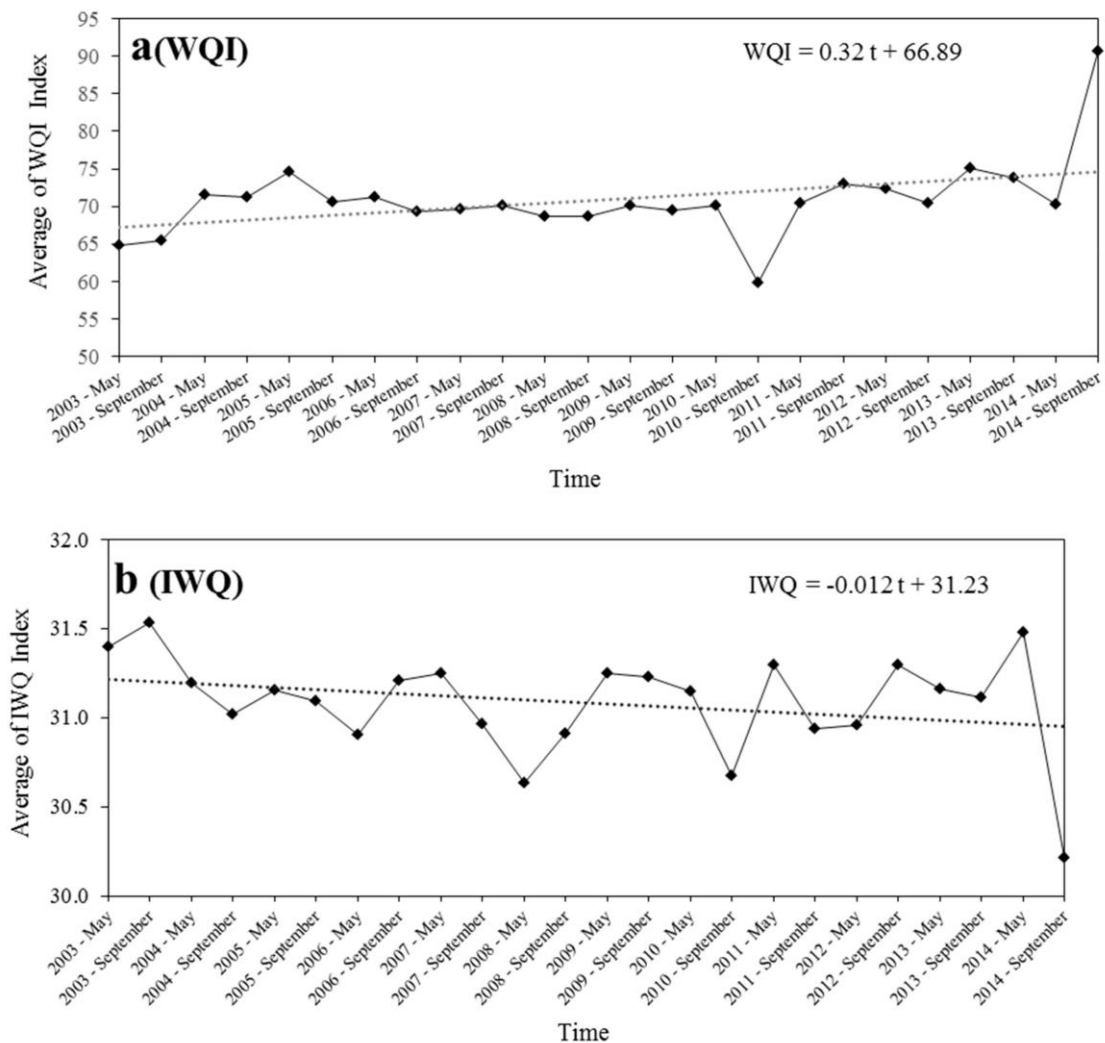


Figure 2. Moderate, and gradual changes in the WQI (a) and IWQ (b) indexes in the entire study area.

Figure 3 shows the geographical distributions of the analysed parameters in the research region based on sample information from 39 wells. It should be noted that the inverse distance weighting (IDW) interpolation technique was used to visualise the distribution numbers. One of the widely used interpolation methods for a variety of engineering issues is the IDW (see, for instance, [44–46]). Based on neighbouring sites, the IDW makes particular parameter predictions. In addition, it was previously noted that there are 81 urban water collecting wells in the research region. Figure 2 shows that the groundwater quality was declining as the WQI grew and the IWQ fell over the period, which is also consistent with Tables 1 and 2's finding that the groundwater quality has a falling tendency. Accordingly, 70 out of 81 wells that feed urban areas with drinking water were classed as having "excellent water," while the other wells were given the "good water" designation (Figure 3a). Out of 50 rural drinking water wells, 27 were rated as having "excellent water," 19 as having "good water," and four as having "poor water." The findings show that urban drinking water wells are generally in extremely good condition. Four rural drinking water wells, however, are in an inappropriate location, therefore either their locations or the water supply for the communities they serve should be altered. In general, it has been discovered that the locations of the urban and rural water wells were deliberately picked. It is advised that drinking water be sourced from the study range's southern and eastern regions, which are the primary aquifer-feeding regions and have extremely good water quality.

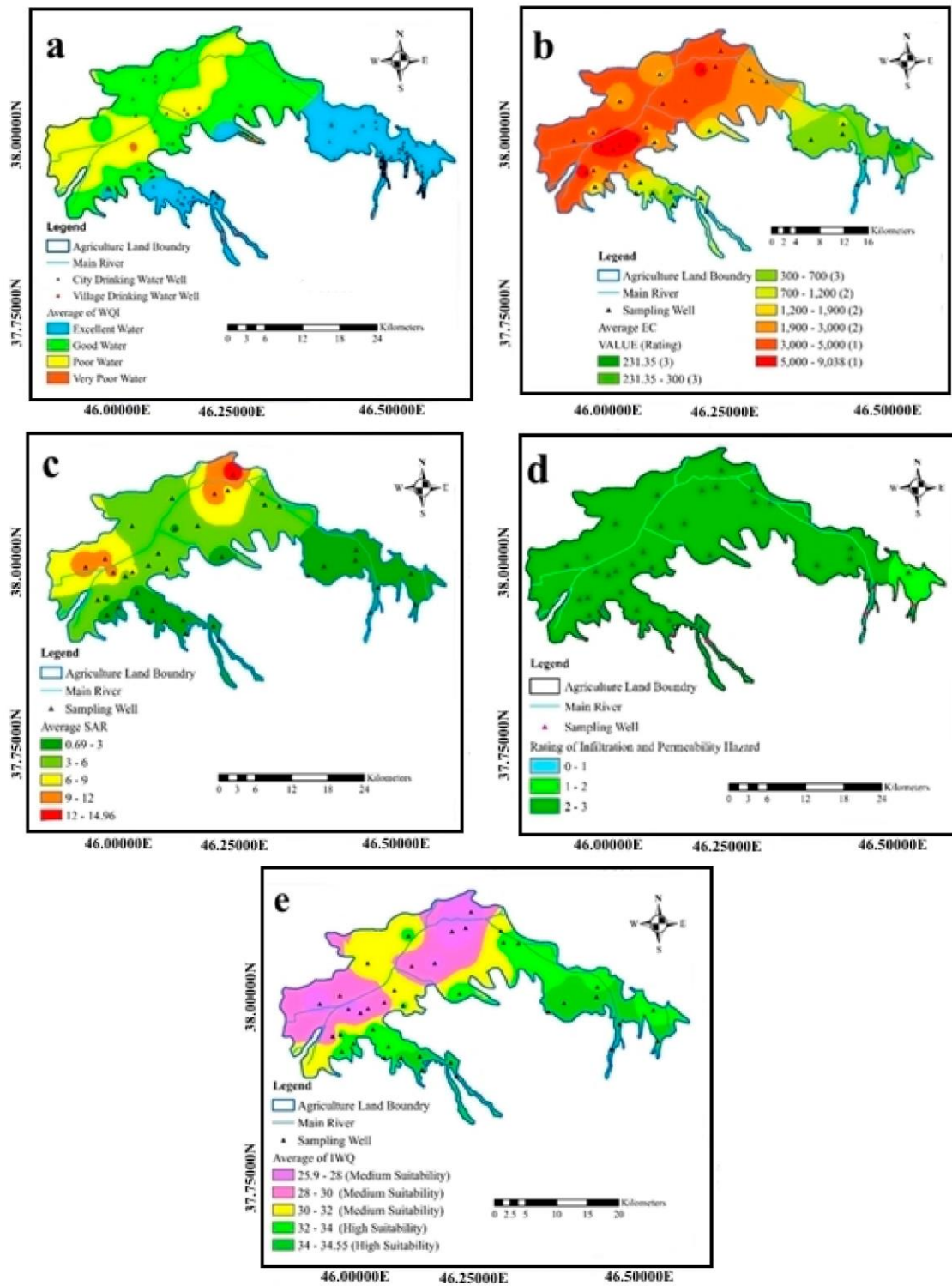


Figure 3. Geographical distribution of studied parameters in the study area ((a): WQI, (b): EC, (c): SAR, (d): infiltration and permeability hazard and (e): IWQ).

Agricultural water quality index is most affected by salinity, permeability, and infiltration hazard weights of 5 and 4, respectively. It should be noted that the weights provided are based on WHO guidelines and norms. Figure 3b depicts the geographical distribution of the average electrical conductivity as determined from 39 wells. The research area's south and east, which are mostly aquifer feeding regions, have the lowest levels of EC, and as one gets closer to the study area's centre, the EC values rise (Figure 3b). According to research by Mosaedi et al., the eastern and central sections of the Tabriz plain are both low in salinity. More so than in the locations where the aquifer is fed, the quality of the subsurface water is less ideal in the centre of the Tabriz plain.

Additionally, 34% (268 km²) of the entire land has an EC between 700 and 3000 (s/cm), 48% of the territory has more EC than 3000 (s/cm), and 18% of the region has an EC amount between 700 and 3000 (s/cm).

The greatest and lowest average SAR values are 0.69 and 14.96, respectively (Figure 3c). The amount of SAR is modest in both the EC and the aquifer feed zone and rises as one gets closer to the north and west of the aquifer.

According to studies, the Tabriz plain's aquifer feeding regions have superior groundwater quality than the rest of this plain.

According to the infiltration and permeability criteria, the research region is deemed hazardous (Figure 3d). The negative impacts of each parameter can be offset by increasing EC and SAR levels in a location. As a result, the infiltration and permeability dangers in the central, northern, and western sections of the research area are minimal due to the high concentrations of EC and SAR in these locations. Figure 3d shows that, on average, 4.21 percent of the area (33 km²) was evaluated as a 1 to 2, while 95.79 percent of the area (758 km²) was ranked as a 2 to 3. In actuality, infiltration and permeability problems in this region are not constrained by agricultural water.

In the study, the IWQ index was derived for the 24 observations between May and September of 2003 and 2014. The minimum and highest IWQ index values were 21 and 35, respectively. Based on the area of Thiessen polygons corresponding to each of the wells, the average area IWQ index was derived. Figure 2b displays the IWQ index change trend over time. The IWQ index is acceptable over time in terms of climate adaptability for farming in the area, according to this figure. A very slight negative IWQ indicator over time demonstrates the viability of the research area's groundwater quality for agricultural use. The required actions must be made to terminate the downward trend in the IWQ index and subsequently advance to a positive trend in order to retain the aquifer's quality. For the whole region, IWQ values range from 25.9 to 34.55 (Figure 3e). The results of IWQ in Figure 3e show that roughly 37 percent (296 km²) of the research area's groundwater has a high compatibility and the remaining 63 percent (495 km²) has a moderate adaptation for agricultural uses based on the aforementioned ranges. The findings also indicate that groundwater in 2227 agricultural wells is somewhat suitable and that groundwater in 1657 agricultural wells is very suitable.

4. Conclusions

In order to preserve the freshwater resources in arid and semi-arid areas, which are crucial for sustainable development, it is critical to identify and manage the groundwater quality. Local legislators and water resource managers can distribute resources for either drinking water or agricultural use depending on the quality of the groundwater in different places. In the Tabriz aquifer, which is situated in the province of East Azerbaijan, northwest Iran, this study intends to pinpoint appropriate sites for water pumping for drinking and agricultural harvest. Indicators were employed in this study to assess the quality of groundwater. The WQI and IWQ indices provide ideal locations for collecting agricultural and drinking water, respectively. These indices are also used to measure the acceptability of water drawn from wells in the research region based on the kind of application. The findings demonstrated that the majority of urban and rural water wells were rated as having "excellent water" and "good water" consistency. There is no low suitability region in the research area's agricultural water compatibility zoning map and the area contains high and medium adaptability groundwater. The study area's WQI and IWQ index variations over time reveal a decline in the quality of the groundwater for drinking and agricultural, respectively. Limiting natural runoff from farms and urban land use can reduce water pollution.

References

1. Hashmi, I.; Farooq, S.; Qaiser, S. Chlorination and water quality monitoring within a public drinking water supply in Rawalpindi Cantt (Westridge and Tench) area, Pakistan. *Environ. Monit. Assess.* **2009**, *158*, 393–403.
2. FAO. *Water Quality for Agriculture*; Food and Agriculture Organization of the United Nations: Rome, Italy, 1994.

3. Tlili-Zrelli, B.; Azaza, F.H.; Gueddari, M.; Bouhlila, R. Geochemistry and quality assessment of groundwater using graphical and multivariate statistical methods. A case study: Grombalia phreatic aquifer (Northeastern Tunisia). *Arab. J. Geosci.* **2013**, *6*, 3545–3561.
4. Venkateswaran, S.; Vijay Prabhu, M.; Mohammed Rafi, M.; Vallel, L.K. Assessment of groundwater quality for irrigational use in Cumbum Valley, Madurai District, Tamil Nadu, India. *Nat. Environ. Pollut. Technol.* **2011**, *10*, 207–212.
5. Jafar Ahamed, A.; Loganathan, K.; Ananthakrishnan, S. A comparative evaluation of groundwater suitability for drinking and irrigation purposes in Pugalur area, Karur district, Tamilnadu, India. *Arch. Appl. Sci. Res.* **2013**, *5*, 213–223.
6. Khan, R.A.; Juahir, H.; Yusoff, M.K.; Zain, S.M.; Hanida, T.I.T. *Using Principal Component Scores and Artificial Neural Networks in Predicting Water Quality Index*; INTECH Open Access Publisher: Rijeka, Croatia, 2012; Volume 271, pp. 283–300.
7. Salahat, M.; Al-Qinna, M.; Mashal, K.; Hammouri, M. Identifying major factors controlling groundwater quality in semiarid area using advanced statistical techniques. *Water Resour. Manag.* **2014**, *28*, 3829–3841.
8. Arumugam, K.; Elangovan, K. Hydrochemical characteristics and groundwater quality assessment in Tirupur region, Coimbatore district, Tamil Nadu, India. *Environ. Geol.* **2009**, *58*, 1509–1520.
9. Amiri, V.; Rezaei, M.; Sohrabi, N. Groundwater quality assessment using entropy weighted Water Quality Index (EWQI) in Lenjanat, Iran. *Environ. Earth Sci.* **2014**, *72*, 3479–3490.
10. Tanji, K.K. *Agricultural Salinity Assessment and Management*, American Society of Civil Engineers; Manuals and Reports on Engineering Practice Number; American Society of Civil Engineers: New York, NY, USA, 1990; Volume 71, 619p.
11. Kwiatkowski, J.; Marciak, L.C.; Wentz, D.; King, C.R. *Salinity Mapping for Resource Management within the County of Wheatland, Alberta, Conservation and Development Branch, Alberta Agriculture*; Food and Rural Development: Edmonton, AB, Canada, 1995; 22p.
12. Mohebbi, M.R.; Saeedi, R.; Montazeri, A.; Azam Vaghefi, K.; Labbafi, S.; Okaie, S.; Abtahi, M.; Mohagheghian, A. Assessment of water quality in groundwater resources of Iran using a modified drinking water quality index (DWQI). *Ecol. Indic.* **2013**, *30*, 28–34
13. Saeedi, M.; Abessi, O.; Sharifi, F.; Meraji, M. Development of groundwater quality index. *Environ. Monit. Assess.* **2010**, *163*, 327–335.
14. Ramakrishnaiah, C.R.; Sadashivaiah, C.; Ranganna, G. Assessment of water quality index for the groundwater in Tumkur Taluk, Karnataka State, India. *J. Chem.* **2009**, *6*, 523–530.
15. Simsek, C.; Gunduz, O. IWQ index: A GIS-integrated technique to assess irrigation water quality. *Environ. Monit. Assess.* **2007**, *128*, 277–300.
16. Adhikari, P.; Shukla, M.K.; Mexal, J.G.; Sharma, P. Assessment of the soil physical and chemical properties of desert soils irrigated with treated wastewater using principal component analysis. *Soil Sci.* **2011**, *176*, 356–366.
17. Debels, P.; Figueroa, R.; Urrutia, R.; Niell, X. Evaluation of water quality in the Chillan River (Central Chile) physicochemical parameters and modified water quality index. *Environ. Monit. Assess.* **2005**, *110*, 301–322.
18. Narany, T.S.; Ramli, M.F.; Aris, A.Z.; Sulaiman, W.N.A.; Fakharian, K. Spatiotemporal variation of groundwater quality using integrated multivariate statistical and geostatistical approaches in Amol–Babol plain, Iran. *Environ. Monit. Assess.* **2014**, *186*, 5797–5815.
19. Negm, A.M.; Armanuos, A.M. GIS-Based Spatial Distribution of Groundwater Quality in the Western Nile Delta, Egypt. In *The Handbook of Environmental Chemistry*; Springer: Cham, Germany, 2016.
20. Narany, T.S.; Ramli, M.F.; Fakharian, K.; Aris, A.Z. A GIS-index integration approach to groundwater suitability zoning for irrigation purposes. *Arab. J. Geosci.* **2016**, *9*, 1–15.
21. Simos, F.S.; Moriera, A.B.; Bisinoti, M.C.; Gimenez, S.M.N.; Yabe, M.J.S. Water Quality Index as a simple indicator of aquaculture effects on aquatic bodies. *Ecol. Ind.* **2008**, *8*, 476–484.
22. Effendi, H.; Wardiatno, Y. Water quality status of Ciambulawung River, Banten Province, based on pollution index and NSF-WQI. *Procedia Environ. Sci.* **2015**, *24*, 228–237.
23. Chen, Z.; Zhu, Z.; Yin, L.; Wei, S.; Deng, L. The changing water quality characteristics from urban drinking water sources in Guangdong, China. *Water Resour. Manag.* **2015**, *29*, 987–1002.
24. Bodrud-Doza, M.; Islam, A.R.M.T.; Ahmed, F.; Samiran, D.; Narottam, S.; Safiur Rahman, M. Characterization of groundwater quality using water evaluation indices, multivariate statistics and geostatistics in central Bangladesh. *Water Sci.* **2016**, *30*, 19–4